K. Hannemann, F. Seiler
(Editors)

Shock Waves

26th International Symposium
on
Shock Waves

Göttingen, Germany
July 15–20th 2007

Proceedings Volume 2

ISSW26

Springer

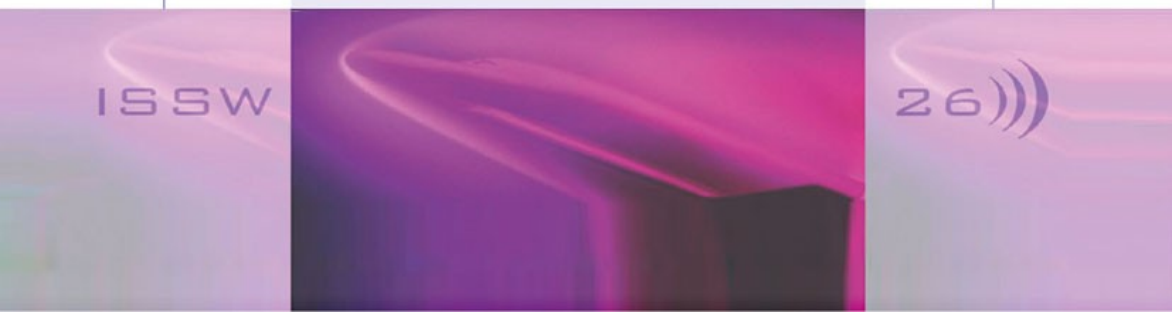

Shock Waves

Klaus Hannemann · Friedrich Seiler (Eds.)

Shock Waves

26th International Symposium on Shock Waves, Volume 2

Springer

Editors

Dr. Klaus Hannemann
German Aerospace Center, DLR
Bunsenstraße 10
37073 Göttingen
Germany
Klaus.Hannemann@dlr.de

Prof. Dr. Friedrich Seiler
French-German Research Institute
of Saint Louis, ISL
5 rue du Général Cassagnou
68301 Saint-Louis
France
Seiler@isl.tm.fr

Co-Editors

Daniel Banuti
Martin Grabe
Volker Hannemann
Sebastian Karl
Jan Martinez Schramm
Julio Srulijes
Jeremy Wolfram

ISBN: 978-3-540-85180-6 e-ISBN: 978-3-540-85181-3

DOI 10.1007/978-3-540-85181-3

Library of Congress Control Number: 2008934453

Cover design: Sumitra Sarma

Printed on acid-free paper

9 8 7 6 5 4 3 2 1

springer.com

Preface

The 26th International Symposium on Shock Waves was held from July 15 to July 20, 2007 in the "Deutsches Theater in Göttingen", Germany. It was jointly organised by the German Aerospace Center DLR and the French-German Research Institute of Saint Louis ISL. The year 2007 marks the 50th anniversary of this symposium which was held for the first time in 1957 in Boston - at that time named "Shock Tube Symposium". After 1967 in Freiburg, being the first symposium which was held outside the United States of America, and 1987 in Aachen, it was an honour for us to host the symposium again in Germany and to celebrate this memorable anniversary. Moreover, we were pleased to organise ISSW26 in the same year in which 100 years of institutionalised German aerospace research is commemorated. This event refers back to the long history of basic and applied contributions to applied mechanics, hydro-, aero-, and gas dynamics which was started in Göttingen by Ludwig Prandtl at the beginning of the last century. In 1907, Ludwig Prandtl founded the "Modellversuchsanstalt für Aerodynamik der Motorluftschiff-Studiengesellschaft" (Institute for Testing of Aerodynamic Models of the Powered Airship Society) in Göttingen and he is therefore considered one of the key founding fathers of institutionalised aerospace research. Later the "Modellversuchsanstalt Göttingen" became the "Aerodynamische Versuchsanstalt AVA" (Institute for Aerodynamic Testing), a precursor of the modern day German Aerospace Center DLR.

After the first and second announcement of the symposium was distributed in summer 2006, 464 expressions of interest from 29 countries were received. The call for abstract submission resulted in a total number of 336 abstracts. Each abstract was reviewed by two members of the ISSW26 Scientific Review Committee which consisted of 49 renowned experts in the field of shock wave research. The final program of the symposium contained nine plenary lectures, 161 oral and 87 poster contributions presented in 47 sessions. The posters were presented in two dedicated sessions without overlapping oral presentations.

Two hundred and eighty two participants, of which 71 were students, from 23 countries registered. The nations from which the participants originated were: Germany (66), Japan (48), Russia (26), USA (25), Australia (16), France (14), Canada (11), India (10), Israel (10), Republic of Corea (10), China (9), United Kingdom (9), Netherlands (5), South Africa (5), Belarus (3), Switzerland (3), Taiwan (3), Brasil (2), Norway (2), Singapore (2), Italy (1), Poland (1) and Ukraine (1). In addition, 50 partners enrolled for the companions program of ISSW26.

Following the opening ceremony, the symposium was started with the Paul Vieille Lecture, given by Prof. Hans Hornung, California Institute of Technology, providing an exciting presentation on: "Relaxation Effects in Hypervelocity Flow: Selected Contributions from the T5 Lab".

A new facet for ISSW was the initiation of the Student Award of the International Shock Wave Institute ISWI. The mission of ISWI, which was founded two years ago, is

to promote international and interdisciplinary collaboration in all areas of shock wave research through the organisation of conferences, awards and honours and to facilitate liaison with other organisations with similar interests and activities. We hope that with the ISWI Student Award we start a tradition for all the following ISSWs which will further strengthen the links between the ISWI and the shock wave symposia. The award was given to the best two student presentations at ISSW26 in Göttingen. Oral- and poster presentations given by the student participants were considered for the prize and the jury consisted of members of the International Advisory Committee and Session Chairpersons of ISSW26. The ISWI Student Award, which was endowed with $1000 US each, was presented during the opening ceremony of the ISSW26 Dinner Banquet by Prof. Kazuyoshi Takayama, President of the International Shock Wave Institute. The winners are:

- Khadijeh Mohri, Imperial College, London, for her presentation on: "Supersonic Flow Over Axisymmetric Cavitites" (together with R. Hillier) and
- Roger Aure, University of Arizona, for his presentation on: "Particle Image Velocimetry Study of Shock induced Single Mode Richtmyer-Meshkov Instability" (together with J.W. Jacobs).

Something unique was the venue of ISSW26. The international shock wave community met in the "Deutsches Theater in Göttingen" (German Theatre) where, during the season, works of classical and modern theatre are performed. Based on the comments we received from many participants we can conclude that our hope that the combination of artistic atmosphere and science will result in an inspiring symposium was fulfilled. The theatre, which was opened in 1890 with the performance of Friedrich Schiller's "Wilhelm Tell", is located right next to the remains of the mediaeval town wall which surrounds the historic city centre of Göttingen. Much of the urban life takes place within the old town walls and all places of interest including hotels and restaurants could be reached by a leisurely ten to fifteen minute walk.

The scientific program was complemented by a number of social events. The lunches were provided in the Old Mensa (refectory) of the University of Göttingen located in the city centre. On Monday evening Göttingen was introduced to the ISSW26 participants during a city tour which finished with a reception of the mayor of Göttingen in the Old Town Hall. The over 1050 years old town of Göttingen is set amid the rolling mountain landscape of southern Lower Saxony in the central part of Germany. The landmark of Göttingen is the Gänseliesel figure on the fountain at the market square in front of the Old Town Hall. This art nouveau statue shows a girl herding geese. It is a tradition that all PhD graduates from the University kiss the statue after passing their examination. This makes her "the most kissed girl in the world". In addition to the charm of the city centre with its evocative relics of past centuries, Göttingen is well known in the scientific community for its large university, numerous research institutes and 44 Nobel Prize winners who lived or worked in Göttingen. On Wednesday, the symposium excursion led the ISSW26 participants to the city of Wernigerode located at the northern border of the Harz mountains. Wernigerode is a town with gorgeous half-timbered houses - the oldest of which can be traced back to the year 1400. The Town Hall is a highlight of medieval architecture and high above the city the Castle of Wernigerode is located, an originally romanesque castle dating from the 12th century which was extensively altered over the centuries. The symposium excursion ended with a barbecue at the Göttingen site of DLR. On Thursday night, the traditional symposium dinner banquet took place in the main foyer, the glass foyer and the "Keller" (cellar) of the Deutsches Theater. The ceremonial

opening of the banquet in the Große Haus of the Deutsches Theater included addresses, the presentation of the ISWI student award, the announcement of the ISSW27 venue and musical entertainment by the "Trio con Brio" of the Göttingen Symphonic Orchestra. On Friday afternoon the ISSW26 was concluded by a facility tour of the Göttingen DLR site.

A companions program was organised during ISSW26, which led the partners and family members of the participants to various locations in the southern Lower Saxony and Göttingen area including the "Sleeping Beauty Castle" Sababurg, the Weser river, Marienburg Castle near Hildesheim, the City of Einbeck, the Plesse Fort, Herzberg Castle, the former German - German border, the Harz mountains and the city of Goslar.

During the meeting of the International Advisory Committee of ISSW26, the venue for ISSW27 which will be held in 2009, was selected. Three excellent proposals were presented to the IAC which shows that there is a continuing interest in ISSW. The 27th International Symposium on Shock Waves will be held in St. Petersburg, Russia and will be chaired by Dr. Irina Krassovskaya of Ioffe Institute, Russian Academy of Sciences. On behalf of the Organising Committee of ISSW26, we congratulate Irina Krassovskaya and wish ISSW27 great success.

ISSW26 could not have been realised without the support of the host institutions, the German Aerospace Center DLR and the French-German Research Institute of Saint Louis ISL, and this is gratefully acknowledged. Further, ISSW26 was generously sponsored by the German Research Foundation DFG and the state of Lower Saxony. The companies LaVision, MF Instruments, Palas, Shimadzu, Springer and VKT could be acquired who supported ISSW26 with a stand at the conference venue.

On behalf of the Organising Committee of ISSW26, we would very much like to thank all participants who came to Göttingen to support the symposium with their attendance and the presentation of a poster or a talk. We would also like to express our gratitude to the members of the International Advisory Committee and the Scientific Review Committee for their continuous support during the preparation and running of the conference. Further, we would like to thank those colleagues who served as session chairperson and who guaranteed an accurate performance of the parallel sessions.

Finally, the support and enthusiasm of all the people who supported the organisation of ISSW26 including the project management of DLR, the logistics section and the secretaries of the DLR Institute of Aerodynamics and Flow Technology, the DLR canteen staff, the ISL team, the students, the team of the Deutsches Theater, the catering team of the Bistro DT Keller and the members of the Spacecraft Section and their families is highly acknowledged. The team spirit of these people was the basis of the realisation of ISSW26 and their friendly appearance was greatly appreciated by the symposium participants.

Göttingen, July 2007

Klaus Hannemann (Chairman)
Friedrich Seiler (Co-Chairman)

The 26th International Symposium on Shock Waves

Hosted by German Aerospace Center, DLR
and French-German Research Institute of Saint-Louis, ISL
Göttingen, Germany
July 15-20, 2007

Chairman

Klaus Hannemann (German Aerospace Center)

Co-Chairman

Friedrich Seiler (French-German Research Institute of Saint-Louis)

Local Organising Committee

Klaus Hannemann
Friedrich Seiler
Sebastian Karl
Jan Martinez Schramm
Sumitra Sarma
Berthold Sauerwein
Julio Srulijes
Susanne Strempel
Alexander Pichler
Jeremy Wolfram

International Advisory Committee

Takashi Abe
Holger Babinsky
Robert Bakos
Gabi Ben-Dor
Salvatore Borrelli
Martin Brouillette
Douglas Fletcher
Nikita Fomin
Sudhir Gai
Boris Gelfand
Victor Golub
Jagadeesh Gopalan
Klaus Hannemann
Ronald Hanson
Richard Hillier
Ozer Igra
Katsuhiro Itoh
In-Seuck Jeung
Zonglin Jiang
Valeriy Kedrinskiy
Shen-Min Liang
Assa Lifshitz
Meng-Sing Liou
Frank Lu
Kazuo Maeno
Richard Morgan
Herbert Olivier
Elaine Oran
Allan Paull
K.P.J. Reddy
Graham Roberts
Akihiro Sasoh
Christof Schulz
Friedrich Seiler
Joseph Shepherd
Beric Skews
Kazuyoshi Takayama
Eleuterio Toro
David Zeitoun
Fan Zhang

Scientific Review Committee

Takashi Abe
Holger Babinsky
Robert Bakos
Gabi Ben-Dor
Martin Brouillette
Douglas Fletcher
Sudhir Gai
Victor Golub
Jean François Haas
Gerald Hagemann
Klaus Hannemann
Marc Havermann
Richard Hillier
Ozer Igra
Katsuhiro Itoh
Mikhail Ivanov
Zonglin Jiang
Mark Kendall
Harald Kleine
Doyle Knight
Wilhelm Kordulla
Assa Lifshitz
Frank Lu
Jan Martinez Schramm
Tim McIntyre
David Mee
Brian Milton
Richard Morgan
Christian Mundt
Herbert Olivier
Allan Paull
Rolf Radespiel
K.P.J. Reddy
Graham Roberts
Akihiro Sasoh
Christof Schulz
Richard Schwane
Friedrich Seiler
Joseph Shepherd
Beric Skews
Julio Srulijes
Johan Steelant
Hideyuki Tanno
Evgeny Timofeev
Euleterio Toro
Zbigniew Walenta
Craig Walton
David Zeitoun
Fan Zhang

Event Coordination and Graphic Design

Sumitra Sarma

Website Programming and Database Support

Jeremy Wolfram

Partners Program

Monika Hannemann

Venue, Deutsches Theater in Göttingen and Deutsches Theater Bistro

Wolfgang Bertram
Carsten Hoffmann
Ulrich Klötzner
Claudia Schmitz

Sponsors

Deutsche Forschungsgemeinschaft
Land Niedersachsen
Deutsches Zentrum für Luft-und Raumfahrt e.V.
Deutsch-Französisches Forschungsinstitut Saint-Louis

Exhibitors

LaVision GmbH
MF Instruments GmbH
Palas GmbH
SHIMADZU
Springer
VKT

Contents

Volume 2

Part XIII Nozzle Flow

Part XIV Numerical Methods

Contents

Volume 1

Part VII Flow Visualisation

Part VIII Hypersonic Flow

Part IX Ignition

Part X

Impact and Compaction

A study of particle ejection by high-speed impacts

M. Anyoji[1], D. Numata[1], M. Sun[1], and K. Takayama[2]

[1] *Center for Interdisciplinary Research, Tohoku University, Aramakiaza 6-3, Aoba, Sendai, 980-8578 (Japan)*
[2] *Biomedical Engineering Research, Tohoku University,Aramakiaza 6-3, Aoba, Sendai, 980-8578 (Japan)*

Summary. The fragmentation of solid plates impacted by a high-speed projectile has been studied intensively in the past. However, the ejection and shattering process of fragmented particles have not been well resolved yet. To simulate the earlier stage of particle ejection, we performed an analogue experiment of the ejection of aluminum spheres attached on a thin aluminum plate in a row and impinged at tis reverse side by a high-spee plastic cylinder of 51 mm in diameter. The ejection of spheres was observed by using a high-speed digital camera and also holographic interefrometry. These image analysis revealed the motion of ejected spheres. .

1 Introduction

Projectile impingements at high speed on a metal plate creates a shock wave propagating in it, which is then reflected from its reverse surface and instantaneously bulges it. Pressures generated behind the shock wave exceed well over the value of yielding stress and then crack propagation behind the shock wave takes place, which results in the fragmentation of the reverse surface of the target plate. This is a brief explanation of debris cloud formation during hypervelocity impacts. In order to collect design data of space debris bumper shields, they performed an analogue experiment [1, 2]. The free flight of micro-particles occurs even in laser ablation assisted drug delivery systems [3]. To instantaneously eject small spherical particles from the plate surface, we impacted with a plastic cylinder, an aluminum plate on the reverse side of which the spheres were attached in a row. The ejection particle was visualized by shadowgraph and the images were recorded sequentially by a high-speed digital video camera and quantitatively by double exposure holographic interferometry. Then we clarified experimentally the process of shattering of aluminum spheres.

2 Experiment

2.1 Facility

We used a gas gun in the Interdisciplinary Shock Wave Laboratory of the Institute of Fluid Science, Tohoku University. Ultra high-density polyethylene cylinders of 51 mm diameter and 55 mm long were projected at a transonic flow range. Figure 1 shows a 5 mm thick aluminum target plate AL5052 of 200 mm by 200 mm and aluminum spheres of 3.2 mm, 4.0 mm, and 4.8 mm, respectively. The spheres were weakly attached in 48 mm length in a row, where the x-axis is defined as the axial direction and y-axis as the vertical direction along the arrayed aluminum spheres. Sphere diameters, numbers, materials, and their weights are tabulated in Table.1. The target plate was cramped at its four corners as shown in Fig. 1(a).

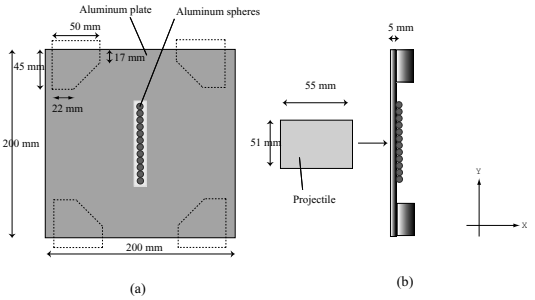

Fig. 1. The target plate and installation of aluminum spheres: (a) frontal view of target plate; (b) side view and impact of the plastic cylinder

Table 1. material information of spheres

Diameter	Number of spheres	Material	Weight per one sphere [g]
3.2 mm	15	Al5052	4.53×10^{-2}
4.0 mm	12	Al2017	9.17×10^{-2}
4.8 mm	10	Al1050	1.58×10^{-1}

2.2 Experimental condition

The gas gun was operated with a diaphragm-less operation system, in which a 51 mm diameter cylinder inserted at the entrance of an acceleration tube, separating test air at 0.1 MPa and room temperature from 1.55MPa helium was held in its initial position with a piston backed up with 1.4MPa helium from behind and then a sudden decrease in the back-up pressure instantaneously released the piston to move backward. Hence the high pressure helium gradually accelerated the cylinder motion. The piston motion was mechanical controlled so that this system warranted a higher degree of reproducibility than conventional diaphragm rupture systems. We achieved a repeatable cylinder impingement onto the target plate. Three experiments were repeated for each sphere size. The optical flow visualization was performed with a commercial flash lump as light source by using shadowgraph and its sequential images were recorded by a high-speed digital video camera of inter-frame time of 16 μs and exposure time of 8 μs. (Hyper Vision HPV-1, Shimadzu Co. Ltd.) Flow fields were quantitatively visualized by using a double exposure holographic interfrometry.

3 Results and Discussion

3.1 High-speed video images

Shadowgraph images are sequentially displayed at time interval of 80 μs. The plastic cylinder impacted on the target plate: at 345 μs in Fig.2; at 342 μs in Fig.3; and at 340 μs in Fig.4. As seen on the second frames in Figs.2-4, the impact flash was observed and the target plate started to deform. The arrayed spheres started to be ejected to move. The plate deformation drove a spherical shock wave, which was precursory to the sphere shattering motion. The shock wave, as later confirmed on the interferograms, was initially

strong enough to accompany its particle velocity, which would accelerate spheres. This is a general trend observed in dusty gas shock tube flows, in which individual dust particles are accelerated behind the incident shock waves, resulting in the non-equilibrium region behind the incident shock.

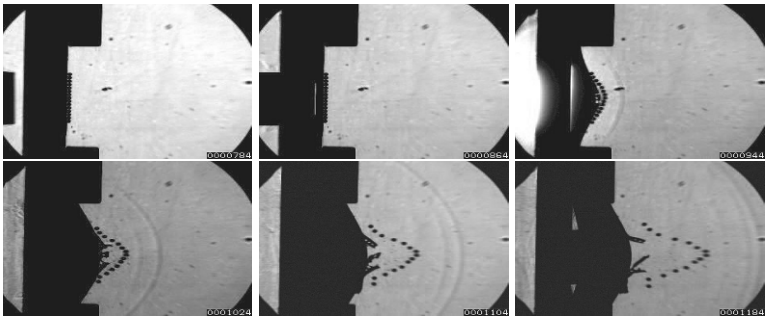

Fig. 2. Spherical diameter of 3.2 mm.

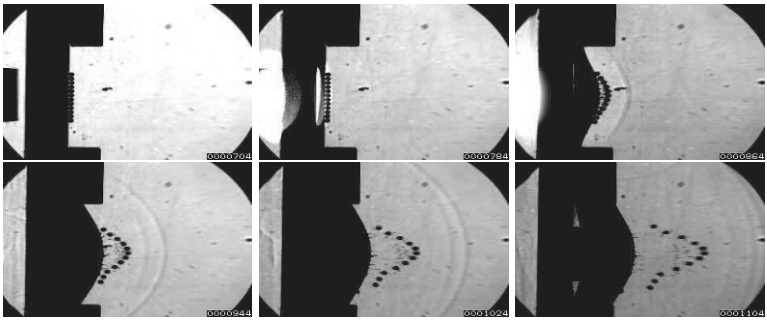

Fig. 3. Spherical diameter of 4.0 mm.

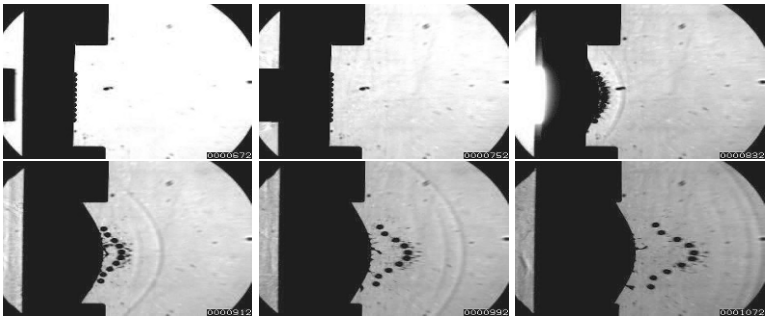

Fig. 4. Spherical diameter of 4.8 mm.

The spheres are departed from the target plates on the fourth frame of Figs. 2-4. The target plate was not ruptured, but the tape attaching to the plate was removed from the plate surface in Fig.2.

3.2 Distribution of spheres

Although the sphere distribution looks initially spherical on the third frame of Figs. 2-4 but transits with the elapsed of time to more or less the Gaussian distribution on the fourth to sixth frames of Figs.2-4. This trend is presumably attributable to the process of target plate deformations. The deformation of target plates is governed by its supporting conditions at its edge. As explained in Fig.1, in this experiment the target plates were cramped at its four corner. Then the process of its deformation can not be axially symmetry. It is also confirmed in this series of experiments, the spheres are moving at constant speed. We recorded images at every 64 μs from the moment of the impact and calculated the center of each sphere from each pixel constituting one sphere. Then sequential distributions of each sphere at given time instance are drawn for individual sphere sizes in Figs.5(a)-(c). We compared the measured spatial distribution of the spheres to the Gaussian distribution and found a good agreement. However, the difference between experiment and the Gaussian one departs with the elapse of time. It is concluded that the Gaussian distribution is a good approximate to describe the sphere distribution.

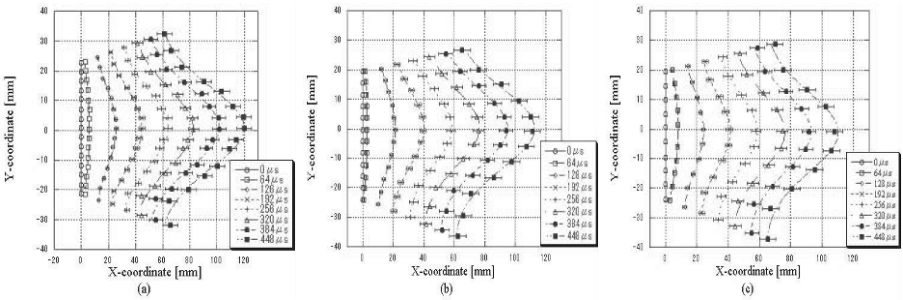

Fig. 5. Sequential distribution of spheres and comparison with Gaussian distribution: (a) 3.2 mm; (b) 4.0 mm; and (c) 4.8 mm

3.3 Velocity and acceleration

We estimated the sphere velocity and the acceleration out of Figs.5(a)-(c) and the results are shown in Figs.6-8 for individual sphere diameters. The x-t diagram and y-t diagram are shown in Figs.6-8(a) and Figs.6-8(b), respectvely. The individual time instants correspond to those in Figs.5(a)-(c). Assuming complete symmetry, we measured only the spheres upper part of the axis.

V_x becomes larger closer to as the central axis. By contraries, V_y becomes smaller closer to the central axis. We confirmed the spheres maintain a constant speed within the frame of the present observation. It may be oversimplification to say that the sphere shattering is analogous to dusty gas flows behind the spherical shock waves. However,

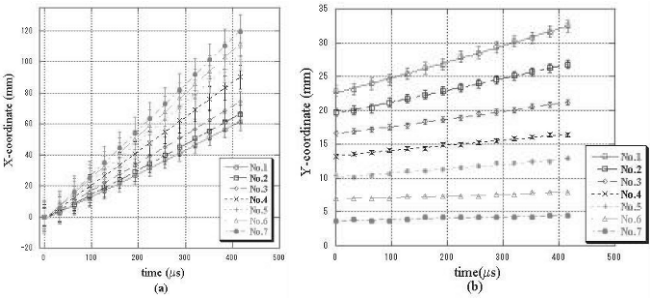

Fig. 6. 3.2 mm: (a)x-t plane; (b)y-t plane

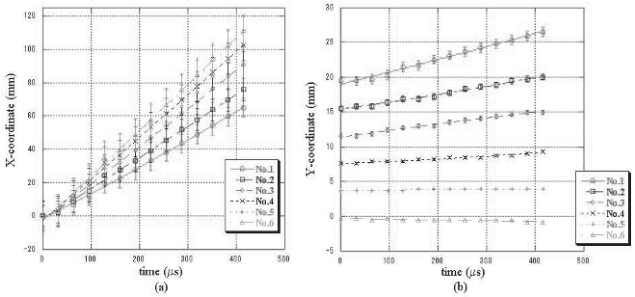

Fig. 7. 4.0 mm: (a)x-t plane; (b)y-t plane

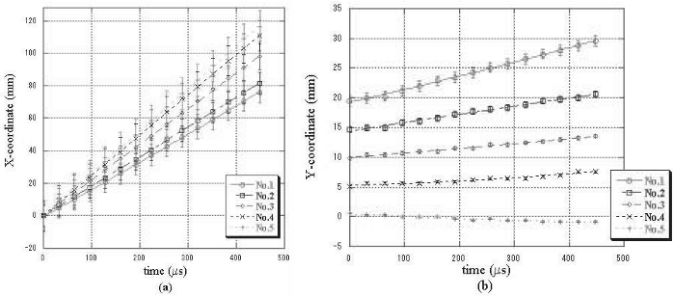

Fig. 8. 4.8 mm: (a)x-t plane; (b)y-t plane

the general trend agrees with such an analogy until we will numerically simulate sphere motion ejected from a high speed impact plate.

3.4 Holographic interferometry

To confirm the presence of the shock wave we performed double exposure holographic interferometric observation. Dark dots show spheres. Fringe distributions are slightly distorted from the axial symmetry but not very significant. Although a preliminary result, a result is shown in Fig.9 for 4.8 mm spheres. Although unobservable on shadow images, the flow field behind the diverging shock wave never be uniform but waves propagating

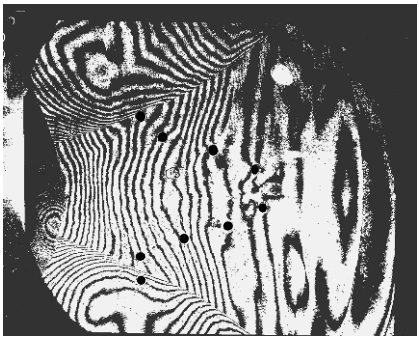

Fig. 9. Holographic interfermetry of shattering 4.8 mm spheres.

vertical direction exist, which may contributed to depart the particle motion from the Gaussian distribution. In the near future these holographic observation systems together with a digital streak recording would conclude flow information and to validate numerical results.

4 Conclusion

The impact generated sphere motion are observed sequentially by shadowgraph, recorded by high-speed digital video camara, and quantitatively by double exposure holographic interferometry. These spheres were ejected by the deformation of target plates and accelerated by the flows behind the impact generated incident shock waves. The region of the constant velocity was so extended, however, we failed to confirm the onset of deceleration. Holographic interferometric observation revealed that the present target plates were supported at their corner, which disturbed the axial symmetry of the flow field from complete symmetry. At the early stage the sphere distribution can be approximated by the Gaussian one. The departure from Gaussian one was attributable to the supporting condition. In the future work, we are planning, to rigorously simulate debris cloud formation, to impact packed spheres. Presumably an approach from a granular flow analyses would provide a good way.

References

1. Piekutowski AJ: *Debris clouds generated by hypervelocity impact of cylindrical projectiles with thin aluminum plates*, Int.J.Impact Engng, vol.5, 1987,pp.509-518.
2. Piekutowski AJ:*Characteristics of debris clouds produced by hypervelocity impact of aluminum spheres with thin aluminum plates*, Int.J.Impact Engng, vol.14, 1993, pp.573-586.
3. Menezes V, Takayama K and S.H.R Hosseini:*Development of a biolistic apparatus for medical applications*, Symposium on shock waves, YOkohama, Japan,2006, 18-B-1-5.

An experimental and numerical study of steel tower response to blast loading

J.D. Baum, O.A. Soto, and C. Charman

Center for Applied Computational Sciences, Special Projects Division SAIC, 1710 SAIC Drive, MS 2-6-9, McLean, VA 22102 (USA)

1 Introduction

Over the last several years we have developed and applied a coupled CFD and CSD methodology for modeling blast wave interaction with structures and the structural response to the blast loading. One of the more interesting and more complex simulations conducted was a simulation of a terrorist attack on a generic steel tower that supports a suspension bridge, modeled as a multi-chamber, multi-floor bridge-support steel tower. The numerical methodology models the HE detonation initiation, the detonation wave propagation within the explosive, detonation products diffraction after detonation completion, blast load interaction with the structure, structural deformation, steel panel fragmentation and blast load diffraction between the accelerating fragments to load the next layer of steel panels (cells). The results demonstrated that structural failure could result from either large pressure loading or high-velocity fragment impact. To validate the results, the University of California, San Diego (UCSD) and Energetic Material Research and Testing Center (EMRTC) of New Mexico Tech (NUMTECH) initiated a test program, under TSWG sponsorship, that tested scaled sections of a steel-tower to blast loading. Simultaneously, SAIC conducted a sequence of numerical simulations of this event. The paper presents the experimental results and the numerical predictions, while concentrating on the analysis of the predictions. It is concluded that the simulations raised some serious issues, which require further precision testing.

2 The Numerical Methodology

Mesh generation for both CSD and CFD models is performed using FRGEN3D [3], which is based on the advancing front method. The CFD mesh is composed of triangular (surface) and tetrahedral (volume) elements. The CSD mesh includes beams, triangular or quad shells and bricks for the solids. The flow solver employed is FEFLO98, a 3-D adaptive, unstructured, edge-based hydro-solver based on the Finite-Element Method Flux-Corrected Transport (FEM-FCT) concept [4]. It solves the Arbitrary Lagrangean-Eulerian (ALE) formulation of the Euler and Reynolds-averaged turbulent, Navier-Stokes equations. The high order scheme used is the consistent-mass Taylor-Galerkin algorithm. Combined with a modified second-order Lapidus artificial viscosity scheme, the resulting scheme is second-order accurate in space, and fourth-order accurate in phase. Other high-order accuracy shock capturing schemes, such as HLLC, WENO, HWENO, etc, are available, and can be used for specific applications. The spatial mesh adaptation is based on local H-refinement, where the refinement/deletion criterion is a modified H2-seminorm [4] based on a user-specified unknown. Most of the shock wave propagation cases require

the use of a blend of density and energy. FEFLO98 supports various equations of states including real air, water, SESAME and JWL with afterburning. The structural dynamics solver are either GA-DYNA3D [5] or SAICSD [8], both are unstructured, explicit finite element codes, well suited for modeling large deformations and provide good base for non-linear materials with elasto-plastic compartmental laws with rupture. Both codes incorporate a large library of materials and various equations-of-state, as well as many kinematic options, such as slidelines and contacts. The structural failure is described using the Johnson and Cook nonlinear plastic hardening function [1] that contains strain rate effects in both the yield and damage functions. The yield stress is a nonlinear function of the effective plastic strain, augmented by a strain rate term which increases the yield strength with increasing strain rate, and a thermal softening term which lowers the yield strength with increasing temperature. Heat is generated in the model by plastic work, and the resulting temperature rise is computed using the specific heat for the material assuming adiabatic conditions. The Johnson and Cook (J&C) model defines the failure strain as a function of the ratio of the pressure stress to the effective stress, strain rate, and temperature [Eq. 81 of the Dyna3D Manual [2]]. The material damage is computed by summation of the plastic strain increments divided by the strain to failure over each time step. Because of the term involving the ratio of pressure stress to the effective stress, the failure strain is large in compressed regions of the model, though little damage will occur in theses compressed regions. When this damage is greater than 1.0, the element is assumed to have failed and is eliminated from the calculation by an erosion algorithm. If the eroded element has any face exposed to the blast pressure, new pressure surfaces are determined and given back to the flow code to evaluate the new external surface of the model and to determine the pressures for the next structural step for the coupled CSD/CFD simulation. In these simulations we are using 60% of the true strain to failure when we evaluate the damage in an element. This is based on engineering judgment and correlation with earlier experiments, adjusted up to account for finer mesh resolution at the failure areas.

Fig. 1. Test especiment before and after the test

3 The Experimental Facility and Results

A field test was conducted at EMRTC to investigate the response of a single row of cells to an explosive load, simulating the response of a full scale section of a typical steel cellular bridge tower to blast loading. The specimen consisted of three cells each 3-6 tall by 3-6 wide and 8-0 in length, constructed of 7/8 A36 steel plates and connected at the

intersections via 8 x 8 x angles and 1 diameter A307 bolts at 4 on center. The specimen was loaded with 220 lbs of flake TNT with a C4 detonator with approximately 6 of stand-off at the midspan of the center cell. The results show a flyer plate of approximately the same dimensions as the charge was created in the top plate of the center cell directly below the applied load. The 2 square impacted the bottom steel plate of the test specimen, creating a second flyer plate. The speed of the first flyer plate before impact with the bottom plate was approximately 3,400 feet per second. In addition to the holes left by the separation of the flyer plates, the test specimens showed significant deformation: the edges of the hole in the top plate showed substantial petalling and tearing of the steel plate. The rupture of the top plate occurred in the center cell where the explosive load was placed. In addition, the bolts and the angle that supported the plates also deformed. The angle pieces stayed connected to the sidewalls of the center cell but the supporting leg was bent. The steel section seen in front of the specimen is what remains of the top plate where it came to rest after the second test. Figure 1 shows the test specimen before (Fig. 1a) and after (Fig. 1b) the test. Figure 1c shows an expanded view of the bottom plate, while Fig 1d shows the two flyer plates. The indentation in the flyer plates was caused by the impact of the charge downwards. The destruction caused by the flyer plates and the plate in the foundation can be seen in Fig 1b. A variety of failure modes were seen in the bottom plate. The bottom plate also deformed before shearing. In addition to the deformation of the plate due to the projectile, one can also see the tearing of the angles and the loss of the connections to the bottom plate. The plate is actually resting on the foundation and is no longer connected to the support angles by bolts.

4 Numerical Results

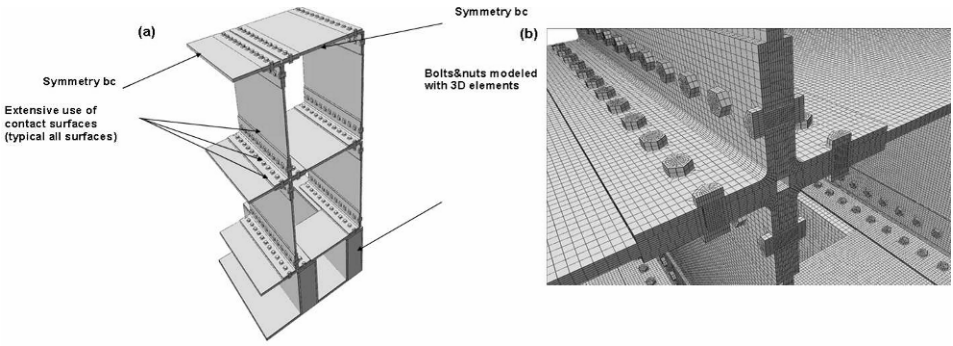

Fig. 2. Numerical model and details of a typical bolted joint

The CSD Model: The model includes only a quarter of the test facility, taking advantage of the double symmetry. The material model used employed the Johnsons and Cook plasticity model, where the A-36 steel parameters where taken of [6]. The A307 bolts were modeled with the same hardening parameters, but with a fracture strain of 18%. The concrete was modeled as rigid. Fracture represented by erosion of elements with damage parameter >1. Contact conditions were used between all parts. The quarter-symmetry CSD model used in the simulations is shown in Figs 2. Figure 2a shows the set-up. The

explosive is set on top, with a standoff distance of six inches. The solid elements were sized 0.4X0.5X0.125 inches for the angles and plates, and 0.125X0.125X0.125 inches for the bolts. The resulting CSD mesh included 868,724 hex elements, 1,094,683 nodal points, 58 contact conditions and 431,482 wet faces the obtain pressure data from the flow solver. Results: The first simulation modeled the structure as plates (shells). As the plate model did not adequately capture the interaction between the bolts, nuts, angles and plates at the connections, it was felt that a 3-D model (solids) would better represent the physics. This model can better represent the complex stress states and produce necking as well as model all six components of the stress. The next issue arose with the failure algorithm. The J&C material model uses true stress true strain (Cauchy stress logarithmic strain). However, deformation can localize in material forming necking at the fracture location. This produced significant mesh sensitivity. The material failure model (ultimate strain value) was adjusted to account for the size of the element relative to gage length and wide variation in response was noted using above approach. To further investigate mesh effect we conducted a sensitivity study that included three plates 6 inch apart. Mesh sizes tested were 1/16, 1/8 and 1/4 inch. The solutions from 1/8 and 1/16 are almost identical, hence the multi-cell models were reworked to include 1/8 inch zone in area where tearing was observed in experiment. The simulation modeled 220 lbs of flake TNT, with a C4 detonator. The charge was placed six inches of standoff at the midspan of the center cell. As no EOS exists (to our knowledge) for flake TNT (flake TNT is usually melted and cast), we conducted several simulations varying the TNT equivalence of the flake TNT. Rough estimate shows that it's TNT equivalence is about 0.25 to 0.3. Naturally, for precision testing and code validation, we require a more precise source definition. The time evolution of the detonation wave propagation in the explosive, and the resulting blast wave evolution are fairly straight forward: charge detonation followed by detonation product diffraction and load on the top surface, followed by top surface failure and blast wave propagation through the cracking steel surface. These are depicted in Figures 3a through 3h. The choice of ultimate strain of 0.6 allows large deformation before plate cracking (Fig 3b) and break-up (Figs 3c and 3d). The resulting flyer plate is strongly deformed (Fig 3e). Similar processes are observed as the flyer plate impacts the second plate, to form a second flyer plate, i.e., significant deformation before plate cracking and formation of a second flyer plate (Figs 3f and 3g). To further investigate the role of the critical effective plastic strain (the ultimate strain value) on energy absorption, flyer plate shape and speed, we varied the ultimate strain value from 0.2 to 0.6. The more brittle material formed a flyer plate with very little deformation. As significantly less energy was spent on plastic work, the flyer plate has a higher velocity and higher kinetic energy, and is capable of penetrating more layers in the adjacent cells than the slower deformed flyer plate (for ultimate strain of 0.6). Another difference between the brittle and ductile materials: for the higher ultimate strain values, the two (or three) flyer plates fly together, while for the brittle materials, the transfer of kinetic energy is almost perfectly, and the impacting plate transferred all of it's kinetic energy to the newly formed flyer plate (Fig 4a). In yet another study we defined the ultimate strain for the top plate as 0.2, and for the second plate as 0.4. Figure 4b shows the top flyer plate to be fairly flat (typical of a brittle material), while the second plate (the more ductile material) deformed significantly before the effective plastic strain surpassed it's ultimate strain value, and the plate broke-off. Comparison of the final status obtained with ultimate strain values of 0.2, 0.4 and 0.6 (0.2 and 0.6 are shown in Figs 3h and 4a, respectively), to the experimental results (Figs 1b to 1d) shows very good reproduction

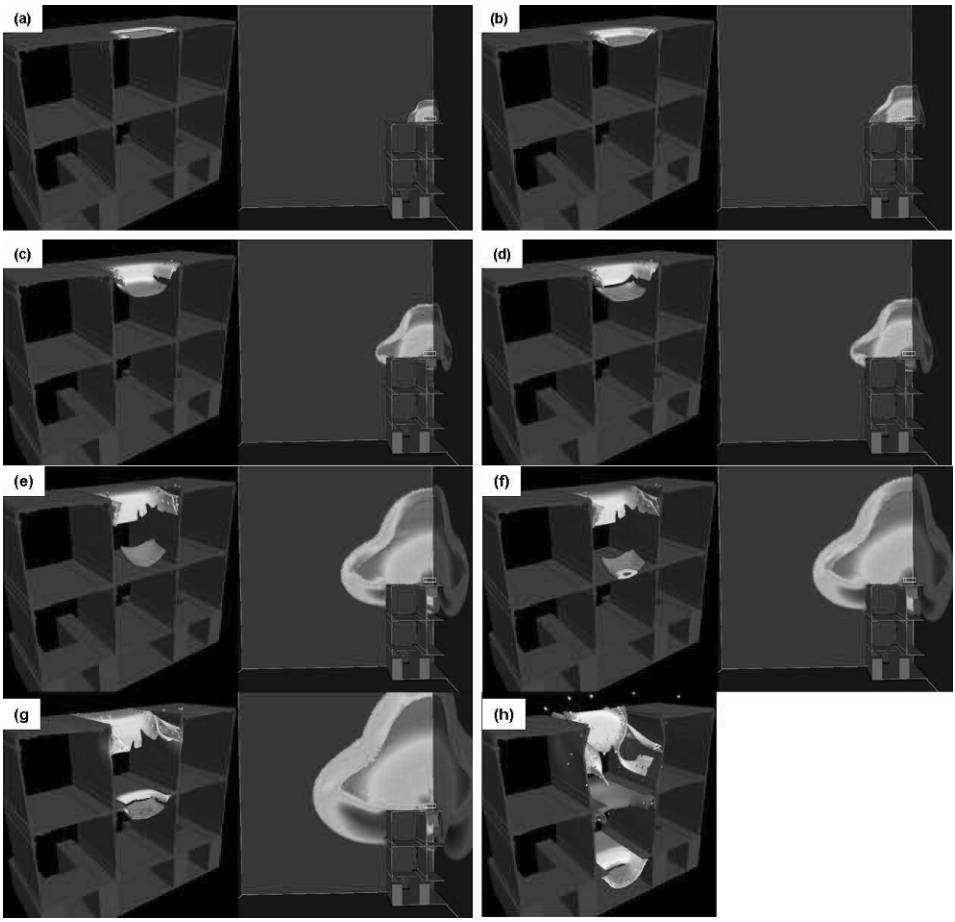

Fig. 3. Evolution of the blast and structural response

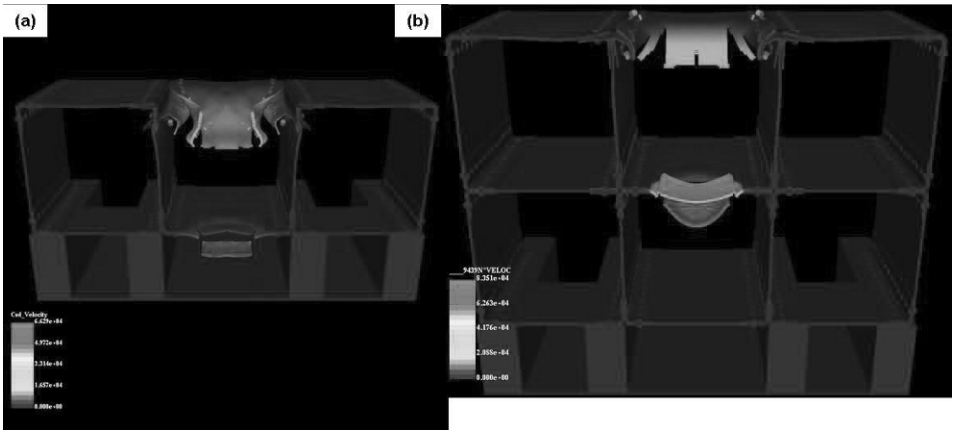

Fig. 4. Evolution of the blast and structural response

of most the deformations discussed above. The size and cut of the predicted flyer plates were almost identical to the experimental one (basically, the explosive box imprint). Both the curvature and speed of the flyer plate best agreed with the results obtained with an ultimate strain value of 0.4. However, these results are inconclusive due to the uncertainty about the source. The results show that determination of the ultimate strain value is critical to modeling the flyer plate shape and speed, and hence the collateral damage inflicted by the charge (i.e., damage to next layer cells). In the next sequence of tests we will use well-characterized ideal explosives, eliminating the issue of an ill-defined source. These should help define the ultimate strain. Following these tests, we will be able to confidently predict the complete tower response to an explosive charge.

5 Conclusions

This paper describes a numerical and experimental investigation directed at improved understanding and modeling of the vulnerability of steel towers to terrorist attacks using bare HE charges. Large scale numerical simulations gave indicated the possible vulnerability of large steel towers to terrorist attacks. As testing of these tower is impractical, it became necessary to validate the predictions against scaled tests. We conducted numerical predictions and experiments under which scaled cells of the steel tower were exposed to blast loading. While the numerical predictions were capable of simulating the damage observed in the experiments, it was impossible to fully validate the predictions, as the explosive used does not have a fully validated equation-of-state. Future tests will be conducted with more cells and with a commonly used ideal explosive (such as C-4, Comp-B, etc.,), to eliminate any uncertainty about the source strength.

References

1. Johnson, G.R. and W.H. Cook, A Constitutive Model and Data for Metals Subjected to Large Strains, High Strain Rates and High Temperatures, Presented at the Seventh International Symposium on Ballistics, the Hague, The Netherlands, April. 1983.
2. Lin, J.I., DYNA3D A Nonlinear, Explicit, Three-Dimensional Finite Element Code For Solid and Structural Mechanics- User Manual, Lawrence Livermore National Laboratory, UCRL-MA-107254, January, 1995.
3. R. Löhner and P. Parikh - Three-Dimensional Grid Generation by the Advancing Front Method; Int. J. Num. Meth. Fluids 8. 1135-1149(1988).
4. R. Löhner and J.D. Baum - Adaptive H-Refinement on 3-D Unstructured Grids for Transient Problems; Int. J. Num. Meth. Fluids 14, 1407-1419 (1992).
5. D. Pelessone and C.M. Charman - A General Formulation of a Contact Algorithm with Node/Face and Edge/Edge Contacts; 1998 ASME Pressure Vessels and Piping Conference, San Diego, Ca, July (1998).
6. Seidt, J.D., Constitutive and Fracture Models for ASTM A36 Hot Rolled Steel, Battelle, Columbus, Ohio, November 2005 (Draft)
7. Optional Strain-Rate Forms for MAT_JOHNSON_Cook and the Role of the Parameter, Len Schwer, March2006, DRAFT
8. O. Soto, Baum, J. Löhner, R., and Mestreau, E. An Efficient CSD FE Scheme for Blast Simulations, presented at the 2007 Coupled Problems Conference, May 21-23, Ibiza, Spain.

DEM simulation of wave propagation in two-dimensional ordered array of particles

M. Nishida[1], K. Tanaka[1], and T. Ishida[2]

[1] *Nagoya Institute of Technology, Gokiso-cho, Showa-ku, Nagoya 466-8555, Japan*
[2] *Graduate School of Engineering, Nagoya Institute of Technology*

Summary. The dynamic response of a two-dimensional particle array subjected to internally bursting load was investigated using a discrete element method. From the distribution of normal contact force between spheres, it was found that the contact forces are reflected and diffracted by the voids and reflected and transmitted by seven alumina ceramic spheres. The particle array was less displaced horizontally layer by layer depending on the change of the contact force distribution.

1 Introduction

Over the last several decades, problems concerning the wave propagation in granular materials, that is, a collection of many solid particles, have become increasingly important in particle technology and granular physics.

In a chain of beads, Nesterenko has been investigating solitary waves both experimentally and theoretically [1]. Recently, many attempts have been made to clarify propagation phenomena of solitary waves in a chain of beads under various conditions [2, 3]. Shukla has investigated stress wave propagation in different arrangements from a single straight chain to a two-dimensional array of discs using dynamic photoelasticity [4]. Britan has studied the propagation of stress waves through a chain of discs experimentally using a high-speed photoelastic diagnostic technique [5].

On the other hand, many attempts have been made to clarify wave propagation phenomena in a two-dimensional array of particles [6, 7]. Sen and Sinkovits investigated the propagation of both small (sound) and large amplitude (shock) perturbations in two-dimensional granular columns. They considered the effects of microstructure due to the presence of voids and impurities [8]. Gilles and Coste examined the time of flight of acoustical wave trains in a two-dimensional array of nylon and steel spheres as a function of the applied stress [9].

Although many papers have been published about propagation phenomena of many types of waves in a three-dimensional array of particles, which is commonly seen in actual granular materials (for example, [10]), the nonlinear properties of wave propagation in two-dimensional array of particles remain unexplained. The present authors investigated the propagation of stress waves in a two-dimensional ordered array of particles [11, 12]. Among many numerical simulation techniques, the discrete element method (DEM) [13] has been widely used in powder technology and physics as one of the most direct and simplest methods for granular matter and powder [14]- [16]. In the present study, the nonlinear propagation of stress waves in a two-dimensional ordered array of particles was investigated by DEM using Thornton's theory [17] for the collision between elastic-perfectly plastic spheres.

2 Numerical analysis

2.1 Particle array

We mainly used mono-size nylon-66 spheres of 1/4 inches in diameter as the components of two-dimensional ordered arrays of particles. As shown in Fig. 1, the nylon spheres were arranged orderly, horizontally, and two-dimensionally in 37 layers of 37 (or 36) spheres each, in a thin rectangular container missing one wall; the total number of spheres was 1351. This means that the gravitational force does not affect the calculated motion of nylon spheres. Three of the container walls were made of polyvinyl chloride (PVC). The simulation was carried out for the case in which the internal load, shown in the enlarged image of Fig. 1, was applied at point A, B or C of the particle array. Seven alumina ceramic spheres were placed in the particle array as shown in the upper half of Fig. 1. The effects of the presence of voids and the material of spheres were also examined.

2.2 Principle of discrete element method

DEM is a means of simulating the movement of granular matter and powder through a series of calculations that trace the motion of individual particles constituting the particle arrays. Equations of translational motion and rotational motion are described by the resultant force and the resultant moment of force exerted by the contacting particles:

$$m_i \frac{d^2 \boldsymbol{x}_i}{dt^2} = m_i \boldsymbol{g} + \sum_{j=1}^{N_c} \boldsymbol{F}_{ij}, \qquad I_i \frac{d\boldsymbol{\omega}_i}{dt} = \sum_{j=1}^{N_c} \left(\boldsymbol{r}_i \times \boldsymbol{f}_{ij} \right). \tag{1}$$

Here, m_i is the particle mass, I_i is the mass moment of inertia, $\boldsymbol{x}_i$ is the displacement vector of the i-th particle, $\boldsymbol{\omega}_i$ is the angular velocity vector of the i-th particle, $\boldsymbol{r}_i$ is the radius vector from the center of gravity of the i-th particle to the point at which frictional force is acting, r_i is the radius of the i-th particle, $\boldsymbol{F}_{ij}$ is the normal contact force vector on the i-th particle exerted by the j-th particle that maintains contact with the i-th

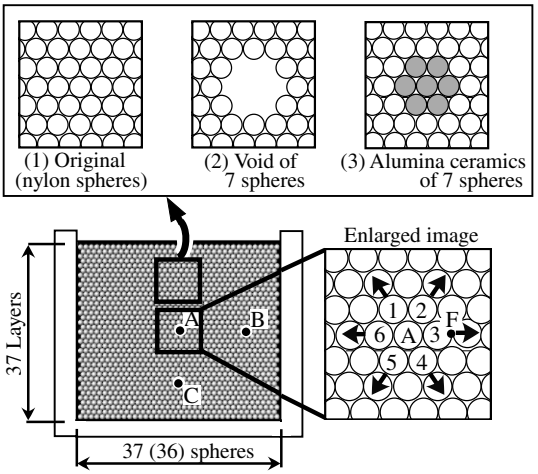

Fig. 1. Initial 2-D array of spheres

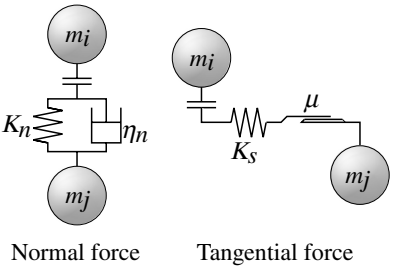

Fig. 2. Model of force-displacement relationship

particle, $\boldsymbol{f}_{ij}$ is the frictional force vector between the i-th and j-th particles, N_c is the number of particles in contact with the i-th particle, $\boldsymbol{g}$ is a gravitational acceleration vector, and t is time.

DEM is based on the hypothesis that disturbances only propagate from a particle to other particles that are in direct contact during a single time step. Therefore, instead of solving the same number of simultaneous equations as contact points, the equation of motion for each particle can be solved independently in each time step.

2.3 Contact force model between two spheres

In the DEM simulation, the particle-particle interaction is one of the most important factors to accurately simulate the movement of particles. In the normal force component, it is assumed that the force-displacement relationship between two spheres is described by a model with a spring, K, and a dashpot, η, as depicted in Fig. 2. Also, a slider element is used to represent Coulomb-type friction between the two spheres in the tangential force component. The normal and tangential force components are separately described, where subscripts n and s indicate the normal and tangential components, respectively. Here, the simplest relationships of each of $\boldsymbol{F}_{ij}$ and $\boldsymbol{f}_{ij}$ with K and η, which were used by Cundall and Strack [13], are employed.

Many models for simulating elasto-plastic contact between two spheres have been proposed in DEM simulations [18, 19]. Among them, in the present simulation we employed Thornton's simple theory for the collision of elastic-perfectly plastic spheres in which maximum pressure at the elastic limit is constant. When the pressure at contact center p_0 is less than the pressure p_y at the contact center when yield occurs, the spring coefficient for normal force component in the force-displacement relationship, K_n, can be determined by Hertz's elastic contact theory. When $p_0 > p_y$, the plastic deformation effect on the force-displacement relationship should be considered. We employed $p_y = 2.8\sigma_y$ in the present simulations on the basis of many papers [18]- [20] with respect to contact mechanics where σ_y is the yield stress of material. Spring coefficient K_s, in the tangential force component, is expressed by the 'no-slip' solution of Mindlin theory [21].

2.4 Parameter determination

It is necessary to determine several material constants and the parameters used in the simulation. The bulk properties of these spheres taken from the data issued by the manufacturers are shown in Table 1.

Table 1. Simulation parameters

Time step Δt [s]	1.0×10^{-7}	Alumina ceramic sphere	
Friction coefficient	0.15	Young's modulus [Pa]	3.90×10^{11}
Spheres diameter [mm]	6.35	Poisson's ratio	0.25
Nylon sphere		Mass [g]	0.52
Young's modulus [Pa]	3.2×10^{9}	PVC wall	
Poisson's ratio	0.33	Young's modulus [Pa]	3.0×10^{9}
Yield stress [Pa]	60×10^{6}	Poisson's ratio	0.30
Mass [g]	0.15	Yield stress [Pa]	65×10^{6}

In the case of low impact velocity, the coefficient of restitution mainly depends on the energy dissipation due to plastic deformation and viscosity. Plastic deformation can be expressed by the spring coefficient of Thornton's theory. To represent energy dissipation due to viscosity, the damping coefficients of dashpot were used. The damping coefficients of dashpots were adjusted to make the coefficient of restitution obtained from DEM simulations conform to that obtained from the results of the impact experiments. The relationships between damping coefficient η_n and contact force component P at each time step are summarized as the following equations:

$$\begin{aligned}
&\text{Nylon sphere} - \text{Nylon sphere:} && [\eta_n/\eta_0]_{\mathrm{NN}} = 0.07/\cosh\{\,0.1(P-10)\},\\
&\text{Nylon sphere} - \text{PVC wall:} && [\eta_n/\eta_0]_{\mathrm{NP}} = 0.05/\cosh\{0.04(P-70)\},\\
&\text{Nylon sphere} - \text{Alumina ceramic sphere:} && [\eta_n/\eta_0]_{\mathrm{NP}} = 0.06/\cosh\{0.05(P-30)\},
\end{aligned} \tag{2}$$

Here, $\eta_0 = 2\sqrt{mK_n}$ is the theoretical critical damping coefficient in a vibration system of a single degree of freedom composed of a mass attached to a spring and a dashpot.

3 Simulation results and discussion

Our simulation results, where internal load was applied at the center of the particle arrays, can be seen below in Figs. 4-9. Figure 3 shows the normal contact force history at point F of sphere 3 in Fig. 1. The maximum contact force of initial load was 50 N, and its pulse duration was 40 μs.

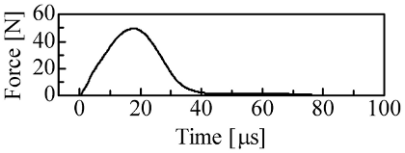

Fig. 3. Normal contact force propagating radially at point F of sphere 3 in Fig. 1

Figure 4 shows the distribution of the normal contact forces in the particle array. The normal contact forces were drawn through the contact points with straight lines whose thicknesses were proportional to their magnitude. The large contact forces propagated radially from the center of the particle array. At about 0.40 ms after initial loading, the normal contact forces between nylon spheres near the walls were large because they were greatly affected by the walls. The peak contact forces decreased rapidly in the first few

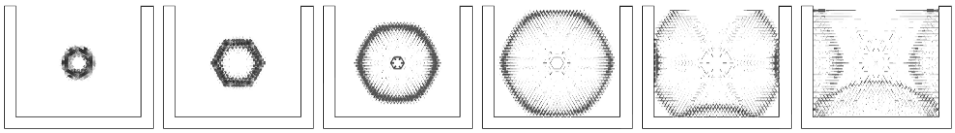

(a) 0.05 ms (b) 0.10 ms (c) 0.20 ms (d) 0.30 ms (e) 0.40 ms (f) 0.60 ms

Fig. 4. Normal contact forces obtained from DEM: initial load at sphere A

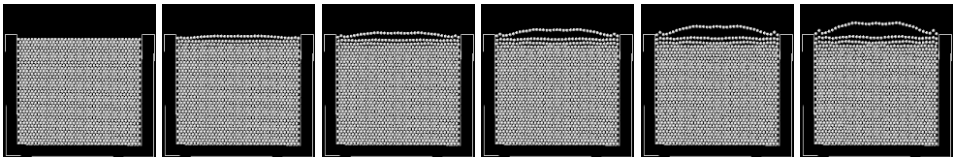

(a) 0 ms (b) 10 ms (c) 20 ms (d) 30 ms (e) 40 ms (f) 50 ms

Fig. 5. Motion of nylon spheres simulated by DEM: initial load at sphere A

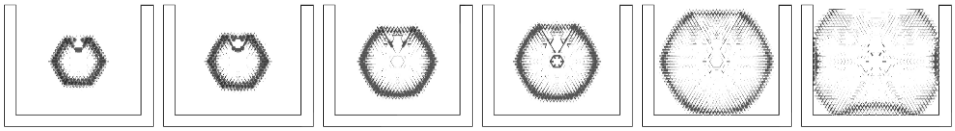

(a) 0.11 ms (b) 0.13 ms (c) 0.18 ms (d) 0.20 ms (e) 0.30 ms (f) 0.40 ms

Fig. 6. Normal contact forces of particle array with void: initial load at sphere A

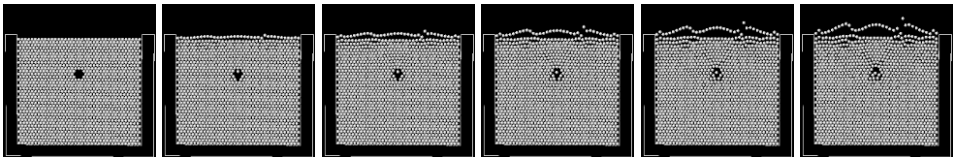

(a) 0 ms (b) 10 ms (c) 20 ms (d) 30 ms (e) 40 ms (f) 50 ms

Fig. 7. Motion of particle array with void: initial load at sphere A

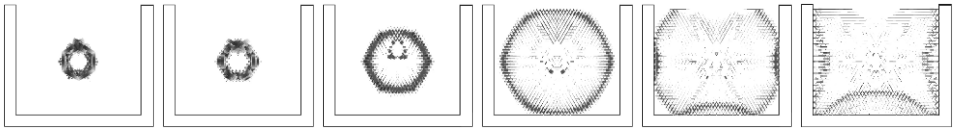

(a) 0.06 ms (b) 0.07 ms (c) 0.15 ms (d) 0.30 ms (e) 0.40 ms (f) 0.50 ms

Fig. 8. Normal contact forces of particle array with alumina ceramic spheres: initial load at sphere A

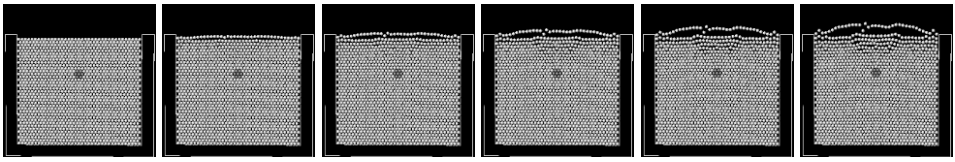

(a) 0 ms (b) 10 ms (c) 20 ms (d) 30 ms (e) 40 ms (f) 50 ms

Fig. 9. Motion of particle array with alumina ceramic spheres: initial load at sphere A

nylon spheres near the initial load, then decayed more gradually, and finally increased slightly in the last few spheres near the wall. Figure 5 shows the motion of the particle array, which was greatly displaced horizontally and symmetrically layer by layer.

Figure 6 shows the distribution of the normal contact forces in the particle array with a void. The void was created by removing seven spheres from the particle array. The contact forces were reflected by the void at 0.11 ms after initial loading. The presence of the void caused local wave scattering and attenuation at 0.18 ms. Figure 7 shows the motion of the particle array with the void. The void caused less movement of the nylon spheres above it.

Finally, the effect of dissimilar material on the distribution of the normal contact forces was examined in Fig. 8 when the void in Fig. 6 and 7 was filled with seven alumina ceramic spheres The large contact forces were reflected by the alumina ceramic spheres at 0.15 ms after initial loading. Figure 9 shows the motion of the particle array with alumina ceramic spheres. Compared to Fig. 5, the alumina ceramic spheres caused slightly less

movement of the nylon spheres above it. The nylon spheres above the alumina ceramic spheres were greatly displaced horizontally layer by layer.

4 Conclusion

The normal contact force between spheres was reflected by the void and the alumina ceramic spheres. They caused less movement of nylon spheres above the void and the alumina ceramic spheres.

Acknowledgement. This study was supported by a Grant-in-aid for Young Scientists (B) (Grant No. 17760077) from JSPS, Japan.

References

1. Nesterenko V. F.: *Dynamics of heterogeneous materials* (Springer, 2001) pp 1-81
2. Melo F., Job S., Santibanez F., Tapia F.: Physical Review E **73**, 041305 (2006)
3. Nakagawa M., Agui J. H., Wu D. T., Extramiana D. V.: Granular Matter **4**, (2003)
4. Rossmanith H. P., Shukla A.: Acta Mechanica **42**, (1982)
5. Britan A., Ben-Dor G., Igra O., Tanaka K., Nishida M.: Dynamics of stress wave propagation through a disc and a chain of discs. In: *Proc. ISSW25* (2004) pp 779-784
6. Shukla A., Sadd M. H., Mei H.: Experimental Mechanics **30**, 4 (1990)
7. Hostler S. R.: Wave propagation in Granular Materials. Ph.D. thesis, California Institute of Technology, (2005)
8. Sen S., Sinkovits R. S.: Physical Review E **54**, 6 (1996)
9. Gilles B., Coste C.: Nonlinear elasticity of a 2D regular array of beads, In: *Powders and Grains*, (AA Balkema, 2001) pp 113-116
10. Mouraille O., Mulder W. A., Luding S.: Journal of Statistical Mechanics (2006)
11. Nishida M., Tanaka K., Ito A., Lu Z.: Impact behavior of two-dimensional particulate aggregation containing dissimilar material layer. In: *Proc. ISSW 24* (2005) pp 1097-1103
12. Nishida M., Tanaka K., Ikeda, Y., Tanaka, Y.: Stress wave propagation in aggregated particles induced by an internally bursting load. In: *Proc. ISSW 25* (2006) pp 791–796
13. Cundall P. A., Strack O. D. L.: Geotechnique **29**, 1 (1979)
14. Herten M., Pulsfor M.: Granular Matter **2**, 1 (1999)
15. Horio M., Kajikawa S.: DEM simulation of industrial issues in fluidized bed reactors. In: *Handbook of conveying and handling of particulate solids*, ed by Levy A., Kalman H. (Elsevier 2001) pp 547-559
16. Hassanpour A., Ghadiri M.: Powder Technology **141**, 3 (2004)
17. Thornton C.: Transaction of ASME Journal of Applied Mechanics **64**, (1997)
18. Li L. Y., Wu C. Y, Thornton C.: Proceedings of Institution of Mechanical Engineers **216**, C4 (2002)
19. Zhang X., Vu-Quoc L.: International Journal of Impact Engineering **27**, (2002)
20. Johnson K. L.: *Contact Mechanics* (Cambridge University Press, 1985) pp 153-155
21. Mindlin R. D.: Transaction of ASME Journal of Applied Mechanics **16**, (1949)

Experiment study of ejecta composition in impact phenomenon

D. Numata[1], T. Kikuchi[1], M. Sun[2], K. Kaiho[3], and K. Takayama[4]

[1] *Graduate School of Engineering, Tohoku University, Katahira 2-1-1, Aoba-Ku, Sendai-Si, Miyagi-Ken, 980-8577, Japan*
[2] *Center for Interdisciplinary Research, Tohoku University, Aramaki aza Aoba 6-3, Aoba-Ku, Sendai-Si, Miyagi-Ken, 980-8578, Japan*
[3] *Institute of Geology and Paleontology, Tohoku University, Aramaki aza Aoba 6-3, Aoba-Ku, Sendai-Si, Miyagi-Ken, 980-8578, Japan*
[4] *Biomedical Engineering Research Organization, Tohoku University, Katahira 2-1-1, Aoba-Ku, Sendai-Si, Miyagi-Ken, 980-8577, Japan*

Summary. Impact tests were held to clarify the relationship between the composition of ejecta and these of the projectile and the target plate under different impact kinetic energy and impact velocity. Two sets of impact experiments were held, one using high carbon chromium bearing steel (SUJ-2) projectile and Al2017-T4 plate (Fe/Al impact), and the other using Al2017-T4 projectile and SUJ-2 plate (Al/Fe impact). The spherical projectile is of 7.94 mm in diameter, made of Al2017-T4 or SUJ-2. The impact velocity considered is from 2.5 to 4.2km/s. By recovering and analyzing the injected SUJ-2 and the Al2017-T4 fragments separately, we can quantitatively measure the composition of the injected fragments, and clarify how it depends upon the material of the projectile and the target plane. We further investigate the effects of velocity and kinetic energy of the projectile on the ejecta composition.

1 Introduction

In the history of the earth, species mass extinction has repeatedly occurred. And, the impact of a huge meteorite on the earth is thought as one of the causes of these mass extinction events [1-4]. The diameter of the colliding meteorite reaches several kilometers, and its speed may reach dozens of kilometers per second. When this meteorite collides with surface of the earth at the hypervelocity ranges, the crater that reaches tens of times the diameter of the meteorite is formed in the collision point, and a large amount of crushed materials of the earth and the meteorite are ejected into the atmosphere. These ejected materials would significantly reduce the amount of sunlight that could reach the surface otherwise, and could remain in the atmosphere for months and years as tiny dusts and gases. The impact of such meteorite is therefore believed to able to change the global weather drastically. The physical and chemical effects of the ejected materials on the weather depend strongly on their compositions.

In this study, we are going to clarify how the ejecta composition is related to the original material of the meteorite and the earth surface by a laboratory experiment. As a part of geophysical application of shock wave research, a hypervelocity impact test was performed in a 15 mm diameter two-stage light gas gun at IFS, Tohoku University. In order to examine the effect of test materials on ejected fragments, spheres made of high carbon chromium bearing steel and AL2017-T4 aluminum alloy were individually projected against aluminum and steel targets. In keeping impact energy of steel and aluminum spheres identical, the impact speed of steel sphere is about 2.5 km/s and that

of aluminum sphere is about 4.2 km/s. We examined not only the impact crater shape but also size and number distribution of ejected fragments.

2 Experimental setup

2.1 Two-stage light gus gun

We used a light gas gun to launch a 15 mm diameter projectile at 1 to 4 km/s into reduced pressure environments down to 50kPa in air. The gun can be operated under two-stage and one-stage modes for launching projectile at different velocity range. Figure 1 shows the gun system consisting of a 51 mm diameter and 3.4 m long pump tube, a high-pressure coupling, a 15 mm diameter and 3 m long launch tube, and a 1.66 m diameter and 12 m long recovery tank which has a test section equipped with two pairs of 600 mm diameter observation windows and three pairs of flash X-ray ports. The observation windows are made of 20 mm thick acryl, which enabled to observe free flight objects.

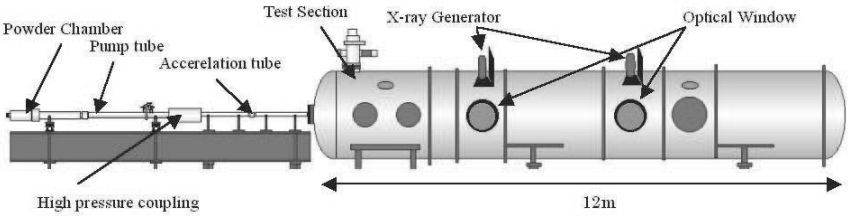

Fig. 1. Schematic of two-stage light gas gun at IFS, Tohoku University

To launch projectiles up to 1.5 km/s, we operated the gun using the single stage mode, in which a cartridge (Winchester 300) filled with high-speed smokeless powder (HS-7 Hodgdon Powder Co.) of 3 g in weight was inserted at the end of the launch tube and ignited with a detonator (GM210M Federal Gold Medal Match). For projectile speed over 1.5 km/s, the two-stage light gas gun operational mode was used instead. A cased charge filled with medium-speed smokeless powder, as propellant charge (H50-BMG Hodgdon Powder Co.) of up to 400 g was inserted in the combustion chamber. To ignite propellant powder in a uniform and controlled fashion, an igniter was inserted in the center of the cased charge.

The igniter contained, in its perforated cylinder, black powder of 13 g in weight and ignited by the Winchester 300 igniter. A 1.5 m long and 15 mm cylindrical tube was connected to the launch tube for attenuating the strong blast wave released from it. This blast remover was basically a perforated tube consisting of four guide rails and a thick wall stainless steel supporting tube. Along the space between two guide rails, 10 mm diameter venting holes were uniformly distributed, through which the precursory blast wave was released into the recovery tank.

A test chamber was placed on a carrier on rails in the recovery tank, so that its position inside of a collimated light beam path passing through the first observation window can be adjusted for the visualization of impact phenomena in the chamber.

2.2 Test chamber for HVI experiments

The test chamber for the present HVI experiments is shown in Fig. 2. It has a single wall structure consisting of stainless steel tube of 200 mm in inner diameter, wall thickness of 25 mm, and 500 mm in length. Target materials and retaining ring are installed in this chamber. The inner wall of this chamber is protected by the silicone rubber sheet of 10mm in thickness. The projectiles are introduced into the chamber through a small diameter entrance hole on the frontal plate as seen in Fig. 2. A sketch of the chamber is depicted in Fig. 2b.

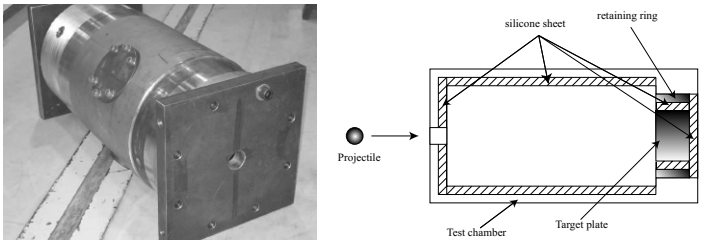

Fig. 2. Test chamber for HVI experiments

2.3 Experimental conditions

Two sets of impact experiments are held, one using high carbon chromium bearing steel (SUJ-2) projectile and Al2017-T4 plate (Fe/Al impact), and the other using Al2017-T4 projectile and SUJ-2 plate (Al/Fe impact). The spherical projectile is of 7.94 mm in diameter, made of Al2017-T4 or SUJ-2. The impact velocity considered is from 2.5 to 4.2km/s. The Experimental setup for the experiments is shown in Fig. 3.

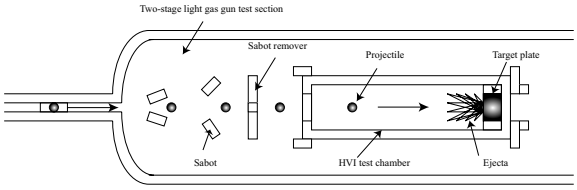

Fig. 3. Experimental setup for HVI tests

We used a 7.94 mm (5/16 inch) diameter spheres to represent a meteorite, and accommodated it in the sabot that consists of four poly-carbonate segments produced by plastic extrusion. The four segments formed a 15 mm diameter and 18 mm long and 3 g weigh cylindrical shape. Upon the release of the sabot and the sphere from the muzzle of the blast remover, the sabot was separated gradually to four segments. The sabot separation was realized by receiving a large aerodynamic force on their blunt frontal surface of the sabot segments.

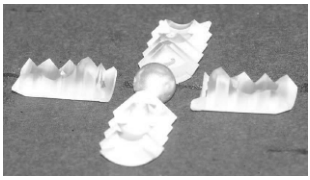

Fig. 4. Spherical projectile and sabot

To promote the sabot separation, we installed a sabot remover before the segments reach the test section, which consisted of a thick steel plate with a hole in the middle. The spherical specimen can pass through the hole but the pieces of sabot segments crashed on the frontal surface and were stopped.

We evacuated the recovery tank by using a rotary pump combined with a mechanical booster pump. The pressure was set to 50 kPa, which can produce aerodynamic forces high enough for spontaneously splitting a sabot from a sphere model.

Three conditions were tested for projectile speeds ranging from 2.5 km/s to 4.2 km/s. The projectile materials, impact velocity, projectile mass, kinetic energy, and target materials of the tests are tabulated in Table 1.

Table 1. Test condition for HVI experiments

	Projectile material	Impact velocity (km/s)	Projectile mass (g)	Kinetic energy (kJ)	Target material
Case 1	Al2017-T4	4.17	0.73	6.35	SUJ-2
Case 2	SUJ-2	2.50	2.04	6.38	Al2017-T4
Case 3	SUJ-2	3.00	2.04	9.18	Al2017-T4

3 Results and discussion

Figure 5 shows two photos of the crater on the target material formed in case 1. The crater is roughly hemispherical, and the local radius on the bottom of the crater is seen to be smaller than that on the top. The surface of this crater is covered with a ruler, and the lip structure is seen on the edge of the crater.

Figure 6 shows the crater on the target material formed in case 2. In this case, the cross-section of the crater looks more like a circular cylindr as shown in Figure 6b. The crater is much deeper compared with case 1.

Therefore, when the projectile has same kinetic energy and the projectile with large density collides with the target plate with small density, it can be confirmed that the depth of the crater tends to grow compared with the case where the projectile with small density collides with the target plate with large density.

A lot of cracks can be confirmed on the surface of the crater, and they have grown in the direction of the projectile impact.

Figure 7 shows the crater on the target material generated as a result of case 3. In this case, it is seen that the crater configuration is similar to the case 2, and the diameter and the depth of the crater are larger than case 2. The number of cracks appeared in the crater section and the lip structure are also larger than the case 2. In case 3, the crack appears almost everywhere on the surface except the vicinity of the crater section.

(a) (b)

Fig. 5. Target plate after impact (Al/Fe impact (Case 1)): impact velocity = 4.17 km/s; (a) frontal view, and (b) side view of crass section

(a) (b)

Fig. 6. Target plate after impact (Fe/Al impact (Case 2)): impact velocity = 2.5 km/s; (a) frontal view, and (b) side view of crass section

(a) (b)

Fig. 7. Target plate after impact (Fe/Al impact (Case 3)): impact velocity = 3.0 km/s; (a) frontal view, and (b) side view of crass section

(a) (b)

Fig. 8. Captured ejecta fragments inside silicone sheet; (a) sample silicone sheet after HVI experiments (Case 1), and (b) relationship between the size and number of ejecta fragments

Figure 8a shows a photograph of the silicone rubber sheet after the experiment. A large amount of impact fragments are captured by the silicon sheet in all cases. However, there is different in the distribution of the impact fragments in case 1 and case 2. In case 2, the amount of impact fragments was less than that captured in case 1, and has concentrated farther from the collision point. It is clear that even for the same kinetic energy, the distribution of impact fragments are greatly influenced by the combination of materials of the projectile and target material. The relationship between the size and number of ejecta fragments inside silicone sheet is shown in fig. 8b. A number and the size of ejecta fragments which captured in the silicon sheet are different according to the impact velocity, the material of the projectile and the target plate.

The total mass of non-penetrated fragments collected in the HVI test chamber is shown in Table 2. The percentage in parentheses of table 2 shows what percentage collected among the mass of the projectile. The mass of the fragments of projectile at case 1 was 52 percent of initial projectile mass, and the remainder was penetrated in the silicon sheet. On the other hand, it was 74 percent of initial projectile mass that was collected at case 2. Though a further verification with a high-speed video camera etc. is necessary in the future experiments, in the case of Fe/Al impact, it was shown that total mass of fragments that originated in the projectile is fewer than the case of Al/Fe impact.

Table 2. Total mass of non-penetrated fragments collected in the HVI test chamber

	Al2017-T4	SUJ-2
Case 1	0.38 g (52.1 %)	1.05 g
Case 2	0.22 g	1.51 g (74.0 %)
Case 3	0.60 g	1.73 g (84.8 %)

4 Conclusions

Impact tests were held to clarify the relationship between the composition of ejecta and these of the projectile and the target plate under different impact kinetic energy and impact velocity. As a result, it is clarified that the distribution of impact fragments are greatly influenced by the combination of materials of the projectile and target material.

References

1. Alvarez LW, Alvarez W, Asaro F, Michel HV: *Extraterrestrial cause for Cretacious-Terinary extinction*, Science 208:1095-1102 (1980)
2. Rampino MR, Adler AC: *Evidence for abrupt latest Permina mass extinction of foraminifera: results of tests for the Signor-effect*, Geology 25:415–8 (1998)
3. Kaiho K: *Planktonic and benthic for aminiferal extinction events during the last 100 m.y*, Palaeoecology 111:45-71 (1994)
4. Kaiho K, Kajiwara Y, Miura Y: *End-Permian catastrophe by a bolid impact: Event of a gigantic release of sulfur from mantle: reply*, Geology September: 865 (2002)

Numerical simulation of the propagation of stress disturbance in shock-loaded granular media using the discrete element method

Y. Sakamura and H. Komaki

Department of Mechanical Systems Engineering, Toyama Prefectural University
5180 Kurokawa, Imizu, Toyama 939-0398, Japan

Summary. By using the discrete element method, we perform numerical simulations of the propagation of stress disturbance in granular media composed of spherical particles placed in a vertical channel with a rectangular cross section. The results show that (1) the shock loads subjected to the uppermost granular particles are transferred through certain paths randomly distributed in the granular medium, (2) the loads are not evenly distributed on the bottom wall as postulated in earlier works, (3) the locally averaged, internal force per unit area introduced in the present work is helpful to understand macroscopic load transfer processes inside shock-loaded granular columns, and (4) the maximum stress is not observed on the bottom wall, but in the upper or middle of the granular column.

1 Introduction

Granular materials can be defined as any materials composed of many individual, macroscopic solid particles, irrespective of particle size [1]. They are ubiquitous in nature and of great importance in applications as diverse as pharmaceutical, food and semiconductor industries [2]. Due to dissipative interactions between grains, granular matter exhibits unique and complex behaviors, which are much different from those of the other familiar forms of matter — solids, liquids or gases [3].

One of the most prominent properties of granular media might be quick dissipation of kinetic energy. In fact, there are many practical applications of granular media as absorbents of mechanical perturbations such as vibration, sound and shock wave. Thus granular materials are expected to be used for protection of people and plants against shock and blast waves. Mainly from this standpoint, the subject of shock wave interaction with granular media has attracted increasing interest in the shock wave research community. Britan and Levy [4] have reviewed recent investigations into this subject in detail. Although earlier efforts such as reviewed in their paper have revealed many important phenomena inside shock-loaded granular media, the dynamics of contact force transfer is still poorly understood.

In the present study, numerical simulations of the propagation of stress disturbance in shock-loaded granular media composed of spherical particles are performed by using the discrete element method (DEM) [5, 6]. The main purpose of the present work is to examine how stress disturbance propagates through the granular media placed in a vertical channel container after shock loading, which is extremely difficult to understand from earlier shock tube experiments (e.g., [7]).

2 Numerical simulation

2.1 Discrete element method (DEM)

DEM is the time-dependent numerical solution of Newton's equation of motion for all particles of which the granular material consists. In the present simulations, the granular media are modeled as assemblies of rigid spherical particles. The equations of translational and rotational motion of the i-th particle are given by

$$m_i \frac{d^2 \boldsymbol{u}_i}{dt^2} = \sum_{j=1}^{N} \boldsymbol{F}_{ij} + m_i \boldsymbol{g}, \qquad I_i \frac{d^2 \boldsymbol{\theta}_i}{dt^2} = \sum_{j=1}^{N} \boldsymbol{M}_{ij},$$

respectively. Here t is the time, m_i is the mass, I_i is the moment of inertia, $\boldsymbol{u}_i$ is the displacement, $\boldsymbol{\theta}_i$ is the angular displacement, $\boldsymbol{F}_{ij}$ and $\boldsymbol{M}_{ij}$ are the force and moment, respectively, exerted on the i-th particle by the j-th particle, N is the total number of particles which contact with the i-th particle, and $\boldsymbol{g}$ is the gravitational acceleration. These equations are numerically integrated based on Cundall's algorithm [5].

2.2 Contact force model

In the present simulations, the normal and tangential contact forces between two particles are calculated using the Voigt model with a no-tension joint [6]. For the tangential force model, a friction slider of Coulomb-type is inserted between the particles to take account of the slip at the contact point. The spring constant in the normal direction is obtained from Hertz's solution of the contact problem [8]. The viscosity coefficient in the normal direction was determined so as to reproduce the results of free fall experiments. On the other hand, the spring constant in the tangential direction is determined using Mindlin's theory [9, 10] and the viscosity coefficient in the tangential direction is evaluated with the critical dumping value.

2.3 Granular media model and simulation parameters

The granular media are modeled as assemblies of 1.5 mm-diameter spherical particles made of a polyacetal resin, which are placed in a vertical channel container with a rectangular cross section ($w \times w$) and a height (d_{L}) such as shown in Fig. 1. The side walls and the bottom wall of the container are made of a polyacetal resin and brass, respectively. The dimensions of the containers are summarized in Table 1. In order to examine the effects of the particle arrangement on the load transfer process, we conducted simulations both for body-centered cubic (BCC) and random assemblies.

The shock loading is achieved by applying a downward step force equally on the uppermost particles in the present simulations. The magnitude of the applied force is estimated from the gas pressure behind a shock wave normally reflected from a flat wall. It is assumed that the Mach number of the incident shock wave is 1.33 and the initial pressure is 0.1 MPa, which correspond to those in shock tube experiments [7].

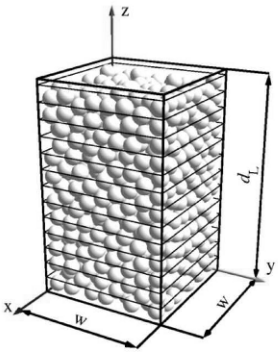

Fig. 1. Granular media model

Table 1. Dimensions of the granular media models

	d_L (mm)	w (mm)
Case 1	20	12
Case 2	20	24
Case 3	60	12

3 Results and discussion

3.1 Contact force distributions

Representative results for BCC and randomly arranged assemblies (both Case 1) are shown in Fig. 2. In this figure, the normal contact force distributions within these granular media 60 and 120 μs after the shock loading are visualized along with the initial arrangements of spherical particles. The pipe segments drawn between the centers of two particles which contact each other designate the load transfer paths and their color indicates the magnitude of the normal contact force.

For the BCC case, the loads are regularly transferred from the top to the bottom as expected. The front of the load transferred region is clearly visible in the snapshot at $t = 60$ μs. When the load front reaches the bottom wall at $t = 120$ μs, the normal contact force on the bottom wall peaks. It should be noted here that the loads are not evenly distributed on the bottom wall as postulated in shock tube experiments [4,7]; the contact forces near the corners of the container are smaller than those in the center area. This fact clearly suggests the great importance of the dimension and the shape of the container to the load transfer processes.

For the randomly arranged case, the situation is more complicated; the shock loads subjected to the uppermost particles are transferred through certain paths randomly distributed in the granular medium called stress chains [11]. Although the load transfer front is barely visible in the snapshot at $t = 60$ μs, the wave-like load transfer process cannot be observed from the snapshot at $t = 120$ μs any longer. We should mention here that several, highly concentrated load paths (designated by the red pipes in the figure) can be seen in the upper region of the granular column. As pointed out in [11], increased contact force along these paths may lead to localized fracture and subsequent friction of

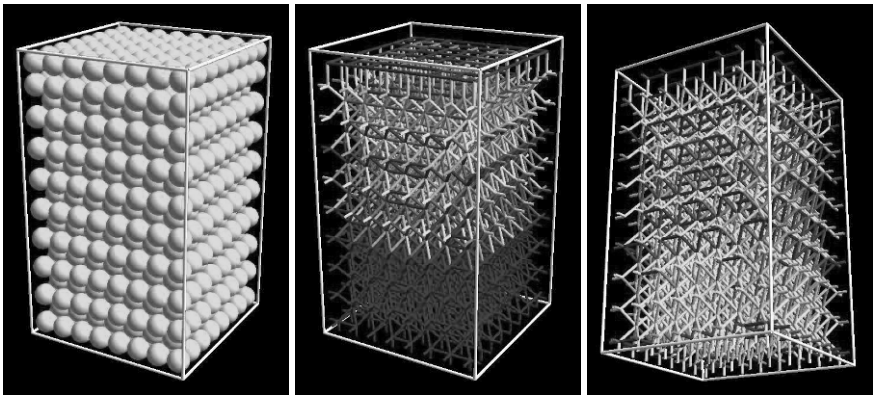

Initial arrangement $t = 60$ μs (top view) $t = 120$ μs (bottom view)

(a) BCC

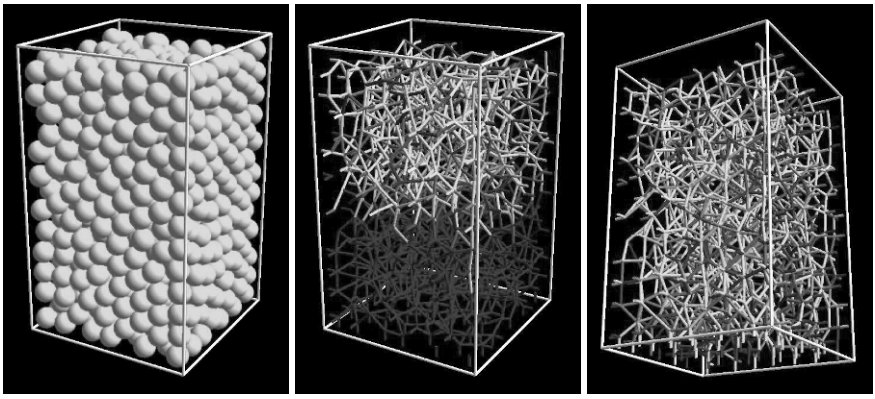

Initial arrangement $t = 60$ μs (top view) $t = 120$ μs (bottom view)

(b) Random

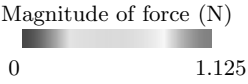

Fig. 2. Arrangement of spherical particles and normal contact force distributions in shock-loaded granular media (Case 1). Here t is the time after the shock impact

newly formed surfaces, which is a possible source of hot spot within reactive granular materials.

3.2 Propagation of the stress disturbance

In order to better understand the load transfer processes in shock-loaded granular media, we calculate the internal normal force per unit area that balances to the external load

applied to the particles inside a sliced region (1.5 mm height) of granular columns, such as illustrated in Fig. 1 (referred to hereafter as "stress"). Figure 3 shows temporal evolutions of the stress distributions inside granular media with different dimensions (Cases 1 to 3). Note that the value depicted in the negative region in the z-axis coordinate represents the stress on the bottom wall.

We can clearly observe wave-like propagation of stress disturbance in granular media from these figures. For relatively shallow granular media (Cases 1 and 2), the loads are transferred to the bottom wall and the oscillations of the stress are observed anywhere in the granular column. For deeper granular media case (Case 3), on the other hand, the load cannot be transferred to the bottom any longer, but rather dumped in the upper region. These results qualitatively agree with those from stress measurements conducted in shock tube facilities [4, 7].

Thus, the proposed stress (locally averaged, internal force per unit area) is found to be helpful to understand macroscopic load transfer processes inside shock-loaded granular media. It is worth pointing out that the maximum stress is not observed on or near the bottom wall even for relatively shallow media cases, but in the upper or middle of the granular column (see Figs. 3 (a) and (b)). It seems to be extremely difficult to explain why this happens by continuum mechanical approaches.

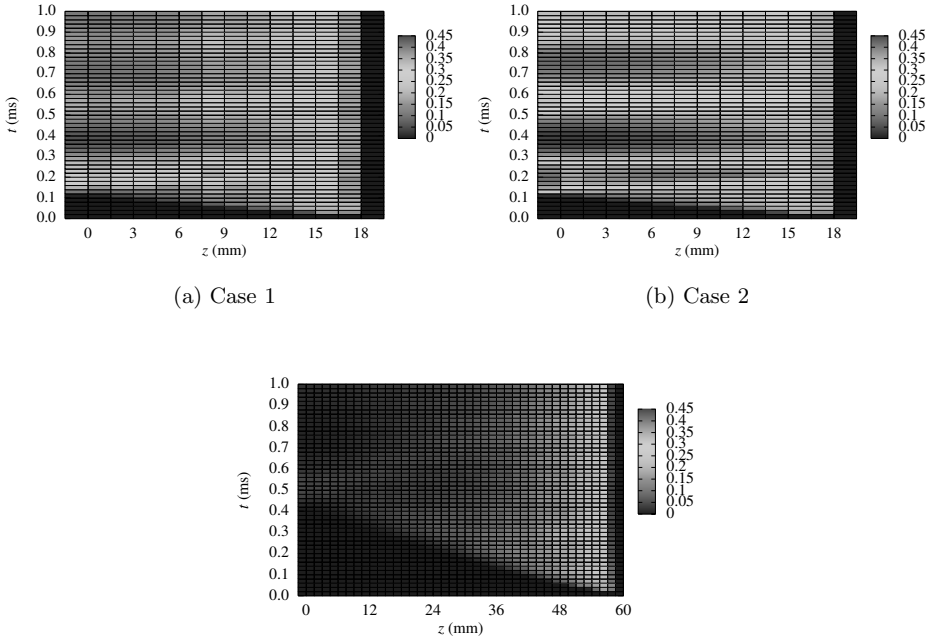

(a) Case 1

(b) Case 2

(c) Case 3

Fig. 3. Temporal evolutions of stress distribution (unit: MPa)

4 Conclusion

Numerical simulations of the propagation of stress disturbance in granular media were performed by using the discrete element method to shed light on complex behavior of shock-loaded granular media. The granular media were modeled as assemblies of spherical particles, which were placed in a vertical channel container with a rectangular cross section. The main conclusions derived from the present work are summarized as follows:

1. The shock loads subjected to the uppermost granular particles are transferred through certain paths randomly distributed in the granular medium (stress chains).
2. The loads are not evenly distributed on the bottom wall as postulated in shock tube experiments conducted previously.
3. The locally averaged, internal force per unit area introduced in the present work is helpful to understand macroscopic load transfer processes inside shock-loaded granular columns.
4. The maximum stress was not observed on the bottom wall even for relatively shallow media cases, but in the upper or middle of the granular column.

Acknowledgement. The authors would like to thank Dr. Junya Kano, Institute of Multidisciplinary Research for Advanced Materials, Tohoku University, for his helpful suggestions in the development of our 3-D DEM code.

References

1. Nedderman, R. M.: *Statics and Kinematics of Granular Materials*, (Cambridge University Press, 1992) p 1
2. Richard, P., Nicodemi, M., Delannay, R., Ribiére, P. and Bideau, D.: Slow Relaxation and Compaction of Granular Systems. Nature Materials **4**:121–127 (2005)
3. Jaeger, H. M., Nagel, S. R. and Behringer, R. P.: The Physics of Granular Materials. Physics Today **49**(4):32–38 (1996)
4. Britan, A. and Levy, A.: Weak Shock Wave Interaction with Inert Granular Media. In: *Handbook of Shock Waves*, vol 2, ed by Ben-Dor, G., Igra, O. and Elperin, T. (Academic Press, 2001) pp 597–666
5. Cundall, P. A. and Strack, O. D. L.: A Discrete Numerical Model for Granular Assemblies. Géotechnique **29**:47–65 (1979)
6. Nishida, M., Tanaka, K. and Takagi, T.: Numerical Simulation on Dynamic Behavior of Granular Materials Subjected to Projectile Impact by Using Discrete Element Method. In: *Proc. of 23rd Int. Symp. on Shock Waves*, ed by Lu, F. K. (2002) pp 655–661
7. Mikami, H., Kaneda, T., Sakamura, Y. and Suzuki, T.: Head-on Collisions of a Planar Shock Wave with a Dust Layer, In: *Theoretical and Applied Mechanics*, vol 49, ed by Kimura, R. (2000) pp 263–270
8. Timoshenko, S. P. and Goodier, J. N.: *Theory of Elasticity*, 3rd edition (McGraw-Hill, 1970) pp 409–414
9. Mindlin, R. D.: Compliance of Elastic Bodies in Contact. J. Appl. Mech. **16**:259–268 (1949)
10. Mindlin, R. D. and Deresiewicz, H.: Elastic Spheres in Contact under Varying Oblique Forces. J. Appl. Mech. **20**:327–344 (1953)
11. Roessig, K. M., Foster, Jr., J. C. and Bardenhagen, S. G.: Dynamic Stress Chain Formation in a Two-dimensional Particle Bed. Exp. Mech. **42**(3):329–337 (2002)

Strain characteristics of aluminum honeycombs under the static and impact compressions

K. Tanaka[1], **M. Nishida**[1], **K. Tomita**[2], **and T. Hayakawa**[2]

[1] *Nagoya Institute of Technology, Gokiso-cho, Showa-ku, Nagoya 466-8555, Japan*
[2] *Graduate School, Nagoya Inst. of Tech., Gokiso-cho, Showa-ku, Nagoya 466-8555, Japan*

Summary. The in-plane static and impact compression phenomena of aluminum honeycomobs were investigated experimentally. Particularly, by defining a "cell-scale strain" and a "macro-scale strain" in the present paper, the relationship between the deformation process of individual cells in the honeycomb and that of the entire honeycom was studied. Also, the effect of strain rate on the deformation and collapse of the aluminum honeycombs and cells was elucidated.

1 Introduction

Cellular solids are composed of a network of cell walls or cell stems. An aluminum honeycomb which is one of typical cellular solids is built up by a lot of polygon cells with thin walls arranged two-dimensionally and has very different mechanical properties from that of mother material owing mainly to the geometrical configulation of cells [1].
Although aluminum honeycombs having been used for reinforcement of thin shell structures, the in-plane characteristics against dynamical loading are not known so much. Tanaka et.al. [2]- [5] invetigated experimentally the in-plane deformation process and wave propagation mechanisms of aluminum honeycombs under impact loading and also they conducted numerical simulations using a shock code, AUTODYN-2D. However, the deformation process of individual cells in the honeycomb and that of the entire honeycomb is very different, it will be very important to study the relationship between the macroscopic deformation and microscopic deformation. Among various investigations, Ohno [6], [7] studied the deformation of cell structures due to the biaxial in-plane loading using homogenization theory and Saiki et. al. [8] studied theoretacally cellular materials under the uni-directional tensile loading. Chen and Jong [9] and Zhu and Mills [10] studied the plastic collapse strength of hexagonal honeycombs by considering the cell wall deformation. Also, Ruan et, al. [11], and Papka and Kyriakides [12] studied the in-plane characteristics of honeycombs numerically.
In this paper, two representataive strain scales, named as a cell-scale strain and a macro-scale strain, are introduced in order to clarify the relationship between the individual cell deformation and entire honeycomb deformation under in-plane static loading and impact loading. Also, the effect of strain rate on the deformation process and plastic collapse strength was examined.

2 A cell-scale and a macro-scale for aluminum honeycombs

Figure 1 shows the geometry of a cell and co-ordinate system where the X_3 axis is taken along the cell axis. According to the theory given by Gibson and Ashby [1], Young's modulus in the X_1 axis, Poisson's ratio and the density are given respectively by

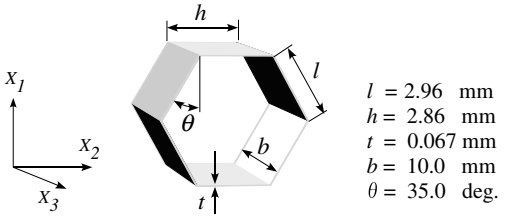

Fig. 1. Geometry of a cell of the aluminum honeycomb used.

$$\frac{E_1^*}{E_s} = \left(\frac{t}{l}\right)^3 \frac{\cos\theta}{(h/l + \sin\theta)\sin^2\theta} \tag{1}$$

$$\nu_{12}^* = \frac{\cos^2\theta}{(h/l + \sin\theta)\sin\theta} \tag{2}$$

$$\frac{\rho^*}{\rho_s} = \frac{(t/l)(h/l) + 2)}{2\cos\theta(h/l + \sin\theta)} \tag{3}$$

where the subscript s denotes the value of the mother material. Also, the plastic collapse strength under the stress in the X_1 direction is given by

$$\frac{\sigma_1^*}{\sigma_{ys}} = \left(\frac{t}{l}\right)^2 \frac{1}{2(h/l + \sin\theta)\sin\theta} \tag{4}$$

where the subscript ys denotes the yield stress of the mother material. The deformation process of individual cells in the honeycomb differs very much from that of the entire honeycom. In order to clarify the relationship between them, we introduce a macro-scale Y_0 which is based on the length of honeycomb in the X_1 direction and a cell-scale y_0 which is based on the cell size in the X_1 direction as shown in Fig.2(A). Six nodes of a cell is denoted by six characters from A to F.

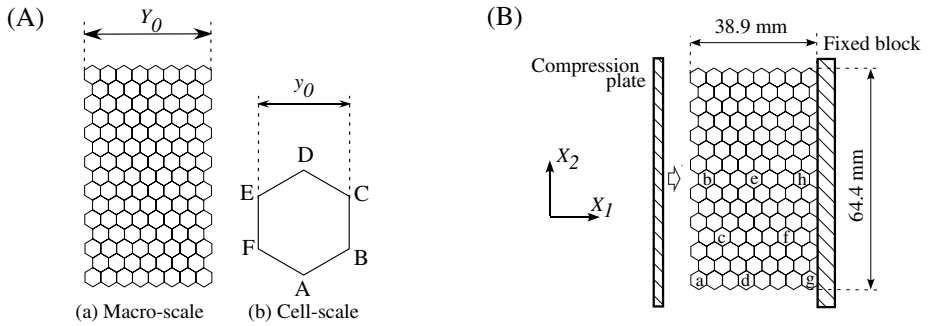

Fig. 2. (A) Definition of two scales in the honeycomb.(B) Arrangement of the honeycomb, compression plate, fixed block and the target cells: a-g.

3 Experiments

An example of the aluminum honeycombs used in the experiments is shown in Fig.2(B). It consists of cells of eight rows and eight columns made of A5052 aluminum alloy. In Fig.2(B), eight characters fram a to g indicate the target cells to be examined later.

3.1 Static compression experiments

Firstly we conducted the in-plane static compression tests in the X_1 direction. An experimetal setup is shown in Fig.3. By using a micrometer head and a compression plate,

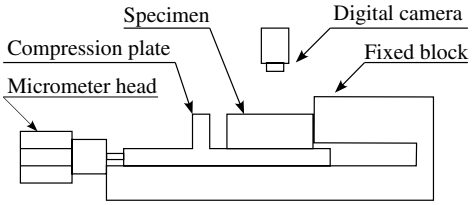

Fig. 3. Experimental setup for the static compression tests.

the honeycomb was compressed slowly in the velocity of 2 mm/min and the pictures of deformed honeycomb were taken by a digital still camera (SONY MVC-FD7) in every 0.5 mm movements of the compression plate. From the pictures, we measured the position of the compression plate, u_{com}, the position of the fixed block, u_{fix}, the initial position of the cell node B, u_{B0}, the initial position of the cell node F, u_{F0}, the initial position of the compression plate, u_0 and the positions u_B, u_C, u_D, u_E, u_F of the nodes B, C, D, E and F, respectively. Then, we defined the cell-scale strain and the macro-scale strain respectively, by

$$\epsilon_{cs} = \frac{\Delta y}{y_0} = 1 - \frac{(u_B + u_C) - (u_E + u_F)}{2(u_{B0} - u_{F0})} \tag{5}$$

$$\epsilon_{ms} = \frac{\Delta Y}{Y_0} = \frac{u_0 - u_{com}}{u_0 - u_{fix}} \tag{6}$$

for the static deformation. The macro-scale strain rate was $\dot{\epsilon}_{ms} = 8.6 \times 10^{-4}\mathrm{s}^{-1}$.

3.2 Impact compression experiments

In order to study the high-strain rate compresion phenomena a small scale gas gun facility shown in Fig.4 was used. An aluminum alloy plate of 320 mm × 40 mm × 12 mm and 0.32 kg was striken on the honeycomb in the X_1 direction. The impact velocities ranged from 5 m/s to 14 m/s. An laser velocimeter (Ono Sokki LV-1710) was used to detect the velocities v_{EF} and v_{BC} of the cell walls EF and BC shown in Fig.2(B). The amount of compression of the target cell in the X_1 direction was calculated by

$$\Delta y = \int_0^t v_{EF} dt - \int_0^t v_{BC} dt \tag{7}$$

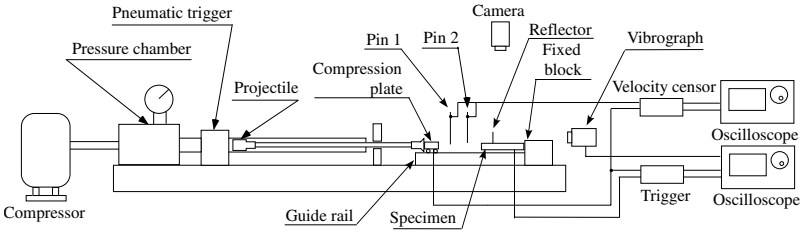

Fig. 4. Experimetal setup for the impact compression tests.

and the cell-scale strain for the impact compression was defined by

$$\epsilon_{ci} = \frac{\Delta y}{y_0} = \frac{1}{y_0}\int_0^t (v_{EF}dt - v_{BC})dt \tag{8}$$

Also, the macro-scale strain for the impact compression was defined by

$$\epsilon_{mi} = \frac{\Delta Y}{Y_0} = \frac{1}{Y_0}\int_0^t v_i dt \tag{9}$$

where v_i is the velocity of the compression plate measured by use of contact pins.

4 Experimental results and discussion.

Figure 5 shows the static compression process of the entire honeycomb. Until the macrscale strain reached about 0.2, the honeycomb was deformed homogeneously. However, when the macro-scale strain exceeded about 0.2, some cells in the central part were collpased locally, which is called as an localized condensation by us and corresponds to the X-type condensation according to Ruan [11]. When the compression was further developed cells near the fixed end were perfectly collpased but cells near the compression plate were partly collapsed and still remained hexagonal shape.

Figures 6 and 7 show the impact compression process of the entire honeycombs for different impact velocities. When the impact velocity was increased, cells near the compression plate were firstly collapsed and the I-type condensation according to Ruan was formed.

In Figs.8(a)-(h), the relationship between the macro-sacle strain and the cell-scale strain of six target cells from a to g is depicted for different strain rates. In Figs.8(a) and 8(g), it is found that the cell-scale strain becomes 1.0 when the macro-scale strain is less than

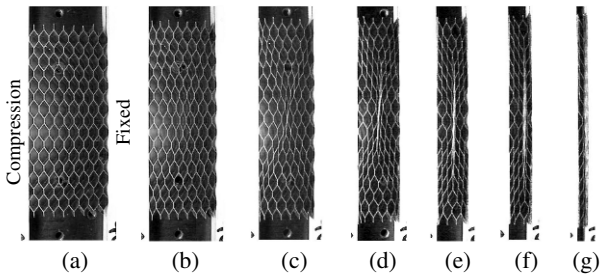

Fig. 5. Collapse of cells under the static compression.$\dot{\epsilon}_{ms} = 8.6 \times 10^{-4}\mathrm{s}^{-1}$.

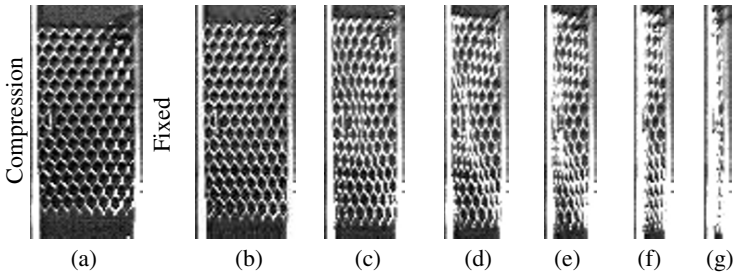

Fig. 6. Collapse of cells under the impact compression.$\dot{\epsilon}_{mi} = 1.3 \times 10^2 \mathrm{s}^{-1}$.

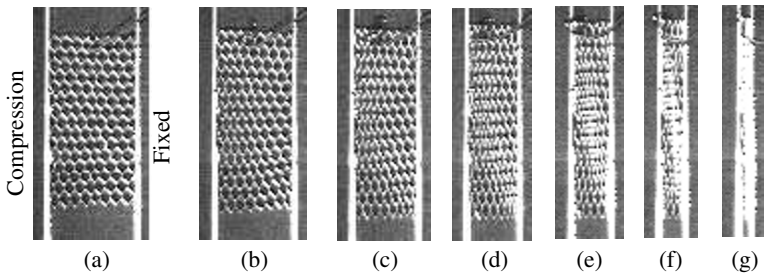

Fig. 7. Collapse of cells under the impact compression.$\dot{\epsilon}_{mi} = 3.5 \times 10^2 \mathrm{s}^{-1}$.

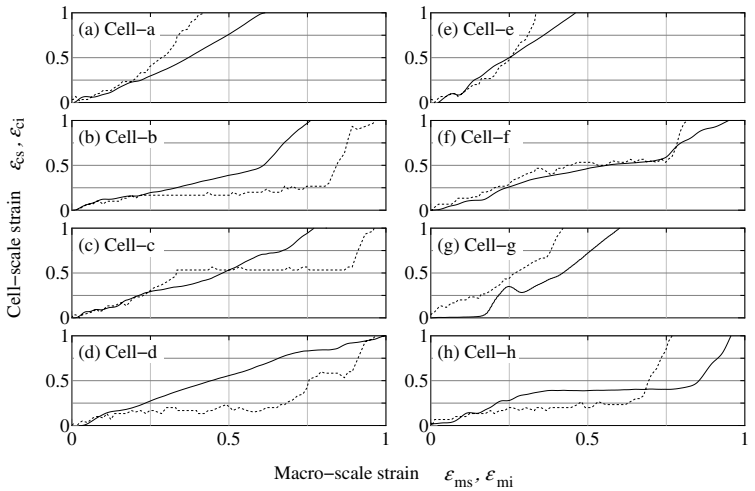

Fig. 8. The relationship between the cell-scale strains and the macro-scale strains for different strain rates. Solid line $-$: $\dot{\epsilon}_{ms} = 8.6 \times 10^{-4} \mathrm{s}^{-1}$, Dotted line $\cdots$: $\dot{\epsilon}_{mi} = 1.3 \times 10^2 \mathrm{s}^{-1}$.

0.5 in the case of static compression, but the cell-scale strain does not reach 1.0 in the case of impact compression. Also, in Figs.8(b) and 8(c), the cell-scale strain becomes 1.0 when the macro-scale strain is 1.0 in the case of static compression, but the cell-scale strain becomes 1.0 when the macro-scale strains is 0.75 in the case of impact compression. On the other hand, as shown in Figs.8(f) and 8(h), the cell-scale strain becomes 1.0 when the macro-scale strain is 0.75 in the case of static compression, but the cell-scale strains becomes 1.0 when the macro-scale strain is 1.0 in the case of impact compression. Thus, the cell-scale distribution depends on the strain rate. Moreover, it is found that the plateau region in the cell-scale strains is observed as the macro-scale strain is increased in the case of static compression but the cell-scale strains are increased linearly in the case of impact compression. Thus, the deformation process of cells is greatly affected by the strain rate. Ruan et. al. [11] suggested by their numerical simulations, the X-type and I-type collopse modes exist. In the case of static compression, the X-type collapse mode appeared in the central portion of the honeycomb. On the otherhand, when the impact velocities are 5 m/s and 14 m/s, the I-type collapse mode appeared near the compression plate in the present experiments. By inspecting the cell deformation process in detailed manner, the X-type mode was transformed to the I-Type mode at the impact velocity of 11.4 m/s. This transition may be caused by the interaction of stress waves and energy dissipation at cell nodes.

5 Conclusion

By the static and impact experiments, it was found that the place of the localized condensation and the collapse mode of cells depend strongly on the strain rate. Also, the deifference of the compression process of cells and entire honeycomb was successfully explained by two representative scales introduced in this paper.

References

1. Gibson, L. J. and Ashby, M. F., *Cellular Solids: Structure and Properties*, (Pergamon Press, 1988, Oxford).
2. Tanaka, K. et al., *Proceedings of the 23th International Symposium on Shock Waves*, (2002), pp. 648-654.
3. Tanaka, K. et al., *Proceedings of the 24th International Congress on High-Speed Photography and Photonics*, SPIE **4183**, (2001), pp. 990-997.
4. Tanaka, K. et al., *Proceedings of the 25th International Congress on High-Speed Photography and Photonics*, SPIE **4948**, (2003), pp. 374-379.
5. Tanaka, K. et al., *Proceedings of the 26th International Congress on High-Speed Photography and Photonics*, SPIE **5580**, (2005), pp. 42-50.
6. Ohno, N. et al., Trans. Japan Society of Mechanical Engineers, Ser. A (in Japanese), **67**, 656, (2001), pp. 618-624.
7. Ohno, N. et al., Trans. Japan Society of Mechanical Engineers, Ser. A (in Japanese), **67**, 658, (2001), pp. 925-932.
8. Saiki, I. et al., Trans. Japan Society of Mechanical Engineers, Ser. A (in Japanese), **69**, 680, (2003), pp. 786-793.
9. Cheng, H. C. and Jong, S. H., Int. J. Mechanical Sciences, **44**, 9, (2002), pp. 1827-1844.
10. Zhu, H. X. and Mills, N. J., Int. J. Solids and Structures, **37**, 13, (2000), pp. 1931-1949.
11. Ruan, D. et al., Int. J. Impact engineering, **28**, 2, (2003), pp. 161-182.
12. Papka, S. D. and Kyriakides, S., Acta Materialia, **46**, 8, (1998), pp. 2765-2776.

Part XI

Medical, Biological, Industrial Applications

Acceleration of cell growth rate by plane shock wave using shock tube

M. Tamagawa, N. Ishimatsu, S. Iwakura, and I. Yamanoi

Kyushu Institute of Technology, Graduate School of Life Science and Systems Engineerig Hibikino 2-4, Wakamatsu-ku, 808-0196 Kitakyushu (Japan)

Summary. This paper describes effects of shock waves on cells to certificate the angiogenesis by shock wave (pressure wave) in the clinical application such as ESW (Extracorporeal Shock Wave). Especially, to investigate the effects of shock waves on the endothelial cells in vitro, the cells worked by plane shock waves using shock tube apparatus are observed by microscope. The peak pressure working on the endothelial cells at the test case is 0.4 MPa. After working shock waves on suspended cells, the disintegration, shape and growth rate (area per one cell and population of cells) are measured by image processing. It is found that the younger generation cells have small differences of shape index, and the growth rate of the shock-worked cells from 0 to 4h are clearly high compared with control ones. It is concluded that once shock waves worked, some of them are disintegrated, but the other has capacity to increase growth rate of cell culture in vitro. This preliminary result will be applied to fundamental investigations about shock wave stimulus on several kinds of cells in future.

1 Introduction

Recently shock wave phenomena in living tissues are being widely applied in the fields of medical and chemical engineering, such as extracorporeal shock wave lithotripsy, drug delivery systems ([2]), bioprocess for environmental protection and tissue engineering. In the field of tissue engineering, the bone therapy to regenerate the bone by extracorporeal shock waves shows the possibility for new therapy. In our previous investigation ([3]), it was found that the all of cells are not disintegrated by high shock wave (0.5 MPa) that has small duration time (50ms). So it is expected that the soft cells such as endothelial cells, cardio cells have a potential to regenerate or growth fast by using high pressure and short duration time from 1 micro s to 100 ms. But lately, Shimokawa et al. reported that extracorporeal focused shock wave (focused shock wave) accelerated cardiogenesys using low level ESW in the clinical application ([5]). They showed the typical photograph of angiograph, which indicates angiogenesis (or cardiogenesys) by extracorporeal focused shock wave. From this excellent study, it is found that the shock wave has ability to regenerate tissue cells. Concerning about the effects of focussed shock waves on living tissue cells and tissues, generally speaking, the focused pressure field in the ESW device is too complicated to estimate worked pressure level, and there should be cavitation bubble near the focused region. Then it is necessary to investigate these fundamental phenomena for effects of shock waves on cell disintegration, growth rate, regeneration.

In this paper, to investigate the effects of shock waves on the endothelial cells in vitro, the cells by plane shock waves in the shock tube are observed by microscope and the growth rate and others are measured by image processing.

2 Experimental apparatus and methods

Endothelial cells were taken from the lumen of pig's aorta by abrading with knife. These cells were cultured on the dish filled with DMEM (GIBCO) including 10 % FBS and 1 % PSN antibiotic mixture in CO_2 incubator under the proper condition (Temperature 310 K, humidity 100%, 5% CO2). Subculture is proceeded by checking 70

As mentioned in the introduction, the key point of this investigation is to use shock waves by simplifying the pressure fields working on the cells. Shock waves to apply endothelial cells are generated by so-called shock tube (Fig.1) . This shock tube has a novel technique that has no diaphragm to generate plane shock waves easily. The feature of the shock tube apparatus is that (1) the shape of the wave is plane and (2) the duration time is long (several 10 ms) compared with laser shock wave and focusing shock wave. As for the apparatus, after several valve operations, the plane shock wave is propagating into the test case located at the wall end in Fig.1. In this test case, the cells were suspended in the cultured liquid and the top surface is wrapped with thin film to prevent the dropping liquid. The important point to set up the test cells is not to include gas bubbles in the wrapped test case, otherwise the effects of bubbles on the cells and pressure fields should be complicated.

Generally, there are two boundary conditions for endothelial cells in the shock wave apparatus. One is the effects of shock waves on suspended cells, the other is fixed cells on the culture dishes. In this paper, only the suspended cells are discussed because setting up the cells is simple operation. . The experimental conditions for shock waves are pressure ratio in the apparatus is 4, Mach number 1.4 in air, shot number is from 1 to 5. Here interval time for each shot of shock wave is 10 - 30 seconds. Figure 2 shows pressure history at the test case. From this result, the peak pressure in the pressure history in air

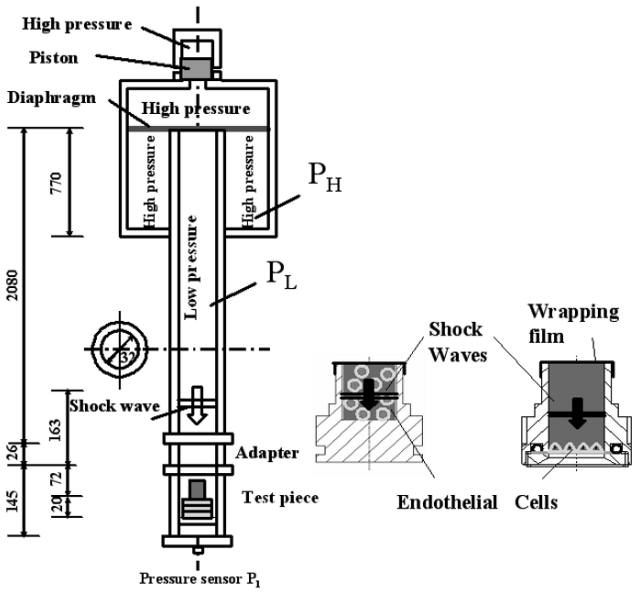

Fig. 1. The schematic of diaphragmless shock tube and test piece with film for shock

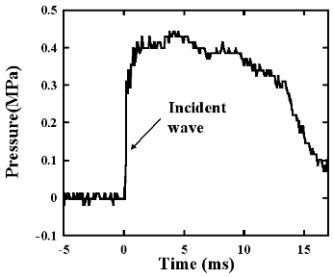

Fig. 2. Pressure history at tube end

at the test case is 0.4 MPa. The pressure sensor is located at the bottom of the shock tube (tube end), so the pressure of incident shock wave in air is estimated to be 0.2 MPa by considering the wave reflection. Then the pressure of incident shock wave in water is estimated to be about 0.4 MPa. The thickness of the shock wave in water is not clear, but usually considered to be several μm. After working shock waves on suspended cells, the disintegration, shape and growth (population of cells and area of cells) are investigated. Every conditions, there are at least one control and one worked cells.

3 Experimental results

3.1 Population of endothelial cells after shock waves

Before observing the deformation and growth of cells, the disintegration rate by shock wave should be checked because the survival number of cells is very important factor for estimating growth rate. The results has already shown that the maximum disintegration of endothelial cells are above 20% at shot number 5.

Concerning about the cell population in the image taken by phase contrast microscopy, it should be taken account of disintegration rate of cells after shock wave with shot number as follows; .

$$N_n = \frac{NS_n}{NS_0} \times (1 - \alpha) \tag{1}$$

Here N_n, N_0 means population of cells at n hours, and population of cells at 0 hour respectively. And N_n is normalized cell population. Figure 3 shows dimensionless population of cells history with shot number. From Fig.3, it is found that according to shot number the population of cells is increasing compared with control cells. In this figure, the population of cells can be counted in the image data, so the error bar and probability is not shown here. It is found that the growth rate of the shock-worked cells from 0 to 4h are clearly high compared with control ones. Especially in case of passage number 3, the population is rapidly increasing by 5 shots shock waves. Concerning about effects of the passage number on the population, the population of several hours of the passage number 3 is about twice as that of passage number 6. This fact also shows that the younger cells have the ability to increase themselves well as mentioned above.

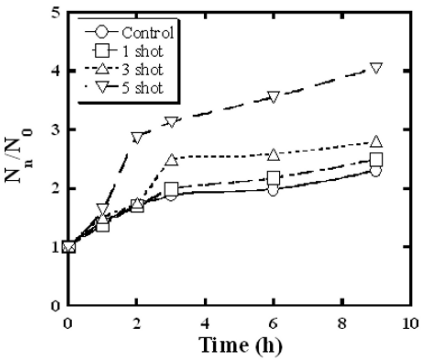

Fig. 3. Population of endothelial cells on the culture dish with shot number

3.2 Gene expression after shock waves

To confirm the capability of acceraltion of cell growth by shock wave, the gene expression is being tested test for these cells by PCR (Polymerase Chain Reaction) method. Quantity of gene expression is estimated as cycline D2

3.3 Discussion

From the above results, it should be discussed about the mechanical stimulus on the cells. Generally the thickness of shock wave is about several μ, this scale is almost the same scale as the cell itself. This scale is very importtant becuase the profile of mechanical stimulus is changed rapidly in the cell compared with other static stimulus.

Using this considerations, then following assumption can be considered. Once the shock wave applied the cell membrane, the cell membrane or the protein on the membrane senses the pressure gradient (normal stress and shear stress) more sensitively than that in case of quasi-static pressure, then the signal from the membrane protein is transmitted inside the cell.

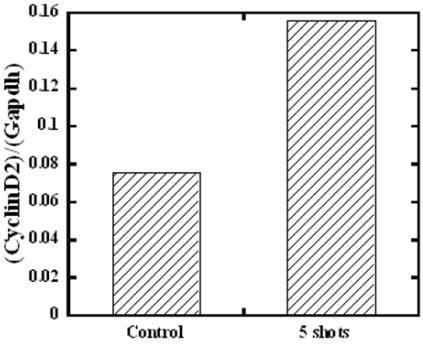

Fig. 4. Effect of shock waves on gene expression of endothelial cells

4 Analysis of propagating shock wave to cell model

4.1 Modeling of propagation shock wave to cell

The computational model is composed of following two stages; (1) Underwater shock wave propagates in the water region (fluid dynamic stage), (2) Propagating shock wave works to the hemisphere cell on the wall (solid dynamic stage). To connect these two computational stages, one dimensional visco-elastic wall model for the fluid-solid interface. The input pressure condition to work this model is important, then the rise time of the pressure wave (shock wave) is defined to be from 0.2 to 12 ns. In this computation, the step pressure with maximum pressure 0.2MPa is worked.

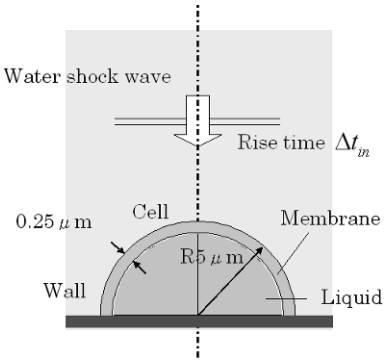

Fig. 5. Model of shock wave propagation to adhesive cell

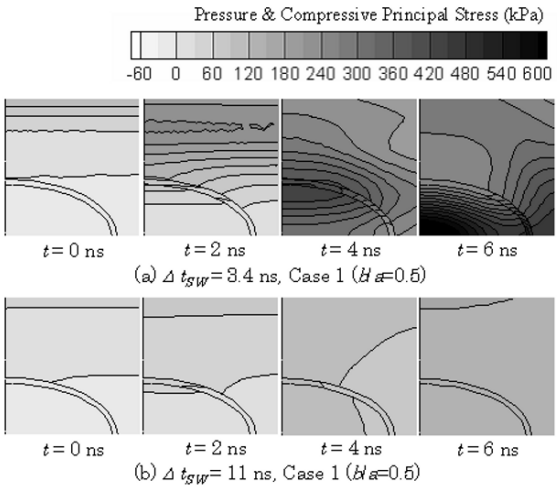

Fig. 6. Pressure and stress wave propagation between fluid and cell

4.2 Computational results and discussion

Figure 6 shows pressure contour after working shock wave to the cell model. Figure 6(a) shows the contour in the case of rise time 3.4 ns, Fig.6(b) shows that in the case of 11 ns. From this, it is cleary found that pressure gradient nrat the cell membrane for the short rise time is larger than that for the long rise time. Then it is considered that the shorter the rise time is, the larger shear stress gradient becomes in the range of 0.2-12 ns. The short rise time has possibility to give large stimulus to the cell membrane or cell.

5 Conclusion

To investigate the effects of shock waves on the endothelial cells in vitro, the cells by plane shock waves were observed. It is concluded that once shock waves worked, some of them are disintegrated, but the other has large ability to increase growth rate of cell culture in vitro. The growth of cells by plane shock waves is also confirmed by the fact that activated gene expression is enhanced. In addition to this, the shorter rise time is, the stimulus to the cell by pressure wave (shock wave) becomes.

In future works, effects of shock waves on the fixed cultured cells in the test case should be done to compare this work, because the normal endothelial cells are fixed on the tissues. And effects of pressure wave forms on the growth rate also should be done because it is important to distinguish the effects of pressure fields.

Acknowledgement. A part of this study was supported by Grants-in-Aid for Scientific Researchon Priority Areas (2) 15086213, Scientific Research (B) (2)16360092, Exploratory Research (2)16656065.

References

1. Ikeda, K.., Matsuda, M., Tomita, K., Takayama, K., Application of Extracorporeal Shock Wave on Bone: Basic and Clinical study, Proceedings of 22nd International Symposium on Shock Waves, Imperial collage, London, 5370, 1999
2. Tamagawa M, Yamanoi I, Fundamental Investigation for Developing Drug Delivery Systems and Bioprocess with Shock Waves and Bubbles, JSME Int'l J., C, 44-4, 1031, 2001
3. Tamagawa M, Akamatsu T, Effects of Shock Waves on Living Tissue Cells and its Deformation Process Using a Mathematical Model, JSME Int'l. J., C, 42-3, 640, 1999
4. Gerhardt, H., Golding, M., Fruttiger, M., Rhurberg, C., Lundkvist, A., Abramsson, A., Jeltsch, M., Mitchell, C., Alitalo, K., Shima, D., Betsholtz, C., VEGF guides angiogenic sprouting utilizing endothelial tip cell filopodia, The Journal of Cell Biology, Vol. 161-6, 1163, 2003
5. Nishida T, Shimokawa H, Sunagawa K et al., Extracorporeal Cardiac Shock Wave Therapy Markedly Ameliorates Ischemia-Induced Myocardial Dysfunction in Pigs in Vivo, Circulation, 9, 3055,2004

Application of shock waves in pencil manufacturing industry

G. Jagadeesh

Department of Aerospace Engineering, Indian Institute of Science, C.V. Raman Avenue, Bangalore - 560 012 India

Summary. A new shock wave generator has been designed, fabricated and tested for preservative impregnation studies into wood slats used for manufacturing pencils in the Shock Waves Laboratory, IISc, Bangalore. Series of experiments have been carried out in the laboratory to achieve satisfactory preservative impregnation into VATTA wood slats. The experiments have shown that it is indeed possible to impregnate preservatives into VATTA wood slats using shock waves and the depth of penetration and the retention of preservatives by wood slats is as good as the conventional methods. This method is expected to result in substantial reduction in the treatment process time compared to conventional methods that are currently being used by the pencil manufacturing industry.

1 Introduction

Shock waves have the ability to instantaneously enhance both static pressure and temperature behind them in any propagating media. In recent times, using the pressure and temperature jumps in a medium behind a shock wave, many innovative applications [1] in different fields are being conceived. While substantial progress has been made in research related to medical applications of shock waves no work has been reported to best of our knowledge on the possible use of shock waves in the area of wood preservation and conditioning. A number of wood preservatives (chemical formulations toxic to wood decay/destroying organisms like fungi, wood destroying termites, marine borers etc)have been developed and are currently in use for improving bio-resistance and thereby enhancing service life for different end uses.

Pencils are commonly made using soft wood. In India a soft wood colloquially termed as *Vatta* wood is used to cover the graphite rods in pencils. In the industry the *Vatta*wood goes through a series of processes including the most important initial stage where water soluble preservative is impregnated into the wood slats. By ensuring proper penetration of these preservatives in the wood the life of the pencils is enhanced. Water soluble preservative with includes a certain percentage of paraffin wax, fatty acids and food preservative is usually used in the pencil manufacturing industry for treating the *Vatta* wood slats. The conventional process currently used in the industry is called the pressure treatment and this usually takes about 8 hours of the manufacturing process cycle. The main focus of the present work is to develop a new shock wave assisted preservative impregnation system [2] for treating *Vatta* wood slats which might result in drastic reduction of process time. Some of the important details of the new technique are described in subsequent sections.

2 Experimental study and results

A new shock wave generator with capability to generate planar shock waves of requisite strengths in the driven section filled with a multi-component viscous fluid is designed, fabricated and tested in the Shock waves Laboratory, IISc, Bangalore. This shock wave generator (Fig.1) comprises of a cylindrical vessel to house the *Vatta* wood slats along with TWO vertical shock tubes. In addition two 6 kW heating rods are also provided inside the cylindrical vessel for heating the water soluble preservative to the required temperature. Figure 2 shows a photograph of the device.A metallic fixture is designed and fabricated to house the slats and orient them in the direction of propagation inside the cylindrical chamber.About 60 wood slats can be housed in one fixture and two such fixtures can be housed inside the cylindrical chamber. Figure 3 shows a photograph of the *Vatta* wood slats placed inside the chamber before the treatment. A fast acting pneumatic valve is used to generate the shockwave and this also enables repeated operation of the device in an industrial environment.

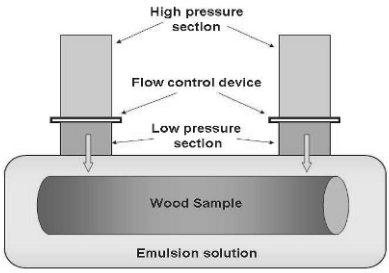

Fig. 1. Schematic diagram of the shockwave generator used in the present study

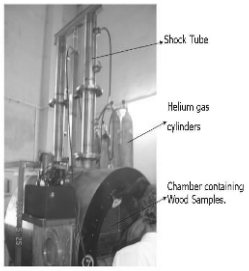

Fig. 2. A photograph of the shockwave generator used for impregnating water soluble preservative into wood

The wood slats fixed vertically in the fixture are completely immersed in the water soluble preservative solution before commencing the experiments. Electric immersion rods are used to enhance the temperature of the preservative solution(fatty acids, water, environmental friendly wood preservative chemicals and paraffin wax) to 70 deg. C. The preservative solution will be virtually boiling at this temperature and most of the paraffin wax would be in the liquid form. Once the required temperature is achieved then wood slats are subjected to shock wave loading.About 4 shots at requisite shock strength seems to give adequate penetration into the wood slats.The wood slats are weighed immediately

Fig. 3. A photograph of the vatta wood slats mounted inside the shockwave generator for treatment

after the treatment and after the samples are completely dry to evaluate the amount of preservative that has gone inside the wood. The depth of penetration and the amount of preservative retention will dictate the quality of the product made using the treated wood.

Figure 4 shows the photograph of the pencils manufactured using *Vatta* wood slats treated using shock wave assisted preservative injection system. The yellow colour wood samples are the raw samples before the preservative treatment. The wood samples after treatment (slightly reddish in colour) are further subjected to sharpenability tests to verify the efficacy of the present method. Although not shown here the pencils made from the wood treated with shock waves are very much comparable to the pencils manufactured from conventional methods. The complete process of shockwave assisted treatment is completed within 10 minutes and there is a great potential to reduce the process cycle time of the pencil manufacturing.

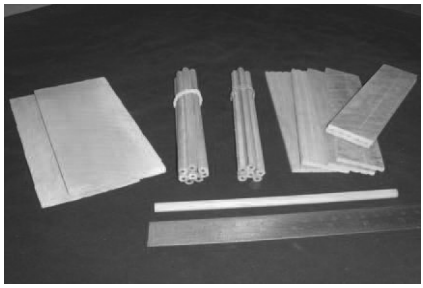

Fig. 4. A photograph of the pencils manufactured from the vatta wood slats treated with shockwaves

It is rather interesting to understand the basic physics involved in the preservative impregnation in wood because of shock wave loading. Any wood slat comprises of both soft wood and hard wood. A micrograph of the softwood sample is shown in Fig. 5. The wood is made up of neatly aligned capillary tubes which run along the longitudinal direction. These tubes are used for transport of fluids in plants or trees. It is speculated at this point of time that because of the shock wave loading the permeability of the wood is enhanced there by allowing more fluid to enter the interior regions through these capillary tubes. However further experiments are necessary to understand the complex shock interaction with a porous media like wood. In this case we also have hot multi-component fluid in which the wood slats are immersed when they are subjected to shock

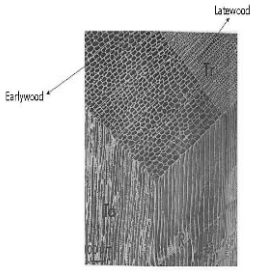

Fig. 5. A micrograph of the softwood

wave loading. The shock wave is generated in air subsequently interacts with the air and hot liquid interface before going through the vertically placed wood slats that are immersed in the hot fluid. Substantial attenuation of the shock wave takes place because of propagation in different media as well as because of heat addition in the hot fluid.

It is also observed during the experiments that the orientation of the wood slat plays a major role in the success of the present method. In the existing method in the industry the wood slats are just bundled together in a jute bag and dumped into the chamber where the entire system with preservative is maintained at a higher pressure for long hours. But the advantage is that you can treat large quantity of wood slats in one shot. One of the important aspects of the present method is we can use the same shock wave generator for drying of the wood slats unlike the conventional systems. We are currently working on shock wave assisted drying of the treated *Vatta* wood slats. Preservative penetration and drying process in the pencil industry consumes almost few days in the manufacturing cycle. In this context the proposed method holds lot of promise for enhancing productivity of pencil industry.

3 Conclusions

A new shock wave assisted preservative impregnation method is developed in IISc for treating *Vatta* wood slats used for making pencils.The results indicate that the quality of pencils made from shock wave treated wood is comparable to the pencils made from existing technology in the industry. The new method is expected to reduce the preservative treatment time in the pencil industry. Future efforts are aimed at extending this novel technique to other industrial applications and understand the underlying science of shock wave interaction with wood immersed in hot non-Newtonian fluids.

Acknowledgement. I would like to thank all the staff of HEA laboratory for the help during the experiments.

References

1. Jagadeesh G, Takayama K: J. of Indian Institute of Science **82**, (2002)
2. Jagadeesh G, K.N. Nataraja and M. Udayakumar: Pressure wave assisted techniques/devices for agriculture, Indian Patent No.454/CHE/2005.

Comparison of methods for generating shock waves in liquids

S. Dion, C. Hebert, and M. Brouillette

Department of Mechanical Engineering, Université de Sherbrooke, CANADA J1K 2R1

Summary. We present two methods for producing high-amplitude pressure pulses in liquids. The electromagnetic generator, commonly used in lithotripters, is difficult to reduce in size, lacks complete control over the pressure pulse and requires high-voltage electronics. On the other hand, a time-reversal method is used to generate high-power acoustic pulses with a low-power electronic piezoeletric transducer.

1 Introduction

As new biomedical and industrial applications of shock waves are emerging, the need to accurately and economically generate shocks is becoming more critical. Since a very large potential resides in biological and medical areas for diagnostic and therapeutic uses, shock waves need to be produced in liquids.

In the past, there have been a number of methods used to produce shock waves in liquids, all characterized by a large and rapid energy deposition, either through the detonation of an explosive, the dumping of electric energy through a spark gap, or the sudden acceleration of a piston, either by electromagnetic (EM) or piezoelectric means. There are well known shortcomings associated with each of these methods, such as the requirement for high-voltage electronics, the manipulation of explosives, insufficient deposited energy or the lack of control of the shock properties. The advantages and disadvantages of each method are summarized in Table 1.

Method	Advantages	Disadvantages
Explosive	Large shock amplitude	Dangerous handling Lack of control
Spark gap	Large shock amplitude	High-voltage
EM piston	Large shock amplitude	High-voltage
Piezolelectric	Ease of control	Low shock amplitude

Table 1. Advantages and disadvantages of common methods for producing shock waves in liquids.

This paper summarizes the results of a study into a conventional method (EM piston) of shock generation in liquids as well as a method exploiting the advantages of piezo generators while avoiding their shortcomings.

2 Electromagnetic (EM) piston generator

The EM shock wave generator comprises two main components, namely a 5-cm diameter coil/membrane assembly, shown in Fig. 1, and a high voltage discharge circuit shown in Fig. 2. This design is based on the device of Mortimer & Skews [1]. The EM generator incorporates a flat coil and a metallic membrane, both held in a non-conductive support. The high-voltage discharge circuit comprises a 25 kV high-voltage power supply, a high-capacity (4 μF) capacitor, a trigger module and a spark gap.

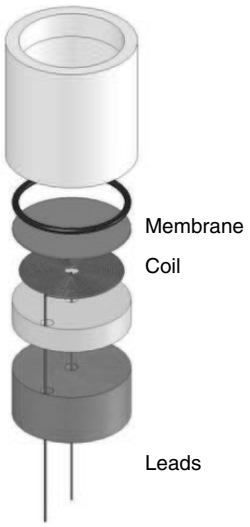

Fig. 1. 5-cm Electromagnetic shock wave generator.

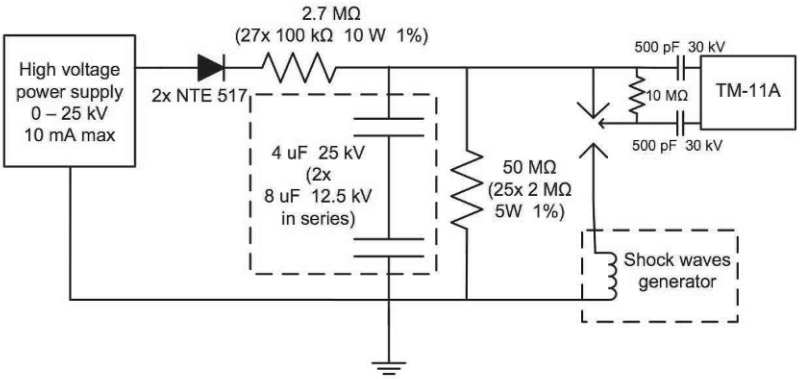

Fig. 2. High-voltage circuit for the electromagnetic shock wave generator.

Operation of the device starts by charging the capacitor with the power supply up to the desired potential. The capacitor's discharge is initiated via the trigger module (TM-11) through the spark gap, which rapidly dumps a high-voltage, high-current electrical pulse into the coil. The magnetic field generated by the coil induces surface currents into the metallic membrane which produce an opposite magnetic field. The resulting strong repulsion force between the coil and the membrane produces a large instantaneous acceleration of the membrane which displaces the water in front of it, which ultimately produces a shock wave. Because of the large repulsion forces within the coil, an initial attempt to operate a 2.5-cm diameter EM generator was not successful as the durability of the device was minimal. Figure 3 shows a typical pressure pulse produced by the 5-cm EM device; shock wave amplitudes up to 400 bars could be generated by the device, with very sharp rise and decay, of the order of 5 μs. Control over the pulse can be achieved solely via the control of the capacitor charge voltage, which basically modulates the pulse pressure amplitude. Once the mechanical and electrical hardware is set, it is not possible to vary the other physical parameters of the pressure pulse, such as pulse duration, for example. This shortcoming, combined with the severe material and safety requirements of high-voltage equipment, makes this method of shock wave generation not the most desirable, or at least, not the most general-purpose.

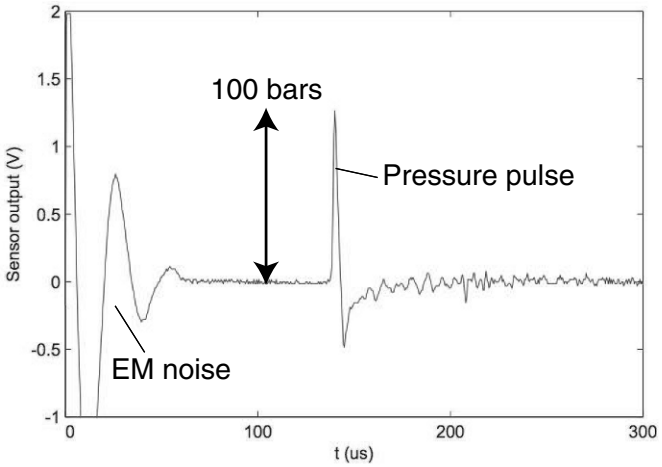

Fig. 3. Typical pressure-time history of shock wave produced with EM shock wave generator.

3 Piezodispersive generator

To minimize these shortcoming, we developed an acoustic pulse amplifier that allows for the controlled generation of high pressure shock waves from the a large number of low amplitude acoustic waves. This technique is based on Time-Reversal Mirror (TRM) technology, as described by Montaldo et al. [2] and Puckett & Peterson [3]. The main advantage of this method, compared to other means of generating high amplitude shocks in liquids, is that it does not requires high voltage equipment, thus considerably reducing cost and electromagnetic noise issues. Also, it can easily be scaled up or down.

First a reference signal is produced with a conventional piezoelectric generator, such as shown in Fig. 4 — this signal is used as the basis for subsequent signal processing. In this example the pressure pulse has an amplitude of about 5 bars and the main peak lasts for about 1 microsecond.

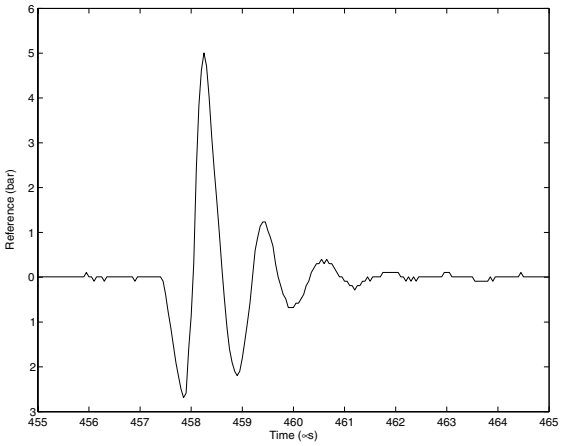

Fig. 4. Example of reference signal for the system.

Secondly, the reference signal is fed into one end of a multi-mode waveguide in order to temporally spread the signal, and the large-time-signature waveform is recorded at the other end with another generator operating as a pressure transducer. An example of a spread reference signal is shown in Fig. 5. We see that the original reference signal has now been temporally spread to over 200 microseconds.

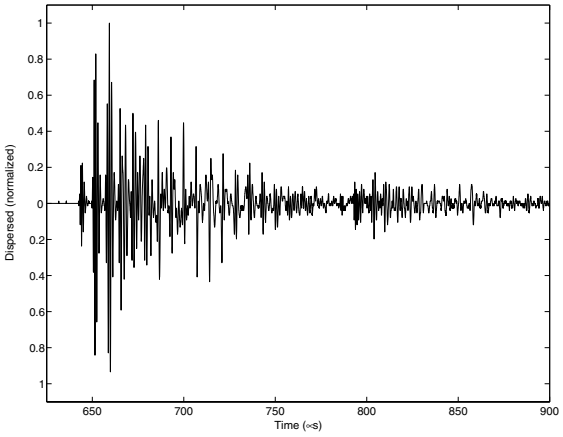

Fig. 5. Temporally-spread signal for the system.

Finally, the temporally-spread signal is time-reversed, amplified and fed back into the waveguide with the same generator. Temporally-inverse propagation thus takes place in the waveguide, leading to the constructive addition of all the pulses in the temporally-spread signal into a large amplitude pulse. Figure 6 shows the pressure trace from a shock wave generated with this device. We see that the amplitude is much larger than that of the reference signal with the same voltage excitation of the piezoelectric generator and, interestingly, the pressure pulse is much shorter than the reference signal (200 nanoseconds vs. 1 microsecond). The last figure actually shows two pressure pulses. The light one is obtained by amplifying the entire processed dispersed signal with the same gain, which leads to about a two-fold amplification from the reference pressure pulse. However, by first clipping the processed dispersed signal to a maximum amplitude, for example 25% as shown in the figure, and then amplifying the clipped signal, higher amplitudes are possible. Amplitudes comparable to those obtained with the EM device are achievable, which are much higher than pressures achievable with current single pulse piezoelectric shock generators.

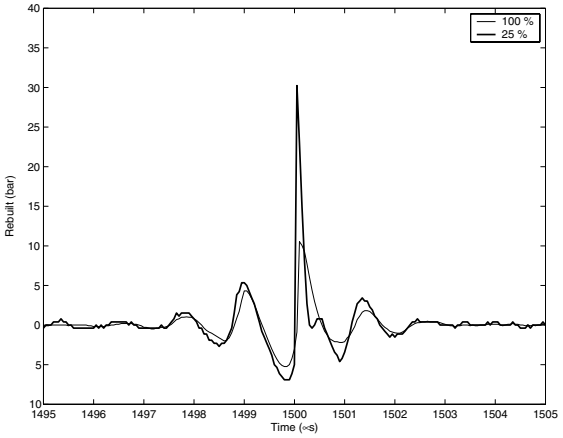

Fig. 6. Typical pressure-time history of shock wave produced with new shock wave generator.

By using different reference signals, a wide array of generated pressure pulses are possible simply by recalling the appropriate waveform from computer memory. Control over the features of the pressure pulse is thus possible with this method.

4 Conclusion

We have presented a conventional and a TRM method for producing high-amplitude pressure pulses in liquids. The EM generator, commonly used in lithotripters, for example, is difficult to reduce in size, lacks complete control over the pressure pulse and requires high-voltage electronics. On the other hand, the TRM method is able to generate high-power acoustic pulse with low-power electronic means while allowing full control.

References

1. Mortimer BJP, Skews B.: Journal of the Acoustical Society of America, **100:3548**, (1996)
2. Montaldo G, Roux P, Derode A, Negreira C, Fink M.: Journal of the Acoustical Society of America, **110:2849**, (2001)
3. Puckett A, Peterson ML.: Acoustic Research Letters Online, **4:31**, (2003)

Gas-phase synthesis of non-agglomerated nanoparticles by fast gasdynamic heating and cooling

A. Grzona[1], A. Weiß[1], H. Olivier[1], T. Gawehn[2], A. Gülhan[2], N. Al-Hasan[3], G.H. Schnerr[3], A. Abdali[4], M. Luong[4], H. Wiggers[4], C. Schulz[4], J. Chun[5], B. Weigand[5], T. Winnemöller[6], W. Schröder[6], T. Rakel[7], K. Schaber[7], V. Goertz[8], H. Nirschl[8], A. Maisels[9], W. Leibold[9], and M. Dannehl[9]

[1] *Shock Wave Laboratory, RWTH Aachen University, 52056 Aachen, Germany*
[2] *German Aerospace Center, Wind Tunnel Department, Linder Höhe, 51147 Köln, Germany*
[3] *Lehrstuhl für Fluidmechanik - Fachgebiet Gasdynamik, TU München, Boltzmannstr. 15, 85748 Garching, Germany*
[4] *IVG, University of Duisburg-Essen, 47048 Duisburg, Germany*
[5] *Institute of Aerospace Thermodynamics, Universität Stuttgart, Pfaffenwaldring 31, 70569 Stuttgart, Germany*
[6] *Institute of Aerodynamics, RWTH Aachen University, 52056 Aachen, Germany*
[7] *Institut für Technische Thermodynamik und Kältetechnik, Universität Karlsruhe, Engler-Bunte-Ring 21, 76131 Karlsruhe, Germany*
[8] *Institut für Mechanische Verfahrenstechnik und Mechanik, Universität Karlsruhe, Straße am Forum 8, 76131 Karlsruhe, Germany*
[9] *Degussa GmbH, Rodenbacher Chaussee 4, 63457 Hanau, Germany*

1 Introduction

Gas-phase synthesized nanoparticles are broadly used in industry, science and measurement technology. Today flame synthesis and hot-wall synthesis are the most widely used methods for industrial production with an annual volume of several million tons. Remarkable is, that the morphology of the synthesized particles does not vary significantly. Most of them are aggregates with a fractal dimension of 1.8 - 1.9 and a geometric standard deviation of the size distribution in the range of 1.5 - 1.7. Former studies indicate that a homogeneous flow field and high heating and quenching rates are of major importance to achieve narrow size distribution and low aggregation. [1]

Therefore, in the frame of the project "Gasdynamically induced nano-particles" supported by the Deutsche Forschungsgemeinschaft (DFG) a novel method for the production of oxide nanoparticles from gas-phase precursors in a shock-wave flow reactor is

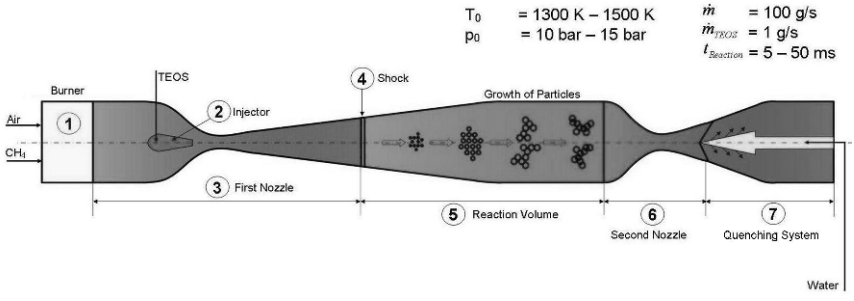

Fig. 1. Principle of operation

presented in this paper. In contrast to conventional methods the gas mixture is instantaneously heated by a stationary shock wave of an overexpanded supersonic nozzle flow. An overview of the principle of operation is given in Fig. 1. Following the injection of the precursor gas (2) the flow accelerates to supersonic flow speed and the reaction is initiated by shock wave heating (4). Chemical processes lead to the generation and growth of nanoparticles in the reaction chamber (5). After an adjustable reaction time depending on the gas velocity and the reactor length, the reaction is terminated due to rapid expansion and, therefore, cooling of the gas in a convergent-divergent nozzle flow (6). The total enthalpy of the flow is finally reduced by injecting water in a quenching system downstream of the second nozzle exit (7). This work is focused on numerical and experimental investigations of the underlying fluid-dynamic and chemical-kinetic requirements, to compose a design strategy of a pilot facility.

2 Numerical Simulation and Comparison with Experiment

The basic layout of the first nozzle (3) is defined by the pre-shock Mach number, the design mass flow rate and the distance from the injection location of the precursor to the shock location. The minimum of this distance follows from the required mixing length of the precursor with the air. The maximum allowable length is prescribed by the ignition delay of the precursor under the given thermal conditions. The throat area of the second nozzle (6) has to be matched, according to the change of the critical density and total temperature as a result of the shock losses, the viscous losses, the reactive heat addition and the wall cooling. In Fig. 2a the static temperature distribution along the axis of the facility is depicted as result of a 3-D numerical simulation. The turbulent simulation (SST-model) includes the effects of the reactive heat addition, wall cooling and temperature dependent fluid properties. In this case the reactive heat is modeled by a prescribed heat addition. The timescales of the shock induced temperature rise and of the aerodynamic quenching are in the order of $\Delta t \approx O(10^{-5}s)$.

The flow accelerates through the first nozzle (3) and reaches the design pre-shock Mach

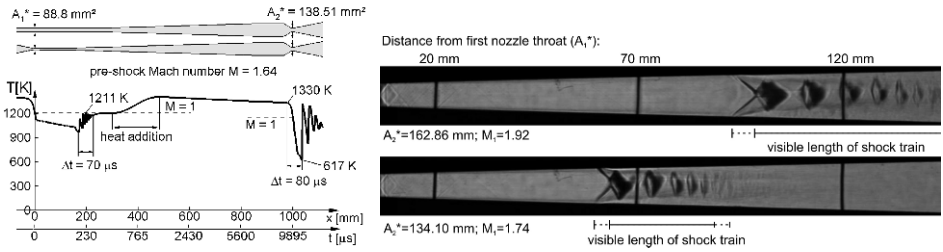

Fig. 2. (**a**) Static temperature distribution along axis - left, 3-D Navier-Stokes simulation (SST-model) supersonic reactor, wall cooling, prescribed heat addition, $Q = \frac{q}{c_p T_{01}} = 0.181$, $T_{01} = 1400\,K$, $p_{01} = 10\,bar$, $p_{exit} = 1.3\,bar$ (**b**) Schlieren pictures of the shock system in the first nozzle for different second throat cross sectional areas - right, experiment at low temperature condition, $T_{01} = 292\ K$, $p_{01} = 4.786\ bar$

number of $M = 1.64$. A well defined sudden temperature rise that leads to instantaneous ignition and precursor decomposition would be achieved by a single normal shock (4). In the actual setup the turbulent boundary layer ahead of the shock is relatively thick

and causes substantial shock/boundary layer interactions. Therefore, the single shock disintegrates into a so called pseudo-shock system; i.e., into a sequence of periodic compression and expansion regions [2], Fig. 2b. The shock system length is depending on the pre-shock Mach number. A pre-shock Mach number change from $M = 1.92$ to $M = 1.74$ results in a decreased shock system length as can be seen in Fig. 2b. Such a shock system leads to a final Mach number immediately downstream of the shock train close to $M = 1$. In order to get closer to the result of a normal shock it is planned to apply active and passive control techniques in the area of the shock boundary/layer interaction. To validate the numerical results prior to the realization of the pilot facility, experiments with non-reactive gases at low temperatures were performed. Figure 3 shows the comparison of 3-D numerically and experimentally obtained static pressure distributions on the side wall (a) as well as experimental and numerical Schlieren pictures of the shock structures and locations (b).

The reaction is modeled by three separately treated parts. The primary reaction is the

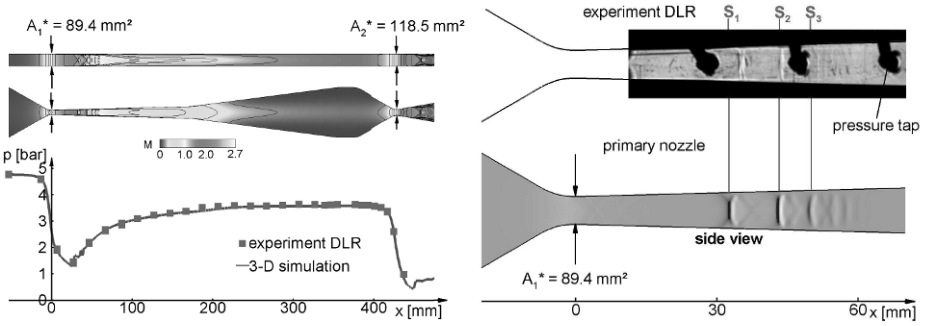

Fig. 3. (**a**) Static pressure distribution on sidewall - left (**b**) numerical/experimental Schlieren picture - right $T_{01} = 292\,K$, $p_{01} = 4.786\,bar$, $p_{exit} = 1.3\,bar$, pre-shock Mach number $M = 1.55$, air, dark areas on Schlieren picture due to pressure tabs on sidewall

decomposition of the precursor and the production of monomers. It is modeled by a one step reaction described by an Arrhenius equation. The secondary reaction, the formation of critical nuclei is modeled by classical nucleation theory (CNT). The tertiary reaction is the particle growth by surface condensation, coagulation and single-aggregation. To simulate the particle growth a local polydisperse, unimodal formulation based on the method of moments is used [3]. This method describes the local particle size distribution caused by turbulent mixing and the coagulation.

3 Investigation of Precursor Injection and Mixing

Rapid mixing of the precursor with the surrounding hot gas flow is crucial to ensure a homogenous mixture of the reactants and to prevent pre-reactions before entering the shock wave region. For this purpose new injectors are developed and tested in a supersonic wind tunnel, to determine the required injector design and mixing length. Additionally Large Eddy Simulation (LES) is used to analyse the mixing process of the precursor with the hot gas flow. The precursor is injected to the subsonic region ahead of the throat of a convergent-divergent Laval nozzle through a series of holes at the trailing edge of the injector. The injection concept is based on a large velocity difference between the hot

gas flow and the injected precursor flow, to generate a strong shear layer and thereby enhance the mixing process. All different types of injectors tested were designed to work in optimal conditions at an injection Mach number of the surrounding flow of M = 0.6. Laser-induced fluorescence (LIF) imaging is used for visualization of the mixing process. This method allows in-situ observation without influencing the process [4]. For the present experiments toluene, a well-studied fluorescent tracer, diluted in nitrogen is used as a substitute of the precursor. The beam of a frequency-quadrupled Nd:YAG laser (266 nm) is formed to a light sheet (0.5 mm thick, 25 mm wide) and passed the flow channel from bottom to top at various positions. An intensified CCD camera is used to record the fluorescence signal. An exemplar experiment of several investigations is shown in Fig. 4a. In this particular experiment the mass flow of the main air stream is 440 g/s. A mass flow of 0.583 g/s toluene diluted in nitrogen 10 l/min is injected at $M = 0.7$. Downstream of the injector a strong LIF signal can be observed. It decreases with increasing distance to the injection because of dilution with air and quenching by oxygen.

The mixing process of the precursor with the hot gas flow is simulated by LES, since so-

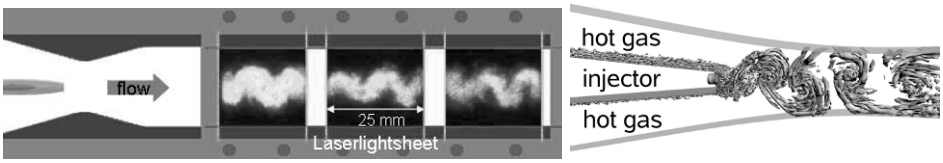

Fig. 4. (**a**) Visualisation of TEOS injection and mixing process by means of LIF - left (**b**) vortex contours from LES colour coded with the pressure - right

lutions based on the Reynolds averaged Navier-Stokes equations cannot predict the wake flow field of the injector with strong embedded vortices with sufficient accuracy. Figure 4b shows the vortex structure for a local Mach number of $M = 0.66$ at the trailing edge of the injector. From the simulation results the relation between mixture homogeneity and geometric parameters like nozzle and injector configuration as well as fluid mechanical parameters such as velocitiy ratio (hot gas flow over injector flow), density ratio, mass-flux ratio and angular momentum can be determined. Different approaches to enhance the mixing performance like vortex generators to create longitudinal vortices and inclined injection jets will be considered and also investigated in experiments. The comparison of experimental results and numerical simulations will be used for mutual validation.

4 Precursor Decomposition, Particle Growth and Measurement

The ignition delay times of tetraethoxysilane (TEOS) are measured in a shock tube of 80 mm internal diameter with a driver section length of 3.8 m and a length of the driven section of 7.2 m. The driver section is filled with helium and an aluminum diaphragm is deployed to achieve the desired pressure difference. Ignition delay times of TEOS mixtures (1 mass percent TEOS in synthetic air) are measured by monitoring the chemiluminescence CH*-signal near 431 nm for frozen post-shock temperatures ranging from 1150 to 1350 K at an average pressure of 8 bar. Both pressure and CH*-emission histories are obtained from a sidewall measurement to determine the ignition delay time. The results of these experiments are depicted as an Arrhenius representation in Fig. 5a showing that the presence of moisture in the mixture increases the ignition delay times of TEOS. Equations to calculate the ignition delay times τ are obtained and are also presented in the figure.

An important aspect of the production of SiO_2 nanoparticles is the characterization of the product. Small-angle X-ray scattering (SAXS) is a powerful technique to characterize particles in the expected size. A single online measurement is sufficient to determine particle size, size distribution, specific area and fractal dimension simultaneously [5]. The used SAXS camera is based on a development of Kratky [6]. With respect to the distinct design of the shock-wave reactor the camera body is splitted to integrate the reaction chamber into the measurement section and to operate the camera while the production of particles is running. Therefore, two major changes are made. A multilayer X-ray mirror (Göbel mirror), which collimates the divergent X-rays into a parallel and monochromatic beam with high brilliance, is established inside the camera and the one-dimensional, gas-filled detector is replaced by a two-dimensional imaging plate detector. Owing to these changes intensity and image quality are increased. Also the solid-state detector can provide higher counting rates and exhibits an efficiency three times as high as the gas-filled detector which leads to a significantly reduced measurement time.
To characterize particles offline a particle sample is extracted from the reaction chamber by a water-cooled probe. It possesses an outside diameter of 7 mm and is composed of four capillaries (Fig. 5b). Nitrogen is used to dilute the sample at the entrance of the probe. Thus, fast quenching of the sample is possible and chemical reactions as well as particle coagulation are stopped immediately [7]. For investigation purposes the particles are separated on a depth filter that can additionally be equipped with a TEM-grid for further analysis.

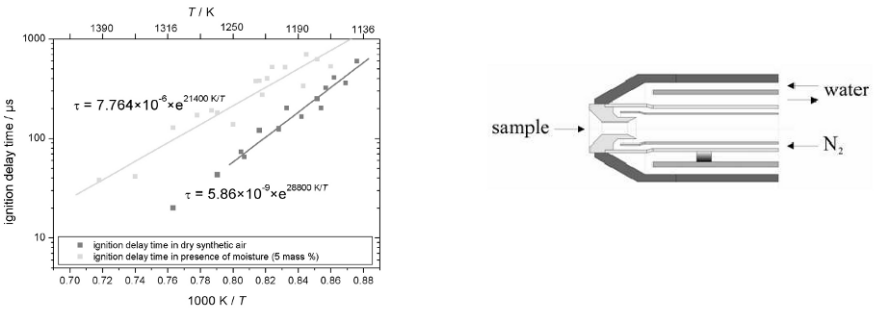

Fig. 5. (**a**) Ignition delay times τ of tetraethoxysilane mixture in dry air (red) and in presence of moisture (green) - left. $[H_2O] = 5$ percent per mass. (**b**) Schematic representation of the sampling probe - right

5 Gasdynamic and Evaporative Quenching

Downstream the reaction chamber particle growth is terminated by the cooling effect of a rapid gasdynamic expansion, thereby accelerating the flow up to a Mach number of 2.5. Subsequently to the gasdynamic cooling the specific enthalpy of the gas stream is reduced by evaporation of injected water. Depending on the gas temperature at the inlet of the second nozzle, a mass flow rate of cooling water between 24.2 and 36.1 g/s is required to prevent exceeding the working temperature of the following exhaust system. Figure 6a shows a basic sketch of the quenching system. The cooling water is fed into the gas stream by injection nozzles, which are distributed on the circumference of a slender

cone placed at the nozzle center line and on the surrounding wall to cover the entire cross section. The inlet pressure varies between 8 and 11 bar. At the injection point of the water jets a normal shock is formed which turns into an oblique shock downstream. High relative velocities between gas flow and water disperses the jet into fragments in the order of 10^{-5} m and smaller. A large specific phase interface is created to enhance water evaporation. Thus evaporation directly counteracts the temperature rise due to the shock system. An experimental Schlieren image of water injection into a supersonic gas flow is shown in Fig. 6b. At the position of the injection the local Mach number is about 2.3. Because in this case the gas is only preheated up to 320 K, this flow does not include water evaporation.

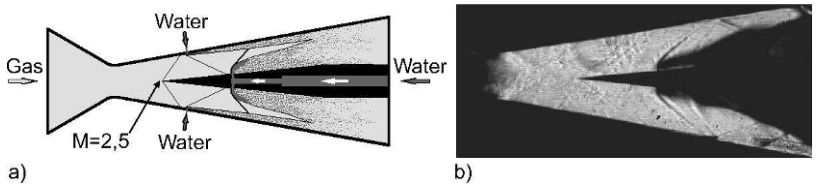

Fig. 6. (**a**) Basic sketch of the quenching system - left (**b**) Schlieren-image of water injection into a supersonic gas flow - right

6 Conclusion und Outlook

A concept for a new shock-wave reactor for producing nanoparticles starting from the gas-phase is presented. Preliminary studies of the gasdynamic behavior of the shock system, the precursor mixing and the water injection have been carried out numerically and in experiment. The gained knowledge is utilized to design and build up a pilot facility which in the near future will be used for experimental studies, including the generation of nanoparticles.

References

1. Schild, A., Gutsch, A., Mühlenweg, H., Pratsinis, S.E., "Simulation of nanoparticle production in premixed aerosol flow reactors by interfacing fluid mechanics and particle dynamics", J. Nanoparticles Res. 1, 305-315, (1999)
2. Matsuo, K., Miyazato, Y., Kim, H.D., "Shock train and pseudo-shock phenomena in internal gas flows", Progress in Aerospace Sciences 35, 33-100, (1999)
3. Friedlander, S.K., "Smoke, Dust and Haze. Fundamentals of aerosol dynamics",Oxford University Press, Oxford, New York (2000)
4. C. Schulz, V. Sick, "Tracer-LIF diagnostics: Quantitative measurement of fuel concentration, temperature and air/fuel ratio in practical combustion situations", Prog. Energy Combust. Sci 31, 75-121 (2005)
5. G. Beaucage, H.K. Kammler, S. Pratsinis, "Particle size distribution from small-angle scattering using global scattering functions", Aplied Crystallography, 37, 523, (2004)
6. O. Kratky, "Neues Verfahren zur Herstellung von blendenstreuungsfreien Röntgenkleinwinkelaufnahmen", Z. Elektrochem. 58, 49, 53, (1954)
7. H.K. Ciezki, B. Schwein, "Investigation of gaseous and solid reaction products in a Stepp combustor using a water-cooled sampling probe", AIAA-paper 96-2768, (1996)

Large-scale simulation for HIFU treatment to brain

Y. Nakajima[1], J. Uebayashi[2], Y. Tamura[2], and Y. Matsumoto[3]

[1] *Intelligent Material and Mechatronics Systems, Toyo University Kawagoe, 350-8585 (Japan)*
[2] *Computational Science and Engineering, Toyo University Kawagoe, 350-8585 (Japan)*
[3] *Mechanical Engineering, University of Tokyo Bunkyo-ku, Tokyo, 113-8656 (Japan)*

Summary. The focused ultrasound wave attracts attention in the medical field in various applications such as High Intensity Focused Ultrasound (HIFU). Amount of sound energy is generated by focused ultrasound in the body of narrow area. Present HIFU treatment cannot be applied to the part surrounded by bones, such as brain, because focal point is changed by refraction and reflection of ultrasound. In this research transskull ultrasound propagation is analyzed by finite difference method for HIFU treatment to brain. Assumption of isentropy and small disturbance of Euler equation gives the governing equation. The density and speed of sound of each medium are given at the center of Cartesian grid cells so as to model arbitrary human body from Computerized Tomography scan images. Transskull focused ultrasound is simulated to examine the effect of the inhomogeneity of the skull and ultrasound frequency to the focus.

1 Introduction

The focused ultrasound wave attracts attention in the medical field in various applications. Amount of sound energy is generated by focused ultrasound in the body of narrow area [1]. It is converted to sound pressure and thermal energy for medical treatment, such as Extracorporeal Shock Wave Lithotripsy (ESWL), High Intensity Focused Ultrasound (HIFU) [2] [3] and so on. In ESWL system, the strong sound pressure is generated by focused ultrasound and calculus is fractured by sound pressure. In HIFU system, the thermal energy is generated by focused ultrasound. Ultrasound is non-invasive and the treatment using focused ultrasound is suitable for medical application.

Present HIFU treatment is only used for superficial part such as prostate, breast and so on and cannot be applied to the part surrounded by bones, such as brain, because focal point is changed by refraction and reflection of ultrasound. In order to apply HIFU treatment to brain, we propose a simulation method to analyze focused ultrasound propagation.

In this research transskull ultrasound propagation is analyzed by finite difference method. Assumption of isentropy and small disturbance of Euler equation gives the governing equation. The density and speed of sound of each medium are given at the center of Cartesian grid cells so as to model arbitrary human body.

The data of human head would be input into computational grid by Computerized Tomography scan (CT scan) [4]. CT scan image is used to measure internal density of skull. Bone has various density and speed of sound. The skull has three-layered structure, structure of porous zone layer, and dense layers. Structure of porous zone is very inhomogeneous. Porosity map is directly linked to CT scan data, called Hounsfield value. Density map and speed of sound map of skull are deduced from porosity map [5].

In the second section the numerical method and the scheme are described. In the third section simulated is three-dimensional transskull focused ultrasound with different frequencies.

2 Numerical method

2.1 Computational grid

The data of human skull by Computerized Tomography scan (CT scan) would input into computational grid. Thus Cartesian grid is used in order to simply input arbitrary shape of human skull. Equal-spacing grid is formed and used throughout the research.

As described in the next part, the density and the speed of sound represent a variation of media in a human body. The values of each medium are given at the center of grid cells so as to simulate arbitrary organs in a human body.

2.2 Governing equation

A governing equation is derived from Euler equation as

$$\frac{\partial^2 p}{\partial t^2} = c^2 \rho \left[\frac{\partial}{\partial x} \left(\frac{1}{\rho} \frac{\partial p}{\partial x} \right) + \frac{\partial}{\partial y} \left(\frac{1}{\rho} \frac{\partial p}{\partial y} \right) + \frac{\partial}{\partial z} \left(\frac{1}{\rho} \frac{\partial p}{\partial z} \right) \right] \tag{1}$$

under assumption of isentropy and small disturbance, where p is acoustic pressure field (scalar), t is time, $\rho(\mathbf{r})$ is the density, $c(\mathbf{r})$ is the speed of sound and $\mathbf{r} = (x, y, z)$ is the position vector.

Equation (1) is discretized as

$$\left. \frac{p^{n+1} - 2p^n + p^{n-1}}{(\Delta t)^2} \right|_{j,k,l} = c^2 \rho \left[\delta_x \left(\frac{1}{\rho} \cdot \delta_x p \right) + \delta_y \left(\frac{1}{\rho} \cdot \delta_y p \right) + \delta_z \left(\frac{1}{\rho} \cdot \delta_z p \right) \right]_{j,k,l}^{n+1} \tag{2}$$

where, $\delta_{(\cdot)}$ is a central difference operator of second or forth order accuracy.

Equation (2) is then second order in time and second or forth in space, and solved by SOR (Successive Over Relaxation) method.

2.3 PML boundary condition

We introduce PML (perfectly matched layer) boundary proposed by Berenger [6] as outer boundary condition in order to prevent fictitious reflections. The original PML boundary gives a dumping term in either x, y or z direction of momentum equations while the dumping terms appear in every direction in the present calculation because we only use one governing equation. Starting again from the Euler equations, one finally obtains,

$$\frac{\partial^2 p}{\partial t^2} = c^2 \rho \left[\frac{\partial}{\partial x} \left(\frac{1}{\rho} \frac{\partial p}{\partial x} \right) + \frac{\partial}{\partial y} \left(\frac{1}{\rho} \frac{\partial p}{\partial y} \right) + \frac{\partial}{\partial z} \left(\frac{1}{\rho} \frac{\partial p}{\partial z} \right) \right] - (\alpha + \beta) \frac{\partial p}{\partial t} - \alpha \beta p. \tag{3}$$

From the matching condition to cancel the fictitious reflection, $\alpha = \beta$ and

$$\alpha = \beta = a \left(\frac{d}{D} \right)^2 \tag{4}$$

is adopted. Here D is the width of PML region, d is the distance from the true boundary in the PML region and a is an arbitrary coefficient.

2.4 Verification of the code

The present code solving Eq. (3) was verified with intensive computations and comparison with the corresponding experiments. The details are found in [7], [8].

3 Transskull focused ultrasound

3.1 Acoustic feature of the skull from CT scan data

In this section, CT scan data is used to make skull model. Figure 1 shows the CT scan of three-dimensional skull used in this research. CT scan image is used to measure internal

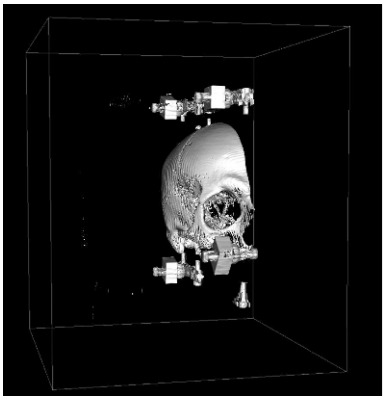

Fig. 1. Computerized tomography scan of three-dimensional skull

density of skull. Skull has various density and speed of sound. The skull has three-layered structure, structure of porous zone layer, and dense layers. Structure of porous zone is very inhomogeneous. Acoustic features of water and skull used in this research are shown in Table 1. The porosity map is directly linked to CT scan data, called Hounsfield value.

	Speed of sound [m/s]	Density [kg/m^3]
Water	1500	1000
Skull	2900	1900

Table 1. Acoustic feature of water and skull

Actual process of making skull model from CT scan data is as follows.

(a). The Hounsfield value is defined by Eq. (5) where μ_x is absorption coefficient of X-ray at each point, μ_{water} is water absorption coefficient of X-ray and μ_{bone} is bone absorption coefficient.
(b). Data of calculation area is extracted.
(c). Porosity distribution Φ is calculated from Hounsfield value distribution by Eq. (6).

(d). Speed of sound is defined by Eq. (7).
(e). Density is defined by Eq. (8)

$$H = 1000\frac{\mu_x - \mu_{water}}{\mu_{bone} - \mu_{water}} \tag{5}$$

$$\Phi = 1 - \frac{H}{1000} \tag{6}$$

$$c = c_{water} + (c_{bone} - c_{water}) \times (1 - \Phi) \tag{7}$$

$$\rho = \Phi \times \rho_{water} + (1 - \Phi) \times \rho_{bone} \tag{8}$$

Figure 2 shows porosity distribution (right) derived from slice of CT scan data (left). Speed of sound and density distribution are then determined from Eqs. (7) and (8).

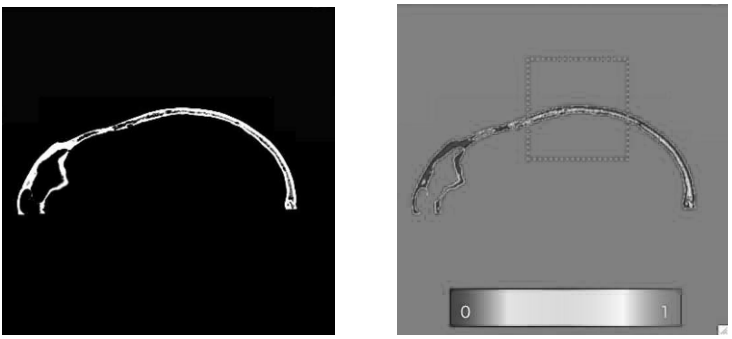

Fig. 2. Slice of the three-dimensional skull data (left) and porosity distribution of the slice (right).

3.2 Simulation of transskull focused ultrasound

Problem setup

As shown in the left of Fig. 3, 66mm×66mm×66mm area is divided into 500^3 grid points where the piezotransducer of 40mm diameter is placed just above the skull. Whole area is filled with water. 0.55MHz and 1.1MHz ultrasound are examined to see the dependency of frequency. The right of Fig. 3 shows an instantaneous pressure distribution of transskull focused ultrasound. Reflected waves and penetrated waves (indicated by red and blue surfaces) are observed.

Penetration, reflection and refraction of waves within the skull

Isosurface of high pressure area around the skull is shown in Fig. 4 when the third wave is penetrating the skull bone. Very high pressure area appears in the bone of high porosity area (left). Area of twice of input pressure level wraps around the high porosity area (center) and part of the waves penetrates the skull with the pressure level of the same of

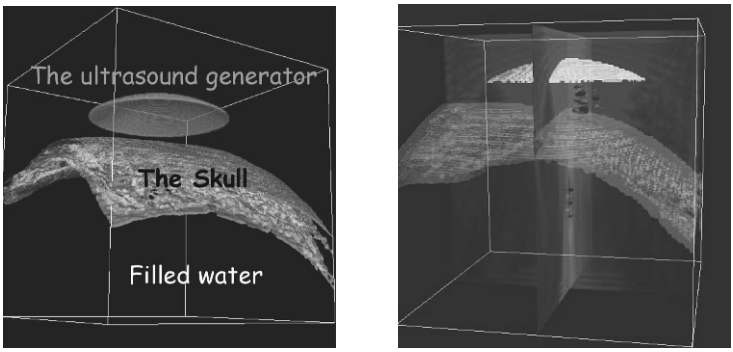

Fig. 3. Setup of transducer and skull (left). Instantaneous pressure distribution of transskull ultrasound (right).

input and also part of the waves reflect at the skull (right). These figures suggest that the behavior of the transskull ultrasound heavily depends on the shape and the composition of the skull.

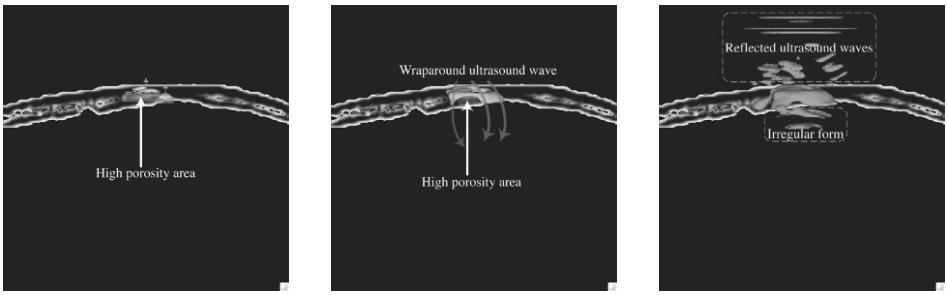

Fig. 4. Isosurface of instantaneous pressure. 4 times (4×) of input pressure level (left). 2× (center). 1× (right).

Dependency of frequency

Ultrasounds of 0.55MHz and 1.1MHz are examined. Figure 5 shows the maximum pressure distribution within a plane and isosurfaces of 1/2 of peak pressure at the focal point. In both cases, ultrasound penetrates the skull and is focused at a certain area. However the shape and the size of the focal area differ. The higher frequency waves have the shorter wavelength and they tend to reflect the inhomogeneity of the skull more. The present result suggests that the control of ultrasound generation both in amplitude and phase be necessary for real applications of HIFU treatment to sharpen the focal point.

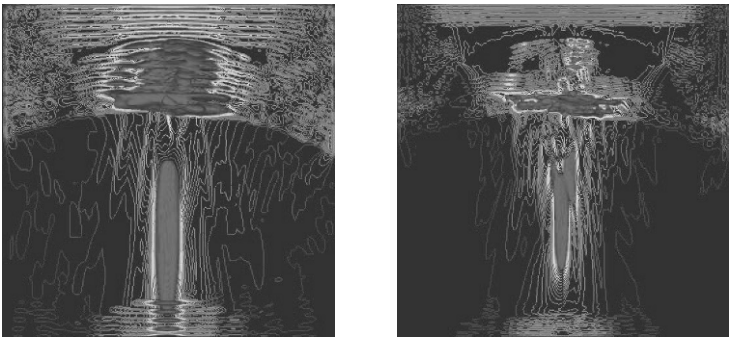

Fig. 5. Maximum pressure distribution of transskull ultrasound. 0.55MHz (left). 1.1MHz (right).

4 Conclusions

In order to apply HIFU treatment to brain, we proposed the method to analyze transskull focused ultrasound based on the CT data of skull and successfully simulated the behavior of penetration, reflection, refraction and focusing of ultrasound in a different media. The high porosity area in the skull bone strongly reflects the ultrasound. The resultant shape of penetrating ultrasound also depends on the frequency. In the next step, absorption by the media should be incorporated into the simulation and will be compared with transskull experiments.

Acknowledgement. The present authors would like to thank Professor M. Fink and Dr. J. -F. Aubry of Ecole Supérieure de Physique et de Chimie Industrielles de la Ville de Paris for providing the three-dimensional CT scan data of the skull.

References

1. Haar, G. T.: Acoustic Surgery. *Physics Today*, 54 (12): 29–34, December 2001.
2. Kennedy, J. F., et al.: High-Intensity Focused Ultrasound for the Treatment of Liver Tumors. *Ultrasonics*, 42 (1-9): 931–936, April 2004.
3. Matsumoto, Y., et al.: Medical Ultrasound with Microbubbles. *Experimental Thermal and Fluid Science*, 29 (3): 255–265, March 2005.
4. Aubry, J. -F., et al.: Relations of Mechanical Properties to Density and CT Numbers in Human Bone. *Medical Engineering & Physics*, 17 (5): 84–93, July 2003.
5. Rho, J. Y., et al.: Experimental Demonstration of Non Invasive Transskull Adaptive Focusing Based on Prior CT Scans. *Journal of Acoustical Society of America*, 113 (1): 323–399, 1995.
6. Berenger, J. -P.: A Perfectly Matched Layer for the Absorption of Electromagnetic Waves. *Journal of Computational Physics*, 114 (2): 185–200, October 1994.
7. Nakajima, Y., et al.: Analysis of Ultrasound Propagation for the Development of the Noninvasive Oncotherapy Device. Selected Articles of the 1st International Conference on the Design Engineering and Science, 79–83, June 2006.
8. Nakajima Y., et al.: Numerical Simulation of Transskull Focused Ultrasound. ECCOMAS-CFD 2006, 149.pdf, September 2006.

Study on application of shock waves generated by micro bubbles to the treatment of ships' ballast water

A. Abe, H. Kanai, H. Mimura, S. Nishio, and H. Ishida

Graduate School of Maritime Sciences, Kobe University
Fukaeminami-machi, Higashinada-ku, Kobe 658-0022, Japan

Summary. This paper reports the fundamental study for development of a ships' ballast water clarifying treatment technology using shock pressures generated by the collapse of micro bubbles. From the microscopic observation, it was confirmed that micro bubbles less than 65 μm in diameter became small in size and disappeared, and the shock wave generation by their collapse was observed by optical visualization method and pressure sheets. The bio-experiments using a marine *Vibrio* sp. were carried out under the three conditions: (1) only use of micro bubbles, (2) only use of 20 kHz ultrasonic waves, and (3) simultaneous use of them. The number of survival cells was investigated under the respective conditions for 12 hours. The inactivation effect on the marine *Vibrio* sp. by simultaneous use of micro bubbles and ultrasonic waves indicated better inactivation than that by the only use of micro bubbles or ultrasonic waves.

1 Introduction

It has been pointed out that ships' ballast water is one of causes of divergence of the marine ecosystem [4]. The development of ballast water clarifying treatment system is an important assignment in the field of maritime sciences. Recently, extensive studies on the treatment of ships' ballast water have been carried out (for example, see [6]). In order to solve the issue of the marine environmental preservation, the authors proposed a new treatment technique of ship's ballast water as a mechanical technology for the inactivation of marine bacteria. The concept of the clarifying treatment method is to use the pressure of shock waves generated by collapse of micro bubbles. They considered that several hundreds MPa of shock pressure generated by collapse of micro bubbles can inactivate marine bacteria at the local micro space around bubbles [3]. If the shock pressure is effective to the inactivation of marine bacteria, it enables us to treat large amounts of ships' ballast water effectively. In general, application of micro bubbles has been studying in the fields of engineering, biology, medicine, etc (for example, see [1,5,7]). However, no reports on the inactivation of marine bacteria directly using micro bubbles were found. In addition, the characteristics of micro bubbles have not been understood well enough. In this study, in order to examine a possibility of inactivation of marine bacteria by micro bubbles, change in size and collapse phenomena of micro bubbles, shock wave generation, and the inactive effects on marine bacteria were investigated experimentally.

2 Experimental

The experimental device consists of an ultrasonic generator (UIP500, Dr. Hielscher), a micro bubble generator using a swirling flow (M2-LM/SCS, Nanoplanet), a radiator

(CCA-1100, Tokyo Rikakikai) and a centrifugal pump (25SCD, Ebara) (see Figure 1). This experimental water channel has a 10 l capacity.

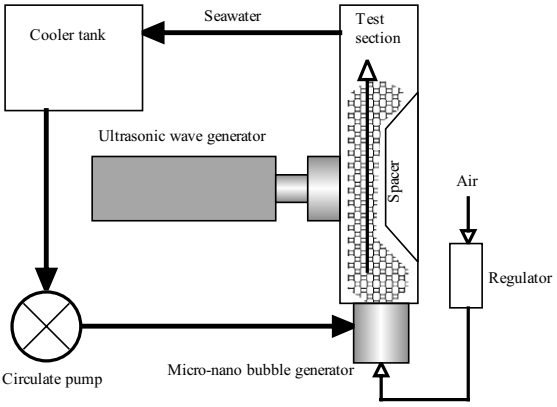

Fig. 1. Illustration of experimental apparatus

It has been well-known that micro bubbles make themselves small and exist in relatively long time after the bubble generation. In order to obtain higher capability for the inactivation of marine bacteria, it is important to understand the behavior of micro bubbles in the water channel. Therefore, micro bubbles were caught using two slide glass plates with a distance of 300 μm near the exit of the micro bubble generator, and the time change of the diameter of micro bubbles were observed by an optical microscope (CX41, Olympus). The collapse of micro bubbles by ultrasonic waves and the generation of shock waves were confirmed by the schlieren visualization method. In addition, shock wave pressures generated by micro jets from micro bubbles were measured with pressure sheets (Prescale, Fujifilm Inc.).

A marine *Vibrio* sp. was used in this study. The marine *Vibrio* sp. belongs to the same generic group of cholera that is one of the bacteria restricted by the international convention regarding the ballast water management. The artificial seawater 10 l, in which NaCl (0.4 M), KCl (10 mM), $CaCl_2{\cdot}2H_2O$ (10 mM), $MgCl_2$ (53 mM), and Na_2SO_4 (28 mM) were dissolved, was used for the experiment. After 10 ml suspension including the 10^8 cfu/ml marine *Vibrio* sp. had been put into the 10 l artificial seawater and stirred enough, seawater was poured into the experimental water channel. The experiment was continued for 12 hours. Samples were taken 10 ml after 1 hour and after then every 2 hours, and they were spread onto an agar plate to check a number of colony after 1/10000 dilution. The number of active bacteria was measured by a colony counting method [2].

3 Observation of micro bubbles in artificial seawater

Figures 2 show micro bubbles produced in freshwater or artificial seawater. The micro bubble generator requires 1.0 l/min air for the best operation. In the case of freshwater, most of air bubbles were not micro size, and the number of bubbles was small. On the other hand, in the case of artificial seawater, micro size air bubbles were generated like a

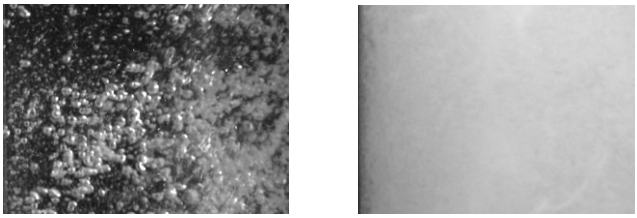

(a) (b)

Fig. 2. Generation of micro bubbles in freshwater (a) and artificial seawater (b)

dense fog in the test section. The reason why a large amount of micro bubbles was easily generated in artificial seawater was considered that the surface tension of seawater was smaller than that of freshwater.

Figures 3 show a time series of the diameter change in artificial seawater. These photos indicate that the bubble diameter decreases from 50 to 3 μm in 650 seconds. It was suggested that the lifetime of a micro bubble was enough long in the test section. Such a slow change in diameter is one of the characteristics of micro bubbles produced by the swirling flow type generator.

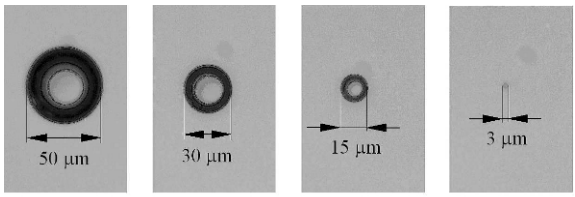

Fig. 3. Time change of the size of a micro bubble 50 μm in diameter

Figure 4(a) shows time change in the diameter of micro bubbles in artificial seawater. This figure indicates that the extinction time increases with increasing the diameter of bubble. It is found that the micro bubbles less than 65 μm in diameter became small size and disappeared, but the 80 μm bubble held its size constant. In addition, it took about sixty seconds for the 20 μm bubble to disappear, and the reducing rate of bubble diameter seemed to be accelerated after the bubble diameter had become 20 μm.

Figure 4(b) shows the relations between the initial volume of micro bubble and the extinction time in freshwater and seawater. In both cases, the initial volumes are positively proportional to the extinction time. From a comparison between them, it was found that the lifetime of micro bubbles in seawater was longer than that in freshwater. The average decreasing rate of volume of micro bubbles in seawater was estimated about 110 $\mu m^3/s$. It seemed that there was similarity between the motion of micro bubbles and that of vapor bubbles.

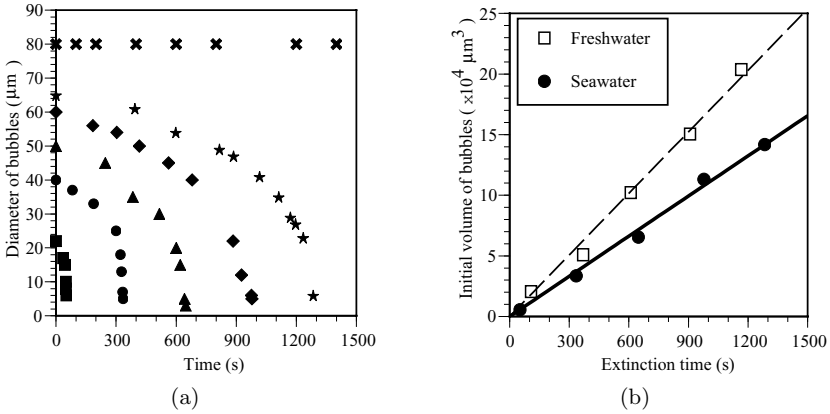

(a) (b)

Fig. 4. Time change in the diameters of micro bubble (a), and relation between the initial volume of micro bubble and extinction time in fresh and seawater (b)

4 Results and discussions

Figure 5(a) shows a photograph obtained by schlieren method, and the density changes in flow field with micro bubbles and ultrasonic waves were visualized. Although there was density non-uniformity in the background, a lot of small circular shadows were shown. We considered that the bright circles around those circular shadows of micro bubbles shows the existence of shock waves generated by collapse of micro bubbles. In addition, as shown in figure 5(b), we obtained a lot of dots on a pressure sheet. They were appeared due to the water jets generated by collapse of micro bubbles.

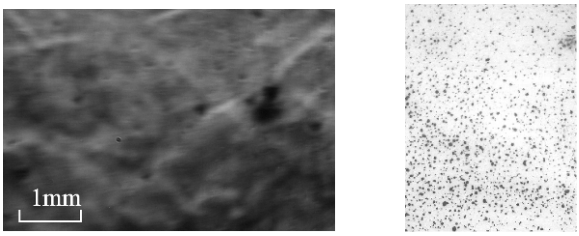

(a) (b)

Fig. 5. Schlieren photograph (a), and reaction of pressure sheet (b)

The bio-experiments using the test section with widths of 5 mm and 20 mm were carried out under the following three conditions: (1) only use of micro bubbles, (2) only use of ultrasonic waves, or (3) simultaneous use of micro bubbles and ultrasonic waves. Figures 6 show the time change of the inactivation ratio of a marine *Vibrio* sp. In these figures, the ordinate axis is represented by -log(N/N_0)C where N is the number of survival bacteria and N_0 means the initial value, and the abscissa is time (hour). In the case of only use of micro bubbles, the inactivation ratio showed slightly increase without relation

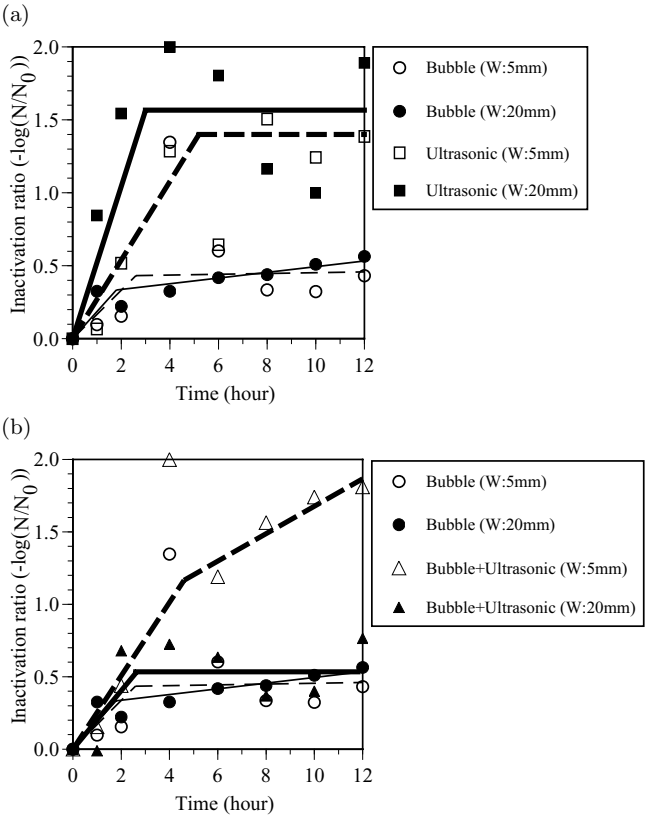

Fig. 6. Time change of the inactivation ratio of a marine *Vibrio* sp.: the results obtained by only use of bubbles and only use of ultrasonic waves in the water channel with widths of 5 mm and 20 mm (a), and the results obtained by only use of bubbles and simultaneous use of bubbles and ultrasonic waves in the water channel with widths of 5 mm and 20 mm (b)

to the width of test section. Figure 6(a) represents the comparison between the result obtained by only use of micro bubbles and that by only use of ultrasonic waves. It is found that the inactivation effect appeared within about early four hours, and after then, the inactivation ratios are approximately constant. In this case, the width of the test section does not relate with the inactivation ratio.

Figure 6(b) shows the result by simultaneous use of micro bubbles and ultrasonic waves. Then, the amount of air introduced into the micro bubble generator was 1.0 l/min that was recommended by the product company as an appropriate value. The experimental result using 20 mm width of test section was similar to the result of only use of micro bubbles. A large amount of micro bubbles probably obstructed the propagation of ultrasonic waves in the test section. In contrast, the result using 5 mm width of the test section increased with increasing time. Therefore, we considered that the ultrasonic waves and their reflection at the surface of spacer in the test section made micro bubbles collapse effectively, and then the marine bacteria were inactivated. From above-mentioned

results, it is concluded that the efficient collapse of micro bubbles is important for obtaining higher inactivation ratio. In the present experiment, it is necessary to decide the appreciate conditions about setting of an ultrasonic transducer, volume of air introduced into the micro bubble generator, and flow velocity through the test section.

5 Conclusions

In the present study, it was shown that micro bubbles less than 65 μm in diameter existed long time in artificial seawater, and shock waves and water jets were generated by collapse of micro bubbles exposed to ultrasonic waves. In addition, the inactivation effect on the marine *Vibrio* sp. by simultaneous use of micro bubbles and ultrasonic waves indicated better inactivation than that by the only use of micro bubbles or ultrasonic waves. These experimental results showed that it is important for inactivation of the marine *Vibrio* sp. to induce the collapse of micro bubbles efficiently. Therefore, it is necessary to examine conditions for the efficient collapse of micro bubbles in order to establish the effective treatment technique of a large amount of ships' ballast water using micro bubbles.

Acknowledgement. A part of the present study has been supported by JSPS under the grant No.B-16360437 and Hyogo Science and Technology Association. The authors would like to express their thanks for the financial support.

References

1. Hashim, M. A., Kumar, S. V., Gupta, B. S., Particle-bubble attachment in yeast flotation by colloidal gas aphrons, Bioprocess and Biosystems Engineering **22**, 4, 333-336, (2000)
2. Mimura, H., Katakura, R., Ishida, H., Changes of microbial populations in a ship's ballast water and sediments on a voyage from Japan to Qatar, Marine Pollution Bulletin **50**, 751-757, (2005)
3. Mimura, H., Abe, A., Katakura, R., Kawasaki, H., Yoshida, K., Ishida, H., Lethality of Shock Pressures to a Marine Vibrio sp. Isolated from a Ship's Ballast Water, Biocontrol Science, **11**, 4, 159-166, (2006)
4. Ruiz G. M., Rawlings T. K., Dobbs F. C., Drake L. A., Mullady T., Huq A., Colwell R. R., Global Spread of Microorganisms by Ships, Nature **408**, 49-50, (2000)
5. Shen, X., Ceccio, S. L., Perlin, M., Influence of bubble size on micro-bubble drag reduction, Experiments in Fluids **41**, 3, 415-424, (2006)
6. Waite T. D., Kazumi J., Lane P. V. Z., Farmer L. L., Smith S. G., Smith S. L., Hitchcock G., Capo T. R., Removal of Natural Populations of Marine Plankton by a Large-scale Ballast Water Treatment System, Marine Ecology Progress Series **258**, 51-63, (2003)
7. Yoshida, Y., Takahashi, Y., Kato, H., Masuko, A., Watanabe, O., Simple Lagrangian formulation of bubbly flow in a turbulent boundary layer (bubbly boundary layer flow), Journal of Marine Science and Technology **2**, 1, 1-11, (1997)

Study of mechanical and chemical effects induced by shock waves on the inactivation of a marine bacterium

A. Abe, Y. Miyachi, and H. Mimura

Graduate School of Maritime Sciences, Kobe University
Fukaeminami-machi, Higashinada-ku, Kobe 658-0022, Japan

Summary. The present paper reports a study on the shock sterilization technique of ships' ballast water. In order to expose cell suspension to strong shock waves, a gas gun experiment was carried out. In this experiment, shock waves in the suspension of a marine *Vibrio* sp. were generated by collision between an aluminum suspension container and an impactor plate accelerated by the gas gun. The changes of shock pressure in suspension were measured by piezofilm gauges and compared them to computational results. The visualization of shock waves in water was carried out by shadowgraph method, and the marine *Vibrio* sp. was observed with an electron microscope. In addition, the affect of free radicals was also investigated using VitC-Na 2 %. It was found that both the dynamic action of shock pressure and the chemical reaction in suspension induced by shock waves were closely related to inactivation of the marine *Vibrio* sp. at an impact velocity lower than about 200 m/s.

1 Introduction

Technological development of treatment of ships' ballast water is an important assignment to preserve the marine environment [6]. The International Marine Organization (IMO) adopted the guidelines of the "International Convention for the Control and Management of Ship's Ballast Water and Sediments" in 2004, and has been implementing a global ballast water management program. Recently, many studies on the management and treatment technique of ships' ballast water have been reported all over the world (for example, see [8]). However, most of studies were intended for marine plankton. The authors consider that it will be important for the treatment of ships' ballast water to sterilize cholera bacteria in the near future. They have started the experimental study on behavior of a marine *Vibrio* sp. exposed to shock waves. In order to exert strong shock waves on the cells, a suspension container made of aluminum was collided with an aluminum impactor plate accelerated by a gas gun. In the previous study, the authors have obtained that the marine *Vibrio* sp. in a suspension container was completely inactivated at an impact velocity larger than about 110 m/s, and then the peak pressure value in the suspension container was more than 200 MPa [1]. However, inactivation mechanism of the marine cells has not been clarified enough.

In the present paper, the propagation process of shock waves in a suspension container was investigated by a numerical simulation and experimental pressure measurements. In order to discuss the mechanical and chemical effects of shock waves on the inactivation of a marine *Vibrio* sp., the damage of a cell wall after shock wave loading was confirmed by a biochemical method and an electron microscopic observation, and the generation of free radicals in suspension was also examined experimentally using VitC-Na 2%. From the above-mensioned results, the contribution of dynamic action of shock wave pressure and chemical reaction in suspension to inactivation of the marine *Vibrio* sp. was discussed.

2 Experimental

2.1 Gas gun and projectile

In this experiment, cell suspension was closed in an aluminum container and compressed by strong shock pressure. The shock pressure was generated by the impact between the suspension container and an aluminum impact plate. The impact plate is an aluminum disk 1 mm in thickness and 38 mm in diameter, and it is attached to the front surface of a projectile accelerated up to an arbitrary velocity by a single-stage gas gun. The gas gun consists in a high pressure chamber, a launch tube, and an impact chamber. The bore of the launch tube is 40 mm and its length is 2 m. The maximum pressure of driver gas in the high pressure chamber was 2 MPa. The impact velocity of projectile was measured by a magnet flyer method. A projectile was made of ABS resin.

2.2 Suspension container

A suspension container was made of aluminum, and its shape was columnar 30 mm in diameter. In the body of container, there was a cavity space to maintain 0.4 ml suspension. The wall thickness of the impact part of the suspension container was 5 mm. In order to improve the precision of plane impact between an impact plate and the suspension container, the container was fixed in a target holder, and set at the exit of the launch tube, as shown in Figure 1. The shock pressure in the suspension was measured by a piezo-film gauge (PVF_2, 11-.125-EK, Dynasen Inc.). The pressure-sensitive area of the gauge is about 9 mm^2, and its thickness is 28 μm.

In the visualization experiment, the rectangular water container with 14 mm $\times$ 20 mm acrylic windows was used. Optical observation of shock waves in the water container was carried out by shadowgraph method.

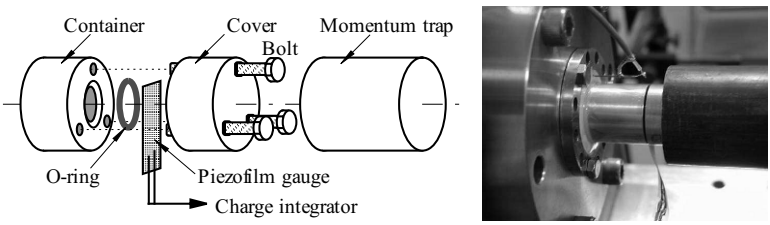

Fig. 1. Assembly and arrangement of a target set

2.3 Judgment of inactivation of marine bacteria

The marine *Vibrio* sp. used in this research belongs to the same generic group of cholera bacteria that was regulated by the international convention for ballast water management. We isolated the marine *Vibrio* sp. from seawater, and cultivated colonies using artificial seawater. Inactivation of the cells after an impact was decided by counting colonies on an agar plate. In addition, the agar plate containing sodium cholate was also used to investigate damage of the outer membrane of cells.

3 Numerical simulation

In order to predict the propagation process of shock waves in cell suspension, the shock wave phenomena generated in a suspension container were calculated by a general purpose transient dynamic finite element program (LS-DYNA, LSTC). The elastic and plastic deformation of aluminum container was represented using the Johnson-Cook model [7]. The Johnson-Cook equation is given by

$$\sigma = (C_1 + C_2\epsilon^N)(1 + C_3 \ln \epsilon^*)(1 - T^{*M}), \tag{1}$$

where σ is the equivalent yield strength, ϵ is the equivalent plastic strain, ϵ^* is the dimensionless plastic strain rate for the reference strain rate (usually equal to 1.0 s^{-1}), and C_i, N and M are constants of the material. T^* is the dimensionless temperature, and it is given by

$$T^* = \frac{T - T_{room}}{T_{melt} - T_{room}}, \tag{2}$$

where T is the current temperature, T_{room} is the ambient temperature, and T_{melt} is the melt temperature. The ABS resin used for the projectile was assumed to be a perfectly elastic material.

For the equation of state of the cell suspension, the Tait equation was used. The Tait equation [3] is defined as

$$P = \alpha \left[\left(\frac{\rho}{\rho_0} \right)^{\beta} - 1 \right], \tag{3}$$

where P is the gauge pressure, ρ is the density, ρ_0 is the initial density, and α and β are constants. In this equation, $\alpha = 304.7$ MPa and $\beta = 7.15$ were used for 0.7 mol/kg of salt water. In order to use the equation 3 in the calculation code, it was transformed to the following polynomial approximation,

$$P = 12951\eta^3 + 6671.2\eta^2 + 2178\eta, \tag{4}$$

where η, $= \rho/\rho_0$ - 1, is compression strain.

4 Results and discussions

4.1 Shock wave generation in a suspension container

Figure 2 shows a comparison between an experimental shadowgraph and numerical pressure distributions obtained at 400 m/s impact velocity. Figure 2(a) shows that a plane underwater shock wave has occurred at the left side boundary, and oblique shock waves generated by the precursive elastic and plastic shock waves in the aluminum frame have propagated from the upper side boundary. From these results, we could obtain good agreements on the position of the plane underwater shock wave and the inclined angle of the first oblique shock wave.

Figure 3 shows a comparison between experimental and numerical pressure changes at 96.2 m/s impact velocity [2]. These results indicate good agreements until about 15 μs. However, the experimental pressure decreases gradually after 15 μs, while the numerical result keeps around 150 MPa. The difference shows the leakage of pressure from the suspension container in this experiment. From the above-mentioned results, it was confirmed that the pressure change generated in suspension by the first shock wave would be simulated quantitatively by the numerical calculation.

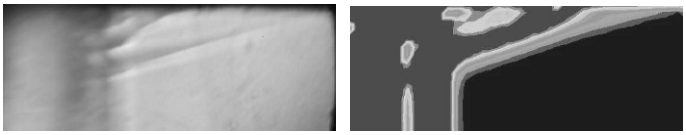

(a) (b)

Fig. 2. Experimental shadowgraph (a), and computational pressure distributions (b), obtained at 400 m/s impact velocity

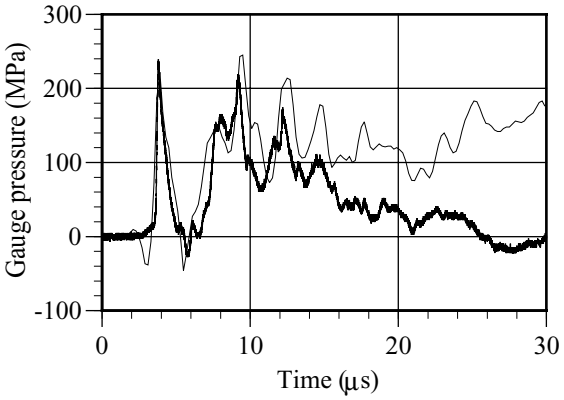

Fig. 3. Comparison of pressure changes: a thin line is computational result, and a bold line is experimental one

4.2 Electron microscopic observation

The marine *Vibrio* sp. was observed with an electron microscope. Figure 4(a) shows an image of the cells before the shock event. It is found that the configuration of a marine *Vibrio* sp. is originally a spheroid of about 1 μm in the major axis. Figure 4(b) and 4(c) are the samples of inactive cells obtained at a low impact velocity less than 100 m/s and at a 266 m/s impact velocity, respectively. It is found that the configurations of inactivate cells after the low velocity impact became like that of red blood cells, while the burst cells were observed at the high impact velocity. In addition, the osmotic pressure of 2 mol NaCl for four hours shriveled the outer membrane of the cells.

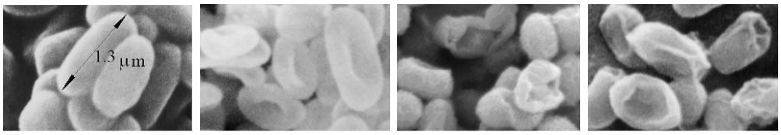

(a) (b) (c) (d)

Fig. 4. Images of a marine *Vibrio* sp. obtained by an electron microscope: picture (a) is the control, and others are the samples of inactive cells obtained at a low impact velocity less than 100 m/s (b) and at a 266 m/s impact velocity (c), and osmotic pressure (d)

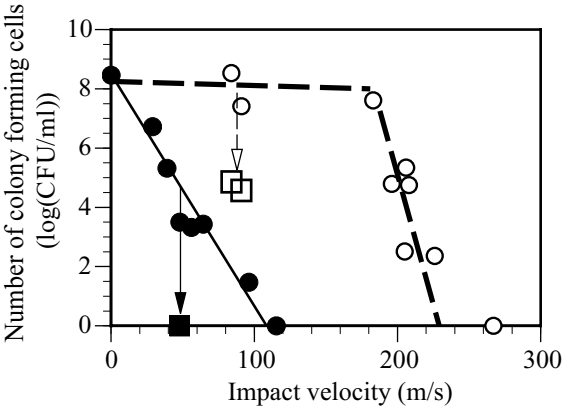

Fig. 5. Relation between survival number of cells and the impact velocity: solid circles indicate the results using normal suspension, a solid square is the result using culture media containing sodium cholate, open circles are the results of addition VitC-Na 2 % to normal suspension, and open squares are the results using the antioxidant agent and culture media containing sodium cholate

4.3 Inactivation effects of shock pressures

The relation between the survival number of the marine *Vibrio* sp. and the impact velocity is shown in figure 5 using solid circles and a solid line [2]. The number of cells decreases with an increase of the impact speed, and the inactivation of the cells are achieved completely at an impact speed larger than about 110 m/s. The peak gauge pressure obtained at 110 m/s in the present suspension container measured about 200 MPa. A solid square in this figure shows the result using an agar plate containing sodium cholate that completely inactivates the marine *Vibrio* sp. damaged on the outer membrane [4,5]. The 10^3 CFU/ml of the cells obtained by the impact velocity of about 49 m/s resulted in the complete inactivation using the sodium cholate. Therefore, it was appeared that the shock pressures generated at an impact velocity lower than 100 m/s gave the damage to the outer membrane of the marine cells.

As shown in figure 3, strong negative pressure has been measured immediately after the arrival of the first shock wave. It was seemed that movement of the cover of suspension container by an inner pressure loading caused the negative pressure, and it was suspected that cavitation bubbles were generated in the container. If cavitation bubbles collapse in the container, the free radicals are produced by the collapse energy of them and act on the marine bacteria. In order to investigate the effects of radicals, the experiment was carried out using the suspension including VitC-Na 2 % that is a representative antioxidant agent. The open circles and the broken lines in figure 5 show the experimental results. It was found that the inactivation of the marine cells was apparently inhibited by the VitC-Na to an impact velocity lower than about 200 m/s. In this case, the complete inactivation effect was obtained at an impact velocity larger than about 250 m/s.

The open squares in figure 5 show the results obtained at the impact velocity about 88 m/s using the suspension added an antioxidant agent and an agar plate containing sodium cholate. In this case, the survival number of cells decreased from 10^8 to 10^5 CFU/ml. The result suggested that the survival cells that had been protected from the

radicals using an antioxidant agent damaged dynamically on their cell wall by shock pressures.

5 Conclusions

The dynamic and chemical effects of shock pressures to the inactivation of a marine *Vibrio* sp. were examined by the shock experiment using a gas gun. From the electron microscopic observation of the shocked cells, it was shown that the configurations of inactive cells were significantly different at the impact velocities. The inactive cells obtained by a low velocity impact showed the configuration like the red blood cells, and the burst of the cells was observed at the high impact velocity. On the other hand, we could not obtain the complete inactivation of the marine *Vibrio* sp. using the suspension with an antioxidant agent at an impact velocity lower than 200 m/s. However, the damage of the outer membrane of survival cells was obviously shown by the bio-experiments using the sodium cholate. Therefore, we consider that the dynamic effects of shock waves will be dominantly at the high impact velocity, but at the low impact velocity dynamic and chemical effects by shock pressures and free radicals contribute to the inactivation of the cells.

Acknowledgement. A part of the present study has been supported by JSPS under the grant No. C-18560768. The authors would like to express their thanks to K. Yoshida for his technical assistance in the electron microscopic observation.

References

1. Abe A., Mimura H., Ikeda T., Katakura R., Shock Compression of Marine Bacterial Cells Enclosed in Aluminum Container, Journal of the JIME **40**(2), 110-115, (2005)
2. Abe, A., Mimura, H., Ishida, H., Yoshida, K., The effect of shock pressures on the inactivation of a marine Vibrio sp., Shock Waves, (2007), submitted
3. Cole R. H., *Underwater Explosions*, Princeton University Press., USA, (1948)
4. Mimura, H., Abe, A., Katakura, R., Kawasaki, H., Yoshida, K., Ishida, H.,Lethality of Shock Pressures to a Marine Vibrio sp. Isolated from a Ship's Ballast Water, Biocontrol Science., **11**(4), 159-166, (2006)
5. Mimura, H., Abe, A., Yoshida, K., Ishida, H., Changes in the Number of Colony-Forming Marine *Vibrio* sp. Cells After Exposure to Shock Pressures in the Presence of Sodium Ascorbate, Bull. Soc. Sea Water Sci., Jpn, **61**(2), 132-133, (2007)
6. Ruiz G. M., Rawlings T. K., Dobbs F. C., Drake L. A., Mullady T., Huq A., Colwell R. R., Global Spread of Microorganisms by Ships, Nature **408**, 49-50, (2000)
7. Rule W. K., Jones S. E., A Revised Form for the Johnson-Cook Strength Model, International Journal of Impact Engineering **21**(8), 609-624, (1998)
8. Waite T. D., Kazumi J., Lane P. V. Z., Farmer L. L., Smith S. G., Smith S. L., Hitchcock G., Capo T. R., Removal of Natural Populations of Marine Plankton by a Large-scale Ballast Water Treatment System, Marine Ecology Progress Series **258**, 51-63,(2003)

The effect of extracorporeal shock wave therapy on the repair of articular cartilage

C.Y. Wen[1], C.H. Chu[2], K.T. Yeh[3], and P.L. Chen[4]

[1] *Department of Aeronautics and Astronautics, Cheng-Kung University, Tainan, Taiwan*
[2] *Department of Orthopedics and Surgery, Show-Chwan Memorial Hospital, Chang-Hwa, Taiwan*
[3] *Department of Pathology, Chang-Hwa Christian Hospital, Chang-Hwa, Taiwan*
[4] *Department of Mechanical and Automation Engineering, Da-Yeh University, Chang-Hwa, Taiwan*

Summary. This study investigated the stimulative effect of extracorporeal shock wave therapy (ESWT) on the articular cartilage regeneration. Eight New Zealand rabbits were used and randomly assigned to A and B groups in the experiment, 4 rabbits for each group. An osteochondral defect, 3 mm in diameter and 3 mm in depth, was drilled in the patellar groove at the distal end of each femur. The left and right patellar defects were designated as the control and experimental samples, respectively. Only the right patellar defects (the experimental group) received 500 impulses of shock waves (at 14 kV) at one week after surgery. At 4 (group A) and 8 (group B) weeks after ESWT, cartilage repair was evaluated macroscopically and histologically. The preliminary results suggested that regeneration of articular cartilage defects might be promoted by ESWT, due to the release of growth-inducing substances such as basic fibroblast growth factor, insulin-like growth factor-I and transforming growth factor-$+\beta$.

1 Introduction

The complete anatomic healing and natural true regeneration of the articular cartilage damage are rare. In fact, in the words of Hippocrates: "ulcerated cartilage is universally allowed to be a troublesome disease." The scarcity of successful therapeutic modalities even colors our view by Hippocrates' opinion.

During the last 60 years[1-3], the natural healing of full-thickness cartilage defects has been extensively studied. Most experimental studies reported the natural healing of the defect at different times after surgery. Investigators have then attemped to improve the healing process by manipulating the defect in specified ways[4-9], including surgically-based attempts undertaken in many clinical centers worldwide.

In recent years the increasing clinical applications of extracorporeal shock wave therapy in the treatment of certain orthopedic conditions including calcifying tendinitis, epicondylitis humeri radialis, calcaneodynia and pseudarthrosis have shown promising results[10-11]. This motivates us to try ESWT on the repair of articular cartilage. The efficacy of ESWT in the case of articular cartilage defects will be examined for the first time in this preliminary study.

2 Materials and methods

2.1 Experimental animals

This research was approved by the Institutional Review Board of Chang-Hwa Christian Hospital, Chang-Hwa, Taiwan. Eight New Zealand white rabbits aged 180 days with

body weight ranging from 3.5 to 4.5 kg were used in this experiment. The rabbits become skeletally mature at this age. The rabbits were divided randomly into two groups: group A and B, of 4 rabbits each. During the study the rabbits were kept in separate cages under standardized conditions according to the requirements of the Taiwan animal protection law and were allowed to have free access to pellet food and water after the surgery and shock wave treatment.

2.2 Experimental setup and procedure

The shock waves were generated by a commercial ESWT system, Ossa-Tron OSA 140. This system consists of a mobile locating C-arm, a laser-beam aiming device and a hydro-electric shock-wave generator. The energy level used in the experimental was 1.2 mJ/mm2, corresponding to the operating voltage of 14 kV.

The rabbit was anesthetized with ketamine (50 mg/kg), Xylazine (5 mg/kg) and Atropin (0.2 mg/kg). After anesthesia was established, a medial parapatellar incision was made over each knee. Medial arthrotomy was performed, and the patella was dislocated laterally, exposing the patellar groove. A cylindrical, full-thickness defect, 3 mm in diameter and 3 mm in depth, was created using a hand drill, penetrating the articular cartilage surface into the subchondral marrow space of the patellar groove of each distal femur (Figure 1). The left and right patellar defects were designated as the control and experimental samples, respectively. At one week after surgery, only the right femoral condyle(served as the experimental sample) received 500 impulses of shock waves at 1 Hz. The left femoral condyle (served as the control sample) received only a chondral defect in the patellar groove. The knee joint of each rabbit was irrigated with normal saline to remove small fragments and debris. The patella was reduced and the subcutaneous tissue and skin were closed with 3-0 nonabsorbable suture in an ordinary manner. The rabbit was injected with Ampicillin (50 mg/kg) to prevent infection. During ESWT, the rabbits were fixed in a device and the right knee joint was held in 30o flection.

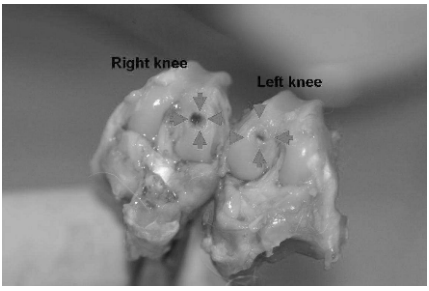

Fig. 1. The left and right patellar defects for rabbit 5.

2.3 Macroscopic and histological examination

Rabbits were randomly assigned to two groups after ESWT, 4 rabbits for each group. Rabbits in groups A and B were sacrificed at 4 and 8 weeks after ESWT, respectively, by intravenous injection of a lethal dose of sodium phentobarbital (100 mg/kg) followed by immediate evaluation of the macroscopic findings in the cartilage. After the macroscopic evaluation was conducted, the distal femurs were resected, fixed with 10

Parameter	Group A Rabbit 1 L R	Rabbit 2 L R	Rabbit 3 L R	Rabbit 4 L R
I Filling of defect	2 2	1 0	2 2	0 0
II Cell type	1 0	2 0	2 0	0 1
III Reconstitution of osteochondral junction	2 1	2 2	2 2	0 0
Parameter	**Group B Rabbit 5 L R**	**Rabbit 6 L R**	**Rabbit 7 L R**	**Rabbit 8 L R**
I Filling of defect	2 0	2 0	2 0	2 2
II Cell type	1 0	1 1	2 2	0 0
III Reconstitution of osteochondral junction	2 0	2 2	2 2	0 0

Table 1. Macroscopic and histological examination of spontaneous repair of articular cartilage. L and R represent left and right knees, respectively. For the parameter I, 0: Obvious; 1: Slight; 2: None. For parameter II, 0: Normal; 1: Mostly hyaline and fibrocartilage; 2: Mostly fibrocartilage. For parameter III, 0: Yes; 1: Almost; 2: Not close.

3 Results

From the parameter I-filling of defect in Table 1, it shows that the over all reparative changes of the experimental group (right knee) is better than the control group (left knee). For the experimental group, White cartilage-like regenerated tissues at the edge of the defect were clearly observed 8 weeks after ESWT (group B), and the depth of the central remaining defect has decreased compared to the 4-week post-ESWT specimens (group A). It demonstrated consistent reparative changes over time.

Figure 2 shows the photomicrographs of repair tissue in the control (left) and experimental (right) groups at 8 weeks after ESWT. There was no reconstitution of osteochondral junction in the control specimen, while in the experimental specimen, hyaline-like cartilage cells were in contact with the rim of the reconstituted subchondral bone and

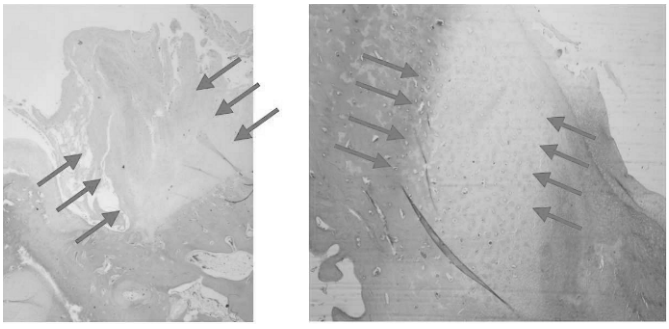

Fig. 2. Photomicrographs (x10) show repair tissue in the control (left) and experimental (right) groups of rabbit no. 5 at 8 weeks (Group A) after ESWT. Arrows indicate the periphery of the created defect.

the cellularity of the repair tissue was greater than that of the adjacent normal cartilage. The subchondral bone at the rim of the defect had matured as a result of remodeling. The outer surface of the repair tissue of the control group is not as smooth as the of the experimental group either.

Figure 3 shows high magnification (x100) of the central areas of repair cartilages in the experimental knee on the right-hand side seen in Figure 2. The experimental defect was filled primarily and uniformly with regenerated hyaline-like articular cartilage. On the other hand, the control defect was primarily filled with fibrocartilage. The histological appearance of specimens from the control group showed poor repair compared to that in the experimental group at the same time after ESWT. Generally speaking, the total macroscopic and histological evaluation at 4 and 8 weeks in the experimental group were better to those in the control group.

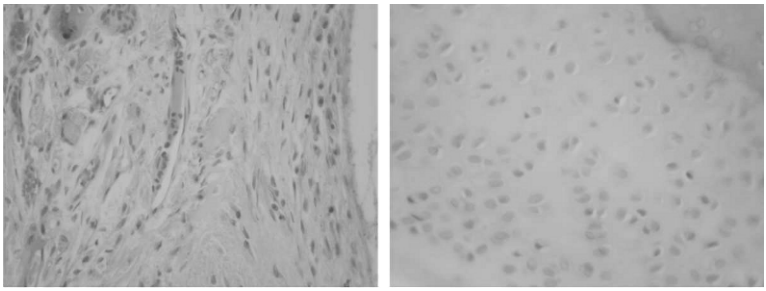

Fig. 3. High magnification (x100) of the central areas of repair cartilages in the experimental knee on the right-hand side seen in Figure 2.

4 Conclusion

The preliminary results suggested that regeneration of articular cartilage defects might be promoted by ESWT, due to the release of growth-inducing substances such as basic fibroblast growth factor, insulin-like growth factor-I and transforming growth factor-$+\beta$.

References

1. Key JA: Experimental arthritis: The changes in joints produced by creating defects in articular cartilage. J. Bone Joint Surg 1931; 13:725-739.
2. Depalma A, Mckeever D, Sudin D: Process of repair of articular cartilage as demonstrated by histology and autoradiography with tritiated thymidine. Clin. Orthop. Relat. Res. 1966; 48:229-241.
3. Mankin HJ, The response of articular cartilage to mechanical injury. J. Bone Joint Surg 1982; 64A:460-466.
4. Grande DA, Pitman MA, Peterson L, Menche D, Klein M: The repair of experimentally produced defects in rabbit articular cartilage by autologous chondrocyle transplantation. J. Orthop. Res. 1989; 7:208-218.
5. Lippiello L, Chakkalakal D, Connolly JF: Pulsing direct current induced repair of articular cartilage in rabbit osteochondral defects. J. Orthop. Res. 1990; 8:266-275.

6. Amlet D, Coutte RD, Abel M, Stewart W, Harwood F, Akeson WH: Rib perichondraial grafts for the repair of full-thickness articular cartilage defects. A morphological and biochemical study in rabbits. J. Bone Joint Surg 1985; 67:911-920.
7. Rothwell AG: Synovium transplantation onto the cartilage denuded patellar groove of the sheep knee joint. Orthopedics 1990; 13:433-442.
8. Hunzlker EB: Articular cartilage repair: basic science and clinical progress. A review of the current status and prospects. Osteoarthritis Cartilage 2002; 10:432-463.
9. Kumagai K, Saito T, Koshino T: Articular cartilage repair of rabbit chondral defect: promoted by creation of periarticular bony defect. Orthopaedic Science 2003; 8:700-706.
10. Heller KD, Niethard FU: Der Einsatz der extrakorporealen Stoßwellentherapie in der Orthopädie-eine Metaanalyse. Z Orthop 1998; 136:390-401.
11. Siebert W, Buch M (eds): Extracorporeal shock waves in orthopaedics. Springer, Berlin Heidelberg New York 1997.
12. Pineda S, Pollack A, Stevenson S, Goldberg V, Caplan A,: A semiquantitative scale for histologic grading of articular cartilage repair. Acta Anat (Basel) 1992; 143:335-340.

The generation of high particle velocities by shock tunnel technology for coating application

X. Luo[1], H. Olivier[1], and I. Fenercioglu[2]

[1] *Shock Wave Laboratory, RWTH Aachen University, 52056 Aachen, Germany*
[2] *Istanbul Technical University, Department of Aerospace Engineering, Istanbul, Turkey*

Summary. For enhancing coating quality, the shock tunnel technology is employed to achieve impact velocities of particles up to 1500 m/s for 10 μm solid particles. A calibration of the nozzle flow has been carried out by using a Pitot rake. The current conditions in the reservoir achieved so far are $p_0 = 140$ bar and $T_0 = 1800$ K. A high speed schlieren system is set up for flow visualization and also for velocity measurement of visible particles. For fine particles, both LDA and PIV methods are used for particle velocity measurements. The achieved results are in good agreement with a quasi-1D prediction.

1 Introduction

Thermal spray processes such as plasma spray, arc spray and high-velocity oxy-fuel spray are widely used for modern coating applications. In these techniques, the coating material suffers very high temperatures, which results in melting and chemical reactions of the coating material. This problem is generally avoided in the cold gas-dynamic spray (CGS) technique [1]. The conventional CGS process basically uses the energy stored in high pressure compressed gas to accelerate fine powder particles to very high velocities in a range between 500 - 1000 m/s [2]. According to the prevailing theory for cold-spray bonding [3], the particle velocity should exceed a minimum (material-dependent) critical velocity to achieve deposition and, therefore, it is desirable to further increase the impacting velocity of particles in order to enhance the quality of CGS and to extend the application range of CGS. A modified cold gas-dynamic spray technique is proposed to increase the solid particle velocity up to 1500 m/s [4]. This method uses the super/hypersonic shock tunnel technology to generate a reservoir condition with high temperature and high pressure. The particles are injected into the nozzle flow downstream of the nozzle throat after the nozzle flow is fully established.

A theoretical model based on gas-particle flows is also presented in [4] to describe the behavior of the flow and the diluted solid particles during the modified cold-spray process. This quasi-1D model is capable to consider non-equilibrium effects of the gas phase due to high reservoir temperatures, and the influence of wall friction and heat transfer. Based on the parametric study [4], a nozzle with optimized theoretical performance has been chosen resulting in a conical nozzle with a half opening angle of 2.8° and a length of 32 cm. The throat diameter amounts to 7.8 mm, and the exit diameter is given by 39.7 mm. The particle injection device is fixed in the LPS (Low Pressure Section) of the shock tube and extends into the supersonic nozzle part. For this, a small tube (outer diameter 3.0 mm, inner diameter 1.2 mm) reaches into the divergent nozzle part so that the injection position is about 52 mm downstream of the throat.

2 Experimental setup and methods

2.1 Shock tunnel and Pitot rake

The shock tube has an outer diameter of 108 mm and an inner diameter of 56 mm. This tube is made by stainless steel and is able to sustain very high pressures up to 1000 bar. A schematic drawing of the setup is shown in Fig. 1. The shock tube has a high pressure section of 2.0 m and a low pressure section of 4.5 m length.

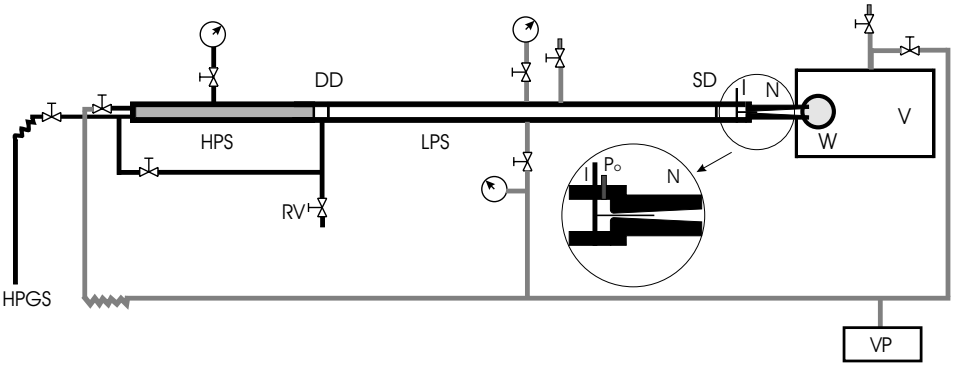

Fig. 1. Schematic drawing of the shock tunnel with peripheries. HPGS, high pressure gas supply; HPS, high pressure section; DD, double diaphragm chamber; LPS, low pressure section; I, injection device; N, nozzle; W, test window; V, vacuum tank; VP, vacuum pump, SD: second diaphragm.

In order to determine the free stream flow conditions downstream of the nozzle exit, a Pitot rake is used, which consists of five Pitot tubes connected with five Kulite pressure transducers, and a sphere installed with a coaxial thermocouple at its stagnation point. The reservoir pressure is directly measured by a Kistler pressure transducer mounted shortly upstream of the nozzle entrance. The reservoir temperature and free stream conditions are derived from the heat flux deduced from the thermocouple signal, the Pitot pressure and the static pressure employing the method described in [5, 6].

2.2 Particle velocity measurement: high speed photo system, LDA and PIV

A schlieren system is set up for flow visualization, which allows to take 16 schlieren photos in one experiment with a time interval between two successive photos of down to 1 μs, which is also very useful for the determination of the velocity of visible particles.

For velocity measurements of fine particles, a laser Doppler anemometer (LDA) system and a particle imaging velocimetry (PIV) system have been set up. In order to measure very high particle velocities, a very small angle is used in the LDA system, which results in a measurement volume of $17 \times 0.16 \times 0.16$ mm^3. For the PIV measurements, a holographic double-pulse laser system (JK Laser system 2000) with a pulse separation time in the microsecond range is adopted to create a laser light sheet (thickness 0.5 mm) perpendicular to the nozzle axis. A Kodak megaplus ES1 CCD camera is employed to

acquire either two images in two frames or one double exposure image in a single frame within a pulse delay in the microsecond range. The image data is then analyzed with the PIV software to obtain the particle velocity field.

3 Results and discussions

3.1 Flow calibration

Measured temperature and pressure histories in the reservoir are shown in Fig. 2. Initially, the HPS is filled with a mixture of helium (partial pressure 140 bar) and air (partial pressure 170 bar), and the LPS is at atmospheric pressure. A pre-cutted copper diaphragm of 0.5 mm thickness is mounted in the nozzle, and the dump tank is evacuated to a low pressure of about 180 Pa. The well validated shock tube simulation code KASIMIR [7] has been utilized for the comparison of the experimental results with the theoretical prediction, shown as dotted lines. An extension of the KASIMIR software package has been done to simulate the case that the driver gas is a mixture of helium and air. It should be mentioned that equilibrium effects are taken into account in KASIMIR. The reservoir temperature in the experiment slightly decreases with time and the testing time is about 2 ms for $T_0 \approx 1700$ K and 5 ms for $T_0 \approx 1500$ K.

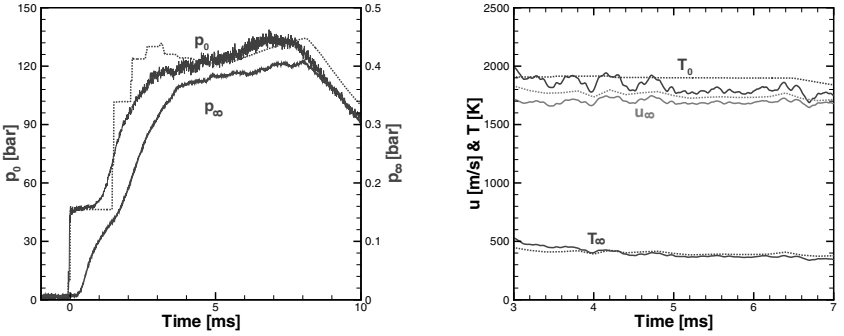

Fig. 2. Experimental results (solid lines) and corresponding numerical results (dotted lines). Reservoir pressure p_0 and static pressure histories p_∞ (left); deduced reservoir temperature T_0, free stream velocity u_∞ and temperature T_∞ (right). Initial condition: $p_4 = 310$ bar (partial pressure of helium 140 bar, partial pressure of air 170 bar), $p_1 = 1$ bar.

By changing the transverse position of the Pitot rake from shot to shot, the Pitot pressure profile along the radius of the nozzle exit has been obtained, see Fig. 3(a). The Pitot pressure is scaled by the actual reservoir pressure because the reservoir pressure slightly varies for every experiment. Each point in this figure represents an average value over the testing time. This Pitot pressure profile clearly indicates that the core flow region of the jet ($0 < r < 12$ mm) is repeatable from shot to shot. Figure 3(b) provides an experimental as well as theoretical relation of the reservoir temperature with the shock speed by KASIMIR. The relatively large scattering of the experimental data in

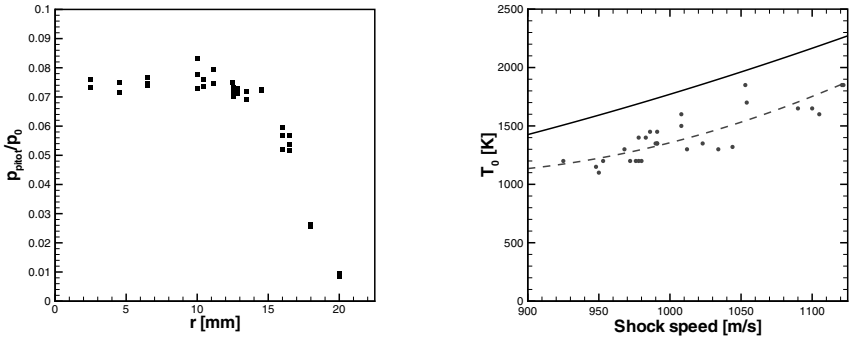

Fig. 3. (a): Pitot pressure profile along the radius at the nozzle exit. **(b)**: Relation of the reservoir temperature with the shock speed. Solid line: theoretical prediction by KASIMIR; dashed line: polynomial fit of experimental data.

Fig. 3(b) is because the partial pressure of helium is not the same for all experiments. Furthermore, the filling process of the different gases is not yet optimized and therefore, might cause variations for each experiment. The general deviation between the theoretical and experimental values in Fig. 3(b) is caused by the mixing process taking place at the contact surface in the experiments.

3.2 Particle velocity measurements

For first experiments, some big glass spheres (diameter 2 mm) were put on a flat surface of the injection device. The particles can be identified in the schlieren photos as shown in Fig. 4. In this case, the particle velocity deduced from the schlieren photos is about 200 m/s. Then smaller glass particles with 0.6 mm diameter are used. The measured mean particle velocity is about 350 m/s, which is almost the same as given by the theoretical prediction (356.6 m/s) utilizing the quasi-1D code, which has also been used for the parametric study. For this experiment the reservoir condition is given by $p_0 = 120$ bar and $T_0 = 1800$ K.

For 15 μm stainless steel particles added on a flat surface of the injection device, the arriving time of particles is first measured by the LDA system with time division of 1 ms, see Fig. 5. It can be found that the particles arrive at the nozzle exit after a delay of 900 μs and the particle flow lasts for several milliseconds. Then a smaller time division (50 μs) is used for the particle velocity measurements. The mean particle velocity measured by the LDA method is about 1050 m/s for the reservoir condition of $p_0 = 140$ bar and $T_0 = 1800$ K.

Up to now, experiments with PIV are still running for different conditions. In this paper, only preliminary results of the PIV measurements are presented for air as driver gas. Fig. 6 shows double-exposure images for the single frame mode for stainless steel particles of mean diameter of 15 μm added in the reservoir (left) and in the injection tube (right). By using the particle-pairing method, it is found that the averaged particle velocity is about 1220 m/s in the left image and 890 m/s in the right image. The cross-

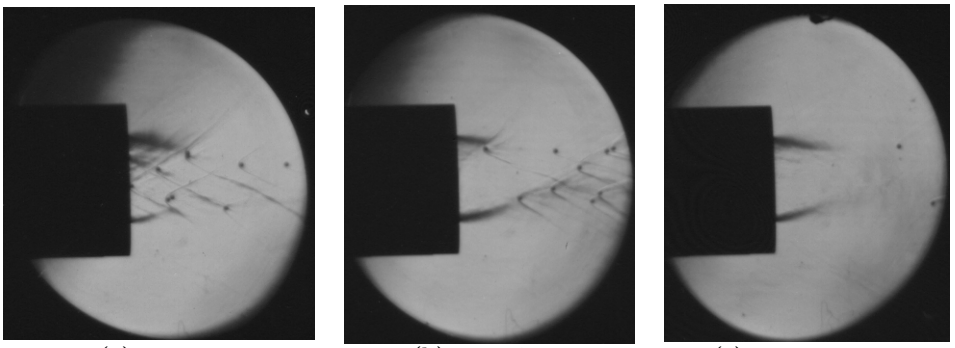

(a) t = 3.30 ms **(b)** t = 3.45 ms **(c)** t = 3.60 ms

Fig. 4. Schlieren pictures for 2 mm glass particles added in the nozzle prior to the experiment.

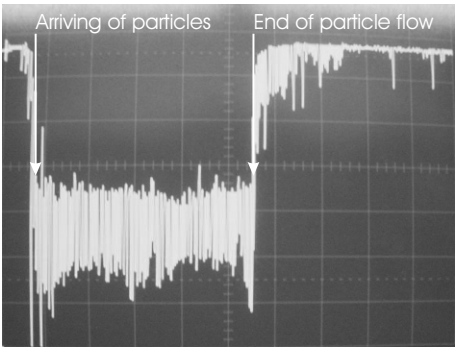

Fig. 5. Determination of the arriving time of particles by the LDA system, time division 1 ms.

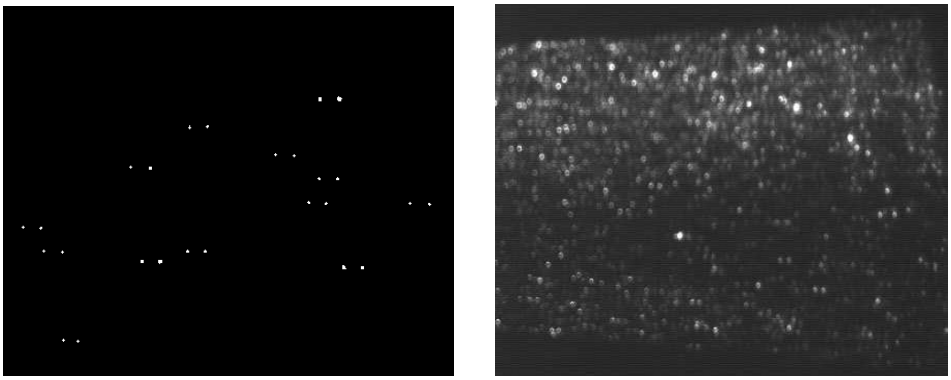

Fig. 6. Double-exposure images in single frame mode for particles added in the reservoir (left, interval 2.2 μs) and in the injection tube (right, interval 1.48 μs). Initial condition: $p_4 = 200$ bar, $p_1 = 1$ bar.

correlation method can also be used to deduce the velocity field by capturing two images in the double frame mode. The mean particle velocity deduced by the cross-correlation method is about 897 m/s, which is the same as for the particle-pairing method.

4 Conclusion

The shock tunnel technology is employed to achieve particle velocities of more than 1000 m/s for 10 μm solid particles. A calibration of the nozzle flow has been carried out by using a Pitot rake and a sphere for measuring the stagnation point heat fluxes. The current conditions in the reservoir achieved so far are $p_0 = 140$ bar and $T_0 = 1800$ K. A high speed schlieren system is set up for flow visualization and also for velocity measurements of visible particles. For fine particles, both LDA and PIV methods are used for particle velocity measurements. Results are in good agreement with the theoretical prediction by the quasi-1D method.

For today's existing technologies, like e.g. plasma coating, the reservoir temperature amounts to 7000-20000 K and the pressure to 1 bar, resulting in a typical particle velocity of about 200-300 m/s. High particle velocities are achieved with the cold gas coating technique, where the reservoir temperature is about 1000 K, the reservoir pressure about 50-100 bar and the typical particle velocity in the order of 600-1000 m/s. This shows that the conditions achieved in this work so far (p_0=140 bar, $T_0 = 1800$ K, expected copper particle velocity for $d = 10\mu$m about 1329 m/s) are already beyond existing technologies. For higher particle velocities, it is still necessary to increase the reservoir condition, for instance to $T_0 \approx 2100$ K and $p_0 \approx 200$ bar, which can be realized by increasing the partial pressure of helium or using pure helium. More PIV experiments will be carried out in the near future for higher reservoir conditions, and different particles in size and material. A substrate will also be mounted near the nozzle exit to study the coating process and to evaluate the quality of the coating layer.

Acknowledgement. This work is supported by the Deutsche Forschungsgemeinschaft (DFG) OL 107/10-2.

References

1. A.O. Tokarev: *Structure of aluminum powder coatings prepared by cold gas dynamic spraying*, Metel Sci., Heat Treat. **35**, 3-4, pp 136–139 (1996)
2. T. Stoltenhoff, H. Kreye, and H.J. Richter: *An analysis of the cold spray process and its coatings*, J. of Thermal Spray Technology **11**, pp 542-550 (2002)
3. M. Grujicic, C. Tong, W.S. DeRosset, and D. Helfritch: *Flow analysis and nozzle-shape optimization for the cold-gas dynamic-spray process*, Porc. Instn Mech. Engrs Part B: J. Engineering Manufacture **217**, pp 1603-1613 (2003)
4. X. Luo, G. Wang, and H. Olivier: *Shock tunnel produced cold gas-dynamic spray: modelling and simulation*, 25th Int. Symposium on Shock Waves, Bangalore, India (2005)
5. H. Olivier: *An improved method to determine free stream conditions in hypersonic facilities*, Shock Waves **3**, 2, pp 129-139 (1993)
6. H. Olivier: *Influence of the velocity gradient on the stagnation point heating in hypersonic flow*, Shock Waves **5**, 4, pp 205-216 (1995)
7. B. Esser: *Die Zustandsgröβen im Stoβwellenkanal als Ergebnisse eines exakten Riemannlösers*, PhD thesis, RWTH Aachen (1991)

Part XII

Multiphase Flow

Cavitation induced by low-speed underwater impact

H. Kleine[1], S. Tepper[1], K. Takehara[2], T.G. Etoh[2], and K. Hiraki[3]

[1] *School of Aerospace, Civil, and Mechanical Engineering, University of New South Wales/Australian Defence Force Academy, Canberra, ACT 2600, Australia*
[2] *Department of Civil Engineering, Graduate School of Science and Engineering, Kinki University, Higashi-Osaka 577-8502, Japan*
[3] *Department of Mechanical and Control Engineering, Faculty of Engineering, Kyushu Institute of Technology, Kitakyushu, Fukuoka 804-8550, Japan*

1 Introduction

The subject of cavitation, that is, the formation and subsequent dynamics of voids within a liquid, has intrigued scientists for centuries, as can be readily seen from the large number of publications on this topic (comprehensive overviews are given, e.g., by Young or Lauterborn et al. [1, 2]). Hydrodynamic cavitation, which is found in fluid machinery or, more generally, in systems where the liquid is accelerated to high fluid velocities, is arguably the most obvious and possibly best known form of this phenomenon. Generally, voids in a liquid can be generated by the application of tension or through the localized deposit of energy [2]. Typically, tension is applied either through hydrodynamic forces in flowing systems (hydrodynamic cavitation) or through pressure and/or tension waves generated in a macroscopically static liquid (acoustic cavitation).

Cavitation can occur not only in technical systems but is also common in biology and medicine. Because of the often highly transient character of the life cycle of the voids within a liquid and their equally often diminutive size, this process is often only recognized with the help of special diagnostics. A recent example in which the (unexpected) existence and subsequently the importance of cavitation processes has only been found by using specialized high-speed photography is the investigation of the snapping shrimp [3].

The present investigation introduces a process of generating tension waves, which to the best of the authors' knowledge has not been reported before in the literature. The phenomenon described here was first discovered by Etoh and Takehara in 2004, when they were experimentally investigating the elasto-hydrodynamic rebound of rigid spheres in a liquid. Theoretical predictions of a low-pressure field and cavitation phenomena in the contact zone during the rebound had been made by Wells and Tsuji [4], and the original intention of the experiments was to determine the characteristics of this region. A new high-speed video camera developed by Etoh et al. [5, 6] and subsequently produced by Shimadzu under the name HPV-1 was the main diagnostic tool for these tests, in which a glass sphere was released under water to impact onto a glass plate (Fig. 1a). Typical drop heights were of the order of 200 mm and glass spheres with diameters between 15 mm and 25 mm were used. While the cavitation zone in the contact region was observed as expected, other cavitation phenomena in substantial distance to the contact zone were also seen (Fig. 1b). These observations led to the investigations described in the following.

Size and material of the spheres together with the drop height dictate that the maximum macroscopic flow velocity is of the order of 1 m/s and thus one order of magnitude below velocities at which hydrodynamic cavitation can be expected. It was initially assumed that jets out of the contact zone might be formed during the impact process and that locally the flow velocity might exceed the cavitation threshold. A series of

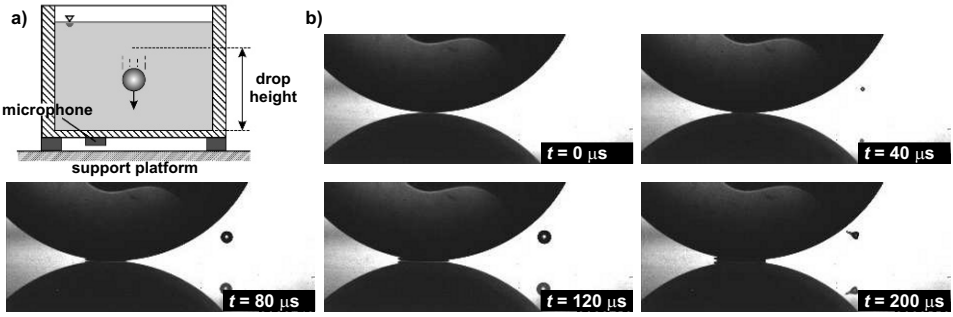

Fig. 1. a) Basic experimental set-up. The camera was triggered on the impact signal provided by the microphone. **b)** Underwater impact of a 20 mm dia. glass sphere on a glass plate in distilled water; impact speed approx. 1.5 m/s. Five frames of a shadowgraph sequence taken with 200 000 fps. $t = 0$ is the instant of impact. Times indicated in the figure have an uncertainty of $\pm 2\,\mu$s, however, time intervals between frames are correct within $0.5\,\mu$s. The camera looked at an angle onto the plate, which leads to mirror images of the sphere and the cavitation bubbles.

preliminary Particle Image Velocimetry (PIV) tests showed, however, that the flow velocities around the sphere remained of the same order of magnitude as the drop velocity. Furthermore, the considerable distance of the bubbles to the contact zone makes hydrodynamic cavitation a less likely cause for the observed process.

Subsequently, it was hypothesized that tension waves caused by the impact be the responsible mechanism for the formation of the observed cavitation. Such waves mostly occur as the result of an inverted reflection of compression waves from an interface across which a substantial difference of acoustic impedance exists [7]. Arguably the most well-known process of this sort is an underwater explosion: the compression wave generated by the explosion (Fig. 2a) reflects as a tension wave at the water/air interface, while a pressure pulse is transmitted into the air. Large clusters of cavitation bubbles form below the water surface almost immediately behind the reflected expansion wave (Fig. 2c). In small-scale tests with charges of 10 mg silver azide, first bubbles occur within $2\,\mu$s after the generation of the reflected expansion wave.

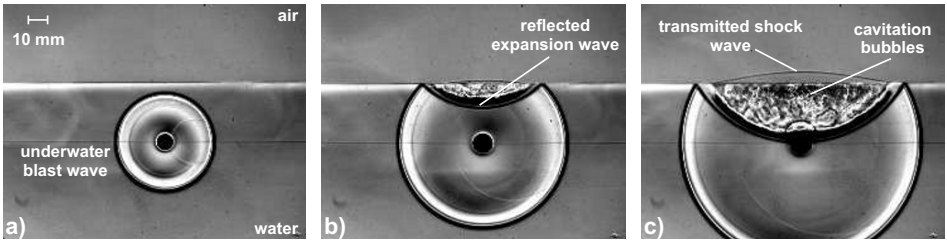

Fig. 2. Underwater explosion of 10 mg AgN_3. Three frames of a schlieren visualization sequence taken with 500 000 fps, time interval between shown frames $\Delta t = 14\,\mu$s.

A similar mechanism can be identified in the case of the low-speed underwater impact of a sphere onto a plate to explain the observed cavitation phenomena outside of the contact zone. The impact at time $t = 0$ generates pressure pulses within each partner of the collision (Fig. 3b). Please note that Fig. 3 is a highly simplified schematic that

only indicates the wave processes believed to be of major importance in this case. Waves that are transmitted into the liquid at the solid/liquid interface by pulses that propagate perpendicularly to the interface, for example, are not shown as their strength is believed to be insignificant. Furthermore, it was not attempted to depict the exact wave configuration within the sphere. Finally, waves caused by the presence of the accelerometer have not been indicated. Once the pressure pulses have reached the respective interfaces to the surrounding medium, namely the top of the sphere and the bottom of the plate, they are reflected as expansion waves. In the case of the plate (thickness d) the reflection occurs at a time $t_1 = d/a$, where a is the sound speed within the plate. When this expansion wave again reaches the upper surface of the plate after a time $t_2 = 2\,d/a$, it propagates into the liquid, where it possibly interacts with the expansion wave generated by the sphere (Fig. 3d). This wave reflection process is repeated several times with ever diminishing amplitudes, but only the first reflection cycle is significant (hence all secondary reflected waves have been omitted in Fig. 3). The tension wave transmitted into the liquid then triggers the cavitation.

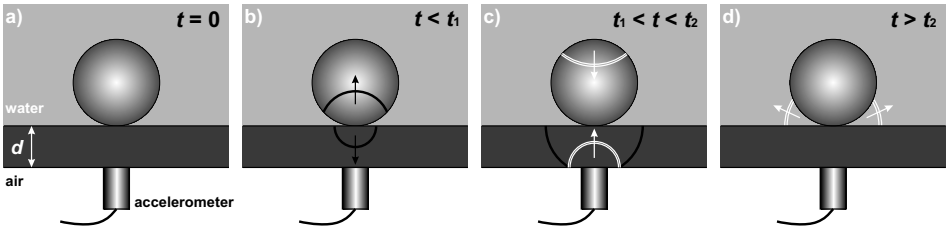

Fig. 3. Simplified schematic of the wave propagation as a result of an elastic collision between a sphere and a plate. **a)** Basic configuration at time of impact. **b)** Generation of pressure pulses in the plate and in the sphere. **c)** Reflection of expansion waves at the interface to medium of lower acoustic impedance. **d)** Resulting tension wave in the liquid.

If the lower side of the impact plate faces a medium of low acoustic impedance, such as sketched in Fig. 3, the reflection process occurs as described in straightforward fashion. If non-submersible transducers are mounted on the bottom as shown in Fig. 3a, such a configuration is automatically achieved. Should there be no substantial air gap between the impact plate and the platform on which the setup is resting (see Fig. 1a), i.e., should the impact plate be in direct contact with this platform, two different scenarios are possible:

- The acoustic impedance mismatch between the impact plate and the support platform is negligible: in this case, the generated pressure pulse would continue to propagate into the support platform. If this platform is of considerable thickness, the inverted reflection would either occur with significant delay or not at all, if the pressure pulse is attenuated in the platform material. In either case, the occurrence of cavitation through the described process is highly unlikely.
- A considerable mismatch in the acoustic impedance exists between the impact plate and the support platform. If the acoustic impedance of the support platform is lower, the reflection proceeds as described in Fig. 3. If it is higher (e.g., when a glass or plexiglass impact plate rests on an optical bench made of metal or granite), the pressure pulse will reflect without inversion at this interface. The inversion only occurs

when this reflected pulse reaches the plate/liquid interface, and it has to go through another reflection cycle before an expansion wave, at a time $t_3 = 4\,d/a$, propagates into the liquid. The cavitation-inducing tension wave is therefore both weaker and more delayed compared to the straightforward reflection case described above, and the resulting cavitation processes, with all other parameters kept constant, will be weaker or possibly not occurring at all.

While pure liquids without any form of contamination can withstand very high tensions without cavitating [7], the presence of contaminants, such as microscopic gas bubbles or minute solid particles, provides nuclei for cavitation and drastically lowers the cavitation threshold [1, 2, 7]. One would therefore expect different cavitation characteristics if liquids with clearly different contamination levels are used, such as distilled water and tap water. The tension wave in the liquid shown in Fig. 3d will therefore only then lead to the onset of cavitation, if it encounters an adequate nucleus.

2 Experiments

In the experimental campaigns that were conducted to investigate the observed cavitation phenomena, the following parameters were varied:

- drop height (from about 150 mm to 1 m);
- sphere size and material (19 mm to 30 mm; glass and stainless steel);
- contamination level of liquid (distilled water and tap water).

For larger drop heights the sphere had to be guided by a rod/rail system in order to achieve reproducible impact positions, while at smaller drop heights ($\leq$ 200 mm), the sphere was simply free-falling. An accelerometer (Bruel and Kjaer Type 4366) was mounted at the bottom of the plate (as sketched in Fig. 3) to detect the arrival of the compression wave passing through the plate and to trigger the high-speed camera (analogous to a digital oscilloscope, the camera can be triggered on any of its hundred frames). Different high-magnification, high-sensitivity schlieren systems with schlieren head focal lengths between 6 m and 9 m were set up to visualize the waves generated by the impact. The camera was the aforementioned Shimadzu HPV-1, while illumination of about 1 ms duration was provided by a strong flash gun (Metz Mecablitz 45 CT-4). The flashlight was triggered by the sphere shortly before impact by interrupting a laser beam located about 2 mm above the plate. The system was synchronized in a way that the flash was approximately at its emission peak when the impact occurred. For direct observation of the impact and the bubble formation, a simple lens-based shadowgraph system was used, which for frame rates up to 125 000 fps could be run with a continuous light source. This system was also used to determine the speed and the acceleration of the sphere during the final 50 mm before impact. It was found that the speed did not exceed 2.7 m/s while acceleration levels within the visible test section were negligibly small – hence it is justified to assume that the sphere moves with constant velocity prior to the impact.

3 Results and discussion

Figure 4 shows frames of a sequence obtained by direct observation, similar to the frames shown in Fig. 1. In this case, the liquid was tap water. The considerably higher degree of

contamination becomes obvious through a significantly larger number of bubbles, which are produced throughout the whole field of view up to a height of about the sphere radius. Bubbles at larger vertical distances from the plate were only observed in less than 1% of all conducted trials.

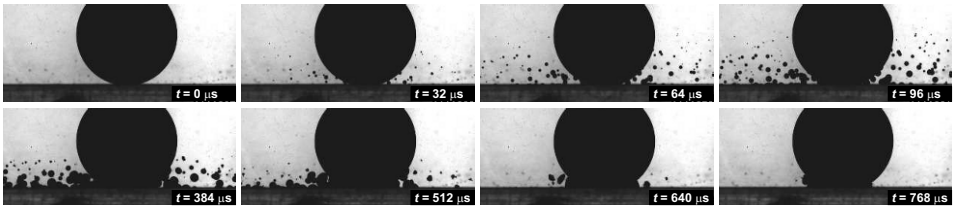

Fig. 4. Underwater impact of a 25 mm dia. steel sphere on a 12 mm thick plexiglass plate in tap water; impact speed approx. 2.5 m/s. Eight frames of a shadowgraph sequence taken with 32 000 fps. $t = 0$ is the instant of impact. Times indicated in the figure have an uncertainty of $\pm 14\,\mu$s due to the low frame rate, however, relative time differences between frames are correct within $2\,\mu$s. During the time interval covered by the shown frames, the steel sphere is essentially motionless. A recognizable rebound only occurs at about $t \approx 800\mu$s, when the initial cavitation activity has terminated.

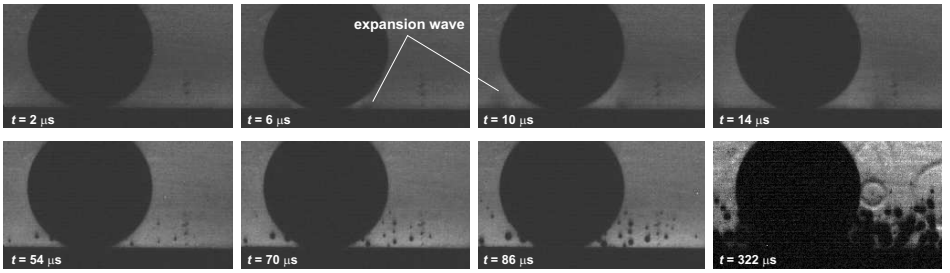

Fig. 5. Underwater impact of a 25 mm dia. steel sphere on a 12 mm thick plexiglass plate in tap water; impact speed approx. 2.5 m/s. Eight frames of a schlieren sequence taken with 250 000 fps. $t = 0$ is the instant of impact. Times indicated in the figure have an uncertainty of $\pm 1.5\,\mu$s, however, relative time differences between frames are correct within $0.5\,\mu$s. In this experiment, bubbles become visible after approx. $50\,\mu$s and begin to collapse about $250\,\mu$s later.

Figure 5 shows a magnified view of the impact zone, taken with a higher frame rate and the schlieren system. In this trial, the camera recording was synchronized with the accelerometer. In the first row of Fig. 5, a wave is seen to emanate from the contact zone. As this is an expansion front, it is not as well defined as a shock wave and its appearance is clearer on the animated visualization than on single frames. In the given experiment, this wave occurs about $5\,\mu$s after the accelerometer registers the impact. This time interval corresponds with sufficient accuracy to the time a pressure pulse needs to traverse the 12 mm thick plexiglass plate, if one assumes a sound speed of 2.6 km/s for plexiglass [8]. Within about $50\,\mu$s after the wave has appeared, first cavitation bubbles become visible (second row, Fig. 5). For the given image resolution, the position of the sphere remains constant during the depicted time, which shows that the characteristic time of the

mechanical impact is orders of magnitude larger than that of the observed wave processes. This supports the assumption that hydrodynamic processes caused by the motion of the sphere have only a minor effect on the formation of cavitation. The generated bubbles undergo typical oscillations and form jets towards the sphere or towards each other, before eventually collapsing. The collapse generates spherical pressure pulses that are similar to blast waves (last frame of Fig. 5).

Tests with a thicker ground plate yielded essentially identical patterns, with the emanation of the expansion wave being delayed by the additional time the wave requires to traverse the thicker plate. The limited variation of drop height and sphere size and material has so far not revealed any obvious trends – cavitation has been seen even for the so far smallest sphere and lowest drop height. Preparations for tests in which the energy of the impact will be systematically varied to determine a threshold for cavitation onset in this test scenario are underway at the time of writing. So far, cavitation has been observed for impact energies around 100 mJ, which is orders of magnitude lower than what is typically found in laboratory-scale underwater explosions (such as the one shown in Fig. 2) or impact slugs such as those used by Trevena [7].

The influence of the expansion wave generated by the sphere is not fully clarified yet. All schlieren records show an emanating expansion wave that appears to be mainly generated within the plate. However, in a brief test series with a hemispherical impact body (in this case a cylinder with hemispherical tip), where the reflected expansion wave from the impact body would not exist or arrive significantly later, no cavitation was observed, although all other parameters were kept constant. This issue requires further studies, which in addition to shape variations of the impacting body will also include the use of materials with significantly different acoustic impedances.

4 Conclusions

The experimental evidence described here has so far supported the hypothesis that elastic waves generated during the impact are the responsible mechanism for the onset of cavitation in the presented low-speed underwater impact scenario. With the help of a newly developed high-speed video camera and a high-sensitivity schlieren system it was also possible to directly visualize the generated tension waves which are considered the cause of the subsequent formation of cavitation bubbles. The tests have also illustrated that considerable cavitation can exist in an environment in which at first sight one would not expect such a process. Impact energies of around 100 mJ have been shown to be sufficient for the generation of cavitation bubbles.

References

1. Young FR: *Cavitation*. McGraw-Hill, London (1989)
2. Lauterborn W, Kurz T, Mettin R, Ohl CD: Adv. Chemical Physics **110**:295 (1999)
3. Versluis M, Schmitz B, von der Heydt A, Lohse D: Science **289**:2114 (2000)
4. Wells J, Tsuji Y: Proc. J.Soc. Multiphase Flow Meeting, Tsukuba (1994)
5. Etoh TG, Poggemann D, Ruckelshausen A et al.: Digest of Technical Papers, ISSCC 2002, pp.46-47 (2002)
6. Etoh TG, Poggemann D, Kreider G et al.: IEEE Trans. Electron. Dev. **50**(1):144 (2003)
7. Trevena DH: *Cavitation and tension in liquids*. Hilger, Bristol (1987)
8. Constantin C: Laser and Particle Beams **22**:59 (2003)

Experimental study of shock wave and bubble generation by pulsed CO_2 laser beam irradiation into muddy water

K. Ohtani[1], D. Numata[1], K. Takayama[2], T. Kobayashi[3], and K. Okatsu[4]

[1] *Institute of Fluid Science, Tohoku University, 2-1-1, Katahira, Aoba, Sendai, Miyagi, 980-8577, Japan*
[2] *Biomedical Engineering Organization, Tohoku University, 2-1-1, Katahira, Aoba, Sendai, Miyagi, 980-8577, Japan*
[3] *Japan Drilling Co., LTD., 2-4-3, Horidome, Nihonbashi, Chuo, Tokyo, 103-0012, Japan*
[4] *Japan Oil, Gas and Metals National Corporation, 1-2-2, Hamada, Mihama, Chiba, 261-0025, Japan*

Summary. This paper reports an experimental result of laser-induced shock waves and bubble generation in muddy water. 5 kW pulsed CO_2 laser beams of 10.6 μm in wavelength diffusively were irradiated repeatedly at 10 Hz onto a biotitegranite surface which was placed at 50 mm deep from clay particle laden water surface. This water mixture was called muddy water of equivalent density of 1.02 g/cc. Repeated exposure of CO_2 laser beams firstly induced a cavitation column in muddy water. The laser energy was transmitted in the cavitation column and by its deposited on the biotitegranite surface, the surface was eventually molten producing spherical glass beads. Repeating this procedure, we found that the laser beam irradiation can excavate the submerged rock surface.

1 Introduction

The motivation of the present project is for the exploitation of high power laser assisted excavation of ocean bottom rocks. Reed et al. [1] irradiated 1.6 kW pulsed Nd: YAG laser beams on a rock surface submerged at 2 mm depth from water surface and confirmed that the rock surface was molten before properly perforated. Encouraged by this finding, we used relatively small diameter CO_2 beams irradiating onto a submerged biotitegranite surface. We found that the laser beam irradiation into water induced underwater shock waves and cavitation bubbles, with which the laser energy was effectively deposited on the rock surface. Brinkmann et al. [2] and Dunn et al. [3] used CO_2 laser-induced bubble column to pierce a submerged acrylic block and found the irradiation for about 4 ms penetrated a 20 mm thick PAA (polyacrylid acid) plate [2].

This paper reports a result of a laser-induced shock waves and bubble generation in muddy water by repeated irradiation of 5 kW pulsed CO_2 laser beams of 10.6 μm wavelength at 10 Hz from water surface. The process of bubble column formation was recorded with a high-speed digital video camera. We confirmed that a biotitegranite submerged in clay particle laden water, muddy water, was excavated.

2 Experimental setup

Figure 1 shows a setup for laser-induced shock wave and bubble generation in muddy water in a 300 mm $\times$ 300 mm $\times$ 300 mm acrylic chamber. Pulsed CO_2 laser (TLF5000AM,

TRUMPF Inc., wavelength of 10.6 μm, nominal power of 5 kW, doughnut mode, pulse frequency variable from 10 to 100 kHz) was irradiated into muddy water. We observed the process of laser-induced bubble formation in water by using a high-speed digital video recording (Phantom V7.3, Vision Research Inc., frame rate up to 180,000 frame/s, sensitivity of 4,800 ISO/ASA monochrome, spatial resolution of 800 pixel $\times$ 600 pixel). The rock specimen was Biotitegranite, relative density of about 2.64 g/cm^3, 70 mm $\times$ 70 mm $\times$ 50 mm, submerged at h = 50 mm deep from muddy water surface. Muddy water is water/bentonite 4 wt% mixture having equivalent density of about 1.02 g/cc. It is noticed that muddy water is traditionally employed to stabilize boring holes by circulating near the boring head. Hence we follow this technical tradition.

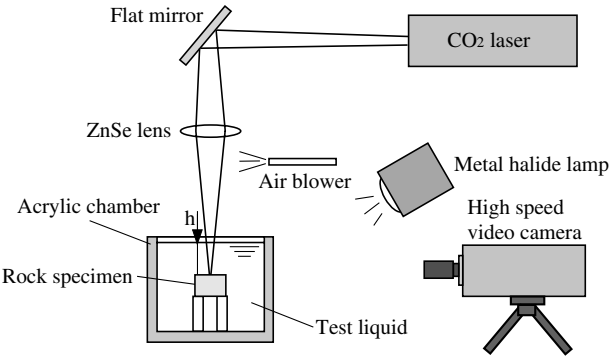

Fig. 1. Experimental setup for bubble generation by pulsed CO_2 laser beam irradiation into muddy water.

3 Result and discussion

3.1 High-speed video recording of pulsed CO_2 laser-induced bubble formation

Time resolved images of pulsed CO_2 laser-induced bubble column formation in water are shown in Fig.2. A pulsed CO_2 laser beam diffusively irradiated the rock specimen at 10 Hz, average energy of 250J/pulse, pulse duration of 50 ms and the observation was performed at interframe time of 55.5 μs, exposure time of 46 μs. Every 5th frame, in other words, 277.5 μs time interval, was sequentially presented.

The bubble was generated at first underneath the water surface in Fig.2(b). With further transmission of laser beams through the growing bubble, local vaporization continued and the bubble diameter was enlarged and bubble length was elongated in Fig. 2(c)-(h). The leading edge of conically shaped cavitation bubble was separated and the split part collapsed due to excited by exposures of pressure waves in Fig. 2(i)-(l). Then the bubble column length became shorter, and a portion was slit, and collapsed repeatedly, which eventually decreased the transmission of laser energy as seen in Fig. 2(m)-(x).

Figure 3 shows the time variation of bubble column length L measured from the surface. L was estimated from the sequential high-speed video images of every 55.5 μs interval. Open circle designates the point in Fig. 2(a)-(x). The bubble length L was

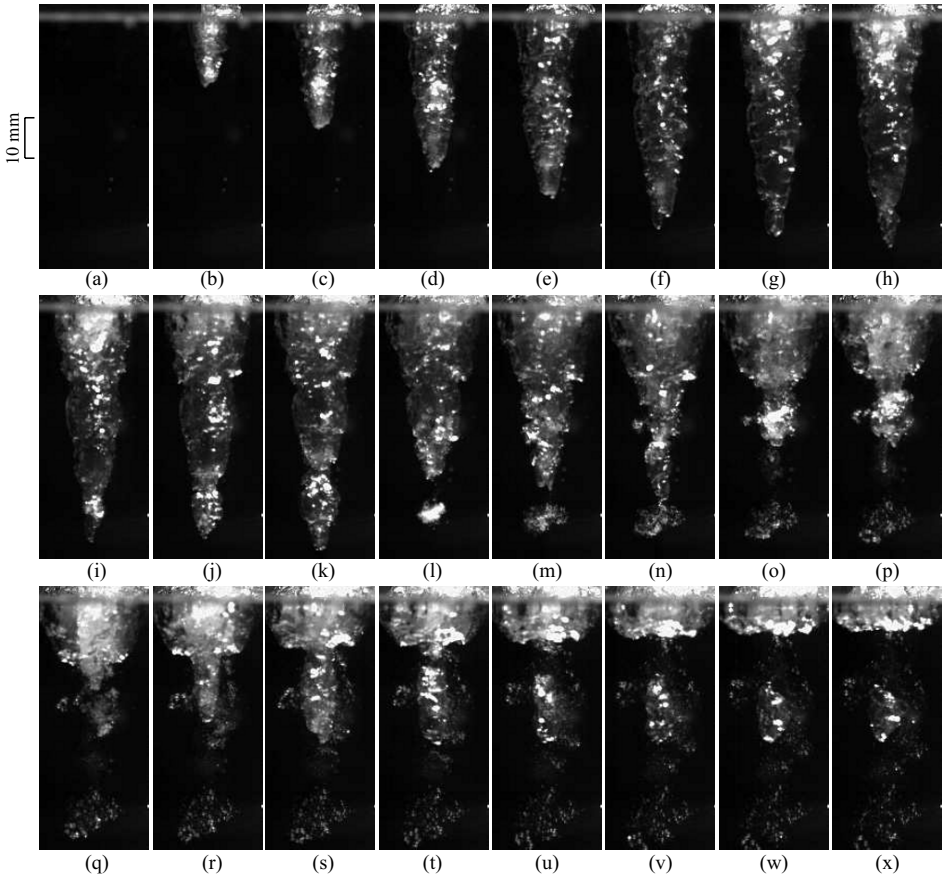

Fig. 2. Sequential photographs of CO_2 laser-induced bubble column. (interframe 55.5μs, exposure time 46μs, the frame interval of 277.5μs)

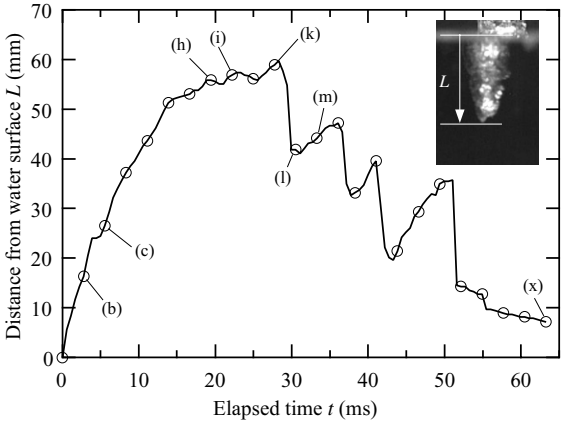

Fig. 3. Time variation of CO_2 laser-induced bubble column.

increased with time during $t = 0 \sim 28$ ms at the specified time instant. The average growth rate of bubble column was 2.1 m/s and the maximum length was 59.7 mm at 28.3 ms.

3.2 Laser-induced excavation in muddy water

Pulsed CO_2 laser beam irradiation onto the biotitegranite specimen submerged at 50 mm depth from muddy water surface is shown in Fig. 4 (left). The direct laser beam irradiation produced about 5 mm diameter damage pattern on the specimen surface. While shifting the irradiation spot as shown in Fig. 4 (right), the damage pattern hole moved in about 15 mm in maximum diameter. A maximum depth of 48 mm was achieved on the specimen surface.

At short time after laser beam irradiation onto the specimen surface, the biotitegranite surface was instantaneously molten and the melt immediately became spherical shape due to the surface tension of molten rock and the rate of its quenching in muddy water environment. Spherical translucent glass beads so far formed were eventually ejected from the bottom of the hole as seen in Fig. 5 (left). Figure 5 (right) shows the histogram of the spherical glass bead diameter. It was ranging about 0.2 to 3 mm in diameter, 0.98 mm in average.

Figure 6 shows the photographs of pulsed CO_2 laser beam irradiation on biotitegranite submerged at 50 mm depth in water and the interframe time of 52.5 μs, exposure time of 47 μs. Laser-induced bubble column front reached the specimen surface and the illumination was observed by reflection of laser beams through/ from the bubble column as seen in Fig. 6 (a). Then after about 11 ms, molten biotitegranite particles were ejected from bottom layer in Figs. 6 (b), (c) and (d). The SiO_2 component of the molten biotitegranite became spherical shape. The glass beads were driven by a shock wave and laser-ablation induced bubble formation at the bottom of the excavation hole.

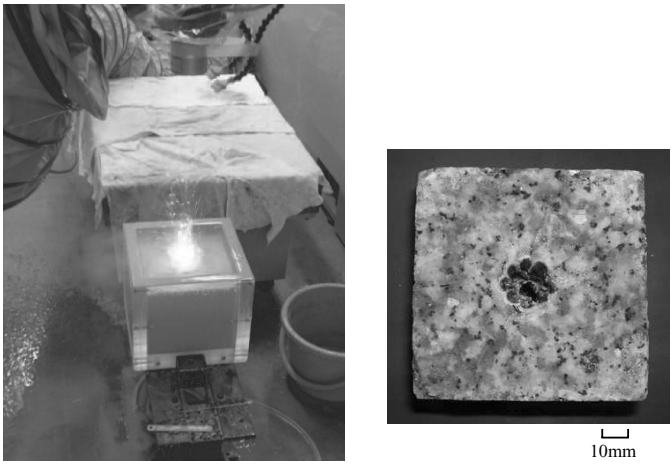

Fig. 4. Photographs of pulsed CO_2 laser beam irradiated on the biotitegranite submerged at 50 mm depth from water surface in muddy water and the excavation hole of the biotitegranite specimen.

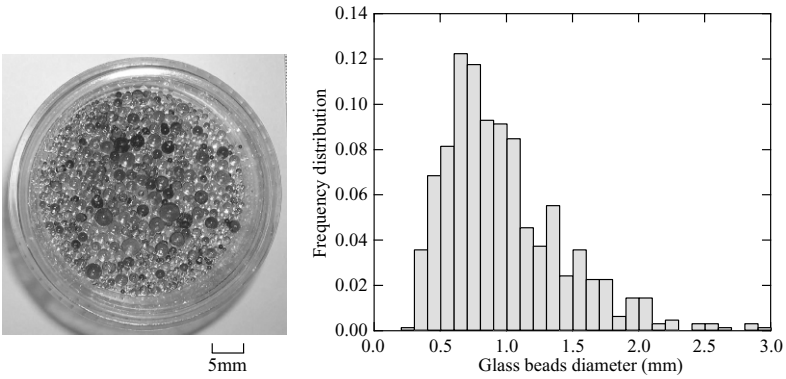

Fig. 5. Photograph of spherical glass beadss and glass beads diameter.

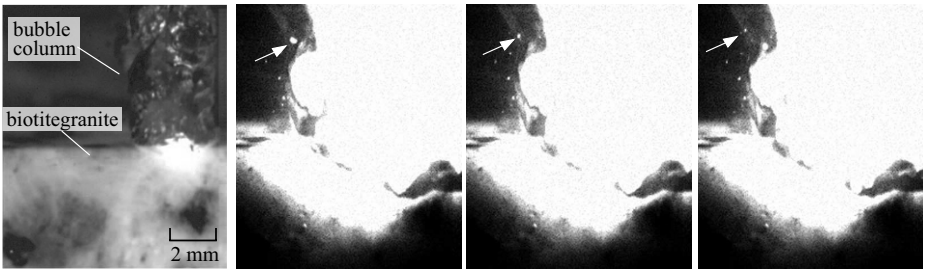

Fig. 6. Photographs of pulsed CO_2 laser beam irradiation on biotitegranite submerged at 50 mm depth in water.

4 Conclusion

A result of shock wave and bubble generation indued by pulsed CO_2 laser beam irradiation into muddy water were presented. The results obtained are summarized as follows:

(1) The process of 5 kW pulsed CO_2 laser-induced bubble column formation was visualized by directly with high-speed recording. CO_2 laser generated bubble column was about 60 mm in length and oscillated.
(2) Pulsed CO_2 laser beam irradiation on the biotitegranite submerged at 50 mm depth from muddy water surface. We succeeded to excavate holes of 15 mm in diameter and 48 mm in depth on the biotitegranite surface. Molten layers of biotitegranite at the bottom of the hole instantaneously shaped into glass beads ranging about 0.2 to 3 mm in diameter and were eventually ejected from the bottom of the hole.

Acknowledgement. The authors wish to acknowledge Messrs. T. Akama, T. Ogawa, S. Hayasaka, K. Kikuta, M. Honna of Institute of Fluid Science, Tohoku University, and Messrs. S. Sanoki, T. Adachi of Japan Drilling Co., LTD. for their assistance in performing the present experiments.

References

1. Reed, C. B., Xu, Z., Parker, R. A., Gahan, B. C., Bataeseh, S., Graves, R. M., Figueroa, H., Deeg, W., Application of high powered lasers to drilling and completing deep wells. Current Annual Report, ANL/TD/TM03-02, Argonne National Laboratory (2003)
2. Brinkmann, R., Theisen, D., Brendel, T., Bringruber, R., Single- pulse 30-J holmium laser for myocardial Revascularization - A study on ablation dynamics in comparison to CO_2 laser - TMR. IEEE Journal of Selected Topics in Quantum Electronics, **5**(4) (1999), pp.969-980.
3. Dunn, I., Bridger, P. M., Duley, W. W., Observation of stable propagation channels for CW CO_2 laser radiation in liquid water. J. Phys. D: Appl. Phys. **26** (1993), pp.1138-1140.

Nonequilibrium ionization of iron nanoparticles in shock front

A. Drakon, A. Emelianov, and A. Eremin

Institute for High Energy Density RAS, Moscow, 125412, Izhorskaya 13/19, Russia

Summary. Experimental observations of ionization in a front of a weak shock wave($2.5<M<3.8$) propagated in inert gas with small admixture of iron nanoparticles were performed. Estimated effective ionization energy showed the values more than ten times less than the work function of bulk iron, which is clearly indicated nonequlibrium nature of the process. Evidences of theoretically predicted zone of the charge separation in front of shock wave were observed.

1 Introduction

In a number of recent studies the considerable nonequilibrium effects in a relaxation zone of shock wave were observed [1–3]. It was shown that most effectively these processes are developed in relatively weak shock waves in the light gases with a small admixture of heavy molecules [2]. Recently, interest to this problem was excited by the experimental evidences of intensive peaks of radiation in the mixtures containing small additives of metal carbonyls $Fe(CO)_5$ [4] and $Mo(CO)_6$ [5]. In both works two various mechanisms of this phenomena have been discussed. The first one links the observed radiation peaks with the high energy collisions in the zone of translational relaxation of shock wave front. The second mechanism assumes, that radiation arises due to the fast recombination of metal atoms formed as a result of immediate decay of carbonyl molecules in a relaxation zone of a shock wave. Independently of real mechanism simple evaluations show that summary energetic barrier for an excitation of observed radiation may amount about 8 eV. Such value can be sufficient for ionization of metal clusters [6]. Since the efficiency of high-energy collisions increases with the growth of cluster-gas molecules mass ratio $R = M/m$ [7], it is especially likely, that the effect of nonequilibrium ionization can be observed in the mixtures, containing iron nanoparticles consisting of 10^4–10^6 atoms. Appearance of free electrons and heavy positively charged particles in front, in turn, may result in a number of electrodynamic effects, caused by a considerable difference of mobility of oppositely charged particles [8–10].

The goal of this study was the experimental investigation of nonequilibrium ionization processes in shock waves propagating in gas mixture at room temperature, containing electrically neutral iron nanoparticles.

2 Experiment

For creation a dredge of iron nanoparticles at room temperature ahead of shock wave an effect of nanoparticle photosynthesis under the influence of UV radiation on $Fe(CO)_5$ containing gas mixture was used. According to results of [11], after exposure of UV radiation on the mixture of $1\%Fe(CO)_5$ + Ar due to photolysis of $Fe(CO)_5$ a supersaturated vapor

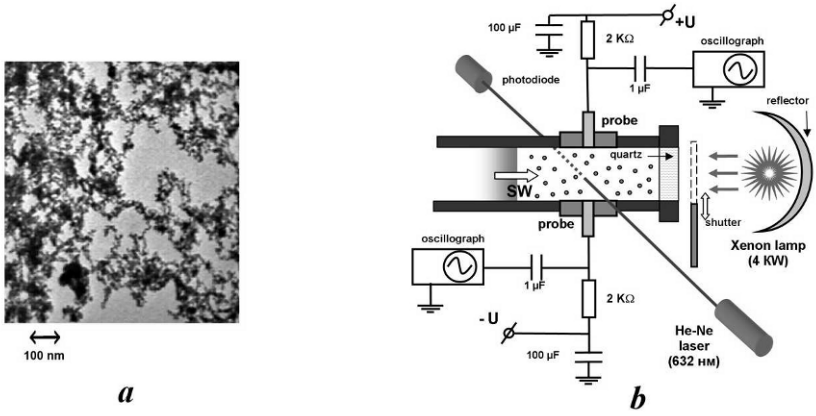

Fig. 1. (**a**) Electronic microphotography of iron nanoparticles samples, formed during UV-photolysis of $Fe(CO)_5$ vapor, (**b**) Experimental setup

of iron atoms is generated, which immediately condense into spherical nanoparticles with diameter 20-40 nm (see Fig. 1a). For that goal shock tube was equipped with the powerful source of UV radiation (4KW xenon lamp) with focusing reflector (Fig. 1b). Radiation was brought into shock tube trough the quartz window in its flange. Directly before shock wave start an investigated volume of shock tube was irradiated during 20 s, which resulted in $Fe(CO)_5$ photolysis, supersaturated iron vapor formation and its condensation to clusters. The process of clusters formation was registered by extinction measurements at wavelength 632 nm. For the measurements of free electron concentration the shock tube was equipped by high-sensitivity electric probes of a special design. Diameter of a probe was 6 mm, the electric voltage on the probes could change in a range -90 ÷ +90 V. For the absolute calibration of the probes a special series of test experiments with the argon containing a natural impurity of sodium was carried out. According to the data of the previous study [12], the natural contents of sodium in the majority of gases (argon, nitrogen, air) is rather stable and equal $(2\pm1)*10^{-5}\%$. In Fig. 2a the characteristic profile of voltage change on a probe with potential +50V behind shock wave at the temperature T = 1710 K is given. Sodium ionization kinetics and achievement of equilibrium level of the signal are clearly seen. In the following Fig. 2b the calibration curve of the probes at U = +50 V is shown. Thus, carried out calibration experiments have shown, that sensitivity of a probe is sufficient for measurement of concentration of electrons from $\geq 10^8$ cm^{-3}, and the resolution time is determined exclusively by the size of a probe and the shock wave velocity.

Experiments in the mixtures containing iron nanoparticles were carried out at relatively low intensity of shock waves ($2.5<M<3.8$), so equilibrium temperature behind shock wave T_2 amounted less than 1500 K and no any equilibrium ionization of easy-ionized admixtures could be expected. Nevertheless, probes have recorded the clearly seen peaks of electron current during shock wave propagation in the mixture, containing iron nanoparticles. In Fig. 3 typical oscillograms observed in experiments are shown.

Upper graph is the extinction of laser beam, which shows an initial extinction of cold particles before the shock wave, a schlieren-peak of shock wave front propagation and the following level of attenuation of beam which is proportional to the particles volume

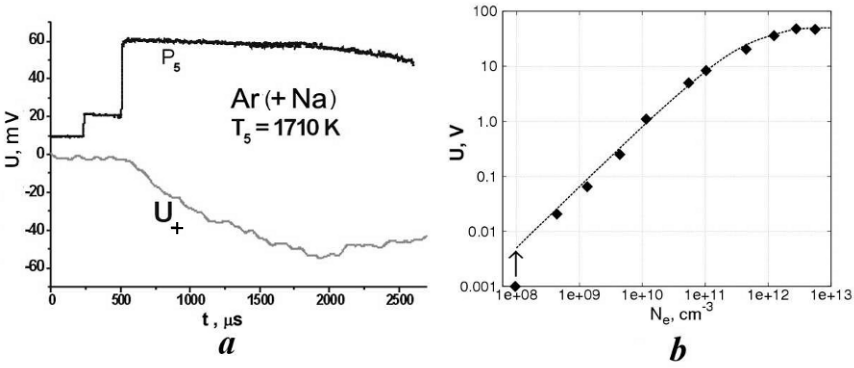

Fig. 2. (**a**) Time profile of the pressure and the voltage on electric probe behind incident and reflected shock waves in Ar with the natural admixture of Na. T_5 = 1710 K, P_5 = 14 bar , U = +50 V, (**b**) Calibration curve for the probe

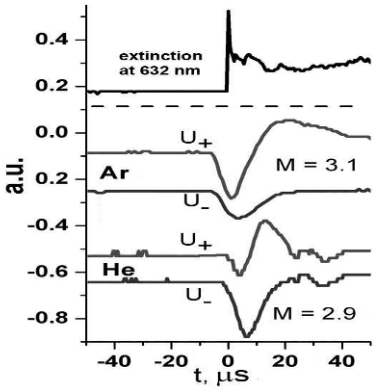

Fig. 3. Typical oscillograms

fraction. Lower plots show the signals of electron current from the probes, which appear few microseconds earlier and disappear few microseconds later than laser schlieren-peak in accordance with the longitudinal size of the probes (6 mm). Amplitude of measured signals varied from 2 up to 20 mV, which corresponds to the concentration of electrons in the range 10^8–10^9 cm^{-3} (see Fig. 2b). Since the mean particle size was about 10^6 atoms and assuming that all Fe atoms of $Fe(CO)_5$ were condensed in nanoparticles, the concentration of particles before shock wave was about 10^{10} cm^{-3}. Thus, due to nonequilibrium processes in a shock wave front only one of 10-100 particles has ejected an electron. It ought to be remarked that peaks of electron current were observed from the probe with positive voltage as well as from the probe with negative voltage up to -50 V, which is the evidence of existence of zone with significant negative potential in a front of a shock wave.

Intensity of both signals grew at increase of Mach number of shock wave and rapidly fell down at pressure decreasing. In the next Fig. 4 all data about maximum amplitudes of increase of the negative voltage on the negative probe normalized on initial mixture

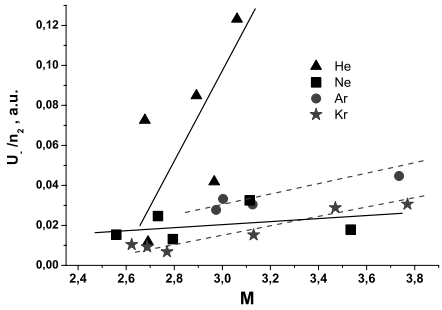

Fig. 4. Maximal amplitudes of increase of the negative voltage on the negative probe in different carrier gases with admixture of iron nanoparticles

pressure measured in different carrier gases are summarized. It is clearly seen that the most sharp increase is observed in helium and the most gentle – in neon. The similar behavior of signals was observed on the probe with positive potential. Thus, the obtained data showed that with the rise of the intensity of a shock wave and the decrease of the weight of carrier gas not only concentration of electron, but also the value of negative potential in front zone were increasing.

3 Discussion

Obtained data are the first evidences of weakly ionized nonequilibrium plasma formation in the front of the weak shock wave propagated in inert gas containing iron nanoparticles. Preliminary analysis already allowed to claim that in front of shock waves with Mach number more then 2.5 free electrons are appearing and due to their fleeing from ionized nanoparticles a zone with negative potential is forming. Charge separation effect in front of shock wave was predicted in a number of theoretical studies [8-10]. These effects could be the most strong at small concentrations of charged particles (large Debye radius) and the large difference in mobility of oppositely charged particles. Performed experiments completely met these conditions. Measured electron concentrations (10^8–10^9 cm^{-3}) correspond to ionization less then 10^{-10}. Mass ratio of positively charged particles and free electrons equals approximately 10^{11} for particles containing about 10^6 atoms. Thus, appearance of zone of separation of rapidly accelerated electrons and slow positively charged particles seems rather probable. Since the potential difference in front zone has to increase with the intensity of charge separation effect, it is reasonable to assume that the value of negative potential in the zone of fleeing electrons would be proportional to the velocity of neutral atoms flow in front of the wave. That assumption is qualitatively confirmed by the next Fig. 5 where ratio of peaks on negative (U_-) and positive (U_+) probes (reflected the value of negative potential in front zone) is plotted as the function of flow velocity behind shock waves in different gases. Another important characteristic of observed phenomenon is the dependence of measured electron concentration on intensity of shock waves. Assuming, that the primary mechanism of electron appearing was an ionization of iron nanoparticles in their collisions with inert gas atoms in the

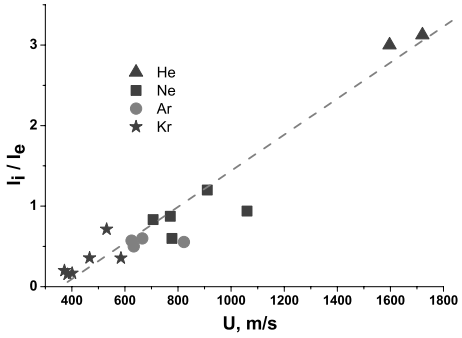

Fig. 5. Ratio of peaks on negative (U_-) and positive (U_+) probes as the function of flow velocity behind shock waves in different gases

front of a shock wave, it is reasonable to assume that the probability of electron detachment should be proportional to the factor $\sim \exp(-2E_{eff}/mu^2)$, where E_{eff} – effective ionization energy (electron work function) of iron nanoparticles, $mu^2/2$ – mean kinetic energy of carrier gas molecules in front of shock wave relatively to the particles before the front. For the other hand the concentration of free electrons n_e emitted from the particles under collisions with fast carrier gas atoms of the shock front should be proportional $N_1{*}n_2$, where N_1 is concentration of nanoparticles before the front and n_2 is gas atoms concentration behind the front. Then, general intensity of the effect and, consequently, integral yield of free electrons, is proportional mass ratio R = M/m. Thus we can assume that observed maximum values of electronic potential on both probes should be proportional $U \sim N_1{*}n_2{*}R$. In the next Fig. 6 the results of all carried experiment are shown as generalized dependence $\ln(U/(N_1{*}n_2{*}R)) \sim 2/mu^2$.

One can see that offered empirical relation successfully described the obtained data. Notable that the value of effective ionization energy E_{eff}, derived from the slope of this

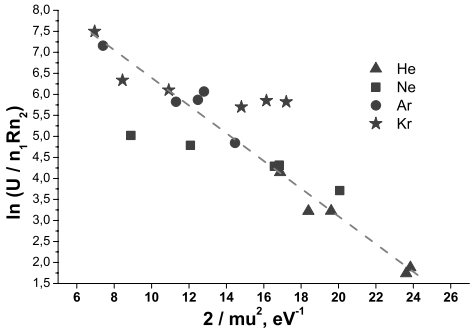

Fig. 6. Boltzmann dependence of measured potentials in a shock wave front in the different carrier gases with admixture of iron nanoparticles on the mean kinetic energy of gas molecules in a shock heated flow

plot , is merely ~ 0.3 eV, that is about 14 times less than the work function for bulk iron. The reason of this discrepancy is most likely the nonequilibrium velocity distribution of carrier gas molecules within shock wave relaxation zone and, thus, inadequacy of term ,,mean kinetic energy" under such conditions. In fact, last achievements in Boltzmann equation solution [2] and especially in DSMC of molecular velocity distribution function transformation [13] in a shock wave front show, that the most essential deviation from the equilibrium are expected in the far high energetic wing ($E > 30E_{eq}$) of distribution function. Therefore the quantitative evaluation of the role of high energy collisions in a shock wave front in observed phenomena of nonequilibrium ionization of iron nanoparticles must be the subject of particular investigation, which is out of frame of present work.

4 Conclusion

A first experimental observation of nonequilibrium ionization and charge separation in front of a weak shock wave propagated in inert gas with small admixture of iron nanoparticles are performed. The peaks of electron concentration from 10^8 up to $10^9 cm^{-3}$ in front of shock waves with Mach number from 2.5 up to 3.8 have been observed. Besides that the increase of the negative voltage on the probe with negative potential up to -50 V was also registered, which is a hint of existence of zone the charge separation in a front of shock wave.

Acknowledgement. The support of this study by the Program P-09 of Russian Academy of Sciences and RFBR is gratefully acknowledged.

References

1. Zeldovich Ia.B., Genich A.P., Manelis G.B.: Dokl. Acad. Nauk SSSR, **248**, N.2, 1979, p.349-351
2. Emelianov A.V., Eremin A.V., Velikodnyi V.Yu.: J.Tech.Phys, **69**, N.9, 1999, p.23-33
3. Divakov O.G., Eremin A.V., Ziborov V.S., Fortov V.E.: Dokl. Ross. Akad. Nauk, **373**, N.4, 2000, p.487-490
4. Kozlov P.V., Losev S.A., Romanenko Yu.V.: J.Tech.Phys. Letters, 2000, **26**, N.22, p.69-75
5. Eremin A.V., Shmakov A.V., Velikodnyi V.Yu., Ziborov V.S.: Nonequilibrium UV radiation of molybdenum atoms in a. weak shock wave front. In: *Abstracts of 24th Int. Symp. Rarefied Gas Dyn.*, July, Bari, Italy, 2004, p.22
6. Nagaev E.L.: Uspekhi Fizicheskikh Nauk, **162**, N 9, 1992, p.49-163
7. Emelianov A.V., Eremin A.V., Velikodnyi V.Yu: Study of non-equilibrium effects within shock front in gas-nanoparticles mixture. In: *Proc. 22-d International Symposium on Shock Waves (ISSW-22)*, London, UK, July 18-23, 1999, p.807-812
8. Velikodnyi V.Yu., Bityurin V.A.: Prikl. Phys., 2002, N.5, p.90-98
9. Rubinstein R., Auslender A. H.: ICASE Report N.2000-3, NASA/CR-2000-210081
10. Biturin V.A., Klyuchnikov N.I.: Fluid Dynamics, 2005, **40**, N.3, p.494-502
11. Emelianov A., Eremin A., Jander, H, Wagner H.Gg: Zeitschrift fur Physikalische Chemie, 2003, **217**, p.1361-1368
12. Eremin A.V., Naboko I.M., Palopezhentsev S.A.: Opt. Spektrosk., 1986, **60**, p.920-927
13. Kulikov S.V., Manelis G.B., Ternovaya O.N.: Chem. Phys. Rep., 2007, **6** (in print).

Non-uniform flow structure behind a dusty gas shock wave with unsteady drag force

T. Saito[1], **M. Saba**[1], **M. Sun**[2], **and K. Takayama**[3]

[1] *Dept. Mechanical Systems Eng., Muroran Institute of Technology, 27-1 Mizumoto-cho, Muroran, 050-8585 Japan*
[2] *Center for Interdisciplinary Research, Tohoku University, 6-3 Aramaki, Aoba-ku, Sendai, 980-8578 Japan*
[3] *Tohoku University Biomedical Engineering Research Organization, Institute of Fluid Science, Tohoku University, 2-1-1 Katahira, Sendai, 980-8577 Japan*

1 Introduction

One of the important subjects of high-speed gasdynamics is the two phase flows of gaseous media loaded with small solid particles (dusty gases). The research field is directly linked to many important applications, such as shock wave interactions with solid particles in a solid-fuel-booster nozzle, high speed flight in the rain, snow, or dust, etc. Accordingly, numerous works on the subject have been reported over the last several decades [1–4]. High-speed flows in dusty gases, especially unsteady ones such as those in a dusty gas shock tube, are quite different from their pure gas counterparts due to momentum and energy exchange between gas and solid particles. The solid particles cannot follow rapid changes in the gas velocity and temperature, exhibiting non-equilibrium shock regions behind shock fronts. The objective of this paper is to quantitatively investigate the effect of unsteady drag force on the structure of this non-equilibrium region behind shock waves traveling through a dusty gas.

One of the crucial parts of dusty gas shock tube flows is drag force modeling by which the interaction between gas and solid particles are defined and, in general, even steady drag force formulae for a sphere are used. This practice, however, may cause some errors for extremely time-dependent flows such as highly dust laden strong shock tube flows. Our recent work showed that the drag coefficient of a sphere passing through a shock wave is extremely time-dependent and shows even negative values for certain period of time due to complex wave interactions [5,6]. In this paper, the non-equilibrium region behind the shock wave traveling through a dusty gas is numerically calculated by implementing unsteady drag forces obtained from the work. The significance of the effect of unsteady drag coefficient has been noted and discussed in the past. However, as far as the authors know, not many quantitative investigations on the subject have been reported, and this work is, based on experimental findings, one of very few self-consistent works on the subject.

2 Unsteady drag force of a sphere passing through a shock wave

The unsteady drag force acting on a sphere was experimentally measured [5, 6]. In the experiments, an aluminum alloy sphere of 80 mm diameter was suspended by thin wire in a 300 mm x 300 mm vertical shock tube. The test section of the shock tube is filled with atmospheric pressure air at room temperature of 293 K. The shock Mach number Ms is 1.22 and the propagation velocity is 414 m/s. Therefore it takes about 500 μs for

the shock wave to pass the sphere model. The force acting on the sphere is measured by a piezoelectric accelerometer (Endevco 2250A-10).

Numerical predictions of the drag forces for different sphere diameters, i.e. from 8 μm to 80 mm, are also carried out. The axisymmetric Navier-Stokes equations with continuity and energy equations are numerically solved. The numerical result for 80 mm diameter is compared with the experimental data for validation and good agreement was obtained.

Figure 1(**a**) is reproduced from [6] and shows unsteady drag forces for different sphere diameters. It is noticed here that the drag coefficient is, in principle, defined for steady flows but in this paper, for the sake of simplicity, we define it as unsteady drag force devided by dynamic force behind the incident shock tube flow. The ordinate of the figure is the drag coefficient of a sphere that is defined as,

$$C_d = \frac{2f}{\rho_0 U_0^2 \pi r^2} \tag{1}$$

where f is the drag force exerted on the sphere and, r the radius of the sphere. The symbols ρ_0 and U_0, respectively, are the characteristic density and velocity taken as the values behind the incident shock wave in the present case. The abscissa is the time normalized by a characteristic time that is defined by, $r/\sqrt{RT_0}$ or $r\sqrt{\gamma}/a_0$ where R and γ are the gas constant and the specific heat ratio, respectively. Symbols T_0 and a_0 are the temperature and the sound speed ahead of the incident shock wave. The value of $\sqrt{RT_0}$=292 m/s is used throughout the work. The trace with high frequency noises in

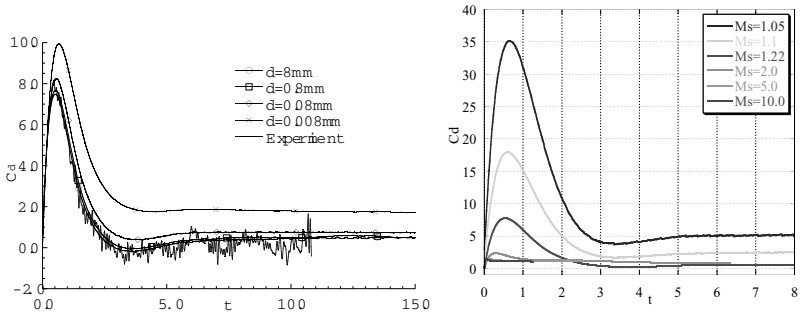

(**a**) (**b**)

Fig. 1. Unsteady drag coefficient: (**a**) Experimental and numerical results for different diameters with Ms=1.22, reproduced from [6]; (**b**) Numerical results for different shock Mach numbers with fixed diamter of 8 mm

Fig. 1(**a**) is the experimental data. It is found that the numerical result and the measured data for 80 mm diameter agree quite well and the numerical one is not shown in the figure for clarity. Also the numerical result of 80 mm diameter is nearly the same as 8 mm one. The most pronounced feature of all traces is that the drag coefficient rapidly increases when the shock wave arrives at the front stagnation point of the sphere. It takes a maximum value at around the normalized time t=1, and then falls to a minimum value at t=3 to 4. The value of the minimum is smaller for larger diameter and is even negative for the sphere diameters of 80 mm and 8 mm. The drag coefficient slowly approaches to

its asymptotic value afterwards. In this study, another series of drag force computations for different shock Mach numbers was carried out with a fixed diameter of 8mm. The incident shock Mach numbers are 1.05, 1.1,1.22, 2, 5 and 10 and the results are shown in Fig. 1(**b**).

3 Quasi-steady analysis of non-equilibrium region behind the shock wave

3.1 Basic equations

Once the velocity and the temperature of gas and solid particles are equilibrated at some distance behind the shock front, the fully developed flow structure of the non-equilibrium region, between the equilibrium region and the shock front, propagates at a constant speed. Then the flow configuration can be regarded as steady relative to the shock front and is numerically obtained by integrating a set of steady equations of mass, momentum and energy conservations [7].

The drag force D and the heat transfer rate Q of a solid particle are expressed via the drag coefficient C_d in Figs. 1 and the Nusselt number Nu as:

$$D = \frac{1}{8}\pi d^2 \rho \left(u - u_d\right) \left|u - u_d\right| C_d \tag{2}$$

$$Q = \frac{\pi d \mu C_p}{\mathrm{Pr}} \left(T - \Theta\right) \mathrm{Nu} \tag{3}$$

where u, T and C_p are the flow velocity, temperature and the specific heat of the gas. The symbols u_d, Θ, C_d and d are the velocity, temperature, specific heat and the diameter of solid particles, respectively.

The Nusselt number Nu depend on the particle Reynolds number and determined from the references [8, 9]. The viscosity coefficient is assumed to depend only on temperature and evaluated by Chapman and Cowling [10] and the Prandtl' number Pr is assumed 0.75.

3.2 Characteristic scales of dusy-gas flows

Some reference scales characteristic to dusy-gas flows are defined. The characteristic velocity is defined as:

$$u_{\mathrm{ref}} = \frac{a_{f,\mathrm{ref}}}{\sqrt{\gamma}} = \sqrt{\frac{p_{\mathrm{ref}}}{\rho_{\mathrm{ref}}}} = \sqrt{\frac{p_1}{\rho_1}}\,, \tag{4}$$

where the subscript 'ref' indicates the reference state and the values p_{ref} and ρ_{ref} are defined from the initial pressure ($p_1 = 101.3$ kPa) and density ($\rho_1 = 1.293$ kg/m^3) of the test gas. The symbol $a_{f,\mathrm{ref}}$ referes to the frozen sound speed of the initial state of the test gas. It is shown that the following characteristic quantity l has the dimension of length [2]:

$$l = \frac{8m}{\pi \rho_{\mathrm{ref}} d^2} = \frac{4}{3}\frac{\rho_p}{\rho_{\mathrm{ref}}}\, d = \frac{4}{3}\frac{\rho_p}{\rho_1}\, d, \tag{5}$$

where ρ_p is the particle material density. The reference length l is used as the length scale in this study. Therefore, the reference time is defined as $\tau = l/u_{\mathrm{ref}}$. The ratio of

mass concentrations α and the ratio of the specific heats β are difined as characteristic parameters of dusty gases as:

$$\alpha = \frac{\sigma_{\rm ref}}{\rho_{\rm ref}} \ , \quad \beta = \frac{C_m}{C_v} \ , \tag{6}$$

where $\sigma_{\rm ref}$ is the initial mass concentration of the solid particles and C_v is the gas specific heat at constant volume. The value of β is assumed to be unity in this study.

4 Numerical results and discussions

Structures of nonequilibrium region behind a shock wave front obtained with the steady and the unsteady drag coefficients are calculated. It is observed in Fig. 1 that the drag coefficient varies significantly with time just behind incident shock waves and then approaches to an asymptotic value. We assume that this asymptotic value is the steady drag coefficient and the first series of calculations (Case 1) is obtained with this steady drag coefficient. The second series of calculations (Case 2) is carried out with the unsteady drag coefficients deduced from the experimental and numerical results shown in Fig. 1.

4.1 Numerical results for Ms = 1.22

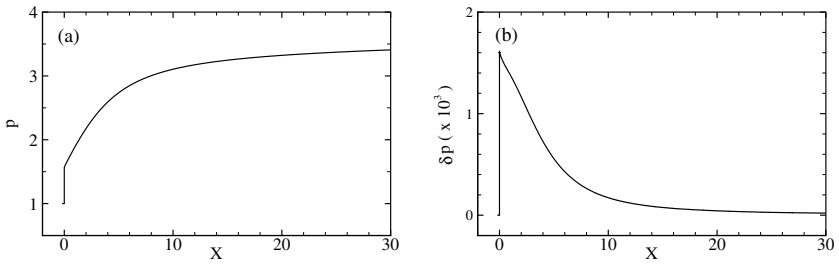

Fig. 2. Pressre profiles for Ms=1.22: (**a**) Case 1 and Case 2, (**b**) Difference between Case 1 and Case 2

Figure 2 compares the pressure profiles obtained for Case 1 and Case 2. As expected, the difference between them is so small that the curves of Case 1 and Case 2 overlap with each other in Fig. 2 (**a**). The difference between the two curves is taken and plotted in Fig. 2 (**b**). This way the effect of the unsteady drag coefficients is clearly observed. It takes a maximum value of about 0.16% of the initital pressure behind the incident shock wave.

The gas density and the particle concentration are shown in Fig. 3 in the similar manner as in Fig. 2. It is seen that the difference of the particle concentration between Case 1 and Case 2 takes a maximum not at the shock wave front but at around x=2 while the difference of the gas density takes maximum just behind the shock wave front.

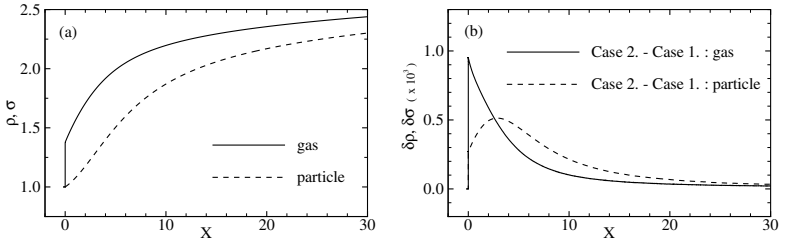

Fig. 3. Gas density and particle concentration profiles for Ms=1.22: (**a**) Case 1 and Case 2, (**b**) Difference between Case 1 and Case 2

4.2 Numerical results for different Mach numbers

Investigations of the effect of unsteady drag force for different incident shock Mach numbers are carried out. Figure 4 shows the differences of Case 1 and Case 2 in the profiles of gas and particle concentrations. It is seen in Figure 4 (**a**) that $\delta\rho$ has a spike at the front and has a maximum some distance behind the shock front for Ms=1.05. When the shock strength is increased the maximum values occure at shock front. Particle concentration in Case 2 becomes significantly larger than that in Case 1 as the shock Mach number is increased. It is found that the effect of the nominal unsteady drag coefficient is more significant for smaller shock Mach numbers. This is due to the fact that the relative significance of the momentum and energy exchanges between gas and particle phases in the initial stage is less for stronger shock waves.

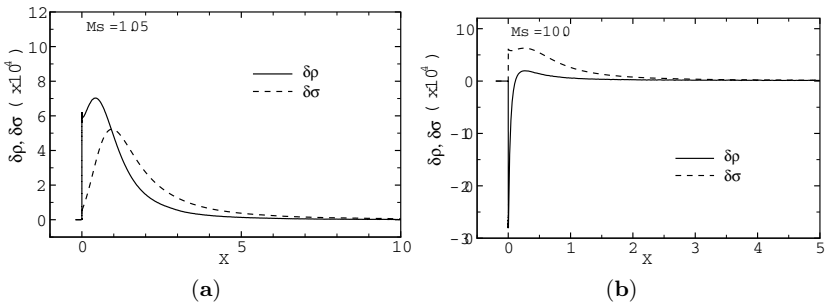

(**a**) (**b**)

Fig. 4. Gas and particle concentration for different Mach numbers: (**a**) Ms=1.05, (**b**) Ms=10.; r=4 mm

4.3 Numerical results for different mass ratios

The ratio of the particle concentration to the gas density α is an important characteristic parameter. Profiles of flow properties with α=10 are calculated and compared with the previous results for $\alpha = 1$. Pressure profiles with $\alpha = 10$ and 1 are compared in Fig. 5. The effect of unsteadiness of the drag coefficient becomes much more significant with increased value of α. The pressure difference between Case 1 and Case 2 is more than 4% with $\alpha = 10$ while it is only 0.16 % when $\alpha = 1$.

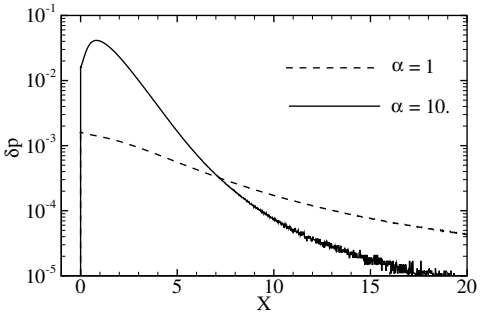

Fig. 5. Comparison of pressure profiles with different particle concentrations $\alpha = 1$ and $\alpha = 10$, $r = 4mm$ and Ms=1.22: solid line; $\alpha = 10$, broken line; $\alpha = 1$

5 Summary

The effect of time dependency of drag coefficient on dusty gas flows is numerically investigated. Dusty gas flows involve many characteristic parameters and we do not intend to clarify the effect for wide variety of their combinations. Instead, we have quantitatively investigated it for some typical cases including our previous works.

It is found that the effect is more significant for lower shock Mach numbers and higher values of the parameter α that is defined as the ratio of the particle mass concentration to the gas density. In general, when the value of α is of the order of unity, contribution of unsteady drag force to flow structures is less significant. However, for dusty gases with higher loading ratio, the effect of unsteady drag force becomes more significant. We plan to verify the usefulness of the present drag force model by performing series of experiments.

References

1. Rudinger, G.: Some properties of shock relaxation in gas flows carrying small particles. Phys. Fluids **12**(5), 658–663 (1964)
2. Miura, H., Glass I.I.: On a dusty-gas shock tube. Proc. R. Soc. Lond. A **382**, 373–388 (1982)
3. Igra O., Takayama, K.: Shock tube study of the drag coefficient of a sphere in a nonstationary flow. In: Takayama, K. (ed.) Proc. of the 18th International Symposium on Shock Waves, Sendai, Japan **1**, 491–497 (1991)
4. Saito, T.: Numerical analysis of dusty-gas flows. J. Comput. Phys. **176**, 129–144 (2002)
5. Tanno, H., Itoh, K., Saito, T., Abe, A., Takayama, K.: Interaction of a shock with a sphere suspended in a vertical shock tube. Shock Waves **13**, 191–200 (2003)
6. Sun, M., Saito, T., Takayama, K., Tanno, H.: Unsteady drag on a sphere by shock wave loading. Shock Waves **14**, 3–9 (2005)
7. Saito, T., Marumoto, M., Takayama K.: Numerical investigations of shock waves in gas-particle mixtures. Shock Waves **13**, 299–322 (2003)
8. Gilbert, M., Davis, L., Altman, D.: Velocity lag of particles in linearly accelerated combustion gases. Jet Propulsion **25**, 26–30 (1955)
9. Knudsen, J.G., Katz, D.L.: Fluid mechanics and heat transfer. McGraw-Hill, New York (1958)
10. Chapman, S., Cowling, T.G.: The mathematical theory of non-Uniform gases. Cambridge University Press (1961)

Numerical study of shock-driven deformation of interfaces

M.-S. Liou[1], C.-H. Chang[2], H. Chen[3], and J.-J. Hu[4]

[1] *NASA Glenn Research Center, Cleveland, OH 44135 (USA)*
[2] *Center for Risk Studies & Safety, University of California, Santa Barbara, CA 93117 (USA)*
[3] *Leader University, Tainan 70970, Taiwan (ROC)*
[4] *Shu-Te University, Kaohsiung 82445, Taiwan (ROC)*

Summary. We employ AUSM$^+$-up to obtain numerical results for studying the deformation of a droplet and an air bubble impacted initially by a passing shock wave, which triggers sequences of an enormously complicated flowfield. Multiplicate shock and rarefaction waves, and contact/slip surfaces have developed and interacted with each other, resulting in incredibly fine structures. Further analysis of the results yields useful insight into the behavior of interface dynamics, providing a new light on the path to understanding of droplet breakup and jet formation.

1 Introduction

The existence of fluid interfaces is a distinct property in many multiphase flows; often they give rise to interesting complex interfacial instabilities and mixing phenomena. Meanwhile, these also pose considerable difficulties in numerical simulation, because the evolution of fluid interface strongly affects the bulk flow field and vice versa. Moreover, the topology of the interface can become extremely complicated to handle algorithmically, as evident in the case of droplet breakup. Numerical results may be afflicted with excessive numerical smearing or catastrophic failure. The problem becomes more challenging when the fluids under consideration have significant disparity in compressibility and density, such as between water and air, where a small imbalance in water density can result in large oscillations in the calculation of pressure. The problem becomes even more stiff if the shock wave and the fluid interface are present simultaneously.

For the current study, we focus on two interface problems in which the motion of interfaces are initiated by an impacting plane shock wave. The first problem is a freely suspended axisymmetrical liquid droplet impinged by an air stream, while the second one is the opposite, an air bubble being impacted by a liquid stream, but leading to two vastly different scenarios.

2 Mathematical modeling and numerical simulation

Contending that direct numerical simulation is still unable to resolve the scales encountered in the problems of interest, we resort to employing the averaged, coarse-grain models [4, 7], or the so-called two-fluid model. As in their turbulence counterparts, major difficulties arise in finding appropriate closure forms (modeling) for the interaction terms introduced during the averaging procedure.

Under this two-fluid model, we adopt the assumption in which the bulk and interfacial pressures of all phases are in equilibrium [7]. The bulk pressure for gas and liquid phases

are represented by the ideal and stiffened gas laws respectively. The interfacial pressure model adopted is originally proposed by Stuhmiller [15] and modified later [3,9].

One of the numerical issues concerning the above set of equations is that it is non-hyperbolic, giving rise to questions such as ill-posedness, which may be manifested as numerical instability and non-convergence. Even though this subject has been brought up frequently in the past publications, mostly for incompressible low speed flows, it has become clear lately that this subject remains open, especially in the high speed regime.

Necessary conditions for rendering the system of equations hyperbolic can be derived [3], involving the solution of a quartic equation, which must be obtained numerically; a detailed account of this subject is provided for a wide range of benchmark problems [3,10].

For the current simulation of interface deformation between air and water, we are employing the capturing approach, rather than the tracking approach, for it is much simpler to deal with complex topological changes, as in atomization of droplets, but at the expense of losing sharpness at the interface. The extent of smearing however can be minimized with an improved numerical method.

The numerical method employed in this study is the AUSM$^+$-up [2, 8] applied to the discrete balance laws of liquid and gas fields, in combination with the stratified flow concept [14]. The derivation of balance laws at the discrete level, i.e., control volume in the Eulerian frame, turns out to be very instructive in guiding the formulation of the numerical method for physical fluxes at the control surfaces [2]. The method has been found to be robust and accurate for several applications in our previous studies [1, 2].

3 Problems involving interface deformation

3.1 Shock-driven deformation of a droplet

Many applications involve dynamics of droplets, such as ink jet, fertilizer application, fuel atomization, chemical agent dispersal, etc. The entire evolution, from deformation to breakup, is extremely complex, the interpretation of experimental observations is limited by perspective views of apparatus, thus hampering the development of a complete theory/model. However, with advances in optics technology, recent findings shed unprecedented insights, allowing a more complete description of the dynamic event from surrounding angles [13, 16], for a shock wave passing over a wall-bounded liquid drop and a freely-suspended drop respectively. Both experiments place optical views at angles oblique to the conventional "side view". As a result, rather startling scenarios about the breakup of a drop has been discovered [16], concluding that there is no Rayleigh-Taylor waves piercing the drop. Instead, they found that an essentially mirror-smooth area in the center persists for several hundred μs, see Fig. 1, while a radially outward flow creates a roughened "muffin-like" periphery. Similar description is also found for a wall-bounded drop [13] in which front, side and back views are depicted. However, events occurring *inside* a drop are still unavailable experimentally.

Numerical approach, on the other hand, can provide *ab initio* deformation, giving an enormously rich description of the dynamics, not only outside but also inside the drop [2]. As a first step to provide confidence in numerical solution of this very complicated problem, we show in Fig. 2 the numerical and experimental snapshots for a drop exposed to a moving shock of $M_s = 3.0$ in air. By observation, it is worth noting that: (1) the back and frontal faces are flattened nearly to the same extent, (2) the "muffin-like" shape is formed with its peripheral region roughened in a wavy fashion, and (3) the numerical

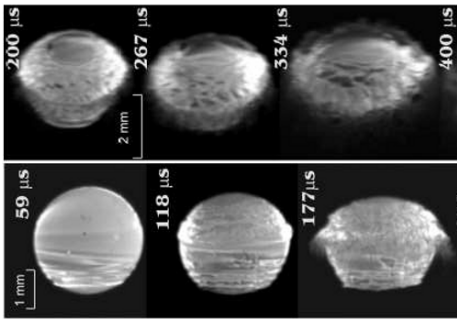

Fig. 1. Laser-induced fluorescence images of a Tri-Butyl-Phosphate drop, flow goes from top to bottom in each frame. Bottom row: side view; Top row: front oblique view at an angle 60 degrees from the flow direction [16].

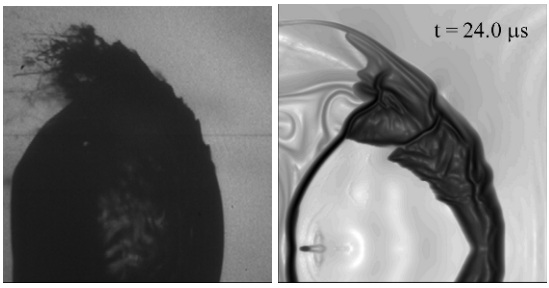

Fig. 2. Comparison of snapshots for the shock-droplet interaction problem. Left: experimental result of a deformed Tri-Butyl Phosphate drop by a shock wave of $M_s = 3.0$, $We = 30,000$ [16]. Right: computed schlieren for $M_s = 3.0$ and $We = \infty$.

result gives evidence that shock wave once transmitted into the drop is trapped inside; it is reflecting back and forth within the drop, with little transmitting out, and is creating a low pressure, cavitating region near the rear stagnation point.

To the 2D cylindrical drops calculated previously, we now add the simulation of an axisymmetrical (spherical initially) drop; sample results are depicted in Fig. 3, along with a comparison with the 2D results at the same instants. In general, their appearances are qualitatively similar, quantitative differences are also obvious. For the spherical droplet, the shock reflection patterns accompanying with the leading shock is more complex, in which a vortical structure emanating from the triple point has interacted with the Mach stem and resulted in a different type of shock reflection. Also, the shock stand-off distance is, as expected, significantly shorter.

3.2 Microjet

Recent interest in medical applications of bubbles has renewed research efforts towards the classical topic of bubble dynamics, especially the high-speed jetting due to bubble collapsing. Examples of applications include the drug uptake enhanced through micro bubbles [6] and ultrasound diagnostics [11]. But, the collapse of a bubble, if not being controlled properly, can also have undesirable side effects of damaging tissues [5]. Thus,

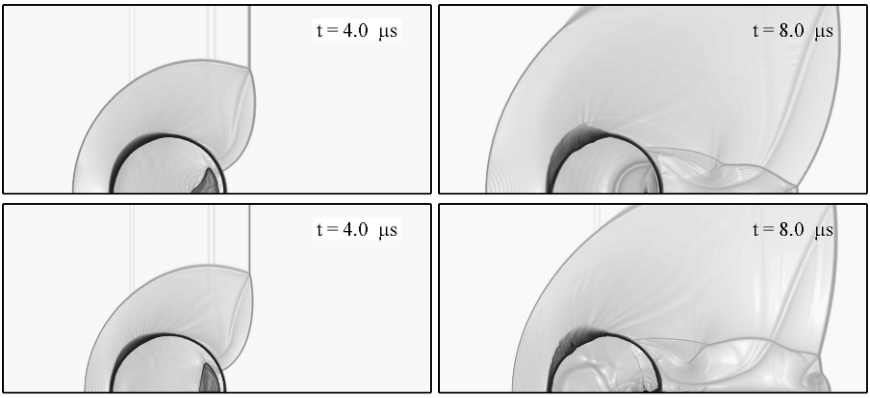

Fig. 3. Images of various instants for 2D (top) and axisymmetric (bottom) shock-droplet interaction problem.

it is important to fully understand the behavior of bubble deformation and collapsing and to know its maximum intensity, e.g., in terms of kinetic energy.

In this study, we attempt to understand the forming of jet by a shock impacting on an extruding curved surface separating water and air columns in a tube, resembling the setup in experiment [12]. Two liquid tubes of diameters of 0.445 mm and 0.29 mm are considered, as shown in Fig. 4. The curved surface is represented as an arc segment of a sphere of radius R_c, intercepted by the tube of radius R, thus the captured spherical surface is included by a cone angle $\phi = \pi - 2\theta$ where θ is the contact angle between the tangent at the intercept and the tube wall. Each diameter takes several tangent angles in the study. The Weber numbers, based on the surface tension between water and air, range from 3,900 to 7,000 for all the cases calculated, hence ignoring the surface tension.

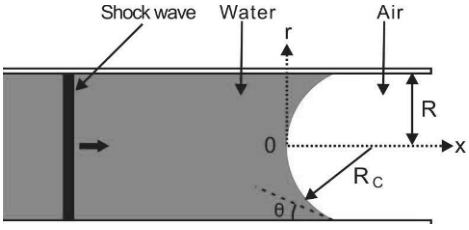

Fig. 4. A schematic of the microjet problem.

Typical sequences of jet formation, taken in experiment [12] are depicted in Fig. 5, together with the calculated pressure contours. Both show that the curved interface is flattened by the impacting sock wave and the central area which is subject to the greatest pressure now moves at the fastest speed, beginning to form a cusp-like jet. The jet continues to accelerate and at the same time is slowed down by the low pressure behind it, thus reaching a maximum speed and decelerating subsequently.

The fluid velocity behind the moving shock is 21 m/s, but the velocity generated in the jet flow, due to the collapsing - forming a singularity at interface, can reach almost

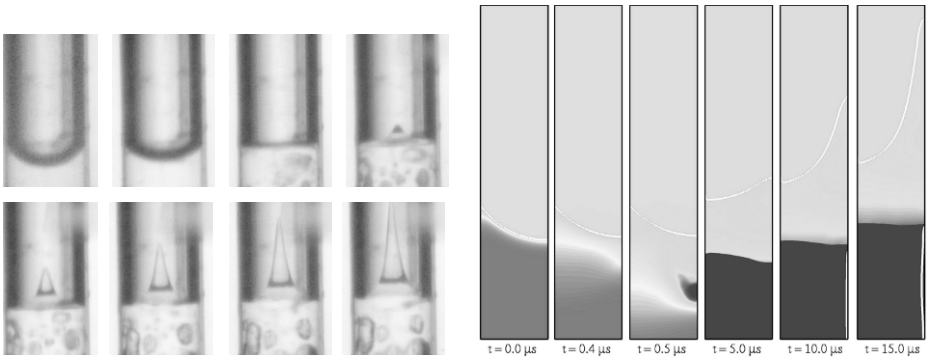

Fig. 5. Images of jet-formation sequences from experiment [12] and computation, in which the calculated jet boundary is denoted by the white lines.

130 m/s! The maximum jet velocity attained for a given shock strength has an interesting geometrical interpretation: it depends only on the ratio of the area exposed to the shock wave to its projection onto the shock wave, A_r.

$$A_r = \frac{4\pi R_c^2 \phi/2\pi}{\pi R^2} = \left(\frac{R_c}{R}\right)^2 \left[2 - \frac{4}{\pi} \arccos\left(\frac{R}{R_c}\right)\right] \tag{1}$$

Figure 6 confirms that a single curve is obtained, irrespective of tube diameters. It also suggests that the maximum velocity is bounded, attaining an asymptotic values that should be determined by the shock strength. Measured maximum velocities [12] are also included for reference; discrepancies between the calculations and measurements are obvious. It is probably premature to draw any conclusion about it since data points are scanty, but clearly indicating the need for detailed data.

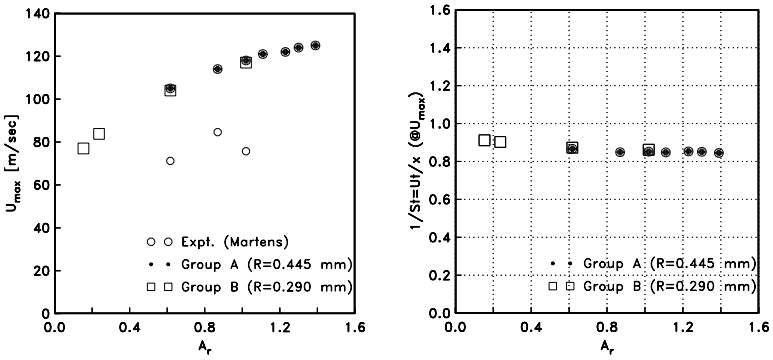

Fig. 6. Maximum jet velocity vs area ratio, showing independence of tube diameters.

As shown in Fig. 6, it is remarkable that the Strouhal number, St, remains essentially constant for all cases, if it is based on quantities when u_{max} is reached. That is,

$$St = \frac{x}{ut}|_{u_{max}} \tag{2}$$

4 Conclusion

A numerical investigation for studying the interface deformation of a droplet and a bubble, separately initiated by a passing shock wave, was conducted. Enormous details rich in physics were revealed, especially in the case of droplet, shedding light on the path to the breakup. It is suspected that the dynamics *inside* the drop is as important as that outside, and may play even a critical role. For the bubble problem, the jetting resulting from the morphological change of interface curvature, from bowl to cusp-like, is obtained, yielding a remarkable result about the maximum jet velocity: (1) it is dependent only on the area ratio between the exposed and projected areas for a given shock strength and (2) the Strouhal number based on the condition at this velocity is essentially constant for all area ratios.

References

1. Chang C.-H., Liou M.-S., Simulation of multifluid multiphase flows with AUSM$^+$-up scheme, Computational Fluid Dynamics 2004, Springer, 613-618, 2005.
2. Chang C.-H., Liou M.-S., A robust and accurate approach to computing compressible multiphase flow: stratified flow model and AUSM$^+$-up scheme, J. Comput. Physics (to appear).
3. Chang C.-H., Sushchikh S., Nguyen L., Liou M.-S., Theofanous T., Hyperbolicity, discontinuities, and numerics of the two-fluid model, 5th Joint ASME/JSME Fluids Engineering Summer Conference and 10th International Symposium on Gas-Liquid Two-Phase Flows, 2007
4. Drew D., Passman S.L., Theory of Multicomponent Fluids, Springer-Verlag, 1999
5. Eizenheofer H., Marlinghaus E., Heine G., Liebich H. G., Brendel W., Delius M., Jordan M., Biological effects of shock waves: Kidney hemorrhage by shock waves in dogs - administration rate dependence, Ultrasound in Medicine and Biology, vol 14, 689-694, 1988
6. Ikink R., Delius M., Wolfrum B., Ohl C. D., Arora M., Drug delivery following shock wave induced cavitationse, 5th International Symp. on Cavitation, 2003
7. Ishii M., Thermo-fluid dynamic theory of two-phase flow, Eyrolles, 1975
8. Liou M.-S., A sequel to AUSM, Part II: AUSM$^+$-up for all speeds, J. Comput. Phys., vol 214, 137–170 2006
9. Liou M.-S., Nguyen L., Chang C.-H., Sushchikh S., Nourgaliev R., Theofanous T., Hyperbolicity, discontinuities, and numerics of two-fluid models, 4th International Conference on Computational Fluid Dynamics, 2006
10. Liou M.-S., Nguyen L., Chang C.-H., Theofanous T., How to solve compressible multifluid equations: a simple, robust and accurate method, AIAA paper 2007–4456, 2007
11. Lohse D., Bubble puzzles, Physics Today, 36–41, February, 2003
12. Martens D., Micro scale jetting by shock wave interaction, Master's Thesis, University of Twente, The Netherlands, 2006
13. Milton B. E., Atomization of liquid droplets on surfaces exposed to moving shock waves, Shock Waves, vol 16, 95–107, 2006
14. Stewart H. B., Wendroff B., Two-Phase Flow: models and methods, J. Comput. Phys., vol 56, 363–409, 1984
15. Stuhmiller J. H., The influence of interfacial pressure forces on the character of two-phase flow model equations, Int. J. Multiphase Flow, vol 3, 551–560, 1977
16. Theofanous T. G., Li G. J., On the physics of aero-breakup, Physics of Fluids (to appear)

Shock and wave dynamics in fuel injection systems

I.H. Sezal, S.J. Schmidt, G.H. Schnerr, M. Thalhamer, and M. Förster

Technische Universität München, Lehrstuhl für Fluidmechanik - Fachgebiet Gasdynamik
D-85747 Garching, Germany

Summary. Due to the exceptional high inlet pressure up to 2000 bar flow dynamics and efficiency of modern injection systems are controlled by high frequency wave dynamics of the compressible liquid flow. Corresponding to alternating shock and expansion waves the liquid fluid evaporates and recondenses instantaneously. Here we present CFD simulations of the time accurate evolution of cavitating flows in 2-D plane and in 6-hole injection nozzles with focus on the wave dynamics just after initialisation of the flow and within the time scale $\Delta t \leq 10^{-4}$ s of pilot and multi-point injection. Due to shock reflections at the bottom of the sack hole the instantaneous maximum pressure increases more than three times higher as compared with the prescribed pressure at the nozzle inlet. For instance, in case of an inlet pressure of 600 bar the maximum pressure in the sack and therefore ahead of the nozzle bore holes reaches about 2100 bar. It is quite reasonable that this amplification of the pressure effects the evolution of the convective flow and therefore the mass flow through the nozzle bore holes.

1 Introduction

Recent developments of fuel injection systems include increasing pressure differences $\Delta p = p_{in} - p_{out}$ up to 2000 bar, as well as individual mass flow control strategies by pilot and multipoint injection with time scales of $\Delta t \leq 10^{-4}$ s. Therefore, the arising flow field inside the injection nozzle experiences variations on multiple time scales. The shortest one corresponds to the propagation of non-linear waves and hence, it is inversely proportional to the speed of sound $c_{liq} = O(1500)$ m/s. An additional time scale is defined by the local flow velocity u which varies within the interval $0 \leq u \leq 400$ m/s during the injection cycle. As wave dynamics and hydrodynamics are strictly coupled, separate consideration of these scales is not possible. Thus, the necessary temporal discretization Δt_{CFD} requires the resolution of the shortest time scale which enforces numerical time steps of the order of 10^{-10} s. Besides these flow dynamic scales, the injection cycle introduces a time scale $\Delta t_{injec} = 10^{-3}$ s as well. Consequently, all scales with $10^{-10} \leq \Delta t \leq 10^{-3}$ s interfere with the dynamic phase transition processes like cavitation and recondensation.

The present investigation focuses on the analysis of the flow field inside 2-D plane and 3-D injection nozzles. Furthermore, a detailed study of the short time flow characteristics at each time scale is performed.

2 Physical Modelling and Numerical Method

2.1 Physical Modelling

In order to resolve wave dynamics in two-phase flows, a fully compressible formulation of the 3-D time dependent Euler equations is necessary. Phase transition is modelled

according to the "Homogeneous Equilibrium" approach, which describes integral average properties of vapour clouds rather than discrete bubble dynamics. The working fluid is water, the thermodynamic properties of water and vapour are expressed by thermal and caloric equations of state, whereas temperature dependent saturation conditions define the two-phase region. The local speed of sound c is calculated according to the corresponding thermodynamic states.

2.2 Numerical Method

Together with the conservation law of total energy the governing equations are hyperbolic in time. Thus a Godunov type method is well suited to calculate the fluxes of the finite volume method. Therefore, an approximate solution of the Riemann problem across adjacent cells is required [1]. However, the classical approaches require substantial modifications to achieve accurate solutions in regions of pure liquid where $M \to 0$ (low Mach number problem). Hence, we developed a modified pressure flux calculation which ensures accurate solutions for $M \to 0$ as well [2]. The time integration of the semi-discrete equations is achieved by an explicit 4-stage Runge-Kutta method with enlarged stability region. Non-linear reconstruction procedures (WENO-3, Van-Leer) ensure high resolution in space. Our recently developed flow solver CATUM (CAvitation TU Munich) is thus second order accurate in space and time. Time accurate resolution of all arising scales in the injection system requires numerical time steps of the order of $\Delta t_{CFD} = 10^{-10}$ s.

At the outlet of the discretisized surrounding domain, weakly reflective boundary conditions are applied. Contrary to classical non-reflective boundary conditions, a prescribed pressure $p_{out,mix}$ is ensured asymptotically. At the inlet similar boundary conditions are applied, p_{in} now resembles the rail pressure. According to the Euler model we presume inviscid adiabatic flow at solid walls.

3 Simulation Results

3.1 2-D Injection Nozzle

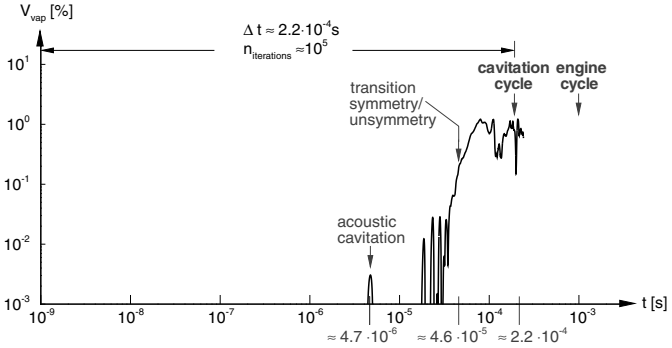

Fig. 1. Time history of the integrated vapour volume V_{vap} [% total volume of the computational domain], $p_{in} = 80$ bar, $p_{out,mix} = 26$ bar, $\Delta t_{CFD} = 10^{-9}$ s.

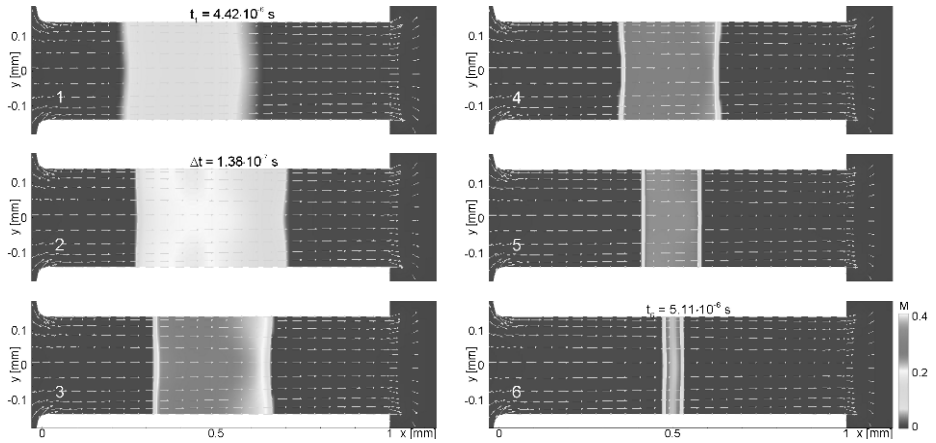

Fig. 2. Acoustic cavitation inside the bore hole, Mach number contours, at $t_1 = 4.42 \cdot 10^{-6}$ s, time interval $\Delta t_{1-6} = 6.90 \cdot 10^{-7} s$, $p_{in} = 80$ bar, $p_{out,mix} = 26$ bar.

In order to highlight fundamental flow details we start with the investigation of a 2-D planar nozzle [3]. The numerical domain includes the nozzle as well as the outflow region. The initial conditions for the entire numerical domain are liquid water at rest at temperature $T_{init} = 293$ K and pressure $p_{out,mix} = 26$ bar. At the inlet we prescribe $p_{in} = 80$ bar. Due to the initially prescribed pressure jump $\Delta p = p_{in} - p_{out,mix} = 54$ bar at the inlet, a shock wave propagates through the nozzle and builds up the convective motion. The shock enforces a reflected rarefaction at the exit of the nozzle. In Fig. 1 the time history of the vapour formation inside the nozzle is shown. The interaction of the

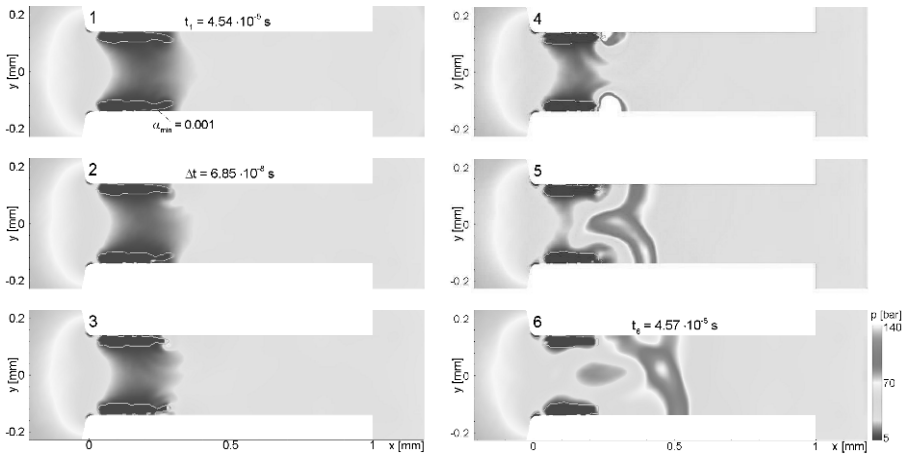

Fig. 3. Transient rearrangement from symmetric to asymmetric cavitation, at $t_1 = 4.54 \cdot 10^{-5}$ s, time interval $\Delta t_{1-6} = 3.43 \cdot 10^{-7}$ s, static pressure contours, $p_{in} = 80$ bar, $p_{out,mix} = 26$ bar.

hydrodynamic flow acceleration with the pressure drop due to rarefaction waves enforces acoustic cavitation at time $t \approx 4.7 \cdot 10^{-6}$ s (Fig. 2). Within 10^{-6} s the evaporated domain recondenses completely. Further acceleration of the flow field results in hydrodynamic cavitation at the inlet of the bore hole. The flow and the cavitation pattern remain symmetric (Pics. 1-2 of Fig. 3) until the intense collapse at the closure region of the cavities induce shock driven instabilities which destroy the flow symmetry (Pics. 3-6 of Fig. 3).

3.2 3-D Injection Nozzle

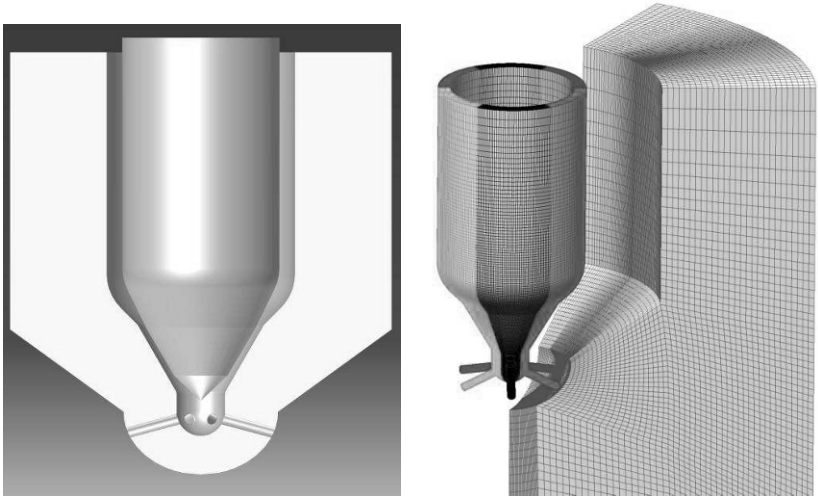

Fig. 4. 3-D 6-hole injection nozzle, geometry and corresponding grid with outflow domain. Each 60 degree section consists of $4 \cdot 10^5$ cells.

In order to study 3-D phenomena a 60 degree section of a multi-hole injection nozzle is discretisized. Fig. 4 shows the geometry and the grid which consists of $4 \cdot 10^5$ finite volumes. The inner diameter of the nozzle is 3.9 mm and the needle diameter is 3.26 mm. Six cylindrical bore-holes with length 1 mm and diameter 0.22 mm are connected to the sack volume. The inlet of the bore-holes are rounded with a radius of wall curvature of $r =$ 0.028 mm. This ensures that the single phase flow remains attached at the nozzle inlet. Again, the entire numerical domain initially contains pure water at rest at $p_{out,mix} = 26$ bar, $T_{init} = 333$ K. At the inlet the prescribed rail pressure is $p_{in} = 600$ bar. The needle position is fixed at maximum lift throughout the simulation.

Figures 5 and 6 depict flow features arising at the shortest time scale $\Delta t \approx 10^{-6}$ s. The initial shock reaches the convergent part of the annular gap between the needle and the inner nozzle wall where area contraction and wall curvature enforce shock focussing and shock deflection respectively (Pics. 1-2 of Fig. 5). Downstream of the needle tip the shock front remains no longer planar. As soon as it interacts with the bore hole inlets diffraction takes place. Thereby, quasi-planar shock waves propagate through the

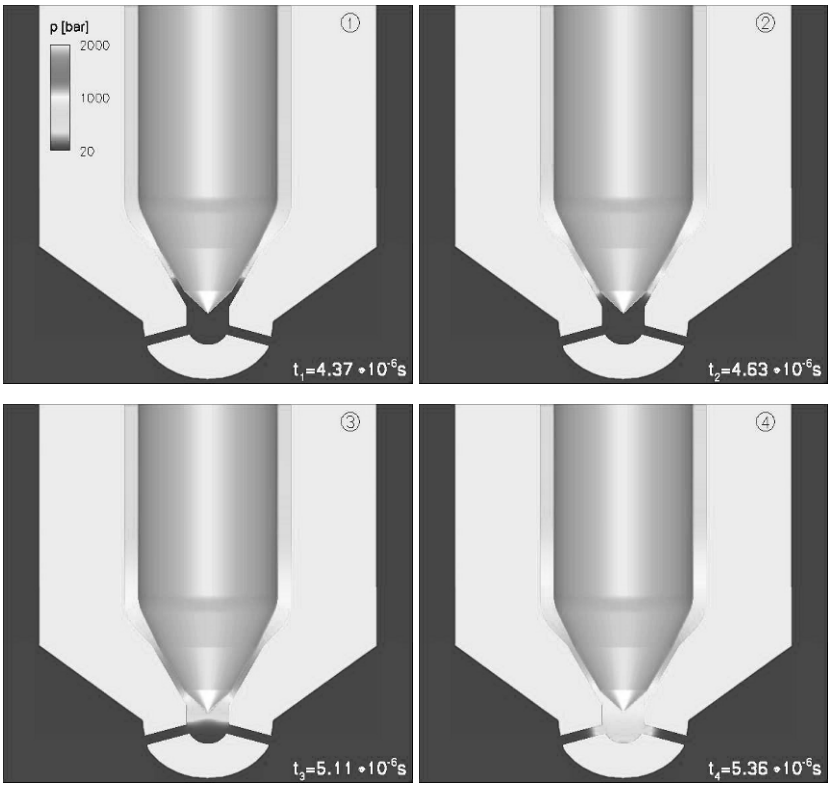

Fig. 5. Pure liquid wave dynamics inside the nozzle as consequence of the initiated shock wave, time interval $\Delta t_{1-4} = 5.36 \cdot 10^{-6}$ s, $p_{in} = 600$ bar, $p_{out,mix} = 26$ bar, $T_{init} = 333$ K, $\Delta t_{CFD} = 10^{-10}$ s.

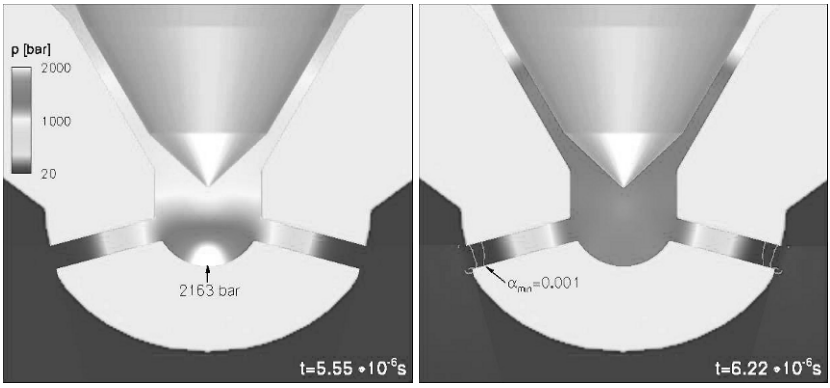

Fig. 6. Shock wave inside the sack-hole, $p_{max} = 2163$ bar (left), acoustic cavitation in the bore-holes (right), $p_{in} = 600$ bar, $p_{out,mix} = 26$ bar, $T_{init} = 333$ K, $\Delta t_{CFD} = 10^{-10}$ s.

bore holes while the primary shock focuses at the bottom of the sack. There the shock focusing results in a maximum instantaneous pressure $p_{max} = 2163$ bar (Fig. 6 - left). As the shock waves reach the exits of the bore holes, reflected rarefaction waves enforce acoustic cavitation (Fig. 6 - right).

For the prescribed pressure difference $\Delta p = p_{in} - p_{out} = 574$ bar steady state supercavitation is observed at $t \geq 10^{-4}$ s (Fig. 7). The resulting contraction of the effective area decreases the mass flow to 76% of its theoretical maximum value.

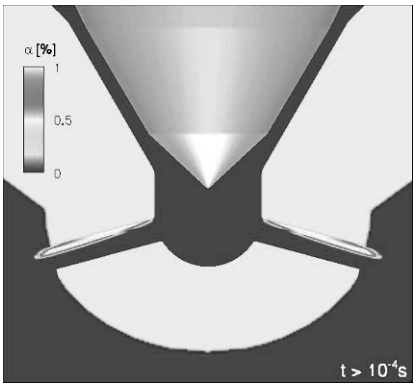

Fig. 7. Steady-state supercavitation in 3-D injection nozzle, at $t \geq 10^{-4}$ s, $p_{in} = 600$ bar, $p_{out,mix} = 26$ bar, $T_{init} = 333$ K, $\Delta t_{CFD} = 10^{-10}$ s.

4 Conclusion and Outlook

The time accurate resolution of the development of the flow inside two injection nozzles is investigated. Thereby, special emphasis is put on different time scales that characterise the flow features during the injection cycle. Wave dynamics dominates during the first microseconds and leads to maximum pressures of more than 2100 bar for a prescribed rail pressure of 600 bar. Acoustic and hydrodynamic cavitation pattern are resolved and the arising steady state mass flow defect of 24% due to supercavitation is analysed. Furthermore, the observed unsteady flow phenomena at $0 \leq t \leq 10^{-4}$ s manifest the necessity of numerical time steps $\Delta t_{CFD} = 10^{-10}$ s in order to predict short time flow characteristics of typical multipoint and pilot injection techniques.

References

1. Toro E.F.: Riemann Solvers and Numerical Methods for Fluid Dynamics. Springer-Verlag (1999)
2. Schmidt S.J., Sezal I.H., Schnerr G.H.: Compressible simulation of high-speed hydrodynamics with phase change. In: Proceedings ECCOMAS CFD 2006 - European Conference on Computational Fluid Dynamics, The Netherlands, CD-ROM publication (2006)
3. Schnerr G.H., Schmidt S.J., Sezal I.H., Thalhamer M.: Shock and Wave Dynamics of Compressible Liquid Flows with Special Emphasis on Unsteady Load on Hydrofoils and on Cavitation in Injection Nozzles. Invited Lecture. In: Proceedings CAV2006 - Sixth International Symposium on Cavitation, The Netherlands, CD-ROM publication (2006)

Shock-induced collapse of bubbles in liquid

X.Y. Hu and N.A. Adams

Lehrstuhl für Aerodynamik, Technische Universität München, 85748 Garching, Germany

Summary. The problem of shock-induced collapse of bubbles in liquid is investigated for 3 types of bubble configuration (bubble row, bubble cluster and bubble matrix) by numerical simulations with a newly developed conservative multi-phase method. The computational results show complex processes which are strongly influenced by the interactions between shock waves, liquid jets, sound waves, vortex sheets and vortices, and bubble oscillations (collapse and rebounce). Some observations and predictions from previous studies are also verified.

1 Introduction

Understanding the high-speed dynamics of bubbles in liquid is important both for fundamental research and applications. The high-speed dynamical phenomena usually are introduced by the collapse of bubbles under certain ambient condition. When a bubble is under shock impact, it begins an asymmetric collapse which is characterized by producing a high-speed liquid jet. The collapse of a single bubble is understood quite well by means of experiments [2] and numerical simulations [3] [4]. However, for the collapse evolving multiple bubbles, while experimental studies were carried almost 20 years ago [1], detailed numerical simulation has not been done for serious difficulties on interface modeling. Recently, we developed a conservative interface method for multi-phase problems [5], which solves the difficulty of conservation for the front tracking method and treats the topological changes naturally by combining interface description and geometric operations with a level set technique. In this paper, we present the simulations with the new method on the collapse of bubbles for 3 types of configuration: bubble row, bubble cluster and bubble matrix.

2 Numerical models

We model the flows of water and air with compressible Eulerian equations in two spatial dimensions, that is

$$\frac{\partial \mathbf{U}}{\partial t} + \frac{\partial \mathbf{F}(\mathbf{U})}{\partial x} + \frac{\partial \mathbf{G}(\mathbf{U})}{\partial y}, \tag{1}$$

where

$$\mathbf{U} = \begin{pmatrix} \rho \\ \rho u \\ \rho v \\ E \end{pmatrix}, \mathbf{F}(\mathbf{U}) = \begin{pmatrix} \rho u \\ \rho u^2 + p \\ \rho uv \\ (E+p)u \end{pmatrix}, \mathbf{G}(\mathbf{U}) = \begin{pmatrix} \rho v \\ \rho uv \\ \rho v^2 + p \\ (E+p)v \end{pmatrix},$$

in which the total energy density $E = \rho e + \frac{\rho(u^2+v^2)}{2}$, e is the internal energy per unit mass. To close this set of equations, the pressure is obtained by the equation of states, which

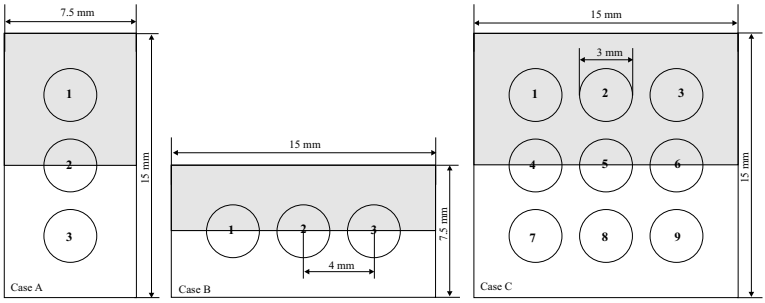

Fig. 1. Schematic for the computational setups for the three cases, in which the computational domains are the dark regions.

is given as Tait's equation for water $p = B\left(\frac{\rho}{\rho_o}\right)^{\gamma} - B + A$ where $\gamma = 7.15$, $A = 10^5$Pa, $B = 3.31 \times 10^8$Pa, and $\rho_o = 1000kg/m^3$, and the idea gas equation for air $p = (\gamma - 1)\rho e$ where $\gamma = 1.4$. At present, no cavitation model is included for water. The evolution of water/air interface is given by the level set equation

$$\frac{\partial \phi}{\partial t} + u\frac{\partial \phi}{\partial x} + v\frac{\partial \phi}{\partial y} \tag{2}$$

in which water is defined in the sub-domain with $\phi > 0$ and air in the sub-domain with $\phi < 0$.

3 Results

In this work, three cases are studied, in which, (Case A) a vertical row of 3 bubbles, (Case B) a horizontal cluster of 3 bubbles and (Case C) a matrix of 9 bubbles are embedded in rectangular or square domains. The schematic for the computational setups are shown in Fig. 1. In all the cases, a planar shock wave with the shock pressure of 0.26 GPa from the left, which is about the same strength as that in the experiment [1], and circular, two-dimensional air bubbles (diameter 3 mm and 4 mm apart) are used. Since a symmetric condition is used for the lower boundary, only the upper half of the domain is computed. An supersonic in-flow condition is used for the left boundary, and an out-flow condition with zero gradient is applied to both the right and the upper boundaries. A gird size of 1.875×10^{-5} mm, and a CFL number of 0.6 are used in all the computations.

Case A Figure 2 shows the density gradients at 4 time instances after the shock wave impinges the bubbles. At the early stage, as shown in Fig. 2a, it is observed that the wave structure comprises the two incident shocks I_1 and I_2 which is weaker for the stronger rarefaction from the two bubble surfaces, the reflection waves R_1 and R_2 which is reflected back and forth from the bubble surfaces to form secondary reflection waves R_2', and the transmitted shocks T inside the bubbles. It is also observed that there are weak sound waves S_1 near the bubble surface, especially the segments with larger curvatures, as shown in Fig. 2b. For bubble 1, because of the asymmetric rarefaction and reflection, the collapse velocity of the upper surface is larger than that of the lower surface. Consequentially, the liquid jet J_1 collides the bubble surface asymmetrically with

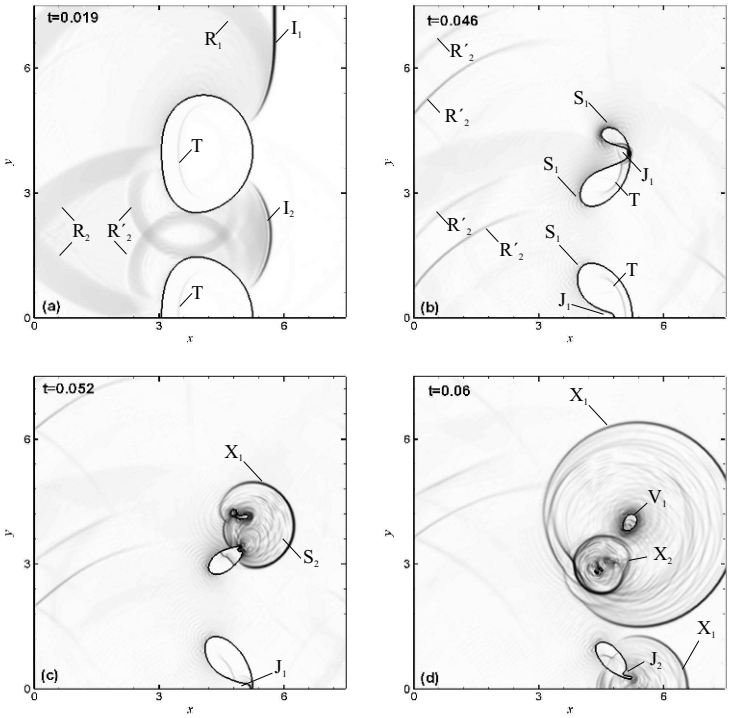

Fig. 2. Case A: Density gradients at 3 time instances.

the speed about 900 m/s (more than twice of the measured value in experiments [1]) and earlier than bubble 2, as shown in Fig. 2b. Note that, before the collision, the transmitted shock wave has been reflected from the bubble surface and collided with the liquid jet. After the collision, a strong explosion wave X_1 is produced and the bubble is split into two bubbles with different sizes. The smaller one quickly comes to its minimum volume, as shown in Fig.2c, and begins to re-bounce and rotate in anti-clockwise, by which sound waves S_2 much stronger than S_1 are produced after X_1. As the present air/water interface is treated as inviscid, sharp density discontinuity, the rotating bubble is actually a closed vortex sheet V_1. On the other hand, the larger one goes for secondary collapse which leads to a secondary explosion wave X_2, as shown in Fig. 2d, with a shock pressure much higher than that of X_1. This result suggests that the secondary collapse is more mechanically destructive than the liquid-jet collision [6]. Comparing to bubble 1, a symmetric but weaker jet J_1 with the speed about 700 m/s leads to a weaker explosion wave and a secondary jet J_2, which will split the upper half of the bubble further.

Case B For bubble 1, after the liquid jet J_1 collides with the bubble surface with the speed about 1100 m/s and produces an explosion wave X_1. The upper half of the bubble forms a new bubble which quickly comes to its minimum volume and begins to re-bounce, companying with several weak explosion waves W_1 and sound waves S_2, as shown in Fig. 3a. The re-bouncing bubble rotates in anti-clockwise and forms a closed

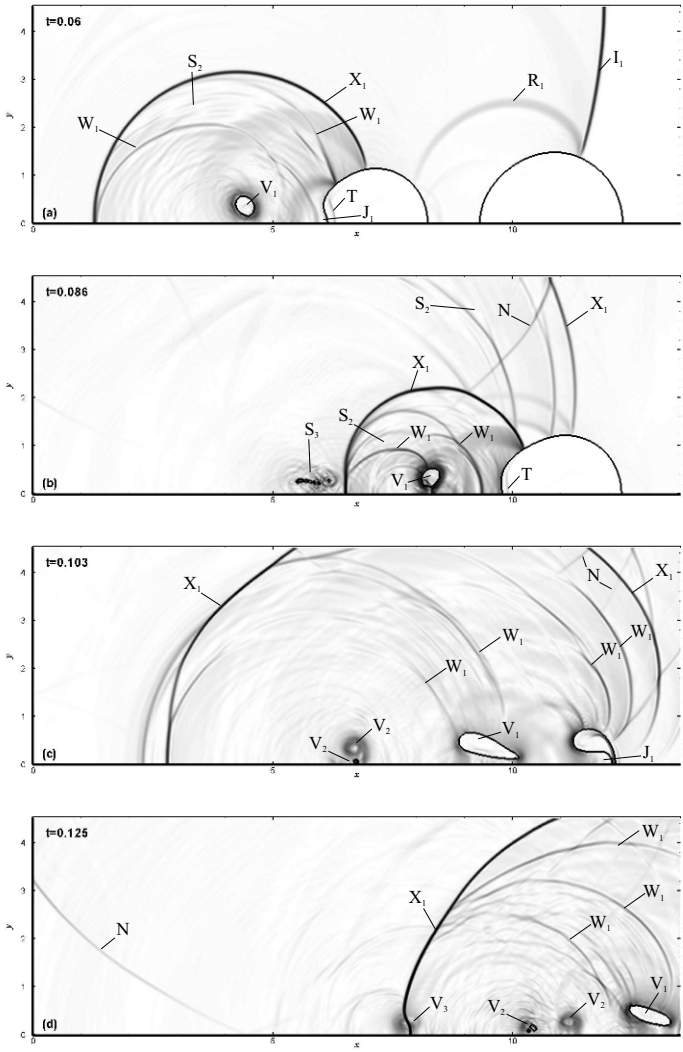

Fig. 3. Case B: Density gradients at 4 time instances.

vortex sheet V_1. The vortex sheet is stretched greatly and generates sound waves S_3, as shown in Fig. 3b. Under the compression of the explosion wave from bubble 2, as shown in Fig. 3c, the vortex sheets collapses finally, by which most of the air mass are split to unresolved bubbles (air mass is deleted in the present model) and only the two tip vortices V_2 are survived. As the tip vortices are attracted to each other, they approach gradually and merge to a single vortex V_3, as shown in Fig. 3d. During the merging process, the last part of air mass is also collapsed into unresolved bubbles. The merged vortex then is impact by the explosion wave originated from bubble 3, which produces

weak compression waves because of the shock/vortex interaction. Note that there are some weak reflection wave fronts N originating from the boundary. These waves are artifacts caused by the simple out-flow boundary condition and have no considerable influence to the global collapse process. Comparing to bubble 1, the behaviors of bubble 2 and bubble 3 are quite similar. The difference is that the explosion waves produced by previously impacted bubbles increase the size and the speed of the liquid jet, as shown in Fig. 3c. The speed of the liquid jet J_1 in bubble 2 is about 1500 m/s and in bubble 3 is about 1600 m/s. On the other hand, if more than 3 bubbles are considered in this case, eventually, the same collapse process will repeat until the end of the bubble cluster. However, as only three bubbles are considered in this case, there is no process after the merge of the tip vortices for bubble 2 and no process after the collapse of the vortex sheets for bubble 3.

Case C In this case, the early stage is quite close to the entire process of Case A. As shown in Fig. 4a, an asymmetric liquid jet with the speed about 900 m/s is produced in bubble 1, which split the bubble into two bubbles with different sizes. While the smaller one quickly goes to re-bounce and forms a vortex sheet V_1, the larger one continues collapse and produces a secondary explosion wave X_2. During the collapse, the bubble is split into 3 tiny bubbles and a strong clockwise vortex V_2 is formed. Comparable weak liquid jet with the speed about 700 m/s is produced in bubble 4, which again produces a weaker explosion wave X_1. The secondary jet in bubble 4 then splits the upper half part of the bubble into two bubbles. By the compression of the explosion waves from bubble 1, these split bubbles collapse and produces a secondary explosion wave X_2 for the larger bubble and a weak explosion wave W_2 for the smaller bubble, which is further split into unresolved bubble, and left an anti-clockwise vortex V_2, as shown in Fig. 4b. After being compressed by the reflected explosion wave Rx_2, the larger bubble collapse again and produces another weak explosion wave W_3. The tiny bubbles and the vortex left from bubble 1 is also compressed by the explosion wave from bubble 4 and the reflected explosion waves. While the collapse and re-bouncing of the tiny bubbles produce several sound waves S_3, the vortex/shock interaction produces two weak explosion waves W_4, as shown in Fig. 4c. Comparing to bubble 1, the liquid jet in bubble 2 is also asymmetric, but with larger size and higher speed (about 1100 m/s). Similarly, the liquid jet produced in bubble 5 has also larger size and higher speed (about 1000 m/s) than that of bubble 4.

4 Conclusion

We have studied the problem of shock-induced collapse of bubbles in liquid by numerical simulations. The results suggest that: (a) the calculated liquid jet speeds are much larger than those measured in experiments; (b) after the first liquid-jet impact, the split bubble may re-bounce quickly or develop to secondary collapse, and the highest pressure happens after the secondary collapse; (c) there are complex interactions between shock waves, vortex sheets or vortices; (d) with the present computational setups, the multiple-bubble collapse increase the size and speed of liquid jets.

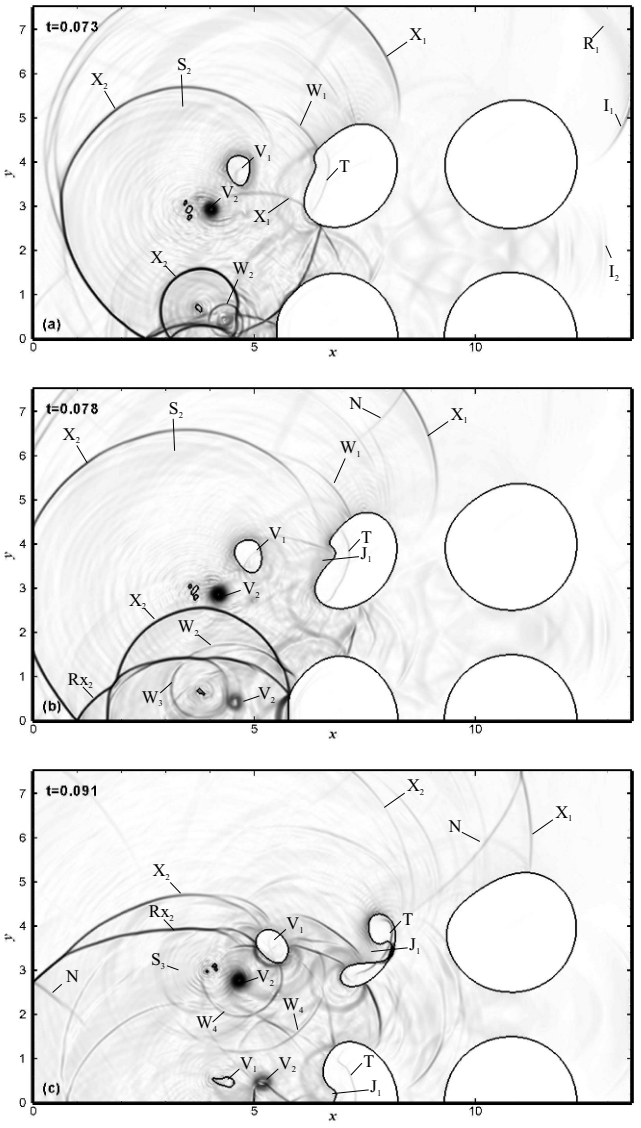

Fig. 4. Case C: Density gradients at 4 time instances.

References

1. Dear JP and Field JE: J Fluid Mech **190** (1988)
2. Bourne NK and Field JE: J Fluid Mech **244** (1992)
3. Ball GJ, Howell BP, Leighton TG, Schofield MJ: Shock Waves **10** 4 (2000)
4. Hu XY and Khoo BC: J Comput Phys **198** 1 (2004)
5. Hu XY, Khoo BC, Adams NA, Huang FL: J Comput Phys **219** 2 (2006)
6. Philipp A and Lauterborn W: J Fluid Mech **361** (1998)

Soot formation, structure and yield at pyrolysis of gaseous hydrocabons behind reflected shock waves

O.G. Penyazkov and K.A. Ragotner

Physical and Chemical Hydrodynamic Laboratory, Luikov Heat and Mass Transfer Institute, National Academy of Sciences of Belarus, 15 P.Brovki str., 220072, Minsk, (Belarus')

Summary. Laser radiation absorption and emission techniques are used to study the kinetics of formation, yield and structure of soot at pyrolysis of methane, acetylene and propane behind the reflected shock waves over the temperature range 1600 - 4000 K. Temperature dependencies for the induction time of soot condensation and yield are obtained from experimental measurements. Analysis of microphotos and electron photographs of carbon materials has shown that fine-dispersed graphite is the main component of their structure over the investigated range of parameters.

1 Introduction

Shock tubes are frequently used for pyrolysis studies, since they permit synthesizing different substances from gas mixtures over a wide range of temperatures and pressures [1–3]. There are many works, in which pyrolysis is considered along with the oxidation process [4,5]. The presence of oxygen exerts an essential influence on the kinetics of chemical reactions, at the same time shifting considered processes into a lower temperature region. In our case, the consideration of the pyrolysis without the oxygen participation makes it possible to investigate it only under pure thermal excitation conditions, which requires higher initial temperatures. The objective of the present work was to investigate the soot formation, structure and yield at the pyrolysis of methane, acetylene, and propane within a wide range of post-shock temperatures.

2 Experimental setup

The square shock tube of 4.5 m long has been applied for these studies (fig. 1). The gas emission behind the reflected shock wave was registered at two wavelengths corresponding to the radiation of the C_2 ($\lambda = 517\ nm$, $\Delta = 5\ nm$) and CH radicals ($\lambda = 430.8\ nm$, $\Delta = 2.5\ nm$). Emissions were detected by interference filters and recorded by photomultipliers. An attenuation signal of laser radiation was recorded by a photoresistor in combination with narrow-band interference filters ($\lambda_1 = 632.2\ nm$, $\lambda_2 = 632.8\ nm$, $\Delta\lambda_2 = 2.6\ nm$) and optical glasses ($KC$-10, KC-13) that used for cutting off a parasitic spectrum caused by gas self-emission at high temperatures.

Since the measuring gas volumes behind the reflected shock wave during observations of the laser absorption and gas emissions were equivalent, the instant of the luminosity peak was chosen as a reference time for measurements of laser absorption coefficients. This criterion corresponded to the maximum of production of C_2 and CH radicals during pyrolysis. The concentration of condensed soot $[C_{soot}]$ was calculated by means of Lambert-Beer's law.

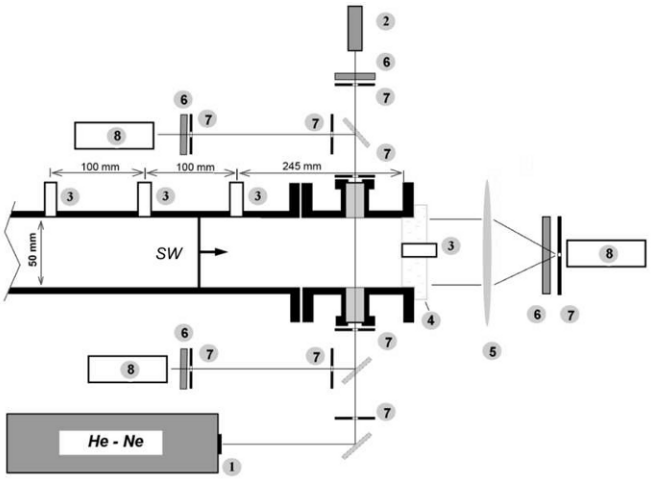

Fig. 1. Test section of the shock tube and the optical setup for pyrolysis studies behind the reflected shock wave. 1 - He-Ne laser; 2 - photoresistor; 3 - pressure sensor; 4 - transparent end wall; 5 - lens; 6 - interference filters; 7 - diaphragm; 8 - photomultipliers.

3 Result

Figs. 2,3 plots obtained temperature dependencies for the induction time of soot condensation and yield at pyrolysis of acetylene and propane behind the reflected shock wave. It is seen that the temperature dependence of soot yield for propane similar to acetylene [1, 2] has a typical "bell-shaped" form. However, a maximal soot yield in propane is located at higher temperatures $2400 - 2800\ K$, and in comparison with the acetylene its profile is essentially broadened.

For the most characteristic parts of the soot yield plots,an analysis of soot fraction microphotos and electron photographs has not revealed the existence of fullerenes and nanotubes in sample materials. It is found that fine-dispersed graphite is the main component of the soot structure at the studied range of pressures and temperatures.

Acknowledgement. This work was supported by the Research Program of the Republic of Belarus "Nanotechnology 1.26".

References

1. Soloukhin R.I., Shock Waves and Detonation in Gases. Moscow: Fizmatgiz, 1963.
2. Bhaskaran K.A., Roth P, The shock tube as wave reactor for kinetic studies and material system. Progress in Energy and Combustion Science, 28, 151-192, 2002.
3. Starke R., Roth P., Soot particle sizing by LII during shock tube pyrolysis of C6H6. Combustion and Flame, 127, 2278-2285, 2002.
4. Hidaka Y., Hattori K., Okuno T., Inami K., Abe T., Koike T., Shock-tube modeling study of acetylene pyrolysis and oxidation. Combustion and Flame, 107, 401-417, 1996.
5. Hidaka Y., Nishimori T., Sato K., Henmi Y., Okuda R., Inami K., Higashihara T., Shock-tube and modeling study of ethylene pyrolysis and oxidation. Combustion and Flame, 117, 755-776, 1999.

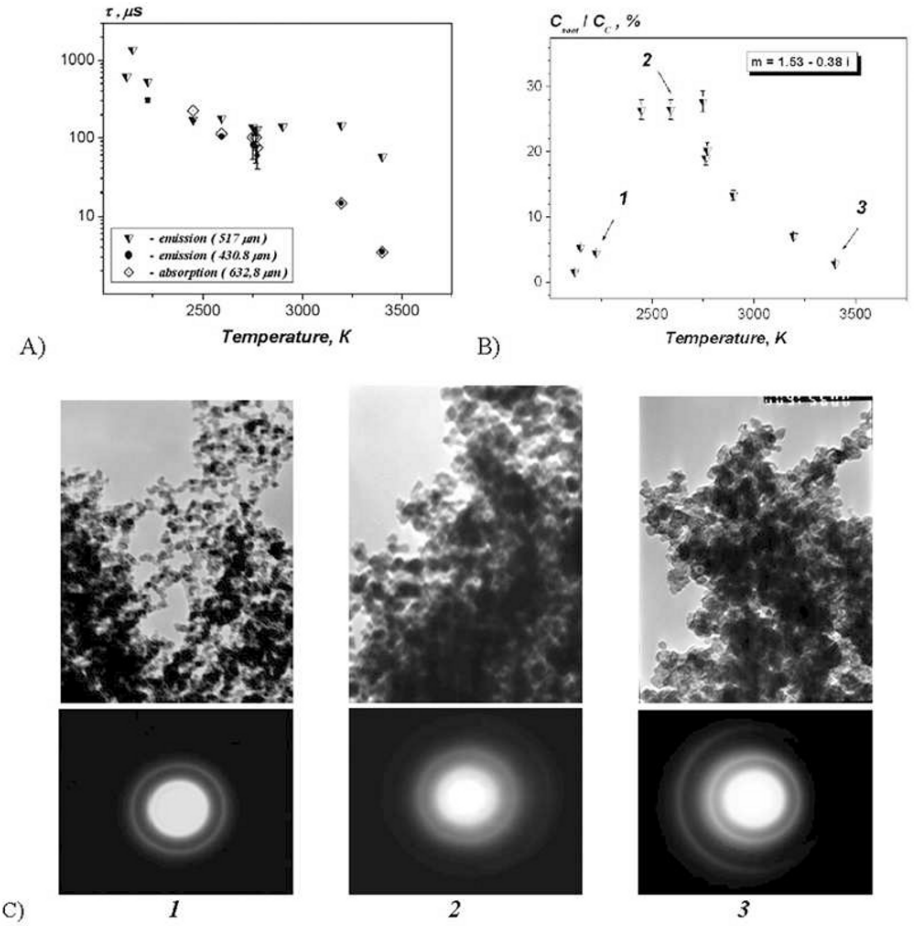

Fig. 2. Induction time (A) and soot yield (B) vs. gas temperature behind the reflected shock wave in C_3H_8/r (4:96) mixture and the microphotos and electron photographs of carbon materials at parts of the dependence (B) during pyrolysis: 1 - 2224 K; 2 - 2590 K; 3 - 3399 K

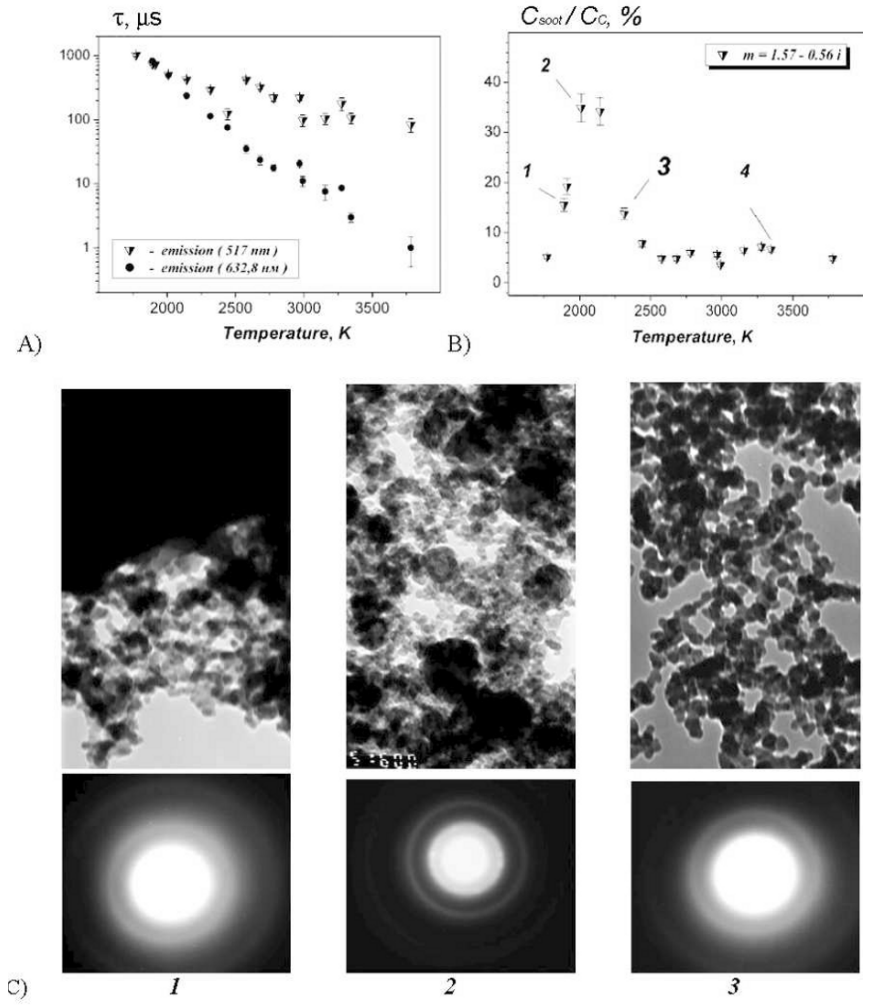

Fig. 3. Induction time (A) and soot yield (B) vs. gas temperature behind the reflected shock wave in C_2H_2/Ar (2:98) mixture and the microphotos and electron photographs of carbon materials at parts of the dependence (B) during pyrolysis: 1 - 1852 K; 2 - 2010 K; 3 - 3277 K;

Two dimensional structure and onset Mach number of condensation induced shock wave in condensing nozzle flows

M. Yu[1], M.L. Wang[1], B. Huang[1], H. Xu[1], Y.J. Zhu[1], X. Luo[2], J.M. Yang[1]

[1] *Department of Modern Mechanics, University of Science and Technology of China,230027 Hefei, P.R. China*
[2] *Shock Wave Laboratory, RWTH Aachen University, 52056 Aachen, Germany*

Summary. The two dimensional structure of condensation induced shock wave in condensing nozzle flows is investigated numerically and experimentally. By means of the dimensional analysis method, two similarity laws of the onset Mach number and structure of condensation shock are obtained for a same parameter, which is the compromise of condensation strength and the energy consumed before condensation. The similarity law of onset Mach number agrees well with the experimental results from other authors.

1 Introduction

Phase transitions of vapor-liquid are often observed in daily life, such as the formation of clouds in the atmosphere and the dew on the leaves. Since the cooling process is often very slow, condensation occurs in equilibrium in these phenomena where significant number of foreign agents (e.g. ions, aerosols, particles) act as condensation nuclei. These phenomena are called heterogeneous condensation. When the characteristic timescale of the cooling is small compared to the timescale of the agglomeration of vapor molecules at foreign agents, the metastable supersaturated state is achieved, and then the condensation nuclei form in the vapor phase itself. This is called homogeneous nucleation. A fast expansion of vapor would cause a fast drop of temperature and a spontaneous condensation, of which the development to liquid phase is dominated by homogeneous nucleation.

Vapor-liquid transitions are also important in many fields of science and technology, such as transonic and supersonic flows, turbo-machinery and propulsion engines. Much work has been done in these fields [1–4].

Since the condensation induced weak shock in the nozzle flow was firstly visualized by Prandtl [5], the studies of non-equilibrium condensation in transonic/supersonic nozzle have been widely carried out by both experiments and numerical simulations [6, 7].The states of nozzle flow are easy to measure; the effects of condensation are easily derived from one-dimensional frictionless gas dynamic models [8]. These models were applied in the dependence of flow states on relative humidity in the supply (Φ_0) and agree well in most experiments. But difficulties arise when the stagnation temperature is varied, and the structure of condensation induced shock wave in the nozzle with high wall curvature hasn't been well studied.

The motivation of present work is to study the structure of condensation shock and the combined dependence of onset Mach number on T_0 and Φ_0 in two-dimensional nozzle with high wall curvature.

2 Experimental setup

We study the condensation of moist air in two-dimensional nozzle both experimentally and numerically. The schematic of experimental setup was shown as Fig. 1, in which the half height of nozzle throat, $y^* = 5.22$ mm; the radius of the wall, $R^* = 24.9$ mm and the width of the nozzle is 13.6 mm. The position and structure of condensation shock are obtained by schlieren method.

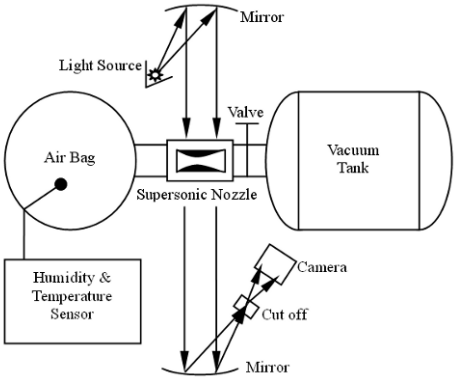

Fig. 1. Schematic of experimental setup

3 Numerical method

In our numerical study we applied the numerical method of ASCE2D [3]. The governing equation for the complete system can be considered as the combination of the moment equations of the size distribution with the Euler equations for time-dependent two-dimensional flow. This method adopts a condensation model consisting of the reduced *Internally Consistent Classical Nucleation Theory* nucleation model and the explicit droplet growth formulation by Gyarmathy [9]. The temperature difference between the droplets and the surrounding gas has been taken into account by applying a wet-bulb approximation. For a detailed description about the condensation model and the numerical method, the reader is referred to [3].

4 Results and analyses

4.1 Different structures of condensation shock

As shown in Fig. 2, the condensation shock trends to be normal shock in slender nozzles, while double λ-shaped shock connected with a Mach stem in the middle appear in the nozzles with high wall curvature. This kind of double-λ structure can be characterized by dimensionless length of Mach stem h_m^*(half Mach stem length h_m normalized by the half nozzle throat height y^*).

The complex structure of condensation shock is the result of non-uniformed expansion of moist air. As shown in Fig. 3(a), the flow near the wall expands faster than that near

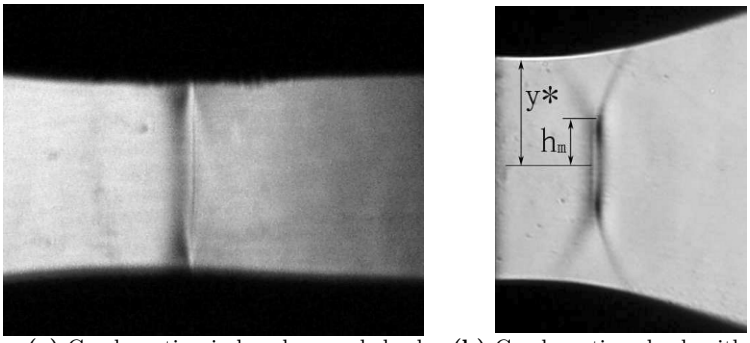

(a) Condensation induced normal shock **(b)** Condensation shock with complex structure

Fig. 2. Different structures of condensation induced shock

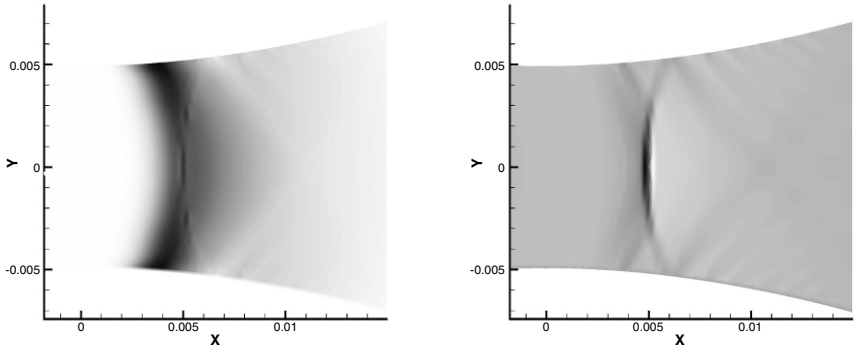

(a) X-gradient of condensate mass fraction **(b)** Digital schlieren

Fig. 3. Numerical simulation of condensation shock with complex structure

the axis and consequently drops faster in temperature. As a result, the condensation happens earlier and more dramatically near the wall, which produces an oblique shock wave (or compressive wave) from each side of the walls. The two oblique shocks meet together near the axis to form a Mach stem. This Mach stem compress the flow and slow down the condensation near the axis. So the non-uniformity of expansion is aggravated. In comparison, if the relative saturation rate is higher, condensation may also induce normal shock in the nozzles with high wall curvature. In this case, the condensation trends to be more uniformed in the flow field.

4.2 Dependence of onset Mach number and dimensionless length of Mach stem on stagnation states

We take the position of Mach stem as where condensation shock onset. Then, the onset Mach number can be calculated based on the one dimensional theory of compressible flows. Results and some simple relations can be found in Table 1 and Fig. 4. It is found

Table 1. Experiment results of Condensation onset Mach number M_c and dimensionless length of Mach stem h_m^*

Φ_0 (%)	69.0	73.5	75.0	77.0	82.0	85.0	92.0	91.0	80.0	80.0	79.5	67.0
T_0 (^{o}C)	18.2	18.3	18.1	18.1	18.6	18.2	18.6	21.4	21.7	25.2	29.1	26.9
M_c	1.39	1.37	1.33	1.31	1.26	1.28	1.23	1.22	1.33	1.26	1.23	1.43
h_m^*	0.095	0.094	0.193	0.225	0.509	0.480	0.538	0.726	0.324	0.517	0.739	0.098

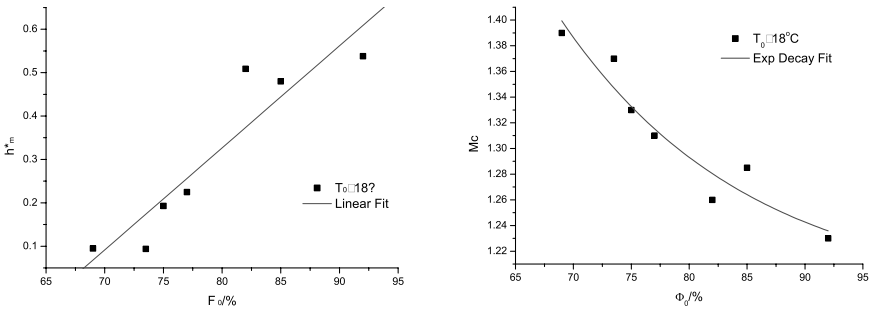

Fig. 4. Simple relations between h_m^*, M_c and Φ_0 at almost constant T_0.

that when Φ_0 goes up, the condensation shock moves upstream and the Mach stem lengthens due to stronger condensation. When T_0 goes up, the Mach stem lengthens at almost the same position. This is a compromise of stronger condensation (pushing the shock forward) and higher temperature (delaying the condensation).

4.3 Dimensional analysis

Firstly, let's analyze the dimensionless length of Mach stem h_m^*. The parameters that may influent h_m^* are stagnation pressure p_0, stagnation temperature T_0, stagnation density ρ_0, relative humidity in the supply $\Phi_0 = p_{v0}/p_{s0}$, where p_{v0} is the vapor partial pressure in the supply, $p_{s0} = p_{s0}(T_0)$ is the saturation pressure for a plane boundary; Geometric parameters: $l = (y^* R^*)^{1/2}$, where y^* is the half height of throat and R^* is the radius of throat wall; Heat capacity C_p and ratio of heat capacity γ; latent heat released by unit mass of vapor L. Besides, the relaxation time τ (duration of condensation) and ΔT_c (the difference between T_0 and condensation temperature) are also very important. Then,

$$h_m^* = F_1(p_0, T_0, \rho_0, p_{v0}, \Phi_0, \Delta T_c, l, y^*, C_p, L, \tau, \gamma) \tag{1}$$

Taking T_0, l and p_0 as basic dimensions, we get:

$$h_m^* = F_2\left(\frac{p_{v0}}{p_0}, \Phi_0, \frac{L}{C_p T_0}, \frac{\Delta T_c}{T_0}, \frac{y^*}{l}, \frac{\tau a^*}{l}, \gamma\right), \tag{2}$$

Where p_{v0}/p_0 is the ratio of vapor in the supply; $L/(C_p T_0)$ is the ratio of latent heat and the heat capacity of unit carrier gas; $y^*/l = (y^*/R^*)^{1/2}$ is the effect of nozzle wall

curvature; $a^* = a^*(T_0)$ is the local sound speed of nozzle throat, l/a^* is the characteristic time of flow near throat,so $\tau a^*/l$ is the ratio of relaxation time and characteristic time.

Since the p_0 is constant, ρ_0 only depends on T_0. C_p, γ and L can also be taken as constant for the ratio of vapor in air is actually very little. Usually 10^{-5} s $< t < 10^{-4}$ s[11] , here we assume $\tau = 5 \cdot 10^{-5}$.

Based on 1-D theory, if T_0 is around 300 K, the temperature near throat will drop to about 240 K and pressure drop to about 0.52 atm. Even if we count in the effect of condensation shock, water should still be in solid phase. Wegener[[1]] had proved that the product of condensation in supersonic nozzle is solid. The critical temperature of the vapor-solid transition is about 273 K, so we take $\Delta T_c = T_0 - 273$.

At last, only y^*, l, T_0 and Φ_0 are left to be control variables. If we define $q = [L/(C_p T_0)] * [p_{v0}/p0] * [\rho_v/\rho_{v0}]$ as the ratio of latent heat and the heat capacity of unit mass unit time at the throat, then we get:

$$h_m^* = F_3\left(\frac{L}{C_p T_0} * \frac{p_{v0}}{p_0} * \frac{\rho_v}{\rho_{v0}}, \frac{\Delta T_c}{T_0}, \frac{\tau a^*}{l}, \frac{y^*}{l}\right) = F_4\left(\frac{qT_0}{\Delta T_c}, \frac{\tau a^*}{l}, \frac{y^*}{l}\right) \tag{3}$$

By linear fit, we can get the similarity law:

$$h_m^* = A\left(\frac{y^*}{l}\right)^{\alpha 1}\left(\frac{\tau a^*}{l}\right)^{\alpha 2}\frac{qT_0}{\Delta T_c} - B \tag{4}$$

Where $A = 3.87, B = 1.02, \alpha 1 = 0.53, \alpha 2 = 0.10$. If we let $X = \left(\frac{y^*}{l}\right)^{\beta 1}\left(\frac{\tau a^*}{l}\right)^{\beta 2}\frac{qT_0}{\Delta T_c}$, which can be view as the compromise of condensation strength and the energy consumed before condensation, the results of table 1 can be redisplayed as Fig. 5 (Left part).

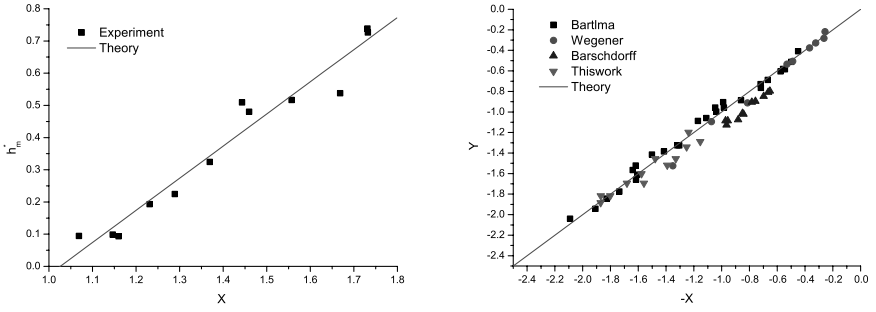

Fig. 5. h_m^* dependence of the compound parameter X (Left) and relation between compound parameter X and Y (Right)

Using the same method, we can also get the similarity law of M_c, which is proved to be a good approximation to the experimental results for several different nozzles, as shown in Fig. 5 (Right part).

$$Y = \ln\left((M_c - C_2)/\left(C_1\left(\frac{y^*}{l}\right)^{\beta 1}\left(\frac{\tau a^*}{l}\right)^{\beta 2}\right)\right), \tag{5}$$

where $C_1 = 0.22, C_2 = 1.00, \beta 1 = -0.51, \beta 2 = 0.67$. C_2 can be viewed as the onset Mach number when the mixture in supply is extremely easy to condense.

5 Conclusions

The two dimensional structure of condensation induced stable shock wave in condensing nozzle flows is investigated both experimentally and numerically. Based on schlieren method, the different structures of condensation shock are characterized and found to be the results of non-uniformity expansion of the flow and the interaction of Mach stem with flow.

With the dimensional analysis method, we found two similarity laws of the onset Mach number and structure of condensation shock which are both depend on the same compound parameter X : the compromise of condensation strength and the energy consumed before condensation. The similarity law of onset Mach number agrees well with the experimental results from other authors. But there is no much work on the 2-D structure of condensation shock for comparison.

References

1. P.P. Wegener and A.A. Pouring: *Experiments on condensation of water vapor by homogeneous nucleation in nozzles*, Phys. Fluids **7**, pp 352–361 (1964)
2. G. H. Schnerr: *2-D transonic flow with energy supply by homogeneous condensation: Onset condition and 2-D structure of steady laval nozzle flow*, Exp. in Fluids **7**, pp 145-156 (1989)
3. X. Luo, B. Prast, M.E.H. van Dongen, H.W.M. Hoeijmakers, and J. Yang: *On phase transition in compressible flows: Modelling and validation*, J. Fluid Mech. **548**, pp. 403–430 (2006)
4. X. Luo, G. Lamanna, A.P.C. Holten, and M.E.H. van Dongen: *Effects of homogeneous condensation in compressible flows: Ludwieg-tube experiments and simulations*, J. Fluid Mech. **572**, pp 339–366 (2007)
5. Prandtl: *Atti del Convegno Volta* **XIV**, 1st edn, Reale Academia D'Italia, Roma (1936)
6. S. Adam and G.H. Schnerr: *Instabilities and bifurcation of nonequilibrium two-phase flows*, J. Fluid Mech. **348**, pp 1–28 (1997)
7. G. Lamanna, J. van Poppel, and M.E.H. van Dongen: *Experimental determination of droplet size and density field in condensing flows*, Exp. Fluids **32**, pp 381–395 (2002)
8. W. Frank: *Condensation phenomena in supersonic nozzles*, Acta Mechanica **54**, pp 135–156 (1985)
9. G. Gyarmathy: The spherical droplet in gaseous carrier streams: review and synthesis. In: *Multiphase Science and Technology* **1**, Springer Berlin (1982)

Part XIII

Nozzle Flow

Design and analysis of a rectangular cross-section hypersonic nozzle

R.S.M. Chue[1], D. Cresci[1], and P. Montgomery[2]

[1] *ATK GASL, 77 Raynor Avenue, Ronkonkoma, NY 11779, USA*
[2] *Aerospace Testing Alliance/AEDC, Arnold AFB, TN 37389, USA*

Summary. A technique for designing rectangular cross-section hypersonic nozzles where all four walls are contoured is presented. Two design variations are shown; one follows directly from a streamtracing method while the other is reshaped to enforce rectangular cross-sections. The former has slightly bulging walls while the latter is easier to manufacture. The application of the true-streamtraced nozzle when integrated with a Flight Acceleration Simulation Test (FAST) technique is also studied. In a FAST test, the simulated flight Mach number is varied by using a reflector plate downstream of the nozzle to generate either an oblique shock or an expansion fan. FAST requires a nozzle with rectangular exit, and therefore the current design method is particularly applicable. The flow quality of the rectangular nozzles as well as the effects of the reflector plate will be discussed.

1 Introduction

It is sometimes desirable to have a rectangular exit nozzle in a hypersonic ground-test facility or in a flight vehicle. Rectangular nozzles could be designed as two-dimensional nozzles where the area expands by having only two of the four walls contoured. However, since the expansion is two dimensional, the design would result in nozzles that are longer than round ones. In addition, when operating in a high temperature environment, such as that in a vitiation-heated test facility, the thin-slit nozzle throat that often results in two-dimensional hypersonic nozzles could lead to severe heating and structural deformation problems. An alternative approach to designing a rectangular exit hypersonic nozzle would be to have all four walls contoured so that the expansion is three dimensional.

This paper serves to demonstrate a technique for designing rectangular hypersonic nozzles that have all four walls contoured using a streamline tracing method. As an illustration, the design of a large-scale hypersonic nozzle with a 1.016 m $\times$ 1.778 m (40 in. $\times$ 70 in.) rectangular cross-section at the exit is shown. Two design variations can be produced from the tools developed at ATK GASL; one is generated using a streamtracing method, and another is further reshaped so that the cross-sectional shape is forced to be exactly rectangular at all axial locations.

As an example for the application of rectangular hypersonic nozzles, a numerical simulation of the true-streamtraced nozzle when integrated with a Flight Acceleration Simulation Test (FAST) configuration is also included in the study. In the FAST test operation, a test technique previously developed at ATK GASL [1], a reflector plate is placed downstream of the nozzle and the plate angle relative to the nozzle is varied during testing as a method to simulate the varying Mach number conditions along a flight trajectory. Note that a rectangular nozzle exit is preferred over a round one for this operation. If a round nozzle is used, the interaction of the circular nozzle flow, which includes the boundary-layer nonuniformity from the nozzle, with the reflector plate would result in a highly three-dimensional flow and would severely affect the test flow quality.

The flow simulations performed include a positive plate rotation to generate an oblique shock to decrease the test flow Mach number, and also a reverse rotation to generate expansion waves and a higher flow Mach number.

2 Rectangular nozzle design

The underlying concept of the design is to use a "parent" nozzle flow field that produces a high-quality nozzle flow while resulting in a compact (i.e., short length) nozzle. An axisymmetric nozzle designed using an analytical method is best suited as the parent flow field. From this, an arbitrarily shaped streamtube would then be "carved" out to obtain the surfaces of any desired nozzle geometry, which in the present case is rectangular. The streamtube is constructed using a streamline tracing procedure where streamlines that would result in a rectangular exit are traced along the axisymmetric flow field. Since no flow can cross a streamline, the carved-out flow field behaves as though the nozzle were still circular. The axisymmetric nozzle design and the streamtracing procedure are applied to an inviscid flow, and the obtained streamlines are corrected for displacement thickness effects as a final step.

The design of a rectangular exit cross-section nozzle can be summarized in the following steps:

(a). An axisymmetric nozzle is designed with an exit diameter that encompasses the desired exit cross section of 1.016 m × 1.778 m (40 in. × 70 in.) This is done using ATK GASL's in-house inviscid method-of-characteristics code (*noz_code*), which generates the supersonic section nozzle wall contour.
(b). An inviscid axisymmetric CFD solution is obtained for the round nozzle geometry.
(c). The desired cross-sectional shape of the nozzle exit is prescribed on the CFD solution. The edges on the nozzle exit are discretized into points. To take advantage of symmetry, investigators need only one quarter of the nozzle geometry in the streamtracing and subsequent CFD analysis.
(d). Streamlines are traced through the inviscid axisymmetric flow field from the nozzle exit discretized points toward the upstream direction and end at the throat location. Note that since the parent flow field is axially symmetric, the CFD solution at any axial location is a function of the radius, but not of the angular orientation. When performing streamtracing, the angular orientation is therefore unchanged along each streamline although this orientation must be preserved in order to reconstruct the three-dimensional position of the final streamline.
(e). Each of the streamlines is corrected for the displacement thickness using ATK GASL's in-house *Sasman-Cresci* code [2].
(f). The true-streamtraced nozzle is then constructed using the family of viscous-corrected streamlines that form the side and top surfaces.
(g). To obtain a nozzle with fully rectangular cross-sections throughout the length, investigators further discretize the nozzle into small, axial increments. At each axial station, the shape is reformed into a rectangle where the cross-sectional area is preserved and the aspect-ratio is fixed to be the same as that at the nozzle exit.

To demonstrate the applicability of the technique for hypersonic nozzles, a design example is presented for a nozzle with a stagnation pressure and temperature of 19.3 MPa and 2610 K, respectively, and a nozzle exit Mach number of 6.25.

The designed nozzles have at least approximately rectangular cross-sections. This is exactly so for the all-rectangular nozzle, since it is enforced to have rectangular sections, but it is approximately true for the pure streamtraced nozzle as well. Furthermore, the throat and the nozzle exit are very close to rectangles even for the true-streamtraced case.

The main difference between the true streamtraced nozzle and the all-rectangular nozzle is that the walls of the former have concave and convex surfaces. This feature is a consequence of the inviscid streamline trajectories rather than of the viscous effects. The true streamtraced nozzle geometry is shown in Fig. 1 with a zoom-in view where the walls can be seen to bulge in and out at different locations. The geometry of the all-rectangular nozzle is shown in Fig. 2.

Fig. 1. Geometry of the true streamtraced nozzle. Left: Full view, right: zoom-in view

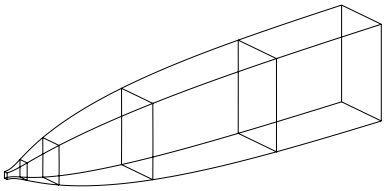

Fig. 2. Geometry of the all-rectangular nozzle

Since the true streamtraced nozzle is directly obtained from the exact streamtube of the parent axisymmetric nozzle, it is expected to adhere more accurately to the theoretical wave-cancelling feature of the method-of-characteristics design. However, the all-rectangular nozzle may be easier and less expensive to manufacture. In the following section, a CFD analysis is carried out to examine the flow quality of the nozzles to determine the best performing design.

3 Computational analysis of designed nozzles

The computational domain includes only the supersonic contours and starts at the nozzle throat plane, where a uniform sonic condition is assumed. The nozzle entrance conditions are obtained using a one-dimensional chemical equilibrium code. The fluid medium is vitiated air consisting of the combustion products from the vitiation heater. High temperature gas dynamics and finite-rate chemistry are captured using a 16-reaction, 12-species kinetics model. The boundary layer is assumed to be fully turbulent, and the two-equation Mentor Shear Stress Transport (SST) k-ω turbulence model is used. The computational code used is GASP version 4.2 [3].

The CFD solution for the true streamtraced nozzle at the design condition is shown in Fig. 3. In the figure, the Mach number contours are shown to illustrate the boundary layer thicknesses on the nozzle walls. Fig. 3a plots the contours on the $z = 0$ symmetry plane, which shows that the boundary layer thickening eventually decreases the core flow

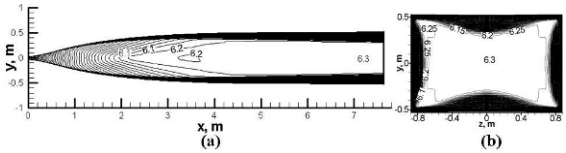

Fig. 3. Mach number contours for true streamtraced nozzle. (**a**) On $z = 0$ symmetry plane, (**b**) at nozzle exit cross section

size near the nozzle exit. Fig. 3b plots the Mach number contours at the nozzle exit and shows a clean flow area of 0.76 m × 1.52 m (30 in. × 60 in.) where the Mach number is very close to the design value of 6.25.

The Mach number contours for the all-rectangular nozzle are shown in Fig. 4. Fig. 4a shows the contours on the $z = 0$ symmetry plane where the boundary layer thickness is seen to be more severe than for the true-streamtraced nozzle and the core flow size is decreased far more than in the true streamtraced nozzle. Fig. 4b plots the Mach number contours at the nozzle exit. Compared to the true streamtraced nozzle (Fig. 3b), the exit flow deviates more from the design Mach number of 6.25 and is more nonuniform. The most noticeable nonuniformities are two round-shaped, low Mach number regions at around $z = 0$ on the y_{max} and y_{min} walls, which decreased the core flow size in the y direction to about 0.508 m (20 in.). Since the only difference between the true streamtraced and the all-rectangular nozzles is that the former follows directly from the method-of-characteristics wave cancelling technique while the latter is reshaped to enforce rectangular cross sections, the poor performance of the latter is a consequence of reshaping that renders the wave mechanics inaccurate. The CFD results therefore demonstrate that the true-streamtraced nozzle can produce better flow quality than the all-rectangular nozzle.

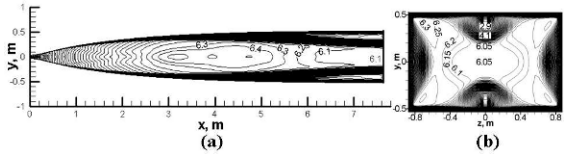

Fig. 4. Mach number contours for all-rectangular nozzle. (**a**) On $z = 0$ symmetry plane, (**b**) at nozzle exit cross section

4 Application of rectangular nozzle to FAST test operation

The Flight Acceleration Simulation Test (FAST) is a ground testing technique previously developed at ATK GASL [1] to simulate the variation of flight conditions along a trajectory in real time. It is used as an example for the application of rectangular exit nozzles. The basic principle behind the FAST technique is that the Mach number in a two-dimensional flow field can be varied by a simple wave process: a shock wave to reduce the Mach number, or an expansion fan to increase it. This process is accomplished by rotating a flat plate (the "reflector plate"), on which the test article is mounted, relative to the nozzle exit. The technique produces the correct flow conditions over the test article by simultaneously varying the test-section Mach number through the strength of the shock wave or expansion fan and the stagnation conditions by varying the pressure and the fuel-air ratio in the vitiation heater. In this manner, a selected segment of a

flight trajectory – including both speed and altitude – can be produced in real time by preprogramming the facility operation [1].

The true streamtraced nozzle is selected for this analysis as its flow quality is superior to that of the fully rectangular nozzle. The nozzle is truncated at 5.4 m (212.56 in.) from the throat location to maximize the core flow size. A reflector plate is placed downstream of the nozzle. The plate is displaced 0.127 m (5 in.) normal from the nozzle wall and is translated 0.0635 m (2.5 in.) axially from the nozzle exit. A "jet stretcher" is assumed to extend the wall contour of the nozzle exit to minimize the disturbances from the edge of the nozzle exit. The jet stretcher walls are taken to be that of the untruncated nozzle contour so that the walls are perfectly continuous between the nozzle exit and the jet stretcher. Beyond the length of the original untruncated nozzle, the top (z) surface of the jet stretcher is open (no wall), whereas the side (y) surfaces are assumed to have fences throughout. The side fences are assumed to have the same wall tangency angles as those at the untruncated nozzle exit.

The nozzle operated with a 10° compression reflector plate is used to generate a test flow that simulates a flight Mach number that is lower than that for the nozzle design condition. The test section is to be located where the oblique shock generated by the reflector merges with the expansion waves generated from the opened top surface. At this location, the flow underneath the oblique shock has the largest core size and is then used as the test flow. The flow field on the $y = 0$ symmetry plane is shown in Fig. 5a.

The flow distributions on a transverse slice taken at where the oblique shock and the top expansion waves merge are shown in Fig. 5b. The useful core flow is in the lower center region, which has a Mach number of approximately 5.5. In the slice, there are two low Mach number distorted flow regions on the side (y_{max}, y_{min}) walls, which are generated by the interaction between the oblique shock and the boundary layers inherited from the nozzle. The distorted regions significantly reduced the core flow width to be about 0.41 m (16 in.) in the y direction. In the z direction, the core flow height based on the flow nonuniformity immediately above the reflector surface is about 0.38 m (15 in.)

The 10° expansion case is similar to the compression case but with the reflector plate tilted downward to generate expansion waves to simulate a flight Mach number that is higher than that for the nozzle design condition. The test section is to be located approximately where the expansion waves generated by the plate merge with the location, the core size is the largest and is used as the test flow. The flow field on the $y = 0$ symmetry plane is shown in Fig. 6a.

The flow distributions on a transverse slice taken near the end of the reflector plate are shown in Fig. 6b. The useful core flow is represented by the lower center region, which has a Mach number of approximately 7.6. Unlike the compression case, there is no shock wave generated on the plate and thus no shock interaction with the inherited viscous flow. As a result, the viscous flow nonuniformity on the y_{max} and y_{min} walls do not

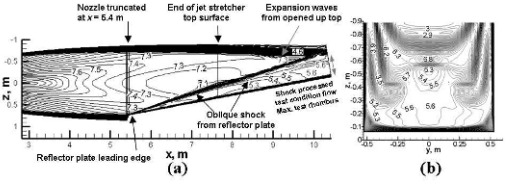

Fig. 5. Mach number contours over reflector plate, 10° compression. (**a**) On $y = 0$ symmetry plane, (**b**) $x \simeq 4.45$ m (175 in.) from nozzle exit

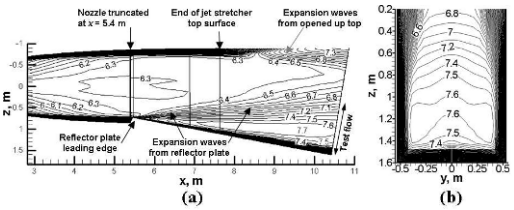

Fig. 6. Mach number contours over reflector plate, 10° expansion. (**a**) On $y = 0$ symmetry plane, (**b**) $x \simeq 5.16$ m (203 in.) from nozzle exit

show any sign of distortion or significant growth; therefore, the flow uniformity is largely preserved. The core flow size is also found to be relatively insensitive to the location of the transverse slice. The high Mach number region is seen to occur just outside the wall boundary layer over the plate, and it gradually decreases in the z direction away from the plate. However, the variation in Mach number is weak and a core flow size of approximately 0.91 m × 0.76 m (36 in. × 30 in. ($y \times z$)) can be obtained.

5 Concluding remarks

A technique is presented for designing rectangular exit nozzles using a streamtracing method. Two nozzle variations are produced, one adheres to the streamtracing procedure and the other is further enforced to be rectangular. Both nozzles have very similar shapes, although the true-streamtraced nozzle has slightly bulging walls. However, the flow qualities delivered by the two nozzles are significantly different from each other. The all-rectangular nozzle suffers from larger boundary layer growth and flow distortions, and thus the core flow size is severely reduced. The true-streamtraced nozzle is therefore a superior design.

The true-streamtraced nozzle is also applied to the FAST facility operation where a reflector plate is added to the nozzle exit. The analysis for the plate rotated 10° into the flow to generate a shock showed a large decrease in core flow area due to the interaction between the shock and the viscous flow inherited from the nozzle. On the other hand, the 10° expansion operation yielded a more uniform flow. This suggests that the test facility should be configured with a nozzle that is designed below the mid-value in the operating range so as to take advantage of the better uniformity in the expansion operations.

Acknowledgement. The authors would like to thank the Test Resource Management Center (TRMC) Test and Evaluation/Science and Technology (T&E/S&T) Program for their support. This work is funded by the T&E/S&T Program through the Arnold Engineering Development Center, Arnold Air Force Base, TN.

References

1. Engers R., Erdos J., Roffe G., Swartwout W.: Flight testing on the ground in the *FAST* facility. ISABE Paper 99-7170, 14th ISABE (1999)
2. Sasman P.K., Cresci R.J.: Compressible turbulent boundary layer with pressure gradient and heat transfer. AIAA J., **4**, 11, Jan. (1966)
3. GASP version 4.2, Aerosoft, Inc, Blacksburg, Virginia, USA (2002)

Effect of nozzle inlet geometry on underexpanded supersonic jet characteristics

N. Menon and B.W. Skews

School of Mechanical Engineering, University of the Witwatersrand, Johannesburg, Private Bag 3, WITS - 2050, South Africa

Summary. A numerical study has been undertaken on underexpanded sonic jets issuing from nozzles of varied inlet geometries. The Mach stem height in the jet issuing from the contoured nozzle has been the greatest over the range of pressure ratios investigated. A vena-contracta effect has been noted in the jet flow field in the cases of nozzles with sharp inlet geometries. The effect of the inlet geometry is to delay the onset of the typical barrel shock structure seen in underexpanded jets. The distortion of the jet boundary results in a smaller Mach stem for the same pressure ratio and exit Mach number.

1 Introduction

Jet flows are an important part of various mixing and thrust producing propulsion systems. Problems associated with combustion and jet noise have been shown to be associated with the jet structure, particularly the existence of shock waves within the jet. The structure of jet flows from underexpanded axisymmetric nozzles have been investigated fairly rigorously over the past half century commencing with the work carried out by Love et al. [1]. Pack [2] provided a method of characteristics approach as early as 1948 to determine the flow field characteristics of an underexpanded jet. A significant amount of work has also been concentrated on the production of noise as a result of the interaction of the shock wave with the turbulent shear layer of the jet (some of the work can be found in [3], [4], [5], [6], [7], [8], [9] and [10]). In the past work has also been concentrated on understanding the initial inclination of the underexpanded supersonic jet as it exhausted from the nozzle. The inclination of the jet boundary was calculated using a method of characteristics based approach for underexpanded jets at moderate pressure ratios exhausting into a quiescent medium [11], for an underexpanded jet at large pressure ratios exhausting into a quiescent medium [12], and for the case of an underexpanded jet exhausting into a supersonic ambient stream [13], [14]. A number of researchers have utilised the approach of solving the Euler [15] or the Navier Stokes ([6], [16], [17] and [18]) equations in cylindrical coordinates to obtain the flow field within an underexpanded axisymmetric jet.

The underexpanded jets were generated by utilising nozzles that were conically divergent (for supersonic underexpanded jets) or smooth contoured nozzles (for sonic underexpanded jets). The effect of conically convergent inlet geometry on the characteristics of the sonic underexpanded jets has not been investigated in the same detail as the cases mentioned earlier. Addy [19] has provided an empirical relation to predict the location and the size of the Mach stem formed in a sonic jet issuing from a conically convergent sonic nozzle. It was observed that the pressure ratio at the onset of the Mach disk formation increased smoothly and continuously with the convergence angle of the nozzle inlet and the Mach disk structure was observed to be stable when the ratio between the stagnation pressure in the nozzle and the ambient pressure was greater than 5.

2 Numerical set-up

The numerical simulation of the underexpanded jet impingement flow was carried out using the commercially available code Fluent 6. The flow was modeled as a viscous flow, with the one equation Spallart-Allmaras turbulence model for closure of the Reynolds Averaged Navier-Stokes equations. The simulation was performed in steady state and convergence was monitored by the log of the residuals of the equations and using a mass flux balance across the inlet and the outlet boundaries of the model. The computational grid was adapted based on the gradient of pressure to obtain the results of adequate resolution.

3 Results and Discussion

The following nozzle inlet geometries were analyzed to determine the effect of the inlet geometry on the underexpanded jet: contoured inlet, , 45^o inlet and an orifice inlet. The nozzles were analyzed to have sonic exits, with the ratio between the exit plane and the ambient atmosphere being varied between 2 and 10 (the ratio is henceforth referred to as PR).

3.1 General description of the flow field

For small underexpansion ratios of the jet (PR = 2), the contoured nozzle results in a well defined barrel shock structure appearing in the flow field as can be seen in figure 1(A). The barrel shock reflects along the jet centerline as a Mach reflection. For the case of the non-contoured inlets (Figure 4 (B) and (C)), the flow field is markedly different. The expansion waves forming at the nozzle exit reflect at the sonic line in the jet boundary as compression waves. These compression waves do not coalesce to form a shock wave before the reflection point as can be seen in figure 1(B) and (C). As the pressure ratio is increased the strength of the barrel shock increases as can be seen in figure 2. The formation of a Mach stem occurs in all of the examined nozzle inlet geometries. The strength of the barrel shock is at its strongest for the case of the contoured nozzle. The formation of the barrel shock in the jet flow stream is nearest to the nozzle exit in the case of the contoured nozzle (Figure 2 (A)). The height of the Mach stem in the nozzle flow field is lower in the case of the 45^o inlet and the orifice nozzle cases (Figure 2 (B) and (C)). Upon increasing the pressure ratio to PR = 10, the shape of the jet flow field remains

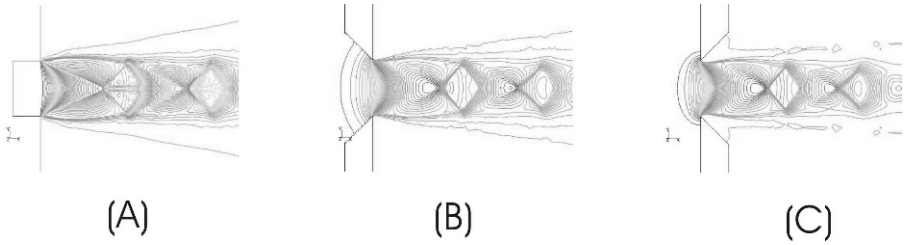

Fig. 1. Density contours of the flow field, M = 1, PR = 2 (A) Contoured inlet (B) 45^o inlet (C) Orifice inlet

essentially similar for the cases of the contoured nozzle and the 45^o inlet nozzle (Figure 3 (A) and (B)). In the case of the nozzle with the orifice inlet however, the expansion of the jet flow as it exits the nozzle is such that the jet boundary touches the nozzle exit face. This causes the jet to expand along the nozzle exit face and not along the jet boundary. The jet boundary in this case originates from the edge of the orifice exit nozzle as can be seen in 3 (C).

3.2 Mach stem heights

A comparison of Mach stem heights non-dimensionalized by the nozzle exit height is shown in Figure 4. The Mach stem height is consistently the greatest for the case of the contoured nozzle. The Mach stem height of the 45^o nozzle inlet is the smallest across the range of pressure ratios examined. The orifice inlet Mach stem height is comparable to the 45^o inlet case until a pressure ratio of 5, after which the Mach stem height for the orifice inlet is greater for pressure ratios of 7 and 10 in comparison the that of the 45^o inlet case. This is as a result of the jet boundary merging with the nozzle exit at higher pressure ratios for the orifice inlet as shown in figure 2 (C). The analytical expressions for the orifice inlet and the contoured nozzle as developed by [19] have also been presented in figure 4 and it is important to note that the analytical expressions under predict the Mach stem height as compared to the simulation results. This is due to the fact that the boundary layer growth in the nozzle geometry has not been accounted for in the case of the contoured nozzle simulation resulting in a flow field that is closer to an inviscid case. The effect of viscosity is evident in the prediction with the analytical expressions as they were developed from experimental results. The effect of inlet turbulence in the development of the jet flow field needs further investigation to ascertain its exact influence.

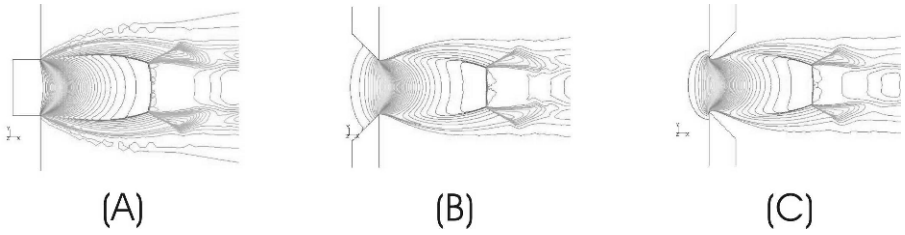

Fig. 2. Density contours of the flow field, M = 1, PR = 5 (A) Contoured inlet (B) 45^o inlet (C) Orifice inlet

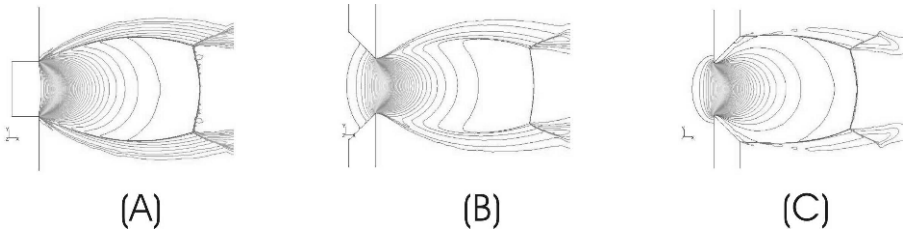

Fig. 3. Density contours of the flow field, M = 1, PR = 10 (A) Contoured inlet (B) 45^o inlet (C) Orifice inlet

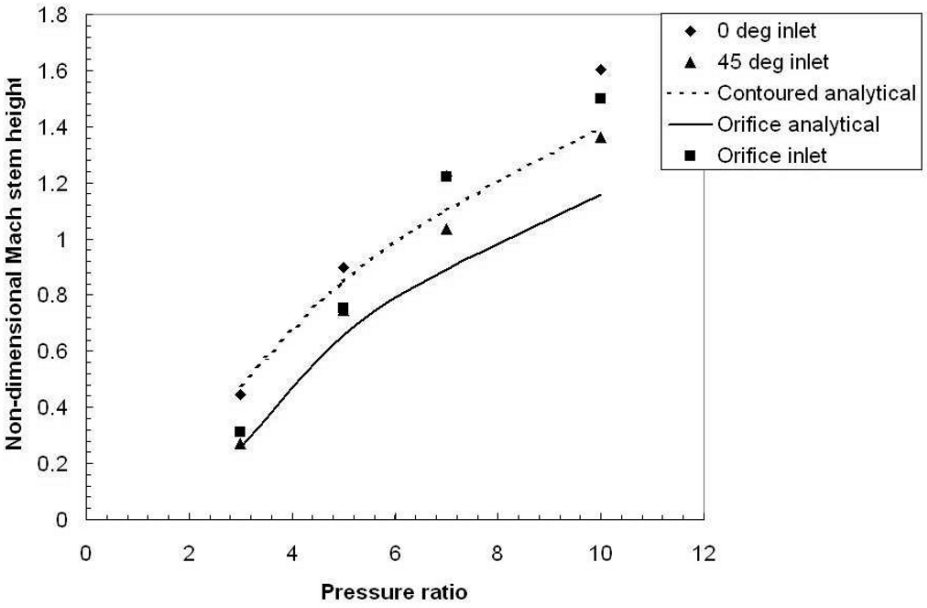

Fig. 4. Non-dimensional Mach stem heights as a function of pressure ratio for various inlet angles

3.3 Effect on jet boundary

The contoured nozzle results in a jet boundary that leaves the nozzle at an angle orthogonal to the nozzle exit face. In the case of the sharp edged nozzle, there is a defined vena-contracta effect that can be seen at the nozzle exit. The vena-contracta effect is most pronounced for the orifice nozzle exit (Figure 5 and 6). There is no discernible change in the shock structure between the jets issuing from the orifice inlet and the 45^o inlet. The vena-contracta in the jet flows results in a narrowing of the jet boundary as it leaves the nozzle exit. This results in a sonic line that is not orthogonal to the nozzle exit

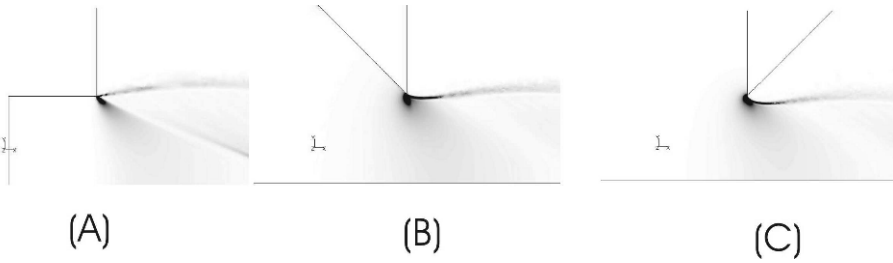

Fig. 5. Pseudo-schlieren images of the flow field in the vicinity of the nozzle exit, M = 1, PR= 2 (A) Contoured inlet (B)45^o inlet (C)Orifice inlet

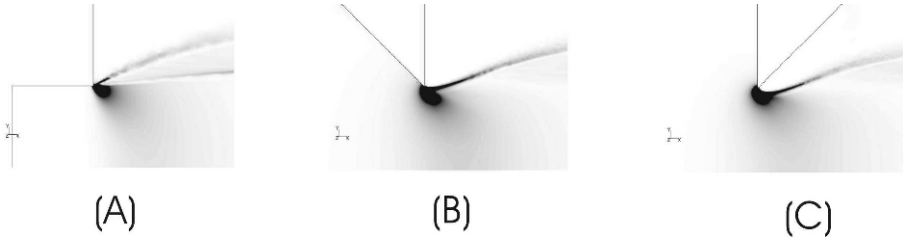

Fig. 6. Pseudo-schlieren images of the flow field in the vicinity of the nozzle exit, M = 1, PR= 5 (A) Contoured inlet (B)45^o inlet (C)Orifice inlet

plane, but curved in space downstream of the nozzle exit. Hence for the case of the 45^o inlet nozzle and the orifice inlet nozzle the flow reaches sonic conditions a small distance downstream of the nozzle exit and not at the nozzle exit in the case of the contoured nozzle.

4 Conclusions

A computational study on underexpanded jet flows issuing from nozzles having varied geometries has been carried out. The main conclusions of the study are:

- The formation of the barrel shock in the jet flow field occurs at the lower pressure ratio in the case of the contoured nozzle in comparison to the other nozzle geometries that have been investigated.
- The Mach stem height is greatest for the case of the contoured nozzle in comparison to the other nozzle geometries that have been investigated over the pressure ratio range between 2 and 10. There is a curvature of the Mach stem in the direction of the flow and the curvature is more pronounced as the pressure ratio is increased.
- The formation of a vena-contracta resulting in a narrowing in the jet boundary is observed in the case of the 45^o and the orifice inlet nozzles.
- The effect of nozzle inlet turbulence needs to be investigated to account for the differences between the analytical prediction of Mach stem height in comparison to the Mach stem height predicted by simulation.

References

1. Love E. S., Grigsby C. E., Lee L. P., and Wooding M. J.: Experimental and Theoretical Studies of Axisymmetric Free Jets, NACA TR R-6 (1959)
2. Pack D. C.: Journal of Mechanics and Applied Mathematics, 1 pp. 1 - 17 (1948)
3. Powell A.: The Aeronautical Quarterly IV pp. 103 - 122 (1953)
4. Powell A.: Proceedings of the Physics Society 66 pp. 1039 - 1057 (1953)
5. Umeda Y. and Ishii R.: Recent Developments in Acoustics 1 pp. 69 - 96 (2003)
6. Siener J. M., Dash S. M., and Wolf D. E.: AIAA Journal, 23 5 (1985)
7. Panda J.: Journal of Fluid Mechanics 363 pp. 173 - 198 (1998)
8. Panda J. and Seasholtz R. G.: Physics of Fluids, 11, 12 (1999)
9. Tam C. K. W., and Jackson J. A.: Journal of Fluid Mechanics, 153 pp. 123 - 149 (1985)

10. Tam C. K. W.: Journal of Sound and Vibration, 121 1 (1988)
11. Love E. S., Woodling M. J., and Lee L. P.: Boundaries of supersonic axisymmteric free jets NACA RM L56G18 (1956)
12. Love E. S, and Lee L. P, Shape of the initial portion of boundary of supersonic axisymmetric free jets at large pressure ratios NACA TN 4185 (1958)
13. Love E. S.: Initial inclination of the mixing boundary separating an exhausting supersonic jet from an ambient supersonic stream NACA RM L55J14 (1956)
14. Vick A. R., Andrews E. H. Jr., Dennard J. S., and Craidon C. B.: Comparisons of experimental free jet boundaries with theoretical results obtained with the method of characteristics NASA TN D-2327 (1964)
15. Katanoda H., Miyazato Y., Masuda M., and Matsuo K.: Shockwaves 10 pp 95 - 101 (2000)
16. Dash S. M., Wolf D. E, and Siener J. M.: AIAA Journal, 23 4 (1985)
17. McDaniel J., Glass C., Staack D., and Miller C.: In Proceesings of the 40th AIAA Aerospace Sciences Meeting and Exhibit (2002)
18. Gribben B. J., Badcock K. J., and Richards B. E.: AIAA Journal 38 2 (2000)
19. Addy A. L.: AIAA Journal 19 1 (1981)

Experimental investigation of shock stand-off distance on spheres in hypersonic nozzle flows

T. Hashimoto*, T. Komuro, K. Sato, and K. Itoh

Japan Aerospace Exploration Agency (JAXA)
Koganesawa 1, Kimigaya, Kakuda, Miyagi, Japan 981-1525

Summary. In order to understand thermochemical non-equilibrium phenomena which occur during re-entry, shock stand-off distances on a simple hemi-spherical model were measured in a high enthalpy shock tunnel. Moreover, from the measurements, the unresolved question of how much influence un-recombinated oxygen atoms and vibrationally excited molecules related to the frozen phenomena of nozzle flows have on the flow was investigated. It was also discussed whether a binary scaling parameter which indicates a non-equilibrium process can accommodate the nozzle flows of a shock tunnel.

1 Introduction

During atmospheric re-entry at speeds of 7 km/s or higher, the air behind the shock wave generated around a body will be compressed and heated to 10,000 K. At these temperatures, real gas effects are dominant and lead to drastic changes in the aerothermodynamic characteristics of the flow. Therefore, the development of thermal protection system against aerodynamic heating and a detailed investigation of aerodynamic characteristics are essential topics to investigate.

Air molecules flowing around re-entry vehicles become vibrationally excited, dissociated and ionized, and the shock layer is in thermochemically non-equilibrium with flow duration times of the same order as the chemical reaction time in air. Since this effects influence aerodynamic characteristics, it is necessary to understand them, particularly for the development of space transportation systems [1].

In the hypersonic regime, a simple geometry is sensitive to real gas effects in the shock layer. In the case of a sphere, the high temperature behind a shock wave brings vibrational excitation and dissociation of air molecules, and the temperature is reduced by heat absorption due to real gas effects. As a result, shock stand-off distances are shortened. Therefore, shock stand-off distances are good reference quantites and useful for validating the results of numerical simulations [2].

As a result, a lot of papers have experimentally, numerically and theoretically investigated shock stand-off distance for high enthalpy flows. Lobb [3] experimentally measured shock wave stand-off distances with a light gas gun and clarified the relationship between flight speed and the shock stand-off distance. Nonaka [4] acquired more detailed data and arranged it according to the binary scaling parameter.

Hornung and Wen [5] measured the shock stand-off distance with a shock tunnel and explained the results by introducing a reaction rate parameter. Olivier [6] further developed this theory and obtained very good agreement with the experimental results.

* Present address: Biomedical Engineering Research Organization, Tohoku Univ., Katahira 2-1-1, Aoba, Sendai, Miyagi, JAPAN 980-8577

A shock tunnel is one of the ground test facilities that can generate high enthalpy uniform flows. However, the test gas remains thermally excited and chemically frozen after it becomes a plasma at the nozzle reservoir and is expanded very rapidly in the nozzle without returning to its original state.

In particular, a not negligible amount of un-recombined oxygen atoms are left in the nozzle flow and, hence, the nozzle flow does not accurately reproduce real re-entry conditions. However, the extent of such a chemically frozen state has not been well examined and this is one of the most serious criticisms made of high enthalpy shock tunnel characteristics. In particular, because of the presence of chemically frozen flow in the nozzle, non-equilibrium effects in the shock layer are weakened.

In the present study, in order to experimentally investigate the influence of the thermochemical non-equilibrium, shock stand-off distances on a hemispherical model were measured in the enthalpy range of 4 to 16 MJ/kg using the High Enthalpy Shock Tunnel (HIEST) at the Japan Aerospace Exploration Agency (JAXA). The obtained results were compared with those from a ballistic range and the effect of changes in the flow density and model radius for a fixed binary scaling parameter and flow velocity was also examined.

2 Test facility and condition

HIEST can produce a test flow with a maximum stagnation enthalpy of 25 MJ/kg and a maximum stagnation pressure of 150 MPa to reproduce the dissociation of molecules in re-entry flight [7]. Three kinds of hemispherical model were manufactured to examine thermochemical non-equilibrium effects by varying the binary scaling parameter. The radii of the models were 25, 40, and 50 mm. The shock stand-off distances were measured from the visualization results using the Schlieren method and pressure measurements were also made near the stagnation point.

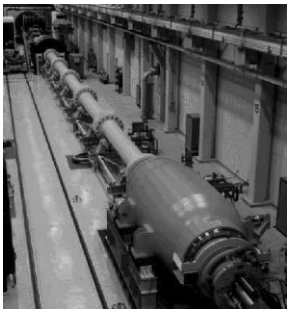

Fig. 1. High Enthalpy Shock Tunnel, HIEST

Table 1 shows the test conditions as calculated by the Nonequilibrium Nozzle Flow (NENZF) code [8]. The binary scaling parameter was set to values of 2.0, 4.0 and 8.0 $\times$ 10^{-4} kg/m^2. The nozzle flow velocities were set to 2.5 to 4.5 km/s, corresponding to enthalpies of 4 to 16 MJ/kg. The test gases were air and nitrogen. A diode pumped solid-state (DPSS) laser was used as a light source and a digital still camera as the recording medium.

Table 1. Test conditions

velocity (km/s)	P_0 (MPa)	ρ (kg/m^3)	R (mm)	ρR (kg/m^2)	test gas
2.5	14.8	0.016	25	4.0×10^{-4}	Air, N_2
3.0	13.0	0.01	40	4.0×10^{-4}	Air, N_2
3.0	38.5	0.03	25	8.0×10^{-4}	Air
3.5	16.7	0.01	40	4.0×10^{-4}	Air, N_2
3.5	35.8	0.021	40	8.0×10^{-4}	Air
3.5	57.8	0.031	25	8.0×10^{-4}	Air
4.0	17.7	0.008	25	2.0×10^{-4}	Air
4.0	17.7	0.008	50	4.0×10^{-4}	Air, N_2
4.0	33.8	0.016	25	4.0×10^{-4}	Air, N_2
4.0	33.8	0.016	50	8.0×10^{-4}	Air
4.5	28.4	0.011	40	4.0×10^{-4}	Air, N_2

3 Test results

Figure 2 shows a Schlieren photograph for an enthalpy of 16MJ/kg, flow velocity of 4.5 km/s and radius of 50 mm as a typical condition. Errors appearing in the data measured from the photographs result from the determination of the shock position and average approximately 2%. The shock stand-off distances, Δ, are normalized by the model radius, R.

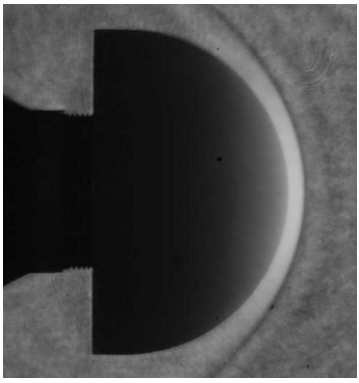

Fig. 2. Schlieren photograph over a sphere for a radius of 50 mm and enthalpy of 16 MJ/kg

Figure 3 shows the test results for ρR=4.0×10^{-4} kg/m^2 and an enthalpy of 4 to 13 MJ/kg when the test gas is nitrogen. The abscissa designates the flow velocity and the ordinate is the normalized shock stand-off distance. The upper solid line designates the analytical results for $\gamma = 1.4$ and the broken line is the prediction of the state of chemical equilibrium at a pressure of approximately 2.7 kPa. Actually, in the higher enthalpy of this range, nitrogen molecules begin to dissociate but the vibration mode is dominant in this region. In the shock tunnel experiments, the nitrogen molecules are not relaxed and reach the nozzle exit in a vibrationally non-equilibrium state due to the frozen phenomena in the nozzle mentioned previously. Therefore, since plenty of excited

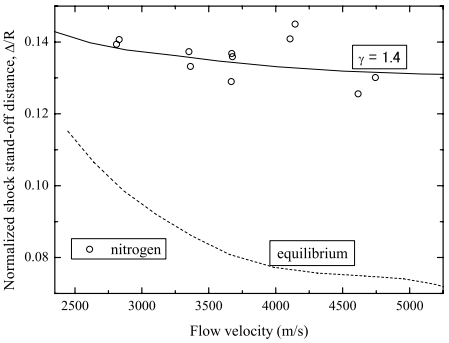

Fig. 3. The normalized shock stand-off distances for nitrogen in HIEST

molecules already exist, the contribution to the internal energy behind the shock wave becomes small and the stand-off distances become relatively long.

The shock stand-off distances measured in HIEST for a test gas of air are plotted in Fig.4 for ρR values of 2.0, 4.0 and 8.0 $\times$ 10^{-4}kg/m^2. The obtained data lie between the curves designated for an ideal gas and for chemical equilibrium. Therefore, the region between the two curves is non-equilibrium region with a finite ρR. Data taken at lower velocities is close to the ideal gas value and, as flow velocity increases, strong non-equilibrium effects clearly appear. It is noted that non-equilibrium effects are exhibited even in the region of 2.5 km/s. Moreover, as the value of ρR increases, the normalized shock stand-off distances approach the equilibrium value.

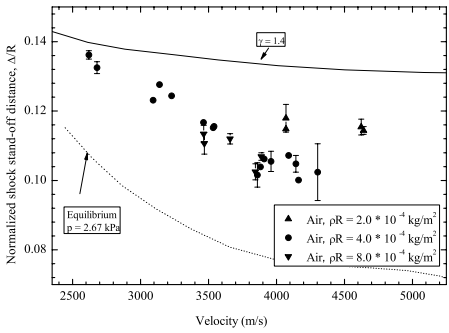

Fig. 4. The normalized shock stand-off distances for air in HIEST

Figure 5 shows a comparison of the normalized shock stand-off distances for ρR = 4.0 $\times$ 10^{-4}kg/m^2. The normalized shock stand-off distances measured in the shock tunnel

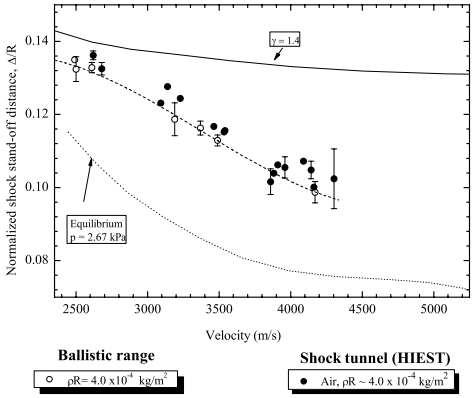

Fig. 5. The comparison of shock stand-off distances between shock tunnel and ballistic range for $\rho R = 4.0 \times 10^{-4}$ kg/m^2

are compared with those obtained in a ballistic range by Nonaka. As the velocity of the flow and the projectile goes up, it is clear that both results have the same tendency. However, the values obtained in the shock tunnel are generally larger than those of the ballistic range. As mentioned above, the shock tunnel test flows keep a higher temperature without returning to their initial state at the nozzle exit. Therefore, the Mach number of the test flows in the shock tunnel becomes lower and that is thought to be one of the causes of the increase in the normalized shock stand-off distance. However, a simple comparison like this is difficult to make due to the presence of other factors. It will be necessary to examine these effects in more detail in the future.

Three values of radius and density are combined in the velocity area of 3.8 to 4.3 km/s and the results of normalized shock stand-off distances at almost constant ρR=4.0 $\times 10^{-4}$kg/m^2 are shown in Fig. 6. The results show good agreement and the binary scaling parameter was found to be established in the non-equilibrium flowfield in HIEST. However, because the density and velocity are calculated from NENZF, further examination is required.

4 Conclusion

In order to experimentally investigate thermochemical nonequilibrium phenomena which occur during re-entry, shock stand-off distances on a simple hemi-spherical model were measured in a high enthalpy shock tunnel. The results summarized as follows:

- Due to the frozen phenomena in the nozzle, the stand-off distances become relatively long for a test gas of nitrogen.
- The shock stand-off distances measured in HIEST for a test gas of air were conducted for three kinds of ρR. As flow velocity increases, strong non-equilibrium effects clearly appear, and as the value of ρR increases, they approach the equilibrium value.

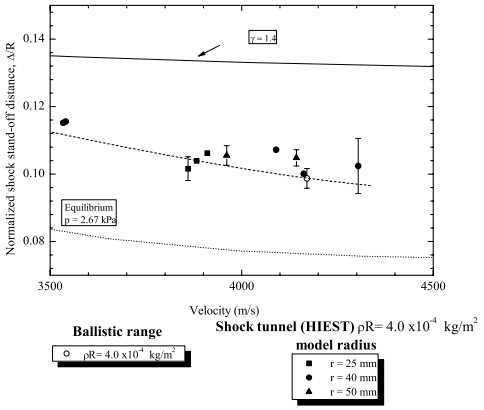

Fig. 6. The normalized shock stand-off distances for different model radius, R = 25, 40, 50 mm, at constant ρR=4.0 $\times$ 10^{-4}kg/m^2.

– The normalized shock stand-off distances measured in the shock tunnel are compared with those obtained in a ballistic range by Nonaka for ρR = 4.0 $\times$ 10^{-4}kg/m^2, and both results have the same tendency. However, a simple comparison is difficult to make due to the presence of other factors. It will be necessary to examine these effects in more detail in the future.

References

1. Anderson J. D. Jr., Hypersonic and High Temperature Gas Dynamics, Mc-Graw-Hill, 1989
2. Park C., Experimental Simulation and Evaluation of Chemical Effects, VON KARMAN INSTITITE FOR FLUID DYNAMICS Lecture Series, 1995
3. Lobb R. K., Experimental Measurement of Shock Detachment Distance on Spheres Fired in Air at Hypervelocities. The high temperature aspects of hypersonic flow (Nelson ed.), Pergamon press, 519-527, 1964
4. Nonaka S., Experimental and Numerical Study on Hypersonic Flows in Ballistic Range, PhD Thesis, Tohoku University, 2000
5. Hornung H. G. and Wen C.-Y., Nonequilibrium Dissociating Flow over Spheres, AIAA Paper 95-0091, 1995
6. Olivier H., A theoretical model for the shock stand-off distance in frozen and equilibrium flows, J. Fluid Mech., Volume 413, 2000
7. Itoh K., Tuned Operation of Free Piston Shock Tunnel, In Proc. 20th International Symposium on Shock Waves, 1995
8. Lordi J. A., Mates R. E., Moselle J. R., Computer Program for the Numerical Solution of Nonequilibrium Expansions of Reacting Gas Mixtures, NASA CR-472, 1959

Mach disk shape in truncated ideal contour nozzles

R. Stark and B. Wagner

German Aerospace Center DLR, Institute of Space Propulsion
Langer Grund, D-74239 Hardthausen (Germany)

Summary. DLR Lampoldshausen carried out cold flow tests to study the flow field in a truncated ideal contour nozzle at low nozzle pressure ratios. A convex shaped Mach disk was found for nozzle pressure ratios less than 10 and a slight concave one for nozzle pressure ratios more than 20. Due to boundary layer transition the convex Mach disk is temporary tilted and redirects the flow towards the nozzle wall. Accompanying numerical simulations compare well with the experiments.

1 Introduction

A series of CFD studies and tests went in for separated nozzle flows in the past. A number of tests showed a significant side load peak for low nozzle pressure ratios (NPR). DLR Lampoldshausen studied this peak [6] experimentally and identified a re-attached flow as an origin. This flow condition was present in thrust optimized parabolic (TOP) nozzles as well as in truncated ideal contour (TIC) nozzles. Re-attached flows are well-known for TOP nozzles where the so called cap shock pattern redirects the flow towards the wall. A competitive CFD study [6] for a TIC nozzle yield a concave bowed Mach disk creating a flow pattern comparable to this cap shock pattern. This bowed mach disk was thought to explain at low NPR a partial redirected flow towards the nozzle wall.
Bowed Mach disks at moderate NPRs could also be found in computations from Nasuti et al. [9] and Pilinski [10]. Frey et al. [5] show a Schlieren image where a shortened TIC nozzle features such a kind of Mach disk. These experimental and numerical studies as well as an intensive discussion within Europe's Flow Separation Control Device Group (FSCD) induced a test campaign studying the Mach disk in TIC nozzles in more detail.

2 Test Setup

The tests were conducted on the horizontal cold flow test position P6.2 using dry nitrogen as a fluid. The maximum total pressure and the minimum total temperature were $5.6\,\mathrm{MN/m^2}$ and $230\,\mathrm{K}$, respectively. The flow passes a settling chamber, a cross-section constriction, and a bending tube section before it accelerates in the convergent-divergent nozzle to supersonic velocity (Figure 1). As the flow pattern at low NPR (< 10) were of interest, where oblique shock and Mach disk are located inside the nozzle, an acrylic glass TIC nozzle was cut step by step from $L/R^* = 12$ down to $L/R^* = 1.75$. It was equipped with up to 50 pressure transducer ports in stream wise direction with a spacing of $2.5\,\mathrm{mm}$ each, starting in the nozzle's throat. The machine-made contour was checked in 3 axial planes and the deviation compared to the design was less than $5\,\mu\mathrm{m}$. The exhaust jet was studied with a Color Schlieren setup based on the dissection technique developed by

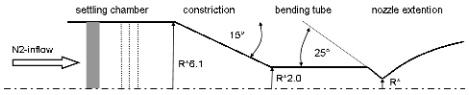

Fig. 1. Sketch of horizontal test section

Cords [2] and improved by Ciezki [1]. Nozzle and test setup are described in more detail in Frey [4] and Stark [13].

3 Discussion of Experimental Results

The obtained flow patterns can be compared to study the influence of the nozzle length on separation location, back pressure, and finally the position and the shape of the Mach disk.

Figure 2a gives the separation locations of all tested nozzle lengths. The data follow a

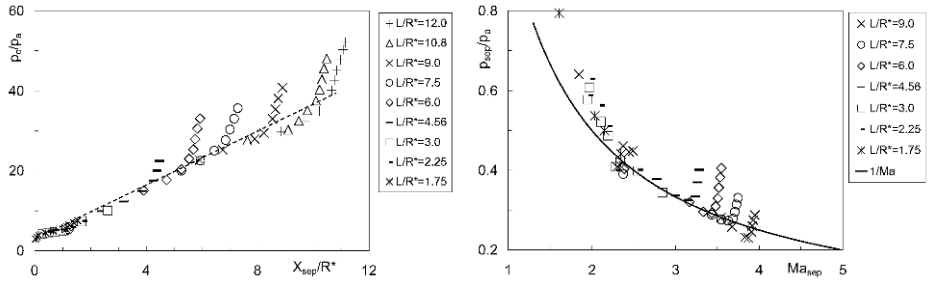

Fig. 2. Averaged separation location. (**a**) Normalized nozzle coordinates versus NPR (p_c/p_a). (**b**) Separation and wall Mach number

linear trend as long as the flow really separates. If the separation zone reaches the nozzle lip, a continued NPR rise only results in a compression of the separation zone, indicated by a distinct gradient change. The discontinuities around NPR = 30 are due to nitrogen condensation resulting in a delayed separation. Thus an influence of the nozzle length on the separation location can be neglected. Figure 2b is a more conventional plot without condensation affected data where the separation pressure (lowest wall pressure) is given as a function of the wall Mach number. The criteria

$$p_{sep}/p_a = 1/Ma_{sep} \tag{1}$$

reproduces the separation pressure data for wall Mach numbers > 2.5 quite well. This trend gets lost for wall Mach numbers < 2.25. The intermediate range around a wall Mach number of 2.4 (representing low NPR of 5) is unstable.

Figure 3a gives the related pressure coefficients as a function of the Reynolds number after Donaldson [3, 7, 12], who studied supersonic tube flows, where p_2 is the pressure

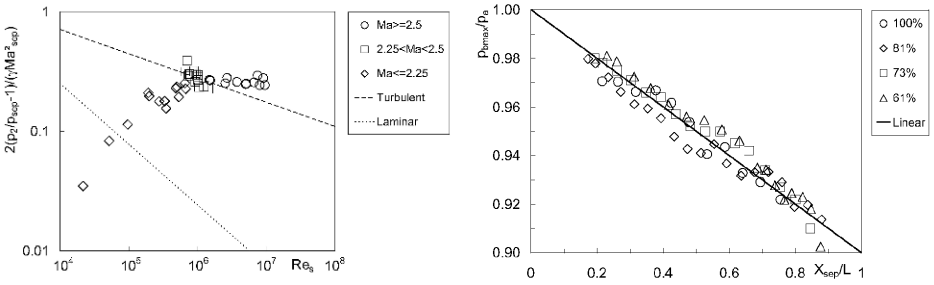

Fig. 3. (**a**) Pressure coefficient and Reynolds number. (**b**) Averaged maximum back pressure

downstream the shock and γ the adiabatic exponent. Only condensation free data were taken into account. Included are critical pressure coefficients for turbulent ($\sim Re_s^{-0.2}$) and laminar ($\sim Re_s^{-0.5}$) separation on flat plates. The squares represent the unstable Mach number region around 2.4. With Reynolds numbers about 10^6, known for laminar-turbulent transition [11], they split up the remaining data in two distinct zones. Separation data for Mach numbers > 2.5 (circles) show a clearly turbulent separation behaviour. The data for Mach numbers < 2.25 (diamonds) a more laminar like. Therefore the separation criteria (1) is valid for turbulent flows.

Figure 3b shows a linear correlation between the maximum pressure inside the separated back flow region p_{bmax}/p_a and the separation location. Compared are results of the several times shortened nozzle (61%, 73% and 81% of initial length). The effective length of the nozzle is hereby negligible and the linear trend of p_{bmax}/p_a converges to 0.9, corresponding with the full flowing nozzle. This is to say: The oblique separation shock re-compresses the flow to $\sim 90\%$ of the ambient pressure and the remaining adaption to ambient conditions takes place over the free jet.

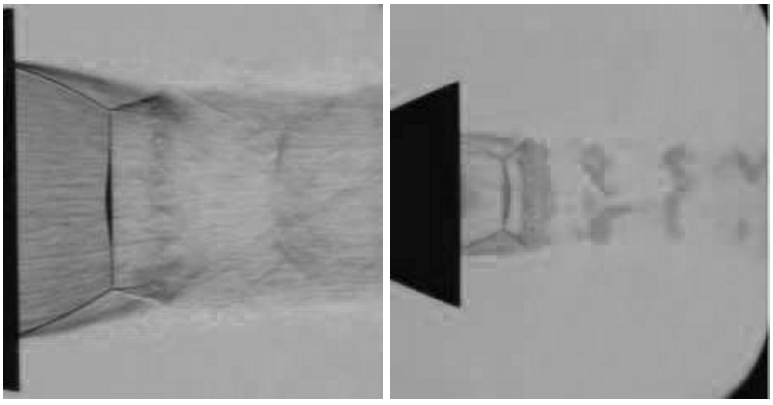

Fig. 4. Schlieren Images (**a**) $L/R^* = 9$; NPR $\simeq 30$; $H_{Mach} = 1.7$ mm. (**b**) $L/R^* = 1.75$; NPR $\simeq 5.5$; $H_{Mach} = 1.8$ mm

In opposite to CFD studies [6,9,10] where clearly bowed concave Mach disks at moderate NPRs were predicted, the Schlieren images only show Mach disks with a slight curvature limited to the centre (Figure 4a). Figure 5a gives the directionless height of the curvature related to the unaffected base as a function of NPR. A maximum is reached for a NPR of 30 to 35. This distribution correlates with the side loads measured for the TIC nozzle of full length by Frey [4] as shown in the graph. A coherence might be given, especially if a vortex is trapped downstream the Mach disk. A second peak is given for NPR below 10. But here the former concave shape turns to a convex one (Figure 4b). Therefore a concave bowed Mach disk at low NPR, as obtained by former CFD studies [6], must be excluded as the origin of a redirected flow towards the wall resulting in side loads.

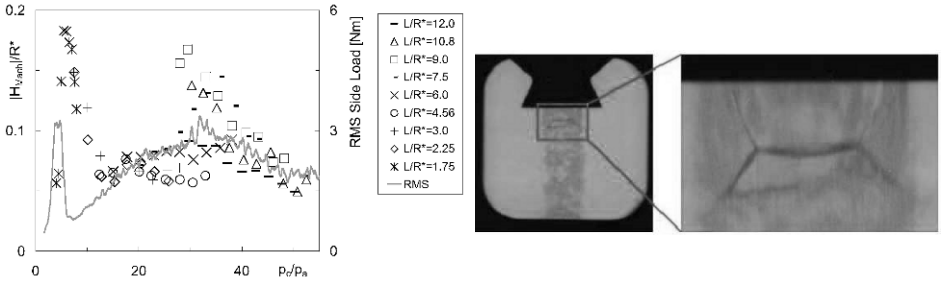

Fig. 5. (**a**) Averaged Mach disk curvature $|H_{Mach}|$. (**b**) Tilted Mach disk; $L/R^* = 1.75$; NPR = 4.93

The pressure coefficients (Figure 3a) show that a re-laminarised boundary layer is present in the nozzle throat. Therefore the separation zone has to pass, during transient start-up and shut-down, through the transition to turbulence again. Its performance changes and the position is abruptly shifted downstream. This process is circumferentially asymmetrical and results in a temporary tilted Mach disk, shown in Figure 5b. In nozzles of full length this tilted Mach disk redirects the flow towards the wall. This is the reason of the partial re-attachment at low NPR causing huge side loads.
This process is locally limited and reversible as the NPR is further increased. It is a close-limited instability in separation behaviour.

4 CFD-Analysis

The Tau-code, developed by DLR [8], was used for accompanying computations. The flow field inside and outside of the nozzle was simulated on axisymmetric hybrid grids. The boundary layer of the adiabatic nozzle wall was resolved by a structured grid consisting out of 30 layers and a y+ value less then 1. The simulated inflow conditions are summarised in Table 1 and they correspond to the experiments shown in Figure 4b. This case was chosen due to the extrem downstream bended Mach disk, the coincidence with the side load peak and former computations of Kwan [6] where a reattached flow

NPR	Simulated gas	T_0 [K]	T_a [K]
5.5	Nitrogen	267	288

Table 1. Boundary conditions for the simulations according to the experiments

could be observed at low NPRs. The boundary conditions are completed with a farfield interpolation based on the ambient conditions during the experiment.

For the given flow conditions the AUSMDV upwind solver with a second order MUSCL gradient reconstruction was applied. The temporal gradients are solved by a three stage Runge-Kutta scheme. Due to the acceptable performance on separated nozzle flows the Spalart Allmaras turbulence model was chosen for the computations.

Residual smoothing was used for a better convergence behavior. The shock pattern and the separated flow at the nozzle wall were achieved on a very coarse grid. Starting from that initial grid and solution, local adaptation was used to refine both the region around the separation point and the Mach disk. The adaptation was successivly continued as described in more detail in Wagner et al. [14]. The development of the wall pressure distribution depending on the grid resolution can be found in Figure 6a starting with the first adapted grid. The results are compared with the measured wall pressures. Due to the minimum of 2.5 mm between the pressure transducers the exact separation position cannot be determined, but the computed pressure distribution compares well with the present experimental values. The dismatch of the first position at $X/R^* = 0.28$ is within the accuracy of the implemented sensor.

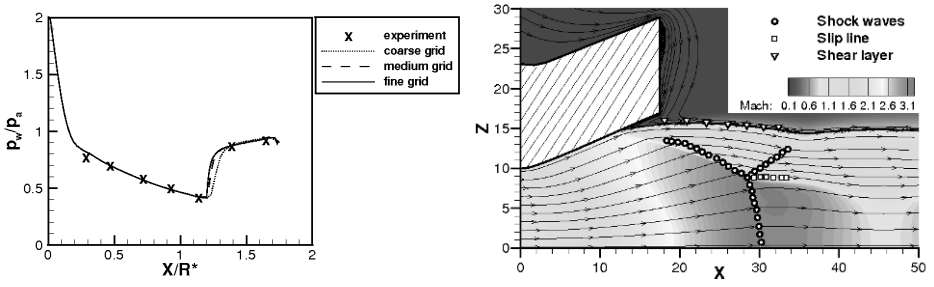

Fig. 6. Numerical Results of the $L/R^* = 1.75$ nozzle (**a**) Pressure distribution. (**b**) Mach number flow field with stream lines compared to experimental data

In Figure 6b the numerical Mach number distribution is overlaid by values taken from the Schlieren image 4b. The shape of the Mach disk and the reflecetd shock are well resolved by the computations. The oblique shock coming from the separation point is more curved in the experiments. Additional to the shock wave position, the trend of both the slip line and the shear layer are extracted from the Schlieren images as far as they were visible and they also compare well with the CFD results.

Both in the experiments and in the computations the Mach disk is bended downstream. The convex shaped Mach disk is the only possability to deflect the divergent flow near the nozzle throat to a parallel flow.

Acknowledgement. The authors would like to thank their colleagues of the 'Flow Separation Control Device' group [5] (CNES, DLR, Astrium ST, ESTEC, ONERA, LEA at Portiers, Snecma, Volvo Aero Corporation) for fruitful scientific exchanges.

References

1. Ciezki H.: Entwicklung eines Farbschlierenverfahrens unter besonderer Berücksichtigung des Einsatzes an einem Stosswellenrohr, Diploma Thesis, Technical University Aachen, 1985
2. Cords P.: A High Resolution, High Sensitivity Colour Schlieren Method, S.P.I.E Journal, Vol. 6, 1968
3. Donaldson C. and Lange R.: Study of the Pressure Rise across Shock Waves Required to Separate Laminar and Turbulent Boundary Layers, NACA RM L52C21, 1952
4. Frey M.: Behandlung von Strömungsproblemen in Raketendüsen bei Überexpansion, Ph. D. Thesis, Universität Stuttgart, 2001
5. Frey M. et al.: Joint European Effort Towards Advanced Rocket Thrust Chamber Technology, 6th International Conference on Launcher Technologies, 2005
6. Kwan W. and Stark R.: Flow Separation Phenomena in Subscale Rocket Nozzles, AIAA Paper 2002-4229, 2002
7. Lawrence R.: Symmetrical and Unsymmetrical Flow Separation in Supersonic Nozzles, NASA CR 92587, 1967
8. Mack A. and Hannemann V.: Validation of the Unstructured DLR-TAU-Code for Hypersonic Flows, AIAA Paper 2002-311, 2002
9. Nasuti F., Onofri M. and Pietropoli E.: Prediction of Shock Generated Vortices in Rocket Nozzles, AIAA Paper 2005-317, 2005
10. Pilinski C. and Nebbache A.: Flow Separation in a Truncated Ideal Contour Nozzle, Journal of Turbulence, Vol. 20, No. 3, 2004
11. Schlichting H.: Grenzschicht-Theorie, 9. Auflage, ISBN 3-540-55744-X, 1997
12. Shapiro A.: The Dynamics and Thermodynamics of Compressible Fluid Flow, Volume 2, ISBN 0-89874-566-7, 1985
13. Stark R. and Wagner B.: Experimental Flow Investigation of a Truncated Ideal Contour Nozzle, AIAA Paper 2006-5208, 2006
14. Wagner B., Karl S. and Hannemann K.: Test Case 1a: Short Nozzle Under Separated Flow Condition Numerical Investigation with the DLR Tau-Code, Proceedings of The FSCD-ATAC Workshop, Noordwijk, 15-16th November, The Netherlands, 2006

Numerical simulation of separated flow in nozzle with slots

I.E. Ivanov[1], **I.A. Kryukov**[2], **and V.V. Semenov**[1]

[1] *Moscow Aviation Institute, Volokolamskoe shosse 4, Moscow, 125993, Russia*
[2] *Institute for Problems in Mechanics, Russian Academy of Sciences, Vernadskii avenue 101-1, Moscow, 119526, Russia*

Summary. A mathematical model and a high-resolution numerical method for numerical simulation of turbulent separated flow in convergent–divergent nozzles are presented. A comparison between numerical calculations and experimental data for plane and axi-symmetric nozzles shows an efficiency and a reasonable accuracy of a numerical code based on the proposed model. A detailed computational study of separated nozzle flows has been conducted for nozzles with one or two circular slots. The possibility for increasing in thrust efficiency is shown under ground conditions due to decreasing of overexpanded flow zone.

1 Introduction

Increase of efficiency of rocket engines due to gas dynamic control of altitude characteristics of a nozzle is considered in this paper.

Improving the power of rocket nozzles is very important to increase the payload of launchers. One of the solutions of this problem which has been obtained consists of increasing the ratio of nozzle areas and controlling the separation flow, in the overexpanded regime, during the first phase of flight. Separation moves the jet detachment point upstream, causing a change in the effective nozzle geometry to one that is shorter and has a lower expansion ratio. For a given nozzle pressure ratio, this alleviates overexpansion and improves thrust efficiency.

Several flow control technologies which have been recently proposed offers further means by which to control and stabilize a separated nozzle flow for performance enhancement. In this paper the control technology by means of creation of one or two circular slots at supersonic part of a nozzle (nozzle with slot) is considered by numerical simulation.

2 Governing Equations

The two-dimensional Favre averaged Navier-Stokes equations, including the equations for the turbulent kinetic energy (TKE) k and the solenoidal dissipation rate ε_s, can be written in the following form

$$\frac{\partial(r\mathbf{Q})}{\partial t} + \frac{\partial(r\mathbf{F})}{\partial x} + \frac{\partial(r\mathbf{G})}{\partial y} = \frac{\partial(r\mathbf{F}_v)}{\partial x} + \frac{\partial(r\mathbf{G}_v)}{\partial y} + r\mathbf{H},$$

where $\mathbf{Q} = (\overline{\rho}, \overline{\rho}\,\widetilde{u}, \overline{\rho}\,\widetilde{v}, \overline{e}, \overline{\rho}\,k, \overline{\rho}\,\varepsilon_s)^T$. The overbar denotes the conventional Reynolds average, while the overtilde is used to denote the Favre mass average. The inviscid fluxes are

$$\mathbf{F} = \begin{pmatrix} \overline{\rho}\,\widetilde{u} \\ \overline{\rho}\,\widetilde{u}^2 + \overline{p} \\ \overline{\rho}\,\widetilde{u}\,\widetilde{v} \\ \widetilde{u}(\overline{e} + \overline{p}) \\ \overline{\rho}\,\widetilde{u}\,k \\ \overline{\rho}\,\widetilde{u}\,\varepsilon_s \end{pmatrix}, \quad \mathbf{G} = \begin{pmatrix} \overline{\rho}\,\widetilde{v} \\ \overline{\rho}\,\widetilde{u}\,\widetilde{v} \\ \overline{\rho}\,\widetilde{v}^2 + \overline{p} \\ \widetilde{v}(\overline{e} + \overline{p}) \\ \overline{\rho}\,\widetilde{v}\,k \\ \overline{\rho}\,\widetilde{v}\,\varepsilon_s \end{pmatrix}.$$

where ρ is the density, u and v are the velocity components, and e is the total energy per unit volume. The fluid pressure is p and the equation of state for the perfect gas is given by

$$\overline{e} = \overline{p} + \frac{1}{2}\,\overline{\rho}\,\widetilde{u}_j\,\widetilde{u}_j + \overline{\rho}\,k,$$

where γ, the specific heat ratio, is taken as 1.4. The viscous fluxes are

$$\mathbf{F}_v = \begin{pmatrix} 0 \\ \sigma_{xx} \\ \sigma_{xy} \\ \widetilde{u}\,\sigma_{xx} + \widetilde{v}\,\sigma_{xy} - q_x \\ \left(\mu + \frac{\mu_t}{\sigma_k}\right)\frac{\partial k}{\partial x} \\ \left(\mu + \frac{\mu_t}{\sigma_\varepsilon}\right)\frac{\partial \varepsilon_s}{\partial x} \end{pmatrix}, \quad \mathbf{G}_v = \begin{pmatrix} 0 \\ \sigma_{xy} \\ \sigma_{yy} \\ \widetilde{u}\,\sigma_{xy} + \widetilde{v}\,\sigma_{yy} - q_y \\ \left(\mu + \frac{\mu_t}{\sigma_k}\right)\frac{\partial k}{\partial y} \\ \left(\mu + \frac{\mu_t}{\sigma_\varepsilon}\right)\frac{\partial \varepsilon_s}{\partial y} \end{pmatrix},$$

and the viscous stress tensor are expressed as

$$\sigma_{ij} = (\mu + \mu_t)\left(2\,\widetilde{S}_{ij} - \frac{2}{3}\frac{\partial\,\widetilde{u}_k}{\partial x_k}\delta_{ij}\right) - \frac{2}{3}\,\overline{\rho}\,k\delta_{ij},$$

where δ_{ij} is the Kronecker delta, S_{ij} is the mean strain rate tensor, μ is the coefficients of molecular viscosity calculated by the Sutherland formula and μ_t is the coefficients of eddy viscosity, respectively. The heat flux is calculated from

$$q_i = -\left(\mu\frac{c_p}{Pr} + \mu_t\frac{c_p}{Pr_t}\right)\frac{\partial\,\widetilde{T}}{\partial x_i},$$

so that the linear gradient hypothesis is used for the turbulent heat flux. c_p is the specific heat at constant pressure, Pr and Pr_t are the laminar and turbulent Prandtl numbers, respectively, and T is the temperature. A constant turbulent Prandtl number is used.

The eddy viscosity μ_t is calculated as

$$\mu_t = c_\mu\,\overline{\rho}\,k^2/\varepsilon_s.$$

The source terms $\mathbf{H}$ can be written as

$$\mathbf{H} = \left(0, 0, \alpha\,\overline{p}\,/r, 0, P_k - \overline{\rho}\,\varepsilon, c_{\varepsilon 1}P_k\frac{\varepsilon_s}{k} - c_{\varepsilon 2}\,\overline{\rho}\,\frac{\varepsilon\varepsilon_s}{k}\right)^T,$$

where P_k is the TKE production, ε is the total dissipation rate of TKE. In the cartesian coordinate system r and α are 1 and 0, respectively, and in the cylindrical coordinate system r and α are y and 1, respectively.

The total dissipation rate is decomposed into the solenoidal dissipation and the dilatation dissipation

$$\varepsilon = \varepsilon_s + \varepsilon_d.$$

In the "standard" $k - \varepsilon$ model [1] constants are

$$c_\mu = 0.09, \quad c_{\varepsilon 1} = 1.44, \quad c_{\varepsilon 2} = 1.92, \quad \sigma_k = 1, \quad \sigma_\varepsilon = 1.3.$$

3 Turbulence modeling

Compressibility and non-equilibrium of turbulence are two important phenomena for turbulence modeling in turbulent flow in rocket engine nozzles. Supersonic flow with large density gradients is realized in diffuser part of nozzle under flight conditions especially when shock waves are generated inside the nozzle. Such situation is typical for separated flow in nozzles.

As follows from DNS data the most important compressibility effect is the dilatation dissipation ε_d. We compared results of numerical simulation of several separated flows in plane and conical nozzles obtained with most dilatation dissipation models described in literature. Overall best results were obtained with models [2] and [3]

$$\varepsilon_d = \left(\alpha_1 \tilde{M}_t^2 + \alpha_2 \tilde{M}_t^4\right) \varepsilon_s, \tag{1}$$

where $\tilde{M}_t = \max(0, M_t - M_{t0})$. Values of constants are $\alpha_1 = 1$, $\alpha_2 = 0$, $M_{t0} = 0$ for the model [2] and $\alpha_1 = 1$, $\alpha_2 = 60$, $M_{t0} = 0.1$ for the model [3].

Due to gas dynamics discontinuities in flow field essentially non-equilibrium regions occurs near discontinuities where the production of TKE is considerable larger than the dissipation. Some non-equilibrium modifications of $k - \varepsilon$ model were studied on basis of numerical simulation of turbulent flows with discontinuities. Special attention was given to compatibility of non-equilibrium modifications with the dilatation dissipation models. We shall describe some studied non-equilibrium modifications of $k - \varepsilon$ model which will be used further.

The renormalization group (RNG) $k - \varepsilon$ model [4] can be considered as the non-equilibrium modification of $k - \varepsilon$ model

$$c_{\varepsilon 1} = 1.42\left(1 - \eta\left(1 - \eta/\eta_0\right)\left(1 + \beta\eta^3\right)\right), \tag{2}$$

where

$$\eta = \sqrt{\lambda / c_\mu}, \quad \eta_0 = 4.38, \quad \beta = 0.012.$$

The ratio of the production of TKE to the dissipation is denoted as $\lambda = P_k / (\overline{\rho}\,\varepsilon)$. The ratio can be considered as the non-equilibrium parameter. Other coefficients of the model are

$$c_{\varepsilon 2} = 1.68, \quad \sigma_k = 0.7179, \quad \sigma_\varepsilon = 0.7179, \quad c_\mu = 0.084.$$

The second non-equilibrium modification is the model [5] which is close to "extended" $k - \varepsilon$ model [6] and is more robust than [6]

$$c_{\varepsilon 1} = 1.44 + 0.3\left(\lambda' - 1\right) / \left(\lambda' + 1\right). \tag{3}$$

The modified non-equilibrium parameter λ' is used in the model which depends on "shear" part of the TKE production

$$P_k' = \mu_t \left(\left(\frac{\partial \widetilde{u}}{\partial y} \right)^2 + \left(\frac{\partial \widetilde{v}}{\partial x} \right)^2 \right).$$

The third modification was proposed in [7] to improve prediction of decaying turbulence at low Reynolds numbers

$$c_{\varepsilon 1} = 1.5, \quad c_{\varepsilon 2} = 1.9\left(1 - 0.11\exp\left(-R_t^2/36\right)\right). \tag{4}$$

4 Numerical method

To solve Navier-Stokes and $k-\varepsilon$ model equations we use a second order of accuracy in time and space Godunov-type method (see [8]). The second order of accuracy is obtained with the application of the MUSCL (monotonic upstream-centered scheme for conservation laws)-Runge-Kutta scheme with essentially two-dimensional reconstruction.

For near wall region the non-equilibrium wall function approach is used. TKE production limiter is used to provide proper dependence of the turbulent energy production term on the mean strain in regions of high velocity gradient.

5 Results and discussion

At first we validated our numerical code by means of comparison of our computed results of separated nozzle flows with experimental results by different authors. The first nozzle is an 11.01° half angle plane convergent–divergent nozzle [9] with a throat width of 27.5 *mm* and an exit width of 42.2 *mm* corresponding to an expansion ratio of 1.797, for a total length of 115.6 *mm*. The inlet temperature is 293°K, the ambient pressure is $p_a = 102387.14$ *Pa*, the ambient temperature is 293°K. The nozzle pressure ratio $n = p_0/p_a$ was varied in the experiment from 1.8 to 8.95.

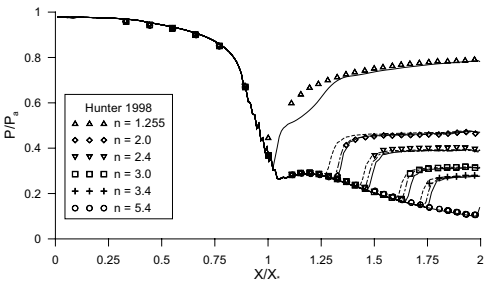

Fig. 1. Wall pressure data for plane nozzle [9]

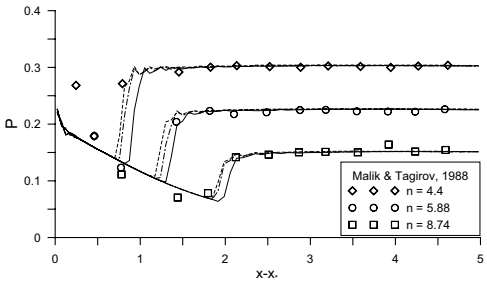

Fig. 2. Wall pressure data for conical nozzle [10]

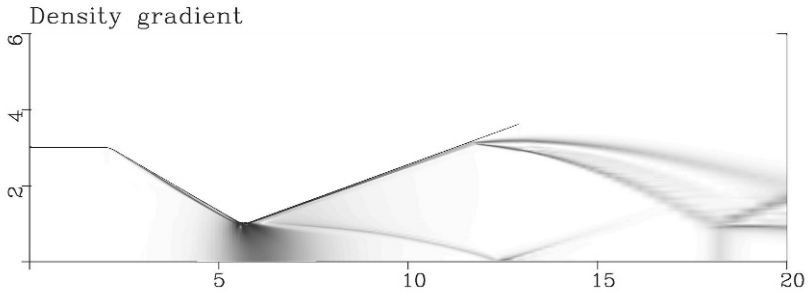

Fig. 3. Numerical Schlieren images of the flow field in the conical nozzle

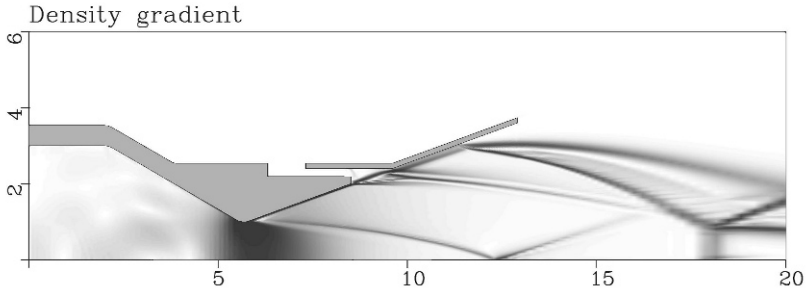

Fig. 4. Numerical Schlieren images of the flow field in the conical nozzle with one slot

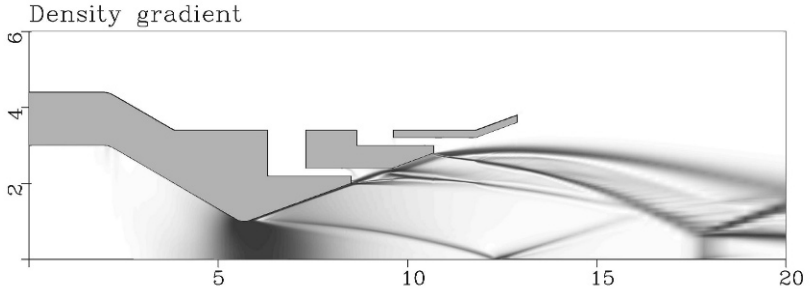

Fig. 5. Numerical Schlieren images of the flow field in the conical nozzle with two slots

Fig. 1 shows computed and measured [9] wall pressure distributions for different nozzle pressure ratios n. The solid, dashed and dash–doted lines correspond to the non-equilibrium modifications (3), (4) and (2), respectively. The dilatation model (1) is used. It can be seen that all three models allow to obtain a separation point position and a recovery pressure level in a recirculation zone after separation point with reasonable accuracy. We might observe in passing that the solution for $n = 1.255$ is unsteady regardless of used model and the shown curve corresponds to arbitrary time.

It is well known that $k - \varepsilon$ model predicts plane flows considerably better than axisymmetric. Therefore the second nozzle used for the validation is an 22.5° half angle conical convergent–divergent nozzle [10] with a throat radius of 5 *mm* and an exit radius of 16 *mm* corresponding to an expansion ratio of 10.24, for a conical part length of 26.52 *mm*. The inlet temperature is 293°K, the inlet pressure is $p_0 = 36$ *atm*, the ambient

temperature is 293°K. Three nozzle pressure ratios n were used in the experiment: 4.4, 5.88 and 8.74.

Fig. 2 shows computed and measured [10] wall pressure distributions for different nozzle pressure ratios n. The solid, dashed and dash–doted lines correspond to the non-equilibrium modifications (3), (4) and (2), respectively. The dilatation model (1) is used. As in the plane case accuracy of separation point and pressure recovery prediction is reasonable. Some discrepancy between measured and computed pressure before separation point can be explained by insufficient nozzle description in [10].

Results of numerical simulation of turbulent nozzle flow are shown on Fig. 3 for a smooth conical nozzle, on Fig. 4 for the same nozzle with one slot, and on Fig. 5 for the same nozzle with two slots. An half-angle of the conical nozzle supersonic part is 20°, a throat diameter is 10 *mm*, a slot width is 1 *mm*. The inlet temperature is 293°K, the ambient pressure is 101250 *Pa*, the ambient temperature is 293°K. The nozzle pressure ratio n is 40. The overexpanded flow regime with separation is realized under such conditions in the smooth nozzle (see Fig. 3). In the nozzle with single slot the separation occurs earlier (for smaller x) than in the smooth nozzle Fig. 4. The overexpanded flow zone decreases providing an increase in static thrust efficiency. In the nozzle with two slots the earliest separation occurs 5 and the overexpanded flow zone is smallest. Further numerical simulation shows that under high–altitude conditions the impulse loss due to a working fluid leakage through the circular slot is small and does not have a pronounced effect on thrust efficiency.

Acknowledgement. The presented research work was supported by the International Science Technical Center (ISTC) within the frames of the ISTC Project 2598.

References

1. Launder B.E., Spalding D.B. : Computer Meth. Appl. Mech. Engn., **3**, 3, 269–289, (1974)
2. Sarkar S., Erlebacher G., Hussaini M.Y., Kreiss H.O. : J. Fluid Mech., **227**, 473–493 (1991)
3. Dash S.M., Kenzakowski D.C., Seiner J.M., Bhat T.R.S. : AIAA Pap., 93–4390, (1993)
4. Yakhot V., Orszag S.A., Thangam S., Gatski T.B., Speziale C.G. : Phys. Fluids A, **4**, 7, 1510–1520, (1992)
5. Chen Y.S. : AIAA Pap., 86–0438, (1986)
6. Chen Y.S., Kim S.W. : NASA Contractor Report, 179204, (1987)
7. Hanjalic K., Launder B.E. : J. Fluid Mech., **52**, 609–638, (1972)
8. Ivanov I.E., Kryukov I.A. : Matematicheskoe modelirovanie RAN, **8**, 6, 47–55, (1996)
9. Hunter C.A. : AIAA Pap., 98-3107, (1998)
10. Malik T.I., Tagirov R.K. : Akademiia Nauk SSSR, Izvestiia, Mekhanika Zhidkosti i Gaza, 6, 60–66, (1988)

Numerical simulation of transient supersonic nozzle flows

A. Hadjadj and Y. Perrot

Institut National des Sciences Appliquées de Rouen, CORIA - Unité Mixte de Recherche C.N.R.S. 6614. Avenue de l'Université, 76801 Saint Etienne du Rouvray, France

Summary. The starting process of supersonic nozzles has been investigated numerically. The objective of this study is to identify the origin of side-loads during start-up and shutdown phases of rocket nozzles. A complex flow structure with significant separated boundary layer and intense moving shocks has been observed. Special attention has been paid to the early phase of the starting process and to the appearance of a strong secondary shock wave due to the change in nozzle area. Shock intensities and velocities are obtained and analysed. The computational results are compared with the experimental data for validation. The flow evolution is proved to be more complex in the presence of turbulence due to a large separation and a strong shock/boundary-layer interaction. In particular, when the recirculation bubble created by the separation shock reaches the nozzle lip, a sudden transition from restricted-shock separation (RRS) to free-shock separation (FSS) patterns is observed. This phenomenon is considered to be one of the basic characteristics of side-loads generation during transient of supersonic nozzles.

1 Introduction

Flow separation control in rocket nozzles is a challenging problem in aerospace science, not only for current engines confronted with problems of thermo-mechanical loads, but also for future engines which could work with very wide separation zones. This phenomenon is related to an usually unstable type of flow occurring in large expansion nozzle and producing unstable forces known as side-loads. Theses forces are prejudicial to the mechanical structure of the nozzle and can cause damages. Basically, the physical

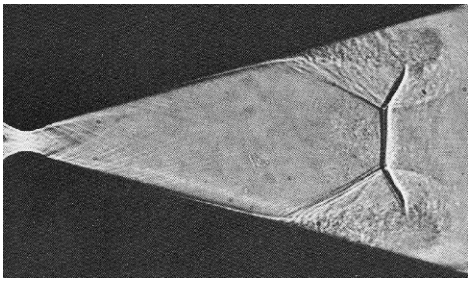

Fig. 1. Starting process in a planar supersonic nozzle [1].

problem met in those configurations is essentially due to the boundary layer separation during nozzle startup process, caused by the ambient high pressure gradient, resulting in a complex phenomenon with shock/shock and shock/boundary layer interactions (see Fig.1). Several complex phenomena, such as boundary layers with adverse pressure

gradients, shocks, induced separation, recirculation bubbles, shear layers can occur in nozzles and may strongly affect the rocket engine's performance.

Transient nozzle flow which exists during engine start-up has been investigated by only a few people. Some experimental work has been performed by Smith [2], Amann [3], Saito *et al.* [4]. Amann [3], for instance, studied the influence of several parameters (nozzle half-angle, throat width and nozzle inlet radius) on the starting process in supersonic nozzles driven by a shock tube. Besides, special interest has been paid to the duration of the starting process, since it decreases the useful testing time of short-duration facilities. However, the evolution of a complex wave structure has also been shown.

From a numerical point of view, some studies were undertaken to simulate nozzle flow transients. Most of the simulations performed were two-dimensional plane or axisymmetric owing to the large amount of computational time required for three-dimensional ones. From previous studies [5,6], it may be concluded from these studies that inviscid computations satisfactorily predict the main flow features (namely the primary and secondary shock waves, multiple shock wave reflections and slip surfaces). Concerning rocket nozzles, Chen and Chakravarty [7] examined the flow structures of the start-up and shut-down processes using a Navier-Stokes solver. The configuration they studied was a sub-scale nozzle of a J-2S rocket engine (i.e. a precursor of the American Space Shuttle main engine). In a recent work, Mouronval *et al.* [8, 9] studied numerically the early transient flow induced in an expanding nozzle by an inflow preceded by an incident planar shock wave using high-order numerical methods. Special attention has been paid to the early phase of the starting process and to the appearance of a strong secondary shock wave. A detailed analysis of the wave structure was given and the mechanism of formation of vortices on the contact surface has been clearly shown as a result of the high accuracy of the simulations.

In this paper, we report recent progress on computations of transient supersonic nozzle flows using both Euler and Navier-Stokes codes. Owing to the large amount of computational time required for a 3D computation, only 2D axisymmetric convergent-divergent nozzles are considered in this study.

2 Inviscid computations

The first part of this paper concerns the transient flow developing in the Vulcain nozzle (designed for the European rocket Ariane V) during the engine start-up. After burning in the combustion chamber, the exhaust gases are expanded in the nozzle to deliver an optimal thrust to the launcher. The starting process begins with the primary shock (blast wave) entering the nozzle and ends when a quasi-steady flow has been achieved. In the simulation, the flow starts at $t = 0$ after the rupture of a diaphragm located at the nozzle inlet that separates two regions of quiescent air. The high-pressure region is at reservoir conditions, pressure P_c=110 bar and temperature T_c=2500 K, whereas the low pressure is at atmospheric conditions, P_a=1 bar and T_a=298 K.

As a first step, viscous effects were neglected during the transient phase in order to focus mainly on the evolution of the rapidly moving shock wave structures which might later interact with viscous effects.

Initially, a strong incident shock moves rapidly through the stagnant low-pressure medium. When the shock enters the divergent part of the nozzle, because the area increases, the flow undergoes an expansion and a contact discontinuity is formed. This

discontinuity quickly becomes distorted owing to a Richtmyer-Meshkov type instability. In addition, a left-running (with respect to the fluid) secondary shock appears and is carried to the right because of the supersonic carrier flow. This shock wave links the high Mach number, low pressure flow, downstream of the throat, with the lower velocity high pressure gas behind the primary shock. The computed flow-field at time $\simeq 2ms$ is shown by schlieren picture (figure 2 - left). The mean flow features (namely the primary and the secondary shock waves, multiple shock wave reflections and slip surfaces) are well reproduced by the simulation. Also figure 2 displays additional details on the multiple wave reflection system (triple points, recompression shocks) formed by the bifurcation of the shocks near the wall as well as the important role played by the internal shock occurring at the nozzle throat.

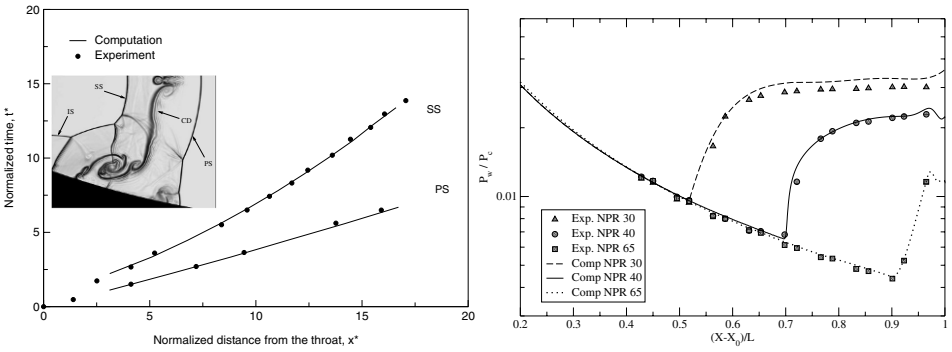

Fig. 2. Comparison of shock-waves trajectories on the axis. All length scales are normalized by the throat height $h_c = 6.15\,mm$ and the elapsed dimensionless time is defined as $t^\star = ta_0/h_c$ where a_0 is the speed of sound of the gas initially at rest ($a_0 \simeq 343\,m.s^{-1}$). The origin of time is chosen in such a way that the primary shock reaches the nozzle throat at $t^\star = 0$ (left). Normalized wall pressure distributions for the TIC nozzle (right).

It should be recalled that the experimental analysis of the transient flow in full scale rocket nozzles is very difficult and expensive, because it would need flow visualizations and measurements inside the divergent section in the few milliseconds of the crucial part of the transient. Therefore, no measurements are available for the Vulcain nozzle.

However, in order to compare our numerical simulations with experiments, we have computed a small scale laboratory nozzle studied experimentally by Amann [3]. The test case consists of a constant-area tube terminated by a 15° plane nozzle whose inlet is rounded. This nozzle is located at the end wall of a shock tube. The general evolution of the wave system in Amman's nozzle is analysed. Good qualitative agreement between numerical and experimental results is obtained (results not shown for concision). Quantitative assessment of the prediction can be achieved by analyzing the movement of the shock fronts. The computed locations of the primary and secondary shocks in the central part of the nozzle are plotted in figure 3 and compared with the experimental results. The agreement is excellent for the primary shock as well as for the secondary one.

3 Turbulent computations

For the second part of this study, we have used a mixed finite-volume / finite element industrial code (N3S-Natur, supported by SNECMA-Motor) based on a multi-dimensional compressible Navier-Stokes solver with an explicit-implicit second order TVD scheme on an unstructured grid. A two-equation $k - \omega$ SST model is used to describe the turbulence. The computations were performed on parallel IBM SP4 machine using $10 \sim 20$ processors.

The test-case considered here is an overexpanded sub-scale rocket-nozzle having a Truncated Ideal Contour (TIC), studied experimentally at ONERA [10]. This nozzle has no internal shock and produces a nearly uniform flow at the exit. For highly overexpanded regimes, *i.e.* when the exit pressure is much lower than the ambient pressure, a separated flow occurs inside the nozzle and evolves as a free jet. An open recirculation zone exists which matches the ambient free-stream to the supersonic carrier flow.

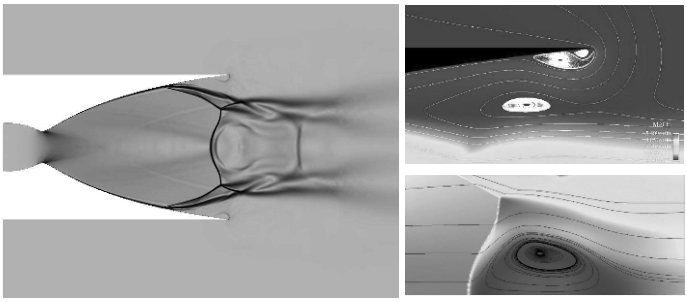

Fig. 3. Steady state solution of the TIC nozzle flowfield at NPR=40. Numerical Schlieren picture (left). Enlargement of the nozzle lip and the Mach disc regions (right).

The computations were carried out using three different Nozzle Pressure Ratios (NPR $= P_c/P_a = 30$, 40 and 65, where P_c and P_a are the chamber and the ambient pressures, respectively). A typical flow separation is shown in Fig. 3. The numerical simulation reveals the existence of a small recirculation bubble trapped between the wall (at the nozzle lip) and the main recirculation zone. It has been shown [11] that this small vortex may play an important role in the amplification of the flow oscillations especially at the end effect regime.

The central part of the jet is characterized by a strong shock waves interaction leading to a curved Mach disc structure with a triple point configuration and a downstream recirculation zone (see Fig. 3 - right). This vortex has been observed in several computations. For instance, Nasuti *et al.* [12] show that the appearance of this vortex is strongly correlated with the upstream non-uniformities of the flow. As expected, in fully expanded steady state flow, no perfect restricted shock separation (RSS) exists in TIC nozzles but an "RSS-like" structure is observed with a cap-shock pattern and a free separation. The corresponding wall pressure distributions are shown in Fig. 2 (right) where the computational results are compared with the experimental data. Excellent agreement is obtained.

To complete this study a transient flow simulation at a very low regime (NPR=5) is investigated. The objective of such investigation is to understand the origin of side-

loads amplification observed during transients in the experiment of a TIC nozzle done by Kwan and Stark [13]. Fig. 4 shows a sequence of numerical pictures, where it is possible to identify different flow structures. In particular, the formation of the secondary shock is clearly visible at the early stage of the start-up process. This strong shock interacts with the boundary layer and large separation occurs. Since the jet plume is not sufficiently formed, the supersonic flow reattached further downstream, leading to a formation of a high-pressure region with a recirculation bubble. A restricted-shock separation (RSS) configuration is then formed, while the major structures of the internal jet remained similar during the transient process. The separated-reattached flow structure moves downstream and gradually discharges from the nozzle exit until a sudden transition from restricted-shock separation (RSS) to free-shock separation (FSS) configuration appears. During a very short time, a high pressure peak was found. The occurrence of the side-loads has been reported when the transition from FSS to RSS occurred during the start-up transient of TOC (Thrust Optimized Contour) nozzles [14], however this phenomenon still yet to be understood in TIC nozzles.

References

1. Van Dyke M., An Album of Fluid Motion, The Parabolic Press, Stanford, California, 1982
2. Smith C. E., The starting process in a hypersonic nozzle, J. Fluid Mechanics, Vol. 24, pp. 625-640, 1966
3. Amann H. O., Experimental study of the starting process in a reflection nozzle, Phys. Fluids, Vol. 12, pp. 150-153, 1967
4. Saito T., Timofeev E. V., Sun M. and Takayama K., Numerical and experimental study of 2-D nozzle starting process, In the proceedings of the 22nd ISSW, paper No. 4090 Imperial College, London, UK, July 18-23, 1999
5. Prodromou P. and Hillier R., Computation of unsteady nozzle flows, In the proceedings of the 18th ISSW, Sendai, Japan, Vol. II, pp. 1113-1118, 1992
6. Igra O., Wang L., Falcovitz J., Amann O., Simulation of the starting flow in a wedge-like nozzle, Int. J. Shock Waves, Vol. 8, pp. 235-242, 1998
7. Chen C. L., Chakravarty S. L. and Hung C. M., Numerical Investigation of Separated Nozzle Flows, AIAA J., Vol. 32, pp. 1836-1843, 1994.
8. Mouronval A.-S., Hadjadj A., Kudryavtsev A. and Vandromme D., Numerical investigation of transient nozzle flow, Int. J. Shock Waves, Vol. 12, pp. 403-411, 2003
9. Mouronval A.-S. and Hadjadj A., Numerical study of the starting process in a supersonic nozzle, J. Propulsion & Power, Vol. 21, pp. 374-378, 2005
10. Reijasse Ph., Morzenski L., Blacodon D. and Birkemeyer J., Flow separation experimental analysis in overexpanded subscale rocket-nozzles, 37th AIAA/ASME/SEA/ASEE Joint Propulsion Conference and Exhibit, AIAA-Paper 2001-3556, 2001
11. Alziary de Roquefort T., Unsteadiness and side-loads in over-expanded supersonic nozzles, Proc. of the 4th European Symposium on Aerothermodynamics for Space Vehicles, Capua, Italy, 15-18 October 2001
12. Nasuti F., Onofri M., and Pietropaoli E., The influence of nozzle shape on the shock structure in separated flows, Proc. of the 5^{th} European Symposium on Aerothermodynamics of Space Vehicles, ESA-ESTEC, 353-358, DLR, Kőln, Germany, November 8-11, 2004
13. Kwan W. and Stark R., Flow separation phenomena in subscale rocket nozzles, 38th AIAA/ASME/SEA/ASEE Joint Propulsion Conference & Exhibit, AIAA paper 2002-4229, 2002
14. Ostlund J., Damgaard T. and Frey M., Side-load phenomena in highly overexpanded rocket nozzles, Journal of Propulsion and Power, Vol. 20, No.4, 2004

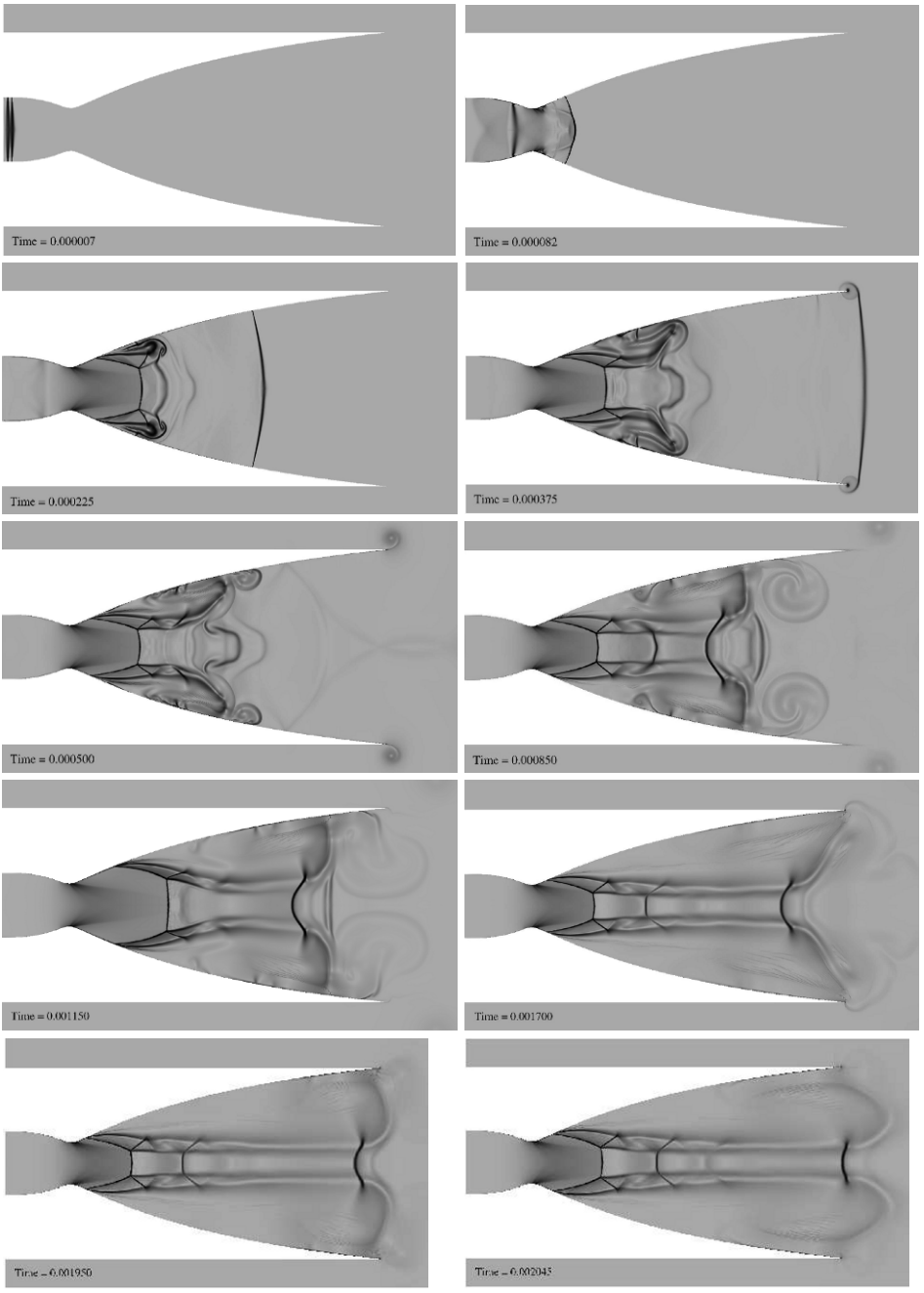

Fig. 4. Formation of shock waves, contact discontinuities and boundary layer separation during the start-up of a Truncated Ideal Contoured (TIC) nozzle (numerical schlieren pictures). TIC nozzle at NPR=10.

Numerical studies of shock vector control for deflecting nozzle exhaust flows

T. Saito and T. Fujimoto

Dept. Mechanical Systems Eng., Muroran Institute of Technology,
27-1 Mizumoto-cho, Muroran, 050-8585 Japan

Summary. Numerical investigations of fluidic thrust vectoring system using secondary jet injected into the main nozzle flow are carried out. Two dimensional Navier-Stokes equations with Spalart-Allmaras turbulence model are used and the numerical results are compared with experimental data obtained by Waithe et al. It is demonstrated that usage of an appropriate turbulence model is essential for studying details of fluidic thrust vectoring system as well as general supersonic nozzle flows.

1 Introduction

Supersonic nozzle flows have been extensively investigated, especially in aerospace and industrial fields for many years. Quasi-one-dimensional theory gives simple and clear solutions of the problem. The actual flows, however, involve complex interactions between shock waves and boundary layers, showing structures sometime quite different from those predicted by the simple theory. Numerical simulations of nozzle flow require great care in preparing proper numerical grids and in choosing appropriate physical and mathematical models for obtaining reasonable solutions. For example, it is not an easy task to simulate non-stationary nozzle starting process even in a very simple two dimensional nozzle [6]. It is found that boundary layer separation on the nozzle side walls plays an important role and must be properly simulated. It then indicated that an appropriate turbulence model is required in order to predict correct boundary layer separation point.

A two dimensional numerical code is developed and tested for its applications to supersonic nozzle flows. After preliminary testing, the numerical code is applied to the experimental work of fluidic thrust vectoring reported by Waithe and Deere [10]. Fluidic thrust vectoring (FTV) is a technique to vary the thrust orientation of nozzle exhaust without resorting to mechanically moving parts and several different methods are proposed [5]. In this paper, we will investigate the so-called shock-vector-type FTV, in that a secondary jet is injected into the supersonic main flow from the nozzle side wall. The main challenges for developing FTV are to find efficient configurations and to achieve linear response. Numerical results are compared with Weithe's data and discussed.

2 Basic equations and numerical methods

Two dimensional Navier-Stokes equations and the conservation laws of mass and energy are numerically integrated [1]. The equation of state for ideal gases is used for closing the system of equations. The numerical scheme WAF (Weighted Average Flux method) developed by Toro [8] is used to solve the convection (or inviscid) part of the basic equations. The scheme is one of higher order extensions of the Godunov scheme and has

the second order accuracies both in space and time. The numerical flux is evaluated from the HLLC approximate Riemann solver [9]. The viscous terms are calculated by using either central differencing or least square method to evaluate the first and second order velocity gradients.

Three turbulence models of Baldwin-Lomax, k-ϵ and Spalart-Allmaras [2, 3, 7] are implemented. Each turbulence model has its own advantages and disadvantages. In this study, since it has successfully been applied to many supersonic flows with boundary layer separations and vortices, Spalart-Allmaras turbulence model is extensively used. The turbulence model is implemented based on Wang [11] with modifications presented by Lei [4]. The modification of Lei increased the robustness of the computations by suppressing the eddy viscosity to an appropriate amount.

3 Numerical grids and code evaluation

Computations of boundary layer developed on a flat plate are carried out as code validation. The results also provide information regarding the necessary space resolution of numerical grids. A flat plate is placed at the bottom of computational domain. Initial conditions of the pressure, density and flow velocity parallel to the plate are 1.013×10^5 Pa, 1.225 kg/m^3 and 500 m/s, respectively. Computations with four numerical grids with

Table 1. Space resolutions of numerical grids next to flat plate

Grid	Δy_{wall} (μm)	y^+
Grid 1	2.0	0.84
Grid 2	3.0	1.25
Grid 3	4.0	1.67
Grid 4	5.0	1.84

different space resolutions are carried out in order to determine appropriate grid size next to the solid plate. The grid sizes of the four different grid types next to the plate surface are listed in Tab. 1. The y^+ values of the first grid point, which is defined by the friction velocity u_* and the kinetic viscosity ν as $y^+ = (yu_*)/\nu$, are also shown in the table. Figure 1 shows profiles of x-component velocity at a down stream location from the leading edge of the plate. The Reynolds number of the location is defined by the distance from the leading edge and is calculated to be 3.5×10^6. This is sufficiently higher than the critical Reynolds number and the boundary layer is expected to be turbulent. Following the convention of boundary layer studies, the velocity in the ordinate is normalized by the friction velocity and y^+ is taken as the abscissa. The solution of the law of the wall that consists of viscous sublayer and the inner layer is also shown in the figure by a solid line. The following formulae for the velocity distribution in the viscous sublayer and the log law are used:

$$\frac{u}{u_*} = y^+ \,, \tag{1}$$

$$\frac{u}{u_*} = 5.6 \log y^+ + 4.9 \,. \tag{2}$$

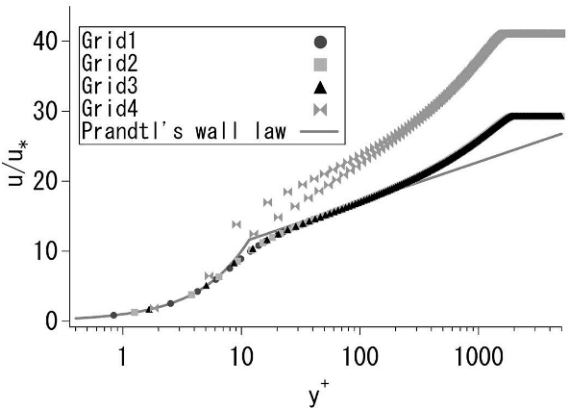

Fig. 1. Velocity distribution of boundary layer on flat plate with Spalart-Allmaras turbulence model

It is found that the numerical code provides solutions that agree well with the law of the wall with all numerical grids except Grid 4. In the outer layer ($y^+ > 500$), the numerical results deviate from the solid line as they should. Although the results from Grid 1 to Grid 3 overlap each other, the solution obtained with Grid 4 deviates significantly from others and oscillates. Grid 4 has the minimum space at the wall Δy_{wall} of 5.0 μm and the value of y^+ is 1.84, which is still well within the viscous sublayer. From these observations in the preliminary computations, we determined that the grid size must be less than 4.0 μm in order to carry out computations with the Spalart Allmaras turbulence model in the current numerical code. Similar tests are also carried out with the k-ϵ turbulence model for the sake of comparison. It is found that the k-ϵ model requires 3.0 μm as the minimum grid size. Although it is not a significant difference, this indicates that the Spalart Allmaras model is more stable than the k-ϵ model.

4 Computations of FTV performance

The specifications of the nozzle are listed in Tab. 2. The secondary jet is injected through 2.03×10^{-3} m wide narrow slit open to the upper nozzle wall. The number of numerical

Table 2. Nozzle specifications from Waithe [10]

Throat area (cm^2)	Exit area (cm^2)	Area ratio	Design pressure ratio	Design Mach number
27.92	50.16	1.85	8.78	2.07

grid points is about 720,000 and the code is executed in parallel with multiple processor elements (PEs) of the Cray XD1 computer system. The MPI parallel libraries are used and the typical wall clock time is about 20 hours using 10 PEs. Comparisons are made on two FTV parameters, (1) the thrust ratio TR and (2) the thrust vector pitch angle

δ_p. The thrust ratio TR is defined as the ratio of the numerically obtained thrust $\mathbf{F}$ and the primary flow isentropic thrust F_i, i.e. $TR = |\mathbf{F}|/F_i$. The numerical thrust vector $\mathbf{F}$ is derived from the formula:

$$\mathbf{F} = \sum [\rho \mathbf{U}(\mathbf{U} \cdot \mathbf{n}) + (p_s - p_\infty)\mathbf{n}] \Delta A, \tag{3}$$

here the summation is taken over the numerical cells at the nozzle exit plane. The symbols $\mathbf{U}$, $\mathbf{n}$, ΔA, p_s, p_∞ are the velocity vector, unit vector in the x direction, projection of each numerical cell area in the x direction, static pressure and ambient pressure, respectively. While the following analytic formula is used for evaluating the ideal thrust:

$$F_i = \sqrt{\frac{2\gamma R}{\gamma - 1}} w_i \sqrt{T_t \left[1 - \left(\frac{p_\infty}{p_t} \right)^{\frac{\gamma - 1}{\gamma}} \right]}, \tag{4}$$

where p_t, T_t, γ and R are the total pressure and temperature, specific heat ratio and the gas constant, resptectively. The mass flow rate w_i is calculated as:

$$w_i = \sqrt{\frac{\gamma}{R}} \left(\frac{2}{\gamma + 1} \right)^{\frac{\gamma + 1}{2(\gamma - 1)}} A_t \frac{p_t}{\sqrt{T_t}}, \tag{5}$$

where A_t is the nozzle throat area. The pitch thrust vector angle δ_p is defined by the x and y components of $\mathbf{F}(F_x,\ F_y)$ as:

$$\delta_p = -\frac{180}{\pi} tan^{-1} \frac{F_y}{F_x}. \tag{6}$$

5 Numerical results and discussion

Table 3. Specifications of secondary jet for three series of computations

	Flow Mach No.	NPR	Pressure [Pa]	Density [kg/m^3]
Case 1	1.0	3.2	2.02×10^5	2.33
		4.4	2.70×10^5	3.11
		5.9	3.56×10^5	4.16
Case 2	0.5	3.2	2.68×10^5	4.66
		4.4	3.57×10^5	6.21
		5.9	4.73×10^5	8.33
Case 3	0.3	3.2	2.94×10^5	7.76
		4.4	3.92×10^5	10.4
		5.9	5.20×10^5	13.9

Numerical calculations of FTV performance with the secondary jet injection are carried out. The aerodynamic conditions of the secondary jet are determined from the experimental conditions: (1) the total pressure of the secondary jet is the same as that of main nozzle flow, (2) the mass flow rate of the secondary jet is 6% of that of main exhausting flow [10]. With the conditions and the known jet slit width, three sets of gasdynamic parameters for the secondary jet are determined for simulations and listed in Tab. 3.

A typical temporal flow field of Case 1 with Spalart Allmaras turbulent model is shown in Fig. 2. When the turbulence model is included, the flow field becomes smooth and stable due to the eddy viscosity. As expected, the boundary layer separation delays with the turbulence model and the separation point is shifted to the down stream directions. Thrust vector pitch angles and the thrust ratios of Case 1, 2 and 3 are plotted in Fig. 3. It is shown that the dependency on the nozzle pressure ratio NPR is well reproduced in all series of Cases 1 to 3. The thrust vector pitch angle becomes smaller with increasing NPR while the thrust ratio increases with NPR. The results of Case 3 best agree with the experimental data. Although we could not figure out what are the exact experimental conditions of the secondary jet from the published reference paper, it is reasonable to say that the secondary jet in the experiments had conditions close to Case 3. It is also found out that the thrust vector pitch angel δ_p is almost linear with the secondary jet Mach number. It is expected that, with the current nozzle configuration, the maximum pitch angle of 15 degrees can be obtained if the secondary jet is in the conditions of Case 1, i.e. choked flow.

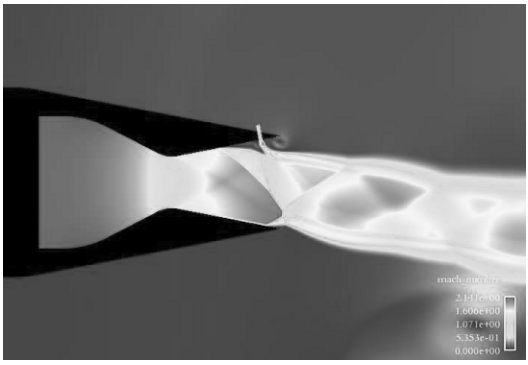

Fig. 2. Flow field with secondary jet with Spalart Allmaras turbulence model: Case 1 with NPR=4.4

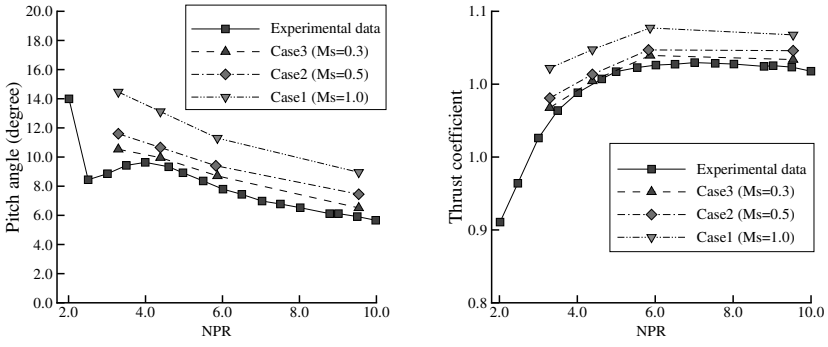

Fig. 3. FTV performance fir Case 1 with NPR=4.4: pitch angle (left); Thrust ratio TR (right)

6 Summary

Numerical code is developed for investigating nozzle flows and applied to simulate FTV operations. The numerical code is based on Navier-Stokes equations with three different turbulence models of Baldwin-Lomax, k-ϵ, and Spalart Allmaras.

Within the range of parameters used in this study, the thrust vector pitch angel is almost linear with the secondary jet velocity. Although the number of simulations is limited in the current study, it is well demonstrated that the numerical method such as the one presented in this paper is useful to establish database for designing and developing the practical hydrodynamic devices such as FTV.

Conducting both experimental and numerical investigations is preferable since any details of them are available for evaluations of numerical code. Details of experiments are also important for tuning a code with turbulence model. We are preparing experimental investigations so that the experimental data can be used for studies of supersonic nozzle flows.

References

1. Anderson, D.A., Tannehill, J.C., Pletcher, R.H.: Computational Fluid Mechanics and Heat Transfer. Hemisphere publishing Corp., New York (1984)
2. Baldwin, B., Lomax, H.: Thin-layer approximation and algebraic model for separated turbulent flows. The 16th AIAA Aerospace Sciences Meeting, Jan. 16-18, Huntsville, Ala., 9p (1978)
3. Jones, W.P., Launder, B.E.: The Prediction of Laminarization with a Two-Equation Model of Turbulence. Int.J.Heat Mass Transfer, **15**, 301–314 (1972)
4. Lei, Z.: Effect of RANS Turbulence Models on Computation of Vortical Flow over Wing-Body Configuration. Trans. Japan Soc. Aero. Space Sci., **48**(161), 152–160 (2005)
5. Mason, M.S., Crowther, W.J.: Fluidic thrust vectoring of low observable aircraft. CEAS Aerospace Aerodynamic Research Conference, 10-12 June 2002, Cambridge UK, 1–7 (2002)
6. Saito, T., Takayama K.: Numerical simulation of nozzle starting process. Shock Waves **9**, 73–79 (1999)
7. Spalart, P.R., Allmaras, S.R.: A One-Equation Turbulence Model for Aerodynamic Flows. The 30th AIAA Aerospace Sciences Meeting, Jan. 6-9, Reno, NV., 22p (1992)
8. Toro, E.F.: A weighted average flux method for hyperbolic conservation laws. Proc. Roy. Soc. london A **423**, 401–418 (1989)
9. Toro, E.F.: Riemann solvers and numerical methods for fluid dynamics. Springer-Verlag Berlin Heidelberg, (1997)
10. Waithe, K.A., Deere, K.A.: Experimental and computational investigation of multiple injection ports in a convergent-divergent nozzle for fluidic thrust vectoring. The 21st AIAA Applied Aerodynamics Conference, June 23-26, Orlando Florida, AIAA-2003-3802, 1–14 (2003)
11. Wang, C.R.: Navier-Stokes Computations With One-Equation Turbulence Model for Flows along Concave Wall Surfaces. NASA/TM-2005-213830 (2005)

Rectangular underexpanded gas jets: Effect of pressure ratio, aspect ratio and Mach number

N. Menon and B.W. Skews

School of Mechanical Engineering, University of the Witwatersrand, Johannesburg, Private Bag 3, WITS - 2050, South Africa

Summary. A numerical and experimental study of the influence of pressure ratio, aspect ratio and Mach number on the underxpanded jet flow from a rectangular nozzle has been carried out. The shock cell length non dimensionalised by the nozzle width has seen to be reducing in magnitude in a linear manner with increasing aspect ratio. The non-dimensionalised Mach stem height increases for small pressure ratios and reduces for larger pressure ratios

1 Introduction

There is limited literature on the detailed structure of the wave system in the near field of an underexpanded rectangular jet. Raman [1] and Alkislar [2] have investigated the shock structure toward developing an understanding of the screech tones emanating from the interaction of the compression waves within the underexpanded jet with the free jet shear layer. Zaman [3] showed that the spreading characteristics of asymmetric jets were not significantly different to that of axisymmetric jets, especially in the cases where the nozzle aspect ratio was close to unity. Mohamed et al., [4] performed an experimental investigation on supersonic jets from rectangular nozzles of aspect ratio 5:1, and characterised the flow regimes and the shock structure for jets in a quiescent atmosphere. Gutmark et al., [5] investigated the spreading characteristics and the flapping modes associated with rectangular underexpanded jets issuing from a nozzle of aspect ratio 3:1 between Mach numbers of 1 and 2.4. A significant variation of the supersonic underexpanded jet was observed from near sonic velocity to higher Mach numbers. Teshima [6] performed experiments on underexpanded air jets exhausting into ambient conditions from rectangular orifices having aspect ratios of 2, 3, 4, 5 and 62 at pressure ratios of up to 500. The jet structure was visualised by using the laser induced florescence method. A hysteresis of shock reflection was observed and reported on. Loh et al., [7] performed computational studies of an underexpanded rectangular jet utilising an unstructured space marching Euler method and was able to obtain reasonable agreement with the experimental findings by Raman [1]. A detailed computational study on the structure of an underexpanded jet from a rectangular nozzle was performed by Rao and Abdol-Hamid [8]. Menon and Skews [9] using the Laser Vapour Screen (LVS) flow visualisation technique were able to capture 'slices' of the flowfield of an underexpanded jet issuing from a square nozzle. They were able to establish that the jet appeared to be behaving as an over expanded jet along the diagonal plane. The origin of the incident shock wave along the central planes of the jet was observed to occur a distance downstream of the nozzle exit. Along the diagonal plane of the nozzle the incident shock wave originated from the corners of the nozzle exit. Numerical studies on underexpanded jet issuing from square and rectangular nozzles (Aspect ratio of 2) showed that the the flow field could be predicted accurately [10].

2 Experimental set-up

The experimental set-up consists of a settling chamber (internal diameter of 120mm) that is supplied with high pressure gas at 15bar from a reciprocating compressor. A sonic nozzle having a square exit profile (10mm x 10mm) is attached to the end of the settling chamber. The flow through the nozzle and settling chamber arrangement is controlled by a throttling valve upstream of the settling chamber. The valve allows for the pressure in the settling chamber to be regulated, and this allows for the underexpansion ratio of the jet to be set as desired. Flow visualisation is achieved through a shadowgraph set up with the image of the flow field being captured onto ISO 400 black and white film.

3 Numerical set-up

The numerical simulation of the underexpanded jet impingement flow was carried out using the commercially available code Fluent 6. The flow was modeled as a viscous flow, with the one equation Spallart-Allmaras turbulence model for closure of the Reynolds Averaged Navier-Stokes equations. The simulation was performed as a steady state solution and convergence was monitored by the log of the residuals of the equations and using a mass flux balance across the inlet and the outlet boundaries of the model.

4 Results and Discussion

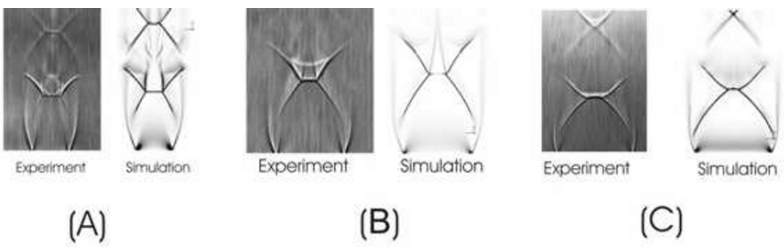

Fig. 1. Experimental shadowgraph and numerical Schlieren images of the flow field on the major axis of an underexpanded jet issuing from a rectangular sonic nozzle at PR = 3; (A) Square nozzle (B) AR = 2 (C) AR = 4

Experimental comparison of the flow fields were obtained for the jet flows issuing from sonic nozzles from various aspect ratio rectangular nozzles. The simulated flow field closely resembles the experimentally observed flow field as can be seen in figure 2. The shock cell length and the height of the Mach stem; non-dimensionalsed with the length of the major axis; have been plotted in figures 2 and 3. There is a steady decrease in the non-dimensional shock cell length for pressure ratios of 2 and 3 as the aspect ratio of the nozzle is increased. The simulation consistently over predicts the non-dimensional length of the shock cell as can be seen in figure 2.

The non-dimensional shock cell length follows a linearly decreasing trend as the aspect ratio of the nozzle is increased (see figure 2). The non-dimensionalised Mach stem height does not follow the same trend as the shock cell length depicted in figure 2. The non-dimensional Mach stem height increases with increasing aspect ratio for the lower pressure ratio of 2, while decreasing with increasing aspect ratio for the higher pressure ratio of 3. For the non-dimensional Mach stem heights the simulation under predicts for the case of the lower pressure ratio, while over predicting for the larger pressure ratio.

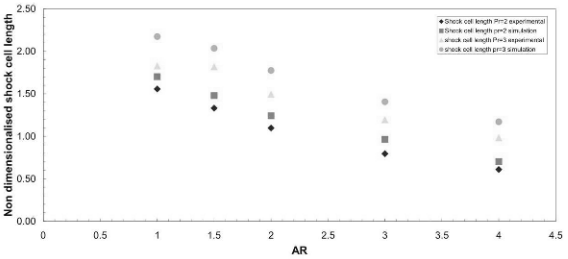

Fig. 2. Non-dimensionalised shock cell length along the major axis of the jet flow

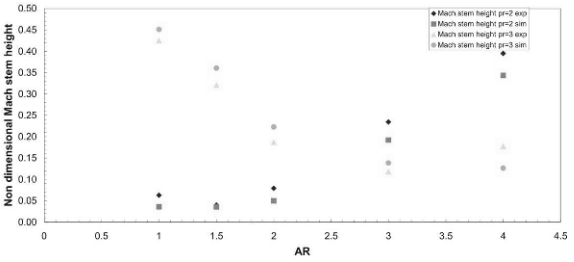

Fig. 3. Non-dimensionalised Mach stem heights on the major axis plane of the jet flow

4.1 General description of the flow field

The flow field of a gas jet issuing from a rectangular nozzle is greatly influenced by the presence of the sharp nozzle corners. Along the major and minor axis of the nozzle the characteristic pattern of expansion wave formation at the nozzle exit followed by the reflection of the expansion fan at the jet boundary as a compression wave can be clearly seen. The compression wave forms into a shockwave that undergoes a regular or Mach reflection based on the underexpansion of the jet.

Along the diagonal of the jet the shock structure is markedly different with the shock wave originating at the nozzle exit, unlike the case along the major and minor axis

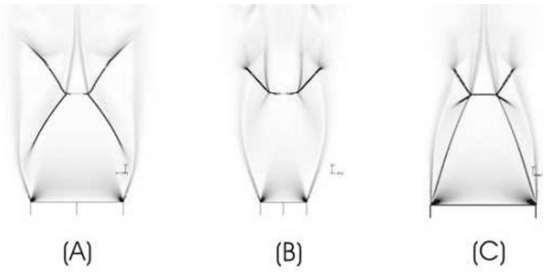

Fig. 4. Flow field along the (A)Major axis (B)Minor axis and (C)Diagonal axis of a rectangular nozzle having an AR = 2

where the incident shock wave originates as the compression waves reflected from the jet boundary, coalesce. The reason for the formation of the shock at the corner of the nozzle can be explained through the cross-sectional slices of the flow field shown in figure 5. The expansion fans originating from the four sides of the nozzle exit lower the pressure of the gas to ambient pressure and cross at the corners of the nozzle, resulting resulting in a pressure drop over the jet boundary lower than the ambient pressure. A shock hence develops at the corner migrating inwards with the expansion fan (as can be seen in the cross- sectional slices in Fig. 5) to equalize the pressure between the ambient medium and the flow within the jet.

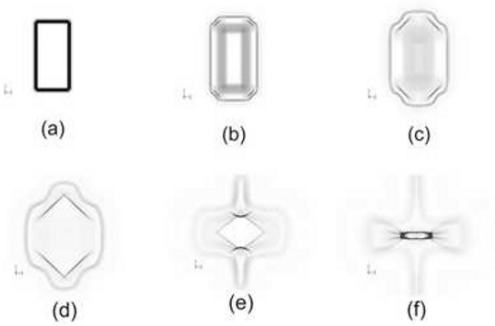

Fig. 5. Cross-sectional slices of the flow field of an underexpanded jet (M = 2, AR = 2, PR = 3) (a)1mm (b)5mm (c)10mm (d)20mm (e)40mm (f)50mm from the exit plane of the nozzle

There is also a marked effect on the shape of the jet boundary as a result of the corners in the nozzle exit. The formation of the incident shock at the corners results in the jet boundary being drawn inwards to the centreline of the jet as the cross sectional slices downstream of the nozzle exit are examined in figure 5. This is consistent with the hypothetical three-dimensional model of the flow field that was developed by Menon and Skews [9].

4.2 Effect of Pressure Ratio

The pressure at the exit plane of the nozzle is greater than the ambient pressure. This results in the jet expanding out of the nozzle. The greater the ratio between the exit plane pressure of the nozzle and the ambient pressure, the greater the expansion of the jet. Increasing the pressure ratio results in transition from regular to Mach reflection for a given exit Mach number and nozzle aspect ratio. The phenomenon is reflected in figure 6 where as the pressure ratio of the jet is increased the transition from regular to Mach reflection occurs.

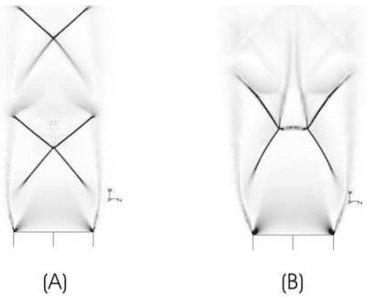

Fig. 6. Flow field along the major axis of a jet issuing from an AR = 1.5 nozzle, M = 1 (A)PR = 2 and (B)PR = 3

4.3 Effect of Aspect Ratio

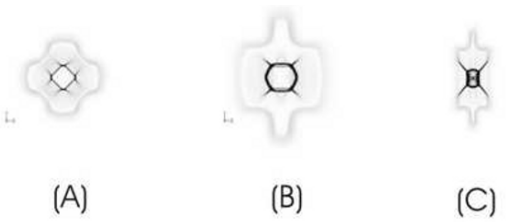

Fig. 7. Crosssectional shapes of the Mach reflection as seen along the axis of the jet M = 1, PR = 3 (A) AR = 1 (B)AR = 2 (C)AR = 4

The effect of the increasing aspect ratio is shown in figure 7 It can be seen that the effect of increasing the aspect ratio on the jet caused a greater distortion of the jet boundary. The Mach stem for a square nozzle has an octagonal shape, while the Mach stem for an underexpanded jet from a nozzle of AR = 2, has a hexagonal shape; the increasing Mach number seemingly working to decrease the facets on the Mach stem. As the aspect ratio is further increased the Mach reflection becomes less complex, appearing to have four sides and aligned to the nozzle exit.

4.4 Effect of Mach number

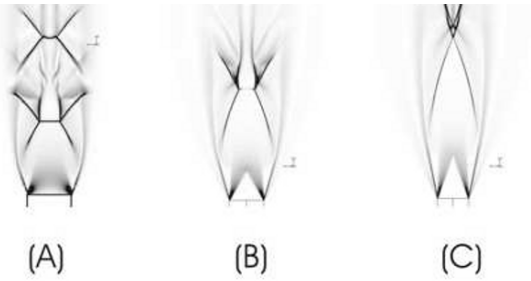

Fig. 8. Flow field along the major axis of a jet issuing from a square nozzle, PR = 3 (A)M = 1 (B)M = 2 (C)M = 3

Increasing the Mach number causes the shock cell length to increase. The Mach reflection is reduced to a regular reflection at a Mach number of 3 for the case of the square nozzle as can be seen in figure 8. A complex system of compression waves can be seen behind the reflection point of figure 8(B) and (C). This phenomenon is being investigated further.

5 Conclusions

A numerical and experimental study of the influence of pressure ratio, aspect ratio and Mach number on the underxpanded jet flow from a rectangular nozzle has been carried out. The results have shown good agreement between the numerical predictions and the experimental observations.

References

1. Raman G.: Journal of Fluid Mechanics **330**, pp. 141 - 168 (1997)
2. Alkislar, M. B., Krothapalli A., and Lourenco L. M.: Journal of Fluid Mechanics **489**, pp. 121 - 154 (2003)
3. Zaman K. M. B. Q.: Journal of Fluid Mechanics **383**, pp. 197 - 228 (1999)
4. Mohamed A., Hamed A., and Lehnig T.: Supersonic rectangular over-expanded jets and two phase flows. In: *Proceedings of the 19^{th} ISABE* (2003)
5. Gutmark E., Schadow K. C., and Bicker C. J.: AIAA Journal **28**, 7 (1990)
6. Teshima K.: Progress in Astronautics and Aeronautics **158** pp. 375 - 380 (1994)
7. Loh C. Y., Himansu A., Wang X. Y., and Jorgenson P. C. E.: *Computation of an underexpanded 3-d rectangular jet by the CE/SE method*, NASA TM 2000-210594 (2000)
8. Rao S. P., and Abdol-Hamid K. S.: *Numerical simulation of jet aerodynamics using the three-dimensional Navier-Stokes code PAB3D*, NASA Technical Paper 3596 (1996)
9. Menon N., and Skews B. W.: In *Proceedings of the 23^{rd} ISSW* (2001)
10. Menon N., and Skews B. W.: In, *Proceedings of the 24^{th} ISSW* (2003)

Part XIV

Numerical Methods

A cartesian grid finite-volume method for the simulation of gasdynamic flows about geometrically complex objects

A. Klomfass

Fraunhofer Ernst-Mach-Institut, Eckerstr.4, 79104 Freiburg, Germany

1 Introduction

The most frequently used concept for the treatment of complex geometries in computational fluid dynamics are certainly unstructured body-fitted grids. An important alternative to unstructured grids are Cartesian grids into which geometrical objects are embedded, especially if compressible inviscid flows are concerned. Methods based on Cartesian grids are computationally efficient, relatively easy to implement and favorable for automatic mesh refinement. Furthermore they are often the best choice for the simulation of flows about moving and deforming objects in fluid-structure interaction. Because of these properties there is a sustained interest in Cartesian grid methods, c.f. [1], [2].

The embedding of a geometrical object into a computational grid leads to three types of grid cells. These are pure fluid cells, cells that are totally masked by the objects, and cells which are intersected (cut) by the object surface. Accordingly, the treatment of embedded objects in a finite-volume scheme requires appropriate methods for the identification of cell types, the determination of geometrical properties of cut cells, and an accurate and stable integration scheme for cut cells. These methods rely on a suitable mathematical representation of the object surface.

The method presented in this paper is based on a discrete point-set representation of embedded surfaces. This representation consists of coordinates and normal vectors for discrete surface points and can be easily derived e.g. from finite-element models of a surface. The discrete point-set provides the identification of all cut cells and allows the calculation of residual cell volumes and residual cell interfaces available to the fluid. A special feature of the scheme is the application of approximate relations for the determination of the residual volumes and cell face areas of cut cells. This makes the scheme very fast, even for cases with moving objects where the evaluations are required in every time step. The method thus provides a very suitable basis for Euler-Lagrange coupled simulations of fluid-structure interactions, c.f. [3].

The paper describes the relevant details of the method and presents results from grid convergence studies for a sphere and a pointed cone. In these studies the geometrical properties of the embedded objects and the transient drag forces generated by a shock induced flow about the objects were evaluated. Furthermore the shock induced flow through a stack of spheres adjacent to a wall is included as an example for complex flow geometries.

2 Basic Finite-Volume Method

The newly developed method has been implemented into the APOLLO code of the Ernst-Mach-Institut, [3]. This code includes a standard finite-volume approximation of the

conservation equations for inviscid, non heat-conducting fluids in Eulerian formulation. For the present purpose, the basic set of finite-volume equations can be written in the following semi-discrete form.

$$V_n \frac{du_n}{dt} = \sum_{l=1,6} (F\mathbf{n}A)_l \tag{1}$$

Here $u = (\rho, \rho\mathbf{v}, \rho e^{tot})^T$ denotes the conservative variables in a cartesian grid cell n with volume V. F, A and $\mathbf{n}$ are the fluxes, the surface areas, and surface normal vectors associated with the six cell faces l of a grid cell, respectively. In our implementation, we use a one-step explicit time integration, together with a HLLC-type flux solver and a MUSCL-type reconstruction based on conservative variables for higher order of accuracy. Some further details are found e.g. in [3].

3 Concepts and Algorithms for embedded Objects

The treatment of embedded objects within the framework of the finite volume method concerns three major issues:

- the identification of cut and masked cells,
- the determination of geometric properties of cut cells, such a residual volume, residual cell face areas, and orientation and size of the embedded surface(s), and
- the time integration of cut cells, including a treatment for cells with small residual volume

In the current work it is assumed, that one or more spatially separated objects are embedded, each of which has a closed surface that is wetted by the fluid on one side only. Furthermore it is assumed that the surface of each object is provided as a finite-element grid, e.g. by a coupled CSD code. Then, for each FE grid a discrete point-set is interpolated, such that each point has a neighboring point at a distance $d < \Delta$, where Δ is the minimum cell length of the fluid grid. Using this point-set as a representation of the embedded surface, it is guaranteed, that each cut cell contains at least one such surface point. Associated with each surface point are – beside the position – a normal vector and a velocity, which are also determined from the FE grid. Given the surface point coordinates, the identification of cut cells is a trivial algebraic procedure if Cartesian grids are used. Upon determination of all cut cells, the masked cells are identified. First, some masked cells adjacent to cut cells are determined through evaluation of the surface normal vectors. The identification of the remaining masked cells is then achieved by exploitation of the fact, that the neighbor of a masked cell is either a cut cell or another masked cell – a direct (face to face) neighborhood of fluid cells and masked cells does not exist in this scheme. Nevertheless can a fluid cell and a masked cell have a common edge or node.

In the next step, the geometrical properties of the cut cells are evaluated. Typically, there are a few surface points within a cut cell. The position, the normal vector and the velocity of these points are then averaged, if they belong to the same object. The averaging effectively defines a single planar embedded surface for each object within a cut cell. Using these averaged values the fraction f of the cell volume occupied by the object is obtained from the following empirical relation.

$$f = \frac{1}{2}\left(1 + \sin(s\pi/2)\right), \quad s = \frac{\max|r_i|}{|r|}\frac{\sum_{i=1,3} r_i n_i \Delta_i}{\sqrt{\sum_{i=1,3} n_i^2 \Delta_i^2}}\,. \tag{2}$$

In this relation $r_i \in [-1, 1]$ denotes the relative position of a point within a grid cell with respect to the grid direction $i = 1, 3 (= x, y, z)$ (on the edges $r_i = -1$ or $r_i = 1$, at the center $r_i = 0$). Furthermore is $\mathbf{n}$ the unit normal vector pointing from the embedded surface into the fluid and Δ_i is the cell size with respect to directions $i = 1, 3$. Once the values of f are known, the fractions h of the cell-face areas blocked by the object are calculated from the blocked volume fractions of the two adjacent cells (denoted by subscripts 1 and 2 in the following relation).

$$\begin{aligned} f_1 + f_2 < 1: \quad & h = \frac{1}{2}\left(\frac{(f_1+f_2)^c - |f_1 - f_2|^c}{1 - |f_1 - f_2|^c}\right)^{1/c}, \\ f_1 + f_2 \geq 1: \quad & h = 1 - \frac{1}{2}\left(\frac{(2-f_1-f_2)^c - |f_1 - f_2|^c}{1 - |f_1 - f_2|^c}\right)^{1/c}. \end{aligned} \tag{3}$$

Both approximate relations (2) and (3) have been derived from a large number of exact geometrical evaluations, where planar embedded surfaces were considered. The exponent c has been determined to c =2.1 in this process.

As the residual volume of the cell must have a closed surface the resulting orientation $\mathbf{n}_{es}$ and area A_{es} of each embedded surface within a cut cell can be obtained from the relation

$$n_{es,i} A_{es} = -\sum_{k=1,6} \left(n_i h A\right)_k, \quad i = 1, 3 \tag{4}$$

Finally, the residual fractions of volume and cell face area available to the fluid, f^* and h^*, are obtained by superposition of all objects present within a cut cell.

$$f^* = \max(0, 1. - \sum_{obj} f), \quad h^* = \max(0, 1. - \sum_{obj} h) \tag{5}$$

Using the quantities as described above the time integration of cut cells is achieved through the modified finite-volume balance equation

$$V_i f_i^* \frac{du_i}{dt} = \sum_{k=1,6} \left(F \mathbf{n} A h^*\right)_k + \sum_{obj} \left(F \mathbf{n} A\right)_{es} \tag{6}$$

The flux F_{es} at an embedded surface is calculated as for any other moving wall boundary. In the present implementation, the fluxes at embedded surfaces are however calculated only with first order of accuracy.

The reduction of the stable time step for a cut cell is estimated from the residual volume fraction. In order to avoid a severe reduction of the time-step size, cut cells with residual volume fractions less than a selected threshold (typically 0.3-0.5) are blended with suitable neighboring cells by conservative averaging. The selection is guided by the direction of the normal vector of the embedded surface.

4 Numerical Tests

In order to test the accuracy of the method a number of different bodies have been embedded into grids of different resolution. Below are presented the results for a sphere

(D=1cm) and a pointed cone (D=1cm, L=1cm) for grids with cell sizes between 0.1cm and 0.01cm. It can be seen in figure 1 that the surface and volume values reconstructed from the embedded surfaces are for all grids very close to the exact values in case of the sphere. This is certainly due to the smoothness of the sphere surface. The results for the cone clearly differ from the latter, due to the presence of the tip and the sharp edge at the circumference of the base. The obtained values however exhibit a straight convergence to the exact values. In a further test series, the embedded bodies were placed in a large number of randomly chosen positions within the grid. It was found that the statistical scatter of the resulting geometrical properties in any case was clearly less than one percent for the cone and 0.1 percent for the sphere. Next, the two bodies were subjected to a

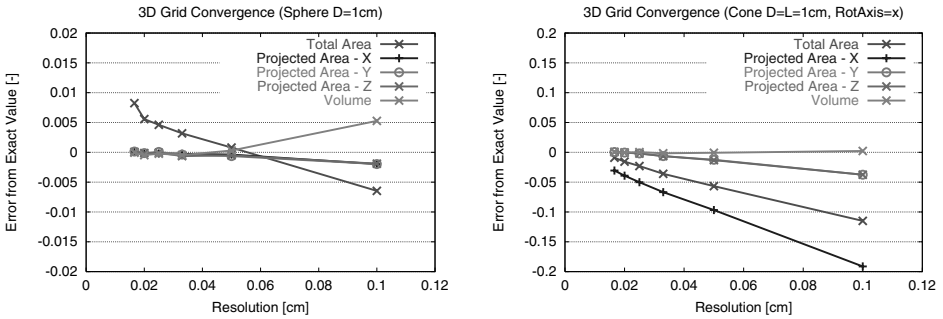

Fig. 1. Grid dependency of geometric properties of the embedded surfaces for sphere (left) and cone (right)

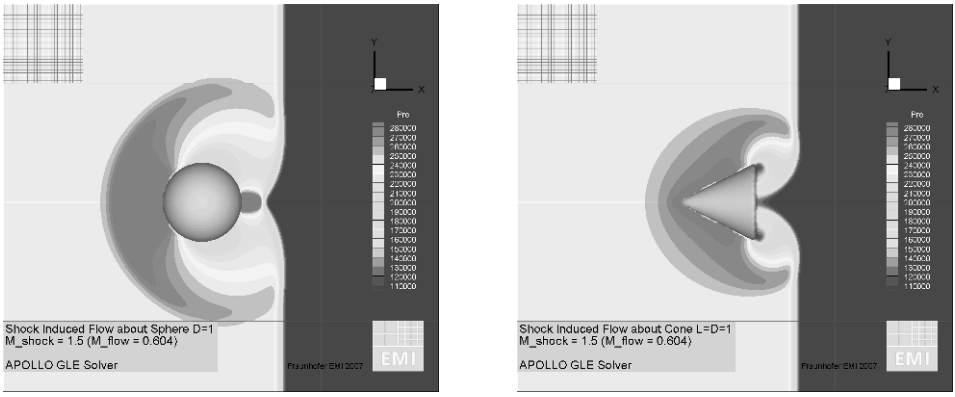

Fig. 2. Instantaneous pressure distribution in the symmetry plane during the refraction of a shock wave about the embedded bodies

shock induced flow of an ideal gas with γ=1.4. Starting from ambient conditions p_0=1 bar, ρ_0=1.187 kg/m^3 a shock wave with shock Mach number 1.5 is refracted around the bodies and induces a homogeneous constant flow with the behind-shock conditions p_s

=2.45 bar, v_s=238 m/s, ρ_s=2.2 kg/m^3 (flow Mach number = 0.6). Figure 3 shows the time dependent drag coefficient ($C_D = 8\ F\ /\ \rho_s\ v_s^2\ \pi\ D^2$) evaluated for different grids. During the refraction phase the drag coefficient reaches a much higher value than in the subsequently reached steady flow phase (note, that for later times the flow past the cone exhibits periodic oscillations). During the refraction phase the computed drag coefficients show a remarkable insensitivity against the grid resolution, while in the steady flow phase the influence of the grid resolution is clearly stronger.

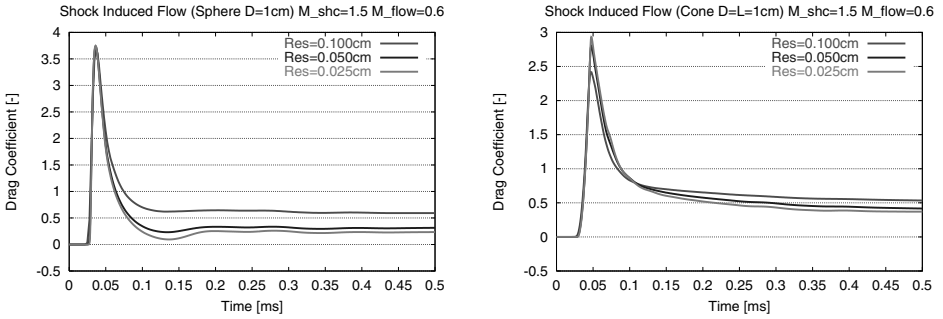

Fig. 3. Transient drag coefficient obtained with different grids

An example for a gasdynamic problem with complex geometry is the shock refraction through a stack of spheres placed onto a rigid surface. Such a configuration might be considered a measure for the protection of shock loaded surfaces. The investigated stack consists of three layers of spheres with diameters 0.433 cm, which are arranged in a regular matrix of cell length 0.5 cm. The middle layer is in a staggered position, such that each sphere of the middle layer is in contact with four spheres of each adjacent layer, see figure 4. The incident shock wave is parallel to the rigid wall and 2 cm away from the wall at t=0. The shock wave has the same conditions as in the examples above. In the simulation a symmetric elementary cross section with lateral dimensions 1cm x 1cm and longitudinal extension of 4cm is modelled. The grid resolution was 0.013 cm. Each layer of spheres was considered an individual embedded object. Figure 5 shows the transient force component normal to the wall on the embedded objects and the wall. Also included is the sum of these forces and the constant force value which would be caused by a normal reflection of the shock wave at the wall without the stack of spheres. It can be seen, that the sum of forces equals the ideal reflection force quite well. This summed force would be applied onto the wall if the spheres were fixed with rigid supports against the wall. The only effect of the stack of spheres is thus the modulation of the force in time.

5 Conclusions

The presented method provides a very flexible, efficient and relatively simple scheme for the simulation of gasdynamic flows about arbitrary geometries. The further development will focus on the treatment of objects which do not posses closed surfaces. Such structures typically feature doubly wetted surfaces, which cannot be handled by the current method yet.

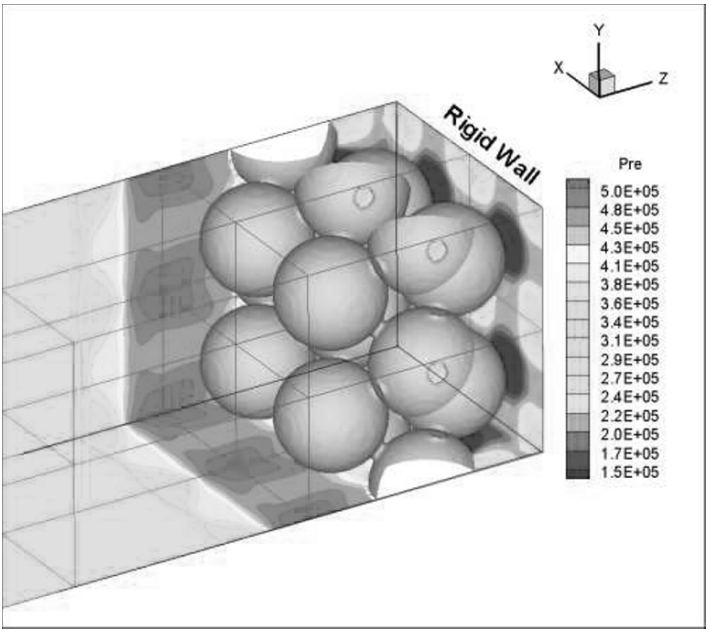

Fig. 4. Instantaneous pressure distribution after the transmission of the shock wave through the stack of spheres and the reflection from the rigid wall

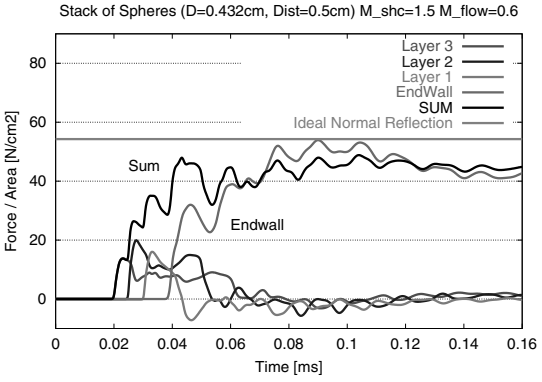

Fig. 5. Normalized force components normal to the wall acting on the individual layers and the wall in comparison with the force for an ideal reflection without the stack of spheres

References

1. H. Luo, J.D. Baum, R. Löhner: A hybrid Cartesian grid and gridless method for compressible flows, Journal of Computational Physics **Vol.214**, Issue 2, pp.618-632 (2006)
2. J. J. Quirk: An alternative to unstructured grids for computing gas-dynamic flow around arbitrarily complex 2-dimensional bodies, Computers & Fluids, **Vol.23**, pp.125-142 (1994)
3. A. Klomfass, K. Thoma: Analysis of Blast loaded Structures by coupled Numerical Simulation. In: *Fluid-Structure Interaction and Moving Boundary Problems*, WITPress (2005)

A discontinuous Galerkin method using Taylor basis for computing shock waves on arbitrary grids

H. Luo[1], J.D. Baum[2], and R. Löhner[3]

[1] *Department of Mechanical and Aerospace Engineering, North Carolina State University, Raleigh, NC 27695 (USA)*
[2] *Center for Applied Computational Sciences, Science Applications International Corporation, McLean, VA 22102 (USA)*
[3] *School of Computational Sciences, George Mason University, Fairfax, VA 22030 (USA)*

1 Introduction

The discontinuous Galerkin methods [1] (DGM) have recently become popular for the solution of systems of conservation laws to arbitrary order of accuracy. The DGM combine two advantageous features commonly associated to finite element and finite volume methods. As in classical finite element methods, accuracy is obtained by means of high-order polynomial approximation within an element rather than by wide stencils as in the case of finite volume methods. The physics of wave propagation is, however, accounted for by solving the Riemann problems that arise from the discontinuous representation of the solution at element interfaces.

In the traditional DG methods either standard Lagrange or hierarchical node-based finite element basis functions are used to represent numerical polynomial solutions in each element. As a result, the unknowns to be solved are the variables at the nodes and the polynomial solutions are dependent on the shape of elements. In this work, a DG formulation based a Taylor basis is presented for the solution of the compressible Euler equations on arbitrary grids, where the numerical polynomial solutions are represented using a Taylor series expansion at the centroid of the cell. The unknown variables to be solved in this formulation are the cell-averaged variables and their derivatives at the center of the cells, regardless of element shapes. Consequently, this formulation is able to offer the insight why the DG methods are a better approach than the finite volume methods based on either TVD/MUSCL reconstruction or essentially non-oscillatory (ENO)/weighted essentially non-oscillatory (WENO) reconstruction, and has a number of distinct, desirable, and attractive features. The developed method is used to compute a variety of shock wave problems on arbitrary grids. The numerical results obtained demonstrated the superior accuracy of this DG method in comparison with a second order finite volume method and a third order WENO method, indicating its promise and potential to become not just a competitive but simply a superior approach than its finite volume and ENO/WENO counterparts for computing shock waves of of scientific and industrial interest.

2 Numerical Method

The Euler equations governing unsteady compressible inviscid flows can be expressed in conservative form as

$$\frac{\partial \mathbf{U}(\mathbf{x},t)}{\partial t} + \frac{\partial \mathbf{F}_j(\mathbf{U}(\mathbf{x},t))}{\partial x_j} = 0, \qquad \text{in } \Omega \tag{1}$$

where, Ω is a bounded connected domain in $\mathbf{R}^d$, d is the number of spatial dimension, and conservative state vector $\mathbf{U}$ and inviscid flux vectors $\mathbf{F}$ are defined by

$$\mathbf{U} = \begin{pmatrix} \rho \\ \rho u_i \\ \rho e \end{pmatrix}, \mathbf{F}_j = \begin{pmatrix} \rho u_j \\ \rho u_i u_j + p\delta_{ij} \\ u_j(\rho e + p) \end{pmatrix}, \tag{2}$$

where the summation convention has been used and ρ, p, and e denote the density, pressure, and specific total energy of the fluid, respectively, and u_i is the velocity of the flow in the coordinate direction x_i. To formulate the DG method, we first introduce the following weak formulation of (1), which is obtained by multiplying (1) by a test function $\mathbf{W}$, integrating over the domain Ω, and performing an integration by parts:

$$\int_\Omega \frac{\partial \mathbf{U}}{\partial t}\mathbf{W}d\Omega + \int_\Gamma \mathbf{F}_j\mathbf{n}_j\mathbf{W}d\Gamma - \int_\Omega \mathbf{F}_j\frac{\partial \mathbf{W}}{\partial x_j}d\Omega = 0, \tag{3}$$

where $\Gamma(=\partial\Omega)$ denotes the boundary of Ω, and $\mathbf{n}_j$ the unit outward normal vector to the boundary. Assume that the domain Ω is subdivided into a collection of non-overlapping elements Ω_e, which can be triangles, quadrilaterals, polygons, or their combinations in 2D and tetrahedral, prism, pyramid, and hexahedral or their combinations in 3D. We introduce the following broken Sobolev space V_h^p

$$V_h^p = \{v_h \in [L_2(\Omega)]^m : v_h \mid_{\Omega_e} \in [V_p^m] \forall \Omega_e \in \Omega\}, \tag{4}$$

which consists of discontinuous vector-valued polynomial functions of degree $p \leq 0$, and where m is the dimension of conservative state vector and

$$V_p^m = \text{span}\left\{\prod_{i=1}^{d} x_i^{\alpha_i} : 0 \leq \alpha_i \leq p, 0 \leq i \leq d\right\}, \tag{5}$$

where α denotes a multi-index. Then, we can obtain the following semi-discrete form by applying weak formulation on each element Ω_e

$$\begin{cases} \text{find } \mathbf{U}_h \in V_h^p \text{ such as} \\ \frac{d}{dt}\int_{\Omega_e} \mathbf{U}_h\mathbf{W}_h d\Omega + \int_{\Gamma_e} \mathbf{F}_j(\mathbf{U}_h)\mathbf{n}_j\mathbf{W}_h d\Gamma - \int_{\Omega_e} \mathbf{F}_j(\mathbf{U}_h)\frac{\partial \mathbf{W}_h}{\partial x_j}d\Omega = 0 \quad \forall \mathbf{W}_h \in V_h^p, \end{cases} \tag{6}$$

where $\Gamma_e(=\partial\Omega_e)$ denotes the boundary of Ω_e, $\mathbf{U}_h$ and $\mathbf{W}_h$ represent the finite element approximations to the analytical solution $\mathbf{U}$ and the test function $\mathbf{W}$, respectively, and both belong to the finite element space V_h^p. Assume that B_i is the basis of polynomial function of degrees p, this is then equivalent to the following system of N equations,

$$\frac{d}{dt}\int_{\Omega_e} \mathbf{U}_h B_i d\Omega + \int_{\Gamma_e} \mathbf{F}_j(\mathbf{U}_h)\mathbf{n}_j B_i d\Gamma - \int_{\Omega_e} \mathbf{F}_j(\mathbf{U}_h)\frac{\partial B_i}{\partial x_j}d\Omega = 0 \quad 1 \leq i \leq \text{N}, \tag{7}$$

where N is the dimension of the polynomial space. In the traditional DGM, numerical polynomial solutions $\mathbf{U}$ in each element are represented using either standard Lagrange finite element or hierarchical node-based basis as following

$$\mathbf{U}_h = \sum_{i=1}^{\text{N}} \mathbf{U}_i(t)B_i(\mathbf{x}). \tag{8}$$

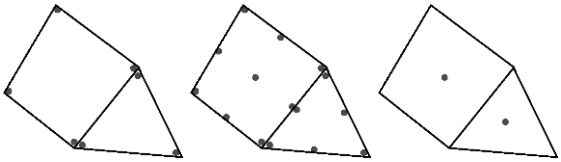

Fig. 1. Representation of polynomial solutions using finite element shape functions (two on the left) and a Taylor series expansion (one on the right)

As a result, the unknowns to be solved are the variables at the nodes $\mathbf{U}_i$, as illustrated in Fig. 1 for linear and quadratic polynomial approximations. On each cell, a system of NxN has to be solved, where polynomial solutions are dependent on the shape of elements. For example, for a linear polynomial approximation in 2D as shown in Fig.1, a linear polynomial is used for triangular elements and the unknowns to be solved are the variables at the three vertices and a bi-linear polynomial is used for quadrilateral elements and the unknowns to be solved are the variables at the four vertices. However, the numerical polynomial solutions $\mathbf{U}$ can be expressed in other forms as well. In the present work, the numerical polynomial solutions are represented using a Taylor series expansion at the centroid of the cell, where the quadratic polynomial solutions, for example, can be expressed as following

$$\begin{aligned}\mathbf{U}_h = \mathbf{U}_c &+ \frac{\partial \mathbf{U}}{\partial x}\,|_c\,(x-x_c) + \frac{\partial \mathbf{U}}{\partial y}\,|_c\,(y-y_c) \\ &+ \frac{\partial^2 \mathbf{U}}{\partial x^2}\,|_c\,\frac{(x-x_c)^2}{2} + \frac{\partial^2 \mathbf{U}}{\partial y^2}\,|_c\,\frac{(y-y_c)^2}{2} + \frac{\partial^2 \mathbf{U}}{\partial x \partial y}\,|_c\,(x-x_c)(y-y_c),\end{aligned} \tag{9}$$

which can be further expressed as cell-averaged values and their derivatives at the centroid of the cell:

$$\begin{aligned}\mathbf{U}_h = \tilde{\mathbf{U}} &+ \frac{\partial \mathbf{U}}{\partial x}\,|_c\,(x-x_c) + \frac{\partial \mathbf{U}}{\partial y}\,|_c\,(y-y_c) \\ &+ \frac{\partial^2 \mathbf{U}}{\partial x^2}\,|_c\,(\frac{(x-x_c)^2}{2} - \frac{1}{\Omega_e}\int_{\Omega_e}\frac{(x-x_c)^2}{2}d\Omega) \\ &+ \frac{\partial^2 \mathbf{U}}{\partial y^2}\,|_c\,(\frac{(y-y_c)^2}{2} - \frac{1}{\Omega_e}\int_{\Omega_e}\frac{(y-y_c)^2}{2}d\Omega) \\ &+ \frac{\partial^2 \mathbf{U}}{\partial x \partial y}\,|_c\,((x-x_c)(y-y_c) - \frac{1}{\Omega_e}\int_{\Omega_e}(x-x_c)(y-y_c)d\Omega)\end{aligned} \tag{10}$$

where $\tilde{\mathbf{U}}$ is the mean value of $\mathbf{U}$ in this cell. The unknowns to be solved in this formulation are the cell-averaged variables and their derivatives at the center of the cells, regardless of element shapes, as shown in Fig. 1. In this case, the dimension of the polynomial space is six and the six basis functions are

$$B_1 = 1, \quad B_2 = x - x_c, \quad B_3 = y - y_c, \quad B_4 = \frac{(x-x_c)^2}{2} - \frac{1}{\Omega_e}\int_{\Omega_e}\frac{(x-x_c)^2}{2}d\Omega$$

$$B_5 = \frac{(y-y_c)^2}{2} - \frac{1}{\Omega_e}\int_{\Omega_e}\frac{(y-y_c)^2}{2}d\Omega,$$

$$B_6 = (x - x_c)(y - y_c) - \frac{1}{\Omega_e}\int_{\Omega_e}(x - x_c)(y - y_c)d\Omega \tag{11}$$

and the discontinuous Galerkin formulation (7) then leads to the following six equations

$$\frac{d}{dt}\int_{\Omega_e}\tilde{\mathbf{U}}d\Omega + \int_{\Gamma_e}\mathbf{F}_j(\mathbf{U}_h)\mathbf{n}_j d\Gamma = 0 \qquad i = 1, \tag{12}$$

$$\sum_{j=2}^{6}\int_{\Omega_e}B_i B_j d\Omega \frac{d}{dt}\begin{pmatrix} \frac{\partial \mathbf{U}}{\partial x}\mid_c \\ \frac{\partial \mathbf{U}}{\partial y}\mid_c \\ \frac{\partial^2 \mathbf{U}}{\partial x^2}\mid_c \\ \frac{\partial^2 \mathbf{U}}{\partial y^2}\mid_c \\ \frac{\partial^2 \mathbf{U}}{\partial x \partial y}\mid_c \end{pmatrix} + \int_{\Gamma_e}\mathbf{F}_j(\mathbf{U}_h)\mathbf{n}_j B_i d\Gamma - \int_{\Omega_e}\mathbf{F}_j(\mathbf{U}_h)\frac{\partial B_i}{\partial x_j}d\Omega = 0 \quad 2 \le i \le 6, \tag{13}$$

Note that in this formulation, the cell-averaged variable equations are decoupled from the equations of their derivatives due to our judicial choice of the basis functions in our formulation and the fact

$$\int_{\Omega_e} B_1 B_i d\Omega = 0, \qquad 2 \le i \le 6. \tag{14}$$

Using this formulation, the similarity and difference between DG and FV methods become clear, and the advantage of the DGM is especially evident in comparison with the FV methods. In fact, the discretized governing equations for cell-averaged variables (12) and the assumption of polynomial solutions on each cell (10) are exactly the same for both methods. The DG(p_0) method, i.e., the DG method using piecewise constant polynomials, exactly corresponds to the first order cell-centered finite volume scheme. The only difference between them is the way how they obtain the high-order polynomial solutions (> 1). In the finite volume methods, the polynomial solutions of degree p are reconstructed using cell-averaged variables from neighboring cells, which can be obtained using either TVD/MUSCL or ENO/WENO reconstruction schemes. Unfortunately, the multi-dimensional TVD/MUSCL reconstruction schemes of arbitrary order based on the extension of one-dimensional MUSCL approach, which are praised to achieve high-order accuracy for multi-dimensional problems, suffer from two shortcomings in the context of unstructured grids: 1) uncertainty and arbitrariness in choosing the stencils and methods to compute the gradients; This explains why a nominally second-order finite volume scheme is hardly able to deliver a formal solution of second order accuracy in practice for unstructured grids, 2) extended stencils required for the reconstruction of higher-order ($> 1^{\text{st}}$) polynomial solutions. This is exactly the reason why the current finite-volume methods using the TVD/MUSCL reconstruction are not practical at higher order and have remained second-order on unstructured grids. When the ENO/WENO reconstruction schemes are used for the construction of a polynomial of degree p on unstructured grids, the dimension of the polynomial space, $N = N(p, d)$ depends on the degree of the polynomials of the expansion p, and the number of spatial dimensions d. One must have three, six, and ten cells in 2D and four, ten, and twenty cells in 3D for the construction of a linear, quadratic, and cubic Lagrange polynomial, respectively. Undoubtedly, it is an overwhelmingly challenging, if not practically impossible, task to judiciously choose a set of admissible and proper stencils that have such a large number of cells on unstructured grids especially for higher order polynomials and higher dimensions. This explains

why the application of higher-order ENO/WENO methods hardly exist on unstructured grids, in spite of their tremendous success on structured grids and their superior performance over the MUSCL/TVD methods. Unlike the FV methods, where the derivatives are reconstructed using the mean values of the neighboring cells, the present DG method computes the derivatives in a manner similar to the mean variables. which is natural, unique, compact, rigorous, and elegant mathematically in contrast with arbitrariness characterizing the reconstruction schemes used in the FV methods with respect how to compute the derivatives and how to choose the stencils. This formulation has a number of distinct, desirable, and attractive features and advantages in the context of DG methods. First, the same numerical polynomial solutions are used for any shapes of elements, which can be triangle, quadrilateral, and polygon in 2D, and tetrahedron, pyramid, prism, and hexahedron in 3D. Using this formulation, DG method can be easily implemented on arbitrary meshes. The numerical method based on this formulation has the ability to compute 1D, 2D, and 3D problems using the very same code, which greatly alleviates the need and pain for code maintenance and upgrade. Secondly, cell-averaged variables and their derivatives are handily available in this formulation. This makes implementation of WENO limiter straightforward and efficient [2], which is required to eliminate nonphysical oscillations in the vicinity of discontinuities. Thirdly, the basis functions are hierarchic. This greatly facilitates implementation of p-multigrid methods [3, 4] and p-refinement. Last, cell-averaged variable equations are decoupled from their derivatives equations in this formulation. This makes development of fast, low-storage implicit methods possible.

3 Numerical examples

Due to page limitation, only a few illustrative examples are presented in this section to demonstrate the accuracy, robustness, and versatility of this DG method. Hancock scheme is used to advance the solution in time in order to achieve the efficiency for time accurate problems and a p-multigrid method [4] is used to accelerate the convergence of the Euler equations to a steady state solution. A WENO-based limiter [2] is used to eliminate nonphysical oscillations in the vicinity of discontinuities.

Example 1: Subsonic flow past a cylinder

This test case is chosen to numerically compare accuracy between DG and FV methods, where a grid convergence study has been conducted for subsonic flow past a circular cylinder at a Mach number of 0.38, and the numerical results are presented in Fig. 2. One can see that the second order DG(P1) solutions on an given meshes are more accurate than the second order finite volume solutions FV(P1) on the globally refine meshes, clearly demonstrating the high accuracy of the DG method.

Example 2: A Mach 3 wind tunnel with a Step

The test case is a classical example for testing the accuracy of numerical schemes for computing unsteady shock waves. The problem under consideration is a Mach 3 flow in a wind tunnel with a step. Fig. 3 shows the computed density contours obtained by the DG method and a third order WENO method, respectively. Note that the same mesh resolution is used for both computations. One can see that the shock resolution of the 3rd order WENO scheme is slightly more diffusive than the present second DG scheme, and the slip line coming from the lambda shock is also more visible in the 2nd DG solution than 3rd order WENO solution, qualitatively demonstrating that the present second order DG solution is as accurate as, if not more accurate than, the third order WENO solution.

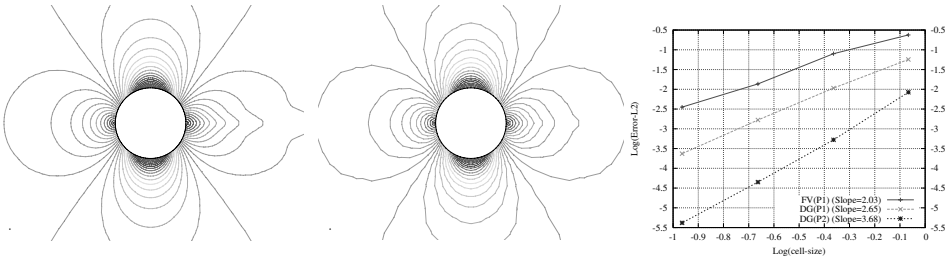

Fig. 2. Computed Mach number contours in the flow field obtained using FV(P1) solution on the 126x33 grid (left), and DG(P1) solution on the 64x17 grid (middle), and the behavior of the error norms with grid refinement for FV(P1), DG(P1), and DG(P2) for subsonic flow past a circular cylinder.

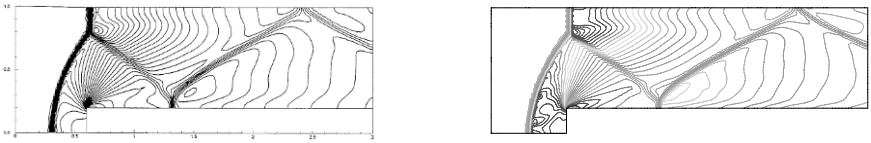

Fig. 3. Computed density contours in the flow field obtained using the 3rd WENO solution (left) and 2nd DG(P1) solution (right)

4 Conclusion

A DG method based a Taylor basis has been presented for the solution of the compressible Euler equations on arbitrary grids. The developed method has been used to compute a variety of time-accurate flow problems on arbitrary grids. The numerical results demonstrated the superior accuracy of this DG method in comparison with a second order finite volume method and a third order WENO method, indicating its promise and potential to become not just a competitive but simply a superior approach than its finite volume and ENO/WENO counterparts for solving flow problems of scientific and industrial interest.

References

1. Cockburn B. and C. W. Shu C. W. : The Runge-Kutta Discontinuous Galerkin Method for conservation laws V: Multidimensional System. journal of computational physics, Vol. 141, pp. 199-224, 1998.
2. Luo H., Baum J.D., and Löhner R. : A Hermit WENO-based limiter for DG method on unstructured grids. journal of computational physics, doi:10.1016/j.jcp.2006,12.017, 2007.
3. Luo H., Baum J.D., and Löhner R. : On the computation of steady-state compressible flows using a discontinuous Galerkin method. International Journal for Numerical Methods in Engineering, doi:10.1002/nme.208, 2007.
4. Luo H., Baum J.D., and Löhner R. : A p-multigrid Discontinuous Galerkin Method for the Euler Equations on Unstructured Grids. journal of computational physics, Vol. 211, No. 2, pp. 767-783, 2006.

A front tracking approach for finite-volume methods

D. Hänel, F. Völker, R. Vilsmeier, and I. Wlokas

Institut für Verbrennung und Gasdynamik, Universität Duisburg-Essen, D-47048 Duisburg, Germany

Summary. A multi-dimensional front tracking concept for Finite-Volume methodd on unstructured grids is presented for solving flow problems with embedded discontinuous solutions. The tracking method is based on the level-set approach on a narrow band in the vicinity of the fronts. The combined finite-volume and tracking method is able to deal with different types of discontinuities in compressible or incompressible fluid flows, as e.g. interfaces or shocks. The flexibility of the tracking method is demonstrated by a number of different flow problems with discontinuities.

1 Introduction

Discontinuous flow features, as material interfaces, shocks or detonations, occur in many flow problems. Such flow features are resolved numerically in the most of cases by capturing methods. However captured discontinuities become smeared out by artificial intermediate states and can therefore falsify the solution. Grid adaption is a practical way in capturing methods to reduce the effects of artificial intermediate states. But a more rigorous and correct way is to treat discontinuities also numerically as discontinuities by shock fitting or front tracking methods. However tracking algorithms, embedded in capturing methods, increase the algorithmic complexity and require additional computational effort. Nevertheless attempts to fitting or tracking were already proposed in early CFD-times, as e.g. in papers by Richtmyer and Morton, 1967, [1] or Moretti, 1987, [2]. One newer promising concept is the level-set method [3, 4], used in the present paper.

The level-set method which is inserted in a finite-volume method is presented in this contribution for tracking of different types of discontinuities on arbitrary, unstructured grids. The method is demonstrated by a number of flow simulations with embedded discontinuities, as interfaces or shocks.

2 Numerical Concept

2.1 Basic Finite-Volume Method

The system of conservation laws for mass, momentum and energy of a general fluid reads:

$$\frac{d}{d\,t}\int\limits_V \mathbf{Q}\,dV + \oint\limits_A \mathbf{H}\cdot\mathbf{n}\,dA = \int\limits_V \mathbf{S}\,dV \tag{1}$$

where Q, H and S represent the conservative variables, the fluxes and the source terms. The equations (1) are solved numerically on arbitrary grids by employing a nodal finite volume method. This method reads for a control volume V_d as sketched in Fig. 1, left:

$$\left.\frac{\Delta \mathbf{Q}}{\Delta t}\right|_{Vd} + Res_{\Delta,Vd} = 0 \qquad \text{with} \qquad Res_{\Delta,Vd} = \frac{1}{V_{Vd}} \sum_{i=1}^{nv} \mathbf{H}_i \, \mathbf{n}_i \, \Delta A_i \tag{2}$$

where Vd is a control volume with the size V_{Vd}. The sum is carried out over all bounding segments. Fluxes are discretized with flux-vector splitting for inviscid contributions and centrally for viscous terms. Artificial compressibility is introduced for low Mach number and incompressible flows. Time integration is performed with an explicit Runge-Kutta time stepping scheme. The whole solution method is integrated in the object-oriented Finite-Volume solution package MOUSE [5], developed at the institute of the authors.

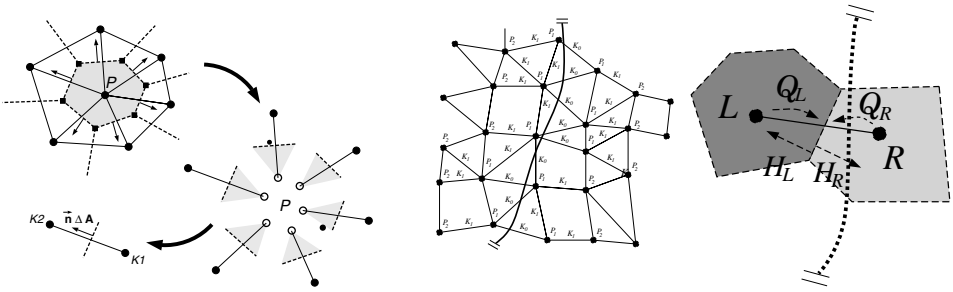

Fig. 1. Grid concept with node centered control volume (left) and grid structure with neighborhood definitions of nodes and edges around a tracked front (middle) and flux separation in cells cut by a front (right)

2.2 Modeling of discontinuities

Discontinuous solutions are mathematically weak solutions of nonlinear, hyperbolic partial differential equations. A typical set of such equations are the Euler equations of compressible, inviscid flows, which may be described in conservative form by Eq. (1). The weak solution of an embedded discontinuity is reads then

$$[\mathbf{H} - \mathbf{c}_d \, \mathbf{Q}]_L^R \cdot \mathbf{n}_d = 0 \tag{3}$$

where $[X]_L^R = X_R - X_L$ defines the jump of left and right variables X over the discontinuity and $\mathbf{c}_d$ is the velocity and $\mathbf{n}_d$ the unit normal vector at the front of the discontinuity. Analyzing Eq. (3) one finds two types of discontinuities, which we call passive and active discontinuities.

Passive or passively transported fronts are material interfaces, contact discontinuities or shear layers, which are transported by the carrier fluid with the flow speed $\mathbf{v}$, i.e. it is $\mathbf{c}_d \cdot \mathbf{n}_d = \mathbf{v} \cdot \mathbf{n}_d$. From the point of view of front tracking the treatment is easier, since the transport velocity $\mathbf{v}$ is available around the front.

Active fronts are shocks or detonation waves. The speed of the front $\mathbf{c}_d$ is usually larger than the velocity $\mathbf{v}$ of the underlying fluid flow, i.e. it is $\mathbf{c}_d \cdot \mathbf{n}_d \neq \mathbf{v} \cdot \mathbf{n}_d$. Its value is ruled by additional physical relations, derived from Eq. (3), known as the Rankine Hugoniot relation in the case of Euler equations. Thus the front velocity $\mathbf{c}_d$ is known only on the front itself, which leads to a more complex formulation of tracking algorithms.

A scalar level-set function $G(\mathbf{x}, t)$ is used to describe the geometry and the transport of the front of a discontinuity. The front itself is defined by a constant value

$G(\mathbf{x},t) = G_0 = const.$, typically chosen to $G_0(\mathbf{x},t) = 0$. Then both sides of the level-set G_0 are distinguishable by the different sign of the level-set function G. The transport of a level-set moving with a propagation speed $\mathbf{c}(\mathbf{x},t)$ reads in the Eulerian frame:

$$\frac{\partial G}{\partial t} + \mathbf{c}_d \cdot \nabla G = 0 \tag{4}$$

In principle, only the level $G_0(\mathbf{x},t) = 0$ is of interest for tracking the front. However, values of neighboring levels of G are still required to evaluate metric coefficients as e.g. the normal vector $\mathbf{n}_d(G)$ at the front. Therefore the level-set function is usually normalized away from the level $G_0 = 0$ to satisfy a slope condition

$$\mid \nabla G \mid = 1. \tag{5}$$

The function G is then a measure of the distance normal to the front, which makes the geometrical exploration of the level-set more accurate. Thus the solution procedure for the level-set function consists of two steps, the transport step, solving Eq. (4), and the normalization step, satisfying Eq. (5) away from $G = 0$. In addition, the local propagation speed of front $\mathbf{c}_d$ has to be determined for active discontinuities (e.g. shocks) by exploring the weak solution.

2.3 Numerical Level-Set Approach

The level-set function is required in the neighborhood of the front only, therefore its definition range is locally restricted to a few number of grid levels around the front (narrow band), sketched in the middle of Fig. 1. Points and edges are marked with P and K respectively and the number index refers to the neighborship level. Edges of type K_0 refer to those hitting the front and the exact front position is described by the value $G = 0$ on these edges upon linear reconstruction. The discrete definition range is dynamic and must be adjusted, if nodes are overrun by the front. If multiple fronts are tracked, the narrow band formulation applies to each of the fronts independently and their discrete definition ranges may overlap in arbitrary ways without restriction.

The propagation step of the front is carried out by an explicit time discretization of equation 4 in the form

$$G^{n+1} = G^n - \mathbf{c}_d \cdot \nabla G^n \, \Delta t. \tag{6}$$

The spatial derivatives of G are constructed by least square approaches. This equation is solved under the assumption of known, frozen velocity $\mathbf{c}_d$ during a time step Δt.

The normalization procedure involves iterations (index k) by pointwise least square approaches and proceeds in two steps. The first step is used to compute the direction of the gradients ∇G^k within the narrow band. The functional value of G^{k+1} is set to satisfy the slope condition Eq. (5) in the second step. Unfortunately the normalization procedure alters slightly the front position, determined before by a linear interpolation for $G = 0$. Additional corrections are still necessary to preserve the exact front position. The normalization procedure is in general the most expensive part of the tracking method, but necessary to preserve sufficient accuracy on an unstructured mesh. More details are found in [6, 7].

The dynamic part of the front tracking method represents the physics of the underlying problem. It has to take into account the jump conditions over the front, it enables the determination of the propagation speed and it couples the states "left" and "right"

to the front with the surrounding solution. The physics can roughly be expressed by the two different types of discontinuities, as classified previously in passive (e.g. material interfaces) and active discontinuities (e.g. shock waves).

The passive discontinuities describe the interface between immiscible fluids which move with the fluid velocity, i.e. $\mathbf{c}_d = \mathbf{v}$. The jump conditions Eq. (3) yield the following conditions at the interface, which couple the left and right states:

$$\mathbf{v}_L \mathbf{n}_d = \mathbf{v}_R \mathbf{n}_d \qquad \text{and} \qquad p_L = p_R$$

The condition of equal pressure $p_L = p_R$ over the front can be substituted by the pressure jump $p_L - p_R = \sigma/R$ in the presence of surface tension σ. The other quantities, as the tangential velocity v_t at the front, the inner energy e or the density ρ are independent each from the other side of the front and are reconstructed by one-sided approximations. Examples for free surfaces are given in [9].

Active discontinuities, like shocks or detonation waves move relative to the carrier fluid $\mathbf{v}$ with the propagation speed $c_n = \mathbf{c}_d \cdot \mathbf{n}_d$. The speed c_n depends on the left and right values Q_L and Q_R at the front, and is calculated from the Rankine-Hugoniot conditions. Typically for shock front calculations is, that supersonic values and one value from the other (subsonic) side, usually the pressure, are prescribed to calculate the shock Mach number Ma_S in the frame moving with the shock. The propagation speed c_n is then determined from Ma_S.

Finite Volume Implementation of the jump conditions is realized for unstructured meshes by the concept of flux separation, formulated first in [8]. All control volumes in Fig. 1, which are cut by the discontinuity, contain now the two states Q_L and Q_R, with their amounts proportional to the partial volumes ΔV_L and ΔV_R. The geometrical determination of these partial volumes is however rather tedious for arbitrary grids, therefore an alternative way is introduced here, called flux separation. It is assumed that a computational cell belongs completely to the state defined by the node in the cell center, as sketched in Fig. 1, right. The fluxes on edges, cut by the front, are then double defined, belonging either to the left or the right cell. The flux difference on such an edge satisfies the jump conditions, since the values Q_L and Q_R satisfy these conditions. If a node gets overrun by the discontinuity, then the corresponding cell is redefined to the new state. In this case the variable set for this node is overwritten by extrapolated values from the corresponding side. In the present version, the time step is restricted to allow at most one neighborhood level to be overrun at once.
The flux separation approach is consistent with the finite volume concept and can be employed to any grid structure. The original control volumes of the mesh are preserved and the need for a sub-cell resolution, rather complex on grids of arbitrary structure, is avoided.

3 Some Applications

A relatively easy problem for front tracking is the formation of a bow shock in front of blunt bodies. The inviscid flow at $Ma_\infty = 2$ past a sphere is computed on a tetrahedral grid and shown in Fig. 2. The left picture shows the initialization of the shock front as a planar surface in front of the sphere and the right one the final tracked position of the shock. Broken partitions of the definition range of the level-set and iso-colors of pressure

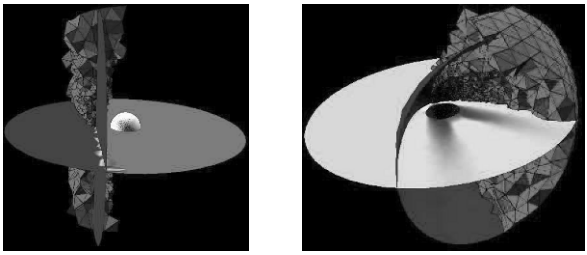

Fig. 2. Inviscid, 3-D flow at $Ma_\infty = 2$ over sphere with initial state (left) and final state (right) of the tracked shock front. Shown are the narrow band of subset grid around level-set and colors of isobars.

on a cut plane are shown in both figures. The bow shock around such simple body is a differentiable surface and is therefore represented very well by a single level-set.
The use of level-sets for non-differentiable and multiple front curves is more problematic. An example of the first kind is presented in Fig. 3 for the supersonic flow at $Ma = 3$ past a set of three cylinders. The front shock is tracked by a single level-set, starting from an initial straight shock as in the previous example. The left figure represents obviously the bow shocks and intersecting points well, but a look in more detail at the zoom in the left picture reveals that existing intersection points of the front are smeared out and are rounded depending on the mesh density.

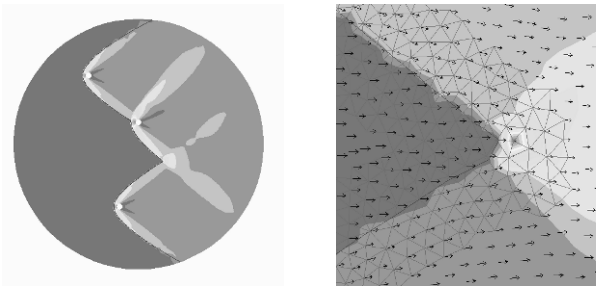

Fig. 3. Inviscid, 2-D flow at $Ma_\infty = 3$ over three cylinders with single tracked shock wave, colors of isobars (left) and zoom of shock crossing area between both lower cylinders with details of pressure values, front level-set, subset mesh and velocity vectors

The smoothing of non-differentiable front curves can be avoided, if additional level-sets are used for each additional discontinuities at intersecting points. First results are achieved for the simpler problem of a regular shock reflection. Another problem are non-closed discontinuities. For example, shocks can degenerate to compression waves or, completely different, a twine in spinnery is moved by the fluid. The authors have proposed here the use of master-slave combinations of level-sets for such non-closed discontinuities. More details are presented in [6, 7].

One example of interface tracking is given in Fig. 4 for the problem of interaction between a helium bubble in nitrogen with a shock wave. The interface between helium and nitrogen is tracked here by using the level-set formulation while the shock wave is

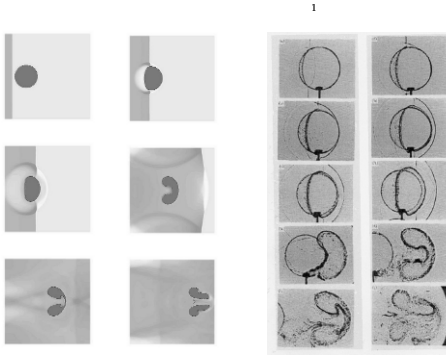

Fig. 4. Simulation of interaction between helium bubble and shock wave in nitrogen (left) and comparison of the density fields at different times with experiment Haas, Sturtevant, JFM,181,(1987)(right). Material interface is tracked by a level-set while the shock is captured

captured. The colors of constant density are in qualitative agreement with those visualized in the experiment by Haas, Sturtevant, JFM,181,(1987). It is to remark that the level-set tracking concept for material interfaces is intensively employed at present to free surfaces and waves in simulations of ship hydrodynamics, [10].

References

1. R. Richtmyer, K. Morton: Difference Methods for Initial value Problems. Interscience, New York, (1967).
2. G. Moretti: A Technique for Integrating Two-Dimensional Euler Equations. Computers and Fluids, vol. 15, pp 59-75, (1987).
3. A. Kerstein, W. Ashurst, F. Williams: Field Equation for Interface Propagating in an Unsteady Homogeneous Flow Field. Phys. Rev. A, vol. 37, pp 2728-2731, (1988).
4. A.J. Sethian: Level Set Methods and Fast Marching Methods: Evolving Interfaces in Computational Geometry, Fluid Mechanics. Computer Vision and Materials Science Cambridge, Cambridge University Press, (1999).
5. O. Gloth, R. Vilsmeier, D. Hänel: Object-oriented programming platform "Mouse", Institute of Combustion and Gasdynamics, Univ. of Duisburg-Essen, *http://www.uni-due.de/ivg* (periodically updated)
6. F. Völker: Verfolgung fluiddynamischer Diskontinuitäten mittels Level-Set-Funktion. Dissertation an der Fakultät für Ingenieurwissenschaften der Universität Duisburg-Essen, (2005).
7. F. Völker, R. Vilsmeier, D. Hänel: A Local Level-Set Method under Involvement of Topological Aspects. In: G. Warnecke (Ed.): Analysis and Numerics for Conservation Laws, p. 233-256, Springer-Verlag Berlin, Heidelberg New York, (2005).
8. O. Gloth, D. Hänel, L. Tran, R. Vilsmeier: A Front Tracking Method on Unstructured Grids. Computer and Fluids, vol. 32, pp 547-570, (2003).
9. F. Bet, D. Hänel, S. Sharma: Numerical Simulation of Ship Flow by a Method of Artificial Compressibility. Twenty-Second-Symposium on Naval Hydrodynamics, pp 522-531, National Academy Press, Washington, (1999).
10. N. Stuntz: Numerische Simulation der Schiffsumströmung mit Berücksichtigung des Propellersogs. Dissertation an der Fakultät für Ingenieurwissenschaften der Universität Duisburg-Essen, (2006).

Behaviour of a bucky-ball under extreme internal and external pressures

N. Kaur[1,2], S. Gupta[1,3], K. Dharamvir[1], and V.K. Jindal[1]

[1] *Department of Physics, Centre of Advanced Study in Physics, Panjab University, Chandigarh-160 014, India*
[2] *Chandigarh College of Engineering and Technology, Chandigarh, India*
[3] *University Institute of Engineering and Technology, Panjab University, Chandigarh, India*

1 Introduction

In a bucky ball, the atoms are all interconnected with each other through sp^2 bonding, thus resulting in exceptional strength. Apart from its hardness, the important fact is that for nanotechnology, useful dopant atoms can be placed inside the hollow fullerene ball. In order to utilize such properties and the strength of this molecule, it is of interest to study its stability under internal and external pressure. Therefore, in this paper, we made an attempt to study the stability of this molecule based on its binding strength. We have used the Tersoff [1, 2] as well as Brenner potential [3] for the intramolecular interactions between the carbon atoms of a bucky ball and compared the two.

There are a number of theoretical and experimental studies available for the phonon modes in C_{60} molecule. Experimental data from Raman scattering [4], Infrared [4, 5] and neutron inelastic measurements [6]provide an overview of the vibrational modes of the C_{60} molecule. Similarly, several calculations of the vibrational frequencies of the C_{60} molecule, using various classical and quantum mechanical theories [7–10], have been performed. In addition, a number of force constant models have been used to calculate the phonon frequencies [11, 12]. For calculating the phonon frequencies, they had first fitted the Raman data to obtain the force constants and then various phonon frequencies had been calculated using these force constants. In order to show the validity of the potential model used by us, we have obtained the stretching force constant of a C_{60} molecule, which would shown to be in good agreement with the theoretical work done by Jishi *et al.* [11] and hence with the experimental observations.

In order to utilize the hardness of a C_{60} molecule as molecular bearings etc., its Bulk Modulus needs to be evaluated. Ruoff and Ruoff [13]estimated the bulk modulus of C_{60} from simple elasticity theory as 843 GPa and, using the Tight Binding method, Woo *et al.* [14] found its value to be 717 GPa. These values have been calculated around zero pressure. In this paper, Bulk Modulus for the C_{60} molecule has been estimated for higher pressures as well. In section 2 we present the theoretical model used to obtain equilibrium structure of a bucky ball. The numerical method and results have been presented in section 3. Section 4 contains discussions and conclusions.

2 Theoretical model

We have used a theoretical model in which the interaction between bonded carbon atoms is governed by (*i*) Tersoff potential [1, 2] and (*ii*) Brenner potential [3]. These potentials have been extensively used to interpret properties of several carbon based systems like carbon nanotubes [15], graphite [1–3], diamond [1–3]and fullerenes [16]. A comparison

of results of structure and bulk modulus under high pressures from these two potentials helps us explore their applicability in high pressure regime.

2.1 Tersoff potential

The form of this potential is expressed as potential energy between any two carbon atoms on C_{60} , say i and j, separated by a distance r_{ij} as

$$V_{ij} = f_c r_{ij}(Ae^{-\lambda_1 r_{ij}} - b_{ij}Be^{-\lambda_2 r_{ij}}), \tag{1}$$

is a function used to smooth the cutoff distance taken as 2.1Å. The state of the bonding is expressed through the term b_{ij} as the function of angle between bond $i-j$ and each neighboring bond $i-k$. The parameters used in this potential have already been given by Tersoff [2]. However some of them have been modified by us (as discussed in section 3.1, para 2) and have been tabulated in table 1.

	$A(eV)$	$B(eV)$	λ_1	λ_2	λ_3
Original	1393.6	346.7	3.4879	2.2119	0
Modified	1380.0	349.49	3.5679	2.2564	0,2.2564

Table 1. The original and modified parameters of the Tersoff potential.

2.2 Brenner potential

The potential energy between any two carbon atoms on C_{60} , say i and j, separated by a distance r_{ij} is given as

$$V_{ij} = V_R(r_{ij}) - B_{ij}V_A(r_{ij}) \tag{2}$$

V_R and V_A are the repulsive and attractive potential energy terms, respectively, which together form a sort of modified Morse potential. In addition, the Brenner potential takes bonding topology into account with the empirical bond order function B_{ij}, whose exact form has been taken from Ref. [3]. Brenner has defined two sets of parameters, henceforth defined as set-1 and set-2, for this potential for carbon systems [3], which have been taken as given in Ref. [3]. Using these potentials, composite energy of all the atoms of the system, given by E is written as

$$E = \Sigma_{ij}V_{ij} \tag{3}$$

where the sum over i and j in Eq. 3 includes all the 60 atoms in the C_{60} molecule.

3 Numerical method and Results

We discuss here the details of numerical methodology and results. We give the essential ingredients and then describe effects of pressure on the molecule.

3.1 Structure and Potential parameters

Two types of bond lengths determine the coordinates of 60 carbon atoms in C_{60} molecule. Single bond b_1, joins a hexagon and a pentagon. The double bond b_2, joins two hexagons and is shorter. These have been measured using nuclear magnetic resonance, and are found to be having lengths 1.46Åand 1.40Å [17] respectively. By using the parameters given by Tersoff, binding energy of the molecule was allowed to minimize using the potential model as given in the earlier section 2.1. To do this the atomic positions of all the 60 atoms were varied to obtain minimum energy configuration. At zero pressure, b_1 and b_2 were obtained to be 1.46Åand 1.42Åwith binding energy 6.72eV/atom as given in table 2. In order to reproduce the bond lengths and the binding energy of C_{60} molecule in closer agreement with the experimental results, the potential parameters given by Tersoff [2]had to be modified. Tersoff has taken λ_3 equal to zero, however in order to see its effect, we have also used a finite value of λ_3. It has been found that the effect of change in λ_3 becomes evident only at high pressures. In table 1, we have tabulated the modified as well as the original potential Parameters [2]. The new bond lengths and energies have been given in tabel 2.

	Calculated				Experimental
	Tersoff potential		Brenner potential		
parameters	original [2]	modified by us	set-1 [3]	set-2 [3]	[17]
Binding energy (eV/atom)	-6.73	-7.17	-7.04	-6.99	-7.04
Bond lengths (Å)	(1.46,1.42)	(1.45,1.41)	(1.45,1.42)	(1.48,1.45)	(1.45,1.40)

Table 2. Comparison between the calculated and experimental Binding energy and bond lengths of a C_{60} molecule with original and modified parameters.

Similarly, energy minimization has been done with Brenner potential using both set-1 and set-2 parameters and the binding energy/atom and bond lengths so obtained for the minimized structures have been tabulated in table 2.

3.2 Pressure effects

To compress or dilate the molecule we multiply each coordinate of 60 atoms by a constant factor $C < 1$ for compression and $C > 1$ for dilation. Each C value determines a +ve (external) or a -ve (internal) pressure. By changing C, we get a new diameter d, (hence a new volume V) and a new binding energy E as shown in figure 1. Thus we get E as a function of V and we get $E(P)$.

We have made the assumption that the shape of the molecule does not change with pressure. This must be true when one deforms the regular C_{60} hydrostatically. Theoretically, this can easily be done by first converting Cartesian coordinates (x, y, z) of 60 atoms into polar coordinates (r, θ, ϕ) and then minimizing the structure allowing only θ and ϕ to change at a fixed radius r of C_{60} molecule.

At zero pressure, each carbon atom in C_{60} has coordination number N as 3 i.e. there are three nearest neighbors within the range of the potential. At some pressure, N changes from 3 to 5 as two more atoms come inside the range of the potential. The value of this pressure is dictated by the potential model.

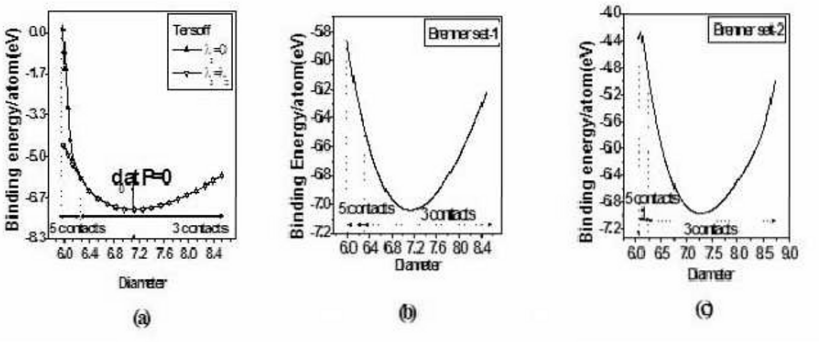

Fig. 1. Binding energy, E, of a relaxed C_{60} molecule at different diameters under Tersoff (a), Brenner set-1 (b) and set-2 (c) potentials.

a) Critical diameters: The molecule can withstand internal and external pressure upto a certain extent. To have a knowledge of these limits, a plot between binding energy/atom, $E(P)$ and diameter of the ball, d as in figure 1 is used. We have been able to minimize the energy of the C_{60} molecule having diameter within certain range, depending upon the potential used, but outside this range minimum energy configuration was not obtained even after a very large number of cycles of iteration as shown in figure 2.

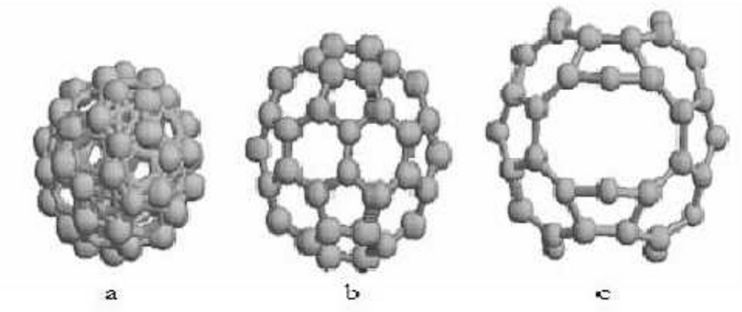

Fig. 2. Molecular structure at critical diameters. The structures $'a'$, $'b'$ and $'c'$ correspond to extreme external, zero and extreme internal pressures respectively.

b) Force constant Double derivative of the binding energy of the molecule with respect to its bond length give the value of force constant. In table 3, we compare the value of bond stretching force constant with other similar work.

c) Bulk modulus Second derivative of the binding energy of the molecule with respect to its volume gives us the bulk modulus and is shown in figure 4. A comparison of various calculations has also been made in table 4.

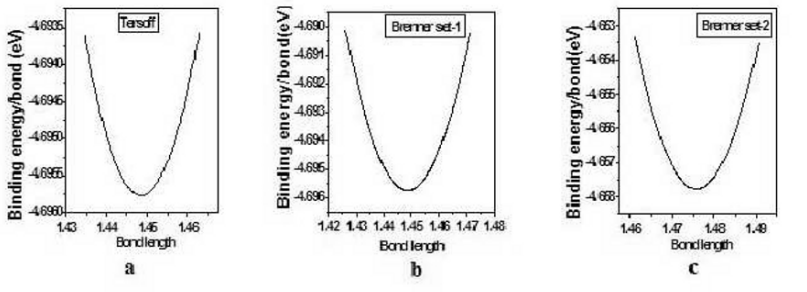

Fig. 3. Binding Energy/bond of C_{60} molecule with varying single bond lengths.

Tersoff	Brenner set-1	Brenner set-2	Jishi *et al.* [11]	Ruoff and Ruoff [13]	graphite [17]	Feldman *et al.* [12]	Cyvin et al. [18]
5.6	3.55	6.51	4.0	6.62	3.5	4.4	4.7

Table 3. Force constants of bond stretching of a C_{60} molecule (mdyne/Å)

Reference	Ruoff *et al.*	Woo *et. al*	Tersoff	Brenner set-1	Brenner set-2
Bulk modulus (GPa)	843	717	674	370	694

Table 4. Bulk modulus of a C_{60} molecule according to various calculations.

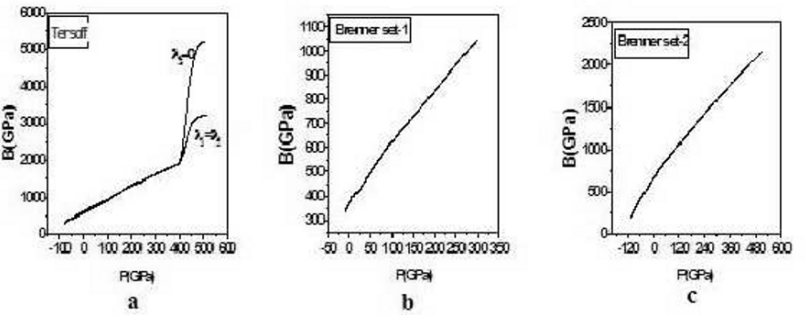

Fig. 4. Variation of bulk modulus with pressure.

4 Discussion

In this paper, we attempt to calculate pressure effects on a C_{60} molecule using Tersoff as well as the Brenner potential for the inter-atomic interactions. With this pressure study, we have been able to calculate the critical diameters, stretching force constant, and Bulk Modulus of a C_{60} molecule at wide ranging pressure values. Although Tersoff potential reproduces the experimental results around zero pressure but at high pressures, as the coordination number increases, the bulk modulus show discontinuity in its value.

This effect gets marginalized by altering the parameterλ_3 to a non zero value which has usually been taken to be zero for carbon systems. We have recalculated the results by taking $\lambda_3 = \lambda_2$ which has already been used to explain the silicon system successfully and figure 4 shows that the discontinuity in the bulk modulus gets diminished by choosing this value. There is a scope for further improvement in the value of this parameter. Usage of Brenner potential does not show such discontinuity. It is quite unexpected that a molecule becomes suddenly so hard. Therefore Tersoff potential is not suitable above approximately 400GPa. However the molecule's behaviour at high pressures may become physically acceptable by choosing appropriate value of parameter λ_3 if we insist on using this potential. The critical pressures corresponding to maximum compression or dilation are about 922Gpa and -134Gpa respectively with Tersoff potential, 535Gpa and -116GPa respectively with Brenner set-1 potential, and 322Gpa and -131Gpa respectively with Brenner set-2 potential. The reliability of these potentials at these extreme pressures is the relevant question here. One has to resort to ab-initio calculations to get exact values, though the estimates provided here using Brenner set-1, can be considered to be quite reliable, as this has provided good estimate of binding energy and bond lengths of C_{60} molecule. We believe that the estimates of critical positive and negative pressures can be useful for planning practical applications related to either high pressure absorption or doping of atoms or molecules in the cage. The results of bulk moduli provide enough motivation for further measurements on this molecule under high pressures.

References

1. J. Tersoff, Phys. Rev. B 37, 6991 (1988).
2. J. Tersoff, Phys. Rev. Lett. 61, 2879 (1988).
3. D. W. Brenner Phy. Rev. B 42, 9458 (1990).
4. D. S. Bethune, G. Meijer, W. C. Tang, H. J. Rosen, W. G. Golden, H. Seki, C. A. Brown, and M.S. Derries, Chem. Phys. Lett. 179,181 (1991).
5. D. S. Bethune, G. Meijer, W. C. Tang, H. J. Rosen, Chem. Phys. Lett. 174, 219 (1990).
6. R. L. Cappelletti, J. R. D. Copley, W. Kamitakihara, Fang Li, J. S. Lannin and D. Ramage, Phys. Rev. Lett. 66, 3261 (1991).
7. R. E. Stanton and M. D. Newton, J. Phys. Chem. 92, 2141(1988).
8. F. Negri, G. Orlandi and F. Zerbetto, Chem. Phys .Lett. 144, 31 (1988).
9. B. P. Feuston, W. Andreoni, M. Parrinello and E. Clementi, Phys.Rev.B 44, 4056 (1991).
10. G. B. Adams, J. B. Page, O. F. Sankey, K. Sinha, J. Menendez and D. R. Huffman, Phys. Rev. B 44, 4052(1991).
11. R. A. Jishi, R. M. Mirie, M. S. Dresselhaus, Phys. Rev. B 45, 13685 (1992).
12. J. L. Feldman, J. Q. Broughton, L. L. Boyer, D. E. Reich and M. D. Kluge, Phys. Rev. B 46, 12731 (1992).
13. R. S. Ruoff, A. L. Ruoff, Appl. Phys. Lett. 59 (13), 23 (1991).
14. S. J. Woo, S. H. Lee, Eunja Kim, K. H. Lee, Young Hee Lee, S. Y. Hwang and Cheol Jeon Phys. Lett. A 162 (1992).
15. S. Gupta, K. Dharamvir and V. K. Jindal, Phy. Rev. B 72, 165428 (2005).
16. D. H. Robertson, D. W. Brenner and C.T.White, J. Phys. Chem. 1999, 15721 (1994).
17. M. S. Dresselhaus, G. Dresselhaus and P. C. Eklund, Science of Fullerenes and Carbon Nanotubes, Academic Press, California 1996.
18. S. J. Cyvin, E. Brendsdal, B. N. Cyvin and J. Brunvoll, Chem. Phys. Lett. 174, 219 (1990).

Investigation of interaction between shock waves and flow disturbances with different shock-capturing schemes

A.N. Kudryavtsev, D.V. Khotyanovsky, and D.B. Epshtein

Institute of Theoretical and Applied Mechanics,
Siberian Branch of the Russian Academy of Sciences, Novosibirsk, Russia

Summary. We simulate transmission of a small-amplitude disturbance wave through a shock wave. Results of our numerical experiments performed with different high-order shock-capturing schemes show that the capability of a scheme to correctly predict the amplification of the disturbances crucially depends on the Riemann solver used in evaluation of numerical fluxes. Incorrectly high amplification rates are produced by the solvers resolving shock waves sharply, with no interior points in numerical profiles of steady shock waves. In particular, both the exact Riemann solver and the popular Roe flux difference splitting demonstrate such unphysical behavior. A possible explanation of such behavior is proposed. More dissipative flow solvers, such as the global Lax–Friedrichs splitting, produce transmission coefficients close to the predictions of linear theory.

1 Introduction

Interaction between shock waves and flow turbulence is an essential feature of many high-speed flows of practical interest. It is well known that the shock wave interactions with boundary layers and free shear flows result in a significant increase in turbulence intensity. Effects of flow disturbances are also important in regular/Mach reflection transition in the dual solution domain, where both types of steady reflections are possible.

When the flow disturbance amplitude is small, linear interaction analysis (LIA), which has been contributed by many authors, most noticeably by [1], can be used to predict the amplification rate. For larger amplitudes, one should rely on direct numerical simulation. The numerical solvers used for this purpose are required to be highly accurate and capture flow discontinuities robustly.

In the last decades a number of sophisticated shock-capturing schemes have been developed for numerical solution of Euler equations. These schemes typically use the high-order TVD (total variation diminishing) or ENO (essentially non-oscillatory) reconstruction of the flow variables, and solve the Riemann problem between two states to obtain the numerical flux on the cell interface.

The purpose of the present study is to investigate capabilities of the different numerical schemes to correctly predict the properties of the disturbance wave transmitted through the shock wave in a few simple model configurations, where the LIA can be applied.

2 Numerical methods

In this study we solve numerically 1D and 2D Euler equations with two different numerical methods. The first method is the finite-volume MUSCL TVD algorithm which utilizes 4th order MUSCL reconstruction of [2] in conjunction with the “minmod” slope limiter. The Riemann solvers used in our numerical experiments are the exact iterative Riemann solver, the Roe flux difference splitting with entropy fix and the van Leer flux vector splitting.

Another class of upwind schemes, which is more attractive to simulate transition and turbulence in high-speed flows, is the ENO (essentially non-oscillatory) and WENO (weighted ENO) schemes. The ENO schemes use an adaptive "smoothest" substencil chosen within a larger, fixed stencil to construct high-order approximation of the solution avoiding the interpolation across discontinuities and preserving uniformly high-order accuracy everywhere where the solution is smooth. The main idea of the WENO schemes is to use a superposition of several substencils with adaptive coefficients to increase the order of approximation even more. In this paper we employ the finite-difference, flux-based, fifth order WENO scheme [3]. The Riemann solvers tested with this numerical algorithm are the Roe flux difference splitting, and more dissipative Lax–Friedrichs flux splitting [3]. In this study we use two different formulations of the Lax–Friedrichs flux splitting: local Lax–Friedrichs (LLF) and global Lax–Friedrichs (GLF). The difference between the two is that the former use local maxima of the eigenvalues as the Lax–Friedrichs coefficients, whereas the latter searches for maxima over the entire range of eigenvalues. The GLF is more dissipative and robust at strong shocks.

Time integration is performed with a 4th order explicit Runge–Kutta scheme.

3 Results and discussion

To investigate capabilities of different shock-capturing schemes to predict amplification of the disturbance wave passing through a shock wave we performed numerical simulations for the one-dimensional problem. We consider the interaction of a fast acoustic wave with an amplitude $\delta p = 1 \times 10^{-4}$ impinging on a steady normal shock. Linear solution for this problem was obtained by Blokhintsev (1945) [4] and Burgers (1946) [5], and can be found in [6].

The flow Mach number is varied between $\mathrm{M} = 2$ and $\mathrm{M} = 10$. The perfect gas with $\gamma = 1.4$ is considered. The length of the computational domain was 5 wavelengths λ of the oncoming disturbance, and the shock was located at $x/\lambda = 1$. The grid was uniform with 200 cells per λ.

Figure 1 presents steady pressure profiles across the shock obtained with different solvers at $\mathrm{M} = 8$. The exact Riemann and Roe solvers yield the exact pressure jump with no intermediate points, whereas more diffusive van Leer and global Lax–Friedrichs splittings produce smeared shock wave with two and four intermediate points, respectively.

In Fig. 2 we plotted the amplification coefficient of the pressure amplitude $\delta p_2/\delta p_1$ and the entropy wave generation coefficient $p_2 \delta s_2/c_p \delta p_1$ versus oncoming flow Mach number M obtained with different schemes. It is clear that the capability of a numerical scheme to predict correctly the amplification of disturbances depends crucially on the Riemann solver used. Incorrectly high amplification rates have been found for the solvers resolving shock waves sharply, with no interior points in numerical profiles of steady shock waves. In particular, both the exact Riemann solver and the popular Roe flux difference splitting demonstrate such unphysical behavior. For example, in the one-dimensional problem both schemes coupled with the MUSCL TVD reconstruction of the 4th order yield the amplification rates of acoustic disturbances close to 300 instead of the theoretical value of 39.2 for a Mach 8 shock wave.

It is a surprising result since the less dissipative approximate Riemann solver of Roe is widely accepted as the most appropriate for simulation of wave-dominated flows encountered in aeroacoustics, boundary layer transition, etc. Such unphysical amplification rates may be connected to the numerical generation of long wavelength noise downstream of a slowly moving shock wave, which was observed in some numerical works (see, e.g. [7]). This phenomenon is caused by periodic increase and decrease in the thickness of shock wave transition while the shock wave oscillates around the stationary position changing its location with respect to grid cell faces and cell centers. In our simulations the shock wave may slowly change its position due to small fluctuations induced in the oncoming flow by the propagating disturbance wave.

On the other side, more diffusive Riemann solvers, which produce shock wave profiles smeared over 3–4 grid cells, predict the amplification rate of small disturbances much better. The van

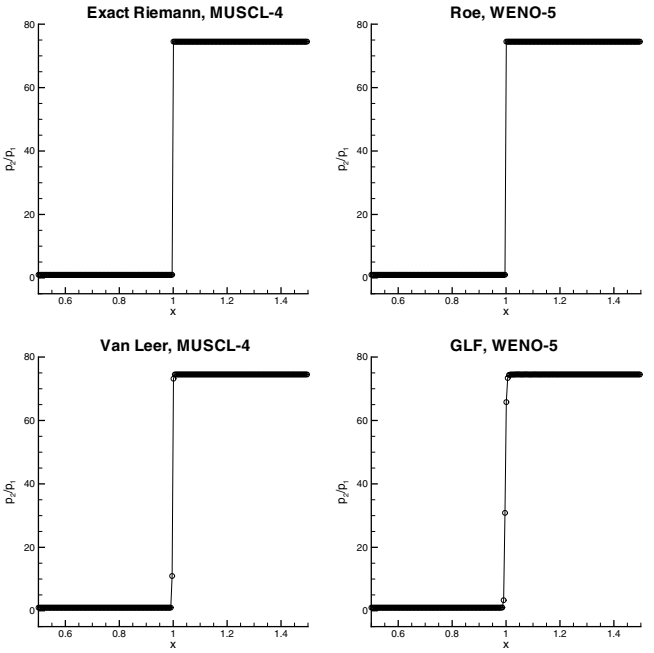

Fig. 1. Steady M = 8 shock wave profiles obtained with different schemes

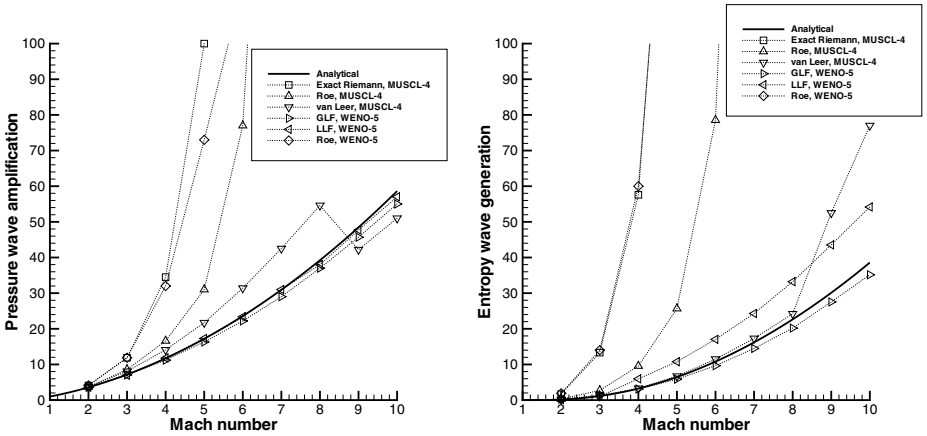

Fig. 2. Pressure wave amplification and entropy wave generation obtained with different schemes

Leer flux vector splitting amplification rates are close to the theoretical curves at low Mach numbers, but tend to deviate as the Mach number grows. Note the sharp change of the slope of the van Leer amplification curves at M ≈ 8. The LLF solver produces almost perfect pressure wave amplification, but its entropy generation is unfortunately much higher than the theoretical curve. We found that close agreement with LIA predictions has been obtained using the 5th order WENO scheme with the global Lax-Friedrichs splitting. The results of these computations are presented in Fig. 3, where the pressure amplitude of the acoustic disturbance interacting with the Mach 8 shock is plotted. It is clear that the transmitted wave amplitude is close to the LIA prediction of 39.2 for the pressure wave amplification. Some high-frequency oscillations are visible in the right plot of Fig. 3 just behind the shock wave located at $x/\lambda = 1$. Although these oscillations are apparently confined within a half-wavelength of the transmitted wave downstream of the shock wave, they may be the reason of slightly lower amplitude of the transmitted pressure wave.

Our two-dimensional computations were performed with an acoustic wave interacting with an oblique shock wave. A comparison of theoretical amplification rates with those obtained using WENO-5 GLF is given in Fig. 4, where the ratio of the pressure disturbance amplitudes behind and ahead of an oblique shock wave is shown as a function of the disturbance incidence angle. The computations are performed for the acoustic waves of amplitude $\delta p_1 = 10^{-4}$ propagating in a supersonic Mach 8 airflow and interacting with a shock inclined at the angle $\alpha = 35^\circ$ to the oncoming flow. LIA transmission coefficients corresponding to this case were obtained using the analytical formulation given in [8]. The angle of the propagation of the acoustic wave was varied in the different computations. It is clear that the amplification rate is close to the linear theory prediction though deviation of the numerically computed amplifications is observed at some angles of incidence.

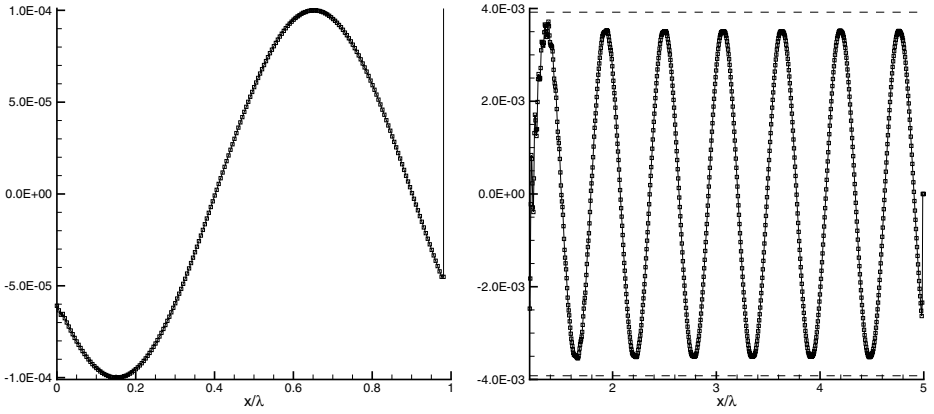

Fig. 3. Pressure amplitude of an acoustic wave interacting with a Mach 8 shock wave obtained with WENO-5 GLF scheme. Shock wave position is $x/\lambda = 1$. Dashed lines correspond to the amplification rate 39.2 predicted by the LIA.

4 Conclusions

Our numerical experiments performed with different high-order shock-capturing flow solvers suggest that the choice of Riemann solver used in evaluating numerical fluxes is extremely important for correct simulation of the transmission of the small-amplitude acoustic disturbance

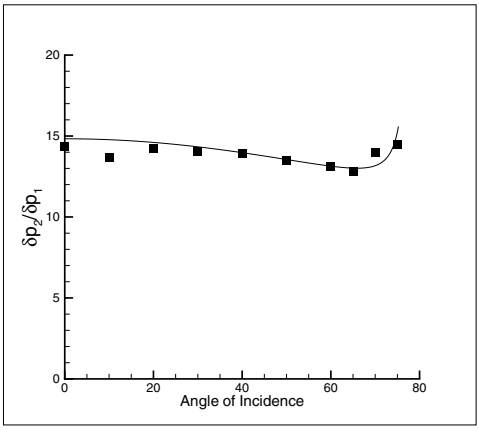

Fig. 4. Pressure amplification rates of an acoustic wave interacting with an oblique shock wave with angle 35° in Mach 8 flow for different angles of incidence of the disturbance wave. Solid line corresponds to the LIA prediction.

wave through a shock. Both the exact Riemann solver and the Roe flux splitting produce amplification rates that are much higher than those predicted by the linear interaction analysis. This discrepancy tends to grow with increasing the Mach number. More diffusive Riemann solvers give amplification rates in much closer agreement with the theory. We found that the global Lax–Friedrichs flux splitting is especially reliable in solving such problems, which was also confirmed in our two-dimensional simulations. A drawback of the global Lax–Friedrichs solver is that its amplification rates are slightly lower than theoretical.

The observed deficiency of the less dissipative Riemann solvers requires thorough investigation. A possible reason for the non-physical amplification of the disturbance wave may be the noise generation mechanism in slowly moving shocks reported in previous studies [7].

5 Future work

We plan to employ the results of this study in investigation of the effects of flow disturbances on regular/Mach reflection transition. It is well known that inside the dual solution domain (DSD) both types of reflection, regular (RR) and Mach (MR) are possible at the same parameters and can be obtained in the numerical simulations. In the wind tunnel experiments the Mach reflection is the preferable shock configuration, which is usually explained by the influence of the wind tunnel disturbances that promote transition from RR to MR at the DSD flow parameters. There is experimental evidence [9] that in low-turbulence facilities both types of reflection are possible in the DSD, and the RR-MR hysteresis is observed at variation of the shock wave angle. However, it is completely unknown what kind of disturbances can cause the RR-MR transition in the DSD in the "noisy" wind tunnels.

We performed some computations with disturbances impinging on the regular shock configuration, but have not yet found any mechanism capable of inducing the forced RR-MR transition. Fig. 5 illustrates the interaction of a planar pressure wave with the RR configuration obtained with the WENO-5 GLF flow solver at M = 8. The amplitude of the pressure disturbance is 0.01. The incident shock angle 35°, which is inside the DSD. The disturbance wave interacts with the incident shocks, transmits through the shocks with amplification, and also generate entropy and vorticity disturbances that travel downstream. Reflections of the acoustic waves between the shocks and the channel walls produce a complex interference pattern. All these

disturbances are then transmitted through the reflected shock waves. The right plot in Fig. 5 shows pressure oscillations behind the reflected shock waves with the amplitude 30–40 times larger of the original pressure wave. These large-amplitude pressure oscillations, however, are insufficient to induce an RR-MR transition in this case.

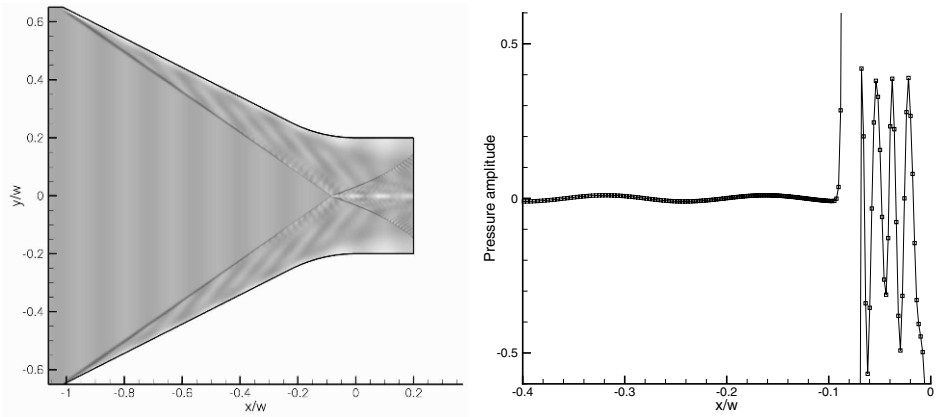

Fig. 5. Interaction of an acoustic wave with regular shock wave reflection in a channel at M = 8. Left figure is the field of total enthalpy; right figure shows the pressure amplitude along the centerline.

Acknowledgement. This study was supported by the Russian Foundation for Basic Research (Grant 05-08-33436).

References

1. S.P. Dyakov: Zh. Eksp. Teor. Fiz. (Sov Phys—JETP) **33** (1957).
2. S. Yamamoto, H. Daiguji: Computers and Fluids **22(2/3)** (1993).
3. G. Jiang, C.-W. Shu: J. Comput. Phys. **126** (1996).
4. D.I. Blokhintsev: Dokl. Akad. Nauk SSSR **47** (1945).
5. J.M. Burgers: Proc. K. Ned. Akad. Wet. **49** (1946).
6. L.D. Landau, E.M. Lifshitz: *Fluid Mechanics, Volume 6 (Course of Theoretical Physics)*, Butterworth-Heinemann, 2nd edition, 1990.
7. T.W. Roberts: J. Comput. Phys. **90** (1990).
8. J.F. McKenzie, K.O. Westphal: Phys. Fluids **11(11)** (1968).
9. M.S. Ivanov et al.: Phys. Fluids **15(6)** (2003).

Novel LBM Scheme for Euler Equations

A. Agarwal[1], A. Agrawal[1], B. Puranik[1], and C. Shu[2]

[1] *Department of Mechanical Engineering, Indian Institute of Technology-Bombay, India.*
[2] *Department of Mechanical Engineering, National University of Singapore, Singapore.*

Summary. Lattice Boltzmann Method (LBM) as a relatively new numerical method has recently achieved considerable success in simulating compressible fluid flows. A hybrid method, which is a combination of the usual Finite Volume Method (FVM) and the LBM, is proposed here to solve the Euler Equations. The inter-cell parameters are obtained by solving the local Riemann problem for each inter-cell using LBM. LBM is a non-iterative process and is thus numerically inexpensive as compared to the Godunov scheme. The proposed scheme is benchmarked for several 1-D problems such as the shock tube problem, the Roe test and the Riemann problem. The results obtained using this hybrid method are compared with those obtained using the Godunov scheme.

1 Introduction

Lattice Boltzmann Method (LBM) has developed as an alternative and promising numerical technique for simulating fluid flows, e.g., [1], [2], [3]. Boltzmann equation is solved to simulate the fluid flow using collision models such as the Bhatnagar-Gross-Krook (BGK) model [4]. The method is computationally less expensive and the boundary conditions can be easily implemented to get high accuracy [5]. It is very effective even with complex boundaries [6] and can also simulate steep shock and contact discontinuity profiles. One of the biggest disadvantages of LBM is that it cannot be used with a non-uniform mesh. FVM along with the use of the Godunov scheme to obtain the interface parameters has been widely used to simulate Euler equations [7]. The key ingredient of this scheme is the solution of a Riemann problem. There is no closed-form solution to the Riemann problem and iterative methods such as the Newton Raphson method are used to obtain the solution. FVM can be used with non-uniform mesh but the use of iterative schemes to obtain the solution of Riemann problem makes the method computationally expensive.

The proposed hybrid method in the present work solves the Euler equations using FVM with the solution to the Riemann problem being obtained by LBM. We employ the compressible perfect gas LB model proposed by Kataoka and Tsutahara [8]. This model allows for the free choice of specific heat ratio. LBM is a non-iterative solver for the Riemann problem and is therefore expected to be more efficient than Godunov scheme. Thus the hybrid method is expectecd to incorporate the advantages of both FVM and LBM.

2 Non-dimensional form of the Euler equations

All variables and equations are expressed in their non-dimensional form for the convenience of numerical calculations and analysis. Let L, ρ_{R0}, and T_{R0} respectively be the

reference length, density and temperature. Then the other non-dimensional variables are defined as

$$t = \frac{\hat{t}}{L/\sqrt{RT_{R0}}},\ x = \frac{\hat{x}}{L},\ y = \frac{\hat{y}}{L} \tag{1}$$

$$\rho = \frac{\hat{\rho}}{\rho_{R0}},\ u_x = \frac{\hat{u_x}}{\sqrt{RT_{R0}}},\ u_y = \frac{\hat{u_y}}{\sqrt{RT_{R0}}},\ T = \frac{\hat{T}}{T_{R0}},\ p = \frac{\hat{p}}{\rho_{R0}RT_{R0}}. \tag{2}$$

The symbol ($\hat{}$) indicates a parameter in its dimensional form.

The two-dimensional time-dependent Euler equations in differential form are

$$U_t + F(U)_x + G(U)_y = 0, \tag{3}$$

where U, F(U) and G(U) are the vectors of conserved variables and fluxes given by

$$U = \begin{bmatrix} \rho \\ \rho u_x \\ \rho u_y \\ E \end{bmatrix},\ F(U) = \begin{bmatrix} \rho u_x \\ \rho u_x^2 + p \\ \rho u_x u_y \\ u_x(E+p) \end{bmatrix},\ G(U) = \begin{bmatrix} \rho u_y \\ \rho u_x u_y \\ \rho u_y^2 + p \\ u_y(E+p) \end{bmatrix}. \tag{4}$$

E (total internal energy per unit volume) is given by

$$E = \rho[0.5(u_x^2 + u_y^2) + e]. \tag{5}$$

Equation of state is given by

$$p = \rho T. \tag{6}$$

A conservative scheme for Eq. 3 is of the form

$$U_{(i,j)}^{n+1} = U_{(i,j)}^{n} + \frac{\Delta t}{\Delta x}[F_{i-1/2} - F_{i+1/2}] + \frac{\Delta t}{\Delta y}[G_{i-1/2} - G_{i+1/2}], \tag{7}$$

where $U_{(i,j)}^{n}$denotes the parameters at the node (i, j) and at time interval n. The inter-cell numerical fluxes F and G are computed using the solution of local Riemann problem. Instead of solving the local Riemann problem in an iterative manner, the LBM scheme is used to calculate inter-cell parameters.

3 LBM scheme for compressible Euler equations

LBM proposed by Kataoka and Tsutahara is used to simulate the inter-cell parameters at the new time step from the known cell and inter-cell parameters at the earlier time step. The solution procedure is non-iterative and is expected to be more efficient than the Godunov scheme where the analytical solution of the local Riemann problem is obtained by iterative procedure.

We now present a synopsis of the LB model developed by Kataoka and Tsutahara. In the Lattice Boltzmann model, the macroscopic variables density, velocity and temperature are defined in terms of a particle velocity distribution function (f_i) as:

$$\begin{cases} \rho = \sum\limits_{1\le i\le I} f_i, \\ \rho u_x = \sum\limits_{1\le i\le I} f_i c_{xi}, \\ \rho u_y = \sum\limits_{1\le i\le I} f_i c_{yi}, \\ \rho[bT + u_x^2 + u_y^2] = \sum\limits_{1\le i\le I} f_i[c_{xi}^2 + c_{yi}^2 + \eta_i^2]. \end{cases} \tag{8}$$

Here, c_{xi} and c_{yi} are the molecular velocities of the particle moving in i^{th} direction (i = 1,2, …, I = 9) and η_i is another variable which has been introduced to control the specific heat ratio. b is a constant which is expressed in terms of specific heat ratio (γ) as

$$b = \frac{2}{\gamma - 1}. \tag{9}$$

The kinetic equation of the non-dimensional form is

$$\frac{\partial f_i}{\partial t} + c_{xi}\frac{\partial f_i}{\partial x} + c_{yi}\frac{\partial f_i}{\partial y} = \frac{f_i^{eq}(\rho, u_x, u_y, T) - f_i}{\epsilon}, \tag{10}$$

where ϵ is the Knudsen number and the distribution function at the old time step is obtained from the equilibrium distribution function, i.e.,

$$f_i^0 = f_i^{eq}(\rho^0, u_x^0, u_y^0, T^0). \tag{11}$$

The two-dimensional Lattice Boltzmann Model is now presented:

$$(c_{xi}, c_{yi}) = \begin{cases} (0,0) & (i=1) \\ v_1\left(\cos\frac{\pi i}{2}, \sin\frac{\pi i}{2}\right) & (i=2,3,4,5) \\ v_2\left(\cos\frac{\pi(i+.5)}{2}, \sin\frac{\pi(i+.5)}{2}\right) & (i=6,7,8,9) \end{cases} \tag{12}$$

and

$$\eta_i = \begin{cases} \eta_0 \ (i=1) \\ 0 \quad (i=2,3,...9) \end{cases} \tag{13}$$

where v_1, v_2 ($v_1 \neq v_2$) and η_0 are non-zero constants.

The local equilibrium velocity distribution function is defined as

$$f_i^{eq} = \rho(A_i + B_i(u_x c_{xi} + u_y c_{yi}) + D_i(u_x c_{xi} + u_y c_{yi})^2) \quad (i = 1,2,3,...9) \tag{14}$$

where

$$A_i = \begin{cases} \frac{b-2}{\eta_0^2}T & (i=1) \\ \frac{1}{4(v_1^2 - v_2^2)}\left[-v_2^2 + \left((b-2)\frac{v_2^2}{\eta_0^2} + 2\right)T + \frac{v_2^2}{v_1^2}(u_x^2 + u_y^2)\right] & (i=2,3,4,5) \\ \frac{1}{4(v_2^2 - v_1^2)}\left[-v_1^2 + \left((b-2)\frac{v_1^2}{\eta_0^2} + 2\right)T + \frac{v_1^2}{v_2^2}(u_x^2 + u_y^2)\right] & (i=6,7,8,9) \end{cases} \tag{15}$$

$$B_i = \begin{cases} \frac{-v_2^2+(b+2)T+u_x^2+u_y^2}{2v_1^2(v_1^2-v_2^2)} \ (i=2,3,4,5) \\ \\ \frac{-v_1^2+(b+2)T+u_x^2+u_y^2}{2v_2^2(v_2^2-v_1^2)} \ (i=6,7,8,9) \end{cases} \tag{16}$$

$$D_i = \begin{cases} \frac{1}{2v_1^4} \ (i=2,3,4,5) \\ \\ \frac{1}{2v_2^4} \ (i=6,7,8,9) \end{cases} \tag{17}$$

The parameters in Eq. 12 and Eq. 13 are chosen to be $v_1 = 1$, $v_2 = 3$, $\eta_0 = 2$. Discretized form of Eq. 10 is used to determine the new inter-cell parameters from the old node and inter-cell parameters in a single time step. In the present work the discretization employed is first order forward in time and first order upwind in space.

4 Results

The hybrid method has been numerically benchmarked against several test cases. These include several one-dimensional initial value problems (IVP) in gas dynamics, demonstrating the generation and propagation of shock waves, rarefaction waves and contact discontinuity waves. Specific heat ratio of the gas in all cases is 1.4 (or $b = 5$) and the time step is set at $\Delta t = \epsilon/4$. All results from this hybrid scheme have been compared with the exact solutions and the results obtained from Godunov scheme.

4.1 The shock tube problem

The rupture of a diaphragm which separates two stationary gases generates a wave system that typically consists of a rarefaction wave, a contact discontinuity and a shock wave. The initial variables of shock tube problem are given by

$$(\rho_L, u_L, T_L) = (1, 0, 1) \quad (x < 0),$$
$$(\rho_R, u_R, T_R) = (5, 0, 1) \quad (x > 0).$$

The pressure and the density profiles within the shock tube at a non-dimensionalized time, $t = 1$, are shown in Fig. 1. It can be noted that the hybrid method is able to capture the wave structure more accurately as compared with the FVM with Godunov scheme.

4.2 The Riemann problem

The Riemann problem is a slight generalization of the shock tube problem in the sense that the two gases on either side of the diaphragm may not be stationary. The given initial conditions generates a centered wave function which consists of two shock waves. The initial variables of Riemann problem are given by

$$(\rho_L, u_L, T_L) = (1, 1, 1) \quad (x < 0),$$
$$(\rho_R, u_R, T_R) = (1, -1, 1) \quad (x > 0).$$

The pressure and the density profiles within the one-dimensional domain at a non-dimensionalized time, $t = 1$, are shown in Fig. 2. It can again be noted that the hybrid method is able to capture the wave structure more accurately as compared with the FVM with Godunov scheme.

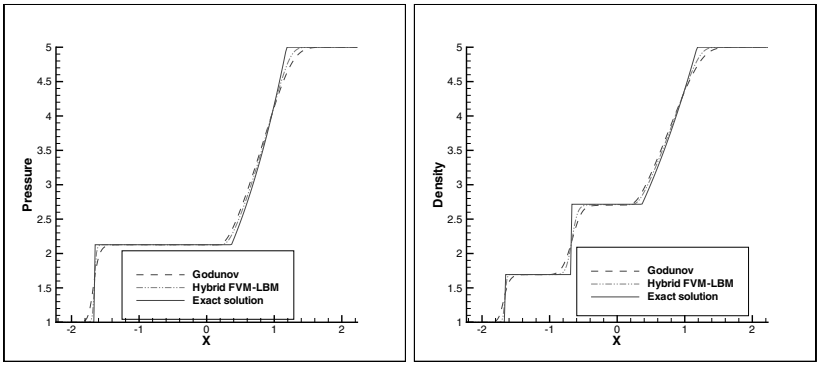

Fig. 1. Shock tube problem: pressure and density profile at $t = 1$ ($\Delta x = 0.02$; $\epsilon = 0.001$)

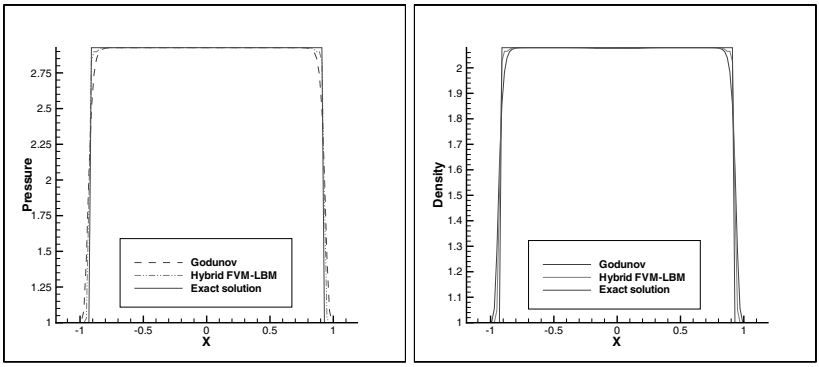

Fig. 2. Riemann problem: pressure and density profile at $t = 1$ ($\Delta x = 0.02$; $\epsilon = 0.001$)

4.3 The Roe test

The given initial condition generates a centered wave function which consists of rarefaction waves. The initial variables of Roe test are given by

$$(\rho_L, u_L, T_L) = (1, -1, 1.8) \quad (x < 0),$$

$$(\rho_R, u_R, T_R) = (1, 1, 1.8) \quad (x > 0).$$

The pressure and density profiles within the one-dimensional domain at a non-dimensionalized time, $t = 0.2$, are shown in Fig. 3. Once again it is seen that the hybrid method is able to capture the wave structure more accurately as compared with the FVM with Godunov scheme.

5 Conclusion

A hybrid method which is a combination of FVM and LBM is presented. The benchmarking tests show that the hybrid FVM-LBM method simulates the shock and contact

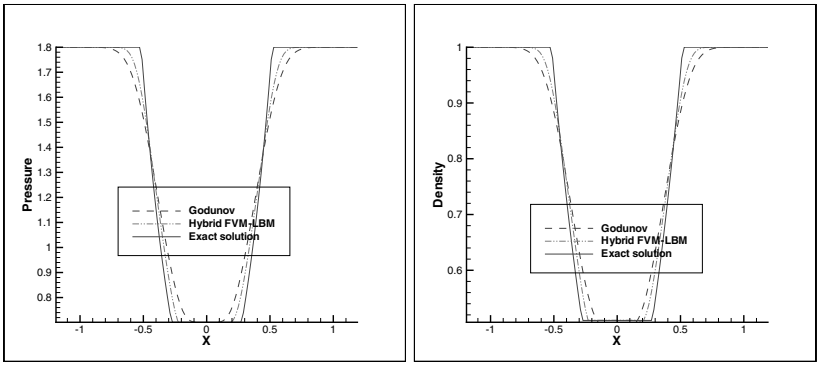

Fig. 3. Roe test: pressure and density profile at $t = 0.2$ ($\Delta x = 0.02$; $\epsilon = 0.001$)

discontinuity profile more accurately as compared to the profiles simulated by the Godunov scheme. The new method is computationally very efficient and this is clearly indicated by the reduced processing times as shown in the Table 1. In order to clearly determine the computational efficiency and accuracy, the hybrid method is required to be employed to simulate multidimensional problems; such efforts are underway.

Table 1. Comparison of processing times for the FVM-LBM scheme and the Godunov scheme

Benchmarking tests	FVM-LBM hybrid scheme	Godunov scheme
Shock tube problem	33.63 seconds	45.71 seconds
Riemann problem	34.78 seconds	46.44 seconds
Roe test (time = 0.2)	7.19 seconds	8.50 seconds

References

1. Succi S.: *The Lattice Boltzmann Equation for Fluid Dynamics and Beyond*, Numerical Mathematics and Scientific Computation, Oxford University Press, 2001.
2. Hudong Chen, Shiyi Chen, Matthaeus, W.H., Recovery of Navier-Stokes equations using a lattice-gas Boltzmann method, Physical Review A, **45**, 8, 5339-5342, 1992.
3. McNamara G. R., Zanetti G., Use of the Boltzmann equation to simulate lattice-gas automata, Physical Review Letters, **61**, 20, 2332-2335, 1988.
4. Bhatnagar P. L., Gross E. P., Krook M., A model for collision processes in gases. I. small amplitude processes in charged and neutral one-component systems, Physical Review, **94**, 3, 511-525, 1954.
5. Maier R. S., Bernard R. S., Grunau D. W., Boundary conditions for the Lattice Boltzmann method, Physics of Fluids, **8**, 7, 1788-1801, 1996.
6. Guo Z., Zheng C., Shi B., An extrapolation method for boundary conditions in Lattice Boltzmann method, Physics of Fluids, **14**, 6, 2007-2010, 2002.
7. Toro E. F.: *Riemann Solvers and Numerical Methods for Fluid Dynamics*, 2nd Edition, Springer Publication, 1999.
8. Kataoka T., Tsutahara M., Lattice Boltzmann method for the compressible Euler equations, Physical Review E, **69**, 056702, 2004.

Numerical simulation of flows with shocks through an unstructured shock-fitting solver

R. Paciorri[1] **and A. Bonfiglioli**[2]

[1] *Università di Roma La Sapienza, Dip. Meccanica e Aeronautica, Via Eudossiana 18, 00184 Rome, (Italy)*
[2] *Università della Basilicata, Dip. di Ingegneria e Fisica dell'ambiente, Viale dell'Ateneo lucano 10, 85100 Potenza, (Italy)*

Summary. A new floating shock-fitting technique featuring the explicit computation of shocks by means of the Rankine-Hugoniot relations has been implemented in an unstructured solver. This paper briefly illustrates the algorithmic features of this orginal technique and the results obtained in the computation of the hypersonic flow past a circular cylinder.

1 Introduction

The computation of flows with shocks by means of the shock-fitting (S-F) technique was proposed by Moretti since the late sixties [1] and adopted by several groups of researchers in the seventies and eighties. Nevertheless, in the nineties the increased computing power along with the availabilty of modern general-purpose codes based on the integral conservation equations produced a loss of interest in the shock fitting techniques.

The complex and difficult implementation of the floating shock-fitting technique in structured-grid solvers has largely contributed to discourage the interest in this type of technique. Indeed, the motion of the shocks throughout the flow-field is obtained by means of floating shock gridpoints which can appear and disappear. This requires the implementation of algorithms which are un-natural in a structured grid setting. As a matter of principle, the management of shock points appears to be simpler within an unstructured grid context. Indeed, the addition, motion and cancellation of shock points and the mesh modifications which are necessary in the neighborhood of the shock front are operations which are less problematic inside an unstructured solver rather than in a structured one.

In the present work, a new floating shock-fitting technique featuring the explicit computation of shocks by means of the Rankine-Hugoniot relations has been implemented in an unstructured solver [2] based on Roe's fluctuation splitting schemes [3].

2 Shock fitting algorithm

The present shock-fitting algorithm is able to compute single shocks occurring within a two-dimensional flow field discretized by an unstructured mesh made of triangles. In its current version, the algorithm does not include any procedure for shock detection and shock interaction. Therefore, the fitted shocks must be present within the flow domain at the beginning of the simulation and no shock interactions between the fitted shocks are presently allowed.

In order to illustrate the algorithmic features of the proposed methodology, let us consider a two-dimensional domain and a shock front crossing this domain at time level t

(see Fig. 1a). The shock front is shown in bold by a polyline whose endpoints are the shock points, marked by squares. A background triangular mesh, whose nodes are denoted by circles, covers the entire computational domain and the position of the shock points is completely independent of the location of the nodes of the background grid. While each node of the background mesh is characterized by a single set of state variables, two sets of values, corresponding to the upstream and downstream states, are assigned to each shock point.

We assume that at time t the solution is known in all grid and shock points. The computation of the subsequent time level $t + \Delta t$ can be split into several steps that will be described in detail in the following sub-sections.

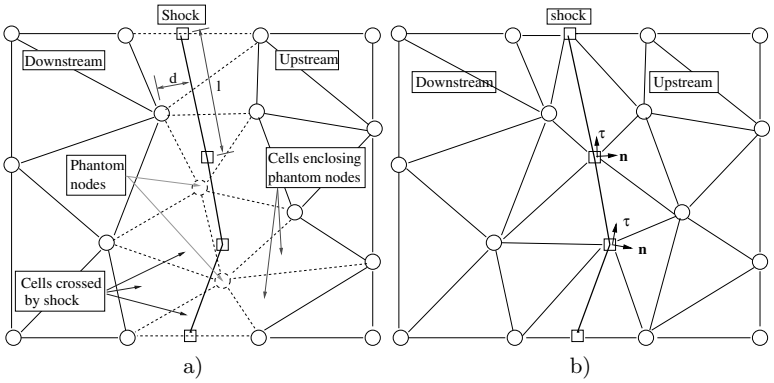

Fig. 1. a) shock front moving over the background triangular mesh at time t: dashed lines mark the cells to be removed; dashed circles denote the phantom nodes; b) the triangulation around the shock has been rebuild

2.1 Cell removal around the shock front

The first step consists in removing the cells around the shock front. More precisely, all cells of the background mesh that are crossed by the shock line are removed along with the mesh points which are located too close to the shock front. These nodes are declared as "phantom" nodes and all cells having at least one phantom node among their vertices are also removed from the background triangulation (see dashed circles and cells in Fig. 1a).

2.2 Local re-meshing around the shock front

Following the cell removal step, the remaining part of the background mesh is split into two regions separated by a hole (or a stripe, if the shock front reaches the outer computational boundary) containing the shock. The hole is then re-meshed using a constrained Delaunay triangulation (CDT): both the shock segments and the edges belonging to the boundary of the hole are constrained to be part of the final triangulation (see Fig. 1b). No further mesh point is added during this triangulation process. At this stage, the computational domain is discretized by a modified mesh in which the shock points and the shock edges are part of the triangulation. This mesh differs from the background mesh only in the neighbourhood of the shock front.

2.3 Computation of the tangent and normal unit vectors

The tangent and normal unit vectors along the shock front have to be computed in each shock point since this is required to properly compute the jump relations (see Fig. 1b). The computation of these vectors in a generic shock point is carried out through specific finite-difference formulas which involve the coordinates of the shock point itself and of its neighbouring shock points that belong to its domain of dependence.

2.4 Solution update using the capturing code

The solution is updated at time level $t+\Delta t$ using the unstructured, shock-capturing code and the modified mesh as input. The modified mesh is split into two non-communicating parts by the shock front which is treated by the code as if it were an internal boundary (see Fig. 2a). This is achieved by replacing each shock point by two superimposed mesh points: one belonging to the downstream region and the other to the upstream region. The downstream and upstream states are correspondingly assigned to each pair of shock nodes. A single time step calculation is performed by the unstructured solver which provides updated nodal values within all grid and shock points at time level $t + \Delta t$. However, the downstream state of the shock points has not been correctly computed except for the following combination of variables:

$$R_d^{t+\Delta t} = a_d^{t+\Delta t} + \frac{\gamma - 1}{2}\mathbf{u}_d^{t+\Delta t} \cdot \mathbf{n} \tag{1}$$

where $\mathbf{n}$ is the shock normal, $a_d^{t+\Delta t}$ and $\mathbf{u}_d^{t+\Delta t}$ are the values of the acoustic and flow velocity of the downstream state of the shock nodes computed by the unstructured solver.

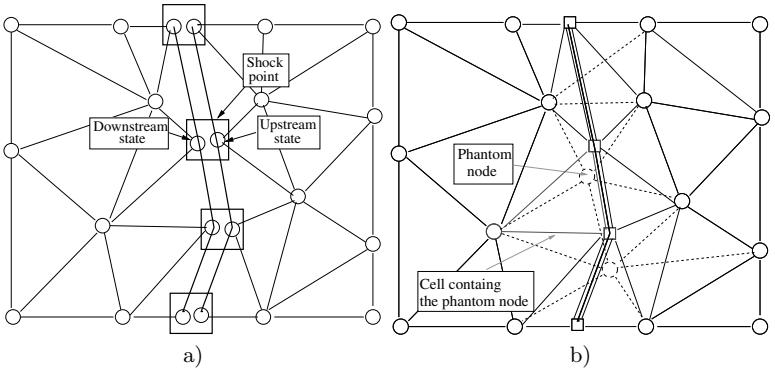

Fig. 2. a) the shock is treated as an internal boundary; b) interpolation of the phantom nodes

2.5 Shock calculation

Each shock point is characterized by an upstream state, a downstream state and a shock speed (w). The upstream state has been updated at time level $t+\Delta t$ in the previous step 2.4. Concerning the downstream state, only the quantity R_d has been correctly updated.

The complete downstream state and the shock speed are computed through a system of five algebraic equations where four equations are the Rankine-Hugoniot relations written with respect to the shock point moving at the unknown speed w. Finally, the last equation of the system is the variable combination of Eq.1 where the value R_d has been computed in the previous step 2.4.

2.6 Interpolation of the phantom nodes

In the previous steps all nodes of the modified mesh have been updated at time level $t + \Delta t$. Nevertheless the phantom nodes, which belong to the background mesh but had been excluded from the modified mesh, have not been updated (see Fig. 2b).

The update of the phantom nodes is performed by first locating each of these within the modified mesh (a search operation which can be efficiently performed on a Delaunay mesh) and then using linear interpolation.

2.7 Shock displacement

The new position of each shock point at time $t + \Delta t$ is computed using the shock speed calculated in the previous step 2.5 by the following first order integration formula:

$$P^{t+\Delta t} = P^t + w^{t+\Delta t}\mathbf{n}\Delta t. \tag{2}$$

The new position of the shock line is obtained (see Fig. 3) by displacing all shock points according to Eq. 2.

2.8 Interpolation of the jumped nodes

During the shock displacement step described in section 2.7, it may occur that the shock passes over several nodes of the background mesh. For instance, in Figure 3 a mesh node whose position at time level t was located in the upstream region, is jumped by the shock, so that its position at time $t + \Delta t$ is in the downstream region. The state of these "jumped" nodes has to be correctly re-computed. This is achieved through linear interpolation. More precisely, the interpolation uses the states of the two shock points belonging to the shock edge jumping the mesh point. In the case shown in the Fig. 3, the jumped node is re-computed by interpolating between the downstream states of the shock points i and $i + 1$ (marked in red).

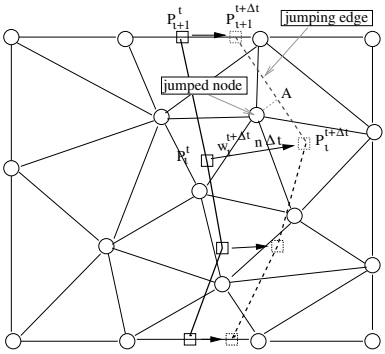

Fig. 3. Mesh points jumped by the shock and their re-computation.

3 Blunt body computation

The test case considers the high speed flow past a circular cylinder at free-stream Mach number, $M_\infty = 20$. The flow is assumed to be inviscid and the solution is computed on a computational domain which surrounds half cylinder. The solution is computed using a very coarse background mesh made of 351 nodes and 29 shock points. Figure 4 displays the background mesh and the modified mesh used during the last iteration. The box on the right, which shows an enlargement of the near shock region, allows to compare these two meshes. It can be observed that these are superimposed everywhere except in the region adjacent to the shock, where the differences between the background (dashed lines) and the modified mesh (continuous lines) are due to the addition of the shock points and edges.

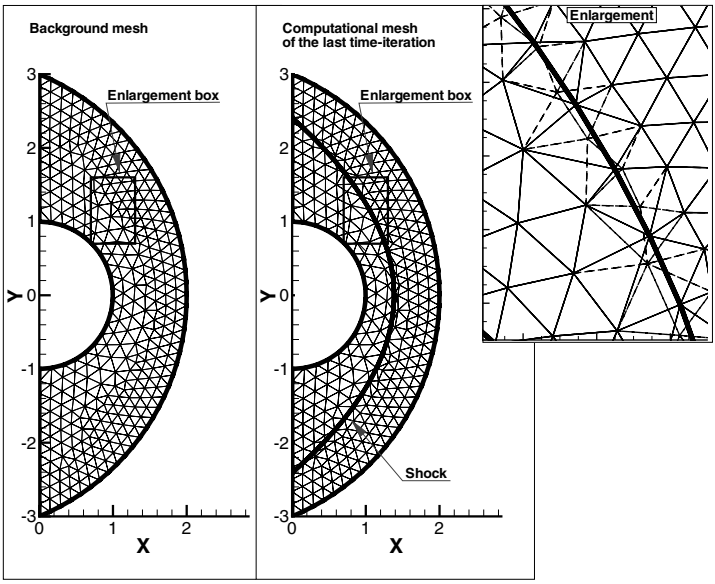

Fig. 4. Comparison between the background and modified mesh of the last time-iteration.

Figure 5 shows the comparison between the solutions computed by the same unstructured code working in shock-capturing and shock-fitting mode. Figure 5 also includes a detailed view of the stagnation point region showing the modifications introduced by the S-F algorithm to the background mesh in order to accomodate the shock line.

The improvements in solution quality due to the shock-fitting technique are evident. In particular, the shock-capturing solution is characterized by a very large shock thickness and by strong spurious disturbances affecting the shock layer region. These disturbances originate from the shock and are caused by the mis-alignment between the edges of the mesh and the shock. On the contrary, the shock-fitted solution shows a very clean field.

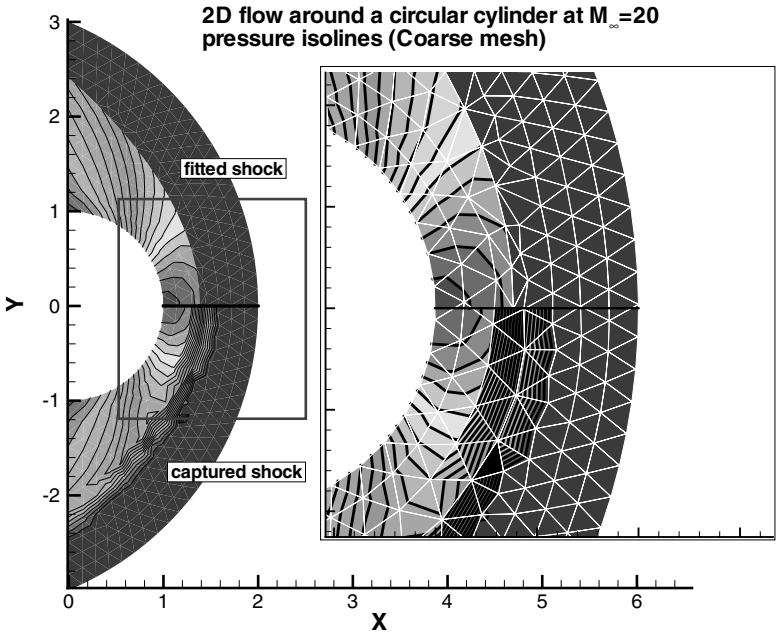

Fig. 5. Coarse grid solutions: comparison between the shock-capturing and shock-fitting solutions

4 Conclusion

The present shock-fitting technique has provided encouraging results and it appears to have a wide developing potential. Concerning the advantages of the proposed implementation of the shock-fitting technique with respect to one adopted in the past in structured-grid solvers, this preliminary work suggests that an important advantage is represented by the easy implementation. Indeed, unstructured solvers easily allow to add and/or remove mesh points and to change the mesh connectivity during the simulation by means of simple operations on the data. Using this capability, it is possible to implement the shock-fitting technique without modifying the computational kernel of the unstructured solver. This reduces the coding effort and it allows to easily couple the proposed shock-fitting technique with other unstructured-grid codes.

References

1. Moretti G. ,Abbett M., A time-dependent computational method for blut body flows, AIAA J 4:2136–2141, 1966
2. Bonfiglioli A., Fluctuation splitting schemes for the compressible and incompressible Euler and Navier-Stokes equations, IJCFD 14:21–39, 2000
3. Deconinck H., Paillère H.,Struijs R., Roe P.L., Multidimensional upwind schemes based on fluctuation-splitting for systems of conservation laws, Journal of Computational Mechanics, 11 (5/6): 23–340, 1993.

Molecular dynamics study of vibrational nonequilibrium and chemical reactions in shock waves

A.L. Smirnov and A.N. Dremin

Institute of Problems of Chemical Physics of Russian Academy of Sciences, Chernogolovka, 142432, Russia

Summary. Energy transfer mechanisms to internal molecular degrees of freedom in shock waves in polyatomic liquids are investigated. The proposed approach uses a new version of the method of nonequilibrium molecular dynamics based on the simplest model potential energy surfaces of reacting polyatomic molecules. The main feature is adaptation of some results and approaches of gas theory to liquids. It is shown that vibrational nonequilibrium is produced by shock compression and influences on chemical reactions. So, the structure of shock waves depends strongly on the peculiarities of vibrational spectra and the structure of normal modes of compounds. The results of numerical simulations demonstrate different shock wave chemistry for substances of almost identical behaviour at static conditions.

1 Introduction

Most liquid explosives consist of polyatomic molecules of complicated structure (ten or more atoms and various bond types). They have high vibrational heat capacity, so that vibrational energy transfer process is of great importance and can influence on the structure of shock and detonation wave in such substances. Available experimental data testify in favour of this opportunity [1]. For example, under shock wave conditions aromatic and aliphatic compounds behave differently, the shock destruction process for aromatic compounds differing from that observed in thermal equilibrium. This was supposed to be connected with the difference in vibrational relaxation times of that compounds.

2 Molecular dynamics

Shock waves in liquids can be simulated by the method of nonequilibrium molecular dynamics [2] based on numerical solution of equations of motion of a large number of atoms. The direct way to account internal degrees of freedom of molecules is to consider the motion of separate atoms on a total potential energy surface (PES). At present numerical simulations of steady state shock waves are carried out usually on empirical PESs. Dynamics of small groups of molecules can be investigated by means of ab initio calculations. Such results involve many details specific to real molecular systems, but it is very difficult to extract any information about individual processes. Besides, both simple ab initio and empirical PESs do not meet precision and reliability requirements. Moreover, they are rather complicated and should be thoroughly examined before used.

In the present work, model PESs are constructed and used as in the previous study [3, 4]. They do not describe rigorously actual molecular systems. However, such PESs have a very simple adjustable structure. Their parameters can be estimated by ab initio calculations for several molecular configurations or can be taken from experiments performed at static conditions.

3 Vibrational energy transfer

Vibrational relaxation theory in gases is well developed at present [5]. It is based on the assumption that intramolecular interactions are much stronger than intermolecular ones. So that corresponding motions are separated in zeroth approximation. Energy exchange processes can be modelled without a detailed dynamical description, i.e. without atomic trajectories based on all atom-atom interactions. The usual way is to put into the Hamiltonian only the terms responsible for the process under investigation. The main result is that the relaxation of mean vibrational energy to its equilibrium value is defined by the Landau-Teller equation

$$dE/dt = -(E - E_0)/\tau$$

where the characteristic time is strongly dependent on temperature and vibrational frequency,

$$1/\tau \approx \left| \int f(t) \cdot \exp(i\omega t)\, dt \right| \approx \lambda^2 \sinh^{-2}(\pi\xi)$$

$\xi = \omega/\alpha v$ - adiabatic parameter, v - the velocity of molecular collision, $\alpha = |(\partial V/\partial r)/V|$ - hardness of intermolecular potential,

$$f = -\frac{\partial V}{\partial x}, \qquad \frac{\partial V}{\partial x} = \lambda \frac{\partial V}{\partial R}$$

The parameters ε and λ determine both rate and special features of vibrational-translational energy exchange in the case of diatomic molecules. These results have been generalized to the case of polyatomic molecules. The parameters λ_k are defined mainly by a structure of normal modes (or by mass ratio in the case of diatomics). They can be determined from the Hessian eigenvectors in some assumptions, but they are treated as independently varying parameters in the current paper. Vibrational-translational exchange rate is proportional to λ at $\lambda \leq 1$. Some nonlinear effects can take place in the case of strong interactions, but they do not affect the dependence of the rate on vibrational excitation of molecules. Some other results and approaches of gas theory have been used as well. Many assumptions are valid for liquids and easily fusible solids. The main difference between gas and liquid is the relative motion of molecules and is taken into account by the simplest variant of molecular dynamics for structureless particles [2].

4 Problem statement

In the absence of chemical reactions, molecules have been simulated by multimode oscillators which interact with each other via isotropic intermolecular potential depending on vibrational coordinates [3]. The Hamiltonian of the system of N molecules:

$$H = \sum_i \left(\mathbf{p}_i^2/2m_i + H_{vib,i} \right) + \sum_{i,j \neq i} V_{ij}$$

here indexes of molecules $i, j < N$, indexes of normal modes $k < K \leq Km$, N_{at} ~10, $K_m = 3N_{at} - 6$, $N \sim 10^3 - 10^6$

The intermolecular potential is taken in the Lennard-Jones form,

$$V_0(r) = 4\varepsilon \left((r_0/r)^{12} - (r_0/r)^6 \right)$$

$$V_{ij} = V_0(|\mathbf{r}_i - \mathbf{r}_j|) \cdot \left(1 + \sum_k \lambda_{ik} x_{ik} + \sum_k \lambda_{jk} x_{jk}\right)$$

and corresponds to the model of "breathing spheres" [5].

The other way to introduce dependency on vibrational coordinates into a simple intermolecular potential is [4]:

$$V_{ij} = V_0(|\mathbf{r}_i - \mathbf{r}_j|), \mathbf{r}'_i = \mathbf{r}_i + \sum_k \lambda_{ik} x_{ik}$$

This formula is more suitable to model chemical reactions due to unlimited vibrational motion. It accounts for a single atom-atom interaction from N_{at}^2 possible ones. Such interactions are almost equivalent from the viewpoint of energy exchange. Simplified forms of intermolecular potential may be used because our goal is not to calculate atomic trajectories. Both techniques permit the splitting into translational and vibrational ones, that are independent on a time step. Thus, conventional monoatomic molecular dynamics is combined with the complicated internal part via a single parameter per each molecule. Pairs of molecules are looked over instead of pairs of atoms, that reduces dramatically calculation expenses from $\approx N_{at}^2 N^2$ to $\approx (N^2 + NK)$

5 Internal Hamiltonian

The internal Hamiltonian corresponds to the sum of harmonic oscillators terms:

$$H_{vib} = (\mu/2) \sum_k \dot{x}_{ik}^2 + U_a$$

$$U_a = (\mu/2) \sum_k \omega_k^2 x_{ik}^2,$$

To take into account unimolecular chemical reactions, the internal part of PES should be changed. In the space of vibrational coordinates of molecules, the simplest PES looks like two minimums with smooth passage through a saddle-point between them. The usual practice is to build such PES from zeroth approximation terms U_a and U_b and interaction U_0 (term's splitting):

$$U = (1/2)\left((U_a + U_b) - \left((U_a - U_b)^2 + U_0^2\right)^{1/2}\right),$$

$$U_b = -Q + (\mu/2) \sum_k \omega_{bk}^2 \left(x_{ik} - x_{bk}\right)^2.$$

The vibrational frequencies in the minimums correspond to normal modes of initial and final molecular states (reagents and products), the level's difference gives a reaction heat effect Q, and the height of the barrier gives an activation energy E_A , that can be adjusted by changing x_{bk}. RRKM theory treats the unimolecular reaction mechanism as separated into two parts, the collisional activation and deactivation process and the microscopic reaction at constant energy. It should be noted that the above information about the PES used here is sufficient to define the chemical system evolution in frames of conventional transition state theory for the case of thermal equilibrium.

6 Results

Numerical calculations have been carried out for different model systems. The cases of both narrow and wide spectra of low frequency vibrations (like benzene and hexane respectively) were considered carefully:

$$(I) \qquad \omega_k = 100, 150, 200, 300, 400, \qquad K = 5,$$

$$(II) \qquad \omega_k = 320, 340, 360, 380, 400, \qquad K = 5.$$

Vibrational heat capacity tends to zero at low temperatures due to quantum effects:

$$C_{vib} \to 0 \qquad at \qquad \theta = \frac{\hbar\omega}{k_B T} \geq 1$$

So, some high frequency modes can not be treated by classical mechanics and they should be excluded. Vibrations can absorb energy at $T < 1000$ K only if $\omega_k < 700cm^1$, so that a very small number of modes should be taken into account in this molecules.

The results of calculations (Figure 1) display that shock wave in a liquid starts with a relatively narrow zone of translational nonequilibrium (shock front). In the case of polyatomic molecules, the front is followed by a relaxation zone in which traslational energy is transferred to internal degrees of freedom of the molecules. In the relaxation zone's head the total energy is allocated on translational, rotational and low frequency vibrational degrees of freedom, so that their mean energies exceed the equilibrium values defined by the temperature far behind the front. The case of wide vibrational spectrum (I) is presented in Figure 1.

Low frequency vibrations are overheated due to exponential term. In absence of low frequency vibrations (Figure 2, II) traslational energy exceeds the equilibrium values for

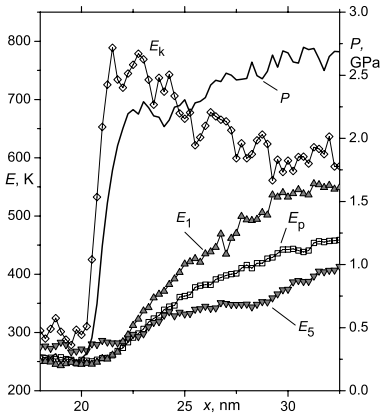

Fig. 1. Pressure P and energies, kinetic E_k, vibrational E_1 and E_5, and total vibrational potential energy E_p versus distance along shock wave propagation, x. System (I).

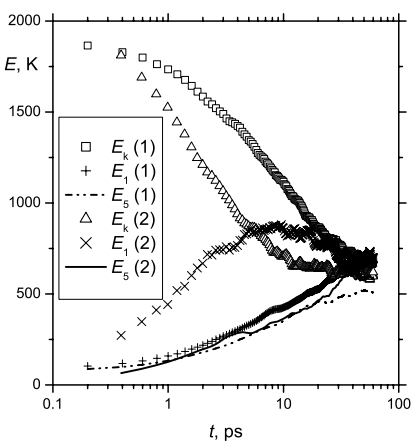

Fig. 2. Energies, kinetic E_k, vibrational E_1 and E_5, versus time. System (I) and (II).

longer period. In the case of narrow spectrum the difference in λ_k can result in vibrational nonequilibrium. If a substance has a large vibrational heat capacity, the overheat can be quite significant and influence chemical reactions in the relaxation zone.

7 Shock wave chemistry

Shock waves are usually simulated by molecular dynamics in very large systems with walls in x dimension and with periodic boundary conditions in y and z dimensions [2]. This is the technique used in current work. The main action of a shock wave is supposed to produce translational nonequilibrium. Some techniques were tested to simulate the shock action in small systems. The most suitable results have been achieved by changing the x size in time, while periodic boundaries in x direction have been used also to exclude near-wall effects. This method is used to compare static and shock wave chemistry in the case of slow reactions. Examples of such calculations are presented in Figure 3 and Figure 4.

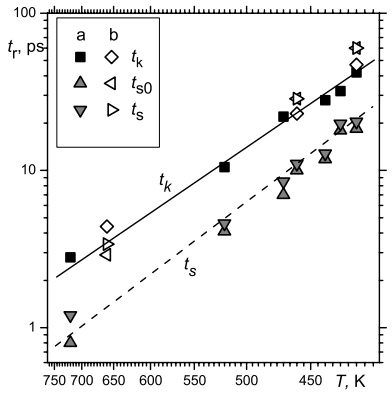

Fig. 3. Chemical reaction time versus temperature. Systems (a) and (b) without heat release. Small volume shock compressed (t_s, t_{s0}) and preheated (t_k) in the same final volume.

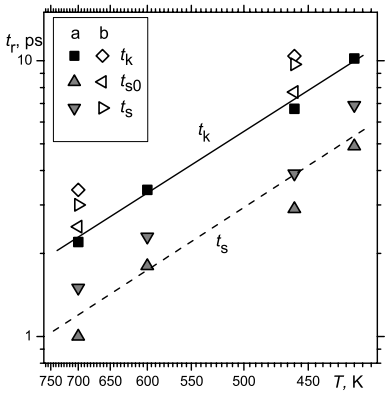

Fig. 4. Chemical reaction time versus temperature. Systems (a) and (b) with heat release (Q=10000 K). Small volume shock compressed (t_s, t_{s0}) and preheated (t_k).

Values (t_s), and t_{s0} are measured from the start and finish of compression. Final volumes are the same for all data points. Compression rate is constant and varies from one point to another. All systems have a narrow spectrum (II), and different sets of λ_k. Both systems presented in Figure 3 permit chemical reaction with an activation energy E_A=3000 K and without heat effect, Q=0. Reaction mode (k=5) of system (a) relaxes faster than other modes (1-4) due to the difference in λ_k, so that it takes more energy than in equilibrium. Reaction rate depends mainly on the mean vibrational energy of the reaction mode and raises compared to thermal conditions. In the case of system (b),

the passive modes (1-4) relax slightly faster than active one. The reaction rate tends to an equilibrium value. Straight line (t_k) approximates the reaction time in system (a) at thermal conditions. It roughly corresponds to both thermal (t_k) and shock compressed (t_s) data for system (b) also. These results demonstrate different shock wave chemistry for substances of almost identical behaviour at static conditions.

The systems presented in Figure 4 permit chemical reaction with an activation energy E_A=4000 K and with heat effect, Q =10000 K. The results and explanation are similar to the previous case (Q=0). However, chemical kinetics in the exothermic case (Q=10000 K) corresponds to a thermal explosion, i.e. the dependence of n on time has accelerated growth, and the process has noticeable ignition delay. While there is decreasing growth without any delay in the isothermic case (Q=0). So, these are quite different processes.

8 Conclusion

The advantages of the model proposed are the following: (i) low calculation expenses, (ii) the simplest way to exclude high frequency vibrations, and (iii) small number of physically significant parameters, that can vary independently. Its basic application seems to estimate some fast transient effects in polyatomic liquids and also to produce input data for problems formulated within the framework of kinetic or phenomenological approaches.

The calculations have shown that vibrational nonequilibrium is produced by shock compression and influences chemical reactions. So, the structure of shock waves depends strongly on the peculiarities of vibrational spectra and the structure of normal modes of compounds.

References

1. Dremin A. N., Babare L. V., The shock wave chemistry of organic substances. In: AIP Conference Proceedings “Shock Waves in Condensed Matter - 1981” (Menlo Park). N.Y., pp. 27-41. 1982.
2. Klimenko V. Y., Dremin A. N., Structure of shock wave front in a liquid. In: Detonation. Chernogolovka, , pp. 79-83, 1978.
3. Smirnov A. L., Karkach S. P., Skrebkov O. V. and Dremin A. N., Molecular dynamics study of vibrational - translational nonequilibrium in a liquid of polyatomic molecules behind shock wave front. Minsk International Colloquium on Physics of Shock Waves, Combustion, Detonation and Non-Equilibrium Processes. MIC 2005, Minsk, 12 - 17 Nov. 2005.
4. Smirnov A. L. and Dremin A. N., Molecular dynamics modelling of shock and detonation fenomena in liquids of polyatomic molecules. In: Proc. of 13th International Detonation Symposium. Norfolk, Virginia. July 23 - 28, 2006.
5. Herzfeld K. F., Litovitz T. A., Absorption and dispersion of ultrasonic waves. N.Y.-Lond.: Acad.Press. 1959.

Parallel algorithm for detonation wave simulation

P. Ravindran and F.K. Lu

Aerodynamics Research Center, Mechanical and Aerospace Engineering Department, The University of Texas at Arlington, Arlington, Texas 76019, USA

Summary. A parallel algorithm which has sufficient scalability for time accurate solution of a propagating detonation wavefront is developed. The emphasis is placed on reduction of computational time without compromising accuracy. The flow was assumed to be unsteady, inviscid and non-heat-conducting and coupled with finite-rate chemistry. A finite volume formulation was employed to ensure conservation and proper handling of discontinuities. A Runge-Kutta second order scheme was utilized for a time accurate solution, with Roe second order flux splitting scheme for spatial solution. For additional higher order spatial accuracy, van Leer MUSCL technique was employed. Equation stiffness was overcome by point implicit treatment of the source terms. The parallel algortihm was developed using Message Passing Interface standard.

1 Introduction

Detonation phenomena have been systematically examined theoretically, experimentally and computationally for over a century, beginning with a one-dimensional propagating detonation front as a discontinuity according to the Chapman–Jouguet (CJ) theory [1,2] and the theory of Zel'dovich, Von Neumann and Döring, which has come to be known collectively as the ZND detonation model [3–5]. The development of numerical techniques for solving high temperature, non-equilibrium flow was pivotal in leading the effort in detonation wavefront simulation. An accurate simulation of the detonation wavefront is a great challenge on computational resources, forcing the use of simplistic approaches which compromises the accuracy of the solution. To overcome these limitations, the solution was initially to employ supercomputers, which in the long run had many inherent difficulties such as their monolithic nature, cooling, bandwidth/latency problems and limited data transmission [6]. In recent years, with the advent of high-performance cluster computing, most of the challenges associated with monolithic supercomputers have been met and addressed.

The development of a parallel algorithm for time accurate solution of a detonation wavefront is reported [7]. The parallel algorithm was developed using the Message Passing Interface standard developed by the Argonne National Laboratory [8] for the purposes of solving the governing equations in a distributed environment.

2 Governing Equations

The time-dependent conservation equations are those for an inviscid, non-heat-conducting, reacting gas flow in which thermal nonequilibrium is modeled with a two-temperature approximation. The conservation equations for the individual species are derived first, and then these are combined to yield the complete set of equations. For

brevity the procedure is summarized here: details can be found in [7]. A simplification comes from the assumption that molecular diffusion is not significant and can be safely neglected when the chemical reactions and the corresponding energy release occur rapidly as in a detonation process. A general representation of species internal energy includes a portion of the internal energy in thermodynamic equilibrium and the remaining portion in a nonequilibrium state. The equilibrium portion of the internal energy is the contribution due to translational and internal modes that can be assumed to be in equilibrium at the translational temperature T. The remaining nonequilibrium portion is the contribution due to internal modes that are not in equilibrium at the translational temperature T, but may be assumed to satisfy a Boltzmann distribution at a different temperature. For the temperature range of interest in the present study, the rotational mode is assumed to be fully excited and in equilibrium with translational temperature T, while the electronic excitation and free electrons modes can be safely ignored.

High temperature flows typically involve some chemical reactions, and the time scale in which chemical reactions take place is important in the estimation of flow field properties. For accurate modeling of a detonation wave, especially in the detonation front where rapid chemical reactions take place in the shock compressed region, species continuity equations based on the chemical kinetics should be solved together with fluid dynamic equations to account for possible chemical nonequilibrium. According to Landau-Teller formulation [10], it is reasonable to assume that the vibrational level of a molecule can change only by one quantum level at a time. This approximation not only reduces the number of species dependent parameters but also simplifies the evaluation of the vibrational relaxation term multiplied by the difference in the translational and vibrational temperature. So, when a point implicit formulation is used on the source terms in the numerical algorithm, the above approximation greatly simplifies an implicit treatment of the temperature difference which drives the relaxation process.

3 Numerical and Parallel Algorithm Formulation

A discretized set of equations has been derived from the governing equations using finite volume approach due to its conservative property. Nonequilibrium flows involving finte-rate chemistry and thermal energy relaxation can be difficult to solve due to stiffness issues associated with varying orders of characteristic time-scales. To overcome this, the point implicit formulation evaluating the source terms at time level $n + 1$ has been an effective method used to numerically integrate stiff systems by effectively rescaling all characteristic times in the flow fields into the same order of the magnitude [11]. An extension of Roe scheme to a thermo-chemical nonequilibrium gas has been used for second order accuracy [12] and higher order approximation using MUSCL approach for added spatial accuracy, has been adapted for this work. A modified Newton-Raphson scheme has been used to calculate temperature at each iteration level. For temporal accuracy, a two-step Runge-Kutta scheme has been implemented.

To adapt the numerical solution to a computer cluster, a parallel algorithm has been designed with the primary objectives being scalability and portability. MPI (Message Passing Interface) has been selected due to its inherent advantages of portability acrss different machine architectures, smooth operation in heterogeneous systems, and to allow efficient implementations across machines of differing characteristics [8]. Figure 1 gives a schematic representation of an instance of data transfer in each iteration. The algorithm implemented has an advantage wherein all the values needed from a neighbor are brought

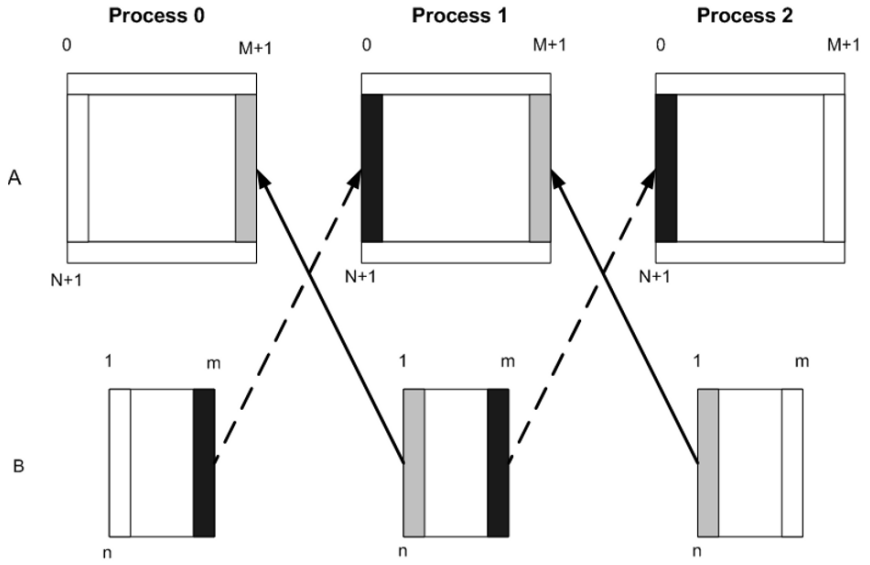

Fig. 1. Block partitioning with overlap and communication pattern

in one message. Coalescing of communications in this manner reduces the number of messages and improves performance.

4 Results

A 50 cm long and 10 cm high channel is used for the detonation channel and the computational domain is discretized into 100×150 grid cells. The grids are clustered near the walls to capture the boundary layer. Adiabatic wall boundary conditions are imposed on the upper and lower sides of the computational domain whereas supersonic inflow and outflow were imposed on the left and right side respectively, with an ambient pressure of 1 atm imposed at the outlet of the channel. Pre-mixed hydrogen-air gas at an ambient pressure of 2 atm and temperature of 500 K is set to flow into the channel with a incoming Mach number of 2. The mixture is ignited by a localized hot-spot at approximately 0.1 m into the channel from the left end. The hot spot is 1 mm long and 5 mm high with a pressure of 30 atm and a temperature of 3000 K. Detonation waves are immediately generated and the initiation and propagation are shown in pressure contour plots in figure 2.

The parallel algorithm was tested on the LoneStar cluster in the Texas Advanced Computing Center, a part of the national TeraGrid project, for benchmarking as well as scalability purposes. Figure 3 illustrated the scalability obtained from the parallel algorithm over a range of processors and increasing iterations. It is observed that with the present algorithm, maximum scalability was obtained when more iterations were computed, which indicates the good performance of the MPI parallel subroutines. As with any parallel algorithm, there would be a point where scalability reduces and the ensuing communications bottleneck would actually increase computation time. Figure 4

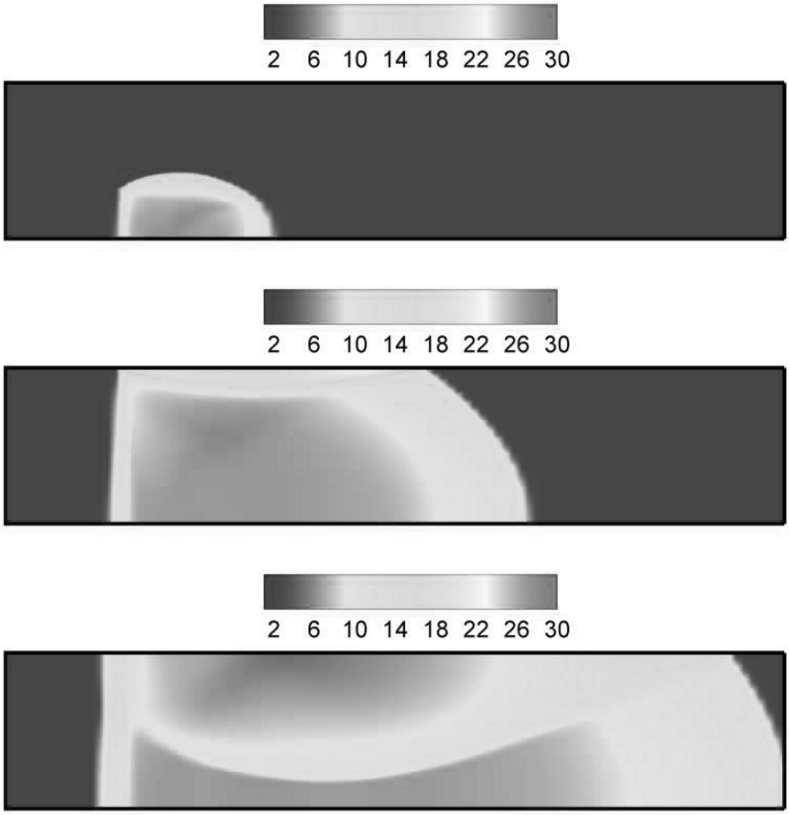

Fig. 2. Pressure contours for a detonation wave propagation in a channel

illustrates the issue of blockage and communication meltdown arising due to increasing communication messages with more number of processors. Figure 5 shows the memory usage of the process threads vary linearly with increasing processors indicating that the algorithm performs effective memory distribution.

The implemented algorithm has proven to be highly efficient and reliable in terms of accuracy and reduces computation time due to good scalability. A detailed study involving computation timelines has been performed and found out to be reasonable within bounds at evidenced by the results.

Acknowledgement. The authors acknowledge the support of the Texas Advanced Computing Center for the computations reported here.

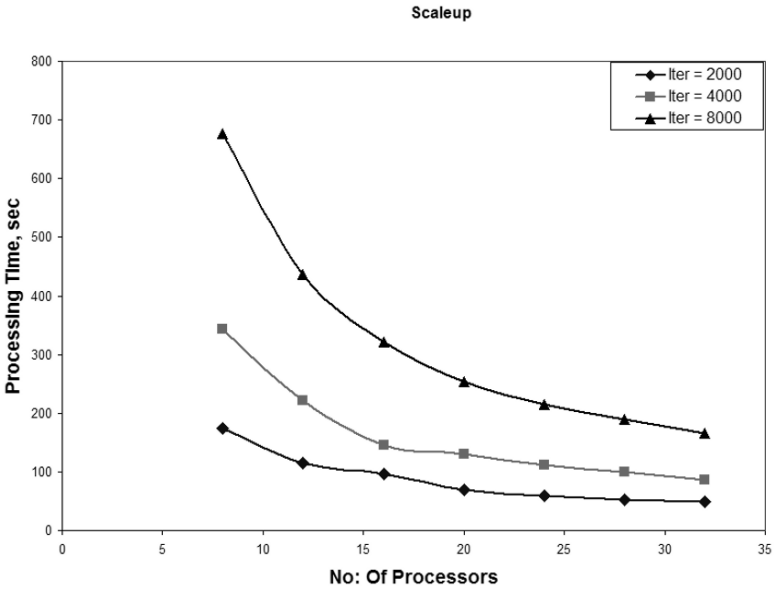

Fig. 3. Scaleup diagram for varying iterations

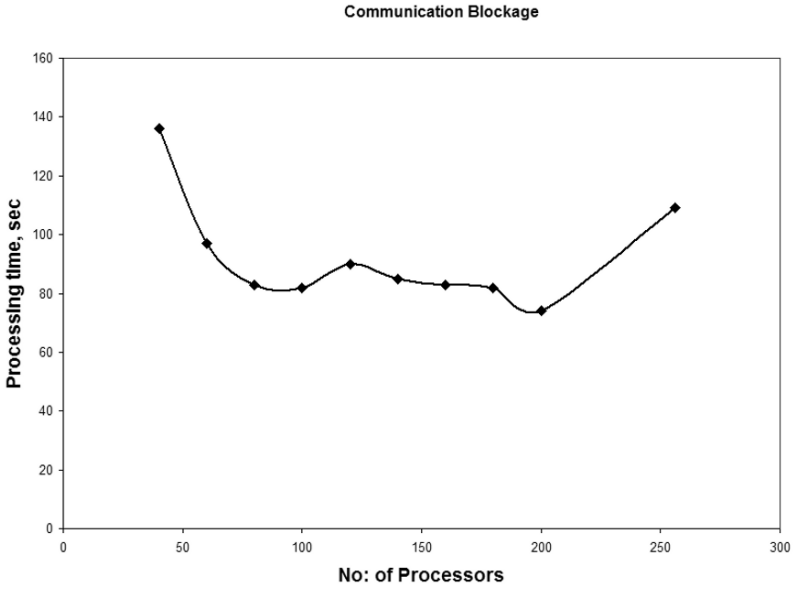

Fig. 4. Communication blockage

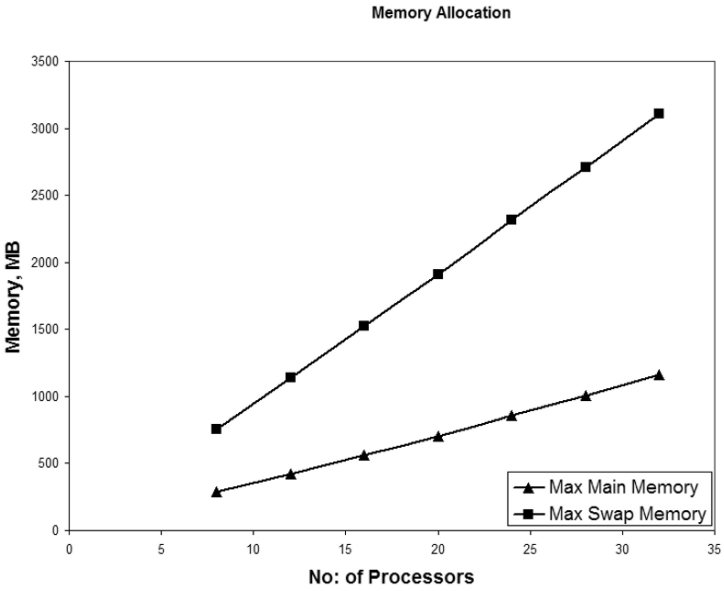

Fig. 5. Main memory and swap memory usage by the process threads

References

1. Chapman, D.L.: On the rate of explosion in gases. In: *Philos. Mag.*, 47, pp. 90–104 (1899)
2. Jouguet E.: On the propagation of chemical reactions in gases. In: *J. de Mathematiques Pures et Appliquees*, 1, pp. 347–425 (1906)
3. Zel'dovich, Ya.B.: On the theory of the propagation of detonations on gaseous system. In: *Zh. Eksp. Teor. Fiz.*, 10, pp. 542–568 (1940)
4. von Neumann, J.: Theory of detonation waves. Progress Report to the National Defense Research Committee Div. B, OSRD-549, (April 1, 1942. PB 31090); In: Taub, A.H. (ed). *John von Neumann: Collected Works, 1903-1957*, Vol. 6, Pergamon Press, New York, 1963
5. Döring, W.: On detonation processes in gases. In: *Ann. Phys.*, 43, pp. 421-436 (1943)
6. Arnold G., Eicker N., Lippert T., Schilling K. (2001): Cluster computing vs. Cray T3E-a case study from numerical field theory In: *Proc 9th Euromicro Workshop on Parallel and Distributed Processing*, Mantova, Italy, pp. 475–479, IEEE Computer Soc, Los Alamitos, California, USA, (Feb 7–9 2001)
7. Ravindran, P.: Numerical simulation of pulse detonation phenomena in a parallel environment. MSAE thesis, University of Texas at Arlington, Arlington, Texas, USA (December 2005)
8. Gropp W., Lusk E., Doss N., Skjellum A.: A high-performance, portable implementation of the MPI message passing interface standard, *Parallel Computing*, 22(6), pp. 789–828 (1996)
9. Gropp W., Lusk E., Skjellum, A.: *Using MPI*, 2nd ed. (MIT Press, 1999)
10. Vincenti, W.G., Kruger, C.H.: *Introduction to Physical Gas Dynamics* (Krieger Publishing Company, 1965)
11. Bussing, T., Murman, E.: Finite volume method for the calculation of combustible chemically reacting flows *AIAA J.*, 26(9), pp. 1070–1078 (1988)
12. Grossmann, B., Cinella, P.: Flux-split algorithms for flows with nonequilibrium chemistry and vibrational relaxation. In: *J. Comp. Phys.*, 88(1), pp. 131–168 (1990)

Shock detection and limiting strategies for high order discontinuous Galerkin schemes

C. Altmann, A. Taube, G. Gassner, F. Lörcher, and C.-D. Munz

IAG - Institut für Aerodynamik und Gasdynamik, Universität Stuttgart, Pfaffenwaldring 21, 70569 Stuttgart Germany

1 Introduction

Discontinuous Galerkin (DG) schemes are a combination of finite volume (FV) and finite element (FE) schemes. While the approximate solution is a continuous polynomial in every grid cell, discontinuities at the grid cell interfaces are allowed which enables the resolution of strong gradients. How to calculate the fluxes between the grid cells and to take into account the jumps is well-known from the finite volume community. Due to their interior grid cell resolution with high order polynomials the DG schemes may use very coarse grids. In this approach the cumbersome reconstruction step of finite volume schemes is avoided, but for every degree of freedom a variational equation has to be solved. The main advantage of DG schemes is that the high order accuracy is preserved even on distorted and irregular grids. In the following we present a DG scheme based on a space-time expansion (STE-DG), which was proposed in [4]. Our scheme features *time consistent* local time-stepping, where every grid cell runs with its optimal time step.

An open issue for DG schemes in general is an efficient shock-capturing strategy. The very successful FV shock-capturing consists of a TVD or WENO reconstruction which is non-oscillatory. In combination with local grid refinement a narrow transition zone at the shock wave is obtained within ~ 4 grid cells. This can also be extended to DG schemes in a way such that the trial function is locally replaced by a reconstructed polynomial. As the efficiency of our STE-DG scheme relies on the locality of the spatial discretization, the use of this shock-capturing technique is cumbersome, especially for high order. Another approach which is more convenient for DG schemes is to keep the large grid cell and to resolve the shock within the grid cell by a narrow viscous profile by locally adding some sort of artificial viscosity. This was recently proposed by Persson and Peraire [5]. Their approach is quite contradictory to FV shock-capturing, since here the order of accuracy is kept high or is even increased locally. Persson and Peraire showed that this strategy captures the shock within a transition zone the size of $\delta = \frac{4h}{p+1}$ where p denotes the degree of the polynomial approximation. In this case the shock profile can be sharpened by increasing the degree of the trial function (p-adaptation). While Persson and Peraire applied this shock-capturing by p-refinement within an implicit scheme, we combine it with an explicit scheme which leads to an anisotropic time step distribution due to the stability restriction. But, due to our local time-stepping feature the efficiency is well preserved.

2 The STE-DG scheme for the Euler equations

2.1 The equations and the semi-discrete variational formulation

The Euler equations in two space dimensions read as

$$\mathbf{U}_t + \mathbf{F}\left(\mathbf{U}\right)_x + \mathbf{G}\left(\mathbf{U}\right)_y = \mathbf{0} \tag{1}$$

with

$$\mathbf{U} = \begin{pmatrix} \rho \\ \rho u \\ \rho v \\ \rho e \end{pmatrix}, \quad \mathbf{F} = \begin{pmatrix} \rho u \\ \rho u^2 + p \\ \rho uv \\ \rho u(e+p) \end{pmatrix}, \quad \mathbf{G} = \begin{pmatrix} \rho v \\ \rho uv \\ \rho v^2 + p \\ \rho v(e+p) \end{pmatrix}, \tag{2}$$

where ρ, u, v, p, and e denote the density, x- and y-velocity, pressure, and specific total energy, respectively. We consider the equation of state of a perfect gas with

$$p = \rho RT = (\gamma - 1)\rho\epsilon \quad \text{and} \quad e = \frac{p}{(\gamma-1)\rho} + \frac{u^2+v^2}{2}, \tag{3}$$

where ϵ denotes the specific internal energy, γ is the isentropic exponent, and R is the gas constant.

The spatial discretization is based on the weak formulation of equation (1). We multiply the Euler equations with an arbitrary test function $\mathbf{\Phi}(\mathbf{x})$, integrate over the grid cell Q_i and use integration by parts for the flux terms to get

$$\int_{Q_i} \mathbf{U}_t \cdot \mathbf{\Phi}\, dx + \int_{\partial Q_i} \mathbf{F}_n \cdot \mathbf{\Phi}\, ds - \int_{Q_i} \left(\mathbf{F}\cdot\mathbf{\Phi}_x + \mathbf{G}\cdot\mathbf{\Phi}_y\right) dx = 0, \tag{4}$$

where ∂Q_i denotes the surface of the grid cell and $\mathbf{F}_n$ is normal component of the flux.

To get the semi-discrete DG scheme we introduce a piecewise polynomial approximation $U_h(\mathbf{x}, t)$, which is defined as

$$U_i(\mathbf{x}, t) := \sum_{l=1}^{N(p)} \hat{\mathbf{U}}_l^i(t)\, \varphi_l(\mathbf{x}) \tag{5}$$

in every grid cell Q_i. Using a trial space of piecewise polynomials with a degree $\leq p$, we can introduce an orthonormal basis $\{\varphi\}_{l=1}^{N(p)}$, where $N(p) = (p+1)(p+2)/2$ in two space dimensions. We choose as test functions the basis functions and get the following $N(p)$ ordinary differential equations for the $N(p)$ unknowns

$$(\hat{U}_l^i)_t = -\int_{\partial Q_i} \mathbf{H}\cdot\boldsymbol{\varphi}_l\, ds + \int_{Q_i} \mathbf{F}\cdot(\boldsymbol{\varphi}_l)_x + \mathbf{G}\cdot(\boldsymbol{\varphi}_l)_y\, dx = 0, \quad l = 1, ..., N(p). \tag{6}$$

As numerical flux we use the HLLC flux (see, e.g., [1]) named $\mathbf{H}$.

2.2 The space-time expansion approach with local time-stepping

For the STE-approach the semi discrete scheme (6) is simply integrated in time. Due to the local time stepping, we give up the assumption that all grid cells run with the same

time step and therefore we do not have any longer a common time level. Let us denote the actual local time level in grid cell Q_i by t_i^n. The degrees of freedom $\hat{\mathbf{U}}_l^{i,n}$ represent the solution at t_i^n in this grid cell. Furthermore, each cell may evolve in time with its local time step Δt_i^n which has to satisfy the local stability restriction, which depends on the grid cell diameter as well as on the order $p+1$, see [4]. With Δt_i^n, the next local time level in Q_i is given as

$$t_i^{n+1} = t_i^n + \Delta t_i^n. \tag{7}$$

The evolution equations for the degrees of freedom read as

$$\hat{U}_l^{i,n+1} = \hat{U}_l^{i,n} - \int\limits_{\partial Q_i} \mathbf{H} \cdot \boldsymbol{\varphi}_l \, ds + \int\limits_{Q_i} \mathbf{F} \cdot (\boldsymbol{\varphi}_l)_x + \mathbf{G} \cdot (\boldsymbol{\varphi}_l)_y \, dx = 0, \quad l = 1, ..., N(p). \tag{8}$$

To evaluate the right hand side of the evolution equations the space-time integrals are approximated by proper Gaussian integration rules. The difficulty is, that the values at the space-time Gauss points are not known. In the STE-approach a space-time Taylor expansion of the approximation U_i at the grid cell barycenter $\mathbf{x}_i$ at time level t_n

$$\widetilde{\mathbf{U}}_i(x,t) := \sum_{l=0}^{p} ((t - t_i^n)\, \partial_t + (\mathbf{x} - \mathbf{x}_i)\boldsymbol{\nabla})^l U(x,t)|_{\mathbf{x}_i, t_n} \tag{9}$$

is used to get an high order approximation at every space-time Gauss point. While the space derivatives are already available within the DG approach, the mixed space-time derivatives are approximated using the (CK-) Cauchy-Kovalevskaya procedure. To replace the time and mixed space-time derivatives the evolution equation is applied several times, see [4] for more details.

As the evaluation of the fluxes between the grid cells on the right hand side relies on neighbor data as well, the local time-stepping algorithm is based on the following evolve condition: The evolution of the DOF are performed, if

$$t_i^{n+1} \leq \min\left\{t_j^{n+1}\right\}, \forall j : \, Q_j \cap Q_i \neq \emptyset \tag{10}$$

is satisfied. This means that an element can only be updated in time, if all neighboring elements' j prospective time level is bigger than the one from element i in concern. This guarantees that the approximate space-time values of the neighbor cells are available. In this manner, the algorithm continues by searching for elements satisfying the evolve condition (10). So all elements are evolved in a suitable order by evaluating the different terms of the right hand side of equation (8) for each element in an effective order. At each time, the interface fluxes are defined uniquely for both adjacent elements, making the scheme exactly conservative, for more details see [2].

3 Sub-Cell Shock Capturing for DG methods

The first step is to detect grid cells in which a strong gradient is approximated and which will lead to spurious oscillations in the approximative piecewise polynomial. In order to determine a suitable sensor for under-resolved parts, we make use of the fact that the solution within each element is represented in terms of an orthogonal basis

$$\mathbf{U}_i(x,t_n) = \sum_{l=1}^{N(p)} \hat{\mathbf{U}}_l^i \mathbf{\Phi}_l. \tag{11}$$

If the underlying exact solution is smooth, we expect the coefficients of the approximation to decay fast. E.g., using the density ρ from the set of conservative variables we apply as proposed in [5] a smoothness sensor in the form

$$S_i := \frac{\sum_{l=N(p-1)+1}^{N(p)} (\hat{\rho}_l)^2}{\sum_{l=1}^{N(p)} (\hat{\rho}_l)^2}. \tag{12}$$

This expression measures the rate of the decay of the magnitude of the coefficients If this rate is low then we have identified a strong gradient which is not well resolved by the local polynomial, e.g. a shock wave. Once the shock has been sensed, we modify the equation locally in this grid cell by introducing an artificial viscosity of the form

$$\mathbf{U}_t + \mathbf{F}(\mathbf{U})_x + \mathbf{G}(\mathbf{U})_y = \nabla \cdot (\varepsilon \nabla \mathbf{U}). \tag{13}$$

The piecewise constant viscosity ε is chosen as a function of the value S_i of the discontinuity sensor and proportional to the available resolution $\sim \frac{4h_i}{p_i+1}$ within the grid cell, see [5] for details. The discretization of the viscous terms is based on exact diffusive Riemann solutions for parabolic equations, see [2] and [3] for details.

4 Results

This section contains results of one- and two-dimensional test cases to show the properties of the STE-DG scheme with this shock-capturing technique.

4.1 Shock Capturing

To demonstrate the capabilities of the shock capturing method we performed a simple test using a Mach 10 shock moving through the computational domain. In addition to our scheme, we performed for comparison the calculation also with a 4^{th} order WENO reconstructed Finite Volume scheme and a 3^{rd} order DG scheme with HWENO limiting. The shock profiles in density together with the grid sizes after $t = 0.16$ are plotted in figure 1.

The 3^{rd} order DG scheme and the 4^{th} order rec. FV scheme both ran on 100 cells, while for the $\mathcal{O}5$ STE-DG scheme only 25 cells were used. One notices that all profiles look rather similar. As expected the DG HWENO and the rec. FV scheme both smeared the shock over 3 cells as usual for these limiting strategies and schemes, respectively. In contrast, the artificial viscosity limiter was able to capture the profile within one cell with almost the same resolution, but using only 1/4 of the HWENO-DG cells.

If this calculation were performed on the same grid, the artificial viscosity method would produce an even sharper shock profile, and would still be able to resolve the shock within just one cell.

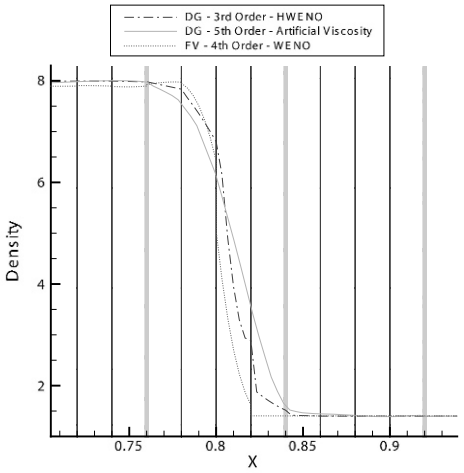

Fig. 1. Comparison of shock capturing properties. Plot of a 3rd order DG scheme, a 4^{th} order WENO reconstructed FV scheme and the 5^{th} order STE-DG scheme with artificial viscosity

4.2 The Double Mach reflection test-case

The Double Mach reflection (DMR) test-case can be considered as a challenging problem for numerical schemes because of different flow phenomena that are lying side by side:

When a Mach 10 shock hits a wedge, a triple-point is formed consisting of two shocks and a slightly unstable contact discontinuity that rolls up at the wedge boundary. To recover the vortex roll-up, the shock capturing has to be performed in a very local way, not affecting the vortices.

Figure 2 shows a density plot of a 6^{th} order calculation as well as a close-up of the triple-point region including some gridcells. One can see that both the shock as well as the vortex are clearly dissolved and - in addition - that the shock profile is captured within only one cell.

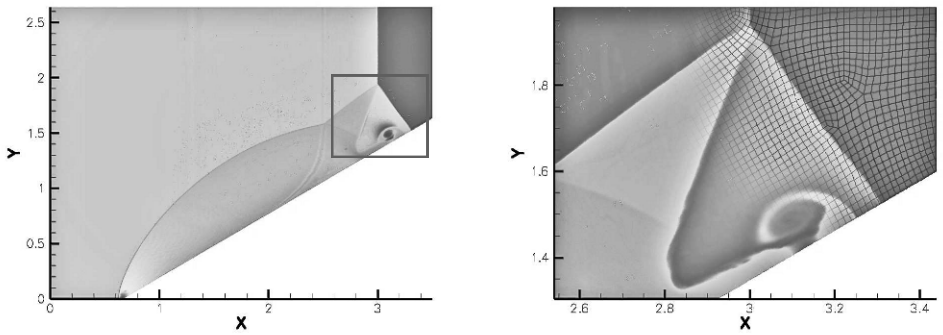

Fig. 2. The double mach reflection problem. Density plot at $t = 0.2$ of the computational domain (left) as well as a zoomed cutout including gridcells (right)

The previously described smoothness sensor and the added viscosity are plotted in figure 3. One can clearly see that viscosity was added only to the strong Mach 10 shock and therefore did not affect the rest of the solution in a bad way.

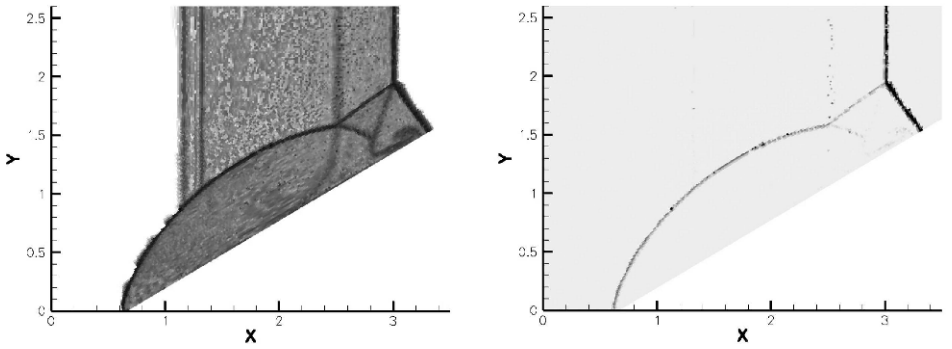

Fig. 3. The double mach reflection problem. Plot of the smoothness sensor (left) and artificial viscosity distribution (right)

5 Conclusion and Outlook

In this paper we combined an explicit space-time DG scheme with the shock-capturing approach of Persson and Peraire [5]. The idea to keep a high order approximation and to add locally artificial viscosity for the subgrid resolution of the shock works also very well also for unsteady problems. To preserve efficiency in the explicit unsteady approach it is essential to use the local time stepping framework.

References

1. E. F. Toro. *Riemann solvers and numerical methods for fluid dynamics.* Springer, second edition, 1999.
2. G. Gassner and F. Lörcher and C.-D. Munz. A Contribution to the Construction of Diffusion Fluxes for Finite Volume and Discontinuous Galerkin Schemes. *J. Comput. Phys.*, 2006. doi:10.1016/j.jcp.2006.11.004.
3. Gassner, G., Lörcher, F., and Munz, C.-D. A discontinuous Galerkin scheme based on a space-time expansion II. Viscous flow equations in multi dimensions. *submitted to Journal of Scientific Computing*, 2006.
4. Lörcher, F., Gassner, G., and Munz, C.-D. A discontinuous Galerkin scheme based on a space-time expansion. I. Inviscid compressible flow in one space dimension. *Journal of Scientific Computing*, 2006. DOI:0.1007/s10915-007-9128-x.
5. Per-Olof Persson and Jaime Peraire. Sub-Cell Shock Capturing for Discontinuous Galerkin Methods. In *Proc. of the 44th AIAA Aerospace Sciences Meeting and Exhibit*, AIAA-2006-1253, Reno, Nevada, January 2006.

The modified ghost fluid method for shock-structure interaction in the presence of cavitation

T.G. Liu[1], W.F. Xie[1], C. Turangan[1], and B.C. Khoo[2]

[1] *Institute of High Performance Computing, 1 Science Park Road, 01-01 The Capricorn, Singapore 117528. email: liutg@ihpc.a-star.edu.sg*
[2] *Department of Mechanical Engineering, National University of Singapore, Singapore 119260.*

Summary. In this work, the modified Ghost Fluid Method (MGFM) is applied to simulate compressible fluid coupled to deformable structure in the presence of both shock and cavitation. Numerical results show that the MGFM for treatment of the fluid-deformable structure coupling works efficiently in all pressure ranges and is capable of simulating both shock loading and cavitation reloading.

1 Introduction

The ghost fluid method (GFM) [1, 2] provides a simple and flexible way of treating the moving material interface in multi-medium flows. On the other hand, it has been found that those GFM-based algorithms of directly using the real fluid pressure and/or velocity to define the ghost fluid status can lead to inaccuracy or even incorrect solution when applied to problems of involving strong shock or jet impact on the material interface [3,4]. As such, utilising the two non-linear characteristic equations intersecting at the interface to predict the ghost fluid status, a modified GFM (MGFM) [3] was developed and found to be robust for gas-gas and gas-water flows. The recent mathematical analysis also affirms that the MGFM is second order accurate in the sense of approximating the exact Riemann problem solution at the interface, while the original GFM [1] has generally no order of accuracy [9]. The intention of this work is to apply the modified ghost fluid method to treat the compressible fluid-compressible structure coupling under strong fluid or shock impact in the presence of cavitation. As we are aware, numerical instability occurring in the vicinity of fluid-structure interface is one of the notorious difficulties in simulating such problems. The appearance of fluid cavitation and cavitation collapse in the later stage of fluid-structure interaction causes even great challenging in the numerical simulation. We will show that these difficulties are overcome well using the modified ghost fluid method to treat the interface.

2 The MGFM for Treating Fluid-Structure Interface

Governing Equations.

The Euler equations for inviscid compressible gases, compressible water, compressible solid or compressible cavitating flow can be written in a consistent form as

$$\frac{\partial U}{\partial t} + \frac{\partial F(U)}{\partial x} + \frac{\partial G(U)}{\partial y} + \frac{\partial H(U)}{\partial z} = 0 \tag{1}$$

$$U = [\rho, \rho u, \rho v, \rho w, E]^T, \qquad F(U) = [\rho u, \rho u^2 + p, \rho uv, \rho uw, (E+p)u]^T,$$

$$G(U) = [\rho v, \rho uv, \rho v^2 + p, \rho vw, (E+p)v]^T, H(U) = [\rho w, \rho uw, \rho vw, \rho w^2 + p, (E+p)w]^T.$$

Here, $p = p(\rho, e)$. ρ is the flow density, (u, v, w) are the flow velocity components in the $x-$, $y-$, and $z-$directions, respectively, p is the flow pressure, E is the total energy given by $E = \rho e + 0.5\rho(u^2 + v^2 + w^2)$ with e as the internal energy per unit mass. Once the equation of state (EOS) is given, the above system is closed for the pure gases and liquid. For gas flow, the EOS is the perfect gas law. For compressible water, the Tait EOS is employed. For compressible solid, the hydro-elastic-plastic EOS [5] is employed. When liquid flow (water) experiences cavitation, we use the isentropic one-fluid cavitation model to constitute cavitating mixture [6].

The Modified Ghost Fluid Method

In an MGFM-based algorithm, the level set technique is usually employed to capture the moving interface. A band of 3 to 5 grid points as ghost cells is defined in the vicinity of the interface. At the ghost cells, ghost fluid and real fluid co-exist. Once the ghost fluid nodes and ghost fluid status are defined for each medium, one employs one's favorite pure/single medium numerical scheme/solver to solve for each medium covering both the real fluid and ghost fluid grid nodes. By combining the solution for each medium according to the new interface location, one obtains the overall solution valid for the whole computational domain at the new time step. The MGFM [3,4] has been shown to be very robust when applied to compressible gas-gas or gas-liquid flow. In the MGFM, the ghost fluid states are defined using predicted interfacial states, which are obtained via solving a defined multi-medium Riemann problem along the normal direction of the interface using the two non-linear characteristic equations intersecting at the material interface. The two nonlinear characteristics intersecting at the interface can be written in association with system (1) along the normal direction of the interface as

$$\frac{dp_{I+}}{dt} + \rho_{IL} c_{IL} \frac{du_{nI+}}{dt} = S_{I+}, \qquad along \qquad \frac{dr_{nI+}}{dt} = u_{nI} + c_{IL}. \tag{2}$$

$$\frac{dp_{I-}}{dt} - \rho_{IR} c_{IR} \frac{du_{nI-}}{dt} = S_{I-}, \qquad along \qquad \frac{dr_{nI-}}{dt} = u_{nI} - c_{IR}. \tag{3}$$

where subscripts I, IL and IR refer to the interface, the left and right sides of the interface, respectively. The subscripts $+$ and $-$ indicate that the derivatives are evaluated and approach from the left and right sides of the interface, respectively. ρ_{IL} (ρ_{IR}) and c_{IL} (c_{IR}) are the density and sound speed on the left (right) side of the interface; S_{I+} and S_{I-} are the remaining terms associated with system (1), which are explicitly treated; u_{nI} and p_I are the normal velocity and pressure at the interface. $r_n = \overrightarrow{r} \cdot \overrightarrow{n}$, $u_n = \overrightarrow{V} \cdot \overrightarrow{n}$ and $\overrightarrow{n} = \bigtriangledown\phi / | \bigtriangledown \phi |$, where $\overrightarrow{r}$ is the position vector and ϕ is the level set function. System (2) and (3) have to be specially solved in order to take into account the shock wave structure interaction and structure elastic-plastic deformation as follows

$$\frac{p_I - p_{IL}}{W_{IL}} + (u_I - u_{nIL}) = \triangle t S_{I+}, \quad \frac{p_I - p_{R2}}{W_{IR}} - (u_I - u_{R2}) = \triangle t S_{I-}. \tag{4}$$

$$W_{IL} = \sqrt{\frac{p_I - p_{IL}}{1/\rho_{IL} - 1/\rho_l(p_I)}}, \quad W_{IR} = \sqrt{\frac{p_I - p_{R2}}{1/\rho_{R2} - 1/\rho_r(p_I)}}. \tag{5}$$

Here, the solid is assumed located on the right side of the interface. u_{R2}, p_{R2} and ρ_{R2} are the solid status after the elastic shock wave when the solid is under elastic and plastic deformation, otherwise, they are taken to be u_{nIR}, p_{IR} and ρ_{IR}, respectively. The detailed derivation of system (4) can be found in [7,8].

Cavitation frequently occurs due to fluid-structure interaction. Once cavitation appears next to the structure, tension waves (negative stress) may exist next to the interface in the structure. As a result, a negative p_{IR} may be erroneously obtained, leading to a negative interfacial pressure calculated using (4). The interfacial pressure, however, should never be negative physically due to the presence of flow cavitation. Special treatment to the interface in such situations, thus, has to be introduced. Because the pressure in the cavitation region is below the saturated vapor pressure, which is very low (can be very close to zero), the pressure change across the interface is small. Furthermore, due to the physical fact that a solid medium is relatively extremely incompressible, the acoustic impedance ($\rho_{IR}c_{IR}$) of solid is very large with a magnitude usually and typically above $O(10^6)kgm/s$. As a result, the magnitude of $dp_{I-}/(\rho_{IR}c_{IR})$ becomes negligibly small (usually less than $1.0^{-5}m/s$). Consequently, equation (3) can reasonably be reduced to

$$-\frac{du_{nI-}}{dt} = S_{I-}/(\rho_{IR}c_{IR}), \qquad along \qquad \frac{dr_{nI-}}{dt} = u_{nI} - c_{IR}. \tag{6}$$

Because the structural stress is not involved in (6), the involvement of negative p_{IR} is avoided when tension waves appear next to the interface inside the structure. A simple yet efficient way to numerically solve (2) and (6) is to assume $\rho_{IR}c_{IR}$ as locally constant. As such, the interface pressure and normal velocity can be directly obtained as follows

$$p_I = p_{IL} + \rho_{IL}c_{IL}[u_{nIL} - u_I] + \triangle t S_{I+}, \quad u_I = u_{nIR} - \triangle t S_{I-}/(\rho_{IR}c_{IR}). \tag{7}$$

Once the interfacial pressure and normal velocity are obtained, one can follow the way described in [7] to obtain the interfacial density and tangential velocity. The predicted interfacial states are then employed to define the ghost fluid states at the ghost fluid points.

3 Applications:Underwater Explosion near a Structure

The MGFM for treating the fluid-structure interface has been extensively tested in [7]. Recently mathematical analysis has further shown that the MGFM applied to treat the fluid-structure coupling reaches higher order accuracy with well-limited conservation errors even if the structure is under elastic-plastic deformation [8]. Here, we apply the MGFM to simulate an underwater explosion near a structure.

The structure is assumed to be a steel wall (deformable). The initial conditions are given as follows. An air cylinder of unit radius is located at the origin (0.0, 0.0) in water and the initial flow parameters inside the air bubble are $\rho_{exp} = 1770kg/m^3$, $p_{exp} = 20000bar$, $\mathbf{V}_{exp} = \mathbf{0}$ and $\gamma_{exp} = 2$. The initial flow parameters for water are $\rho_l = 1000kg/m^3$, $p_l = 1bar$ and $\mathbf{V}_l = \mathbf{0}$. The computational domain is a rectangular region with $x \times y \in [-6,6] \times [-6,6]$ and the planer wall is located at the straight line $y = 3$. The water-structure interface is treated using the MGFM developed in this work. The liquid-bubble interface is also handled using the MGFM [3,4].

Once the explosion is initiated, a strong underwater shock is generated and it impacts the wall soon. As a result, part of the shock will be transmitted inside the flexible wall

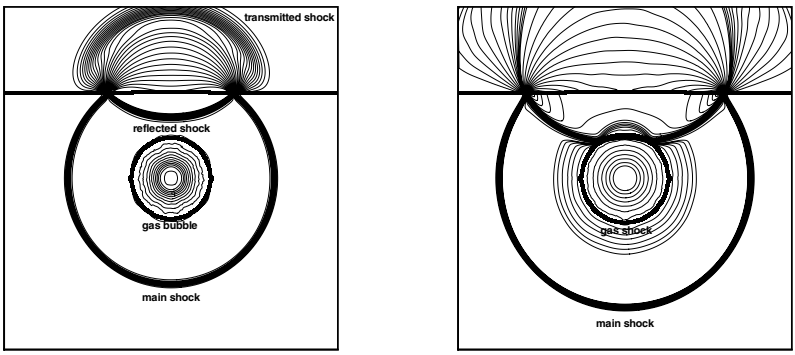

Fig. 1. pressure contours at t=1.5ms (left) and t=2.0ms (right)

and part of the shock is reflected back into the water (see the left figure in Figure 1). As the sound speed of the structure is faster than that of water, the transmitted shock wave inside the structure is propagating ahead of the incident shock in water, resulting in a precursive wave propagating along the structure surface and soon out of the computational domain (see the right figure in Figure 1). The reflected shock wave interacts with the air bubble, leading to a strong reflected rarefaction wave moving towards the wall. After this rarefaction wave reaches and reflects from the wall, cavitation occurs near the wall. As the flow moves back to compress the cavitation, the cavitation will collapse towards the wall; a pressure surge is then generated. Figure 2 show the pressure contours at $t = 3.75ms$ and $t = 4.25ms$. Figure 3 shows the corresponding void fraction

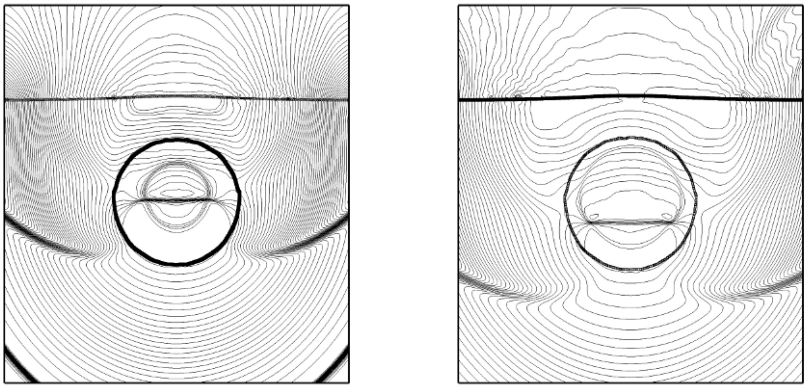

Fig. 2. pressure contours at t=3.75ms (left) and t=4.25ms (right)

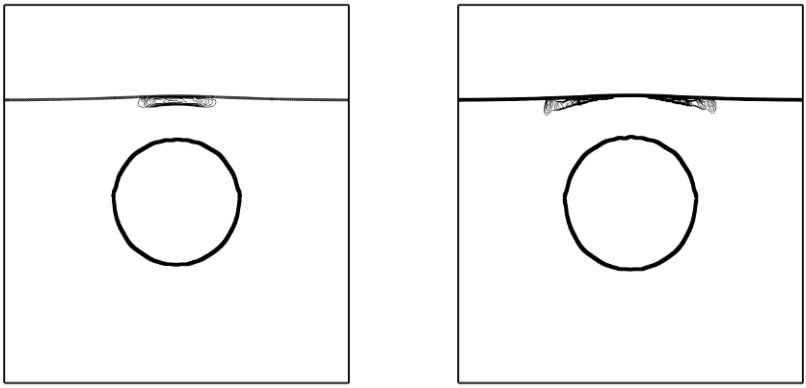

Fig. 3. void fraction contours at t=3.75ms (left) and t=4.25ms (right)

contours in the respective time moments. At the time of $3.75ms$, the cavitation has been generated and is expanding (see the left figure in Figure 3), while it is shrinking at the time of $4.25ms$ (see the right figure in Figure 3). The cavitation collapse causes a water jet towards the structure, leading to the generation of pressure surge. Such a pressure surge results in the second impact towards the structure. To better observe the process of cavitation creation and collapse and the effect of structure flexibility on the cavitation collapse, the pressure history at the centre of planar wall is recorded (see Figure 4). In Figure 4, the recorded first pressure peak is due to the underwater shock impact, while the second pressure peak is due to cavitation collapse.

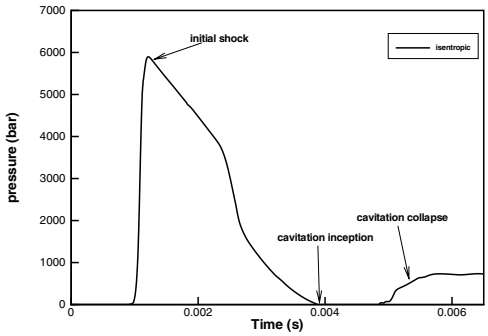

Fig. 4. Recorded pressure history at the center of the wall surface

4 Conclusions

In this work, the modified Ghost Fluid Method (MGFM) was applied to treat the compressible fluid coupled to deformable structure under strong shock impact in the presence of cavitation. To define the ghost fluid states when the structure is under plastic deformation, an approximate Riemann problem solver (ARPS), which is able to take into account the structure plastic deformation, has been developed. To handle and simulate cavitation structure interaction, the non-linear characteristics intersecting at the material interface has been specially solved in order to obtain a physically reasonable interface state and thus define the ghost fluid states in such situations. Numerical results showed that the MGFM indeed works efficiently under such extreme environments.

References

1. Fedkiw RP, T Aslam, B Merriman and S Osher (1999) A non-oscillatory Eulerian approach to interfaces in multimaterial flows (the Ghost Fluid Method), J. Comput. Phys., 152:457-492.
2. Fedkiw RP (2002) Coupling an Eulerian Fluid Calculation to a Lagrangian Solid Calculation with the Ghost Fluid Method, J. Comput. Phys., 175:200-224.
3. Liu TG, Khoo BC and Yeo KS (2003) Ghost fluid method for strong shock impacting on material interface, J. Comput. Phys., 190:651-681.
4. Liu TG, Khoo BC and Wang CW (2005) The ghost fluid method for compressible gas-water simulation. J. Comput. Phys., 204:193-221.
5. Tang HS and Sotiropoulos F, (1999) A second-order Godunov method for wave problems in coupled solid-water-gas systems, J Comput. Phys., 151:790-815.
6. Liu TG, Khoo BC and Xie WF, (2004) Isentropic one-fluid modelling of unsteady cavitating flow, J Comput. Phys., 201:80-108.
7. Liu TG, Khoo BC and Xie WF, (2006) The modified ghost fluid method as applied to extreme fluid-structure interaction in the presence of cavitation, Comm. Comput. Phys., 1:898-919.
8. Liu TG, Xie WF and Khoo BC, (2007) The modified ghost fluid method for coupling of fluid and structure constituted with Hydro-Elasto-Plastic equation of state, SIAM J. Sci. Comput., accepted.
9. Liu TG and Khoo BC, (2007) The accuracy of the modified ghost fluid method for gas-gas Riemann problem, Applied Numerical Mathematics, in press.

Transient aerodynamic forces experienced by aerofoils in accelerated motion

H. Roohani[1] **and B.W. Skews**[2]

[1] *University of Johannesburg, PO Box 17011, Doornfontein 2028, Johannesburg, South Africa*
[2] *University of the Witwatersrand, PO Wits 2050, Johannesburg, South Africa*

1 Introduction

In the study of forces acting on an aerofoil nearly all past work was conducted on objects moving at constant speed through the fluid. This has seldom been extended to accelerating bodies, even though objects experience acceleration and /or retardation in most practical applications.

As an example, when graphs of the variation of lift or drag versus Mach number were plotted for an aerofoil, these were based on steady state flight [1]. In other words sufficient time was allowed to lapse at each specific Mach number for aerodynamic equilibrium to be reached, before the lift or drag forces were determined. However, in accelerated motion there is no time for equilibrium to be reached at each Mach number. An example of this for the simple case of a particle moving through speed of sound is given by Lilley and Yates [2]. Therefore the graph of lift or drag versus Mach number for an accelerating object should differ from the steady state scenario as given, for example, by Whitcomb [3].

The main reason for the limited study of accelerated motion in compressible fluids was that computational techniques were not sufficiently developed in the past. However, recent developments in Computational Fluid Dynamics have made it possible to model such problems.

2 Modelling Techniques

2.1 Steady state

In order to model an object moving with constant velocity through a compressible fluid two techniques can be used. The first is to move the reference frame of the object at the desired velocity. This technique moves the object and the meshed domain simultaneously at the required velocity while the far field fluid remains stationary.

The second technique requires the use of pressure far-field boundary conditions. These are used in Fluent to model free stream conditions at infinity, with free stream Mach number and static conditions being specified. Although this technique only specifies the velocity at the far-field, sufficient time is allowed in steady state simulations for the system to reach equilibrium. This will result in the entire flow field to be moved at the required velocity and the reference frame of the object to be kept stationary, hence producing results identical to the case of the moving reference frame described above.

2.2 Accelerating objects

Fluent does not have the facility for the linear acceleration of the reference frame of an object. The moving reference frame technique can only solve problems with constant

velocity as described above. Therefore, in order to deal with acceleration using Fluent, the reference frame of the object must be kept stationary and the entire flow field must be accelerated.

It is important to note that accelerating the entire flow field cannot be achieved merely by accelerating the velocity at the far field. Any change at the far-field will propagate through the medium at the speed of sound and will be experienced by an object and by the fluid surrounding the object only some time after the change has taken place. In contrast, when an object is physically accelerated through a particular fluid, the changes in the velocity of that object are experienced instantaneously by the fluid immediately surrounding the object and are propagated outwards.

In order to successfully model the case of an accelerating object by moving the flow field, the fluid at far field and the fluid inside the boundaries of the meshed domain must be accelerated simultaneously with equal acceleration. The far field is accelerated by a user-defined function, which determines the changing value of the input velocity at a given time. The fluid inside the boundaries must be accelerated using momentum and energy source terms. These are derived from the momentum and energy equations, which are built into the Fluent source code. They are also introduced with the help of a user-defined function. This technique was recommended by Fluent for the linear acceleration of an object in compressible fluids in external aerodynamic problems. Accelerating the entire flow field and keeping an object stationary is equivalent to accelerating the reference frame of the object in the opposite direction and keeping the fluid stationary.

3 Comparison of the Aerodynamic Effects Experienced by Aerofoils at Constant Velocity and in Accelerated Motion

Four aerofoils with cord lengths of 1m were used in this investigation. The first was a subsonic symmetrical aerofoil, NACA 0012, which provided a good starting point for testing the effects of acceleration. The second was a subsonic asymmetrical aerofoil, NACA 2412. This was used to confirm the findings from the first aerofoil, but also provided the opportunity to compare the effects of acceleration on different aerofoil profiles. Two supersonic aerofoils were also used. These were a diamond shaped aerofoil and a biconvex aerofoil, each with a cord length of 1m and a maximum thickness of 0.1m. A particularly high acceleration was chosen to enhance the differences between the steady and accelerating scenarios. All aerofoils were subjected to the following conditions:

Free stream temperature	= 300 K
Atmospheric pressure	= 101325 Pa
Acceleration	= 1041 m/s^2
Range of Mach numbers	= 0.1 to 1.3
Angle of attack	= 4 degrees

Initially steady state simulations were conducted for each aerofoil, at Mach numbers ranging from 0.1 to 1.3. Then each aerofoil was subjected to an acceleration of 1041 m/s^2 through the same range of Mach numbers. Graphs of lift drag, and pitching moment versus Mach number were plotted for the aerofoils. For comparison the steady and the unsteady graphs were plotted on the same set of axes. Aerodynamic coefficients were not used because there is no reference density and velocity.

Figures 1 and 2 show the steady and unsteady drag variations for the aerofoils over the entire range of Mach numbers (0.1 to 1.3).

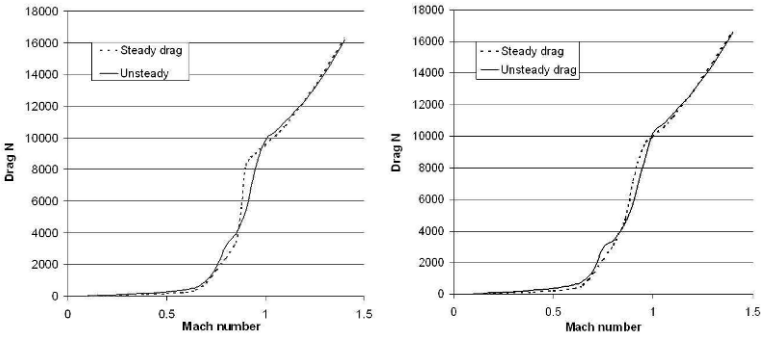

Fig. 1. Steady and unsteady drag variation with Mach number for the symmetrical (NACA 0012) (left) and asymmetrical (NACA2412) (right) aerofoils. Acceleration = 1041 m/s^2 (106g) for the unsteady state.

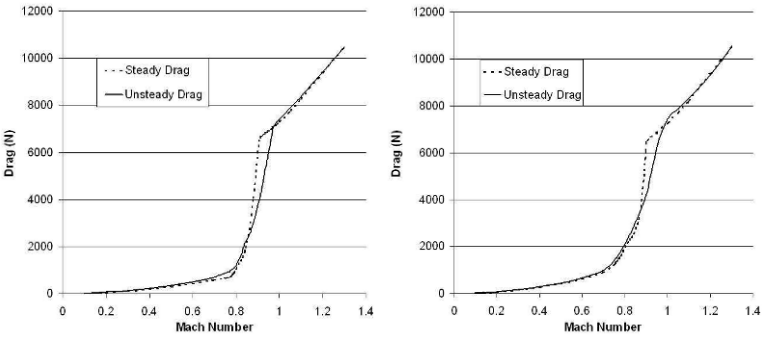

Fig. 2. Steady and unsteady drag variation with Mach number for the biconvex (left) and the diamond shaped (right) aerofoils. Acceleration = 1041 m/s^2 (106g) for the unsteady state.

In figure 3 the subsonic portion of the graph for the symmetrical aerofoil (NACA0012) is plotted in order to improve clarity. This shows that, for these Mach numbers, the unsteady drag is higher than the steady state drag. The same was found to be true for all the other aerofoils. However in the transonic and supersonic regions this situation reverses back and forth several times.

Figures 4 and 5 show the steady and unsteady lift variations with Mach number. In the subsonic region the unsteady lift is lower than the steady state values. However in the transonic region, due to separation occurring on the upper surface of the aerofoils a sudden drop in the lift forces are observed. This is due to the fact that in the areas where separation occurs the pressure rises substantially due to appearance of the transonic shock, thus reducing the pressure differential between the bottom surface and the

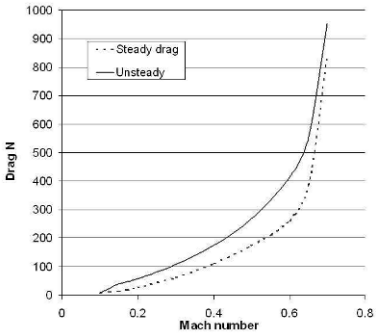

Fig. 3. Steady and unsteady drag variation with subsonic Mach numbers for the symmetrical aerofoil (NACA 0012). Acceleration = 1041 m/s^2 (106g) for the unsteady state.

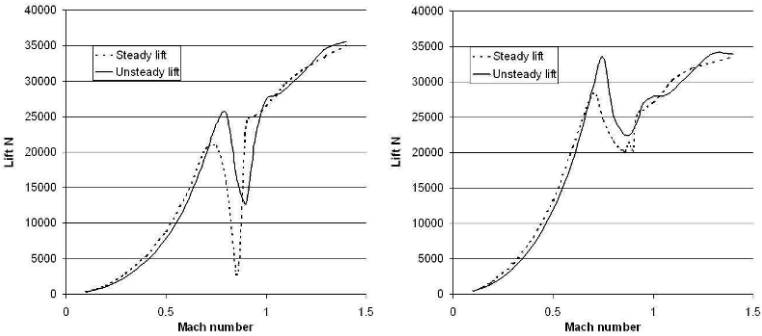

Fig. 4. Steady and unsteady lift variation with Mach number for the symmetrical (NACA 0012) (left) and asymmetrical (NACA2412) (right) aerofoils. Acceleration = 1041 m/s^2 (106g) for the unsteady state.

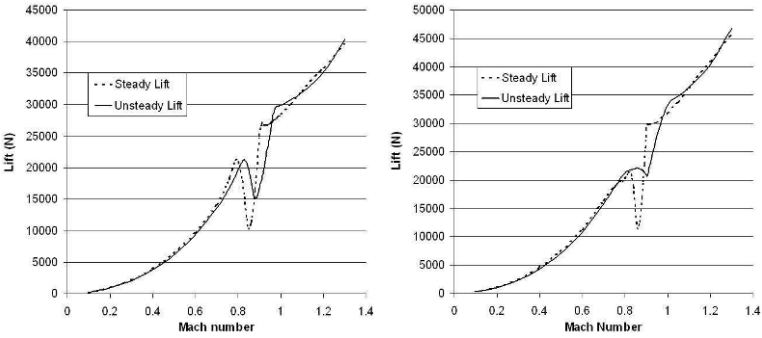

Fig. 5. Steady and unsteady lift variation with Mach number for the biconvex (left) and diamond shaped (right) aerofoils. Acceleration = 1041 m/s^2 (106g) for the unsteady state.

top surface of the aerofoil. As a result sudden changes take place in lift in this region, resulting in very significant differences between the steady and unsteady scenarios. In the supersonic region the unsteady lift values fluctuate above and below the steady state values.

Graphs of the steady and unsteady pitching moment versus Mach number are shown in figures 6 and 7. In the subsonic region, for these aerofoils, the difference between the steady and the unsteady values are less significant than the transonic and supersonic regions. In the supersonic region the unsteady moment fluctuates above and below the steady values, as was the case with lift and drag. However, the greatest difference between the steady and unsteady pitching moments is observed in the transonic range of Mach numbers.

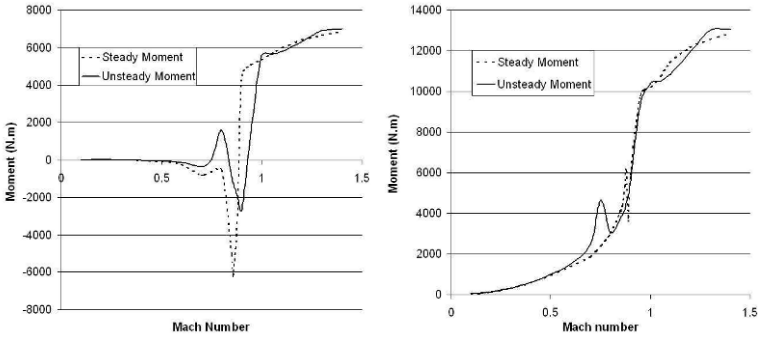

Fig. 6. Steady and unsteady moment variation with Mach number for the symmetrical (NACA 0012) (left) and asymmetrical (NACA2412) (right) aerofoils. Acceleration = 1041 m/s^2 (106g) for the unsteady state.

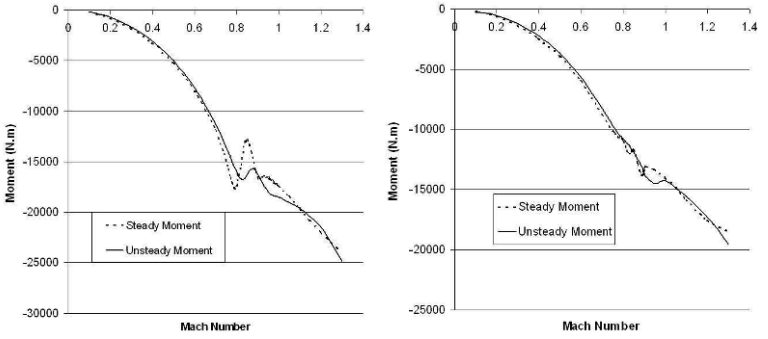

Fig. 7. Steady and unsteady moment variation with Mach number for the biconvex (left) and diamond shaped (right) aerofoils. Acceleration = 1041 m/s^2 (106g) for the unsteady state.

In order to explain some of the effects observed, it is important to note that when an object is accelerated in a compressible fluid, the unsteady flow field generated is not

allowed sufficient time to reach equilibrium and the flow pattern at a specific Mach number is therefore quite different to the steady state flow pattern at that same Mach number. As a result, the unsteady lift, drag and pitching moment at any given Mach number should also be different to the steady state values.

In the transonic region these effects are more pronounced because of the movement of shock induced point of separation, on the upper surface of the aerofoils, with changing Mach number. This can drastically affect the lift and moment even when the change in Mach number is small. Therefore, when accelerating through transonic Mach numbers, the unsteady condition of the flow field has a more pronounced effect on the aerodynamic forces and moments. The graphical representation of the results, confirm this explanation.

A more detailed explanation, regarding the different effects of acceleration, requires more investigation. Acceleration effects could be dependant on body shape, angle of attack of the aerofoil and other factors such as atmospheric conditions. For the moment it is sufficient to note that, acceleration changes the flow field around an object and consequently the aerodynamic forces and moments on that object, for a given Mach number.

4 Conclusions

- In comparison with the steady state values, in the subsonic region, acceleration produced a reduction in lift and an increase in drag. However, the pitching moment values changed less significantly in the subsonic region.
- In the transonic and supersonic regions, the differences between the steady and unsteady values fluctuated, with the largest differences observed in the transonic region.
- Acceleration had a similar effect on the lift, drag and pitching moment of these aerofoils. However, changes in these effects as a result of changing aerofoil profile, were observed specially in the transonic region. Additional investigation is required in order to determine the ideal aerofoil profile, which would be used to reduce acceleration effects.

References

1. Oosthuizen P.H. and Carscallen W.E.: *Compressible Fluid Flow*, 1st International Edition (McGraw Hill, 1997) pp 213-215.
2. Lilley G.M. and Yates A.H.: *Some Aspects Of Noise From Supersonic Aircraft*, Journal Of The Royal Aeronautical Society, June (1953).
3. Whitcomb R.T.: *A Study Of The Zero-Lift Drag-Rise Characteristics Of Wing-Body Combinations Near The Speed Of Sound.* National Advisory Committee for Aeronautics - Report 1273.

Part XV

Plasmas

Relaxation dynamics of porous matter under intense pulsed irradiation

V.P. Efremov[1], B.A. Demidov[2], A.N. Mescheryakov[1], A.I. Potapenko[1], and V.E. Fortov[1]

[1] *Institute for High Energy Densities, Russian Academy of Sciences, Izhorskaya str. 13/19, Moscow, 125412, Russian Federation*
[2] *Russian Scientific Center "Kurchatov Institute", Kurchatov sq. 1, Moscow, 123182, Russian Federation*

1 Introduction

Porous media have large and increasing number of applications in Inertial Confinement Fusion, high energy densities physics, Warm Dense Matter research and so on. In many of the applications the media is subjected to the intense volume energy deposition [1, 2]. While the properties of the porous matter under shock loading are well known for many substances, the behavior of the media under intense pulsed volume heating remains the topic of the research interest.

Currently the heating of the porous matter is assumed as *direct and momentary* transition from the heterogenous porous media into the uniform plasma. Actually it's the transition from the solid matter of the pore walls into homogenous plasma. We suggest to pay more attention to the *homogenization* stage [3, 4]. The duration of the stage can be comparable to the time of irradiation for the novel facilities.

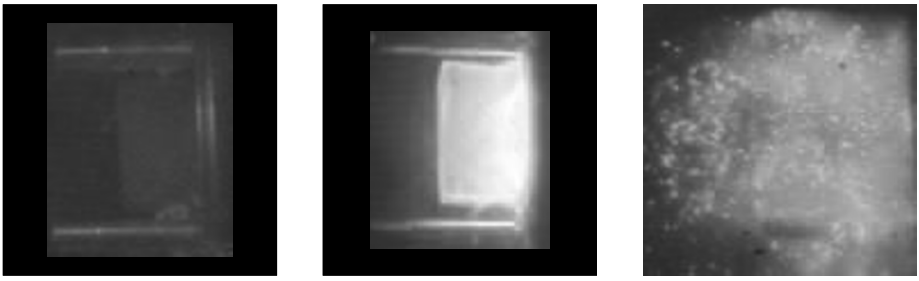

Fig. 1. Aerogel sample ($0.15\,\mathrm{g/cm^3}$ SiO_2) expansion after irradiation. Left-to-right: before irradiation; 50 ns after beginning of irradiation; $300\,\mu$s after irradiation

Porous medium under high-rate energy deposition (in our case irradiation) turns into homogeneous plasma by means of complex hydrodynamic and radiation processes (see Fig. 1). Three images of the Fig. 1 represent the successive stages of the porous media irradiation. On the middle image the energy deposition zone being transformed into plasma and the still intact non-irradiated part of the sample are shown. The right image demonstrates the complete destruction of the specimen with its splinters intermixed with the expanding plasma.

Despite the lowered average density of the porous material it has generally the same microscopic density of the matrix as the continuous material does. Hence the decreased values of volume energy density should not be mistakenly taken for the real thermodynamical state of the material being heated.

The collapse of the expanding pore wall material inside the pore void could lead to the energy compression and create hot spots throughout the media. In this case a relatively small portion of the matter has dramatically elevated temperature, pressure and ionization in comparison with the average values. Such hot spots can produce higher energy radiation and even damage the fuel capsule wall in some ICF target designs.

Our approach is to create the thermodynamical model of the porous media behavior applicable to various sorts of porous materials (e.g. organic foams, metal foams, aerogels etc.). In order to achieve this, we are using the numerical modelling of the experimental irradiation scheme as well as analytical model of the pore material expansion.

2 Experimental setup

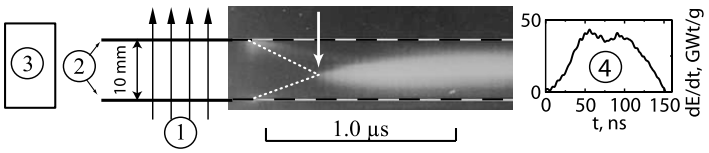

Fig. 2. Experimental setup and streak camera record. 1 - pulsed electron beam, 2 - Al foils, 3 - camera, 4 - beam power profile. Arrow shows the time of collision. Dashed lines are the initial foil position, dotted lines represent the estimated expansion paths of the average velocity (10 km/s).

Because the pores in the real porous media are too small and irregularly shaped to be studied directly we propose the physical modelling scheme. The porous media is substituted with the set of the two or more thin parallel foils (see Figure 3). The foils are irradiated with the powerful pulsed energy flux. We've used the electron beam with the following properties: electron energy 0.3 MeV, beam current 10-30 kA, duration 100 ns FWHM as the energy source. Foil thickness was considerably smaller than the electron stopping range so the foil heating was almost spatially uniform. Mostly the aluminum foils were used because the equation-of-state of aluminum is well developed for the wide range of energies. Distance between the foils (5–10 mm) was smaller than the beam radius so the collision can be considered one-dimensional near the beam axis. The beam pulse time was considerably longer than the acoustic relaxation time for the foils, so their heating was almost isobaric.

The phenomena of foil heating, expansion and collision were studied with streak and frame cameras. Because the frame cameras could record only two images we used experimental setups involving several foils with different spacing so they represented various stages of the collision process on the same image. Spatial beam profile was measured with pin-hole camera. The beam voltage and current profiles were also recorded.

3 Experimental results

Figure 3 represents the frame camera images of the above mentioned multi-foil setup. Images **(a)** and **(b)** represent the successive stages of the aluminum foil interaction while image **c** shows the possibility to use this method to study dielectric media. But we haven't modelled the data obtained for mica yet due to more complicated equation-of-state in comparison with aluminum.

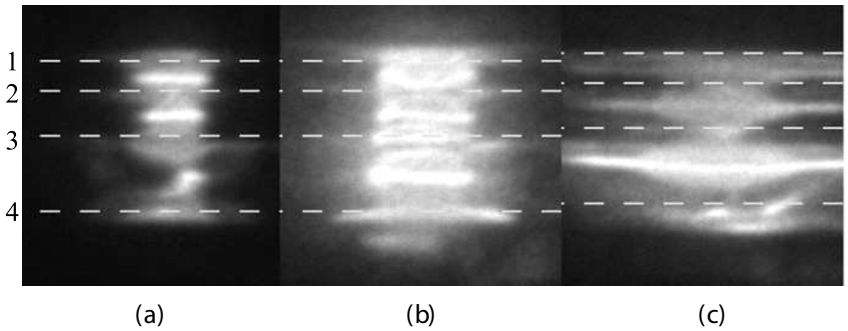

Fig. 3. One-dimensional collapse of thin films (initial positions are shown with dashed lines). Left-to-right: 10 μm Al, 80 ns after irradiation; the same sample 150 ns after irradiation; 14 μm mica, 150 ns after irradiation. The pulsed electron beam has propagated upwards.

It's hard to derive numeric values from the frame images. Nonetheless they demonstrate very good flatness of collision near the beam axis, allowing us to use less involved 1D model. The accurate measurements of expansion velocity were performed with streak camera.

The typical streak camera recording is shown at Fig. 2. The both foils demonstrate considerable heating and light radiation during the time of irradiation. After the end of pulse the expanding foil material gradually cools down and dims. Later the streams from the both foils collide in the void between them creating bright flash inside the interaction zone.

Because the movement of the most rarefied outer layer of the expanding foil could not be directly traced by the direct means we have taken its average expansion velocity as the ratio between the half interfoil distance and the time interval between energy deposition and the very beginning of collision. The experimental measurements of expansion velocity are shown at Fig. 4.

4 Analytic model

The presented analytic model follows closely the model presented in [5]. We solve the basic system of hydrodynamics equations:

$$\frac{\partial \rho}{\partial t} + \frac{\partial (\rho v)}{\partial x} = 0 \tag{1}$$

$$\rho \left(\frac{\partial v}{\partial t} + v \frac{\partial v}{\partial x} \right) = -\frac{\partial P}{\partial x} \tag{2}$$

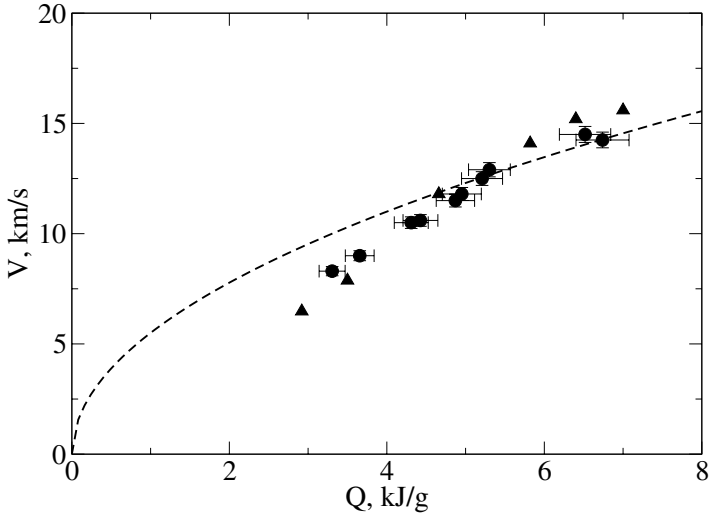

Fig. 4. Velocity of expanding 10 μm Al foil vs. specific deposited energy. Circles — experimental results, triangles — numerical simulation, dashed line — analytical solution.

$$\frac{\partial}{\partial t}\left(\rho\epsilon + \frac{\rho v^2}{2}\right) = -\frac{\partial}{\partial x}\left[\rho v\left(\epsilon + \frac{v^2}{2}\right) + Pv\right] + \rho H, \tag{3}$$

where H is the specific energy deposition. The value of H was calculated from the recorded beam current and voltage using the semi-empirical algorithm of electron energy deposition [6]. The model of ideal gas was used as the equation-of-state. The results are shown at Fig. 4 as the dashed line. The velocities given there correspond to sufficiently rarefied steady flows studied at the experiments. That's why the curve is essentially even simpler self-similar solution for the centered rarefication wave:

$$v = \frac{2C}{\gamma - 1}, \tag{4}$$

where C is the sound velocity, $\gamma = C_P/C_V$ is the adiabatic exponent. Time history of the analytic solution was used to check the numerical model given below.

5 Numeric simulation

The simulation of electron stopping was carried out by Monte-Carlo technique using ENDF/B-IV libraries. Target expansion was described by the system of one-dimensional radiation hydrodynamics equations in Lagrange coordinates [7] in the approximation of two-temperature [8] single-velocity [9, 10] approximation. Numerical estimates for solid and liquid phases were based on Mie-Gruneisen equation. Plasma phase was simulated within the approximation of the local applicability of Saha equation. Considering that the viscous heating occurs for the ion component only [11] and the energy transfer between the components is much slower process, the electron gas is compressed adiabatically with the electric forces. Considering this within the context of quasineutral plasma we have the electron density n_e correlate with the ion density n_i by the average ion charge $\overline{\zeta}$

$$n_e = \overline{\zeta} n_i \tag{5}$$

The following equation is used for the heat flux due to thermal conductivity:

$$\Omega = -\alpha_m \rho r^\nu \frac{\partial T}{\partial m} \tag{6}$$

there α_m is the thermal conductivity coefficient considered constant for the given media, ρ is the media density.

To compute the change of the electron component energy due to atom or ion ionization the following formula was used:

$$Q_I = \left(\frac{N_A I}{\mu_a}\right) \frac{\partial \overline{\zeta}}{\partial t} \tag{7}$$

there I is the current atom ionization potential, N_A is the Avogadro number, μ_a is the atomic mass.

In so doing the degree of ionization $\overline{\zeta}$ (average ion charge) and the value of I are computed in approximation of local applicability of Saha equation depending on the electron temperature T_e.

The values of I and $\overline{\zeta}$ are derived from the following equation (for the single chemical element):

$$I(\overline{\zeta} + 0.5) = k_B T_e \ln\left(\frac{A_C T_e}{\overline{\zeta} n_i}\right)^{3/2}, \tag{8}$$

there $A_C = (4\pi m_e k_B/h^2)^{3/2}$, k_B is the Boltzmann constant, $n_i = \rho N_A/\mu_a$ is the ion density.

To describe the thermal radiation transfer and its influence on the energy deposition in target the conjugation of volumetric radiation for the optically thin target layers and radiation heat conductivity for the inner optically thick layers were used.

The results of expansion simulation for various deposited energy Q are given at Fig. 4.

One-dimensional modelling shows what for collapse of the expanding streams at 12.2 km/s the initial temperature inside the collision zone is 5–6 times fold higher than the maximum temperature inside the foil bulk during irradiation.

6 Conclusion

The method of the detailed investigation of the porous medium homogenization and relaxation under fast energy deposition was proposed. The velocity of expansion of 10 μm Al foils as function of deposited energy was measured. Numerical and analytical models were used to interpret the obtained results.

References

1. Pikuz S.A., Efremov V.P., Faenov A.Ya. *et al.* Investigation of heavy ions tracks energy deposition inside solid media by methods of x-ray spectroscopy. J. Phys. A: Math. Gen., vol. 39, no. 17, 2006, pp. 4765–4769

2. Demidov B. A., Efremov V. P., Ivkin M. V. *et al.* Evolution of the glow of an aerogel irradiated with a high-power pulse electron beam. Technical Physics, vol. 45, no. 7, 2000, pp. 870–877
3. Efremov V., Demidov B., Mescheryakov A. *et al.* Physical modeling of porous media behavior in targets for inertial fusion. NIM–A, 2007 (in press)
4. Khalenkov A. M., Borisenko N. G., Kondrashov V. N., Merkuliev Yu. A. ,Limpouch J., Pimenov V. G. (2006) Experience of micro-heterogeneous target fabrication to study energy transport in plasma near critical density. Laser and Particle Beams vol. 24, pp. 283–290
5. R. London, M. Rosen, Hydrodynamics of exploding foil x-ray lasers. Phys. Fluids, vol. 29 no. 11, 1986, pp. 3813-3822
6. Tabata T., Ito R. An algorithm for the energy deposition by fast electrons. Nuclear Science and Engineering, vol. 53, 1974, pp. 226-239
7. A. A. Samarski, Yu. P. Popov. Raznostnye metody resheniya zadach gazovoi dinamiki. M.: Nauka, 1980, 352 p. (in Russian)
8. Yu. V. Afanas'ev, E. G. Gamalii, V. B. Rozanov. Osnovnye uravneniya dinamiki i kinetiki lazernoi plazmy. Trudy PhIAN SSSR, 1982, vol. 134, pp. 10-31 (in Russian)
9. W. C. Mead, E. M. Campbell, K. G. Estabrook *et al.*, Laser-plasma interactions at 0.53 mm for disk targets of varying Z. Phys. Rev. Letters, vol. 47, no. 19, 1981, pp. 1289-1292
10. G. J. Pert, Two-dimensional hydrodynamic models of laser-produced plasmas, J. Plasma Physics, vol. 41, part 3, 1989, pp. 263–280
11. Ya. B. Zel'dovic, Yu. P. Raizer. Fizika udarnyh voln i vysokotemperaturnyh yavlenii. — M.: Nauka, 1966, 688 p. (in Russian)

Shock wave interaction with nanosecond transversal discharges in shock tube channel

I.A. Znamenskaya[1], D.A. Koroteev[1], D.M. Orlov[1], A.E. Lutsky[2], and I.E. Ivanov[3]

[1] *Faculty of Physics, Lomonosov Moscow State University, Leninskie Gory, Moscow, Russia*
[2] *Keldysh Institute of Applied Mathematics RAS, Miusskaya sq. 4, Moscow, Russia*
[3] *Moscow Aviation University, Volocolamskoye sh. 4, Moscow, Russia*

Summary. Discontinuity breakdown conditions were realized experimentally by instant homogenous energy input in front of shock wave. Energy deposition was conducted using nanosecond gas discharges in spatial and surface area. A shock tube and special type of nanosecond electric discharge with plasma electrodes were used for this research. One and two-dimensional numerical simulation under experimental conditions has been undertaken. Pressure, density, temperature and velocity fields have been examined. Comparison of numerical data and schleiren images of shock wave after its interaction with discharge area was conducted. The configuration of disturbed shock wave was found to be in a good correspondence with one from numerical calculations. Numerical results showed possibility to achieve Richtmyer-Meshkov type instability without membrane.

1 Introduction

It is well known fact that high capacity electric discharges may cause sufficient perturbations in gas flows. Discharges are also known as a tool for visualization of gas flow discontinuities [1]. During the last decades there is a growth of interest directed to the possibility of flow control by using plasma technologies. A number of the publications devoted to this subject are overviewed in [2]. The majority of the published data deal with research in the field of interaction between the supersonic gas flow and low temperature plasma area formed by electric discharge. Most of the research groups examine the quite long-termed quasi-stationary or high-frequency electric discharges. In this paper we consider nanosecond transversal spatial and surface discharges realized experimentally in supersonic flow with a shock wave. Research conducted in field of plasma physics especially for such type of electric discharge [3] showed that sufficient part of electric energy goes directly in translational degrees of freedom. In the other words, applied discharges provide a rapid heating of local gas area. Numerical simulations under experimental conditions are also presented.

2 Experimental technique

Experimental setup was built for the purposes of studying the non-stationary processes of interaction between the subsonic and supersonic gas flows with/without discontinues and spatial or surface short-termed electric discharge. In this context "short-termed" means that discharge current duration ($\sim$200 ns), is much lower than characteristic time of gasodynamic processes realized in the setup ($\sim$10 μs). So, the impact of the discharge could be considered as instant from the gasodynamical point of view. The setup configuration for the given problem is shown on the figure 1 (left). The two main parts were

shock tube and electric discharge chamber. Shock tube had a channel (low pressure section) with the rectangular profile 24×48 mm. It allowed to generate shock waves with Mach numbers $M = 1 \div 6$, using helium as a driver gas and the air as a driven one. The discharge chamber was mounted with the shock tube's channel and it has the same profile. Top and bottom walls of the chamber were plasma electrodes which produced the ultraviolet glow for the pre-ionization of spatial discharge area. The surface discharge of plasma electrodes was also used as the independent source of energy impact in a special series of experiments. The sidewalls were made of quartz glass to make the discharge glow and shock formations visible by the optical means, or using shadow and schlieren technique. The length of the discharge section was equaled 100 mm. Special scheme was created to make the discharge initiation on the different stages of shock wave moving through the discharge chamber.

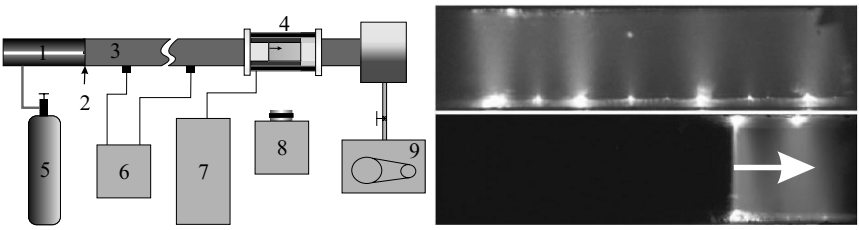

Fig. 1. Left: experimental setup. Right: discharge glow images in motionless gas (top) and in the case when shock wave is in discharge camber (bottom). 1- high pressure section, 2- membrane section, 3- flow channel, 4- discharge section, 5- high pressure helium accumulator, 6- flow parameters control, 7- high voltage setup, 8- discharge glow control, 9- vacuum pump

3 Analysis of discharge's glow

Spatial discharge. As it was mention above, the discharge current time interval was about 200 ns. So from the gasodynamical point of view discharge can be considered as instant and shock wave was nearly motionless during the energy input time. It was possible to record the integral (in respect to time) discharge glow redistribution by photo cameras (figure 1 (right)). As it can be seen from the figure 1 (right) if there is no flow in discharge area, glow is quite homogenous all over discharge section. But if the discharge was initiated at the moment when shock wave front situated in the discharge section, the glow concentrates in the low pressure area in front of shock wave. The phenomenon of discharge "self localization" in front of shock wave was observed for all the variety of shock wave positions in discharge section. Accumulation of the discharge glow in the low pressure area is caused by the following phenomena. The local conductivity of the air is the very sensitive function of Townsend parameter E/N (where E is the electric field strength and N is concentration of neutral particles in discharge plasma). As the E/N changes by the orders of magnitude over the shock front, local conductivity in low pressure area is much higher than beyond the shock. So we conclude the dominant part of experiment plasma flux localizes in front of shock wave. The indirect confirmation of this thesis is in the dependance of local flow intensity I on distance x [cm], which was covered by shock wave along the discharge section before the moment of discharge

initiation. This dependance is well approximated by the function $I(x) = 10I_0/(10 - x)$, $x \in [0; 9.5]$, where I_0 is local glow intensity in motionless gas. Kinetic calculations in [3] confirm this conclusion directly.

Sliding discharge. The experiments with sliding discharges without spatial phase showed that its glow has nearly similar properties. It is quite homogenous in motionless gas and has the dimensions of $100 \times 35 \times 0.5$ mm. It concentrates in low pressure area when plane shock wave is in discharge chamber. In the other words, in last case we experimentally realized "instant" ionization of low pressure areas of plasma sheets which were placed at the opposite walls of flow channel. Generally, glow intensity as a function of x behave similarly to the spatial glow. At some conditions the special effects of glow redistribution were observed (figure 2).

Fig. 2. Left: glow behind SW $M = 2$; $x = 9.4$ cm; $P_0 = 25$ torr Right: spatial glow $M = 2.6$; $x = 8.5$ cm; $P_0 = 25$ torr

At some parameters, there was an additional surface glow behind the shock wave front. It was observed at low Mach numbers $M \sim 2 - 3$, quite low initial pressures $P_0 \sim 25$ torr and $x > 7$ cm. At Mach numbers $M \sim 4 - 5$, more lower initial pressure $P_0 \sim 4 - 7$ torr we could observe the development of surface discharge into the spatial glow in the low pressure area in front of shock wave at $x \in [5; 10]$. So, we can evaluate the maximum density of energy deposition according to shock wave position and glow intensity. Maximal energy magnitude was 10 eV/particle (or 0.2 J/cm^2).

4 Discharge as a source of instant heating

It was shown theoretically [3], that about 50% of discharge's energy goes directly to the gas heating. VT relaxation time for the other part of discharge's energy is quite long, so under the experimental conditions setup we may consider only instant part of energy release. Thus discontinuity breakdown conditions were realized experimentally. For sliding discharge of plasma electrodes this fact was confirmed experimentally [4]. It is shown [3], that energy input goes in the gas area in front of shock wave and its density equals $q = q_0 V_0/V$. In this formula q_0 is energy input density when there is no shock wave in the discharge chamber, V_0 is volume of discharge section, V is volume of the discharge section area that is in front of shock wave. So the conditions, realized in the setup were used as the boundary and initial conditions for numerical simulation of the processes arising after instant energy release. The surface discharge of plasma sheets, which also concentrates in front of shock wave, was also accounted in 2D numerical simulations.

5 Numerical simulation of flow under the experimental conditions

Spatial energy input. Numerical simulation was conducted within the mathematical model of 2D time-dependent Euler equations. The generalized Godunov finite-difference scheme with piecewise linear representation of gas dynamical fields was used. This approach provides a second order space and time approximation for sufficiently smooth solutions. The problem statement is presented on left part of figure 3. At the initial time moment a plane shock front moving with $M = 3$ from left to right is located at $x = 0$. According to the experimental conditions the energy input which was going to the volumetric part of the discharge $0 < x < 1.5$, $|y| < 1.1$ (domain 2 on figure 3) equaled 0.83 J. Each of the plasma sheets (electrodes) $1.1 < |y| < 1.2$ (domains 3 on figure 3) provided the energy inputs of $0.11J$. According to the previous investigations [4] it was assumed that 50% of energy goes to the instant heating (to transnational degrees of freedom). In the case considered the volumetric energy input density is 16.75% with respect to the total energy behind the shock. So, there are 5 domains with constant flow values at the initial moment. On each boundary of these domains the discontinuity breakdown takes place. The subsequent flow is characterized by the complicated 2D process of interaction and evolution of these secondary discontinuities.

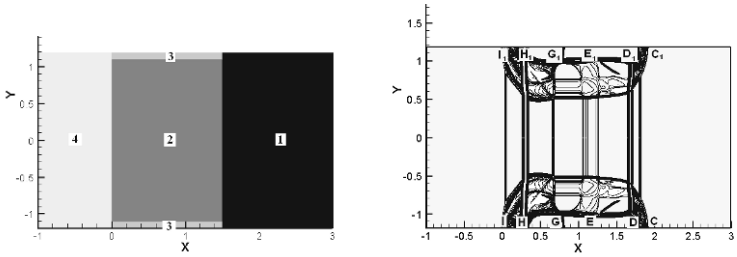

Fig. 3. Left: initial pressure distribution for 2D numerical simulation. Right: density gradient isolines after 0.15 dimensionless time units

Due to the flow symmetry the 2D calculations were held using the grid with 1280x256 cells in half plane $y > 0$. Near the walls in the "hot" regions the shock waves I_1I, C_1C, G_1G and tangential discontinuities H_1H, D_1D (figure 3 (right)) move faster then on the symmetry plane $y = 0$. Furthermore, the discontinuities formed on the plasma sheets boundaries spread and interacts in perpendicular direction. The line of tangential discontinuity D_1D which initially coincides with the boundary of energy input domain twists rapidly due to accelerated motion near the walls. That stage is shown on figure first two pictures of figure 4.

At some time moment shock wave G_1G, which is also twisted, reaches tangential discontinuity D_1D. As the result of their interaction we have two shock waves: reflected and passing. The amplitude of tangential discontinuity D_1D perturbations grow intensely (figure 4). Such flow properties could be considered as a special case of Richtmyer-Meshkov instability [5] (figure 4).

Numerical calculations conducted for experimental conditions distinctly reflect nonlinear and transitional phases of Richtmyer-Meshkov instability development (formation

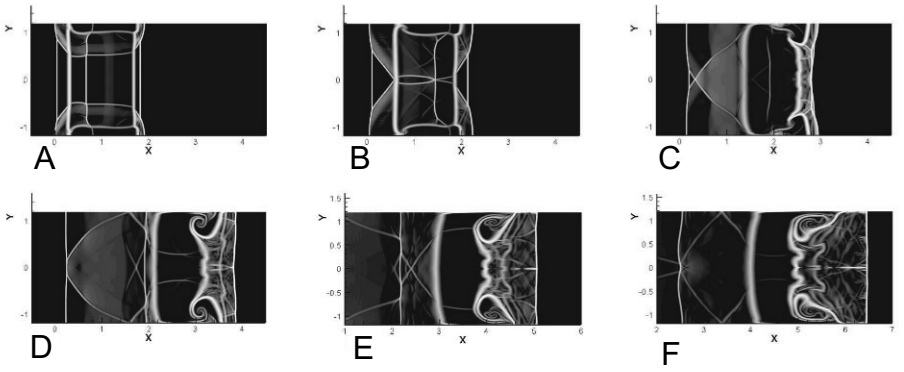

Fig. 4. Density gradient at the consequent time moments

of light gas bubbles which penetrate in dense gas and mushroom-like structures development). They presented on last four pictures of figure 4. Numerical study of turbulent stage requires more complicated mathematical model which account viscosity and involve higher order numerical schemes and grids with much higher spatial resolution.Adequacy of calculations is supported by experimental shadow image of the flow area after energy input (see figure 5 (left)). Time-dependent behavior of Fourier-modes of tangential gap curve is presented on figure 5 (right). These data were obtained by means of discontinuity-fitting method.

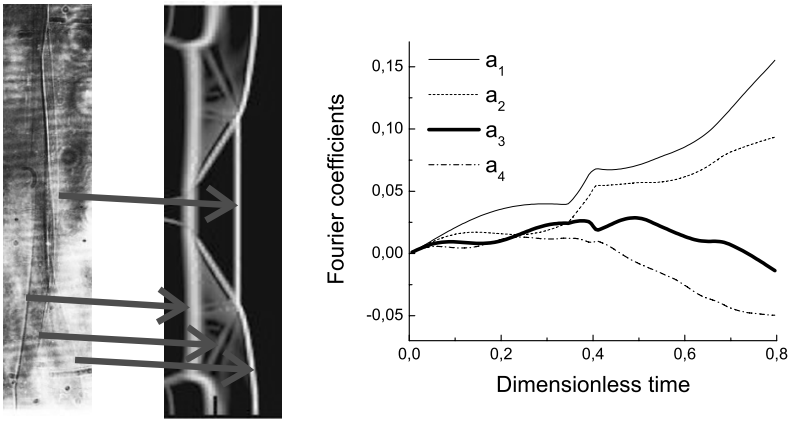

Fig. 5. Left: flow structure near passed shock wave. Right: fourier modes of permutated tangential gap vs dimensionless time

Surface energy input. For simulation of instant surface energy input of plasma sheet areas in front of shock wave we used CFD model based on 2D unsteady Navier-Stokes equations. The parameters of instant energy input correspond experimental ones

(figure 6 (left)). Evolution and stability of shock wave after pulse ionization of channel walls surface was studied. Shock wave interaction with pulse surface discharge includes shock-shock interaction (with transversal shock wave caused by quick energy surface input) and shock interaction with non-equilibrium non-stationary nearwall layer is shown on figure 6 (right). CFD simulation results were found to be in correspondance experimaneal images.

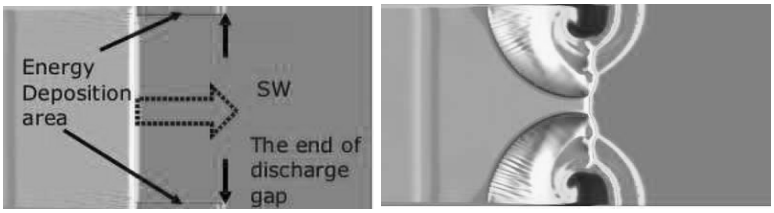

Fig. 6. Left: initial conditions $M = 2.2$; $x = 90$ mm; $W = 0.2$ J/cm^2. Right: density isosurfaces at 15 μs

6 Conclusion

Possibility of experimental realization of discontinuity breakdown conditions by instant energy release in localized area of the gas flow was shown. That type of energy input leads to formation of new discontinuities that can be used in flow control technologies. Results of numerical simulation show the possibility of Richtmyer-Meshkov type instability realization without using additional membranes in flow channel.

Acknowledgement. Researches were conducted at support of RAS Program 9 and RFBR grant 05-08-50247

References

1. Nishio M., Method for visualizing streamlines around hypersonic vehicles by using electrical discharge, AIAA Journal 30 (6), 1662-1663, 1992
2. Bletzinger P., Ganguly B.N., Van Wie D., Garscadden A. Plasmas in high speed aerodynamics, J. Phys. D: Appl. Phys. 38, R33-R57, 2005
3. Znamenskaya I.A., Koroteev D.A., Popov N.A., A nanosecond high-current discharge in a supersonic gas flow, High Temperature. 43(6), 817-824, 2005
4. Znamenskaya I.A., Lutsky A.E., Mursenkova I.V., The surface energy deposited into gas during initiation of a pulsed plasma sheet discharge, Technical Physics Letters 30(12), 1036-1038, 2004
5. Richtmyer R.D., Taylor instability in shock acceleration of compressible fluids, Comm. Pure. Appl. Math. 13, 297-319, 1960

Temperature measurements in the arc heated region of a Huels type arc heater

K. Kitagawa[1], Y. Miyagawa[2], K. Inaba[2], M. Yasuhara[1], and N. Yoshikawa[3]

[1] *Dept. of Mechanical Engng., Aichi Institute of Technology, Toyota, Aichi 470-0392, Japan.*
[2] *Graduate student, Aichi Institute of Technology*
[3] *Dept. of Aerospace Engng., School of Graduate Studies, Nagoya University, Nagoya, Aichi 4648603, JAPAN*

Summary. An arc heating performance of an arc heated wind tunnel is studied to apply for thermal protection technology of reentry flow of earth type planets in hypersonic flight environments and for disposal of industrial and medical waste in the environmental problem. The purpose of the present work is to study basic problems of an arc heating performance of a Huels type arc heater to obtain temperatures from emission spectra profiles in the plenum region. The increase of discharge current are decreasing T_v of the nitrogen molecule, while T_v of the ionized nitrogen molecule changes non-monotonically by effect of arc heating in the plenum region. Rotational temperatures T_r of N_2^+ is measured to be in between 3800 to 3500K for $R(8) - R(30)$ of the rotational quantum number, respectively.

1 Introduction

Electric arc heaters have been used for aeronautical testing of thermal protective materials for hypersonic fright [5, 10] and disposal of toxic wastes after high temperature burning. Hollow type arc heated wind tunnels are constructed for high enthalpy hypersonic flow [1], of with segmented constrictor type, Huels type or Hybrid type. These arc heated wind tunnels have different experimental ranges of gas enthalpy, stagnation temperature and stagnation pressure. Characteristic performance of an arc heated wind tunnel is an important for thermal protection technology of reentry flow into the earth and the other planets, and high temperature property(3000K$\sim$) and to get an accurate estimation of necessary conditions for the power source of the arc heater. Hollow type arc heated high enthalpy wind tunnels are developed and operated such as Huels type [9], Hybrid type [8] or Segmented-constrictor type designs [3, 13].

The purpose of the present work is to study an arc heating performance of a Huels type arc heater including mass flow rate, discharge current and discharge voltage of hot gas, and to obtain temperatures from emission spectra profiles of molecular bands using pure nitrogen and Air as the working gas.

2 Experimental facility and apparatus

2.1 Huels(Hüls) type Arc heater

Huels type DC-arc heater is designed and constructed in Aichi Institute of Technology, and shown schematically in Fig. 1. Huels type arc heater has series of hollow type cathode and anode electrodes, connected to the supersonic nozzle and low density tank with 1m in diameter and 2m in length. Measured quantities are the mass flow rate m(g/sec) and

the temperature T_{01} before heating, the discharge voltage V(V), the discharge current I(A) of the plasma arc, and the pressure p_w of the arc heated tube wall at location B in the plenum region [8][9]. Each component of the arc heater and the supersonic nozzle are independently cooled by cooling water. The inner diameter d and outer diameter d_o of the cathode and anode are 12 and 18mm, respectively. The throat diameter d_t and exit diameter d_e of the supersonic nozzle are 3.5 and 10.5mm, respectively, and Mach number M is about 3.0. The unit consists of two coaxial tubular electrodes separated by an insulator(Teflon) in the plenum chamber. Working gases are injected tangentially into the plenum chamber to make swirl for arc stabilization. Both cathode and anode are made of oxygen free copper. To avoid any undesirable concentrated current spot of discharge at some fixed position of the heating tube surface, a magnetic coil system is attached to the cathode side of arc heater coaxially to the tube axis. This B_x rotate the current spot in the tube by the Lorentz force, and thus avoiding the heated up damage by concentrated spot. The pressure in the low density tank is kept at 13.3Pa(0.1torr) and the stagnation pressure at location B is at 0.1213MPa. The discharge currents are at 80, 100 and 120A, respectively. The mass flow rate depends on the discharge current and stagnation pressure. Test gases used are pure nitrogen, air and carbon dioxide.

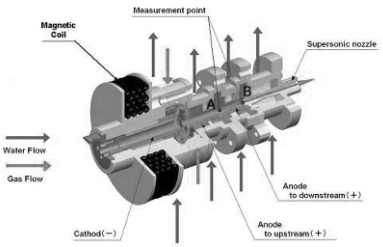

Fig. 1. Schematic view of Huels type arc heater.

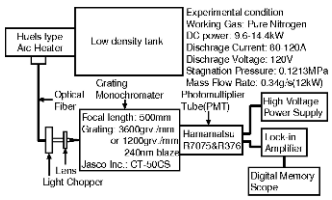

Fig. 2. The optical arrangement of the spectroscopic measurement system.

2.2 Spectroscopic measurement apparatus

The high resolution spectroscopic measurement [2, 11, 12, 14] of the radiation yields a direct evaluation of the vibrational and rotational temperature in the plenum region of arc heater. The optical arrangement of the spectroscopic measurement system is shown in Fig. 2 [8, 9]. The emission spectra profiles from hot gas in the plenum region of arc heated wind tunnel are spectroscopically measured at 78(location A in Fig. 1) and 36mm(location B in Fig. 1) upstream of sonic throat in an arc heater. The monochromator with the focal length of 500mm (Jasco Inc., CT-50CS), uses high resolution grating systems (3600grooves/mm and/or 1200grooves/mm on 240nm blaze). The entrance and exit slit widths are from 0.02 to 0.04mm. The scanning speed of monochromator is about from 1.7 to 5.0nm/min, giving high spectrum resolution. The intensity of spectral light is measured using the photomultiplier tube(PMT, Hamamatsu Photonics R7057 and/or R376) powered by a high voltage power supply(Hamamatsu Photonics C3350). For the emission experiments, the PMT are connected to a lock-in amplifier (NF Co. Ltd., LI5640) whose output are recorded with a digital oscilloscope (Yokogawa Electric Co. Ltd., DL716). Wavelength is calibrated by using gas discharge lamp (Hg), which radiates

well known spectrum. Typically, averages of 300 individual spectra are recorded and the error of temperature measurements amount $\pm(200 \sim 400)$K of vibrational temperatures T_v and $\pm(300 \sim 600)$K of rotational ones T_r, respectively.

3 Results and Discussion

3.1 The 1D stagnation temperature

1D (one dimensional) stagnation temperature T_0 is defined as the one deduced from one dimensional nozzle flow relation, assuming that the heated reactive gas [4] is in thermodynamic equilibrium from the heating tube end down to the choked sonic throat of the supersonic nozzle. 1D nozzle flow theory shows that the ratio $(p_0 - p_w)/p_0$, the difference between stagnation pressure p_0 and pressure p_w divided by p_0, corresponding to the present area ratio A/A_t (A:sectional area of the tube, A_t:throat area of the supersonic nozzle) amounts about 0.001%, and p_w can be approximated by p_0 within about 0.1% of error. Figs. 3 and 4 show the 1D stagnation temperature T_0 plotted against stagnation pressure p_0 under discharge currents for pure Nitrogen, Air and carbon dioxide, respectively. In these figures, the 1D stagnation temperature T_0 increase as the stagnation pressure goes up (p_0=0.05∼0.25MPa). The 1D stagnation temperatures T_0 are evaluated to be in between 1300K to 2300K for pure nitrogen and air, while its T_0 in between 1300K to 2000K for carbon dioxide. These differences of temperature ranges T_0 can be possible, which is coming from the difference of specific heat ratio of heated reactive gas.

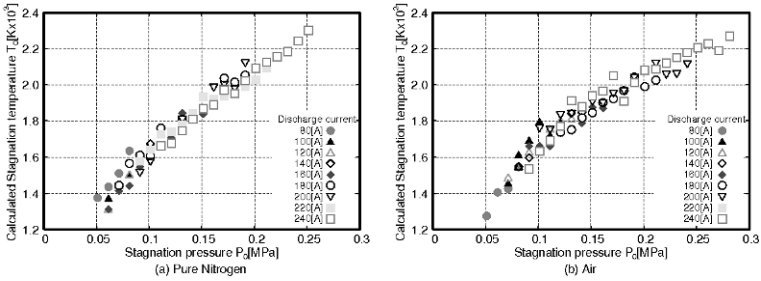

Fig. 3. $T_0 - p_0$ relations at several current conditions, for pure N_2 and Air.

3.2 Spectroscopic measurement of plasma arc

A typical scan of spectra profiles at location B for N_2 and Air plasma arc are shown in Figs. 5 and 6, respectively. The emission spectra are obtained by scanning over the desired wavelength range in 5min of arc heater running time. The identified transitions are attributed to N_2^+ 1-, N_2 2+ and CNV band systems. In Figs. 5 and 6, the vibrational level spectra for ionized nitrogen molecule and molecular clearly show the alternating intensity due to the nuclear spin of one for the nitrogen. In Fig. 6, the spectral lines of CNV have strong signal intensity that exist contamination of arc heated flow by ablation of electrode or insulator of arc heater. The emission spectra profiles can be used to evaluate

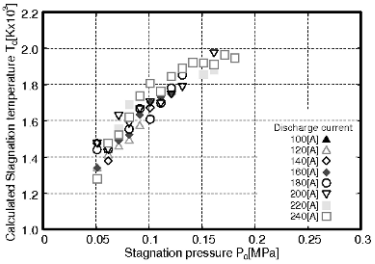

Fig. 4. $T_0 - p_0$ relations at several current conditions, for carbon dioxide.

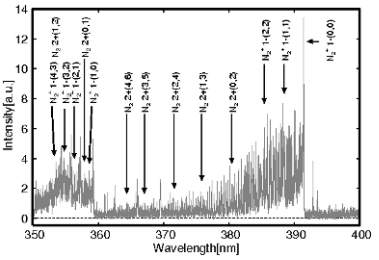

Fig. 5. Measured emission spectra of N_2 plasma arc in the plenum region.

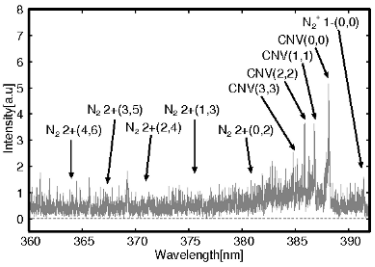

Fig. 6. Measured emission spectra of arc heated air flow in the plenum region.

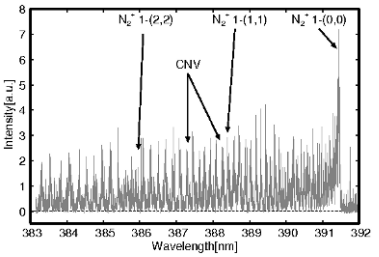

Fig. 7. Measured vibrational and rotational emission spectra showing N_2^+ 1- band system at location B in the plenum region.

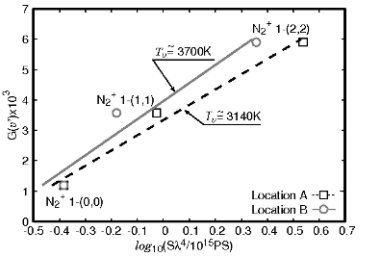

Fig. 8. Boltzmann plot of N_2^+ 1- vibrational level from N_2 plasma arc at both location in the plenum region.

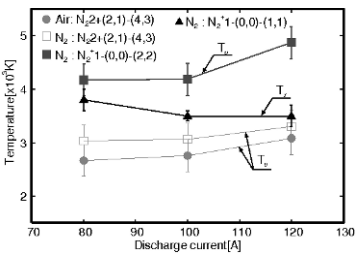

Fig. 9. Comparison of vibrational temperature and rotational temperature for arc heated flow.

the local gas temperatures that exist in an ionized molecular, molecular and atomic gas flow by exploiting the dependences of signal intensity on the temperature dependent population distributions. Vibrational temperatures T_v for plasma arc are determined from Boltzmann plot method by using the ratio of band heads from different vibrational levels of same species. Figure 8 shows the Boltzmann plot [6, 7] of vibrational level at both location in the plenum region. Circles and squares denote at location A and B in the plenum region, respectively. The solid line corresponds to data group with circles location B, and the dotted line to that with squares at location A in the plenum region.

Vibrational temperature T_v for N_2 plasma arc obtained from average inclination line close to (0,0)-(1,1)-(2,2) in N_2^+ 1-, are determined to be about 3140K at location A, and about 3700K at location B, showing that T_v increases due to arc heating in plenum region. Averaged values of vibrational temperature at location B are shown in Fig. 9 as a function of discharge current. Blue squares with solid line correspond to label N_2^+ 1- for N_2 plasma arc, squares with solid line to label N_2 2+ for N_2 plasma arc and red circles with solid line to label N_2 2+ for Air plasma arc. The scatter of vibrational temperature measurements for N_2^+ 1- and N_2 2+ are $\pm(200 \sim 300)$K and $\pm(200 \sim 400)$K respectively under the discharge current range. Vibrational temperatures of N_2^+ and N_2 are measured to be in between 3600 to 5300K and in between 2600 to 3900K, respectively. Results for N_2 plasma arc show that the vibrational temperature T_v for ionized N_2^+ 1- are greater than that for N_2 2+, corresponding to the ionized nitrogen molecule increase with decreasing the nitrogen molecule. Discharge current increases with decreasing T_v of the nitrogen molecule, while T_v of the ionized nitrogen molecule change non-monotonic with increasing discharge current. For Air plasma arc, the discharge current increase with increasing T_v of the nitrogen molecule, which is lower than measured vibrational temperature values for N_2 plasma arc.

Rotationally resolved emission scans are performed by slowly scanning the monochromator from the N_2^+ 1-(0,0) band head at 391.14nm through 380nm, as shown in Fig. 7. The rotational level spectra clearly show the alternating intensity due to the nuclear spin of ionized nitrogen molecule. The P-branch emission lines overlap with R-branch at 391.14nm through 390nm. Neglecting Boltzmann plot of P-branch lines, the first line is used for temperature measurements from $R(8)$ for N_2^+ 1-. The Boltzmann plot of R-branch emission lines trace for $R(8) - R(28)$ of N_2^+ with even rotational quantum number. Averaged values of rotational temperature as a function of discharge current at location B, are shown in Fig. 9. Triangles with solid line indicate by the label N_2^+ 1-. The scatter of the rotational temperature measurements for N_2^+ 1- are $\pm(300 \sim 500)$K under the discharge current range. Rotational temperatures T_r of N_2^+ are measured to be in between 3800 to 3500K for $R(8) - R(26)$ of the rotational quantum number. The discharge current increase with decreasing T_r of the ionized nitrogen molecule, which are lower than measured vibrational temperature values. These indicate that the thermal equilibrium is not reached at location B in the plenum region of present Huels type arc heater.

4 Conclusion

The present research is to study an arc heating performance of high efficiency arc heated wind tunnel and database of spectra profiles in plasma flow. In order to experimentally investigate these problems, arc heated wind tunnel is traditionally used, which provide an insight to establish analytical modeling of an arc heated flow.

A method of estimating 1D stagnation temperatures is proposed from the measured stagnation pressure and mass flow rate, with the aid of a high temperature gas table. The 1D stagnation temperature T_0 increase as the stagnation pressure goes up. T_0 are evaluated to be in between 1300K to 2300K for pure Nitrogen and Air, and in between 1300K to 2000K for carbon dioxide, respectively. Spectral profiles in an arc heated flow of pure nitrogen are obtained to estimate the vibrational and rotational temperatures from N_2^+ 1- and N_2 2+ bands in the plenum region of the Huels type arc heater.

The vibrational-rotational spectra profiles can be separated using a high resolution grating system and a quick response PMT of the spectroscopic measurement system. Vibrational temperatures of N_2^+ 1- and N_2 2+ for N_2 plasma arc are measured to be in between 3600 to 5300K and in between 2600 to 3900K, respectively. The increase of discharge current are decreasing T_v of the nitrogen molecule, while T_v of the ionized nitrogen molecule changes non-monotonically by effect of arc heating in the plenum region. Rotational temperatures in R-branch ($\Delta J = +1$) of N_2^+ 1- for N_2 plasma arc is measured to be in between 3800 to 3500K. Difference of T_r and T_v shows that the thermal equilibrium is not reached at location B in the plenum region of present Huels type arc heater.

References

1. Cohen, L.M., Hanson, R.K.: Emission and Laser-Induced Fluorescence Measurements in a Supersonic Jet of Plasma-Heated Nitrogen, J. Phys. D: Appl. Phys., **25**, pp. 339-351(1992)
2. Czernlchowski, A.: Temperature Evaluation from the partially Resolved 391 nm N_2^+ band, J. Phys. D: Appl. Phys., **20**, pp. 559-564(1987)
3. Donohue, J.M., Fletcher, D.G., Park, C.S.: Emission Spectral Measurements in the Plenum of an Arc-Jet Wind Tunnel, AIAA Paper 1998-2946(1998)
4. Hilsenrath, J., Klein, M., and Wolley, H.W.: Tables of Thermodynamics Properties of Air including Dissociation and Ionization from 1500K to 15000K, AEDC-TR-59-20(1959)
5. Hinada, M., Inatani, Y., Yamada, T., Hiraki, K.: An Arc Heated High Enthalpy Test Facility for Thermal Protection Studies, ISAS Rep. No.664, ISAS(1996)
6. Huber, K.P., Herzberg, G.: *Molecular Spectra and Molecular Structure, IV Constants of diatomic molecules*, pp. 426-427(1979)
7. Jarmain, W.R., Fraser, P.A., Nicholls, R.W.: Vibrational Transition Probabilities of Diatomic Molecules: collected results N_2, N_2^+, NO, O_2^+, Transition probabilities, pp. 228-233(1953)
8. Kitagawa, K., Mori, Y., Yoshikawa, N., Yasuhara, M.: Characteristics of High Efficiency Arc Heated Wind Tunnel, Proc. 23rd Int. Sympo. on Space Technology and Science, ISTS2002-e-54p(2002)
9. Kitagawa, K., Miyagawa, Y., Inaba, K., Yoshikawa, N., Yasuhara, M.: Spectroscopic temperature measurements in the plenum region of a huels type arc heated wind tunnel, Proc. 25th Int. Sympo. on Space Technology and Science, ISTS 2006-e-13(2006)
10. Kubota, K., Funatsu, M., Shirai, H., Tabei, K.: Spectroscopic Measurements of Micro-air Plasma-Jets at an Atmospheric Pressure(in Japanese), Trans. of the Japan Soc. of Mech. Engng Part B, 17-7, pp. 1806-1812(2005)
11. Muntz, E.P.: Measurement of Rotational Temperature, Vibrational Temperature, and Molecule Concentration, in Nonradiating Flow of Low Density Nitrogen, Institute of Aero physics University of Toronto, UTIA Report No.71, AFSOR TN 60-499(1961)
12. Parigger, C., Plemmons, D.H., Hornkohl, J.L., Lewis, J.W.: Temperature Measurements from First-Negative N_2^+ Spectra Produced by Laser-Induced Multiphotn Ionization and Optical Breakdown of Nitrogen, Applied Optics, 34-18, pp. 3331-3335(1995)
13. Park, C.S., Newfield, M.E., Fletcher, D.G., Gökcen, T.: Spectroscopic Measurements of Shock Layer Flows in an Arc Jet Facility, J. Thermophysics and Heat Transfer, 13-1, pp. 60-67(1999)
14. Robben, F., Talbot, L.: Some measurements of Rotational Temperatures in a Low Density Wind Tunnel using Electron Beam Fluorescence, Institute of engineering research University of California Barkeley, California, Report No.AS-65-5(1965)

Part XVI

Propulsion

A model to predict the Mach reflection of the separation shock in rocket nozzles

F. Nasuti and M. Onofri

Sapienza University of Rome, Dipartimento di Meccanica e Aeronautica
Via Eudossiana 18, 00184 Rome (Italy)

Summary. In case of high overexpansion, the exhaust jet of the supersonic nozzle of rocket engines separates from nozzle wall because of the large adverse pressure gradient. At the same time, to match the pressure of the separated flow region, an oblique shock is generated which evolves through the supersonic jet starting approximately from the separation point. This shock reflects on the nozzle axis with a Mach reflection. Thus a peculiar Mach reflection takes place whose features depend on the upstream flow conditions, which are usually not uniform. A simplified model is presented which is a first step to predict the expected features of Mach reflection depending on the nozzle shape and on the position of the separation point along the divergent section of the nozzle.

1 Introduction

Large liquid rocket engines experience during their startup a relatively long time of overexpanded operation, with high side loads which may affect the structural integrity of nozzles [1]. This phase lasts a time of the order of the second, that is much larger than characteristic time-scales of the flow. Therefore, it is possible to analyze the phenomenon by steady-state solutions at different ratios between chamber and ambient pressure (that is at different degrees of overexpansion).

The operating condition at pressure ratio (PR, the ratio of chamber to ambient pressure) much lower than the design value, which is only reached at the end of the startup transient, yields a separation of the boundary layer. The flow separation in a supersonic stream is associated with the generation of an oblique shock wave, the separation shock wave, allowing also the supersonic stream to recover the ambient pressure value (see Fig. 1). This shock reflects on the nozzle axis with a Mach reflection. The characteristics

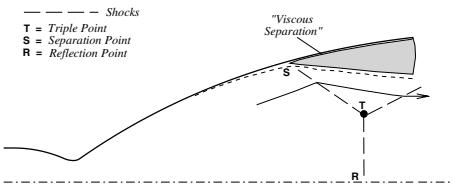

Fig. 1. Separation shock Mach reflection without flow reattachment.

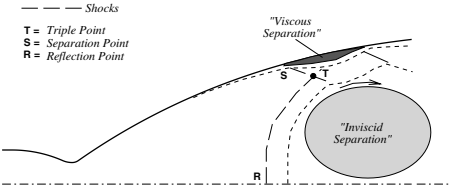

Fig. 2. Separation shock Mach reflection with flow reattachment.

of the separation shock and of its reflection on the symmetry axis have a decisive influence on the evolution of the flow, including the possible flow reattachment following flow

separation, which has been considered of crucial importance to determine the strength of the above mentioned side loads [1–3]. A typical configuration of separation-shock reflection presenting flow reattachment is shown in Fig. 2. In that case the flow non-uniformity ahead of the shock is such to generate a vortex in the core of nozzle flow and to move the supersonic jet behind the oblique shock towards the wall.

On the basis of published numerical and experimental studies of the phenomenon [4,5], the present study aims to discuss a simplified model to predict the expected kind of Mach reflection of the separation shock and thus the possible consequences in terms of generation of side loads.

2 Separation shock Mach reflection

To study a model for the separation-shock Mach reflection in a supersonic nozzle, is necessary to recall simpler flow structures, for which models have been published in the literature. The basis of the following discussion is the model introduced by Li and Ben-Dor [6]. This model deals with the Mach reflection generated by a finite-length planar wedge placed in a uniform supersonic stream and is able to predict the Mach stem height and position by the analysis of the interaction between the supersonic expansion fan at the end of the wedge and the subsonic converging stream-tube generated behind the Mach stem. It is based on a well-defined structure for the Mach reflection, which needs a number of conditions to be satisfied. For instance, if a pressure ratio through the separation shock of 4.0 is considered, the upstream Mach number has to be in the range $2.15 - 3.17$ (ratio of specific heats $\gamma = 1.4$).

2.1 Oblique shock in a planar uniform flow

Among the possible cases studied in [6], the case with the reflected shock impinging exactly on the corner of the wedge is examined here. In fact, as shown by the schematic

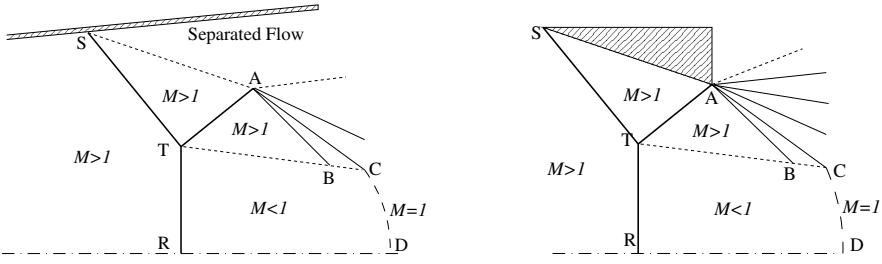

Fig. 3. Special case of Li and Ben-Dor model for the analysis of separation-shock reflection in nozzles. Left: schematic of shock pattern in overexpanded nozzles; right: schematic of Li and Ben-Dor model shock pattern when the reflected shock impinges on the wedge corner.

of Fig. 3, the basic separation-shock reflection in overexpanded nozzles (Fig. 1), is quite similar to that particular case of wedge generated shock reflection. According to the model of [6], among the possible positions of T along the separation shock starting in S, the correct position must be such that the area ratio CD/TR is the sonic one, on the

basis of the average subsonic Mach number evaluated behind the shock TR. Beside that, to close the problem, the position of the point C has to be determined with respect to S, T, and A. The point C is defined as the point on the contact discontinuity TBC where the flow becomes again horizontal. Thus AC is taken as the Mach line corresponding to horizontal flow (Prandtl-Meyer expansion between the Mach lines AB and AC changing the flow direction from TB to horizontal). The length of AC, and thus the position of C, is then easily computed by a mass balance between ST and AC.

The model implemented for the uniform planar flow shows a good agreement with numerical results confirming the findings of [6]. For example, a comparison with numerical results is shown in Figure 4a for the case with upstream Mach number $M = 2.7$ and pressure ratio through the separation shock $p_a/p_s = 4.0$.

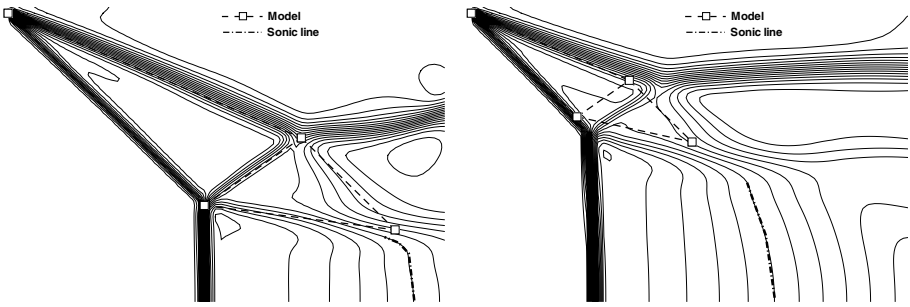

(a) planar flow (b) axisymmetric flow

Fig. 4. Comparison of CFD (Mach number contour lines) and model results for the case of uniform flow with $M = 2.7$ and pressure increase through the separation shock $p_a/p_s = 4.0$.

2.2 Oblique shock in an axisymmetric uniform flow

While in case of planar flow either regular or Mach reflection can occur depending on upstream flow conditions and separation-shock pressure ratio, in the axisymmetric case only the Mach reflection is possible. In fact, the flow turning downstream of the separation-shock yields a pressure increase which eventually leads to an increase of the shock strength and thus of the shock slope. In the present study it will be assumed that the downstream pressure and shock-slope growth along the separation shock ST, which is caused by the axisymmetric channel narrowing behind it, is a secondary effect and thus it will be neglected. It could be introduced as an improvement of the present model in future studies. The further hypothesis is made that the supersonic stream between the incident and the reflected shock (region STA in Fig. 3) and between the reflected shock and the slipstream discontinuity evolving downstream of the triple point (region ATBC in Fig. 3) behaves like in the planar case. Note that in this case it is assumed again that the Mach line AC is straight, but the position of C is now evaluated by the axisymmetric mass balance between ST and AC. Finally, the computation of the position of the triple point T is made considering the axisymmetric area ratio between the circles with radii TR and CD. Because of the larger number of simplifying assumptions, the agreement with numerical

results is less precise than in the planar case. Nevertheless, considering the simplicity of the model, the results show a good agreement (Figure 4b).

2.3 Nonuniform flow

In the study of Mach reflection of the separation shock in overexpanded nozzles it has to be considered that the axisymmetric flow upstream of the separation shock is neither horizontal nor uniform. Rather, the flow direction and Mach number show radial and axial gradients, whereas the assumption of isentropic flow ahead of the shocks can still be made. The first problem to face in modeling Mach reflection for nonuniform upstream flows is

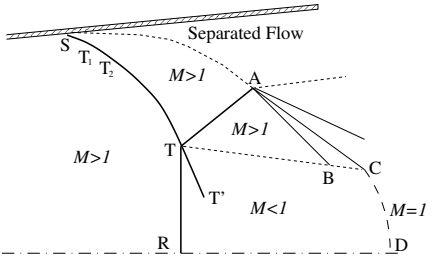

Fig. 5. Schematic of nonuniform flow model for Mach reflection.

to model the region STA (Figure 5). As a first attempt, in the present study, constant pressure is assumed in this region. This assumption neglects axisymmetric effects as made in the foregoing section, moreover it neglects the role that gradients of flow Mach number and direction have on the pressure evolution. However, because the upstream pressure and flow direction are not uniform, the constant downstream pressure value can only be obtained through a curved shock ST of varying intensity. To compute the separation shock, the present model therefore proceeds as follows. Starting from S an elementary part ST_1 is built on the basis of flow conditions upstream of S. The next elementary part of ST (that is T_1T_2) is calculated from the upstream flow conditions in T_1, and so on up to a point T' where the shock becomes a strong shock (subsonic flow behind it). The triple point T must belong to the line ST' and its position can be found by an iterative process which searches for the supersonic flow evolution in TAC and the subsonic flow evolution in RTCD that lead to the same point C, as done in the foregoing sections. For each iteration, a position of T is assumed, and a triple point three-shocks solution is computed. The strong shock solution is used, as done in the foregoing sections, to determine the subsonic flow Mach number behind TR. However, differently than in 2.1-2.2, in this case there is neither a single Mach number nor a single flow direction value, both ahead of the shock TA and in the region TAC: the reflected shock solution in T is then assumed as a uniform flow solution in the region TAC. Taking these uniform values of pressure, Mach number and flow direction, a straight reflected shock is built and the position of the point A is obtained from the mass-flow-rate balance between ST and TA. At this point a uniform flow is avaliable downstream of the reflected shock representing the supersonic flow conditions, as well as the average subsonic Mach number behind the Mach stem. Thus the model can find the final position of T by analyzing the area ratio between the circles of radii TR and CD. If the area ratio is the sonic one the iteration

process ends, else a new position of T is selected and a new iteration is made. The present model can be used to study the evolution of the separation shock for varying PR in a nozzle, once a Euler solution is computed by CFD. For instance, the separation point and the value of pressure in the separated flow region can be obtained by using the wall pressure computed by CFD and a separation criterion. Then the separation shock ST can be computed taking from the CFD solution the properties of the nonuniform flow upstream. At this point it is possible to use the above described model as all information needed is available. Typical results obtained with the present approach for the truncated ideal contour nozzle discussed in [7] are displayed in Figure 6. These results have been

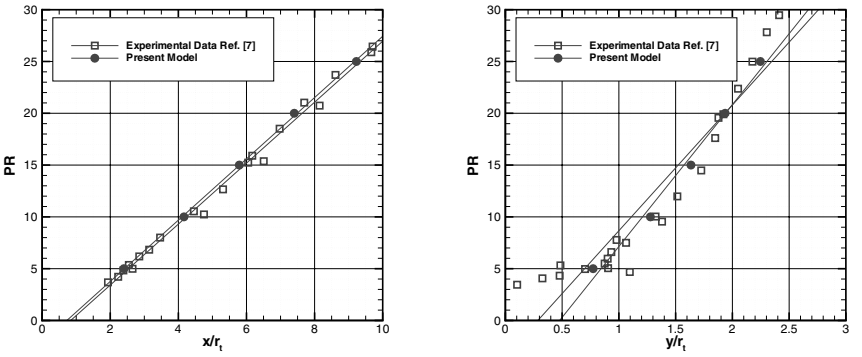

(a) axial position (b) radial position

Fig. 6. Triple point position: comparison of present model results and experimental data.

obtained by taking the separation location from the experimental data rather than also introducing the uncertainty coming from the separation criterion. It is interesting to note that a good agreement of the position of the triple point with experimental data is obtained, although the comparison with CFD results shows some differences in the flow structure downstream.

2.4 Nonuniform flow with inviscid separation

The model presented in the foregoing section can be applied to the case of overexpanded nozzle, provided that the flow conditions are such that the hypotheses of the model of [6] are valid. In this sense, it should be noted that, the range of validity of the model is in principle very narrow: the upstream Mach numbers must be in the range $1.7 - 3.2$ (values relevant to flows with ratio of specific heats $\gamma = 1.4$) if the separation pressure ratio is in the range of $2.5 - 4.0$. However, the flow pressure upstream of the separation shock usually decreases and the flow Mach number increases moving from S to T and thus a pressure ratio larger than the separation one and a larger Mach number are found ahead of the triple point. This property enlarges the range of validity of the model for overexpanded nozzles. Nevertheless, it must be remembered that the model has been introduced for uniform flow and thus the results can only be considered reliable in case

of slight radial nonuniformities. In the other cases, a limitation for the application of the model is due to the shape of the Mach disk (TR). In fact, the model described above assumes that a converging channel takes place behind TR, but this is not always the case in overexpanded nozzles. To better understand this limitation it can be useful to analyze the evolution of the Mach stem starting from the axis (that is going from R to T), and assuming constant pressure downstream (Fig. 7). The figure shows that there

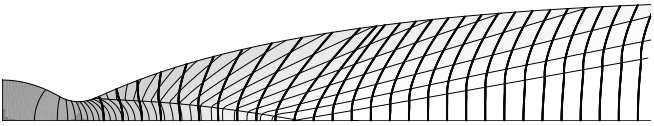

Fig. 7. Mach stem of the separation shock reflection assuming constant pressure downstream in an ideal nozzle.

is a region where strong radial gradients take place. When the Mach stem lies in these regions it can be expected that it bends downstream, rather than upstream, and thus a triple point with a "diverging" channel will take place, rather than a "converging" one.

3 Conclusion

A first step in the development of a model for the study of the Mach reflection of the separation shock in overexpanded rocket nozzles has been presented. The model only addresses the case of nozzles with slight radial gradients, for which it shows a good agreement with experimental data. The next step of the study will be the extension of the model to the cases leading to the "inviscid separation".

References

1. Nave L., Coffey G., Sea level side loads in High-Area-Ratio Rocket Engines, AIAA Paper 73–1284, 1973
2. Nasuti F., Onofri M., Viscous and Inviscid Vortex Generation During Startup of Rocket Nozzles, AIAA Journal, vol. 36, pp. 809-815, 1998
3. Frey M., Hagemann G., Restricted Shock Separation in Rocket Nozzles. J Propulsion and Power, vol. 16, pp. 478-484, 2000
4. Onofri M., Nasuti F., The Physical Origin of Side Loads in Rocket Nozzles, AIAA Paper 99–2587, 1999
5. Nasuti F., Onofri M., Pietropaoli E., Shock-Generated Vortices in Rocket Nozzles, AIAA Paper 2005–317, 2005
6. Li H., Ben-Dor G., A Parametric Study of Mach Reflection in Steady Flows, Journal of Fluid Mechanics, vol. 341, pp. 101-125, 1997
7. Stark R.H., Wagner B.H., Experimental Flow Investigation of a Truncated Ideal Contour Nozzle AIAA Paper 2006-5208, 2006

Computation of hypersonic double wedge shock / boundary layer interaction

B. Reinartz and J. Ballmann

RWTH Aachen University, Lehr- und Forschungsgebiet für Mechanik
Templergraben 64, 52062 Aachen (Germany)

1 Introduction

Within the frame of the Research Training Group "Aerothermodynamic Design of a Scramjet Demonstrator for Future Space Transportation Systems" a combined numerical as well as experimental analysis of hypersonic inlet flows has been initiated. For an air breathing hypersonic propulsion system, the engine inlet consists of a series of exterior compression ramps and a subsequent interior isolator/diffusor assembly. Compression of the incoming flow is thereby achieved through oblique shock waves. Two phenomena characterize the technological problems of the engine: on the one hand, the interaction of strong shock waves with thick hypersonic boundary layers causes large separation zones that reduce the captured mass flow and thus the engine performance. On the other hand, the high total enthalpy of the flow leads to severe aerodynamic heating, further enhanced by turbulent heat fluxes.

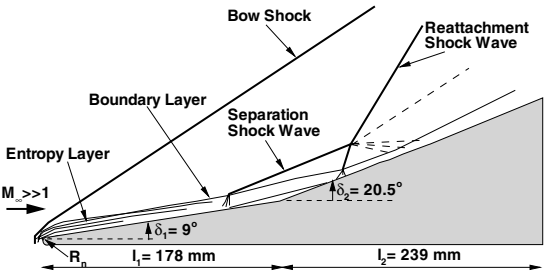

Fig. 1. Shock / boundary layer interaction schematic on a blunt double wedge configuration

To improve the accuracy of numerically simulating the exterior inlet compression, the computation of the double wedge configuration shown in Fig. 1 has been initiated in correspondence to a recent experimental study [1] investigating the effect of different wall temperatures (T_W = 300K, 600K, and 760K) as well as different leading edge radii (R = sharp, 0.5 mm, and 1 mm) on the flow separation. A preliminary quasi–steady 2D analysis [2] showed the flow to be transitional. In the current paper, the effect of different turbulence models on the size of the separation and on the peak values for pressure and surface heat flux are investigated.

2 Numerical Method

2.1 Navier–Stokes Solver FLOWer

The FLOWer code [3] is applied, which solves the unsteady compressible Navier–Stokes equations using a cell–centered finite volume method on block–structured grids. An advection upstream splitting method (AUSM) Flux Vector splitting is used for the inviscid fluxes and second order accuracy in space is achieved by means of a monotonic upstream scheme for conservation laws (MUSCL) extrapolation where a van Leer limiter function is used to guarantee the total variation diminishing (TVD) property of the scheme. The diffusive fluxes are discretized by central differences. Time integration is performed by a five–step Runge–Kutta method. To enhance convergence, a multigrid method, implicit residual smoothing, and local time stepping for steady–state computations are applied.

2.2 Turbulence Modeling

In case of turbulent flow, a wide variety of compressible low Reynolds number turbulence models based on the Reynolds averaged Navier–Stokes equations are available in FLOWer. Already well proven are the eddy viscosity models where a linear dependence of the Reynolds stress tensor on the strain rate tensor is assumed. Depending on the model, different numbers of transport equations for some turbulent quantities are solved which are then used to compute the eddy viscosity. Here, the one-equation Spalard–Allmaras (SA) and the Strain-Adaptive Linear Spalard–Allmaras (SALSA) model [4] as well as the two-equations k-ω model of Wilcox [5] are applied. Also tested is the more recently developed Shear Stress Transport (SST) k-ω model of Menter [6] which is a combination of the Wilcox model close to wall with the k-ϵ model further off.

However, for wall dominated flows with thick boundary–layers, strong shock / boundary–layer interaction and with separation, as they are of interest here, the assumption of a linear dependence between the Reynolds stress tensor and the strain rate tensor is not always valid. Therefore, two relatively newly implemented differential Reynolds stress models (RSM) [7,8] are also tested in the double–wedge simulations. Those models solve transport equations for each component of the Reynolds stress tensor as well as for an additional length scale. Thus, they are computationally expensive. Furthermore, they decrease the stability of the numerical scheme. Hoewever, RSM computations show promising results, especially for separated flows. The first model applied is the Wilcox stress-ω model (Wilcox RSM) [8] which is a combination of a simplified version of the Launder-Reece-Rodi (LRR) model where Wilcox ω-equation is used for supplying the length scale to close the system. The second model uses the modified LRR model by Wilcox close to the wall, the Speziale-Sarkar-Gatski (SSG) in the farfield and Menter's ω-equation for closure. Accordingly, that model is called SSG/LRR-ω model [7].

Like the flow equations, the spatial discretization of the turbulent transport equations is performed using an AUSM upwind scheme with van Leer limiter for the convective and central discretization for the diffusive terms. In addition to the stability problems inherent in the differential Reynolds stress models, the low Reynolds number damping terms as well as the high grid aspect ratio near the wall make the system of turbulence equations of all models stiff. To increase the numerical stability of turbulent flow simulations, the time integration of the turbulence equations is decoupled from the mean flow equations, and the turbulence equations are solved using a diagonal dominant alternating direction implicit (DDADI) scheme [9].

2.3 Boundary Conditions

At the inflow boundary, the freestream conditions of the experimental investigation listed in Table 1 are prescribed. The turbulent values are determined by the specified freesteam turbulence intensity of $Tu_\infty = 0.5$: $k_\infty = 1.5(Tu_\infty u_\infty)^2$ and $\omega_\infty = k_\infty/(0.001 \times \mu)$. For the supersonic outflow, the variables are extrapolated from the interior. At solid walls, the no-slip condition is enforced by setting the velocity components, the turbulent kinetic energy and the normal pressure gradient to zero. The specific dissipation rate is set proportionally to the wall shear stress and the surface roughness. The energy boundary condition is directly applied by prescribing the wall temperature when calculating the viscous contribution of wall faces. Three different wall temperatures are simulated: $T_W =$ 300 K, 600 K and 760K. In case of two–dimensional computations, the FLOWer code is run in a special mode for plane flow.

Table 1. Test conditions

M_∞	Re_∞ [1/m]	T_0 [K]	T_∞ [K]
8.3	3.76×10^6	1420	102

Because there is no transition model available in FLOWer, the transition process is modeled by switching on the respective turbulence model at a certain streamwise location. For all transitional computations shown in this paper, the first wedge has been computed laminar and a turbulence model has been used for the flow computation on the second wegde. Thus, the hinge line represents the chosen point of transition.

2.4 Computations

The FLOWer computations are performed on the SunFire SMP–cluster of RWTH Aachen university as well as on an IBM p690 cluster of Research Centre Jülich. The parallelization is jointly based on FLOWer's block–based MPI (message passing interface) formulation as well as on an OpenMP shared memory parallelization. A complete validation of the FLOWer code has been performed by the DLR prior to its release [3] and continued validation is achieved by the analyses documented in subsequent publications [10,11]. The accuracy of the current investigation is evaluated by comparison with the experimental results.

3 Results

The computation of the double wedge configuration shown in Fig. 1 has been initiated in correspondence to a recent experimental study [1] investigating the effect of different wall temperatures ($T_W =$ 300K, 600K, and 760K) as well as different leading edge radii ($R =$ sharp, 0.5 mm, and 1 mm) on the flow separation. Figure 2 shows the computed Mach number distribution for a cold model with a slightly blunted leading edge and a large separation. Detail A shows the detached bow shock in front of the leading edge which converges towards an oblique first ramp shock. The separation shock meets the

bow shock at the first triple point (TP1) forming a combined shock which again meets the reattachment shock at the second triple point (TP2). Streamlines are included in Detail B to show the size of the separation zone and the shear layer above. To model the transitional flow behavior, the flow on the first wedge has been computed laminar but an SSG/LLR-ω turbulence model was used on the second wedge.

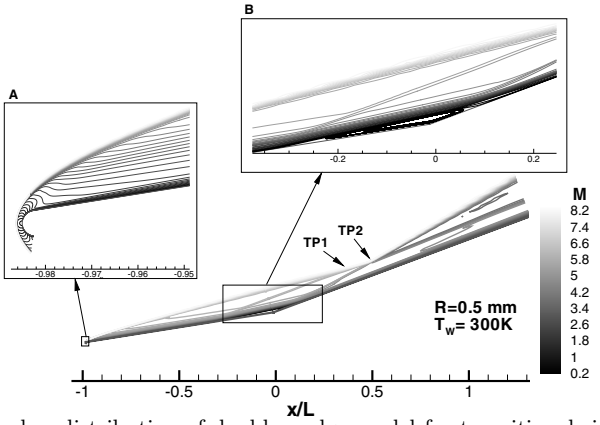

Fig. 2. Mach number distribution of double wedge model for transitional simulation with the SSG/LLR-ω turbulence model. (R= 0.5 mm, T_W= 300 K, TP=triple point). Details of bow shock (A) and separation region (B, incl. streamlines)

Figure 3.a shows the Stanton number distributions for laminar, turbulent and transitional simulations in comparison to experimental and theoretical results. The transitional analysis was initiated because on the one hand pure laminar computations overpredict the size of the separation and at the same time underpredict the peak heating near reattachment by about one order of magnitude. On the other hand, in pure turbulent simulations the flow does not separate at all which is shown exemplary for an SSG/LLR-ω model in Fig. 3.a. Comparison of the experimental data with the results of a self similar theory [12] indicate that at least the incoming flow prior to separation seems to be laminar. Since the shear layer above the separation is the most unstable region in the flow, the shear layer Reynolds number based on the definition of Birch and Keyes [13] is used to analyze the state of the flow. The plotted data in Fig. 3.b. represent the Reynolds number based on the high-speed flow above the layer and on the distance along the shear layer from the point of separation. According to Birch and Keyes, transition in a free shear layer formed by shock interactions occurs at shear layer Reynolds numbers between 30,000 to 65,000. Thus, the Reynolds number values of Fig. 3.b indicate a certain degree of turbulence in the shear layer right after the boundary layer separates. Because the point of separation is not known a priori and depends on the turbulence model used, the hinge line between the first and the second wedge is chosen as point of transition. In Fig. 3.a, the results of a transitional analysis also applying the SSG/LLR-ω model show that the overall agreement with the experimental data is improved. The size of the separation is now slightly underpredicted, causing the recompression shock wave to be steeper than in the measurements. However, because the last two heat flux sensors were not working during the tests on the blunted model, the measurements may miss the actual Stanton number peak downstream of reattachment.

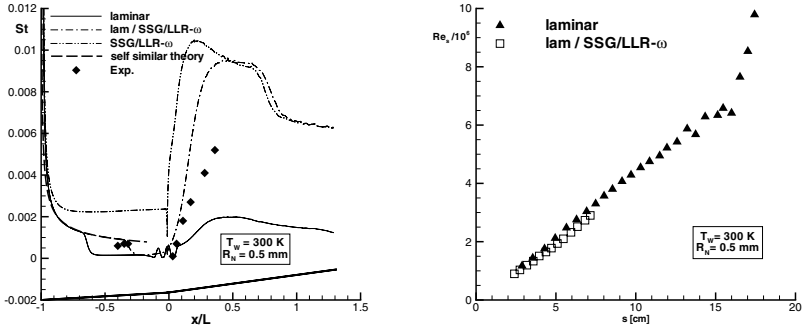

Fig. 3. Stanton number distributions and shear layer Reynolds number based on Birch and Keyes definition [13] for different simulations. Comparing results of laminar, turbulent and transitional computations with experimental data taken from Neuenhahn et al. [1]

Figure 4 compares the results of transitional simulations using different turbulence models and showing a noteworthy influence of the turbulence model on the flow solution. The SSG/LLR-ω model best predicts the size of the separation and only slightly underpredicts the pressure peak. However, it does not meet the distribution of the Stanton number on the second wedge. This is best represented by the Wilcox stress-ω model which otherwise overpredicts the separation region. The two two-equations models lie somewhat in between the two Reynolds stress models and seem to give a good but not exact estimation of the wall distributions of heat flux and pressure. Currently, the effect of moving the point of transition upstream is investigated. This analysis might improve the agreement between CFD and experiment further.

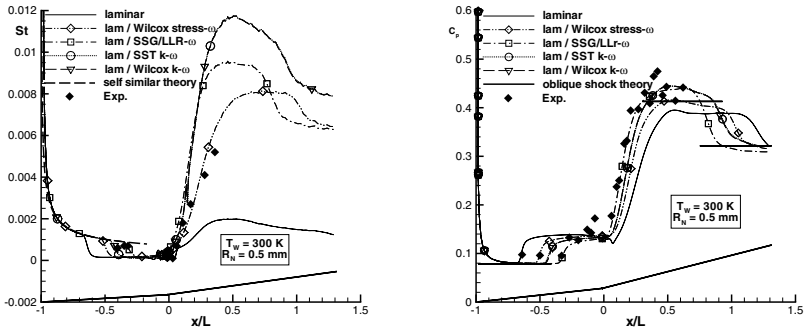

Fig. 4. Stanton number distributions and pressure coefficient distributions for different simulations. Comparing results of laminar and different transitional computations with experimental data taken from Neuenhahn et al. [1]

4 Conclusions

In oder to improve the predictability of supersonic inlet flows, detailed numerical simulations are performed for an experimental double wedge test case. Comparison of the measured Stanton number distribution with laminar and turbulent results indicates that

the double wedge flow is transitional. Further analysis of the shear layer Reynolds number shows that the flow downstream of separation is already turbulent. Different turbulence models have been applied to this test case showing a noteworthy influence on the results. Currently, the effect of the point of transition is investigated.

Acknowledgement. This work has been financially supported by the Deutsche Forschungsgemeinschaft (DFG) within the frame of the Research Training Group GRK 1095/1 "Aerothermodynamic Design of a Scramjet Propulsion System". Appreciation is expressed to the Shock Wave Laboratory of the RWTH Aachen University for the supply of the measurement data.

References

1. T. Neuenhahn and H. Olivier: *Influence of the wall temperature and the entropy layer effects on double wedge shock boundary layer interactions*, AIAA Paper 2006-8136 (2006)
2. B.U. Reinartz, J. Ballmann, and R.R. Boyce: *Numerical Investigation of Wall Temperature and Entropy Layer Effects on Double Wedge Shock / Boundary Layer Interactions*, AIAA Paper 06-8137 (2006)
3. N. Kroll, C.-C. Rossow, K. Becker, and F. Thiele: *The MEGAFLOW Project*, Aerospace Science and Technology **4**, 4, pp 223-237 (2000)
4. P.R. Spalart and S.R. Allmaras: *A One-Equation Turbulence Model for Aerodynamic Flows*, AIAA Paper 92–0439 (1992)
5. D.C. Wilcox: *Turbulence Energy Equation Models*, Turbulence Modeling for CFD **1**, 2nd ed, pp 71–170, DCW Industries, Inc., La Canada, CA (1994)
6. F.R. Menter: *Two-Equation Eddy-Viscosity Turbulence Models for Engineering Applications*, AIAA Journal **32**, 8, pp 1598–1605 (1994)
7. B. Eisfeld and O. Brodersen: *Advanced Turbulence Modelling and Stress Analysis for the DLR-F6 Configuration*, AIAA Paper 2005-4727 (2005)
8. B. Eisfeld: *Implementation of Reynolds stress models into the DLR-FLOWer code*, DLR, Institute of Aerodynamics and Flow Technology, IB 124-2004/31 (2004)
9. J.E. Bardina, P.G. Huang, and T.J. Coakley: *Turbulence Modeling Validation, Testing, and Development*, NASA Technical Memorandum 110446 (1997)
10. T.A. Coratekin, J. van Keuk, and J. Ballmann: *On the Performance of Upwind Schemes and Turbulence Models in Hypersonic Flows*, AIAA Journal **42**, 5, pp 945–957 (2004)
11. B.U. Reinartz, J. Ballmann, C. Herrmann, and W. Koschel: *Aerodynamic Performance Analysis of a Hypersonic Inlet Isolator using Computation and Experiment*, AIAA Journal of Propulsion and Power **19**, 5, pp 868–875 (2003)
12. J. Anderson: *Hypersonic and High Temperature Gas Dynamics*, MacGraw–Hill (1989)
13. S.F. Birch and J.W. Keyes: *Transition in Compressible Free Shear Layers*, Journal of Spacecraft and Rockets **9**, 8, pp 623–624 (1972)

Disintegration of hydrocarbon jets behind reflected shock waves

I. Stotz[1], **G. Lamanna**[1], **B. Weigand**[1], **and J. Steelant**[2]

[1] *Institut für Thermodynamik der Luft- und Raumfahrt, Universität Stuttgart Pfaffenwaldring 31, 70569 Stuttgart (Germany)*
[2] *Propulsion and Aerothermodynamics Division, ESTEC-ESA Keplerlaan 1, 2200 AG Noordwijk (The Netherlands)*

Summary. A shock tube facility to generate a high pressure and temperature test environment has been built and characterised. Shock tube experiments were performed to study the disintegration of liquid hydrocarbon jets at elevated pressures and temperatures. Shadowgraph images of the spray were acquired and analysed. The objective of this paper is to show the feasibility of a shock tube to investigate hydrocarbon spray injection and disintegration processes performed at conditions relevant to different propulsion systems. First results using shadowgraph imaging are presented and compared to literature data.

1 Introduction

Thorough understanding of the injection, disintegration and combustion processes of liquid jets is of particular importance with respect to many propulsion systems (rocket engine, gas turbines, direct injection engines). Shock tubes have been used for gas-phase, multiphase flow and combustion studies for many years as they can produce high pressures and temperatures in a controlled environment and in a highly repeatable manner. A comprehensive review on the application of shock tubes to heterogenous flow, mixing and combustion studies is provided by Petersen [1]. In the present application a shock tube is used to provide basic information on the injection and disintegration processes of hydrocarbon (n-dodecane) jets at temperatures and pressures typical for many propulsion systems. A description of the design and performance of the facility used in this study is given in [2], thus only a brief overview is presented here.

The break-up of (liquid) jets is influenced by several interacting forces with varying importance depending on the disintegration mode [3, 4]. The mechanism of disintegration can be divided into two macroscopic zones, the primary and the secondary break-up region. The primary jet break-up modes can be divided into different regimes (see Figure 1(a)) depending on the injection velocity, the injection pressure, and the ambient conditions. The experiments performed in the course of this study can all be assigned to the atomisation regime.

The macroscopic dispersion, jet spreading angle and liquid/dense core length, are important parameters to describe spray disintegration (see Figure 1(b)). The spreading angle θ is directly related to the amount of surrounding gas introduced into the jet (entrainment) and is influenced by the forces acting on the jet at the nozzle exit. The parameter most frequently used to classify the spreading angle is the ratio of the test gas density to the density of the injected fluid (ρ_g/ρ_f) [5, 6]. In the present study, the spreading angle is defined at $x = 60D$. The liquid or dense core length L_{Core} of a jet is a measure for the axial penetration depth into the test environment. The *liquid core* can be either specified as the intact core ("connected liquid") or as the dense core (high

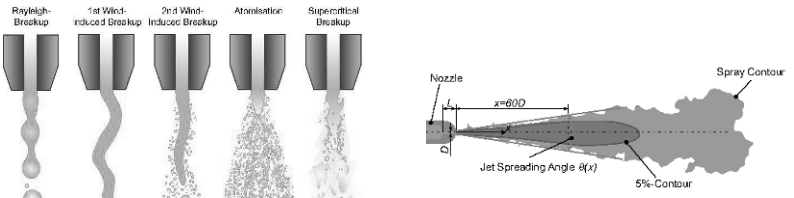

(a) Primary jet break-up regimes (b) Nozzle/jet parameters

Fig. 1. (a) Jet disintegration regimes, increasing (relative) injection velocity/pressure from left to right. (b) Definition of the nozzle geometry and the macroscopic jet parameters.

liquid/gas density ratio). It is very difficult to precisely measure the dense core length by optical means as the core is surrounded by a dense cloud of droplets. Hence the results from this study show only a qualitative trend for different operating conditions. The quantitative results are fairly high and are thus reckoned to overestimate the actual core length (represented here by the 5%-intensity contour in the shadowgraph images).

2 Test facility

2.1 Shock Tube Design

The double-diaphragm shock tube (DDST) consists of a 3.0 m long driver section followed by a short buffer section with a length of 60 mm. The driven section is approximately 8.4 m long. All these components have circular cross-sections with internal diameters of 72 mm. A special feature of the DDST is the transition to the square test section (50 mm x 50 mm) by the introduction of a skimmer. The skimmer and the test section are 1.0 m long in total leading to an overall facility length of about 12.4 m. A sketch of the facility is given in Figure 2. Optical access to the region of interest is provided by flat UV-grade fused-silica windows encompassing the last 60 mm of the test section and its full duct height.

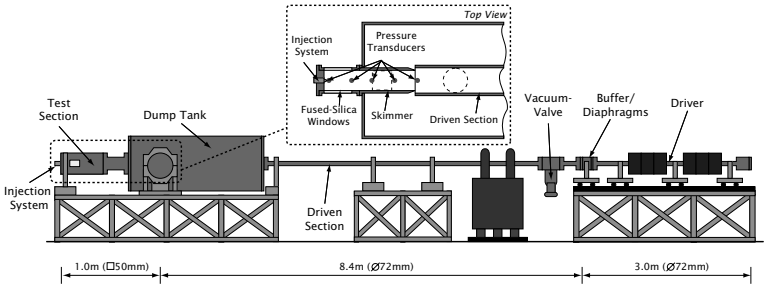

Fig. 2. Schematic of the Double-Diaphragm Shock Tube.

Pressure profiles are measured at several locations in axial direction with fast-response piezoelectric pressure transducers. Typical reflected shock pressures vary from 10 to

50 bar, temperatures typically range from 800 to 2000 K with a maximum test time of about 5 ms. In the endwall of the test-section a fast-response fuel injector is flush-mounted. The fuel back-pressure can be varied from 100 bar to 1400 bar. The injector used in this study has an internal diameter of D =150 μm and a length to diameter ratio of $L/D = 7$.

2.2 Performance and Test Conditions

The shock tube was characterised using different mixtures of helium and argon as the driver gas and argon and nitrogen as the bath gas in the driven section. In the present application a mixture of 80% helium and 20% argon as the driver gas and pure argon as the test gas are used throughout all experiments. The experiments were performed at equal driver to driven pressure ratios $p_4/p_1 = 18$ resulting in similar initial shock Mach numbers of about $M_S = 1.9$ and reflected shock temperatures of approximately $T_{5,0}$ =910 K with pressures ranging from $p_{5,0} = 10 - 38$ bar. Due to non-ideal effects, the conditions behind the reflected shock wave are not constant and both pressure and temperature experience a linear increase with time. The increase in pressure and temperature can be quantified by calculating their slopes $(\mathrm{d}{p_5}^*/\mathrm{d}t)$ and $(\mathrm{d}{T_5}^*/\mathrm{d}t)$. These values are normalised by their initial post-shock values (${p_5}^* = p_5/p_{5,0}$; ${T_5}^* = T_5/T_{5,0}$), yielding for experiments performed at $p_4/p_1 = 18$: $(\mathrm{d}{p_5}^*/\mathrm{d}t) = 63\,\mathrm{s}^{-1}$ and $(\mathrm{d}{T_5}^*/\mathrm{d}t) = 24\,\mathrm{s}^{-1}$. The operating conditions of the present study are given in Table 1.

Condition No.	M_S [-]	$p_{5,0}$ [bar]	$T_{5,0}$ [K]	$\overline{p}_5$ [bar]	$\overline{T}_5$ [K]
I	1.89 ± 0.007	10.38 ± 0.13	899 ± 8	11.15 ± 0.02	935 ± 8
II	1.90 ± 0.005	15.86 ± 0.13	911 ± 7	16.84 ± 0.07	941 ± 7
III	1.88 ± 0.008	18.34 ± 0.27	891 ± 6	19.53 ± 0.33	921 ± 8
IV	1.90 ± 0.009	23.34 ± 0.37	914 ± 6	24.91 ± 0.21	952 ± 6
V	1.92 ± 0.006	30.56 ± 0.29	925 ± 3	32.18 ± 0.28	960 ± 5
VI	1.90 ± 0.010	37.93 ± 0.91	910 ± 9	39.64 ± 0.86	942 ± 11

Table 1. Experiments performed in the present study with the respective incident shock Mach numbers and reflected and test pressures and temperatures

3 Spray Measurements

Figure 3(a) shows the chamber conditions and the injection process at different stages before and after shock reflection, Figure 3(b) gives a sample false colour shadowgraph image of the spray, acquired at *Condition No. II*. The test conditions for the injection experiments are quoted as the mean values for the injection period. The beginning of which coincides with the initiation of fuel injection while its end is marked by the point in time when the shadowgraph image is acquired (i.e. quasi-steady injection is established). The fuel (n-dodecane) was injected at constant differential pressures of $\Delta p_f = 200$ bar (fuel to chamber) and at temperatures T_f of about 293-298 K.

3.1 Time Dependence of the Injection Process

Test time limitations to about 4-5 ms make it necessary to establish quasi-steady injection within a very short time. The injection system starts introducing fuel about 400 μs

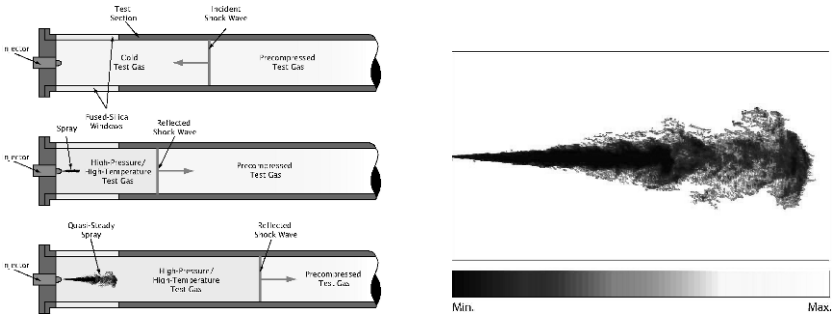

(a) Principle of fuel injection (b) False colour shadowgraph image

Fig. 3. Fuel injection behind reflected shock wave (a) and typical false colour shadowgraph image of the spray after conditioning (b).

after triggering and therefore fulfills the requirement of rapid injection. Furthermore the fluid flow has to reach quasi-steady conditions within the test time. Therefore a series of single shot images was acquired at different time steps after injection was initiated and both the spreading angle θ at $x = 60D$ and the dense core length L_{Core} were determined. Figure 4 shows the results of the jet spreading angle θ and the dense core length L_{Core} acquired at different times for *Condition No. IV*. As both these properties stay fairly constant after 800 μs, it was concluded that quasi-steady injection can be assumed for times greater 800 μs. As a result of these observations it was decided to conduct instantaneous measurements at (1600 μs) after fuel injection, as transitory effects have apparently vanished and the jet has reached a quasi-steady state at this point in time.

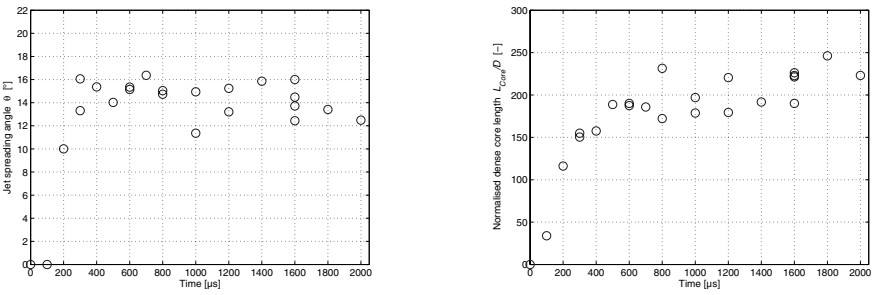

(a) Spreading angle θ (b) Dense core length L_{Core}

Fig. 4. Temporal evolution of jet spreading angle (a) and dense core length (b).

3.2 Spreading Angle

The jet spreading angle θ in the close-up range of the nozzle defines the initial growth rate of the spray. For the experiments performed, exclusively positive spreading angles have been detected being an indication of the atomisation regime. They were determined

at an axial distance $x = 60D$. The results of the analysis are presented in Figure 5(a) plotted in a log-log-diagram together with results and correlations from other sources. The tangent of the spreading angle ($\tan\theta$) is therein plotted versus the gas to injectant density ratio (ρ_g/ρ_f), a curve fit to the experiments yields

$$\theta = 1.58 \left(0.02 + \sqrt{\frac{\rho_g}{\rho_f}}\right). \tag{1}$$

This equation is very similar to the theoretical equation proposed by Reitz and Bracco [5] for steady-state diesel-like sprays with nozzle length to diameter ratios of $L/D = 4$. The slopes match very well, the absolute values are slightly higher which might by caused by the position and the method of how the jet spreading angles were determined. The curve-fitted equation by Naber and Siebers [7] overestimates the spreading angles, especially for lower density ratios, its slope is considerably smaller than that of this study. Naber and Siebers [7] conducted transient measurements of a liquid fuel jet injected into a high-pressure environment with the same nozzle length-to-diameter ratio $L/D = 4$ as Reitz and Bracco [5].

3.3 Dense Core Length

The results for the dense spray core length L_{Core} are shown in the log-log-diagram in Figure 5(b), which plots the dimensionless dense core length (L_{Core}/D) versus the chamber to injectant density ratio. The slopes of the curves agree fairly well with that of the upper and lower bound for diesel-like sprays by Chehroudi et al. [8] and that obtained by Chehroudi et al. [9] for cryogenic nitrogen jets. The normalised dense core length L_{Core}/D can be approximated by the curve fit applied to the experimental data, yielding

$$\frac{L_{Core}}{D} = 15 \left(6.2 + \sqrt{\frac{\rho_f}{\rho_g}}\right). \tag{2}$$

The very high values of the dense core length lead to the assumption that a considerable part of it actually comprises very dense separated droplets and its absolute value is thus overestimated. The overall trend however is captured fairly well.

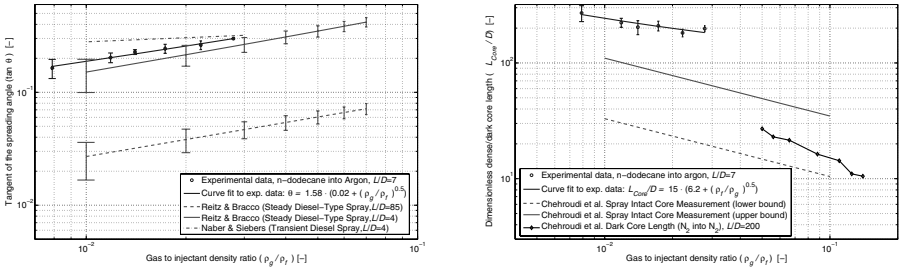

(a) Spreading angle θ (b) Dense core length L_{Core}

Fig. 5. Spreading angle (a) and dense core length (b) as a function of the gas to injectant density ratio (ρ_g/ρ_f).

4 Conclusion

Liquid fuel jets were injected into the high pressure and temperature region behind reflected shock waves. The experiments conducted show the feasibility to investigate jet disintegration processes using a shock tube. Quasi-steady injection conditions were reached within a fraction of the overall test time. The results of the measurements of the jet spreading angle generally agree well with those found in literature, the dense core lengths observed are considerably higher compared to other experiments. Further experiments using additional measurement techniques are planned in order to get a better understanding of the processes involved and to further increase the accuracy of the results.

Acknowledgement. This work was performed within the *Long-Term Advanced Propulsion Concepts and Technologies (LAPCAT)* project investigating high-speed airbreathing propulsion. *LAPCAT*, coordinated by *ESA-ESTEC*, is supported by the *EU* within the 6^{th} *Framework Programme* Priority 1.4, Aeronautic and Space, Contract no.: AST4-CT-2005-012282. Further information can be found on: `http://www.esa.int/techresources/lapcat`.

References

1. E.L. Petersen: *Solid- and Liquid-Phase Combustion Measurements Using a Shock Tube: A Review*, JANNAF 37^{th} Combustion Subcommittee Meeting, pp 567-588, JANNAF, 13–17 November (2000)
2. I. Stotz, G. Lamanna, B. Weigand, and J. Steelant: *A Double-Diaphragm Shock Tube for Hydrocarbon Disintegration Studies*, 14th AIAA/AHI Space Planes and Hypersonic Systems and Technologies Conference, AIAA-2006-8109, AIAA, 6–9 November (2006)
3. R.D. Reitz: *Atomization and other Breakup Regimes of a Liquid Jet*, PhD thesis, Princeton University, Princeton, NJ (1978)
4. W.O.H. Mayer and J. Telaar: *Investigation of Breakup of Turbulent Cryogenic Variable-Density Jets*, Atomization and Sprays **12**, 5&6, pp 651-666 (2002)
5. R.D. Reitz and F.V. Bracco: *On the Dependence of Spray Angle and other Parameters on Nozzle Design and Operating Condition*, SAE International Congress and Exposition, SAE Paper No. 79049 (1979)
6. B. Chehroudi, D. Talley, and E. Coy: *Initial Growth Rate and Visual Characteristics of a Round Jet into a Sub- to Supercritical Environment of Relevance to Rocket, Gas Turbine, and Diesel Engines*, 37^{th} AIAA Aerospace Sciences Meeting and Exhibit, Reno, USA, January 11–14 (1999)
7. J.D Naber, D.L. Siebers: *Effects of Gas density and Vaporization on Penetration and Dispersion of Diesel Sprays*, SAE International Congress and Exposition, SAE Paper No. 960034 (1996)
8. B. Chehroudi, S.H. Chen, F.V. Bracco, and Y. Onuma: *On the Intact Core of Full-Cone Sprays*, Society of Automotive Engineers Congress and Exposition Transaction Papers, Paper No. 850126 (1985)
9. B. Chehroudi and D. Talley and E. Coy: *Fractal Geometry and Growth Rate of Cryogenic Jets Near the Critical Point*, 35^{th} AIAA/ASME/SAE/ASEE Joint Propulsion Conference and Exhibit, AIAA 99-2489, Los Angeles, California, USA, June 20–24 (1999)

Experimental and numerical investigation on the supersonic inlet buzz with angle of attack

H.-J. Lee[1] **and I.-S. Jeung**[2]

[1] *Graduate Student, Dep. of Aerospace Eng., Seoul National University, Seoul, Korea*
[2] *Dep. of Aerospace Eng. and Institute of Advanced Aerospace Technology, Seoul National University, Seoul, Korea*

1 Introduction

During inlet buzz, supersonic inlets exhibit considerable oscillation of the shock system in front of the inlet and corresponding large pressure fluctuations downstream. Inlet buzz is highly undesirable because of the decrease in efficiency or the total failure of the engine operation resulting from large fluctuations. Therefore, the effort to understand the nature and cause of this phenomenon is important in order that the starting of buzz can be predicted and more effectively avoided without losing performance, which results in many researches up to now. After Oswatitsch's first observations, Ferri and Nucci [1], in 1951 and Dailey [2], in 1954 carried out the two main experimental studies on the inlet buzz, which allowed them to identify two different mechanisms that can trigger inlet buzz. After that, although the inlet buzz phenomenon has long been studied, the understanding of its mechanism remains incomplete. Moreover, the study of buzz phenomenon at the external off-design conditions such as an angle of attack is not conducted so much. In a this view, the scope of this study is to investigate the general characteristics of the inlet buzz at the external design and off-design conditions. Experiments and numerical simulations were conducted to obtain the effect of angle of attack on an inlet buzz.

2 Experimental and Numerical Method

The Wind Tunnel The experiment was conducted using free-jet type supersonic blow-down wind tunnel in Seoul National University. The facility allows approximately 6∼8 second of run time. The test section has a square shape of 10.9 by 10.9 Cm. The inflow freestream Mach number was 2.5 and the upstream total pressure was 900kPa.

The Inlet Model The inlet model used in this experiment is a generic, axisymmetric, external compression inlet, with a cowl lip diameter of 14mm, as shown in Fig. 1∼2. Corresponding to simplistic design, the model has a single compression surface on the center-body, a fixed geometry, and no bleed system. The optimum half cone angle was decided as 30° according to the Oswatitsch's experimental results [3]. After that, inlet throat height was determined so that the entrance flow is not choked at the throat using simple Euler numerical analysis. The inlet throat height is 2.1mm; the total length is about 170mm. The throat length is 5mm to supply the uniform flow to downstream. The angle of subsonic diffuser is designed 5° according to Ref. [4].

Pressure Measurement Wall static pressure measurement were obtained at 8 stations on the inside of surface of the cowling, see Fig. 1. Pressures were measured on the upper(station 1∼4) and lower(station 5∼8) surface each. During stable operations, the pressure was measured by conventional strain gauge type. For the cases of unstable operation, dynamic pressure sensor transducers were used and sampled at 10kHz.

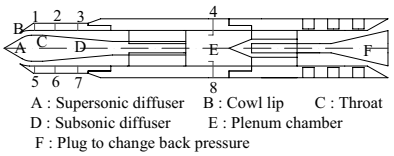

Fig. 1. Drawings of the Model

Fig. 2. Inlet Model installed in Wind Tunnel

Shadowgraph Flow Visualization Shadowgraph flow visualization was used to capture the external shock formation in front of the inlet. The shadowgraph pictures were taken using high resolution camera (EOS 20D, Cannon) which have 1/8000sec of the shutter speed for the stable operation, and images were recorded for unstable operations using a high speed camera (Ultima APX, Photoron) operating at 6000 frames per second.

Numerical Method 3D CFD analysis using Reynolds Averaged Navier-Stokes equation was conducted to understand characteristics of the internal flow inside the inlet. The inflow and outflow conditions was the same as experimental condition and used the supersonic boundary condions. No-slip wall condition was used and Roe's FDS with 3rd order is used as a spatial discretization. Fully Implicit scheme for time integration and Menter's SST turbulent model was adapted with total grid number of 1 million.

3 Results and Discussion

The inlet operating conditions were varied by changing the position of the back plug as shown Fig. 1, which controlled the exit jet area. The back plug position is identified by the area ratio, AR, defined as the ratio of the geometrical exit jet area to the cross-sectional area at the throat section. Experiments were conducted at AR 1.34∼0.366. Also, experiments for angle of attack, AOA, were conducted at 2° and 4° to obtain its effect on the inlet flow characteristics. With the manually operated plug, each operating condition is tested separately for each tunnel run. The wall static pressure, shadowgraphs, FFT analysis were used to deduce information about the buzz cycle.

3.1 Operation with no Angle of Attack

Overall operations

The results of the wall static pressure measurements vs. AR are shown in Fig. 3 and Fig. 4 is the shadowgraph visualization results. This figure shows the static pressure of each measuring station plotted against the AR. The static pressure trends were divided into 5 flow operating regimes, as follows.

Regime (1) : The external shock formation was invariant as supercritical mode. It can be seen that the static pressure is rising with decreasing AR, when the exit jet flow is closing down and the terminal shock, in fact intensified shock train is moved forward.
Regime (2): External shock formation is still invariant and plenum chamber pressure is maximum condition called critical operation mode. It is supposed that the terminal

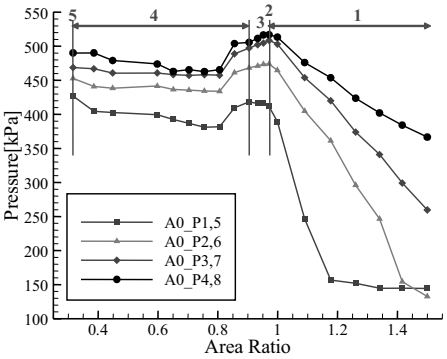

Fig. 3. Pressure Distributions vs. AR at AOA 0°

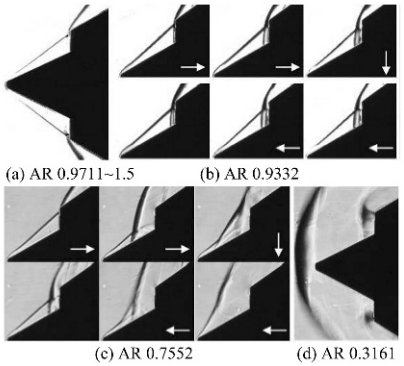

Fig. 4. Shadowgraphs vs. AR

shock exist on the cowl-lip in this condition. Operation at AR=0.9711 belongs to this regime. The results of the visualization are shown in (a) of Fig. 4 for regime (1) and (2).
Regime (3): The cone separation, which is part of the subcritical shock, appears as shown in (b) of Fig. 4. As further reduction in AR forces the cone separation to move more forward, three shocks are seen in compression surface and the vortex sheet to move outward to the cowling wall. Although it was not big, the terminal shock was moving near the cowl continuously and slightly. Operations at AR=0.9332∼0.9522 belong to here.
Regime (4): The inlet buzz takes place in this regime, as indicated by oscillation of the shock wave and the large fluctuation of the static pressures. Two buzz modes was observed, intermittent and continuous mode. During buzz operation, three shocks and separation on the compression surface are shown in (c) of Fig. 4.
Regime (5): As shown in (d) of Fig. 4, the shock was detached from the inlet totally and the inlet is unstarted. In this condition, all of regions of inlet are subsonic and pressures of all stations are not different largely. AR= 0.3161 is the beginning of this regime.

Buzz with no Angle of Attack

Characteristics as AR In the regime (4) for the buzz operations in Fig. 3, we could observe the two buzz modes, the intermittent and continuous buzz mode as AR. The intermittent buzz was observed at the larger AR=0.8556∼0.9044 relatively and the continuous buzz was observed at the low AR=0.3161∼0.7552. During of the intermittent buzz operation, shock stood on near the cowl-lip for a long time, 0.02∼0.07sec. as like subcritical mode and then the oscillation of shock system repeated 1∼3 times. After that subcritical mode was preserved again. During the continuous buzz mode, there was no time that the shock system stood on near cowl-lip as subcritical mode and the shock was oscillated continuously. The dynamic pressure profiles from the subcritical to continuous buzz mode during time of 60ms are shown in Fig. 5. The large fluctuations of the pressure data were not observed in all stations for the subcritical mode. But as AR decreases slightly, the buzz initiated intermittently and the large fluctuations of pressure were seen. As AR decreases, the duration that the subcrtical mode preserves decreased gradually. For this intermittent buzz mode, the frequency of buzz onset was not constant but its onset frequency was increased as AR decreased. When AR was reduced below AR=0.8059, the time that the inlet is operated at the subcritical mode was disappeared

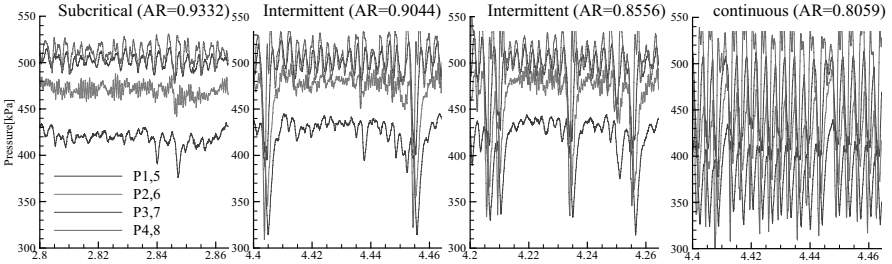

Fig. 5. Dynamic Pressures vs. AR during 60ms

totally and the buzz was initiated continuously as shown Fig. 5. The fundamental frequency of inlet buzz was from 200Hz to 450Hz from the FFT results. The fundamental frequencies for the buzz cycle were the same on the all stations at the same AR condition. But the amplitude was largest at the plenum chamber. Also, the fundamental frequency and amplitude of plenum chamber were increased as AR decreasing. However the amplitude of all stations except the plenum chamber was not increased largely.

One Cycle Analysis about General Buzz

The general buzz cycle observed from results consists of 3 phases from Fig. 6.

(Phase 1) Subcritical: The shock is expelled upstream; the separation on the compression surface grows up, and obstructs an inlet throat. Because of the obstruction the entrance mass flow decreases and the chamber pressure decreases abruptly.

(Phase 2) Reattachment: The subcritical shock moves downstream back into the inlet and cone separation disappeared; when the pressure downstream of the shock is sufficiently low, the shock-induced separated flow area on the ramp disappears. The terminal shock then bluntly moves downstream. As the separation zone disappears and the entrance mass flow increases, the chamber pressure increases again.

(Phase 3) Restart: The inlet remains at the supercritical condition; the inlet entrance is not obstructed anymore and pressure of the chamber increase as the flow fills-up.

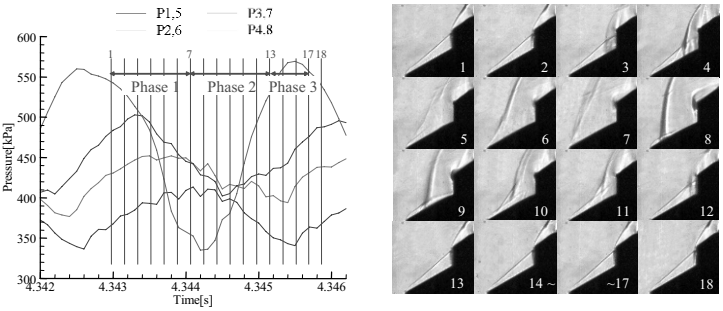

Fig. 6. Pressure Signals during a Buzz cycle and Shadowgraph Visualization (AR=0.7036)

The terminal shock moves forward and the flow become subcritical again; the terminal shock is expelled because of the high pressure inside the inlet, and a new cycle may begin.

3.2 Operations with Angle of Attack

To investigate the effect of an AOA on the buzz, we conducted the experiments of AOA 2°, 4° at the same AR of AOA 0°. There are some characteristics when the inlet is operated at a finite AOA for the stable operation conditions. The shadowgraphs and numerical result at AOA 2°, 4° for the stable operation conditions are shown in Fig. 7. When the free-stream is not parallel to the centerbody axis, the shock structures becomes asymmetric with respect to the centerbody. As a result, a leading conical shock angle increases and the shock becomes weaker on the leeward side compared to the AOA 0°, and the vice versa on the windward side. This results in distortion of the reflecting shock structure. Thus, the normal shock moves further upstream on the windward side and is skewed at the subsonic diffuser. Vortex sheets originating from the shock intersection point enter the inlet duct at the windward side. Due to this vortex sheet running into the inlet the flow is separated on the cowl surface. When the inlet operates at a finite AOA, owing to the different flow direction, it captures more air flow on the wind ward side than on the leeward side. But the flow is more compressed on the windward side since the shock originated on the compression surface is stronger on windward side. These characteristics affect on that of buzz also. As the AOA increases, the locations of the normal shock on both sides move upstream at the same AR. The pressure distribution as AOA at the same AR=0.9991 is shown in Fig. 8. As mentioned above, the operation mode is changed a series of process, supercritical, critical, subcritical, intermittent buzz, continuous buzz, unstart as AR decreases. But when the inlet operates with a finite AOA, the AR which changes the operation mode is larger. As shown in Fig. 8, the inlet model operated as supercritical mode at the AR=0.9991 with no AOA, but did as intermittent buzz mode at same AR when the inlet operated with AOA 4°. In addition, although the AR is the same, the operation mode is changed from supercritical to buzz mode as AR increases, which results in the decreasing of the plenum chamber pressure. The shadowgraph images at AR=0.8059 with AOA 2° is shown in Fig. 9. When the inlet operates at AOA 2°, 4°, the static pressure on the leeward was higher than that of on the windward although the detached shock was observed. Therefore, as the terminal shock is moved upstream at the buzz operation condition, the shock is moved more largely on the leeward side as shown in Fig. 9. The separation size originated on the compression surface was larger on the leeward surface and the buzz becomes asymmetric. However the procedure of one buzz cycle was the same as that with no AOA.

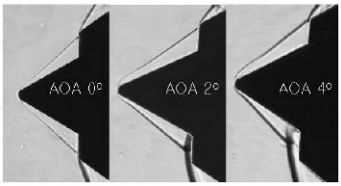

(a) External Shock Formation vs. AOA

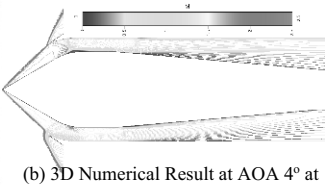

(b) 3D Numerical Result at AOA 4° at Supercritical Mode

Fig. 7. Shadowgraph Visualization vs. AOA and Numerical Result

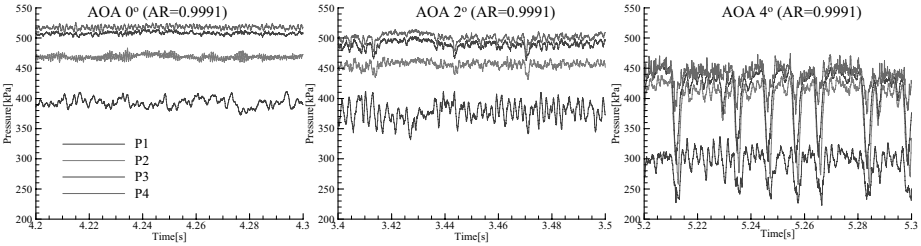

Fig. 8. Comparisons of Pressure Distribution as AR at the same AR

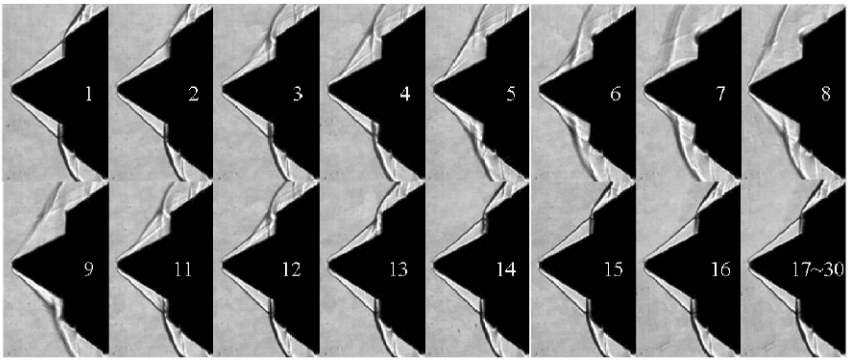

Fig. 9. Shadowgraph Visualization at AR =0.8059 with AOA 2 °

4 Conclusions

A supersonic inlet model was tested in the supersonic blowdown wind tunnel of SNU at Mach number of 2.5. Experiments were conducted with various AR and AOA for the generic, axisymmtric, single-surface external compression inlet model. The characteristics of buzz were observed for the various AR and AOA from the experimental results.

Acknowledgement. This research is supported by the NRL Program of KOSEF (M1050000007 2-05J000007210), Agency for Defense Development and FVRC of SNU, and by the second stage of BK21

References

1. Ferri, A., and Nucci, L. M.: *The Origin of Aerodynamic Instability of Supersonic Inlets at Subcritical Conditions*, edition (NACA RM L50K30,1951)
2. Dailey, C. L.: Supersonic Diffuser Instability. Ph.D. Thesis, California Institute of Technology, CA (1954)
3. Oswatitsch, K.: *Pressure Recovery for Missiles with Reaction Propulsion at High Supersonic Speeds*, edition (NACA TM-1140, 1948)
4. John ,J . M.: *Inlets for Supersonic Missiles*, edition (AIAA Education Series, 1990) pp.23-54

Experimental investigation of inlet injection in a scramjet with rectangular to elliptical shape transition

J.C. Turner and M.K. Smart

Center for Hypersonics, University of Queensland, Brisbane (Australia)

1 Introduction

REST Inlets

The scramjet used in this investigation employed a 3D inlet with a rectangular to elliptical shape transition (REST). REST inlets developed by Smart [5] are of fixed geometry and mixed compression. These inlets transition smoothly from a semi-rectangular capture area with flat bottom and sides to an elliptical throat and isolator. The capture shape allows for several REST modules to be mounted side by side on a compression forebody. The inlets have curved leading edges and a highly swept cowl. This configuration gives moderate internal contractions allowing the inlets to be self starting in flight, despite their fixed geometry.

Radical farming

This investigation was concerned with a flight condition at enthalpies corresponding to Mach 8 flight. Ignition of a fuel-air mixture in a scramjet operating at these relatively low enthalpies and with limited compression can be problematic. Initial analysis of the REST inlet showed a core-flow temperature at the isolator exit of 790K which is too low for spontaneous ignition of a premixed hydrogen-air mixture. Radical farming offers an alternative means of promoting ignition [4]. This technique relies on the 2D structure of oblique shocks and expansions to generate high temperature regions in the combustor. As the mixture passes though successive regions of high temperature, radicals necessary for the chain-branching process are generated and then frozen in the flow. In this way staged ignition can occur as the flow passes through successive high temperature regions. Ignition can therefore be achieved in combustor flows of lower average temperature. Inlet injection is necessary for this ignition method as it delivers premixed fuel-air to the sites of elevated temperature.

Inlet injection

Inlet injection is the process of introducing fuel into the inlet airflow of a scramjet engine. One of the chief benefits of inlet injection is a reduction in the length of the combustion chamber required for efficient burning. A significant fraction of the total skin friction drag on a scramjet is attributable to the high-density flow in the combustor [1].

2 Experiment

The T4 reflected shock tunnel was used to conduct an experimental campaign to investigate injection of hydrogen fuel in the inlet of a REST scramjet at a Mach 8 flight

condition. In order to conduct the experiments a suitable operating condition was required for the shock tunnel. Mach 8 flight corresponds to a total enthalpy (H_o) around 3MJ/kg, which is at the low end of the facility's operating range. Although matching H_o is critical in combustion experiments, particular attention was also given to replicating the static pressure, temperature and flow-speed of the flight condition.

A scramjet model was fabricated from a readily machinable polymer material. The 1280mm long model consisted of a short forebody plate, REST inlet, elliptical combustor and elliptical expansion nozzle. The model was suspended from the roof of the shock tunnel's test section exposing the inlet to the core of the test flow (figure 1).

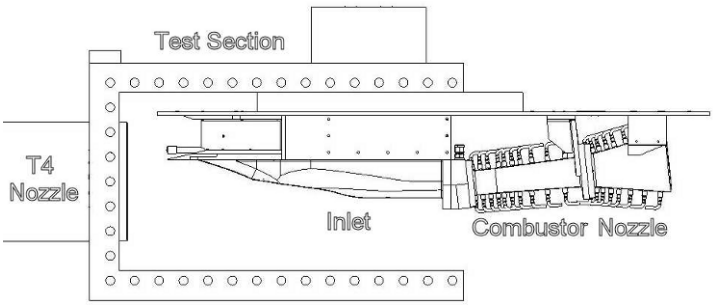

Fig. 1. Experimental model in T4 test section

The experiments were to asses the ability of inlet injection to facilitate ignition when used in conjunction with radical farming. If radical farming was to occur the location of ignition should correspond to a region of high temperature. Pressure rise due to combustion was shown by comparison with shots where combustion is suppressed using a nitrogen test gas. The point of the first pressure rise due to combustion can be readily located, indicating the where ignition has occurred. A number of runs where conducted over a range of equivalence ratios to map the performance of the engine.

2.1 Flight & Test Condition

The nominal trajectory of the flight was dictated by the competing requirements of adequate combustion pressures and dynamic pressure limits for the vehicle. A flight altitude of 30km was used to determine the required design parameters for the engine, the corresponding dynamic pressure was 52kPa. The nominal flow properties for the flight condition are shown in table 1.

Table 1. Nominal flight and test conditions

	$Mach$	p [kPa]	T [K]	H_o [MJ/kg]
freestream	8.1	1.2	227	3.2
forebody	6.7	3.6	320	3.2
test condition[a]	6.7	3.0	333	3.1

[a] T4 nozzle exit properties calculated using NENZF code. [3]

Forebody angles less than 5^o are structurally difficult to realise, while larger angles lead to higher shock losses. The forebody of the vehicle was assumed to have a 6^o deflection angle. A test condition was chosen to simulate the flow conditions on the forebody of a flight vehicle. The nominal test condition for the experiments is shown in table 1.

The average total enthalpy of the condition achieved in the test facility was 3% lower than the nominal forebody condition used to design the engine. During the test program the total enthalpy ranged between 2.8 and 3.2 MJ/kg, corresponding to a flight Mach numbers between 7.8 and 8.1.

Static pressures archived where 17% lower than required, leading to lower combustor pressures than desired. This change in pressure corresponds to an altitude of just over 31km at the nominal flight speed.

2.2 Scramjet Model

Space constraints in the T4 test section meant a full 6^o forebody could not be incorporated into the experimental model. Rather than simulating the freestream flow, T4 was configured to reproduce the flow conditions on the forebody. The model therefore consisted of a shortened forebody aligned with the test flow and the REST scramjet module.

The experimental model consisted of three components, a REST inlet, divergent elliptical combustor and elliptical nozzle. The REST inlet was designed to give a static pressure of 50kPa at the start of the combustor, at the nominal flight condition. The total geometric contraction ratio of the inlet was 5.68 of which 2.08 was internal. The capture area of the REST inlet was approximately $74cm^2$. The combustor has a area ratio of 2, with a constant area section 3 times its throat height. The elliptical nozzle was a ruled surface with a 10^o expansion corner and area ratio of 5.

At the end of the inlet the flow was turned to align the combustor flow with the freestream. As the forebody was assumed to be 6^o, a bend of the same angle was required. This was considered to be advantageous for radical farming as it introduced additional non-uniformity into the combustor flow. The isolator length was carefully chosen to ensure a shock impingement at this location, increasing the shock strength. Care was taken to ensure that the pressure increase at this point would not exceed the Korkegi separation limits [2].

Fuel injection was by means of portholes in the walls of the model at 45^o to the local flow direction. The injectors in the inlet consisted of three portholes of 2.2mm diameter a distance of 460mm upstream of the combustor entrance. The combustor injectors consisted of eight portholes of 1.5mm diameter around the perimeter at the start of the combustor.

2.3 Instrumentation

The scramjet model was instrumented with transducers along upper (body-side) and lower (cowl-side) surfaces in order record static pressures at the walls. These transducers were of the Kulite XTEL-190 series.

As test times are only a few milliseconds the response time of the measurement system must be adequate to accurately measure pressure changes. To achieve this the transducers are mounted directly behind a 2mm deep pressure tap in the wall surface. This requirement placed restrictions on the locations where measurements could be made

due to the bulk of the transducers. This was a particular issue in the forward part of the inlet, the locations of the transducers can bee seen in figure 2.

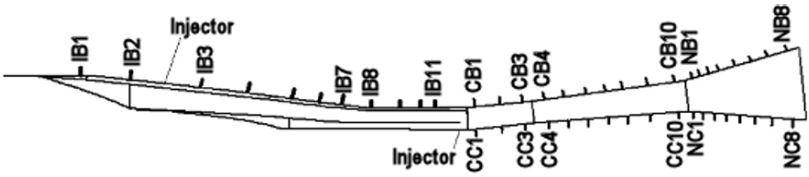

Fig. 2. Transducer positions

An additional pressure transducer was mounted above the leading edge of the model to obtain pitot pressure measurements. The pitot probe was fitted with a PCB pressure transducer.

Signal conditioning consisted of amplification and anti-alias filtering of the pressure signals followed by 4 into 1 multiplexing prior to recording. The data acquisition system consisted of a single BCD transient recorder developed for the Center for Hypersonics. An acquisition sample rate of 1us was used giving a sample rate of 4us for each multiplexed pressure signal.

3 Results and Discussion

A number of shots were conducted in order to acquire data needed to map the performance of the scramjet model. A list of flow properties including equivalence ratio (ϕ) for selected shots are provided in table 2. Ignition was achieved for all the equivalence ratios tested. This was significant due to the low core flow temperature in the combustor. For inlet injection above ϕ=0.72 the model became choked due to boundary layer separation in the combustor, leading to an engine unstart.

Table 2. Selected shots

Shot	Test gas	H_o [MJ/kg]	p_e [kPa]	T_e [K]	Injection	ϕ
1	*air*	3.05	2.96	338	*none*	0.0
2	*air*	3.04	2.95	336	*inlet*	0.67
3	*nitrogen*	3.08	2.85	317	*inlet*	0.69
4	*air*	3.03	2.95	336	*combustor*	0.67
5	*nitrogen*	3.08	2.80	318	*combustor*	0.78

The flow through the engine is dominated by oblique shock and expansion waves, this can be seen in the fuel off pressure distribution plot (figure 3). For clarity only body-side data for shots listed in table 2 are presented in figure 3. Pressure data are corrected for shot to shot variation by $\overline{p_s}/p_s$[1] then normalised using the average static pressure of

[1] p_s is the T4 stagnation pressure

the test flow $\overline{p_e}^2$. Wall pressures for nitrogen shots were combustion was suppressed are plotted for comparison purposes.

The inlet injection case in figure 3 shows addition of fuel clearly increased the pressure levels in the latter part of the inlet. The pressures in the inlet are essentially the same for the suppressed and unsuppressed combustion cases. This is an indication that combustion did not occur in the inlet despite the presence of fuel. No evidence of combustion on the inlet was found for any inlet injection shots in the experiment. For the combusting case the high pressure at 820mm was of particular interest as this corresponded to the second high temperature region the flow encountered. Ignition was most likely to have occurred at this point because of preexisting radicals in the flow and the prevailing conditions in the combustor. The pressure rise due to combustion can be clearly seen in the combustor and nozzle beyond 820mm. The first transducer indicating a pressure rise due to combustion was at the location of the second high temperature region on the body-side of the engine. There is no discernible ignition delay indicating that radical farming is promoting ignition of the fuel mixture.

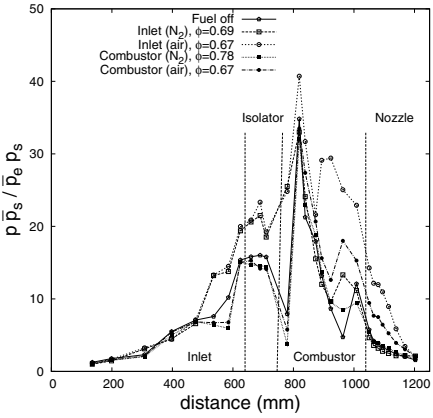

Fig. 3. Body-side wall pressure distributions

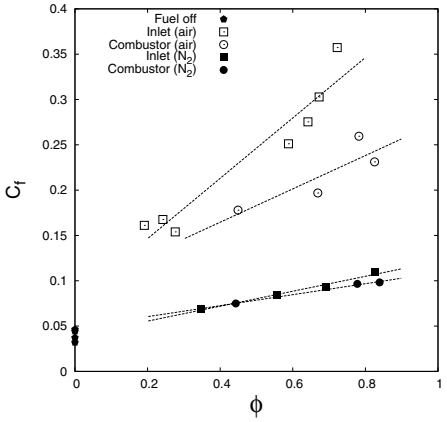

Fig. 4. Integrated inviscid thrust coefficients

The example of combustion chamber injection in figure 3 shows the pressure rise in the combustor is lower than the inlet injection case for a similar equivalence ratio. No significant combustion pressure rise was seen in the first half of the combustor, however the presence of combustion is notable. It is believed that shock heating is the primary ignition mechanism in this case. Reduced thrust when compared with inlet injection was a result of the delayed ignition and poorer mixing.

Thrust was calculated by integrating pressures over incremental areas through the inlet, combustor and nozzle of the model. These results are presented in figure 4 as thrust coefficients. The thrust coefficients are calculated using freestream values for dynamic pressure and full capture area ($C_f = T_{inc}/\frac{1}{2}\rho_\infty U_\infty^2 A\infty$). The accuracy of the incremental thrust calculation is dependent on the uniformity of the flow and the number of pressure measurements in the model. As the flow through the experimental model was non-uniform the calculated thrust coefficients are considered to be estimates only. Thrust coefficients

[2] p_e is equivalent to the forebody static pressure p_1

for the inlet and combustor injection are plotted against equivalence ratio, Both air and nitrogen cases are given. The thrust produced by inlet injection was consistently higher than that of the combustion chamber injection. The difference appeared more pronounced as the equivalence ratios were increased.

Thrust coefficients for non-combusting nitrogen shots indicate that there was a significant amount of thrust due to mass addition alone. Interestingly the nitrogen thrust coefficients for inlet and combustor injection were similar in magnitude. This suggests that the increase in drag due to inlet injection was not significant. The reason was that the increase in inlet pressure due to injection was most pronounced in the isolator where the contribution to inviscid drag was minimal.

4 Conclusions

Ignition occurred across the range of equivalence ratios at a nominal test enthalpy of 3.1MJ/kg, using both inlet injection and wall-based combustion chamber injection. The significance of Radical farming on ignition is unclear although ignition appeared to be initiated at a high temperature region.

Inlet injection shows an increase in pressures on the inlet. Comparisons with Nitrogen shots, where combustion is suppressed, show that this is due to the mass addition alone. No burning appears to be evident on the inlet across the range of equivalence ratios tested.

The increase in pressures in the inlet result in a small drag penalty. This appears not to be significant and is offset by the expansion of the additional mass through the exhaust nozzle

Inlet injection produces higher incremental thrust than injection on the walls of the combustion chamber. This difference is consistent across the range of equivalence ratios tested, indicating that mixing is enhanced, leading to higher combustion efficiencies.

References

1. Goyne, C. and Stalker, R. J: Shock tunnel skin friction measurements in a supersonic combustor. Journal of Propulsion and Power, **15**, 3 (1999)
2. Korjegi, R, H.: Comparison of shock-induced two and three-dimensional incipient turbulent separation, AIAA Journal **13**, 4 (1975)
3. McIntosh, M. K.: Computer Program for the Numerical Calculations of Frozen and Equilibrium Conditions in Shock Tunnels, Technical Report, Australian National University (1968)
4. Odam, J.: Scramjet Experiments using Radical Farming. PhD, Mechanical Engineering. Brisbane, University of Queensland (2004)
5. Smart, M. K.: Design of three-dimensional hypersonic inlets with rectangular-to-elliptical shape transition. Journal of Propulsion and Power **15**, 3 (1999)

Experimental investigation on staged injection in a dual-mode combustor

S. Rocci Denis, D. Maier, and H.-P. Kau

Lehrstuhl für Flugantriebe, Technische Universität München
Boltzmannstraße 15, D-85748 Garching bei München, Germany

1 Introduction

To guarantee good performances of airbreathing hypersonic vehicles, the air stream entering the combustion chamber for a flight Mach number above 6 has to be supersonic [1]. As a consequence, the typical dwell time of the flow in the combustor (τ_R) is limited to 1 ms; within this time the processes of fuel injection, mixing and combustion have to be completed.

The injection system should guarantee both a good macroscale mixing to obtain a homogeneous mixture in the combustor and an efficient microscale mixing to promote the reactions at the molecular level. Moreover, the injector should be designed to support production of radicals and mixture ignition within the shortest ignition delay time (τ_I) possible, i.e. it should act as a flame holder. Finally, the disturbance induced to the main flow and the associated losses should be minimized.

After some years of research on supersonic combustion with ramp injectors [2], the work at the test facility of the Institute for Flight Propulsion (LFA) of the *Technische Universität München* was focused on a strut injector with a cylindrical flame holder positioned in its wake [3–5].

The strut has recently been improved to reduce the pressure losses and to extend the durability of the system. To increase the overall equivalence ratio, a second injection stage consisting of an open cavity has been implemented further downstream.

This paper presents the experimental investigations on the strut as a single stage injector and the first results obtained with the combination of strut and cavity for a combustor entrance Mach number of 2.2 and a total temperature of the supplied airflow ranging between 600 K and 1000 K.

2 Experimental Setup

2.1 Test facility

Air is supplied to the direct connected test facility at a pressure of 1 MPa and at a maximum flow rate of 0.5 kg/s. An interchangeable Laval nozzle accelerates the flow to supersonic speeds. For the present investigations the Mach number at the combustor entrance has been set to a value of 2.2.

The airflow is continuously pre-heated by an electric heat exchanger and then vitiated through catalytic pre-combustion of hydrogen on a Platinum-Palladium solid catalyst up to a maximum of 1200 K. For the presented investigations the temperature is limited to 1000 K to extend the test time. Hydrogen is supplied both to the test section and to

the catalyst, while methane is only supplied to the test section for the main supersonic combustion. Oxygen is added to the supplied air upstream of the electric heater and counterbalances the amount reacting on the catalyst.

To monitor the static pressure distribution in the combustor thirteen pressure taps are implemented along the bottom wall. A total pressure probe and a total temperature sensor measure the conditions at the combustor exit. A Schlieren optic setup is used to determine the exit Mach number (M_{CE}).

2.2 Combustion chamber

The combustion chamber has a length of $360\,mm$ and an entry cross section of $25\times27\,mm^2$ and consists of two modules. The strut injector is positioned in the first module, which is 160 mm long and has a constant cross section. The cavity is placed in the second module that diverges by 4° over 200 mm to counteract the pressure increase due to combustion. Figure 1 shows the combustor in the configuration with staged injection; the static pressure taps are visible on the wall. The walls are made of stainless steel and have quartz windows to enable optical access for non-intrusive measurement techniques. The combustion chamber is not cooled.

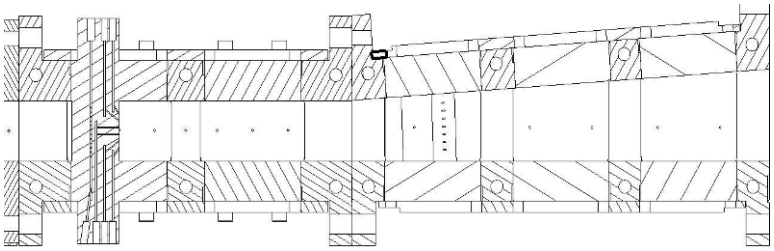

Fig. 1. Cut of the combustion chamber with strut injector and cavity.

2.3 Strut injector

The strut (detailed in Figure 2) is made of Alloy 800H and features an apex half-angle of 7.5°, $23\,mm$ length, $27\,mm$ width and $2\,mm$ thickness, i.e. much smaller than the previous versions [3–5], to reduce the aerodynamic losses. To obtain a more homogeneous fuel distribution, the number of injection holes has been increased for both axial and normal injection and the distance between the orifices has been reduced.

The goal is to exploit the subsonic wake of the strut and the vortices created at its trailing edge to generate a recirculation zone with higher temperature in the middle of the supersonic airflow. Hydrogen (Figure 2, holes **B**) and either air or oxygen (Figure 2, holes **C**) at sonic speed and at a temperature of about $290\,K$ are injected axially into this region to vary the mixture ratio. A laser beam is focused into the mixing zone to ignite the mixture. The dwell time of the radicals in the recirculation zone is long enough to support propagation of the reaction after few laser pulses so that a pilot flame can be stabilized. Methane is injected at approximately $570\,K$ through the series of holes **A** on both sides of the strut normally to the surface.

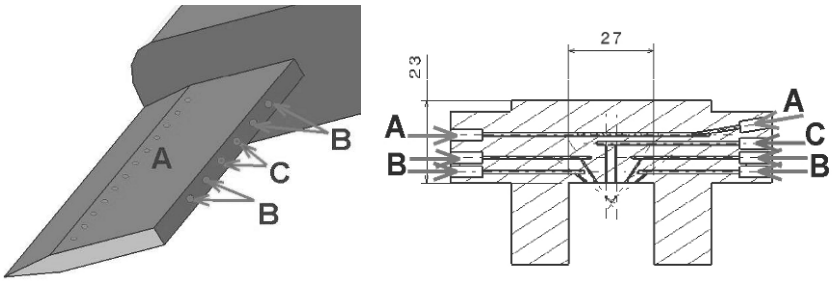

Fig. 2. 3*D* view *(left)* and axial cut *(right)* of the strut.

2.4 Cavity injector

According to previous studies [1, 6, 7], the cavity design has been a trade off between enhancing the overall equivalence ratio and minimizing the drag associated with the use of a cavity.

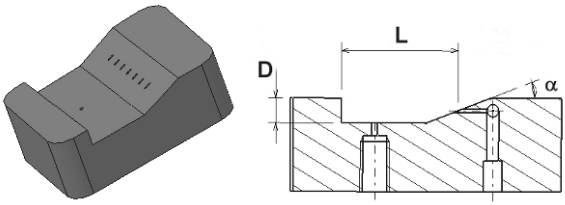

Fig. 3. 3*D* view *(left)* and cut *(right)* of the cavity.

The cavity (see Figure 3) has a 4 *mm* depth (D) and a 20 *mm* length (L) measured from the front wall to the middle of the slanted rear wall ($\alpha = 20°$). The injection holes are fitted along the direction of the stream lines.

Because of its length-to-depth ratio (L/D) the cavity is classified as open [1,7], i.e. the shear layer detaching at the front cavity lip will reattach at the cavity rear wall and not on its floor. The choice of an open cavity has been made to limit drag and total pressure losses [1]. The cavity drag coefficient also depends on the geometry of the back wall; for the present investigations α has been set to 20° according to the results of Samimy [6].

2.5 Gas sampling probe

To complete the information on the combustion process and on the aerodynamics of the flow exiting the combustor, a gas sampling probe has been designed based on the work of Mitani et al. [8]. The probe is made of Alloy 800H and it is water cooled (open cycle). The geometry of the probe tip allows sample collection under supersonic conditions to prevent friction choking and heating up of the gas. This feature and the heat exchange along the probe body support freezing of the reactions. The composition of the samples is then determined by means of gas chromatographic analysis.

3 Results and Discussion

3.1 Results for the strut as a single injection stage

First tests aimed to study different pilot flames, i.e. lean to rich mixtures and using either air or oxygen as additional oxidiser (Figure 2, line **C**). The wake of the strut is suitable to stabilize both H_2-O_2 and H_2-Air flames for different values of the equivalence ratio (ER) and without the flame holder [3–5], which was the main source of total pressure losses. Additionally, with the injector being shorter, the boundary layer grows slower on the strut walls, hence reducing the friction losses.

In both cases the flame is stable over a broad operation range and the wall static pressure distributions (p_{Wall}) indicate similar combustion modalities. The maximum pilot air massflow rate is limited due to testbed conditions, so that only a rich flame can be stabilized. As long as air can be entrained into the pilot zone from the surrounding supersonic flow, the flame burns stably, but ignition of the main methane combustion leads to choking of the pilot flame because of a lack of oxidiser. On the contrary, the oxygen massflow rate is not limited so that stoichiometric conditions could be tested as well: in this case the pilot flame can sustain the main methane combustion. The mixture ratio in the pilot zone turned out to be a key factor in the overall combustion stabilization process: stoichiometric conditions are necessary to have stable combustion of pilot and main flames. To guarantee ER = 1 for the H_2-Air case, a higher air massflow rate would be needed, but due to the abovementioned testbed constraints further tests have been carried out only with H_2-O_2 pilot flames.

The next step has been a detailed investigation of the main methane combustion for different values of the injected massflow rate (Figure 2, line **A**). Table 1 summarizes the test conditions that are examined below, while Figure 4 shows the corresponding wall pressure distribution in the combustor.

Table 1. Test conditions summarize

Condition	H2 [mg/s]	O2 [mg/s]	CH4 [g/s]
S1_FOFF	0	0	0
S1_COM_PF	150	820	0
S1_COM_CH4_4	150	820	1.5
S1_COM_CH4_5	150	820	3
S1_COM_CH4_6	150	820	4.5

The overall static pressure distribution is first analysed based on the fuel-off case, to provide an insight into the aerodynamic phenomena occurring in the combustor. The first p_{Wall} peak is caused by the shock at the strut leading edge, while the second and third peaks by shock reflections. In the diverging module the supersonic flow expands and p_{Wall} decreases, except for the taps 9 and 13, again due to shock reflections, although the p_{Wall} rise becomes lower as the shocks weaken.

The interaction of the aerodynamic phenomena with thermodynamic effects due to combustion of both pilot and main flames is now discussed and the results are compared with those of the corresponding cold tests (without combustion) to quantify the effective combustion pressure rise. For the pilot flame the first sensors detect values matching those of the fuel-off case, i.e. no thermal choking occurs in the combustor. The higher level of

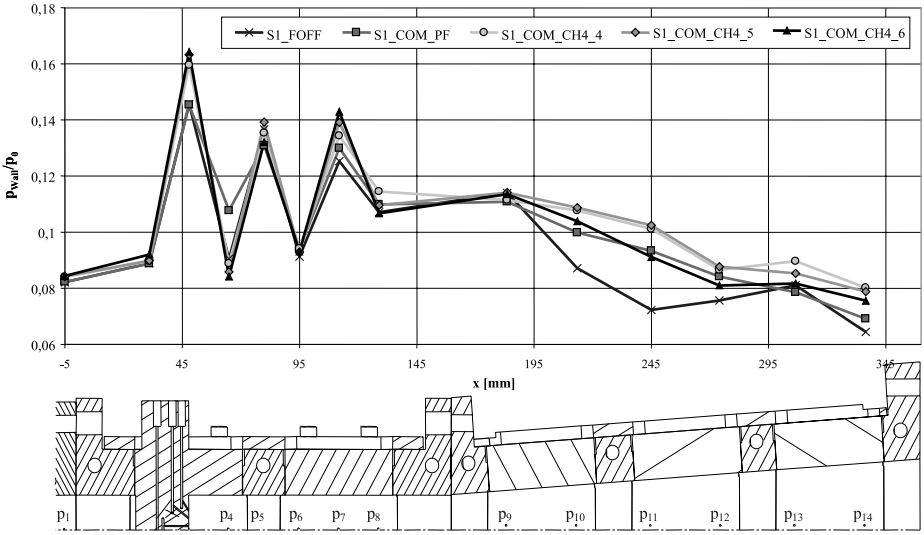

Fig. 4. Wall pressure distribution in the combustor.

p_4 is due to combustion heat release: the cold test confirms only a 5% contribution of fuel injection to the total Δp. The higher level of p_{Wall} and its decrease in the diverging section indicate supersonic conditions: the contribution of combustion heat release to the overall Δp_{10} and Δp_{11} is up to 96% and 95% respectively, and up to 74% for Δp_{12}. Disappearance of the p_{Wall} peaks at taps 9 and 13 points out that the combustion process now controls the aerodynamic effects of shock reflections.

All curves relating to methane combustion show a higher p_3 level due to mass injection straight upstream of the pressure tap. The combustion heat release is shifted further downstream (p_4 is again lower and p_5, p_6 and p_7 are only slightly different than in the cold tests). This suggests that, although CH_4 already reacts behind the strut, combustion occurs in a weak regime and becomes stronger further downstream, preventing thermal choking. Unlike for the pilot flame, combustion does not control the aerodynamics and the p_{Wall} peaks are detected again, although shifted when compared to the fuel-off case.

The lower pressure increase for the richer CH_4 flame indicates weaker combustion. For increasing fuel massflow rate the flame becomes shorter and analysis of the exhaust gases shows that a higher amount of CH_4 remains unburned. The gas sampling probe has been placed at different positions across the combustor exit cross section and the results show that CH_4 remains confined in the middle of the supersonic stream. This indicates a low mixing level between the fuel and the supersonic air and makes this injection system unsuitable to reach adequate overall ER values. All experimental data (observation of the flame structure, gas sampling results and total conditions at the combustor exit) suggest a stratification of the combustor flow. In the central layer (in and close to the strut wake) the fuel-air mixture is homogenous and the combustion rather strong; this flow leaves the combustor at a Mach number ranging from 1.6 to 1.8, depending on the equivalence ratio. At higher ER the flame is shorter and the flow behind it is easier accelerated from the surrounding flow, which explains the higher M_{CE}. On the contrary,

the next layer (basically air with less or no fuel) is slower at higher ER ($M_{CE} \approx 1.6$) because of higher losses of kinetic energy associated to the entrainment of the central layer. The most external stratum consists of the boundary layer flow.

3.2 Results for the combination of strut and cavity injection

First tests have been carried out to monitor the changes in the mixing and combustion processes and in the wall pressure distribution while varying the amount of methane injected through the strut and the cavity.

Because of the fuel injection in the diverging section, a first wall pressure peak appears immediately downstream of the cavity and the value of the measured static pressure increases with the amount of injected fuel. For higher amounts of CH_4, a second peak appears further downstream, indicating heat release through combustion. Nevertheless, most of the CH_4 leaves the combustor unburned, as the available length is too short for a sensible amount of fuel to react. This could be due to the temperature of the CH_4 injected at this stage, which is about $260\,K$ to provide some cooling of the combustor wall. Further tests will be carried out with injection of pre-heated methane through the cavity, to investigate the influence of the longer τ_I.

The experimental data suggest that the CH_4 jet does penetrate into the supersonic flow, but it does not mix with the hot gases of the flame stabilized through the first stage. The jet appears to modify the flame direction because of the different pressures and temperatures of the gases and an additional layer of CH_4-rich flow can be observed.

References

1. A. Ben-Yakar, R.K. Hanson, *Cavity Flame-Holders for Ignition and Flame Stabilization in Scramjets: an Overview*, Journal of Propulsion and Power, vol 17, number 4, pp 869-877 (2001)
2. R. Hönig, D. Theisen, R. Fink, G. Kappler, *Experimental Investigation of a SCRAMJET Model Combustor with Injection Through a Swept Ramp Using Laser-Induced Fluorescence with Tenable Excimer Lasers), 26th Symposium on Combustion, The Combustion Institute, Neapel, Italy (1996*
3. S. Rocci-Denis, A. Brandstetter and H.-P. Kau, *Experimental Study on Transition between Ramjet and Scramjet Modes in a Dual-Mode Combustor*, AIAA-2003-7048 (2003)
4. S. Rocci-Denis, D. Maier, W. Erhard and H.-P. Kau, *Free Stream Investigations on Methane Combustion in a Supersonic Air Flow*, AIAA-2005-3314 (2005)
5. A. Brandstetter, *Betriebsverhalten einer Dualmodus-SCRamjet-Modellbrennkammer mit Wasserstoffverbrennung*, Dissertation, Lehrstuhl für Flugantriebe, TU München, (2004)
6. M. Samimy, H.L. Petrie, A.L. Addy, *Study of Compressible Turbulent Reattaching Free Shear Layers*, AIAA Journal, vol 24, number 2 (1986)
7. A.J. Neely, C. Riley, R.R. Boyce, N.R. Mudford, A.F.P. Houwing, M.R. Gruber, *Hydrocarbon and Hydrogen-Fuelled Scramjet Cavity Flameholder Performances at High Flight Mach Number*, AIAA-2003-6989 (2003)
8. T. Mitani, M. Takahashi, S. Tomioka, T. Hiraiwa, K. Tani, *Measurements of Scramjet Engine Performance by Gas Sampling*, AIAA 98-1590 (1998)

Performance of a scramjet engine model in Mach 6 flight condition

S. Ueda, T. Kouchi, M. Takegoshi, S. Tomioka, and K. Tani

Japan Aerospace Exploration Agency JAXA, Kakuda Space Propulsion Center
1 Koganesawa Kimigaya Kakuda, Miyagi 981-1525, (Japan)

1 Introduction

The supersonic combustion ramjet (scramjet) is expected to be the most effective propulsion system for space transportation and hypersonic transportation of the next generation. Japan Aerospace Exploration Agency, Kakuda Space Propulsion Center (JAXA-KSPC) has been conducting firing tests of a variety of sub-scale scramjet engine models in Mach 4, 6, 8 simulated flight conditions using Ramjet Engine Test Facility (RJTF). [1] At each flight condition, the engines produced thrust greater than the engine drag. However, under relatively low Mach number conditions such as Mach 4 and 6, the obtained thrusts in these tests were insufficient because unstart transition occurred at fuel equivalence ratios less than unity. A modified sidewall-compression-type scramjet engine ($E2$) was fabricated to improve engine performance. It was designed to reduce distortions caused by the swept angle in the frame and the airflow. For this purpose, the $E2$ model has no swept angle on the sidewalls except in its inlet section. Starting in 1998, the $E2$ model was tested with several struts and ramp blocks under Mach 8 flight conditions. [2] In the present study, we attempted to apply boundary-layer bleeding and multi-stage fuel injection schemes, such as strut first-stage injection and sidewall second-stage injections from several streamwise locations, to the $E2$ model under Mach 6 flight conditions. [3] [4] [5] Experimental results were compared with CFD analysis of the whole engine.

2 Experimental Apparatus

Combustion tests were carried out under Mach 6 simulated flight conditions using the RJTF, which is a free-jet-type high enthalpy wind tunnel with a rectangle nozzle 510 mm $\times$ 510 mm. The engine entrance conditions assuming that the stream has passed the forebody shock wave at Mach 6 are indicated in Table 1. To obtain a high total temperature flow, a storage air heater was used. The velocity boundary-layer thickness at the nozzle exit was evaluated from pitot pressure measurements. Figure 1 shows a schematic view of the sub-scale engine model ($E2$) tested in this study. The engine had a sidewall compression inlet with a swept angle of 45 degrees and a sidewall expansion nozzle. The engine consisted of two sidewalls, a top wall and a cowl. The overall length, height and width of the engine were 2198.4 mm, 250 mm and 200 mm, respectively. A strut was installed between the sidewalls in the engine to enhance flow compression. The geometrical contraction ratio of the inlet, which is the ratio of the area of the inlet entrance to that of the inlet exit, was 5 with the strut.

The leading edge of the cowl was located at the inlet exit to allow spillage of the incoming air to the external flow for better starting performance. The backward facing

Mach number	5.3
Stagnation pressure (MPa)	4.8
Stagnation temperature (K)	1480
Boundary-layer thickness (mm)	50

Table 1. Test condition of Mach 6 at RJTF

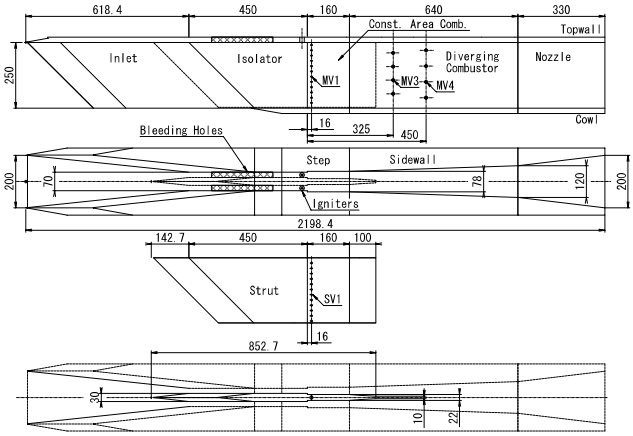

Fig. 1. Schmatic views of a scramjet engine model ($E2$)

steps of 4 mm in height on the sidewalls and strut at the junction of the isolator and combustor were used for flame holding. The combustor consisted of a constant cross-sectional area duct ($C.C.$) and a diverging one ($D.C.$). The main fuel injectors ($MV1$ and $SV1$) were located 16 mm downstream of the step in the $C.C.$ section, and secondary fuel injectors ($MV3$ and $MV4$), for the multi-stage fuel injection, were located 325 mm and 450 mm downstream of the step in the $D.C.$ section. The fuel mass flow rate (m_f) of 142 g/s corresponded to the bulk equivalence ratio (Φ) of unity assuming the air capture ratio of 0.81 obtained by CFD. [6] A torch-igniter (TI) [7] was installed on the top wall 20 mm upstream of the step to enable stable ignition under Mach 6 flight conditions, which were near a lower limit of self-ignition. The boundary layer was bled through porous holes on the top wall around the inlet exit at a mass flow rate of 60 g/s, which was about 1.2 % of the total air flow. The thrust was measured by means of a force measurement system (FMS). Its error was $\pm$ 50 N. Wall temperature and pressure distributions, heat flux distributions on the sidewall within the combustor section were measured. Gas sampling was conducted at the engine exit using water-cooled sampling rakes to ensure reaction quenching during the sampling process. [8]

3 Numerical techniques

The numerical method employed consisted of the full three-dimensional compressible Reynolds-averaged Navier-Stokes equations with a finite rate chemistry. [9] The solution algorithm [10] was based on a cell-vertex, upwind, finite-volume scheme for an arbitrarily

shaped cell. The algorithm adopted the hydrogen-oxygen reaction which consisted of nine species (H_2, O_2, H_2O, H, HO_2, OH, O, H_2O_2 and N_2) / seventeen elementary reactions. N_2 was assumed to be inert. The turbulent eddy viscosity was evaluated by the one-equation turbulence model proposed by Goldberg and Ramakrishnan. [11] The turbulent Prandtl number was 0.9 and the turbulent Schmidt number was 1.0. [12] The dynamic pressure at the entrance of the inlet is 106 kPa. The Reynolds number (R_e) based on the engine height was 2.1×10^6. Its displacement thickness (δ^*) and momentum thickness (θ) were 20 mm and 2.9 mm, respectively. All solid walls were non-slip and isothermal, wall temperature (T_w) of 300 K. For computations, the wall share stress (τ_w) and the heating rate on wall (q_w) were calculated using the velocity and temperature gradient on the walls. These gradients were evaluated by a method based on Gauss' theorem.

4 Results and discussion

Figure 2 shows the thrust increment from the no fuel condition (ΔF) versus Φ. As for the single-staged fuel injection from sidewall (MV1) and strut (SV1), ΔF stayed in low level when Φ was lower than 0.4, referred as "weak combustion". [13] However, ΔF jumped suddenly to a higher level at $\Phi = 0.4$, referred as "intensive combustion". With further increment of Φ, ΔF dropped drastically to a much lower level and the engine went into un-start. Un-start transition occurred at $\Phi = 0.7$, and thus ΔF was limited to 1850 N.

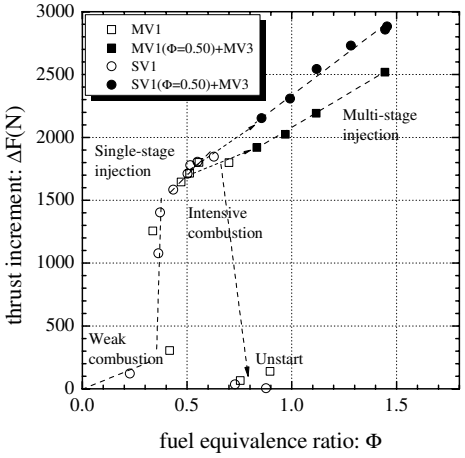

Fig. 2. Thrust increment from no fuel condition.

Figure 2 also shows ΔF versus the equivalence ratio (Φ) for the multi-staged fuel injection. While first stage fuel injection was fixed to $\Phi = 0.50$, the second-stage fuel injection was increased. Un-start transition did not occur with boundary layer bleeding up to $\Phi = 1.45$. As a result, we achieved the purposes of this study, i.e., by the multi-stage injections and the boundary-layer bleeding, un-start transition was suppressed and ΔF increased to 2880 N, which was about 1.5 times larger than the maximum achieved with single-staged injection in the Mach 6 tests. The maximum net thrust (ΔF_{int}) was 1850 N, with estimated internal drag ($D_{int} = 1030$ N).

To validate the CFD code, numerical results of wall pressure distributions were compared with the experimental data. Figures 3 show the comparison of experimental and CFD pressure distribution on the sidewall. Pressures are normalized by the total pressure of the incoming free stream. The broken line and the open symbols denote the results for the no fuel case, while the solid line and the solid symbols are those for the combustion case. The abscissa is the distance from the leading edge of the top wall. The half flow path on the horizontal plane is also shown at the top of each figure for the reference of the measuring position. These numerical results showed good agreement with the experimental data for no fuel case. However, numerical results showed higher pressure at $D.C.$ region in the combustion case. This result indicated that numerical analysis over-estimated the combustion effect by the secondary fuel injection.

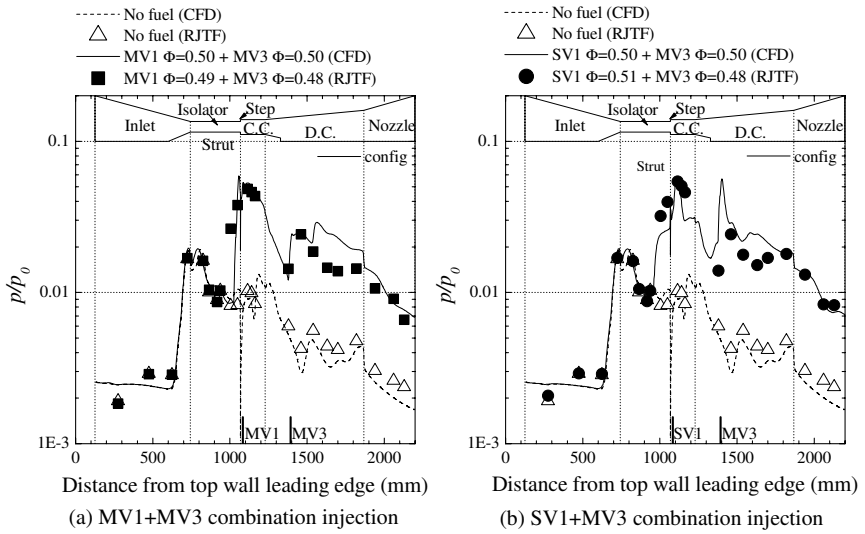

Fig. 3. Comparison of the numerical and experimental pressure on the side wall: y/H = 0.5.

Figure 4 (a) shows heat flux distribution on the sidewall with the $MV1 + MV3$ and $SV1 + MV3$ combinations. Difference of the heat flux between sidewall fuel injection ($MV1$) and strut fuel injection ($SV1$) indicated that combustion occurred mainly near the injection wall due to insufficient penetration into the core flow. As the second-stage fuel burnt in the $SV1 + MV3$ combination, the heat flux on the sidewall increased drastically in the downstream half of the $D.C.$ section. Though the combusted gas near the sidewall was more fuel-rich for the $MV1 + MV3$ combination, the resulting heat flux was comparable to that with the $SV1 + MV3$ combination. The experimental results of heat flux were higher than the numerical results. One of the reasons of the difference is strong distribution of heat flux at the combustor region. Figure 4 (b) shows numerical results of adiabatic wall temperature on the sidewall with the $MV1 + MV3$ combination. CFD result shows that the adiabatic wall temperature is kept a high value in the combustor section.

Figure 5 show the fuel concentration at the engine exit with the $MV1 + MV3$ and $SV1 + MV3$ combination, respectively, at $\phi_{1st} = 0.36$ and $\phi_{2nd} = 0.36$ for both

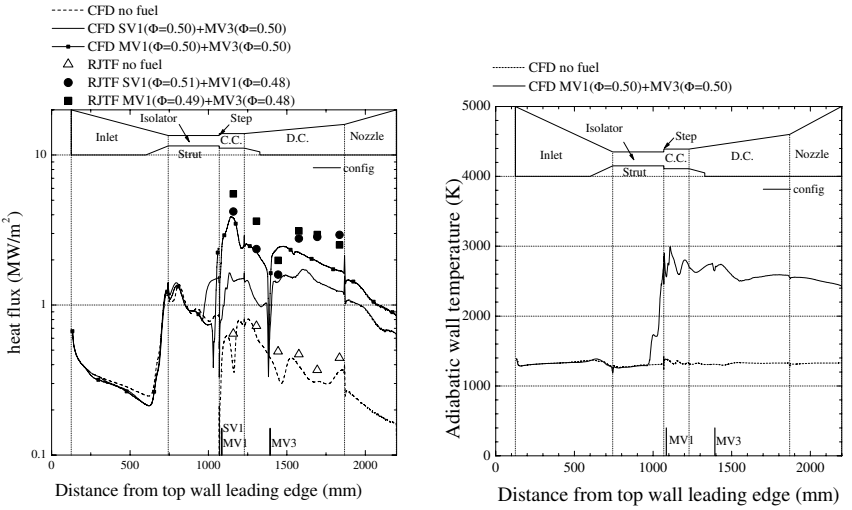

(a) Heat flux on the side wall (b) Adiabatic wall temperature on the side wall

Fig. 4. Heat flux and adiabatic wall temperature on the side wall: y/H = 0.5

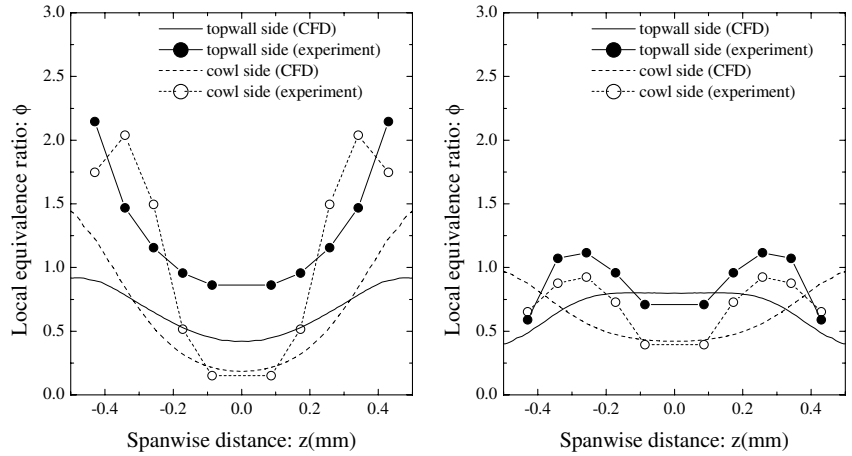

(a) MV1(ϕ=0.36)+MV3(ϕ=0.36) combination injection (b) SV1(ϕ=0.36)+MV3(ϕ=0.36) combination injection

Fig. 5. Local equivalence ratio at the nozzle exit of the engine.

combinations. Unfortunately, gas sampling could not be conducted at higher flow rates (ϕ of 1 or above), because the probe initiated combustion of the unburned fuel, which led to a facility unstart due to thermal choking of the diffuser flow. Sampling and Pitot pressure measurements were carried out along two horizontal lines, 63 mm from the top wall (top wall side) and 66 mm from the cowl (cowl side). It should be noted that the half spanwise region was used for gas sampling and the other half was used for Pitot pressure measurement. Therefore, data points on the non-measured side were copied from the measured side. With the $SV1 + MV3$ combination injection, fuel distribution was

more uniform (with a peak local equivalence ratio of about 1.2) compared with that of the $MV1 + MV3$ combination injection with a peak local equivalence ratio of above 2. Experiments and CFD simulation agree well qualitatively.

5 Conclusion

Mach 6 tests of a scramjet engine model ($E2$) were carried out in RJTF and the effects of the multi-staged fuel injection and the boundary-layer bleeding. The heat flux to the engine wall was measured and compared with CFD analysis. The following results were obtained.

- By applying the multi-staged fuel injection and boundary-layer bleeding, the engine operated without un-start transition around the fuel equivalence ratio (Φ) of 1 or above. Especially for the strut injection ($SV1$), the thrust increment from the no fuel condition (ΔF) increased to 2880 N.
- The CFD results show good agreement with the experimental data qualitatively. However, CFD analysis over-estimated the combustion effect by the secondary fuel injection.

References

1. Miyajima, H., et al., RJTF construction group, Ramjet Engine Test Facility, NAL TR-1347, 1998.
2. Hiraiwa, T., et al., Experiments on a Scramjet Engine with a Ramp-Compression Inlet at Mach 8, Journal of Propulsion and Power, Vol.22, No.2, pp. 440-446, 2006.
3. Ueda, S., et al., Mach 6 Tests of a Scramjet Engin with Multi-Staged Fuel Injection, AIAA Paper 2006-1027, 2006.
4. Ueda, S., et al., Performace Comparison of Combined Fuel Injection Methods in a Staged-Combustion Scramjet Engine, Proc. 21th ISTS, pp. 121-126, 2006.
5. Ueda, S., et al., Evaluation of Heat-flux on Scramjet Engine Wall in Mach 6 Flight Condition, IAC-06-C4.5.4, 2006.
6. Kouchi, T., et al., Numerical Experiments of Scramjet Combustion with Boundary-Layer Bleeding, AIAA Paper 2003-7038, 2003.
7. Kobayashi, K., et al., H2/O2 Torch Igniter for Scramjet Engine Tests, ISTS 2004-a-20, 24th ISTS, 2004.
8. Mitani, T., et al., Analysis and Application of Gas Sampling to Scramjet Engine Testing, Journal of Propulsion and Power, Vol.15, No.4, pp.572-577, 1999.
9. Kouchi, T., et al., Heat Flux Prediction for Scramjet Engines, ISTS 2004-a-08, 2004.
10. Kodera, M., et al., Numerical Analysis of Scramjet Combusting Flows by Unstructured Hybrid Grid Method, AIAA paper 2000-0886, January 2000.
11. Goldberg, U. C., and Ramakrishnan, S. V., A Pointwise Version of Baldwin-Barth Turbulence Model, Comp. Fluid Dyn., Vol. 1, pp. 321-338, August 1993.
12. Kodera, M., et al., Scramjet Inlet Flow Computations by Hybrid Grid Method, AIAA paper 98-0962, January 1998.
13. Kanda, T., et al., Mach 6 Testing of a Scramjet Engine Model, Journal of Propulsion and Power, Vol. 13, No. 4, pp. 543-551, 1997.

Radiatively cooled scramjet combustor

R.G. Morgan and F. Zander

Centre for Hypersonics
The University of Queensland, Brisbane, 4072 (Australia)

1 Introduction

The construction of combustion chambers for scramjets that can survive the heating loads and dissipate the energy of a flight effectively remains a great challenge. In addition to surviving the conditions of supersonic combustion, the structure must be designed to minimise weight to optimise the performance of the engine. Previous engines have only sustained combustion for a short duration, in the order of seconds, hence the heating problem has not been as severe as for longer duration flights. Future flight programs at UQ and around the world are looking towards longer burn times in the order of minutes which requires a combustor that can maintain structural integrity for the duration of the flight whilst dissipating a significant amount of heat. An example of this is the X-1 engine, part of the X-51A program, which is currently slated for a 5 minute flight test in 2009 [1]. The use of composites offers a solution to many of these problems [2] and this paper investigates the use of composite materials for a combustor, in conjunction with the use of regenerative cooling and internal radiative heat transfer for thermal equilibration.

2 Conditions Analysed

Two different flight conditions have been considered for the analysis, a Mach 8 flight at 27km altitude and a Mach 10 flight at 30km altitude. The inlets used were 4 shock inlets (3 external, 1 internal) and have been designed such that the post inlet static temperature and pressure were approximately 1000K and 1 atm pressure and for minimal total pressure loss. The inlets were calculated on a 2D basis resulting in lengths of 4m and 7m for the Mach 8 and Mach 10 cases respectively. This can be seen in Fig. 1.

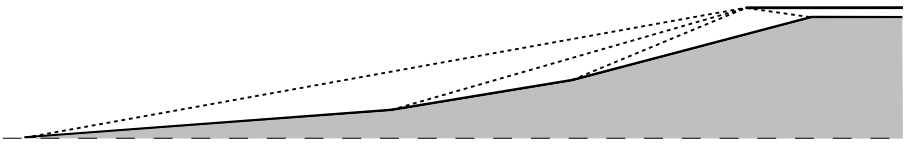

Fig. 1. Schematic of Scramjet Inlet.

The combustor analysed was 1m in length. Although the analysis was purely 2D an elliptical combustor shape was assumed to calculate the capture area. The major chord has a length of 0.1m and the aspect ratio is 1.8. One side of the combustor was considered to be exposed to the atmosphere allowing heat to be radiated out, while the other side

was surrounded by the fuel manifold as shown in Fig. 2. The combustor is manufactured from a reinforced carbon-carbon (RCC) composite whose thickness is dependent on the case being considered. The conductivity of the combustor material is a very important property as the heat from the boundary layer needs to be conducted through the wall to be removed from the combustor system. The thermal conductivity value of RCC used was 5W/mK which was taken from Dowding [3]. This was the result of experimental testing with RCC in the direction perpendicular to the fibres as would be the case for a combustion chamber designed for hoop stress. The RCC is treated throughout as a grey body radiator with an emissivity value of 0.9. The fuel manifold is manufactured from inconel with assumed properties of a melting temperature in excess of 1600K and a thermal conductivity of 20 W/mK [4]. The exact configuration of the fuel lines within the manifold was not considered however a value of 3mm was used as the average distance between the external surface of the manifold and the fuel. To ensure that the fuel manifold does not reach the melting temperature of inconel and to set the heat transfer through the manifold provision is made for graphite insulation to be inserted between the RCC and the manifold. The thickness required is a function of the RCC temperature and is stated in the results for each case. The fuel used for this analysis is octane with a combustion heat release of 44MJ/kg. The equivalence ratio used is 0.67.

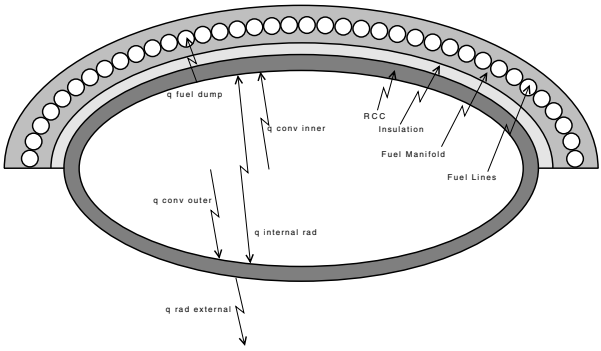

Fig. 2. Schematic of combustor cross section (not to scale)

3 Analysis Procedure

The analysis conducted was completed for steady state conditions with equilibrium energy balance and an approximate model to give a preliminary indication of whether the concept is viable. Transient effects were not considered and will still require analysis at a later time to allow for any additional effects not considered by the steady state calculations. The first stage of the analysis was to calculate an approximate inlet length to allow for the different convective heating rates resulting from distance from the leading edge. This calculation was done using a 2D approximation and resulted in lengths of 4m and 7m for the Mach 8 and Mach 10 cases respectively. These lengths are overestimations of a 3D inlet length and the 3D compression effects will significantly reduce the length to

reach the desired conditions of 1000K and approximately 100kPa. A quick calculation of varying lengths showed that the convective heat transfer difference for 2m to 7m only changed by approximately 0.1MW/m^2. Although this is a significant amount of heat it accounted for less than 12.5% of the heating rate at the inside wall. This variation reflects on the thermal design at different stations along the combustor. The results of the current preliminary analysis show there is still heat dump reserve in the fuel which can be utilised for a fully 3D analysis which will result in higher heating loads.

A simplified combustion model was used - 100% combustion efficiency was assumed with total conversion of chemical energy to heat energy. NASA's CEA program was used to calculate the combustion temperature of 2500K assuming a constant pressure throughout the process. This temperature is assumed to be constant down the entire length of the chamber. The heating considered was the convective heat flux from the flow, conduction to the fuel lines and the radiative heat flux between the walls and away from the external surface. Radiation absorption of the gas was calcualted however it was shown that the gas absorbed less than 1% of the total heat flux and thus was ignored for further calculations. The fuel was calculated to provide a heat dump equivalent to 1MW/m^2 on the internal wall.

The calculation of the convective heat transfer was done using (1) from Stollery [5] which is based on the Eckert reference enthalpy method. This analysis is for a flat plate, accounting for changing pressures across shocks, in hypersonic flow and has been shown in previous experimental testing to give reasonable agreement with overall heat flux loads [6]. This shows that for this stage of analysis the 2D approximation is useful for the preliminary design.

$$\dot{q}_w = \frac{0.0296}{Pr^{\frac{2}{3}}}\rho^* u_e (H_r - H_w)\left(\frac{\rho^* u_e x}{\mu^*}\right)^{-\frac{1}{5}} \tag{1}$$

The solution is computed using 1mm increments down the length of the combustor. The conduction axially along the combustor is negligible in comparison to the convective and radiative heat loads and has been left out of the analysis. At each point the inside wall temperature is calculated for an equilibrium net flux where radiation between the walls, convection from the flow and heat dump to the fuel was calculated. This is done initially for an assumed external wall temperature. After this the outside wall temperature is calculated for equilibrium net flux including radiation between the walls, convection from the flow and radiation into the atmosphere. Changing the external wall temperature changes the radiation flux to the inside wall creating the iterative process which is repeated until both walls are within 1kW/m^2 of equilibrium. Repeating this process down the length of the combustion chamber enables a plot of the wall temperatures to be created showing the equilibrium condition.

The outside wall of the combustor uses radiation to the atmosphere to dump most of the heat. In calculating the equilibrium the convective heat transfer, radiation to or from the inside wall and radiation to the atmosphere are considered. RCC wall thicknesses of 1mm and 3mm are used for the Mach 8 and Mach 10 cases. The conduction across the wall is calculated to enable a realistic estimate of the radiation heat dump to be calculated. The temperature drop reduces the radiation heat flux and must be considered when designing the combustor. In both cases the outside wall temperature is greater than the inside wall temperature meaning that there is radiation to the inside wall and the extra heat is dumped into the fuel.

The inside wall has similar heat transfer terms as the outside wall. The convection to the wall from the flow, radiation between the walls and the conduction through to

the fuel. This is again solved for the equilibrium wall temperature. The heat dump to the fuel is calculated using an inconel fuel manifold and octane heat sink data produced by Huang [7]. Using inconel as the fuel manifold material allows the maximum possible temperature of the manifold to be fixed at 1100K which is well below the melting point and does not affect the structural integrity. With this knowledge and an assumed average distance from the outside of the manifold to the fuel of 3mm the temperature of the fuel lines can be calculated. The fuel lines were assumed to be 5mm diameter pipes covering the entire internal surface of the combustion chamber wall. A rough estimate of the heat flux convectively transferred to the fuel could then be calculated for the given conditions from the mass flow rate, equivalence ratio and the energy of combustion. This resulted in a value of approximately 1MW/m^2 and is adequate to vapourise and crack the fuel at the given mass flow rate. This calculation required an iterative process as the amount of heat sink provided by the fuel is dependent on the temperature that it can be raised to, however this in turn is dependent on the heat flux into the fuel. A factor of 0.8 was used in the calculation to allow for extra losses in the process.

4 Results

The results of the calculations show that the wall temperatures for the two cases only vary by approximately 100K down the length of the combustion chamber. The plots in Fig. 3 show the inside and outside wall temperature for the Mach 8 and Mach 10 cases. The Mach 8 plot shows that the wall temperatures for this case are quite moderate with the inside wall ranging from 1300-1400K and the outside wall ranging from 1700-1800K. These temperatures are well within the operating limits of RCC. The results for the Mach 10 case show the large increase in the heating problems. In this case the wall temperatures are reaching approximately 2700K which produces much greater materials selection problems for the combustion chamber. The small fluctuations seen in the plot are due to the coarseness of the data in the look-up tables used.

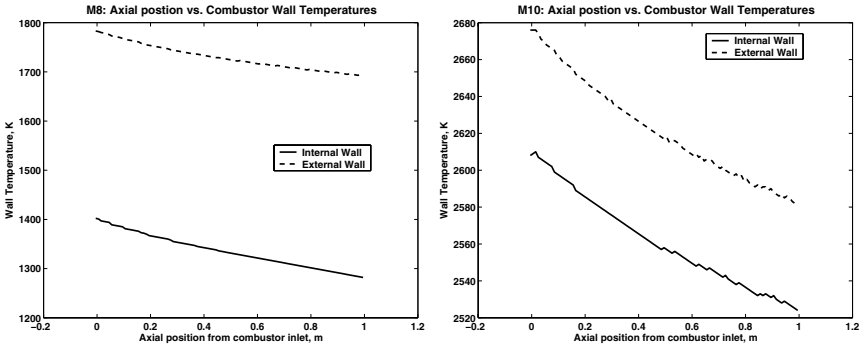

Fig. 3. Internal and external wall temperatures for the M8 (left) and M10 (right) flight cases.

The analysis shows that equilibrium will be achieved at these wall temperatures with approximate heat flux terms as shown in Table 1. A negative value of the $\dot{q}_{int.rad}$ term

indicates radiation from the external wall to the internal wall. The values shown are at a length of 0.5m from the end of the inlet. These will vary for different points along the combustion chamber.

Table 1. Wall heat transfer values at the mid point of the combustor for M8 and M10

Mach No.	Wall	Wall Temp [K]	$\dot{q}_{conv}$ [MW/m^2]	$\dot{q}_{int.rad}$ [MW/m^2]	$\dot{q}_{fueldump}$ [MW/m^2]	$\dot{q}_{ext.rad}$ [MW/m^2]
8	internal	1331	0.70	-0.29	1.00	-
8	external	1724	0.67	-0.29	-	0.38
10	internal	2557	0.78	-0.22	1.00	-
10	external	2618	1.14	-0.22	-	0.92

From the calculation of the heat loads one important factor was the requirement of a layer of graphite insulation to protect the fuel manifold. This is selected by setting the temperature of the fuel manifold at the specified 1100K, knowing the wall temperature and heat transfer rate from the previous calculations and then computing the required thickness using standard conduction theory. The Mach 8 case averaged a thickness of approximately 0.1mm and the Mach 10 case required 1.5mm. The actual insulation thickness values drop linearly down the length of the combustion chamber as the wall temperature decreases. In the Mach 8 case the insulation can be disregarded as the fuel manifold can withstand the slight increase in temperature that will result. The Mach 8 case represents a design that would be feasible for use in the near future using the RCC as the structure for the combustion chamber. Previous studies [8] show that at these temperatures the RCC will not undergo any ablation, the only major effect is that of oxidation. This has also been shown on the space shuttle as the conditions are similar to those experienced on the wing leading edges and nose. This will not present a problem for the length of flights being considered here. For future applications with longer flight paths this issue will need to be addressed with the use of oxidation resistant coatings such as silica carbide. The Mach 10 case presents much higher heat flux rates and required wall temperatures for the equilibrium case. With current materials this may be feasible for a short duration flight (∼seconds), however for a longer flight other new methods will be required to either offer greater heat sinks or to enable the walls to withstand the greater thermal loads. Ablation is one good option that the use of composite materials enables. For a certain duration of flight ablation of the chamber walls can be used to dissipate large amounts of heat, however further research is required into the effects of the changing geometry on the combustion.

5 Discussion

As this is a preliminary analysis of the specified combustor configuration there are many details that require further investigation. This investigation has shown that the use of a composite combustor is potentially feasible for future flights and is an area of interest that should be pursued further. One of the major factors of the design are the properties of the RCC used for the combustion chamber. A review of the literature has shown that there are many widely varying results for the RCC properties. The reason for this discrepancy is that the properties are highly dependent on the manufacturing techniques.

This justifies the use of the properties as chosen, however for further design some collaborative research must be undertaken in which the materials and design can be tailored towards the same objectives. The second part that needs much further investigation is the use of a hydrocarbon fuel, in this particular case octane, as an endothermic heat sink. Further work would require design and testing of the method of heat transfer to the fuel. The design of the fuel pipes to allow full heat transfer to the fuel and the values that can be obtained with different pipe sizes and layouts would need investigation. Of particular interest would be the convective heat transfer to the fuel running through the fuel pipes.

6 Conclusion

This preliminary study of the use of RCC as a combustor material for a scramjet shows that the concept is viable. The high strength to weight ratio of RCC offers great advantages for future designs. The equilibrium heat balance is satisfied with hot yet sustainable wall temperatures which is good for the thermodynamic cycle as it allows regenerative cooling to be used which heats and cracks the fuel enabling higher efficiency combustion. The results show that the M8 flight would be easily achievable however the upper limit is as yet unknown. This will depend on the material properties that can be achieved and further design of the endothermic heat sink system. The results of this study justify the further investigation into the concept which will be shown at the Australian Fluid Mechanics Conference at the Gold Coast in December 2007. This work is supported by the ARC Discovery Grant.

References

1. Hughes D.: Toward a Practical Scramjet. *Aviation Week and Space Technology*, 166(18):93, May 2007
2. Bouquet C., Fisher R., Larrieu J. M., Uhrig G., Thebault J.: Composite Technologies Development for Scramjet Applications. *12th Space Planes and Hypersonic Systems and Technologies* AIAA 2003-6917, 2003
3. Dowding K. J., Beck J. V., Blackwell B.F.: Estimation of directional-dependent thermal properties in a carbon-carbon composite. *International Journal of Heat and Mass Transfer* 39(15):3157-3164, Oct. 1996
4. Laubitz M. J., Cotnam K. D.: Thermal and electrical properties of inconel 702 at high temperatures. *Canadian Journal of Physics* 42(1):131-152, Jan. 1964
5. Stollery J. L., Coleman G. T.: A Correlation between Pressure and Heat Transfer Distributions at Supersonic and Hypersonic Speeds. *Aeronautical Quarterly* 26(4):304-315, Nov. 1975
6. Morgan R. G., Stalker R. J., Shock Tunnel Measurements of Heat Transfer in a Model Scramjet, *AIAA Paper* 85-908, 1985
7. Huang H., Sobel D. R., Spadaccini L.J., Endothermic Heat-Sink of Hydrocarbon Fuels for Scramjet Cooling, *AIAA Paper* 2002-3871, 1985
8. Williams S. D., Curry D. M., Chao D. C., Pham V. T.: Ablation Analysis of the Shuttle Orbiter Oxidation Protected Reinforced Carbon-Carbon. *Journal of Thermophysics and Heat Transfer* 9(3):478-485, Jul 1995

Thrust vectoring through fluid injection in an axisymmetrical supersonic nozzle: Theoretical and computational study

N. Maarouf[1], M. Sellam[1], M. Grignon[1], and A. Chpoun[12]

[1] *Laboratoire de Mécanique et d'Energétique d'Evry, Université d'Evry Val d'Essonne 40 rue du Pelvoux, 91020 Evry-Cedex, France*
[2] *ICARE-CNRS, 1C avenue de la recherche scientifique, 45071 Orleans Cedex France*

Summary. A Numerical and modeling study has been accomplished to investigate the effects of a secondary injection in an axisymmetrical, convergent-divergent nozzle for fluidic thrust vectoring purpose. The annular secondary gas injection in the axisymmetrical nozzle causes complex effects (boundary layer separation, shock wave interaction,...). The present paper focuses on the results of some computational and modeling investigations, where the influence of some parameters (pressure ratios, injection slot size and location, injected mass flow rates...) are studied. To perform this work, a 3D Navier-Stokes calculations, with several turbulence models were used. Previously, a theoretical model of a secondary injection in a primary jet had been constructed. To characterize the separation zone caused by the injection, different correlations have been tested. The results indicate that fluidic annular injection in an axisymmetrical nozzle can produce significant thrust-vector angles up to 16°. The nozzle pressure ratio and the mass flow rate ratio were in the range of 2 to 10 and 2 to 7% respectively. Some results were validated on NASA experiments in both 2D and axisymmetric tests.

1 Introduction

Fluid injection in the divergent of a supersonic nozzle is an attractive way to produce vectored thrust since it can remove the need for complex mechanical devices. In the past many works were devoted to the planar nozzle flow: Waithe et al. (2003) [1], Mangin et al.(2006) [2]. Such concept of thrust vectoring is currently applied for some recent jet-fighters with planar nozzles producing low nozzle exit Mach numbers. However, fluidic thrust-vectoring may be interesting in the case of axisymmetrical nozzles as well. For example for satellite attitude control system, thrust-vectoring may reduce the number of supersonic fixed nozzles. One of the aims of this work is to investigate the influence of numerous parameters which govern the behavior of the injection of a secondary jet flow in a supersonic stream and its subsequent influence on the amount of thrust-vectored angle, as it was done for planar nozzles.

The present paper shows that it is possible to construct a simple engineering model to investigate those parameters. In the case of an axisymmetrical nozzle, the model shows that additional parameters appear and must be taken into account. To validate the analytical model, extensive numerical 3D calculations using a Navier-Stockes finite volume solver have been carried out. The results were also compared to some of existing experimental data from NASA both for 2D and 3D configurations which give a significant confidence of the model.

Nomenclature

A_e,A_t	Exit and throat section
b	Injector width
C_{pmax}	Pressure coefficient corresponding to the stagnation pressure
c_d	Discharge coefficient
F_a,F_n	Axial and normal forces
h	Step height
M_k	Mach number behind the shock wave
M_0, P_0	Mach and pressure before the shock
NPR	Nozzle pressure ratio
P_{oj}	Total injection pressure
q_0	Dynamic pressure before the shock
SPR	Secondary pressure ratio
X, Y	Axial and normal direction
X_t	Throat axial location
y_j	Nozzle radius at injection plan
γ	Specific heat ratio
δ	Pitch thrust vector angle (vectorisation)
φ	Injection angle

2 Analytical Model

As it was pointed out in some previous works Spaid et al.(1968) [3], the two dimensional flow, resulting from gaseous secondary injection into a supersonic stream, is quite similar to the supersonic flow passing over a forward-facing step. From this idea, an analytical model of the flow field can be built. The main purpose is then to calculate an effective step height h which can be used as a scale parameter for the entire flow field (three dimensional effects are neglected in this case).

Different assumptions and simplification are proposed: No mixing occurs between the secondary and primary flows, the interface between the two flows is a rounded forward-facing step. The secondary gas expands isentropically to the free-stream static pressure and then is turned parallel to the wall.

As for the 2D nozzle, in the case of an axisymmetrical flow, the application of the momentum balance over the control volume, sketched in figure 1, leads to the following equation for the penetration height h of the step:

$$\frac{\pi}{4}q_0 C_{pmax} h^2 - \frac{2}{3}q_0 C_{pmax} y_j \varphi h = 2c_d b y_j \varphi \gamma P_{0j} \left(\frac{2}{\gamma+1}\right)^{\frac{1}{\gamma-1}} \left[\frac{1}{\gamma^2-1}\left(1-\left(\frac{P_0}{P_{0j}}\right)^{\frac{\gamma-1}{\gamma}}\right)\right]^{1/2} \quad (1)$$

This equation solved for h and combined with the separation criterion leads to the location of the separation point using the same method as for 2D case, Mangin et al. [2].

The Campbell and Farley criterion, below, estimates the mach number ratio through a separated shock wave. The criterion is evaluated for conical nozzle separation with nozzle divergence half-angle up to 29° Campbell et al. [5]. The mach number ratio is approximated by the following correlation.

$$\frac{M_k}{M_0} = 0.76 \quad (2)$$

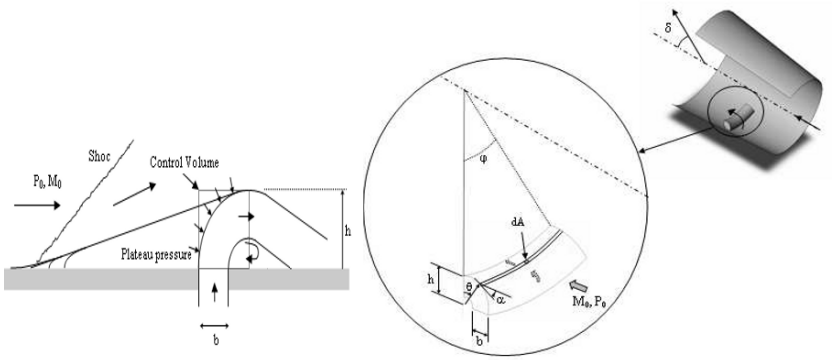

Fig. 1. 2D injection modeling (left), Sketch for pressure integral derivation, 3D case (right)

The thrust vector angle δ is calculated in the thrust-vector plane at which the resultant thrust-vector is deflected from the nozzle axis from equation 3.

$$\delta = tan^{-1}(F_n/F_a) \tag{3}$$

In this work, the injection slot has the form of a slit-like annular orifice. The main feature of the flow, in this case, is a separation line which occurs in front of the injector. This zone extends towards and laterally on both sides of the injector, where the influence of the injected gas becomes increasingly low. In this model, a constant separation line is assumed in front of the injector, and the side separation lines are described by a polynomial functions.

3 Computational method

Numerical method

The numerical study was performed using a finite volume code (CFD-FASTRAN) to solve the steady three-dimensional Navier-Stokes equations with a time marching scheme. Time integration is achieved using a fully implicit scheme. Local time stepping is also used to accelerate convergence to steady state solution. Flux vectors are evaluated, at each time step, using Roe's upwind flux difference splitting, with a MINMODE flux limiter in order to achieve a high-order spatial accuracy. The solution was allowed to converge until the L_2 norm of the density residual dropped at least by four orders of magnitude.

Computational grid and geometry

Finite volume grids were constructed using a cartesian grid generator. The computational domain includes the convergent-divergent nozzle and the downstream zone. The total number of cells is up to 47 000 for 2D Nozzle and 1 300 000 for 3D nozzle. The refinement of the grids near the wall was such as the first cell-height was about y^+=1 for the Spalart and Baldwin-Lomax turbulence model and about y^+=30 for k-ε.

The nozzle used in the 2D study was a non-axisymmetric convergent-divergent nozzle with a design nozzle pressure ratio NPR_D of 8.78, a nominal throat area of 0.0028 m^2, and a width of 0.10 m, section ratio A_e/A_t=1.78 and exit mach M_e=2.2. While the axisymmetrical CD nozzle has a section ratio A_e/A_t=1.75, NPR_D=8.26 and M_e=2

4 Results

4.1 Planar nozzle

The figure 2 shows analytical, experimental and computational static wall pressures (upper and lower surface for computational results) for NPR= 4.6 and SPR=0.7 (4.4% of primary mass flow rate). The injection port is located at X/X_t=1.78. The model predicts a static pressure along the wall (injection side) which correlates well with experimental and numerical data. The plateau pressure and the origin of the interaction between the primary and secondary flows are well evaluated by the calculations. As shown in figure 3, the fluidic injection causes an oblique shock wave upstream of the injection port. The CFD predicts the shock wave location at X/X_t=1.56 on the upper surface compared to the shock wave location at X/X_t=1.53 in the experimental data for NPR=4.6. CFD also predicts a slightly stronger shock wave on the upper surface compared with the experimental data (the plateau pressure is greater). The results give a vectorisation angle of 7.5° for the model, 9.4° for CFD for k-ε turbulence model., while the experimental data gives, δ=7°.

In this case, turbulence modeling was required to predict solutions for the flow field. We used essentially the 2-equation k-ε turbulence model. The results for a wide range of test cases show that this model produces very good agreement with experimental data for flows with adverse pressure gradients, separation zones and shock-boundary layer interactions. Figure 2 presents the distribution of pressure on the upper surface of the nozzle for different turbulence models i.e. k-ε, Baldwin-Lomax and Spalart-Allmaras models. The corresponding thrust - vector angles δ are respectively: 9,45 , 9,04 and 9,76.

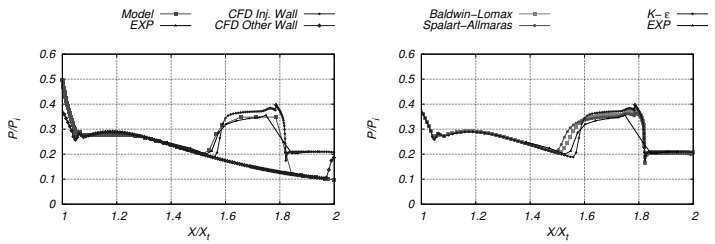

Fig. 2. Upper wall pressure from modeling, CFD and experiments (2D Nozzle)(left), Wall pressures for several turbulence models (right)

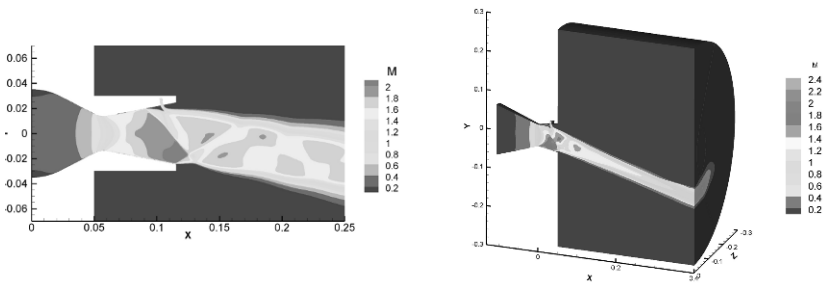

Fig. 3. Mach number counters for computational injection in 2D Nozzle (left), 3D nozzle (right).

4.2 Axisymmetrical nozzle

3D nozzle flow configurations have been investigated to highlight the influence of the three main parameters NPR, SPR and φ. In addition, a comparison between the model, the numerical simulations results and experimental data was done for NPR ranging from 3 up to 12 while SPR was varied from 0.3 to 1.2 (SPR=1.0 corresponds to primary mass flow rate of 7.2 % for the proposed geometry). We have used the K-ε turbulence model for the numerical simulation. Figure 4 shows the distribution of wall pressure for the divergent part of the nozzle. A zone of plateau pressure in front of the injector and a zone of pressure gradient on the two edges can be noted. The vertical force component of the vectored thrust originates from the integrated effect of these pressure distributions. A very strong pressure can be noticed just in front of the injector. This implies the presence of a second oblique shock and a fluid recirculation.

The variation of the injection angle is presented on the figure 4, the vectorisation is important for φ=90°, the separation line is closer to the nozzle throat. The vectorisation decreases for the low values (φ <90°) because of weak aspect ratios (length/width) of the orifice, which causes a very important friction in the orifice. While for the large values, back-pressure starts to appear on the other half of the nozzle, a negative force pushes the nozzle against direction of the injected gas. A vectorisation of 15.5° is obtained numerically while the experiment gives 16° for the case of φ=60°, Wing et al. [4].

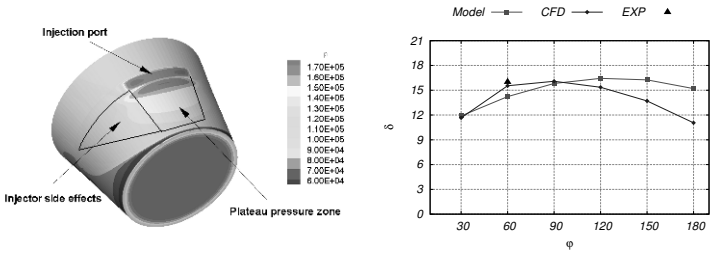

Fig. 4. Distributions of wall pressures in the axisymmetric nozzle wall for φ=60°, NPR=3, SPR=1 (left), Thrust vector angle versus injection angle for NPR=3, SPR=1 (right)

As a function of NPR, the results are shown on figure 5 at SPR=1 and φ=60°. The lower NPR represents a free separation in the divergent nozzle, and a maximum value of the vectorisation. While one realists that the vectorisation decreased for the higher

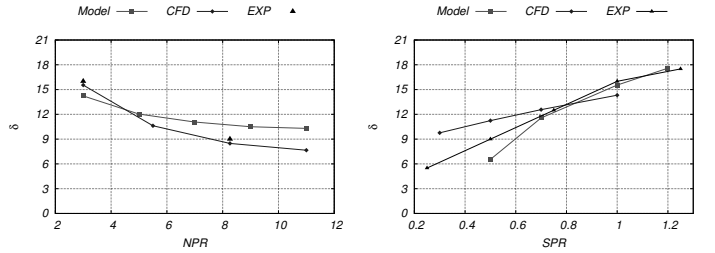

Fig. 5. Thrust angle versus NPR in the axisymmetric nozzle for φ=60, SPR=1 (left), Thrust angle versus SPR for φ=60°, NPR=3.0 (right)

NPR. The maximum efficiency thrust is for NPR_D (adapted nozzle value). Two points present the experiments results, for NPR=3, δ=16° and for NPR_D=8.26, δ=8.5°.

As seen in figure 5, the results of thrust angle as a function of secondary pressure ratio SPR for NPR=3.0 and φ=60° are presented. Lower SPR represents a low flux of the momentum and a small value of equivalent step height.

5 Conclusion and further work

The objective of this study was to investigate fluid injection in a two-dimensional and axisymmetrical CD supersonic nozzle for fluidic thrust vectoring through modeling and computational means. A theoretical model based on the semi-empirical approach has been constructed for this study. Several annular ports were tested in the 3D case without increasing the secondary flow rate. Results of 2D study indicate a good agreement between the model calculations and the experimental and numerical results. Results of 3D study indicate that the code is valid for predicting the internal performance quantities of a 3D convergent divergent nozzle with annular injection port. Fluidic thrust vectoring of the axisymmetric jet up to 16° was accomplished. Future studies will be dedicated to different configurations with multiple injection ports and for different injection port locations.

References

1. Kenrick A. Waithe and Karen A. Deere, Experimental and computational investigation of multiple injection ports in a convergent-divergent nozzle for fluidic thrust vectoring. AIAA-2003-3802
2. B. Mangin, A. Chpoun, L. Jacquin, Experimental and numerical study of the fluidic thrust vectoring of a two-dimensional supersonic nozzle. Private communication.
3. F. W. Spaid, E. E. Zukoski, A study of the interaction of gaseous jets from transverse slots with supersonic external flows. AIAA journal, Vol. 6, 1968
4. David J. Wing, Victor J. Giuliano, Fluidic Thrust Vectoring of an axisymmetric exhaust nozzle at static conditions. FEDSM97-3228, 1997
5. C. Campbell, J. Farely, Performence of several conical convergent-divergent rocket-type exhaust nozzles. NASA TN D-467, September 1960
6. G. Masuya, N. Chinzei and S. Ishii, Secondary gas injection into a supersonic conical nozzle AIAA Journal, Vol. 15, March 1977
7. E. Erdem, K. Albayrak and H. T. Tinaztepe, Parametric study of secondary gas injection into a conical rocket nozzle for thrust vectoring. AIAA 2006-4942

Part XVII

Rarefied Flow

On shock wave solution of the Boltmann equation with a modified collision term

S. Takahashi and A. Sakurai

Tokyo Denki University, 101-8457 Tokyo, (JAPAN)

Summary. Although the existence problem of the shock wave solution for the Boltmann equation has bee much studied in many decades, this problem has been still open. Additionally even for any approximated equation, e.g., BGK model, no satisfactory answer has obtained. We consider the existence of shock wave solution for the Boltmann equation with a modified collision term in which the distribution function is approximated by its 13 moments, originally proposed by Oguchi. The model or O-model, unlike previous ones, expresses the collision term in an explicit function of molecular velocity and this enables us to examine directly the singular nature of the equation to have existence of shock wave solution.

1 Introduction

The problem of finding a shock wave solution of the Boltzmann equation has a long history probably since R. Becker [1] commented that the Navier-Stokes system could be inadequate for the shock structure problem especially for stronger shock cases and the kinetic approach by the Boltzmann equation should be used for this. There have been numerous studies on this subject especially because it has been utilized for a kind of test problem for a new kinetic model with approximated equation. Most of these are however, approximate solutions including numerical ones, and a very few of them are exact to limited cases even for any approximate equation, e.g., BGK model as we can see in Nikolaenko [2], Caflish and Nikolaenko [3], Bose, Iller and Ukai [4]. So we can say that this problem is still open.

We consider the shock wave solution of the Boltzmann equation with a modified collision term in which the distribution function is approximated by its 13 moments, originally proposed by Oguchi [5] (O-model) as it is formulated in the following section 2. Approximate solution of this equation was sought in [6], which was constructed in neglecting the singular nature near the uniform sub- and supersonic regions. Here we investigate the problem in a way of showing the existence of a solution.

2 Shock structure problem of the Boltmann equation with a modified collision term

We consider the shock structure problem for a steady planar shock wave whose front is normal to the x-dimension and consider the molecular velocity distribution function $F(\mathbf{v}, x)$ of the molecular velocity $\mathbf{v} = (v_x, v_y, v_z)$. We use the Boltmann equation with a modified collision term, which is proposed by Oguchi [5]. It is derived from the original collision expression by performing the integrals in assuming local Maxwellian for the distribution function. It looks similar to BGK and Shakov [7] models but it is different in

expressing the collision term in an explicite function of molecular velocity $\mathbf{v}$. It becomes to the present case of steady one-dimensional flow for the Maxwell molecular model in dimensionless form based on the representative collision frequency ν_-, the temperature T_-, the pressure p_-, and the density n_- as,

$$\begin{aligned} &v_x \frac{\partial F}{\partial x} = \Pi, \\ &\Pi \equiv -\frac{n\nu}{(\pi T)^{3/2}} \exp\left(-\frac{V^2}{T}\right) \quad \cdot \left[\frac{3p_{xx}}{4pT}\left(V_x^2 - \frac{V_y^2+V_z^2}{2}\right) + \frac{q_x V_x}{pT}\left(\frac{2V_x^2}{5T} - 1\right)\right] \\ &\equiv \Pi_1 p_{xx} + \Pi_2 q_x \end{aligned} \tag{1}$$

where

$$\begin{aligned} &n(x) = \int F d\mathbf{v}, \quad u(x) = \frac{1}{n}\int F v_x d\mathbf{v}, T(x) = \frac{2}{3n}\int F V^2 d\mathbf{v}, \\ &p = nT, p_{xx}(x) = 2\int F V_x^2 d\mathbf{v} - p, \quad q_x(x) = \int F V^2 V_x d\mathbf{v}. \end{aligned} \tag{2}$$

Here

$$\mathbf{V} = (V_x, V_y, V_z) = (v_x - u, v_y, v_z). \tag{3}$$

The distribution function F becomes the Maxwell distribution function $F_\pm$ in the uniform subsonic and supersonic regions as $x \to \pm\infty$ or

$$F(\mathbf{v}, x) \to F_\pm \equiv \frac{n_\pm}{(\pi T_\pm)^{3/2}} \exp\left(-\frac{V^2}{T_\pm}\right), \tag{4}$$

as $x \to \pm\infty$ where $n_\pm$, $T_\pm$ and $u_\pm$ are the values for $x \to \pm\infty$.

3 Shock wave solution

3.1 Construction of moment equations

Although eq. (1) is still of integro-differential type as the original Boltzmann kinetic equation, its collision term is expressed in an explicit function of $\mathbf{V}$ given by five moments, n, u, p (or T), p_{xx} and q_x in eq. (1) as functions of x only. Accordingly, we may derive relations between these moments by integrating eq. (1) with certain weights, from which we may determine these variables.

We first obtain three relations by integrating eq. (1) over $\mathbf{v}$, using the weights 1, v_x and v^2 and utilizing the conservation laws of mass, momentum and energy as

$$nu = C_1, nu^2 + \frac{1}{2}(p + p_{xx}) = C_2, nu^3 + \frac{5}{2}pu + up_{xx} + q_x = C_3 \tag{5}$$

where $C_1 = n_-u_- = n_+u_+$, $C_2 = n_-u_-^2 + \frac{1}{2}p_- = n_+u_+^2 + \frac{1}{2}p_+$, $C_3 = n_-u_-^3 + \frac{5}{2}p_-u_- = n_+u_+^3 + \frac{5}{2}p_+u_+$.

We next consider two more moment integrals given as

$$\int \frac{\partial F}{\partial x} d\mathbf{v} = (p.v.)\int \frac{\Pi}{v_x} d\mathbf{v}, \quad \int V^2 \frac{\partial F}{\partial x} d\mathbf{v} = (p.v.)\int \frac{V^2}{v_x}\Pi d\mathbf{v}. \tag{6}$$

We get from eq. (6) that

$$\frac{dn}{dx} = -\frac{n\nu}{pT}\left[\frac{3}{4}up_{xx}\left\{-1+\left(\xi^2-\frac{1}{2}\right)\frac{I}{\xi}\right\}+\frac{2}{5}q_x\left\{\xi^2-1-\xi^2\left(\xi^2-\frac{3}{2}\right)\frac{I}{\xi}\right\}\right]$$
$$\equiv Ap_{xx}+Bq_x, \tag{7}$$

$$\frac{dp}{dx} = \frac{2}{3}\left[\left(u^2+T\right)\frac{dn}{dx}+\frac{n\nu}{p}\left\{\frac{3}{8}up_{xx}\frac{I}{\xi}+\frac{2}{5}q_x\left(\xi I-1\right)\right\}\right]$$
$$\equiv Cp_{xx}+Dq_x, \tag{8}$$

where

$$\sqrt{\pi}I(\xi) = (p.v.)\int_{-\infty}^{\infty}\exp\left(-\frac{V_x^2}{T}\right)\frac{dv_x}{V_x+u} = 2\mathrm{e}^{-\xi^2}\int_0^{\infty}\exp\left(-\eta^2\right)\frac{\sinh(2\xi\eta)}{\eta}d\eta,$$

with $\xi = \dfrac{u}{\sqrt{T}}$, $\eta = \dfrac{v_x}{\sqrt{T}}$.

From above we obtain a first-order differential equation for $p(n)$, $n_- \le n \le n_+$,

$$\frac{dp}{dn} = \frac{Cp_{xx}+Dq_x}{Ap_{xx}+Bq_x}, \tag{9}$$

with the condition $p(n_\pm) = p_\pm$. Eq. (9) becomes singular as $0/0$ at two ends of $n = n_\pm$ or $(n,p) = (n-n_\pm, p-p_\pm)$, since both p_{xx} and q_x should vanish there, which correspond to $x = \pm\infty$. We examine the nature of the solution there. This is a type of singular two point boundary value problem of a first order differential equation, we have found that the nature of the solution near $n = n_+$ is of node type while it is of saddle point type near $n = n_-$. Accordingly (i) we have two regular solution curves starting from $(n_-,\, p_-)$ of which one stretches towards to an area near $(n_+,\, p_+)$ while (ii) any solution curve near $n = n_+$ approaches to the point $(n_+,\, p_+)$. (iii) Further, solution passing a point $(\tilde{n}, \tilde{p})$ of $n_+ < \tilde{n} < n_-$, $p < \tilde{p} < p_+$ is regular and unique in $n_+ < n < n_-$ as far as the magnitude of the parameter M_- is close to 1 or $M_- - 1$ is small enough. Combine all three facts of (i), (ii), (iii) above, we can see that there exist a unique smooth solution of eq. (9) starting from $(p_-,\, n_-)$ and ending at $(p_+,\, n_+)$.

3.2 Local solutions near the end points

We show the local existence for the equation of the form

$$\frac{dy}{dx} = \frac{cx+dy+g(x,y)}{ax+by+f(x,y)} \equiv \frac{Q(x,y)}{P(x,y)}, \tag{10}$$

with constant values a, b, c, d provided that $x = 0$ is a saddle point or a nod and f/x^2 and g/x^2 are bounded near $x = 0$. Function $v = y/x$ satisfies

$$v' = \frac{1}{x}\left(\frac{c+dv}{a+bv}-v\right)+\frac{\zeta}{x}, \zeta = \frac{Q}{P}-\frac{c+dv}{a+bv}.$$

The solution is of the form $(v-p)^\alpha(v-q)^\beta x = V$ for integral constant V and $\alpha\beta > 0$ for saddle point type and $\alpha\beta < 0$ for nod type. It follows that

$$\begin{aligned}\frac{dV}{dx} &= \frac{\partial V}{\partial x} + \frac{\partial V}{\partial v}\frac{dv}{dx} \\ &= V^{1-\beta}x^{\frac{1}{\beta}}\left(v+\frac{a}{b}\right)(v-p)^{\frac{\alpha}{\beta}-1}\frac{\zeta}{x}. \\ \beta(V^{\frac{1}{\beta}})' &= x^{\frac{1}{\beta}}\left(v+\frac{a}{b}\right)(v-p)^{\frac{\alpha}{\beta}-1}\frac{\zeta}{x}.\end{aligned} \tag{11}$$

We construct a solution with $\lim_{x\to 0} v(x) = q$. For $\varepsilon(x) = v(x) - q$, it follows that

$$\begin{aligned}|\varepsilon(x)|_\infty &\le \frac{x}{\beta+1}\left|\left(v+\frac{a}{b}\right)(v-p)^{-1}\frac{\zeta}{x}\right|_\infty \\ &\le \frac{x}{b(\beta+1)}\frac{N_1|\varepsilon|_\infty + N_2}{|(\varepsilon+q-p)(b\varepsilon+a+bq+\frac{f}{x})|_\infty},\end{aligned} \tag{12}$$

with

$$N_1 = |b|\left|\frac{g}{x^2}\right|_\infty + |d|\left|\frac{f}{x^2}\right|_\infty, \quad N_2 = |a+bq|\left|\frac{g}{x^2}\right|_\infty + |c+dq|\left|\frac{f}{x^2}\right|_\infty.$$

Thus $|\varepsilon(x)|_{L^\infty([0,x_0])}$ is bounded for sufficiently small x_0, although N_1 and N_2 include ε. Since $v = y/x$ and $\varepsilon(x) = v(x) - q$, $|y(x) - qx| < Lx$ for $x \in (0, x_0)$ with some $L > 0$. Thus we can construct a local solution if $f(x,y)/x^2$ and $g(x,y)/x^2$ are bounded for (x,y) with $|y(x) - qx| < Lx$ and $x \in [0, x_0]$. In our problem of eq. (9),

$$AD - BC = -\frac{1}{20Tu}\left(\frac{n\nu}{p}\right)^2\frac{1}{\xi}\{\xi(6\xi^2-5)I^2 + 2(-5\xi^2+2)I + 4\xi\}.$$

We see $\mathbf{D}_+ > 0 > \mathbf{D}_-$ for $M_- = \sqrt{6/5}$.

Boundedness of f/x^2 and g/x^2 for f, g in eq. (10) provided that $|y(x) - q| < Lx$ is shown by

$$\begin{aligned}&\xi^2 - \xi_-^2 = C_1\left(\frac{u}{p} - \frac{u_-}{p_-}\right) = C_1\frac{p_-x - u_-y}{(y+p_-)p_-} = O(x), \\ &\xi^n - \xi_-^n = O(x), \quad n = 1, 2, 3, \cdots, \\ &I(\xi) - I(\xi_-) = I'(\xi_0)(\xi - \xi_-), \quad \xi_0 \in (\xi_-, \xi).\end{aligned} \tag{13}$$

Using the $p(n)$ function determined above, the functions $n(x)$, $p(x)$ $(-\infty < x < \infty)$ can be derived from eqs. (7), (8) combined with boundary conditions of $n(\pm\infty) = n_\pm, p(\pm\infty) = p_\pm$. It is possible as far as the upstream Mach number M_- is not so greater than 1 as it was shown in its approximate solution [6], where it was $M_- < 1.82$.

3.3 Construction of distribution function F

Now we determine the distribution function F. It is readily seen that once u, T are given as functions of x as above. F can be obtained simply by integrating both sides of eq. (1) over x from $x = -\infty$ to $x = \infty$ to yield

$$v_xF = v_xF_- + \int_{-\infty}^{x} \Pi dx$$

which can be transformed into a more convenient form. By eqs. (7) and (8), the collision term in eq. (1) turns to

$$\Pi = [(D\Pi_1 - C\Pi_2)\frac{dn}{dx} + (-B\Pi_1 + A\Pi_2)\frac{dp}{dx}](AD - BC)^{-1} \equiv \tilde{\Pi}\frac{dn}{dx},$$

So that $\int_{-\infty}^{x} \Pi dx = \int_{n_-}^{n} \tilde{\Pi} dn$ and $v_x F = v_x F_- + \int_{n_-}^{n} \tilde{\Pi} dn$. Notice that the above equation satisfies the boundary condition automatically as far as the integral exists since its right side term is to be given in a function of v and $n(x)$ only.

We seek here an explicit expression of F directly from eq. (1). We look for a solution F of eq. (1) subject to the boundary conditions of eq. (3) provided that u and T are given. We represent the solution by the Hermite expansion as done in [8] which is for the original Boltzmann collision model, although it is misleading in mixing of using constant and variable temparature T. We determine the coefficient and consider its summability.

For the Hermite basis defined by $H_i(\eta) = (-1)^i \dfrac{d^i\omega}{d\eta^i}/\omega,\ \omega(\eta) = \dfrac{1}{\sqrt{2\pi}} \mathrm{e}^{-\frac{\eta^2}{2}},\ (-\infty < \eta < \infty)$ we represent $F = F(x, v_x, v_y, v_z)$ by a Hermite series expansion in the form of

$$F = \left(\frac{2}{T}\right)^{\frac{3}{2}} \Omega(W) \sum_{i,j,k=0}^{\infty} a_{ijk}(x) H_{ijk}(W), \tag{14}$$

where we set

$$\begin{aligned} &(W_x, W_y, W_z) = \sqrt{\frac{2}{T}}(V_x, V_y, V_z), \\ &\Omega(W) = \omega(W_x)\omega(W_y)\omega(W_z), \\ &H_{ijk}(W) = H_i(W_x)H_j(W_y)H_k(W_z). \end{aligned} \tag{15}$$

Now we set by eq. (1)

$$\int H_{ijk} \frac{\partial}{\partial x}(v_x F) dv = \int H_{ijk} \Pi dv, \tag{16}$$

to have equations for a_{ijk}. We have

$$i!j!k! \left\{ b'_{ijk} + u' b_{i-1,j,k} + \frac{T'}{4}(b_{i-2,j,k} + b_{i,j-2,k} + b_{i,j,k-2}) \right\} = \Pi_{ijk} \tag{17}$$

for

$$\begin{aligned} &b_{ijk} = \left(\sqrt{\tfrac{T}{2}}\right)^{i+j+k} \left\{ \sqrt{\tfrac{T}{2}}(i+1)a_{i+1,j,k} + u a_{ijk} + \sqrt{\tfrac{T}{2}} a_{i-1,j,k} \right\} \\ &a_{ijk} = 0, \text{ for } i, j, k < 0 \end{aligned} \tag{18}$$

and

$$\begin{aligned} \Pi_{ijk} = &-\tfrac{3}{8}\nu a_{200} \int \Omega H_{ijk}(2H_{200} - H_{020} - H_{002}) dW \\ &-\frac{1}{20}\nu\{6a_{300} + 2(a_{120} + a_{102})\} \int \Omega H_{ijk}(H_{300} + H_{120} + H_{102}) dW, \end{aligned} \tag{19}$$

Now we consider the general summability of series expansion. Letting $c_{ijk} = \sqrt{\frac{T}{2}}^{i+j+k} a_{ijk}$, series

$$S_i = \sum_{j,k} b_{ijk}, \quad d_i = \sum_{j,k} c_{ijk}$$

satisfy

$$
\begin{aligned}
S_i &= (i+1)d_{i+1} + ud_i + \frac{T}{2}d_{i-1} \\
S_i' &+ u'S_{i-1} + \frac{T'}{4}(2S_i + S_{i-2}) = M_i
\end{aligned}
\tag{20}
$$

The summation $S = \sum_i S_i$ satisfies

$$
S' + u'S + \frac{3}{4}T'S = M,
$$

for $M = \sum \frac{1}{i!j!k!}\Pi_{ijk}$. Since S is obtained by

$$
S = e^{-(u+\frac{3}{4}T)} \int e^{u+\frac{3}{4}T} M dx,
$$

$S < \infty$ implies $\lim S_i = 0$. We see $\lim d_i = 0$.

To consider the convergence of the right hand side of (14) as function of (x, v_x, v_y, v_z), we obtain that

$$
\left| \sum_{i,j,k=0}^{\infty} \sqrt{\frac{T}{2}}^{i+j+k} a_{ijk}(x) \right| < \infty \tag{21}
$$

for $T(x) < 2$.

4 Conclusion

We consider the Boltzmann equation with a modified collision term in which the distribution function is approximated by its 13 moments, originally proposed by Oguchi [5]. We establish first the solution of moment equations, and secondary determine the distribution function itself from the moments provided above. We also construct the solution in the Hermite polynomial expansion by utilizing the orthogonality of the Hermite polynomials and obtain equations for the coefficients. We show a summability of the coefficients.

References

1. Becker, R., Stosswelle und Detonation, Zeitschrift f. Physik 8 321-, 1922
2. Nikolaenko B., A general class of nonlinear bifurcation problems from a point in the essential spectrum, and applications to shock wave solutions of kinetic equations. Applications of Bifurcation Theory, Academic Press, 333-357, 1977.
3. Caflisch R. E., Nikolaenko B., Shock profile solutions of the Boltzmann equation. Commun. Math. Phys. 86, 161-194, 1982.
4. Bose C., Illner R., Ukai S., On shock wave solutions for discrete velocity models of the Boltzmann equation. Transport Theory and Statistical Physics, 27 (1), 35-66, 1998.
5. Oguchi H. and Soga T., Computation of rarefied gas flows at near-equilibrium state by discrete-velocity-ordinate method. In: Shen C, et al. (eds) Rarefied Gas Dynamics. Peking University Press, Beijing, 285-297, 1997.
6. Nagai R, Homma H, Maeno K, Sakurai A Shock-wave solution of the Boltzmann kinetic equation in a 13-moment approximation. Shock Waves (DOI)10.1007/s00193-003-0208-z, 2003.
7. Schakov, E. M., Kinetic model equations and numerical results, Rarefied Gas Dynamics, by H. Oguchi, University of Tokyo Press, Tokyp, 137-148, 1984.
8. Grad H., On the kinetic theory of rarefied gases. Comm. Pure Appl. Math. 2 (4) 331-407, 1949.

Rotational-translational relaxation effects in diatomic-gas flows

V.V. Riabov

Department of Computer Science, Rivier College, Nashua, New Hampshire 03060 USA

1 Introduction

The problem of deriving the nonequilibrium gas dynamic equations from the first principles of the kinetic theory of gases was studied by Ferziger and Kaper [1] in the cases of near-equilibrium and slow-relaxation processes of the energy exchange between internal and translational degrees of molecular freedom. The case of the arbitrary energy exchange ratio was analyzed in [2], [3], [4], [5] for polyatomic gas mixtures.

In the present study the problem of redistribution of translational and rotational energy has been solved for diatomic gases within the framework of the Chapman-Enskog method [1], [5], [6] and the Parker model [7] in the general case of the arbitrary energy exchange ratio. The gasdynamic equations, transport coefficients and relaxation time have been found for nonequilibrium processes in diatomic gases [5], [6]. The calculations of relaxation time, viscosity, thermal conductivity, and diffusion coefficients are carried out in the temperature range from 200 K to 10,000 K for nitrogen by using the technique of integral brackets [1], [4]. The calculated parameters are compared with the values obtained by the approximate method [8] as well as data from experiments [9], [10] in ultrasonic, shock-wave, and vacuum devices. The correlation of theoretical and experimental data is satisfactory. The applicability of one- and two-temperature relaxation models for para-hydrogen at the rotational temperature range from 0 to 1200 K is discussed. The numerical solutions of the Navier-Stokes equations are analyzed for spherical expanding nitrogen flow and supersonic flow near a sphere.

2 Rotational relaxation time estimations

Two definitions of relaxation time are widely used. In the first case the expression for the temperature dependence of the relaxation time, $\tau_{\mathrm{R1}}(T)$, is obtained by using the Chapman-Enskog iteration method of solving the Boltzmann equation for a gas of particles with internal degrees of freedom [1]. In the second case the relaxation time, $\tau_{\mathrm{R2}}(T)$, is found directly from the relaxation equation (see Eq. (17) from [6]) by calculating the rate of increase of the internal energy of the molecules that originally were not excited [11].

In the present study parameters $p\tau_{\mathrm{R1}}(T)$ and $p\tau_{\mathrm{R2}}(T)$ are calculated for nitrogen by formulas (18)-(20) from [6]. Multifold integrals are calculated at 200 points over the range 200 K $\leq T \leq$ 10,000 K, using the Monte-Carlo technique [5], with 4000 tests at each point. The data for intermediate points are determined by using cubic splines [6]. The estimated accuracy of the calculations is 1.5 percent. The higher orders of the theory of perturbations [6] make a substantial contribution at $T < 400$ K, and the accuracy of the calculations is lower under these conditions. The results of calculations $p\tau_{\mathrm{R2}}$ and $p\tau_{\mathrm{R1}}$

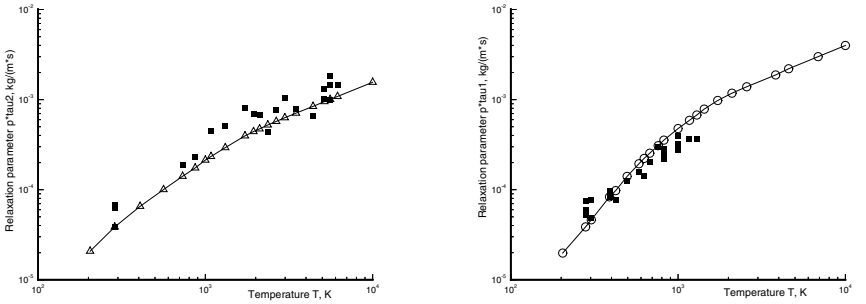

Fig. 1. Parameters $p\tau_{\mathrm{R}2}$ (*left*) and $p\tau_{\mathrm{R}1}$ (*right*) versus temperature T

are shown in Fig. 1 (solid lines). The experimental data (filled squares) were acquired in [9], [10]. The calculations show that at 200 K $\leq T \leq$ 10,000 K, $p\tau_{\mathrm{R}1}$ is 2 or 2.5 times as large as $p\tau_{\mathrm{R}2}$. This difference is apparently due to the adiabatic nature of the energy exchange between the highly excited rotational states of the molecules [5]. The effect of the initial energy distribution at rotational levels was not considered in this comparison. The quantity $p\tau_{\mathrm{R}1}(T)$ was used for interpreting the experimental data on the scattering and absorption of ultrasound, where the effect of the ultrasound frequency on $p\tau_{\mathrm{R}1}$ was disregarded [9]. The quantity $p\tau_{\mathrm{R}2}(T)$ was used for interpreting the data of experiments in shock tubes. The available experimental data [9], [10], both on ultrasound and on shock waves, differ from one another by 200-300 percent, which is approximately equal to the difference between $p\tau_{\mathrm{R}1}$ and $p\tau_{\mathrm{R}2}$, as evident from Fig. 1.

3 The effect of initial rotational energy distribution

The effect of the initial energy distribution at rotational levels has been estimated in [5] under the assumption that at initial time the distribution corresponds to the Boltzmann distribution with rotational temperature $T_{\mathrm{R}} > 0$. Therefore, the translational-rotational relaxation time becomes a function of both T and T_{R} (see Eq. (1.7) in [5]). The parameter $p\tau_{\mathrm{R}2}(T, T_{\mathrm{R}})$, calculated for nitrogen at $T = 1000$ K, decreases from 2.13×10^{-4} kg/(m·s) for $T_{\mathrm{R}} = 0$ K to 5.24×10^{-5} kg/(m·s) for $T_{\mathrm{R}} = 800$ K.

The problem of a proper selection of the relaxation time [$\tau_{\mathrm{R}2}(T)$ versus $\tau_{\mathrm{R}2}(T, T_{\mathrm{R}})$] for a more accurate description of the manner in which the system approaches equilibrium is studied for para-hydrogen. The solution of the kinetic equation in τ approximation (see Eq. (17) in [6]) was compared with the solution obtained by numerical integration of the system of kinetic equations for the occupancies of the individual rotational levels [5]. In these calculations, the constants of the rotational-transfer rates were estimated within the framework of the effective-potential method [12]. The calculation results are shown in Fig. 2 (*left*), where parameters $p\tau_{\mathrm{R}2}(T, T_{\mathrm{R}})$, estimated at constant temperature $T =$ 400 K, (triangles) are compared with the results of numerical integration of the system of kinetic equations (circles). The point $T_{\mathrm{R}} = 0$ K of the first curve corresponds to $p\tau_{\mathrm{R}2}(T)$. A dependence of the relaxation time on T_{R} is observed. Therefore, the use of a function

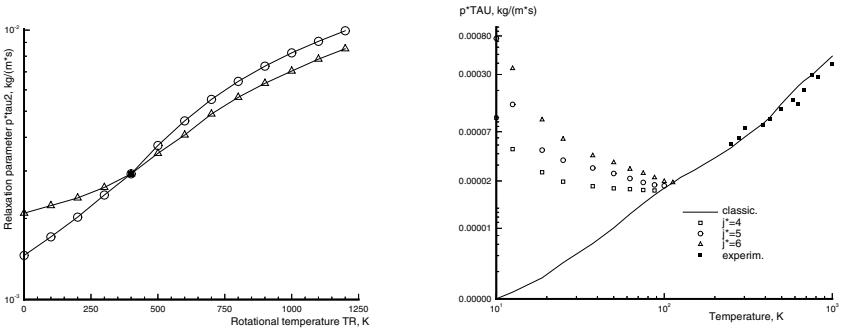

Fig. 2. The rotational relaxation parameters $p\tau_{\mathrm{R}2}(T,\, T_{\mathrm{R}})$ in para-hydrogen at constant temperature $T = 400$K (*left*) and in nitrogen expanding into a vacuum (*right*)

$p\tau_{\mathrm{R}2}(T,\, T_{\mathrm{R}})$ significantly improves the approximate solution of the relaxation equation, and the initial distribution of energy at rotational levels should be taken into account within the framework of the τ approximation.

4 Rotational relaxation in freely expanding gas flows

Studies [13], [14] of the rotational relaxation in expanding gas flows discovered a significant decrease of the gas density downstream that leads to a decrease in the number of molecular collisions. The departure of the gas rotational energy from the equilibrium value was observed.

Lebed and Riabov [15], [16] studied another cause for the rotational energy departure. At the decrease of kinetic temperature T_{t}, adiabatic collision conditions [17] should be taken into account, and the relaxation time τ_{R} increases due to the sharp decrease of the rotational transfer probabilities. Using this method [15], the relaxation times were calculated for nitrogen at stagnation temperature $T_0 = 295$ K [see Fig. 2 (*right*)] under the conditions of aerodynamic experiments in underexpanded jets [13], [14], [16]. The calculations based on the classical concept [7] [see solid line in Fig. 2 (*right*)] do not show a tendency of increasing $p\tau_{\mathrm{R}}$ with the decrease of T_{t} under adiabatic rotational energy exchange conditions. At temperatures $T_{\mathrm{t}} > 273$ K, numerical results correlate well with experimental data [9], [10]. In the expansion of nitrogen, starting at $T_0 = 300$ K, the maximum population of molecules occurs at rotational levels J from 6 to 4 [15], [17]. The results of calculating $p\tau_{\mathrm{R}}$ for $J = 6$, 5, and 4 are shown in Fig. 2 (*right*) (empty triangles, circles, and squares, correspondingly). The values of $p\tau_{\mathrm{R}}$ increase with decrease of T_{t}. At $T_{\mathrm{t}} > 100$ K, the adiabatic condition breaks down, and the parameter $p\tau_{\mathrm{R}}$ could be estimated by the Parker's model [7].

For qualitative estimations, the energy relaxation time is replaced by the relaxation time of the level J. This approximate method [15] correctly represents the nature of the R-T nonequilibrium process, i.e., an increase of $p\tau_{\mathrm{R}}$ with decreasing T_{t}. Figure 3 (*left*) shows the distributions of rotational temperature T_{R} along the axis of nitrogen jet. The result of using the classical mechanics concept [7] is shown there by diamonds. The curves

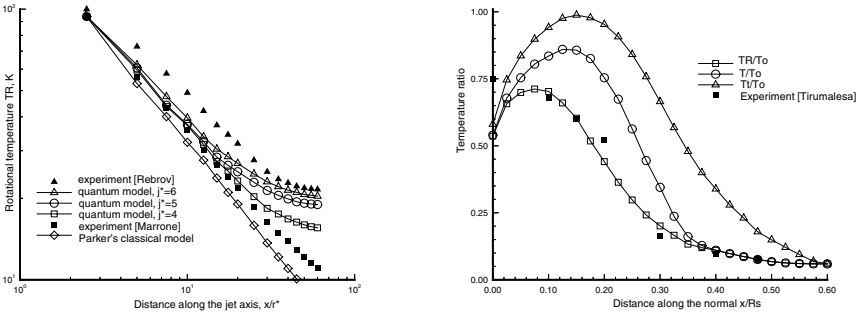

Fig. 3. The rotational $T_{\rm R}$ and translational $T_{\rm t}$ temperatures in spherically expanding flow of nitrogen (*left*) and at the stagnation streamline near a sphere (*right*)

marked by empty triangles, circles, and squares were obtained for values of $p\tau_{\rm R}$ at $J = 6$, 5, and 4, correspondingly. The calculations were made at $\mathrm{K} = \rho u r/(p\tau_{\rm R}) = 2730$, $p_0 r_{\rm j} = 240$ torr·mm and $T_0 = 295$ K.

The experimental data ((filled squares) [13], (triangles) [14]) for $T_{\rm R}$ are upper and lower bounds on the distribution of rotational energy along the nitrogen jet. Numerical results, based on the quantum concept of rotational energy exchange, correlate well with the experimental data [14]. The data contradicts the classical model predictions [7] of $T_{\rm R}$. The experimental and computational results demonstrate the necessity of considering the quantum concept in describing R-T relaxation in underexpanded jets. This concept was used in evaluating various relaxation models in expanding low-density nitrogen flows [18].

5 Transport coefficients in non-equilibrium diatomic gases

The analytic formulas for transport coefficients were found by Lebed and Riabov (see Eqs. (21-29) in [6]): the coefficients of shear viscosity corresponding to rotationally inelastic and elastic collisions, η and η_0; the corresponding values of the thermal conductivity, λ and λ_0; and the self-diffusion coefficient of the elastically colliding molecules, D_0. The simplest approximations for the thermal conductivity coefficient λ were analyzed in [1], [5], [6], [8]. The first approximation [8] was based on the diffusive transfer, but it disregarded the relaxation of the rotational energy. The relaxation was taken into account partially in the next, second, approximation [8] for the thermal conductivity coefficient λ_2. Triangles and circles in Fig. 4 (*left*) show η and η_0, correspondingly, as given by Eqs. (21-29) from [6], while the filled squares indicate the experimental data of Vargaftik [19]. The difference between η and η_0 is evaluated as 5 percent in the low-temperature regime. At temperature $T > 1000$ K these values correlate well with each other. The parameter $\rho D_0/\eta_0$ is approximately constant and equals to 1.20.

Triangles in Fig. 4 (*right*) show λ, as given by Eqs. (21-29) from [6]. Circles correspond to the Mason and Monchick's second approximation [8], λ_2. The filled squares indicate the experimental data of Vargaftik [19]. The present analysis shows that the correlation between the exact solution, the Mason and Monchick's second approximation [8], and

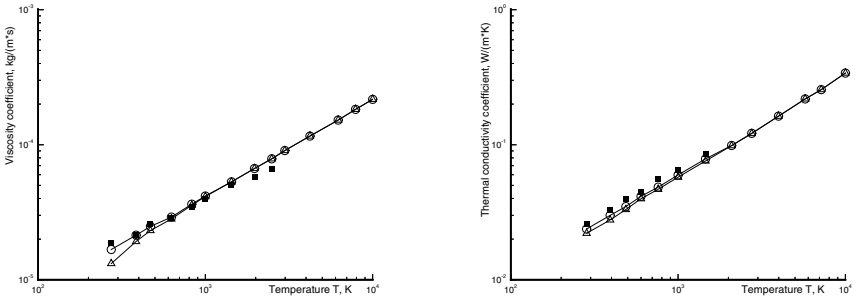

Fig. 4. Viscosity (*left*) and conductivity coefficients (*right*) in nitrogen

experimental data [19] is acceptable. The small discrepancy between the theoretical values of η and λ and the experimental data (see Fig. 4) can be eliminated by a proper choice of the molecule collision potential at $T < 1000$ K.

6 Rotational relaxation in viscous gas flow near a sphere

The combined effect of the rotational-translational relaxation and the viscosity and thermal conductivity processes is studied here by solving the full system of the Navier-Stokes equations and the relaxation equation (see Eq. (42-46) from [6]) with the implicit numerical technique [20]. The flow of molecular nitrogen was assumed to be undisturbed on the outer boundary of the computational region. At the spherical surface the slip, temperature and rotational energy jump conditions [20] were used.

The distributions of the nonequilibrium rotational ($T_{\rm R}$, empty squares) and translational ($T_{\rm t}$, triangles) temperatures are shown in Fig. 3 (*right*) for flow at Knudsen number $Kn = 0.08$ (or Reynolds number $Re_0 = 16.86$), Mach number $M = 9$, stagnation temperature $T_0 = 298$ K, and temperature factor $t_{\rm w} = 0.3$. In the viscous shock layer near a sphere, a significant difference between the translational and rotational temperatures can be observed. The shock-layer becomes thicker under the nonequilibrium flow conditions than in the case of equilibrium flow at $T_{\rm R} = T_{\rm t}$ [see circles in Fig. 3 (*right*)]. The numerical results for $T_{\rm R}$ correlate well with the experimental data [21] [marked by filled squares in Fig. 3 (*right*)], obtained in a wind tunnel by the electron-beam diagnostics.

7 Conclusion

The calculations of relaxation time, viscosity and thermal conductivity, and diffusion coefficients were carried out by using the Monte-Carlo simulation technique for nitrogen at 200 K $\leq T \leq$ 10,000 K . The calculations and available experimental data show that the rotational relaxation time, $\tau_{\rm R1}$, obtained by using the Chapman-Enskog iteration method, is 2 or 2.5 times as large as the time $\tau_{\rm R2}$, which is found directly from the relaxation equation. The difference is apparently due to the adiabatic nature of the energy exchange

between the highly excited rotational states of the molecules. The quantity $p\tau_{R1}$ is used for interpreting the experimental data on the scattering and absorption of ultrasound. The quantity $p\tau_{R2}$ is used for interpreting the data of experiments in shock tubes. The use of a function $p\tau_{R2}(T, T_R)$ significantly improves the approximate solution of the relaxation equation, and the initial distribution of energy at rotational levels should be taken into account within the framework of the τ approximation.

Acknowledgement. The author expresses gratitude to I. V. Lebed for his participation in this study.

References

1. J. Ferziger, H.G. Kaper: *Mathematical Theory of Transport Processes in Gases* (North-Holland, Amsterdam-London 1972)
2. M.N. Kogan, N.K. Makashev: Fluid Dynam. **13**, 126 (1978)
3. B.V. Alekseev: Tekhn. Eksper. Khimiya **5**, 88 (1969)
4. V.A. Matsuk, V.A. Rykov: J. Appl. Mech. Techn. Phys. **18**, 61 (1978)
5. I.V. Lebed, V.V. Riabov: J. Appl. Mech. Techn. Phys. **24**, 447 (1983)
6. V.V. Riabov: J. Thermophys. Heat Transf. **14**, 404 (2000)
7. J.G. Parker: Phys. Fluids **2**, 449 (1959)
8. E.A. Mason, L. Monchick: J. Chem. Phys. **36**, 1622 (1962)
9. C.A. Brau, R.H. Jonkman: J. Chem. Phys. **52**, 474 (1970)
10. J.A. Lordi, R.E. Mates: Phys. Fluids **13**, 291 (1970)
11. B.F. Gordiets, A.I Osipov, L.A. Shelepin: *Kinetic Processes in Gases and Molecular Lasers* (Nauka, Moscow 1980)
12. H. Rabitz, S.H. Lam: J. Chem. Phys. **63**, 3532 (1975)
13. P.V. Marrone: Phys. Fluids **10**, 521 (1967)
14. B. Borzenko, N. Karelov, A. Rebrov, R. Sharafutdinov: J. Appl. Mech. Techn. Phys. **17**, 20 (1976)
15. I.V. Lebed, V.V. Riabov: J. Appl. Mech. Techn. Phys. **20**, 1 (1979)
16. V.V. Riabov: J. Aircraft **32**, 471 (1995)
17. I.V. Lebed, S.Ya. Umanskii: Khimiya Vysokikh Energii **10**, 501 (1976)
18. L. Gochberg, B. Haas: AIAA Paper 95-2070 (1995)
19. I.B. Vargaftik: *Handbook of the Thermophysical Properties of Gases and Liquids* (Nauka, Moscow 1972)
20. V.V. Riabov: Fluid Dynam. **15**, 320 (1980)
21. D. Tirumalesa: AIAA J. **6**, 369 (1968)

Shock wave solution of molecular kinetic equation for source flow problem

M. Tsukamoto and A. Sakurai

Tokyo Denki University 101-8457 Tokyo, (JAPAN)

Summary. We compute shock wave solution for a 2D source flow problem of the Boltzmann equation. Results are compared with the one by the Navier - Stokes system as well as an experimental result observed in a steady radial flow between two flat plates.

1 Introduction

The purpose of this study is to find shock wave solution of the Boltzmann equation for 2D source flow. The problem of steady radial flow is a setting where the velocity is in radial direction and the flow quantities as velocity u , pressure p , density N and temperature T are all functions of radius r only. In spit of this simple setting, the problem is quite involved and was studied in some detail in the past based on various types of fluid dynamics models ([3], [2], [5], [6], [7]). But very nature of the mysterious features to the solution of these equations has been remained unsolved. There has been also some renewed interests on this problem in connection with various practical subjects such as gas flow through an orifice (Yamane et al(1984), and a different approach by a kinetic model ([1]). We use the Boltzmann equation with BGK collision model for this problem and compare the solution curves with those by the Navier-Stokes equations and experimental result given in Yamane et al(1984).

2 Basic equations

We utilize the usual practice of time dependent approach to find the steady flow starting from an appropriate initial state. We use time - dependent Boltzmann equation with BGK collision model for the distribution function $f(\xi, \alpha, \xi_z, r, t)$ in cylindrical coordinates system with radius r in non - dimensional form ([4] , Doi & Ooshima (1998)). For the actual calculation, we use the reduced distribution functions g, h, G, H as

$$g = \int_{-\infty}^{\infty} f d\xi_z, h = \int_{-\infty}^{\infty} {\xi_z}^2 f d\xi_z, G = \int_{-\infty}^{\infty} F d\xi_z, H = \int_{-\infty}^{\infty} {\xi_z}^2 F d\xi_z. \tag{1}$$

, where F is the local Maxwellian. Then the Boltzmann equation with BGK model is written for present problem of axial symmetry in a non - dimensional form as

$$\frac{\partial g}{\partial t} + \xi \cos\alpha \frac{\partial g}{\partial r} - \frac{\xi \sin\alpha}{r} \frac{\partial g}{\partial \alpha} = \frac{1}{2} R_{e2} N (G - g)$$

$$\frac{\partial h}{\partial t}+\xi\cos\alpha\frac{\partial h}{\partial r}-\frac{\xi\sin\alpha}{r}\frac{\partial h}{\partial\alpha}=\frac{1}{2}R_{e2}N(H-h)$$

$$G=\frac{N}{\pi T}\exp\left(-\frac{C^2}{T}\right),H=\frac{1}{2}GT,C^2=\xi^2-2u\xi\cos\alpha+u^2,$$
$$N=N\left(r,t\right)=\int\xi g d\xi d\alpha,u=u\left(r,t\right)=\frac{1}{N}\int\xi^2 g\cos\alpha d\xi d\alpha,$$
$$T=T\left(r,t\right)=\frac{2}{3N}\left(\int\xi\left(\xi^2 g+h\right)d\xi d\alpha-Nu^2\right),p=NT,R_{e2}=\frac{\varrho_2\xi_2 r_2}{\mu_2},$$

where R_{e2} expresses Reynolds number at $r=r_2$ through Karmanfs relation

$$K_nR_{e2}=\sqrt{\frac{8\gamma}{\pi}}M_2 \tag{2}$$

for Maxwell molecular model and the Knudsen number $K_n=\frac{l_2}{r_2}$, where M_2,l_2 are respectively the Mach number and the mean free path at $r=r_2$. And

$$\xi^2=\xi_r^2+\xi_\theta^2,\xi_r=\xi\cos\alpha,\xi_\theta=\xi\sin\alpha,\alpha=\tan^{-1}\frac{\xi_\theta}{\xi_r},0\leq\xi<\infty,-\pi\leq\alpha\leq\pi \tag{3}$$

We consider two bounding surfaces at $r=r_1$ and $r=r_2$ and assign boundary values for g,h and T,u,N there as

$$g=\frac{N_2}{\pi T_2}\exp\left(-\frac{C^2}{T_2}\right),h=\frac{1}{2}GT_2,u_2=m_s(given)$$

at $r=r_2$ and

$$g=\frac{N_1}{\pi T_1}\exp\left(-\frac{C^2}{T_1}\right),h=\frac{1}{2}GT_1,T_1=given,u_1=given,N_1=\frac{m_s}{u_1r_1}$$

at $r=r_1$. The initial condition for them is given as

$$g=\frac{N}{\pi T}\exp\left(-\frac{C^2}{T}\right),h=\frac{1}{2}gT,T=T_2,u=0,N=N_2$$

for $r_1<r<r_2$

3 Results and discussion

For numerical integration, we set $N_2=T_2=1$, $u_2=0.1$ at $r=r_2=1$, and use $u_1=0.80,1.0,1.4,1.6$. We start the computation from the initial condition above with one of the u_1 values above and an appropriately given T_1 value, and perform computation until we have steady flow, and then repeat the process by changing T_1 values to have a steady solution which is uniform near $r=1$. To the typical case of $R_{e2}=100$ or equivalently $K_n=0.017$ we have $T_1=0.70,0.60,0.23$ and 0.015 respectively for

$u_1 = 0.80, 1.0, 1.4$ and 1.6. The result is shown in Fig.1, where the number density N , the velocity u , the temperature T , the pressure p and the constant mass flow m_s to show the consistency of the computation are expressed. These curves show little difference between them in their shock - wave like feature, except for the $u_1 = 1.6$ case ,to which velocity curve starts from its maximum limit and decreases monotonically to zero. To this case, the temperature curve shows that it starts from the absolute zero and monotonically increases to a uniform state as $r \to 1$. The pressure curve starts also from zero to become uniform as $r \to 1$. Mass flow should remain constant. In Fig.2, the velocity curves are compared with corresponding ones obtained by the Navier- Stokes equations. The solution obtained here is in general similar to the one by the Navier - Stokes system. The behavior of the velocity curve near the source seems to be more natural than the one for the Navier- Stokes system, which reaches to its maximum limit at the point far from the source indicating a nature of the singularity there. Shown in Fig.3 is corresponding shock wave pattern appearing in an experiment by Yamane et al(1984), which is observed in a steady radial flow between two flat plates.

Conclusion

Although the overall feature of the solution obtained here is similar to the one by the Navier - Stokes solutions, the behavior of the velocity curve near the source is seems to be more natural than the one by the Navier- Stokes system, which reaches to its maximum limit at the point far from the source indicating a nature of the singularity there.

References

1. Gusev.VN,Vlasov.VI: Rerefied gas flow from a spherical sink and source. Prc 21st RGD, 1998
2. Ladyzhenskii.MD: On the efflux of a viscous gas into vacuum. J Appl Math Mech 26, 965-974, 1962
3. Levey.H: Two-dimensional source flow of a viscous fluid. Quart Appl Math 12, 25-48, 1954
4. Onishi.Y,Doi.T,Ooshima.T: Motions of a vapor between the spherical condensed phases.Prc 21st RGD, 1998
5. Prosnak.W: Shock wave in a two-dimensional radial flow. Archiwum Mechaniki Stosowanei 8,617-645, 1956
6. Sakurai.A: On the theory cylindrical shock wave. J Phys Soc Japan 4, 199-202, 1949
7. Shusser.M,D.Weihs: Two-dimensional compressible viscous sink flow. Fluid Dynamic Res 15,349-364, 1995
8. Yamane.R,Oshima.S,Takahashi.M,Tamaki.H: Trans. Jpn.Soc. Mech. Engrs. 50(453),1213-1221, 1984

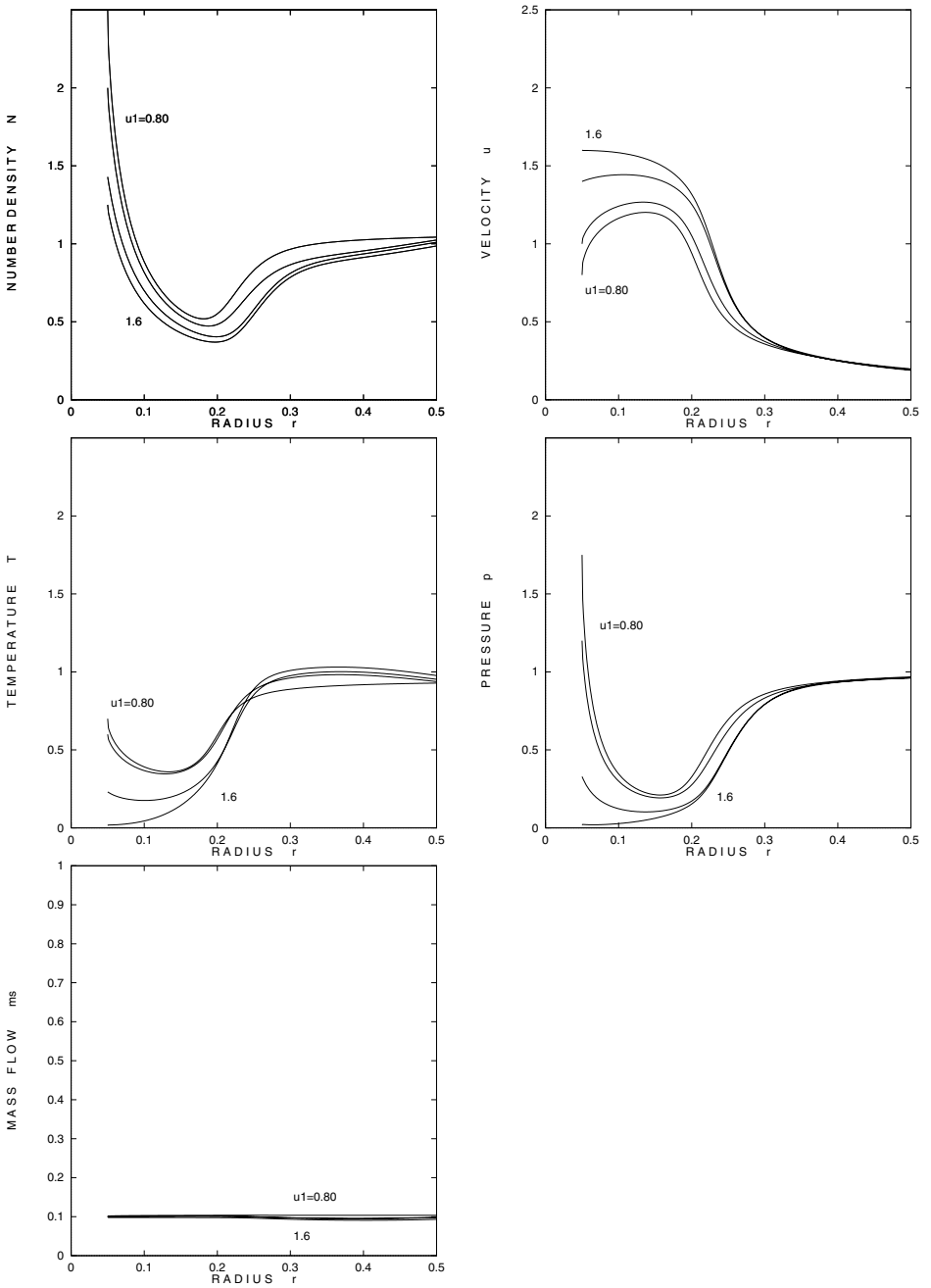

Fig. 1. Shock wave solution curves for cylindrical source flow of the Boltzmann equation: Distributions of number density , velocity , temperature , pressure , mass flow , Re=100, $u_1 = 0.8, 1.0, 1.4, 1.6$

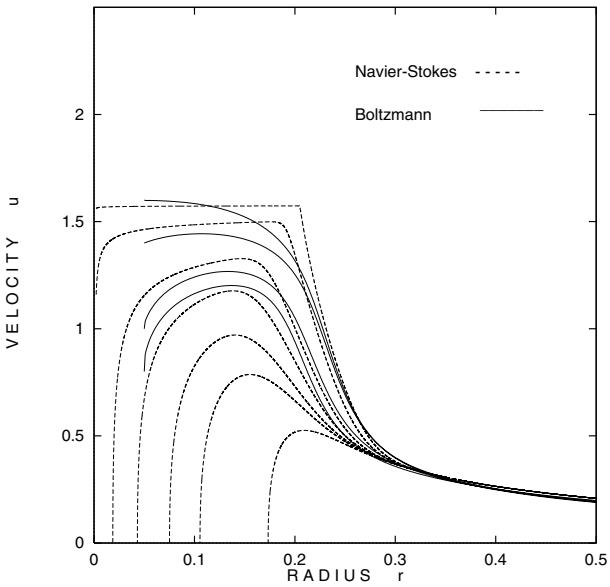

Fig. 2. Shock wave solution curves for cylindrical source flow with Boltzmann and Navier-Stokes equations. Re=100, $u_1 = 0.8, 1.0, 1.4, 1.6$.

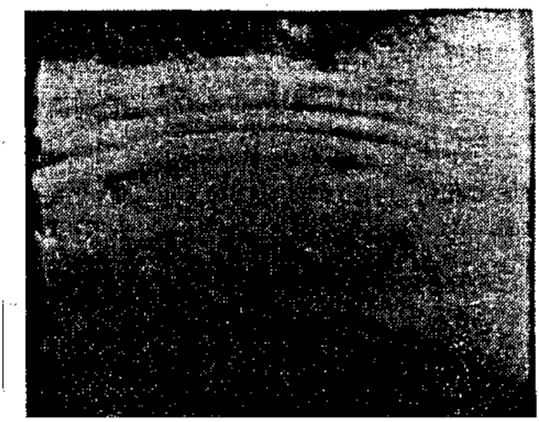

Fig. 3. Schlieren photograph including shock wave for source flow by [8] appearing in a steady radial flow between two flat plates.

Part XVIII

Richtmyer-Meshkov

Computations in 3D for shock-induced distortion of a light spherical gas inhomogeneity

J.H.J. Niederhaus[1], D. Ranjan[1], J.G. Oakley[1], M.H. Anderson[1], J.A. Greenough[2], and R. Bonazza[1]

[1] *Department of Engineering Physics, University of Wisconsin-Madison 1500 Engineering Drive, Madison, WI 53706 (USA)*
[2] *Lawrence Livermore National Laboratory, Livermore, CA 94550 (USA)*

Summary. Results are presented from a series of 3D numerical simulations for shock-bubble interactions, for a spherical helium bubble in air or nitrogen initially at atmospheric pressure ($A \approx -0.75$), accelerated by a planar shock wave of Mach number $M = 1.45$, 2.08, or 2.95. The simulations are carried out using a multifluid, adaptive Eulerian Godunov code at a fine-grid resolution of R_{100}. The computed solutions clearly resolve well-known shock refraction and vortex formation processes. Further, distinct, counter-rotating secondary vortex rings are observed to form in the flowfield as a result of irregular shock refraction effects. The temporal development of the the bubble's streamwise dimension and the mixing of bubble and ambient fluid are shown to collapse onto nearly self-similar trends on timescales based on a 1D gasdynamics analysis.

1 Introduction

A useful means of characterizing the development of an inhomogeneous medium under acceleration by a shock wave is to consider shock-bubble interactions. These may be viewed as a simplified form of shock-accelerated inhomogeneous flows found in, for example, the interstellar medium [1] and inertial confinement fusion devices [2]. In shock-bubble interactions, a shock wave propagates over a single discrete inhomogeneity of circular cross-section. The bubble is compressed and deformed, and, in the case of a spherical bubble, a vortex ring is produced in the post-shock flowfield.

The development of the flowfield in shock-bubble interactions is driven by three nonlinearly coupled and simultaneous physical processes: (1) shock compression of the inhomogeneity; (2) reflection, refraction, and diffraction of the shock wave by the inhomogeneity [3]; and (3) vorticity generation. For spherical bubbles, baroclinic vorticity generation ($\nabla\rho \times \nabla p \neq 0$) results in the formation of a primary vortex ring, as well as subsequent, smaller secondary vortex rings.

In the 1D analog to a shock-bubble interaction, a shock wave interacts with a gas slab embedded in the medium. The slab gas state may be tracked during this interaction by solving a system of equations based on the Rankine-Hugoniot conditions, with appropriate matching conditions at the interfaces. The resulting properties of the slab fluid may be regarded as a baseline with which to compare the properties of a shocked bubble. Such an approach has been used successfully by Giordano and Burtschell [4] to predict the density of shocked bubbles. The one-dimensional analysis also yields characteristic velocities useful in timescaling: the incident shock wave speed W_i, the transmitted shock wave speed (in the bubble) W_t, and the post-shock ambient flow speed u_1'.

Here, we consider a particular variety of shock-bubble interactions, where a planar shock wave propagating in a gas medium interacts with a light spherical gas inhomogeneity. The bubble fluid is helium, and the ambient fluid is air or nitrogen. An Atwood

number can be defined for these gas pairings as $A = (\rho_2 - \rho_1)/(\rho_2 + \rho_1) \approx -0.75$, where ρ_2 is the bubble fluid density, and ρ_1 is the ambient fluid density. Three scenarios are considered, including shock wave Mach numbers $M = 1.45$, 2.08, and 2.95. These flows are simulated using a multifluid Eulerian Godunov code in a quarter-symmetry geometry, as shown in Figure 1(a). The simulated shock-induced bubble deformation and vortex ring formation (reflected to all four quadrants) for $M = 2.08$ is shown in Figure 1(b). Two integral diagnostics are applied to the resulting datasets in order to characterize the temporal development of the shocked bubble dimensions and the extent of mixing.

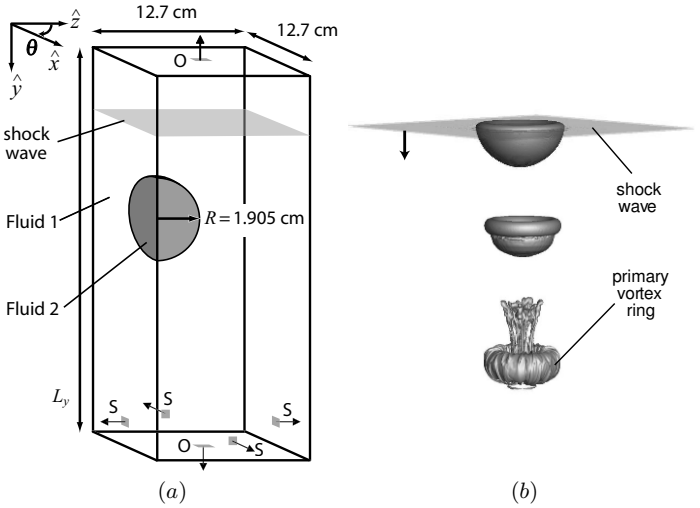

Fig. 1. (a) Schematic view of three-dimensional Cartesian geometry used in the present simulations (not drawn to scale.) "S" indicates symmetry boundary conditions; "O" indicates outflow boundary conditions. (b) Simulated deformation of a helium bubble during and after interaction with a $M = 2.08$ shock wave in air.

2 Setup of 3D simulations

Simulations are performed in 3D using an adaptive hydrodynamics code called *Raptor*, which integrates the compressible Euler equations using an operator-split second-order Godunov method (see Colella, 1985 [5]). Multifluid capturing capability is incorporated by adopting a volume-of-fluid technique similar to that of Miller and Puckett (1996) [6]. The integration kernel is embedded within the block-structured adaptive mesh refinement (AMR) framework of Berger and Oliger (1984) [7], to maximize spatial resolution and accuracy for regions of interest that move across the Eulerian mesh.

The calculations using *Raptor* are set up in Cartesian mesh subtending a quadrant of a typical shock tube flow field, including a quarter-spherical bubble of radius $R = 1.905$ cm. Refinement of the grid in the bubble region yields an effective spatial resolution of Δ=191 μm, corresponding to approximately 100 highest-level grid points in a distance R. In the initial condition, shown schematically in Figure 1, a planar shock wave propagates in the $+y$-direction, approaching a quarter-spherical bubble of helium, embedded in an

otherwise uniform air or nitrogen environment at atmospheric temperature and pressure. A smooth interface is created in the initialization using a subgrid volume-of-fluid model to suppress "stairstep" features. Boundary conditions indicated in Figure 1 are applied to enforce symmetry and capture shock reflections at the sidewalls, but not the endwalls.

Gas	$\mathcal{M}$ [g/mole]	γ	c [m/s]	ρ [kg/m^3]
He	4.003	1.667	1007	0.1614
N_2	28.013	1.399	348.9	1.129
Air	28.967	1.399	343.0	1.168

Table 1. Initial properties of gases present in the current calculations, including the molar mass $\mathcal{M}$, the ratio of specific heats γ, the initial sound speed c, and the initial density ρ. The initial pressure and temperature in the system are 98, 217 Pa and 293 K, respectively.

The three scenarios considered here are intended to correspond to the scenarios considered in the experimental work of Ranjan *et al.* [8]. Properties of the gases included in these simulations are shown in Table 1, and important parameters for each of the scenarios, including dimensionless parameters and various characteristic speeds, are listed in Table 2. Although direct comparison of experimental and numerical results is beyond the scope of the present study, the experimental data are also presented in this meeting, and direct comparison will be made in future publications.

Scenario #	Gas pair	M	A	W_i [m/s]	u_1' [m/s]	W_t [m/s]
1	Air-He	1.45	-0.757	497.4	217.4	1235
2	Air-He	2.08	-0.757	713.4	457.3	1529
3	N_2-He	2.95	-0.750	1029	759.2	1948

Table 2. Overview of flow parameters for three simulations, including the incident shock Mach number M, the Atwood number A at the unshocked interface, and lab-frame speeds W_i, u_1', and W_t of the incident shock wave, shocked ambient gas, and transmitted shock wave, respectively.

3 Flow visualizations

Slices through simulated flowfields for the $M = 2.95$ air-helium scenario are shown in Figures 2-3. In Figure 2, the density is shown on the left, and the vorticity magnitude ω on the right, where $\omega \equiv \boldsymbol{\omega} \cdot \boldsymbol{\theta}$, $\boldsymbol{\omega} = \nabla \times \mathbf{V}$, and $\boldsymbol{\theta}$ is the azimuthal unit vector. Contours of the bubble fluid volume fraction $f = 0.01$ and $f = 10^{-7}$ are overlaid on the density plots. In Figure 3, f is plotted for later times on the left, on a logarithmic scale, with ω on the right. The slice is oriented at an angle of $\theta = \pi/6$ to the $x = 0$ plane, and shock wave motion is downward. In these plots, the action of the processes described in Section 1 is depicted. The transit of the incident shock wave results in strong axial compression of the bubble volume, seen in Figure 2(a). A complex pattern of discontinuities is set up in the density field near the bubble surface as the shock wave passes over it, including a Mach stem and triple point, visible in Figure 2(b-d). Baroclinicity gives rise to the

development of sheets of vorticity enveloping the bubble. These sheets roll up later in time to produce the distinct vortex rings seen in Figure 2(e-f) and in Figure 3.

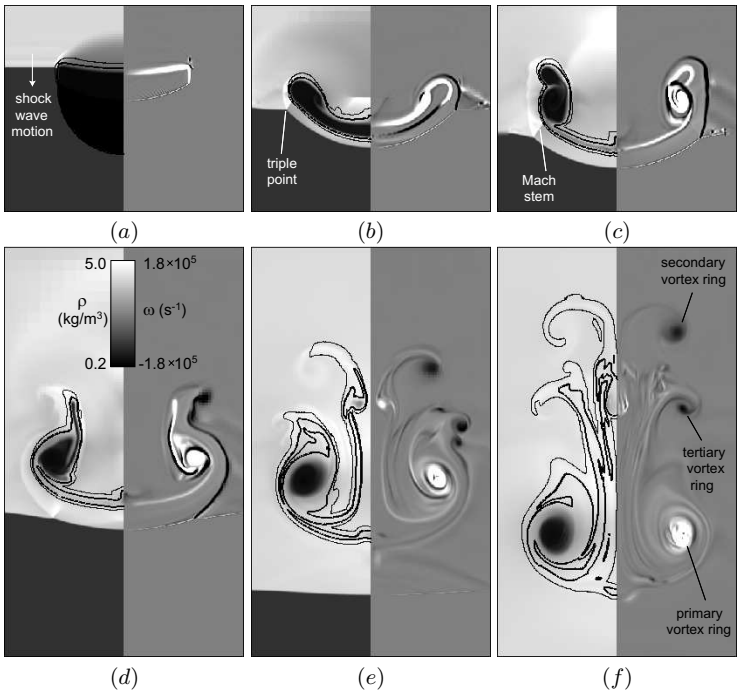

Fig. 2. Computed density (left) and vorticity magnitude (right) field for a M=2.95 air-He shock-bubble interaction. Overlaid are contours of $f = 0.01$ (heavy line) and $f = 10^{-7}$ (light line). Scaled times (tW_i/R): (a) 0.7, (b) 2.2, (c) 4.1, (d) 6.3, (e) 12.5, (f) 18.8.

An important feature of the computed flowfields is the appearance of secondary and tertiary vortex rings in the upstream region. These vortices rotate in the opposite direction as the primary vortex ring, and thus drive the late-time elongation of the shocked bubble. They are initiated by the triple point, which forms as a result of irregular shock refraction in the bubble. The triple point traces a slip surface in the flowfield, which rolls up to form the secondary, counter-rotating vortex ring. The development of secondary and tertiary vortex rings continues to late times, as shown in Figure 3.

4 Streamwise bubble dimension

As can be seen in Figures 2 and 3, the length of the mixing region grows steadily even at late times in these scenarios. This length L is obtained from the computed data here by measuring the distance along the y-axis between the upstream and downstream extremities of the $f = 0.01$ contour. This is normalized by the initial bubble diameter $D = 2R = 3.81$ cm and plotted in Figure 4(a). These data indicate the axial compression

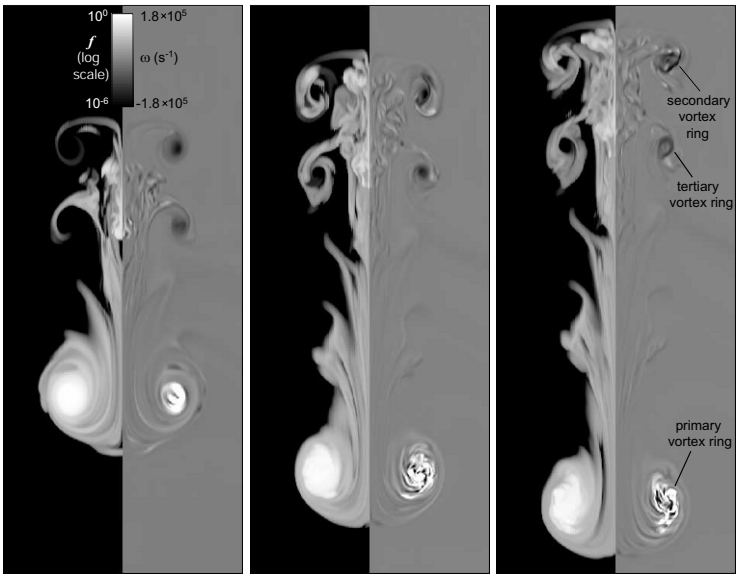

Fig. 3. Computed He volume fraction (left) and vorticity magnitude (right) field at late times for a M=2.95 air-He shock-bubble interaction. Scaled times (tW_i/R): (a) 24.1, (b) 33.5, (c) 37.8.

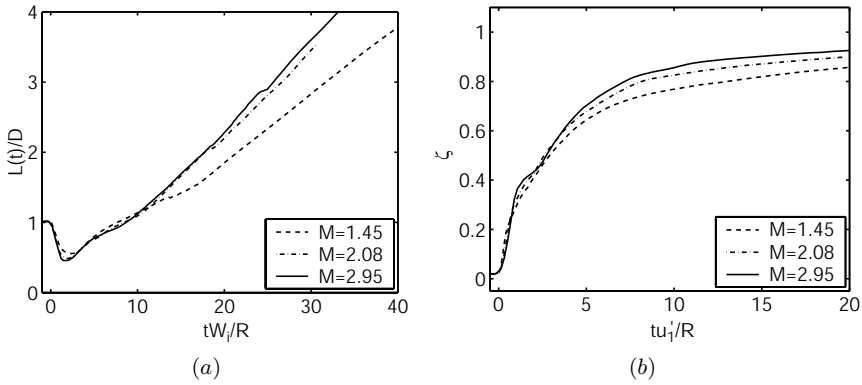

Fig. 4. Plots over dimensionless time of (a) the streamwise dimension of the shocked bubble, and (b) the extent of bubble and ambient fluid intermingling.

of the bubble during initial shock passage ($tW_i/R < 2$), followed by a period of nearly constant streamwise growth, which continues through the duration of the simulations. The data collapse nearly to a single trend on the dimensionless timescale tW_i/R, although the $M = 1.45$ growth becomes relatively slow after $tW_i/R \approx 12$, perhaps due to weaker secondary vortex ring development. The trends all reach a minimum around $tW_i/R = 2$, when the incident shock wave and triple point have overtaken the bubble completely.

5 Fluid intermingling

As a bubble is compressed, deformed, and axially elongated in a shock-accelerated flow, the bubble fluid mixes into the ambient medium. Although the present simulations include no explicit treatment of dissipative effects, and therefore cannot be expected to capture the diffusive aspects of molecular mixing, the convective intermingling of fluids in the simulations is an important and relevant feature. For the current simulations, this intermingling is characterized by measuring the mean ambient-fluid volume fraction in the bubble region. This quantity is obtained here as $\zeta = 1 - \int f dV / \int_B dV$, where B is the region where $f > 0$, and dV is a differential volume element. The parameter ζ is plotted for each of the three scenarios in Figure 4(b) on the dimensionless timescale tu'_1/R. The trends in ζ collapse nearly to a single curve, particularly at early times, on a timescale based on the post-shock ambient fluid speed u'_1, rather than either the incident or transmitted shock wave speeds. This reflects the fact that mixing of the bubble fluid into the ambient medium is driven by velocity shear.

6 Conclusions

The current simulations provide a numerical counterpart to the shock tube experiments of Ranjan *et al.* [8]. A series of integral diagnostics have been applied to the simulation data in order to characterize two particular aspects of shock-bubble interactions, including streamwise bubble deformation and mixing. We have seen that temporal trends in different quantities characterizing these effects follow different timescales. However, in general, characteristic velocities obtained from 1D gasdynamics are effective in collapsing these data. In ongoing and future work, collapsed trends in these quantities from experiments and simulations will be compared directly.

References

1. Klein, R.I., Budil, K.S., Perry, T.S., Bach, D.R. The interaction of supernova remnants with interstellar clouds: experiments on the NOVA laser. Ap. J., 583:245–259, 2003.
2. Collins, T.J.B., Poludnenko, A., Cunningham, A., Frank, A. Shock propagation in deuterium-tritium-saturated foam. Phys. Plasmas, 12:062705, 2005.
3. Haas, J.-F., Sturtevant, B. Interaction of weak shock waves with cylindrical and spherical inhomogeneities. J. Fluid Mech., 181:41–76, 1987.
4. Giordano, J., Burtschell, Y. Richtmyer-Meshkov instability induced by shock-bubble interaction: numerical and analytical studies with experimental validation. Phys. Fluids, 18:036102, 2006.
5. Colella, P. A direct Eulerian MUSCL scheme for gas dynamics. SIAM J. Sci. Stat. Comput., 6(1):104–117, 1985.
6. Miller, G.H., Puckett, E.G. A higher-order Godunov method for multiple condensed phases. J. Comput. Phys, 128:134–164, 1996.
7. Berger, M., Oliger, J. Adaptive mesh refinement for hyperbolic partial differential equations. J. Comput. Phys., 53:484–512, 1984.
8. Ranjan, D., Niederhaus, J., Motl, B., Anderson, M., Oakley, J., Bonazza, R. Experimental investigation of primary and secondary features in high-Mach-number shock-bubble interaction. Phys. Rev. Lett., 98:024502, 2007.

Experimental investigation of shock-induced distortion of a light spherical gas inhomogeneity

D. Ranjan, J.H.J. Niederhaus, J.G. Oakley, M.H. Anderson, and R. Bonazza

Department of Engineering Physics, University of Wisconsin-Madison
1500 Engineering Drive, Madison, WI 53706 (USA)

Summary. Results are presented from experiments studying the interaction of a planar shock wave of strength $1.4 < M < 3.0$ with a spherical soap bubble composed of helium. Flow visualizations are obtained using planar laser diagnostics. The imaging technique used here takes advantage of the atomization of the liquid bubble film by the incident shock wave. The early phase of the interaction is dominated by the phase reversal process and the formation of a primary vortex ring. Further, at late times, the growth of counter-rotating secondary vortical features are observed in the case of a high-Mach number experiment. The temporal development of the shocked bubble dimensions are analyzed on a non-dimensional time scale for incident shocks within a range of Mach numbers.

1 Introduction

The Richtmyer-Meshkov instability (RMI) occurs at an interface between two fluids when the passage of a shock wave results in the baroclinic deposition of vorticity on the interface due to the misalignment of local pressure and density gradient ($\nabla\rho \times \nabla p \neq 0$). The presence of non-linear acoustic effects (shock refraction, diffraction, and reflection) along with interface instability, including non-linear growth and transition to turbulence, makes the RMI one of the most challenging problems in fluid dynamics. The shock-bubble interaction (SBI) is a fundamental configuration for studying shock-accelerated inhomogeneous flows (SAIF), *i.e.*, an extension of the RMI.

The phenomenon of SAIF takes place in a wide variety of energy- and spatially-scaled applications. It can be applied to study the fragmentation of gallstones or kidney stones by shock waves [1] as well as to study the interaction of supernova remnants with interstellar clouds [2]. It also finds application in atmospheric sonic boom propagation, supersonic combustion, and shock mitigation in foams and bubbly liquids. In the case of inertial confinement fusion (ICF), the turbulent mixing consequent to the RMI poses a significant limitation in achieving thermonuclear ignition. The turbulent mixing between the deuterium-tritium (DT) fuel and ablator material results in lowering the fusion yield. The emergence of ICF as a potential power source in the late 1960s has been a significant impetus for investigating shock-accelerated inhomogeneous flows.

Experimental investigations of the interaction of shock waves with curved interfaces has been inspired by the research performed in early 1960s to characterize the interaction of a shock wave with a flame front roughly spherical in shape. Curved flame fronts, when accelerated by a shock wave, undergo heavy distortions such as phase reversal and spike formations. The current experimental study is motivated by the seminal work of Haas and Sturtevant [3] and the recent work of Layes *et al.* [4,5]. These previous experiments were conducted in horizontal shock tubes with the bubble supported by a holder and subjected to a $M < 1.3$ shock wave in air. The shadowgraph images suggested the presence of a

vortex ring; however, due to the integral visualization technique employed, the detailed structure of the vortex was not captured. The recent high-Mach number experiments by Ranjan *et al.* [6] show the presence of secondary vortex rings at late times which are absent in the case of low-Mach number experiments. In this paper we are reporting results from experiments studying the interaction of a planar shock wave of strength $1.4 < M < 3.0$ with a spherical soap bubble composed of helium.

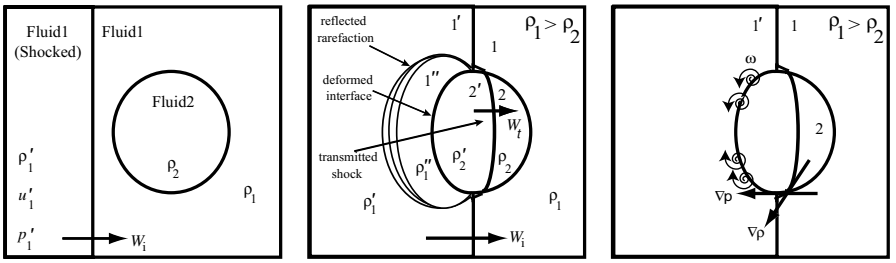

Fig. 1. Schematic diagram of shock reflection, transmission and vorticity distribution in the early phase of a shock-bubble interaction for a light bubble: (*a*) pre-shock; (*b*) post-shock wave pattern; (*c*) vorticity distribution.

Figure 1 shows the wave pattern and vorticity deposition during the early phase of a shock-bubble interaction for a light bubble. At low angles of incidence, regular refraction occurs where the transmitted wave and the incident wave intersect the interface at the same point. At higher angles, various aspects of irregular refractions are observed where usually the interaction of the transmitted wave with the interface runs ahead of the incident wave or of a Mach stem, as shown in Figure 1(*b*). Figure 1(*c*) shows the direction of the vorticity vector($\boldsymbol{\omega}$) which corresponds to the sign of the $\nabla\rho \times \nabla p$ term in the vorticity equation :

$$\frac{\mathrm{D}\boldsymbol{\omega}}{\mathrm{D}t} = (\boldsymbol{\omega} \cdot \nabla)\,\mathbf{u} - \boldsymbol{\omega}\nabla \cdot \mathbf{u} + \frac{\nabla\rho \times \nabla p}{\rho^2}. \tag{1}$$

2 Experiment Description

The shocked-bubble flow field is visualized experimentally using a specially-equipped setup [6] installed in the Wisconsin Shock Tube Laboratory (WiSTL) at the University of Wisconsin-Madison. The centerpiece of the WiSTL facility is a 9.2 m, vertical, closed duct of 0.254 × 0.254 m square internal cross section, designed with an impulsive load capability of 25 MPa to accommodate static and dynamic loads associated with strong shocks. A downward-moving shock wave is released by discharging a boost tank, through a fast-opening valve, into the driver section, pressurized to about 95% of the diaphragm rupture pressure. In these experiments, the retractable injector system has been inverted so that the bubble can rise freely once released from the injector, without hitting the injector itself. The release and free rise of the bubble are recorded at 250 fps with a CCD camera (DALSA CA-D1-0256A) and front lighting. This allows the capture of the evolution of the bubble during its release from the holder and provides an initial condition

image of the bubble prior to (within 10 ms) shock interaction. After release, the bubble oscillates on a time scale of 100 ms, remaining nearly spherical. This setup results in clean experiments and disruption to the planar shock wave is minimized.

The evolution of the flow structures is captured using planar laser imaging. The flow is illuminated with a pulsed Nd:YAG laser (Continuum Surelite II) and a Lambda Physik excimer laser (LPX210). The laser beam is formed into a plane and transmitted through the center of the bottom of the shock tube. The Nd:Yag laser is capable of two pulses separated by a minimum of 100 ns, with a pulse width of 10 ns duration. Three 1024×1024 pixel array Andor (model 434) CCD cameras are used to capture the Mie scattered light resulting from the laser interaction with the soap film solution. As the shock wave passes through the bubble, the film gets atomized. The size of the atomized droplets is dependent on the shock wave strength [7] as shown in Figure 2. At lower Mach number, it may be noted that, because of the lower energy deposited by the shock wave on the bubble film, the atomization is less efficient.

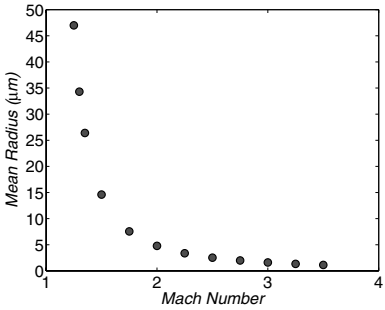

Fig. 2. Average droplet size as a function of shock wave strength.

Scenario #	Bubble gas	Ambient gas	M	A	W_i [m/s]	u_1' [m/s]	W_t [m/s]	u_1'/c_1'
1	Helium	Air	1.45	-0.757	503.8	220.0	1241	**0.56**
2	Helium	Air	2.08	-0.757	722.7	462.7	1548	**1.01**
3	Helium	Nitrogen	2.95	-0.750	1040	767.0	1971	**1.35**

Table 1. Experimental study overview. M is the Mach number of the initial incident shock wave; A is the pre-shock Atwood number at the bubble surface. W_i, u_1', W_t and c_1' represent the incident shock wave speed, flow speed of the shocked ambient gas, transmitted shock wave speed in helium, and sound speed in the shocked ambient gas, respectively.

The shock strengths are chosen to investigate the distortion of the bubble in regimes where the post-shock velocity in the ambient gas is less than, approximately equal to, and greater than, the local sound speed. The experimental scenarios are presented in Table 1. Numerical results [8] corresponding to these three scenarios are also presented in this meeting. Several experiments have been conducted and reproducibility of the initial condition between different experiments is quite good with bubble diameters in the range $D = 3.8 \pm 0.2$ cm.

3 Flow visualizations

Experimental images representing light scattered from atomized film material present in the bubble midplane for the $M = 2.08$ air-helium scenario are shown in Figure 3. The time has been non-dimensionalized as $\tau = 2tW_t/D$. The merits of different non-dimensional time scales will be discussed later in Section 4. The initial stage of shock interaction with the bubble results in the axial compression of the bubble as seen in Figure 3(a) where the transmitted shock wave is still inside the bubble. Two faint outlines are visible at the downstream side of the bubble. One can argue that one of them represents the bubble surface while the second one represents the transmitted shock wave.

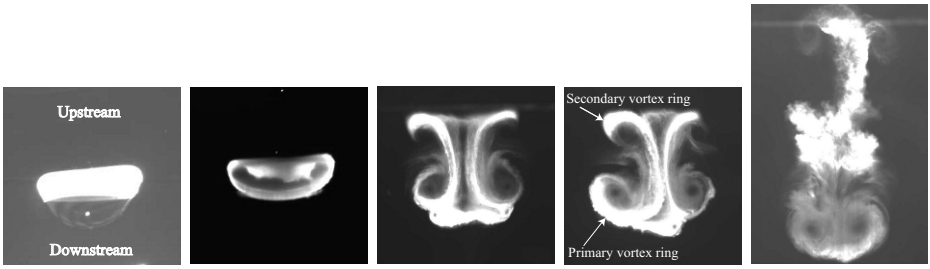

Fig. 3. Experimental images of a shocked ($M = 2.08$) helium bubble in air: (a) $\tau = 2.0$, (b) $\tau = 6.6$, (c) $\tau = 37.9$, (d) $\tau = 41.8$, (e) $\tau = 63.4$.

Figure 3(b) shows the bubble after the incident shock wave has completely traversed the bubble periphery. The maximum compression is seen at this time. During this period of shock interaction, vorticity is deposited on the bubble interface which leads to the formation of the primary vortex ring as seen in the Figure 3(c) at the downstream end of the bubble. An axial velocity in the flow field induced by the primary vortex ring appears to entrain fluid from the center portion of the bubble, swirling into the vortex ring. The other notable feature seen in these experiments is the presence of the counter-rotating secondary vortex ring in the upstream region of the bubble (see Figure 3(c-e)). Recently, the presence of a secondary vortex ring has been reported by Ranjan *et al.* [9] for a $M = 2.95$-accelerated helium bubble in nitrogen. These features are generated by complex shock refraction and reflection phenomena arising at high Mach numbers outlined by Niederhaus *et al.* [8].

4 Results

In order to study the compression and unstable growth of the bubble, the axial ("height,"h) and lateral ("width," w, upstream as well as downstream) dimensions of the shocked bubble are measured over time. The downstream width represents the width of the distorted bubble across the primary vortex ring, whereas, the upstream width represents the width across the helium lobes or the secondary vortex ring. In the analysis, the length scales are non-dimensionalized by the initial diameter ($L_h = h/D$ and

$L_w = w/D$). Figure 4 shows the evolution of the axial extent of the bubble for all the three scenarios. The data have been plotted on three different non-dimensional time scales. The

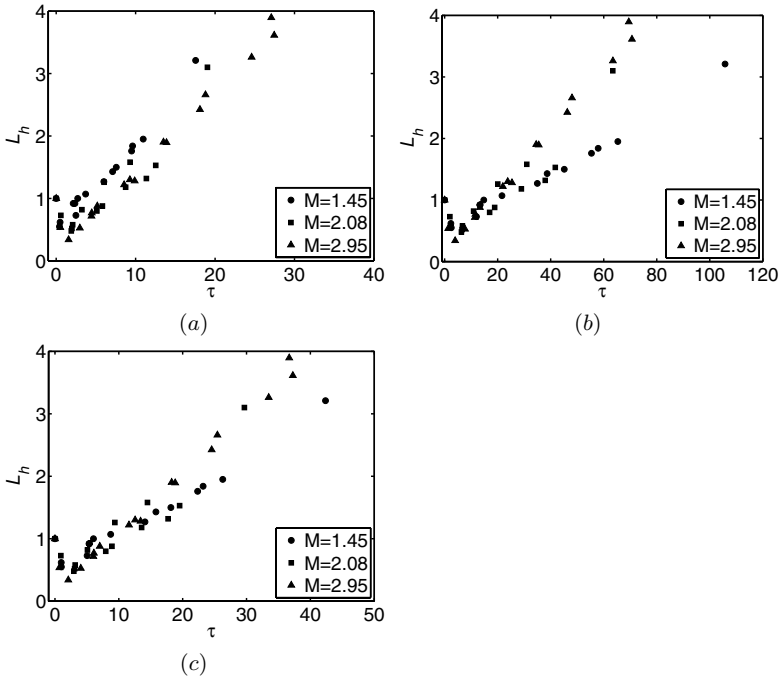

Fig. 4. Axial (height) extents of the bubble normalized by initial bubble diameter D, plotted as a function of the dimensionless time τ: (*a*) $\tau = 2tu_1'/D$,(*b*) $\tau = 2tW_t/D$, (*c*) $\tau = 2tW_i/D$.

earliest post-shock image shows an initial compression of the bubble which can be seen in Figure 4. In all the three cases, the growth of the bubble after compression is approximately linear with time. Figure 4(*c*) shows that the non-dimensionalization based on incident shock wave speed (W_i) does the best job in collapsing the data to a single trend, although, the $M = 1.45$ growth becomes slower at late times. The observed difference is attributed to the formation of the counter-rotating strong secondary vortex ring in the high-Mach number scenario which is absent in the case of low-Mach number experiments. Figure 5 shows the lateral extents of the bubble for $M = 1.45$ and $M = 2.08$ scenarios. At early times, the shock compression leads to the initial flattening of the bubble. In both cases, the width reaches a plateau at late times. Similar trends for width have been reported for the $M = 2.95$ scenario by Ranjan *et al.* [9] and the $M = 1.24$ scenario by Layes *et al.* [5].

5 Conclusions

The present work represents a novel experimental approach which takes advantage of planar imaging, higher shock strengths than previous experiments, and a flow that is un-

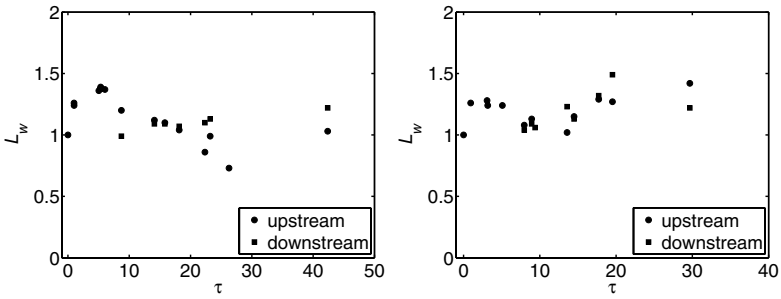

Fig. 5. Lateral (width) extents of the bubble normalized by initial bubble diameter D, plotted as a function of the dimensionless time $\tau = 2tW_i/D$: (*a*) $M = 1.45$, (*b*) $M = 2.08$.

obstructed by bubble holders or injectors. The early time behavior of the shocked bubble can be collapsed to a single trend using dimensionless timescale based on incident shock wave speed. Growth rate for the high-Mach number scenario is significantly different than the low-Mach number cases at late times.

References

1. Gracewski, S.M., Dahake, G., Ding, Z., Burns, S.J., Everbach, E.C., 1993. Internal stress wave measurements in solid subjected to lithotripter pulses, *J. Acoust. Soc. Am.* **94**, pp. 652-661.
2. Klein, R.I., Mckee, C.F., Colella, P., 1994. On the hydrodynamic interaction of shock waves with interstellar clouds. 1: Nonradiative shocks in small clouds, *Ap. J.* **420**, pp. 213-236.
3. Haas, J.-F., Sturtevant, B., 1987. Interaction of weak shock waves with cylindrical and spherical inhomogeneities, *J. Fluid Mech.* **181**, pp. 41-76.
4. Layes, G., Jourdan, G., Houas, L., 2003. Distortion of a spherical gaseous interface accelerated by a plane shock wave, *Phys. Rev. Let.* **91**, 174502.
5. Layes, G., Jourdan, G., Houas, L., 2005. Experimental investigation of the shock wave interaction with a spherical gas inhomogeneity, *Phys. Fluids* **17**, 028103.
6. Ranjan, D., Anderson, M., Oakley, J., Bonazza, R., 2005. Experimental investigation of a strongly shocked gas bubble, *Phys. Rev. Let.* **94**, 184507.
7. Cohen, R. D., 1991. Shattering of a liquid drop due to impact, *Proc. R. Soc. Lond. A* **435**, pp. 483-503.
8. Niederhaus, J. H. J., Ranjan, D., Oakley, J. G, Anderson, M. H., Greenough, J. A., Bonazza, R., 2007. Computations in $3D$ for a shock-induced distortion of a light spherical gas inhomogeneity, ISSW26, paper:2691.
9. Ranjan, D., Niederhaus, J., Motl, B., Anderson, M., Oakley, J., Bonazza, R., 2007. Experimental investigation of primary and secondary features in a high Mach number shock-bubble interaction, *Phys. Rev. Let.* **98**, 024502.

Hot wire, laser Doppler measurements and visualization of shock induced turbulent mixing zones

C. Mariani, G. Jourdan, L. Houas, and L. Schwaederlé

Polytech' Marseille, DME, IUSTI/UMR CNRS 6595, Université de Provence
Technopôle de Château-Gombert, 13013 Marseille (France)

1 Introduction

This paper presents the works carried out at Université de Provence (IUSTI) [1] and [2] and at the Commissariat l'Energie Atomique (CEA/DIF) [3] and [4] on the Richtmyer-Meshkov instability (RMI) of gaseous interfaces in shock tubes and on the turbulent mixing zones arising from it. The RMI occurs when a shock wave impulsively accelerates an interface of gases of different densities which are initially separated by a very thin membrane. On average, the shock and the interface are coplanar but any geometric perturbations on the gaseous interface, either set initially or created at shock passage, will lead to locally non parallel pressure and density gradients. This generates a sheet of vorticity on the interface which deforms it and leads to a turbulent mixing layer. This mixing layer can then be excited by subsequent waves, first and most strongly by the transmitted shock after its reflection on the shock tube end wall. This planar shock-interface interaction followed by re-shock excitation is analogous to the dynamics of the interface between thermonuclear fuel and shell material occurring in inertial confinement fusion targets with a spherical centripetal incident shock/compression and centrifugal reflected shock. Since mixing may impede the fusion process, it is important to predict it with modeling. Recently, at CEA/DIF, shock tube mixing experiments have been used in order to help the research on turbulent mixing modeling [5] and direct numerical simulation [6]. In the two last decades, we have jointly investigated this turbulent mixing zone in shock tube by various techniques, schlieren and shadowgraph visualizations, x-ray average density measurements, differential interferometry, laser-doppler velocimetry (LDV) at CEA, schlieren and shadowgraph visualisations, average density measurements by infrared laser emission and absorption and hot wires (CTHWA) at IUSTI.

2 Experiments

In the present experiments, the air/SF_6 interface is initially materialized by a thin nitrocellulose microfilm maintained next to a metallic wire mesh with a wire spacing of 1.8 mm. Thus the forcing wavelength of the RMI is 1.8 mm in both transverse directions with an unknown initial amplitude estimated at 1-3 mm. The length of the SF_6 chamber is 250 mm for the two common shock tube experiments (CTHWA, LDV and schlieren) but lengths of 200 and 300 mm are also used at CEA/DIF for LDV and schlieren visualization respectively. For this fast to slow case, the Mach 1.2 incident shock wave in air is transmitted as a Mach 1.3 shock in SF_6 thus accelerating the flow to about 70 m/s. After its reflection on the end plate, the interaction of the returning shock of Mach 1.3 reverses the flow to about -25 m/s. The subsequent interaction with the second reflected wave, a rarefaction, brings the gases to a velocity of 10 m/s.

2.1 Experimental set-up at IUSTI

At IUSTI, the horizontal 85 mm by 85 mm shock tube is equipped with three hot wire probes supported close to the test section center by prongs inserted from the end plate as shown in Fig. 1. Each wire can be set at a different abscissa, thus each shock tube run provides three heat transfer measurements. The CTHWA output voltage is a function of local gas characteristics: velocity, density, temperature, viscosity and heat conductivity [1] and [2]. Using Wilke and Vassilievski laws for the transport coefficients in the mix and the simplifying hypothesis of a linear temperature variation in the mix, this voltage depends on velocity and concentration only. For sampled instants we calculate all possible values of hot wire signal for a logical range of velocity and concentration in the mix, then match it to the experimental signal in order to obtain a probable pair of velocity and concentration. We found that the evolution of the concentration profile is much less sensitive to the range of velocity then the velocity profile. The CTHWA is a good mixing zone detector. However, the intrusive nature of the probe makes it less useful for the re shocked mixing zone because the reflected shock waves propagates along the prongs and the wire is located in their wakes. At 80 kHz, the frequency response of the hot wire is also too limited.

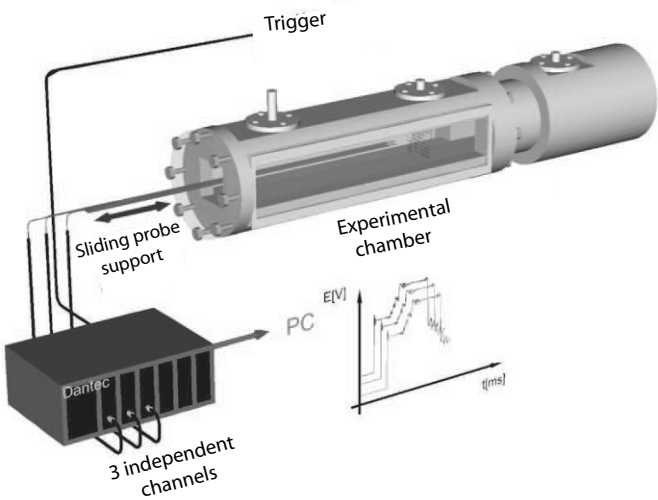

Fig. 1. Observation section and hot wire anemometer setup on IUSTI shock tube.

3 Experimental set-up at CEA/DIF

As seen on Fig. 2, at CEA/DIF we use a two component LDV in a vertical 130×130 mm^2 shock tube to obtain axial and transversal velocity components at various abscissa along the shock tube axis. Prior to the run, air and SF_6 are seeded with incense smoke and olive oil droplets (μm size) respectively. The LDV provides a velocity data point whenever

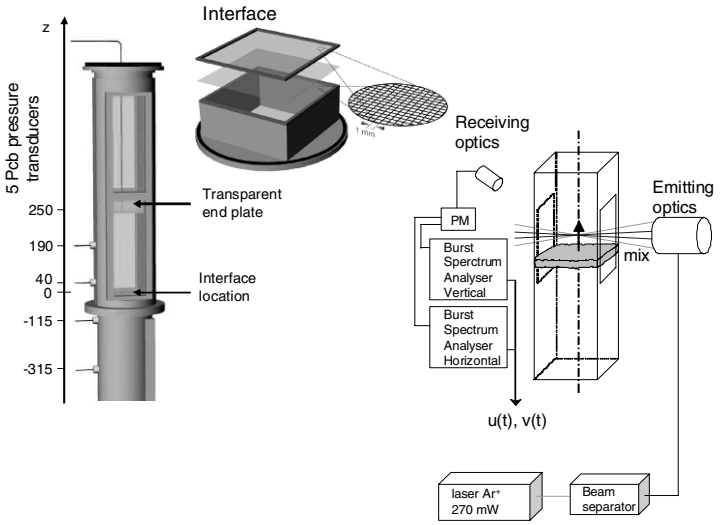

Fig. 2. Observation section and laser doppler anemometer setup on CEA shock tube.

a particle crosses the measuring volume (intersection of two pairs of laser beams) and the Doppler shifted light diffused from it reaches the receiving optics. We found that the membrane fragments dramatically reduce the data rate in the mixing zone. Many identical runs are thus needed at each location to obtain velocity profiles in the mix [3] and [4].

3.1 Comparisons of preliminary CTHWA and LDV data

Figure 3 presents a superposition of CTHWA and LDV raw signals obtained, respectively, on IUSTI and CEA/DIF shock tubes, for similar conditions, i.e., an air/SF_6 interface, materialized by a 0.5 μm nitrocellulose microfilm, accelerated by a 1.2 shock wave Mach number. Note that the SF_6 chamber is 250 mm in the case of the common experiments while the shock tube cross sections is 85×85 mm^2 at IUSTI and 130×130 mm^2 at CEA/DIF. In the experiments by [3] at CEA/VM, a vertical shock tube (cross section 80×80 mm^2) was used with an incident shock wave Mach number of 1.45 in SF_6 and a air chamber 300 mm long. The comparison of the two diagnostics has been obtained for three different locations (44 mm, 88 mm and 147 mm) from the initial position of the interface, the last one corresponding, approximately, to the abscissa of re shock-interface interaction. The gas flows at the two first measurement locations at 70 m/s between passage of the incident and re shock and slows down to -20 m/s after re shock. Before reflected shock (at 44 mm, 88 mm), the CTHWA detects the mixing zone as a clear drop of signal, while the LDV indicates its passage by a relative rarity of velocity points. Although the passage times of the different singularities of the flow are in approximate agreement, the mixing zone passage occurs later at IUSTI than CEA/DIF, owing to small differences in gas composition (higher leakage at IUSTI across the membrane prior to the run) and sometimes weaker shock waves at IUSTI. Before the re shock, the CTHWA allows a clear detection of the mix boundaries, while the LDV suffers from a dramatic reduction of

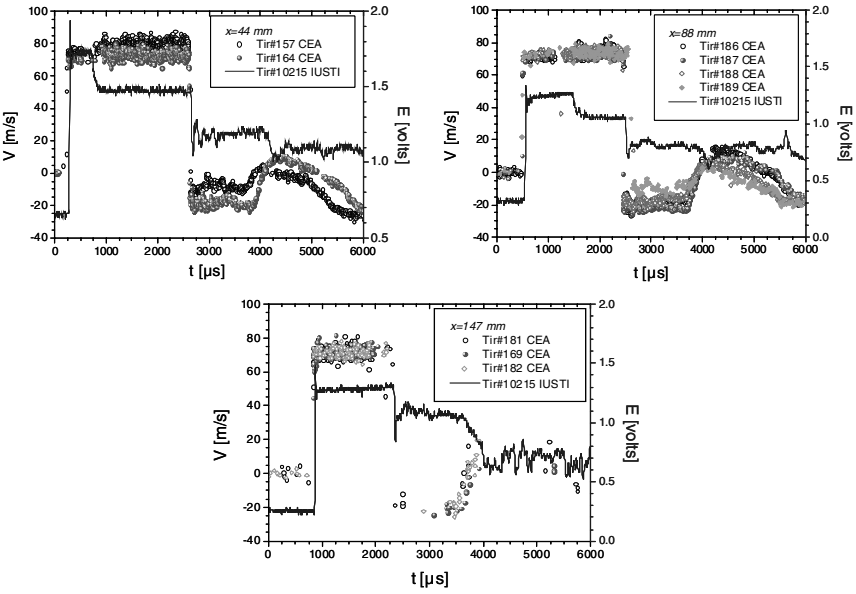

Fig. 3. Comparison of CTHWA and LDV raw signals obtained for similar conditions (air/SF_6, M_{is}=1.2).

the acquisition rate, presumably because of the interception of the laser beams by the membrane fragments. In order to still confront two experiments undertaken on different apparatus we have compared the experimental x-t diagrams and mixing zone thickness obtained from schlieren visualization at CEA and from CTHWA signals at IUSTI in Figure 4. These two graphs confirms the good agreement of experiments of CEA and IUSTI and allows us to think that the two techniques, although presenting each one advantages

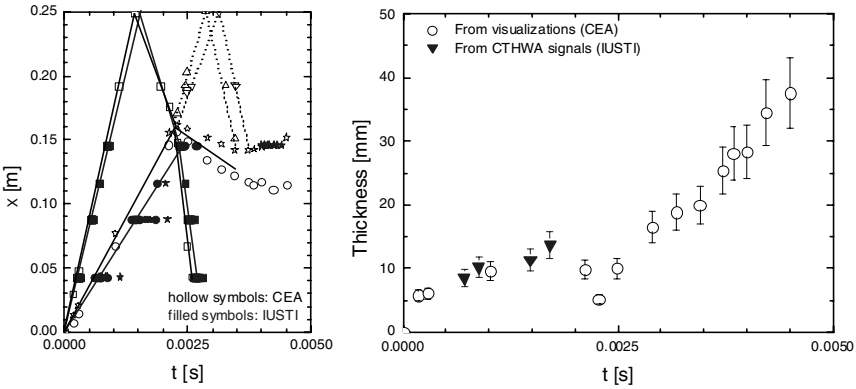

Fig. 4. Comparison of x-t diagrams and mixing zone thickness obtained from schlieren visualizations (CEA) and CTHWA signals (IUSTI) for similar conditions (air/SF_6, M_{is}=1.2).

and disadvantages, are complementary. We could conceptually combine the two diagnostics by using the range of velocities measured with the LDV in one experiment for determining with the inverse method for CTHWA, the evolution of the concentration in the other.

3.2 Insight into the more recent LDV results

For the subsequent LDV campaign at CEA/DIF, a wire mesh of spacing of 1 mm is added below the microfilm in order to maintain it in a planar horizontal position below the upper grid of spacing 1.8 mm. Many (up to 38) identical runs are needed at each location to measure the velocity mean, variance (turbulent kinetic energy per unit mass) and rms (root mean square of the velocity data) in the mix. Before re shock, the small scatter of the velocity points is on the order of the noise in the pure gases. After re shock, their much larger scatter confirms that the mix is turbulent. Schlieren visualization performed for two lengths of SF_6, 250 and 300 mm, indicated that the post re shock growth rate is higher for the longer SF_6 section. This is confirmed by 3D simulation [6] whereas the visualization results of [7] for shorter SF_6 lengths indicated nearly identical growth rates. We compared the LDV results obtained for two lengths of SF_6, 200 and 250 mm and for slightly different incident shock wave Mach numbers in air, 1.18 and 1.21. The LDV measurement positions at 105 and 135 mm for SF_6 lengths 200 and 250 mm respectively, allowed probing the thin and fast mixing zone briefly before re shock and the thick and stagnant mixing zone for a long time after re shock. The post re shock rms or variance is significantly higher for 250 mm than for 200 mm, and slightly so for Mach 1.21 than Mach 1.18, i.e. for a longer delay between incident and reflected shock and for the slightly higher incident shock Mach number. This confirms the trend observed with schlieren viualization between 300 and 250 mm. More details on LDV results (amplification by the re shock and anisotropy of the turbulent velocity field) will appear later in [4] but the comparison between schlieren visualisation from the actual experiment and from the 3D numerical simulation has recently been published in [6].

4 Summary

This work presents two methods for point measurements in mixing zones induced by Richtmyer-Meshkov instability in shock tubes. The constant temperature hot-wire anemometer exploited at IUSTI is an intrusive technique, but allows a clear detection of the mixing zone boundaries before re shock. Concentration profiles can be obtained by the inverse method in which concentration is allowed to vary between 0 and 1 and the velocity between set values. The CTHWA method appears reasonably accurate before re shock for volume fraction estimates. The LDV technique provides only few data points and is less useful before re shock. The use of LDV pioneered at CEA/VM [3] for TMZ measurements can give precise information on velocity providing turbulent kinetic evaluation but remains a very tedious work : several tens identical shock tube shots at each locations are needed for statistical convergence. However, contrary to the CTHWA, LDV is more useful for the measurement of velocity after reshock. Here, preliminary LDV results are compared to hot wire results and show a good agreement with the two techniques. So, we consider to really combine the diagnostics on the same shock tube experiment by positioning next to each other the hot wire probe (2.5 mm long and 5 μm

in diameter) and the LDV measuring volume (0.2 mm wide and 1-5 mm long). Thus each velocity data point from the LDV will remove this unknown from the CTHWA equation to yield the concentration. This may be difficult as the hot wire might be coated by the seeding droplets and often destroyed by the membrane fragments, but is worthwhile experimenting with in future campaigns. In any case, it appears that the velocity data from the LDV, however tediously gathered over dozens of runs are more readily adaptable to a direct comparison with modeling and simulation results. On the contrary, the output of the CTHWA, a convolution of at least velocity, molar fraction and temperature in the mix, are better suited to a convolution of simulation results: i.e. the use of these three calculated values from the simulation in the heat transfer equation of the CTHWA. This also means that the calibration parameters of the device are determined from the known zones of this unsteady flow: for instance the hot wire signal from the pre- and post-shocked pure gases, air and SF_6. The IUSTI team was partially supported by several grants from CEA/DIF. L. Schwaederlé also worked on visualization and preliminary LDV results as postdoc at CEA/DIF. The staff members of CEA/DIF, D. Counilh, J.-F. Haas, P. Montlaurent and A. Perez are very thankful to him and to the undergraduate students A. Lassis, G. Seguin, R. Molle and N. Perrin.

References

1. Jourdan G., Schwaederlé L., Houas L., Haas J.F., Aleshin A.N., Sergeev S.V. and Zaytsev S.G., 2001. Hot wire method for measurements of turbulent mixing induced by Richtmyer-Meshkov instability in shock tube. *Shock waves* **11**, 189-197.
2. C. Mariani, L. Schwaederlé, G. Jourdan and L. Houas, 2007. Comparison ot hot wire and laser Doppler measurements in shock-induced mixing zones *10th IWPCTM - Paris (France) July 2006, M. Legrand and M. Vandenboomgaerde editors - CEA/DIF* 226-229.
3. Poggi F., Thorembey M.H. and Rodriguez G., 1998. Velocity measurements in turbulent gaseous mixtures induced by Richtmyer-Meshkov instability. *Phys. Fluids* **10** (11), 2698-2700.
4. Haas J.F., Counilh D., Schwaederlé L., Mariani C., Jourdan G., and Houas L., ,Visualization and point measurements of velocity and density in air/SF_6 turbulent mixing zones induced by the Richtmyer-Meshkov instablity, 2007. *Turbulent Mixing and Beyond Workshop 2007 - Trieste (Italy), 18-26 August 2007, Snezhana Abarzhi editor.*
5. Grégoire 0, Souffland D, Gauthier S (2005) A second-order turbulence model for gaseous mixtures induced by the Richtmyer-Meshkov instabilities, 2005. J. of Turbulence 6 (29), 2005
6. Boulet M, Griffond J (2007) Three-dimensional numerical simulation of experiments on Richtmyer-Meshkov induced mixing with reshock, 2007. Proceedings of the 10th IWPCTM - Paris, France, July 2006, Legrand and Vandenboomgaerde editors, CEA/DIF, 33-36.
7. E Leinov, A Formoza, O Sadot, A Yosef-Hai, G Malamud, Y Elbaz, A Levin, D Shvarts and G Ben-Dor, 2007. Experimental investigation oh hydrodynamic instability induced by multiple accelerations of a contact surface between two fluids. Proceedings of the 10th IWPCTM - Paris, France, July 2006, Legrand and Vandenboomgaerde editors, CEA/DIF, 188-193.

Investigation on the acceleration of sinusoidal gaseous interfaces by a plane shock wave

C. Mariani[1], G. Jourdan[1], L. Houas[1], M. Vandenboomgaerde[2], and D. Souffland[2]

[1] *Polytech' Marseille, DME, IUSTI/UMR CNRS 6595, Université de Provence Technopôle de Château-Gombert, 13013 Marseille (France)*
[2] *CEA-DAM/DIF/DCSA/SSEL, BP12, 91680 Bruyères-le-Châtel (France)*

1 Introduction

The impulsive acceleration of a perturbated interface, separating two gases of different densities, leads first to the growth of the initial perturbations then to the mixing of the two fluids and finally, for long times, to the development of turbulent structures. The mixing process is known as the Richtmyer-Meshkov instability ([1], [2]) and is of great interest in several fields of research (astrophysics, aeronautics,...) and especially in Inertial Confinement Fusion to better understand the loss of energy which prevents the spontaneous chain reactions. When a plane shock wave passes through a sinusoidal gaseous interface, a deposition of vorticity occurs on the perturbations where gradients of density and pressure are not colinear. Then, these initial interfacial perturbations evolve through linear and non linear stages to form a mixing zone (MZ).

The following experimental work concerns the growth of macroscopic sinusoidal perturbations of a gaseous interface after an impulsive acceleration caused by a shock wave. This study was performed in our T200 horizontal 20 cm×20 cm square cross section shock tube. The high pressure, low pressure and experimental chambers are respectively 1.65 m, 5 m and 0.48 m long. T200 shock tube allows to generate shock waves which Mach number ranges from 1.1 to 3. The diagnostic device is the laser sheet visualization which gives a 50 frames film of a longitudinal section of the flow (frames are spaced by 500 μs to 20 μs). It is composed with a pulsed copper vapor laser (pulse frequency ranges from 2 to 50 kHz), an optical system to transform the laser beam in a laser sheet and a high speed rotating drum camera (which turns up to 300 m/s). Dynamic PCB pressure gauges give temporal evolution of the pressure and set off the measurements.

2 Experimental results

The aim of the present work is to follow the whole linear and the earliest non linear stages of growth of macroscopic interfacial sinusoidal perturbations of small amplitudes. The initial interface is materialized by a double layer nitrocellulosic film (1 μm thick) put on a grid designed with computer and made by stereolithography. This technique allows to obtain grids whose meshes form a perfect sinusoid of chosen and reproducible dimensions. We use two different sinusoids to observe the evolution of the perturbations. The first one (grid 1) is characterized by an initial amplitude of 3 mm and a wave length of 80 mm. The second (grid 2) is characterized by an initial amplitude of 6 mm and a wave length of 120 mm, as shown in figure 1.

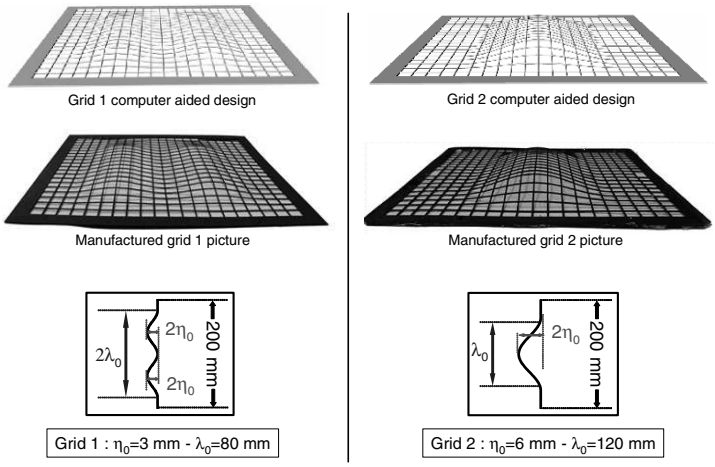

Fig. 1. Scheme, pictures and dimensions of the two used sinusoidal grids

Furthermore, two gas couples are used: an air/SF_6 interface to consider the case where the incident shock wave passes from a light gas to a heavier one and an air/helium interface to consider the opposite case. Each initial interface (*i.e.* each gas couple associated with each grid) is accelerated by incident shock waves of two different intensities (about 1.15 and 1.4) in order to better understand the influence of the Mach number on the growth of the sinusoids. The experimental conditions are given in table 1. As regards the

#Run	Gas 1	Gas 2	#grid	W_{iSW} (m/s)	M_{iSW}	kη_0	A*	η_0^* (mm)	ΔU$_{exp}$(m/s)
T200#113	incensed air	SF_6	1	405	1.18	0.23	0.696	2.5	62
T200#114	incensed air	SF_6	1	400	1.17	0.23	0.693	2.5	68
T200#116	incensed air	SF_6	2	394	1.15	0.34	0.695	5.6	60
T200#117	incensed air	SF_6	2	405	1.18	0.34	0.695	5.5	56
T200#118	incensed air	air	2	392	1.14	0.23	$\simeq 0$	2.2	105
T200#120	incensed air	SF_6	1	476	1.39	0.22	0.720	2.1	126
T200#121	incensed air	He	1	403	1.17	0.20	-0.785	1.7	132
T200#123	incensed air	He	1	466	1.36	0.22	-0.800	1.0	240
T200#124	incensed air	He	2	393	1.14	0.34	-0.761	5.0	105
T200#125	incensed air	He	2	481	1.40	0.34	-0.808	3.2	248
T200#126	incensed air	SF_6	2	490	1.43	0.35	0.723	5.0	135

Table 1. Summary of the experimental conditions. W_{iSW} is the incident shock wave velocity, M_{iSW} is the incident shock wave Mach number, k is the wave number, η_0 is the pre-shock amplitude, A* is the post-shock Atwood number, η_0^* is the post-shocked amplitude and ΔU is the post-shock velocity jump

other experimental parameters, we use a laser frequency of 10 kHz and a camera speed of 180 m/s and we seed the air in the low pressure chamber with incense smoke during 15 minutes before running the experiment.

Figures 2 and 3 present exemples of laser sheet frames obtained respectively from air/SF_6 and air/He single runs. The flow typologies are different for the two cases: in the

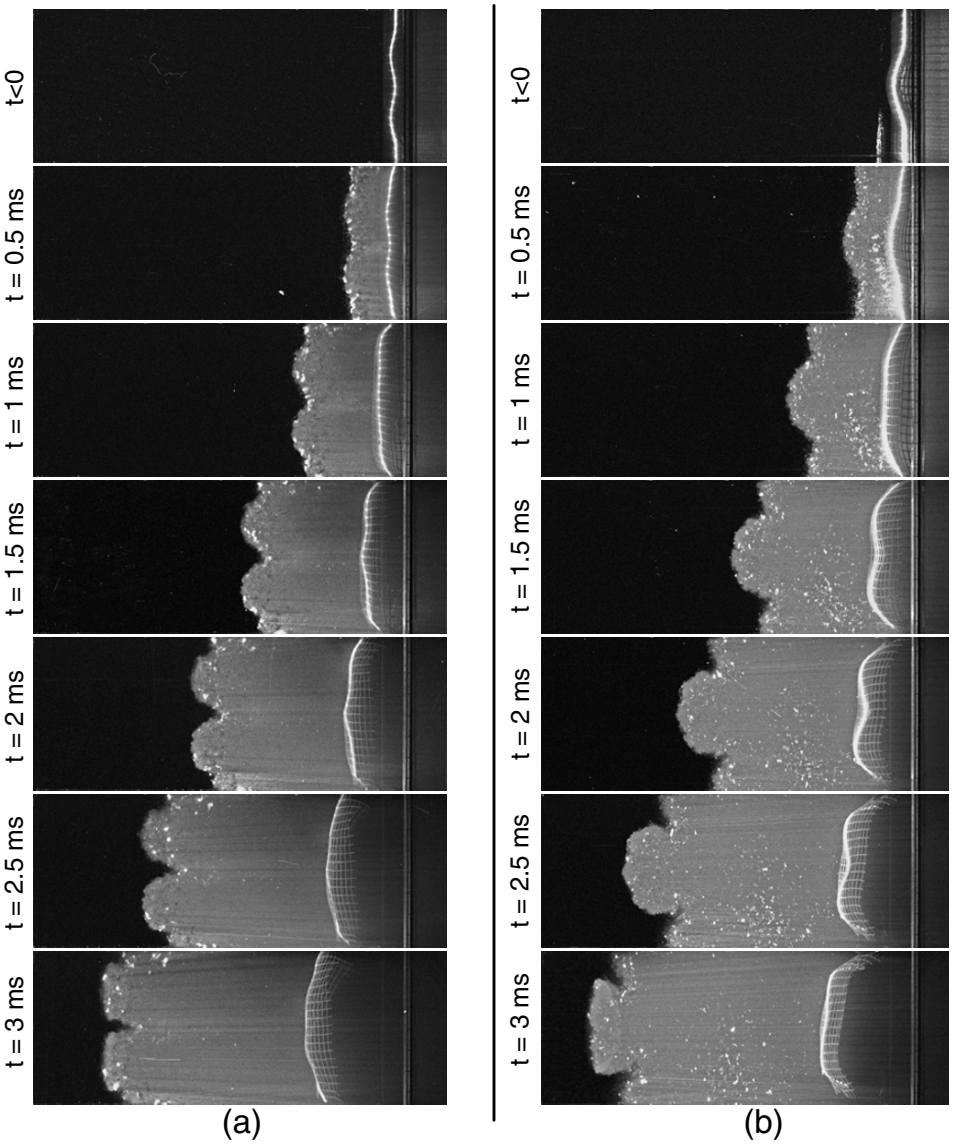

Fig. 2. Laser sheet frames of two air/SF_6 experiments: (a) T200#120 - grid 1 - M_{iSW}=1.39 – (b) T200#126 - grid 2 - M_{iSW}=1.43

air/SF_6 light/heavy gas configuration, the incident shock wave compresses the initial perturbations and accelerates them. They begin to grow directly in their initial orientation until the come-back of the reflected shock wave that stops and reverses the growth. In the air/He heavy/light gas configuration, initial perturbations reverse with the passage of the shock and the reversal sinusoids grow in their new orientation. The reflected shock wave more accelerates the phenomena. On these pictures appear the residual pieces of

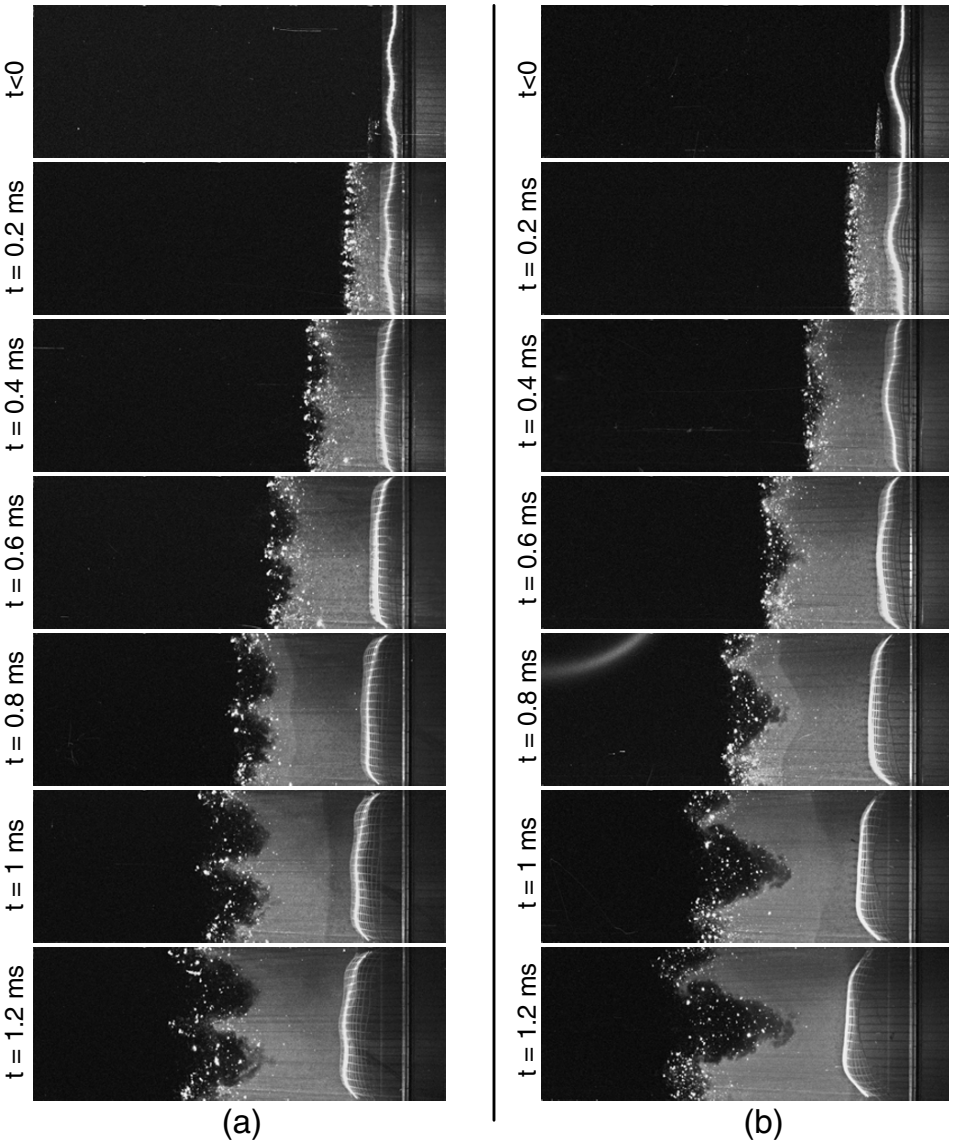

Fig. 3. Laser sheet frames of two air/He experiments: (a) T200#123 - grid 1 - M_{iSW}=1.35 – (b) T200#125 - grid 2 - M_{iSW}=1.40

nitrocellulose membrane which more diffract the laser light. Their influence on the mix process will be considerate further. The frames show also the destruction of the grid but its influence on the mixing zone is negligible because it happens more tardily.

The peak to peak measurement of the amplitude of the perturbations allow to quantify the growth. Its evolution according to time was the subject of many experimental([3], [4], [5]) and theoretical studies ([6], [7]). This evolution is represented in figures

4 and 5 in a dimensionless axis system for both the light/heavy and the heavy/light configurations. We also plotted the linear theory of Richtmyer and two non linear theories (only available for light/heavy experiments); the one of Sadot et al. [6] and the other of Zhang and Sohn [7]).

Richtmyer [1] integrated the governing equations of the flow at first order and gave by this way a linear approach of the growth of the perturbations which applies only after the compression phase (incompressible fluid) and for small amplitudes compared with wave length. The amplitude according to time is given by: $\eta(t) = \eta_0^* + k\Delta U A^* \eta_0^* t$, where η_0 is the amplitude after the compression, $k = \frac{2\pi}{\lambda}$ is the wave number,ΔU is the velocity jump after the first impulsive acceleration and A^* is the post shock Atwood number.

Sadot *et al.* work on flow equations expanded to second order. Their model takes into account the asymptotic behavior reached by the the growth velocity at advanced times of mix and highlights a dissymmetric aspect of the evolution; the sinusoids that grow from the light gas to the heavier one (bubbles) are slower than the ones that grow from the heavy gas to the lighter one (spikes).

The model of Zhang and Sohn is a Padé approximation to third order solution of the flow equations. It allows to describe very non linear evolutions of the perturbations.

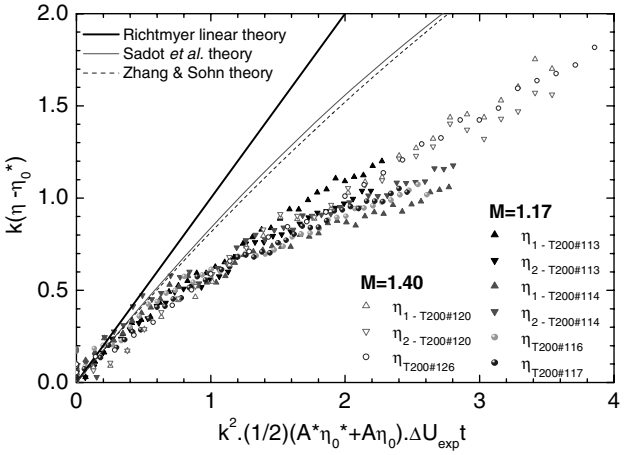

Fig. 4. Dimensionless peak to peak measurements of the amplitude of the sinusoidal perturbations of light/heavy (air/SF_6) interfaces

3 Discussion

The present experimental conditions ($k\eta_0 \ll 1$) were chosen to follow the linear and the earliest non linear stages of growth of the initial perturbations. Our results agree very well with Richtmyer linear theory in the heavy/light (air/He) case, as can be clearly seen in figure 5. However, in the ligth /heavy (air/SF_6) experiments, the growth rates of perturbations follow a unique trend, whatever the Mach number and the initial perturbations are, which is much below the ones predicted by the theoretical models, even non linear. At the present time, the difference between experiments and models is attributed to the membrane particles which are more present near the interface in this gaseous

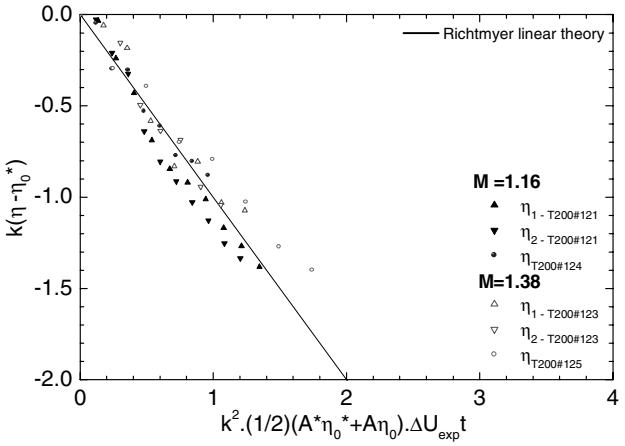

Fig. 5. Dimensionless peak to peak measurements of the amplitude of the sinusoidal perturbations of heavy/light (air/He) interfaces

configuration. Effectively, when we observe in details the air/SF_6 laser sheet sequences, we can note that the presence of the membrane seems to prevent the interpenetration of the two gases and makes difficult the measurement of the peak to peak amplitude and particularly in the region of the spikes.

References

1. Richtmyer, R.D., 1960, Taylor instability in shock acceleration of compressible fluids. *Commun. Pure Appl. Math.*, **13**, pp. 297-319
2. Meshkov, E.E., 1969, Instability of the interface of two gases accelerated by a shock wave. *Sov. Fluid Dyn.*, **4**, 101
3. Jourdan, G. and Houas, L., 2005, High-amplitude single-mode perturbation evolution at the Richtmyer-Meshkov instability. *Phys. Rev. Lett.*, **95**, 20 , pp. 204502.1-204502.4
4. Collins, B.D. and Jacobs, 2002, J. W, PLIF flow visualization and measurements of the Richtmyer-Meshkov instability of an air/SF_6 interface. *J. Fluid. Mech.*, **464**, pp. 113-136
5. Puranik, P. B., Oakley, J. G. Anderson, M. H. and Bonazza, R.,2004, Experimental study of the Richtmyer-Meshkov instability induced by a Mach 3 shock wave. *Shock Waves*, **13**, 6, pp. 413-429
6. Sadot, O., Erez, L., Alon, U., Oron, D., Levin, L.A., Erez, G., Ben-Dor, G., and Shvarts, D., 1998, Study of nonlinear evolution of single-mode and two bubble interaction under Richtmyer-Meshkov instability. *Phys. Rev. Lett.*, **80**, 8, pp. 1654-1657
7. Zhang, Q. and Sohn, S., 1997, Nonlinear theory of unstable fluid mixing driven by shock wave. *Phys. Fluids*, **9**, 4, pp. 1106-1124

Particle image velocimetry study of shock-induced single mode Richtmyer-Meshkov instability

R. Aure and J.W. Jacobs

Department of Aerospace & Mechanical Engineering, University of Arizona, 1130 N. Mountain Ave., Tucson, AZ 85721, USA

1 Introduction

The Richtmyer-Meshkov (RM) instability occurs when a perturbed interface between two gases of different densities is given an *impulsive* acceleration due to the passage of a shock wave. The impulsive acceleration causes the initial perturbation to grow into complex mushroom-like structures. The instability is closely related to the Rayleigh-Taylor instability which exhibits similar behavior, but under the influence of *constant* acceleration. The RM instability derives its name from the analytical and numerical work of Richtmyer [1], which was later confirmed in shock tube experiments by Meshkov [2]. The instability is of great fundamental interest in fluid mechanics and physics. The instability has been attributed as a source of significant mixing in supernovas [6] and supersonic combustion [8], as well as one of the major obstacles in attaining positive-net-yield inertial confinement fusion [7].

The mechanism primarily responsible for the instability is the deposition of baroclinic vorticity according to the two-dimensional, compressible vorticity equation,

$$\rho \frac{D}{Dt}\left(\frac{\omega}{\rho}\right) = \frac{1}{\rho^2}\nabla\rho \times \nabla \tag{1}$$

The vorticity is produced by the misalignment of pressure and density gradients which occurs when the shock (∇p) passes through the interface between the two different density gases ($\nabla\rho$). But, additional vorticity can be generated in later stages. Shortly after the shock passage the perturbation begins to increase in amplitude. The heavy gas penetrates upward into the light gas forming what is termed the spike, while the light gas penetrates down into the heavy gas forming the bubble. The vorticity on the interface is convected toward the spike while the interface rolls up forming vortices. As the roll-up progresses additional baroclinic vorticity is deposited on the interface near to the vortex cores. At this point, the dominant pressure gradient is the one resulting from the centripetal acceleration of the vortex. The deposited vorticity due to this pressure gradient is often referred to as secondary vorticity.

Jacobs & Sheeley [3] showed that if one assumes the flow field to be that given by linear stability theory, the circulation, calculated by integrating the vorticity over one-half wavelength of the interface, is given by,

$$\Gamma = 4\frac{\dot{a}_0}{k} \tag{2}$$

where k is the wave number and $\dot{a}_0$ is the initial growth rate. If it is assumed that viscous dissipation and the baroclinic generation of secondary vorticity is negligible, one would expect the circulation to be constant during the evolution of the instability following

the shock interaction. Peng *et al.* [9] have shown numerically that for cases with a large density difference, the circulation is not constant, but increases in time. However, no experimental measurements of vorticity and circulation for the RM instability currently exist to verify this claim.

2 Experimental Set-up

Early shock tube experiments [2] [10] used a shaped membrane often supported by a mesh of wires to define the initial perturbation. This technique has its advantage in establishing a sharp, well defined and repeatable initial perturbation. The disadvantage with this technique is that pieces of the membrane, which is shattered by the impinging shock wave, are entrained in the flow. The pieces disturb the flow and the growth of the instability and, in addition, impede the use of advanced visualization techniques such as Planar Laser Induced Fluorescence (PLIF), Planar Rayleigh Scattering and Particle Image Velocimetry (PIV).

Jones & Jacobs [4] developed a membraneless technique to generate the initial perturbation in RM shock tube experiments and used Mie scattering for visualizing the flow. PLIF was later successfully implemented in this apparatus [5]. The diagnostics implemented in these earlier studies yield limited quantitative information. In order to obtain additional quantitative information, these earlier studies have been extended by implementing PIV. Note that this is not the first application of PIV in this type of experiment. Prestridge *et al.* used PIV in their study of shock accelerated gas curtains [11], but because only one of the two gases is seeded the obtainable data is limited.

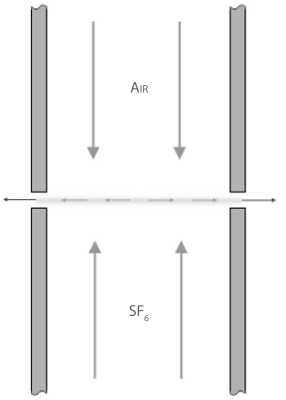

Fig. 1. Generation of interface

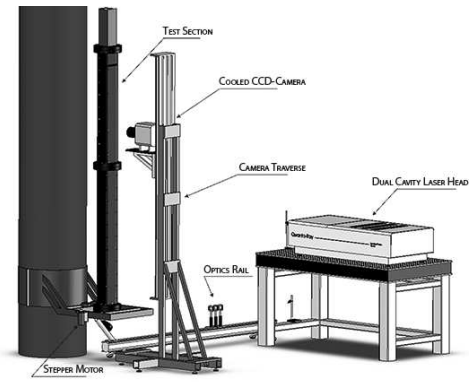

Fig. 2. Test section and instrumentation

The experimental set up used in the present experiments is an improved version of the set up used by Jones & Jacobs [4], the main difference being a longer shock tube and improved diagnostic. The set up consists of a 10 m long vertical shock tube. The shock tube has a 3.7 m long driver, and a 6.3 m long driven section with a 88.9 mm square

cross-section. The 2 m long test section has a transparent acrylic front face. A diffuse interface is generated by two opposing gas flows meeting and exiting through two narrow slots at the top of the test section as shown in figure 1. The light gas (air) enters through a plenum at the top of the driven section. The heavy gas (SF_6) enters trough a similar plenum at the bottom of the test section. Both gases are seeded with 0.30μm polystyrene Latex spheres by atomizing a water suspension. The Atwood number in the experiment is 0.66. The interface between the two gases is given an initial sinusoidal perturbation by gently oscillating the driven section. A weak shock wave ($M_s = 1.21$) is generated by puncturing the polypropylene diaphragm separating the driver and driven section. One double exposed image per experiment is obtained by illuminating the seeded flow using a dual cavity pulsed Nd:YAG laser. The laser beams are focused and expanded to a 1 mm thick light sheet using a system of spherical and cylindrical lenses, and enters the shock tube through a window in the bottom of the test section. The image is captured using a cooled CCD camera which is mounted on a vertical rail system aligned with the test section. The test section and instrumentation is illustrated in figure 2. Analysis of the PIV images is accomplished using DaVis FlowMaster software by LaVision.

3 Experimental Results

Due to the nature of the experiment and the diagnostics used only *one* image per experiment can be obtained. In order to study the development of the instability a large number of single experiments must be performed. Due to slight variations in the initial shock strength and perturbation amplitude, at least three experiments were performed at each time increment. The initial pre-shock amplitude in these experiments was 3 mm. Figure 3 shows a selection of images forming a time sequence obtained from these experiments. The sequence consists of vorticity fields obtained from PIV compared to PLIF images. Note that the PLIF images are only used to illustrate the approximate stage of development and are not from the same experiment since the experimental set up is not capable of simultaneous PIV and PLIF.

The results show that the shock interaction deposits a vorticity distribution on the interface with maximum values at the points where the slope of the perturbation is the largest and which decays to zero at the positions with minimum interface deflection. The deposited vorticity causes the instability to grow and at later times form mushroom structures as the vorticity distribution collapses to form vortices. At later stages a secondary instability develops on the arms of SF_6 spiraling inwards to the vortex cores. It can be observed in this sequence that the half spike developing at the wall of the test section is strongly influenced by the boundary layer. This can be observed in both the PLIF and PIV images. Furthermore, the influence is more prominent at later times as the thickness of the boundary layer grows.

An important factor in PIV is the resolution. The resolution is limited by the number of pixels available on the CCD-chip and the size of the interrogation windows used in the PIV algorithm. The resolution limitations are most prominent in the experiments presented in figure 3 where the entire shock tube is imaged. Note that the vortex appears as a solid core of vorticity of one sign. Some additional experiments were conducted with the camera placed nearer the shock tube such that only the vortex core was imaged. The result of one of these experiments is presented in figure 4. The increased resolution in this smaller area now reveals that the vortex, in fact, consists of vortex sheets. In addition, secondary vorticity of opposite sign (blue) can now be observed. Possibly more

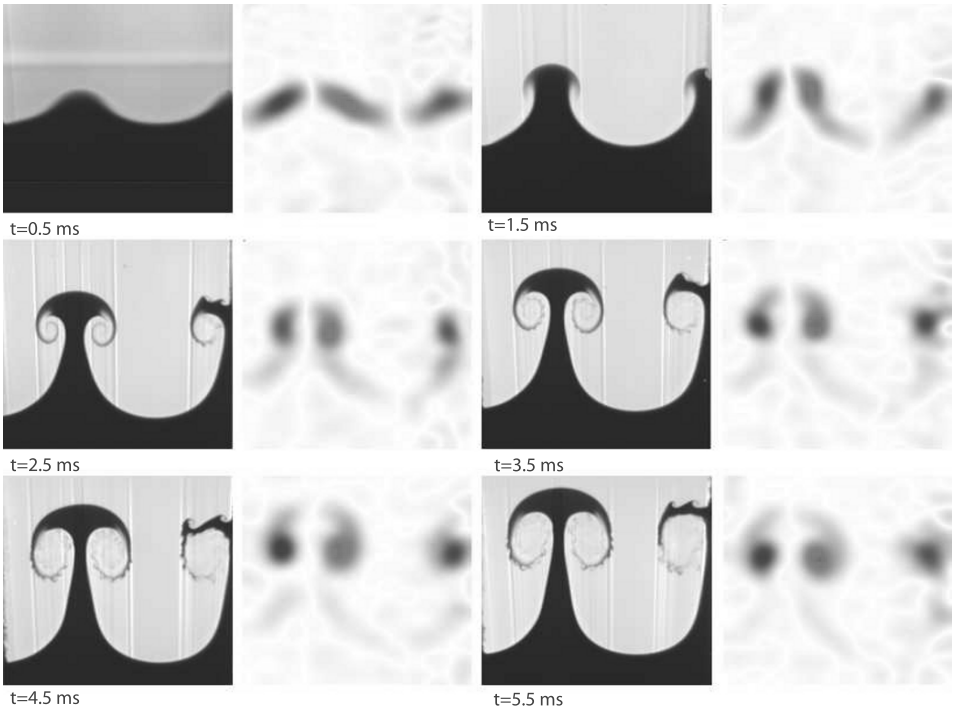

Fig. 3. A comparison of PLIF and PIV images in the 1 1/2 wavelength experiment.

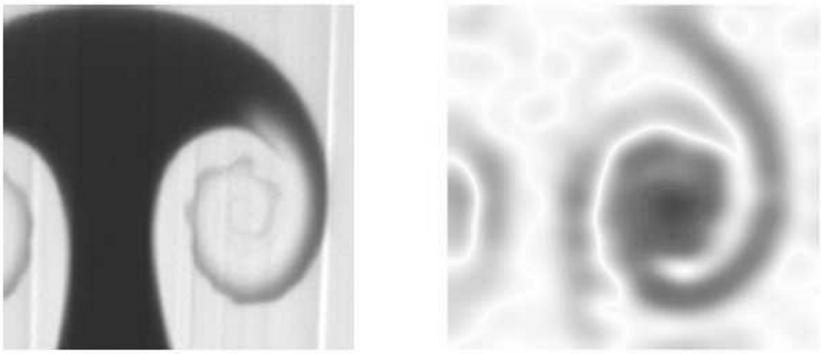

Fig. 4. Improved resolution of small scales when only vortex core is imaged.

interesting, are the small bumps in the vorticity distribution that can be observed in this image. If compared to the PLIF image on the left it is apparent that the wavelength of these bumps is of the same order as that of the secondary instability visible in the PLIF experiment.

Circulation is an important quantity in this flow as it determines the growth rate of the instability. Also important is the fact that because circulation is an integrated measurement, it is insensitive to the resolution issues described above. The circulation was extracted from the vorticity field measurements by integrating the vorticity over the area of a rectangular box covering one half wavelength. The vertical sides of the box were aligned with the center of the spike and the center of the bubble and the horizontal sides were placed as far as possible away from the interface. Figure 5 shows the measured circulation vs. time for an experimental series using a 2 1/2 wavelength ($k = 176\,\mathrm{m}^{-1}$) sinusoidal initial perturbation with a pre-shock amplitude of approximately 1.1 mm. The circulation measurements in this plot are for the right half of the spike that is closest to the center of the shock tube (i.e., the centermost vortex). This vortex was chosen to minimize the effects of the boundary layers on the shock tube walls. The line passing through the data is a curve fit, presented only for illustration of the general trend. The horizontal line shows the circulation estimate using equation (2) with the initial growth rate extracted from the experiments. The general trend shows that the circulation is approximately constant in the early stages of development until significant roll-up has taken place. At this point the generation of secondary vorticity becomes important, causing an overall increase in vorticity and hence circulation. This increase continues until a stage where the vortex cores become turbulent. Turbulent mixing of the two gases causes a decrease of both $\nabla\rho$ and ∇p reducing the generation of secondary vorticity, and the circulation reaches a plateau. If the circulation was tracked further in time, one would expect a decrease in circulation due to viscous dissipation. The trend of the curve agrees well with what is observed in previous numerical simulations. The scatter in the data is due to the

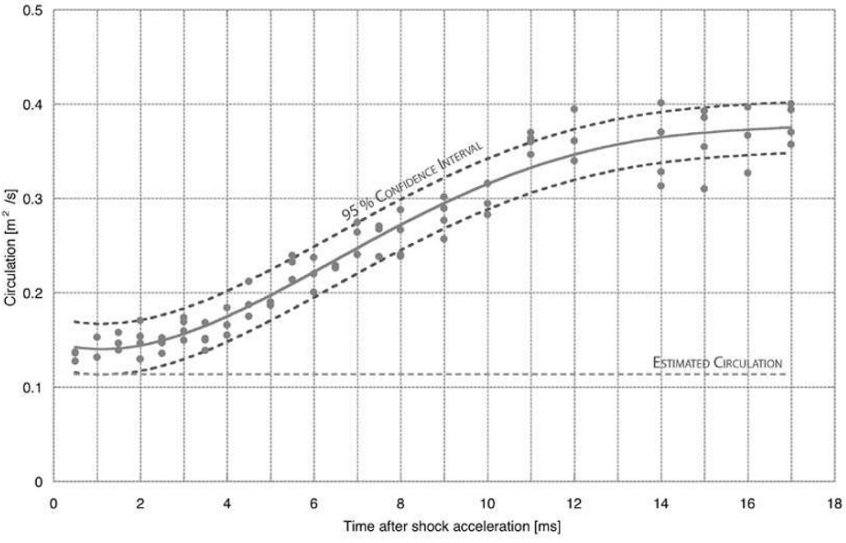

Fig. 5. Evolution of circulation vs. time after shock acceleration.

slight variations in the initial conditions and is one of the shortcomings of the current set up where only one image per experiment is acquired.

4 Conclusion

PIV has been implemented successfully for the full flow field in the Richtmyer-Meshkov instability shock tube experiments. Several experimental series with varying initial perturbation amplitude and wavelength have been performed and the capabilities of the method in these experiments have been tested. The experiments have shown that PIV is an effective diagnostic method for extracting velocity measurements from these experiments. Vorticity distributions and the circulation over one half wavelength have been extracted from the velocity field measurements and the generation of secondary vorticity has been observed. The results show that there is an increase in circulation with time due to the generation of secondary vorticity and that the circulation eventually stabilizes when the vortex cores become turbulent. It has been shown that the largest obstacle for the effective use of this technique in these experiments is the limited resolution of PIV. Increased resolution is needed to obtain correct magnitudes and resolve small structures. Due to the nature of the experiment slight variations in initial conditions result in data scatter.

This research was supported by Lawrence Livermore National Laboratory.

References

1. Richtmyer, R.D., *Taylor Instability in Shock Acceleration of Compressible Fluids.* Commun. Pure Appl. Math., **8**, 297 (1960).
2. Meshkov, E.E., *Instability of the Interface of Two Gases Accelerated by a Shock Wave.* Fluid Dyn., **4**, 101 (1969).
3. Jacobs, J.W., Sheeley, J.M., *Experimental Study of Incompressible Richtmyer-Meshkov Intability.*
4. Jones, M.A., Jacobs, J.W., *A Membraneless Experiment for the Study of Richtmyer-Meshkov Intability.* Phys. Fluids, **9**, 3078-3085 (1997).
5. Collins, B.D., Jacobs, J.W., *PLIF Flow Visualization and Measurements of the Richtmyer-Meshkov Instability of an Air/SF_6 Interface.* J. Fluid Mech., **464**, 113-136 (2002).
6. Arnett, W.D., Bachall, J.N., and Woosley, S.E., *Supernova 1987A,.* Annu. Rev. Astron. Astrophys., **27**, 629 (1989).
7. Lindl, J.D., McCrory, R.L., and Campbell, E.M., *Progress Toward Ignition and Burn Propagation in Internal Confinement Fusion.* Phys. Today, **45**, 32 (1992).
8. Markstein, G.H., *A Shock Tube Study of Flame Front-Pressure Wave Interaction.* 6th Interantional Symposium on Combustion, Reinhold, 1957, pp. 387-398.
9. Peng, G., Zabusky, N.J., and Zhang, S., *Vortex-Accelerated Secondary Baroclinic Vorticity Deposition and Late-Intermediate Time Dynamics of a Two-Dimensional Richtmyer-Meshkov Interface.* Phys. Fluids, **15**, 3730-3744 (2003).
10. Alesin, A.N., Gamalii, E.G., Lazareva, E.V., Lebo, I.G., and Rozanov, V.B., *Nonlinear and Transitional States in the Onset of the Richtmyer-Meshkov Instability.* Sov. Tech. Phys. Lett., **14**, 466-468 (1988).
11. Prestridge, K., Rightley, P.M., Vorobieff, P., Benjamin, R.F. and Kurnit, N.A., *Simultaneous Density-Field and PIV of a Shock-Accelerated Gas Curtain.* Exp. Fluids, **29**, 339-346 (2000).

Richtmyer-Meshkov instability in laser plasma-shock wave interaction

A. Sasoh[1], **K. Mori**[1], **and T. Ohtani**[2]

[1] *Department of Aerospace Engineering, Nagoya University, Furo-cho, Chikusa-ku, Nagoya 464-8603, Japan*
[2] *Department of Aerospace Engineering, Tohoku University,6-6-1 Aramaki-aza-Aoba, Aoba-ku, Sendai 980-8579, Japan, currently JFE Engineering Co., Tokyo 100-0005, Japan.*

Summary. The interaction between a laser plasma bubble and a shock wave involving a Richtmyer-Meshkov instability was experimentally studied via framing Schlieren visualization with a new experimental arrangement. The plasma bubble was generated by irradiating a TEA (Transversely-Excited Atmospheric) CO_2 laser pulse onto a parabolic mirror made of aluminum. After the laser pulse, the plasma bubble expanded and drove a spherical shock wave. The shock wave was reflected against the parabola, and interacted with the plasma bubble itself. In the interaction, a sharp interface is generated without membrane so that undesired membrane-oriented disturbances were eliminated. The flow visualization was conducted with various ambient pressure and laser energy, thereby obtaining different jet formations patterns.

1 Introduction

Richtmyer-Meshkov instability [1, 2] is initiated by baroclinic interaction between a density and pressure gradients. Because such interaction evolves to complicated flows, which cannot be fully predictable only through computational fluid dynamics – experiment still has an essentially important role in investigating the related phenomena. In most of past works [3–5], a density discontinuity was formed using a layer of membrane or its equivalent such as soap bubble. However, the interaction was fluid-dynamically contaminated due to the fragments of the membrane. An interface can be generated by the impingement of opposing flows [6, 7]. However, the flexibility of such experiment is rather limited. In our past work, we developed a new setup in which Richtmyer-Meshkov instability could be studied as the interaction between the laser-induced plasma bubble and a shock wave which was driven by the plasma bubble itself [8, 9]. The published contents were only a small fraction of the series of experiments. In this paper, we will report further experimental results.

2 Baroclinic motion of bubble

The production of a vorticily is formulated by taking a rotation of Euler's equation:

$$\frac{d\omega}{dt} = \{\omega \cdot \nabla\}\mathbf{u} - \omega\{\nabla \cdot \mathbf{u}\} + \frac{1}{\rho}\nabla\rho \times \nabla P \tag{1}$$

The third term on the right-hand side of Eq 1 corresponds to the baroclinic term. Figure 1 schematically illustrates the deformation of a bubble, that is a low-density sphere, experiencing a shock wave loading. The bubble interface acts as a density discontinuity, and the shock wave a pressure discontinuity. A plane shock wave is incident to the bubble

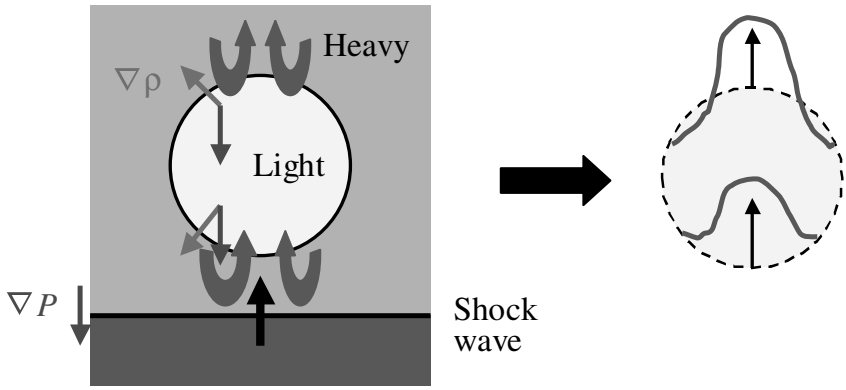

Fig. 1. Barochlinic motion in plasma bubble-shock wave interaction

upward. Following the baroclinic term in Eq. 1, the convexity of the bubble lower part is reversed, whereas the upper part obtains a positive gain. As a result, a 'reversal' jet is formed from the bottom to the top of the bubble.

3 Apparatus

Figure 2 schematically illustrates the test section of the present experiment. The cylindrical test chamber was 300 mm in inner diameter and 300 mm in length along the horizontal axis. Near the center of the chamber, an aluminum parabolic mirror was set so that its axis was aligned with a radius of the test chamber. The diameter of the parabola was 42 mm, the focal length 21 mm. A TEA CO_2 laser pulse was directed along the parabola axis through a ZnSe window. The effective beam diameter incident onto the parabola was controlled by the diameter of the iris placed above the window. The full width at half maximum of the primary laser power peak was 0.2 μs; 90 % of the total energy, E, was irradiated in 3 μs.

Initially, the test chamber was evacuated using a turbo-molecular pump that was backed by a rotary pump to 10^{-3} Pa. Then the test gas was introduced to the 'ambient' pressure, P_0. In this study, krypton, was examined as the test gas. Time evolution of the laser-induced flow was visualized through a Schlieren system, recorded onto a high-speed framing camera (HyperVision HPV-1, Shimazu Co. 10^6 frame/s at maximum, resolution; 312 × 260 pixels). A xenon flush lamp was used as the light source. The collimated light beam for the visualization was supplied along the axis of the test chamber.

4 Results and discussions

Figures 3 to 7 show the visualized laser-induced events. A sharp interface over a single test gas species is produced without any material and disturbance associated with the separation. As was discussed in Ref. [9], the large-scale baroclinic vortex motion is similar with respect to the ratio of laser energy to the ambient pressure although small-scale perturbations are enhanced at high ambient pressures.

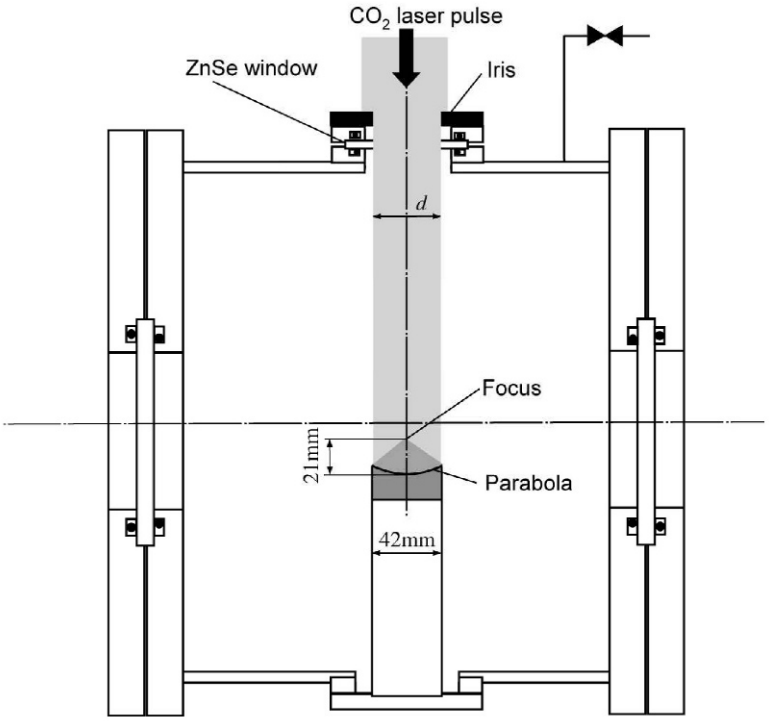

Fig. 2. Experimental setup

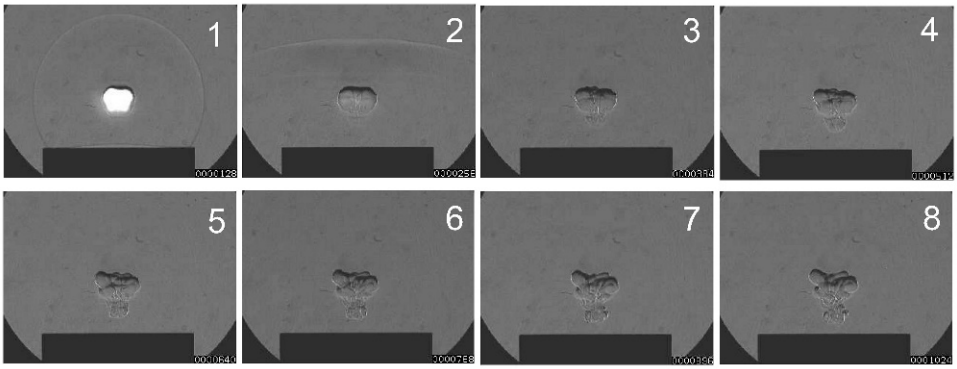

Fig. 3. Framing Schlieren images, $P_0 = 100$ kPa, $E = 0.5$J, framing interval; 128 μs.

Figure 3 to 5 show framing Schlieren images for different E at P_0 =100 kPa. When the laser energy is small, E =0.5J (Fig. 3) or E =1.2J (Fig. 4), the bubble motion is governed by the interaction with laser beam; the effect of the reflected shock wave is small. In these cases, the plasma bubble was made extruded towards the parabolic mirror. This behavior is commonly observed when focusing a laser pulse in gas. [10] However, with even larger

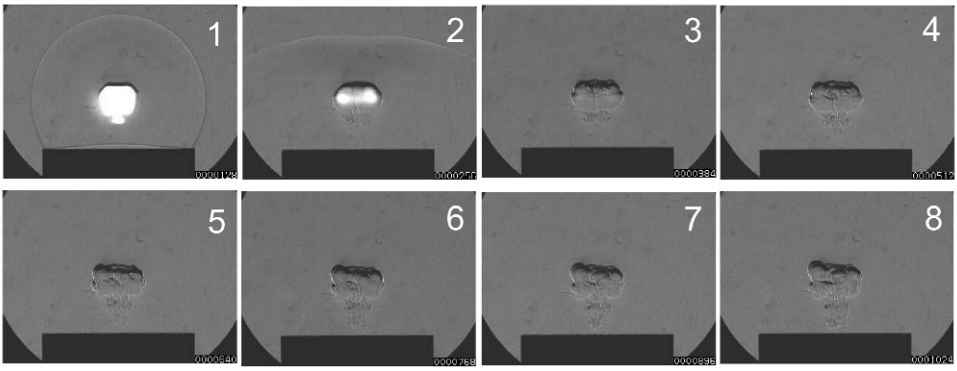

Fig. 4. Framing Schlieren images, $P_0 = 100$ kPa, $E = 1.2$, framing interval; 128 μs.

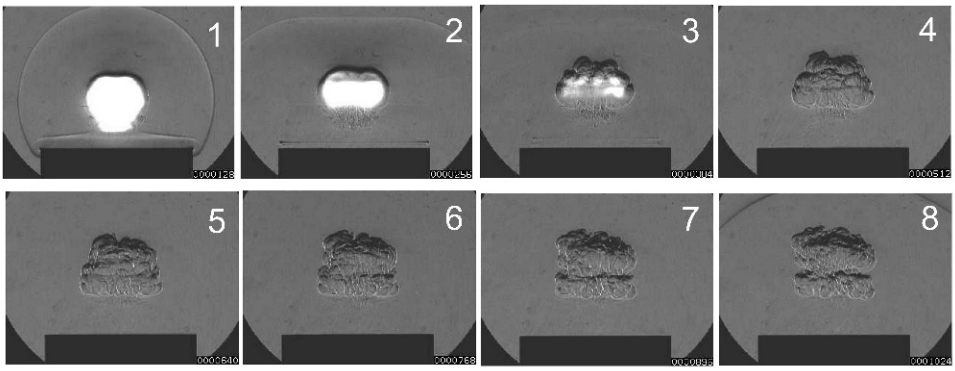

Fig. 5. Framing Schlieren images, $P_0 = 100$ kPa, $E = 3.3$J, framing interval; 128 μs.

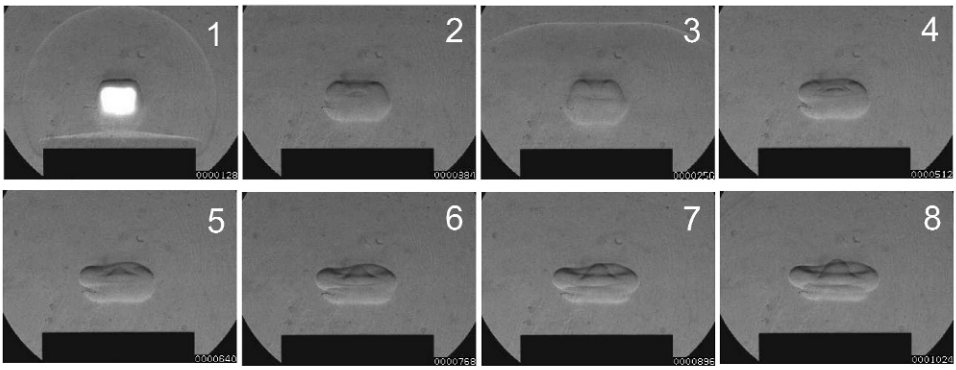

Fig. 6. Framing Schlieren images, $P_0 = 20$ kPa, $E = 0.5$J, framing interval; 128 μs.

E (=3.3 J, Fig. 5), the baroclinic motion became dominant, the bottom portion of the bubble reversed its convexity, forming a upward jet motion.

At a lower P_0 (=20 kPa, Figs. 6 and 7), the impact of the laser pulse of the same energy became larger than that at P_0 = 20 kPa. At E = 0.5 J (Fig. 6), jet motion downward or upward was not observed. The plasma bubble was deformed from a sphere to a disk shape, while at P_0=100kPa (Fig. 3) the downward jet appeared. With the larger energy, E =1.2 J (Fig. 7), the baroclinic effect dominated in the bubble motion. The bubble reversal occurred as the result of the upward jet.

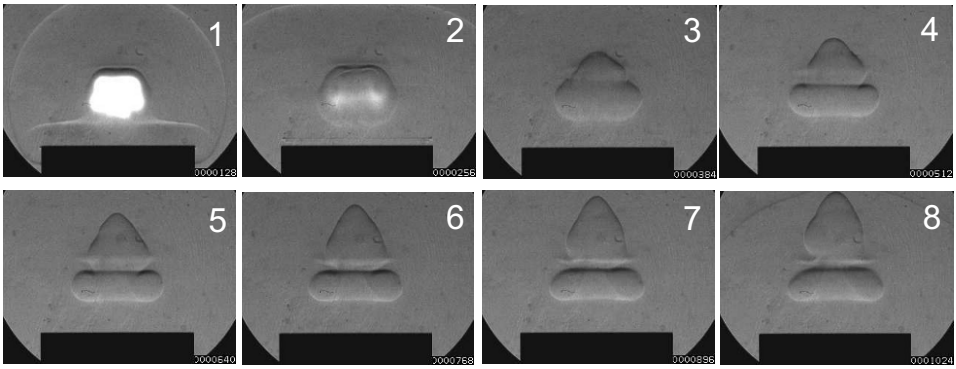

Fig. 7. Framing Schlieren images, P_0 = 20 kPa, E = 1.2J, framing interval; 128 μs.

5 Conclusion

In the interaction between a laser-induced plasma bubble and a shock wave which is driven by the bubble itself, the bubble motion was influenced by the laser-plasma interaction and the plasma-shock wave interaction. Depending on the impact of the shock loading, the interaction yielded different topological change of the bubble. When the shock loading was strong, the baroclinic effect dominated – the reversal jet appeared upward. With smaller impact, the laser-plasma interaction beat the former; the downward jet appeared.

References

1. Richtmyer RD: Comm. Pure & Appl. Math. **XIII** (1960), 297
2. Meshkov EE: Soviet Fluid Dynamics **4** (1969), 101
3. Erez L et al: Shock Waves**10** (2000), 241
4. Hosseini SHR & Takayama K: Phys. Fluids**17** (2005), 084101
5. Layes G, Jourdan G & Houas L: Phys. Rev. Lett. **91** (2003), 174502
6. Jones MA & Jacobs JW: Phys. Fluids **9** (1997),3078
7. Jacobs JW & Krivets VV: Phys. Fluids **17** (2005),034105
8. Yu X et al : Sci. Tech. Energetic Materials **66** (2005), 274
9. Sasoh A, Ohtani T & Mori K : Phys. Rev. Lett. **97** (2006), 205004
10. Bradley D et al : Combust & Flame **138** (2004), 55

Shock tube experiments and numerical simulation of the single mode three-dimensional Richtmyer-Meshkov instability

V.V. Krivets[1], C.C. Long[1], J.W. Jacobs[1], and J.A. Greenough[2]

[1] *University of Arizona, 1130 N. Mountain Ave., Tucson AZ 85721 USA*
[2] *Lawrence Livermore National Laboratory, 7000 East Avenue, Livermore CA 94550 USA*

Summary. A vertical shock tube is used to perform experiments on the single-mode three-dimensional Richtmyer-Meshkov Instability. The interface is formed using apposed flows of air and SF_6 and the perturbation is created by the periodic motion of the gases within the shock tube. Planar laser induced fluorescence is used for flow visualization. Experimental results were obtained with a shock Mach number of 1.2. A three-dimensional numerical simulation of this experiment was conducted the results of which are compared with the experimental images and measurements.

1 Experimental set-up

Membraneless Richtmyer-Meshkov instability experiments have previously been carried out in a vertical shock tube using a single-mode two-dimensional initial perturbation [1], [2]. The present study utilizes the apparatus and experimental techniques of these previous investigations modified to allow the generation of a single-mode three-dimensional initial perturbation.

A 5.16 m long vertical shock tube with a 10.2 cm diameter round driver, and a 8.9 cm square test section is used for this study. The light gas (air) enters the tube at the top of the driven section immediately below the diaphragm, and the heavy gas (SF_6) enters at the bottom of the test section. The gases exit the shock tube through a series of small holes in the test section walls, leaving behind a flat, diffuse interface (figure 1). In the previous study [3] the initial perturbation was generated by periodically oscillating the square shock tube, laterally, in the diagonal direction to produce a nearly single-mode three-dimensional standing wave. Unfortunately, this method is capable of producing perturbations of only very small amplitude ($ka_{0-} = 0.16$). More recently we have found that we can produce similar three-dimensional standing waves using vertical oscillation in which the gas column within the shock tube is oscillated using the periodic motion of a piston mounted at the bottom of the test section. This oscillating flow inside of the tube generates a single-mode three-dimensional standing wave and forms an initial perturbation on the interface which has a larger value of ka_{0-}. A weak shock wave ($M = 1.2$) is generated in the shock tube by manually puncturing a polypropylene diaphragm. The flow is visualized in these experiments utilizing planar laser induced fluorescence (PLIF). The light gas is seeded with nearly saturated acetone vapor and illuminated by the fourth harmonic of a pulsed Nd:YAG laser positioned at the lower end of the shock tube. The the laser's output is passed through circular and cylindrical lenses and reflected upward through a window in the shock tube end wall producing a light sheet that illuminates a thin cross section of the interface. The resulting fluorescent image is captured by a thermoelectrically cooled CCD camera. The initial interface is shown in the figure 2 just before and after shock wave passage. In these experiments

the instability was initiated with a square, single-mode three-dimensional perturbation of the form

$$\eta(x, y) = a_0 \cos(k_x x) \cos(k_y y) \tag{1}$$

where $k_x = k_y = \sqrt{2}\pi/W$ and $W = 8.9\,\mathrm{cm}$ is the width of the test section side wall. The x and y axes are directed trough diagonal of the tube cross section and η is the vertical displacement of the interface. In this particular image the spike is positioned at the center of the shock tube and the laser sheet spans the test section diagonal yielding views of the maximum and minimum penetration.

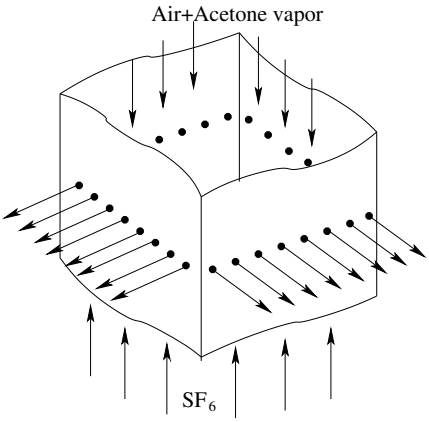

Fig. 1. The formation of a flat interface by stagnation flow.

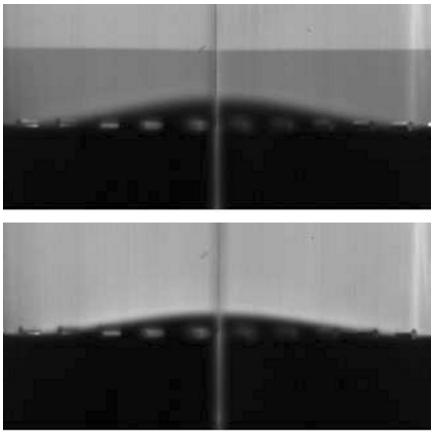

Fig. 2. PLIF images showing the reshock and postshock interface shape.

2 Numerical simulation

The code Raptor, a multi-dimensional Eulerian adaptive mesh refinement (AMR) code, is used for the three-dimensional computations. It was developed and is currently supported by AX-Division at Lawrence Livermore National Laboratory (LLNL). Raptor uses a block-structured approach to adaptivity [4], whereby blocks or patches of the computational domain are refined in space and time. The refined grid layout is constructed as a hierarchy with the coarse resolution grid covering the entire computational domain. Finer levels are strictly contained within the next coarser level, thus creating a nested grid hierarchy. The individual patches or blocks are the basic elements of parallelization. The blocks on a particular level are distributed among the available processors. This approach has successfully been applied to a wide range of massively parallel computers available at LLNL such as the Intel Xeon based ALC/MCR with 1920 processors, Itanium based Thunder with 4096 processors and the IBM BG/L with 131072 processors [5].

The underlying integration method is based on the original higher-order Godunov scheme developed by Colella [6]. It has been extended to multiple materials (with distinct equation-of-states) by Miller and Puckett [7] and generalized to miscible materials by Greenough et al. [8].

The computations presented here use a domain that models the entire shock tube length and square cross-section. This allows naturally accounting for re-shock by placement

of a solid reflecting at the same location as in the experimental apparatus. The re-shock problem will be addressed in future work. The base grid is $960 \times 16 \times 16$ cells in the x, y and z directions, respectively, where the yz plane is the square cross-section. Two levels of refinement are used, each by a factor of 4, bringing the final effective resolution to 256×256 in the yz plane. The streamwise direction (x) is also refined to the same spatial resolution using an automatic refinement procedure that captures the evolving instability for all time. Its extent is dictated by the mixing layer growth. During shock acceleration, the shock wave is refined but after shock passage it is de-refined back to the coarsest level, for efficiency. All computations presented were run on the IBM uBGL computer, which is a small 2048 processor version of the larger BGL machine.

3 Results

Figure 3 shows a comparison of experimental PLIF images along with similar images from the numerical simulation. The computations show generally good agreement with the experiments. However, the numerical results show a clear lack of vortex development compared with the experiments. The resolution is a key component in resolving vortex development, and as noted, this is a relatively low resolution simulation. Without the proper resolution, the vortex roll-up is not as strong. Another matter of interest is that

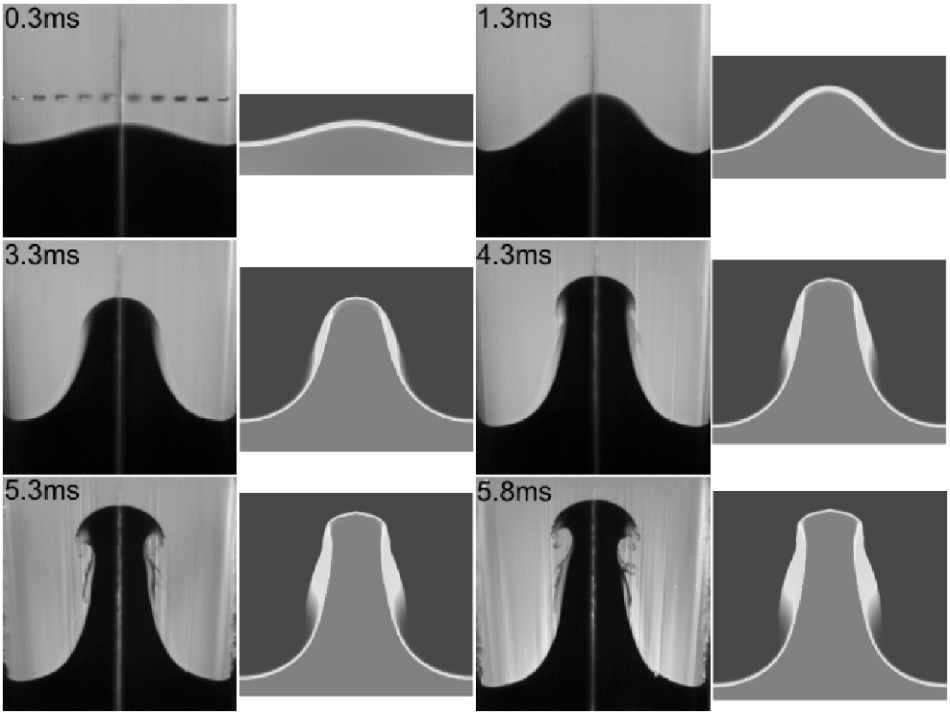

Fig. 3. A sequence of PLIF images (diagonal slices) along with corresponding concentration maps obtained from the simulation.

previous 3-D results [9] have shown two pairs of vortex rings for each bubble/spike pair — one surrounding each spike and one surrounding each bubble (figure 4). However, both the experiment and computation shown in figure 3 clearly show only one vortex per half wavelength. It should be noted that the earlier experiments were carried out with a relatively low-Atwood number fluid combination ($A = 0.15$), and that the present study has a significantly larger Atwood number ($A = 0.65$). To better illustrate this difference in topology, figure 5 is a three-dimensional view of the interface obtained from the computations at approximately 6 ms after shock interaction. One can clearly observe the strong vortex ring surrounding the spike along with what could be described as a much weaker ring surrounding each bubble. We believe that this difference in topology is the direct result of the difference in the value of the Atwood number. Note that one should expect lower Atwood number flows to posses the symmetry expressed by the double ring configuration. Whereas one might expect higher Atwood number instabilities to lose this symmetry yielding configurations similar to those observed in the higher Atwood number results presented here. One can reasonably argue that increasing the Atwood number causes the vortex ring surrounding the spike to increase in strength at the expense of that surrounding the bubble. One would then expect the stronger ring to stretch the weaker one into the configuration depicted in figure 5. Figure 6 is

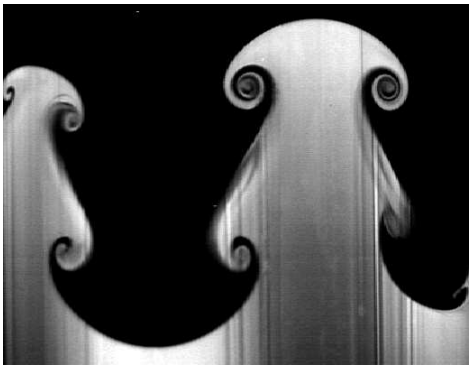

Fig. 4. 3D experiment with incompressible fluids $A = 0.15$, diagonal slice, from [9].

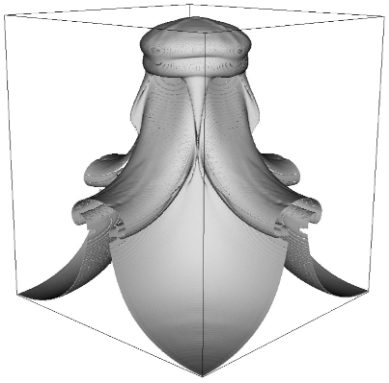

Fig. 5. 3D numerical 3D surface plot of the interface at the 50% concentration level.

a comparison of experimental and numerical amplitude measurements, defined as the average of the bubble and spike amplitudes. The comparison shows excellent agreement despite differences in interface roll-up. In figure 7 the experimental data is plotted in nondimensional form to allow comparison with the earlier 2D [2] and 3D [3] experiments carried out at different Mach numbers and with different perturbation amplitudes and wavelengths. This comparison clearly shows the three-dimensional experiments to grow faster (in this dimensionless sense) than their two-dimensional counterparts, a fact also observed in similar comparisons with lower Atwood number incompressible experiments [9]. Note that the faster nonlinear growth of three-dimensional RM instability is well known and is captured by existing models for the late time growth.

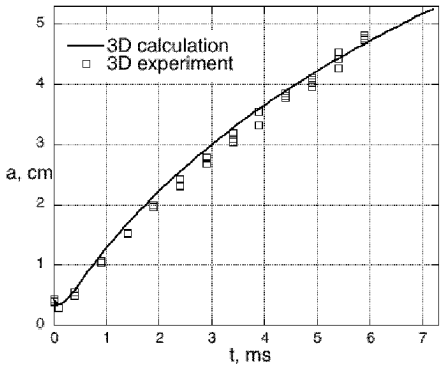

Fig. 6. Amplitude vs. time: experiment and calculation.

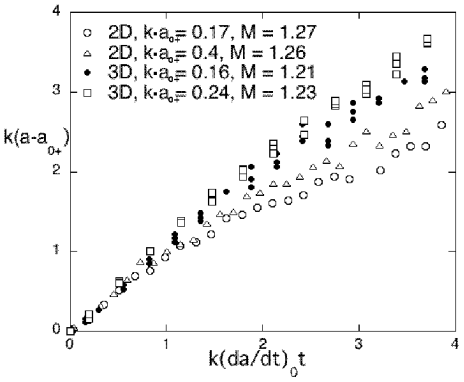

Fig. 7. Evolution of experimental amplitudes in nondimensional coordinates.

4 Conclusions

The three-dimensional Richtmyer-Meshkov instability using a square single-mode perturbation has been investigated both experimentally, in shock tube experiments, as well as with matched numerical simulations. Relatively good agreement between PLIF images and experimental concentration maps is observed. However, the relatively low resolution simulations do not achieve the same degree of vortex roll-up as that observed in the experiments. Amplitude measurements, on the other hand, show excellent agreement between experiment and simulation, illustrating the relative insensitivity of amplitude measurements to fine interface features. Both experiment and computation illustrate a pronounced difference between the interface topology of this relatively high Atwood number instability and earlier lower Atwood number experiments. The earlier lower Atwood number experiments showed a more symmetrical vortex configuration of symmetric vortex arrays while the larger Atwood number flow clearly shows asymmetry with essentially only a single array of vortex rings surrounding only the spikes. This difference can very logically be attributed to the effect of the Atwood number to produce asymmetry in RM flows.

This research was supported by Lawrence Livermore National Laboratory.

References

1. Collins B.D., Jacobs J.W. PLIF Flow visualization and measurements of the Richtmyer-Meshkov instability of an air/SF_6 interface. J. Fluid Mech. 464, 113-136 (2002).
2. Jacobs J.W., Krivets V.V. Experiments on the late-time development of single-mode Richtmyer-Meshkov instability. Phys. Fluids. 17, 034105 (2005).
3. Krivets V.V., Stockero J.D., Jacobs J.W. Experimental study of single-mode Richtmyer-Meshkov instability for 2D and 3D perturbations. Poster presentation IWPCTM Cambridge (2004).
4. Berger M., Colella P. Local adaptive mesh refinement for shock hydrodynamics. J. Comput. Phys. 82 (1), 64-84 (1989).

5. Rendleman C. A., Beckner V. E., Lijewski M., Crutchfield W. Y., Bell J. B. Parallelization of structured, hierarchical adaptive mesh refinement algorithms. Computing and Visualization in Science 3, 147-157 (1998).
6. Colella P. A direct Eulerian MUSCL scheme for gas dynamics. SIAM J. Sci. Stat. Comput. 6, 104-117 (1985).
7. Miller G.H., Puckett E.G. A high-order Godunov method for multiple condensed phases. J. Comput. Phys. 128, 134-164 (1996).
8. Greenough J. A., Beckner V., Pember R. B., Crutchfield W. Y., Bell J. B., Colella P. An adaptive multifluid interface-capturing method for compressible flow in complex geometries. AIAA paper 95-1718 (1995).
9. Chapman P.R., Jacobs J.W. Experiments on the three-dimensional incompressible Richtmyer-Meshkov instability. Phys. Fluids 18, 074101 (2006).

Shock wave induced instability at a rectangular gas/liquid interface

H.-H. Shi[1] **and Q.-W. Zhuo**[2]

[1] *College of Mechanical Engineering and Automation, Zhejiang Sci-Tech University, Xiasha Higher Education Zone, Hangzhou 310018, China*
[2] *Institute of Mechanics, Chinese Academy of Sciences, 15 Beisihuanxi Road, Beijing 100080, China*

Summary. This paper reports an experimental research of Richtmyer-Meshkov (RM) instability at a gas/liquid interface. The experiment was conducted in a vertical rectangular shock tube which has an inner dimension of 35 mm times 35 mm. Different tests with shock wave Mach number of 1.36, 1.50 and 1.58 were tested. The later development of the RM instability was recorded by a CCD camera. The related parameters such as the spike and bubble heights were measured.

1 Introduction

Shock wave induced instability at an interface between two fluids with different densities, namely Richtmyer-Meshkov (RM) instability, has important applications in a wide range of technology fields. For example, it is seen in inertial confined fusion, Supernova explosion, Scramjet engine, underwater supersonic jet, etc. Although the RM instability has been studied for more than 40 years since the pioneering work of [9], many things remain unclear. Particularly, when the Atwood number approaches to 1, there are few experimental data which are necessary to verify the existing theoretical and numerical results ([1], [7] and [6]).
The existing experimental results of RM instability are mostly from shock tubes experiments at a gas/gas interface ([2], [8]). In contrast to a gas/gas interface, a gas/liquid interface has a large density ratio between the two fluids so that it provides a sharp distinction in flow visualization without using tracing particles or dye additives. It also has the advantages of free from the effects of membrane which separates the gases or gas diffusion [3]).
[5] and [4] carried out experiments of Rayleigh-Taylor (RT) instability at an air/water interface. Probably it was [12] firstly conducted a RM instability experiment at a gas/liquid interface using gels as the liquid phase. By using a vertical circular shock tube with 34 mm inner diameter, [13] and [10] studied RM instability phenomena with different air/liquid combinations which enabled them to verify the effect of fluids surface tension and viscosity on the development of the RM instability. In their experiments, it has been found that single-mode instability always appears. However, when the circular shock tube is replaced by a rectangular one which has almost an identical geometrical size of 35 mm square length, complex events such as multimode instability appear ([11], [14]).

2 Experimental Devices and Method

Figure 1 shows the experimental setup of the vertical rectangular shock tube. It mainly consists of (1) a 200 mm long high pressure section filling with helium gas; (2) a 750

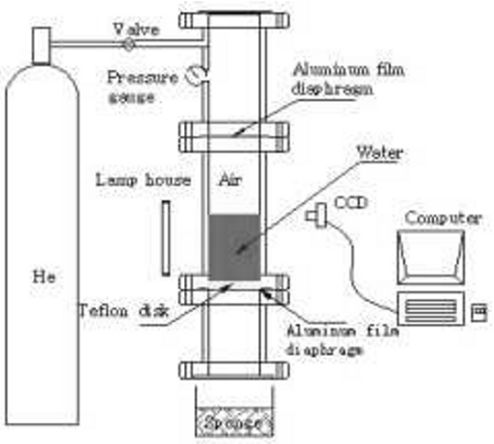

Fig. 1. Schematic of the experimental devices

mm long low pressure section at atmosphere; (3) a 200 mm long discharging section. All the tubes have the same square section and the width of the inner dimension is 35 mm. The high pressure and the low pressure sections are separated by a 36 or 60 μm thick aluminium diaphragm. The low pressure and the discharging sections are separated by a thinner aluminium diaphragm of 15 μm thickness. Water is filled into the low pressure section which has two side windows for observation. At the bottom of the water column, a 1 cm thick and 33 mm length square Teflon plate is placed to make sure the lower water surface keep plane shape in motion. When the helium gas pressure in the high pressure section reaches the rupture pressure, a shock wave forms and moves downwards. When the shock wave impacts on the water column and accelerates it, the RM instability occurs.

A Germany made Basler-A310b type CCD camera was applied for the flow visualization. The framing rate was 100 fps and the exposure time was set at 20 μs. A 300 mm long lamp whose illumination intensity was adjustable was used as the back lighting. Figure 2 gives

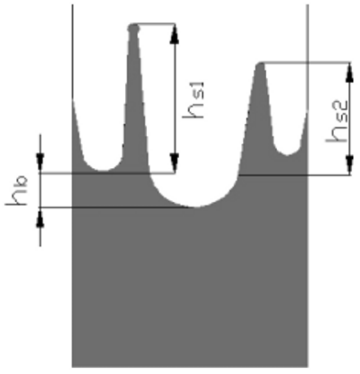

Fig. 2. Definition of the spike and bubble heights

the definition of the spike and bubble heights h_s and h_b during RM instability. If multiple spikes or bubbles appear, then an averaged value is taken, e.g. $h_s = (h_{s1} + h_{s2})/2$.

3 Experimental Results

Figures 1-3 show the CCD photographs of RM instability on an air/water interface at different shock waves Mach numbers of 1.36, 1.50 and 1.58 respectively. Because the length of the observation window in the shock tube is given as 250 mm, it is seen from Figs. 1-3 that as the increase of Mach number the frame number of the captured sequences reduces from 8 in Fig. 1 to 5 in Fig. 3. An interesting phenomenon is found that multimode instability occurs in the three cases, that is, multiple spikes and bubbles with different heights appear. Furthermore, from Figs. 3g-3h, Figs. 4e-4f and Figs. 5d-5e, it is seen that 3-dimensional instability has been developed at the later stage. These phenomena are not seen in the experiment of a circular shock tube with almost an identical geometrical dimension, where only single-mode instability occurs ([13]) and [10]).

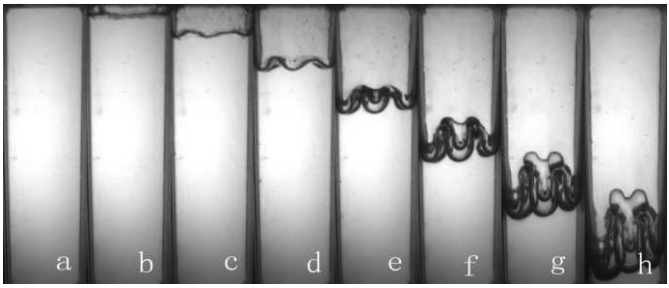

Fig. 3. Photographs of RM instability at rectangular air/water interface. The upper is air and the below is water. Shock wave (Ms = 1.36) goes downwards. Interframe time = 10 ms

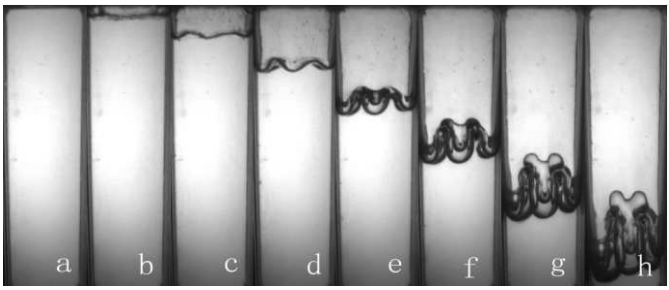

Fig. 4. Photographs of RM instability at rectangular air/water interface. The upper is air and the below is water. Shock wave (Ms = 1.50) goes downwards. Interframe time = 10 ms

This may be attributed to that the four corners of the square cross-section generate multi-wavelength initial disturbances on the air/water interface. Mathematically, the probability of the occurrence of the instability may be distributed all over a rectangular interface whereas it is mostly concentrated at the center of a circular interface. This is

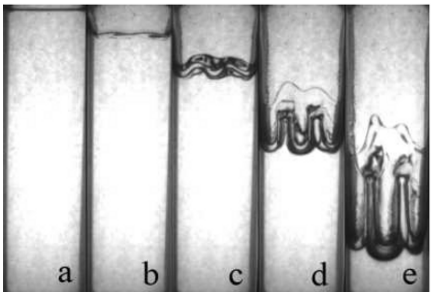

Fig. 5. Photographs of RM instability at rectangular air/water interface. The upper is air and the below is water. Shock wave (Ms = 1.58) goes downwards. Interframe time = 10 ms

why the instability always firstly occurs at the center of a circular gas/liquid interface ([13] and [10]).

Figures 6(a)-6(c) are relationships of the measured averaging spike and bubble heights h_s and h_b against time t. Obviously, the growth rate of the spike and bubble heights increases with the increase of the shock wave Much number M_s. At the time of 40 ms, h_s is about 25 mm when the Mach number is 1.58 whereas in the cases of Mach numbers 1.50 and 1.36, the spike heights are about 11 mm and 6 mm respectively. In accordance with the theory of [1], the spike or bubble height can be expressed as

$$h_s = \alpha_s t^{\theta_s}, h_b = \alpha_b t^{\theta_b} \tag{1}$$

when the Atwood number $A = (\rho_1 - \rho_2)/\rho_1 + \rho_2$ is 1, $\theta_s = 1$ and $\theta_b = 0.4$, where ρ_1 and ρ_2 are densities of the heavy and light fluids respectively. The powers of time θ_s and θ_b are called growth rates. From the experimental results shown in Figs. 6(a)-6(c), it is found that $\theta_s = 1$ and $\theta_b = 0.54$. The measured value of the growth rate for the bubble height is greater than that predicted by [1].

Within the time range of present study, the spike and bubble heights h_s and h_b have about one order difference in magnitude. This fact and their tendency of growth are quite close to the experimental results of RM instability at a circular air/water interface (see Fig. 10 in [13]). The experimental result of RM instability at an air/decane interface indicates that, until a time of 30 ms, the difference between h_s and h_b is not as large as that of an air/water interface and they are in the same order of magnitude ([10]). The experimental result of RM instability at an air/glycerin interface shows another special tendency of growth. The high viscosity of glycerin prevents the growth of the spike and makes its height almost be same as that of the bubble. Meanwhile in this case, it is found that both h_s and h_b become linear functions, that is, both θ_s and θ_b approach to 1. The viscosity effect is believed to be the reason why the bubble height growth rate in the present experiment is about half of that at an air/glycerin interface.

4 Conclusions

(1) At a rectangular gas/liquid interface, multimode and 3-dimensional RM instabilities occur whereas they may not happen at a circular gas/liquid interface. (2) The measured values of the growth rates for the spike and bubble heights at the air/water interface are

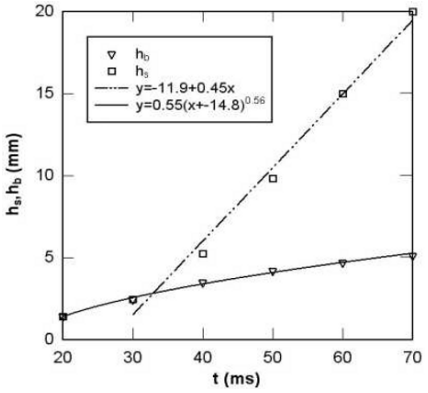

(a) Mach number 1.36

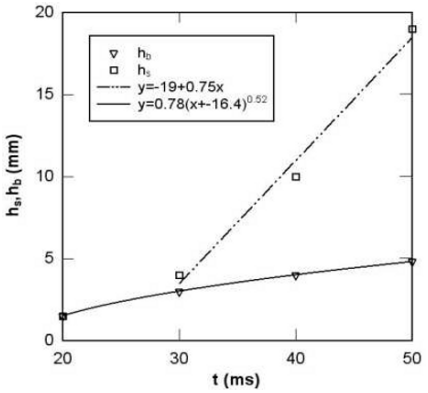

(b) Mach number 1.50

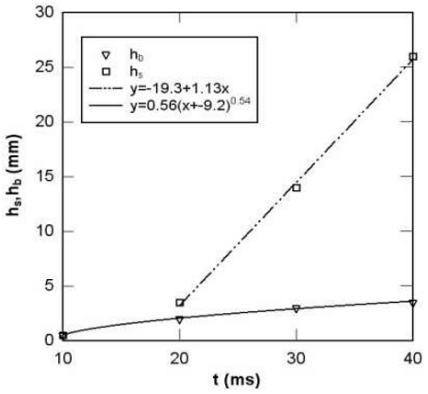

(c) Mach number 1.58

Fig. 6. Growth of the spike and bubble heights at different shock Mach number

1 and 0.54 respectively. The former is same as that predicted by [1]. However, the latter is greater than the value of [1] and is about half value of the growth rate at an air/glycerin interface. (3) Comparing this work with [13], it may suggest that if averaging spike and bubble heights are taken into account, the interface geometry may neither influence the global characteristics of RM instability nor the growth tendency.

Acknowledgement. This work has been supported by the National Natural Science Foundation of China (Grant No.10672144), the Open Research Funding of LHD of Institute of Mechanics of CAS and the Bairen Plan of Chinese Academy of Sciences.

References

1. Alon U, Hecht J, Ofer D, Shvarts D et al. (1995) : *Power Law and Similarity of Rayleigh-Taylor and Richtmyer-Meshkov Mixing Fronts at all Density Ratios* Physical Review Letters, **74** : 534-537.
2. Ben-Dor G, Igra O, Elperin T (2001) : *Handbook of Shock Waves* Academic Press, New York, Vol.2, Chapter 14, pp.489-543.
3. Benjamin RF (1991) : *Shock and Reshock of an Unstable Fluid Interface. Proc 3rd Int Workshop on the Physics of Compressible Turbulent Mixing. Abbey of Royaumont, France, June 17-19*, pp.325-332.
4. Jacobs JW and Catton I (1988) : *Three-Dimensional Rayleigh-Taylor Instability: Part 2, Experiment* J Fluid Mech, **187**:353-371.
5. Read KI (1984) : *Experimental Investigation of Turbulent Mixing by Rayleigh-Taylor Instability* Physica D, 12:45-58.
6. Mikaelian KO (2005) : *Richtmyer-Meshkov Instability of Arbitrary Shapes* Phys Fluids, 17(3):034101 (online).
7. Peng G, Zabusky NJ, Zhang S (2003) : *Vortex-Accelerated Secondary Baroclinic Vorticity Deposition and Late-Intermediate Time Dynamics of a Two-Dimensional Richtmyer-Meshkov Interface.* Phys Fluids, 15(12):3730-3744.
8. Puranik PB, Oakley JG, Anderson MH, Bonazza R (2004) : *Experimental Study of the Richtmyer-Meshkov Intability Induced by a Mach 3 Shock Tube.* Shock Waves, 13:413-429.
9. Richtmyer RD (1960) : *Taylor Instability in Shock Acceleration of Compressible Fluids* Commun Pure Appl Math, 13:297-319.
10. Shi HH and Kishimoto M (2003) : *Fluid Mechanics in the Transient Acceleration of a Liquid Column* Explosion and Shock Waves, 23:391-397. (in Chinese).
11. Shi HH and Zhuo QW (2007) : *Evolution of the Fluid Mixing Zone in Richtmyer-Meshkov Instability at a Gas/Liquid Interface* Chinese J Theor Appl Mech, **39** (3):417-421. (in Chinese).
12. Volchenko OI, Zhidov IG, Meshkov MM, Rogachev VG (1989) : *Growth of Localized Perturbations at the Unstable Boundary of an Accelerated Liquid Layer* Sov Tech Phys Lett, 15:19-21.
13. Wang XL, Itoh M, Shi HH and Kishimoto M (2001) : *Experimental Study of Rayleigh-Taylor Instability in a Shock Tube Accompanying Cavity Formation* Jpn J Appl Phys, **40**:6668-6674.
14. Zhuo QW and Shi HH (2007) : *Experimental Study of Richtmyer-Meshkov Instability at a Gas/Liquid Interface in a Shock Tube* J Exps Fluid Mech, **21**, (1):25-30. (in Chinese).

Part XIX

Shock Boundary Layer Interaction

An investigation into supersonic swept cavity flows

B. Reim, S.L. Gai, J. Milthorpe, and H. Kleine

School of Aerospace, Civil, and Mechanical Engineering, University of New South Wales/Australian Defence Force Academy, Canberra, ACT 2600, Australia

Summary. The paper presents results of an investigation of the flow characteristics of swept cavities in a Mach 2 supersonic stream. The unsteady features of the flow within the cavities were of primary interest. The length to depth ratio of the cavities studied were typical of the shallow 'open' and 'closed' type, respectively. The results of the swept cavities, when compared to those obtained for straight cavities (of the same streamwise length to depth ratios), showed some significant differences. In particular, with the 'short' swept cavity, the flow appears to be of the quasi-open type, distorted slightly by the spanwise flow across the cavity. In the case of the 'long' swept cavity, flow features resembling the transitional closed to closed type appeared to exist across the span.

1 Introduction

Designers of missiles, re-entry vehicles, and aircraft, encounter a variety of design problems related to the flow characteristics in and around cavities. A number of investigations of these problems have been conducted over the years to increase our understanding of cavity flow fields at subsonic through to hypersonic speeds. It has been known that depending on the cavity length to depth ratio (l/d), the cavity may be either 'open' or 'closed'. An open cavity can sustain self-induced oscillations within the cavity with distinct resonant frequencies. A closed cavity, on the other hand, sustains an unsteady pressure field with a broadband spectrum and no well-defined frequency. The result in either case is an increase in drag but more importantly, structural fatigue and buffeting due to pressure oscillations and far field noise radiation, both of which exert a baleful influence on the airframe structure and the environment.

While the flow characteristics pertaining to straight cavities, wherein both the cavity leading and trailing edges are normal to the oncoming flow direction, are now fairly well understood, similar information in regard to swept cavities, where the leading and trailing edges of the cavity are at yaw to the oncoming flow direction, is quite sparse, especially at supersonic speeds. Studies by Tracy & Plentovich [1] have considered the effects of yaw but their studies were restricted to a yaw angle of 15° and a Mach number of $M = 0.9$. The work by Disimile & Orkwis [2], although done at a Mach number of 2, describes the flow in a very short open cavity ($l/d = 2$) and concentrates mainly on the variation of sound pressure levels in the cavity with yaw.

The present paper describes an experimental investigation conducted to determine the flow characteristics of swept cavities in the supersonic flow regime at a freestream Mach number of 2. The investigation focused on the unsteady flow behaviour of swept cavities, both open and closed. The streamwise length to depth ratios of cavities studied were 8 and 16, typical of shallow open and closed type cavities. The cavity sweep angles tested were 0° (straight), 15° and 45°. When compared with the datum case of the straight cavity (0°), the swept cavities showed some distinct and unusual differences.

2 Experimental details

The experiments were conducted in a blow-down supersonic wind tunnel of cross-section 155 mm (height) × 90 mm (width) at a freestream Mach number of 2. A flat plate 280 mm long and 8 mm thick and spanning the full width of the tunnel was mounted along the axis of the tunnel. To investigate the cavity pressure field, an instrumented cavity was installed, equipped with five fast response miniature Kulite gauges (XCQ-062), one each on the two faces of the cavity and three on the cavity floor, in line with the flow. Three cavity yaw angles, 0°, 15°, and 45°, were achieved by using interchangeable inserts to define the cavity geometry. For all the cavities, an inboard distance of 116 mm from the leading edge of the flat plate was maintained. The cavity depth was 4 mm. Two models of the cavity were used in tests. The short swept cavity, with a streamwise length to depth ratio l/d of 8 was equivalent to an open straight cavity. The long swept cavity had a streamwise length to depth ratio l/d of 16 and was equivalent to a closed straight cavity. Because of the sweep, the 'effective' length to depth ratios of the cavities for sweep angles 15° and 45° were 7.7 and 5.65 in the case of the open cavity and 15.45 and 11.31 in the case of the closed cavity, respectively. The value 11.31 borders on the 'transitional closed' according to Tracy & Plentovich [1]. A perspective view of the swept cavity model and its installation in the test section is shown in Fig. 1.

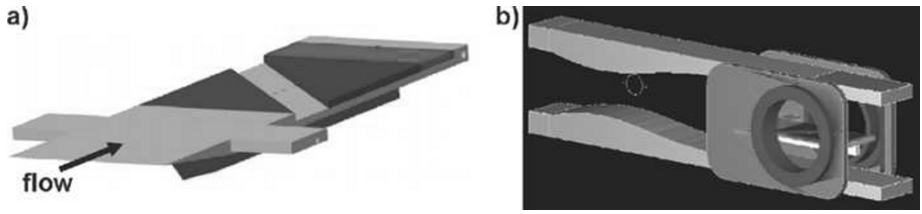

Fig. 1. (a) Swept cavity model arrangement, showing removable inserts to change sweep angle and aspect ratio (b) Integration of swept cavity model in test section

Colour schlieren images of the flow in the cavities were obtained using a flash light source with a pulse width of 200 μs. Time-resolved monochrome schlieren images were taken with a high-speed camera and a flash light source that provided a pulse of 1 ms duration. However, the size of the test section windows allowed one only to 'look through' cavities with yaw angles of 0° and 15°.

3 Results and discussion

3.1 The boundary layer at the cavity leading edge

The separating boundary layer at the cavity leading edge is known to influence the characteristics of the cavity flow. Charwat et al. [3] point out that the ratio of the separating boundary layer thickness to cavity depth, δ/d, is an important parameter and that the effect of increasing the boundary layer thickness for a constant depth cavity is to smooth out the adverse pressure gradient effects in the cavity and increase the skin friction on the cavity floor. Secondly, Zhang and Edwards [4] suggest that the boundary

layer, through the separated shear layer amplification of vortical disturbances, plays an important role in sustaining the open cavity oscillatory mechanism, although oscillatory frequency prediction models do not take into account the finite thickness of the boundary layer.

In the present experiments, the oncoming boundary layer at the cavity was measured 13 mm ahead of the cavity leading edge and was found to be turbulent and about 2.2 mm thick. The unit Reynolds number at the cavity was 43 million per metre. Based on the cavity length, it varied between 13.8×10^5 and 27.6×10^5. The measured boundary layer thickness agreed well with that calculated for a turbulent boundary layer using the criterion of Crocco and Lees [5].

3.2 Analysis of oscillatory modes in open cavities

Figures 2a through to 2e show spectra of pressure oscillations for the straight and swept open cavity configuration. Discrete resonant frequencies occur in the straight (0°) cavity as well as the cavity with 15° yaw. They are particularly predominant on the rear face of the cavity. With the 45° yaw, the picture is significantly different. The spectra from the transducers on the floor are all broadband showing no discrete frequencies and continuously decreasing sound pressure levels. The front face spectrum shows a near constant sound pressure level but no discrete frequencies. The rear face transducer spectrum shows a peak at 18 kHz but not a sharp discrete tone. The broadband nature of spectra of cavities with 45° sweep would indicate that the unsteady pressure oscillations occur in all directions inside the cavity with this sweep angle and cover a continuous range of frequencies.

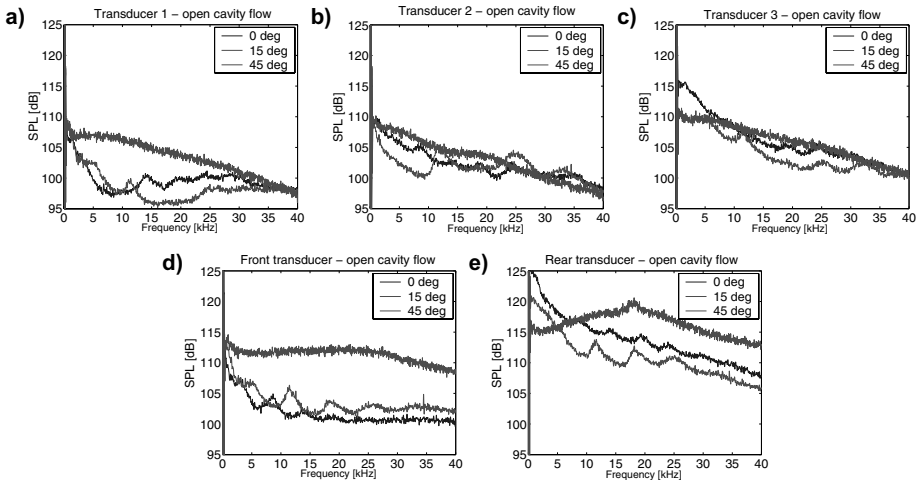

Fig. 2. Pressure oscillations within an open cavity at various sweep angles

It is of interest to compare the above frequencies and modes with theoretical predictions based on the modified Rossiter formula for the Strouhal number [6]:

$$\frac{fl}{U} = \frac{n-\beta}{\frac{U}{U_c} + \frac{Mcos\psi}{\sqrt{1+(\frac{\gamma-1}{2})M^2cos^2\psi}}} \tag{1}$$

where $n = 1, 2, ...$ is the mode number, β is the phase lag, f is the oscillation frequency, U_c is the convection velocity, and l is the cavity length. U and M are the freestream velocity and Mach number, respectively, and ψ is the yaw angle. γ is the ratio of specific heats of the gas. For high Mach numbers and shallow cavities, experimental evidence [6] suggests that $\beta \approx 0.25$ and $U/U_c \approx 0.6$ independently of the freestream temperature, the cavity width (w), and the Reynolds number based on the cavity length.

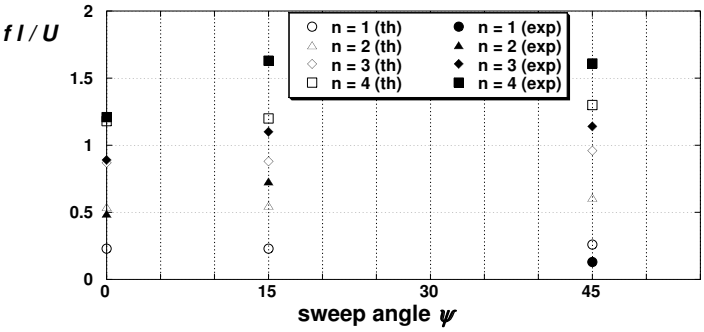

Fig. 3. Comparison between experimental and theoretical Strouhal numbers as a function of sweep angle for open cavities

Figure 3 shows the comparison between the theoretical Strouhal numbers, as calculated above, and the experimental ones obtained from the spectra. It is seen that the spectra are dominated by the second, third and fourth Rossiter modes ($n = 2, 3, 4$). The agreement between the experimental and theoretical values is very good for the modes $n = 2, 3, 4$ in the case of the straight cavity, but with sweep the discrepancies increase. There is an indication that the Strouhal number increases slightly with sweep for a given mode, but the results are too few to draw any definite conclusion.

3.3 Comparison of open and closed swept cavity flows

The experiments confirmed that both straight and swept closed cavities did not show any discrete frequencies but a broadband spectrum for all yaw angles. This is consistent with the fact that in a closed cavity oscillatory behaviour is inhibited, because the flow first attaches to and then separates from the cavity floor.

Figure 4 shows the time-averaged sound pressure levels (SPL) as a function of the transducer location on the cavity floor and the cavity face for both open and closed cavities. For the open cavity, there is a monotonic rise in the average SPL on the floor, regardless of the sweep. On the front and rear faces, however, there is an increase in SPL with sweep. With the closed cavity, on the other hand, while the results for the straight and 15° swept cavities are consistent, those with the 45° sweep do not show any consistent trend. This is not altogether surprising as this flow is dominated by strong cross flows in the spanwise direction with the result that the effect of shear layer impingement at

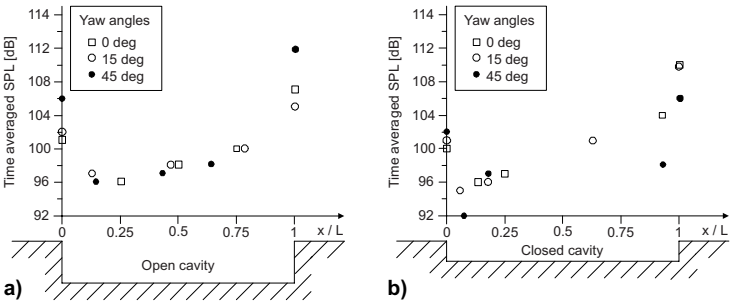

Fig. 4. Comparison of time-averaged sound pressure levels (SPL) as function of position within the cavity for open (a) and closed (b) cavity flow

the trailing edge would be weaker. The strong presence of cross flows was verified in additional experiments using oil flow visualisation.

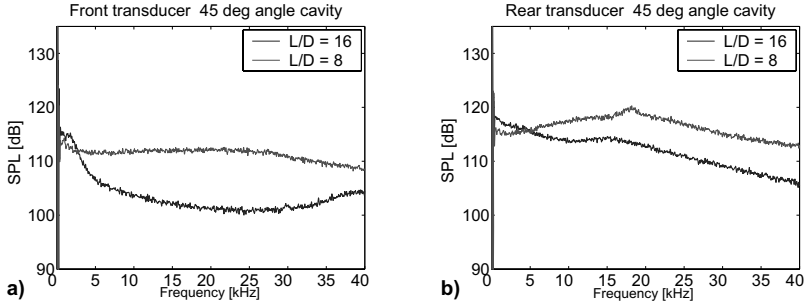

Fig. 5. Comparison of pressure oscillations at the cavity face, open and closed swept cavities; sweep angle $\psi = 45°$

Figure 5 compares the pressure oscillations for 45° swept open and closed cavities. While there are no significant peaks in the spectra, the sound pressure level for the short swept (open) cavity is generally higher.

3.4 Flow visualisation

Figures 6a and 6b show direction-indicating colour schlieren images of open and closed cavities with a 15° sweep angle. In the open cavity flow (Fig. 6a), the shear layer forming at the leading edge slightly deflects upwards causing a shock at the leading edge of the cavity. The shear layer subsequently thickens bridging the cavity before impinging on the trailing edge which gives rise to a vortex seen as a red spot at the corner surrounded by a yellow region. As a consequence of the shear layer impingement, pressure waves (seen as pink and violet regions) are generated which propagate within the cavity upstream towards the leading edge thus setting off the oscillatory mechanism. Additional time-resolved visualisation has clearly shown this wave propagation. The trailing edge shock and expansion zones are also visible.

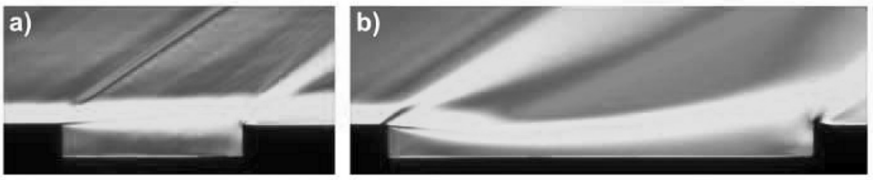

Fig. 6. Schlieren images of open (a) and closed (b) swept cavity at $\psi = 15°$

The closed cavity (Fig. 6b) flow is characterised by a very distinct concave curvature of the shear layer as the flow separates from the leading edge. It attaches to the floor and then separates before reattaching at the trailing edge. Thus there is a broad compression region (seen in pink) spanning most of the cavity floor. In the case of the straight cavity, this compression region narrows down to two shock waves, whose location corresponds to the beginning and the end of the compression region seen in the swept cavity case. Although the spectra showed no discrete frequencies, one can notice intense vortical flows and pressure waves emanating from the cavity trailing edge region and along the length of the cavity between the floor and the shear layer. The schlieren images thus broadly confirm the trend seen in the pressure data.

4 Conclusions

The unsteady pressure field of swept cavities of yaw angles 0°, 15°, and 45° was investigated and showed the following features:

- In the case of an open swept cavity, the straight (0°) and the 15° yaw angle results both showed discrete resonant tones while the 45° yaw angle cavity showed a broadband spectrum with no discrete frequencies. The agreement between the calculated and experimental Strouhal numbers was very good for the second, third and fourth Rossiter modes for the straight cavity but with increasing yaw, the agreement became poor. Also, for a given mode, there was a trend towards a small increase in Strouhal number with increase in yaw.
- In the case of the closed swept cavity, no discrete frequencies were observed in the spectra at all yaw angles and also the average sound pressure levels were lower than those of the open cavity.
- The flow features visualised by means of colour schlieren photography showed good qualitative agreement with the pressure field data.

References

1. Tracy GS, Plentovich EB: NASA TM 4436 (1993)
2. Disimile PJ, Orkwis PD: J Propulsion & Power **14**:392 (1998)
3. Charwat AE, Roos AN, Dewey FC, Hitz JA: J Aero. Sciences **28**:457 (1961)
4. Zhang X, Edwards JA: Aeronautical J **92**:355 (1992)
5. Crocco L, Lees L: J Aero. Sciences **19**:181 (1952)
6. Howe MS: *Acoustics of Fluid-Structure Interactions*, Cambridge University Press (1998)

Axisymmetric separated shock-wave boundary-layer interaction

N. Murray and R. Hillier

Department of Aeronautics, Imperial College London

1 Introduction

This paper presents a fundamental experimental study of a separated shock-wave / turbulent boundary-layer interaction in a hypersonic, turbulent flow, conducted using the Imperial College Mach 8.9 hypersonic gun tunnel. The objective is to produce the highest quality two-dimensional flow, in this case using an axisymmetric arrangement of a cowl (shock generator) and centrebody (test surface). This methodology follows the cowl-induced attached and separated interactions produced by Boyce and Hillier [11].

2 Experimental Techniques

2.1 Facility

Experiments were carried out with the cowl-centrebody configuration shown in figure 1(a), with nominal conditions of a Mach number of 8.9 and Reynolds number of 48 million/m, total temperature and pressure of $1105°K$ and 60 MPa respectively. The total run-time of the tunnel is approximately 20 ms, with steady conditions of 5 ms. The centrebody leading edge flowfield is shown in figure 1(b). The centrebody boundary layer becomes turbulent approximately 3 centrebody diameters downstream of the leading edge while the interactions occur approximately 11 diameters downstream of the leading edge.

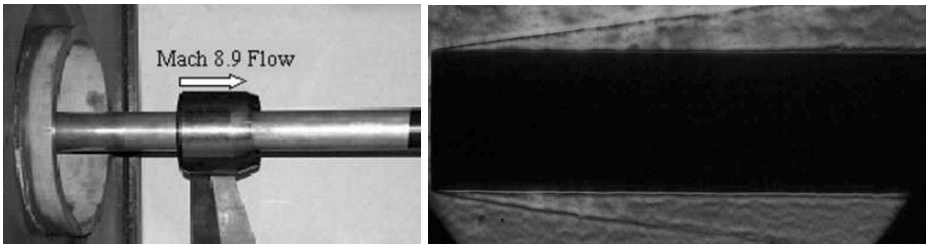

(a) Experimental Setup (b) Centrebody LE flowfield

Fig. 1. Experimental setup consisting of the centrebody and cowl in the test section of the tunnel and a schlieren picture of the centrebody leading edge flowfield.

Pressure measurements are taken using Kulite QC series transducers inserted into the centrebody. Heat transfer measurements are taken using in-house manufactured thin

film resistance temperature gauges. The temperature history recorded during a run is converted to heat transfer using the method of Cook and Felderman [2]. Oil-flow visualisations were conducted by wrapping the centerbody with a thin sheet of black plastic for contrast and painting on a film of oil and titanium oxide paste with photographs taken (1 ms exposure) during the steady run time.

3 Experimental Results

The cowl was designed with an internal compression angle of 10 degrees, providing a shock wave of sufficient strength to separate the boundary layer. Schlieren pictures of the separated region from two separate runs are shown in figure 2. The locations (1), (2) and (3) are at constant spatial positions and demonstrate that there is small scale flapping or movement of the separated flow field. The size of the bubble is noticeably smaller in Run 2 and the locations and angles of the separation and reattachment shock waves are different. These two pictures were chosen as they show the maximum captured deviation in the bubble size and separation shock wave but other pictures captured large deviations in the reattachment shockwave. The kinks and broadness of the separation and reattachment shock waves would also suggest high frequency unsteadiness within the small time-frame of the spark source. The incident shock wave on the other hand is steady.

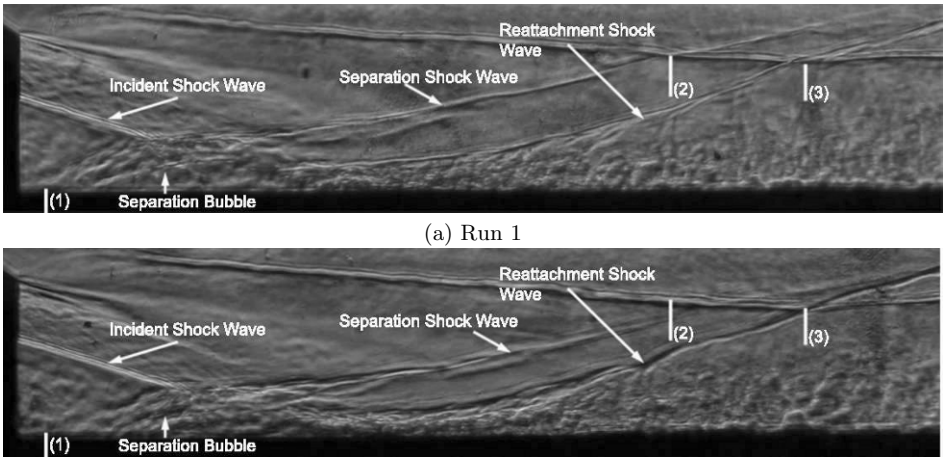

(a) Run 1

(b) Run2

Fig. 2. Schlieren visualisation depicting a detail of the separation region.

The axial pressure and heat-transfer distributions, averaged over the steady run window and taken at three azimuthal positions, are shown in figure 3. In both cases, the data collapse onto one mean profile emphasising the high degree of axisymmetry that was achieved. Achieving this is a basic requirement in the establishment of benchmark data.

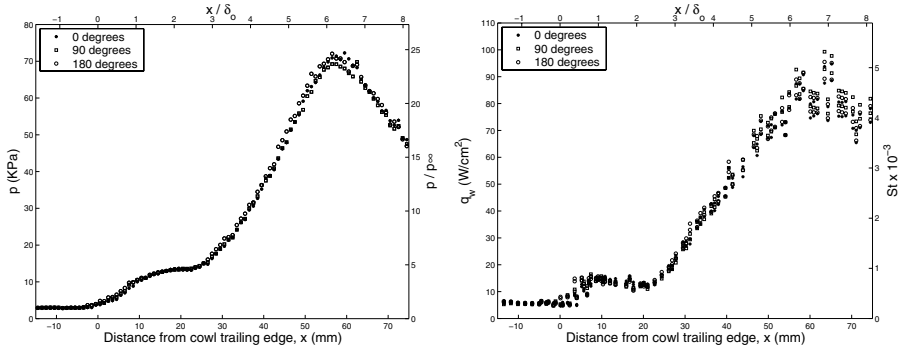

(a) Surface Pressure (b) Surface Heat-transfer

Fig. 3. Axisymmetric surface data on centrebody, measured at three azimuthal positions.

Despite the level of axisymmetry displayed by the heat-transfer data, the experimental scatter becomes noticeable at a streamwise point of $\sim 40mm$ and increases up to the heat-transfer peak. This can be related to surface striations caused by Görtler-type vortices, seen during oil-flow visualisations. These striations start at a streamwise position of approximately 40 mm and continue to develop until 60 mm downstream of the cowl trailing edge (see figure 4). The beginning and development of these striations is consistent with the increased scatter in the heat-transfer profiles.

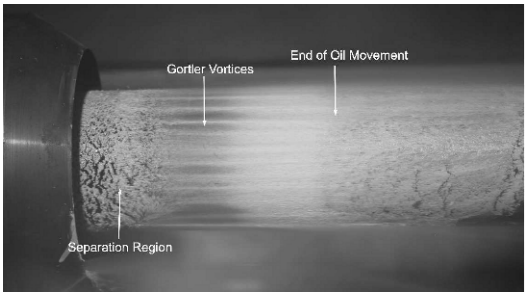

Fig. 4. Oil-flow visualisation depicting surface striations caused by the formation of Görtler-type vortices.

The visualisation shows that there are approximately 12 striations between 0° and 180° representing a "wavelength" of about 19.6 mm and a distance between striations of 9.8 mm. Görtler suggested that the average distance between striations should be 2.5δ (where δ is the local boundary layer thickness) - this was later verified by Hopkins et al. [12] to be accurate to within 20%. An estimate of the boundary layer thickness between the 40 and 45 mm, taken from the schlieren visualisations, is approximately 3.45 mm, so that the distance between striations in the oilflow is about $\approx 2.8\delta$.

Comparison with visualisations taken during repeated runs shows that the azimuthal location of the striations varies from run to run, indicating that the vortices are not fixed

and could be moving around the centrebody azimuth during run-time. However, if this were happening during the oil-flow visualisations, a smeared striation pattern should be expected rather than the defined pattern captured here. It seems likely that the presence of the oil, and of course of the underlying plastic, could be "freezing" the vortices. Either the initial striations formed in the oil prevent further movement by creating valleys in the oil film or small air pockets under the plastic, which would move from run to run due to wiping and recoating of the oil, could be forcing the location of the instability mode.

The re-attachment line can also be estimated using oil-flow visualisations and is approximately $\sim 33mm$ downstream of the cowl trailing edge.

4 Pressure and Heat-Transfer Transformation

There exist analytical models to describe approximately the relationship between surface pressure and heat-transfer [3,4], in high Reynolds Number attached flows, which use the Reynolds analogy and the Crocco relation. Equation 1, due to Coleman et al. [3], provides the predicted heat-transfer ratio Q_P (local value normalised by pre-interaction value) in terms of the corresponding pressure ratio p_r. This equation was previously shown by Murray [9] and Murray and Hillier [7,8] to be consistent through an attached interaction when the flow is in local equilibrium, i.e. in regions where changes in the local pressure gradient are small. They showed that in non-equilibrium regions, troughs can form at the pre-interaction and peak regions (see figure 5(a)) and that these troughs were not predicted by equation 1.

The equation assumes that the pressure gradient only effects the energy thickness and not the shape of the velocity profile. This explains the break down in the trough regions since these regions are dominated by inertial response (diffusive timescales are large compared to inertial timescales). This assumption must also break down in separated regions. The accuracy of equation 1 shown in previous studies [8, 9] implies that the energy thickness can dominate the changes in heat-transfer through most of a SWBLI.

$$Q_P = \left(\frac{6p_r + 1}{p_r + 6}\right) \frac{[M_\infty^2 p_r(p_r + 6)]^{0.65}}{[(6p_r + 1)M_\infty^2 - 5(p_r^2 - 1)]^{0.15}[M_\infty^2(6p_r + 1)]^{0.5}} \tag{1}$$

One of the most evident features of CFD modelling of turbulent flows is its ability to predict the surface pressure of attached flows and its relative inability to do the same for heat-transfer [5, 6, 9]. This means that equation 1 is an important indication of the expected surface heat-transfer due to a computational surface pressure profile (provided the flow satisfies the assumptions of the theory). Murray [9] used this transformation to predict surface heat-transfer through an attached interaction based on computational surface pressure (see figure 5(a)). The resulting heat-transfer predictions were more accurate than that predicted by CFD (which in this case used Menter's one equation variant of the $k - \epsilon$ model).

If this transformation is used for this separated interaction as in figure 5(b), there is very good agreement between the measured and transformed heat-transfer data outside of the separated region. It is tempting to consider the breakdown of the relationship in the separated region to be an indication of the location of the separation and reattachment points. There is in fact excellent agreement between the reattachment point predicted by oil-flow visualisations and that assumed using equation 1 (both giving it as 33 mm downstream of the cowl trailing edge). An intuitive argument can be made that since the

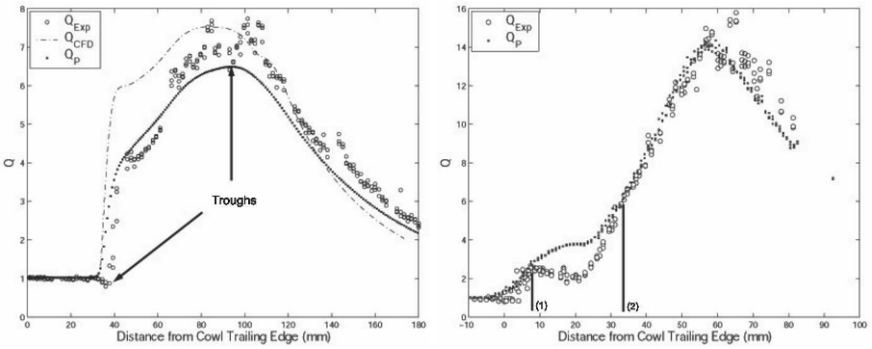

(a) Attached interaction from Murray [9]. (b) Separated interaction.

Fig. 5. Comparison between pressure and heat transfer profiles when transformed using equation 1. Q_{Exp} is the experimental heat-transfer ratio through the interaction, Q_{CFD} is the computational heat-transfer ratio through the interaction, Q_P is the predicted heat-transfer ratio.

transformation gives a very accurate indication of reattachment it should do the same for separation. The locations of separation and reattachment based on this hypothesis are noted on the figure as (1) and (2) respectively.

5 Free-Interactions

The notion of a free interaction has been used since Chapman et al. [10] noticed that for some separated flows, parts of the surface pressure curve - up to and through the separation region - were identical regardless of the strength of the incident shock. This situation is called a free interaction. Chapman documents the existence of a free interaction throughout the separation bubble, including reattachment in a laminar flow but casts doubt on the existence of a free interaction after the separation point in turbulent flows.

To isolate whether or not this axisymmetric separated flow constitutes a free-interaction it must be compared with a separated flow that has a similar incoming boundary layer, since Chapman et al [10] found that the pressure rise through a free-interaction scales with C_f. Williams [13] created a separated SWBLI in the Imperial College Gun Tunnel using a flare / centrebody configuration, using the same test conditions as these experiments, so results from his experiment can be compared with the present work.

To compare the rises in both pressure and heat-transfer through the interactions produced by the cowl and flare they are plotted together, with an offset in the streamwise direction such that the most upstream points of influence of the interactions coincide. The resulting plots are shown in figure 6. The comparisons for both surface pressure and heat-transfer display a perfect correlation between both datasets up to the plateau region, demonstrating that there exists a free-interaction up to this point. The two interactions were also shown to constitute a free-interaction at reattachment by Murray [9].

The existence of the free-interaction for the two different separation scales implies that the unsteadiness of the separated region seen in figure 2 is driven by the incoming boundary layer and not by the separation scale itself. If this were not the case, the

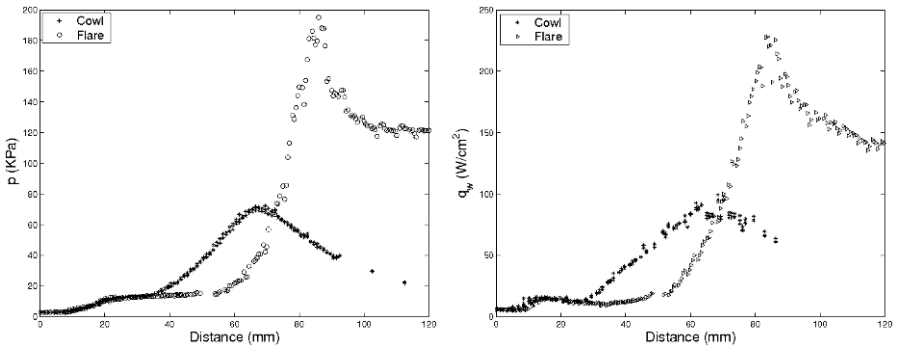

(a) Pressure. (b) Heat-transfer.

Fig. 6. Comparison of pressure and heat-transfer rise due to separation to isolate whether or not a free-interaction exists. Included is current data and that from Williams [13].

tendency of unsteadiness to smear surface profiles would mean that the pressure rise through a free interaction would depend on both C_f and the separation scale.

Acknowledgement. This research is funded by EPSRC and DSTL.

References

1. Needham D.A., Elfstrom G.M., Stollery J.L., Design and operation of the Imperial College number 2 hypersonic gun tunnel, Imperial Collge London, 1970, Aero Report, 70-04
2. Cook W.J., Felderman E.J., Reduction of data from thin film heat transfer gauges: a concise numerical technique, AIAA Journal, 1966, 4-3, 561–562,
3. Coleman G.T., Stollery J.L., Heat transfer from hypersonic turbulent flow at a wedge compression corner, J Fluid Mech, 1972, 56, 741–752.
4. Back L.H., Cuffel R.F., Changes in Heat Transfer from Turbulent Boundary Layers Interacting with Shock Waves and Expansion Waves, AIAA Journal, 1970, 8 No.10, 1871–1873.
5. Narayanswami N., Horstman C.C., Knight D.D., Computation of Crossing shock/Turbulent Boundary Layer Interaction at Mach 8.3, AIAA Journal, 31-8, 1993, 1369–1376.
6. Zha G.C., Knight D.D., Three-Dimesnsional Shock/Boundary-Layer Interaction using Reynolds Stress Equation turbulence Model, AIAA Journal, 34-7, 1996,
7. Murray N., Hillier R., Hypersonic ShockWave/Turbulent Boundary Layer Interactions In A Three-Dimensional Flow, AIAA, AIAA-2006-0121, 2006.
8. Murray N., Hillier R., Separated Shockwave / Turbulent Boundary Layer Interactions at Hypersonic Speeds, AIAA, AIAA-2006-3038, 2006.
9. Murray N., Three-Dimensional Turbulent Shock-Wave / Boundary-Layer Interactions in Hypersonic Flows, Imperial College, UK, 2007.
10. Chapman D.R., Kuehn D.M., Larson H.K., Investigation of separated flows in supersonic and subsonic streams with emphasis on the effect of transition, NACA,1356,1958,421–460.
11. Boyce R.R., Hillier R., Shock-induced three-dimensional separation of an axisymmetric hypersonic turbulent boundary layer, AIAA Journal,2000,2000–2226.
12. Hopkins E.J., Keating S.J., Bandettini A., Photographic Evidence of Streamwise Arrays of Vortices in Boundary-Layer Flow, NACA, 1960,TN D-328.
13. Williams S., Three-Dimensional Separation of a Hypersonic Boundary Layer, Imperial College, UK,2004.

Computational studies of the effect of wall temperature on hypersonic shock-induced boundary layer separation

L. Brown[1], C. Fischer[2], R.R. Boyce[1], B. Reinartz[2], and H. Olivier[2]

[1] *University of New South Wales at the Australian Defence Force Academy, Northcott Drive, Canberra, ACT 2600, Australia*
[2] *RWTH Aachen University, D-52064 Aachen, Germany*

1 Introduction

This paper shall present the numerical results of an investigation into the effect of wall to freestream temperature on boundary layer separation for a nominal flat plate/ 15degree compression corner. The numerical results will be compared to the experimental results of Bleilebens and Olivier [1]. The major findings from their study showed a distinct trend for boundary layer separation size to increase with wall-to-freestream temperature ratio; that the separation process was dictated purely by laminar effects; and that the separated shear layer transitioned to turbulence during the reattachment process. The transitional behaviour of the reattaching shear layer was characterised in their results through high Stanton number distributions post-reattachment and the observance of Gortler vortices in the infrared thermography images.

Reinartz et al [2] focussed upon assessment of the role of wall temperature and entropy layer effects for double wedge configurations, but featured an initial numerical study into the flat plate/ compression corner of Bleilebens and Olivier upon which this paper is founded. The present investigation shall build and expand upon these initial calculations. The compression corner calculations showed agreement with the separation size growth encountered during the Bleilebens and Olivier [1] experiment with increasing wall-to-freestream temperature ratio. Although the results from the FLOWer CFD code agreed well for separation size, the pressure level over the separation bubble was found to be considerably higher than that found experimentally. The 2D laminar simulations calculated with the CFD++ code overpredicted the experimental separation and the pressure level within the separation bubble, however. The expansion process post reattachment was also found to be under-predicted for both CFD codes used; these discrepancies were attributed to 3D effects neglected within the simulations. Significant improvement in the 2D double-wedge simulations were found when a turbulence model was applied at the hinge line between the first and second ramps.

A schematic (from Bleilebens and Olivier [1]) of the typical flow is given in Figure 1. The figure depicts the recirculation zone produced by the separated boundary layer; the separation and reattachment shocks; the 'triple point' where these shocks intersect and the expansion fan issuing from this intersection that is necessary for matching the pressure between streamlines that pass through the separation and reattachment shocks and streamlines that pass through the main ramp shock.

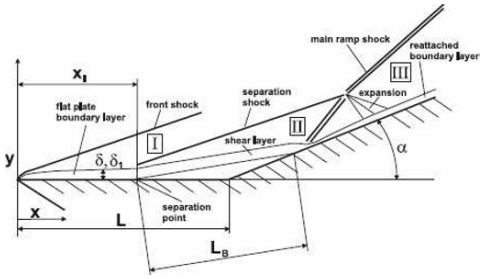

Fig. 1. Figure 1. Schematic of compression corner flow (Bleilebens and Olivier [1])

2 Numerical Method

The commercial code CFD++ (Goldberg et al [3]) was used in all of the simulations presented here. The code is a time accurate, unstructured, multi grid solver. It has a number of turbulence models, ranging from one to three equation models. The code has been developed for high speed applications and has been extensively validated for supersonic and hypersonic flow regimes, unlike many other codes whose foundations are in low speed industrial applications. Finite rate chemical reactions are also incorporated into the code.

All of the calculations were performed with a multi-species air mixture with frozen reactions. This was done because, while the low total enthalpy (3MJ/kg) of the freestream means that the effects of chemistry in the flow are negligible, the freestream was generated by expanding from a stagnant reservoir and was slightly dissociated. Modelling of the equilibrium thermodynamics of the mixture was therefore desirable to ensure congruity between numerical and experimental conditions. The turbulent calculation was conducted using the one equation Spallart-Almaras turbulence model. Based on the measurements of Bleilebens and Olivier a non-uniform inflow condition was applied to the inflow boundary of the numerical domain to accurately simulate the diverging conditions emanating from the nozzle of the TH2 shock tunnel at Aachen; these are tabulated in table 1.

Ma_∞	7.37	h_∞	0.25MJ/kg	M_{NO}	0.02285
Re_∞	$3.98\times10^6/m$	p_0	17.4MPa	M_N	0
T_∞	250K	h_0	2.98MJ/kg	$\Delta M/M$	$0.112/m$
p_∞	1983.8Pa	T_0	2500K	$\Delta u/u$	$0.055/m$
ρ_∞	$0.027kg{\cdot}m^{-3}$	M_{N2}	0.76186	$\Delta p/p$	$-0.525/m$
u_∞	2350m/s	M_{O2}	0.21268	$\Delta\rho/\rho$	$-0.443/m$

Table 1. Freestream conditions for numerical simulation of TH2 condition II

Two mesh strategies were employed for this study, a fully structured and a hybrid scheme (with structured elements for the boundary layer, a dense region of unstructured elements in the vicinity of the separated shear layer and a coarser resolution for the far field). An example of each is shown in Figure 2. The wall boundary condtions consisted of 37mm cold wall followed by a heated wall with mean temperatures of 293K, 546K and 779K for the three cases considered.

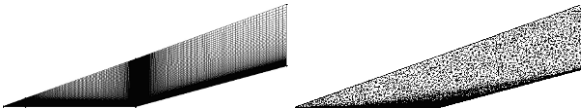

Fig. 2. (left) Structured Mesh, (right) Hybrid Mesh

It has been found that compression corner flows at hypersonic Mach numbers are extremely mesh sensitive (Reinartz et al [2,4]). A mesh dependency study for the hybrid mesh (above) by Reinartz et al [4] found there to be a significant effect of the rate of change of cell size when transitioning from an initial coarse mesh at the start of the flat plate to the fine mesh in the vicinity of separation. Mesh dependence studies for both mesh strategies exhibited mesh independence to further mesh refinement, with consideration to the cell size ratio accounted for only in the hybrid variant.

3 Results

Figure 3 shows the surface pressure coefficient measurements from both the experimental and numerical studies for 2D calculations. The pressure has been non-dimensionalised to local pressure coefficients using the local values of the non-uniform freestream conditions as reference quantities. The length scale is normalised with respect to model length and has been centred on the hinge line.

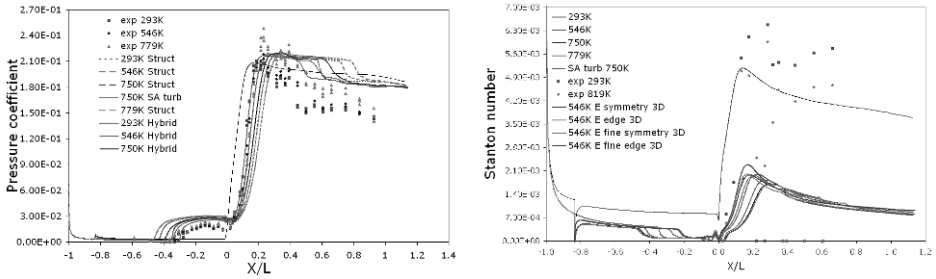

Fig. 3. (left) 2D Pressure Coefficient, (right) Stanton Number Distributions

All of the laminar cases show separation of the boundary layer and demonstrate an increase in separation size with increasing wall-to-freestream temperature ratio. The turbulent case (computed for 750K) does not exhibit boundary layer separation due to the higher momentum within the boundary layer ensuring it remains attached. The fully structured mesh calculations predict a significantly larger separation size, whereas the hybrid calculations conform to the experimental data far more favourably. At this time we have not definitively proven the cause of this anomaly and it warrants further investigation. The results from the hybrid mesh agree well with the size of separation indicated by the experimental pressure measurements, indicating a purely laminar effect

as found experimentally. There is a clear discrepancy between the pressure level within the separation bubble for the 2D laminar simulations and the measured values, however. None of the laminar simulations found any appreciable change in peak pressure during the reattachment process with increasing wall temperature, whereas there is a distinct peak in the 779K experimental results. This tendency was also found in the calculations of Reinartz et al [2].

Figure 3 presents the Stanton number comparison (similarly referenced to local freestream conditions) between the experiment and numerical simulations. The discontinuity at x/L = -0.8 is due to the step change from the cold to hot wall. It is clear from the figure that the laminar calculations vastly under-predict the Stanton number distribution downstream of the hinge line, whereas the turbulent calculation produces a Stanton number distribution far more inline with that found experimentally. This data leads to the conclusion that while the flow undergoes laminar separation it transitions to turbulence in the vicinity of reattachment. The application by Reinartz et al [2] of a turbulence model from the compression corner onwards is therefore a plausible engineering approach to assume for these flows.

The formation of Gortler vortices were cited by Bleilebens and Olivier [1] as further evidence that the flow transitions from a laminar to turbulent regime during reattachment. Various authors have numerically studied the stability of shock-induced separated boundary layers subject to small amplitude disturbances. Pagella and Rist [5] and Balakumar et al [6] found that over the separation bubble the amplification of small scale disturbances were suppressed until post-reattachment. The findings of Pagella that increased wall temperature exacerbates boundary layer instability growth provide some insight as to the significant difference between the 779K results and the other temperatures measured experimentally. Further analysis of the numerical results to characterise the Gortler number and assess the stability of the boundary layer over this region would provide deeper insight

3.1 3D simulations

Preliminary 3D runs have been performed to address the issue of edge effects present within the experiment. At this stage these calculations have not been shown to be mesh converged and are based on the fully structured 2D mesh. The results of these 3D calculations, however, provide significant insight into the role that edge effects play. Accurate simulation of these edge effects is thought to be important since the spillage of flow off the side of the model can communicate itself to the model centreline quickly via the subsonic separation zone. Depicted in Figure 4 is the symmetry plane and a plane located at the corner in the crossflow direction. Selected streamlines originating near the symmetry plane have also been plotted. As can be seen there is considerable communication through the separated region to the edge, with the separation size decreasing significantly as the edge is approached and multiple vortex structures propagating from the centreline to the edge of the model.

Figure 5 depict Mach contours of transverse slices located upstream of separation, within the separation bubble and downstream of reattachment respectively. The contribution of edge effects within the expansion region is clearly visible, thus supporting the conjecture of Reinartz et al [2] pertaining to the under-prediction of this process within 2D simulation.

The Cp plot can be found in Figure 6 comparing the 3D and 2D structured mesh results for the 546K wall temperature case and also comparing coarse (5M cells) and

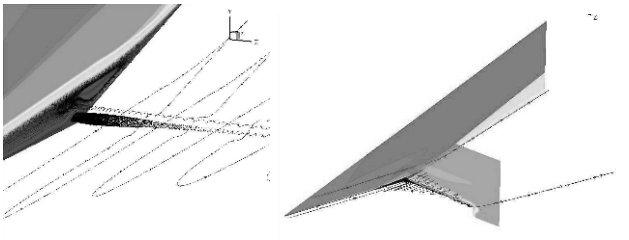

Fig. 4. 3D Centreline and Crossflow

Fig. 5. z-plane Mach Contour, x/L=-0.26, x/L=0 and x/L=0.67

fine (16M cells) meshes for the symmetry plane and edge distributions. Figure 3 showed the 3D Stanton numbers, and as expected they are grossly under-predicted due to the imposition of laminar flow conditions. The centreline pressure coefficient distribution for the fine mesh shows reasonable agreement with the experimental data for separation size and pressure level. The recompression process is predicted well and expands post-reattachment to levels akin to those found in the experiment. The 3D effects due to edge effects are therefore seen to be considerable and contribute significantly to the difference between the 2D calculations and experiment. The results are not mesh converged however.

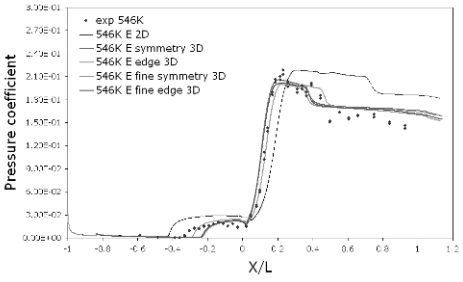

Fig. 6. 3D Pressure Coefficient

4 Conclusions

The study has shown agreement with the findings of Olivier and Bleilebens [1]. The effect of increasing wall-to-freestream temperature ratio increases the size of separation.

The separation process is dominated by laminar effects, with transition to turbulence occurring after the separation process. Significant mesh sensitivity has been found to occur for these flows. 3D effects have been identified as having a considerable effect upon the surface pressure distribution. Spillage from the centreline of the model off the edge of the model occurs and contributes to the reduced separation bubble pressure measured during the experiment when compared with 2D laminar calculations. 3D effects also significantly contribute to the expansion fan (issuing from the intersection of the ramp, separation and reattachment shocks) impingement upon the model surface and the ensuing surface pressures that this produces.

References

1. Bleilebens M., Olivier H., On the influence of elevated surface temperatures on hypersonic shock wave/boundary layer interaction at a heated ramp model, Shock Waves 15:301-312, May 2006
2. Reinartz B., Ballmann J., Boyce R.R., Numerical Investigation of Wall Temperature and Entropy Layer Effects of Double Wedge Shock/ Boundary Layer Interactions, AIAA Paper 2006-8137, 2006
3. Goldberg U., Batten P., Palaniswamy S., Chakravarthy S., Peroomian O., Hypersonic Flow Predictions Using Linear and Nonlinear Turbulence Closures, AIAA J. of Aircraft, Vol. 37, No. 4, 671-675, 2000
4. Reinartz B., Ballmann J., Fischer C., Boyce R.R., Brown L., Shock Wave/ Boundary Layer Interactions on Hypersonic Intake Flows, 2nd European Conference for Aero-Space Sciences, Brussels, Belgium, July 1-6, 2007
5. Pagella A., Rist U., Instability and Transition in Shock-Induced Separation Bubbles, Meeting Proceedings RTO-MP-AVT-111, Prague, Czech Republic, 2004
6. Balakumur P., Zhao H., Atkins H., Stability of Hypersonic Boundary Layers over a Compression Corner, AIAA Journal, Vol. 43, No. 4, April 2005

Dynamics of unsteady shock wave motion

P.J.K. Bruce and H. Babinsky

Department of Engineering, University of Cambridge, Trumpington St., Cambridge CB2 1PZ, UK

Summary. An experimental study of a normal shock wave subject to unsteady periodic forcing in a parallel walled duct has been conducted. Measurements of the pressure rise across the shock wave have been taken and the dynamics of unsteady shock wave motion have been analysed from high speed schlieren images. The velocity of shock wave motion is shown to be related to the instantaneous pressure ratio across a shock wave. The relative importance of geometry and pressure perturbation frequency on dynamic shock wave behaviour is considered and the concept of a critical frequency is proposed, which relates the two. In the absence of flow separation the effects of viscosity on the dynamics of unsteady shock wave motion appear to be small. Further work establishing non-dimensional relations is proposed to improve the general applicability of the findings of this study.

1 Introduction

Shock wave / boundary layer interactions (SBLIs) occur in many high speed aerodynamic applications and often have detrimental effects on performance. In many instances, interactions have been observed to exhibit significant unsteady behaviour. Due to the large changes in local flow properties that occur across shock waves, the presence of unsteady effects can lead to large and undesirable local fluctuations in properties such as pressure and the rate of heat transfer. Current understanding of the mechanisms that govern unsteady SBLIs has not yet reached the level where unsteady effects can be reliably predicted. For this reason, modern design methods use rules of thumb and large safety margins to avoid designing applications where unsteady SBLIs are likely to be present. This cautious approach of avoiding, rather than designing for, SBLI unsteadiness is a limiting factor in the design of modern high speed aerodynamic applications.

It is widely accepted that many examples of unsteady shock wave behaviour, such as buffeting of transonic aerofoils [1] and buzz or engine unstart in supersonic engine intakes, are caused by periodic pressure perturbations downstream of the shock wave. On a transonic aerofoil, these may come from the aerofoil's wake while, in an aero-engine, they might originate from the face of the compressor. Despite the serious safety and performance implications of phenomena such as transonic buffeting and engine unstart, no reliable techniques for predicting their characteristics exist. In a previous study [2], it was found that unsteady SBLIs are influenced by a combination of viscous and inviscid factors but their relative effect on the oscillation amplitude was not studied. At very high frequencies, the amplitude of shock wave motion is known to be very small and of little concern. With decreasing frequency however, the amplitude of unsteady shock wave motion has been shown to increase [3], though the reasons for this are not well understood. It is the aim of the present study to address this particular issue.

2 Experimental Methods

Experiments have been performed in the blowdown-type supersonic wind tunnels of the University of Cambridge. The tunnels have a rectangular working section with a constant cross section 114 mm wide and 178 mm high. For the present study, an elliptical cam was mounted at the beginning of the first diffuser, 790 mm downstream of the mean shock position, as shown in fig. 1(a). During tunnel runs, the tunnel stagnation pressure was held constant and the cam was rotated at frequencies between 8 and 46 Hz to produce a periodic variation in tunnel back pressure at a frequency double that of cam rotation. Fig. 1(b) shows measurements of static pressure beneath the rotating cam at a cam rotational frequency of 20 Hz. It can be seen that the pressure varies almost sinusoidally, and this was observed to be the case at all frequencies tested. This fluctuating back pressure caused the position of the tunnel's normal recovery shock wave to oscillate about its mean position. The tunnel operating parameters were chosen so that the shock wave was located at the centre of the working section window under steady flow conditions.

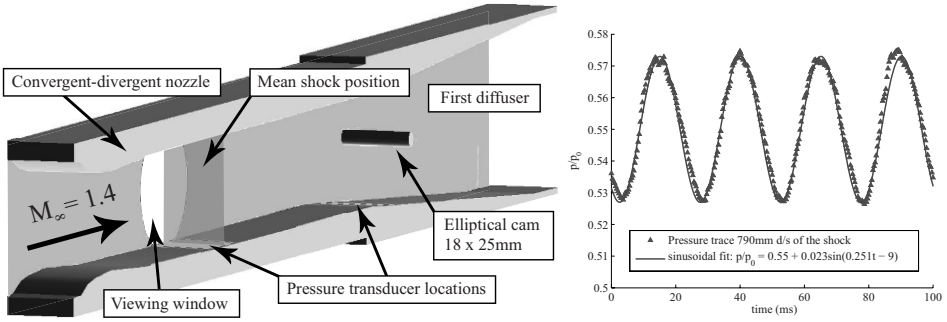

a) Wind tunnel working section b) Tunnel back pressure

Fig. 1. Experimental arrangement

Wall static pressure measurements were obtained using eight Druck PDCR-200 series pressure transducers located directly beneath 0.5 mm diameter holes in the areas of the tunnel floor highlighted in fig. 1(a). High speed schlieren images were obtained using a Photron FASTCAM-ultima APX high speed camera at shutter speeds of 1/6000 s and a resolution of 512x512 pixels.

Analytical and computational study

In addition to experiments, a simple analytical and computational study of a normal shock wave of strength $M_\infty = 1.4$ in a duct subject to downstream pressure variations has been conducted. Parallel and diverging duct geometries were investigated, as shown in fig. 2. In all cases, the magnitude of downstream pressure perturbations have been scaled to match those measured experimentally.

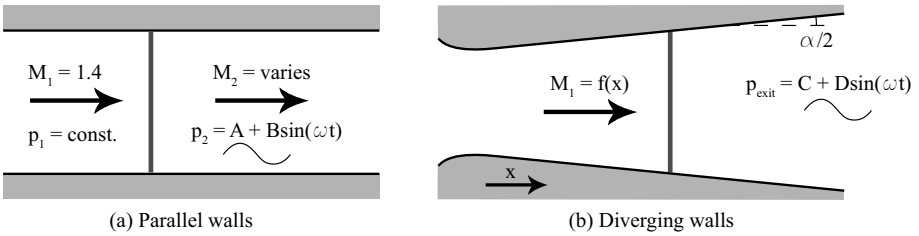

(a) Parallel walls (b) Diverging walls

Fig. 2. Duct geometries used for the analytical and computational study

3 Results

When subjected to sinusoidal variations of downstream pressure, the normal shock wave undergoes consistent and repeatable periodic motion. Fig. 3(a) shows plots of position, velocity and acceleration for a complete cycle of periodic shock wave motion at a shock wave oscillation frequency of 40 Hz. Fig. 3(b) shows a selection of schlieren images that correspond to the points in the cycle marked A, B, C and D. All images measure approximately 110 mm by 40 mm and the flow is from left to right. The arrows on the images indicate the direction of shock wave motion.

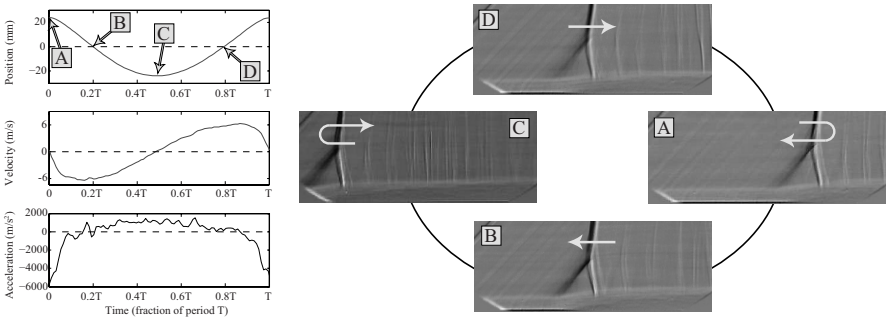

(a) Dynamics (b) Schlieren images

Fig. 3. Results for a shock wave oscillation frequency of 40 Hz

The skewed velocity variation is caused by bunching and spreading of compression and expansion waves, respectively, as they travel upstream from the cam. This is most clearly seen by the spike in the acceleration plot at position A, which is due to bunching of compression waves leading to a very rapid rise in pressure behind the shock wave which encourages upstream motion. Results at all frequencies are broadly similar to those presented in fig. 3. The main difference is that amplitudes decrease and accelerations increase with increasing frequency. Peak velocities at all frequencies are around 7 m/s

in both the upstream and downstream directions, which is of the order of ±2% of the freestream velocity, $U_\infty = 410$ m/s. This corresponds to a change in the relative Mach number of the shock wave of the order of ±2%.

Fig. 4 shows the pressure rise at two points of the unsteady SBLI cycle when the shock wave is in same place but traveling in different directions (points B and D in fig. 3) compared to the pressure rise through a steady SBLI at $M_\infty = 1.4$. Also marked on the graph are two predicted downstream pressures. These were calculated based on the expected pressure rise across the interaction for the instantaneous relative Mach numbers shown on the images, scaled to the same constant upstream pressure as the steady interaction.

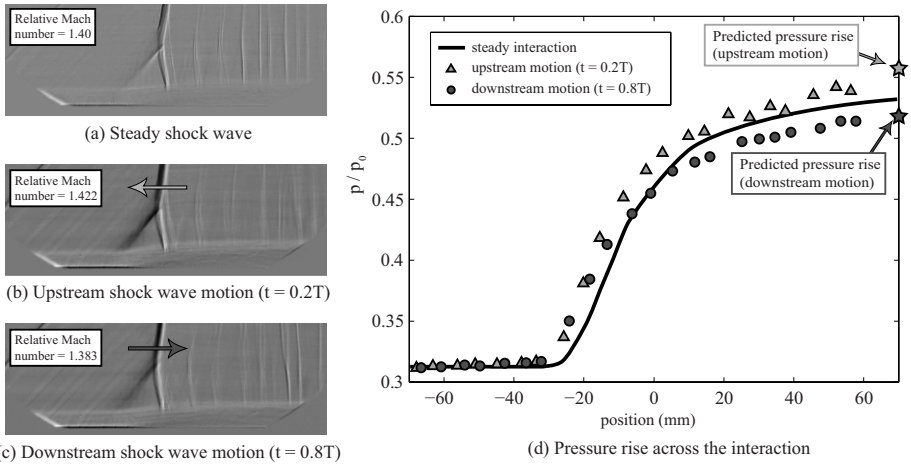

Fig. 4. Comparison of pressure rise during upstream and downstream shock wave motion for a shock wave oscillation frequency of 70 Hz

The predicted pressure rises closely match the experimental measurements in fig. 4 and this suggests that the pressure jump across the unsteady SBLI depends only on the flow Mach number relative to the shock wave. This implies that the velocity of shock wave motion can be determined analytically for a given (varying) pressure ratio. Furthermore, given the pressure variation driving shock wave motion, the shock wave trajectory can easily be calculated by integrating the predicted shock wave velocities, thus yielding the amplitude of shock wave motion. Fig. 5 shows the results of such a calculation for various frequencies of pressure fluctuation, together with experimentally measured amplitudes.

The agreement between prediction and experiment is very good. This clearly suggests that unsteady shock wave motion is simply the mechanism by which a shock wave changes its strength to satisfy an imposed varying pressure ratio. For a given pressure fluctuation, shock wave velocities should therefore be independent of frequency and this is indeed the case, as previously observed. Experimentally measured amplitudes are in general around 20% below the analytical prediction, which suggests that other, most likely viscous, factors are also of some importance.

Fig. 5 predicts that oscillation amplitudes become infinitely large for frequencies tending to zero. While this is correct for a truly inviscid parallel duct, it clearly cannot be

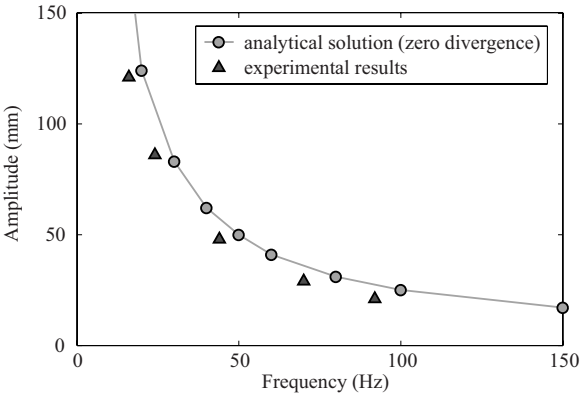

Fig. 5. Comparison of analytical and experimental results

the case in a diverging duct. The effect of divergence has been studied computationally using a simple 1D Euler scheme. The results for a number of different duct divergence angles are presented in fig. 6.

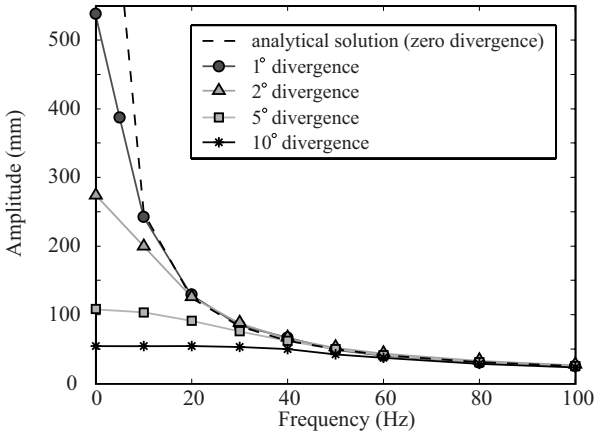

Fig. 6. Effect of divergence

The results show that at low frequency, the amplitude of shock wave motion tends toward limit amplitudes. These correspond to the difference in the steady shock wave positions at the extremes of the duct exit pressures. These effectively set the 'steady state' upstream and downstream positions of the shock wave and hence the 'zero-frequency amplitude'. At higher frequencies, the amplitude of shock wave oscillation is largely independent of divergence angle and very closely matches the analytical prediction for parallel ducts. Fig. 7 shows the general shock wave behaviour.

For a given geometry and imposed downstream pressure perturbation, a critical frequency exists such that: At frequencies below f_{crit}, the amplitude of shock wave motion is primarily determined by the divergence of the duct and is independent of frequency, while

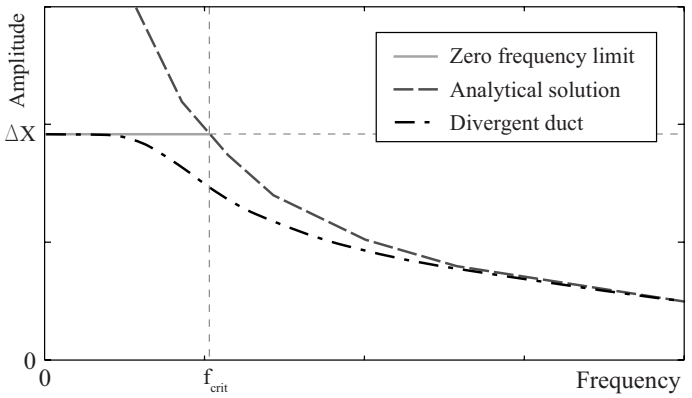

Fig. 7. Amplitude - frequency relation in a diverging duct

at frequencies above f_{crit}, the amplitude becomes almost independent of duct divergence and is only a function of frequency. The implications of this are potentially significant, and the ability to predict the critical frequency could be of great use to designers.

4 Conclusion

Experiments studying the dynamics of unsteady shock wave motion have been performed. The relationship between the amplitude and frequency of unsteady shock wave motion has been measured and a model for the situation of a normal shock wave in a diverging duct has been outlined. A critical frequency is proposed that relates the relative importance of geometry and the frequency of pressure perturbation to dynamic shock wave behaviour. Simple inviscid analytical and computational schemes have been observed to capture the overall physics of the situation, suggesting the effects of viscosity are small in the current setup. The findings of this work have implications for the unsteady performance of applications such as transonic diffusers, mixed compression engine inlets and transonic aerofoils. Further work is needed to establish non-dimensional relations and allow a more fundamental analysis of the problem and greater applicability to real-world situations.

References

1. Lee, B.H.K.: Self-sustained Shock Oscillations on Airfoils at Transonic Speeds, Progress in Aerospace Sciences 37, pp147–196, 2001
2. Bruce, P.J.K. and Babinsky, H.: An Experimental Study of Unsteady Separated Shock Wave Boundary Layer Interactions, AIAA Paper 2007-1140, 2007
3. Galli, A. and Corbel, B. and Bur, R.: Control of Forced Shock-Wave Oscillations and Separated Boundary Layer Interaction, Aerospace Science and Technology 9, pp653–660, 2005

Experimental investigation of heat transfer characteristic in supersonic flow field on a sharp fin shape

J.W. Song[1], J.J. Yi[1], M.S. Yu[2], H.H. Cho[1], K.Y. Hwnag[3], and J.C. Bae[3]

[1] *Department of Mechanical Engineering, Yonsei University, 120-749, Republic of Korea*
[2] *Department of Mechanical Engineering, Yonsei University, 120-749, Republic of Korea, presently National Science Museum Planning Office, Ministry of Science and Technology, 427-060, Republic of Korea*
[3] *Agency for Defense Development, P.O. Box 35, Yuseong, Daejeon*

1 Introduction

The development of a supersonic speed flight, one problem of practical importance is the inviscid/viscous interaction between shock wave and turbulent boundary layer. High local surface heat transfer could cause the burn-out of important units protruded into a supersonic flow field. Also, the large spatial difference of heating rates could bring a large thermal stress on a vehicle surface. For last decades, many researchers have tried to understand the flow structure and heat transfer phenomena near the protruding body in a supersonic flow. Aso[1] has measured pressure and heat flux distribution in the separated flow region by sharp fin and Stanton number is calculated from the measured heat flux. He showed the increase in pressure distribution and heat transfer in a separated and a reattachment flow region. However, this test needs a long test time for measuring two-dimensional distribution with 10 array sensors. Alvi[2] showed the sharp fin generating lambda-shock structure by using PLS (Planar Laser Scattering) imaging technique. But the investigation focused only on a shock visualization. Lu[3] proposed the correlation between a Mach number and an angle made by inviscid shock wave trace. But Lu's experiment also did not contain the pressure and heat transfer distribution data either. Knight[4] has conducted the numerical simulation and the experiment for the backward of a sharp fin in supersonic turbulent flow. Rodi[5] has studied the comparison of pressure distributions between a sharp and a blunt fin. Even in this test, he failed to include the heat transfer distribution to the results. In this study, heat transfer near a sharp fin was investigated. The fin rotating angle is considered as a parameter. We took the surface temperature images using an infra-red camera for the turbulent flow separated regions near sharp fins. To satisfy the constant heat flux condition on a surface, we made a thin foil heater which can be installed to the bottom surface near the fin. For the understanding of flow characteristics around a fin, the oil-lampblack method was also conducted.

2 Experimental Program

2.1 Supersonic blow-down tunnel

Figure 1 is the schematic diagram of the blow-down tunnel used in this study. Before the tunnel, there are the high pressure flow generating equipments consisting of air compressor, buffer, filters and storage tanks. The compressor can compress the air up to

20MPa and the pressurized air is stored to air tanks whose storage capacity is $1.8m^3$, respectively. Compressed air is going through the buffer tank and cooled down. When experiment starts, the compressed air is supplied from tanks to the stagnation chamber lowering its pressure level 150 to 6 down by a pressure regulator. In the inlet part of stagnation chamber, the cone-type separator and the 5 stages screen are installed to increase the flow uniformity and the lower turbulence level in a stagnation chamber. Settled flow in a stagnation chamber is accelerated through a supersonic nozzle whose designed Mach number of nozzle is three. The accelerated flow enters into the test chamber, where the pressure transducer and the windows for shock visualization are prepared. After the test chamber, the diffuser and the silencer are positioned for the pressure recovery and the noise reduction, respectively.

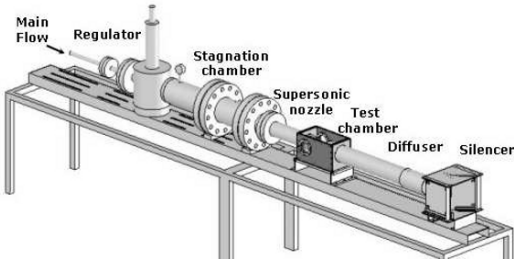

Fig. 1. Schematic diagram of Supersonic blow-down tunnel

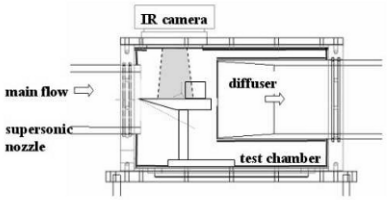

Fig. 2. Schematic diagram of Test Chamber

2.2 Test model and other supplement equipments

Figure 2 is the schematic diagram of a test chamber. Test chamber is located between a forward nozzle and a backward diffuser. And test model, which is installed inside of test chamber, is generated shock wave. When the experiment is started supersonic air is passes around a fin and motivating shock wave. This shock wave could interact with a boundary layer resulting in the change of surface temperature distribution and these variations of temperature were measured by an infra-red camera. During the test, a test chamber should be maintained in a nearly vacuum state. Therefore, the test chamber should be tightly sealed up after installing the test model and an infra-red camera. Sharp fin was used as a protruded body and the fin-installed test model is illustrating well Fig. 3. Fin was made of Aluminum. In a sharp fin case, the considered wedge angle were 12.5 °,15 °,17.5 °, and 20 °. All fins were unswept type. To produce a constant heat flux condition on a considered surface around the fin, the thin foil heater is designed and manufactured. The total thickness of a heater is 0.2mm. The electric resistance is 200Ω for a sharp fin. Heater were adhered to the teflon block by RTV. Below the thin foil heater, the teflon block and the mineral wool are positioned as thermal insulators with thickness and respectively as shown in Fig. 3. The infer-red camera has a 0.03K resolution and its frequency is almost 1Hz. And also camera has spatial resolution of 300×200 pixel. On the most of test model and test chamber, the flat black lacquer sprayed and its emissivity is found to be about 0.89 from the calibration test and is considered when the result of

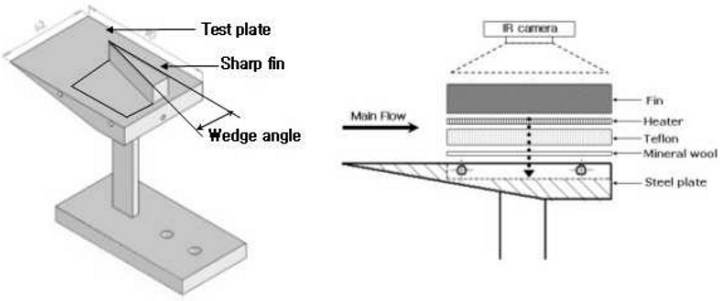

Fig. 3. Illustration of Sharp fin and Test plate

infra-red image is processed to calculate the surface distribution on a surface. To the foil heater, the direct current is supplied by the power whose maximum voltage and current are 200V and 20A, respectively. And the current value is monitored during the test by checking the voltage drop across the shunt positioned in the middle of an electric circuit. The most of voltage signals from sensors such as pressure transducer and thermocouples are received by the voltmeter and processed in a computer.

2.3 Experimental condition and test procedure

The upstream Mach number is about 3 and the unit Reynolds number in an free stream is about $5 \times 10^7/m$, respectively. Figure 4 shows the pressure and the temperature in the stagnation chamber and the pressure in a test chamber during the test. During the test, stagnation and test chamber pressure are almost maintained to be 6atm and 0.16atm, respectively. The stagnation chamber temperature also reaches to the steady state condition in nearly ten seconds although slight decrease is observed due to the gas expansion in air tanks and the Joule-Thompson effect at the valve and the pressure regulator. In this condition, Mach number is about three which is calculated by equation 1 as follows.

$$\frac{P_0}{P} = \left[1 + \frac{(k-1)}{2} M^2\right]^{\frac{k}{k-1}} \tag{1}$$

The experiments are conducted under the constant heat flux condition. Heat flux was calculated by equation 2.

$$\dot{q} = \dot{q}_g - \dot{q}_l \tag{2}$$

$\dot{q_g} = I^2 R$: generating heat flux on heater
$\dot{q_l}$: heat loss in the backward of the test plate
I : measured electrical current , R : electrical resistance of a thin foil heater

By the analysis of 1-dimensional transient conduction problem, heat loss is estimated to be about 8% when heat flux is $23,000 W/m^2$.
Heat transfer coefficient is calculated by following equation 3.

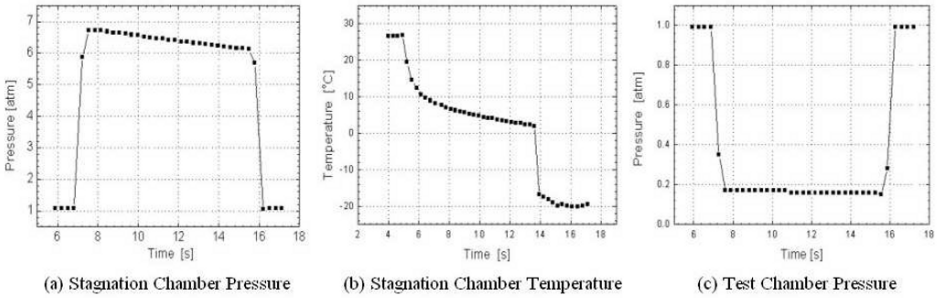

(a) Stagnation Chamber Pressure (b) Stagnation Chamber Temperature (c) Test Chamber Pressure

Fig. 4. Graph of chamber pressure and temperature

$$h = \frac{\dot{q}}{T_w - T_{aw}} \left[1 - (\frac{\xi}{x})^{0.9} \right]^{-\frac{1}{9}} \tag{3}$$

T_w : measured surface temperature
$T_{aw} = T_0 \frac{1+r\frac{k-1}{2}Ma^2}{1+\frac{k-1}{2}Ma^2}$: adiabatic wall temperature
r, k and Ma are the freestream recovery factor, specific heat ratio and Mach number.

3 Discussion of Results

3.1 Oil and lampblack method

We used oil and lampblack method in order to see the surface flow streak line which can be varied by the flow field change due to a protruded fin. We spread on the smooth surface of the test plate the mixture of carbon powder and silicon oil that is viscous enough not to be flown off in the flow. Figure 5 is the picture of streak line of sharp fin with a wedge angle of 20 degree. In Fig. 5, both of 1st and 2nd separation lines can be observed. These separation lines are also observed in case of wedge angles of 12.5 ° and 17.5 ° in Fig. 6.

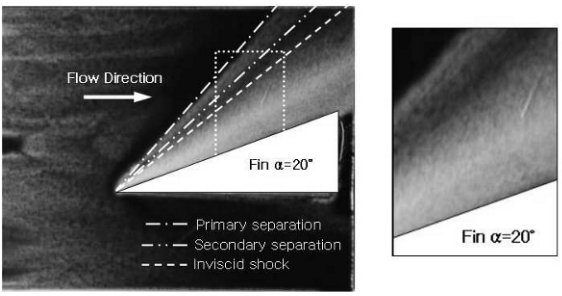

Fig. 5. Flow visualization by oil and lampblack

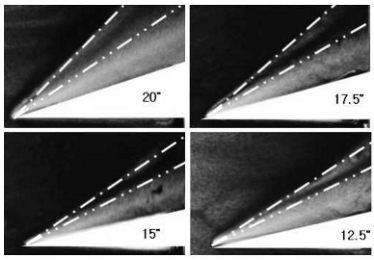

Fig. 6. Flow visualization by oil and lampblack on different wedge angle sharp fin

For the relation between fin wedge angle and 1st separation line angle , linear correlation equation is obtained and plotted in Fig. 7 together with an experimental result. First flow separation line is known to appear slightly ahead of the inviscid shock wave line. This flow separation in an upstream of inviscid shock wave is induced due to the upstream propagation of an increased pressure by the interaction between an inviscid shock wave and a boundary layer. Secondary separation line tends to be obscure with decreasing fin wedge angle. Especially, in a case of fin wedge angle less than 12.5 °, the secondary separation line cannot be observed.

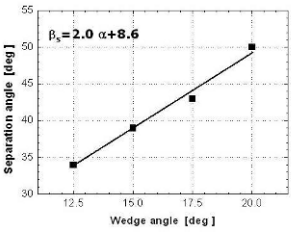

Fig. 7. Plot of 1st separation line angles to fin wedge angle

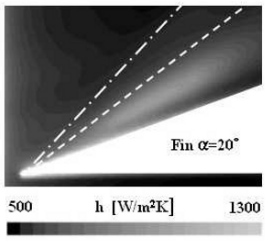

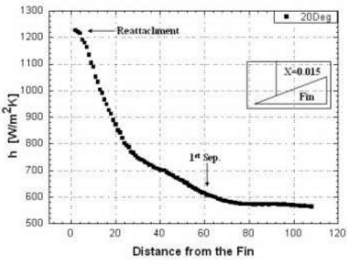

Fig. 8. Convective heat transfer coefficient distribution of sharp fin

3.2 Convective heat transfer coefficient

Convective heat transfer coefficient was calculated by surface temperature distribution with an infra-red thermography. Figure 8 shows an obtained distribution of convective heat transfer coefficient for the case of fin wedge angle 20 °. 1st separation line and inviscid shock line were also illustrated in Fig. 8 for reference. Heat transfer coefficient starts to increase gradually in a downstream from the point of flow separation. It has the highest value of $1200 W/m^2K$ at the region expected as a reattachment region. It is 2.5 times as high in that of the region where there is no interference between a boundary layer and a shock wave. The reason for this is as follows: Separated boundary layer flow impinges the flat surface in the region between fin and inviscid shock with a high turbulence level resulting in a high heat transfer. Heat transfer coefficient and pressure distribution are shown in Fig. 9. In this figure, it can be found that the second flow separation does not affect the heat transfer phenomena while the surface pressure changes largely. Figure 10 shows the more wedge angle increases, the more peak heat transfer coefficient value increases. Also, as the angle of the inviscid shock wave increases, the area becomes resulting in a wide heat transfer promoted area as shown in Fig. 10.

4 Conclusion

In this study, aerodynamic heating phenomena caused by interaction of shock wave with the turbulent boundary layer was investigated. An experimental study was performed for convective heat transfer around fin in supersonic flow field. During the experiment,

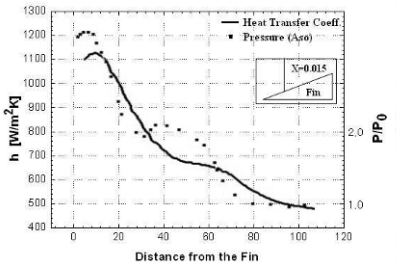

Fig. 9. Comparison with pressure and heat transfer coefficient distribution on sharp fin

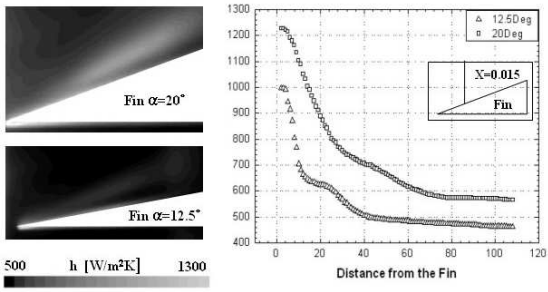

Fig. 10. Convective heat transfer coefficient distribution for different wedge angle

the wedge angle is considered as a parameter. Convective heat transfer coefficient of sharp fin increase gradually after 1st separation line. We found that the peak value of heat transfer coefficient appears at the location where the flow reattachment is expected. Distributions of pressure and heat transfer coefficient are similar in most area but 2nd separation did not affect on distribution of heat transfer coefficient unlike distribution of pressure. The distribution of heat transfer coefficient for sharp fin at the expected region of reattachment is 2.5 times higher than that of none interference region. The value of heat transfer coefficient increases with wedge angle. As wedge angle increasing, high heat transfer coefficient maintained region is also increasing.

Acknowledgement. This work was supported by Defense Acquisition Program Administration and Agency for Defense Development under the contract UD060016AD.

References

1. Shigeru Aso, Masanori Hayashi and Anzhong Tan : The Structure of Aerodynamic Heating in Three-Dimensional Shock Wave/Turbulent Boundary Layer Interactions Induce by Sharp Fin and Blunt Fins. AIAA, 89-1854
2. F. S. Alvi and G. S. Settles : Physical Model of the Swept Shock Wave/Boundary-Layer Interaction Flow Field. AIAA Jouna , Vol. 30, No. 9, September 1992
3. F. K. Lu, G. S. Settles and C. C. Horstman : Mach Number Effects on Conical Surface Features of Swept Shock-Wave/Boundary-Layer Interactions, AIAA Jounal, Vol. 28, No. 1, January 1990
4. Doyle D. Knight, T.J. Garrison, G.S. Settles, A.A. Zheltovodov, A.I. Maksimov and A.M. Shevchenko, and S. S. Vorontsov : Asymmetric Crossing-Shock-Wave/Turbulent-Boundary-Layer Interaction, AIAA Jounal, Vol. 33, No. 12, December 1995
5. P. E. Rodi and D. S. Dolling : Behavior of Pressure and Heat Transfer in Sharp Fin-Induce Turbulent Interaction", AIAA Jounal, Vol. 33, No. 11, November 1995

Experimental investigation of the sliding electric frequency mode arc discharge in the subsonic and supersonic flow

V.S. Aksenov[1], S.A. Gubin[1], K.V. Efremov[1], and V.V. Golub[2]

[1] *Moscow Engineering Physics Institute, Kashirskoe shosse 31, Moscow, 115409, Russian Federation*

[2] *Institute for High Energy Densities, Russian Academy of Sciences, Izhorskaya str. 13/19, Moscow, 125412, Russian Federation*

1 Introduction

The plasma of the discharge, initiated along a surface of wing or the fuselage, is promising aircraft control facility. Strong shock wave formation at air gap disruption by the sliding discharge (SD) changes a flow over aircraft surface and creates an impulse for changing a trajectory of flight (see Figure 1). Critical existence conditions measurements of the sliding discharge in an air flow are important for its application in supersonic aircraft. These conditions at supersonic flows were investigated earlier [1], [2]. The purpose of this work is to direct measure of efficiency SD to create impulse obtained by wing in the subsonic and supersonic air flow.

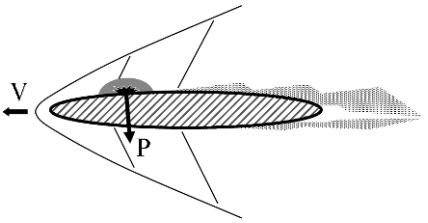

Fig. 1. General diagram of the discharge action to the aircraft wing

2 Experimental setup

The sliding arc discharge was studied in a frequency mode in air flow. Used air flows were created by ventilator or by air outflow to the vacuumed capacity. In this work the investigated discharge is the air disruption between electrodes and a surface of a semiconducting coal-graphite rod (Figure 2a). Direction of discharge is perpendicular to a flow and smooth up with a surface of streamline bodies (wedge with a 10 degree streamlined corner or wing model). The discharged gap between electrodes was 4 cm - 8 cm. The voltage between electrodes was registered. Process of discharge was recorded by video camera. Scheme and photo of investigated wing model are shown on Figure 3. We used two flow-generated modes: flow with velocity 520 m/s (pressure in nozzle 0.16 atm) and flow with velocity 200 m/s (pressure in nozzle 0.24 atm). Investigated wing with discharger and wind tunnel are shown on Figure 4.

For measuring impulse from the discharge, aerodynamic balances were constructed. Own oscillation frequency of balance was of about 100 Hz. The cable and strain gauge

were protected from the airflow and heat exchange as minimum for 30 seconds. Strain gauge receives effort to perpendicular of model wing plane. The calibration of aerodynamic balances was produced by falling of calibrated preliminary heated clay ball. Shock from ball was inelastic.

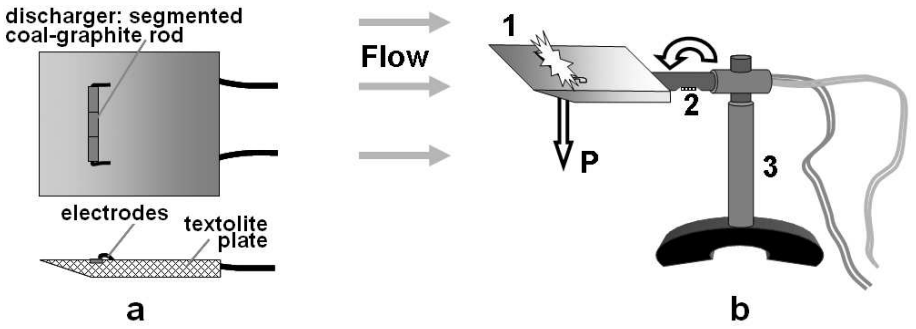

Fig. 2. a - Scheme of supersonic wing model with segmented discharger. Wedge with the sizes of a plane 8 cm x 12 cm. Discharged gap is 4 cm (between electrodes). **b** - Scheme of measuring of discharge impulse using aerodynamic balances in air flow. 1 - wing model with segmented discharger (upper plane of wedge it is parallel to flow), 2 - strain gauge, 3 - the rigid support

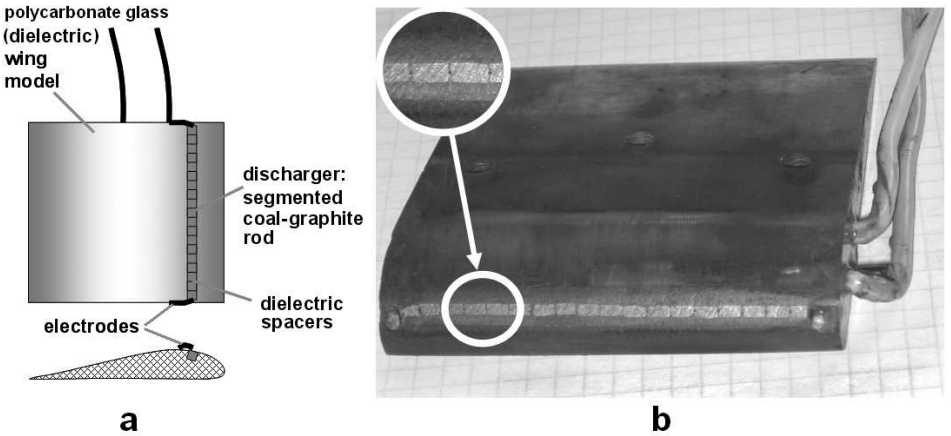

Fig. 3. a - Scheme of wing model. The discharged gap between electrodes is 8 cm. **b** - Photo of investigated wing

3 Experimental results

First experiments with slow air flows (with speed 40 m/s) demonstrated no visible influence of flow on the discharge. It was shown that the major determining factors of stability of the discharge were an intensity of a field on an discharger, size of discharger segments, a warming up of electrodes and pressure (electric durability of air depends on pressure).

All experiments carried out by us confirm the possibility of stable excitation of the sliding discharge in wind tunnel at air flow velocities from 200 m/s up to 520 m/s and intensity of an electric field from 0.5 kV/cm up to 1.0 kV/cm (Figure 5). Frames 1 - 4 on

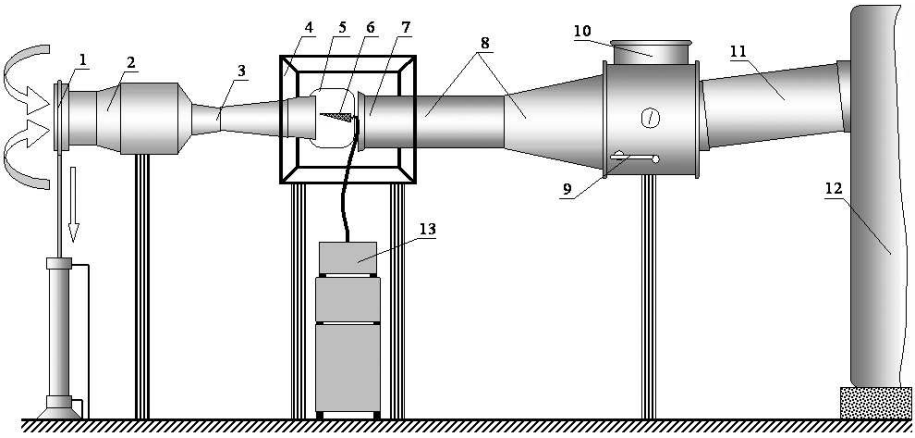

Fig. 4. Experimental setup: supersonic wind tube. 1 - pneumatic cutoff plate-bolt, 2 - receiver, 3 - supersonic nozzle, 4 - Eiffel's camera, 5 - window, 6 - is model wing-discharger, 7 - the entrance of diffuser, 8 - diffuser, 9 - the drive of vacuum lock, 10 - vacuum lock, 11 - connecting conduit, 12 - vacuum gas holder (120 cubic meters, 10 mm Hg), 13 - apparatus counter with the power unit of the discharger

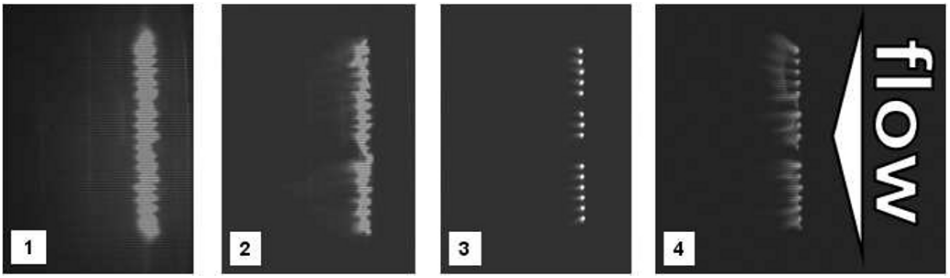

Fig. 5. The frames of wing-discharger work in the airflow with velocity of 200 m/s (frequency - 10 Hz, energy of one discharge - 15 J)

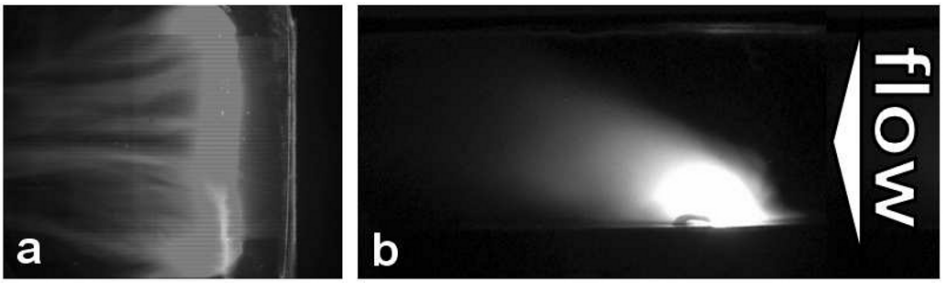

Fig. 6. a - Work of discharger in the wind tunnel. The flow velocity is 520 m/s, frequency - 10 Hz, energy - 150 J. **b** - The work of wedge-shaped discharger in the pulsed operation with the capacity energy 270 J in the airflow 520 m/s, flow direction is from right to left. Wing is located horizontally

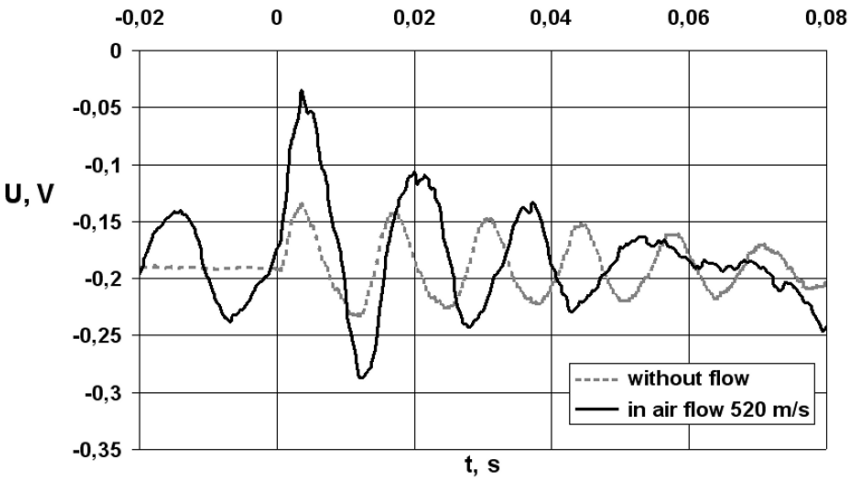

Fig. 7. Oscillogram of the action of the typical discharge with the energy 265 J on the wing in quiescent air and in the supersonic airflow (520 m/s)

Figure 5 - were recorded with exposure time 0.03 s for different discharges. Flow velocity (200 m/s), frequency (10 Hz), energy (15 J) were the same. Frame 1 is typical SD. Frame 2 demonstrates SD with one segment lost. Frame 3 and 4 is work of discharger when three segments were lost by flow, but discharger continued to functionate. Discharger energies were 8 J - 40 J at brought average power from 100 W up to 500 W. Discharges frequency was varied up to 40 Hz. Work of more powerful discharger in the wind tunnel with supersonic flow (520 m/s), frequency - 10 Hz and energy - 150 J is shown on Figure 6. It is well visible (Figure 6a) the removal of the SD plasma by the supersonic flow and the expansion of the erosion products of discharger material.

Action of discharge impulse on wing surface in air flow has been measured according scheme on Figure 2b. These measurements were carried out for various wing profiles and discharge energies. Oscillograms of discharge action with the energy 265 J on the wing in quiescent air and in the supersonic airflow (520 m/s) are shown on Figure 7. Time of one SD was about 5 - 10 μs. Discharge was carried out at the zero time. Dashed line on Figure 7 corresponds to discharge in motionless air. Solid line on Figure 7 corresponds to discharge in supersonic airflow. The difficulty of treatment of oscillograms with the supersonic flow consists in the presence of the strong sustained own oscillations. This is connected with the streamline around the tail end of the wing and knife-holders. As a result we have observed different forms of oscillograms in dependence on the switching moment of discharge relatively to phase of the own system oscillations. We took into account this at obtaining mechanical impulse value.

For the quantitative assessment of pulse action on wing, we had suggested value - efficiency of the discharge:

$$Efficiency = \frac{Impulse}{Deposited\ energy} = \frac{P}{E}, \left[\frac{N \cdot s}{J}\right] \tag{1}$$

where P is mechanical impulse created by SD with energy E. As the energy of the discharge in this work we mean energy of capacity. Energy transferred to the discharge plasma is about 10% - 20% E ([3]).

Obtained experimental efficiency as function of discharge energy is shown on Figure 8. We can see that for all investigated discharges the value of impulse is slightly depended on flow presence. The efficiency of the of discharge action falls with increasing of discharge energy.

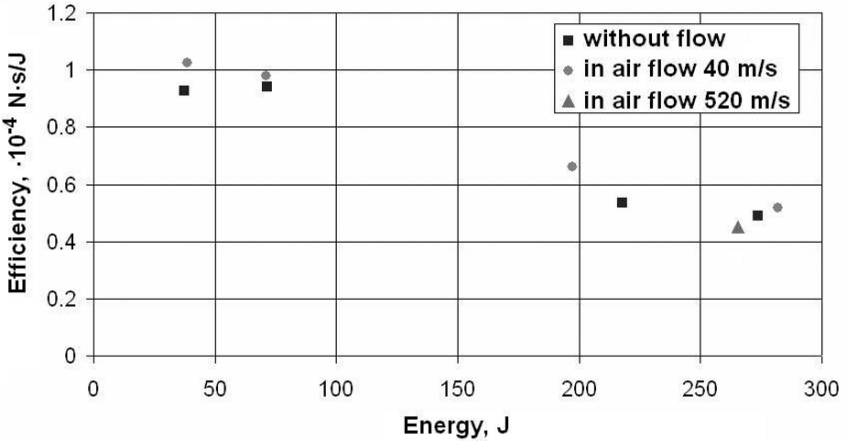

Fig. 8. Efficiency as function of discharge energy

Probably it is connected with the decreasing of the diameter of initial plasma channel of electrical discharge. The more precise interpretation of this phenomenon requires the microscopic examination of the discharge plasma dynamics. But, for investigated range of energies it follows that weak discharges with the energy about 50 J are more preferable than more powerful ones. In the supersonic flow (520 m/s) the measurements were carried out only with the high energy SD about of 265 J. For smaller energies poor relationship between signal and noise was observed. That is action from the discharge was compared with the own wing oscillations.

In perspective applications of the SD, the discharger is proposed to establish directly on the external elements of aircraft. Therefore it is necessary to investigate the possibility of its use in the real weather conditions (increased humidity, fog, rain and etc.) Model wing-discharger was placed into the water-air flow (40 m/s). Discharger functioned both in the the water-air flow and in the water layer on the completely moistened wing surface. Discharges with the energies 10 - 100 J were tested both in the pulse and in the frequency modes (up to 10 Hz during not less than 15 seconds). The flow rate of water from the sprayer was 6 g/s.

4 Conclusions

1. Possibility of the stable excitation of the frequency mode sliding discharge in the wind tunnel with the speeds of airflow to 520 m/s was shown. Necessary electric field was located in the range from 0.5 kV/cm to 1.0 kV/cm. Energies of discharges with a frequency of up to 40 Hz were 8 J - 40 J with the average power input from 100 W to 500 W.

2. Efficiency sliding discharge for creation mechanical impulse as faction of deposited energy is evaluated.

3. The possibility of the functioning of the sliding frequency electrical discharge in the conditions of high humidity in the subsonic flow was tested and verified.

Acknowledgement. Present work was made due to the partial support of presidium RAS programs. The authors are appreciate to professor E. Son for the given possibility to use wind tunnel in MIPT.

References

1. V.S. Aksenov, V.V. Golub, S.A. Gubin, V.P. Efremov, I.V. Maklashova, A.I. Kharitonov, Yu.L. Sharov Sliding Electric Arc Discharge as a Means of Aircraft Trajectory Control Tech. Phys. Letters, vol. 30, No. 10,pp. 871-873, 2004
2. V.S. Aksenov, S.A. Gubin, D.V. Blagodatskih, M.V. Bragin, V.V. Golub, V.V. Volodin, I.N. Laskin Active Flow Control by the Sliding Electric Arc Discharge, European conference for aerospace sciences, July 4-7th 2005
3. V.V. Golub, V.S. Aksenov, D.I. Baklanov, V.V. Volodin, S.V. Golovastov, S.A. Gubin, V.P. Efremov, A.S. Savel'ev, V.E. Fortov, Yu.L. Sharov Issledovanie vliyaniya magnitnogo polya na initsiirovanie detonatsii iskrovym razryadom v vodorodo-vozdushnoi smesi, Dokladi Akademii Nauk vol. 404, N 3, pp. 321-326, 2005

Experimental study of two-dimensional shock wave/turbulent boundary layer interactions

A.G. Dann, R.G. Morgan, and M. McGilvray

Centre for Hypersonics, University of Queensland, Brisbane, Australia

1 Introduction

For high speed air-breathing engines, knowledge of the point at which boundary layer separation occurs limits the design parameters. Shock wave/turbulent boundary layer interaction is a common occurrence in supersonic flows with almost any flow deflection accompanied by shock formation. Incident shock interactions occur when the shock that impinges on the boundary layer is generated by an external source. These allow for the study of the interaction of bulk flow compression without the added effects of streamline curvature and hence are used for this work. They are particularly important for scramjet studies which involve ducted flows where there is a requirement to add as much heat and pressure as possible. However analytical means of modeling separated flow are not advanced.

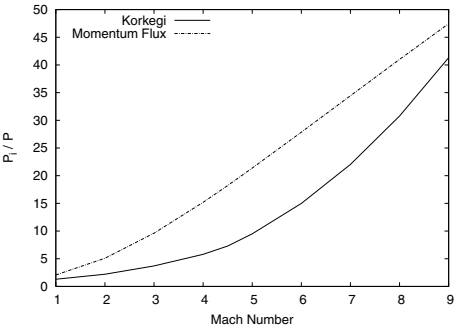

Fig. 1. Comparison of the Korkegi correlations with the momentum equation.

One of the most well known and used empirical correlations for the prediction of separation of turbulent boundary layers was developed by Korkegi [1,2]. In 1975 Korkegi [2] published the criteria for two-dimensional (non-skewed) incipient turbulent boundary-layer separation due to shock wave/boundary layer interactions (1) and (2) where p_i/p is the pressure ratio across the shock wave. The above correlations have been plotted in Fig. 1.

$$p_i/p = 1.0 + 0.3M^2 \, for \, M \, < \, 4.5 \tag{1}$$

$$p_i/p = 0.17M^{2.5} \, for \, M \, \geq \, 4.5 \tag{2}$$

These two-dimensional correlations were formulated with data from nine sources where $Re_\delta > 10^5$. The correlations do not include the effects of Reynolds number or wall temperature variations; the author arguing that they were relatively small second order effects. The correlations developed by Korkegi have been successfully used by air-breathing engine designers [3, 4] despite their simplicity in an area of much complexity. To make further progress in this area a model is needed which uses information about the process by which the pressure ratio is achieved.

An analysis based on momentum arguments previously published [5], has also been used as a comparison (see Fig. 1). This analysis has resulted in (3) where $D = \int_0^\delta \frac{1}{\delta}\frac{\rho}{\rho_\infty}(\frac{u}{u_\infty})^2 dy$ and is Mach number dependent. To allow ease of comparison this equation has been presented in the same form as the Korkegi correlations (see (1) and (2)) accepting that the coefficient D is not constant and contains the momentum integral across the boundary layer.

$$\frac{p_i}{p} = \gamma M^2 D + 1 \tag{3}$$

2 Experimental Program

2.1 Facility

The experimental data for the following work has been obtained from T^2 [5], a small free-piston reflected shock tunnel at the University of Queensland. The experimental results have been formulated from the one condition with stagnation conditions as shown in Table 1. The nozzle exit conditions, also presented in Table 1, were calculated using equilibrium chemistry isentropic process from the stagnation results. These are based on the measured stagnation pressure, and the nozzle exit static and pitot pressures. The estimated Reynolds number is $7.5 \times 10^6/m$ which is likely to produce a turbulent boundary layer in the experimental model.

Table 1. Experimental stagnation and nozzle exit conditions

Stagnation Conditions		**Nozzle Exit Conditions**	
Stagnation pressure	$30.7MPa$	Density	$0.08kg/m^3$
Stagnation Temperature	$1310K$	Static pressure	$2.1kPa$
Incident Shock Speed	$1100m/s$	Pitot pressure	$200kPa$
		Velocity	$1700m/s$
		Mach no.	8.65

2.2 Experimental Model

Scramjet combustor flows are characterised by a complex combination of multiple shock and expansion wave system originating from the intake compression and from heat release due to combustion. The traversing of these shocks through boundary layers limits the pressure rise which can be sustained without separation; which in turn limits the propulsive efficiency. In order to study this process from a fundamental point of view, a

model was designed to create two sets of shock-expansion pairs which could traverse the boundary layer at preset distances.

The T^2 experiments involve an instrumented aluminium circular duct of inner diameter 38mm and length 420mm. The duct was instrumented longitudinally with eight PCB pressure transducers and six quartz thin-film heat transfer gauges. The model (Fig. 2) incorporates an inlet with a conically shaped cowl (not shown), and a shock generator incorporating two cones of 15° semivertex angles. The generator was moved incrementally rearward using the same condition at each shot in order to provide more data points and hence greater resolution. At the point of shock wave/boundary layer interaction the maximum change in boundary layer thickness by utilising this procedure is approximately ±5% which is not considered significant in terms of the parameters being studied. The duct is sufficiently long so as to allow development of a turbulent boundary layer that will thereby interact with the conical shocks created from the cones. The existence of a turbulent boundary layer was verified by comparison of experimental heat transfer data with laminar and turbulent correlations [6].

In order to avoid unwanted shock and expansion wave effects the model has been designed so that the first reflected shock is swallowed by an inner cylinder and removed from the area of interest. The second shock generator is able to be moved forward or rearward to adjust the second shock wave/boundary layer interaction position.

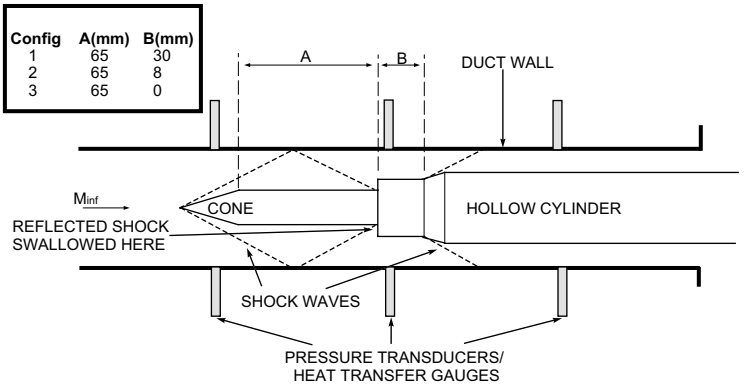

Fig. 2. Two-shock experimental model (not to scale).

Data was recorded for three model configurations as shown in Fig. 2. The first configuration was to confirm that the pressure and heat flux peaks corresponded to the generation of shocks by the cones and not other features of the model i.e. the second cone was positioned far downstream, the second was based on results of a viscous CFD simulation that showed separation after the second cone interaction, and the third was with the second cone as far forward as possible and still allowing the first reflected shock to be swallowed.

3 Results and Discussion

The pressure ratio over both interactions has been compared to the correlations of previous researchers. The Korkegi correlations connect Mach number with incipient separation pressure ratio, independently of process. Despite the practical utility of the empirical correlations, its simplistic nature implies there will be limits to its validity in complex flow situations. In particular, after a preliminary (sub-separation) perturbation to a turbulent boundary layer, there may be some degree of recovery of the original velocity profile which may increase the level of unfavorable pressure rise it can contain before full separation occurs. This can be controlled in the model by variation of the distance between the two interactions.

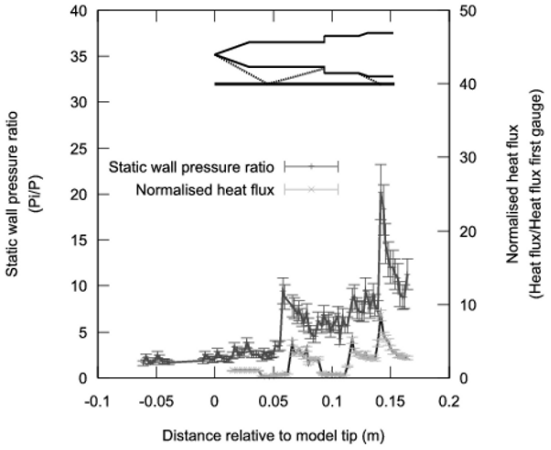

Fig. 3. Static wall pressure ratios and normalised heat flux data for two shock model, configuration 1

Configuration 1 (Fig. 3) shows two distinct shock wave/boundary layer interactions at 0.057 m and 0.138 m which approximately agrees with perfect gas calculations. The static wall pressure and heat flux before the first interaction are reasonably consistent with minor fluctuations probably due to weak viscous interaction and diverging inlet flow. After the first interaction the pressure drops slightly and stays at a fairly constant level before rising slightly, possibly as a result of viscous interaction due to the hollow cylinder leading edge, before rising sharply as a result of the second cone interaction. The heat flux data shows a significant drop after the first cone interaction to levels similar to that before the interaction. There is a rise corresponding to the slight pressure rise just before the second shock interaction. The pressure data most clearly shows that the first reflected shock wave is effectively swallowed by the hollow cylinder since there are very few pressure fluctuations between the first and second interactions.

Configuration 2 (Fig. 4) shows three distinct peaks: the first two corresponding to shock wave/boundary layer interactions generated by the cones and the third due to a reflected shock. These locations agree with the estimated interaction locations. After the first interaction the pressure drops slightly but stays at a higher level than before the

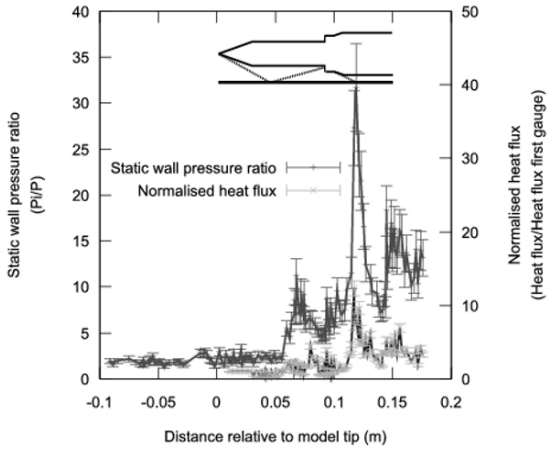

Fig. 4. Static wall pressure ratios and normalised heat flux data for two shock model, configuration 2

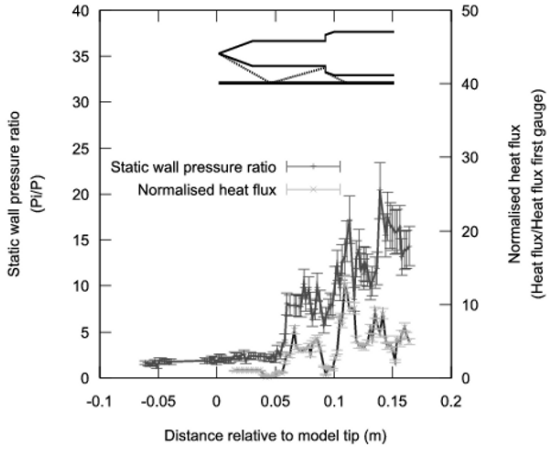

Fig. 5. Static wall pressure ratios and normalised heat flux data for two shock model, configuration 3

interaction before rising sharply as a result of the second cone interaction. The heat flux data shows a similar trend to the pressure data however the first cone interaction is not well defined.

Configuration 3 (Fig. 5) shows three distinct peaks: the first two corresponding to shock wave/boundary layer interactions generated by the cones and the third due to a reflected shock. There appears to be fairly constant pressure between the two cone interactions. The heat flux data also has three distinct peaks corresponding to the same perturbations as the pressure data but with a significant drop just before the second cone interaction.

The pressure ratios over both interactions for each configuration were calculated using the static pressure at the start of the inlet taken to be the nozzle static pressure and the static pressure at its highest point during the second interaction. Table 2 shows the comparison of pressure ratios for the different configurations using the Korkegi correlations, the momentum flux equation and the data derived from the current experiments.

Table 2. Comparison of pressure ratios for Mach 8.65 condition data

Configuration	Korkegi	Momentum Flux Eq	Experimental
1	37.41	44.19	20.19
2	37.41	44.19	31.72
3	37.41	44.19	17.18

This comparison indicates that according to empirical and analytical correlations, separation would not occur for any of the configurations studied. The pressure ratio for Configuration 3 is the lowest which may be due to the absence of any viscous interaction prior to the second cone interaction. Since the pressure ratio in Configuration 2 is the highest, the distance from the hollow cylinder inlet and the second cone may represent a critical value whereby the amount of viscous interaction and the proximity of the two interactions is coupled. The experiments presented here provide non-separated heat flux and pressure reference data which will be used to help interpret subsequent data from separated flows.

4 Conclusion

A model has been successfully tested which enables a hypersonic turbulent boundary layer to be subjected to two quantified compression-expansion systems, with an adjustable axial separation between them. This enables the separation characteristics of boundary layers to be studied for a range of compression histories, providing fundamental data for the development of more complex separation models. The operation of the model has been demonstrated for pressures below the critical separation levels. On-going work will now extend the experiments to pressure levels which will induce separation.

References

1. Korkegi R. H., Simple correlation for incipient turbulent boundary-layer separation due to a skewered shock wave, *AIAA Journal*, 11(11):1578-1579, Nov. 1973.
2. Korkegi R. H., Comparison of shock-induced two- and three-dimensional incipient turbulent separation, *AIAA Journal*, 13(4):534-535, Apr. 1975.
3. Smart M.K., Design of three-dimensional hypersonic inlets with rectangular-to-ellipitcal shape transition, *Journal of Propulsion and Power*, 15(3):408-416, May 1999.
4. Mitani T., Sakuranaka N., Tomioka S., Kobayashi K., Boundary-layer control in Mach 4 and Mach 6 scramjet engines, *Journal of Propulsion and Power*, 21(4):636-641, 2005.
5. Dann A. G., Denman A. W., Jacobs P. A., Morgan R. G.: Study of separating compressible turbulent boundary-layers, AIAA Paper 2006-7943, 2006.
6. Morgan R. G., Stalker R. J., Shock Tunnel Measurements of Heat Transfer in a Model Scramjet, *AIAA paper 85-908*, 1985.

Flow simulation of inlet components using URANS approach

N.N. Fedorova, I.A. Fedorchenko, and Y.V. Semenova

Khristianovich Institute of Theoretical and Applied Mechanics,
Siberian Division of Russian Academy of Sciences,
Institutskaya 4/1, 630090 Novosibirsk (Russia)

1 Introduction

In inlets, a boundary layer passes through a system of shock waves and expansion fans in optional combination. These numerous interactions may lead to the boundary layer separation and cause the inlet unstart. Double ramp configuration is often used for external pre-compression. The choice of ramp angles and a distance between ramps is of great importance to provide a necessary level of pre-compression and to avoid a flow separation. The parametric computations performing within a wide range of gasdynamic and geometric parameters provide a basis for the choice of optimum configurations. But these problems demonstrate a certain level of simulation complexity connected with intricate flow structure and turbulent character of a boundary layer. Many important flow features are not well-understood even in a case of two-dimensional flow. Recent progress in using LES and DNS for modeling of SWTBLI gives us a big hope to improve the situation. But at present, these approaches seem to be too expensive for engineering applications.

In the paper, the unsteady Favre-averaged Navier–Stokes equations closed by Wilcox turbulence model [1] are used. The numerical investigation is carried out by an original 2D URANS–based code, developed at ITAM SB RAS, Novosibirsk, Russia [2]. Two flow configurations are simulated under the conditions of real experiments. The geometry of the computational domain is shown in Fig. 1. The domain was restricted by the inlet (1) and outlet (2) sections, rigid wall on the bottom (3) and free artificial boundary on the top (4). The inlet section (1) was chosen downstream from the transition region and upstream from the interaction zone to provide there the undisturbed turbulent boundary layer with integral parameters close to those in the experiments. At the rigid surface (3), no-slip velocity and adiabatic temperature were specified. At the outlet section, "soft" extrapolated conditions were used. At the top boundary, the non-reflecting conditions for all the gasdynamic parameters were kept. A regular grid was used in calculations,

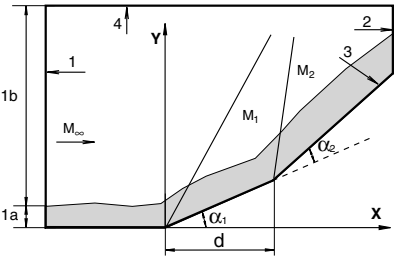

Fig. 1. Computation domain and types of boundary conditions

condensed to the rigid walls and consisted of $200 \div 300$ nodes in y–direction and $300 \div 500$ nodes in x–direction. The minimal y step was chosen to keep $y^+ < 1$ for the first grid point adjacent to the wall.

2 Double ramp flow — Case 1

The first configuration has fixed ramp angles (11° and 9°) and variable distance between the ramps ($0 \div 39$ mm). The purpose of the investigation was to design an optimal configuration with minimal length and pressure drag. These computations were performed under the conditions of experiments conducted in IAG, Stuttgart [3] for the three sets of flow parameters. Some results have been presented earlier in [4], namely, of incoming Mach number $M_\infty = 2.54$ and unit Reynolds number $Re_1 = 12.7 \cdot 10^6$ 1/m and of $M_\infty = 2.995$ and $Re_1 = 7.5 \cdot 10^6$ 1/m. In present paper, simulations are carried out for the parameters as follows: $M_\infty = 2.513$, $Re_1 = 9.82 \cdot 10^6$ 1/m, total pressure $P_0 = 93400$ Pa, total temperature $T_0 = 283$ K. The boundary layer thickness before the first ramp is $\delta = 5.15$ mm.

The numerical results and experimental data on a wall pressure distribution are presented in Fig. 2, a, where the solid lines represent the numerical solutions, and the symbols correspond to the experimental data. The numbers on the lines stand for the following distances: *0* – $d = 0$ mm, *1* – 8.24 mm, *2* – 9.43 mm, *3* – 10.97 mm, *4* – 21.58 mm, *5* – 39.24 mm. A satisfactory agreement of the calculated and measured results both for short and long distances d between the kinks is observed.

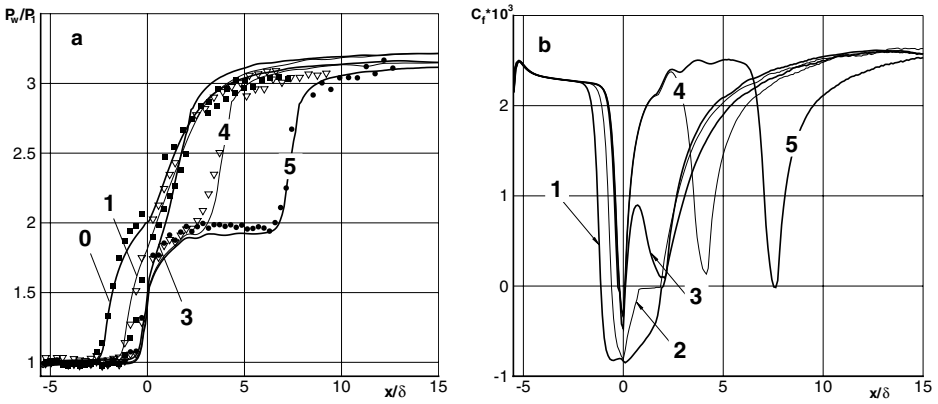

Fig. 2. Experimental and calculated wall pressure (a) and skin friction (b) distributions for $\alpha_1 = 11°$, $\alpha_2 = 9°$, $M_\infty = 2.513$ and various d

The analysis of the skin friction coefficient behavior presented in Fig. 2, b, allows estimating the separation sizes for each ramp length. Three flow regimes can be distinguished similar to those described in [4]. The first one is a coupled regime where the separation zones induced by the two shocks are combined in one large separation (line *1* in Figs. 2). The second regime is a transitional one with a short detached zone at the first angle and a zero skin friction coefficient area downstream (line *2*). The third

regime results in two spaced shocks, with a short separation in the vicinity of the first kink and an attached flow at the second kink (lines *3–5*). In case of the third regime with d increasing, the flow tends to separate again near the second kink. Analysis of the wall skin friction distributions indicates that the optimal distance between the kinks is $11 \div 12.4$ mm, or, in terms of d/δ, is $2.13 \div 2.4$, as it guarantees the minimal pressure drag along with a short ramp length. Together with presented results, the influence of the Reynolds number and heat transfer behavior were studied numericallly.

3 Double ramp flow – Case 2

The second configuration has a fixed distance between the ramps (100 mm) and the second ramp angle of 18°, but a value of the first ramp angle is changeable (7°, 11° and 15°). The main goal of these calculations was to investigate the influence of preliminary pressure gradient on the boundary layer separation properties in the second interaction. This configuration was computed under experimental condition given in Table 1. The experiments have been performed in ITAM SB RAS (Novosibirsk) blow-down wind tunnel. Experimental data [5] on pressure distributions and boundary layer integral parameters for a single ramp of $\alpha_1 = 7°$, 11° and 15° were used for verification of numerical results. In Table 1 the freestream Mach numbers M_∞, Mach numbers behind the first (M_1) and second (M_2) interactions are shown, calculated by inviscid theory. The absence of some data for $M_\infty = 2$ means that there is no oblique shock wave attached to the second ramp angle. The case $M_\infty = 2$ and $\alpha_1 = 15°$ was not computed since for this geometry the flow was subsonic at the outlet section that made it difficult to compute in a frame of existing numerical algorithm.

Table 1. Flow parameters

M_∞	$P_0 \times 10^5$, n/m^2	T_0, K	$Re_1, \times 10^6$/m	α_1	M_1	M_2
2	2.1	287.8	25.7	7	1.75	-
				11	1.6	-
3	4.208	288.1	33	7	2.65	1.85
				11	2.45	1.7
				15	2.25	1.53
4	10.3	271.2	54	7	3.49	2.41
				11	3.21	2.24
				15	2.92	2.04

The static pressure and skin friction distributions along the model for $\alpha_1 = 7°$, 11°, 15° and $\alpha_2 = 18°$ at different M_∞ are shown in Figs. 3 – 5. The solid lines present the results of the calculations, the lines 1, 2 and 3 denote computational results for $M_\infty = 4, 3$ and 2, correspondingly. Dashed lines stand for the inviscid solutions and symbols correspond to the experimental results [5] for single ramp flows.

For $\alpha_1 = 7°$, for all considered freestream Mach numbers the attached flow was realized in the vicinity of the first ramp (Fig. 3). When the ramp angle increases up to 11°, the small local separation zone near the first ramp arises at $M_\infty = 2$, whereas at $M_\infty = 3$ and 4 the flow remains attached (Fig. 4). It is necessary to note that at $M_\infty = 2$,

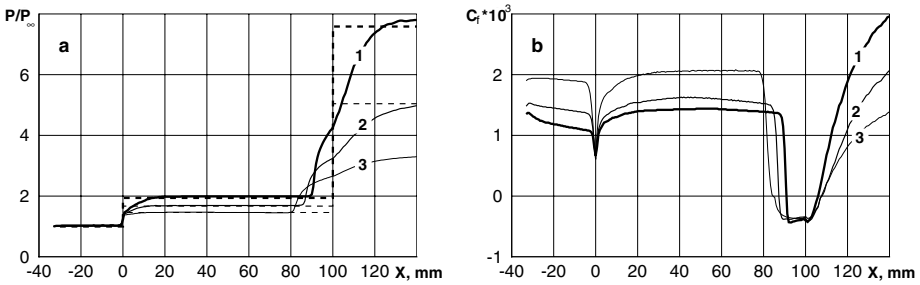

Fig. 3. Static pressure (a) and skin friction (b) distributions at various M_∞, $\alpha_1 = 7^\circ$

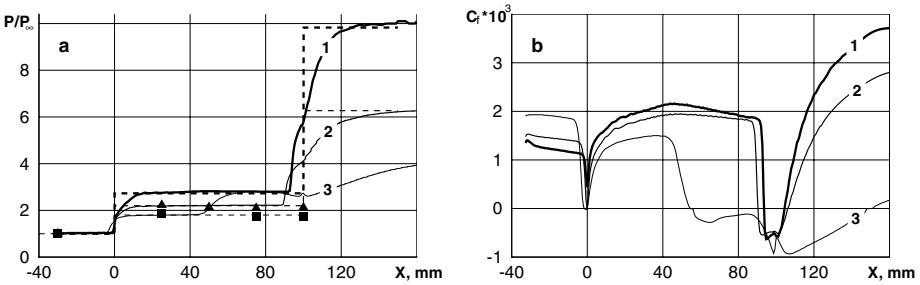

Fig. 4. Static pressure (a) and skin friction (b) distributions at various M_∞, $\alpha_1 = 11^\circ$

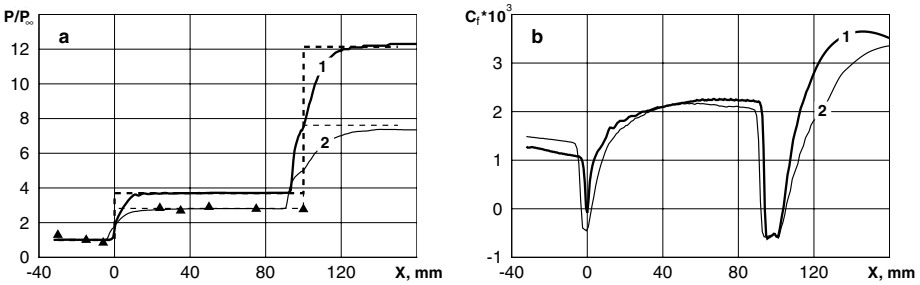

Fig. 5. Static pressure (a) and skin friction (b) distributions at various M_∞, $\alpha_1 = 15^\circ$

$\alpha_1 = 11^\circ$, the extensive separation zone is observed in the vicinity of the second ramp (Fig. 4). Such a big separation scale is due to the fact that behind the first interaction the external flow Mach number is rather low $M_1 = 1.6$. For this Mach number the shock wave detaches from the ramp, i.e. the normal shock is formed near the surface. Interaction with the normal shock results in development of an extensive separation zone and the flow gets subsonic at the outlet section. As it was mentioned above, the transonic flow at $M_\infty = 2$, $\alpha_1 = 15^\circ$ was not computed. For $\alpha_1 = 15^\circ$, a local separation zone exists in the vicinity of first ramp at $M_\infty = 3$ (Fig. 5), but at $M_\infty = 4$ the flow is attached.

For all considered M_∞ and α_1 values the flow was separated in the vicinity of the second ramp, but with M_∞ increasing, the size of the separation zone had been reduced.

The influence of the α_1 values on the flow structure in the vicinity of the second ramp ($\alpha_2 = 18°$) was studied numerically. To compare, the single 18°–ramp flow simulations have been performed at freestream Mach numbers corresponding to M_1 values presented in Table 1 and turbulent boundary layer thickness close to that behind the first interaction. Results of this comparison at $M_\infty = 3$ for the two various pre-interaction strengths are presented in Figs. 6, a, b. Here line 1 stands for the skin friction distribution along the single 18° ramp at $M_\infty = 2.45$ (Fig. 6, a) and $M_\infty = 2.25$ (Fig. 6, b). Line 2 shows the skin friction behavior along the double ramp in the region adjacent to the second 18° ramp. Figure shows that in a case of equilibrium boundary layer ($\alpha_1 = 0°$), an extensive separation zone exists in the vicinity of the $\alpha = 18°$ ramp. But a separation size decreases significantly if we put before this 18° ramp an additional ramp of 11° or 15°. In Fig. 7, the same results obtained at $M_\infty = 4$ for the two strengths of pre-interaction are presented: $\alpha_1 = 11°$ (a) and $\alpha_1 = 15°$ (b) with the line notations similar to those in Fig. 6.

Computations have shown that pre-interaction with shock wave raises an ability of a boundary layer to resist a separation. It may be due to the fact that a preliminary pressure gradient promotes an increase of mass flow pulsations and level of turbulence before the second interaction. Such a tendency can be observed at all M_∞ and angles of the first ramp $\alpha_1 = 11°$ and 15°. At $M_\infty = 3$, the effect of pre-interaction is more

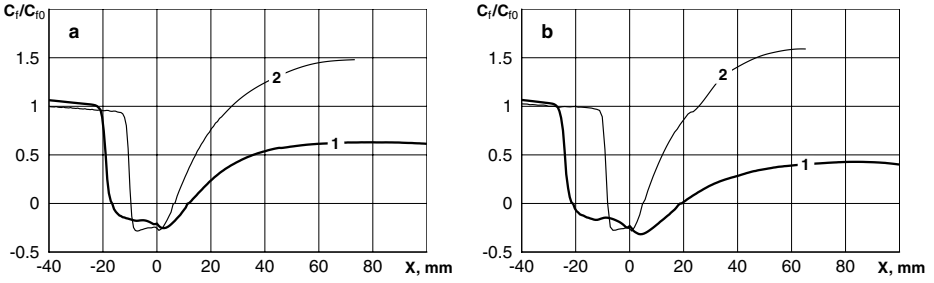

Fig. 6. Computed skin friction distributions at $M_\infty = 3$ with $\alpha_1 = 11°$ (a) and 15° (b)

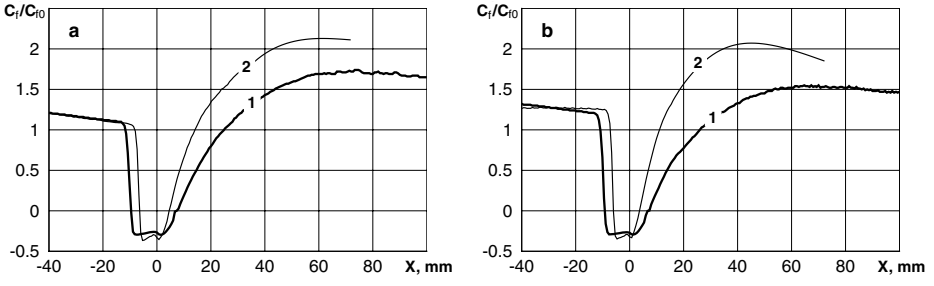

Fig. 7. Computed skin friction distributions at $M_\infty = 4$ with $\alpha_1 = 11°$ (a) and 15° (b)

pronounced than at $M_\infty = 4$ since the scale of separation at single ramp is much larger for a lower Mach number.

4 Conclusion and future work

In the paper, the pressure gradient action on a 2D turbulent boundary layer was studied by means of mathematical modeling at $M_\infty = 2 \div 4$ and ramp angles from 7° to 18°. The URANS-based simulation of the double ramp supersonic configuration has been carried out. An ability of the averaged Navier-Stokes equations to predict flow behavior in the vicinity of such geometry is found out to be reasonable. A good agreement with the experimental wall pressure distributions has been obtained. Three flow regimes have been observed and the optimal ramp lengths have been estimated.

It was shown numerically that pre-interaction with a shock wave leads to a considerable reduction of separation at the second ramp. The effect is observed at $\alpha_1 = 11°$ and 15° and is substantial for smaller M_∞. The separation scale at the second ramp depends on a pre-interaction intensity. If a flow is attached at the first ramp, visible separation length reduction has not been achieved that allows us to suggest that the shock pre-interaction effect is related to turbulization action of local separation zone arising in the first interaction. Further, a history of turbulent boundary layer characteristics behind first and second interactions will be studied. Future work will also include different geometries and ramp angle combinations. The critical distances d between ramps will be determined at which the effect of the separation reduction is not observed at various Mach numbers.

Acknowledgement. The work was supported by Russian Foundation for Basic Research, grant 05-01-00684 and German Research Association (DFG), Research Training Center 1095/1.

References

1. Wilcox, D.C.: *Turbulent modeling for CFD*, (DCW Industries Inc., 1993)
2. A.V. Borisov, N.N. Fedorova: Thermophysics and Aeromechanics **4**, 1 (1996) pp 69–83.
3. U. Gaisbauer, H. Knauss, S. Wagner: Experimental Investigation about External Compression of Highly Integrated Airbreathing Propulsion Systems. In: *Basic Research and Technologies for Two–Stage–to–Orbit Vehicles*, WILEY-VCH (2005) pp 347–364.
4. U. Gaisbauer, H. Knauss, S. Wagner, Yu.V. Kharlamova, N.N. Fedorova: Experimental Investigation and Numerical Simulation of Supersonic Turbulent Flows in Vicinity of a Double-Ramp Configuration. In: *Proc. of Intern. Conf. on Methods of Aerophys. Research.* vol 4, ed by A.M. Kharitonov (Publishing House "Nonparel", Novosibirsk, 2004) pp 137–142.
5. M.A. Goldfeld, V.V. Zatoloka: Izvestia AN SSSR **3**, 13 (1979) pp 40–47.

Fluidic control of cavity configurations at transonic and supersonic speeds

C. Lada and K. Kontis

The University of Manchester, Manchester, M60 1QD, UK

Summary. An experimental study has been conducted to investigate open and closed cavity configurations with and without fluidic control at transonic and supersonic speeds. The cavity models were of $\frac{L}{D}$ = 2, 6, 11 and 18. The investigation was carried out at Mach numbers of 0.8, 1.4 and 1.7. The passive flow control technique employed wedges of 15^o, 30^o, 45^o and 60^o were placed at the leading and trailing edge of each cavity. Pressure measurements, and oil flow, were employed to examine the characteristics of the induced flowfield. Experimental results revealed the basic flow features and defined the cavity flow field types.

1 Introduction

Roshko [1], Krishnamurty [2] Rossiter [3], and Sarohia [4] are some of the early investigators that studied the resulting flow field inside cavities. The main variable affecting cavity flow is the length-to-depth ratio. The first classification occurs in deep-cavity flow (open cavity), where the aspect ratio is less than 10; there is a large recirculation zone with one stationary, vortical structure and the shear layer bridges the cavity. In the second classification, where the aspect ratio is greater than 13, the cavity is considered shallow, (closed cavity) and creation and rollup of vortices at the leading edge of the cavity takes place. The last classification occurs in cavities with aspect ratio that lies between the open and closed,(transitional cavities). Johannesen [5] in 1954 using Schlieren photography and pressure measurements, typified the open cavity flow by a series of weak compression waves above the shear layer. The intensity of the compression waves increased up to the critical aspect ratio. A breakthrough study was published by Rossiter [3] in 1964. He suggested that the momentary flow separation at the leading edge results in periodic shedding of localised vortices, producing acoustic tones.

A major issue that occurred after the aerodynamics and the acoustics inside the cavities were understood, was to control the cavity flows in order to eliminate or alleviate all the undesired phenomena. There are some interesting recent reviews by Colonius [6], who provided a summary of numerical simulations on active flow control of acoustic resonance and Cattafesta et. al. [7], who reviewed the experimental work on the same field.

2 Experimental Set-up

The experiments took place in the Plint TE25/A Supersonic Wind Tunnel, at Mach numbers of 0.8, 1.4 and 1.7. The$\frac{L}{D}$ ratios chosen to cover open transitional and closed cavity flows are 2, 6, 11, and 18. The length of each is set to 90 mm. There are 33 static pressure tappings; the pressure tappings inside the cavity are placed in three lines parallel to each other and to the direction of the flow. Four different wedges were manufactured

for each cavity model. The wedges were designed at four different angles of 15^o, 30^o, 45^o and 60^o and placed at the edges of the cavity.

Average pressures inside and outside of the cavities were obtained via the aid of pressure transducers. Oil flow technique was employed to visualise the surface flow inside and outside the cavities.

3 Results and Discussion

The most effective wedge for cavity $\frac{L}{D}$=2 was that of 30^o. At a freestream Mach number of 0.8 and the 30^o wedge placed at the cavity leading edge, the pressure was increased over the cavity floor. The pressure coefficient distribution has a concave up shape, meaning that the flow recirculates with less momentum compared to the no control case. The pressure at the trailing edge dropped, meaning that the wedge interacts in an efficient way with the shear layer impingement and the natural feedback loop for resonance is disturbed.When the 30^o wedge was placed at the cavity trailing edge, similar effects were obtained. The pressure coefficient was similarly distributed over the cavity floor, but the magnitude was decreased in that case, Fig. 1.

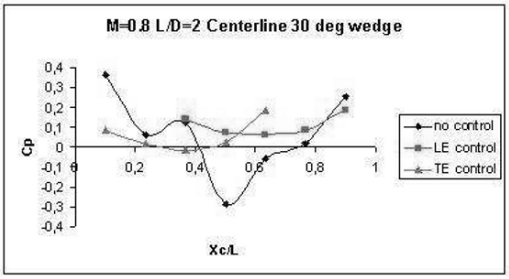

Fig. 1. Pressure Distribution on Cavity Floor For $\frac{L}{D}$=2, M=0.8 no control case and with 30^o wedge placed at leading and trailing edge

As the Mach number was increased to Mach no. of 1.4, the magnitude of the pressure coefficient is smaller for both the leading and the trailing edge wedge, compared to the no control case because less free stream flow becomes entrained into the cavity. Again there are indications that the feedback loop is disturbed since the pressure recorded at the traling edge is reduced.

The oil flow results show that the flow bridges the cavity, impinges on the trailing edge and entrains inside. It separates just ahead of the wedge and a large recirculation region is formed on top and bottom corner, Fig. 2.

At Mach number 1.7, the wedge located at the trailing edge causes the pressure along the cavity floor to increase dramatically. This indicates that it probably worsens the cavity oscillations instead of suppressing them. This is not the case for the leading edge wedge, that reduced the magnitude of pressure and caused an almost uniform pressure distribution.

The most pronounced effect for cavity $\frac{L}{D}$=6 was again that of 30^o. The pressure distribution became more uniform when the wedge was placed at the cavity leading edge and there is no indication of flow recirculation inside the cavity. A pressure drop was observed at the cavity trailing edge, meaning that acoustic suppression may be

Fig. 2. Oil Flow Picture on Cavity Floor For $\frac{L}{D}$=2, M=1.4 no control case and with 30^o wedge placed at leading and trailing edge

possible.The 30^o wedge placed at the trailing edge of the cavity changed the flowfield from open to transitional.The pressure distribution shows a large longitudinal pressure gradient, causing the problem of store nose-up pitcing moment. Fig.3

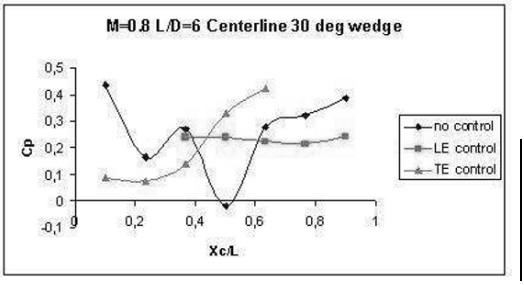

Fig. 3. Pressure Distribution on Cavity Floor For $\frac{L}{D}$=6, M=0.8 no control case and with 30^o wedge placed at leading and trailing edge

As the Mach number increased the effect of the 30^o wedge placed at the leading edge became minimal. As the Mach number increased to 1.4, a typical open cavity pressure distribution was observed, but the magnitude of pressure dropped meaning that less flow has entrained the cavity. At Mach no. 1.7 the flowfiled changes to transitional again, without indications of large longitudinal pressure gradient.

The oil flow results show a similar behaviour as the one described for $\frac{L}{D}$=2. The only difference is that only one vortical structure is formed at the top corner, Fig. 4. Similar results were obtained for the three different Mach numbers.

For $\frac{L}{D}$=11 and 18, a transtional cavity flow field occurs. Since acoustic fields exist in transitional-open cavities and store-nose up pitching moments exist in transitional closed cavities, controlling the flow aims in suppressing the acoustic modes in transitional open cavities as well as decreasing the longitudinal pressure gradients in transitional closed cavities so that the problem of store nose-up pitching moment is not severe. At M=0.8 the cavity flow field is transitional closed. When the Mach number increased from 0.8 to 1.4 and finally to 1.7 the flow field changed from transtional closed to transtional open.

At M=0.8 the cavity is transitional closed type. Figure 5, show an increase of pressure along the cavity floor, for both the leading and trailing edge case. When the wedge was placed at the leading edge, the recirculatory region just after the leading edge moved a bit further closer to the trailing edge and the increase of pressure at that region suggests

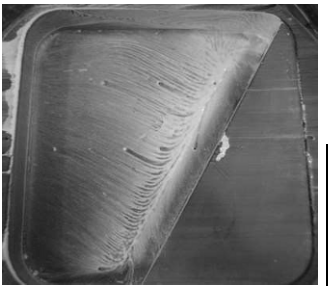

Fig. 4. Oil Flow Picture on Cavity Floor For $\frac{L}{D}$=6, M=0.8 no control case and with 30^o wedge placed at leading and trailing edge

that momentum was reduced. This is the most effective flow control case, since the longitudinal pressure gradient in the cavity is slightly decreased compared to the no control or the trailing edge control case. When the wedge was placed at the trailing edge the only effect that had on the flow field was that the pressure was increased along the cavity floor, meaning that more flow entrains the cavity. Similar effects were observed for greater Mach numbers.

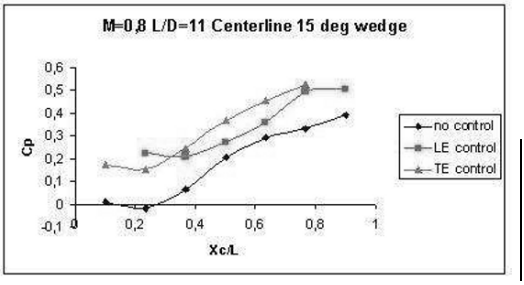

Fig. 5. Pressure Distribution on Cavity Floor For $\frac{L}{D}$=11, M=0.8 no control case and with 15^o wedge placed at leading and trailing edge

The oil flow results show no indication of shear layer impingement on the cavity floor and the flow field obtained is similar to the transitional open cavities flow field without flow control. The shear layer bridges the cavity, impinges on the trailing edge wall and entrains.The flow separates again just ahead of the wedge and there is a vortical structure shown on the top corner. Fig. 6

For $\frac{L}{D}$=18, the 15^o wedge case placed at the leading edge of the cavity caused the flow inside the cavity to behave as in transitional closed cavities. The pressures measured close to the leading edge of the cavity were increased compared to the no control case and the overall distribution show that a lower adverse pressure gradient was observed.There is a low pressure region at $\frac{Xc}{L}$=0.4, where separation occurs.The pressures measured at the trailing edge of the cavity were unaffected compared to the no control case. When the wedge was placed at the trailing edge, the pressure distribution shows a dramatic increase of pressure close to the cavity leading edge and then a constant drop until $\frac{Xc}{L}$=0.6, which is also the point of separation. Fig.7.

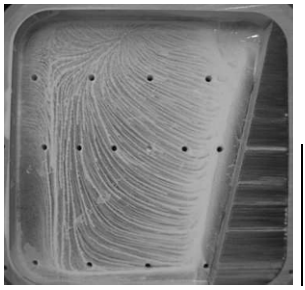

Fig. 6. Oil Flow Picture on Cavity Floor For $\frac{L}{D}$=11, M=0.8 no control case and with 15^o wedge placed at leading and trailing edge

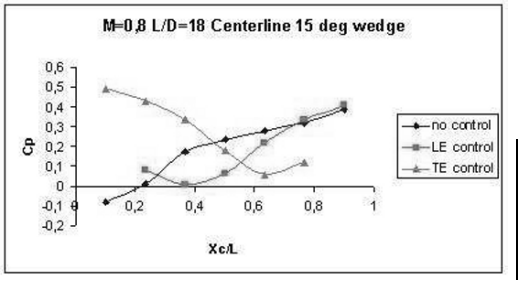

Fig. 7. Pressure Distribution on Cavity Floor For $\frac{L}{D}$=18, M=0.8 no control case and with 15^o wedge placed at leading and trailing edge

When the Mach number increased to 1.4, the leading edge wedge does not affect the flow field, and at 1.7 the pressure drops dramatically indicating that less flow entrains the cavity. The wedge placed at the trailing edge causes the same effects for greater Mach numbers as those described for the 0.8 M case.

The oil flow reults for the $\frac{L}{D}$=18 cavity show that the shear layer impinges in the middle of the cavity floor and also the impingement line is parallel to the wedge. Again the same vortical structure is obtained as those described in previous cases. Fig. 8

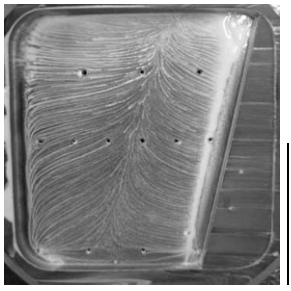

Fig. 8. Oil Flow Picture on Cavity Floor For $\frac{L}{D}$=18, M=0.8 no control case and with 15^o wedge placed at leading and trailing edge

4 Conclusions

Experimental results reveal the basic flow features of cavities with passive flow control at transonic and supersonic speeds. The wedges for the open control case cavities placed at the cavity leading edge, appear to reduce the pressures measured at the cavitis trailing edge, and to interact in an efficient way with the shear layer so the natural feedback loop for resonance is disturbed. For the transitional case cavities the wedges placed at the leading edge decreased the longitudinal pressure gradients so that the problem of store nose-up pitching moment is not severe.

References

1. Roshko, A., "Some Measurements of Flow in a Rectangular Cutout", NACA Technical Note 3488, August 1955.
2. Krishnamurty, K., "Acoustic Radiation from Two Dimensional Rectangular Cutouts in Aerodynamic Surfaces," NACA Technical Note 3487, August 1955.
3. Rossiter, J. E.,"Wind-Tunnel Experiments on the Flow Over Rectangular Cavities at Subsonic and Transonic Speeds," British Aeronautical Research Council Reports and Memoranda No. 3438, 1964.
4. Sarohia, V., "Experimental Investigation of Oscillations in Flows Over Shallow Cavities", AIAA Journal, Vol. 15 No. 7, July 1977, pp 984-991.
5. Johannesen, N. H., "Experiments on Supersonic Flow Past Bodies of Revolution with Annular Gaps of Rectangular Section", Phil. Mag., Series 7 Vol. 46 No. 372, pp. 31-39, 1955.
6. Colonius, T., "An Overview of Simulation, Modeling, and Active Control of Flow/Acoustic Resonance in Open Cavities", AIAA 2001-0076, Jan. 2001.
7. Cattafetsa, L., Williams, D., Rowley, C., and Alvi, F., "Review of Active Control of Flow Induced Cavity Resonance", AIAA 2003-3567, Jun. 2003.

Front separation regions for blunt and streamlined bodies initiated by temperature wake – bow shock wave interaction

P.Y. Georgievskiy[1] **and V.A. Levin**[2]

[1] *Institute for Mechanics MSU, 1 Michurinskiy pr., Moscow 119192, Russia*
[2] *Institute for Automation and Control Processes, 5 Radio st., Vladivostok 690041, Russia*

Summary. Front separation flows supported by an upstream energy deposition are examined. It is shown that a reason for separation region formation is an interaction of a thin high temperature wake ("thermal spike") which is formed downstream a localized energy deposition region with a shock layer upstream of a body. Some simplified analytical models are applied to describe a front separation phenomenon. To realize steady flows with isobaric front separation regions in numerical experiments the "method of transformation of energy deposition" is proposed. The method is applied for both blunt as well as streamlined "thermal spiked" bodies to realize conical front separation regions. "Shock-free" separation flows initiated by subsonic "thermal spikes" are particularly examined.

Introduction

Historically an idea of improvement of aerodynamic characteristics of bodies by a localized energy deposition in an upstream supersonic flow was proposed in Russia in the meddle 80-ies. From the very beginning a local energy deposition was considered as an instrument for control of a supersonic flow over large bodies. In this case the mechanism of a wave drag reduction was a formation of front separation regions ahead of a fore surface of bodies.

Georgievsky, Levin [1] and Yuriev et al. [2] have shown the possibility of wave drag reduction for blunt bodies. Stabilization of an optical discharge in a supersonic flow of argon that was obtained by Tretiyakov et al. [3] was the first experimental confirmation for the possibility of the controlled electrodeless energy deposition in a high speed flow. Nemchinov et al. [4] has found a "forerunner" effect for a shock wave – a rarefied channel interaction, and has formulated the "thermal spike" conception for wave drag reduction of blunt bodies. The model of "steady isobaric front separation region" was introduced by Guvernjuk, Savinov [5]. The possibility of an effective control of flows over blunt and streamlined bodies by a localized energy deposition in an upstream flow in a steady and a pulse-periodic modes was shown by Georgievsky, Levin [6, 7]. Term "effective" means, that a small energy deposition into a small region upstream of a large body produces a wave drag reduction, when the saved power is much higher than a consumed one. The recent surveys for application of an upstream energy deposition for supersonic aerodynamics problems were performed by Zheltovodov [8] and Knight et al. [9].

1 Formulation of the problem

To describe supersonic flows with an energy deposition the mathematical model of the "energy source" was applied. Euler equations for an unsteady motion of an inviscid perfect gas presented in a vector form are:

$$\frac{\partial \rho}{\partial t} + \operatorname{div} \rho \mathbf{V} = 0,\ \frac{d\mathbf{V}}{dt} + \frac{1}{\rho} \operatorname{grad} p = 0,\ \frac{\partial e}{\partial t} + \operatorname{div}(e+p)\mathbf{V} = \rho Q,\ e = \frac{p}{\gamma - 1} + \frac{\rho \mathbf{V}^2}{2} \quad (1)$$

where p is the static pressure, ρ is the density, $\mathbf{V}$ is the velocity vector, e is the total energy per volume unit and Q is the energy input per mass unit per time.

Only axially symmetrical flows were examined. Depending on a problem specific cylindrical r, z or spherical R, θ coordinates were applied. The energy input Q in cylindrical coordinates is defined by:

$$Q(r, z, t) = Q_0 f(t) \exp\left(- \left(\frac{r}{\Delta r} \right)^2 - \left(\frac{z - z_0}{\Delta z} \right)^2 \right) \quad (2)$$

where Q_0 is the magnitude, $\Delta r, \Delta z$ are "effective radii" and z_0 is the location of the energy source center on the symmetry axes. It must be noticed, that a space distribution (2) is of "Gaussian type", so that $\dot{Q} > 0$ for each point in a calculation region. But it is not a problem for numerical simulation because of exponential decreasing of the energy input with a distance from the energy source center.

For a flow over the energy source without a downstream body the similarity criteria can be formulated:

$$\gamma = \text{const},\ M_\infty = \text{const},\ Q_0 \Delta z = \text{const},\ \frac{\Delta r}{\Delta z} = \text{const} \quad (3)$$

The explicit MacCormack scheme [10] of a second order accuracy with coordinates and time (for interior points on smooth solutions) was used for a numerical simulation. Discontinuities (shock waves and tangential surfaces) were not specially allocated and were calculated using regular algorithm. Typical parameters for an upstream flow were $\gamma = 1.4, M_\infty = 2$. The time marching procedure was used to establish steady solutions or to examine unsteady processes. Courant-Friedrichs-Lewy stability condition was used to determine the time step. Spherical coordinates were used for blunt bodies and cylindrical coordinates – for streamlined bodies. Mesh resolution was depended on the situation and typically was 400×360 points for spherical coordinates R, θ and 400×800 for cylindrical coordinates r, z.

2 Simplified schemes for front separation regions formation

In the present paper the Guvernjuk, Savinov [5] model of the "isobaric front separation region" was be applied to found separation region geometry in the presence of the high temperature wake. If the energy source cross size approaches to zero, whereas the similarity conditions (3) are held, then the temperature and other gasdynamics parameters on the symmetry axes are constant (cross direction distributions are self-similar). At the limit the separation region becomes conical (Fig.1, left). According with [5] it was assumed that the static pressure inside conical separation region was equal to a total pressure in the wake behind the locally normal shock (or simply the total pressure for subsonic wake). Depending on the "thermal spike" heating parameter ω the front separation region angle α, the oblique shock angle β and conical flow in the shock layer were determined.

Nemchinov et al. [4] "forerunner" scheme for a normal shock – a high temperature wake interaction is presented on Fig.1 (right). For the initial moment of the contact of

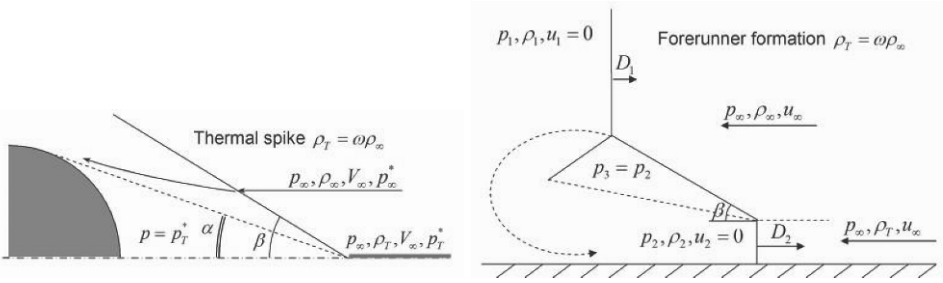

Fig. 1. Simplified schemes for front separation regions formation: left – the "thermal spike" scheme for the conical front separation region; right – the "forerunner" scheme for the normal shock – the high temperature wake interaction.

the primary normal shock with a high temperature cloud the situation of the "random discontinuity decomposition" is taking place. So the secondary normal shock moves upstream the temperature wake with the velocity D_2, that is higher than the primary shock velocity D_1 . So the two-dimensional unsteady structure with oblique shock and triple point configuration appears. Nemchinov et al. [4] have found wonderful in its simplicity formula for the oblique shock angle β:

$$\sin\beta = \sqrt{\omega} \tag{4}$$

The flow scheme, presented on Fig.1 (right), shows the turn-inside effect for the stream formed by the gas particles passed through the oblique shock (the "forerunner stream").

3 Front separation regions formation for blunt bodies

If the energy source is "powered on" in the uniform upstream flow, then the high temperature cloud appears. The elongation of the cloud is provided by the drifting effect of the upstream flow and by the acceleration of hot particles by the pressure gradient behind the bow shock (if the "flow choking effect" is observed [6]). In any case when the cloud contacts the shock layer the process of the high temperature wake – the shock layer interaction starts. The initial stage of this process can be described by the Nemchinov "forerunner" model, so the "forerunner stream" appears (the blunt body can be considered as a reason for a normal shock existence). If similarity criteria (3) are satisfied for different size energy sources, then on this stage flowfields looks very similar. If the temperature wake is enough thick, then the stream spreads over the lateral surface of the body and the steady isobaric front separation region forms. But for thin temperature wakes the "forerunner stream" turns inside the front separation region – this way the circulating flow arises (Fig.2, left). The constant inflow of additional gas into the separation region results in its enlargement in a cross direction with the next periodical blowout of an extra gas – the pulsations of front separation region appears (Fig.2, right). That's why Nemchinov et al. [4] have made a conclusion, that only pulsing regimes are realizable for front separation regions initiated by the "thermal spike".

To realize steady flows with isobaric front separation regions in numerical experiments the "method of transformation of energy deposition" is proposed. Initially, the steady solution with the isobaric front separation region was found for the enough large energy

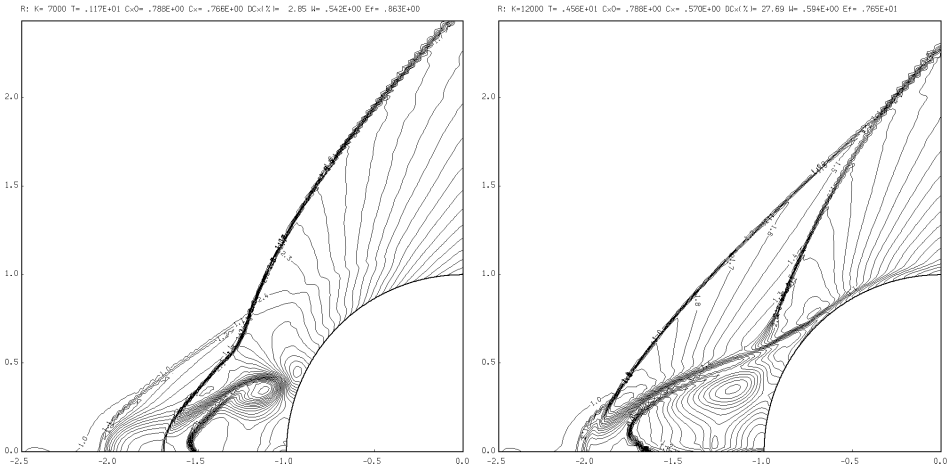

Fig. 2. Formation of pulsing separation regions for blunt bodies: left – the "forerunner stream" turns inside the front separation region; right – the enlargement of front separation region in cross direction (density isolines).

source. Then the energy source radius was decreased from the large value down to the small one (similarity criteria (3) were held). Finally the flow with the accurate isobaric front separation region for the small energy source (Fig.3, left) was found instead of the pulsing flow, that was observed when the same energy source was "powered on" in the uniform upstream flow (Fig.2, right).

Similar idea was applied to find "shock-free" regimes for the flow over the sphere. "Shock-free" deceleration regimes are characterized by a continuous deceleration of a

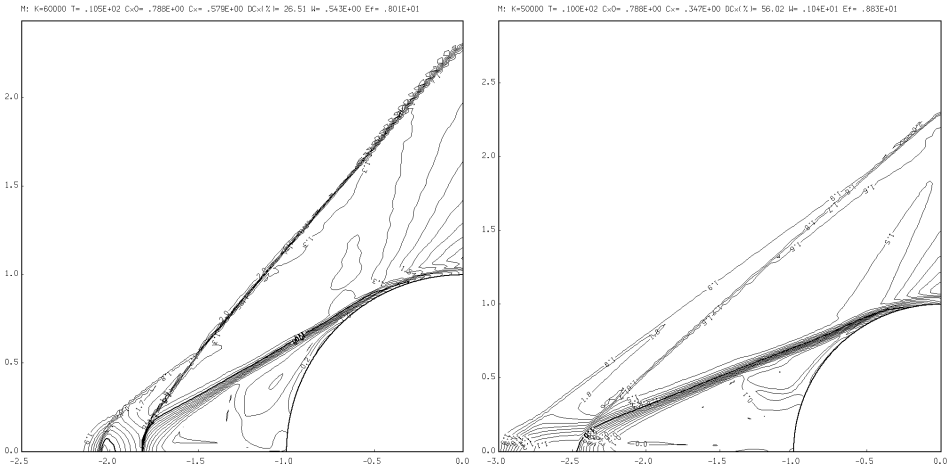

Fig. 3. Flows with steady isobaric front separation regions initiated by thin temperature wakes, that were calculated by the "method of transformation of energy deposition": left – spherical energy source; right – elongated energy source, "shock-free" regime (Mach numbers isolines).

flow inside a temperature wake from a supersonic speed down to a subsonic one so that only weak hanging shock appears on the periphery of a flow. Such regimes were observed in [6] for a supersonic flow over elongated energy sources. But if the elongated energy source is powered on in the uniform upstream flow, then because of the "forerunner stream" capturing effect a very unstable pulsing flow was observed. On Fig.3 (right) the same energy source was compressed from a large spherical source during the numerical procedure. This way the accurate steady flow with the isobaric conical front separation region was found.

4 Front separation regions formation for streamlined bodies

The supersonic flows over streamlined bodies of the unit midsection where examined. Class of ogival-type bodies was constructed by the rotation of the circle arc around the arc chord.

For energy sources of a small elongation (for spherical energy sources for example) the "flow choking" effect is taking place [6], supersonic temperature wakes arise and regular flow regimes are observed. No separation regions appear and hot particles are spread around the lateral surface of the body. In the temperature wake region the obliquity of the apex shock changes or, if the ogival body apex angle is larger than the critical for the local Mach number in the temperature wake, the bow shock appears (Fig.4, left).

For elongated energy sources the "shock-free" deceleration effect is taking place, subsonic temperature wakes arise [6] and the situation radically changes. The irregular regimes are observed for the flows over ogival bodies (Fig.4, right). The stable composite-type conical front separation regions appear – partially the regions are filled by the high temperature slow moving gas and partially by the slow vortex flow. The "shock-free" regime is realized – only hanging shocks appears on the periphery of the flow (according to the new "effective" body shape). It must be mentioned that the effect of "forerunner stream" capturing was observed for very thin temperature wakes only. The flow for $\Delta r = 0.1$ was calculated by the "direct" powering on the energy source in the uniform flow and the "transformation" method was applied for Fig.4, (right) $\Delta r = 0.1 \rightarrow \Delta r = 0.05$. Thus the energy deposition into an elongated region can be used for initiation of front separation regions for streamlined bodies.

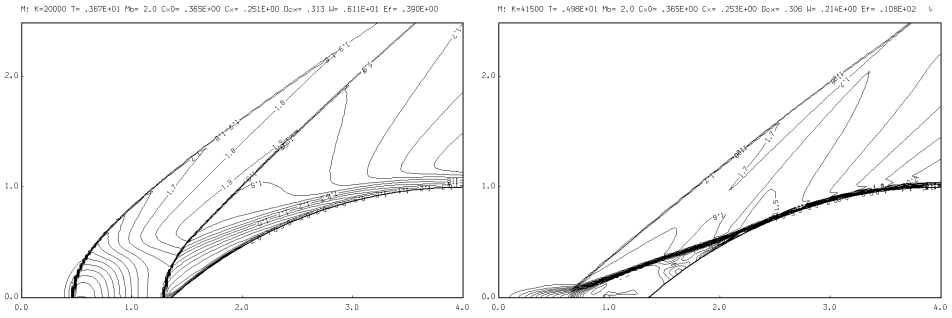

Fig. 4. Regular and irregular flows over the ogival-type body: left – spherical energy source, thick temperature wake; right – elongated energy source, thin temperature wake (Mach numbers isolines).

Conclusions

Front separation flows supported by an upstream energy deposition are examined. It is shown that a reason for separation region formation is an interaction of a thin high temperature wake which is formed downstream a localized energy deposition region (or the "thermal spike") with a shock layer upstream of a body. The Guvernjuk-Savinov model of isobaric front separation region was applied for the analytical describing of the conical flow over "thermal spiked" bodies. The Nemchinov "forerunner" model was used for explanation of the effect of "forerunner stream" formation during the temperature wake – the shock layer interaction. It was shown that the "forerunner stream" formation is a reason for pulsations of front separation regions. To realize steady flows with isobaric front separation regions in numerical experiments the "method of transformation of energy deposition" is proposed. The method is applied for both blunt as well as streamlined "thermal spiked" bodies to realize conical front separation regions. "Shock-free" separation flows initiated by subsonic "thermal spikes" are particularly examined.

Acknowledgement. These investigations are financially supported by Russian Academy of Sciences (P9.2 program), Russian Foundation for Basic Research (grant 05-01-00003) and Russian Federal Agency on Science and Innovations (grant NSh-6791.2006.1).

References

1. Georgievsky P., Levin V. : Supersonic Flow over Bodies in the Presence of External Energy Input. Letters to Journal of Technical Physics (in Russian), vol. 14, no. 8, 1988.
2. Borzov V., Rybka I., Yuriev A. : The Estimation for Power Input Using for Wave Drag Reduction of a Body in a Supersonic Flow. Journal of Engineering and Physics (in Russian), vol. 63, no. 6, 1992.
3. Tretiyakov P., Grachev G., Ivanchenko A. et al. : Stabilization of an Optical Discharge in a Supersonic Flow of Argon. Proceedings of Russian Academy of Sciences (in Russian), vol. 336, no. 4, 1994.
4. Artem'ev V., Bergel'son V., Nemchinov I., Orlova T., Smirnov V., Khazins V. : Change of Regime in Supersonic Flow past an Obstacle Preceded by a Thin Channel of Reduced Density. Fluid Dynamics (Historical Archive), vol. 24, no. 5, 1989.
5. Guvernjuk S., Savinov K. : Shock Layer Structure for the Barrier in the Wake-type Nonuniform Supersonic Flow (in Russian). Institute for Mechanics of Moscow State University, Paper no. 4047, 1990.
6. Georgievskii P., Levin V. : Control of the Flow past Bodies Using Localized Energy Addition to the Supersonic Oncoming Flow. Fluid Dynamics, vol. 38, no. 5, 2003.
7. Georgievsky P., Levin V. : Bow Shock Wave Structures Control by Pulse-Periodic Energy Input. AIAA Paper 2004-1019, 2004.
8. Zheltovodov A. : Development of the Studies on Energy Deposition for Application to the Problems of Supersonic Aerodynamics. Institute of Theoretical and Applied Mechanics, Russian Academy of Sciences, Preprint no. 10-2002, Novosibirsk, Russia, 2002.
9. Knight D., Yan H., Candler G., Kandala R., Elliot G., Glumac N., Zheltovodov A., Pimonov E. : High Speed Flow Control Using Pulsed Energy Deposition. Proceedings of European Conference for Aerospace Sciences (EUCASS), Moscow, Russia, July 4-7, 2005.
10. MacCormack R. : The Effect of Viscosity in Hypervelocity Impact Cratering. AIAA Paper 1969-354, 1969.

Pressure waves interference under supersonic flow in flat channel with relief walls

M.-C. Kwon, V.V. Semenov, and V.A. Volkov

Moscow state Aviation Institute, Dept. of Rocket engines, Volokolomskoe Shosse 4, 125493 Moscow, Russia

Summary. In a number of cases, surfaces of channel walls are distorted in the process of operation so that periodically reiterative dimples and convexities are formed. Thus, additional wave drag appears when such relief structures are flowed by the supersonic gas stream. There are theoretical data on relief surfaces wave drag only for some simplest forms of relief, but there are practically no experimental data. This work suggests the method which allows obtaining within the limits of linear approximation the exact formula for wave drag of channel walls with the arbitrary plate in the first and subsequent interference zones. By the example of sinusoidal relief it is demonstrated that pressure waves interference can lead to both increasing and decreasing of wave drag.

1 Formulation of the problem

Consider flat stationary supersonic flows of ideal gas in the channel between walls with flat relieves are represented schematically on Fig. 1.

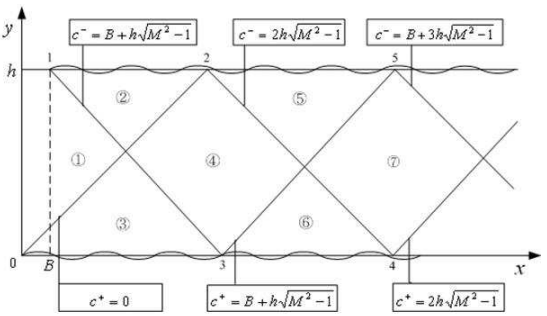

Fig. 1. Schema of relief channel and interference zones

Let functions $\xi_0(x)$ and $\xi_h(x)$ to describe relieves in bottom and upside wall.

$$y_{wo} = \xi_x(0),\ x \in [0, L_0]; \quad y_{wh} = \xi_h(x),\ x \in [B, B + L_h]. \tag{1}$$

It is obvious that functions $\xi_0(x)$ and $\xi_h(x)$ should be continuous. As it is shown in work [1], generally their derivatives of function $\xi_0^{'}(x)$, $\xi_h^{'}(x)$, $\xi_0^{''}(x)$, $\xi_h^{''}(x)$ are possible to suppose sectionally continuous.

In addition assume that functions $\xi_0(x)$, $\xi_h(x)$, $\xi_0^{'}(x)$, $\xi_h^{'}(x)$ in the range of definition satisfies the restrictions:

$$\xi_0(x) \ll L_0,\ \xi_h(x) \ll L_h,\ \ |\xi_0^{'}(x)| \ll 1,\ \ |\xi_h^{'}(x)| \ll 1. \tag{2}$$

Usually suppose that dimensionless pressure disturbance, density and speed are too small:

$$\frac{\delta p}{\kappa p} = \Psi \ll 1; \quad \frac{\delta \rho}{\rho} = E \ll 1; \quad \frac{\delta U}{U} = \Phi \ll 1; \quad \frac{\delta V}{V} = \Theta \ll 1. \tag{3}$$

If the restrictions (2), (3) are executed, the boundary conditions on walls of the channel can be set in linearized form:

$$\frac{\delta V}{U}|_{y=0} = \Theta|_{y=0} = \xi_0^{'}(x), \quad \frac{\delta V}{U}|_{y=h} = \Theta|_{y=h} = \xi_h^{'}(x). \tag{4}$$

Thus local and total wave drag coefficients on walls, it is possible to express through the value of function Ψ:

$$c_{px_0} = \frac{2}{M^2}\Psi_{wo}(x)\xi_0^{'}(x), \quad c_{px_h} = -\frac{2}{M^2}\Psi_{wh}(x)\xi_h^{'}(x). \tag{5}$$

$$c_{pL_0} = \frac{2}{M^2 L_0}\int_0^{L_0}\frac{2}{M^2}\Psi_{wo}(x)\xi_0^{'}(x)dx,\ c_{pL_h} = -\frac{2}{M^2 L_h}\int_B^{B+L_h}\frac{2}{M^2}\Psi_{wh}(x)\xi_h^{'}(x)dx. \tag{6}$$

where M is Mach number of uniform flow.

For the decision of assigned task, it is enough to solve the two equations of two unknown functions Θ, Ψ. If conditions (2), (3) are executed, this system can be written down according to [5]:

$$(M^2-1)\frac{\partial \Psi}{\partial x} + M^2\frac{\partial \Theta}{\partial y}, \quad M^2\frac{\partial \Theta}{\partial x} + \frac{\partial \Psi}{\partial y}. \tag{7}$$

These equations were derived by D.E. Blohinzeva [4] . However, direct application methods in the works [1-3] for decision of the boundary problems (4), (7) appear impossible, so it is difficult to generalize because of intricateness of calculations. Therefore in the given work instead of the D.E. Blohinzeva's method [4], the initial boundary problems (4), (7) are solved by means of the method characteristics [5].

General solutions of linearized system

In case of $M > 1$, we can define the reduced transverse coordinate $\tilde{y}$ and the reduced function of pressure $\tilde{\Psi}$, such that:

$$\tilde{y} = y\sqrt{M^2-1}, \quad \tilde{\Psi} = \Psi\sqrt{M^2-1}/M^2. \tag{8}$$

Substituting (8) into (7), we have:

$$\frac{\partial \tilde{\Psi}}{\partial x} + \frac{\partial \Theta}{\partial \tilde{y}} = 0, \quad \frac{\partial \Theta}{\partial x} + \frac{\partial \tilde{\Psi}}{\partial \tilde{y}} = 0. \tag{9}$$

The general solutions of system (9) agree to [5], such that:

$$\Theta = I^+(c^+) + I^-(c^-), \quad \tilde{\Psi} = I^+(c^+) - I^-(c^-), \quad c^{\pm} = x \mp \tilde{y}. \tag{10}$$

Functions $I^+(c^+)$ and $I^-(c^-)$ are the Riemann intervals, and it's lines agree to $c^{\pm} = const$, where $c^{\pm}$ are characteristics. When we solve the boundary problems, concrete view of functions $I^+(c^+)$ and $I^-(c^-)$ are defined by the method of characteristics [5] on the given boundary conditions (4).

Linearized models of discontinuous characteristics According to definition of shock as gas dynamics parameters, discontinuous characteristics for any function $f(c^+, c^-)$ can be written as:

$$[f]_{c^+=a} = \lim_{c^+ \to a+0} f(c^+, c^-) - \lim_{c^+ \to a-0} f(c^+, c^-) ,$$
$$[f]_{c^-=b} = \lim_{c^- \to b+0} f(c^+, c^-) - \lim_{C^- \to b-0} f(c^+, c^-). \tag{11}$$

Substituting the general solution (10) into definitions (11), we have:

$$[I^-]_{c^+=a} = 0 \Rightarrow [\Theta]_{c^+=a} = [I^+]_{c^+=a}, \quad [\tilde{\Psi}]_{c^+=a} = [I^+]_{c^+=a} ,$$
$$[I^+]_{c^-=b} = 0 \Rightarrow [\Theta]_{c^-=b} = [I^-]_{c^-=b}, \quad [\tilde{\Psi}]_{c^-=b} = -[I^-]_{c^-=b}. \tag{12}$$

From (12) only one of invariants has break in discontinuous characteristic, namely the sign coincides with a sign on this characteristic.

2 Wave drag and interference in channel

Wave drag in channel walls depends not only on their relief, but also on initial disturbance entering into the channel. In our study, it is supposed that the interference of waves is caused only by relief wall and that initial disturbance into the channel is equal to zero. This assumption makes the boundary problems (4), (9) explicitly same as [1]. When slope angles of leading edges in both upside and bottom wall are distinct from zero, also as well as in break point, oblique shock wave or expansion wave is appeared. It is modeled by "discontinuous" characteristics [1] within the limits of linear approximation. Therefore it can be supposed that disturbance from the bottom wall is extended from its leading edge to downward stream along the characteristic $c^+ = 0$, and from upside wall- along the characteristic $c^- = B + \tilde{h}$. All flow areas are designated on Fig. 1.

According to the characteristics method and boundary problems, we can obtain pressure distributions in each wall of channel:

$$\tilde{\Psi}_{w0} = \xi_0^{'}(x), \quad 0 < x < B + \tilde{h} ,$$
$$\tilde{\Psi}_{w0} = \xi_0^{'}(x) - 2\xi_h^{'}(x - \tilde{h}), \quad B + \tilde{h} < x < 2\tilde{h}. \tag{13}$$

$$\tilde{\Psi}_{wh} = -\xi_h^{'}(x), \quad B < x < \tilde{h} ,$$
$$\tilde{\Psi}_{wh} = -\xi_h^{'}(x) + 2\xi_0^{'}(x - \tilde{h}), \quad \tilde{h} < x < B + 2\tilde{h}. \tag{14}$$

Substituting (13), (14) into (6), we can receive the coefficients of wave drag on walls:

$$c_{pL_0} = \frac{2}{L_0\sqrt{M^2-1}} \left\{ \int_0^{B+\tilde{h}} [\xi_0^{'}(x)]^2 dx + \int_{B+\tilde{h}}^{L_0} \xi_0^{'}(x)[\xi_0^{'}(x) - 2\xi_h^{'}(x - \tilde{h})]dx \right\},$$
$$\tilde{h} \le L_0 \le 2\tilde{h} ,$$
$$c_{pL_h} = \frac{2}{L_h\sqrt{M^2-1}} \left\{ \int_B^{\tilde{h}} [\xi_h^{'}(x)]^2 dx + \int_{\tilde{h}}^{B+L_h} \xi_h^{'}(x)[\xi_h^{'}(x) - 2\xi_0^{'}(x - \tilde{h})]dx \right\},$$
$$\tilde{h} \le L_h \le 2\tilde{h} . \tag{15}$$

In each of formulas (15), the first term- it is the contribution of region where disturbance does not come from other wall, and the second - the contribution of the first interference zone on the given wall.

Interference of wave drags in channel As an example, we consider the particular case that leading edges are not displaced relatively to each walls and both lengths and relieve of them are identical.

$$B = 0, \quad L_0 = L_h = L, \quad \xi_0(x) = \xi_h(x) = \xi(x) \;\Rightarrow\; \xi_0^{'}(x) = \xi_h^{'}(x) = \xi^{'}(x). \tag{16}$$

Then we can obtain the coefficient of total wave drag of channel:

$$c_{pL_\Sigma} = \frac{4}{L_0\sqrt{M^2-1}} \left\{ \int_0^{\tilde{h}} [\xi^{'}(x)]^2 dx + \int_{\tilde{h}}^{L} \xi^{'}(x)[\xi^{'}(x) - 2\xi^{'}(x-\tilde{h})]dx \right\}, \; \tilde{h} \le L \le 2\tilde{h}. \tag{17}$$

Consider the particular case of sine wave relieves:

$$\xi(x) = A\cos(2\pi/\lambda) \;\Rightarrow\; \xi^{'}(x) = -2\pi A/\lambda \sin(2\pi/\lambda). \tag{18}$$

And define two dimensionless parameters and the total wave drag of channel in case of periodic relieves depends on these parameters:

$$\Lambda = \frac{L}{h\sqrt{M^2-1}} = \frac{L}{\tilde{h}}, \quad K = \frac{L}{\lambda}. \tag{19}$$

ParameterΛ is the interference number, K is the wave number. It fully characterizes modes of interference. Actually, when $\Lambda < 1$, any disturbances are generated by one wall can not reach to the other walls so that interference zones on both walls are absent. In this case the total coefficient of wave drag of the channel can be written:

$$\Lambda \le 1 \;\Rightarrow\; c_{pL_\Sigma} = \frac{16\pi^2}{L\sqrt{M^2-1}} \int_0^L [\xi^{'}(x)]^2 dx. \tag{20}$$

Substituting profile (18) into (20), we have:

$$\Lambda \le 1, \; c_{pL_\Sigma} = \frac{16\pi^2(\frac{A}{\lambda})^2}{L\sqrt{M^2-1}} \int_0^L \sin^2(2\pi\frac{x}{\lambda})^2 dx = \frac{8\pi^2}{\sqrt{M^2-1}}(\frac{A}{\lambda})^2[1 - \frac{\sin(4\pi K)}{4\pi K}]. \tag{21}$$

When $1 < \Lambda \le 2$, each region of walls has the first interference zone so the characteristics are appeared in these regions. Substituting profile (18) into (17), and using replacement of integration variable, we have:

$$c_{pL_\Sigma} = \frac{16\pi^2(\frac{A}{\lambda})^2}{L\sqrt{M^2-1}} \{ \int_0^1 \sin^2(2\pi K\eta)d\eta - 2\int_{1/\lambda}^1 \sin(2\pi K\eta)\sin[2\pi K(\eta - \frac{1}{\lambda})]d\eta \}. \tag{22}$$

Both integrals in curly bracket in (22) are expressed through elementary functions. This final result can be presented as:

$$1 < \Lambda \le 2, \quad c_{pL_\Sigma} = \frac{16\pi^2}{M^2-1} \left(\frac{A}{\lambda}\right)^2 N(K,\Lambda)\,,$$

$$N(K,\Lambda) = \frac{1}{2}\left(1 - \frac{sin(4\pi K)}{4\pi K}\right) - \left(1 - \frac{1}{\Lambda}\right)\cos(2\pi\frac{K}{\Lambda}) + \frac{\cos(2\pi K)}{2\pi K}\sin\left[2\pi K\left(1 - \frac{1}{\Lambda}\right)\right]. \tag{23}$$

Function $N(K, \Lambda)$ is enough complex. Flow satisfies the value $\Lambda = 2$ when the characteristics beginning on leading edges, after reflection precisely reach on edge assignment of the same wall. In this case the first interference zone is closed, consequently resonance effects take place. In fig. [2], [3], [4], we reduce some graphics illustrating behavior of function $N(K, \Lambda)$ in regions $1 < \Lambda \leq 2$.

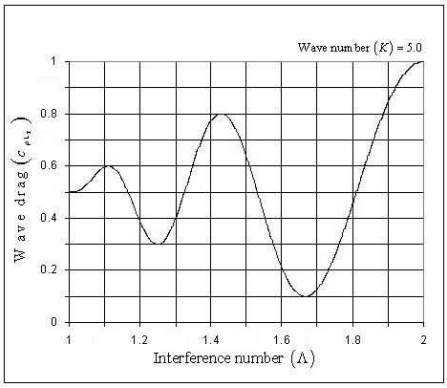

Fig. 2. Value of wave drag at odd wave number($K = 5.0$) has maximum value that is equal to unit. It is exceeding twice as much as total wave drag value in same two plates. (at $\Lambda = 2.0$)

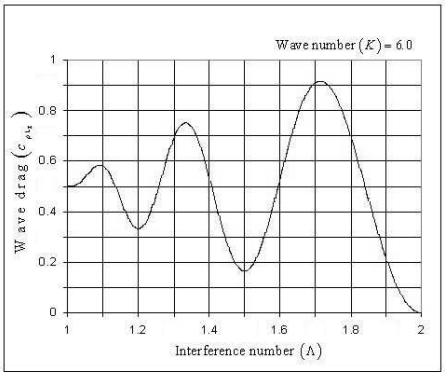

Fig. 3. Value of wave drag at even wave number($K = 6.0$) has minimum value that is equal to zero. (at $\Lambda = 2.0$)

In Fig. [4], it is shown that the minimum value of wave drag is equal to zero at all even values of wave number, when interference number is $\Lambda = 2$. Also we can see that the overall maximum value of wave drags is approximately equal to 1.06, it is realized at $K \approx 0.8$. Consequently, the local maximum value of wave drags little bit exceeding unit and monotonously tends it with growth K, when wave number is odd natural numbers. As we said, in the plane of parameters Λ and K, there are set of numerable points $K_n \approx n$

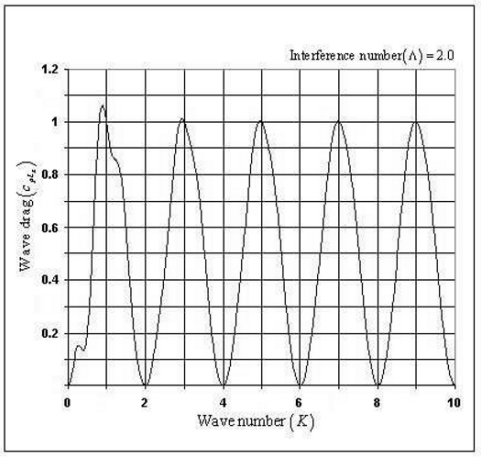

Fig. 4. Interference number (Λ) = 2.0

at $\Lambda = 2$, and resonant effects are shown as that wave drags have the local maximum and minimum values.

3 Conclusion

Flow regimes with interference number are formulated in the range $\Lambda \leq 2$. It is possible to calculate analytically or numerically the factors of wave drag in rectilinear flat channels with any relief walls, which have finite number of break points. In our study, theories are based on linearized equations of gas dynamics. Its predictive ability now is not doubted, because it was successfully applied to the decision of many problems of applied aerodynamics [3], [4], [5]. It is necessary to proof the results of his study; not for confirmation of the theory, and for definition of the boundary area which was considered in this work.

Acknowledgement. This work was supported by the Korea Science and Engineering Foundation Grant (No. M06-2004-000-10006).

References

1. Kwon M. C., Volkov V. A.,Semenov V. V. : The exact solution of linearized problems under supersonic flow in relief flat, Aerospace MAI Journal**13**, 2, pp36-40. (2006)
2. Semenov V. V. : Wave drag of the wavy surface in the reaction nozzle and flying vehicle, Journal Aviationnaya technika , 4, pp18-22. (2000)
3. Chorny G. G. : Gas dynamics, Nayka (1998)
4. Blohinzeva D. E. : Acoustics of non-homogenous flow, Nayka (1998)
5. Godynov S. K. : Equations of mathematical physics, Nayka (1971)
6. Kwon M. C. : Differential apparatus for research of wave drag of projection surface. Master's thesis, MAI, Russia (2006)

Progress in time resolved flow visualisation of shock boundary layer interaction in shock tunnels

N. Mudford[1], S. Wittig[2], S. Kirstein[3], R. Boyce[1], and R. Hruschka[1]

[1] *University of New South Wales, ADFA Campus, Canberra, Australia*
[2] *RWTH, Aachen University*
[3] *Technische Universität München*

1 Introduction

Shock wave boundary layer interactions (SWBLI) are found in abundance in flows in and around vehicles in hypersonic flight. In SWBLI's, the adverse pressure gradient produced by a shock impinging on a boundary layer strongly decelerates the low momentum flow in the boundary layer. In severe cases, this reverses the flow and causes the boundary layer to separate from the surface on which it formed. The subsequent behaviour of the separated flow can have severe consequences for vehicle handling or integrity. For example, if the free shear layer created by the separation reattaches to the surface, it produces very high localized heat fluxes which can weaken the structure or even burn a hole in it. Unchecked growth of a separated flow in a scramjet flowpath may unstart the engine. Thus the incentives for understanding SWBLI's are many and compelling.

2 Experiments

The SWBLI here is produced by a forward facing step on a straight, thin walled, circular pipe with a sharp leading edge. This geometry has many of the features of flat plate flow without the edge effects. The experiments were conducted in the T-ADFA Free Piston Shock Tunnel (FPST) at the Australian Defence Force Academy. Diagnostics included conventional schlieren, near-resonantly enhanced schlieren and surface heat flux measurements. The schlieren images were captured using an ultra high speed camera, yielding a detailed record of the steady nozzle flow establishment and separated flow development and oscillatory behaviour.

2.1 T-ADFA Free Piston Shock Tunnel, the SWBLI model

T-ADFA has a 5.0 m long, 124 mm i. d. compression tube and a piston mass of 8.0 kg. The shock tube length and diameter are 6.4 m and 50 mm respectively. The hypersonic nozzle used here is a 7.5° half angle conical nozzle having a 12.7 mm throat diameter and a 305 mm exit diameter. The combined test section and dump tank has a 585 mm i. d. and 3.6 m length. Optical access to the test section is via 200 mm diameter windows.

High enthalpy (A) and low enthalpy (B) air flow conditions were used here. The ESTC shock tube flow program [1] and the STUBE nozzle flow program [2] calculate the test section flow conditions from the initial shock tube fill pressure, the primary shock speed, the nozzle reservoir plateau pressure, nozzle geometry and the thermophysical properties of air. The relevant conditions are presented in Table 1. Pitot pressure normalised to nozzle reservoir pressure, p_{pitot}/P_{res}, 65 mm and 275 mm downstream of the nozzle exit

Table 1. Nozzle reservoir and nozzle exit flow conditions. H_0 = total enthalpy, $m_{i,\infty}$ = mass fraction of species i. Other symbols have their usual meanings. Subscripts: res = nozzle reservoir plateau condition, ∞ = test section freestream.

Flow Condition	H_0 (MJ/kg)	P_{res} (MPa)	T_{res} (K)	p_∞ (Pa)	T_∞ (K)	ρ_∞ (g/m^3)	u_∞ (km/s)	M_∞	$m_{O2,\infty}$	$m_{O,\infty}$	$m_{NO,\infty}$
A	13.74	10.63	6985	363	583	1.95	4.58	9.2	0.0900	0.1171	0.0484
B	4.08	11.5	3055	242.9	137	6.14	2.47	10.9	0.2097	0.00055	0.0423

are within $\pm 5\%$ of $3.3 * 10^{-3}$ and $2.3 * 10^{-3}$, respectively, inside the ~ 200 mm diameter core flow for both flow conditions [3].

The model consists of a 50 mm o. d. straight pipe with axis parallel to the oncoming flow. The pipe's sharp leading edge narrows to a 35 mm i. d. via a conical contraction at 20° to the oncoming flow. The impulsive flow from the nozzle starts and maintains a hypersonic flow within the pipe, as evidenced by the absence of any disturbance ahead of the pipe entrance in Fig. 4. A 70 mm o.d. collar clamped to the outside of the pipe produces the 10 mm high step that creates the SWBLI studied here.

2.2 Diagnostics

Initially a conventional Z-type schlieren system with two 305 mm FL mirrors, illuminated by a 300μs duration flash lamp, was used. The slit-like source mask and the knife edge where aligned parallel to the leading edge shock. The images were recorded by the Shimadzu HPV-1 with framing rates between 250 and 125 $kfps$ and exposure times between 1 and 4 μs.

In the second version of the schlieren system, the highly enhanced refractivity in the vicinity of the lithium D2 line at 670.78 nm was exploited to increase system sensitivity. The test gas was seeded with lithium (Li) vapour by putting Li foil into the shock tube near its downstream end. The dense, high temperature test gas evaporates some of the Li and carries it into the test section. A single-longitudinal-mode diode laser was employed as a light source but its low power necessitated a decrease in the schlieren system cutoff ratio. Thus almost no undeflected light was blocked by the knife edge, resulting in dark spots on the schlieren images reflecting flowfield density gradients. Absorption resulted in further darkening of regions with relatively high density.

Surface heat flux was measured using two 5.3 mm long, 0.25 mm wide, $\sim 0.3\mu m$ thick platinum thin film gauges sputtered onto a Macor substrate consisting of a 50 mm o.d. insert closely matched to the pipe outer wall [4]. This insert was set to a number of positions along the model by means of spacers. The two gauges are arranged circumferentially on the insert and have an axial separation of 12.5 mm.

3 Results and Discussion

3.1 Starting process and approach to steady test flow

The standard theory of hypersonic nozzle starting begins with a Primary Starting Shock (PSS) accelerating the resident gas initially in the nozzle. This shock is driven by the pressure exerted by the test gas issuing from the nozzle throat. Ideally, a contact surface

then exists between the test and resident gases. The deceleration of the test gas creates an upstream facing Secondary Starting Shock (SSS). Depending on the flow conditions, a non-steady expansion may exist between the SSS and the steady flow that follows these nonsteady disturbances. Figure 1 shows six frames of conventional schlieren video from two condition B shots [3] with the leading edge and the collar 25 mm and 275 mm, respectively, downstream of the nozzle exit. The sequence commences as the PSS approaches the collar and ends 872μs later in the steady separated test flow. The existence of a well defined double shock system is confirmed by Figs. 1(a) and (b) which clearly show the PSS and SSS, respectively, to be nearly straight. Between these two shocks, the flow is seen to be highly non-uniform and non-steady.

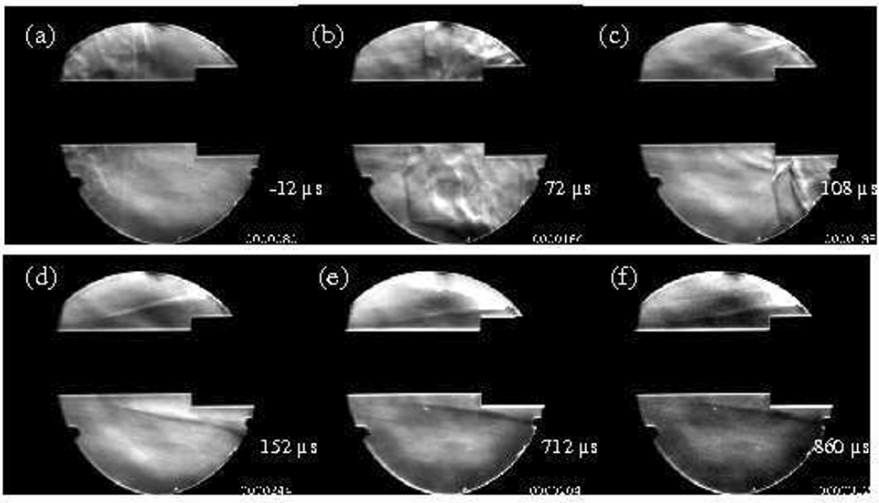

Fig. 1. Nozzle starting flow and the development of steady separated flow over the collar. Times in μs are after the arrival of the Primary Starting Shock at the collar forward face.

Fig. 1(c) shows the flow as the SSS clears the collar forward face. A bow wave, which began forming while the collar was enveloped by the starting shock system, is traveling upstream from the collar. As it proceeds it weakens and forms itself into a conical separation shock, as seen in Fig. 1(d). Gradually, this separation shock weakens further and attains a quasi-steady state, as seen in Figs.1(e) and (f). The video shows weak disturbances and unsteadiness about the average separation shock position during this steady flow period but no corresponding disturbances are seen in the leading edge interaction shock.

3.2 Near-resonantly enhanced schlieren in the high enthalpy flows.

During the passage of the starting shock system, in these shots, there is strong but patchy refraction and absorption of the laser light. Particularly strong refraction is expected for the test gas between the PSS/SSS contact surface and the SSS as this gas should be heavily doped with Li having come from the downstream end of the test gas slug which

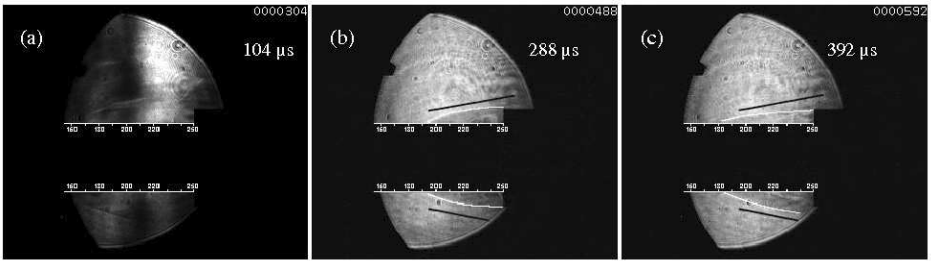

Fig. 2. Schlieren sequence of high enthalpy flows seeded with Li. White drawn curve shows the recirculation zone boundary. Dark drawn lines show the steady separation shocks' average positions. Note these images are inverted compared with those of Figs. 1 and 4

would be in intimate contact with the Li sample as it partially vapourises. Figure 2(a), taken $104\mu s$ after PSS arrival at the collar, shows the arrival of very highly refracting gas, the leading edge of which is thought to be the PSS/SSS contact surface. Between Figs. 2(a) and (b), refraction is so strong that the laser light is often almost entirely blocked. Very high refraction ceases upon the departure of the SSS, in Fig. 2(b).

In Figs. 2(b) and (c) a recirculation zone can be seen ahead of the collar. For clarity, white lines have been drawn along the zone boundaries. Black lines have been drawn at the steady flow separation shocks' average positions obtained from conventional schlieren images at the same flow condition. In Fig. 2(b), the zone is 50 mm long while in Fig. 2(c) it is 70 mm long. After this, the recirculation zone is no longer visible implying that the freestream Li concentration is then too low to offset the small cutoff ratio.

A possible interpretation of the observations is as follows. During the passage of the starting shock system, the gas within the recirculation zone has a high Li vapour concentration. After the passage of the SSS, the slow mass transfer in and out of the recirculation zone causes the Li vapour to linger in the zone although its concentration has dropped markedly in the surrounding flow. The absence of Li vapour in the recirculation zone $\tau = 100\mu s$ later suggests that this is the characteristic residence time of fluid in the zone. The freestream flow speed is $u_\infty = 4.58\ km/s$ and recirculation zone length is $L_r \sim 60\ mm$. Under this interpretation, Li vapour is depleted after $(u_\infty \tau / L_r) = 7.6$ passes of the recirculation zone.

3.3 Surface heat flux

The Stanton number based on freestream conditions, St_∞, is shown in Figure 3 for the high enthalpy shots for the clean pipe and for the pipe with the collar fitted with its upstream face at $x = 250\ mm$. This figure shows that the separation point is ~ 60 to 70 mm upstream of the collar front face, where St_∞ begins to fall sharply below its clean pipe values. This is close to the recirculation zone length estimated from Fig. 2(c), discussed above.

3.4 Foreign objects

Several of the videos show solid objects passing through the field of view. Some of them seem to collide with the collar and, when they do so, they often emit a bright flash.

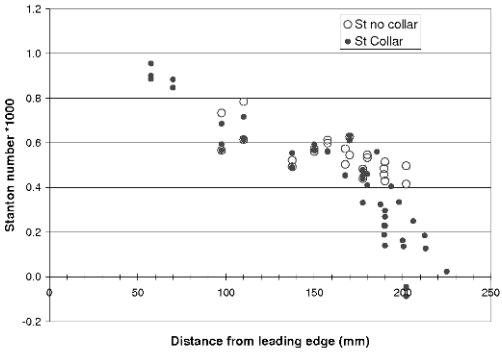

Fig. 3. Stanton number of heat flux on the pipe outer surface with and without collar attached for the high enthalpy shots. Collar front face is at $x = 250\ mm$.

These solids are almost certainly either fragments of the mylar diaphragm, originally sealing the nozzle entrance, or fragments of the main, mild steel diaphragm or, in the Li seeded flows, Li fragments. The models suffered some impact damage during the tests, as models do in the tunnel, indicating that the objects are probably metallic implying that all such objects in the conventional schlieren shots are main diaphragm fragments. Also, given that Li partially evaporates on shock reflection in the shock tube, the thin mylar diaphragm should mostly evaporate in these conditions.

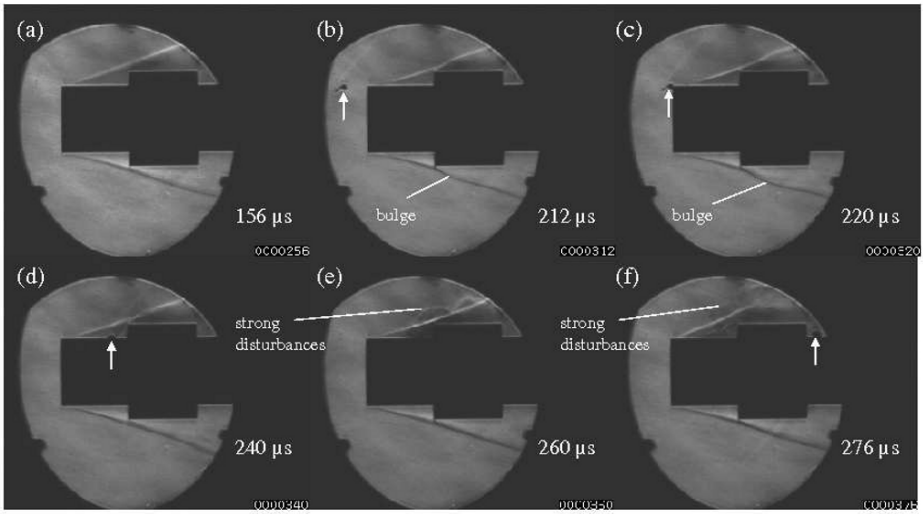

Fig. 4. Flight of foreign object, indicated by arrow, through the flow field. Low enthalpy condition. Collar 50 mm from model leading edge. Times in μs are times after Primary Starting Shock arrival at collar.

One such event is shown in Figure 4 for conventional schlieren shot 159. The object's speed is constant throughout and is $\sim 2.0\ km/s$. A barely visible, upstream facing bow shock exists around the object as seen in Fig. 4(a). As the object comes into line with the model leading edge, in Figs. 4(b) and (c), the separation shock, which until this time has been fairly steady, develops a distinct bulge aft of the collar front face. As the object aligns itself with the collar front face, blast-wave-like disturbances emanate from that region (Figs. 4(d) to (f)). The fact that the object re-appears aft of the collar and that its speed is constant throughout imply that the object itself does not collide with the collar. Thus it seems that the disturbance to the separated flow on the model is caused by its interaction with the bow wave about the particle. Most of these objects are only $O(mm)$ in diameter but their presence has profound, persistent effects on the flow. This may be the cause of many of the disturbances commonly seen on surface measurement traces in shock tunnel flows.

4 Conclusion

The high speed video camera used here to capture schlieren images has permitted the acquisition of detailed data on flow development in shock tunnels that was previously only rarely glimpsed. This has demonstrated that the long standing model of the nozzle starting process, involving Primary and Secondary Starting Shocks, is indeed closely followed in the tunnel. The near-resonantly enhanced schlieren has added to this by making visible the contact surface, thought to exist between the two starting shocks, and providing a measure of the ratio of the starting shock layer thicknesses. This optical technique has also yielded an estimate of recirculating flow residence time and the boundary layer separation length. The latter was in close agreement with the separation length obtained from surface heat flux measurements. The final surprising revelation is the strong and long lasting effects on flow of diaphragm debris passing close to the model flows. Previously, it was thought that debris significantly affected flows only upon collision with the model and that the effects were short lived.

The near-resonantly enhanced schlieren technique shows great promise in a number of other ways. A planned boost to diode laser power and improvement of methods of Li seeding into the steady flow, should increase sensitivity of the technique and further expand exploration of the flow behaviours.

References

1. McIntosh, M.K.: *Computer code for the numerical calculation of frozen and equilibrium conditions in shock tunnels*, Technical Report, Department of Physics, Australian National University,Canberra, ACT, 1968.
2. Vardavas, I.: Modelling reactive gas flows within shock tunnels. Australian Journal of Physics **37**, 1984
3. Kirstein, S.: The behaviour of hypersonic shock-induced boundary-layer separation with strong real gas effects, University of New South Wales, ADFA, (2006)
4. Dorner, S.S.: Transient heat flux measurements of laminar and turbulent boundary layers in a hypersonic shock tunnel. Technical University of Munich, Munich, (2006)

Study on convective heat transfer coefficient around a circular jet ejected into a supersonic flow

J.J. Yi[1], J.W. Song[1], M.S. Yu[2], and H.H. Cho[3]

[1] *Graduate school of Mechanical Engineering, Yonsei University 120-749, Republic of Korea*
[2] *Graduate school of Mechanical Engineering, Yonsei University, presently National Science Museum Planning Office, Ministry of Science and Technology, 427-060, Republic of Korea*
[3] *Mechanical Engineering, Yonsei University 120-749, Republic of Korea*

1 Introduction

The secondary jet injection into a supersonic cross flow can be observed in various situations such as a thrust vector control of a rocket and fuel injection of a scramjet engine, etc. The secondary jet in a supersonic flow acts as blocking body to the approaching cross flow although it is a fluid. When the blocking body exists in a supersonic flow, a complex structure of shock waves is produced. Many investigations have been conducted about the blocking bodies in a supersonic flow. Schuricht and Roberts[3] took surface temperature images using a TLC (Thermochromic Liquid Crystal) thermography to calculate the convective heat transfer coefficient. Yu[4] has measured the heat transfer coefficient around a protuberant cylinder body in supersonic flow by using a infra-red camera. There are some papers published about the pressure distribution around secondary injection hole in supersonic flow. Everett[5] has measured the pressure distribution around the circular secondary injection hole using PSP (Pressure Sensitive Paint), which show that the maximum pressure appeared on the side of injection hole. Huang[6] reported the crescent shape dimple around secondary injection hole which is installed at Titan IV SRM nozzle. Huang concluded that the high pressure and heat transfer cause the ablation around secondary injection. Although there are lots of studies on flow field and heat transfer about the cylindrical body and fin, there is little information about the heat transfer around a secondary jet. In this study, the convective heat transfer coefficient was measured around a circular secondary jet ejected into the supersonic flow field. The wall temperature measurement around the injection nozzle was conducted using an infra-red camera. A constant heat flux was applied to the wall around the secondary nozzle. For the different jet to freestream momentum ratio, the stagnation pressure of the secondary injection was controlled. The measured temperature is used to calculate the convective heat transfer coefficient. The comparison of the heat transfer coefficient distribution and the pressure distribution which is measured by Everett[5] was made in the center line.

2 Experimental facilities and data reduction

2.1 Supersonic blow-down tunnel

A supersonic blow-down tunnel was made for this test. In experimental facilities, there is the high pressure flow supplement system consisting of air compressor, coolers, filters, and air tanks. The air is compressed up to about 200atm. The compressed air is stored about 150atm in air storage tanks which has a $1.8m^3$ storage capacity. In the test, the compressed air is supplied from storage tanks to the stagnation chamber lowering the

pressure level down to 6.8atm by a pressure regulator. In the inlet diffuser of stagnation chamber, there are a cone-type separator and 5-stage screen installed for lowering the turbulence level and increasing the flow uniformity. The pressure and temperature in stagnation chamber are measured during the experiments. Figure 1 shows the pressure and temperature in freestream stagnation chamber. Stabilized air is passed through the nozzle for accelerating velocity to Mach 3. The accelerated air enters the test chamber. The test model which is placed in test chamber goes through the supersonic field. In test chamber, the static pressure was measured at 0.17atm. From the secondary injection tank, the air is passed through the pressure regulator lowering the adequate pressure for fitting the jet to freestream momentum ratio. In the secondary injection stagnation chamber, the air is stabilized and the stagnation pressure is measured. In the test model, there is the secondary flow passage for guiding the flow to test surface.

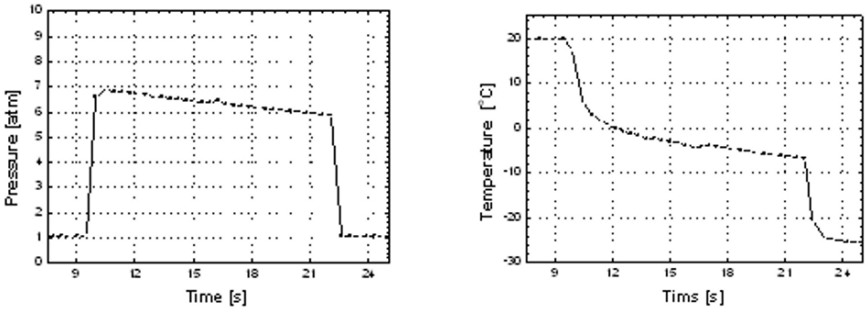

Fig. 1. The stagnation pressure and temperature at freestream stagnation chamber

2.2 Test model and other supplement equipments

Figure 2 shows the test model and the electrical foil heater in the experiment of the secondary injection. The considered surface where the secondary injection hole is located and the temperature was measured was placed on the electrical foil heater to satisfy the constant heat flux condition. At the back of the heater, a 5mm thickness Teflon block was placed to prevent the heat loss. For uniform constant heat flux condition around the secondary injection. The foil heaters resistance which was employed in the secondary injection experiment is 267Ω. The electrical source of the heater is the direct current supplied by the electrical power (200V, 20A). The supplied current value was monitored during the test by checking the voltage drop across the shunt placed in the middle of the electrical circuit. Most of voltage signals from sensors such as pressure transducers and thermocouples are received by the voltmeter (Agilent, HP34970A) and processed in a computer. The surface temperature on a considered surface was measured using the infra-red camera (Jenoptik, Varioscan3011-ST). The error estimation is 13.39 %. The major errors were caused by heat loss to the back of test and the heat resistance. The surface temperature was measured by the infra-red camera which was installed at the upper wall of test chamber. The secondary flow enters through the passage installed below of the test model surface. The secondary flow reached the Mach number 1 when it passed through the secondary flow nozzle, satisfying the chocking condition.

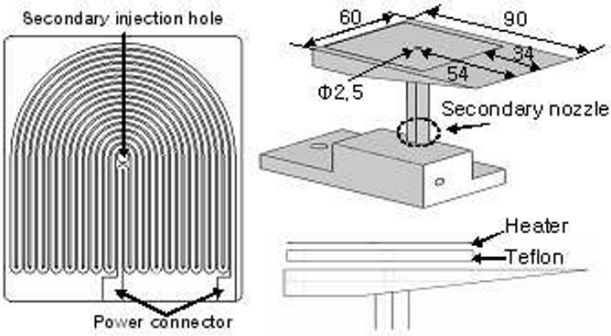

Fig. 2. The test model and heater pattern

2.3 Experimental condition and data reduction

The experiments were conducted under the constant heat flux condition on a considered surface. The freestream Mach number was about 3 and the unit Reynolds number was about $5.0 \times 10^7/m$. During the experiments, the stagnation chamber pressure was almost maintained to be 6.3atm although the chamber temperature decreased gradually due to the gas expansion in storage tanks and the Joule-Thomson effect at the valves and the pressure regulator. The heat flux was fixed at about 30,000 W/m^2. The heat flux value was calculated applying the following Eq. 1

$$\dot{q} = \dot{q}_h - \dot{q}_l \tag{1}$$

$\dot{g}_h$ is the heat generation of heater and it can be calculated using Eq. 2

$$\dot{q}_h = I^2 R \tag{2}$$

I is the current which is supplied heater and R is the heater resistance. $\dot{q}_l$ is the heat loss in the backward of test surface. The heat loss was estimated by the analysis of the one dimensional transient conduction problem and the flat surface condition was applied as boundary condition. The heat loss analysis process was conducted by the commercial code, Fluent vs. 6.2.16. When about 30,000W/m^2 heat is generated by the heater, the total heat loss was calculated to 6 % of the total heat flux. The heat transfer coefficient is calculated using Eq. 3

$$h = \frac{\dot{q}}{T_w - T_{aw}} \left[1 - \left(\frac{\xi}{x} \right)^{0.9} \right]^{-\frac{1}{9}} \tag{3}$$

where, T_{aw} was calculated by Eq. 4

$$T_{aw} = T_0 \frac{1 + r\frac{k-1}{2} Ma_\infty^2}{1 + \frac{k-1}{2} Ma_\infty^2} \tag{4}$$

The recovery factor, , is $Pr_{air}^{1/3}$. For controlling the jet to freestream momentum ratio, the secondary stagnation pressure was controlled by the pressure regulator. Equation 5 shows the definition of jet to freestream momentum ratio.

$$J = \frac{(\rho V^2)_j}{(\rho V^2)_\infty} = \frac{(\gamma p M a)_j}{(\gamma p M a)_\infty} \tag{5}$$

In the experiment, the freestream Mach number and the static pressure at the test chamber were 3 and 0.17atm, respectively. The static pressure at the secondary injection hole was governed by the stagnation pressure at the secondary injection stagnation chamber.

3 Results

3.1 The oil streak pattern

The experiments about the oil streak pattern were conducted with respect to jet to freestream momentum ratio. Figure 3 shows the results of the oil streak pattern. When the jet to freestream momentum ratio was increased, the length of the first separation and second separation was increased. When the jet to freestream momentum ratio was 1.17, the first separation length in a center line was expected to occur at about 2.25D upstream of secondary injection hole diameter and the second separation distance in center line was 1.2D upstream of secondary injection hole diameter. When the jet to freestream momentum ratio was 2.15, the first separation line appeared on 3.5D and the second separation line was believed to occur at about 1.6D upstream of the secondary injection hole diameter. When the jet to freestream momentum ratio was increased, the separation length was far from the secondary injection hole. The reason of this flow separation is known to be the reverse gradient of a surface pressure in a flow direction. When the momentum ratio increases, the surface pressure behind the inviscid shock wave around the secondary injection hole is increased and it could be propagated further upstream. This upstream pressure propagation is thought to cause the earlier flow separation for the higher jet to freestream momentum ratio.[7]

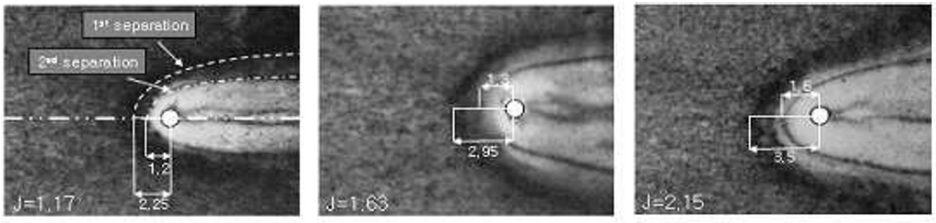

Fig. 3. The results of the oil streak pattern with respect to jet to freestream momentum ratio

3.2 Heat transfer coefficient

Figure 4 shows the contours of the convective heat transfer coefficient with respect to the jet to freestream momentum ratio on the surface of the test model. In Fig. 4, the

white circle in the middle of all figures represents the secondary injection hole. From the leading edge of the test model to the first separation, the convective heat transfer coefficients have the tendency to decrease because of the development of the boundary layer. Behind the first separation line, the heat transfer coefficient increases. Also, when the jet to freestream momentum ratio increases, the heat transfer coefficient around the secondary injection hole increases. As shown in the figure, the maximized region of the heat transfer coefficient appears on the both sides of the secondary injection hole. Figure 5 shows the comparison between heat transfer and surface pressure. In the case of the surface pressure distribution, the results of Everett[5] were referred. Everett conducted the pressure measurement test using PSP (Pressure Sensitivity Paint) for various jet to freestream momentum ratios such as 1.2, and 2.2. In this study, the jet to freestream momentum ratios were 1.17, and 2.15. Therefore, two results can be compared each other qualitatively. In Fig.5.a, the jet to freestream momentum ratios of the heat transfer coefficient and pressure distribution are 1.17 and 1.2, respectively. Two distributions of heat transfer coefficient and surface pressure show a similar pattern each other although the heat transfer coefficient doesn't show any change in the pressure plateau region. The maximum values of heat transfer coefficient and surface pressure appear similarly just in front of an injection hole. The same results appear in Fig. 5.b. In the Fig.5.b the jet to freestream momentum ratios of the heat transfer coefficient and pressure distribution are 2.15 and 2.2, respectively. The value of the convective heat transfer coefficient and

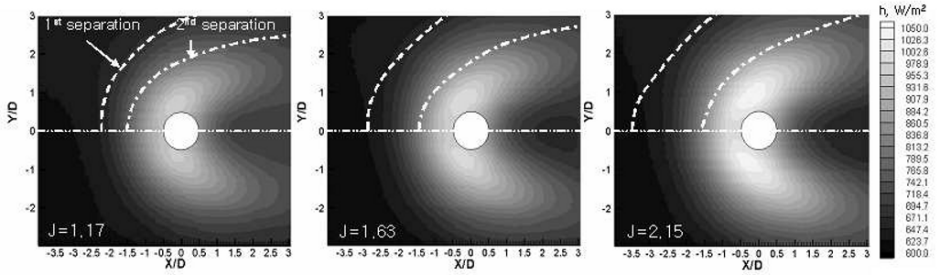

Fig. 4. The results of the convective heat transfer coefficient with respect to jet to freestream momentum ratio

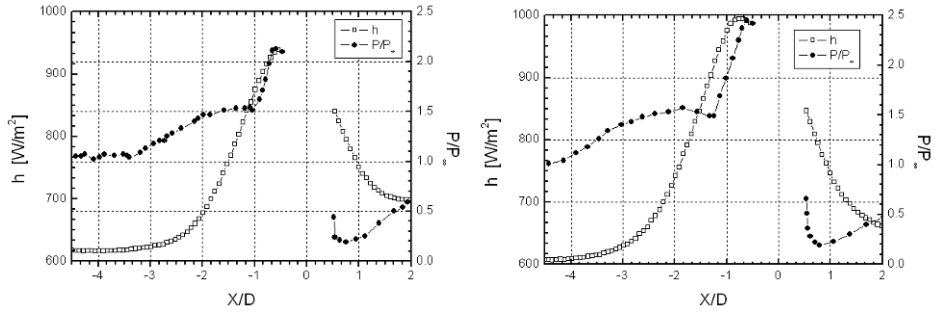

Fig. 5. The comparison between the heat transfer coefficient and pressure distribution in a center line, $a.J = 1.17(left), b.J = 2.15(right)$

the pressure was increased with respect to jet to freestream momentum ratio. The peak point locations of the heat transfer coefficient and the surface pressure are observed at the almost same position.

4 Conclusion

The measurement of the convective heat transfer coefficient was conducted for the flat surface where the secondary jet was ejected into the supersonic cross-flow. Also, the comparison between the heat transfer coefficient distribution and surface pressure distribution along the center line was performed. The results of the oil streak pattern around the circular secondary injection hole showed that the separation length was increased with increasing the jet to freestream momentum ratio. In this turbulent flow separation region, the surface heat transfer is promoted and the effected region becomes larger with increasing jet to freestream momentum ratio. Surface pressure shows a similar pattern with the surface heat transfer coefficient and has the peak value at the same position where the maximum heat transfer coefficient appears.

References

1. Hung, F. T., and Clauss, J. M. : Three-Dimensional Protuberance Interference Heating in High-Speed Flow. AIAA Paper 80-0289, Jan. 1980
2. Aso, S., Hayashi, M., and TAN, A. : Aerodynamic heating phenomena in three dimensional shock wave/turbulent boundary layer interactions induced by sweptback blunt fins. AIAA 28th Aerospace Sciences Meeting, AIAA-1990-381, AIAA, Washington D.C.
3. Schuricht, P.H., and Roberts, G. T. : Hypersonic interference heating induced by a blunt fin. AIAA 8th International Space Planes and Hypersonic System and Technologies Conference, AIAA-1998-1579, AIAA, Washington D.C.
4. Yu, M.S., Yi, J.J., Cho, H.H., Hwang, G.Y. and Bea, J.C. : A Study of the heat transfer around a cylindrical body protruded into a supersonic flow-field. AJCPP2006-22143, 2006
5. Everett, D.E., Morris, M.J., Wall pressure measurements for a sonic jet injected transversely into a supersonic crossflow : Journal of Propulsion and Power, Vol. 14, No. 6, November-December, pp. 861-868, 1998
6. Huang. W.M., Mistrek, D.L., and Murdock J.W. : Nozzle erosion induced by thrust vector control injection, AIAA paper 96-2638, 1996
7. Stollery, J.L. : Glancing shock-boundary layer interactions, AGARD-R-764, 1990

The effect of boundary layer transition on jet interactions

G.S. Freebairn, N.R. Deepak, R.R. Boyce, N.R. Mudford, and A.J. Neely

School of Aerospace, Civil and Mechanical Engineering, University of New South Wales, Australian Defence Force Academy, Canberra, 2600, Australia

1 Introduction

Transverse injection into high speed cross flows has been considered for a large number of applications over the past fifty years. Reviews by Margason [1], Spaid and Cassel [2] and Roger [3] contain several hundred theoretical, experimental and numerical references relating to jet interaction (JI) research. The most significant part of this work relates to use of transverse injection for vehicle reaction control(RC).

Precise vehicle control is of critical importance in any flight environment, but particularly at hypersonic speeds. One of the key findings to come out of the NASP and Hyper-X hypersonic vehicle development programs, for instance, was the need for robust flight control systems and algorithms to cope with the strong aerodynamic non-linearities associated with hypersonic flight [4]. The challenge faced by designers wishing to incorporated RC systems into these vehicles is that activation of RC jets can generate very strong, complex interactions. These can substantially alter the effective forces generated if the jet were exhausting into a quiescent medium, as well as causing aerodynamic interference that may extend for a considerable distance downstream. The development of accurate control algorithms and systems requires an awareness of the scales and sensitivities of these interactions over the entire flight envelope.

As a class of shock wave boundary layer interaction (SWBLI), the aerodynamic interference resulting from the interaction of the jet plume with the cross flow is strongly dependent on the state of the oncoming boundary layer [5]. Most of the existing JI research pertains to turbulent interactions generally associated with low altitude supersonic flight, although considerable research has also focused on high altitude hypersonic applications where boundary layers are typically laminar. In light of this, it may be concluded that interactions with both fully laminar and fully developed turbulent boundary layers are now reasonably well understood.

The same cannot be said when the boundary layer is in a state of transition from laminar to turbulent or where transition takes place within the interaction [6, 7]. This has implications for the application of RC technology to an increasing range of vehicles including reusable launch vehicles, hypersonic cruise vehicles, hypersonic interceptors and reentry vehicles where boundary layer transition is an important issue [8].

The present authors are unaware of any specific published examples of transitional supersonic or hypersonic jet interaction data but this paper will highlight some recent related evidence that justifies a more systematic study of the phenomenon. It will then outline some of the challenges of applying present JI methodologies to transitional phenomena and outline plans for a supersonic flight experiment to compliment the ground testing and numerical studies.

2 The jet interaction

The salient features and surface pressure distributions resulting from the interaction of an underexpanded jet plume with a high speed cross flow are shown in Fig. 1.

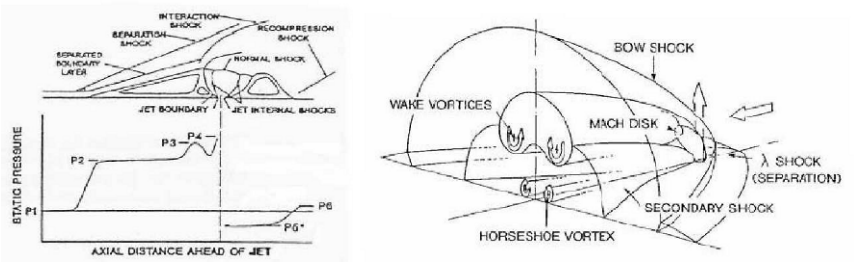

Fig. 1. The jet interaction showing **(a)** the primary features and pressure distributions in the nozzle centreline plane (Ref. [9]) and **(b)** the 3-D vortex structure (Ref. [10])

The expanding plume obstructs the cross flow creating a strong interaction, or barrel, shock before being brought back to ambient pressure through a normal shock known as a Mach disc. The strong adverse pressure gradients associated with the barrel shock induce upstream boundary layer separation in a nearly parabolic arc about the jet. This is accompanied by a weaker separation shock and at least two counter-rotating horseshoe vortices as determined by boundary conditions. A second smaller separated flow forms just downstream from the jet and this is followed by a recompression shock at the flow reattachment point. The elevated upstream surface pressures(P_2 to P_4), offset slightly by the lower pressures in the jet wake(P_{6^*}), are the source of the force amplification that characterises the JI.

Many studies have identified the need to place RC jets as far downstream from the vehicle's centre of gravity as possible to maximise force amplification and minimise adverse interference effects [3]. Defining a vector force amplification factor $\mathbf{K_F}$ as the ratio of the total force produced by the sum of the thrust $\mathbf{T}$ and aerodynamic interference $\mathbf{F_{JI}}$, to the thrust of the jet in a vacuum T_v,

$$\mathbf{K_F} = \frac{\mathbf{T} + \mathbf{F_{JI}}}{T_v} \tag{1}$$

amplification factors of up to three have been measured for these configurations [3].

Conversely, if performance or design constraints require the placement of the RC jets on the forward part of the vehicle, a considerable portion of the body is subjected to aerodynamic interference generated by the interaction. The horseshoe vortices may wrap around the body with the associated high surface pressures on the underside of the vehicle now acting to reduce the effective jet thrust. This can result in force deamplification and KF values as low as 0.5 [6]. When these non-localised pressure distributions span the centre of gravity significant variations in the associated turning moments may also result.

3 Evidence for transitional jet interaction effects

As part of an investigation into the wrap around of the separation front about a conical body in a fully laminar Mach 8 flow, Kumar et al [11] observed that the separation line became extremely unsteady as the freestream pressure was reduced. These results are reproduced in Fig. 2. The jet centre is marked by the vertical arrow towards the rear of the model while the discrete points and dashed lines represent the measured position and theoretical predictions based on an analytic blast wave model, respectively, of the separation shock. It was postulated that this was a result of boundary layer transition although no further analysis was presented.

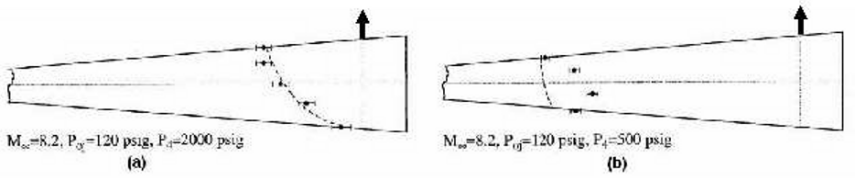

Fig. 2. Comparison of the predicted and measured separation fronts induced by a jet located toward the rear of a slender cone (jet centre marked by vertical arrows) in a Mach 8.2 flow for a **(a)**fully laminar, and **(b)** transitional boundary layer (Ref. [11])

It should be noted that the considerable difference in the separation lengths between Fig. 2 (a) and (b) is primarily due to the reduction in the freestream-to-jet total pressure ratio (P_4/P_{0j}). This increases the effective obstruction created by the plume and hence the forward extent of the separation region. As illustrated in the following example transition within the boundary layer is associated with a reduction in separation length.

In a related study of SWBLI Murphree et al [7] examined the effects of transition on vertical cylindrical post induced separation in Mach 5 flows. Although there are several fundamental differences, the horseshoe vortex systems generated by a cylindrical post and the jet plume share many features [12].

By tripping the boundary layer and forcing transition at different locations, they compared laminar, transitional, and turbulent interactions. Surface streak line visualisations of the three cases are reproduced in Fig. 3. Pockets of both laminar-like and turbulent-like flow separations similar to those observed in Ref. [11] were visible for the transitional case (Fig. 3(b)). This was attributed to the presence of turbulent spots flowing into the SWBLI. More work is required to understand these flows.

Importantly, to our knowledge, no published data exist for transitional JI in high speed flows, with the possible exception of Ref. [7]. It is possible that similar behaviour to that observed in the cylindrical post case would be observed for a JI. It is also possible that transition can be triggered in the JI separated flow region, as observed in the hypersonic flat plate compression corner studies of Bleilebens and Olivier [13]. Particular attention must be paid to the effects on surface pressure distributions and the behaviour of the horseshoe vortices. This will have implications for control system design.

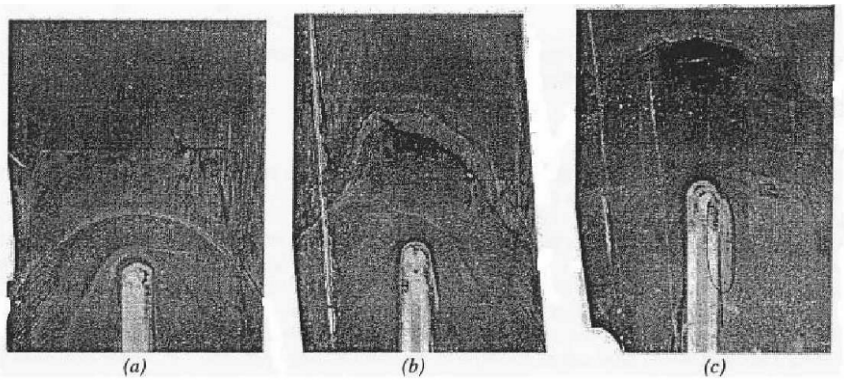

Fig. 3. Surface streak line visualisation of post induced interactions on a flat plate in Mach 5 flows. **(a)** fully turbulent, **(b)** transitional, and **(c)** laminar (Ref. [7])

4 Prediction Methodology

One reason for the extensive body of work on JI is that, for even the simplest missile-like geometries, the force and moment amplification factors are strongly dependent on a number of parameters including the freestream and jet flow properties as well as the vehicle and jet nozzle geometries [3]. The general approach to quantifying these relationships for use in flight control algorithms, as outlined in Ref. [6], begins with the application of analytical modeling to derive appropriate scaling laws. Parametric computational fluid dynamics (CFD) [14] and wind tunnel studies [11], are then conducted around these scaling laws. Curve fits are applied to the resulting data giving correlations relating the induced forces and moments to the parameters of interest.

The most widely used analytical model treats the jet plume as a blockage [11, 15]. Assuming that mainstream flow and geometrical similitudes are maintained this reduces to the extensively verified momentum scaling law

$$\frac{P_{0j}A^*}{qA_v} \tag{2}$$

where P_{0j}, A^*, q and A_v represent the total pressure of the jet, the effective nozzle area, the mainstream dynamic flow pressure, and the vehicle reference area respectively.

One of the major challenges in applying this methodology to transitional phenomena relates to the lack of understanding of the transition process itself. The growth and development of disturbances responsible for transition is thought to depend on a number of factors including surface conditions and geometry, freestream conditions and the presence of boundary layer instabilities [8]. However, efforts to characterise this phenomena using experimental or CFD techniques have so far met with little success.

This has implications for scaling laws and correlations derived from ground testing. Despite recent advances in low noise, or quiet, wind tunnel technology [16], measurements of transitional phenomena are always compromised by free stream turbulence introduced from the active boundary layers of the tunnel walls [17]. In these high noise environments the mechanisms responsible for transition in flight may be bypassed altogether [8, 16] and it currently not clear what impact this will have on the extension of ground based transitional JI results to the flight environment.

There are also considerable challenges associated with numerically simulating the complexities of three-dimensional transitional and turbulent high speed SWBLI's [18]. Although it is possible to simulate turbulent spots at desired upstream locations and observe the effect on the interactions or obtain predictions of the integrated surface pressures from uniform interactions produced by CFD, these results must be carefully, and thoughtfully, evaluated against experimental data.

5 Flight Experiment

To this end a coupled ground test/CFD/flight test is being conducted by the authors in order to investigate JI behaviour in supersonic and hypersonic flows. The flight payload is currently under development and is scheduled for launch on a supersonic rocket in 2008. It consists of a 3:1 ogive and cylindrical afterbody with an overall length of 1440mm and an outside diameter of 343mm(Fig. 4).

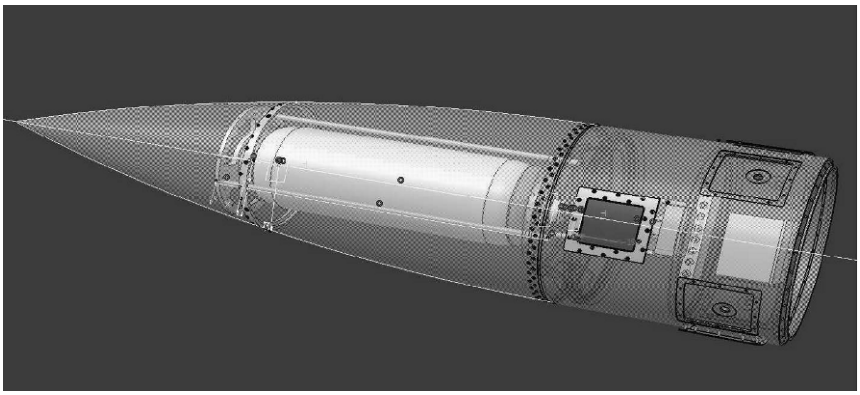

Fig. 4. Flight experiment configuration

The jet interactions will be generated by two sonic nitrogen jets. These are positioned normal to the surface on opposite sides of the afterbody half a body diameter downstream from the end of the ogive and will be pulsed simultaneously to maintain stability. The precise nozzle diameters and flow pressures will be finalised following the completion of a parametric study, similar to that discussed in Sect. 4, being conducted at present.

Instrumentation for the flight includes surface pressure and heat flux sensors, positioned in order to characterise the footprint of the JI as the vehicle descends from laminar through transitional to turbulent flows. The surface around one of the jets will be painted with a temperature sensitive paint as part of a related proof-of-concept study.

Based on calculations conducted using the criterion for boundary layer transition from Ref. [17], for a nominal velocity of $M_\infty = 3.2$ in the standard atmosphere, the altitude range chosen to achieve the desired range of flow conditions will be from approximately 25 down to 10 km. Transition about the jet is expected to occur at around 17 km giving a comprehensive data set for comparison with ground testing and CFD.

6 Conclusion

An understanding of the interaction of underexpanded jet plumes from reaction control systems with high speed cross flows over the entire flight envelope is essential to the development of accurate control algorithms for future hypersonic applications. Jet interactions with both laminar and fully turbulent boundary layers have received considerable attention but transitional interactions remain poorly understood.

There is some evidence suggesting the simultaneous presence of laminar-like and turbulent-like behaviour in the interaction but more work is required to understand the effect of this on surface pressure distributions and vortical flow structures, particularly for vehicle configurations using forward mounted RC systems. To this end a closely coupled program of numerical, and experimental (both ground based and flight) programs is currently being undertaken to gain further insight into this complex phenomenon.

References

1. Margason R. J.: Fifty years of jet in cross flow research. AGARD-CP-534, 1993
2. Spaid F. W. and Cassel L. A.: Aerodynamic interference induced by reaction control, AGARDograph, AGARD-AG-173, NATO, 1973
3. Roger R. P.: The aerodynamics of jet control for supersonic/hypersonic endo-interceptors: lessons learned, AIAA Paper 99-16653, 1999
4. Fidan B., Mirmirani M., and Ioannou P. A.: Flight dynamics and control of air-breathing hypersonic vehicles: review and new directions, AIAA Paper 2003-7081, 2003
5. Dolling D. S.: Fifty years of shock-wave/boundary layer interaction research: what next? AIAA J., vol. 39, no. 8, 2001
6. Cassel L. A.: Applying jet interaction technology, J. Spacecraft and Rockets, vol. 40, no. 4, 2003
7. Murphree Z. R., Jagodzinski J., Hood E. S., Clemens N. T., and Dolling D. S.: Experimental studies of transitional boundary layer shock wave interactions, AIAA Paper 2006-326, 2006
8. Schneider S. P.: Flight data for boundary-layer transition at hypersonic and supersonic speeds, J. Spacecraft and Rockets, vol. 36, no. 1, 1999
9. Powrie H. E. G., Ball G. J., and East R. A.: Experimental study of the interaction of a two dimensional reaction control jet with a hypersonic flow, IUTAM Paper, 1992
10. Dickmann D. A. and Lu F. K.: Jet in supersonic crossflow on a flat plate, AIAA Paper 2006-3451, 2006
11. Kumar D., Stollery J. K., and Smith A. J.: Hypersonic jet control effectiveness, Shock Waves, vol. 7, 1997
12. Kelso R. M.: Horseshoe vortex systems resulting from the interaction between a laminar boundary layer and a transverse jet, Phys. Fluids, vol. 7, no. 1, 1995
13. Bleilebens M., Olivier H.: On the influence of elevated surface temperatures on hypersonic shockwave / boundary layer interaction at a heated ramp model, Shock Waves, vol. 15, no. 5, 2006
14. Praharaj S. C., Roger, R. P., Chan S. C., and Brooks W. B.: CFD computations to scale jet interaction effects from tunnel to flight, AIAA Paper 97-0406, 1997
15. Mahmud Z., and Bowersox R. W.: Aerodynamics of low blowing ratio fuselage injection into a supersonic freestream, J. Spacecraft and Rockets, vol. 42, no. 1, 2005
16. Horvath T. J., Berry S. A., Hollis B. R., Chang C. L., and Singer B. A.: Boundary layer transition on slender cones in conventional and low disturbance Mach 6 wind tunnels, AIAA Paper 2002-2743, 2002
17. Anderson J. D.: *Hypersonic and High Temperature Gas Dynamics*, (AIAA, 1989), p. 275
18. Malmuth N. D.: Theoretical aerodynamics in today's real world: opportunities and challenges, AIAA J., vol. 44, no. 7, 2006

The influence of wall temperature on shock-induced separation

C.A. Edelmann[1], G.T. Roberts[2], L. Krishnan[2], N.D. Sandham[2], and Y. Yao[3]

[1] *Institute of Aerodynamics and Gasdynamics, Pfaffenwalding 21, D-70550 Stuttgart, Germany*
[2] *School of Engineering Sciences, University of Southampton, Hants SO17 1BJ, UK*
[3] *School of Engineering, Kingston University, London SW15 3DW, UK*

Summary. Two-dimensional numerical simulations are carried out to investigate the influence of wall temperature on the extent of the separation bubble produced when a planar shock impinges on a laminar boundary layer growing on a flat plate. The results are compared with empirical and theoretical correlations derived previously by other workers.

1 Introduction

Shock/boundary layer interactions (SBLI) are complex phenomena associated with supersonic and hypersonic flight that can have profound effects on the aerodynamic behaviour of a high speed vehicle. For example, strong interactions result in separation of the boundary layer, which can affect the aerodynamic forces and moments and, especially in the hypersonic case, cause a significant enhancement in the surface heating near reattachment. For these reasons, SBLI phenomena have been investigated for many years (see, for example, the review paper by Dolling [1]). Despite the significant body of work that has been undertaken, some aspects of the fundamental behaviour of SBLI remain relatively unexplored, or unknown. This includes the influence of wall temperature on the flowfield structure and topology, which is the topic under investigation in this paper.

Figure 1 shows a SBLI created by a shock wave impinging on a flat plate over which a boundary layer is growing. If the incident shock is of sufficient strength, the boundary layer will separate, causing separation and reattachment shocks to form. One of the primary parameters of interest is the separation bubble length $l_b = x_r - x_s$, where x_s and x_r are, respectively, the separation and reattachment points. It is well-known that a laminar SBLI is more prone to separation than a turbulent SBLI [1], and that the shock strength (characterised by the overall pressure ratio p_3/p_1, see Fig. 1) required to induce separation increases as the flow Mach number increases.

Katzer [2] carried out a series of numerical simulations of a shock impinging on a flat plate laminar boundary layer over a range of freestream Mach numbers $1.414 \leq M_1 \leq 3.4$ and Reynolds numbers $10^5 \leq Re_{x_i} \leq 6\times10^5$, with overall pressure ratios in the range $1.20 \leq p_3/p_1 \leq 1.80$. Here x_i is the distance from the leading edge of the flat plate to the point of shock impingement in the absence of the boundary layer. Katzer observed that the growth of the bubble length l_b was approximately linear with pressure ratio over the range of conditions he investigated, and proposed the following correlation law:

$$L_b = \frac{l_b}{\delta^*_{x_i}} \frac{{M_1}^3}{(Re_{x_i}/C)^{\frac{1}{2}}} = 4.4P \tag{1}$$

where $\delta^*_{x_i}$ is the undisturbed (i.e. no shock) displacement thickness at x_i, the Chapman-Rubesin parameter $C = (\mu_w T_1)/(\mu_1 T_w)$ and $P = (p_3 - p_{inc})/p_1$, where p_{inc}/p_1 is the shock pressure ratio required to produce incipient flow separation.

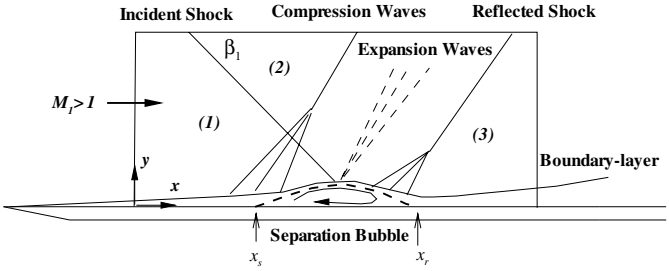

Fig. 1. Typical SBLI characteristics with impinging shock

In principle, Katzer's correlation accounts for variations in wall temperature implicitly through $\delta^*_{x_i}$ (which will be smaller for a cold wall than a hot wall) and explicitly through the Chapman-Rubesin parameter. However, in Katzer's work the ranges of Mach number and overall pressure ratio were limited and he only considered adiabatic walls. Krishnan et al. [3] also considered effectively adiabatic wall conditions, but extended the Mach number range up to $M_1 = 6.85$ and overall pressure ratios up to 5.89. From these results it was observed that the Katzer-type correlation was not linear over these extended pressure ratio ranges and, instead, proposed a revised correlation law:

$$L_b = \frac{4.4P}{1 + 0.1P} \tag{2}$$

Bleilebens and Olivier [4] recently reported the results of experiments carried out on a heated flat plate/compression ramp model on which a laminar SBLI was created at $7.1 \leq M_1 \leq 8.1$. Although the flow configuration is different to the impinging shock case, according to the free-interaction concept [5] the flowfield characteristics are similar for a given overall pressure ratio. Bleilebens and Olivier observed that, for a given ramp angle (which governs the overall pressure ratio) the bubble length increased as the wall temperature was increased with respect to the freestream temperature. They were unable to correlate their experimental results using Katzer's Eqn. (1); however, they did find that their data correlated reasonably well if, instead of evaluating the boundary layer displacement thickness and Reynolds number at the ramp hinge line (equivalent to the inviscid shock impingement point in the impinging shock case), they evaluated these parameters at the separation point. In this case they found their data were correlated by

$$L_b = (4.4 - 0.2\frac{T_w}{T_1})P \tag{3}$$

However, a potential difficulty with this modified correlation is that, unlike Katzer's correlation (Eqn. (1)), it is not possible *a priori* to estimate the separation location, and hence evaluate the Reynolds number and boundary layer displacement thickness at separation.

2 Numerical method

In this paper we explore the effect of wall temperature variations by carrying out two-dimensional numerical simulations of an impinging shock interacting with a laminar boundary layer, using a high-order unsteady Navier-Stokes code [6]. In the present case we are only concerned with the properties of the steady flow. These are obtained by running the simulation until such time that the properties of primary interest (e.g. the bubble length, l_b) are no longer changing significantly. It is worthwhile noting here that Katzer's criterion for convergence (based on decay of residuals below a threshold value) was not found to be an adequate check for stationary values of the bubble length and that, in some cases, much longer runs were necessary to achieve convergence.

The implementation of this code to the present study is similar to that described in Yao et al. [7]. The range of Mach numbers ($M_1 = 2.0$, 4.5 and 6.85) and overall pressure ratios are similar to those reported by Krishnan et al. [3] and, as in that previous work, the freestream Reynolds number at the shock impingement location is held constant at $Re_{x_i} = 3 \times 10^5$. However, in this present work we carry out simulations with a cold wall ($T_w = T_1$) and with a hot wall ($T_w = T_{aw}$). In both cold and hot wall cases the freestream Reynolds number (at a given Mach number) remains constant. Here the adiabatic wall (or recovery) temperature is calculated for a flat plate: $T_{aw} = [1 + r(\gamma - 1){M_1}^2/2]T_1$ with a recovery factor $r = \sqrt{Pr}$ for a laminar boundary layer, where Pr is the Prandtl number ($Pr = 0.72$ was assumed here).

The boundary conditions applied to the computational domain (illustrated as the rectangular box region in Fig. 1) were as described in Yao et al. [7], except that both cold and hot wall boundary conditions were applied to the lower boundary, as described above. The baseline grid used here was [N_x, N_y] = [257, 129], as in Krishnan et al. [3], but the domain sizes were adjusted carefully to suit the flow configurations. Checks on sensitivity to the domain size and grid refinement were carried out, but typically the bubble length remained within 5% of the baseline value, except near incipient separation particularly with the hot wall. In these cases a finer grid gave a significantly larger bubble length, which made estimation of the incipient pressure ratio difficult. This is discussed later.

3 Results

Figure 2 is a plot of the Reynolds number based on bubble length (Re_{lb}) against the overall pressure ratio, for all the cases considered here. Several features immediately become clear from this plot: the bubble length grows rapidly with overall pressure ratio at low Mach numbers, less so at high Mach numbers; the bubble length is greater for a hot wall than for a cold wall, at a given overall pressure ratio (this observation is compatible with that of Bleilebens and Olivier [4]); the overall pressure ratio required for incipient separation increases with Mach number and is greater for a cold wall than a hot wall. In addition, close observation of the data plotted in Fig. 2 reveals that the variation of bubble length with pressure ratio at $M_1 = 2$ is approximately linear (as observed by Katzer [2]), but at higher Mach numbers the variation is non-linear, both near incipient separation (particularly for the cold wall cases) and at high pressure ratios (particularly in the hot wall cases, as found by Krishnan et al. [3]).

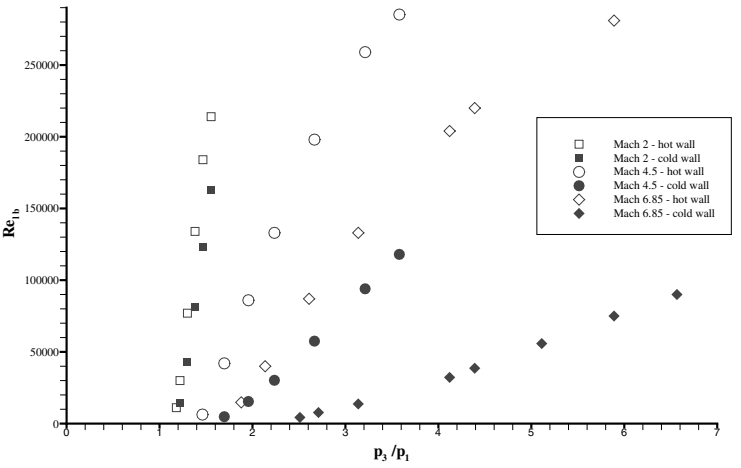

Fig. 2. Reynolds number based on bubble length vs. overall pressure ratio

In order to test Katzer's bubble length correlation over the range of Mach numbers, overall pressure ratios and wall temperatures considered here, we first need to examine the incipient separation condition.

3.1 Incipient separation

From his numerical results Katzer [2] verified that the shock strength required for incipient separation scaled according to the laws of the free interaction theory. He did this by estimating his incipient pressure ratio p_{inc}/p_1 by linear extrapolation of his bubble length vs. overall pressure ratio data back to a point where $l_b = 0$. He then verified that the following expression was valid for his range of test conditions:

$$\frac{p_{inc} - p_1}{p_1} = \frac{1}{2}\gamma {M_1}^2 P_{inc}[c_{f_i}/({M_1}^2 - 1)^{\frac{1}{2}}]^{\frac{1}{2}} \tag{4}$$

where he found the constant of proportionality to be $P_{inc} = 1.85\sqrt{2}$. He argued that the latter value was similar to that found experimentally and numerically by other workers, but also noted the difficulty in evaluating p_{inc}/p_1 precisely. Note that Eqn. (4) implicitly shows some sensitivity to wall temperature via the undisturbed (i.e. no shock) skin friction coefficient, c_{f_i}, evaluated at the (inviscid) shock-wall impingement point.

We have evaluated the incipient pressure ratios for our present cases and have plotted these in Fig. 3. In this plot we show the linear correlation of best fit to our data (from which P_{inc} can be determined as $1.7\sqrt{2}$) and compare that with Katzer's correlation. Although these two lines do not differ greatly, it appears that our data for cold and hot walls do not fully correlate via Eqn. (4), i.e. there is an additional wall temperature dependency that has not been accounted for. However, also note the significantly large error bars concerning our own data, which result from the uncertainty in extrapolating the data in Fig. 2 linearly back to $Re_{lb} = 0$, when it is clear that the data are non-linear in that region, and also the sensitivity to grid resolution noted earlier.

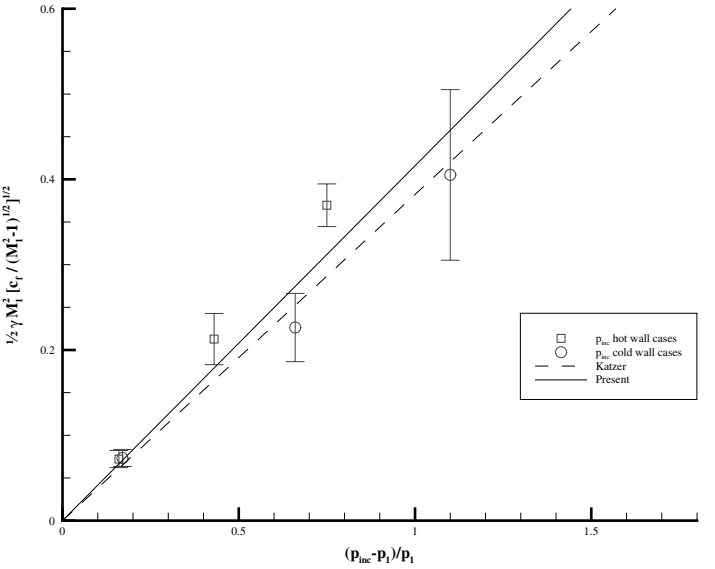

Fig. 3. Incipient separation correlation [2]

3.2 Bubble length correlation

Fig. 4 is a plot of the non-dimensional bubble length L_b, defined in Eqn. (1), against $P = (p_3 - p_{inc})/p_1$. In this plot, p_{inc}/p_1 has been estimated from Eqn. (4) with $P_{inc} = 1.7\sqrt{2}$, as discussed above. Also shown on this plot are the linear correlation due to Katzer [2], and the non-linear correlation found by Krishnan et al. [3] for adiabatic walls over the extended Mach number and overall pressure ratio range considered here.

As can be seen, although there is some significant scatter in the data when plotted in this form, most of the data correlate reasonably with Katzer's linear curve up to a value of $P \approx 2.0$. Above this value, a non-linear dependence is apparent for the adiabatic wall cases, as noted by Krishnan et al. The major departure from Katzer's linear correlation occurs for data obtained for the Mach 6.85 cold wall case. These data show a non-linear behaviour, with a non-dimensional bubble length L_b significantly smaller than those of the other cases considered here. For this case the ratio of wall-to-adiabatic wall temperature was approximately 1:9, indicating that heat transfer to the wall would be very strong. It therefore appears that Eqn. (1) does not fully account for wall temperature effects.

It should be noted that the revised correlation of Bleilebens and Olivier [4], given in Eqn. (3), does not offer any improvement: in general this correlation over-predicts the values of L_b for the cold wall cases and under-predicts the values for the hot wall cases. It therefore does not seem to account for wall heat transfer effects correctly.

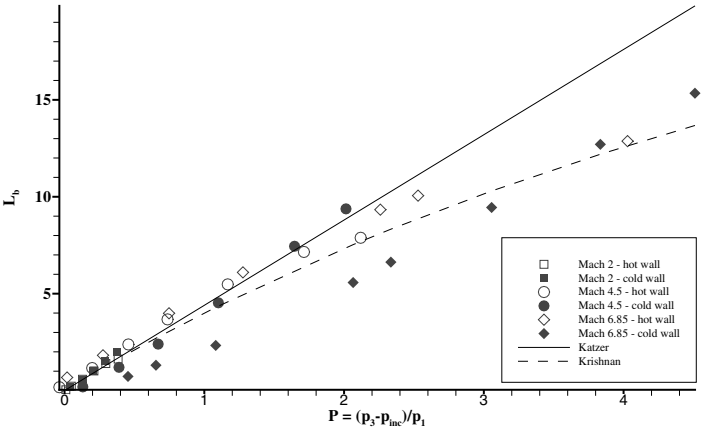

Fig. 4. Bubble length correlation [2]

4 Concluding remarks

From the numerical simulations that have been carried out, it appears that the separation bubble length correlation proposed by Katzer [2] does not apply to SBLI with very large overall pressure ratios (and hence massive separation), particulary at high Mach numbers, nor does it fully account for wall temperature effects, again particularly at high Mach numbers. Part of the discrepancy may be due to the difficulty (and consequent uncertainty) in predicting incipient separation. It would appear that further work is necessary to resolve these issues.

References

1. Dolling DS: Fifty years of shock-wave/boundary layer interaction research: what next? AIAA J. **39**, 8 (2001), pp. 1517–1531
2. Katzer E: On the lengthscales of laminar shock/boundary layer interaction. J. Fluid Mechanics, **206**, (1989), pp. 477–496
3. Krishnan L, Yao Y, Sandham ND and Roberts GT: On the response of shock-induced separation bubble to small amplitude disturbances. Modern Physics Letters B, **19**, 28-29, (2005), pp. 67–70
4. Bleilebens M and Olivier H: On the influence of elevated surface temperatures on hypersonic shock wave/boundary layer interaction at a heated ramp model. Shock Waves, **15**, 2006, pp. 301–312
5. Chapman DR, Kuehn, DM and Larson HK: Investigation of separated flows in supersonic and subsonic streams with emphasis on the effects of transition. NACA Report 1356, 1958.
6. Sandham ND, Li Q and Yee HC: Entropy-splitting for high-order numerical simulation of compressible turbulence. J. Computational Physics, **178**, 2 (2002), pp. 307–302
7. Yao Y, Krishnan L, Sandham ND and Roberts GT: The effect of Mach number on unstable disturbances in shock/boundary layer interactions. Physics of Fluids, **19**, 5, 2007, paper 054104 (15 pp.)

Wave drag reduction by means of aerospikes on transonic wings

M. Rein, H. Rosemann, and E. Schülein

Institute of Aerodynamics and Flow Technology, German Aerospace Center
Bunsenstr. 10, 37073 Göttingen, Germany

1 Introduction

Wave drag and shock induced boundary layer separation are important issues of flows around transonic wings. At transonic speeds the supersonic flow regime that is formed locally above wings, is terminated by a shock wave. This happens especially under off-design flight conditions and results in a wave drag. In addition, the shock-boundary layer interaction can cause a separation of the boundary layer and can thus lead to further losses and, eventually, to buffeting. These phenomena limit the maximum economic cruise speed of airplanes. The negative effect of the transonic flow regime can be mitigated by controlling the shock terminating the supersonic region above the wing. In the past many different concepts based, for example, on passive ventilation (perforated plates, slots, grooves), active suction, contour bumps or adaptive walls have been persued [1–3]. Mostly, these control methods are based on a two-dimensional approach, i.e., control devices are applied unifomly along the whole span. More recently, also three-dimensional control devices have been shown to positively affect lift and drag [4–7]. All these approaches have in common that measures for controlling the shock are applied directly at the surface of the wing. However, a control of the shock wave is also possible by placing external devices above the surface of the wing into the supersonic flow regime. The latter concept that is related to the one of aerospikes on blunt bodies, is studied in the present paper. As in the case of flow control measures that are applied directly at the surface of a wing the basic idea of aerospikes is achieving the pressure rise across a system of oblique and normal shocks instead of across a single normal shock thus reducing wave losses. In the present investigation oblique shocks were produced by disturbing the supersonic flow above the wing. In a test series the effectiveness of a variety of different spike-shaped bodies placed above a transonic wing was tested in the DNW-TWG, Göttingen. In addition to pressure measurements a colour schlieren system was set up for providing information about the influence of spikes on the flow field. In the following, first basics of aerospikes on transonic wings are explained. Then, wind tunnel experiments are described and results of measurements are presented and discussed. This is followed by a conclusion.

2 Aerospikes on transonic wings

The drag reduction mechanism of spike-shaped bodies that are placed in the supersonic flow above a transonic wing is based on the generation of wake flows and oblique shock waves interfering with the virtually normal shock terminating the supersonic region (Fig. 1). In this manner instead of an abrupt pressure rise across a single shock the pressure increases more gradually thus limiting losses. Since the spike is located above

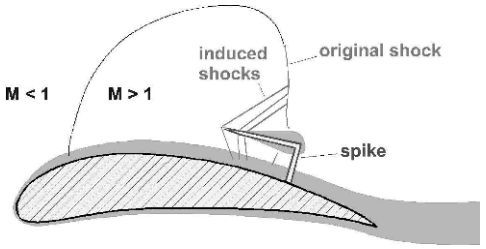

Fig. 1. Mode of action of a spike on a transonic wing

the surface of the wing the boundary layer on the wing is not directly disturbed. In the streamwise direction the exact position of the spike is likely to be of little influence on its efficiency because the properties of the wake are only little dependent on the streamwise location of the spike. The height H at which the spike is arranged above the surface should be chosen so that the shock is especially weakened in its lower part where the shock strength is greatest. Typical dimensions depend on the chord length c and the Mach angle μ. Similarly, in order to weaken the shock over the whole span width several spikes need to be placed next to each other in spanwise direction (Fig. 2).

Bodies of various geometries can be conceived acting as wake and shock inducing spikes. In the following, results are reported that were obtained with a cylindrical body

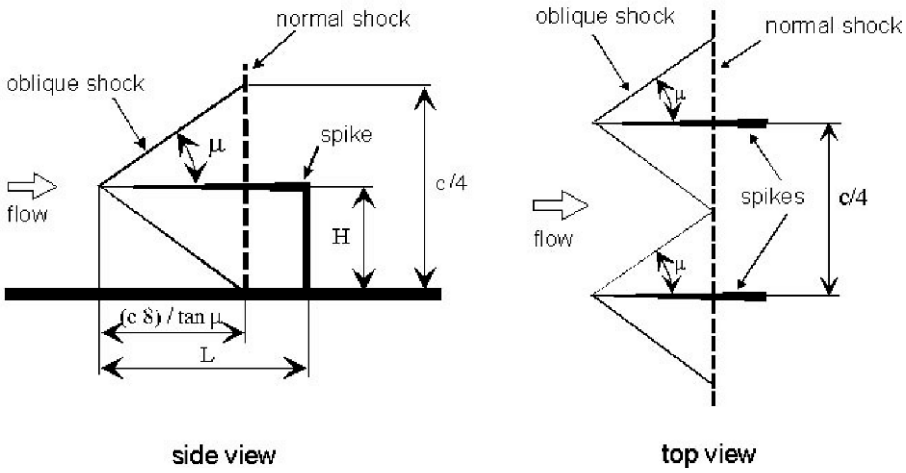

Fig. 2. Region of influence of a spike.

having a needle-like tip (cylindrical spike), a punctured pipe that was open at its leading end (punctured pipe) and a cone (conical spike). The cylindrical spike was chosen to resemble aerospikes as used on the nose of supersonic aircraft. Since the Reynolds number in the wind tunnel tests performed in the present study was much smaller than under real flight conditions a punctured pipe was then used in order to produce a wake like flow by jets that are ejected out of little holes arranged along the cylindrical surface of the pipe. Finally, a well defined displacement of the flow was achieved by means of the conical spike.

3 Wind tunnel tests

A 400mm-chord model of the transonic airfoil VC-Opt [8] was mounted in the 1m x 1m adaptive walls test section of the TWG. Onto the top of the VC-Opt model a single spike was placed the tip of the spike being located about in the middle of the chord (Fig. 3). Slender schlieren windows were fitted into the 2D-support right above the airfoil and a colour schlieren system was set up for observing the flow field. Lift and drag were determined by pressure measurements. On the wing the static pressure was obtained via pressure taps that were arranged in a slightly diagonal manner thus avoiding interferences between the taps. The drag was calculated from total pressure data obtained by wake-rake measurements one and a half chord lengths behind the trailing edge. The rake was laterally displaced with respect to the spike because the hold of the spike produces a wake that causes an effect opposing drag reduction by weakening the shock. Tests were performed at a Reynolds number of $Re \approx 5 \cdot 10^6$ and at two Mach numbers, $M = 0.775$ and $M = 0.795$, respectively.

Fig. 3. Transonic wing with conical spike in the DNW-TWG

In Fig. 4 schlieren pictures of the flow around the VC-Opt model without and with spikes are shown for a Mach number of $M = 0.795$ and an angle of attack of $\alpha = 3°$. Due to the slenderness of the schlieren windows the spikes are not always fully visible. A comparison of the pictures of the flow around the clean airfoil and the flow around airfoils with spikes shows only little differences. This is due to the span width ($1m$) being much greater than the size of the spike (diameter $2 - 12mm$). However, a shock wave

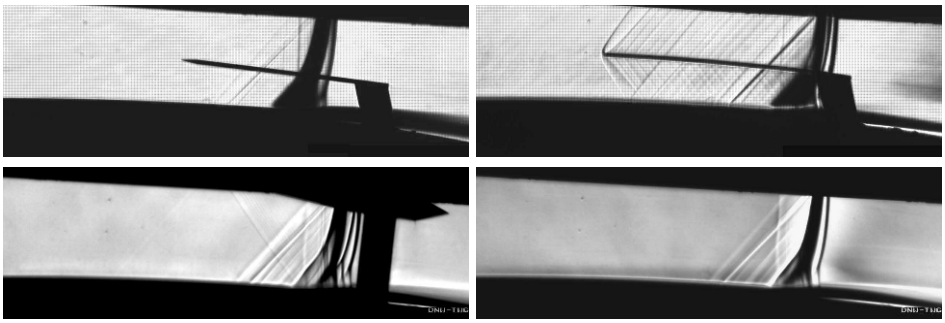

Fig. 4. Schlieren pictures of spike, punctured pipe, conical spike and clean airfoil. Mach number: $M = 0.795$, angle of attack: $\alpha = 3^\circ$.

and Mach lines originating from the tip and the surface of the spike, respectively, can clearly be seen for the case of the conical spike and the punctured pipe. Lift and drag polars were obtained also for configurations not shown in Fig. 4. Here, those for a clean airfoil and for an airfoil with a cylindrical spike, a punctured pipe and a conical spike are compared to each other (Fig. 5). In the case of the cylindrical spike the displacement of the wake rake was two and a half percent and in all other cases it was ten percent of the chord length. At certain angles of attack there is a gain in lift and the drag is clearly reduced. This effect is most pronounced for the conical spike, i.e., for that body which produces the greatest displacement of the flow.

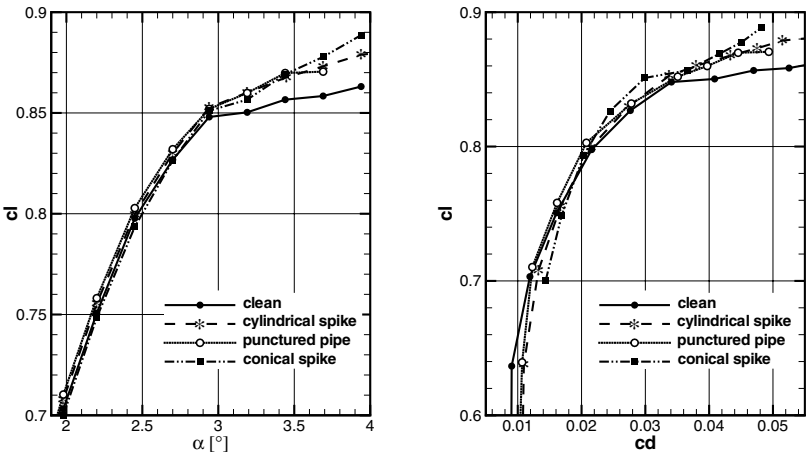

Fig. 5. Effect of different spikes on lift and drag

4 Conclusion

A preliminary study of the effect on the wave drag of aerospikes placed on top of transonic wings has been presented. Since the Reynolds number formed with the diameter of the model of a cylindrical spike is relatively small when compared to real flight conditions the efficiency of the cylindrical spike was less than expected. In order to produce larger disturbances in the supersonic flow field above the wing spikes of other geometries have also been tested. For certain angles of attack, $\alpha > 2.5°$, a gain in lift and a reduction of drag has been observed. Thus, the concept of using aerospikes on transonic wings clearly shows a potential for reducing wave drag. The shape of the spikes needs a further optimization taking into account real flight Reynolds numbers. Furthermore, it is important to obtain more global information on the wave drag by perfoming wake-rake measurements at different lateral positions thus resolving the spanwise distribution of the sectional drag and determining the influence of the hold of the spike. In this several spikes should be arranged next to each other in spanwise direction on top of the wing. In future tests schlieren pictures may not be of primary importance. Then integral values of forces such as lift and drag can be directly obtained by using a wind tunnel balance.

References

1. E. Stanewsky, J. Fulker, J. Delery and J. Geissler (Eds.): *Drag Reduction by passive Shock Control - Results of the Project EUROSHOCK*, Notes on Numerical Fluid Mechanics, Vol. 56, Vieweg Verlag, Braunschweig, Wiesbaden 1997.
2. E. Stanewsky, J. Delery, J. Fulker, and P. de Matteis (Eds.): *Drag Reduction by Shock and Boundary Layer Control - Results of the Project EUROSHOCK II*, Springer Verlag, Berlin, Heidelberg, New York 2002.
3. D. M. Bushnell: *Shock Wave Drag Reduction*, Annu. Rev. Fluid Mech. **36** (2004), pp. 81-96.
4. P. R. Ashill and J. L. Fulker: *A Review of Flow Control Research at DERA*, in: Meier, G.E.A. and Viswanath, P.R. (Eds.), IUTAM Symposium on Mechanis of Passive and Active Flow Control, Kluwer, Dordrecht 1999, pp. 43-56.
5. A. N. Smith and H. Babinsky: *Experimental Investigation of Transonic Aerofoil Shock / Boundary Layer Interaction Control Using Streamwise Slots*, in: Sobieczky, H. (Ed.), IUTAM Symposium Transsonicum IV, Kluwer, Dordrecht 2002, pp. 285-290.
6. G. Dietz, *Passive Shock Control Concept for Drag Reduction in Transonic Flow*, J. Aircraft **42** (2005), pp. 794-798.
7. D. W. Bechert, E. Stanewsky and W. Hage, W., *Windkanalmessungen an einem Transsonik-Flügel mit strömungsbeeinflußenden Massnahmen*, DLR-Report No. IB 223-99/B3-1, Berlin, Göttingen 1999.
8. K. Richter and H. Rosemann, *Experimental investigation of trailing edge devices at transonic speeds*, The Aeronautical Journal **106** (2002), pp. 185-193.

Wave drag reduction concept for blunt bodies at high angles of attack

E. Schülein

German Aerospace Center DLR,
Institute of Aerodynamics and Flow Technology,
Bunsenstraße 10, 37073 Göttingen (Germany)

Summary. The present investigation is an attempt to improve the aerodynamic effectiveness of aero-spikes located at the nose of supersonic blunt bodies flying at a wide range of angles of attack (AoA). For this purpose, the use of pivoting spikes, which can maintain their favorable alignment relative to the incoming flow independent from the body's orientation, is proposed. The proof-of-concept experiments for the pivoting spikes have been conducted in the Ludwieg Tube Facility at DLR Göttingen at Mach 2, 3 and 5 for angles of attack from 0 to 30 degrees. The model tested is a cylindrical body with a hemispherical nose. Additionally to the body equipped with a pivoting spike the reference body without a spike and the body with a conventional fixed spike were investigated. The results containing shadowgraph visualizations, direct force measurements and infrared heat flux measurements show the clear adventages of the pivoting spikes.

1 Introduction

Modern highly agile missiles equipped with a radar or infrared seeker mostly have relatively blunt hemispherical nose shapes. The reason is the requirement of an as undisturbed as possible signal transmission through the nose structure for optimal seeker functionality as well as the reduction of the heating loads on the dome structure at supersonic speeds. However the blunt nose shape leads to very high aerodynamic wave drag accompanied by high structural pressure loadings.

Conventional aero-spike devices help to protect the dome and to reduce the wave drag of blunt bodies at supersonic speeds. These devices mounted in the front of bodies can lead to distinct wave drag reductions of more than 50% in straight cruise flight [1]. The effect is induced by the interaction of the bow shock wave with the spike's boundary layer, which results in a flow separation with the formation of a conical shear layer that covers the spike and the majority of the dome and transforms the strong bow shock into a weaker shock system.

The presence of a spike in front of the blunt body, however, can lead to an increase in local thermal loadings due to the reattachment of a disturbed turbulent flow at the dome [2]. A spike seems to reduce the heat fluxes only if the separated boundary layer remains laminar and the spike is sufficiently long [3], [4]. The additional negative effect of the conventional mounting of a spike with an alignment along the body-axis is the very low device effectiveness with respect to wave drag reduction at relatively high angles of attack. As proven many times (e.g. [5]), the effect of a spike decreases quickly with increasing angle of attack α. The worst effect is however, that at moderate and high angles of attack the complex 3-D shock/shock/boundary-layer interactions can lead to very irregular and high heating peaks near the spike root [6]. The resulting high wall-temperature gradients are very dangerous because they can lead to damage of the dome structures due to high thermal strains.

The goal of the present investigations is the examination of innovative pivoting aero-spikes, which can maintain their alignment relative to the incoming flow independent of the body's orientation. This should consequently alleviate some disadvantages of conventional spikes in the wide AoA-range.

2 Test models and measurement techniques

The wind tunnel tests have been carried out with using a simplified axially symmetric hemisphere-cylinder model with a diameter D of 60mm and a length L of 200mm. Three model configurations were investigated: a) reference blunt body without spike, b) the blunt body equipped with a conventional fixed spike, and c) the blunt body with a novel pivoting aero-spike. Some spikes used have a diameter d_S of 6mm and different lengths L_S between 10mm and 200mm. They were screwed into the hemispherical body by threaded pins. The nose-tips of the spikes were either simply cut flat or had an additional tip-body, such as a flat-edged disc, a sphere or a double-cone 20°/45°, all with a maximal diameter d_D of 15mm ($d_D = 0.25D$). An additional test model with a prototype of a pivoting spike-device, which uses the weathercock principle for the self-maintaining of its alignment relative to the incoming flow, has also been investigated. This device uses aerodynamic stabilizers mounted downstream on levers. The rotation axis of this device is oriented perpendicularly to the longitudinal axis of the body and crosses it approximately at the center of the hemisphere.

The investigations were conducted in the Ludwieg Tube Facility at DLR Göttingen at Mach 2, 3 and 5 for a constant Reynolds number, based on the body diameter, of 1.5×10^6. The body's angle of attack was varied from 0 to 30 degrees.

The standard shadowgraph technique was used in this investigations to visualize the effect of different spike configurations. The recording of shadowgrams was made by a high speed camera ($PHOTRON\ Ultima\ APX - RS$) with a frame rate of 3kHz and an exposure time of 50μs.

For the force measurements an internal 6-component balance of the TASK-Corporation was utilized. In present work, only the effect of the used spikes on the drag, lift and pitching moment is analyzed. The reference parameters for the aerodynamic coefficients are the cross-sectional area $\left(A = 2827.4mm^2\right)$ and the length of the body ($L = 200mm$). The moment reference point lies on the body's axis at 154.3mm from the tip. The drag coefficients presented here correspond to the extracted forebody drag.

For the heat transfer measurements the Quantitative Infrared Thermography (QIRT) technique was applied. For this purpose a thick walled model was fabricated from black $PLEXIGLAS$ with low thermal conductivity. The time history of the test-surface temperature was recorded during the wind tunnel run and then used to determine the heat transfer rate under the assumption of a semi-infinite wall thickness. The local heat flux rates $\dot{q}$ obtained are converted to Stanton numbers as $St = \dot{q}/(\rho_\infty U_\infty c_p(T_0 - T_w))$, where: ρ_∞ and U_∞ are the freestream density and velocity; c_p is the specific heat capacity of air at constant pressure; T_0 and T_w are the total and model-wall temperatures. More details of the QIRT-technique used can be found in [7].

3 Results and discussion

3.1 Flowfield structure and heat flux distribution

Figure 1 shows a set of shadowgrams and Stanton number distributions obtained at $\alpha = 20^\circ$ and $M_\infty = 2$. These results show the effect due to the fixed or pivoting flat-edged spikes with a length of $L_S = 0.75D$ compared with the reference blunt body

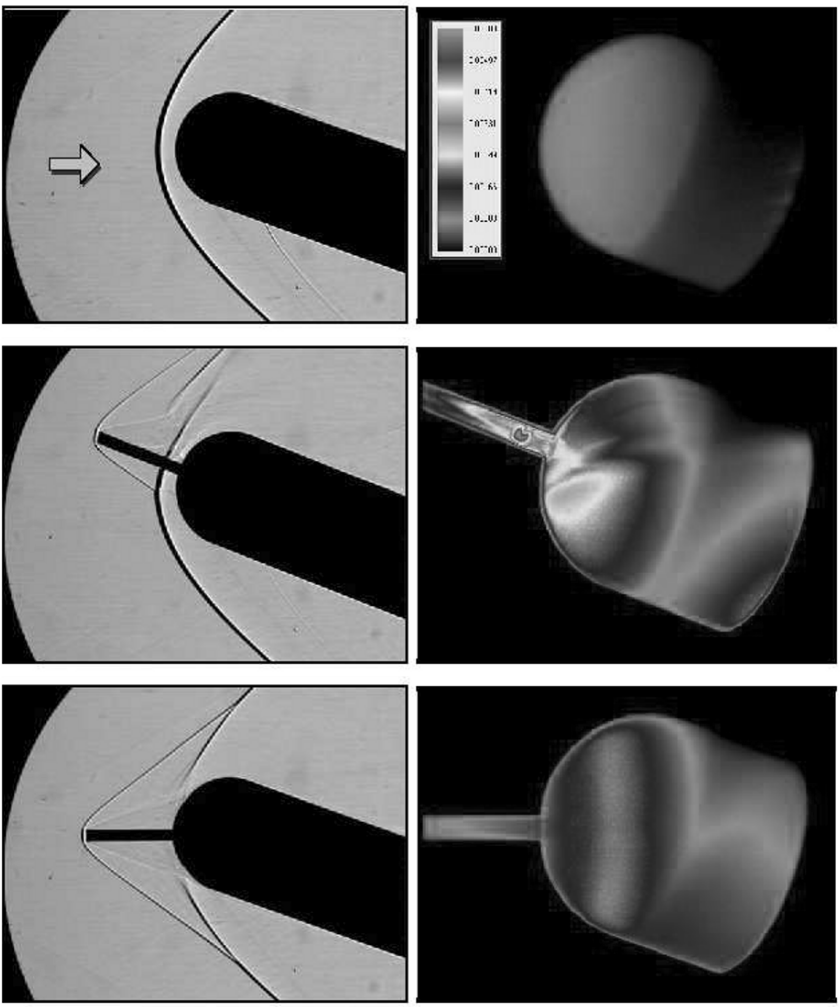

Fig. 1. Effect of fixed and pivoting spikes on the shock wave structures (left column) and quantitative Stanton number distributions on the hemisphere (right column) at $M_\infty = 2$, $Re_D = 1.5 \times 10^6$ and $\alpha = 20^\circ$: top pictures - reference body without a spike; middle pictures - body with a conventional fixed spike $L_S = 0.75D$, and bottom pictures - body with a pivoting spike of the same length

without a spike. The shadowgrams (left column) show for spiked bodies the typical wave structures, which consist at least of two shock waves coming from the spike's nose and from the reattachment region on the hemisphere, and the viscous shear layers limiting the separation region. Opposite to the effect of the conventional fixed spike, the separation zone around the pivoting spike remains quite symmetrical also at this high incidence angle and is very similar to that at $\alpha = 0°$. Furthermore, the comparison shows weaker shock waves in the presence of the pivoting spike not only upstream of the hemisphere but also along the wave-fronts far from the interaction zones.

The quantitative Stanton number distributions shown in Figure 1 (right column) confirm the increase of local heat fluxes in presence of a spike in front of the blunt body, due to the reattachment of the disturbed shear layer at the hemisphere. The maximal Stanton number measured for the pivoting spike configuration is 2.14 times bigger than for the reference blunt body without a spike. The reason is apparently the different state of the boundary layer at the given Reynolds number: laminar on the reference body and turbulent on the spiked body. The more negative effect of a fixed spike configuration is visible in the irregular heating peaks due to complex 3-D interacting flows near the stagnation region. The pivoting spike caused a smoother heat flux distribution at significantly lower heating levels. The maximal Stanton number measured for the fixed spike configuration is around 5.1 times greater than for the reference blunt body without a spike, and consequently nearly 2.4 times as high as that measured for the pivoting configuration.

3.2 Aerodynamical effectivness of pivoting spikes

The results of force and moment measurements show that the pivoting spikes oriented in the flow direction are responsible for the higher performance of blunt bodies than the conventional spikes. Figure 2 demonstrates the effect of fixed and pivoting spike-discs ($L_S = 1.0D$, $d_D = 0.25D$) compared with the performance of the reference body without a spike at $M_\infty = 5$. Both top plots clearly show that the forebody drag reduction effect of a fixed spike-disc decreases rapidly with increasing incidence angle α. The results agree very well with the observations of [5] and show that at approximatelly $\alpha > 15°$ the fixed spike-disc configuration generates even higher drag levels than the reference blunt body. The pivoting configuration shows, in comparison, a very stable behavior and substantial drag reductions in the entire *AoA*-range. Even at $\alpha = 30°$ this configuration still shows over 30% improvement over the reference body drag.

The comparison of the pitching moment behavior (left bottom plot) shows another advantage of the pivoting spike technology. The conventional fixed spike-disc leads understandably to an increase of the pitching moment, which would need to be compensated in a real flight, but the pivoting configuration reduces the destabilising moment. Furthermore, the lift-over-drag ratio of the body is clearly increased by the movable spike-device over the entire *AoA*-range, with respect to the reference blunt body. This is also caused by the optimized spike effect due to the decrease in the drag.

Similar tendencies were observed at other investigated flow conditions and types of spikes, such as sphere-tipped and cone-tipped spikes, where a distinct effect of the pivoting spikes on the control of the flow structure was always noticeable. The wind-tunnel tests with the prototype of a self-orienting spike-device were also successful. These additional results could not be presented here because of lack of space.

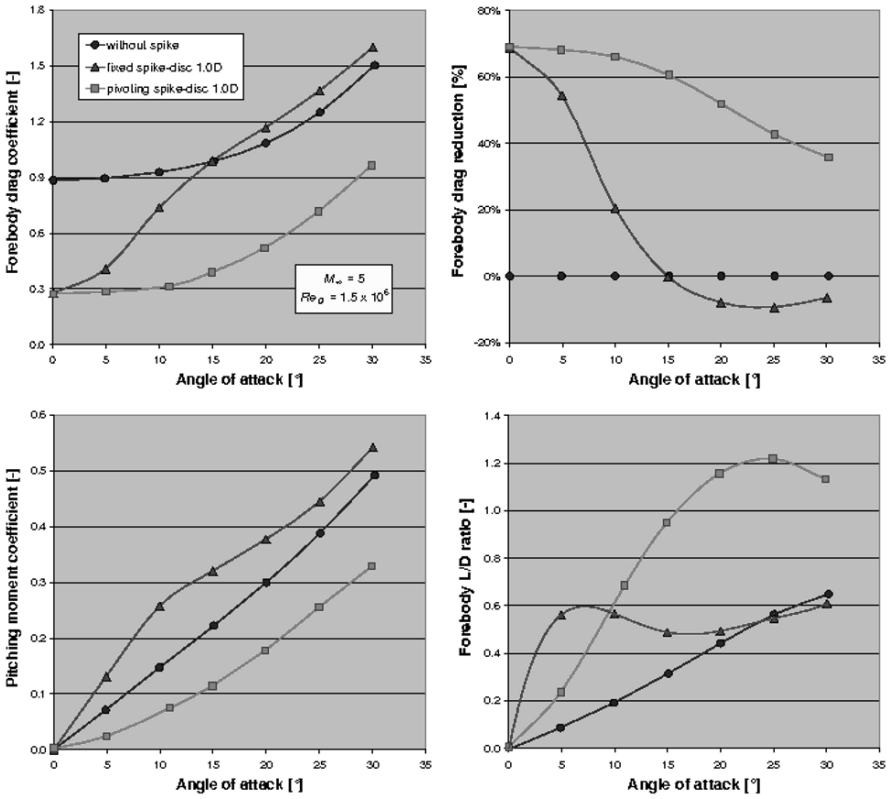

Fig. 2. Effect of fixed and pivoting spike-discs ($L_S = 1.0D$) on the aerodynamic performances at $M_\infty = 5$ and $Re_D = 1.5 \times 10^6$

4 Conclusions

The presented experimental results show clearly that the pivoting spikes are better than the conventional fixed spikes in all categories. All investigated spike types (flat-edged, sphere-tipped, disc-tipped, and cone-tipped spikes) show the advantages of the pivoting concept. Compared to conventional fixed spike-configurations the pivoting spikes:

- show a very stable behavior and distinct drag reductions over the whole *AoA*-range up to 30 degrees;
- caused at incidence a desirable decrease in the pitching moment and increase in the lift-over-drag ratio;
- lead to a smoother heat flux distribution and to clearly lower heating levels.

References

1. Chang, P.K.: Separation of Flow. Pergamon Press, 1970, 777 p.
2. Crowford D.H.: Investigation of the Flow Over a Spiked-Nose Hemisphere-Cylinder at a Mach number of 6.8, NASA TN-D118, Dec. 1959.

3. Bogdonoff S.M. and Vas I.E.: Prelimenary Investigations of Spiked Bodies at Hypersonic Speeds, Wright Air Dev. Center TN 58-7 (AD 142 280), March 1953.
4. Motoyama N., et al.: Thermal Protection and Drag Reduction with Use of Spike in Hypersonic Flow, AIAA-2001-1828, 2001.
5. Gnemmi P., Srulijes J., Roussel K., Runne K.: Flowfield Around Spike-Tipped Bodies for High Attack Angles at Mach 4.5. J. of Spacecraft and Rockets, Vol.40, No.5, pp.622-631, Sep.-Oct. 2003.
6. Menezes V., Saravanan S., Jagadeesh G. and Reddy K.P.J.: Experimental Invetsigations of Hypersonic Flow over Highly Blunted Cones with Aerospikes, AIAA-Journal, Vol.41, No.10, Oct. 2003, pp.1955-1966.
7. Schülein E.: Skin Friction and Heat Flux Measurements in Shock Boundary Layer Interaction Flows, AIAA-Journal, Vol.44, No.8, Aug. 2006, pp.1732-1741.

Wave processes on a supercritical airfoil

A. Alshabu, H. Olivier, V. Herms, and I. Klioutchnikov

Shock Wave Laboratory, RWTH Aachen University, Templergraben 55,52062 Aachen, Germany.

Summary. A shock tube with a rectangular test section is utilized to study the transonic flow about an airfoil model of a constant chord length. Upstream moving pressure waves are observed in experiment as well as in numerical simulation of a supercritical airfoil flow for different flow regimes. Both experimental and numerical results show that the observed waves are coupled with vortex generation in the boundary layer as well as wake fluctuations. The measured wave frequencies are in the order of 1-2 kHz. Using statistical means the wave speeds and wave propagation direction could be determined.

1 Introduction

An interesting phenomenon is observed when performing transonic flow studies on an airfoil. Pressure waves initiate near the trailing edge or/and in the wake and star propagating upstream in the subsonic region where they interact with the incoming flow, strengthen before becoming apparently weaker and almost disappear near the leading edge. Both, experimental and numerical investigations [1] show that the propagation of the observed waves is coupled with vortex generation in the boundary layer and wake fluctuations.

Upstream moving waves have already been experimentally observed during the phenomenon of periodic shock motions on airfoils. These waves are associated with wake fluctuations due to unsteady shock motions and termed 'Kutta waves' by Tijdemann [4]. The waves presented in this paper, however, have also been observed for flow conditions, for which no shock or shock oscillations occur. The authors suppose that the vortex generation in the boundary layer and their interaction with the trailing edge play a key role in the generation of these waves.

In the past, upstream moving waves have also been observed in compressible subsonic flows around slender bodies, for which a regular Karman vortex street occurs. However, these waves have been observed as a distortion affecting the vortex street formation and had not been further investigated. Seiler and Srulijes [6] investigated these waves more in detail. In their work they reported that the formation of vortices at the trailing edge in compressible subsonic flows is coupled with the emission of upstream moving pressure waves. It was concluded that the waves represent a weak acoustic phenomenon.

In this paper experimental and numerical results will be presented aiming at the better understanding of the wave processes described above.

2 Measurement and Numerical Technique

The test facility used is a modified shock tube with a rectangular test section (280x200 mm) to perform airfoil testing at transonic Mach numbers and relatively high

Reynolds numbers extending up to 38×10^6 based on a chord length of 100 mm [5]. The flow behind the incident shock wave provides the testing flow for a measuring period of about 5 ms. Figure 1, left, shows a longitudinal cut of the test section. The tested model is the BAC3-11 airfoil of 200 mm span and 80 mm chord length. To perform pressure measurements 11 miniature pressure transducers have been mounted directly underneath of pressure taps of 0.6 mm diameter. The natural frequency (Helmholtz resonator [3]) of the resulting configuration consisting of pressure tap, transmitting volume and sensor, is about 6 kHz. High speed photography is used to obtain highly time-resolved shadowgraphs of the flow. Figure 1 , right, shows a typical example of a Pitot and static pressure history measured in the test section. Due to shock tube boundary layer effects both pressures slightly increase with time. For data reduction a time window is chosen between 8 and 12 ms during which the free stream Mach number changes only by 1.4 %

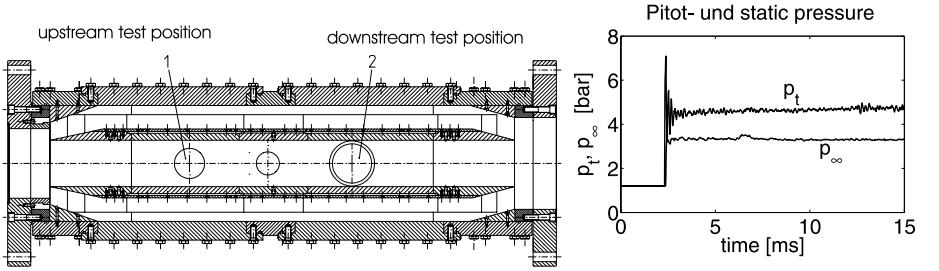

Fig. 1. Longitudinal cut of the test section(left), example of Pitot and static wall pressure histories measured in the test section of the transonic shock tube (right)

For numerical simulations a finite difference method based on WENO difference operators of high order ($N = 5, 7, 9, ...$) is applied for the approximation of the inviscid fluxes [4]. The 2-dimensional flow simulation is carried out on a C-H type grid with 1280x130 grid points on the RWTH Sun Fire cluster using 20 CPUs. No-slip boundary conditions are applied at solid walls with boundary layer related quantities $\Delta x^+ < 20$ and $\Delta y^+ < 1$.

3 Results

The experiments have been conducted at a chord Reynolds number range of 0.7 to 4×10^6 in order to study transition effects. The Mach number ranged between 0.6 and 0.8 at zero incidence. Figure 2 shows time-resolved shadowgraphs for an experiment with a Mach number of 0.71 and a Reynolds number of 3.0×10^6. The wave structure on the upper side of the airfoil as well as the upstream propagation of the waves can be easily seen. An increase of the wave intensity is also seen in the expansion region of the flow. The intensity of the waves decreases however, as they move further upstream towards the leading edge, where they become almost invisible depending on the sensitivity of the shadowgraph system.

Figure 3 , left, shows a similar wave structure obtained by numerical simulations for the same flow conditions. As can be depicted from Figure 3 , left, the wave generation is

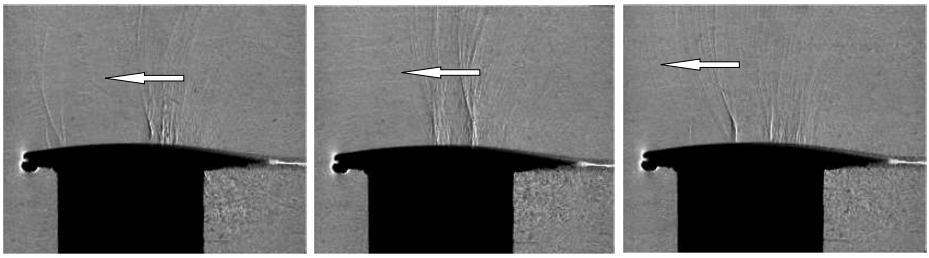

Fig. 2. Time-resolved shadowgraphs showing the upstream wave propagation on the upper side of the airfoil BAC3-11; Ma = 0.71, Re = 3.0×10^6, $\alpha = 0^o$

coupled with vortex generation in the boundary layer. In Figure 3 , right , it is seen that these vortices propagate downstream and interact with the trailing edge and/or the wake causing the waves to initiate. Hence, the vortex generation in the boundary layer seems to play an important role for the wave generation. The authors suppose that in order to stop the wave generation the vortex generation and the interaction of the vortices with the trailing edge respectively should be hindered.

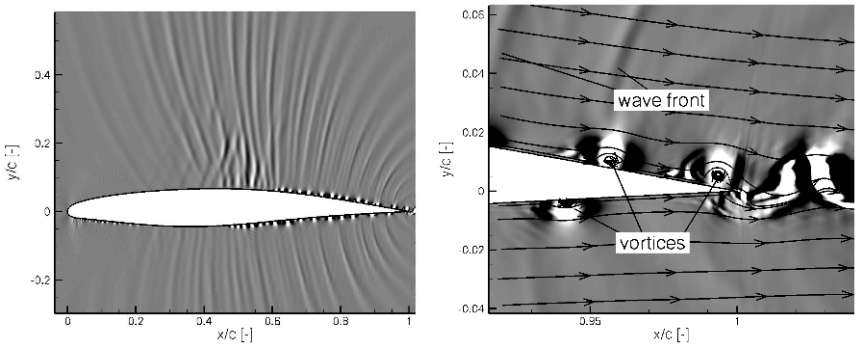

Fig. 3. Numerical results: Wave structure on the upper side of the airfoil BAC3-11; Ma = 0.71, Re = 3.0×10^6, $\alpha = 0^o$ (left), vortex interaction at the trailing edge (right)

Accompanied to flow visualizations, pressure measurements on the upper side of the BAC3-11 airfoil have been performed. Figure 4 shows some selected pressure histories for the experiment shown in Figure 2. Pressure fluctuations in the pressure histories due to wave processes presented above are easily seen. Starting from the trailing edge, the intensity of these fluctuations increases in the region of maximum flow expansion before it strongly decreases in the vicinity of the leading edge emphasizing the conclusion made from the shadowgraphs. As described in the following these fluctuations have been analyzed by statistical means [2].

The left and right parts of Figure 5 show the wave intensity at different Mach and Reynolds numbers respectively. Shown in Figure 5 is the standard deviation of the cor-

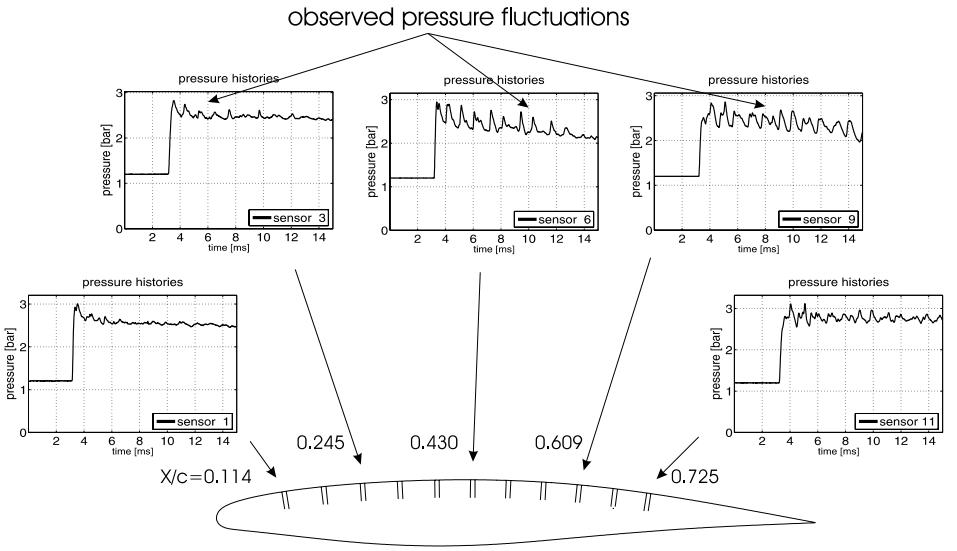

Fig. 4. Observed pressure fluctuations on the upper side of the BAC3-11, Ma = 0.71, Re = 3.0×10^6, $\alpha = 0^o$

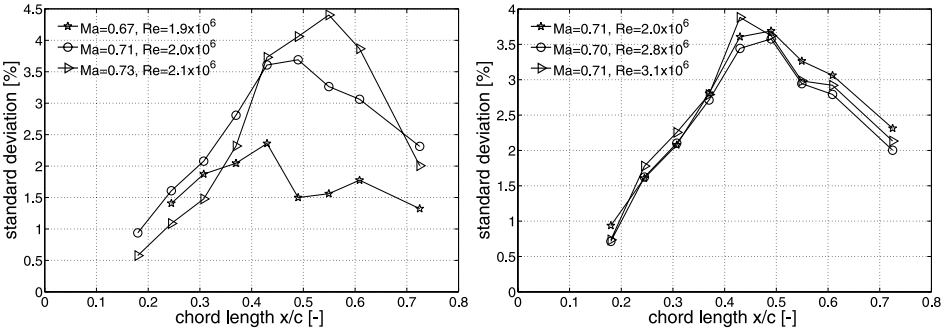

Fig. 5. Wave intensity at different Mach (left) and different Reynolds numbers (right)

responding pressure signals for the time period from 8 to 12 ms normalized with the corresponding free stream static pressure p_∞. The standard deviation, which can be regarded as a measure of the wave intensity confirms the conclusion made above. In all plots the wave intensity reveals a maximum in the region of the maximum flow velocity and decreases rapidly towards leading and trailing edges. Further, as it can be depicted from the left part of Figure 5 higher Mach numbers produce larger wave intensities. In the right part of Figure 5, it might be deduced that a small increase in the Reynolds number of about 1×10^6 results in small increase of the wave intensity. The Reynolds number influence on the wave intensity seems not to be as strong as that of the Mach number. However, a final conclusion demands the investigation of the Reynolds number influence in a wider range. The left part of Figure 6 shows exemplary a Fourier analysis of the pressure history of sensor 9. Two predominant frequencies of about 1 and

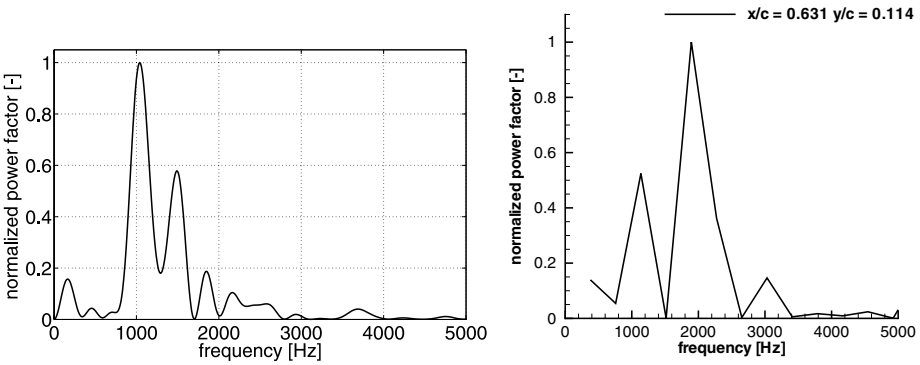

Fig. 6. Power spectral density of the pressure signal of sensor 5 (left) and the corresponding numerical result (right); Ma = 0.71, Re = 3.0×10^6, $\alpha = 0^o$

1.5 kHz can be depicted in Figure 6, left. The right part of Figure 6 shows the corresponding numerical result. The power spectrum of the pressure fluctuations corresponds to propagating pressure waves near the upper side of the airfoil (x/c = 0.631, y/c = 0.114) outside of the boundary layer. As it can be deduced from Figure 6 , right, two predominant frequencies of about 1.2 and 1.9 kHz agree well with experimental data. No significant Mach and Reynolds numbers dependence of the wave frequencies was found in the investigated range.

Two-point cross correlation of the pressure histories is used to determine the propagation direction and speed of the pressure waves. The left and right parts of Figure 7 show the obtained wave speed with respect to the airfoil at different Mach and Reynolds numbers respectively. Regardless of the rough spatial resolution, the figure shows an expected behaviour of the wave speed. It can be easily seen that in all plots the wave speed is lowest in the region of high local flow velocities and increases further downstream in the recompression zone of the airfoil. As can be depicted from the left part of Figure 7 higher Mach numbers result in an overall decrease of the wave speed. Further, as shown in the right part of Figure 7 the wave speed increases for higher Reynolds numbers.

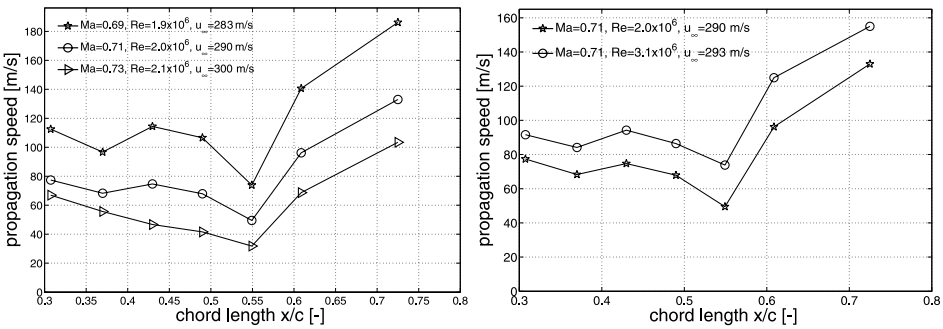

Fig. 7. Wave speed at different Mach (left) and different Reynolds numbers (right)

4 Conclusion

Results of a research work focussing on unsteady wave processes being observed for the flow on a supercritical airfoil were presented. The experiments were performed in a modified shock tube with a rectangular test section, in which both Reynolds and Mach numbers can be separately varied in a wide range. Time-resolved shadowgraphs reveal clearly the existence of upstream moving pressure waves. These waves initiate near the trailing edge and/or in the wake and propagate upstream. The vortex generation in the boundary layer seems to play the major role in the wave generation process. Time-resolved pressure measurements performed show pressure fluctuations due to the wave processes mentioned above. The Fourier analysis of the pressure histories reveals two predominant frequencies in the order of 1 and 2 kHz. Using two-point cross correlation wave speed and wave propagation direction have been determined. The wave intensity was found to increase with higher Mach and lower Reynolds numbers. Further, the determined wave speed, relative speed to the airfoil model, increases with increased Reynolds and decreased Mach numbers. Numerical results agree well with experimental data.

References

1. Alshabu A., Olivier H., Klioutchnikov I., Investigation of upstream moving pressure waves on a supercritical airfoil, Aerospace Science and Technology (10), May 2006, pp. 465-473
2. Berndat J. S., Piersol A. G., Measurement and Analysis of Random Data, John Wiley and Sons, Inc., 1966
3. Göpel W., Hesse J., Zemel J. N. (Eds.), Sensors- A comprehensive Survey. Band 7. Wiley-VCH Verlaggesellschaft, Weinheim, 1994
4. Klioutchnikov I., Ballmann J., "DNS of Transitional Transonic Flow about a Supercritical BAC3-11 Airfoil using High-Order Shock Capturing Schemes", DLES VI, Springer-Verlag, ERCOFTAC Series, 2006, V.10, pp. 737-744
5. Olivier, H. Reichel, T. Zechner, M.: Airfoil Flow Visualization and Pressure Measurements in High-Reynolds-Number Transonic Flow, AIAA Journal, Vol. 41, No. 8, Aug. 2003, pp. 1405-1412
6. Seiler F., Srulijes J., Vortices and pressure waves at trailing edges, Proceedings of the 16th International Congress on High Speed Photography and Photonics, Strasbourg, France, 1984
7. Tijdeman, H., Investigation of the Transonic Flow around Oscillating Airfoils, National Aerospace Lab., NLR TR-77090, Amsterdam, The Netherlands, Oct. 1977

Part XX

Shock Propagation/Reflection

α_1, β_1, β_2 - root characteristics of multiply possible theoretical solutions of steady Mach reflections in perfect diatomic gases

J.-J. Liu[1] **and T.-I. Tseng**[2]

[1] *Department of Engineering Science, National Cheng Kung University, Tainan, Taiwan ROC*
[2] *National Center for High-Performance Computing, Hsinchu, Taiwan ROC*

Summary. The existence of the jump in β_1=β_2 double roots in the three-shock theoretical solutions of steady Mach reflections on the (θ_1, M_0) plane is determined for the first time, θ_1 is flow deflection behind the incident shock, M_0 is the incident shock Mach number. This jump behavior of β_1=β_2 double roots explains the occurrence of newly found α_1=β_2 double roots of multiple theoretical solutions of steady MR in perfect diatomic and triatomic gases. The critical condition determining the location of M_0 of this jump, for gas specific heats ratio of 1.4, is obtained to occur at α_1= β_1= β_2 triple roots where M_0=3.41485. There are two findings closely associated with this jump behavior of β_1=β_2 double roots: 1, the α_1 solutions cease to become physically meaningful for $M_0 > 3.41485$; 2, α_1=β_2 double roots do not exist for $M_0 < 3.41485$.

1 Introduction

This work is an extension of Liu [1-3] and Liu et al. [4] reporting on multiplicity regimes of three-shock theoretical solutions of steady Mach reflections (MR) in perfect diatomic and triatomic gases. The existence and basic characteristics of newly found α_1= β_2 double roots of three-shock solutions of steady MR are verified and analyzed in perfect diatomic and triatomic gases [3.4]. As noted earlier [1], the problem of three-shock confluences of MR phenomena in steady flow is important both theoretically and practically. Academically, the problem of weak pseudo-steady MR has attracted attentions of researchers in areas of physics, mathematics, and engineering for more than half of century. A change of coordinates from laboratory to self-similarly propagating triple-point makes pseudo-steady MR equivalent to steady MR in the vicinity of the triple-point. Henderson [5] showed that the equation of motion of a confluence of perfect-gas three-shock waves (i.e. steady MR) could be reduced to a single polynomial equation of tenth degree with the pressure ratio across the Mach stem as the variable. Henderson [5] then gave the maps of the multiplicity of theoretical three-shock solutions on the (θ_1, M_0) plane for $\gamma = 1.1$, 9/7, 7/5 and 5/3 where m = 0, 1, 2 for the former two gases and m = 0, 1, 2, 3 for the latter two (m, the number of physically significant roots). Liu [1,2], on the other hand, pointed out that there exist regimes of m = 3 for $\gamma = 1.1$ and 9/7, and there are erratum in Henderson's multiplicity map for $\gamma = 7/5$. The reason for these mistakes are incorrectness in computed β_1=β_2 double-root lines. Henderson [5] reported that the β_1=β_2 double-root line and triple-root (II) curve coincide over the entire M_0 range considered for γ=1.1, and they merge for $M_0 > 3$ for $\gamma = 7/5$. Liu [1,2], however, showed that these two lines coincide only at $M_0 = 2.41$ and 3.117 for $\gamma = 9/7$ and 7/5, respectively. We show here that these two lines affect the map of the multiplicity of three-shock theoretical solutions of steady MR significantly. Needless to say, the newly found α_1=β_2 double roots not only change the β_1=β_2 double-root line, but dramatically alter the multiplicity

map of steady MR. Liu [3] remarked that the occurrence of α_1=β_2 roots implies the existence of a possible discontinuity behavior in the β_1=β_2 double-root line. The aim of this work is the determination of the location of the jump in β_1=β_2 double-root line of theoretical solutions of steady MR on the (θ_1, M_0) plane. Another motivation of this work stems from the above-mentioned link between theoretical solutions of a steady MR, where exact solutions are available, and those of a pseudo-steady MR. Henderson's 1987 work [6] on pseudo-steady MR, which was based on his 1964 work [5] on steady MR, is the most frequently referred theoretical analysis for describing the problem of the von Neumann paradox of weak pseudo-steady MR. However, are these two Henderson's works correct?

2 Analysis

The tenth degree polynomial equation of perfect-gas three-shock confluences given by Henderson [5] is of the form: $R_i T_i = 0$ (i=1,2,..9), where R_i and T_i are algebraic polynomials of degree 6. The tenth degree polynomial equation obtained by Liu [1] is of the form $\sum_{n=0}^{10} C_n x^n = 0$, where $C_n\,'s$ are too lengthy to be given here. For example, the numbers of different terms in coefficients C_3 and C_4 are 748 and 778, respectively. This tenth degree polynomial equation is used for calculating all possible three-shock theoretical solutions for a given condition of a steady MR. An intermediate form of this equation is given in [1].

According to Henderson [5], a physically significant solution of a steady MR requires that the pressure behind the Mach stem be larger than that behind the incident shock. There exist double incident Mach line degeneracies, D_1, double reflected Mach line degeneracies, D_2, a physically possible α_1 solution, a physically impossible α_2 solution. This gives a total of six roots with two pairs of complex roots left. He used symbols β_1, β_2 to represent a second and third appearances of physically possible solutions when one of the two pairs becomes real. In the following, we explain nomenclature used in obtaining multiple three-shock solutions by applying it to a steady MR of $M_0 = 4.015$, $P_1 = 6.215$, $\gamma = 1.4$. Figure 1(a) shows (p - θ) shock polar diagrams illustrating multiply possible three-shock solutions for this steady MR, where m = 2. There is one regular reflection solution RR (weak), one backward-facing reflected shock solution β_1, one forward-facing reflected shock solution β_2. The α_1 root is not physically realizable in this case. The physical plane corresponding to β_1 is shown in Fig. 1(b). The wave configuration is drawn according to calculated results of the β_1 solution, and it agree reasonably well with that of the actual experiment of this case reported in JFM (2002, 459). Note the vast differences among β_1, β_2 and α_1 solutions, and not all intersection solutions lead to physically meaningful results. Liu et al. [4] reported the link between the occurrence of α_1=β_2 roots and a possible jump behavior in β_1=β_2 root-line. More specifically, possible jump behaviors of β_1=β_2 root-line were found to be located in narrow ranges near M_0=3.5 and 2.3 for $\gamma = 7/5$ and $9/7$, respectively. Searching for the exact location of the jump of the β_1=β_2 double-root line on the (θ_1, M_0) plane are carried out by systematically examining multiply possible solutions at different $M_0\,'s$ by varying θ_1 from upper forbidden sonic conditions to their minimum incident Mach angle conditions. Three series of sequential solutions of $M_0 = 3.4$, 3.41484 and 3.45 are reported.

3 Locating the jump of β_1=β_2 double roots line by examining theoretical solutions of steady MR at different M_0's

Earlier works of one of the authors [1-4] have explained mathematical and physical meanings for the occurrences of possible theoretical α_1, β_1, β_2, D_2, D_1 and α_2 solutions of perfect-gas steady MR. Owning to the usefulness of (p - θ) shock polar representation of theoretical MR solutions, the results illustrating in Figs. 2-4 are self-explanatory. In particular, solutions of the upper sonic forbidden condition are marked as M_1=1, D_2=α_1, marked as Triple-root (I), D_2=β_1 as Triple-root (I) or (II), D_2=β_2 as Triple-root (II). Solutions of forward- and backward-strong/weak separating, forward- and backward-sonic, forward/backward separating, von Neumann and limiting incident shock Mach angle conditions, β_1=β_2, α_1=β_2 are correspondingly marked. Therefore, only brief descriptions regarding main features of multiply possible solutions are provided for M_0 = 3.4 and 3.45. Detailed discussions on behaviors of α_1, β_1 and β_2 solutions are given for M_0 = 3.41485, where the jump in β_1=β_2 is located. Figures 2 and 4 give systematic shock polar solutions for M_0 = 3.4 and 3.45, respectively. There are similarities and differences in these two series theoretical solutions. Similarities are θ_1 locations of the solutions of triple-root (I) and (II), forward/backward separating, forward- and backward- sonic and von Neumann conditions. However, significant differences are θ_1 locations of β_1=β_2 double roots. Particularly, α_1=β_2 double roots, which occur twice in M_0 = 3.45, do not exist in M_0 = 3.4. The reason for this apparently large difference in θ_1 location in such a narrow variation of M_0 and the occurrence of α_1=β_2 may be understood when one compares calculated solutions of M_0 = 3.4 and 3.5 with those of M_0 = 3.41485. The critical condition for occurring the jump in β_1=β_2 double roots is now found to be the α_1=β_1=β_2 triple-root condition at M_0=3.41485, θ_1=36.4344, shown in Fig. 3(b). One observes that the α_1 solutions cease to become physically realistic, for they are unable to move above D_2 for $M_0 > 3.41485$. After the occurrence of α_1=β_1=β_2, α_1 and β_2 disappear immediately, and the β_1 moves towards the forward-facing, then backward-facing branches of the reflected shock polar. From the incident polar viewpoint, the β_1 moves from the weak to the strong branches. As for the various specific MR solutions, they are marked in Fig. 3. Most interesting cases are α_1=β_2 roots whose first appearance is the merge of the α_1 and β_2 roots and their second appearance is the separation of these two roots, when $M_0 > 3.41485$. Finally, this obtained jump behavior of β_1=β_2 double-root line, occurring at M_0=3.41485, $29.8438° \leq \theta_1 \leq 36.4344°$, is added to the map of the multiplicity of theoretical three-shock solutions of steady MR of perfect diatomic gases on the (θ_1, M_0) plane. This is shown in Fig. 5(a). Important locations delineating different regimes of multiplicities of steady MR are marked as points a to k. Their definitions are given accordingly there. Locally enlarged view near the β_1=β_2 jump of 5(a) illustrating various separating or limiting properties of steady MR solution curves are shown in Fig. 5(b).

4 Conclusions

The existence of the jump in β_1=β_2 double roots in the three-shock theoretical solutions of steady Mach reflections on the (θ_1, M_0) plane is determined for the first time, θ_1 is flow reflection behind the incident shock, M_0 is the incident shock Mach number. This jump behavior of β_1=β_2 double roots explains the occurrence of newly found α_1=β_2 double

roots of multiple three-shock theoretical solutions of steady MR in perfect diatomic and triatomic gases. The critical condition determining the location of M_0 of this jump, for gas specific heats ratio of 1.4, is obtained to occur at $\alpha_1 = \beta_1 = \beta_2$ triple roots where M_0=3.41485. There are two findings closely associated with this jump behavior of β_1=β_2 double rots: 1, the α_1 solutions cease to become physically meaningful for $M_0 > 3.41485$; 2, α_1=β_2 double roots do not exist for $M_0 < 3.41485$.

References

1. Liu J. J. : A map of multiplicity of perfect-gas three-shock theoretical solutions of steady Mach reflection in diatomic gases, The 5th Int'l Workshop on Shock/Vortex Interactions. Kaohsiung, Taiwan, 120-127, 2003
2. Liu J. J. : Multiply possible three-shock theoretical solution of steady Mach reflections in triatomic perfect-gases, The 5th Int'l Workshop on Shock/Vortex Interactions. Kaohsiung, Taiwan, 105-111, 2003
3. Liu J. J. : A new kind of double roots of three-shock theoretical solutions of steady Mach reflections in perfect triatomic gases, The 28th National Conference on Theoretical and Applied Mechanics, 659-666, 2004
4. Liu J. J., Lin C. C., Chou C. A. : The existence of α_1=β_2 double roots in the three-shock theoretical solutions of steady Mach reflections in perfect diatomic gases, AASRC/CCAS Joint Conference, 2005
5. Henderson L. F. : On the confluence of three shock waves in a perfect gas, Aeronautical Quarterly, vol. 15, 181-197, 1964
6. Henderson L. F. : Regions and boundaries for diffracting shock wave systems, ZAMM, vol. 67, 2, 1987

.

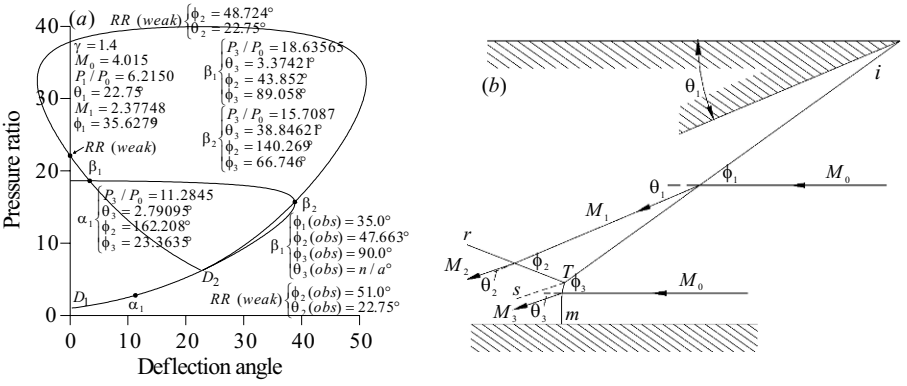

Fig. 1. Steady MR shock polar diagram (a) showing multiple solutions and the physical plane of the β_1 solution for M_0 =4.015, θ_1=22.75°, γ=1.4, where i, incident shock; r, reflected shock; m, Mach stem; s, slipstream. (0), (1), (2), (3), respectively, are flow regions as defined, ϕ_n, wave angles, θ_n, deflection angles, T, triple-point, χ, triple-point angle, M_s, incident shock Mach number, θ_w, wedge angle, M_n, flow Mach number.

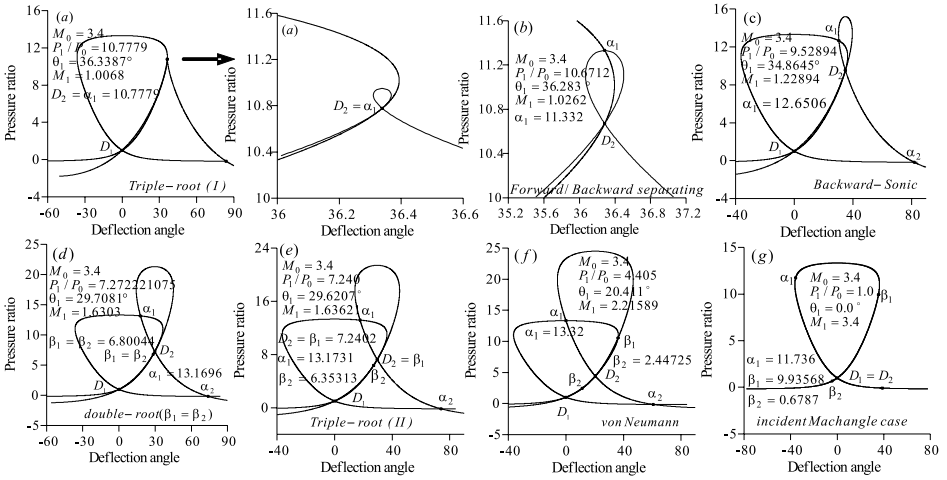

Fig. 2. Sequential (p-θ) shock polar solutions of steady MR of $M_0 = 3.4$

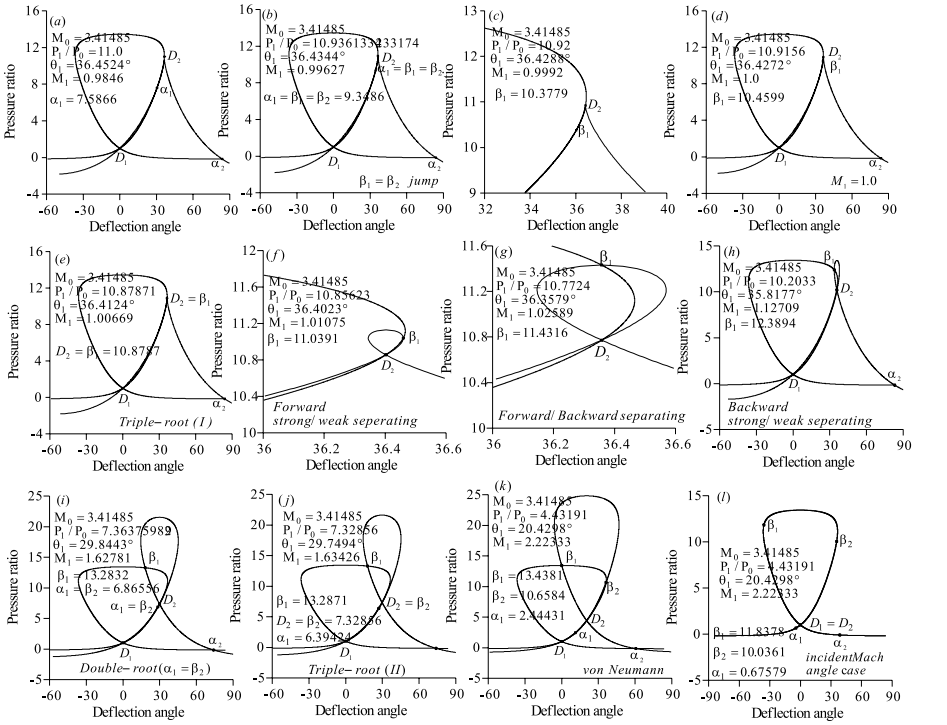

Fig. 3. Sequential (p-θ) shock polar solutions of steady MR of $M_0 = 3.41485$

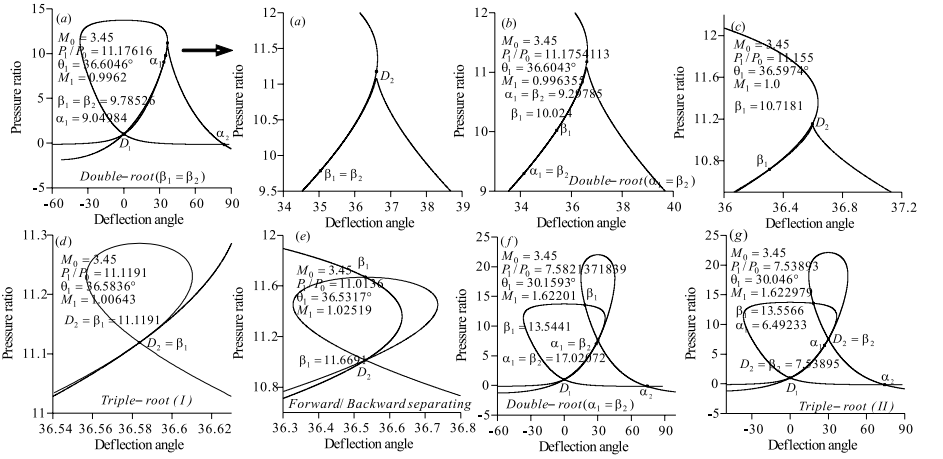

Fig. 4. Sequential (p-θ) shock polar solutions of steady MR of $M_0 = 3.45$

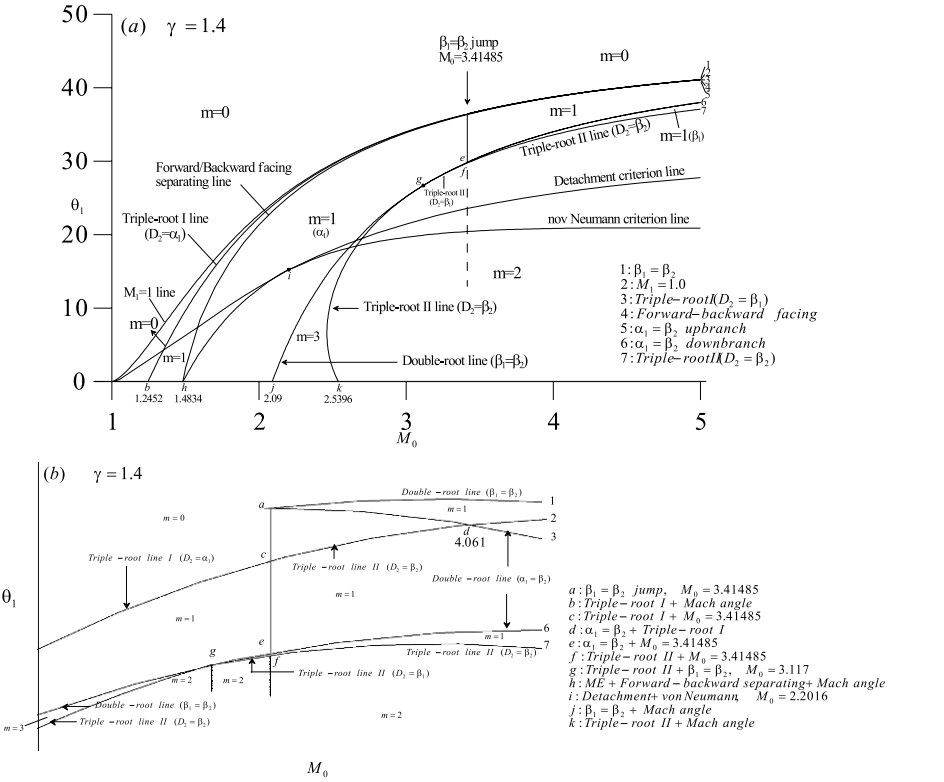

Fig. 5. The map of multiplicity of theoretical three-shock solutions of steady MR in perfect diatomic gases on the (θ_1, M_0) plane. (b) Locally enlarged view (not in proportional to actual curves) near the β_1=β_2 jump showing solution curves of β_1= β_2 jump and various separating and limiting conditions of different resimes of (a).

A calculator for shock wave reflection phenomenon

M. Sun

Center for Interdisciplinary Research, Tohoku University, Sendai 980-8578, Japan *

Summary. We develop a numerical tool, as simple as a calculator, by integrating all numerical related issues, such as grid generation, boundary and initial conditions setup as a whole, for simulating shock wave phenomenon. Unlike available numerical codes that generally require the knowledge of mathematics to run them, the present calculator is developed for the phenomenon and set physical quantities as input parameters. As a result, for obtaining a numerical result of shock reflection, one can run it by only specifying shock Mach number, the wedge angle and the ratio of specific heats. The software is available from website $http:\backslash\backslash www.flowwatch.net\backslash dl\backslash swr.html$. The methodology is applicable for the simulation of other basic shock phenomenon as well.

1 Introduction

Numerical techniques for the simulation of shock wave phenomenon have grown matured especially in the last two decades, as a key research field of computational fluid dynamics (CFD). Numerous commercial software and non-commercial algorithms have been developed in laboratories over the world. The use of these software requires the knowledge of mathematical modeling of physical flows, such as boundary and initial conditions. In practice, in order to get a numerical result, one has to spend days or weeks to master them, so that the CFD is sometimes forbidden for these who do not want to spend time on numerics although they want to get numerical results for reference.

This work is devoted to constructing a *virtual* shock tube that is based on physical models, such as wedges, cones, similar to those used in a real lab. We try to integrate all numerical related issues, such as grid generation, the setup of boundary and initial conditions as a whole, for a given model, and hide these numerical issues from end users. Consequently, one can obtain a numerical result by only specifying phenomenon-related physical parameters, as one performed an experiment shot.

The methodology is applicable to broad classes of shock wave phenomena. In this paper, only a two-dimensional wedge and an axisymmetric cone is considered to demonstrate the methodology. The shock interaction with them is called shock wave reflection. Shock wave reflection, a basic phenomenon in shock dynamics, can be fully determined by three parameters as

$$f = f(M_s, \theta_w, \gamma), \tag{1}$$

where M_s is the Mach number of the incident shock wave, and θ_w is the angle of the wedge for a 2-D reflection or the semi-apex angle of a cone for an axisymmetric reflection.

* Also Interdisciplinary Shock Wave Laboratory, Transdisciplinary Fluid Integration Research Center, Institute of Fluid Science, Tohoku University, Sendai 980-8577, Japan

Relation (1) is valid for the inviscid and the ideal gases with the constant adiabatic index of γ. A sketch of the phenomenon is shown in Fig. 1.

The phenomenon of shock wave reflections has been investigated for over one century, and a recent state-of-the-knowledge review was given by Ben-Dor (2006), and more details have been studied and reported by those therein referred to. The phenomenon has been documented according to observed reflection patterns, and the well-known analytical models are based on the invicid assumption. Therefore, these reflection pattern can be well predicted by the Euler equations. In fact, the Euler equations provide the set of solutions of the phenomenon more accurate and more general than any invicid analytical model. Nowadays, it is fairly easy to obtain a numerical solution of the equations by CFD.

In this paper, we attempt to construct a virtual lab that can visualize and display the reflection pattern in a computer, taking full advantage of the advanced solution techniques developed in CFD for compressible flows. The software is made so simple that anyone can easily get a quick image of reflection pattern. Once the three parameters are specified, the corresponding numerical image will be shown by one click. It is as simple as a "calculator "that frees people from evaluating basic algebraic operations. It is hoped that the calculator for shock reflection can free people from studying CFD and running shock tubes for the phenomenon. The calculator and a few numerical examples are introduced in section 2.

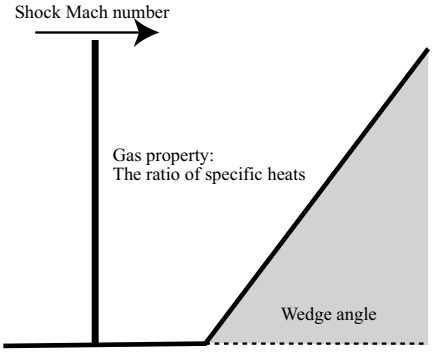

Fig. 1. Three parameters in shock wave reflection over a 2-D wedge or an axisymmetric cone

2 Overview of the calculator

The calculator has been designed and built in the way that can be easily applied to other shock wave phenomena in addition to shock wave reflections. It consists of two main modules, Problem Module and CFD Module, and a graphical user interface (GUI), as depicted in Fig. 2.

2.1 Problem Module

A Problem Module selects and optimizes the computational model for a given flow phenomenon according to the input parameters. Physical parameters must be defined for a

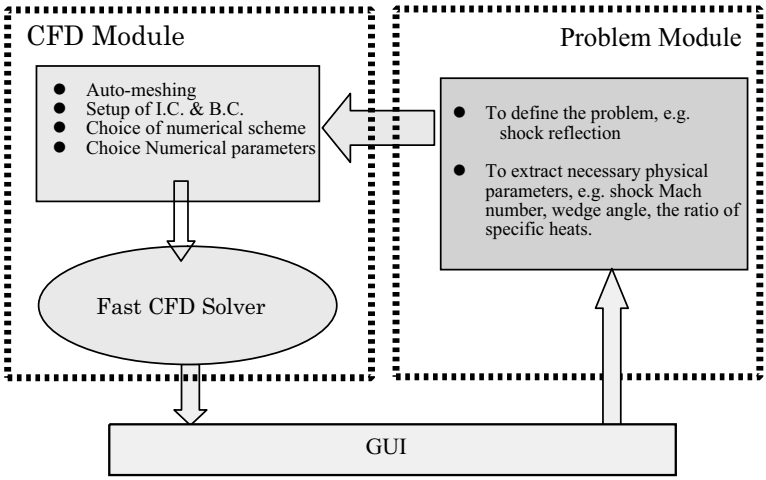

Fig. 2. Schematic of the calculator for shock wave dynamics

user to input. For the sake of users, the parameters should be simple, and the number of them should march with to the mathematical model to be solved. Three parameters are required for shock wave reflections over a wedge or a cone, shock Mach number (M_s), wedge angle (θ_w) and the ratio of specific heats (γ), when solving compressible Euler equations for the ideal gases, as written in Figure 2. The algebraic range of the parameters are set as follows: $M_s \in [1.001, 10]$, $\theta \in [0°, 90°]$, and $\gamma \in [1.001, 2.]$. Since the assumption of the ideal gas is not accurate for high temperature, the upper limit of shock Mach number is set to be 10.

Problem Module further defines what required for initializing the CFD Module, such as setting the computation domain, boundary and initial conditions, the CFL number for the numerical scheme, etc. These are unusually done by a CFD person to start a computation using any software or algorithm.

Problem Module can contain numerous flow cases that represent typical flow phenomena, such as flows over a circular cylinder. For each case, one needs to select the minimum flow parameters in order to complete the theoretical model that approximates the flow phenomenon, and defines other numerical issues that are required by the CFD module for obtaining a result efficiently, accurately and robustly. Notice that an end-user of the present calculator does not need to specify these issues, which requires a thorough understanding of CFD.

2.2 CFD Module

Once the parameters for a flow phenomenon are specified in Problem Module, CFD module takes them as input parameters and show interactive results automatically through the GUI. It requires the kernel algorithm of CFD module to be able to realize all functions that a good commercial software can do, such as grid generation, flow simulation, and plotting results. Among many other technical issues in CFD module, the robustness of a flow solver is the most challenging in the realization of the calculator working for any input parameters.

The CFD solver used for simulation shock wave reflection is based on an in-house code, VAS2D. It was developed based on solution-adaptive unstructured quadrilateral grids for easy vector and parallel processing on supercomputers, while maintaining its high efficiency on personal computers [2]. VAS2D can simulate unsteady/steady, inviscid/viscid, frozen/equilibrium compressible flows for arbitrary geometries with two spatial coordinates (2-D planar and axisymmetric). The conservation laws are discretized by the finite volume method. The second-order spatial accuracy is achieved by a MUSCL-type linear reconstruction, and the MINMOD limiter is used for suppressing possible oscillations around large gradients. A few Riemann solvers has been included in the VAS2D, such as the exact Riemann solver, HLL and HLLC approximate Riemann solvers [4]. In the calculator, the AUFS solver [3] is used by default. The two-step Runge-Kutta scheme was used for achieving second order temporal accuracy.

A grid is automatically generated for any given wedge angle. Totally 19 grids were generated using a meshing tool for every 5 degrees from 0° to 90°, and stored as a grid database. For other angles between, the grid is obtained by modifying and smoothing the grid having the closest wedge angle from the grid database. This strategy is extremely robust, and it can create a grid for any wedge angles, although it can be replaced by a meshing tool that however may possibly crash for some unknown wedge angles.

In fact, constructing the good Problem and CFD modules is much tougher than making CFD software as those available in the market. In the case of commercial codes, one needs to setup parameters, and to optimize the parameters as well for obtaining a good result. In the present calculator, all these are conducted automatically on the background. Extensive experience on CFD and a thorough understanding of fluid dynamics are essential to realizing the automatic optimization.

2.3 Graphical User Interface

The graphical interface of the calculator is, as shown in Fig. 3, designed for parameter input and displaying results. An end-user just needs to specify three parameters, shock Mach number, the angle and the ratio of specific heats on the left panel of the main window interface as shown in Fig. 3a, and the numerical result will be shown on the right as shown in Fig. 3b.

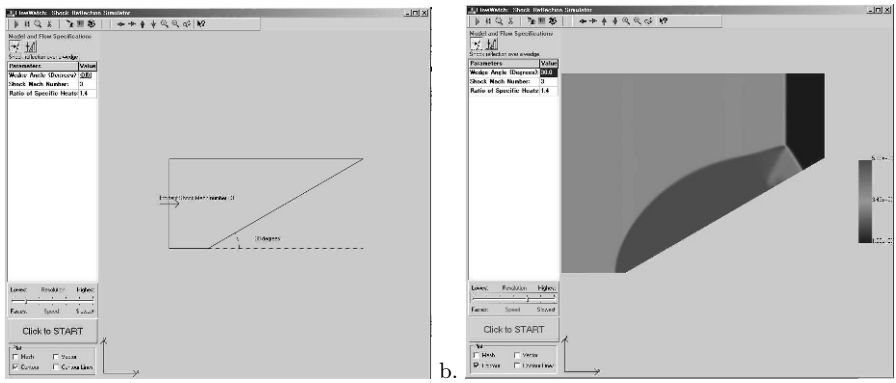

a. b.

Fig. 3. Graphical user interface of the calculator: a) three parameters are defined on the left panel; b) the dynamic numerical result will be shown on the right window.

The intermediate numerical results during computation and the final result can be depicted. One can stop, restart or give pause to the process of computation by clicking the corresponding icon above. The displayed image is created by an efficient post-processing package that provides a few commonly-used functions, including plotting color/line contours, velocity vectors, drawing numerical mesh, or any combination of them. An example of solution-adaptive grid together with density contours is shown in Fig. 4 for the shock wave of $M_s = 3$ reflecting over a 30° wedge. An image can be moved or zoomed in or out, and one can also zoom in the interested portion of the image by mouse. The image shown on the right window of the calculator can be copied, and pasted directly in Microsoft Word, Adobe Photoshop, and others.

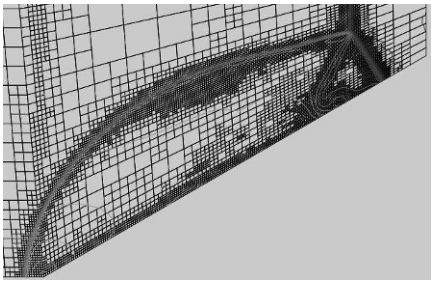

Fig. 4. Density contours with correspoding 4-level adaptive grids

The calculator provides a control for the end-user to select the resolution needed. It appears as a horizontal scroll bar on the left panel. In the CFD Module, it actually reflects the level of refinement. If the scroll bar is moved to the leftmost end, the computation will use the initial grid without any grid refinement. If it is set to the rightmost end, a 6-level refinement will be used. It is set to 1-level refinement by default.

A high resolution result requires more computer time to complete, so that one has to make a trade-off between resolution and speed. Fig. 5 shows a typical result. The computation is conducted on a desktop computer with Window XP operating system and Intel Xeon(R) 1.6GHz CPU. A high resolution result can resolve the wave pattern in more details, while requires more computer time. Notice that it takes about 4 times as much computer time for the increase of one level refinement. For a uniformly structured grid it takes 8 times instead, so that the calculator is about one order faster than the algorithms using uniform grid to achieve the high-resolution result.

3 Concluding remarks

A calculator for simulating shock wave reflections has been proposed. All numerics-related issues have been carefully considered inside. Anyone interested in shock wave phenomena can use it without learning CFD, for example, pure experimenters, engineering students, and so on. The software is available from our website $http:\backslash\backslash www.flowwatch.net$. The methodology followed is applicable to other flow phenomenon. Toward the buildup of a virtual shock wave laboratory, a software package including more models that represents other shock wave phenomenon is under development, and will be distributed through the website.

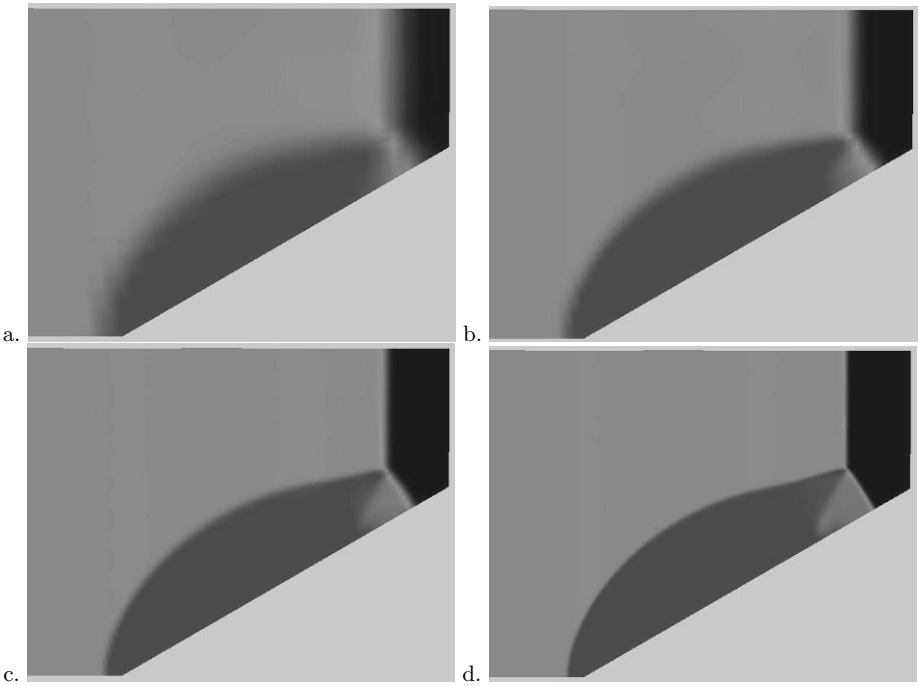

Fig. 5. Results for a shock wave of $M_s = 3$ over a wedge of $\theta_w = 30^\circ$, resolution versus speed: a) 1-level refinement, desktop time required for the computation $T \approx 1s$; b) 2-level refinement, $T \approx 4s$; c) 3-level refinement, $T \approx 16s$; d) 4-level refinement, $T \approx 65s$.

The author thanks Dr. Hongwei Zheng from National University of Singapore for his help in designing and improving the graphical user interface.

References

1. Ben-Dor G. (2006) A state-of-the-knowledge review on pseudo-steady shock-wave reflections and their transition criteria, Shock Waves, V15: 277-294.
2. Sun M., Takayama K. (1999) Conservative smoothing on an adaptive quadrilateral grid, J. of Computational Physics, V150: 143-180
3. Sun M., Takayama K. (2003) An artificially-upstream flux vector splitting scheme for the Euler equations, J. of Computational Physics, V189: 305-329
4. Toro E.F. (2005) Riemann Solvers and Numerical Methods for Fluid Dynamics, Springer

A parametric study of shock wave enhancement

D. Igra[1] **and O. Igra**[2]

[1] *RAFAEL, Aerodynamics Group, P.O.Box. 2250, Haifa 31021, ISRAEL*
[2] *Department of Mechanical Engineering, Ben Gurion University, Beer Sheva Israel*

Summary. The flow field developed behind a shock wave propagating inside a constant cross-section conduit is solved numerically. The ambient gas is composed of pairs of air-helium layers having a continually decreasing width. It is shown that a meaningful pressure amplification can be reached behind the transmitted shock wave. By proper choice of the number of air-helium layers and their width reduction ratio, pressure amplification as high as 7.5 can be obtained.

1 Introduction

It is well known that the pressure jump across a given shock wave increases when it propagates in a conduit whose cross-section is continually reduced [1], or in the case of a spherically imploding shock wave [2]. In both cases the flow cross-section is reduced toward zero. A question arises whether or not this is a necessary condition for pressure amplification. In our previous work [3] we have demonstrated that it is possible to create a pressure amplification by using alternating layes of different gases. The gas into which the shock propagates consists of layers of light and heavy gases in which the thickness of each successive heavy layer is less than that of the foregoing. The same is true for the light gas layers.

In the current work a parametric study is conducted with the aim of finding a two layered, light-heavy gas, arrangement that yields maximal shock enhancement. As in our earlier study [3] here too the heavy and the light gases are air and helium, respectively. Effects associated with changes in following parameters were investigated:

- The number of alternating heavy/light gas layers.
- The applied reduction ratio between successive layer's thicknesses.
- The initial shock wave Mach number.

In the current paper it was possible to obtain a pressure amplification that is more than 7.5 times higher than the pressure prevailing behind the incident shock wave. Details regarding the numerical method used in the present solution are given in [3].

2 Results and discussion

In the considered case, an incident shock wave, propagating in helium ($M_s = 2$), collides head-on with alternating layers of air and helium. In the sequence of these layers each successive pair of Air/He layers has half the width of the upstream pair (i.e., layer's reduction ratio, δ, $\delta = 2$). The resulting flow from the interaction of a transmitted shock wave with these layers of Air/He is solved numerically for the following initial conditions: $M_s = 2$, $P_0 = 100$ kPa , $\rho_{air} = 1.25$ kg/m^3 and $\rho_{He} = 0.166$ kg/m^3.

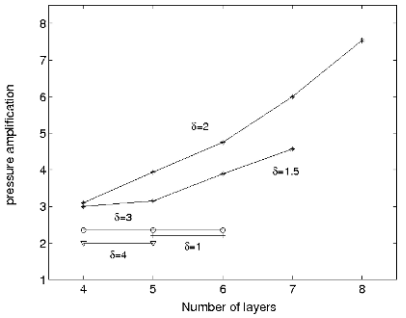

Fig. 1. Pressure amplification versus number of air/helium layers. Initial conditions are: $M_s = 2$, $P_0 = 100$ kPa , $\rho_{air} = 1.25$ kg/m^3 and $\rho_{He} = 0.166$ kg/m^3.

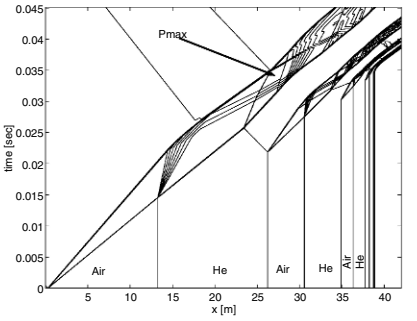

Fig. 2. Density contours for the case having 5 air/helium layers, $\delta = 3$ and other initial conditions as in Fig. 1.

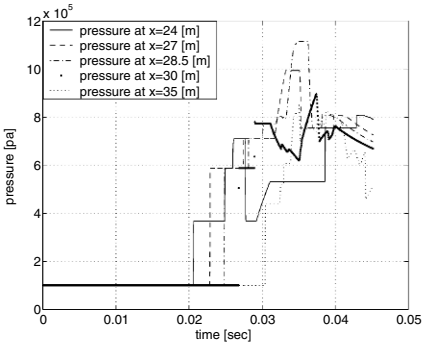

Fig. 3. Pressure histories computed at a few different locations along the conduit for the conditions indicated in Fig. 2.

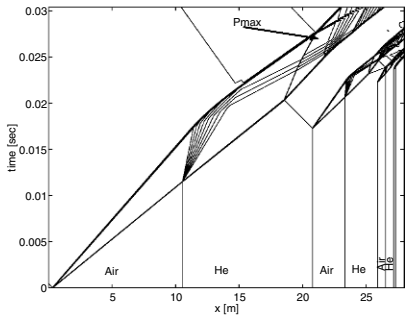

Fig. 4. Density contours for the case having 5 air/helium layers, $\delta = 4$ and other initial conditions as in Fig. 1.

It is reasonable to assume that the attained maximum pressure is influenced by the specific choice of the number of alternating air-helium pair used in the solution and the value chosen for δ. δ is the width ratio between neighboring pair of air-helium layers. In addition, the Mach number of the incident shock wave will most probably influence the value of the attained maximum pressure. In the following these effects are discussed.

As a first step we check the effects associated with changes in the number of alternating heavy-light gas layers on the obtained pressure amplification. By pressure amplification we mean the ratio between the maximum pressure reached behind the transmitted shock wave and the pressure prevailing behind the incident shock wave. In all investigated cases the width of the thinnest (final) layer was kept constant. This was reached by adding appropriately thick layers upstream of the thinnest layer. The initial conditions were kept as mentioned earlier, i.e., $M_s = 2$, $P_0 = 100$kPa ,$\rho_{air} = 1.25$ kg/m^3 and $\rho_{He} = 0.166 kg/m^3$.

Obtained results are shown in Fig. 1 for five different width reduction ratios. For the cases $\delta = 1.5$ and $\delta = 2$ increasing the number of alternating air/helium layers results in

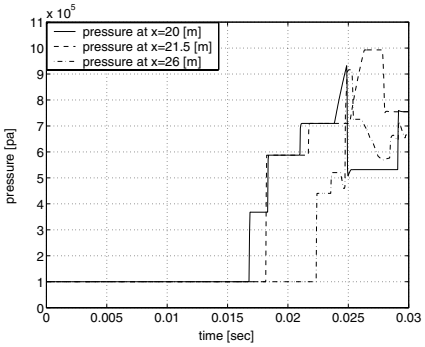

Fig. 5. Pressure histories computed at a few different locations along the conduit for the conditions indicated in Fig. 5.

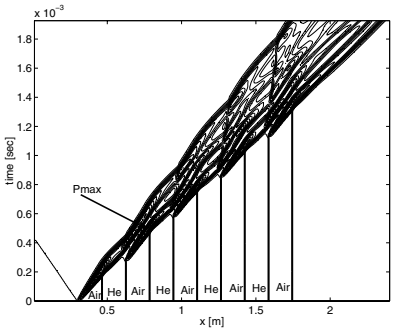

Fig. 6. Density contours for the case having 5 air/helium layers, $\delta = 1$ and other initial conditions as in Fig. 1.

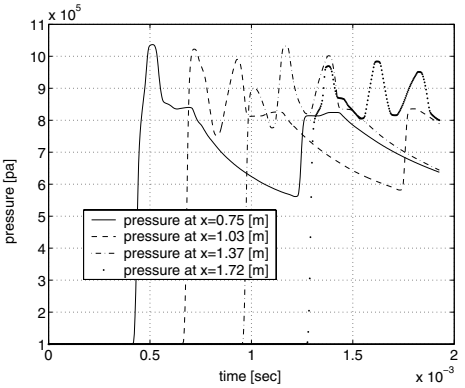

Fig. 7. Pressure histories computed at a few different locations along the conduit for the conditions indicated in Fig. 6.

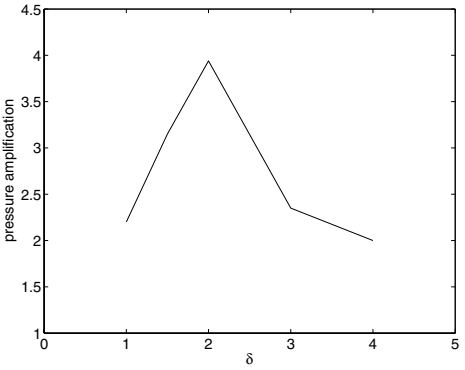

Fig. 8. Pressure amplification ratio. Initial conditions as in Fig. 1 with 5 alternating air-helium layers.

an increase in the obtained pressure amplification. It is also apparent from Fig. 1 that increasing the reduction ratio δ, from 1.5 to 2, for a given number of layers, results in a significant increase in the obtained pressure amplification.

However, when increasing the reduction ratio to 3 or more, increasing the number of layers has practically no effect on the obtained pressure amplifications. The reason for this behavior can be explained by examining Fig. 2 (showing lines of constant density for the case in which $\delta = 3$ and the number of alternating air-helium layers is 5), and Fig. 3. It is evident from Fig. 2 that maximum pressure occurs in the first pair of air-helium layers. It is also evident from Fig. 3 that indeed the highest pressure is found on the curve showing pressure history computed at $x = 28.5$ m, i.e. within the first air-helium layer. Pressure histories computed at either $x < 28.5$ m or $x > 28.5$ m reach a lower maximum pressure. This maximum pressure is about $11 * 10^5$Pa, which results in a pressure amplification of 2.31 only.

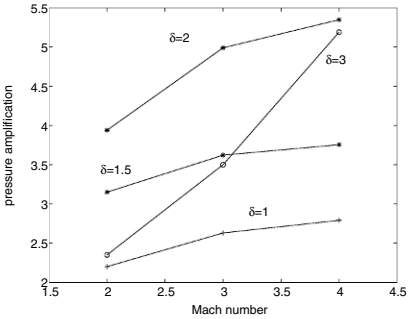

Fig. 9. Pressure amplification versus the incident shock wave Mach number.

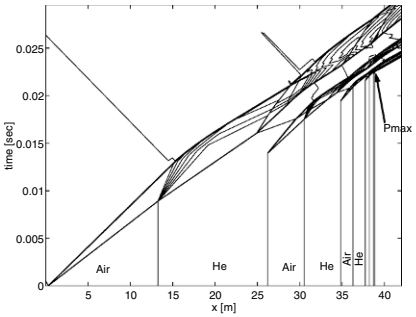

Fig. 10. Density contours for the case having 5 air/helium layers, δ=3 Initial conditions are: $M_s = 3$, $P_0 = 100$ kPa , $\rho_{air} = 1.25$ kg/m^3 and $\rho_{He} = 0.166$ kg/m^3.

A significantly higher value is reached when δ=2 and the number of alternating air-helium layers was 6. At these conditions: $P_{max} = 2.2 * 10^6$ Pa. In addition, for δ=2 and 5 layers a pressure amplification of about 4 was obtained as shown in Fig. 1. However in both cases when δ=2 the maximum pressure was in the thinnest air layer. Similar behavior is observed when changing the number of alternating air/helium layers to 4 and δ to 4. It is evident from Fig. 4, showing lines of constant density, that here again maximum pressure is reached within the first pair of air-helium layers. It is suggested in Fig. 5 that this maximum pressure is only 10^6 Pa; significantly smaller than that observed for δ=2 where the maximum pressure is reached further downstream (at the thinnest air layer). As a reference, results obtained for the case in which the number of alternating air-helium layers is 5 and δ=1 (i.e., a sequence of alternating air-helium layers all having the same width), are shown in Figs. 6 and 7. It is evident from these figures that maximum pressure is reached in the first pair of air/helium layers and this maximum is barely over 10^6Pa. In summary it is apparent that maximum pressure amplification is reached when δ=2 as shown in Fig. 1.

The next parameter to be checked is the reduction ratio, δ; effects associated with changes in δ on the obtained pressure amplification are shown in Fig. 8. In this case the number of air/helium layers was kept constant at 5 and all other initial condition are as in the previous case. As already shown (in Fig. 1), increasing δ within the range $1 < \delta < 3$ results in meaningful pressure amplifications. However, further increase in δ results in significant decrease in the obtained pressure amplification. It was shown that for $\delta > 3$ the maximum pressure is reached in the first pair of air/helium layer thereby excluding further pressure amplification.

The last case to be studied is the effect that changes in the incident shock wave Mach number have on the obtained pressure amplification. In this case the number of air-helium layers was set at 5 and the following values of δ were investigated; δ = 1, 1.5, 2 and 3. Other initial conditions were kept as in the previous cases. Summary of the obtained results are shown in Fig. 9. The following is apparent from Fig. 9.

- As could be expected for all δ's, increasing the incident shock wave Mach number results in an increase in the obtained pressure amplification.

- For $1 < \delta \leq 2$ a similar (moderate) increase in pressure amplification is observed when increasing the incident shock wave Mach number. However, for $\delta = 3$ a significantly larger increase in pressure amplification is evident for increasing values of M_s. The reason for this behavior is the fact that when $1 < \delta \leq 2$ the maximum pressure is achieved in the thinnest air layer while in the case when $\delta = 3$, for $M_s = 2$ the maximum pressure is found in the first pair of air/helium layer (the thickest layers, see Figs. 2 and 3); it moves to thinner layers when M_s is raised above 2. It is apparent from Figs. 10 and 11 that with increase in the incident shock wave Mach number (to $M_s = 3$) the maximum pressure is found in the thinnest layer.
  The fact that in the considered case the highest pressure is found in the thinnest layer is similar to what was observed in [3], where results obtained for δ=2, are shown. It is also evident from Fig. 11 that indeed the highest pressure is found on the curve showing pressure history computed at $x = 38.86$ m, i.e. within the thinnest air layer. Pressure histories computed at $x < 38.86$ m reach lower maximum pressure. This maximum pressure is about $38 * 10^5$Pa, which yields a pressure amplification of 3.5.

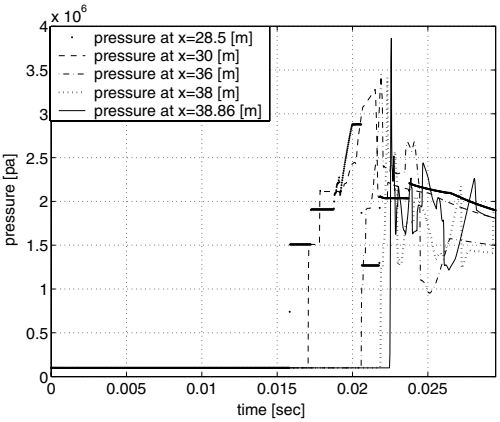

Fig. 11. Pressure histories computed at a few different locations along the conduit for the conditions indicated in Fig. 10.

3 Conclusions

It is shown that significant shock wave enhancement is achievable in a one-dimensional flow (constant flow cross-section) by employing alternate layers of heavy and light gases. Several parameters affecting the alternating air-helium layers were studied to find out how to obtain maximal pressure amplification. It was shown that in the case when $M_s = 2$, δ= 2 and the transmitted shock wave passes through 8 alternating air/helium layers a pressure amplification of about 7.5 is possible. Higher pressure amplifications can be reached by increasing the number of alternating air/helium layers.

References

1. Whitham, G.B.:Linear and Nonlinear Waves. John Wiley and Sons, New York (1974)
2. Higashino, F.: Shock wave focusing. In Handbook of Shock Waves, Eds. Ben-Dor G, Igra O and Elperin T, Academic Pres (2001).
3. Igra, D. and Igra, O. : Shock Wave Enhancement. ISSW 24, Beijing China, 2004.

A secondary small-scale turbulent mixing phenomenon induced by shock-wave Mach-reflection slip-stream instability

A. Rikanati[1], O. Sadot[2 3], G. Ben-Dor[3], D. Shvarts[1 2 3], T. Kuribayashi[4], and K. Takayama[4]

[1] *Department of Physics, Ben Gurion University, Beer-Sheva 84015, Israel*
[2] *Department of Physics, Nuclear Research Center, Negev 84190, Israel*
[3] *Department of Mechanical Engineering, Ben Gurion University, Beer-Sheva 84015, Israel,*
[4] *Interdisciplinary Shock-Wave Research Center, Institute of Fluid Science, Tohoku University, Sendai, Japan*

Summary. Secondary small-scale Kelvin-Helmholtz instability, developing along the Mach reflection slip-stream, was investigated. This instability is the cause for thickening the slipstream. Growth rates of the large-scale Kelvin-Helmholtz shear flow instability are used to model the evolution of the slip-stream instability in ideal gas. The model is validated through experiments measuring the instability growth rates for a range of Mach numbers and reflecting wedge angles. Good agreement is found for Reynolds numbers of $Re > 2 \times 10^4$ This work demonstrates, for the first time, the use of large-scale models of the Kelvin-Helmholtz instability in modeling secondary turbulent mixing in hydrodynamic flows, a methodology which could be further implemented in many important secondary mixing processes.

1 Introduction

The hydrodynamic instability developed on a contact surface between two fluids due to constant (Rayleigh-Taylor Instability) or impulse (Richtmyer-Meshkov Instability) accelerations has a great importance in achieving gain in laser driven inertial confinement fusion (ICF) as well as in many astrophysical processes [1], [2], [3]. The secondary turbulent mixing in these complex unstable hydrodynamic flows increases the mixing process. In those application the unstable interface between two layers evolves as bubbles (penetration of the light fluid into the heavy fluid) and spikes (penetration of the heavy fluid into the light fluid). The dynamics of the bubbles and spikes increases the shear flow on the contact surface and initiates the secondary small scale Kelvin-Helmholtz instability. In the present study we generate the small scale Kelvin-Helmholtz instability on a slipstream (SS) of a Mach reflection. Mach reflections (MRs) are well known shock-wave related phenomenon occurring when an oblique shock wave reflects from a rigid wall (or interacts with a second shock wave) and are of great importance in many hydrodynamic flows [4]. The basic feature of a Mach reflection is that of the three shocks structure gives rise to the slipstream (SS) instability. Through modeling this instability, as described first in [5] and in this paper, we implement a technique for understanding secondary turbulent mixing. The MR three shocks structure is a phenomenon widely demonstrated in many experimental works (see e.g., [4]), as well as in the example from the current work illustrated in Fig. 1). The three shocks structure appears when the inclination angle, between the incident shock and the bounding wall, is smaller than a critical angle defined through the detachment criterion [6], which depends on the shock-wave Mach number and the material equation of state. In the MR structure, the SS is of a unique

hydrodynamic nature, being a discontinuity which is not a shock. The SS separates between two regions (regions 2 and 3 in Fig. 1) of different densities $\rho_2 \neq \rho_3$ and tangential velocities $u_2^{\parallel} \neq u_3^{\parallel}$ but of equal pressures ($p_2 = p_3$) and of normal velocities ($v_2^{\perp} = v_3^{\perp}$) i.e., a shear flow. As can be seen from Fig. 1, the SS discontinuity thickness increases downstream from the triple point (TP). So far, the leading assumption for the cause of this instability was related to the viscosity generated boundary layer effect [4]. As is the case in the SS discontinuity, the Kelvin-Helmholtz (KH) shear flow instability [7] occurs when two fluids flow with proximity to each other with a tangential velocity difference, defined as the shear velocity. Under this instability, small perturbations on the two fluid interface evolve into a formation of vortices causing the two fluids to turbulently mix. Here, we demonstrate that the KH instability is the cause for the SS thickening, which generates secondary small-scale turbulent mixing. By implementing previously reported KH large scale instability growth rates [7], [8], we try to model the spread angle of the SS instability as a function of the MR flow parameters.

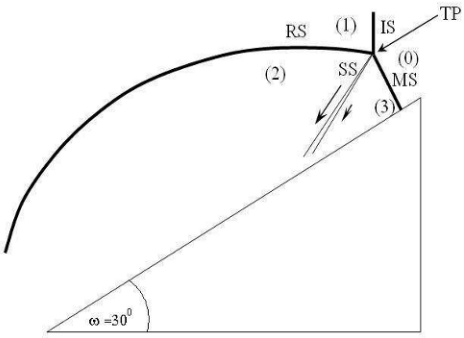

Fig. 1. Mach reflection with a wedge angle of $w = 30^0$ (see text for further experimental details). Marked are the following features: the incident shock (IS), the Mach stem (MS), the reflected shock (RS), the triple point (TP), the slip stream (SS), Four flow regions are distinguished: the nonshocked air (0), the shocked air above RS (1), the shocked air behind RS (2), and the Mach-stem shocked air (3).

2 Model Description

The attempt to numerically deduce secondary mixing phenomena through the solution of the full 2D or 3D Euler equations is expected to be very difficult, if at all possible. This is due to the very large number of computational cells required to describe both the large-scale and the small-scale mixing processes. The width of the KH large-scale turbulent mixing zone (TMZ) evolves with time according to $\delta h(t) = c \cdot \Delta v \cdot t$ as expected from dimensional considerations, where v is the shear velocity, t represents the evolution time, and $c = 0.19 \pm 0.01$ is a dimensionless constant derived experimentally [7], numerically, and recently even theoretically [8]. It is convenience to measure the KH evolution spatially in most experiments, i.e., as a function of the advection distance from the mixing starting point. From this, the temporal growth can be related to the spatial growth by

assuming that the average flow flows downstream with the fluid average velocity, resulting in $\delta h(x) = 2 \cdot c \cdot (v_2 - v_3)/(v_2 + v_3)$ where v_2 and v_3 are the two fluid velocities and c is the previously mentioned dimensionless constant. To this equation, two corrections must be introduced. The first, as reported in [8], is for cases of fluids of two different densities, and the second is for high Mach number flows ($\Delta v/a \geq 1$ where a is the fluid average sound speed). Following these two corrections, the TMZ width $\delta h(x)$ becomes:

$$\delta h(x) = (0.38 \pm 0.02)\frac{S(v_2, v_3)}{1 - 2\phi_d(\rho_2, \rho_3)S(v_2, v_3)} \times \phi_{HiMach}(\Delta v/a) \tag{1}$$

Where

$$\phi_d(\rho_2, \rho_3) = \frac{1}{2}\left|\frac{1 - \sqrt{\rho_3/\rho_2}}{1 + \sqrt{\rho_3/\rho_2}}\right| \tag{2}$$

and

$$S(v_2, v_3) = \frac{v_2 - v_3}{v_2 + v_3} \tag{3}$$

$$\phi_{HiMach}(\Delta v/a) = \frac{1}{2}\left(1 - tanh\left(2\left(\frac{\Delta v}{a} - 1.2\right)\right)\right) \tag{4}$$

is the high Mach correction which is based on a parametric fit of the results shown in [9]. Finally, based on Eq. (1), the spread angle of the spatially growing instability is found from:

$$\theta_{spread} = arctan\left(\frac{\delta h(x)}{2x}\right) \tag{5}$$

For the growth of the SS instability, v_2, v_3, ρ_2, and ρ_3 need to be known. These physical properties are the velocities (in the frame of reference moving with the triple point) and the densities of regions 2 and 3 in Fig. 1. All are analytically calculated using the three-shock theory of von Neumann [6]. The theory is based on the traditional shock-wave conservation equations which are implemented for a single oblique shock. For an ideal gas (see [10]), the flow parameters behind an oblique shock can be analytically derived through a set of analytical relations, as a function of the shock inclination angle and the preshock conditions. In Fig. 2 the sheer velocity and the Atwood number

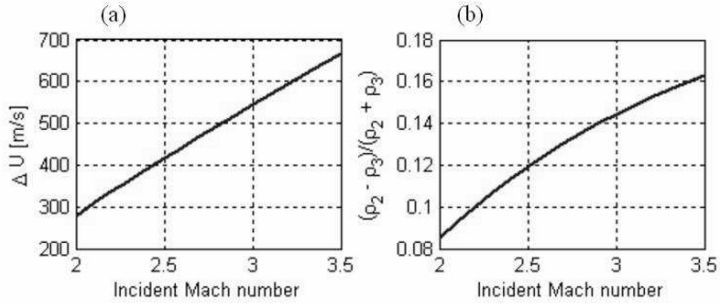

Fig. 2. Mach reflection calculation, using analytical solution of the conservation equations. From the solution the sheer velocity along the slip-stream was found (a) and the density relation (Atwood number) (b).

$A = (\rho_2 - \rho_3)/(\rho_2 + \rho_3)$ vs. the incident shock wave Mach number in the case of 45^0 wedge. To obtain the solution, one has to implement these relations three times, once for each shock in the three-shock confluence, demand a closure relations of pressure equalization between regions 2 and 3, and zero perpendicular velocity, and assume that the Mach stem is perpendicular to the wedge. Once the flow parameters are known, the four physical parameters mentioned above are easily obtained. From the analytical solution it is found that the spread angle depends only on the incident shock-wave Mach number, the reflecting wedge angle, and the adiabatic index of the gas, while the initial density and pressure are of no importance. In Fig. 3(B), one can see the resulting SS instability spread angles for MR in air ($\gamma = 1.4$) as a function of the incident shock-wave Mach number for reflecting wedge angles of $w = 20^0, 30^0, 40^0, 45^0$. Notice that, initially, the expected spread angle increases with the increase in Mach number or wedge angle, until a value of about 8^0, after which the spread angle decreases. This effect is a result of the Mach number reduction factor of Eq. (1).

3 Experimental apparatus and results

Experiments were conducted in order to verify the model predictions, using a shock-tube facility at the Interdisciplinary Shock-Wave Research Center of the Institute of Fluid Science, Tohoku University. The tube allows the generation of Mach $1.1 - 5$ shock waves passing through a rectangular tube having a 10 cm by 18 cm cross section. Near the end of the tube, a steel wedge with a varying angle was placed in the test section, and holographic interferometry images were taken of the MR generated from the shock-wedge interaction. For further details on the shock tube and the interferometry technique, see [6] and [11]. Experiments were done with ambient air at an initial pressure of $P_0 = 10.1kPa$, wedge angles of $w = 20^0, 30^0, 40^0, 45^0$, and incident shock-wave Mach numbers of $Mi = 1.55, 1.9, 2.3, 2.78$. In Fig. 3(A) an image from the experiment is presented for a constant wedge angle of $w = 40^0$ and for all four Mach numbers. It is evident that, as the gas on the two sides of the SS flows away from the triple point, the SS thickness linearly increases. A density profile is evident through the increasing spacing between the fringes along the SS. Notice that, as predicted by the model, the spread angle increases with increasing Mach number. In order to quantitatively analyze the model predictions, a detailed comparison of the measured and predicted spread angles was done for all Mach numbers. Spread angle measurements were taken between two straight lines bounding the SS thickening region. The results are plotted in Fig. 3(B) as a function of the incident shock-wave Mach number for reflecting wedge angles of $w = 20^0, 30^0, 40^0, 45^0$. In the figure, reasonable agreement is demonstrated except for the $M < 2$ where low pressures were used. In order to understand the cause for the disagreements, the discrepancy between the model predictions and the experimental results is plotted in Fig. 4 against the SS shear velocity Re number. From the figure, it is clear that all of the experiments conducted at $Re > 2 \times 10^4$ show good agreement with theory. Note that in the experiments conducted at $M = 1.55$ with $P_0 = 10kPa$ no spread angle was noticed, while, for the $M = 1.5$ experiment with $P_0 = 100kPa$ very good agreement with the model is obtained. The important difference between these two experiments is the higher densities obtained at the $P_0 = 100kPa$ experiments, introducing weaker kinematic viscosities and larger Re numbers (see caption of Fig. 4). Together with Fig. 4, it is clear that the disagreements between the model and the experiments are due to viscous effects, which are not accounted for in Eq. 1. The viscous effects, serving as a secondary mix cutoff stabilizing mechanism (through a cutoff Re

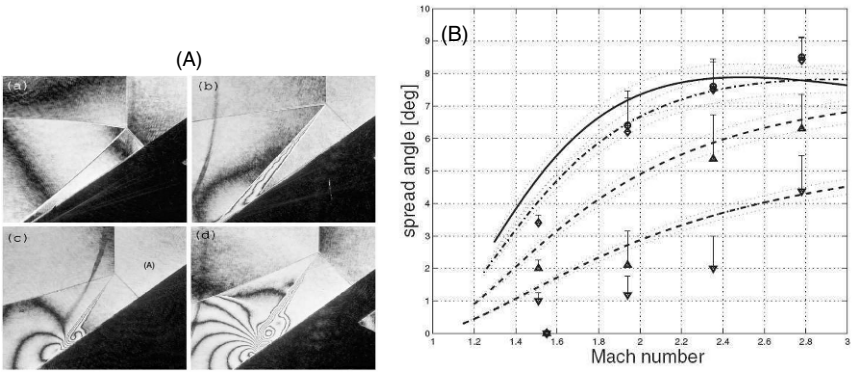

Fig. 3. A) Holographic interferometry images for MRs with a wedge angle of $w = 40^0$ and incident shock-wave Mach numbers of $Mi = 1.55$ (a), 1.9 (b), 2.3 (c), and 2.78 (d). Two white lines in (b) bound the SS, demonstrating the growth angle measurement technique.
B) SS instability spread angle as a function of incident shock-wave Mach number. Theoretical predictions in thick lines: $w = 45^0$ (solid line), $w = 40^0$ (dashed-dotted line), $w = 30^0$ (upper dashed line), and $w = 20^0$ (lower dashed line). Thin lines around the thick lines mark the error in the model prediction [see Eq. (1)]. Experimental results and error bars are also plotted; All the experiments were conducted with ambient air at $P_0 = 10.1kPa$, apart from the $M = 1.5$ experiments conducted at $P_0 = 100kPa$.

number), are a well known phenomenon. And the critical Re number, measured at 2×10^4, is similar to critical Re numbers demonstrated for several other mixing phenomena, such as secondary mixing at the Richtmyer-Meshkov and KH instabilities [2], [3].

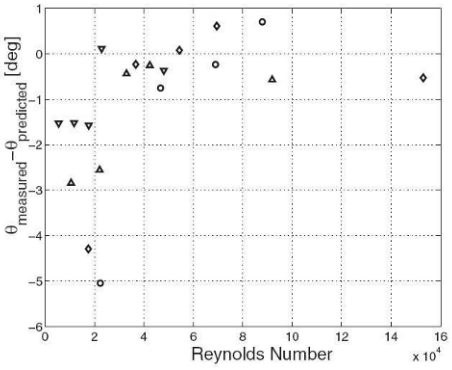

Fig. 4. Predicted spread angle subtracted from the measured spread angle, as a function of the SS Re number. $(\bigcirc), (\diamond), (\triangle), and (\bigtriangledown)$ mark experiments conducted at $w = 45^0, 40^0, 30^0$, and 20^0, respectively. Experiments conducted at an initial pressure of $100kPa$ resulted in Re numbers of $Re = 15.3 \times 10^4, 9.2 \times 10^4$, and 4.8×10^4 for $w = 40^0, 30^0$ and 20^0, respectively.

4 Summary

It is shown that existence and width of a secondary small-scale turbulent mixing zone can be predicted by simple analytical procedure based on models of large-scale KH instability growth. The densities, viscosities, velocities, and average sound speed, are the quantities obtained from this model. Using this technique, the evolution of the SS instability of an MR was analytically characterized. Good agreement was achieved with an experimental evaluation of the SS spread angle, conducted at Mach numbers of $Mi = 1.5 - 2.78$ and spread angles of $w = 20^0 - 45^0$. A critical Re number of 2×10^4 was found to distinguish between turbulent and laminar flows, thus indicating secondary turbulent mixing generated through the evolution of the KH instability as the cause for the SS discontinuity thickening. The success in modeling secondary mixing using large-scale models of the KH instability should provide a guideline for future research in secondary turbulent mixing phenomena.

Acknowledgement. The financial support of the Interdisciplinary Shock-Wave Research Center of the Institute of Fluid Science, Tohoku University, for conducting the experimental phase of the presented research and helpful discussions with Dr. D. Oron are acknowledged by the authors.

References

1. S. P. Regan et al., Phys. Rev. Lett. 89, 085003 (2002).
2. Y. Zhou, H. F. Robey, and A. C. Buckingham, Phys. Rev. E 67, 056305 (2003).
3. P. E. Dimotakis, J. Fluid Mech. 409, 69 (2000).
4. G. Ben-Dor, Shock Wave Reflection Phenomena (Springer- Verlag, Berlin, 1992).
5. A. Rikanati, O. Sadot, G. Ben-Dor, D. Shvarts, T. Kuribayashi and K. Takayama Phys. Rev. Lett. 96, 174503, (2006).
6. J. von Neumann, Navy Department, Bureau of Ordinance, Washington, DC, Explosives Research Report No. 12, 1943.
7. G. L. Brown and A. Roshko, J. Fluid Mech. 64, 775 (1974).
8. A. Rikanati, U. Alon, and D. Shvarts, Phys. Fluids 15, 3776 (2003).
9. S. A. Ragab and J. L. Wu, Phys. Fluids A 1, 957 (1989).
10. H. Li and G. Ben-Dor, J. Fluid Mech. 341, 101 (1997).
11. F. Ohtomo, K. Ohtani, and K. Takayama, ShockWaves 14, 379 (2005).
12. American Institute of Physics Handbook, edited by Dwight E. Gray (McGraw-Hill, New York, 1972).

Analytical reconsideration of the so-called von Neumann paradox in the reflection of a shock wave over a wedge

E.I. Vasilev[1], T. Elperin[2], and G. Ben-Dor[2]

[1] *Department of Computational Mechanics, Volgograd University, Volgograd, Russia*
[2] *Pearlstone Center for Aeronautical Engineering Studies, Department of Mechanical Engineering, Faculty of Engineering Sciences, Ben-Gurion University of the Negev, Beer Sheva, Israel*

Summary. Experimental investigations on the reflection of plane shock waves over straight wedges indicated that there is a domain, the *weak shock wave domain*, inside which the resulted wave configurations resemble a Mach reflection although the classical three-shock theory does not provide a solution. This paradox is known as the *von Neumann paradox*.

While numerically investigating this paradox Colella & Henderson (1990) suggested that the observed reflections were not Mach reflections but *von Neumann reflections*, in which the reflected wave at the triple point was not a shock wave but a compression wave.

Vasilev & Kraiko (1999) concluded in the course of their numerical investigation, that the wave configuration includes in addition to the three shock waves a very tiny Prandtl-Meyer expansion fan centered at the triple point. This wave configuration, first predicted by Guderley (1947), was recently observed experimentally by Skews & Ashworth (2005) who named it *Guderley reflection*.

It has been found, in the course of the present study, that there are in fact three different reflection configurations inside the weak shock wave domain:

– A von Neumann reflection - vNR,
– A yet not named reflection - ?R,
– A Guderley reflection - GR.

The transition boundaries between MR, vNR, ?R and GR and their domains have been determined analytically. The reported study presents a full solution of the weak shock wave domain, which has been puzzling the scientific community for a few decades.

1 Introduction

Mach (1878) discovered in his pioneering experiments two types of shock waves reflection configurations: regular reflection, RR, and irregular reflection, IR, with a triple point, that was later named *Mach reflection*, MR. In order to describe the shock waves configuration in the vicinity of a triple point von Neumann (1943a, 1943b) suggested a simple three-shock waves theory, 3ST, based on the conservation equations across an oblique shock waves and appropriate boundary conditions.

Discrepancies between von Neumann's 3ST and experiments were detected first by White (1952), who recorded MRs in a parameter domain not allowed by the 3ST. This discrepancy, later confirmed by many investigators, is the *von Neumann paradox*.

A theoretically consistent solution instead of the 3ST was suggested first by Guderley (1947), who concluded that a supersonic patch exists behind the triple point. The isentropic solution of Guderley could not eliminate the contradiction in von Neumann's theory since it did not include a tangential discontinuity; however, it contained two

important elements: a reflected shock wave that was directed against the flow; and a supersonic patch behind the triple point.

The first serious attempt to simulate shock wave reflection under the conditions of the von Neumann paradox was undertaken by Colella & Henderson (1990), who concluded that the reflected shock wave degenerated near the triple point into a continuous compression wave. However, Olim & Dewey (1992) showed that experiments comply with this hypothesis only when $M_S < 1.05$, or for wedge angle $\theta_W < 10°$. Under different conditions the reflected wave propagates with supersonic velocity, and it is a shock wave with finite amplitude. This suggests that the smearing of the shock wave front in Colella & Henderson's (1990) numerical calculations was a numerical artifact of their shock capturing scheme.

Vasilev (1998) using a very high resolution numerical scheme and new front tracking techniques confirmed the principal points of Guderley's solution. The calculations revealed the existence of an expansion fan emerging from the triple point with a supersonic patch behind it. These results allowed formulating a *four-wave theory*, 4WT, that resolved the von Neumann paradox. The four-wave theory complies fairly well with the experiments of Olim & Dewey (1992). Vasilev & Kraiko (1999) performed similar calculations on adaptive grids. They showed that the numerical results agreed with a generalized three-wave/four-wave theory in the whole range of the wedge angles.

The final closure to the 50-year history of the von Neumann paradox was achieved recently by Skews & Ashworth (2006) who detected, using a large-scale installation, the above-mentioned expansion fan.

2 Present Study

The *three-shock theory*, 3ST, makes use of the conservation equations across the three shock waves and appropriate boundary conditions across the slipstream across which the pressure remains constant and the streamlines are parallel, $\theta_1 \pm \theta_2 = \theta_3$. The latter BC divides the 3ST into two types:

- A "standard" three-shock theory for which $\theta_1 - \theta_2 = \theta_3$
- A "non-standard" three-shock theory for which $\theta_1 + \theta_2 = \theta_3$.

Colella & Henderson (1990) concluded that:

- When the solution of the 3ST results in a standard solution, $\theta_1 - \theta_2 = \theta_3$, the reflection is an MR, and
- When the solution of the 3ST results in a non-standard solution, $\theta_1 + \theta_2 = \theta_3$, the reflection is a vNR.

As shown subsequently while the first conclusion is correct the second one is only partially correct, since there are cases in which the 3ST does have a non-standard solution but the solution is not physical. Hence, the second conclusion should be modified to:

- When the solution of the 3ST results in a non-standard solution, $\theta_1 + \theta_2 = \theta_3$, the reflection is a vNR **provided that the solution is physical**.

This conclusion contradicts the concept forwarded by Colella & Henderson (1990) that the vNR resolves the "von Neumann paradox", since the vNR takes place not when the 3ST does not have a solution, but when the 3ST provides a "non-standard" solution.

However, there are still two unresolved situations:

(a). The 3ST provides a "non-standard" solution, which is not physical.
(b). There are experimental situations in which the recorded reflections resemble MRs in a domain where the 3ST does not provide any solution. This, in fact, is the "von Neumann paradox".

Guderley (1947) resolved this paradox almost over 60 years ago. He claimed that in addition to the three shock waves that meet at the triple point, there are cases in which a very tiny Prandtl-Meyer expansion fan complements the wave configuration. Hence, rather then a three-shock wave confluence there is a four-wave confluence. Following Skews & Ashworth (2005) this reflection, shown schematically in figures 1c, is called *Guderley refection*, GR. As it turned out, the forgoing presentation still does not provide

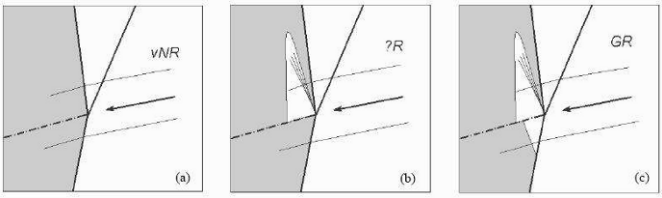

Fig. 1. Illustration of the wave configurations of (a) von Neumann reflection, (b) the newly presented reflection, and (c) the Guderley reflection (gray denotes subsonic flow).

a full picture of the phenomenon, since there are situations between the a vNR and a GR domains for which non of these two reflection configurations is possible, and there is a yet another wave configuration there.

This is shown in figure 2 by means of the evolution of the (I-R)-polars combinations as the complementary wedge angle, $\theta_W^C = 90° - \phi_1$, is decreased from 41°, for which the reflection is an MR, to 38.2°, 34.5°, 33.9°, 32.5°, 31.8° and finally to 30°, for $M_S = 1.47$ and $\gamma = 5/3$. Figure 2a shows the (I-R)-polars for $\theta_W^C = 41°$. The intersection of the I- and R-polars results in a standard solution of 3ST ($\theta_1 - \theta_2 = \theta_3$) and the resulting reflection is an MR. Figure 2a also reveals that the flows on both sides of the slipstream of the MR, near the triple point, are subsonic. At $\theta_W^C = 38.2°$, $\theta_2 = 0$ is reached (figure 2b). This is the MR↔vNR transition point. Figure 2b also reveals that $M_2 < 1$ and $M_3 < 1$. Figure 2c shows the (I-R)-polars for $\theta_W^C = 34.5°$. The intersection of the I and R polars results in a non-standard solution of the 3ST ($\theta_1 + \theta_2 = \theta_3$). The resulting reflection is a vNR (figure 1a). The flows on both sides of the slipstream of the resulted vNR are subsonic. At $\theta_W^C = 33.9°$ (figure 2d) the subsonic branch of the I-polar intersects the R-polar exactly at the sonic point of the R-polar, hence, $M_2 = 1$ and $M_3 < 1$. This situation marks the point beyond which the 3ST has a solution which is not physical! Therefore, this is the point at which the vNR terminates and gives rise to another reflection that was earlier termed ?R (figure 1b), i.e., figure 2d represents the vNR↔?R transition point, and also the point at which solutions of the three-shock theory (3ST) are not physical anymore and hence it should be replaced a four-wave theory (4WT), i.e., 3ST↔4WT. At $\theta_W^C = 33.4°$ (figure 2e) the I- and R-polars still intersect, along their weak-solution branches, i.e., $M_2 > 1$. This solution, which implies that the reflected shock wave is directed towards the oncoming flow and that the flow in state (2) is supersonic, is not

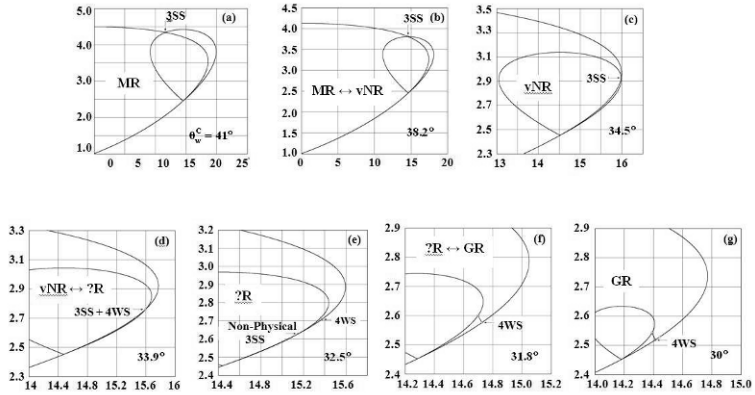

Fig. 2. The (I-R)-polars combinations for $M_S = 1.47$ and $\gamma = 5/3$. The sonic point is marked on all the shock polars.

physical! The (I-R)-polars of the alternative 4WT, which results in a ?R, is shown by the line bridging a subsonic state on the I-polar [state (3)] with the sonic point of the R-polar [state (2)]. At $\theta_W^C = 31.8°$ (figure 2f) the I- and R-polars do not intersect at all and the 3ST does not provide any solution. Based on the 4WT of Vasilev (1999) the sonic points of the I- and the R-polars are bridged, hence $M_2 = 1$ and $M_3 = 1$. This is the point at which the ?R terminates and the GR forms (figure 1c). At $\theta_W^C = 31°$ (figure 2g) the I- and R-polars do not intersect and the 3ST does not provide any solution. The I- and the R-polars are bridged at $M_2 = 1$ and $M_3 > 1$. A Prandtl-Meyer expansion fan, similar to the one mentioned above bridges the flows in states (2) and (3) whose conditions are sufficient to support a Prandtl-Meyer expansion fan. The vNR, ?R and GR are shown in figure 1. In the vNR all the flow regions behind the reflected shock wave and the Mach stem are subsonic. Hence, the triple point is embedded in a subsonic flow with a logarithmic singularity (except for the incoming flow behind the reflected shock wave). In the ?R there is one supersonic patch (white area) that extends from the slipstream towards the reflected shock wave with a Prandtl-Meyer expansion fan inside it. In the GR there are two supersonic patches. One, similar to that in the ?R, and one that extends between the slipstream and the Mach stem. Hence while in the ?R there are two subsonic patches near the triple point, in the GR there is only one subsonic patch. Thus, the vNR, ?R and GR are characterized by different number of subsonic patches with logarithmic singularity at the triple point.

The evolution of the types of reflection that are encountered when θ_W^C is reduced for $M_S = 1.47$ and $\gamma = 5/3$ and the appropriate transition criteria between them are summarized in table 1.

The transition criteria are shown in figure 3a. Figure 3b present the domains of and the transition boundaries between the various shock wave reflections in the (M_S, θ_W^C)-plane for $\gamma = 1.4$. Line 1, $\phi_2 = 90°$, is the MR↔vNR transition line. Above this line $\phi_2 < 90°$ and the reflection is an MR. Line 2, $M_2 = 1$, is the vNR↔?R transition line. This line also separates between the domains in which the 3ST does or does not have a physical solution, i.e., the 3ST↔4WT. Line 3, $M_3 = 1$, is the ?R↔GR transition line. Line 4 is the line on which $M_1 = 1$. Below this line the flow behind the incident shock

$\theta_W^C \& \phi_1$	Mach Number in State(2)	Mach Number in State(3)	
$\theta_W^C = 41.0°(\phi_1 = 49.0°)$	$M_2 < 1$	$M_3 < 1$	MR
$\theta_W^C = 38.2°(\phi_1 = 51.8°)$	$\phi_2 = 90°$		MR↔vNR
$\theta_W^C = 34.5°(\phi_1 = 55.5°)$	$M_2 < 1$	$M_3 < 1$	vNR
$\theta_W^C = 33.9°(\phi_1 = 56.1°)$	$M_2 = 1$		vNR↔?R 3ST↔4WT
$\theta_W^C = 33.4°(\phi_1 = 56.6°)$	$M_2 = 1$	$M_3 < 1$	?R
$\theta_W^C = 31.8°(\phi_1 = 58.2°)$	$M_3 = 1$		?R↔GR
$\theta_W^C = 31.0°(\phi_1 = 59.0°)$	$M_2 = 1$	$M_3 > 1$	GR

Table 1. Reflection processes when θ_W^C is decreased for $M_S = 1.47$ and $\gamma = 5/3$.

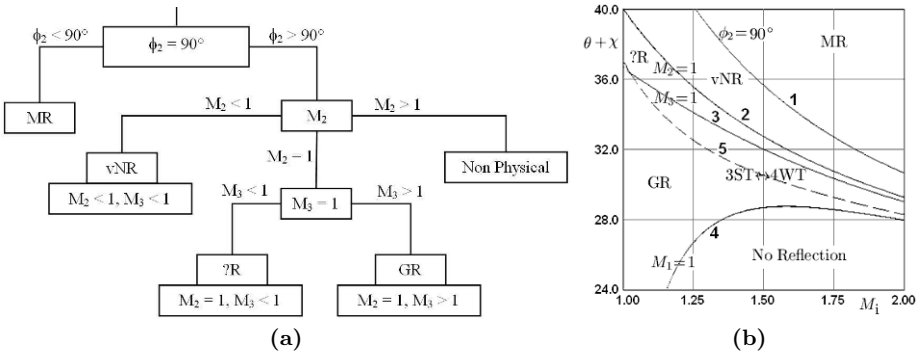

Fig. 3. (a) Evolution tree type presentation of the transition criteria between the various reflections. (b) Domains of and transition boundaries for $\gamma = 7/5$.

wave is subsonic and no reflection can take place! Line 5 divides the (M_S, θ_W^C)-plane into two domains: above it the 3ST has at least one solution (not necessarily physical) and below it the 3ST does not have any solution. Consequently, between lines 2 and 5 the 3ST has a solution, which is not physical. The von Neumann paradox existed inside the domain bounded by lines 2 and 4. Guderley (1947) resolved the paradox in the domain bounded by lines 3 and 4 by forwarding the four-wave concept. The reflection in this domain is a GR (figure 1c). The reflection that takes place inside the domain bounded by lines 2 and 3 is ?R, which is shown in figure 1b. In summary, the MR-domain is above line 1; the vNR-domain is between lines 1 and 2; the ?R-domain is between lines 2 and 3; the GR-domain is between lines 3 and 4; and the NR-domain is below line 4. The 3ST has at least one (not necessary physical) solution in the domain above line 5 and no solutions in the domain below line 5.

3 Summary

The reflection of weak shock waves has been reconsidered using shock polars. It has been pointed out that the vNR-concept that was forwarded by Colella & Henderson (1990) as a resolution of the von Neumann paradox is not correct, since it occurs under conditions for which the three-shock theory (3ST) does have a solution.

Based on the boundary condition across the slipstream the solutions of the three-shock theory were classified into "standard-3ST solution" and "non-standard-3ST solution".

It was shown that there are two situations in the non-standard case: a situation in which the 3ST provides solutions of which at least one is physical and a situation in which the 3ST provides a solution which is not physical, and hence no reflection having a three-shock confluence can take place there.

In addition, it was shown that there are cases in which the 3ST does not provide any solution. The reflection domain in these cases could be either a ?R (figure 1b) or a GR (figure 1c) that both include an Prandl-Meyer expansion fan but differ in the number of their supersonic patches. The GR was suggested by Guderley (1947) as his resolution of the von Neumann paradox, and the ?R was first suggested by Vasilev (1999).

The domains and transition boundaries between the above mentioned four types of reflection that can take place in the weak shock domain were elucidated.

Acknowledgement. This study was conducted under the auspices of the Dr. Morton and Toby Mower Chair of Shock Wave Studies.

References

1. Colella, P. and Henderson, L.F., 1990 The von Neumann paradox for the diffraction of weak shock waves. J. Fluid Mech., 213, 71 94.
2. Guderley, K.G. 1947 Considerations on the structure of mixed subsonic-supersonic flow patterns. HQ Air Materiel Command, Wright Field, Dayton, Ohio., Tech. Report F-TR-2168-ND.
3. Mach, E., 1878 Uber den verlauf von funkenwellen in der ebene und im raume. Vienna Acad. Sitzungsberichte. 78, 819 838.
4. Neumann, J. von, 1943a Oblique reflection of shocks, *Explosive Research*. Rep. 12, Navy Dept., Bureau of Ordinance, Washington, DC, USA.
5. Neumann, J. von, Refraction, intersection and reflection of shock waves. NAVORD Rep. 203-45, Navy Dept., Bureau of Ordinance, Washington, DC, U.S.A., 1943b.
6. Olim, M. and Dewey, J.M., 1992 A revised three-shock solution for the Mach reflection of weak shocks. Shock Waves, 2, 167 176.
7. Skews, B.W. and Ashworth, J.T., 2005 The physical nature of weak shock wave reflection. J. Fluid Mech., 542, 105-114.
8. Vasilev, E.I., 1998 High-resolution simulation for the Mach reflection of weak shock waves. Proc. ECCOMAS 4th Comput. Fluid Dyn. Conf. Athens, Greece, 1(1), 520-527.
9. Vasilev, E.I., and Kraiko, A.N. 1999 Numerical simulation of weak shock diffraction over a wedge under the von Neumann paradox conditions. Comput. Math. Math. Phys., 39(8), 1335 1345.
10. White, D.R., 1952 An experimental survey of the Mach reflection of shock waves. Princeton Univ., Dept. Phys., Tech. Rep. II-10, Princeton, N.J., USA. See also Proc. 2nd Midwest Conf. Fluid Mech., Ohio State Univ., 3, 253 262.

Blast loads and propagation around and over a building

C.E. Needham

Applied Research Associates, Southwest Division, Albuquerque, New Mexico 87110 USA

Summary. Recent interest in blast propagation in urban environments has demonstrated a need for a fast running model to approximate the modifications to the blast environment caused by the interaction with buildings. A series of first principles calculations was completed which provides a data base for describing the interaction of buildings with blast waves of various yields. Using this data base, ARA has developed a fast running model to describe this interaction.

The interaction of a blast wave with a structure involves complex flow phenomena. Modeling of this interaction with a fast running PC based method presents some interesting challenges. Reflection of a planar shock from the front face of a rectangular structure with a normal angle of incidence can be handled fairly well with the application of the Rankine-Hugoniot (R-H) relations to get the peak reflected pressure. Knowledge of the building dimensions determines the rarefaction wave propagation from each edge of the building. The R-H relations can then be applied to obtain the stagnation pressure behind the incident wave. If we simply change the incident wave to a curved front, impinging the structure at an angle other than 90 degrees, the problem becomes more complex.

The model described in this paper provides not only the load as a function of time at any point on any surface of a rectangular structure from an arbitrary blast wave, it also provides the pressure waveform in the "shadow" of the building. This model is based on results of first principles, high resolution CFD calculations, supported by experimental data and the TNT standard. The model accounts for the effects of vortices forming and shedding from the edges of the building and follows the shock around multiple corners.

Examples and comparisons of the results of the model with first principle calculations are presented for several shock strengths and building orientations.

This work was funded by the Defense Threat Reduction Agency (DTRA).

1 Introduction

Obtaining accurate loads on simple structures has been a task relegated to three dimensional hydrodynamic computer codes. In order to resolve peak pressures from blast wave loading has required fine zoning and run times of hours to tens of hours or more. ARA undertook a task to make a number of such three dimensional calculations for simple rectangular parallelepipeds exposed to blast waves originating from different yields at varying distances and at different incident angles to the structure. The structure dimensions were varied to determine the effects of the ratios of different dimensions, such as height to width and width to length. (Varying the size is the equivalent of changing the yield.)

Additional calculations were made to examine the effects of neighboring buildings on the flow around a single building. Variations were made in building length, separation, height and width. The addition of a second building introduces significant perturbations to the flow which extend to 4 or 5 building dimensions beyond the structure. The model

development described here follows the historical perspective beginning with the simplest principles. Whereever possible, the model attempts to follow physical principles rather than fits to a data base. The first principles calculational results are used as the guideline and for the evaluation of the adequacy of the models as they are developed.

2 The Blast Standard

ARA uses the TNT blast standard for all condensed high explosives. We realize that there are differences in detonation properties and that a TNT detonation does not accurately represent C-4 for instance. To make this method workable and not too complicated, we use the principle of "equivalent yield". Rather than making a detailed comparison of pressure or impulse as a function of range and dynamically adjusting the effective yield to match the observed behavior relative to TNT, we assume that the total detonation energy relative to TNT can be used to provide the appropriate pressure and impulse as a function of range to within 10 or 15 percent. The TNT standard generates all hydrodynamic parameters as a function of range at a given time. Thus the full positive and negative phases of pressure, density and velocity are defined at any time after detonation. These fits include the effects of the detonation products and the dynamic pressure associated with them. The TNT standard is very fast on any modern PC and provides an evaluation for a few thousand points at a given time in about 1 second.

The standard procedure for finding the loads on a planar surface is to use the incident overpressure and a reflection factor. This is a well defined procedure and can be done using the Rankine-Hugoniot relations when the shock arrival is perpendicular to the wall. The peak reflected overpressure is calculated from the equation:

$$OP_{ref} = 2 * OP_{inc} + (\gamma + 1) * DP_{inc} \tag{1}$$

where γ is the ratio of specific heats of the air (typically = 1.4) and DP is the incident dynamic pressure. When the shock incidence angle is not 90 degrees, either tables or reflection factor plots (e.g., Fig. 1) can be used to determine the peak reflected pressure.

This paper presents an alternative, reasonably easy to use, and more accurate model for defining structural loads from external detonations. The free field wave forms for any hydrodynamic parameter (pressure, density, velocity, energy density, temperature, etc.) are defined by the TNT Standard. For reflection from a planar surface, the principle of image bursts is used. An image burst is used to represent the interaction of a blast wave with a reflecting surface. Figure 2 (left) illustrates the image burst concept. A detonation of yield Y1 occurs at a distance R from a planar reflecting surface. The resultant pressure on the reflecting surface can be represented by treating the surface as a perfectly reflecting plane and replacing the plane by a perfectly symmetric image burst. The image burst is placed the same distance from the plane and is given the same yield as the actual detonation. This has been done very successfully in experiments where shock reflections were studied in the absence of a boundary layer.

In order for this to be done numerically, a set of shock interaction rules, known as the LAMB addition rules, were formulated some years ago. The LAMB addition rules listed in Table 1 have been used by a number of fast running engineering codes with great success. The application of these rules to finite sized buildings with a face perpendicular to the incident shock is straight forward by simply limiting the region of interaction to the solid angle of the shock front intercepted by the face of the building. When the

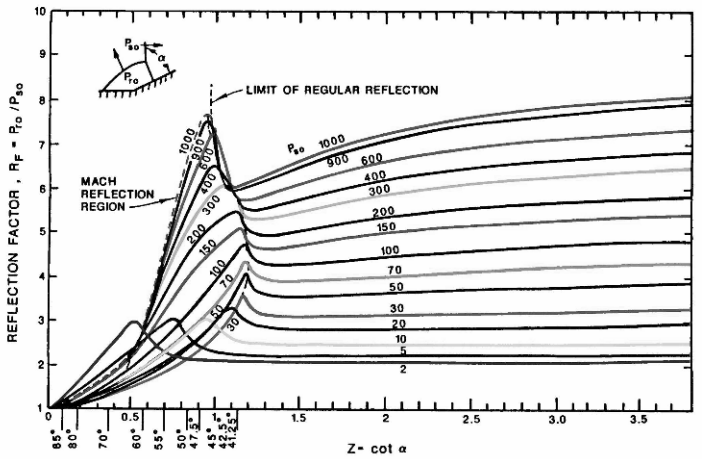

Fig. 1. Reflection factor for blast waves in air as a function of angle

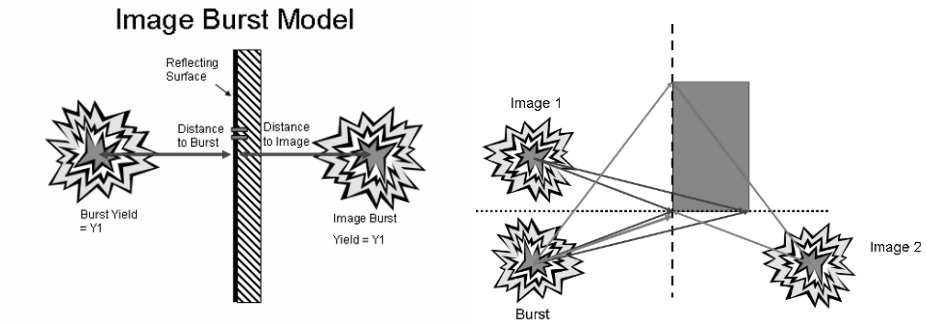

Fig. 2. The image burst concept (left). Image burst locations for arbitrary structure orientation (right).

"Conservation of Mass"

$$\bar{\rho} = \rho_0 + \sum_{i=1}^{N} \Delta\rho_i$$

"Conservation of Momentum"

$$\vec{V} = \frac{\sum_{i=1}^{N} \rho_i \vec{V}_i}{\bar{\rho}}$$

"Conservation of Energy"

$$P = P_0 + \sum_{i=1}^{N} \Delta P_i + 1.2\left(\frac{1}{2}\left(\sum_{i=1}^{N} \rho_i \left|\vec{V}_i\right|^2\right) - \frac{1}{2}\bar{\rho}\left|\vec{V}\right|^2\right)$$

Table 1. The LAMB Addition Rules

building is at an arbitrary angle to the incoming shock, there are two reflecting surfaces requiring two separate image bursts. Figure 2 (right) illustrates the pairings of the image bursts with the real burst.

The addition rules are applied to the area to the bottom of the structure in the illustration for the original burst and image burst 1. They are applied not only to the surface of the structure but within the volume affected by the combination of bursts. In the region to the left of the structure, the addition rules are applied to the original burst and image burst 2 only. The rules are applied to all points on the left surface of the structure and to the volume to the left of the structure which is influenced by those two bursts.

By using the addition rules for a sufficient number of points on the surface of the building, pressure loading waveforms can be constructed as a function of time and impulses calculated at any number of arbitrary points on the faces of the building. We have now completed the loading for the easy surfaces of the building. The loads on the sides and back of a structure which are not in the direct line of sight, present a special problem. The remainder of this paper discusses the approach used in modeling the shock as it surrounds and loads the structure.

3 A Simple model for propagating Blast Waves around corners

Several calculations were made using the three dimensional SHAMRC CFD code (AMR version of SHARC) to describe the loading on a single building. The pressure time histories were recorded on all sides of the building. In order to gain some understanding of the behavior of the shock as it engulfs the building we monitored the pressures at a number of points on the various walls and in the near field as a function of time. The calculation was for a 2000 pound TNT charge detonated approximately 70 feet from the front face of the building. In figure 3, the points on the yellow line labeled SHAMRC results were taken along a line from the detonation point to the corner of the building, along the side of the building and around the back side of the building. The curve labeled TNT standard is the free field peak overpressure as a function of range for the 2000 pound charge. For comparison, I plotted the peak overpressure at twice and four times the distance for the free field overpressures. I noted that the pressure at the shock front dropped as it rounded the corner of the structure and the decay fell parallel to the overpressure curve at twice the distance. Further, I noticed that the peak overpressure dropped to correspond to the pressure at 4 times the distance when it rounded the second corner at 117 feet to the backside of the building.

To find the overpressure at the point of interest we calculate the total distance from the burst point to the point of interest by summing the distance from the burst to the corner of the building, Rc, plus the distance from the corner of the building to the point of interest, Rw. This is used to find the radius of the shock when it reaches the point of interest:. $R_t = R_c + R_w$. In fact, the shock did travel that distance to get to the point of interest. The resulting shock geometry is shown in figure 4 (left). Note the curvature and "delay" of the shock as it travels around the building.

When we evaluate the pressure from the model at that range, we find it is higher than what was calculated by the first principles code. Using the observation from figure 3 and the results of the first principles calculation, we developed the relation that the pressure at the point of interest is the pressure at the radius equal to:

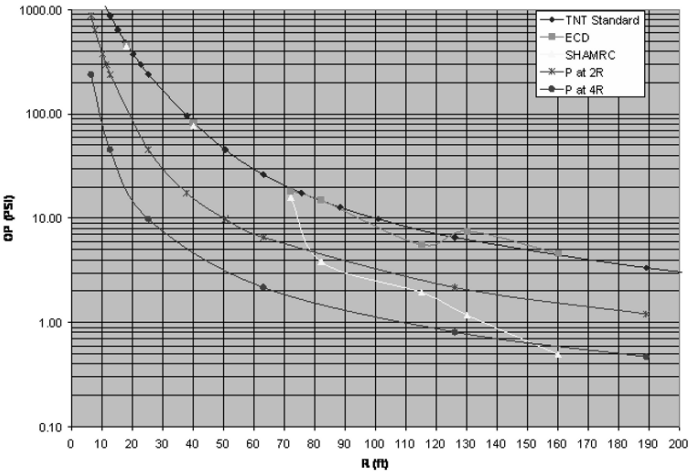

Fig. 3. Overpressure vs. Range for 2000 pound TNT detonation

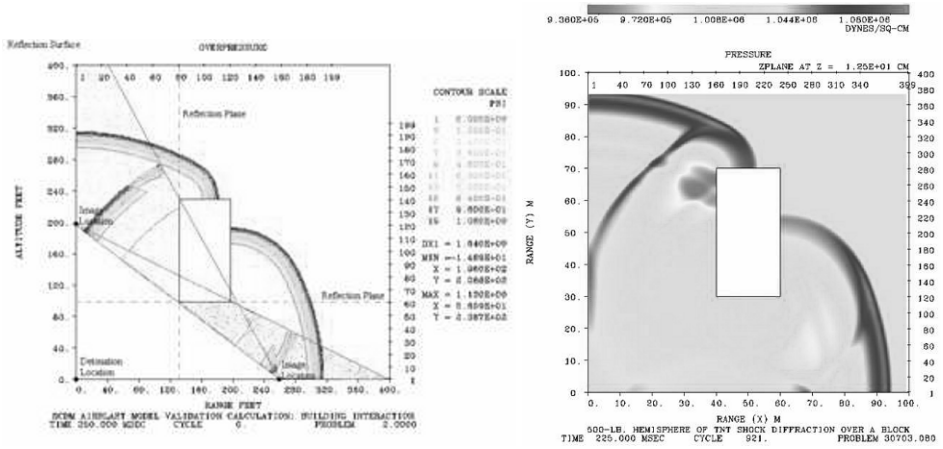

Fig. 4. Combined shock geometries for an asymmetric burst location. Results of simple model (left) and first principles code (right)

$$R_p = R_t * (1 + \sin\theta) \tag{2}$$

Thus we have a two step procedure for determining the refracted shock geometry and the refracted shock pressure. We have found that this procedure can be used to describe not only the peak overpressure, but provides a good approximation to the time history of the overpressure. Note that this procedure accounts for the discontinuous drop in overpressure as the shock reaches the corner of the structure.

This procedure works equally well for the shock being refracted around a second corner. The radius for the shock is measured as the sum of the radius from the charge to the first corner plus the radius along the length of the building plus the radius from the

second corner to the point of interest:

$$R_t = R_c + R_w + R_s \tag{3}$$

The pressure at the point of interest is found by evaluating the pressure from the TNT standard at a distance of

$$R_p = R_t * (1 + \sin\theta) * (1 + \sin\alpha) \tag{4}$$

The total time history can be constructed by calling the TNT standard at a sequence of times for the same point.

This method also permits the use of LAMB addition rules for the combination of shocks that come from the different sides or over the top of the structure. This method can then account for the interaction and stagnation of shocks on the backside of a building. One of the complications with combining the shocks that have followed various paths is that only the minimum path length should be used for each surface of the building.

When the shock geometry changes are included, the results of the shock locations for both reflected and refracted shocks are shown in figure 4 (left). The shaded yellow and green areas show the regions of influence for the reflections of the two image charges. Figure 4 (right) shows the results of a first principles SHAMRC calculation of a similar scenario. Note the agreement in shock geometry for both the diffracted and reflected shocks.

4 Conclusions and Future Development

This method appears to provide satisfactory airblast environment definition for the loading of a single rectangular based structure and in the surrounding near field to the structure. The TNT standard and the LAMB addition rules remain essentially unchanged over the last several years and have proven very useful and reasonably accurate for a wide variety of shock applications.

A number of three dimensional calculations have been completed for a few selected yields using side by side structures The calculations used three different values for the separation distance and four different values for the building length, while the height and width were held constant. Attempts to model the multiple building blast wave interactions have not yet produced a viable model The reflected overpressure on the front face of the buildings is readily calculated using standard image burst techniques, however modeling the remainder of the field with a fast running method has not yet been solved.

Blast propagation through windows and doors

C.E. Needham

Applied Research Associates, Southwest Division, Albuquerque, New Mexico 87110 USA

Summary. A challenging blast propagation problem is the detailed description of a blast wave propagating through a window or doorway either from the inside to the exterior, from the exterior to the interior or from room to room. A number of three dimensional first principles calculations of blast loading on structures have been carried out and compared with experimental data. The combined calculational and experimental results were used as a data base for a number of geometric variations of building size, opening size and charge location. Derived from this large data base, ARA has developed a fast running model.

This paper describes the development of a fast running model based on physical principles and conservation laws. Comparisons of the results of the fast running model with the waveforms in the data base illustrate the principles used in the model. Results of the model are then compared to first principles waveforms and with experimental waveforms from recent multi-room internal detonations which were not a part of the data used for development of the model.

Application of physical principles leads to a much more robust and adaptable model than "fitting" parameters to a data base.

This work was sponsored by the Defense Threat Reduction Agency (DTRA).

1 Background

A method has been developed to predict the blast wave time history in a fast running engineering level model for propagation from room to room through doorways and windows. The method is based on the TNT standard for high explosive detonations, geometrical considerations and the basic properties of blast waves. The model was developed using the results of two and three dimensional hydrodynamic computer code calculations as a data base for understanding the refraction and flow of shocks through openings. We have attempted to retain as much physical meaning in the method as possible and have avoided using numerical fits or correlations.

2 TNT Standard

ARA uses the TNT blast standard for all condensed high explosives. The TNT standard generates all hydrodynamic parameters as a function of range at a given time. Thus the full positive and negative phases of pressure, density and velocity are defined at any time after detonation. These fits include the effects of the detonation products and the dynamic pressure associated with them. The model returns the values for pressure, density and velocity at any point in space and time. The TNT standard is very fast on any modern PC and provides an evaluation for a few thousand points at a given time in about 1 second.

3 Internal Blast Propagation with Floor and Ceiling

A detonation occurs between two planes of infinite strength and infinite extent (the floor and ceiling). The volume into which the energy expands is restricted and the energy density is proportionally increased above that of a free expansion. The initial calculations were made for the case of a 100-kg charge of TNT, detonated at mid-height between the planes separated by distance H.

Figure 1 shows the pressure distribution calculated by the first principles code, SHARC, at a time of 5.8 ms after the detonation at mid height of a three meter high room. This is for a two dimensional axi-symmetric geometry with the detonation taking place on the axis of symmetry. The initial shock has reflected at least twice from the floor and ceiling. The shock approaching the wall is nearly planar. The results of this calculation were used at different times as initial conditions for a series of three dimensional calculations to determine the shock behavior in the second room as a function of stand off distance of the charge in the first room.

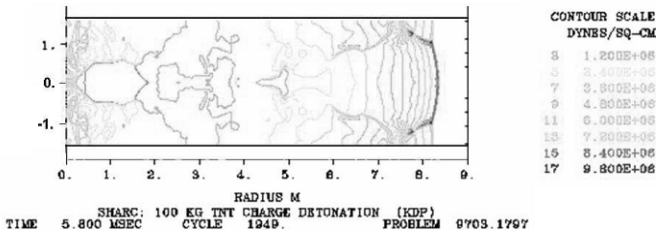

Fig. 1. Pressure distribution at 5.8 ms for a blast wave with floor and ceiling

Figure 2 shows the pressure distribution for a one meter standoff distance, with a one square meter opening when the charge is placed in line with the opening. The reflected pressure in the donor room is nearly 400 bars while the maximum pressure in the second room is only 40 to 50 bars. The three dimensional calculations included an array of pressure monitoring stations in the second room. The pressure-time histories recorded at these stations were used as the data base for determining the distribution of the pressure, dynamic pressure and corresponding impulses as a function of location relative to the opening and the charge placement.

For a free air sphere, the energy of the detonation is contained in a volume $V_f = 4\pi R^3/3$, where R is the shock radius. For containment between two planes, after the initial reflection has occurred, the volume containing the energy can be approximated by: $V_c = \pi R^2 H$where H is the distance between the planes and R is the distance from the charge parallel to the planes. Contained in this volume is the detonation energy Y_0. Taking the ratio of the two volumes:

$$V_c/V_f = 4R/3H \tag{1}$$

The yield ratio for the effective yield of the detonation at distance R from the charge between planes is $4R/3H$ for $R \geq 3H/4$. Thus at R = 3H, $Y = 4Y_0$. There will be a rapid transition between free field and this effective yield at distances from R = H/2 to R = 1.33 H.

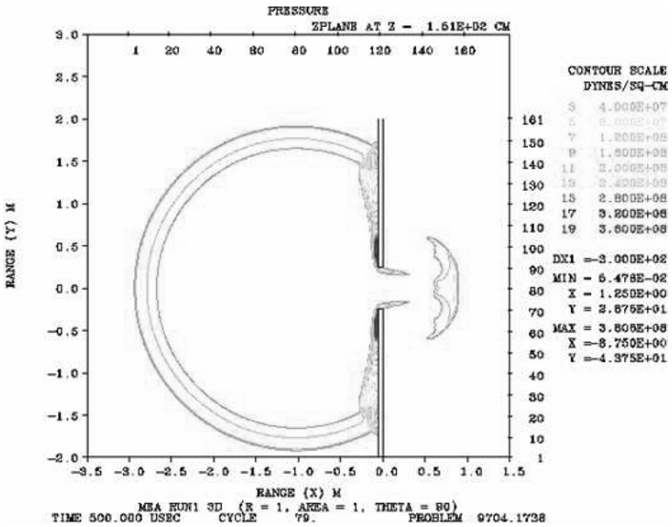

Fig. 2. Three dimensional results at mid-height at 0.5 ms, for a one meter standoff, charge in line with opening

A model based on the above assumptions has been developed which provides the overpressure and impulse for an arbitrary high explosive detonation in a room with a finite ceiling height. The next step was to estimate the blast propagated through a finite opening and its distribution on the far side of the wall. There may or may not be a ceiling over the burst, thus, the model works as well for bursts outside a building and entering as for a burst inside a building and exiting or propagating from room to room inside a building.

4 Blast Propagation through an Opening in a Wall

The assumption here is that the wall is infinite in extent and has a single opening of area A. The model makes no assumptions about the shape of the opening because this would require specific information on the design of the building. The problem is to define the distribution of pressure on the far side of the wall as a function of range and incident angle to the opening on the detonation side, the opening area, the range, and the angle from the opening on the far side of the wall.

First, we use the example problem where the angle between the opening and the detonation is perpendicular (90 degrees) to the wall. The energy going through the opening is the fraction of the energy contained in the solid angle between the detonation point and the opening area. Thus the energy fraction through the opening is

$$E_f = (2A/3)R_0/(4\pi {R_0}^3/3) = A/(2\pi {R_0}^2) \leq 1 \tag{2}$$

At the door opening the effective yield is the original yield Y_0, but the energy passing through the door is $Y_1 = Y_0 A/(2\pi {R_0}^2)$. The yield therefore transitions as $(R_0/R)^2$

between the limits of 1 at the opening and $A/(2\pi {R_0}^2)$, where R is the total distance from the burst and R_0 is the radius from the burst to the opening.

As the shock progresses through the door, this fraction of energy is redistributed, but not uniformly. The angular distribution of the energy on the far side of the wall is proportional to the ratio of dynamic pressure Q to the overpressure. Thus, at very low overpressures the opening will behave like a source of the reduced yield located at the center of the opening. At high overpressures the source will be directional, with a preferential direction aligned with the radius vector to the charge. Any point in alignment with the door opening will see the original yield for a greater distance than those points in the shadow region of the wall. The dynamic pressure at high overpressure is 2.5 times the overpressure. The overpressure, being a scalar, attempts to redistribute the energy equally in all directions. The dynamic pressure is directed and attempts to continue carrying the momentum and energy in the direction of the vector from the charge.

5 Angular Dependence of Transmitted Wave

If we let Φ be the angle between the radial from the charge to the edge of the opening and the radial from the edge of the opening to the target point, we require the integral of the energy distribution over Φ to be Y_1, the energy through the opening. When Φ is $\pm 90^o$, the energy is proportional to ΔP (the overpressure, a scalar). We define angle α to be the angular width of the opening. When Φ is outside the angular opening defined by α, the energy distribution is proportional to the ratio of the component of the dynamic pressure Q to the overpressure in the direction of the target point. Figure 3 illustrates the geometry and the angle relationships. For an ideal gas ($\gamma = 1.4$),

$$Q = \frac{5(\Delta P)^2}{2(7P + \Delta P)} \tag{3}$$

Therefore, $\frac{Q}{\Delta P} = \frac{5\Delta P}{2(7+\Delta P)}$, if we let $P_{ambient} = 1$. The proportion of energy in the direction Φ is thus defined as $\frac{\Delta P + Q\cos\Phi}{\Delta P + Q}$ and the effective yield is calculated accordingly. Because the effective yield is specified at each target point, the model produces not only the arrival and peak overpressure, but complete waveforms of all blast parameters. These waveforms may be integrated to provide impulses directly.

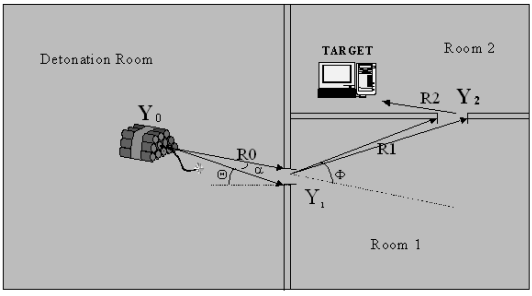

Fig. 3. Definition of the geometry for multiple room propagation

6 Blast Propagation through a Second Opening to a Third Room

Whether the source is in another room, or is in the open on the other side of the wall, the effective yield at the opening is modified by the same function of the opening area as described above. For the case of a second opening in the non-blast room, the effective yield at the center of the second opening becomes the effective yield as adjusted by the distance and angular position relative to the first opening. As the blast propagates through the second opening, the effective yield is further reduced by the opening area ratio and the angular adjustment, just as the yield was changed by passage through the first opening.

7 Comparisons of Model and First Principles Calculations

The model was exercised against a large number of three dimensional first principles (SHARC) hydrodynamic calculations. Figure 4 shows the results of the pressure distribution in the second room for the case of a 100 kg TNT detonation placed 1 meter in front of a 1 square meter opening into the second room. For perfect agreement, the data would fall on the diagonal line. Points above the line indicate that the model is higher than the SHARC results and points below the line indicate that the model gives lower pressures than SHARC. The model is on the low side at low values, but is consistently within a factor of two of SHARC. The deviation at low overpressures is not considered to be a serious problem because the low overpressures are less important for most structure response.

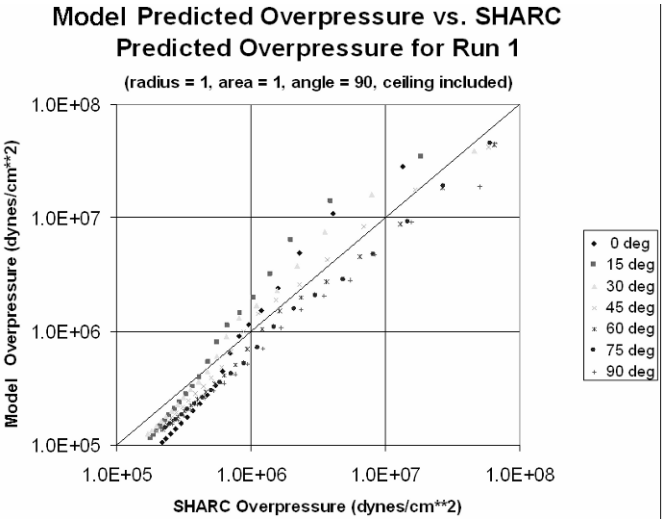

Fig. 4. Comparison for a charge aligned with the opening

Figure 5 shows the overpressure comparison for the case of the detonation being 4 meters from a 4 square meter opening at a 60 degree angle. For this larger distance, and

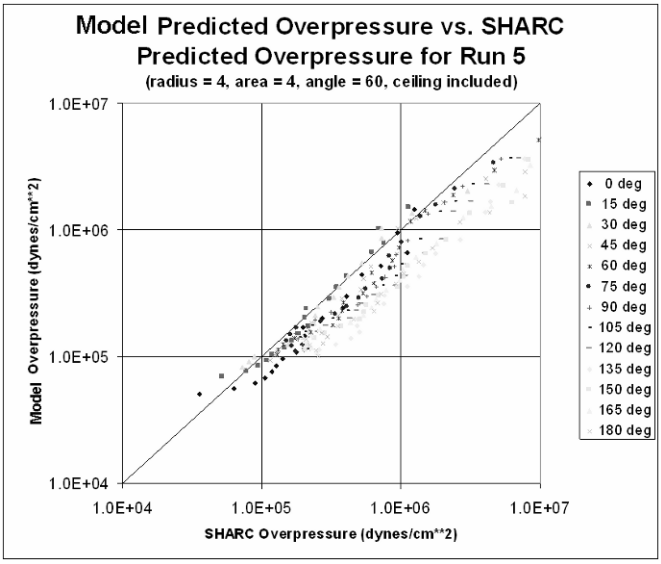

Fig. 5. Comparison for the charge at 60 degrees from the opening

therefore less divergent flowfield, the model consistently tracks the SHAMRC results at all pressure levels and there is no falloff at the lower pressures. The largest differences occur when the position in the second room is on a line perpendicular to the line of sight at the opening and is minimal when the points fall along the line of sight.

8 Conclusions

The algorithm presented here provides a very fast and efficient method of defining the air blast propagated into a second room through a relatively small opening. This method provides not only the peak overpressure waveforms as a function of time, but the dynamic pressures as well. These waveforms may also be integrated to provide the overpressure and dynamic pressure impulses at any location in the second room.

The model is readily extended to the propagation of a shock through a second opening into a third room. This is accomplished by redundantly applying the same rules to the second opening as were applied to the first opening.

The accuracy of the model (less than a factor of 2) is sufficient for most applications and is well within the known frangibility limits of most structures. Most overpressure points in the second room fall within 25% of the first principles calculations. One of the advantages of this method is that it requires no image bursts or shock addition logic.

Improvements to the model which could be easily implemented include varying the yield in the second room using a similar algorithm to what is used in the detonation room to account for the reflections from the floor and ceiling. The effects of reflections from the walls of the detonation room and the second room could be included by adding image bursts and including the LAMB addition rules.

Blast wave discharge into a shelter with inlet chevron

A. Britan, Y. Kivity, and G. Ben-Dor

Shock Tube Laboratory of Protective Technologies Research and Development Center, Faculty of Engineering Sciences, Ben-Gurion University of the Negev, Beer-Sheva, Israel

Summary. The concept of passive shock deflectors investigated in this paper allows an easy entry of a shock wave into a shelter, while initiating further reflections and turbulent vortices by diffracting the transmitted shock over a single 90°-chevron facing the incoming flow. Gas dynamic aspects of different chevron placements that control the variation in the attenuation capacity were investigated experimentally, using pressure measurement and shadowgraph photography.

1 Introduction

When a blast wave hits a shelter, the passive shock deflectors (PSD) is expected to minimize the effects of the blasts wave entering the shelter through the air conditioning ducts or other apertures. The damping capacity of various PSD represented by screens, perforated plates or granular beds is based on strong viscous losses [1–3]. In the barrier suggested in [4], back-to-back placed triangular bars have increased resistance due to the strong reflected waves and the diffraction over the large angle. The PSD reported in [5] was supposed to raise additional energy losses due to converging-diverging shocks inside the chevron shown in Fig. 1a. However, our previous tests [2] revealed that several adjacent plates separated by air gaps, play the same role and compare favorably with the downstream pressure field reported in [5]. Since in the real practice optimal PSD has also to minimize the loads on the air conditioning duct, the relative geometry and dimension of a PSD is important. To quantify the matter we replaced the long and narrow conduit investigated in [2] with the $10mm$ wide test section shown in Fig. 1b. In this case, the flow pattern closely resembles the dynamics of the shock wave in the flow area marked by a circle in Fig. 1a, while with a longer distance between the exit of the shock tube and the confining walls. A single 90°-chevron could be placed at various distances, x, from the opening cross-section of $20mm \times 10mm$ providing different blockage for the outflow resulted by the incident shock wave with the Mach number $M_S = 1.3$. The diaphragmless shock tube having a cross section of $32mm \times 32mm$, optical shadowgraph system and the pressure transducers T0 and T1 were the same as in [2]. The pressure transducers T2 and T3 were positioned as shown in Fig. 1b. In order to investigate the role of the geometric factor the distance x was changed between $0.05h$ and $7.5h$.

2 Results and Discussion

2.1 Sensitivity of the pressure to the geometric factor

The insert in Fig. 2a shows two typical profiles of temporal pressure variations. At the entrance to the test section (port T1), the pressure sharply rises first across the incident

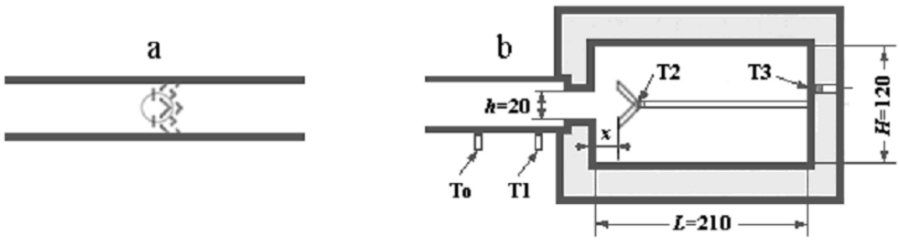

Fig. 1. (a) schematics of the chevron based deflector investigated in [2] and (b) the shock-tube-test-section used in this study.

shock wave to a certain value, remains constant and then increases to the value P_5 across the shock wave reflected back from the test-section entrance. At port T3 the pressure rise seems rather gradual and is considerably lower compared with the equilibrium pressure level P_5 registered at port T1. This difference is a clear evidence of the attenuation caused by the expansion of the shock wave inside the test section and its diffraction over the chevron. Several peaks in the front of the pressure trace T3 show that when the precursor shock wave hits the back wall, it is more likely a series of shocks than a single front. When the chevron is shifted towards the back wall the amplitudes of the first peak, (A) and the third peak, (B), according to the data in Fig. 2a increase and the attenuation performance decreases. It is worthwhile noting that the attenuation coefficient, k, is sensitive to the downstream shift of the chevron until $x/h \leq 2 \div 3$, while a further increase in x becomes ineffective. Considering the typical pressure trace shown in the insertion to Fig. 2b, one can refer first to a high-pressure peak registered in the port T2. This peak is a clear evidence of the fact that the precursor shock entering the chevron accelerates toward the vortex. Thereafter the gas stagnation near the vortex take turns to an expansion behind the reflected shock. As a result, the pressure at port T2 gradually reduces to the "steady" level marked by an arrow. According to the data in Fig. 2b the Peak and the Steady curves reach maximum ($k_1 = 1.75$ and 0.9 subsequently) when the geometric factor is small $x/h \leq 2$. The value $k_1 = 1$ in the Peak curve, corresponds to the conditions when the effect of the flow contraction inside the chevron is minimal, while constant vales, about $k_1 \approx 0.5$ in the Steady curve show that at $x/h > 3$ chevron has no advantages over a straight reflecting plate of the same length.

2.2 Development of flow structure

When the planar shock wave interacts with a 2D-area enlargement as shown in Fig. 3a it undergoes transition to cylindrical geometry and the post shock flow field expends around a 90° corner. Nonlinear variations in the pressure and density jump at the shock wave front give rise to baroclinic torque. This in turn, produces two opposite vortex cores with large density gradients. The resulted shear layer is unstable and quickly breaks-up to a series of small, separate vortices visible after about $t = 200\mu s$. The starting jet with the barrel shock and small scale vortices within the extended turbulent zone already appears at $t = 259\mu s$. Up to this stage, viscosity has no effect on generation, spreading and break-up of these structures [6]. Meanwhile the precursor shock wave continues to expand until it reflects at the confining walls. Once the reflected shock wave reaches the vortex cores,

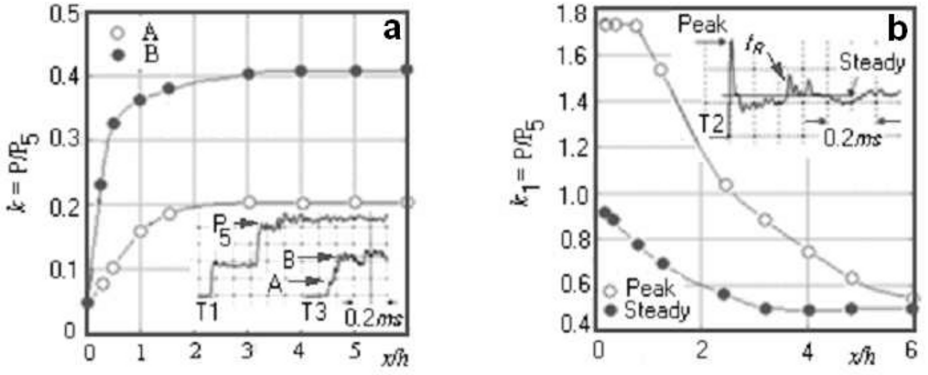

Fig. 2. Experimental data demonstrating the role of the geometric factor in the pressure history registered at ports T1 to T3.

at $t = 295\mu s$, a second stage in the flow history begins [6]. During this stage, the reflected shock splits into two parts. One part is seen to be sucked into the turbulent zone where the viscosity acts simultaneously with the baroclinic torque. The other part, outer part of the reflected shock wave, that is connected to the precursor shock wave forms a triple point and then moves towards the flow axis. Notice that a Mach disc becomes visible at this stage in the center of the starting jet while the reflected shock wave converges to the flow axis. The pictures obtained at $t = 323\mu s$ and $t = 414\mu s$ show dynamics of the flow pattern before and after the shock wave reflection at the centerline.

The wave propagation history into the test section that contains a chevron is evident from figures 3b and 3c. The major effect is a blockage of the gas flow that restricts the starting jet at the cost of an increased flow rate in the radial direction. When the chevron is shifted downstream from the shock-tube output, more space for longitudinal development of the starting jet is left. To clarify the phenomenon the flow pictures of Fig. 3b have to be compared first with those in Fig. 3a. When the distance x is small, the precursor shock wave striking the chevron at $t = 44\mu s$ is mostly planar. At $t = 52\mu s$ it forms regular reflections with oblique shocks on the upper and lower walls when accelerated towards the vertex. Once reaching the vertex, the resulting curved reflected shock moves back at $t = 82\mu s$. Non-regular reflections of the oblique shocks form at the entrance to the transition section a complex structure with a Mach disc. High-pressure difference, in this region, forces the reflected shock wave to enter the transition section at $t = 116\mu s$. Further propagation of the reflected shock wave is followed with back and forth movements of the triple points over the front of the reflected shock wave. The picture obtained at $t = 132\mu s$, demonstrates this feature shortly before the triple points coalesce first at the front center. The oblique shock interacts at the flow axis and causes the local pressure to increase. The second pressure jump at this point, is reached when the oblique shock waves, reflected from the side-walls, meet each other again after $t = 186\mu s$. These repeatable reflections of the oblique shocks are responsible for non-steadiness of the pressure history near port T2. When coupled with the curved reflected shock that moves upstream and finally enters the transition section, both these phenomena manifest that the chevron at this stage forms a common duct with a transition section. A small air gap between the shock tube and the chevron ($x/h = 0.25$) provides

a single means for stagnated gas to be discharged into the main flow. Starting from $t = 146\mu s$ the discharged flow becomes supersonic and remains unchanged even after interaction with the reflected shock wave at $t = 322\mu s$. This means that the transient flow inside the chevron behaves as a closed system that is "unaware" of any variations in the outside pressure field. The influence of the geometric factor on the dynamics of the flow pattern is quite pronounced in the shadowgraphs of Fig. 2c. The longer distance, x, allows more time for the expansion fans to interact with the shock wave front and finally coalesce at the flow axis. As a result, the precursor shock wave becomes curved long before it strikes the chevron at $t = 64\mu s$. At $t = 114\mu s$ the backward faced pair of the reflected oblique shock waves interacts with the vortices at the input corners and gives rise to a new curved shock. This so-called diaphragm shock wave is clear evidence that the local flow in this area is supersonic [7]. At $t = 128\mu s$ the diaphragm shock wave and

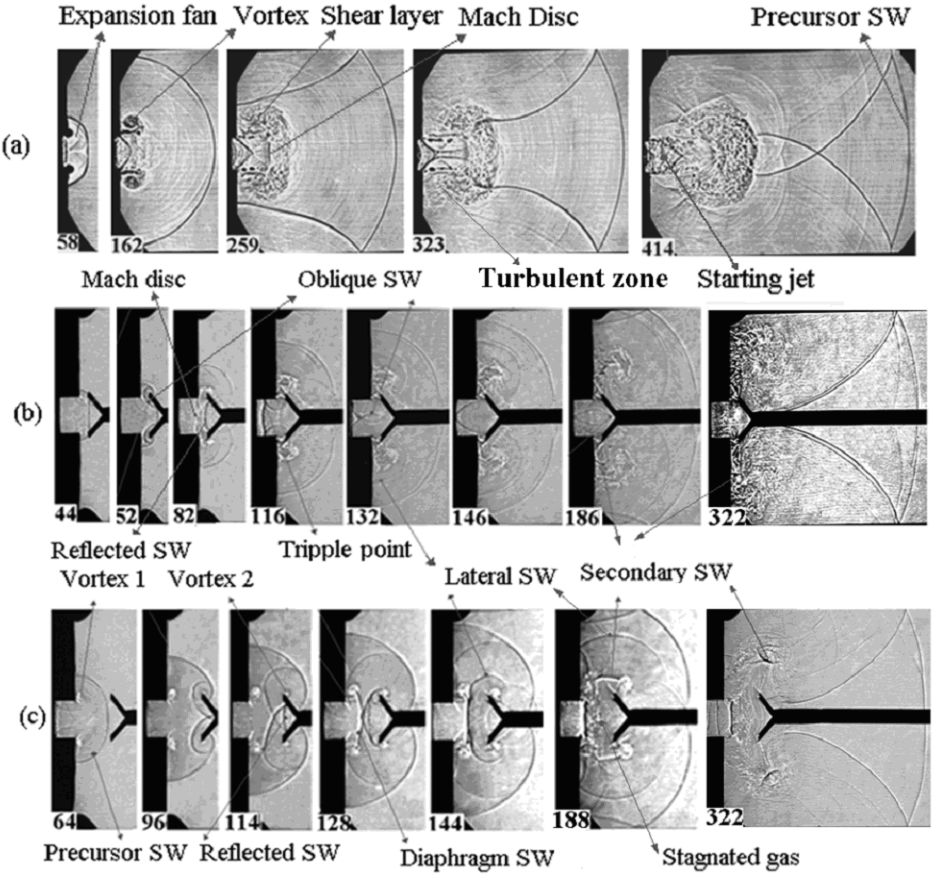

Fig. 3. Typical shadowgraphs demonstrating the propagation of the shock wave inside the empty shelter (a) and effect for two values of geometrical factor: $x/h = 5/20 = 0.25$ (b) and $x/h = 20/20 = 1$ (c). The time, in μs, is assumed to be zero for the instant that the incident shock wave is reflected at the entrance to the transition section.

reflected shock, both resting on the vortices, form a new X-shaped configuration with the extended area of the stagnated gas downstream. At $t = 144\mu s$ this so-called "bubble" of stagnated gas splits into the lateral shock wave that looks as a sharp front separated at its one end from the chevron and moving toward the confining walls. This allows the stagnated gas to expand and supersonic flow sheds "vortex 2" from the back edges of the chevron at $t = 188\mu s$. However, when compared with the last shadowgraphs of Fig. 3b it is seen that configuration developed for $x/h = 1$ is less stable and could break down earlier once the shock wave reflected from the confining wall arrives. This demonstrates that a local supersonic flow over the sharp edge of the chevron and resulted secondary shock wave are both sensitive to disturbances from the backside of the flow field.

3 Discussion and Conclusions

Since detailed pattern of the shear layer instability and turbulent mixing is currently incomplete any experimental evidence in this field has a great advantage [7]. To explain these mechanisms the blast intensity, geometric factor x/h and the dimensions of the shelter, have to be considered. Restricting, ourselves to a single effect caused by the distance x on the pressure coefficients, k and k_1, other parameters of the problem: M_S, h, H and L were set to be constant. Judging from Fig. 2a it appears that the sensitivity of the coefficient k to variations in x ceases for $x/h > 2$. Since Fig. 2b imposes a similar, while less stiff, restriction on the coefficient k_1, it follows that a direct control of the pressure history for optimization purposes is really productive. However, analysis that is more extensive requires also processing of a full series of the flow field pictures (Fig. 3 shows only selected pictures of this series). Typical results of this processing in Fig. 4 show that the trajectories of the precursor shock wave (1) and the turbulent zone (2) are both sensitive to the blockage effect. As to the close position of the chevron (when $x = 5mm$), this fact could be best understood if one refers to the curved rotational flow environment propagating along the vertical wall visible in Fig. 3b. Due to strong energy-losses inside a supersonic jet the longitudinal velocity of the precursor shock in this case is 11% smaller than the case of the empty section. However, the lateral movement of the precursor shock is insensitive to this effect and related trajectories in Fig. 4b coincide with each other. A closer look at Fig. 4b clearly shows that significant effect on the related trajectories appears once the precursor shock wave reflected from the sidewall further interacts with the turbulent zone. Whereas in the empty chamber this interaction causes total stagnation of the turbulent zone, in the test section containing a chevron, the resulted stagnation of the turbulent zone is negligibly small. The physical consequences of this interaction become more apparent after the analysis of the flow patterns in Fig. 3c. The quasi-steady conditions behind the diaphragm shock wave are kept until the closed structure of lateral, diaphragm and reflected shock waves protects this area from the higher backpressure. Once the shock wave reflected from the confining wall destroys the situation this leads to entrainment of the surrounding pressure visible at $t = 322\mu s$ (the related jump, t_R in the pressure trace of Fig. 2b, appears in response to this feature). Similar pressure jumps while shifted in accordance with the arrival time of the reflected shock wave to transducer T2, were registered only for $x > 25mm$. This quantifies the range of the geometrical factor $0 < x/h < 1.25$ when supersonic jet near the vertical wall is stable for a long time and the protection is optimal.

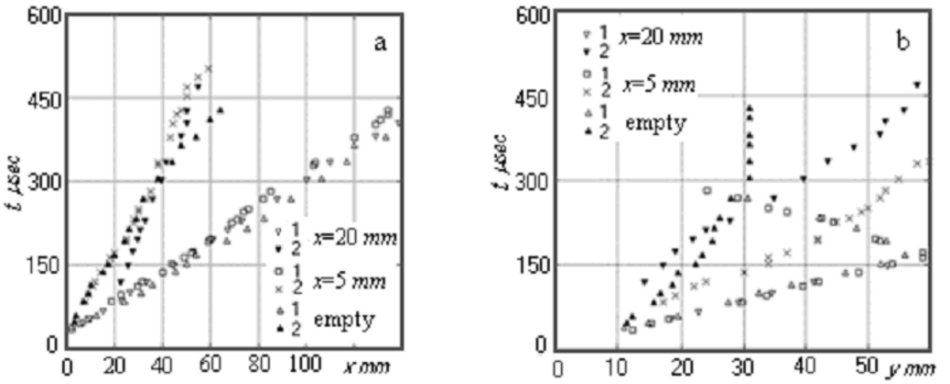

Fig. 4. Time-distance trajectories of the precursor shock wave (1) and turbulent zone (2) propagating in horizontal (a) and vertical (b) directions.

References

1. Britan, A., Ben-Dor, G., Igra, O. and Shapiro, H., 2001, Shock waves attenuation by granular filters, Int. J. Multiphase Flow, **27**, 617-63.
2. Britan, A., Kivity, Y. and Ben-Dor, G., 2005, "Passive deflector for attenuation of shock waves", Proc. ISSW25, Bangalore, India, 504.
3. Britan, A., Igra, O., Ben-Dor, G. and Shapiro, H., 2006, Shock wave attenuation by grids and orifice plates, Shock Waves **16**, 1, 1-5.
4. Skews, B.W., Draxl, M.A., Felthin, L. and Seitz, M.W., 1998, Shock wave trapping. Shock Waves **8**, 21-28.
5. Baum, J.D. and Lohner, R., Numerical design of a passive shock deflector using an adaptive finite element scheme on unstructured grids, AIAA Paper 92-0448.
6. Abate, G. and Shyy, W., 2002, Dynamic structure of confined shocks undergoing sudden expansion, Prog. Aerospace Sci., **38**, 23-42.
7. Jiang, Z., Onodera, O. and Takayama, K., 1999, Evolution of shock waves and the primary vortex loop discharged from a square-cross section tube. Shock Waves **9**, 1-10.

Computational and experimental investigation of dynamic shock reflection phenomena

K. Naidoo* **and B.W. Skews**

School of Mechanical Engineering, University of the Witwatersrand, Johannesburg, 2050, South Africa

Summary. This paper reports the development of an experimental facility for the investigation of dynamic, two-dimensional shock reflection phenomena generated by a rapidly pitching wedge in proximity of an ideal wall. CFD simulations of the rapidly pitching wedge are used to analyse dynamic flow field phenomena and response of the triple point below and within the dual solution domain. Computed, unsteady pressure traces on the reflection plane are also analysed.

1 Introduction

Consider the shock wave reflection pattern generated by a wedge of infinite span in close proximity to an ideal wall. The regular reflection (RR) and Mach reflection (MR) configurations possible in a steady supersonic freestream are well known, as well as the steady state transition criteria between these configurations. Transition criteria for the steady, two-dimensional case were published by Ben-Dor [1]. These transition criteria are not valid for the rapidly pitching wedge in which there are significant dynamic effects. Transition between RR and MR and other unsteady phenomena observed for the rapidly pitching, two-dimensional wedge was presented by Felthun and Skews [2] and Naidoo and Skews [3].

This research paper documents progress on the development of an experimental test rig for the investigation of unsteady shock reflection phenomena. Computational fluid dynamics (CFD) was used to investigate some of the unsteady flow field phenomena. An analysis of the computed unsteady flow field, triple point response and the static pressure traces on the reflection plane is presented.

2 Experimental facility development

A facility is being developed for the experimental investigation of two-dimensional, unsteady shock reflection phenomena generated by a rapidly pitching wedge in close proximity to an ideal wall (Fig. 1). This facilty is being developed for the 450mm x 450mm supersonic blow-down wind tunnel at the Council for Scientific and Industrial Research, South Africa. The rig consists of two wedges positioned symmetrically about a horizontal plane, to simulate the effect of an ideal, smooth reflection surface. A large wedge aspect ratio of 4.5 was used to ensure approximate two-dimensional flow on the wedge centre plane. The motion of both wedges is synchronized to maintain a horizontal symmetry plane.

* Present Address: CSIR - Defence Peace Safety and Security, Aeronautics Systems Competency, PO Box 395, Pretoria, 0001, South Africa

Currently, the rig is only capable of gradual wedge pitch rates to approximate the steady state case. This rig will be modified for rapid rotation of the wedges and will be achieved with a spring loaded actuator. The mechanism has been designed to achieve instantaneous maximum pitch rates of approximately 25000.0 deg/s. Tests were conducted to generate steady state, reference flow field data at freestream Mach numbers, $M_\infty = 2.0$ and $M_\infty = 3.0$. Flow visualization was achieved with three-colour schlieren (Fig. 2). Flow field images will be acquired with a high speed digital camera for the dynamic tests.

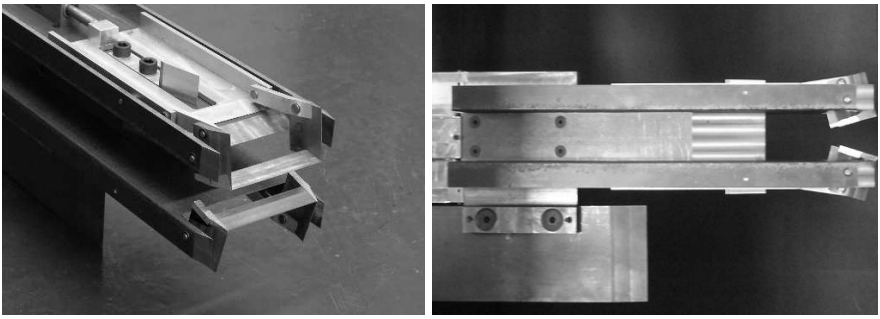

Fig. 1. Experimental test rig for the investigation of dynamic shock reflection phenomena

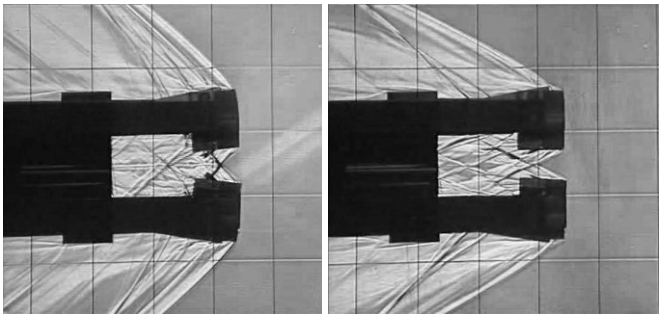

Fig. 2. Three-colour schlieren images captured during reference tests

3 Numerical simulations

Euler simulations in Table 1 were carried out with a vertex centred, Arbitrary Lagrangian Eulerian, finite volume scheme on unstructured triangular meshes [2]. The numerical method enables dynamic adaptive refinement, ideally suited to moving boundary problems in supersonic flows. Steady state, supersonic freestream conditions were established before the wedge, of constant chord $w = 60.0$ mm, was pitched at a rapid and constant rate. Solutions were tested for grid dependence and a fine grid was used for all flow field computations. Any flow solution dependence on the fine grid is small compared to the dynamic effects observed in this study. These test cases briefly explore the effect of M_∞, pitch rate and pitch direction on Mach stem growth, for fixed trailing edge separation,

g, as well as fixed leading edge separation, h. Results are valid for the specified initial wedge incidence angle, θ_i. Maximum pitch rate, per freestream condition, was specified by scaling the wedge trailing or leading edge tangential speed, V_T, with the freestream acoustic speed, a_∞, i.e. $V_{Tmax} = 0.1a_\infty$.

Table 1. Dynamic test matrix, $\gamma = 1.4$

Case	M_∞	Pitch Rate ($^\circ/s$)	$\frac{g}{w}$	$\frac{h}{w}$	θ_i	Case	M_∞	Pitch Rate ($^\circ/s$)	$\frac{g}{w}$	$\frac{h}{w}$	θ_i
1	4.0	+8500.0	0.48	-	19.0	7	2.0	+12500.0	0.65	-	8.0
2	4.0	+17000.0	0.48	-	19.0	8	2.0	+25000.0	0.65	-	8.0
3	4.0	+17000.0	-	0.85	19.0	9	2.0	+25000.0	-	0.85	8.0
4	4.0	-8500.0	0.48	-	26.5	10	2.0	-12500.0	0.65	-	15.5
5	4.0	-17000.0	0.48	-	26.5	11	2.0	-25000.0	0.65	-	15.5
6	4.0	-17000.0	-	0.85	26.5	12	2.0	-25000.0	-	0.85	15.5

3.1 Flow field characterization

The computed flow field for case 12 is discussed here. Density contours for case 12 are shown in Fig. 3. A history of static pressure traces through the reflection point on the ideal wall are shown in Fig. 5. Mach stem height history is shown in Fig. 6(a).

A steady MR is established at wedge incidence, $\theta = 15.5^\circ$. The wedge is pitched instantaneously at -25000.0 deg/s about its leading edge. Initially, the triple point maintains its vertical position. The wedge surface is moving away from the reflection plane and a weak expansion region is setup on the wedge surface. At $\theta = 13.5^\circ$, the acoustic pulses from the moving wedge surface reach the triple point and the Mach stem height, m, increases. The Mach stem height reaches a maximum at approximately $\theta = 8.7^\circ$ and decreases subsequently. In case 12, the pitch rate and initial wedge incidence are such that the Mach stem height has a finite value at $\theta = 0.0^\circ$. The rapid pitch generates an inverse MR. This can be observed from Fig. 3(e) and Fig. 3(f), i.e. the shear layer is directed away from the wall. Also, the pressure traces in Fig. 5 show that while the reflection pattern is MR, the static pressure rise through the reflection point decreases with decreasing wedge incidence. At $\theta = 0.0^\circ$ the wedge sheds the shock wave system, hereafter referred to as the "orphan"shock system. The "orphan"shock system washes downstream below $\theta = 0.0^\circ$.

3.2 Transition of the "orphan"shock system

Just below $\theta = 0.0^\circ$, the "orphan"shock system maintains the basic anatomy of the oblique shock system previously attached to the wedge leading edge (Fig. 4). There still remains an incident oblique shock wave, a small Mach stem and a reflected oblique shock wave at $\theta = -0.5^\circ$. As the "orphan"shock system washes downstream the incident oblique shock begins to diminish in strength (Fig. 5). At the same time the triple point continues to move toward the wall. At the time $\theta = -1.5^\circ$ the "orphan"shock system transitions from MR to RR. There is a discontinuity in static pressure rise through the reflection point

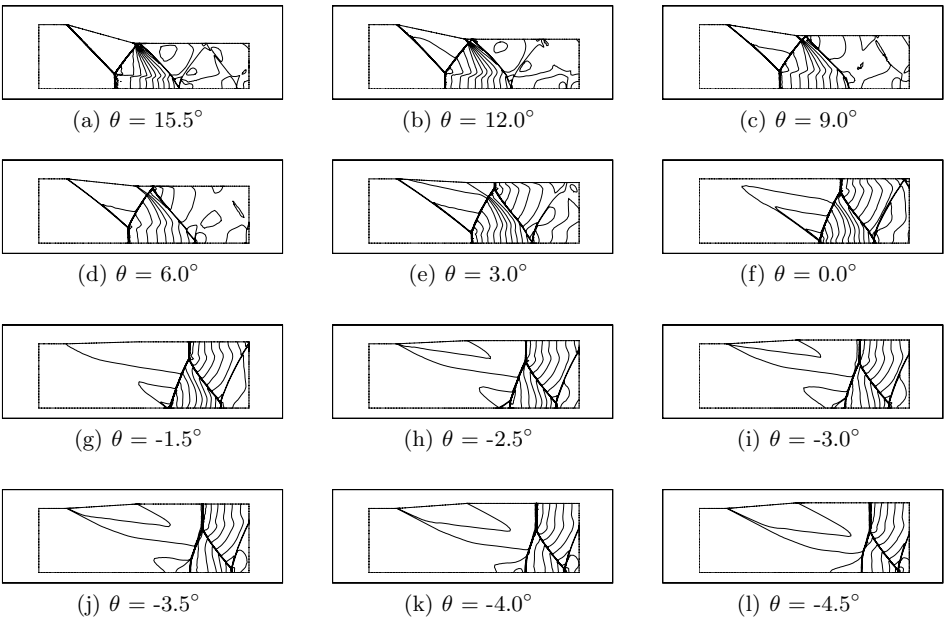

Fig. 3. Dynamic MR → RR : case 12

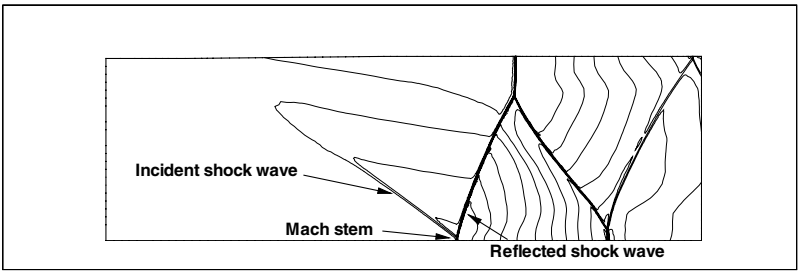

Fig. 4. Anatomy of the "orphan shock"system at θ = -0.5° : case 12

on the wall on transition from MR to RR due to the inverse MR. This discontinuity is effected through a normal shock between the reflected wave and the wall (Fig. 3(h) - 3(l)). The normal shock moves downstream relative to the "orphan"shock system. The shock wave system upstream of the normal shock becomes too weak to notice on the density contour plots. The bow wave at the wedge leading edge is now a Prandtl-Meyer expansion whose influence propagates towards the wall resulting in additional wave modification.

3.3 Unsteady static pressure characterization on the reflection plane

Pressure scans through the reflection point on the wall, for case 12, are shown in Fig. 5. As the wedge is pitched about its leading edge, the pressure rise through the reflection point decreases continuously until transition to RR. The pressure rise at transition, θ = -1.5°,

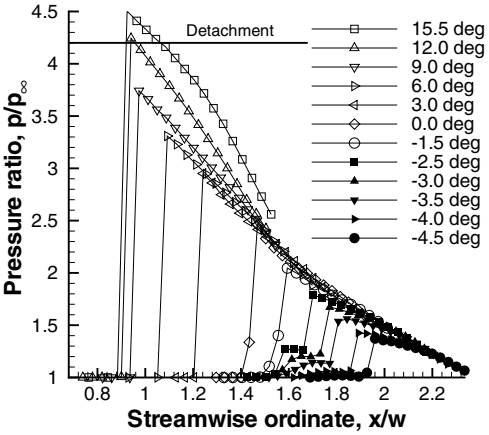

Fig. 5. Unsteady static pressure response on the reflection plane : case 12

is approximately 51.2% below the theoretical detachment condition. Due to the inverse MR configuration observed for these dynamic cases (MR → RR only), a discontinuity in pressure rise is expected across transition. This is achieved through a normal shock that propagates downstream between the reflected shock and the wall. The moving normal shock can be seen in the pressure traces for $\theta <$ -1.5°.

3.4 Unsteady triple point response

MR → RR

$M_\infty = 2.0$ (Cases 10, 11 and 12): In contrast to case 12, the Mach stem development history for case 11 in Fig. 6(a) demonstrates a noteworthy difference. In case 11 the triple point maintains its initial vertical location. At $\theta = 13.0°$ the Mach stem height decreases. Unexpectedly, at approximately $\theta = 9.0°$, the triple point begins to move away from the wall. At approxiamtely $\theta = 6.5°$, the triple point eventually begins its final movement toward the reflection plane. This fundamental difference lies in the fact that the wedge leading edge and incident shock attachment point is fixed for case 12 and moving for case 11. Case 10 demonstrates a similar characteristic to case 11, with the exception that transition to RR occurs at approximately $\theta = 4.5°$ due to the smaller pitch rate. Complete understanding of this complex, non-linear phenomena requires detailed understanding of the acoustic properties of the dynamic flow field.
$M_\infty = 4.0$ (Cases 4, 5 and 6): The triple point response trends in Fig. 6(b) are similar to those observed at $M_\infty = 2.0$ for rotation about the wedge leading edge and trailing edge.

RR → MR

$M_\infty = 2.0$ (Cases 7, 8 and 9): Mach stem growth in Fig. 6(a) is approximately quadratic. The wedge incidence angle at transition is dependent on pivot point and rotation rate for a specified initial wedge incidence.

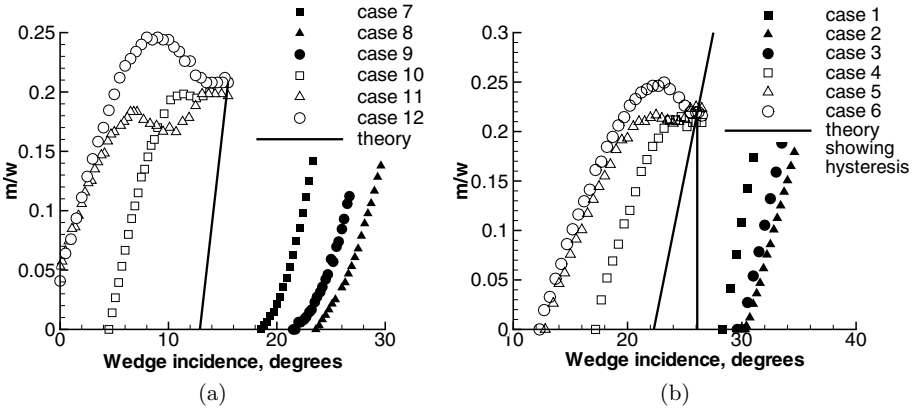

Fig. 6. Dynamic Mach stem growth at (a) $M_\infty = 2.0$ and (b) $M_\infty = 4.0$

$M_\infty = 4.0$ (Cases 1, 2 and 3): Mach stem growth in Fig. 6(b) is approximately linear. Once again, the dependency on rotation rate and pivot point is demonstrated. It is not known, at this stage, whether the Mach stem growth trend is quadratic for larger pitch rates at M_∞=4.0.

4 Conclusion

Transition from MR to RR was demonstrated for the unsteady, "orphan"shock system with CFD. Pressure traces on the reflection plane show, very clearly, the nature of the inverse MR before transition to RR as well as the development and movement of the normal shock between the reflected wave and the reflection plane after transition to RR. Complex triple point behaviour was observed at $M_\infty = 2.0$ and $M_\infty = 4.0$. For a particular freestream condition and initial wedge incidence these phenomena demonstrate a strong dependence on wedge pitch rate, direction of rotation and pivot point.

References

1. Ben-Dor G: Hysteresis phenomena in shock wave reflections in steady flows. **Proceedings, 22nd International Symposium on Shock Waves**, Paper 6000 (1999)
2. Felthun LT, Skews BW: Transition Between Regular and Mach Reflection in Dynamic Compressible Flows. **AIAA Journal**, 2002-0549 (2002)
3. Naidoo K, Skews BW: Dynamic shock reflection phenomena in ideal, two-dimensional flows. **Proceedings, 25th International Symposium on Shock Waves**, Paper 1187 (2005)

Computations of shock wave propagation with local mesh adaptation

B. Reimann[1], V. Hannemann[2], and K. Hannemann[2]

[1] *German Aerospace Center DLR, Institute of Aerodynamics and Flow Technology, Lilienthalplatz 7, 38108 Braunschweig, Germany*
[2] *German Aerospace Center DLR, Institute of Aerodynamics and Flow Technology, Bunsenstr. 10, 37073 Göttingen, Germany*

1 Introduction

The numerical simulation of discontinuous flow phenomena results in high demands related to the used computational grids. A high resolution of the grid is required to resolve shock waves and contact surfaces. This leads, especially for unsteady flows with moving structures, to grids with a large number of points. Local mesh adaptation allows to reduce the computational effort by refining the mesh only in regions where it is necessary. In the present paper a numerical simulation of the shock tunnel flow in the High Enthalpy Shock Tunnel Göttingen (HEG) is performed. Local grid adaptation is used to capture shocks and contact discontinuities. Of particular interest for the shock tunnel performance and the investigation of driver gas contamination is the shock reflection process and the interaction between the reflected shock, the boundary layer and the contact surface separating the test gas from the driver gas.

2 High Enthalpy Shock Tunnel Göttingen

The HEG of the German Aerospace Center (DLR) is a free piston driven shock tunnel. The facility operates in reflected mode. Air accelerates a piston (up to 800 kg) down the 33 m long compression tube, which compresses the driver gas helium to a pressure up to 100 MPa. After rupture of the stainless steel main diaphragm which separates driver and test gas a strong shock wave propagates down the 17 m long and 0.15 m diameter shock tube. The shock wave reflects from the end wall and compresses the test gas to the high pressure, high temperature nozzle supply condition. When this nozzle reservoir region is formed the test gas expands though a 3.75 m long conical hypersonic nozzle with a throat diameter of 22 mm and an exit diameter of 0.88 m. The total enthalpy and

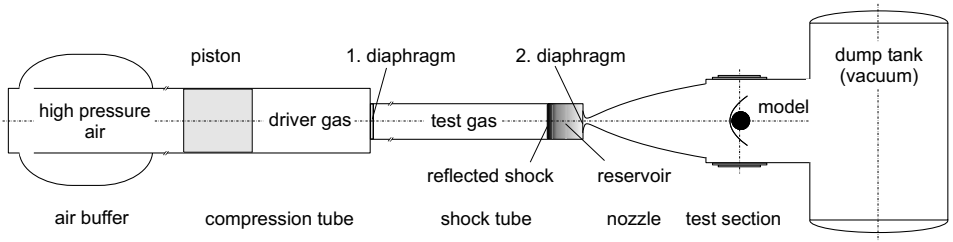

Fig. 1. Schematic drawing of the High Enthalpy Shock Tunnel Göttingen.

the Mach number of the flow depend on the operating conditions and range from 1.7 to 23 MJ/kg and 6 to 8, respectively. Figure 1 shows a sketch of the HEG.

2.1 Driver gas contamination

In the ideal shock tunnel the test time ends with the arrival of the expansion wave (reflected from the piston) or the contact surface at the nozzle entrance. Stalker and Crane [7] showed that non ideal behavior can shorten the test time dramatically. The interaction of the reflected shock wave with the shock tube boundary layer leads to a bifurcation of the reflected shock. The bifurcation affects the reservoir region and causes, after interacting with the contact surface region, a jet of driver gas near the wall. The reason for this is the lower compression hence deceleration of the fluid across the two oblique shocks compared to the normal reflected shock wave. The test time ends ahead of time when this jet enters the nozzle throat. Chue and Eitelberg [1] show results of a perfect gas computation of the reservoir region in HEG using a structured CFD code. Based on this results a method proposed by Sudani et al. [8] to capture the driver gas jet has been developed and tested in HEG by Hannemann et al. [3]. Figure 2 shows the reservoir region of the HEG. The principle of the contamination process and the capturing device (sleeve) is shown. A particle stopper in front of the nozzle throat avoids that particles from the primary diaphragm enter the nozzle.

Fig. 2. Sketch of the shock tunnel reservoir region and schematic of the driver gas contamination process. Reflected shock wave (RS), boundary layer (BL), contact surface (CS), separation (S), sleeve (SL), nozzle throat (NT), and particle stopper (PS).

3 Numerical method

3.1 DLR TAU code

The flow solver used in the present study is the DLR TAU code. It is a finite volume Euler/Navier-Stokes solver, which can handle structured, unstructured, and hybrid meshes. The Reynolds averaged Navier-Stokes (RANS) equations are discretized by a finite volume technique using tetrahedra, prisms, hexahedra and pyramids. In the two dimensional and axisymmetric cases all points are located in two planes with identical grid point distributions. The grid consequently contains only triangular and rectangular prisms. The upwind scheme AUSMDV with second order MUSCL reconstruction is used for the inviscid fluxes. For the time discretization an approximately factorized LU-SGS, as well as a Runge-Kutta scheme are implemented. For acceleration, local time stepping, multigrid and explicit residual smoothing are available. Furthermore, parallel computing is possible via domain splitting and Message Passing Interface (MPI) communication. To model the mixing process of two gases a mass conservation equation is solved for each component. In each cell the mixture is considered to be homogeneous.

3.2 Grid adaptation technique

Grid adaptation by cell division offers the possibility to insert additional points only in regions where clustering is necessary. The later removal of these points allows to keep the locally higher resolution for a calculation of unsteady flow only as long as necessary. Difference and gradient based indicators of any available flow variable can be used to mark edges for adaptation. Restrictions for edge marking are the undercut of a given minimum edge length and the total number of points. Figure 3 shows exemplary the refinement of a simple grid.

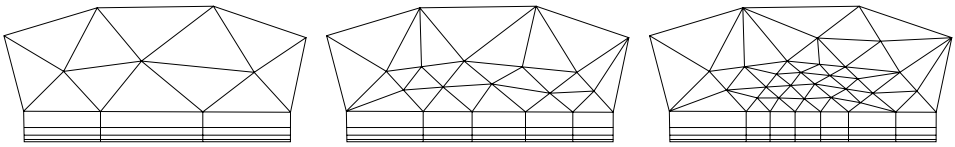

Fig. 3. Example of the hybrid grid adaptation. Initial grid (left) and the grid after the first (middle) and second (right) adaptation cycle.

4 Validation

As a validation test case the inviscid interaction between a weak normal shock and a cylindrical refrigerant R 22 ($CHClF_2$) bubble in air was simulated. The test case is described by Quirk and Karni [6]. At the beginning the bubble with a diameter of 50 mm is in mechanical and thermal equilibrium with the surrounding air. The shock Mach number is 1.22. The initial rectangular grid covering a region of 44.5×890 mm is discretized with 8982 triangles (4786 points). The grid is pre-refined at the locations of the shock and the contact surface. Figure 4 shows the initial, pre-refined grid and the grid after 1173 adaptation steps. The computation starts with the shock 247.5 mm upstream of the center of the bubble. All initial values are given in Table 1. The minimal bisected edge length is 0.125 mm the upper limit of points is 500000. Figure 5 shows a series of schlieren pictures of the interaction. In the upper half of each frame the computational result and in the lower half the experimental result from Haas and Sturtevant [2] is shown. The numerical results are in excellent agreement with the experiments. Due to the lower

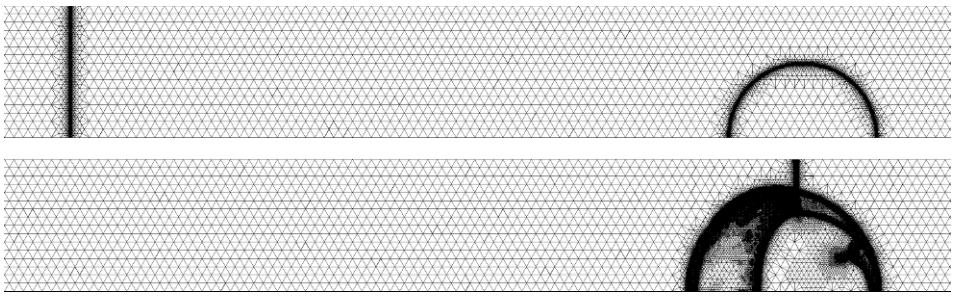

Fig. 4. Cutout of the computational mesh. On the top the initial grid is shown. Ten adaptation steps have been used to pre-refine the grid. Below the same cutout after 1173 adaptation steps.

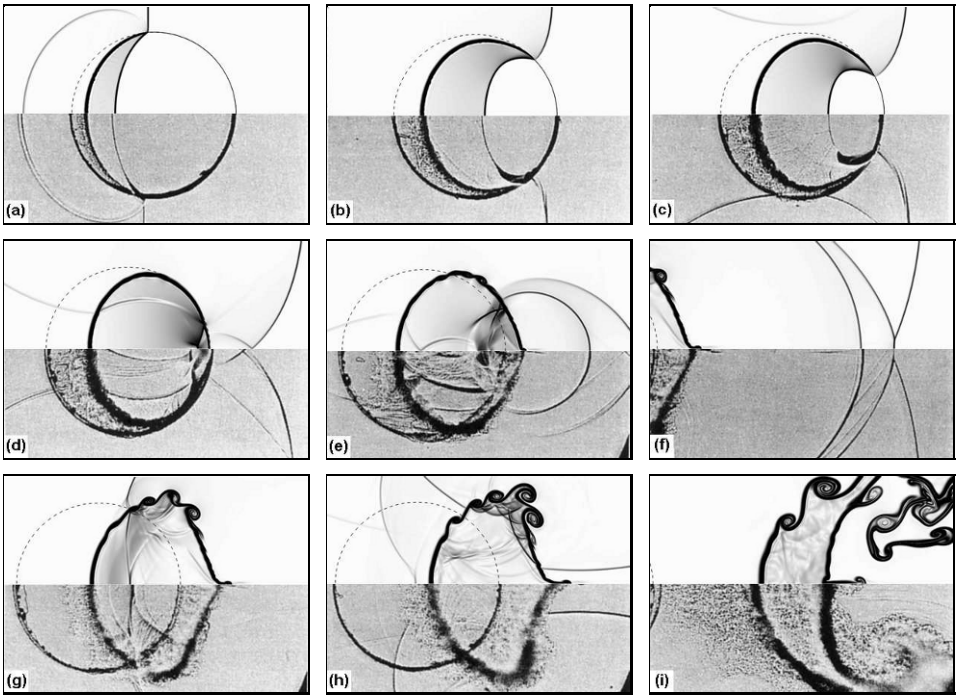

Fig. 5. Numerical (upper) and experimental (lower) schlieren images of the interaction of a weak shock wave with a cylindrical refrigerant bubble. (a) 55 μs, (b) 115 μs, (c) 135 μs, (d) 187 μs, (e) 247 μs, (f) 318 μs, (g) 342 μs, (h) 417 μs, and (i) 1020 μs. The time is measured from the point when the shock reaches the bubble. The experimental pictures are taken from Haas and Sturtevant [2].

speed of sound of the refrigerant the shock inside the bubble moves slower. The bubble behaves like an acoustic focusing lens. The accelerated contact surface is deformed and a Richtmyer-Meshkov instability is observed.

Table 1. Initial conditions for shock-bubble interaction simulation.

	R [J/(kg K)]	γ	T [K]	ρ [g/m^3]	u [m/s]
R22 bubble	91	1.249	298.0	3736.448	0.0
surrounding air	287	1.4	298.0	1184.727	0.0
post shock air	287	1.4	339.881	1630.616	115.438

5 HEG shock tunnel flow

The computational domain covers a 1.275 m long cutout including the the shock tube end section and the nozzle throat region. The tube diameter is 0.15 m. The flow is assumed to be axially symmetric. Figure 2 shows, in addition to the sketch of the driver gas

contamination process, a part of this domain. The position of the downstream boundary was chosen in such a way that the flow is supersonic, so that an extrapolating boundary condition can be used. An isothermal, no slip boundary condition was employed at the shock tube walls, nozzle throat, particle stopper and sleeve. Turbulence was modeled by the one-equation formulation given by Spalart and Allmaras. A shock wave moving in a tube into stationary gas results in the generation of a boundary layer at the wall. To simulate the unsteady growing boundary layer at the inflow plane an analytical solution given by Mirels [5] was implemented. The test gas is assumed to be in thermochemical equilibrium, while the driver gas is assumed to be a perfect gas. The initial values of the simulation are the measured fill pressure and temperature of the shock tube and the shock velocity of the incident shock wave. From these data a post shock state can be computed. 35.5 μs after shock reflection the driver gas enters the inflow plane. This point results from simulations of the HEG flow using the one-dimensional code L1d developed by Jacobs [4]. The initial conditions are listed in Table 2. Figure 6 shows on the left-hand side computed schlieren pictures of the reservoir region in HEG. On the right-hand side the driver gas mass fraction is shown. The series start 25 μs before shock reflection. The time between the pictures is 50 μs. On the first two pictures the incident shock wave moves over the sleeve and the particle stopper. Due to the supersonic flow behind the incident shock a bow shock is formed in front of the sleeve and particle stopper. 75 μs after shock reflection the bifurcation of the reflected shock as a result of the interaction with the boundary layer can be observed below the sleeve. This triple point travels upstream until it interacts with the contact surface. After 175 μs the contact surface can be seen at the left boundary of the depicted part of the cpmputational domain. Because of the shock tube boundary layer the driver gas close to the wall is slowed down. Between 275 μs and 325 μs the formation of the driver gas jet can be observed. The bifurcation disappears when the shock enters the driver gas. Due to the fact that the sleeve is closed at the end the pressure inside is rising during shock reflection. Before the major part of the helium enters the sleeve the air exhausts. These outflowing air pushes the contact surface upstream.

Table 2. Initial conditions for HEG simulation

	Gas	T [K]	ρ [g/m^3]	u [m/s]
test gas (initial)	air (equilibrium)	292.0	287.636	0.0
test gas (post shock)	air (equilibrium)	6123.9	2754.190	4209.152
driver gas	He (perfect gas)	2000.0	1375.660	4209.152

6 Conclusion

Unsteady local grid adaptation is applicable to capture moving structures like shocks and contact surfaces. The simulated shock-bubble interaction is in very good agreement with experimental results. For the simulated HEG shock tunnel flow a driver gas jet reaching the nozzle is not observed when the sleeve is present. Outflowing gas from the sleeve supresses the developing driver gas jet.

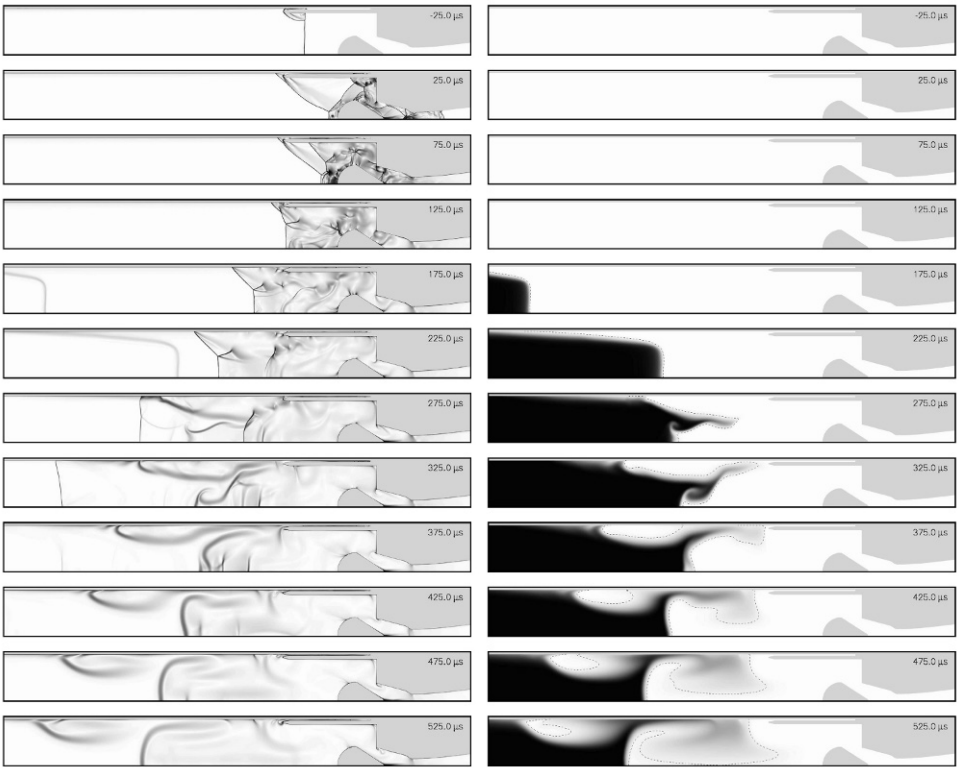

Fig. 6. Numerical schlieren images (left) and driver gas mass fractions (right) of the shock tunnel flow in the reservoir region in HEG. The time is related to shock reflection. The dashed line in the images on the right-hand side mark a helium mass fraction of 5%.

References

1. Chue, R. M. S., Eitelberg G: Studies of the transient flows in high enthalpy shock tunnels, Experiments in Fluids, **25**, 5–6, pp. 474–486 (1998).
2. Haas, J.-F., Sturtevant, B.: Interaction of weak shock waves with cylindrical and spherical gas inhomogeneities, J. Fluid Mech., **181**, pp. 41–76 (1987).
3. Hannemann, K., Schnieder, M., Reimann, B., Martinez Schramm, J.: The Influence of Driver Gas Contamination in HEG, AIAA Paper 2000-2593 (2000).
4. Jacobs, P.: Shock Tube Modelling with L1d, Research Report 13/98, Department of Mechanical Engineering, The University of Queensland (1998).
5. Mirels, H.: Turbulent Boundary Layer Behind Constant Velocity Shock Including Wall Blowing Effects, AIAA J., **22**, 8, pp. 1042–1047 (1984).
6. Quirk, J. J., Karni, S.: On the dynamics of shock-bubble interaction, J. Fluid Mech., **318**, pp. 129–163 (1996).
7. Stalker, R. J., Crane, K. C. A.: Driver Gas Contamination in a High-Enthalpy Reflected Shock Tunnel, AIAA J., **16**, 3, pp. 277–279 (1978).
8. Sudani, N., Valiferdowski, B., Hornung, H. G.: Test time increase by delaying driver gas contamination for reflected shock tunnels, AIAA Paper 98-2771 (1998).

Diffraction of two-shock configuration over different surfaces

M.K. Berezkina, I.V. Krassovskaya, and D.H. Ofengeim

Ioffe Physical Technical Institute, St.Petersburg, 194021, Russia.

1 Introduction

Diffraction of shock configuration is the second stage of non-stationary process of interaction of a shock wave with a 2D body. The two-shock system is formed as a result of the regular reflection of an incident shock wave from the first planar inclined surface of a 2D body. On the second surface diffraction of SW system occurs. Diffraction of two-shock configuration over convex and concave cylindrical surfaces with a continuously changing angle of diffraction has been numerically considered by Berezkina et al [1], [2].

The peculiarity of the diffraction of a two-shock configuration is that both incident and reflected waves diffract simultaneously. In view of the fact that not a single shock but a two-shock configuration interacts with the second wedge, the role of the reflected shock should be clarified. Instead of two-shock, a new three-shock configuration of confluence type is formed, two shock waves of which set bound the disturbed domain. The inner structure of the perturbed zone is determined by the interference of two flows: the flow initiated by the shock waves, which forms the outer boundary of the diffraction zone and the expansion flow at the top of the body. At the present paper the numerical data of a shock wave interaction with a two-faced convex wedge are given. Numerical simulation is performed for various diffraction angles. Influence of the diffraction angle on the flow structure inside the perturbed area is shown. The role of the second wave of the two-shock configuration in the process of diffraction over the second wedge is revealed.

2 Statement of the problem

The phenomenon under consideration is the flow caused by interaction of a planar shock wave with a two-faced convex wedge. The angles of the first and second surfaces are β_1 and β_2, respectively. The problem is solved for the model of perfect gas with constant specific capacity ratio γ, in the absence of viscosity and heat conductivity. Integration of the Euler equations was made with the help of a code [3].

3 Results and discussion

A single shock wave experiences diffraction when it interacts with a surface at the angle $\alpha > 90°$. When a two-shock configuration diffracts over a surface, the term "diffraction" should be refined or defined more precisely. As it was shown by Berezkina at al [1], the diffraction phenomenon of the two-shock system takes place over the second horizontal surface of the double wedge, when the angle between the incident shock and the surface

equals to 90°. In the present paper the numerical results of the process of interaction of a shock wave with the double wedge for various angles of the second wedge are reported. The incident shock Mach number $M_I = 2.09, \gamma = 1.29$ and the angle of the first wedge $\beta_1 = 48°$ were fixed but the angle of the second wedge β_2 varied. The list of variants under consideration is presented in Table 1. α is the angle between the incident shock front and the second wedge surface. At the given initial parameters a regular reflection takes place on the first surface.

Table 1. Variants of body geometry under consideration

No.	1	2	3	4	5	6	7
α, °	83.4	90.0	96.6	108	114	120	180

In Fig. 1a, b the numerical temperature contours for $t = 1.5$ are given for var.1 and var.6, respectively. At the point $t = 1$ the two-shock configuration passes by the leading edge of the second wedge. The angle of the second wedge β_2 is positive for var.1 but negative for var.6. It is also clear, that diffraction over the second surface is to occur for var.6. In accordance with the values of the incident shock Mach number and the angle of the second wedge, one could expect that, for var.1 the reflection will occur not only on the first surface (regular reflection) but also on the second one (irregular reflection). Using the elementary three-shock theory, the parameters of the shock wave configuration for $M_I = 2.09$ and $\beta_2 = 6.6°$ were calculated. In the frame of Landau's concept of "directed" shock, this configuration is interpreted as *confluence*, because it contains two *incoming* (incident and reflected) and one *outgoing* (Mach stem) shocks. The Mach stem has to be planar and perpendicular to the wedge surface. As Fig. 1a shows, a new three-shock system of confluence type forms on the second surface. As compared to theoretically possible configuration mentioned above, this structure has a curved rather than a planer resulting wave D. Moreover, the additional tangential discontinuity is pronounced rather well near the triple point T_0. In the present case not a single shock but two shocks interact with the second wedge simultaneously. We believe, that the role of the reflected wave R of the two-shock configuration is dominant in the process of bending around the leading edge. It pushes off the incident shock I from the second wedge and diffracts over the

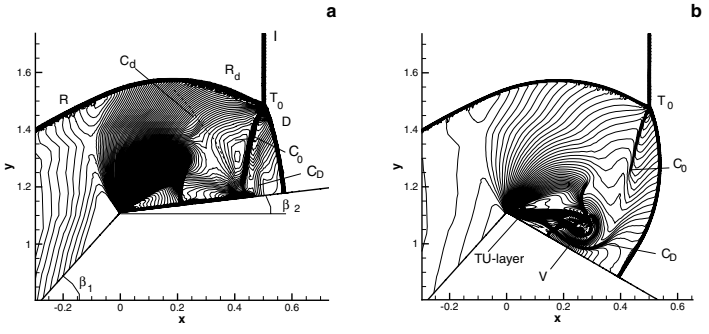

Fig. 1. Temperature contours for $t = 1.5$: (**a**) — var.1, (**b**) — var.6

second surface itself. The attributes of shock diffraction such as curved front R_d and contact surface C_d can be seen in Fig. 1a (the contact surface is weak and can be noticed near the wedge). Interaction of the perturbed part R_d of the primary reflected shock with an undisturbed incident shock I results in confluence system forming. The contact discontinuity C_0 emanating from the triple point does not reach the wedge surface. The resulting wave D also diffracts over the second wedge. It is curved and yet another contact surface C_D arises. That is, in spite of the fact that the second angle is positive, diffraction but not irregular reflection takes place.

The flow pattern for the large negative angle of the second wedge is shown in Fig. 1b. It is interesting to note that the trajectory of the triple point and, consequently, characteristics of the outer three-shock configuration are the same as in the previous example. The shape of the resulting wave is different. The contact surface emanating from the triple point reduces. The additional contact discontinuity has no contact with the solid wall. It is curved and forms the some kind of virtual cavity, which is located above the second wedge.

Fig. 2 illustrates an influence of the diffraction angle on the inner structure of the diffraction zone. The fragments of the flowfield for $t = 2.0$ as the temperature isolines are given in Fig. 2a–d for vars. 1, 3, 4, 7, respectively. The instant streamlines (the solid lines with the arrows) are also represented. The main feature of the inner structure is the gasdynamic system consisting of the secondary shock (shock wave configuration) and the element, which is referred to as either slipstream [4], [5] or TU-layer [6]. The

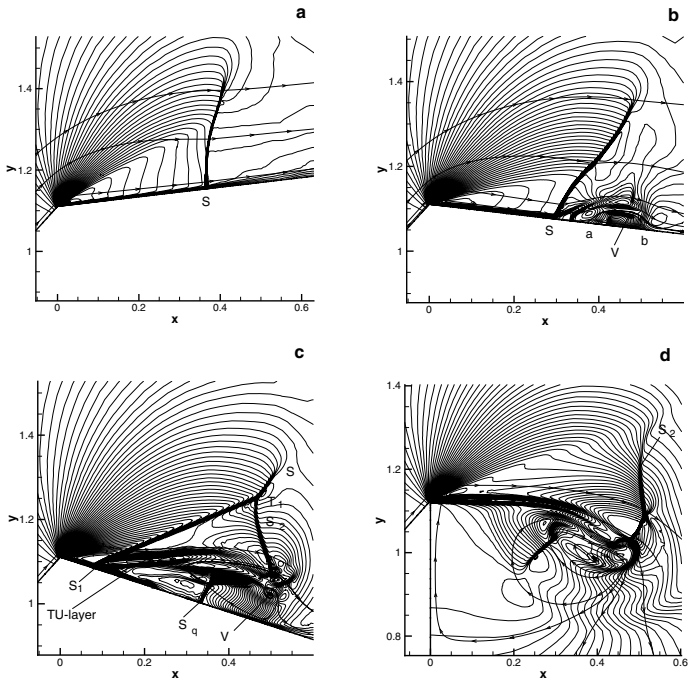

Fig. 2. Flow patterns as temperature contours with imposed instantaneous streamlines for the different angles of diffraction. $t = 2.0$

system matches the accelerated flow downstream of the expansion wave to the lower velocity, high-pressure flow behind the diffracted shock. In the case of var.1 ,2 the balance between these two flows maintains a single secondary rearward-facing shock wave S (the stagnation wave). The foot of the wave is planar and perpendicular to the solid wall. The TU-layer is not pronounced (Fig. 2a). The flow remains attached to the solid surface after passing the edge.

When the diffraction angle is increased (Fig. 1b) the angle of the expansion fan is also increased. The stagnation wave front is curved, and its foot is inclined to the second wedge surface. Behind the stagnation wave the TU-layer emanating from the wall is formed. It should be emphasized once again, that the element has the structure of a layer with temperature maximum in the middle. As the streamlines demonstrate, the local closed separation zone occurs on the surface of the second wedge. Downstream of the separation point there exists a bubble made of a recirculating flow, bounded a streamline that separates the recirculating flow from the flow streaming from upstream down. The separation point does not coincide either with the coordinate of S_1 or coordinate of the TU-layer. Above and below the separation line one can see the additional recompression shocks.

At the diffraction angle equal to 108° (Fig. 2c), instead of a single stagnation wave we see the three-shock configuration of stagnation. In contrast to the previous examples, the coordinate of the shock S_1 is much closer to the leading edge of the second wedge. The TU-layer is clearly seen. The coordinate of S_1 is the same the coordinate of the lower boundary of the TU-layer. The loose end of the TU-layer is rolled-up. The reason of such structure of the end of the TU-layer is a vortex, which produces mixing of cool and hot gases. The separation of flow takes place. The separation zone is unclosed. To decelerate the gas that is transported towards the leading edge by the vortex, a recompression shock is formed. It extends from the surface, where it is perpendicular to it, into the TU-layer. The loose end of the recompression shock splits into the three-shock configuration.

In case of diffraction over the vertical wall (Fig. 2d), the flow separates just in the leading edge of the second wedge. Such separation can be defined as inertial separation. The TU-layer originates at the leading edge. The spiral structure of the loose end is well pronounced. The shock configuration of stagnation is degenerated into one unattached shock wave. There is plenty of room for the development of vortex flow. The supersonic recirculating flow is decelerated by the recompression wave, which is also unattached.

The overall development of the flow as temperature contours with imposed instantaneous streamlines at consecutive points of time is given in Fig. 3 for var.5. As the numerical data shows, the trajectory of the three-shock configuration is practically straight line. The contact discontinuity, emanating from the point T_0, does not reach the surface of the second wedge. As for the contact surface C_D, which should be referred as attribute of resulting shock D diffraction, it gains the strength near the wall. It can be seen as a narrow gradient layer adjacent to the solid surface of the second wedge (Fig. 3b-d). This contact discontinuity bounds the area, in which the system, combining the flow passing the expansion fan with the flow initiated by the diffracted shock, exists. As Fig. 3 shows, it consists of the TU-layer, the above-layer secondary three-shock configuration of stagnation and under-layer recompression wave. At $t = 1.5$ (Fig. 3a) the shock S_1 extends from the point, which is located at some small distance away from the leading edge. The strength of S_1 along its contour is variable. The TU-layer emanates from the same point. In the course of time this point slides to the leading edge (Fig. 3d). It should be pointed out that the shape of the shock S_1 is changeable in time. It is convex at the

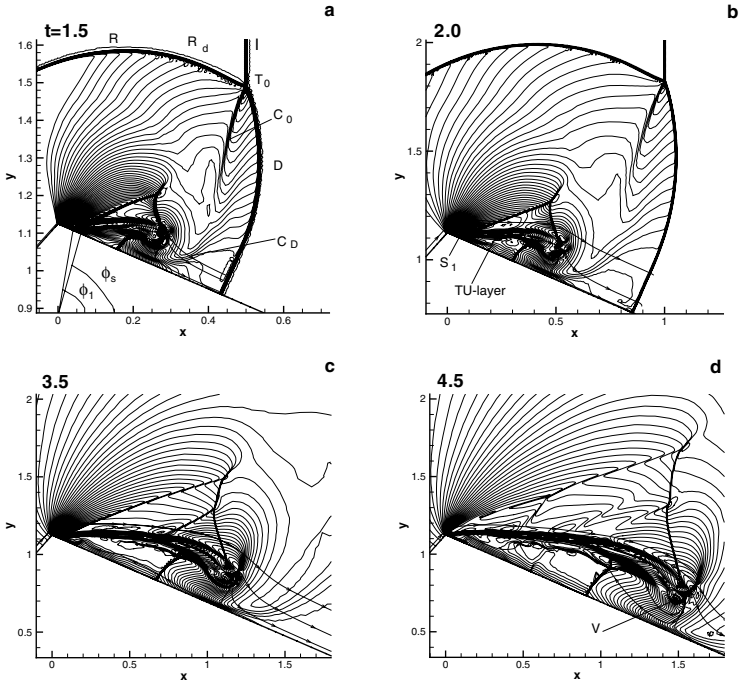

Fig. 3. Evolution of the flow field as temperature contours with imposed instantaneous streamlines for var.5

beginning of the process and then transforms into concave. While the shock wave S_1 is sliding to the leading edge, it degenerates into a Mach line (Fig. 3d). The instantaneous streamlines illustrate the presence of the vortex flow, which is developed near the loose end of the TU-layer. The vortex arises on the second surface and then moves away from the leading edge. The vortex produces mixing of cool and hot gases and this action leads to structuring of the end of the TU-layer. The flow after passing the expansion remains attached to the surface and separates at the point located on a small distance from the edge.

The location of the separation point on the second wedge is also changed. The dependence of the angular coordinate ϕ_s of the separation point and the angular coordinate ϕ_1 of the shock S_1 on time are shown in Fig. 4c. To find out the reason of the behavior of these values, we examine the behavior of the flow parameters before the expansion fan. In Fig. 4a, b the profiles of pressure p and the flow Mach number M along the first and second surfaces of the two-faced wedge are plotted for $t = 1.5$ and $t = 4.5$, respectively. The pressure before the expansion is strongly changed in time. The velocity of flow before the expansion decreases from supersonic (Fig. 4a) up to subsonic (Fig. 4b). As a result, the parameters behind expansion and the angle of the expansion fan are also changed. At the very beginning of the diffraction process the pressure behind of the expansion wave drops to the value much less than the pressure in undisturbed gas. As well as the pressure after the diffracted shock is gradually decreased to the value less than the pressure in undisturbed gas. The stagnation shock S_1 and recompression shock S_q originate to level

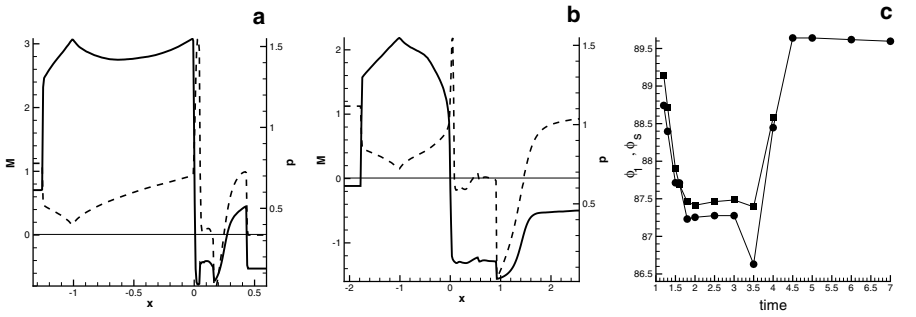

Fig. 4. (**a, b**): Profiles of pressure p *(solid line)* and the flow Mach number M *(dashed line)* on the first and the second surfaces, (**a**) $t = 1.5$, (**b**) $t = 4.5$; (**c**): The motion of the angular coordinate of the shock S_1 *(squares)* and of the separation point *(circles)* along the second wedge

the pressure. For $t = 4.5$ the pressure just after the expansion fan becomes equal to the pressure in undisturbed gas.

4 Conclusions

Diffraction of a two-shock configuration over surfaces of different shape is investigated. The results are summarized as follows: (i) New three-shock configuration of confluence type forms immediately at the beginning moment of diffraction. The resulting shock wave, which emanates from the triple point, experiences diffraction over the second surface itself. In case of the large initial diffraction angle the foot of the resulting wave comes to the second surface in the form of sonic line. Transformation of the resulting wave into a shock wave along its complete contour takes an interval of time. (ii) The general structure of the interior flow depends strongly on the value of a diffraction angle. (iii) Interaction of two-shock configuration with a compressive angle can result in not only reflection but also diffraction. (iv) In dependence of the diffraction angle, the regimes with separation, without separation and with local separation zone (separation bubble) occur.

References

1. Berezkina MK, Krasovskaya IV, Ofengeim DKh: Tech. Phys. **51**, 7 (2006) pp. 827–833
2. Berezkina MK, Krasovskaya IV, Ofengeim DKh: Peculiarities in diffraction of two-shock configuration over a concave cylindrical surface. ISIS17, Rome (2006)
3. Voinovich PA: Two-dimensional locally adapted unstructured unsteady Euler code. St. Petersburg. Advanced Technology Center (unpublished) (1993)
4. Skews BW: J. Fluid Mech. **29** (1967) pp. 705–719
5. Kleine H, Ritzerfeld E, Gronig H: Shock wave diffraction - new aspects of an old problem. In: *Shock Waves at Marseille*, vol.IV (1995) pp. 117–122
6. Berezkina MK, Krasovskaya IV, Ofengeim DKh : Tech.Physics Letters **30**, 12 (2004) pp. 1017–1019

Drainage and attenuation capacity of particulate aqueous foams

A. Britan, M. Liverts, and G. Ben-Dor

Shock Tube Laboratory, Pearlstone Center for Aeronautical Engineering Studies, Department of Mechanical Engineering, Ben-Gurion University of the Negev, Beer-Sheva, Israel

Summary. It is well established, nowadays, that if the particles added to aqueous foams are hydrophilic, have proper size and shape they concentrate within the Plateau borders and decrease the liquid drainage. The fact that solid additives can increase the protective performances of a particulate aqueous foam is also well known and even patented. This study bridges the gap between these two different features, which have been investigated to date independently. The experimental finding that small particles (about $45\mu m$ coal fly ash) slow down temporal and spatial variations of the liquid fraction clarified in the drainage tests was further related to the dynamics of the shock wave propagation in a shock tube. To the best of our knowledge, the results that are reported for the first time can help in better understanding the fundamentals of shock wave/particulate foam interaction.

1 Introduction

High attenuation capacity of aqueous foams stems from the ability of the foam cells to store the impact energy when deformed. In spite of the closed-cell structure that includes bubbles, films, Plateau borders and nodes, this feature in aqueous foams resembles similarity to that inherent to the polymeric foams [1]. However, since the drainage reduces its density and thus, impairs its attenuation capacity, efforts to slow down the foam drainage are crucial for practical usage. Control over the transient liquid fraction, $\varepsilon = V_l/V_f$, (V_f is a foam volume and V_l is a volume of the foaming liquid) could be accomplished with the increased viscosity or inclusion of high concentrated molecular surfactant to the foaming solution. When compared to these methods, stabilization by solid additives could be competitive enough providing that the particles are cheap and have the appropriate wetting behavior. Moreover, whereas in order to slow down the drainage rate the particles have to be light and small, in order to improve the damping capacity of aqueous foams they have to be large and heavy. Hence, the proper solution is a compromise complying with these contradictory requirements [2]. There are evidences that when the foam drains the solid additives concentrate within the Plateau borders and nodes that serve as the channels for resulted interstitial flow of the foaming liquid [6]. If so, the drainage rate has to depend on the particles concentration, $n = m_p/m_{total}$, (m_p - mass of the added particles, m_{total} - mass of the particulate foaming solution). However, since the solid additives also change the viscosity of the foaming solution, unambiguous interpretation of the final effect is rather difficult. This uncertainty has long been a matter of discussion in early studies describing the attenuation of sound by the particulate foams. Whereas [3] demonstrated that the attenuation increases when the concentration rises; the data reported in [4] show inverse dependence of the sound attenuation on the particles concentration. However, recent experiments revealed that when the concentration exceeds a certain "critical" value, further attenuation of the sound contrary to the expectations has to decrease [5]. Generally speaking, the conclusion whether the role of particles is positive or not, depends

on their concentration, n, diameter, d_p and the material characteristics of the particles. Among the few understood effects, we emphasize that small, micron-size particles "armor" the bubbles surface and make the foam cell more stabile while particles of larger diameter rupture the films and increase the drainage rate [7]. From this, it follows that only particles that pass freely through the network of the foam cells and prevent it from rupturing can reduce the drainage rate. The maximum diameter of these particles, d_p^*, is best approached by the equation relating the cross section area of node, A_n, to the mean value of the bubble radii, r_b, namely: $A_n \simeq 0.161 r_b^2$ [2]. To proceed further, we need to link the cross section, A_n, to the node diameter, d_n, and accomplish that task by requirement that $d_p^* \leq d_n$. Assuming that the mean bubble radius registered in these tests was 20 to $80\mu m$, d_p^* cannot exceed about $45\mu m$. In searching for suitable solution in these tests a powder of coal fly ash ($\rho_s = 2000 kg/m^3$) was added in variable proportions to wet aqueous foam with initial density $\rho_f = 200 kg/m^3$. Since the focus is on the plausible effects, the mechanisms responsible for the observed phenomena as well as physical-chemical properties of the solid and liquid fractures are still to be determined. The merit of the powder, known in advance, is that it is cheap and could be easily handled from the wastes of any working cycle utilizing coal fuel. After dry heating and subsequent sieving through the mesh N45 the resulted spherical particles easily mix with the foaming liquid and further disperse over the aqueous foam sample inside a blender.

Conceptually, the material testing is identical with free drainage of aqueous foam of known initial liquid fraction, $\varepsilon_0 = 0.2$, seeded with variable concentrations of solid additives. For this purpose the foam sample was left to drain for a long time period ($\Delta t \approx 60 min$) when confined inside the transparent test cell having a square cross-section of $32mm \times 32mm \times 420mm$. Transient conductivity of the aqueous foam column registered at the top, middle and bottom cross sections was converted to local water content, $\varepsilon(t)$. Each test of this series was accomplished with the pictures of the drained liquid accumulated on the test cell bottom [1] and particles' concentration, n, in subsequent tests was gradually increased from $n = 0$ to $n = 0.33$.

For the shock tube tests the same transparent test cell was filled with regular ($n = 0$) or particular ($n = 0.2$) aqueous foam and then was attached to the shock tube channel having a cross section, $32mm \times 32mm$ [1]. Before the head-on impacts by the shock wave, it was also left to drain during various times $0 < \Delta t \leq 60 min$. Distinctive features of these experiments are:

(a). Highly repeatable intensity of the impact conditions in subsequent tests (a diaphragmless vertical shock tube with fast opening pneumatic valve ensures a constant value of Mach number in the range $M_S = 1.32 \pm 0.02$);
(b). Known character of the spatial distribution of the water content, $\varepsilon(x)$, over the foam column length. Notice that this characteristic was identified in the material testing at each instant of time $0 < \Delta t \leq 60 min$.

When the results of this series were compared to each other, the role of the parameters Δt and n on the shock wave/foam interaction becomes apparent. To quantify the matter a comparative analysis was applied to the propagation velocity and to the post shock overpressure registered upstream (T_1 and T_2), inside (T_3 to T_6) and at the bottom of the aqueous foam column or at the end wall of the test cell (T_7) [1]. Commercial surfactant ATC-787F for the aqueous foam was purchased at Kidron Industrial Materials Ltd. (Israel) while the powder of the coal fly ash was supplied by the Rotenberg power station in Ashkelon (Israel).

2 Obtained results and Discussion

2.1 Drainage rate and dynamics of the liquid fraction

The total effect of the solid additives on the holdup histories of the foaming liquid accumulated at the test cell's bottom is evident in Fig 1a. As we move from regular ($n = 0$)

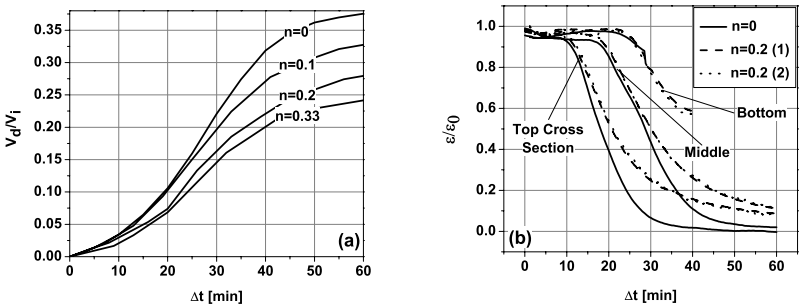

Fig. 1. (a) Transient holdup (V_d and V_i - volumes of drained and initial foaming solutions correspondingly) and (b) liquid fraction registered inside the aqueous foam column as a function of concentrations n. Curves (1) and (2) are shown to ensure repeatability of the results obtained in subsequent tests with the particulate foam.

to particulate ($0 < n \leq 0.33$) aqueous foam it is seen that the higher the concentration is, the slower is the flow rate of the drained liquid. The liquid fraction in Fig. 1b is a local parameter that is sensitive to the transient balance between the foaming liquid that enters from above and that flowing out from the observed cross section of the foam column. Initially, the liquid fraction, ε, is uniform throughout, but when the drainage proceeds, the foam top dries faster, as it does not receive any liquid from above. With time, depletion profile is seen to develop at the top and gradually moves toward the bottom where the registration of the water content, $\varepsilon(t)$, was interrupted at $\Delta t \approx 30min$ due to the arrival of the drained liquid to the conductivity sensor. It is clear that eventually the liquid fractions registered in all the three cross sections have to approach the steady state values that are equal over the full column length. Solid additives do not violate the common tendency, while they appear to increase the resistance of the Plateau borders to the drained liquid flow. This feature has no practical importance during the initial, so called induction period when the liquid fraction is constant, while changes significantly the later histories of the liquid fraction observed at $\Delta t > 15min$ in particulate foam with $n = 0.2$. As the result the dashed and the dotted curves in Fig. 1b start to convert to the steady state level earlier than those for the regular ($n = 0$) foam. When comparing the data obtained for the top, middle and bottom cross sections, non-homogeneity or difference in the water content over the foam column length becomes important during the time period $10min < \Delta t < 40min$. It is a matter of fact that when compared to a particulate foam ($n = 0.2$) the regular foam ($n = 0$) dries out faster. At least at the top and the middle cross sections the drain rate of the regular foam is higher. Particulate

foams take a longer time to reach equilibrium. The value of final liquid fraction is about twice higher than that in the regular ($n = 0$) aqueous foam.

2.2 Shock wave/foam interaction

The physical behavior of a compressible cellular material interacting with a moving shock wave depends on the profile and strength of the shock wave as well as on the material properties. A drained aqueous foam seeded with solid particles, appears to be affected also by the time duration, Δt, and by the concentration, n. Although to explain the behavior, all these characteristics have to be varied, only a single set of impact conditions pertaining to the variable parameter, Δt, in the regular ($n = 0$) and particulate ($n = 0.2$) aqueous foams will be discussed here. At the first stage we focused on the trajectories of the shock waves moving over the regular ($n = 0$) aqueous foam shown in Fig. 2. When the incident shock waves (In) approaches the foam column it is reflected back

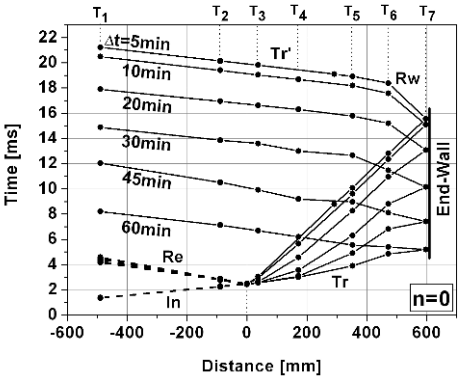

Fig. 2. x-t diagram of the shock wave/aqueous foam interaction.

at the air/foam interface as a reflected shock (Re). The shock wave (Tr) transmitted inside the foam is further reflected back at the end-wall and propagates upstream as the reflected shock wave (Rw). The straight-line trajectories of the transmitted shock wave, Tr, registered at the early stage of the foam drainage ($\Delta t = 5$ and $10min$) ensure that the initial non-homogeneity of the aqueous foam column that is impacted in shock tube tests is negligible. However, later on, starting from $\Delta t \geq 20min$, this non-homogeneity exerts primary control over the propagation trajectories of both the transmitted, Tr, and reflected, Rw, shock waves. The most interesting details of the flow history occur near the end-wall. Non-linear trajectories, Rw, between pressure ports T_6 and T_7 are indirect evidence that the reflected shock wave refracts at the air/foam interface. In contrast to these findings, near constant trajectory of the shock wave, Tr', is coupled with its extremely high velocity to the left of port T_6. This suggests that transducers T_3 to T_5 become progressively uncovered by foam and thereby are exposed in time to air external to the aqueous foam column. If the duration of the foam drainage proceed later than $\Delta t > 30min$, the trajectories of the transmitted shock wave, Tr, near the port T_6 break.

A key reason for this finding is that the foam column by that time lost about 25% of its initial water content and the issued liquid is accumulated at the end-wall of the test section. This water layer is gradually thickened in time and finally bridges the gap to port T_6. As a result, the incoming shock waves refracts at the water surface as though it is a solid wall [1]. Similar consideration is valid for the analysis of the-end wall pressure profiles shown in Fig. 3. In fact, the longer the duration of the aqueous foam drainage is,

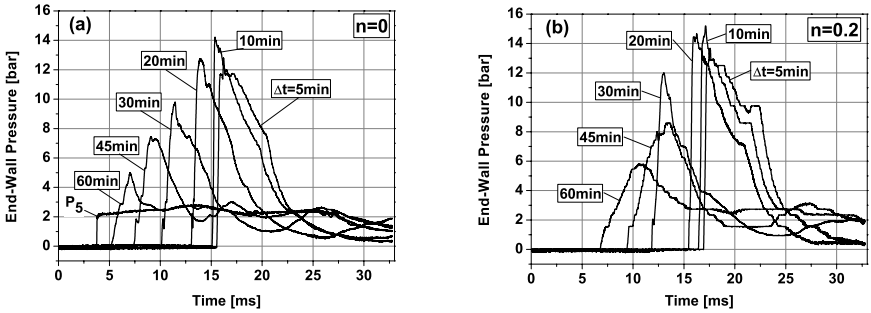

Fig. 3. End-wall pressure profiles in the regular (a) and particulate (b) aqueous foams

the thicker is the water layer. If so, the expansion fan arising when the reflected wave, Rw, interacts with the foam face finally reaches the end-wall and restricts the amplitude of the pressure trace registered at T_7. However, in spite of this, the peak pressures transmitted to the end-wall in the regular ($n = 0$) and especially in the particulate ($n = 0.2$) aqueous foam significantly exceed the normal reflection pressure, P_5, registered without foam (shown in Fig. 3a). This pressure enhancement usually addressed to the momentum imparted to the foam skeleton by the shock, requires a larger impulse from the wall to bring the foam to rest. When comparing the pressure traces in Figs. 3a and 3b it is evident that in both cases the foam column delays the arrival of the shock wave at the end-wall. In similar the drainage duration and the resulted non-homogeneity reshape the profiles, substantially reducing the peak pressure. The data in Fig. 4b quantify this finding demonstrating the role of particles in both phenomena.

3 Conclusions

The use of coal fly ash in reducing the drainage rate, $d\varepsilon/dt$, of wet aqueous foam with initial liquid fraction of $\varepsilon = 0.2$ was demonstrated based on the results of the free drainage tests. The aqueous foam becomes more stable when the concentration is raised from $n = 0$ to $n = 0.33$.

Using shock tube tests, a comparative analysis of the regular ($n = 0$) and the particulate ($n = 0.2$) aqueous foam revealed significant pressure enhancements at the shock tube end-wall for both cases. Whereas the drainage reduces this effect, the final conclusion is that within the range of the studied conditions this material has no advantage as

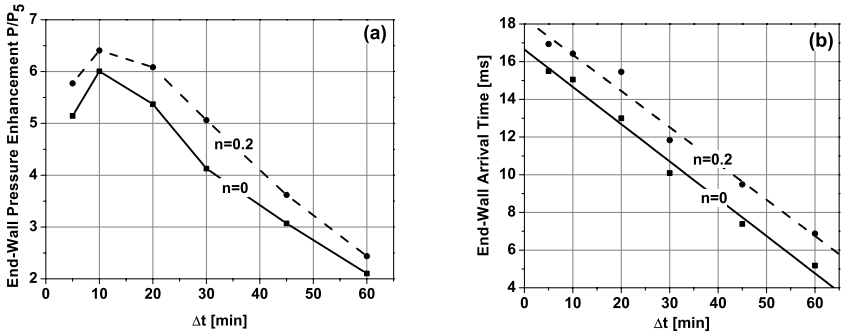

Fig. 4. Pressure enhancement registered at the end-wall (a) and time of arrival of the transmitted shock wave (b) as function of the drain time Δt.

protection against normal impact of shock wave. In contrary because the solid particles reduce the drainage rate and additionally remove kinetic energy from the shock wave, particulate foam is more effective in delaying the velocity of the transmitted shock wave, Tr. This so-called "delay" mechanism of the shock wave attenuation increases with particle concentration, n, and could be particularly important when applied to blast waves, since it provides additional time for the blast to decay within the protective barrier.

Acknowledgement. The authors are thankful for the valuable discussions with Prof. George Kaptay from the University of Miskolc, Hungary. This study was conducted under the financial support of the Israel Science Foundation (Grants No. 278/03 and No.154/04). The study was conducted under the auspices of the Mower Professorial Chair of Shock Wave Studies.

References

1. Britan, A., Ben-Dor, G., Shapiro, H., Liverts, M. and Shreiber, I., Drainage effects on shock wave propagating through aqueous foams, Colloids and Surfaces, accepted for publication, 2007.
2. Weaire, D. and Hutzler, S., The Physics of Foams, 28-29, Oxford, UK, 1999.
3. Moxon, N.T., Torrance, A.C. and Richardson, S.B., The attenuation of acoustic signals by aqueous and particulate foams, Applied Acoustics, **24**, 193-209, 1988.
4. Shushkov, G.A. and Feklistov, V.N., Acoustic properties of gas-liquid foams with solid particles, Akusticheskiy Zhurnal (in Russian), **41**, 2, 1995.
5. Shreiber, I., Ben-Dor, G., Britan, A. and Feklistov, V., Foam self-clarification phenomenon: An experimental investigation, Shock Waves, **15**, 3-4, 199-205, 2006.
6. Ip, S.W., Wang, Y. and Toguri, J.M., Aluminium foam stabilization by solid particles, Can. Metallurgical Quart, **38**, 81-92, 1999.
7. Kaptay, G., Interfacial criteria for stabilization of liquid foams by solid particles, Colloid and Surfaces A: Physicochem. Eng. Aspects, **230**, 67-80, 2004.

Effect of acceleration on shock-wave dynamics of aerofoils during transonic flight

H. Roohani[1] **and B.W. Skews**[2]

[1] *University of Johannesburg, PO Box 17011, Doornfontein 2028, Johannesburg, South Africa*
[2] *University of the Witwatersrand, PO Wits 2050, Johannesburg, South Africa*

1 Introduction

When studying the aerodynamic flow field around objects moving through compressible fluids, it is expected that there would be a difference between the flow field around an object moving at constant velocity with the flow field around an accelerating object moving at the same instantaneous Mach number. This is because during acceleration the fluid around an object does not have sufficient time to reach equilibrium and is therefore always in a transient state.

It has already been shown by H. Roohani and B.W. Skews [1], that the aerodynamic forces and moments acting on an aerofoil can be significantly affected by acceleration. The objective of this paper is to show that the flow field around an accelerating object is also affected and to use this to suggest an explanation for the changes that take place in the aerodynamic forces.

As the greatest difference in aerodynamic forces caused by acceleration are observed in the transonic range of Mach numbers, this is the main focus of this investigation.

2 Modelling Techniques

2.1 Steady state

In order to model an object moving with constant velocity through a compressible fluid two techniques can be used. The first is to move the reference frame of the object at the desired velocity. This technique moves the object and the meshed domain simultaneously at the required velocity while the far field fluid remains stationary.

The second technique requires the use of pressure far-field boundary conditions. These are used in Fluent to model free stream conditions at infinity, with free stream Mach number and static conditions being specified. Although this technique only specifies the velocity at the far-field, sufficient time is allowed in steady state simulations for the system to reach equilibrium. This will result in the entire flow field to be moved at the required velocity and the reference frame of the object to be kept stationary, hence producing results identical to the case of the moving reference frame described above.

2.2 Accelerating objects

Fluent does not have the facility for the linear acceleration of the reference frame of an object. The moving reference frame technique can only solve problems with constant velocity as described above. Therefore, in order to deal with acceleration using Fluent,

the reference frame of the object must be kept stationary and the entire flow field must be accelerated.

It is important to note that accelerating the entire flow field cannot be achieved merely by accelerating the velocity at the far field. Any change at the far-field will propagate through the medium at the speed of sound and will be experienced by an object and by the fluid surrounding the object only some time after the change has taken place. In contrast, when an object is physically accelerated through a particular fluid, the changes in the velocity of that object are experienced instantaneously by the fluid immediately surrounding the object and are propagated outwards.

In order to successfully model the case of an accelerating object by moving the flow field, the fluid at far field and the fluid inside the boundaries of the meshed domain must be accelerated simultaneously with equal acceleration. The far field is accelerated by a user-defined function, which determines the changing value of the input velocity at a given time. The fluid inside the boundaries must be accelerated using momentum and energy source terms. These are derived from the momentum and energy equations, which are built into the Fluent source code. They are also introduced with the help of a user-defined function. This technique was recommended by Fluent for the linear acceleration of an object in compressible fluids in external aerodynamic problems. Accelerating the entire flow field and keeping an object stationary is equivalent to accelerating the reference frame of the object in the opposite direction and keeping the fluid stationary.

3 The effects of acceleration on aerofoil aerodynamics during transonic flight

Two subsonic aerofoils, NACA 0012 and NACA 2412, and two supersonic aerofoils were used. The supersonic aerofoils were of biconvex and diamond shaped profiles. All aerofoils had cord lengths of 1 m and the supersonic ones had a maximum thickness of 0.1 m. These aerofoils were subjected to a very high acceleration in order to enhance the differences between the constant velocity and accelerating scenarios. They were all subjected to the following conditions:

Free stream temperature	= 300 K
Atmospheric pressure	= 101325 Pa
Acceleration	= 1041 m/s^2
Range of Mach numbers	= 0.1 to 1.3
Angle of attack	= 4 degrees

Initially steady state simulations were conducted for each aerofoil, at Mach numbers ranging from 0.1 to 1.3. Then each aerofoil was subjected to an acceleration of 1041 m/s^2 through the same range of Mach numbers. Pressure plots and flood plots were compared at each instantaneous Mach number, taking note of the difference between the constant velocity and the accelerating scenarios in each case. As expected the greatest difference was observed in the transonic region. Apart from the significant difference in the general shapes of the pressure and flood plots, in this region, at each instantaneous Mach number, acceleration brought about a shift in the point of flow separation on the upper and lower surfaces of the aerofoils.

In figures 1 and 2 the pressure and the flood plots for the symmetrical subsonic aerofoil (NACA 0012) are shown at a Mach number of 0.9. The shift in the point of flow separation brought about by acceleration is apparent.

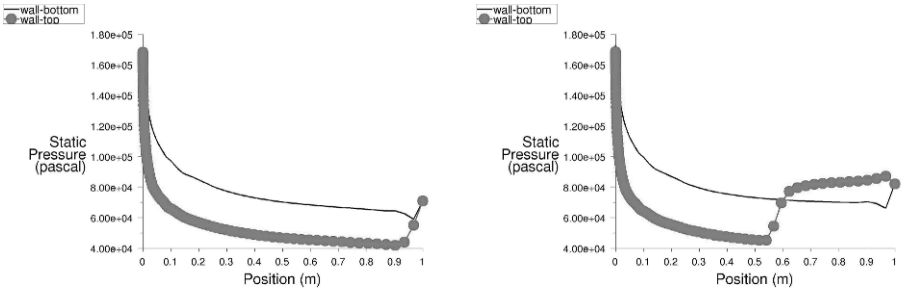

Fig. 1. Steady (left) and unsteady (right) pressure versus position for NACA 0012, Mach number 0.9, acceleration 1041 m/s^2 for the unsteady case.

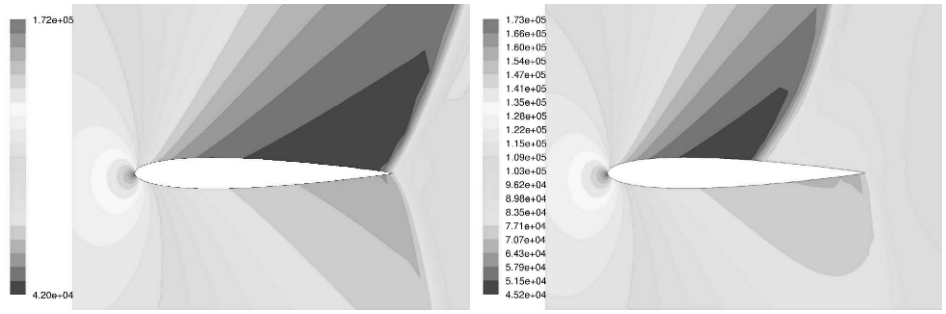

Fig. 2. Steady (left) and unsteady (right) pressure flood plots for NACA 0012, Mach number 0.9, acceleration 1041 m/s^2 for the unsteady case.

Figures 3 and 4 represent a comparison of the pressure and flood plots for the asymmetrical aerofoil (NACA 2412) at Mach 0.91 with similar results. Again the pressure plots and the flood plots show a difference in the shock-wave induced point of flow separation between the steady and unsteady scenarios. In figures 5 and 6 a supersonic diamond shaped aerofoil is used. Here acceleration affects the flow so drastically that the results are visible on both the top and the bottom surfaces of the aerofoil. Shockwaves are present on both surfaces and they are affected by acceleration.

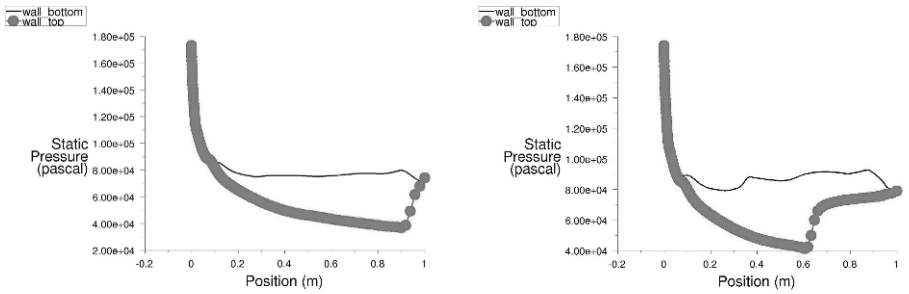

Fig. 3. Steady (left) and unsteady (right) pressure versus position for NACA 2412, Mach number 0.9, acceleration 1041 m/s^2 for the unsteady case.

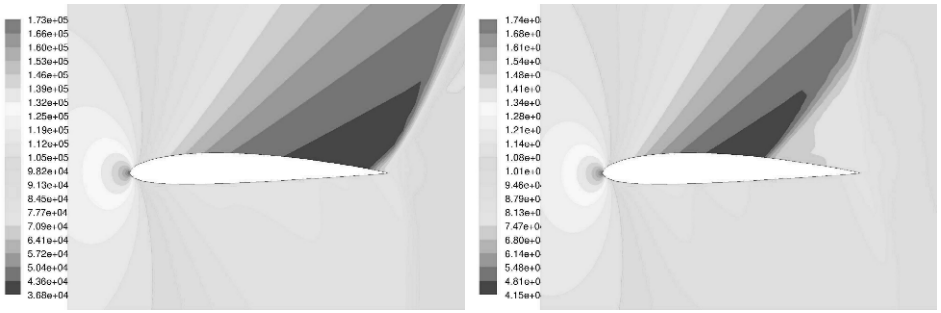

Fig. 4. Steady (left) and unsteady (right) pressure flood plots for NACA 2412, Mach number 0.9, acceleration 1041 m/s^2 for the unsteady case.

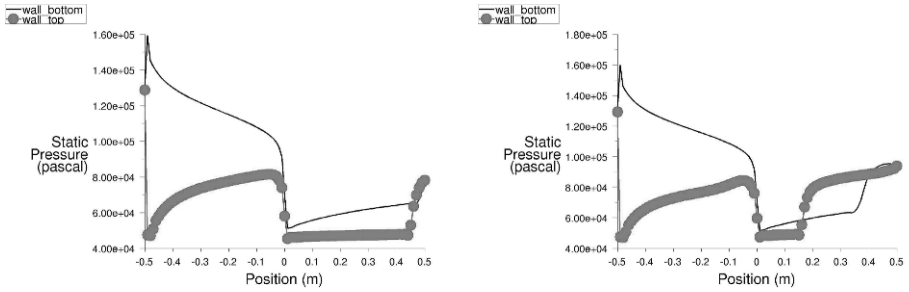

Fig. 5. Steady (left) and unsteady (right) pressure versus position for the diamond shaped aerofoil, Mach number 0.9, acceleration 1041 m/s^2 for the unsteady case.

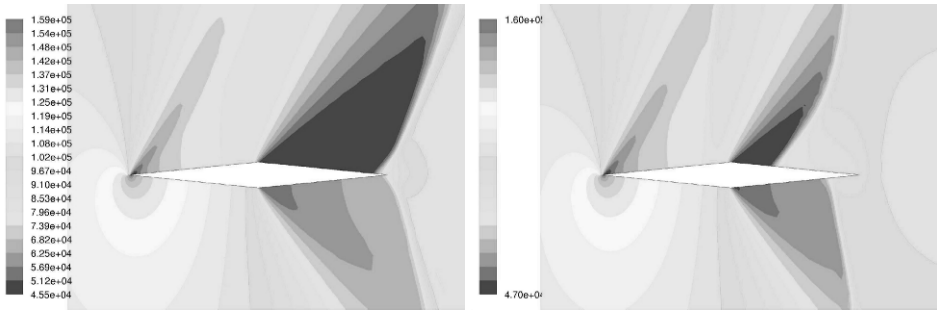

Fig. 6. Steady (left) and unsteady (right) pressure flood plots for the diamond shaped aerofoil, Mach number 0.9, acceleration 1041 m/s^2 for the unsteady case.

Finally simulations testing a biconvex aerofoil showed similar effects. These are shown in figures 7 and 8.

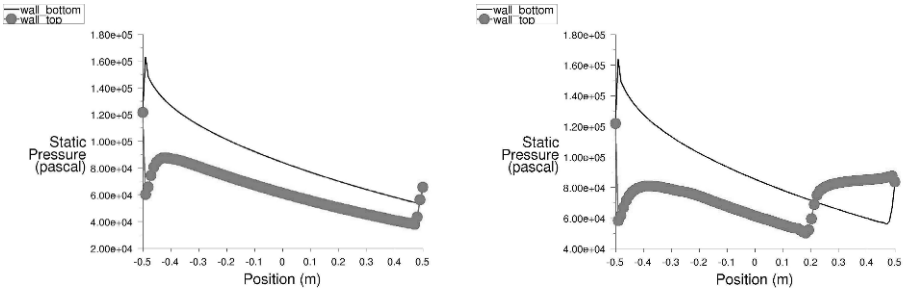

Fig. 7. Steady (left) and unsteady (right) pressure versus position for the biconvex aerofoil, Mach number 0.9, acceleration 1041 m/s^2 for the unsteady case.

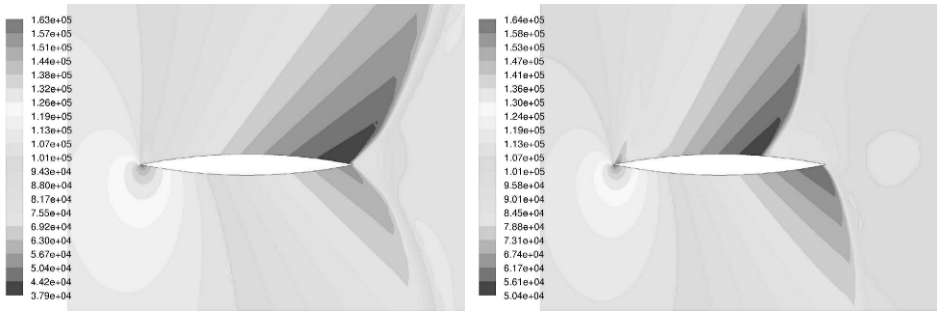

Fig. 8. Steady (left) and unsteady (right) pressure flood plots for the biconvex aerofoil, Mach number 0.9, acceleration 1041 m/s^2 for the unsteady case.

The effects observed can be explained by noting that during acceleration the flow field is always in a transient state. It does not have time to reach equilibrium. When an object is accelerated through transonic Mach numbers the shock-induced point of flow separation shifts with changing Mach number. However due to the fact that equilibrium is never reached, the position of the shockwave at a specific Mach number is not the same as it would have been under constant velocity conditions. This causes the unsteady aerodynamic forces and moments, in the transonic region, to be significantly different to those of the steady state condition. This effect is far less severe for the subsonic and supersonic Mach numbers.

4 Conclusions

- When comparing steady and unsteady scenarios significant differences in pressure plots and flood plots are observed in the transonic region.
- These were mainly because for the same instantaneous Mach number acceleration brings about a shift in the position of the shock induced point of flow separation.
- To varying degrees, the above phenomenon was observed in all aerofoil profiles, which were tested. However at this point it is premature to claim that changing the aerofoil profile will reduce the effect of acceleration and this must be a subject for future investigations.

References

1. Roohani H. and Skews B.W.: *Transient aerodynamic forces experienced by aerofoils in accelerated motion*, ISSW26, July (2007).

Effects of precursory stress waves along a wall of a container of liquid on intermittent jet formation

A. Matthujak[1], K. Pianthong[1], M. Sun[2], K. Takayama[3], and B.E. Milton[4]

[1] *Department of Mechanical Engineering, Faculty of Engineering, Ubon Ratchathani University, 34190, Thailand*
[2] *Interdisciplinary Shock Wave Research Laboratory, Institute of Fluid Science, Tohoku University, Sendai, Japan*
[3] *Tohoku University Biomedical Engineering Research Orgization, Tohoku University, Sendai, Japan*
[4] *School of Mechanical and Manufacturing Engineering, The University of New South Wales, Sydney, 2052, Australia*

Summary. This paper describes results of pressure measurements and double exposure holographic interferometric visualization of waves propagating in a conically shaped container of liquid during high-speed liquid jets generation by impact acceleration method using a vertical two-stage light gas gun. To verify the contribution of longitudinal and transversal waves created in metal containers, we used a 10.6 mm x 10.6 mm container of water with thick acrylic observation windows and quantitatively visualized waves by using double exposure holographic interferometry. We found the presence of stress waves released in water, whose effect was cancelled with wave interaction in the container.

1 Introduction

The characteristic of high-speed liquid jet (water jet and liquid fuels jet) generated by high-speed impact technique has been extended in many papers [1, 2]. At the projectile impingement on the container of liquid, prior to shock generation in liquid, longitudinal and transversal waves created in a metal part of the container, these stress waves are released forming a precursory shock wave. The wave interactions inside a container of liquid and the contribution to these waves to jet formation are not yet thoroughly resolved. Even though there are few researches that have attempted to describe such wave interactions and contribution, all of the researches are only analytical and numerical study [3, 4] so that the experimental study is still needed for verification and clarification.

To identify the stress waves, we constructed a 10.6 mm x 10.6 mm cross sectional container of water and visualized, by using double exposure holographic interferometry, impact generated shock waves in water and also shock waves released in water by stress waves in metal walls.

2 Experimental facility

We used an impact driven method for jet generation [5]. The liquid contained in the nozzle cavity is impacted by a high velocity projectile. The high speed projectile needed in this technique is produced by the vertical two stage light gas gun (VTSLGG), shown in Fig. 1 . The component detail and the operation procedure of the VTSLGG have been described [5]. Note that the impact velocity (V_p) of 300 m/s, the conical nozzle and water is used for high-speed liquid jet generation in this experiment.

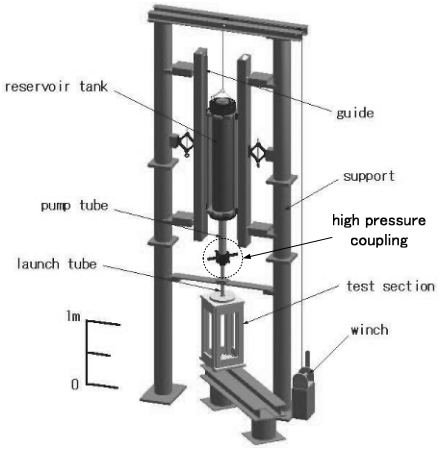

Fig. 1. Vertical two-stage light gas gun (VTSLGG)

3 Pressure measurement in a nozzle cavity

3.1 Pressure measurement

For pressure measurements, we used a 0.1 mm diameter optical fiber probe pressure transducer (FOPH2000 RP Acoustics Co.Ltd.), which is one of the most sophisticated pressure transducers commercially available and inserted it into a 0.7 mm diameter nozzle hole as shown in Fig. 2a. Being so thin, it was supported by a jig and inserted in the center of the nozzle hole exactly parallel to the nozzle axis. The plastic shroud of optical fiber was removed and glued in the jig as shown in Fig. 2b.

The output signal from optical fiber pressure transducer, which is the temporal variation of pressures at a spot of 0.1mm diameter, can be detected at a high frequency response of 100 MHz by a photodetector and stored in a digital oscilloscope. The principle of the optical fiber pressure transducer is found in [6]. The tip of the pressure transducer is positioned exactly at 4 mm from the bottom of the nozzle. The schematic diagram of its setting is shown in Fig. 2b.

3.2 Results and discussion

We observed negative pressures in the nozzle at the projectile impact as shown in Fig. 3. From the preliminary test, we found that such negative pressures detected with the optical fiber pressure transducer are attributable to impact flash and have no physical significance.

We observe the pressure fluctuation and 3 peak over-pressures, marked as A, B and C appear. These peak pressures A, B, and C correspond to the shock waves originated from longitudinal and transversal waves initially propagating in the container metal wall and spontaneously released into water and the incident shock wave in water, respectively. Then, the following three peak over-pressures marked at points D, E and F correspond to 1.24, 0.602 and 0.273 GPa, respectively. The time intervals of peak pressures between D and E ($\Delta t'_1$) and between E and F ($\Delta t'_2$) are 45.08 and 38.82 μs, respectively. From high-speed liquid jet visualization in Fig. 4, time intervals Δt_1 between 1^{st} and 2^{nd} jet tips and Δt_2 between 2^{nd} and 3^{rd} jet tips are 24 and 32 μs, respectively.

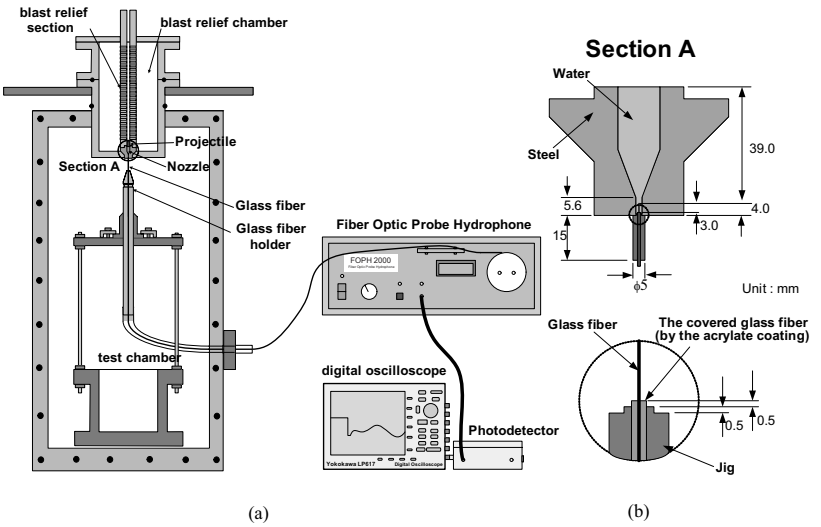

Fig. 2. (a) Pressure measurement system (b) Optical fiber pressure transducer setting

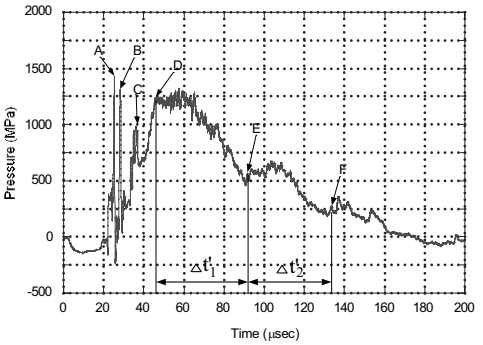

Fig. 3. Pressure history inside the nozzle, V_p = 308 m/s

Peak pressures at D, E and F correspond to multiple shock reflections in water, which drive corresponding jets at time intervals of Δt_1 and Δt_2. Due to the insertion of the jig at the nozzle exit hole, pressures increases inside the nozzle take longer holding time and resulting higher pressures destroyed the jig which was tightly glued in the nozzle hole.

4 Precursory released stress waves in water

We visualized, by using double exposure holographic interferometry, the wave motion in the square container (shown in Fig. 5a) after piston impingement. Time markers are attached on these sequential interferograms. However, although the experiments were repeatable, the time marker and the corresponding wave position slightly scattered within a few $\pm\mu$s. Selective sequential holographic interferogrms are shown at V_p = 362 m/s are presented in Figs. 6a-h : (a) 8 μs; (b) 15 μs; (c) 21 μs; (d) 32μs; (e) 64 μs; (f) 80 μs; (g) 90 μs; and (h) 114 μs.

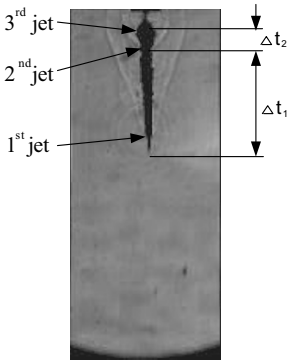

Fig. 4. Intermittent water jet acceleration (from [6])

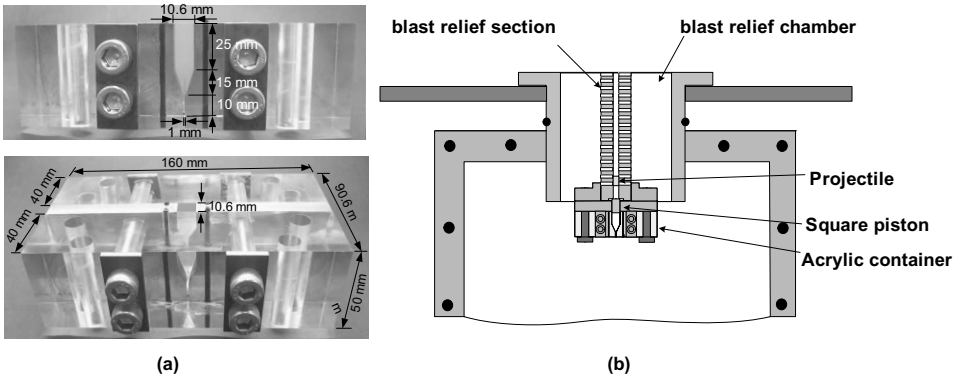

Fig. 5. (a) A 10.6 mm x 10.6 mm square cross sectional nozzle, notice very thick acrylic wall thickness (b) A square cross sectional nozzle arrangement

At 8 μs after the impingement, in Fig. 6a, longitudinal and transversal waves in the metal wall and acrylic windows are spontaneously released into water and formed oblique shock waves. As longitudinal and transversal wave speeds in the steel wall are 5.9 km/s and 3.2 km/s, respectively, and those in acrylic are 2.7 km/s and 1.4 km/s, respectively, and much faster than the sound speed in water. The inclination angle of these oblique shock waves θ is expressed by a_{water} / $a_{solid} = \sin\theta$ where a_{water} and a_{solid} are sound speeds in water and solid, respectively. An oblique shock wave L observable in Fig. 6a is a released longitudinal wave and is inclined about 28°, whereas one defined by this relationship is about 15°. The experimental inclination angle is closer to one defined for the oblique shock wave into water corresponding to the transversal wave.

Fringes distributed normal to the solid wall correspond to the shock wave LA released from the longitudinal wave in acrylic, which nearly merge with the released transversal wave T from metal wall. At the spot where the normal shock and oblique shock intersect, the oblique shock changes of its inclination angle of 5°, which implies the merger of T and LA. The second normal shock corresponds to shock wave in water S, which were formed by piston compression. It should be noticed that fringes observable in front of L are caused by temperature fluctuations in water.

L and T passing through the tapered parts of the nozzle reflected obliquely interacted two-dimensionally with each other. Released waves and S are still identified in Fig. 6b,c

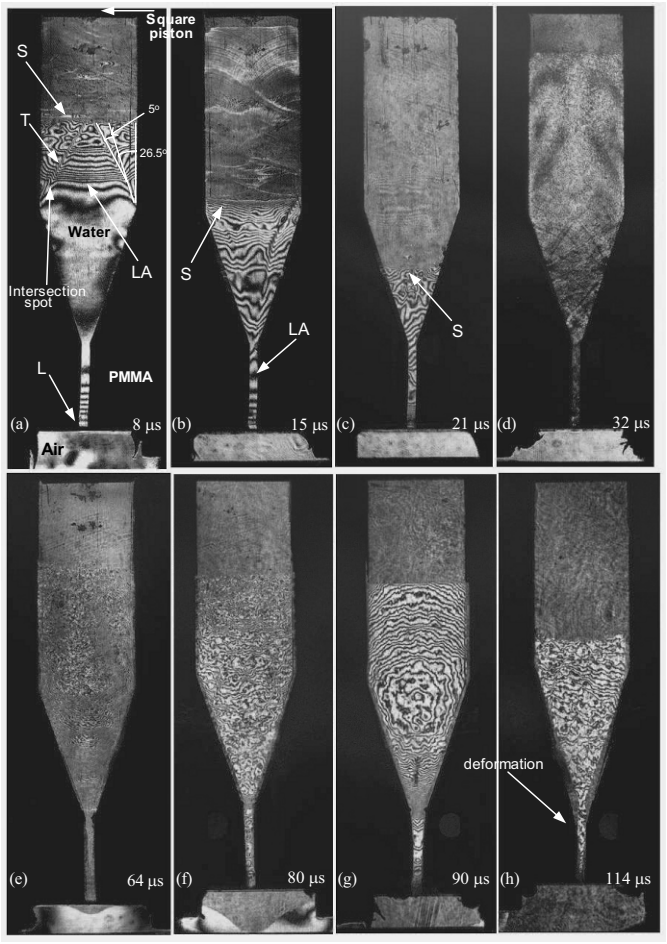

Fig. 6. Sequential holographic interferograms of precursory stress waves in metallic side wall and shock waves released in water, V_p = 362 m/s at the elapsed time of :(a) 8 μs; (b) 15 μs; (c) 21 μs; (d) 32 μs; (e) 64 μs; (f) 80 μs; (g) 90 μs; and (h) 114 μs. Notice main shock wave and precursory stress waves in the metal wall and acrylic windows.

and moved into the nozzle part enhancing pressures. Container shapes are different between the present square cross sectional case and conical one in Fig. 3. The mode of projectile impacts is different between the present case and that in Fig. 3. In the square cross sectional container, the projectile impacted on the square piston in Fig. 5b, whereas in the circular cross sectional container, the projectile directly impacted the liquid surface. If one neglects all these differences and compares Fig. 6, for the sake of simplicity, with the pressure measurements in the nozzle hole as shown in Fig. 3, A and B marked in Fig. 3 correspond to L and T, and C in Fig. 3 corresponds to S.

The top part in Fig. 6d-g corresponds to D in Fig. 3, which consists of the assembly of wavelets and reflected shock waves, exhibiting a totally disturbed region. Despite of

the difference of container geometries and projectile impact characteristic in Fig. 3 and Fig. 6, the time variations of wave motion and pressures show many common features.

We put a Mylar diaphragm of 50 μm in thickness at the nozzle exit to hold liquid from the vertical nozzle hole. As seen in Figs. 6f-h, it did not rupture immediately after the high pressure loading but started to gradually bulge and eventually ruptured at about 90 μs after the projectile impingement. At that time, the piston shown as dark area on the top started to move downward. With the jet initiation, the resulting nozzle flow thickens boundary layer displacement thickness and hence reduces water mass flow rate. Simultaneously, the metal wall deformation became visible as seen in Fig. 6h. With the initiation of nozzle flows, expansion waves propagate from the nozzle to the piston surface. Such multiple reflections of shock waves and expansion waves eventually accelerate intermittently liquid jets.

5 Concluding Remarks

From the pressure history and sequential holographic interferograms inside the acrylic container, we found that: 1) longitudinal and transversal waves did exist in metal parts of the container and also in acrylic observation windows; 2) before the nozzle flow started, these waves and their reflected waves coalesced with a main impact generated shock wave; 3) the primary jet was driven by pressures of 12.4 GPa caused by 300 m/s projectile impingement; 4) successive shock reflections inside the container of liquid drove intermittent multiple liquid jets; 5) the contribution of released longitudinal and transversal waves to multiple jet formation is marginal; and 6) negative pressures detected with the optical fiber pressure transducer are attributable to impact flash and have no physical significance.

Acknowledgement. We wish to acknowledge Mr. S. Haysaka of Tohoku University for his encouragement and devotion in conducting the present experiments and all staff members of the Interdisciplinary Shock Wave Research Laboratory. We also wish to express gratitude to T. Kikuchi and D. Numata who helped in setting up the optical system. The first author would like to express his acknowledgement to Royal Thai Government for financial support. This project was in part supported by the Grant-in-Aid for Science Research No. 12 CE 2003 offered by the Ministry of Education, Culture, Sport, Science and Technology, Japan.

References

1. Shi, H.H.: Study of Hypersonic Liquid Jets. Ph.D. thesis, Tohoku University, Sendai, Japan(1994)
2. Pianthong, K., Milton, B.E., Behnia, M.,: Generation and shock wave characteristics of unsteady pulsed supersonic liquid jets. Journal of Atomization and Sprays **13 5-6**, 475-498 (2003)
3. Glenn, L.A.: The mechanics of the impulsive water cannon. Computers and Fluids **3**, 197-215 (1975)
4. Lesser, M.: Thirty years of liquid impact research: a tutorial review, Wear **186-187**, 28-34 (1995)
5. Matthujak, A., Hosseini, S.H.R., Takayama, K., Sun, M., Voinovich, P.: High speed jet formation by impact acceleration method. Shock Waves Journal (in press)
6. Staudenraus, J., Eisenmenger, W.:Fiber-optic probe hydrophone for ultrasonic and shock-wave measurements in water. Ultrasonic **31 (4)**, 267-273 (1993)

Experimental investigation of tripping between regular and Mach reflection in the dual-solution domain

C.A. Mouton and H.G. Hornung

Graduate Aeronautical Laboratories, California Institute of Technology, Pasadena, CA, USA

Summary. Experiments were conducted in the Mach 4.0 Ludwieg tube facility at the California Institute of Technology. First, the hysteresis phenomenon, first proposed by [1] is explored. Second, tripping from regular reflection to Mach reflection by depositing laser energy onto one of the wedges is considered. These experimental results are compared with numerical computations and theoretical estimates.

A double wedge model was constructed with the lower wedge being fixed and the upper wedge being adjustable. This asymmetric configuration was chosen for simplicity and follows the work of [2] and [3].

Computationally, the hysteresis phenomenon is easy to demonstrate. However, experimentally, due to tunnel noise, the hysteresis phenomenon is more difficult to show and the maximum angle to which regular reflection can be maintained is reduced. This angle is a qualitative measure of the quietness of the tunnel.

In order to demonstrate the hysteresis phenomenon, the upper adjustable wedge was set so that the shock angles are well below the von Neumann condition, and therefore only regular reflection is possible. As the upper wedge angle is increased into the dual solutions domain, at some point a sudden transition to Mach reflection with a finite Mach stem height occurs. Further increase of the upper wedge angle causes the Mach stem to grow further. If the upper wedge angle is then decreased, the Mach stem height is decreased continuously until it reaches zero at the von Neumann condition and regular reflection is restored.

Experiments were conducted moving the upper wedge at different speeds to study the effect of the wedge speed on transition. It was found experimentally, that if the wedge was moved quickly, regular reflection could be maintained further into the dual-solution domain. This is believed to be due to the fact that the wedge spends less time at any given angle so that the chance of a sufficiently strong disturbance occurring is smaller.

By depositing laser energy on the lower wedge a small blast wave is created. This disturbance can be compared to the disturbance from a solid particle impacting the wedge. Using high-speed cinematography we can capture the disturbance to the incident shock. Soon after the disturbance is introduced, a small Mach stem is formed and grows to its steady-state height. This growth rate is compared with theoretical calculations.

The importance of energy deposition location is also discussed. If the energy is deposited far downstream on the wedge, it has to be very strong to reach the incident shock; however, if the energy is deposited far upstream, it also has to be very strong, because it will weaken before it reaches the reflection point. Therefore, there is an optimum location, in terms of minimum energy required to cause transition from regular to Mach reflection. This is also explored computationally, and for downstream locations, a theoretical estimate of the energy required is presented.

1 Experimental Setup

Several experiments were conducted using the Ludwieg Tube at the Graduate Aeronatuical Laboratories of the California Institute of Technology (GALCIT). The details of the facility and the specific test setup will be discussed in this chapter.

1.1 Ludwieg Tube

A Mach 4 nozzle was designed, constructed and taken into operation for the existing Ludwieg tube at GALCIT. The Ludwieg tube consists of a 17 m long 300 mm inner diameter tube, a transition piece to allow for the upstream insertion of particles, an axisymetric nozzle, a diaphragm station (located either just upstream of the throat or downstream of the test section) and a dump tank.

Before a run, the tube is filled with the test gas at a pressure of up to 700 kPa and the dump tank is evacuated. To start the run, the diaphragm is ruptured, thus causing an expansion wave to propagate through the nozzle and into the tube. During the time it takes for the expansion wave to travel to the end of the tube and for the reflected wave to return to the nozzle, the reservoir conditions for the nozzle flow are almost perfectly uniform, thus giving a constant condition test time of 80 ms to 100 ms.

A Mach number of 4 was chosen because it is necessary to operate at a Mach number for which the dual-solution domain has a shock angle range that is not too small. Also, to avoid having to heat the gas in the tube, it is necessary to operate at a Mach number no higher than 4, to avoid condensation of the test gas in the nozzle expansion.

Since the expansion takes only about 100 ms to travel from the nozzle to the end of the tube and back, any time that the flow needs to establish itself in the nozzle reduces the test time. It is therefore important that the nozzle design allows for a relatively fast startup process. Computations done assuming an infinite dump tank and a diaphragm downstream of the nozzle show a 20 ms startup time, which is quite acceptable and is almost identical to the startup time with the previous Mach 2.3 nozzle.

The Ludwieg tube was equipped with a high speed schlieren system. The primary component of the system is a Visible Solutions Phantom v7.1 camera. At the full resolution of 800×600 px the camera has a frame rate of 4,800 fps.

Early experiments showed that the flow, using the downstream diaphragm, did not properly start. An image taken half way through the test time is shown in Figure 1. The maximum steady flow time achieved with this configuration was no more than 20 ms.

Euler computations using the Amrita system [4] were conducted to understand the problem, in particular, the problem was modeled with a finite dump tank to understand the importance of the back pressure as well as the shock generated when the diaphragm is ruptured.

1.2 Upstream Diaphragm Station

Further computations done using Amrita, with the diaphragm moved just upstream of the converging nozzle section showed no problems with flow unstart and also produced a flow start time of only 3 ms, as opposed to the 20 ms required with the downstream diaphragm.

Unfortunately, there are significant drawbacks to having the diaphragm upstream of the test section. Specifically, the ruptured diaphragm will cause disturbances due to its

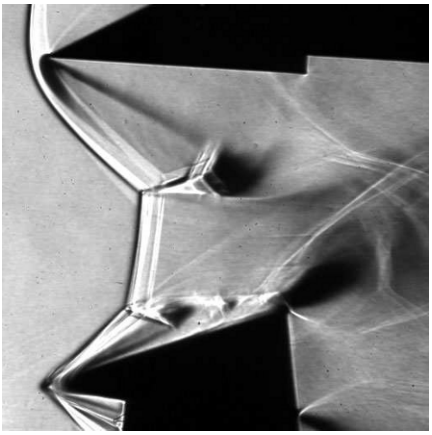

Fig. 1. Experimental flow at approximately 50 ms into the test time showing unstart with a downstream diaphragm.

Fig. 2. Simulation showing the starting of the nozzle, 2.7 ms afterthe rupturing of the diaphragm located just upstream of the converging section of the nozzle. The left boundary condition, just upstream of the throat, is extrapolated, while the right boundary condition, at the end of the dump tank, and the outer wall of the dump tank are reflective.

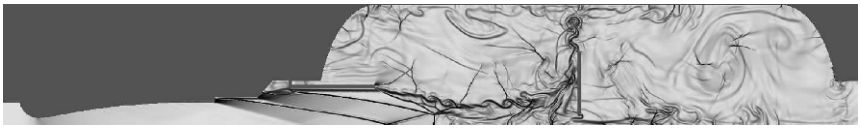

Fig. 3. Simulation showing the correctly started flow 50.1 ms after the rupturing of the diaphragm located just upstream of the converging section of the nozzle. The left boundary condition, just upstream of the throat, is extrapolated, while the right boundary condition, at the end of the dump tank, and the outer wall of the dump tank are reflective.

presence as well as due to the production of small pieces of debris. Experiments conducted using an upstream mylar diaphragm of 5 mils had a first startup process, and unstart of the flow was not experienced until after the reflected expansion wave from the tube returned to the test section.

1.3 Adjustable Wedge Model

A double wedge model was constructed with the lower wedge being fixed at an angle of 23.6° and the upper wedge being adjustable. The upper wedge angle is controlled using a rotary servo motor with a 5:1 gear ratio. The assembly of the adjustable wedge is shown in Figure 4. The wedge is supported by two vertical posts, and its motion is controlled by a connecting rod, which is connected to the motor.

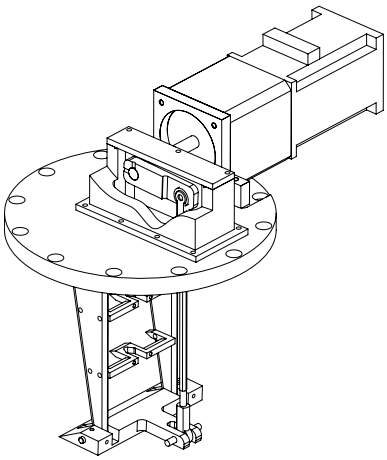

Fig. 4. Wedge assembly consisting of a wedge, a connecting rod, a support structure, a motor, and a gearhead.

2 Experimental Mach Stem Heights

The current experimental results for the Mach stem height, at various upper wedge angles, are plotted, along with the theoretical calculations, the previous experimental results of Hornung and Robinson [5], and the current computations, in Figure 5. Very good agreement between the theoretical, computational, and current experimental work is seen. The experimental work of Hornung and Robinson consistently show higher Mach stem heights than the current experiments.

2.1 Experimental Mach Stem Growth

The growth rate of the Mach stem can be measured from the new experimental data. With the wedges in the dual-solution domain with regular reflection, energy was deposited on the lower wedge. The deposition of energy causes the flow to trip from regular reflection to Mach reflection. Since the initial flow is inside the dual-solution domain, where the steady-state Mach stem height is finite, the Mach stem quickly grows to this steady-state height.

Figure 6 shows the measured Mach stem heights at various times together with theoretical estimates. The experiments show a near linear growth rate, until the steady-state height is reached. The initial rapid growth of and subsequent asymptotic approach to the steady state predicated by the theory is not observed. Very good agreement is seen between the steady-state height, as well as with the time required to reach the steady-state height. The video from which the growth rate was measured was recorded with $38\,\mu$s between frames.

3 Conclusions and Future Work

The Ludwieg tube facility at the California Institute of Technology was retrofitted with a Mach 4.0 nozzle. This Mach number is large enough to provide a sufficiently large

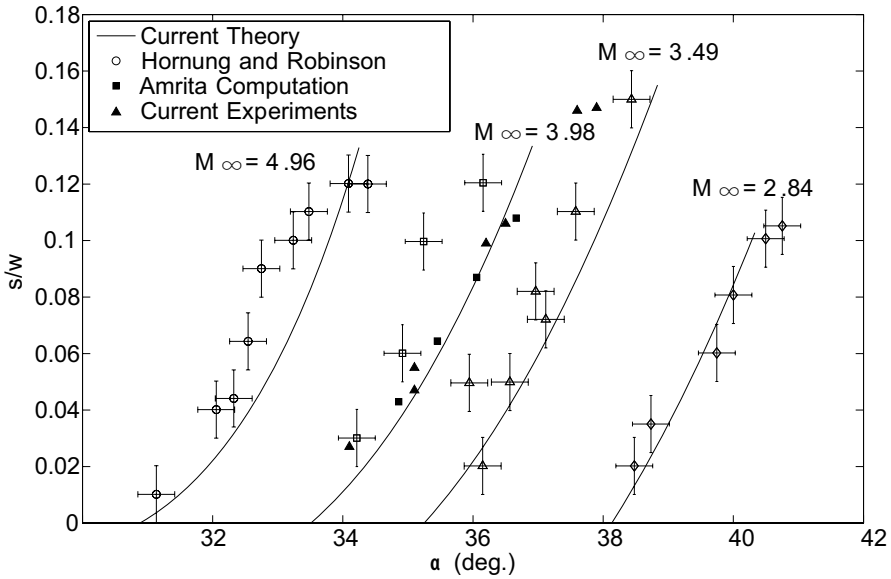

Fig. 5. Comparison of current experimental Mach stem height results against the theoretical estimates, measurements by Hornung and Robinson [5], as well as current computational work done using Amrita. $\gamma = 1.4$ and $g/w \approx 0.4$.

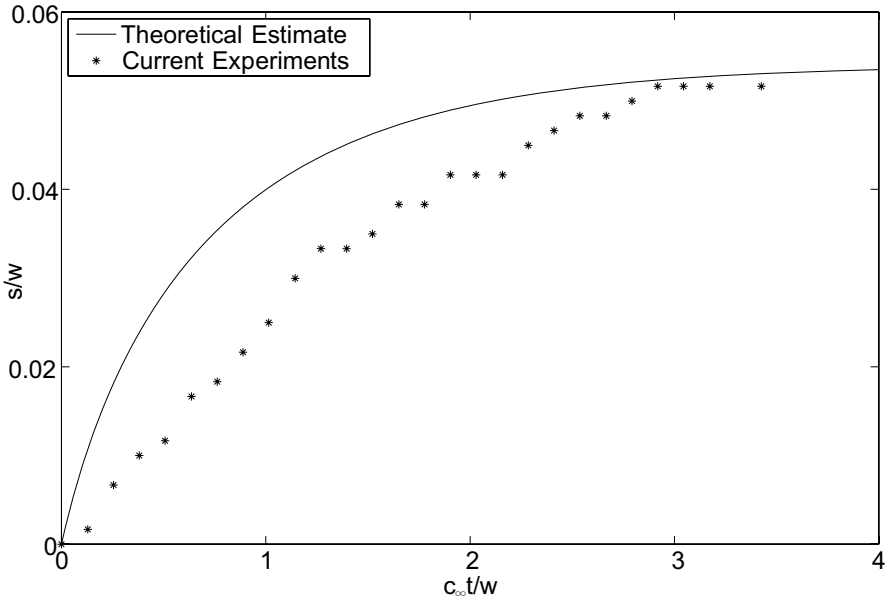

Fig. 6. Comparison of current experimental Mach stem growth rates with the theoretical estimate. $\gamma = 1.4$ and $g/w \approx 0.4$.

dual-solution domain, while being small enough not to require preheating of the gas. The test time of the facility is 100 ms, which requires the use of high-speed cinematography and a fast motor to rotate the wedge.

The first experiments conducted on shock reflection in the Ludwieg tube verified the hysteresis phenomenon. The ability to enter the dual-solution domain with regular reflection is a qualitative measure of the quietness of the facility. Hysteresis was successfully demonstrated in the Ludwieg tube facility. The experiments show that in the Ludwieg tube facility, regular reflection could be maintained till approximately half way between the von Neumann condition and the detachment condition.

Energy deposition studies were performed using a 200 mJ Nd:YAG laser. The disturbance caused by the blast wave from the laser is seen to affect the incident shock, and in some cases cause transition from regular reflection to Mach reflection. The location on the wedge where the energy is deposited is found to be an important criterion in whether or not transition occurs. This finding is consistent with the numerical work presented in this thesis, which shows that the energy required to cause transition is dependent on the location where the energy is deposited. Future studies should measure the amount of energy deposited on the wedge, so that an accurate minimum energy for transition can be calculated as a function of deposition location. The best way to measure the energy deposited is to visualize the blast wave caused by the energy deposition. Attempts to do this in the current experiments were unsuccessful, because the densities required to visualize the blast wave were so high that the blast wave was nothing more than a Mach wave, and therefore an energy could not be calculated.

Experiments were also performed to measure the Mach stem height and its growth rate. These results are compared with the theoretical estimates presented in this thesis. Excellent agreement between the steady-state Mach stem height and the theoretical estimate is seen. Comparisons of Mach stem growth rate with theoretical estimates show significant differences, but do show good agreement in the time required to reach the steady-state height. The reasons for these differences are unknown, and may be attributable to three-dimensional effects.

Acknowledgement. This work was funded by the Air Force Office of Scientific Research, under the supervision of Dr. John Schmisseur

References

1. H.G. Hornung, H. Oertel, and R.J. Sandeman: *Transition to Mach Reflection of Shock-Waves in Steady and Psuedo-Steady Flow with and without Relaxation*, Journal of Fluid Mechanics **90**, pp 541–547 (1979)
2. M. Ivanov, G. Klemenkov, A. Kudryavtsev, S. Nikiforov, A. Pavlov, V. Fomin, A. Kharitonov, D. Khotyanovsky, and H.G. Hornung: *Experimental and Numerical Study of the Transistion between Regular and Mach Reflections of Shock Waves in Steady Flows*, The 21st International Symposium on Shock Waves (1997)
3. N. Sudani, M. Sato, T. Karasawa, J. Noda, A. Tate, and M. Watanabe: *Irregular Effects on the Transition from Regular to Mach Reflection of Shock Wave in Wind Tunnel Flows*, Journal of Fluid Mechanics **459**, pp 167–185 (2002)
4. J.J. Quirk: *Amrita - A Computational Facility (for CFD modelling)*, VKI 29th CFD Lecture Series, ISSN 0377-8312 (1998)
5. H.G. Hornung and M.L. Robinson: *Transition from Regular to Mach Reflection of Shock-Waves Part 2. The Steady-Flow Criterion*, J. of Fluid Mechanics **123**, pp 155–164 (1982)

Interferometric signal measurement of shock waves and contact surfaces in small scale shock tube

S. Udagawa[1], K. Maeno[2], I. Golubeva[3], and W. Garen[4]

[1] *Graduate School of Science and Technology, Chiba University, 1-33 Yayoi, Inage, Chiba, 263-8522, Japan*
[2] *Faculty of Engineering, Chiba University, 1-33 Yayoi, Inage, Chiba, 263-8522, Japan*
[3] *Department of Engineering, University of Archangelsk, 163002, Uferstrasse 17, Archangelsk, Russia*
[4] *Department of Phototnics, University of Applied Science Oldenburg/Ostfriesland/Wilhelmshaven, Constantiaplatz 4, Emden, 26723, Germany*

Summary. In this study we have performed the experiment under the several pressure conditions by using the mini-shock tube of 3mm diameter, which was developed by Garen, by using the interferometric signal measurement with the collimated and polarized laser beams. It is confirmed that the shock waves do not propagate at constant velocity in this mini-shock tube. We have also performed a numerical simulation by using two-dimensional and axi-symmetric N-S equation to compare with the experimental results. The experimental results are shown with the numerical results on the x-t diagram. It is confirmed that the influence of the friction between the test gas and the wall produces the difference between the inclinations of *x-t* curves of the diagram.

1 Introduction

Recently, the micro-shock wave becomes noticed particularly on the several science fields[1][2]. The diffusive transport phenomena such as heat conduction with the wall and the shear stress lead to remarkable deviation from the ideal shock behavior in a narrow channel, which was described by Brouillette[3]. The scaling parameter S is expressed as following equation.

$$S = \frac{Re \cdot D}{4L} \tag{1}$$

Here, Re and D are the Reynolds number and a diameter of the shock tube respectively, and L is the distance between the shock wave and the contact surface between driver - and driven gas. For example, the formula of the Hugoniot curve for the density ratio in front and behind a shock wave can be expressed as follows:

$$\frac{\rho_2}{\rho_1} = \frac{(\gamma_1+1)M^2 + \frac{2\gamma_1 M}{Pr}\cdot\frac{1}{S} + \left(\frac{1}{S}\right)^2 \frac{2\gamma_1}{Pr}}{(\gamma_1-1)M^2 + \frac{1}{S}\cdot\frac{2}{M\cdot Pr} + 2} \tag{2}$$

If S becomes infinite, the well known ideal density ratio is derived:

$$\frac{\rho_2}{\rho_1} = \frac{(\gamma_1+1)M^2}{(\gamma_1-1)M^2+2} \tag{3}$$

Shock waves at micro scales may be highly suitable in the field of medical engineering and further applications[2][4][5][6]. Garen, et.al had performed the shock wave measurements by using the uniquely developed diaphragm-less driver section with specially designed laser differential interferometer in the shock tube of 3mm diameter. It

is also shown experimentally that the Mach number of the shock wave depends on the Reynolds number and is no longer only a function of the initial pressure ratio across the quickly opening valve p_4/p_1 but also is strongly correlated to the Reynolds number at the narrow channel[7].

As the results it is shown that the diaphragm-less driver section and the laser differential interferometer are highly suitable for generating and measuring the shock wave propagation in the small diameter tube. However, the experiments have not been performed at the different positions. Therefore, catching the shock waves and the contact surfaces along the axial direction are of great importance. We have performed the further experiment under the same pressure conditions at the different positions in the diameter of 3mm shock tube by using the diaphragm-less driver section and the laser differential interferometer which are developed by Garen, et.al. Additionally we have performed a numerical simulation for comparison with the experimental results.

2 Experimental setup

Figure 1 shows the schematic diagram of our shock tube, which consists of the high pressure chamber and the low pressure chamber (glass shock tube). The low pressure chamber has an inner diameter of 3mm and length of 920mm. The high pressure chamber, which has got a simple structure, consists of the quickly opening valve including the rubber, the pressure chamber for the valve, and the outer diaphragm. The high pressure air from the compressor is filled into the pressure chamber for the valve through the piping system and is monitored by a pressure gauge after controlling the pressure p_{valve}. Additionally, the quickly opening valve operates by manually bursting the outer diaphragm which is settled on the rear side of the pressure chamber. Here, p_4 and p_1 are the pressures in the high pressure chamber for the shock tube and the low pressure chamber respectively. The pressure p_4 has to be kept lower than p_{valve} to separate the high pressure chamber from the low pressure chamber as the initial condition. The distance x between the quickly opening valve and one of the laser beams of two interferometers is taken from 168 to 858mm. The initial pressure ratio across the quickly opening valve p_4/p_1 is set up 20. We have performed the experiment under the same pressure ratio p_4/p_1 which was obtained by changing the pressures p_4 and p_1. Helium and air have been used as the driver gas, and air has been used as the test gas.

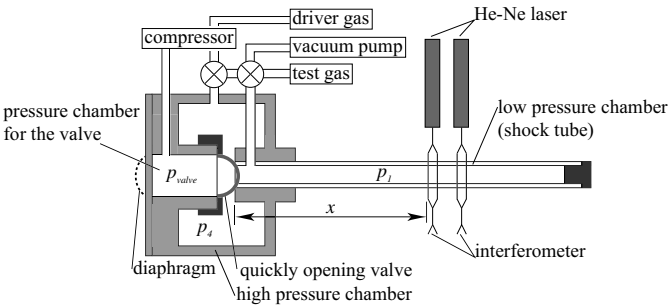

Fig. 1. Schematic diagram of a mini shock tube

3 Numerical simulation

In the small scale shock tube flow analysis, the dominant equation for the flow condition is classified by Knudsen number Kn, which is expressed as the following equation.

$$Kn = \frac{\lambda}{d} \tag{4}$$

Here, λ is the mean free path of the gas molecule and d is the diameter of the tube. If Kn becomes smaller than 0.01, the condition becomes continuum flow which is described by Navier-Stokes (N-S) equation. If Kn becomes between 0.01 and 0.1, the condition becomes slip flow which is described by N-S equation with slip wall condition. In the small scale shock tube flow Kn behind the shock wave is expressed as equation (5).

$$Kn = \frac{k_b}{\sqrt{2}\pi\sigma^2 d} \frac{2 + (\kappa_1 - 1)M^2}{(\kappa_1 + 1)M^2} \frac{T_1}{p_1} \tag{5}$$

Here, λ, k_b, T_1 and σ are the mean free path, Boltzmann constant, absolute temperature of the test gas, and a diameter of the test gas molecule. Kn in our experimental conditions calculated from equation (5) is smaller than 0.01 for air and helium. Thus, it is valid that N-S equation is appropreately used for numerical simulation. In the numerical simulation the grid points are 15 for r direction and 9200 for x direction respectively, and the real grid size is 0.1mm square. Two-dimensional and axi-symmetric N-S equation system is used in this analysis for a circular tube flow. AUSM-DV scheme is used for numerical analysis of the convection terms. MUSCL scheme is used to obtain the higher oder accuracy for space to increase the resolution. The second ordered Runge-Kutta scheme is used for the time integration. The viscous coefficient is calculated from Sutherland's equation. The pressure ratio p_4/p_1 is 20 and the pressure at the high pressure chamber p_4 is 1000mbar respectively. The driver and the test gas are air.

4 Results and Discussion

Figures 2 (a) and (b) show the x-t diagrams from the experiments. The horizontal and the vertical axes are the distance x between the position of the quickly opening valve at the initial condition and the measurement position, and the time t from the quickly opening valve has opened. Figure 2 (a) shows the results which were obtained by using air as the driver and test gas. Figure 2 (b) presents the results which were obtained by using helium as the driver gas and air as the test gas. The opened points and the normal points show the measured positions of the contact surface and the shock wave, respectively for both graphs. The lozenge points show the result for the case of p_4=1000 and p_1=50mbar. The square points show the result for the case of p_4=750 and p_1=37.5mbar. The trianglar points show the result for the case of p_4=500 and p_1=25mbar.

The propagation of the shock waves is confirmed in Figures 2 (a) and (b). It is occured that the shock waves were not been generated from the starting point. The shock wave forming distance depends on the opening time of the quickly opening valve. Additionally we have successed to catch the contact surfaces propagating from behind the shock waves. The contact surfaces were not clearly caught, after the center of the shock tube in the case by using air as the driver gas, near the end wall of the shock tube in the case by using helium as the driver gas. The reason without catching the contact surfaces is

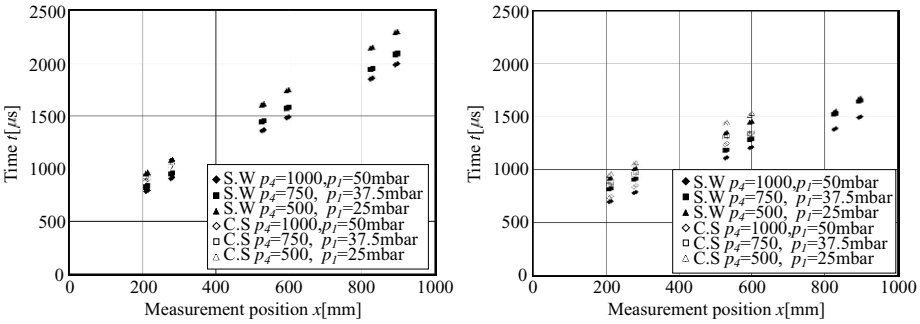

Fig. 2. (a) x-t diagram by using air as the driver and test gas (left), (b) x-t diagram by using helium as the driver gas and air as the test gas (right)

attributed to that the density change is too small in the case by using air as the driver gas, and the density gradient across the contact surfaces is too small by diffusion effect of the gases. Generally it is well known that the velocity of the shock wave depends on the pressure ratio p_4/p_1 as the Rankine-Hugoniot relation. However, the experimental results have denoted that the velocity of the shock wave also depends on the driver pressure p_4 and test pressure p_1 themselves. The distance L between the shock wave and the contact surface, which is used in the scaling parameter S, converges to steady value with propagating the shock waves, which is very small value.

Figures 3 (a) and (b) show the x-v diagrams from the experiments. The horizontal and the vertical axes are the distance x between the position of the quickly opening valve at the initial condition and the measurement position, and the velocity v of the shock wave. Figure 3 (a) shows the result which was obtained by using air as the driver and test gas. Figure 3 (b) shows the result which was obtained by using helium as the driver gas and air as the test gas. The normal points show the velocity of the shock waves for both graphs. The lozenge points show the result for the case of p_4=1000 and p_1=50mbar. The square points show the result for the case of p_4=750 and p_1=37.5mbar. The trianglar points show the result for the case of p_4=500 and p_1=25mbar.

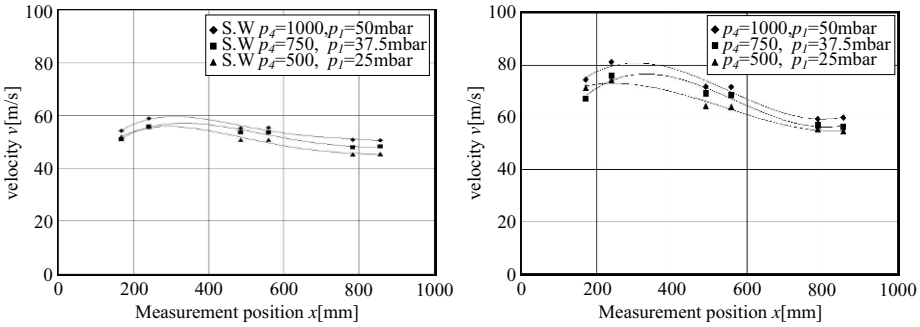

Fig. 3. (a) x-v diagram by using air as the driver and test gas (left), (b) x-v diagram by using helium as the driver gas and air as the test gas (right)

The velocities of the shock waves are accelerated near the quickly opening valve in both graphs. It is occured that the shock waves still have not been fully formed near the quickly opening valve, which is an aggregation of the pressure waves. Generally, the shock wave has propagated at the same velocity in the shock tube after the acceleration for the case of a large shock tube diameters. However, the shock waves become decelerated after indicating the maximum at approximately x=300mm. The reason of the deceleration is considered to the effect of the friction between the gas and the shock tube wall. This deceleration is one of the remarkable characteristic phenomena in the small scale shock tube.

Figure 4 shows the comparison of the experimental results and the CFD results on the x-t diagram. The vertical and holizontal axes are the time t and the measurement position x. In this case the driver gas and the test gas are air, and the driver gas pressure p_4 and the test gas pressure p_1 are 1000 and 50mbar respectively. The CFD results have the offset value of 450μs for the time direction to compare with our diaphragm-less experimental results. The gradient of the shock waves shows a good agreement with the experimental and the CFD results. However, the gradient of the contact surface obtained from the experimental results has the difference from the CFD results. This difference shows that the behavior of the shock waves has been influenced by the friction between the wall and the driver gas behind the contact surface, as it propagates in a small channel.

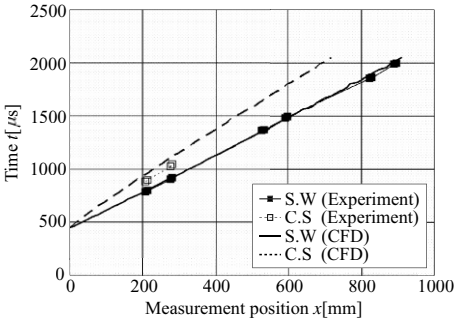

Fig. 4. Comparison of the experimental results and the CFD results on the x-t diagram (p_4=1000mmbar, p_1=50mmbar, driver/test gas: air/air)

5 Conclusion

In this paper we have performed the experiment by using a mini shock tube of 3mm diameter, which was developed by Garen, under the same pressure ratio condition by changing the measurement position for the case of air as the driver and test gas, and helium and air as the driver and test gas, respectively. We have also performed the numerical simulation for two-dimensional and axi-symmetric N-S equation. From our results the following points can be concluded.

(a). It is confirmed that the shock wave propagate with acceleration near the quickly opening valve in a small scale shock tube. The cause of acceleration is attributed to that the shock wave forming distance depnds on the opening time of the quickly opening valve.

(b). We have successed to catch not only the shock waves but also the contact surfaces by using the specially designed double laser interferometer. The contact surfaces are not clearly caught near the end wall of the shock tube. The reason without catching the contact surfaces is attributed to that the density gradient across the contact surfaces is too small by diffusion effect of the gases.

(c). The velocity of the shock waves is no longer only a function of the pressure ratio p_4/p_1 but also is correlated to the initial driver pressure p_4 and p_1 at a small scale shock tube.

(d). The shock waves are decelerated after indicating the maximum at approximately x=300mm. The cause of deceleration is attributed to the effect of the friction between the gas and the shock tube wall. This deceleration is one of the remarkable characteristic phenomena of a small scale shock tube.

(e). The behavior of the shock waves and contact surfaces obtained from the experiments has the difference between the numerical simulation. The reason of the difference is considered to the friction between the wall and the gas.

Acknowledgement. The first author would like to express his best gratitude to German Academic Exchange Service (DAAD). This work was performed during the author's stay in Germany, financed by a scholarship from DAAD.

References

1. W. Garen, et.al.: A novel mini-shock tube for generating shock waves at micro scales in turbulent and laminar gas flows. In: *Proceedings of 25th International Symposium on Shock Waves*, ed by K.P.J. Reddy (Springer-Verlag, 2005) pp.746-750.
2. K. Takayama.: Applications of shock wave research to medicine. In: *Proceedings of 22nd International Symposium on Shock Waves*, ed by G.J. Ball, et.al. (1999) pp.321-326.
3. M. Brouillette: Sock waves at micro scales, Shock Waves, **vol.13**, (2003) pp3.-12.
4. B.J. Belhouse, et.al.: Needle-less delivery of drugs, in dry powder form, using shock waves and supersonic gas flow. In: *Proceedings of 21st International Symposium on Shock Waves*, (1997) pp.51-56
5. M.A.F. Kendall: The gas-particle dynamics of a high-speed needle-free drug delivery system. In: *Proceedings of 22nd International Symposium on Shock waves*, ed by G.J. Ball, et.al. (1999) pp.605-610.
6. D.D. Dlott: Nanoshocks in molecular materials, Accounts of Chemical Research, American Chemical Society, **vol.33**, (2000) pp.37-45.
7. W. Garen, et.al.: Shock tube for generating weak shock waves, AIAA-Journal, **vol.12**, (1974) pp.1132-1134.

Investigation of a planar shock on a body loaded with low temperature plasmas

F.-M. Yu and M.-S. Lin

Institute of Aeronautics and Astronautics,
National Cheng Kung University, Tainan 701, Taiwan

Summary. The qualitative study of the interaction between planar shock wave and a hemisphere-cylinder model with and without corona discharge plasma from its copper head have been done in the shock tube facility of Institute of Aeronautics and Astronautics in National Cheng-Kung University. With the incident Mach number of 1.3-1.69, the shock wave reflected on the model with regular reflection and transition to Mach reflection have been observed for model without corona discharge plasma. With the corona discharge plasma effect from the model copper head, the similar shock wave patterns were observed. However, a widening thickness of the shock and a shortening of the length of the Mach stem were observed and the location of the triple point is closed to the model surface. The curvature of the reflected shock wave is being increased. From the measured pressure signal of the relative strength of the shock reflection from the model head, a longer time is need and the measured signal strength is much smaller. It has clearly shown that under the effect of corona discharge plasma the shock reflection from the model head with a smaller speed and a much weaker strength. This is a strong indication that the corona discharge plasma can decrease the strength of shock wave properly.

1 Introduction

The directly energy addition in front of a moving object has been proposed to reduce the aerodynamics drag in supersonic flight. The former experiments demonstrated that with a direct energy addition in the shock wave the original strong bow shock wave produced by blunt body can be reduced to a weaker benign conical shock wave [1] [2]. Some experimental results from wind tunnel testing as well as the numerical results from CFD have shown the plasma induced drag reduction by locally applied high energy to some special positions in the stream [3]. The study indicates that there are three main reasons for drag reduction under the plasma shock wave interaction conditions. It includes the gas heating in the discharge which may lead to decrease of the local flow Mach number and shock wave structure rearrangement, the ionization in the discharge plasma which may cause the changes of gas density and the charged particles from the plasma which may lead to upstream momentum transfer [4]. It has shown that a proper gas energy arrangement between body and the shock wave has a major effect on the strength of the detached shock. Based on this consideration, an experiment has been prepared by loading a blunt body model which has a hemispherical copper front surface with an extra high voltage (200KV) in a shock tube facility and to examine the shock reflection over the model with low temperature plasma discharge in front of it. Since low temperature plasma technology is a comprehensive science and the control cost is low. There are five categories of low temperature plasma discharge techniques, which are glow discharge plasma, corona discharge plasma, dielectric barrier discharge plasma, RF discharge plasma, and microwave discharge plasma [5]. Normally, corona discharge (PCD) and dielectric barrier discharge (DBD) are relatively suitable discharge modes

and the average energy of electrons of them is in the range of 1 eV to 10 eV. For the convenient on the arrangement of model inside the shock tube facility, a corona discharge plasma technique is being used.

2 Experimental Setup

The experiment has been done in the shock tube facility of Institute of Aeronautics and Astronautics in National Cheng-Kung University. The sketch of shock tube facility and the major dimensions are shown in Figure 1. The test section with square inner section (66.4mm × 66.4mm) and a length of 1000mm is connected at the end of driven section. A pair of windows with a diameter of 34mm locates on both sides of test section to observe the flow field. Two piezoelectric pressure transducer and charge amplifier (Model 113A24 and Type 507, PCB) are employed in this experiment to derive the shock speed in test section. The data acquisition is done by a transient recorder (Model W+W700, Kontron). A cylindrical model with a hemispherical copper front surface of a total length

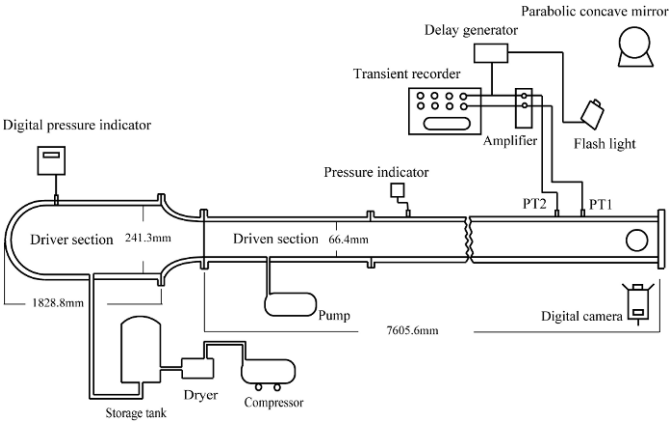

Fig. 1. Layout of the shock tube facility

of 70 mm is mounted at the center of the end plate of the driven section. The diameter of the spherical nose model is 15 mm which is attached to a cylinder body of bakelite with a length of 55 mm as shown in Figure 2. The high voltage power system is obtained from modifying of a stun gun power supply system which is operated by a 6V battery. The high voltage power system is packaged inside a metal box to prevent from electromagnetic interference with the electronic equipments in the laboratory. It offers a working voltage of 200KV, a working current of 0.8 amp, and a working time of 5 seconds. A color Schlieren technique is used to visualize the flow and wave structure in the shock tube. The light source has pulse duration of 650ns and pulse power of 6 J per pulse (PALFLASH500, Photonics Co.). A digital camera is employed at the ISO of 800 to record the Schlieren picture (Nikon D100). The layout of the color Schlieren is shown on Figure 2 also.

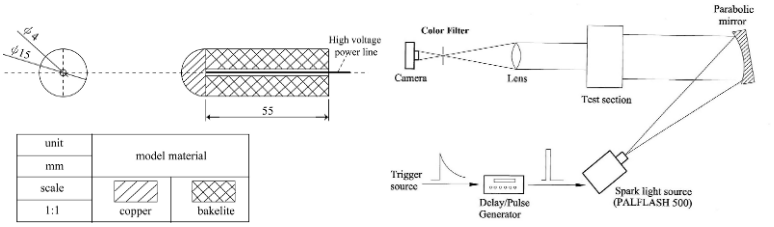

Fig. 2. The schematic configurations of testing model and color Schlieren system

3 Results and Discussion

The typical results of a pair of color Schlieren pictures of planar shock reflection from a hemisphere-cylinder model with an incident shock wave Mach number of Ms=1.36 is shown in Figure 3.. The dissection of the color filter is designed with green as a reference color between colors of blue and red. The light refracts from high density region toward low density region will offer red color and for opposite refraction direction it is of blue color. On both pictures show that on the top of model head, the light refracts from the high density region toward low density region so the color of reflected shock wave is blue and the incident shock is of red color. A more saturation on color indicates a higher density gradient in flow field. For the incident planar shock wave from Ms=1.36 to Ms=1.67, the results of color Schlieren pictures indicate it reflects from the model to form a regular reflection (RR) pattern as it is passing the model head. Following with shock wave propagates downstream the model head surface, the angle between the incident shock and the tangent on its root over the hemisphere is increasing and the regular reflection pattern is gradually transition into a Mach reflection (MR) pattern as shown. However, since the density gradient exists for both horizontal direction and vertical direction near the triple point, in such a three dimensional flow field only a weak light deflection in horizontal direction near this position and which can not be resolved by

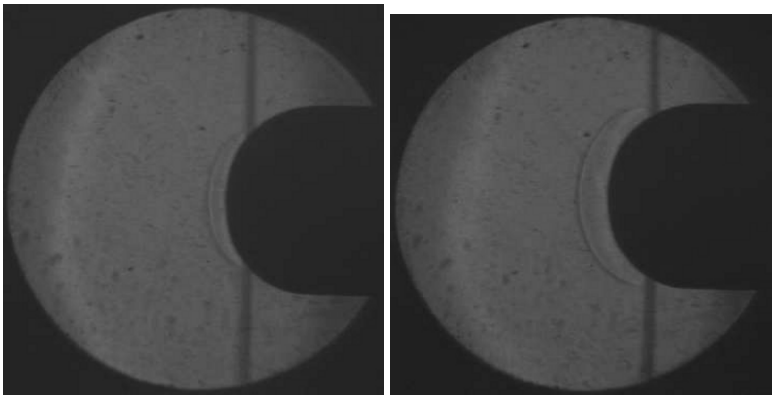

Fig. 3. Typical Color Schilieren pictures of shock reflection on model head at Ms=1.36

current optical arrangement. Thus it can only show the background color of green here. The typical Schlieren pictures of shock wave reflection on a hemisphere-cylinder model with and without corona discharge plasma effect over the model head are shown on Figure 4. For the condition of Ms=1.55. With the effect of plasma, the shock reflection is under the influences of an inhomogeneous gas temperature distribution on the hemisphere surface due to corona discharge. It leads to a spreading, broadening and weakening of the shock reflection on it as observed on the Schlieren pictures on Figure 4. The effect becomes clearer as the reflection shock wave moving away from the model head as shown on Figure 5. It also shows that the curvature of the reflection shock is increased. Under the effect of plasma, a widening thickness of the shock and a shortening of the length of a Mach stem are observed and the location of the triple point is close to the model surface which causes the radius of curvature of the reflected shock wave decreased. For the

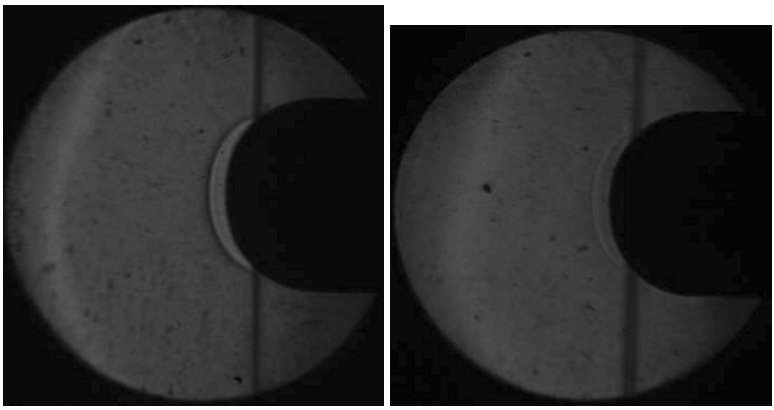

Fig. 4. Typical Color Schilieren pictures of shock reflection on model head at Ms=1.55, Right: with conrona discharge plasma, Left: without.

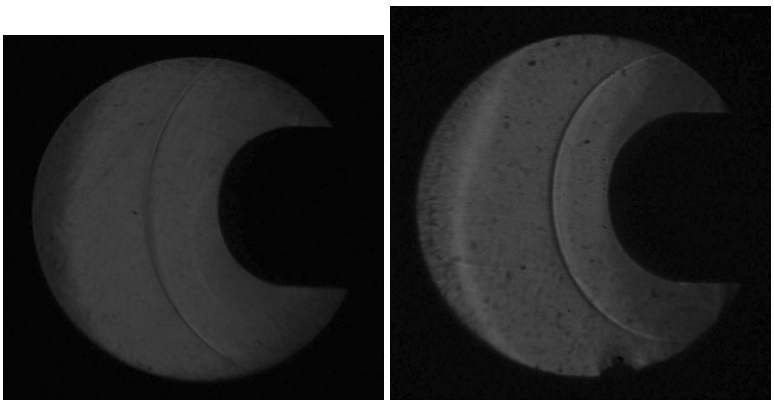

Fig. 5. Typical Color Schilieren pictures of shock reflection away from model head at Ms=1.55, Right: with conrona discharge plasma, Left: without.

incident planar shock wave from Ms=1.36 to Ms=1.67, the color Schlieren observation indicates that dispersion of reflection shock increases with the increasing of incident shock wave strength. Moreover, it depends not only on the shock strength but also on the propagation distance over the surface with corona discharge plasma.

A typical comparison on the measured pressure signal of the relative strength of the shock reflection from the model head with and without corona discharge plasma for Ms=1.55 is shown on Figure 6. With corona discharge plasma, it takes a longer time and the measured signal strength much smaller for a reflected shock to reach the pressure transducer. It is clearly shown that under the effect of corona discharge plasma the shock reflection from the model head with a smaller speed and a much weaker strength. It indicates the corona discharge plasma can decrease the strength of shock wave properly.

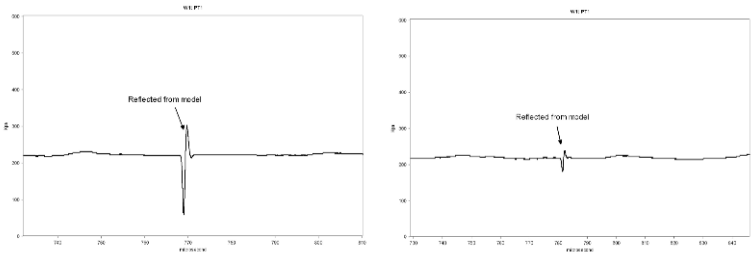

Fig. 6. The measured pressure signal on the relative strength of the shock reflection from model head at Ms=1.55, Right: with corona discharge plasma, Left: without.

4 Conclusion

With the incident Mach number of 1.3-1.69, the shock wave reflected on the hemisphere-cylinder model with regular reflection and transition to Mach reflection pattern have been observed for model without corona discharge plasma. With the corona discharge plasma effect from the model copper head, the similar wave patterns were observed. However, a widening thickness of the shock and a shortening of the length of the Mach stem were observed. With the location of the triple point is closed to the model surface which causes the radius of curvature of the reflected shock wave decreased. From the measured pressure signal of the relative strength of the shock reflection from the model head, a longer time is need and the measured signal strength is much smaller. It has clearly shown that under the effect of corona discharge plasma the shock reflection from the model head with a smaller speed and a much weaker strength. It is a strong indication that the corona discharge plasma can decrease the strength of shock wave properly.

References

1. Sohail H. Zaidi, M. N. Shneider, D. K. Mansfield, Y. Z. Ionikh, and R. B. Miles, Influence of Upstream Pulsed Energy Deposition on a Shockwave Structure in Supersonic Flow, AIAA Paper 2002-2703, 2002

2. [2] Yu. Z. Ionikh, N. V. Chernysheva, A. P. Yalin, S. O. Macheret, L. Martinelli, and R. B. Miles, Shock Wave Propagation through Glow Discharge Plasmas: Evidence of Thermal Mechanism of Shock Dispersion, AIAA Paper 2000-0714, 2000
3. Sun Zongxiang, Progress in Plasma Assisted Drag Reduction Technology, Advances in Mechanics, Vol. 33, No. 1, 2003
4. V. I. Khorunzhenko, D. V. Roupassov, and A. Yu. Starikovskii, Hypersonic Flow and Shock Wave Structure Control by Low Temperature Nonequilibrium Plasma of Gas Discharge, AIAA Paper 2002-3569, 2000
5. Eliasson B, Kogelschatz U. IEEE Transaction on Plasma Science, 1991, vol. 19, No. 6, pp. 1063-1077

Numerical, theoretical and experimental study of shock wave reflection from a layer of spherical particles

E. Timofeev[1], G. Noble[1], S. Goroshin[1], J. Lee[1], and S. Murray[2]

[1] *Department of Mechanical Engineering, McGill University, 817 Sherbrooke St. West, Montreal, Quebec H3A2K6, Canada*
[2] *DRDC Suffield, Box 4000, Stn Main Medicine Hat, Alberta T1A 8K6, Canada*

1 Introduction

The problem of a shock wave interacting with a porous medium (reflection and transmission) is of interest to both, practical applications and fundamental gasdynamic theory. For practical applications, a porous medium can be used to attenuate both the reflected and transmitted shock wave. From the fundamental theory point of view, the transient gasdynamic processes subsequent to reflection off a porous interface and the propagation of the dispersive shock wave through the porous medium are not well understood both qualitatively and quantitatively. The majority of the investigations to date are concentrated on the propagation of the transmitted shock [1]. Much less attention has been devoted to the reflected shock from the porous interface. The objective of the present study is to access the effectiveness of the porous interface in attenuating the reflected shock.

2 Experiments

Shock wave reflection from a packed bed of spheres has been studied using two detonation-driven shock tubes (a vertical one, 15 cm in diameter, and a horizontal one, 30 cm in diameter) for incident shock wave Mach numbers of 1.6, 2.0, 2.1, and 2.4. For each of these Mach numbers, six sphere diameters (steel balls) have been tested: 0.125, 0.25, 0.50, 0.75, and 1.0 inches in the 15 cm diameter tube and 2.5 inches in the 30 cm diameter tube. PCB pressure transducers have been used as the main diagnostic tool.

The 15 cm diameter tube was oriented vertically for all experiments in order to allow the packed bed of spheres to be maintained at one end without the need for a retaining screen. Due to the weight of the 30 cm diameter tube it was mounted horizontally. Thus, several small parallel rods were fixed in front of the packed bed to contain the 2.5 inches diameter spheres at the end of the tube. It was determined that the thin rods (0.25 inches in diameter spaced by 2 inches) used in the 30 cm diameter tube did not interfere appreciably with the reflection from porous media.

The strength of the reflection is quantified by a ratio comparing the experimental pressure ratio with the pressure ratio for a plane shock wave at the same incident Mach number M_s reflecting normally from a solid impermeable wall:

$$R_{\mathrm{exp/solid}} = \left(\frac{p_3}{p_1}\right)_{\mathrm{exp}} \Big/ \left(\frac{p_3}{p_1}\right)_{\mathrm{solid}} \cdot 100\% \quad , \tag{1}$$

where p_1 is the initial pressure in the test section and p_3 is the pressure behind the reflected shock.

For the reflection of a plane shock wave with a step-like profile from a solid wall we should obviously get $R_{\text{exp/solid}} = 100\%$ regardless of the incident Mach number value. In our experiments, the incident shock is followed by the expansion waves (due to the finite size of the driver and the Taylor wave profile of the detonation wave in the driver section). For shocks traveling at approximately $M_s = 2.0$, a good agreement (discrepancy is less than 1%) between the experimentally and theoretically determined reflected shock pressures is obtained. For slower shocks, near $M_s = 1.6$, the experimentally determined reflected shock pressure is approximately 94% of the theoretically predicted value. For shocks traveling near $M_s = 2.4$, the experimentally determined reflected shock pressure is approximately 104% of the theoretically predicted pressure. This trend should be taken into account when interpreting the results obtained for shock wave reflection from packed beds of spheres.

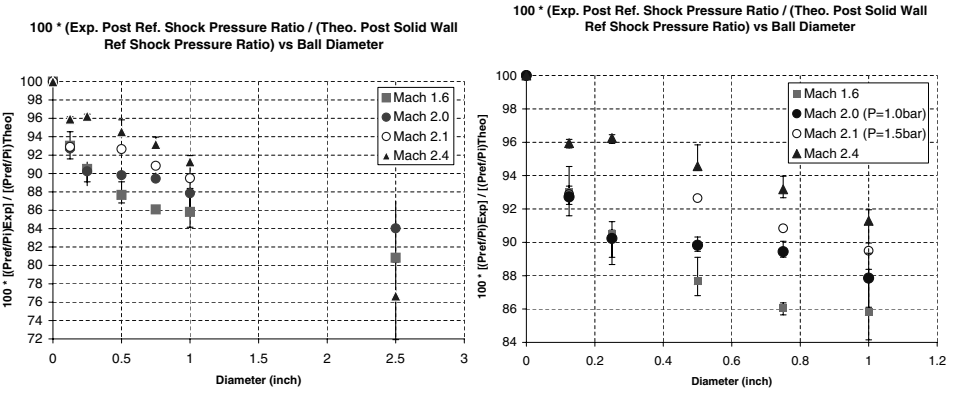

Fig. 1. Experimental results for reflected shock wave attenuation with a packed bed of spheres. The right image enlarges the results for smaller ball diameters (all obtained using the 15 cm diameter shock tube).

Figure 1 shows the experimental results obtained for shock waves at $M_s = 1.6$, 2.0, 2.1 and 2.4 reflecting off a packed bed of spheres. Two general trends can be seen. First, as the ball diameter decreases while the incident shock strength is kept constant, the reflected shock strength increases toward 100% corresponding to the reflected shock strength for a solid impermeable wall. In other words, the attenuation of the reflected shock would be more effective if large balls were used.

Second, keeping the ball diameter constant as Mach number of the incident shock is increased, it is seen that the ratio of the experimentally determined reflected-shock pressure to the theoretical value for reflection from a solid wall increases. In other words, for a given ball diameter, the relative strength of the measured reflection from porous media increases as the strength of the incident shock is increased, i.e., porous media attenuates more effectively the reflection of shock waves with lower incident shock Mach numbers. However, it should be emphasized that the influence of the incident shock Mach number is, in fact, much less pronounced if we take into account that in our

experiments the intensity of the reflected shocks corresponding to lower incident shock Mach numbers (1.6) is underestimated while for higher incident shock Mach numbers (2.4) it is overestimated as explained above.

3 Theoretical analysis

For the open area ratio and incident shock Mach number values of our experiments, the flow through the packed bed of spheres is choked at the minimum area shortly after the incident shock enters the granular media (see also [2]). The condition of choking allows the calculation of the reflected shock wave intensity using simple theoretical considerations.

The Mach number M_3 behind the reflected shock under the choking condition can be obtained from the open area ratio f using the well-known area-Mach number relation for quasi-one-dimensional isentropic flow:

$$\frac{1}{f} = \frac{1}{M_3} \cdot \left\{ \left(\frac{2}{\gamma+1} \right) \left[1 + \frac{\gamma-1}{2} M_3^2 \right] \right\}^{\frac{\gamma+1}{2(\gamma-1)}} . \tag{2}$$

The ratio $p_{31} = p_3/p_1$ can be obtained using the following expression:

$$\frac{p_{31}}{p_{21}} = 1 + \frac{(p_{21}-1)\sqrt{1 + \frac{\gamma+1}{\gamma-1} \cdot \frac{p_{31}}{p_{21}}}}{\sqrt{p_{21}\left(\frac{\gamma+1}{\gamma-1} + p_{21} \right)}} - \gamma M_3 \sqrt{\frac{\gamma-1}{2\gamma} \frac{p_{31}}{p_{21}} \left(\frac{\gamma+1}{\gamma-1} + \frac{p_{31}}{p_{21}} \right)} , \tag{3}$$

where $p_{21} = p_2/p_1$ and p_2 is the pressure behind the incident shock. This equation is valid for $M_3 = 0$ as well, resulting then in the pressure ratio p_{31} for the reflection from a solid impermeable wall.

Finally, a ratio, $R_{\text{porous/wall}}$, between the reflected-shock pressure ratio for porous medium reflection and the reflected shock pressure ratio for solid wall reflection is written analogously to Eqn. (1) as:

$$R_{\text{porous/wall}} = \left(\frac{p_3}{p_1} \right)_{\text{porous}} / \left(\frac{p_3}{p_1} \right)_{\text{wall}} \cdot 100\% . \tag{4}$$

The open area ratio f can be related to the porosity ϵ using the packing angle ω (60° in Fig. 2a):

$$\epsilon = 1 - \frac{\pi}{6(1-\cos\omega)\sqrt{1+2\cos\omega}} , \quad f = 1 - \frac{\pi}{4\sin\omega} . \tag{5}$$

It is illuminating to plot the attenuation ratio vs. porosity for the same incident shock Mach numbers as were tested in the experiments, see Fig. 2c. Since increasing ball diameters corresponds to increasing porosity, Fig. 2c should be considered as the theoretical counterpart of Fig. 1 summarizing all experimental results. It is seen that Fig. 2c demonstrate the same trends which were mentioned when discussing the experimental results: (a) For the same incident shock Mach number, medium with higher porosity leads to better relative attenuation of the reflected shock; (b) For the same porosity, higher

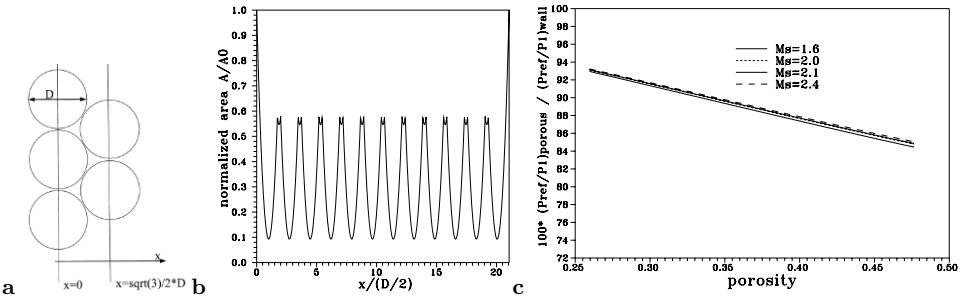

Fig. 2. a Schematic of two adjacent layers of spheres; **b** Corresponding area variation; **c** Theoretical ratio of the strength of the shock wave reflected from a porous medium to the strength of the shock wave reflected from a solid impermeable wall for different Mach numbers of the incident shock wave as a function of porosity.

incident shock Mach number results in relatively stronger reflected shock. As seen in Fig. 2c, the theory predicts rather insignificant (less than 0.5%) variation of the relative attenuation ratio with the incident shock Mach number. The scatter of the experimental results in Fig. 1 is of the order of 6-8%. This can be explained by the fact that in our experiments with the reflection from solid wall we have about 10% scatter of the relative attenuation ratio for different Mach numbers around the exact value of 100%: from 94% to 104%. Normalization of the experimental results for a packed bed of spheres by their counterparts for solid wall reflection (as opposed to the normalization by the theoretical pressure ratio as in Eqn. 1) brings the experimental values for different Mach numbers much closer, as predicted by the theory.

Basing on the data available in literature [3–5], it is reasonable to assume that for the smallest (0.125 inches) balls the porosity is about 0.36, and hence, according to Fig. 2c, the relative attenuation ratio is about 89-90%. The largest (2.5 inches) balls would correspond to the porosity value in the range 0.45-0.50, with the relative attenuation ratio of 84-86%. These numbers are somewhat less than we have in the experiments (Fig. 1). This is because in the theory we assume that as long as the flow chokes, no disturbances come out of the porous medium and propagate upstream, and thus the intensity of the reflected shock does not change with time. In fact, some compression waves reflected from the granular filter internal structures may propagate upstream, catch the reflected shock and amplify it. This phenomena is addressed in more detail below when discussing numerical simulation results.

4 Numerical modeling

To achieve a better understanding of the reflection and transmission phenomena from a porous bed, numerical modeling of shock wave reflection from porous media is also carried out using quasi-one-dimensional approach and the Euler (i.e. inviscid, non-heat-conducting) gas model. The quasi-one-dimensional Euler equations are solved using a second-order in space and time Godunov-type upwind finite-volume scheme on an unstructured adaptive mesh [6]. The porous media is represented by an area variation cor-

responding to the most densely packed bed of spheres with the packing angle of $\omega = 60°$ (Fig. 2a). Slicing the bed with planes normal to the incoming flow direction, the following normalized area distribution can be obtained from geometrical considerations (not taking into account boundary effects):

$$\frac{A}{A_0} = \begin{cases} 1 - \dfrac{\pi}{2\sqrt{3}}[1 - \overline{x}^2], & \text{if } 0 \le \overline{x} \le \sqrt{3} - 1; \\ 1 - \dfrac{\pi}{2\sqrt{3}}\big[-2\overline{x}^2 + 2\sqrt{3}\,\overline{x} - 1)\big], & \text{if } \sqrt{3} - 1 \le \overline{x} \le 1; \\ 1 - \dfrac{\pi}{2\sqrt{3}}\big[1 - (\sqrt{3} - \overline{x})^2\big], & \text{if } 1 \le x \le \sqrt{3}; \end{cases} , \tag{6}$$

where $\overline{x} = x/(D/2)$. Equation (6) is graphically represented in Figure 2b.

Figure 3 shows the result of shock wave ($M_s = 2.0$) reflection from a packed bed of spheres modelled by the area variation of Eqn. (6) (Fig. 2b). Twelve ball layers are considered which roughly corresponds to the experiments with 2.5 inches balls in the 30 cm diameter shock tube. The packed bed is considered to be adjacent to a wall, so that no transmitted shock takes place. It is seen that the intensity of the reflected shock varies gradually and initially it is lower than it would be at the solid wall reflection. At later moments, the intensity increases due to disturbances coming upstream from the packed bed. It is not possible to track individual disturbances coming upstream. Figure 3b shows a part of the x-t diagram of Fig. 3a in the vicinity of the entry (reflection) plane using much smaller contour steps as compared to Fig. 3a. This helps to visualize some disturbances coming upstream but still it would be difficult to pinpoint their origin.

It is required about 9 thicknesses of the porous layer for the reflected shock to fully recover its intensity to the level of the reflected shock from impermeable solid wall. In

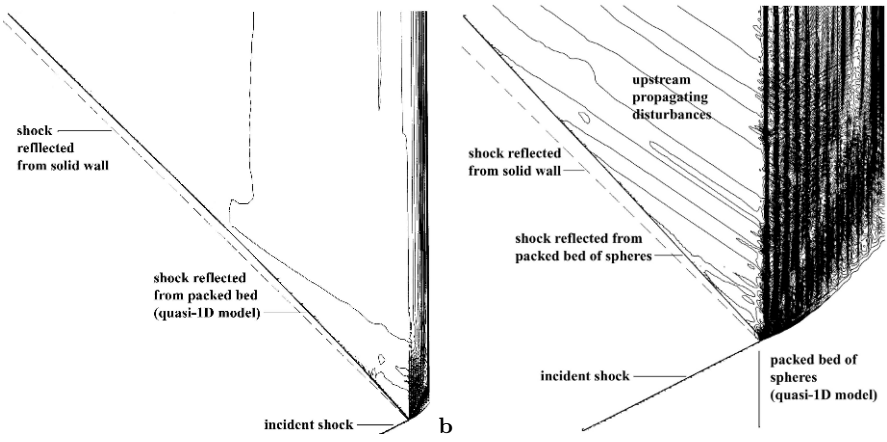

Fig. 3. a Plane shock wave ($M_s = 2.0$) interaction with a packed bed of spheres (12 layers) modeled by area variation given by Eqn. (6) (see also Fig. 2a,b). Solid lines represent x-t diagram of the process. Dashed line corresponds to the reflection of the same shock from the solid wall. **b** Detail of the x-t diagram shown in Fig. 3a in the vicinity of the reflection plane.

our particular experiments, in which the granular medium section was either 67 cm (the 30 cm diameter tube) or 30 cm (the 15 cm diameter tube) long, that makes quite long distances: about 6 m and 3 m, respectively. This implies that using pressure transducers located close to the reflection plane, as we do, it is possible to measure the reflected shock strength near the reflection plane without significant spatial/temporal averaging. At the same time, it is obvious that to get very accurate experimental measurements for such a gradual, long distance variation over the whole range is a challenge.

In experiments, due to dissipative effects inside the porous media, the reflected shock strength would not asymptote to the solid wall reflection value. At the same time, the incident shock wave and the waves generated by it inside the porous media undergo reflections and these reflected shock (compression) waves propagate upstream and strengthen the reflected shock. That is why our experimental results (Fig. 1) are somewhat higher than the values given by the choked flow theory (Fig. 2) which does not consider such reflected disturbances.

5 Conclusions

Our overall conclusion is that porous media in the form of a packed bed of solid particles is not a very effective way to decrease the intensity of the reflected shock wave, especially so if porous layer is attached to a solid wall, so that no transmitted shock/flow occur. The best possible attenuation does not exceed 15%, as compared to the reflection from a solid wall without any porous media. To achieve better attenuation, higher porosities (open area ratios) should be used, i.e. larger and perhaps more irregular granular particles. The reflected shock is better attenuated if the other end of granular filter is left open allowing a continuous propagation of the transmitted shock and flow through the filter. When resorting to the quasi-one-dimensional modeling (theoretical under the choked flow assumption or numerical), we should use in the model the same open area ratio as in the actual medium to be modeled. Hence, the porosity measurements with the subsequent deduction of open area ratio are important. In case there are no appreciable disturbances propagating upstream from the granular filter and subsequently catching up with the reflected shock, the quasi-one-dimensional inviscid model provides reliable estimates of the reflected shock intensity. If such disturbances are present, the reflected shock will be somewhat stronger than predicted by the model.

References

1. Timofeev E., Lee J.: Shock wave interaction with granular materials: a literature review and some preliminary considerations. Report, SWACER Inc., Montreal, February 2004
2. Franks W.J.: UTIA Tech. Note No. 13, May 1957
3. Medvedev S.P., Frolov S.M., Gelfand B.E.: Eng. Phys. J. (USSR) **55**(6), 924-928 (1990)
4. Slungaard T.: Hydraulic resistance, shock wave attenuation and gaseous detonation extinction in granular materials. PhD thesis, Norwegian Univ. of Science and Technology (2002)
5. Zieve R.: http://london.ucdavis.edu/∼zieve/Research/balls.html (2004)
6. Tahir R., Timofeev E.: `Solver I` – One-dimensional, multi-gas, adaptive, unstructured, time-dependent CFD application for MS Windows. Email: rabi.tahir@rogers.com, timofeev@sympatico.ca (1999-2007)

Numerical simulation of interactions between dissociating gases and catalytic materials in shock tubes

V.V. Riabov

Department of Computer Science, Rivier College, Nashua, New Hampshire 03060 USA

Summary. A numerical method has been developed to study interactions between gas flows and catalytic materials of the shock-tube end after shock wave reflection at high temperature conditions. The study is based on computations of nonequilibrium multicomponent gasdynamic parameters in air and analysis of the nonsteady-state thermal boundary layer near the tube end.

1 Introduction

Shock tubes have become widely used to study thermodynamic processes in high temperature gas flows [1], [2] and chemical kinetics [3], [4]. Flow parameters behind incident and reflected shock waves were analyzed by Gaydon and Hurle [1], Bazhenova et al. [2], Sturtevant and Slachmuylders [5], Goldsworthy [6], Johannesen et al. [7], and Hanson et al. [8]. It was found that the gas behind the reflected shock wave is practically at rest in the laboratory coordinate system, and the temperature in this area is approximately twice as high as behind the incident shock wave.

The purpose of the present study is to analyze heat transfer processes at the catalytic materials of the shock-tube end after shock wave refraction in terms of the model of the nonsteady-state nonequilibrium thermal boundary layer developed by Provotorov and Riabov [9], [10], [11]. The analysis [9] covered the time interval from 10^{-9} sec to 2.5 μsec, and it was restricted by the applied numerical method. In the present study we have developed the numerical algorithm and studied gasdynamic parameters and component concentrations in the layer for the time interval up to 100 μsec. The parameters behind the reflected shock wave [1], [2], [9], [11] were evaluated as the external boundary conditions for the layer. The nonequilibrium parameters in this area are the functions of initial parameters such as pressure and temperature in the shock-tube channel, velocity of the incident shock wave, etc. The dissociation, recombination and exchange reactions [4], [12] among the air components (O_2, O, NO, N_2, and N) were considered. At the shock-tube end a union boundary condition [5], [6], [7], [9] for temperature and heat flux was used, as well as a boundary condition for recombination of atomic components. Unfortunately, the identical experimental data are unknown to the author.

2 Gas flow behind the incident shock wave

We have considered the simplest model [1], [2], [9] of the one-dimensional inviscid dissociating gas flow behind the incident shock wave, which propagated in an ideal air with parameters of pressure $p_1 = 1$ and 100 Pa, and temperature $T_1 = 295$ K at constant velocity $U_S = 5$ km/s. The system of chemical reactions occurring in the five-component mixture and reaction constants used in the present study were described in [4], [12].

The algorithm of calculation of the parameters behind the incident and reflected shock waves is described by Provotorov and Riabov [9] in detail. The system of algebraic-differential equations [9] has been solved at each point of the flow field behind the incident shock wave under the assumption that air is not dissociated on the shock wave front. A modified Newton's method [13] with optimal choice of iteration step was used for numerical solution of the equations. The flow parameters behind the incident shock wave

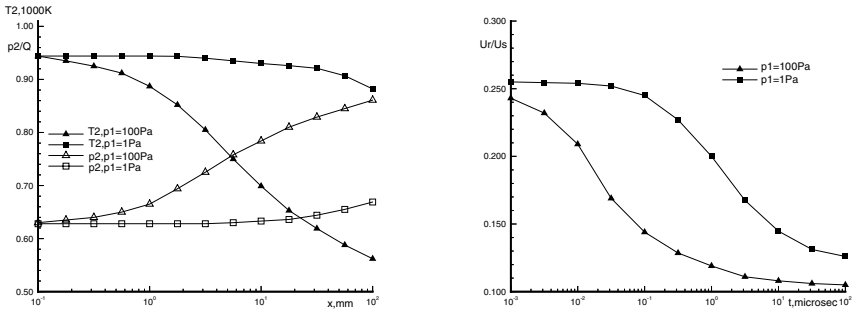

Fig. 1. Temperature T_2 and pressure p_2 behind the incident shock wave as a function of distance from the wave front (*left*), and velocity of the reflected shock wave U_{R} as a function of time (*right*) at various initial pressure parameters: $p_1 = 1$ Pa (*squares*) and $p_1 = 100$ Pa (*triangles*)

are shown in Fig. 1 (*left*). The solutions obtained for temperature and pressure are typical for dissociating gas flows with nonequilibrium relaxation [1], [2], [7], [8], [9]. For small time interval ($t \approx 10^{-8}$ sec) the gas state is frozen [2], while at large distances from the shock wave (at $t \geq 10^{-5}$ sec and $p_1 = 100$ Pa) the flow parameters tend to their limiting equilibrium values [2]. With decrease in initial pressure up to $p_1 = 1$ Pa the equilibrium state is reached at significantly distances, while at $t < 10^{-5}$ sec the flow parameters differ little from frozen.

3 Gas flow behind the reflected shock wave

The reflected shock wave is propagated in the disturbed field after the incident shock wave [7], [8]. The velocity of the reflected shock wave U_{R} as a function of time, for two cases of pressure $p_1 = 1$ and 100 Pa, is plotted in Fig. 1 (*right*) (squares and triangles, correspondingly). The decrease of the values U_{R} indicates the nonequilibrium type of chemical reactions behind the incident shock wave [8]. The magnitude of pressure p_1 defines the time required for attainment of the steady-state distribution. And this time is less by approximately a factor of 100 for the case of $p_1 = 100$ Pa. Therefore, the parameter U_{R} becomes very convenient for experimental verification of the nonequilibrium parameters in the areas behind the shock and near the end of the tube.

Using the technique developed by Provotorov and Riabov [9], the distribution of temperature T_3 and pressure p_3 behind the reflected shock wave was calculated. The computational technique was used as the same one that was discussed above for the case

of the incident shock wave. The computational results are shown in Fig. 2 (*left*) at the same cases of the initial pressure p_1. The distribution of temperature T_3 [see Fig. 2 (*left*)] is similar to the distribution of the velocity U_R of the reflected shock wave and it can be useful for the identification of the type of the chemical processes behind the shocks [7], [8]. The values of temperature T_3(t) were used as the external ("outer") boundary conditions for temperature in the thermal viscous layer near the tube end. Figure 2 (*left*) presents

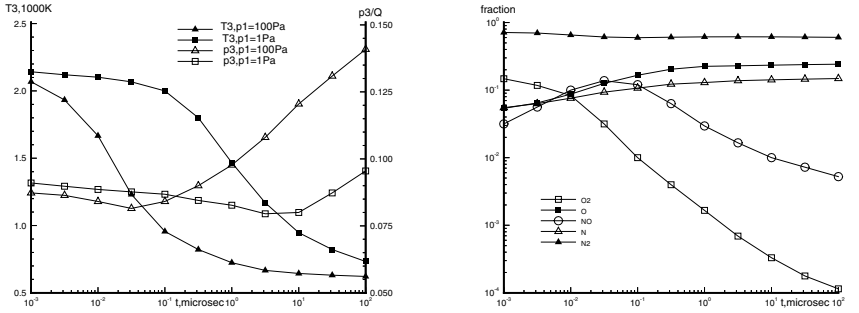

Fig. 2. Temperature T_3 and pressure p_3 behind the reflected shock wave as a function of time at various initial pressure parameters: $p_1 = 1$ Pa (*squares*) and $p_1 = 100$ Pa (*triangles*) (*left*), and mass fractions α_i in air behind the reflected shock wave at $p_1 = 100$ Pa (*right*)

also the computational results for pressure p_3 behind the reflected shock wave as a function of time. This parameter is the most conservative one. Nevertheless, for the case of the large value of initial pressure $p_1 = 100$ Pa (triangles) the significant increase of the values p_3 is observed after the short initial time-interval of decreasing. This is a result of the influence of different types of chemical relaxation processes behind the incident wave with initial pressure p_1 [5], [6], [8], [9]. The initial decrease of p_3 is explained by rapid chemical relaxation behind the reflected shock wave [8]. As presented in Fig. 2 (*left*), the temperature distribution T_3(t) indicates this type of chemical process in the region. In the case $p_1 = 100$ Pa, the flow behind the reflected shock wave is close to a state of local thermodynamic equilibrium [2], while in the other case $p_1 = 1$ Pa, the flow is significantly in nonequilibrium [8], [9]. The function p_3(t) can be used for the prediction of pressure in the thermal viscous layer near the tube end, and it correlates with the value of pressure p_w(t) at the tube end.

Additional important information is the distribution of the air components behind the reflected shock wave. This data [shown in Fig. 2 (*right*)] has been used as external boundary conditions for the component mass concentrations in the thermal viscous layer under the considered conditions.

4 The thermal viscous layer near the tube end

Behind the reflected shock wave the thermal viscous layer begins to grow near the tube end [5], [6], where a union boundary condition for temperature and heat flux is used,

as well as a boundary condition for recombination of atomic components. The acceptable model of a nonsteady-state nonequilibrium thermal boundary layer [6], [9] could be considered in this area. The gasdynamic functions in the layer are determined by the following dimensional parameters [9]: t_*, ρ_*, μ_*, $p_* = \rho_* {U_S}^2/2$, $l = U_S t_*$, $\delta_* = (\mu_* t_*/\rho_*)^{0.5}$, $u_* = \delta_*/t_*$, which are the characteristic time, density, viscosity, pressure, length, and layer thickness. Below we treat all functions and variables as dimensionless, referenced to their characteristic values.

Comparing the values of two parameters l and δ_*, the main perturbation parameter ϵ can be introduced:

$$\epsilon^2 = (\delta_*/l)^2 = \mu_*/(\rho_* {U_S}^2 t_*)$$

Using the perturbation technique, the independent variables and functions in the near-wall flow area at the tube end can be described in terms of series [9], [10]:

$$x = \epsilon x^{(1)} + ..., t = t^{(0)}, u = \epsilon u^{(1)} + ..., T = T^{(0)} + ..., \rho = \rho^{(0)} + ..., \alpha_i = {\alpha_i}^{(0)} + ...$$

If we substitute transformation (3) in a system of nonsteady-state one-dimensional Navier-Stokes equations and transform to the limit $\epsilon \to 0$, we obtain the system of equations of the thermal nonequilibrium boundary layer that was analyzed by Provotorov and Riabov [9], [10] in detail. Air is considered as a multicomponent system of five components (O_2, O, NO, N_2, and N). The mass diffusion flux, viscosity, and heat conductivity of multicomponent gas mixture were calculated by the approximation method of Riabov [17]. To satisfy the continuity equation identically, the stream function ψ was introduced, as well as new independent variables:

$$\psi'_t = -\rho u; \psi'_x = \rho; \tau = t; \eta = \psi/(2t)^{0.5}$$

After transformations we obtain a system of partial differential equations of the parabolic type. A finite-difference approximation to the boundary-layer equations, with boundary conditions mentioned above, was constructed analogous to the method using a matrix variant of Keller's two-point "box scheme" [14], [15], [16]. The spatial and time variables were approximated by the second order terms. The finite-difference stability analysis has been performed by Denisenko and Provotorov [14] in terms of the spectral method. The two-point difference equations were solved by the matrix regularization technique of Provotorov [15].

5 Heat flux at the catalytic wall

The calculated values of heat transfer coefficient $C_h = q/(\rho_1 {U_S}^3)$ are shown in Fig. 3 (*left*) for the range of time $t = 10^{-8} - 10^{-4}$ sec and initial pressure $p_1 = 1$ and 100 Pa (triangles and squares, correspondingly). At $t < 1$ μsec the heat flux values differ by a factor of 50. At $t > 10$ μsec this difference is less significant. The thermal layer state approaches equilibrium at $p_1 = 100$ Pa, and the heat flux values are almost the same for various catalytic materials (see Fig. 3 (*left*); filled triangles for Pyrex, empty triangles for nickel). At lower initial pressure $p_1 = 1$ Pa, processes within the thermal layer are of a strongly nonequilibrium character. For this case, the influence of catalytic properties

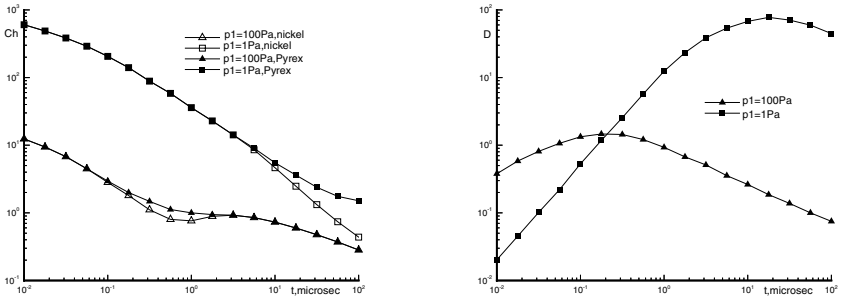

Fig. 3. Heat transfer coefficient $C_{\rm h}$ (*left*) and normalized thermal boundary layer thickness D $= 10^5\delta/(U_{\rm S}t_*)$ (*right*) at the end wall of the shock tube for various wall catalytic properties and initial pressure parameters: $p_1 = 1$ Pa (*squares*) and $p_1 = 100$ Pa (*triangles*)

of the wall material is significant. For different catalytic materials [see Fig. 3 (*left*); filled squares for Pyrex, empty squares for nickel] the values of heat transfer coefficient $C_{\rm h}$ differ by a factor of 6 at t > 30 μsec. This phenomenon can be applied to the identification of catalytic properties of heat protection materials.

6 The chocking effect in the thermal viscous layer

Figure 3 (*left*) shows the anomalous behavior of the $C_{\rm h}$(t) function for large times (t $>$ 0.4 μsec) at $p_1 = 100$ Pa. It indicates on the "chocking" effect in the thermal boundary layer. The time development of thermal layer thickness D $= 10^5\delta/(U_{\rm S}t_*)$ is shown in Fig. 3 (*right*). The thermal boundary layer thickness is defined as

$$\delta = (2\tau)^{0.5} \int_0^{\eta_\delta} \rho^{-1}{\rm d}\eta.$$

Here parameter η_δ is the η value at the external boundary of the thermal layer. Parameter t_* is equal to 100 μsec.

In the case $p_1 = 100$ Pa there exist well-defined moments in time at which the layer thickness (triangles) reaches a maximum value. Pressure behind the reflected shock wave p_3(t) begins to grow at these moments [see Fig. 2 (*left*), triangles]. This flow regime is characterized by the value $p_1 = 100$ Pa. The similar effect is also identified for larger times (t > 20 μsec) at lower initial pressure $p_1 = 1$ Pa [see squares in Fig. 3 (*right*)]. Such a mechanism is possible only in nonequilibrium gas, where physical and chemical processes allow maintaining a positive pressure gradient dp/dt [8], [9]. The chocking is caused by decreasing the layer thickness δ, when the pressure p_3(t) is increasing.

7 Conclusion

A method based on the numerical analysis of the thermal boundary layer near the shock tube end has been developed for studying heat transfer properties of catalytic materials

at high temperatures. The dependence of heat flux and pressure at the shock tube end as well as reflected shock wave velocity upon time provides valuable information on the characteristics of the thermal boundary layer near the tube end and catalytic-wall properties. The same flow characteristics can be used for determination of the discovered chocking effect of the nonsteady-state nonequilibrium thermal boundary layer near the tube end.

The analysis was made in terms of one-dimensional nonsteady flow models. In future studies the possible effects of the boundary layers on the tube sidewall should be taken into consideration. However, the problem of an interaction between the sidewall boundary layers with the thermal boundary layer at the shock tube end wall would require a three-dimensional analysis for a correct interpretation of future experimental results.

Acknowledgement. The author expresses gratitude to V. P. Provotorov for participation in developing numerical algorithms.

References

1. A.G. Gaydon, I.R. Hurle: *The Shock Tube in High-Temperature Chemical Physics* (Reinhold, New York 1963)
2. T.V. Bazhenova, L.G. Gvozdeva, Yu.G. Lobastov: *Shock Waves in Real Gases* (Nauka, Moscow 1968)
3. M.W. Slack: J. Chem. Phys. **64**, 228 (1976)
4. C. Park, J.T. Howe, R.L. Jaffe, G. Candler: J. Thermophys. Heat Transf. **8**, 9 (1994)
5. B. Sturtevant, E. Slachmuylders: Phys. Fluids **7**, 1201 (1964)
6. F.A. Goldsworthy: J. Fluid Mech. **5**, 164 (1959)
7. N.H. Johannesen, G.A. Bird, H.K. Zienkiewicz: J. Fluid Mech. **30**, 51 (1967)
8. R.K. Hanson, L.L. Presley, E.V.Williams: Numerical solutions of several reflected shock-wave flow fields with nonequilibrium chemical reactions. NASA TN D-6585 (1972)
9. V.P. Provotorov, V.V. Riabov: J. Appl. Mech. Techn. Phys. **28**, 721 (1987)
10. V.V. Riabov, V.P. Provotorov: AIAA Paper 2071 (1994)
11. V.V. Riabov, V.P. Provotorov: J. Thermophys. Heat Transf. **9**, 363 (1995)
12. V.P. Provotorov, V.V. Riabov: Tr. TsAGI **2111**, 142 (1981)
13. V.V. Ermakov, N.I. Kalitkin: J. Comput. Math. Math. Phys. **21**, 235 (1983)
14. O.V. Denisenko, V.P. Provotorov: Tr. TsAGI **2269**, 1 (1985)
15. V.P. Provotorov: Tr. TsAGI **2436**, 165 (1990)
16. V.V. Riabov: Three fast computational approximation methods in hypersonic aerothermodynamics. In: *Computational Fluid and Solid Mechanics*, ed. by K. J. Bathe (Elsevier: Boston 2005), 819–823
17. V.V. Riabov: J. Thermophys. Heat Transf. **10**, 209 (1996)

Numerical simulation of shock waves at microscales using continuum and kinetic approaches

D.E. Zeitoun[1], Y. Burtschell[1], I. Graur[1], A. Hadjadj[2], A. Chinnayya[2], M.S. Ivanov[3], A.N. Kudryavtsev[3], and Y.A. Bondar[3]

[1] *Université de Provence, Ecole Polytechnique Universitaire de Marseille–DME, 13453 Marseiile (France)*
[2] *LMFN-CORIA CNRS UMR 6614, 76800 Saint Etienne du Rouvray (France)*
[3] *ITAM, Siberian Division of Russian Academy of Sciences, 630090 Novosibirsk (Russia)*

Summary. Numerical simulations of shock wave propagation in microchannels and microtubes have been performed using three different approaches: the Navier-Stokes equations with the velocity slip and temperature jump boundary conditions, the statistical Direct Simulation Monte Carlo (DSMC) method for the Boltzmann equation, and the model kinetic Bhatnagar-Gross-Krook (BGK) equation. The influence of the viscosity and heat-conductivity, the wall heat transfer losses, and the rarefaction effects has been studied and the results obtained with different approaches have been compared.

1 Introduction

A rapid progress in micromachining techniques during the last two decades has resulted in the fabrication and utilization of micro-electromechanical systems (MEMS) and nano-electromechanical systems (NEMS). In the aerospace applications, many micromachines, such as micropumps, microturbines, microvalves, micronozzles etc. involve flows of gases (or liquids), both in subsonic and supersonic speed range. Due to very small size of MEMS, flows in them have many important features that are different from those in macromachines. An important problem in the development of MEMS is the design of devices that are able to produce mechanical work from chemical heat release, i.e. the micro-engines. At the miniaturization level, the time scales associated with heat loss mechanisms are reduced dramatically while the characteristic time scales for heat release stay virtually independent of scale. Thus, the efficiency of conventional devices such as internal combustion engines and gas turbines is seriously degraded when they are scaled to small sizes. One possibility to overcome this difficulty is to increase the rapidity of heat release using shock-induced (and/or shock-assisted) combustion. However, this technique requires a deeper insight into the mechanisms governing the microscale shock wave phenomena. The effects of viscosity and heat-conductivity, the heat losses due to the wall heat transfer, the non-equilibrium phenomena observed in rarefied flows are of importance for shock wave propagation and interaction at microscales while they are usually can be neglected for macroscale shock waves.

The investigations of viscous and rarefaction effects on shock wave propagation in shock tubes at low initial pressure were started many years ago [1–3]. The most prominent phenomena observed and investigated in these studies were shock wave deceleration, contact surface acceleration and, as a result, a significant decrease in time interval between the arrivals of the shock wave and the contact surface. Recently, a renewed interest to shock waves at microscales resulted in new experimental and numerical studies of these phenomena [4–6].

Numerical investigations of gas microflows require the development of appropriate and efficient numerical tools. If the flow Knudsen number $\mathrm{Kn} = \ell/L < 0.1$ (where ℓ is the mean free molecular path and L is characteristic length scale) then the continuum description based on the Navier-Stokes equations with the wall boundary conditions, which take into account the velocity slip and temperature jump, can be generally applied. Otherwise, the kinetic approach based on the Boltzmann equation for the distribution function should be invoked. The most well-known numerical tool for solving the Boltzmann equation is the Direct Simulation Monte Carlo (DSMC) method, which, in recent decades, was successfully used for the simulation of various rarefied flows, especially in the aerospace applications. However, like any statistical techniques, the DSMC method suffers from the statistical noise, this problem is particularly severe for low-speed and/or unsteady microflows. Another approach, which one considers as a promising alternative, is the direct solution of kinetic equations with high-resolution finite-difference schemes. Since the direct finite-difference solution of the Boltzmann equation is very resource-consuming due to the complicated form of its collision integral term, the model kinetic equation, such as the Bhatnagar-Gross-Krook (BGK) one, can be solved instead. In the model equation the collision integral is replaced by a simple term describing relaxation to the equilibrium distribution function.

The primary objective of the present paper is to simulate numerically the shock wave propagation in the microscale channels and tubes using all three above-mentioned techniques. The investigation is aimed at both validating the numerical solvers for their applications to microflows and better elucidating the physical phenomena accompanying the shock waves at microscales.

2 Numerical techniques

The unsteady flow in a micro shock tube (plane microchannel or round microtube) which occurs after the rupture of a diaphragm separating initially the gases at different pressures is considered solving the Navier-Stokes, Boltzmann and BGK equations.

Two different compressible Navier-Stokes codes are used for continuum modeling of the viscosity and heat-conductivity effects on shock wave propagation at microscales: the CARBUR solver developed at IUSTI [7] and the solver from ITAM [8]. Both the codes solve the Navier-Stokes equations on a structured quadrilateral grid using modern high-resolution shock-capturing schemes for evaluating the convective fluxes and the central finite differences to calculate the diffusive terms. An additional feature of the CARBUR code is its capability of simulating multispecies and chemically reacting flows.

Rarefaction effects are taken into account by imposing the velocity slip and temperature jump boundary conditions on the solid wall deduced from from an approximate solution of the kinetic equation in the Knudsen layer [9].

The DSMC computations were performed using the SMILE software system [10] developed at the ITAM and based on the majorant frequency scheme. SMILE employs two independent grids: the first one to organize particle collisions, and the second one for sampling of macroparameters. Both grids are based on uniform rectangular background cells, which are split into smaller cells, if necessary. The collisions between the molecules are performed using the Variable Hard Sphere (VHS) model, the diffuse reflection model with complete energy accommodation is employed at the channel wall.

The BGK-type model kinetic equation for the distribution function $f(\mathbf{x}, \mathbf{v}, t)$

$$\frac{\partial f}{\partial t} + \mathbf{v} \cdot \frac{\partial f}{\partial \mathbf{x}} = \nu \left(f^{eq} - f \right), \tag{1}$$

where f^{eq} is the equilibrium distribution function, $\mathbf{v}$ is the molecular velocity, $\nu = p/\mu$ is the collision frequency (p is the pressure) has been solved with a finite-difference solver based on the discrete ordinate method in the velocity space and the 3rd or 5th order WENO scheme [11] in the coordinate space. The numerical integration in the velocity space is performed using the composite Simpson rule. The Maxwell diffuse reflection boundary condition is imposed on the distribution function at the wall surface.

It is well known that the original BGK equation with the Maxwellian equilibrium distribution function leads to an incorrect value of the Prandtl number. To circumvent this problem, f^{eq} is modified as proposed by Shakhov [12] (S-model).

3 Comparison of results from continuum and kinetic models

All above-mentioned approaches have been applied on the same test case. The chosen test case is the propagation of a shock wave in a plane microchannel with the height $2H = 5$ mm and the length $L = 32H$. Argon is employed as both driven and driver gas. The initial pressures on two sides of the diaphragm are $p_1 = 44.2$ Pa and $p_2 = 11.9p_1$, which corresponds, in the ideal inviscid case, to Mach number $M_s^{theor} = 1.6$. The initial gas temperature is 300 K and the same value is taken for the wall temperature. At these conditions, the Knudsen numbers calculated for low-pressure and high-pressure gases are $\mathrm{Kn}_1 = \ell_1/H = 0.05$ and $\mathrm{Kn}_2 = \ell_2/H = 4.2 \cdot 10^{-3}$ respectively. The viscosity is taken proportional to $T^{0.81}$.

Owing to the problem symmetry, all computations are performed in the half of the complete domain. The Navier-Stokes simulation has been performed on the grid of 1280×40 cells. For the DSMC computations about 110 million of model particles, 1.5 million of collisional cells, and 15.000 of macroparameter cells have been used. The size of collisional cell and time step value were significantly smaller than local mean free path and local mean collision time, respectively. All presented DSMC results are obtained using time averaging over the interval of 100 time steps (=1 μs) to reduce the statistical scatter. The coordinate grid size for the BGK computations is the same as for the Navier-Stokes simulations while 33×33 points are utilized in the velocity space.

The temperature flowfields at $t = 80$ μs obtained with three different approaches are given in Fig. 1. It is evident that generally the flowfields are in good agreement, however the DSMC results suffer from a statistical noise in the low-pressure gas. The distributions of longitudinal velocity along the line of symmetry at $t = 80$ μs are shown in Fig. 2.

The shock wave position X_s and velocity have been extracted from the density distributions along the symmetry line. The time dependencies of X_s in three computations are very close to one another. The shock wave Mach numbers M_s as functions of non-dimensional time $\tau = ta_1/H$ (where a_1 is the velocity of sound in the lower-pressure gas) are given in Fig. 3. Data scattering in M_s is basically due to difficulties of accurate extraction of this quantity from numerical data. At the first moments, the shock velocity exceeds the theoretical inviscid value because of viscous widening of the discontinuous initial profile. However, it rapidly decreases down to $M_s \approx 1.3$.

Numerical simulations have also been performed for tenfold decreased level of the initial pressures so that $\mathrm{Kn}_1 = 0.5$ and $\mathrm{Kn}_2 = 4.2 \cdot 10^{-2}$. The velocity distributions for this case are given in Fig. 4. As can be seen, now there is a bigger difference between

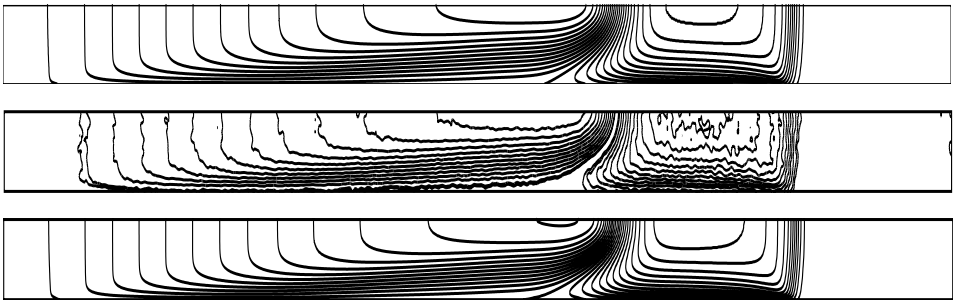

Fig. 1. Temperature flowfields at $\mathrm{Kn}_1 = 0.05$ obtained in Navier-Stokes (top), DSMC (middle) and BGK (bottom) simulations.

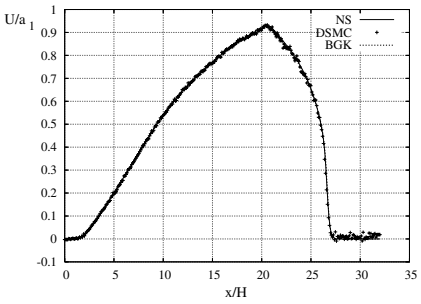

Fig. 2. Velocity distributions along the line of symmetry at $\mathrm{Kn}_1 = 0.05$.

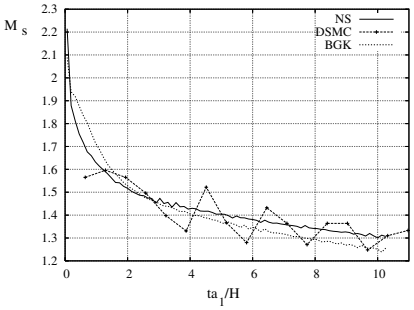

Fig. 3. Shock Mach number vs time at $\mathrm{Kn}_1 = 0.05$.

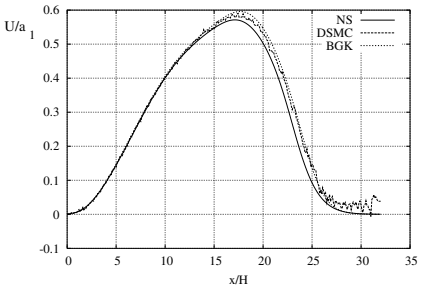

Fig. 4. Velocity distributions along the line of symmetry at $\mathrm{Kn}_1 = 0.5$.

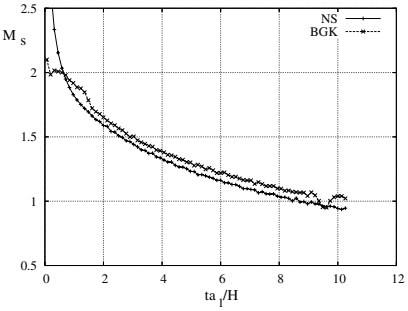

Fig. 5. Shock Mach number vs time at $\mathrm{Kn}_1 = 0.5$.

the Navier-Stokes computation and two kinetic approaches. The time dependencies of M_s are shown in Fig. 5. The velocities decrease rapidly and become sonic in the end of computation.

4 Parametric study of shock wave propagation with Navier-Stokes solver

The dependence of shock wave propagation on the Knudsen number and on the initial pressure ratio has been studied by the continuum approach. The Navier-Stokes equations have been solved for a plane microchannel with $L/H = 100$ using the grid consisting of 4000×40 cells. Three different values of $\mathrm{Kn}_1 = 0.01$, 0.05, and 0.25 have been considered at the initial pressure which correspond the theoretical shock wave Mach number $\mathrm{M}_s^{theor} = 1.6$. The obtained evolution of shock wave Mach numbers is shown in Fig. 6

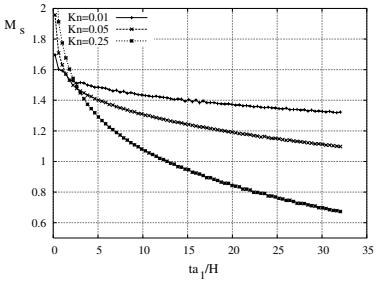

Fig. 6. Shock wave Mach number at $M_s^{theor} = 1.6$ and different Knudsen numbers.

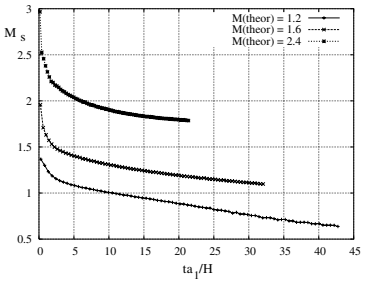

Fig. 7. Shock wave Mach number at $\mathrm{Kn}_1 = 0.05$ and different M_s^{theor}

For the lowest value of Kn the shock wave may be hardly identified, which is probably explains the values of $\mathrm{M_s} < 1$ observed at later time moments (the shock wave position has been determined as a point where the density $\rho = 1.05\rho_1$).

Computations with the fixed $\mathrm{Kn}_1 = 0.05$ and pressure ratios corresponding to ideal Mach numbers $M_s = 1.2$, 1.6, and 2.4 have also been performed. The results are shown in Fig. 7.

5 Shock wave propagation for different driven and driver gases

In order to obtain higher Mach number in microtubes, different driver/driven gases have to use. The CARBUR code [7] allows to perform these computations. A detailed numerical description of the flow in a microtube can be found in [6]. In the present study, H_2/N_2 are the driver/driven gases at the temperature T=300K. The diameter and the length of the tube are respectively 5 mm and 0.5 m, the pressure ratio $P_4/P_1 = 156$, which corresponds to an ideal Mach number equal to 5. The scaling ratio S_c=$Re_1 D/4L$, based on the low pressure tube length, is respectively equal to 0.1 for P_1=40 Pa and 0.025 for P_1=10 Pa. Figure 8 shows the shock position against time (left) and the evolution of the Mach number along the tube (right) for the two different initial low pressure. It can be noted the strong decrease of the shock strength along the tube an this effect is more and more important when the initial pressure decreases for the same pressure ratio. After only a distance of 10 cm after the diaphragm location, the shock Mach number is

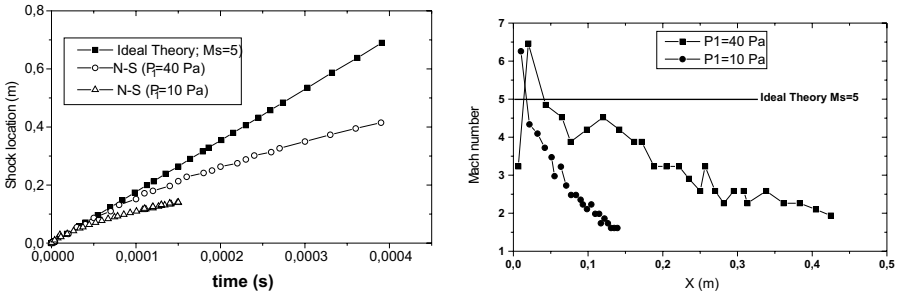

Fig. 8. Shock position vs time (left) and Mach number along the tube (right).

of 1.5 when the pressure P_1=10 Pa. As noted in [6], these effects cannot describe by the previous 1D models [3, 5].

6 Conclusion

The shock wave propagation in the microtubes and microchannels has been studied using three different approaches. The results obtained with all three approaches are in good agreement for the investigated range of Knudsen numbers. The strong decreasing of the shock strength and its propagation velocity along the tube has been observed.

Acknowledgement. The authors gratefully acknowledge the support for this work from the National Center of Scientific Research (CNRS, France), project PICS-2006 and from Russian Foundation for Basic Research, RFBR project 06-01-22000.

References

1. Duff R. E., Shock-tube performance at low initial pressure. Phys. Fluids, vol. 2, no. 2, 1959
2. Roshko A., On flow duration in low pressure shock tube. Phys. Fluids, vol. 3, no. 9, 1960
3. Mirels H., Test time in low pressure shock tube. Phys. Fluids, vol. 6, no. 9, 1963
4. Sun M., Ogawa T., Takayama K., Shock propagation in narrow channel. 23rd Int. Symposium on Shock Waves (July 22-27, 2002, Fort Worth, Texas, USA).
5. Brouillette M., Shock waves at microscales. Shock Waves, vol. 13, no. 1, 2004
6. Zeitoun D. E., Burtschell Y., Navier-Stokes computations in micro shock tubes. Shock Waves, vol. 15, no. 3-4, 2006
7. Burtchell Y., Cardoso M., Zeitoun D.E. Numerical analysis of reducing driver gas contamination in impulse shock tunnels. AIAA Journal, vol. 39, no. 12, 2001
8. Markelov G. N., Kudryavtsev A. N., Ivanov M. S. Continuum and kinetic simulation of laminar separated flow at hypersonic speeds. J. of Spacecraft and Rockets, v 37, N 4, 2001
9. Kogan M. N. Rarefied Gas Dynamics. Plenum, N. Y., 1969
10. Kashkovsky A. V., Markelov G. N., Ivanov M. S., An object-oriented software design for the direct simulation Monte Carlo method. AIAA Paper 2001-2895, 2001
11. Jiang G.-S., Shu C.-W. Efficient implementation of weighted ENO schemes. J. Comput. Phys, vol. 126, no. 1
12. Shakhov E. M. Methods of Rarefied Gas Dynamics. Nauka, Moscow, 1974

Numerical simulation of weak steady shock reflections

M. Ivanov[1], D. Khotyanovsky[1], R. Paciorri[2], F. Nasuti[2], and A. Bonfiglioli[3]

[1] *Institute of Theoretical and Applied Mechanics of the Russian Academy of Sciences, Institutskaya str. 4/1, 630090 Novosibirsk (Russia)*
[2] *Sapienza Università di Roma, Dip. Meccanica e Aeronautica, Via Eudossiana 18, 00184 Rome (Italy)*
[3] *Università della Basilicata, Dip. di Ingegneria e Fisica dell'ambiente, Viale dell'Ateneo Lucano 10, 85100 Potenza (Italy)*

Summary. The reflection of weak shocks constitutes an interesting problem from a modeling point of view. The discussion about the von Neumann paradox and the Guderley's triple shock wave solution are an example of this interest. In the present paper the attention is focused on those steady state reflections where the Von Neumann theory fails or does not provide the "classical" solution with incident and reflected shocks belonging to opposite families. Contrarily to the theory, numerical solutions of these problems show a Mach reflection similar to von Neumann triple point solution, provided that the computed shocks have a physical or numerical thickness. These special cases of Mach reflections are discussed with the help of numerical solutions obtained by different approaches based on shock capturing and shock fitting, respectively.

1 Introduction

The whole range of steady-state reflection of shock waves in supersonic flows is completely defined by two parameters: the upstream Mach number M_∞ and the deviation angle Θ_1 which generates the incident shock wave. According to the values of these parameters the incident shock wave can reflect on a solid wall parallel to the free-stream direction with a regular or a Mach reflection. The discussion on the conditions leading to one or the other kind of reflection are well-known and reported on gas-dynamics textbooks. Nevertheless, at low free-stream Mach number, a special kind of shock reflection takes place also known as von Neumann paradox. These special cases are easily understood with the help of shock polars (Figure 1). The shock polar is the locus of the possible shock solutions for an assigned upstream Mach number on a $\Theta - p/p_\infty$ plane, where Θ is the flow velocity angle and p/p_∞ is the pressure downstream the shock wave normalized with respect to free-stream. Usually the incident-shock polar is plotted with the symmetry axis at $\Theta = 0^o$, whereas the reflected-shock polar is plotted with the symmetry axis at $\Theta = \Theta_1$ where Θ_1 is the deviation angle provided by the incident shock. In case of regular reflection (Figure 1a) the flow pressure downstream of the reflected shock is identified by the value at the intersection between the reflected-shock polar and the $\Theta = 0^o$ axis. In case of Mach reflection (Figure 1b) the flow pressure and deviation angle downstream of the triple point (and the reflected shock) are identified by the intersection point between the incident- and reflected-shock polars, whereas the locus of flow pressures and deviation angles downstream of the Mach stem is identified by the branch of the incident-shock polar from the triple point to the $\Theta = 0^o$ axis.

The case of von Neumann paradox (Figure 1c) is that occurring at low free-stream Mach number when the reflected-shock polar intersects neither the vertical axis nor the incident-shock polar. In these special cases of weak Mach reflections the three shock theory of Von Neumann fails, whereas numerical solutions have been obtained with different

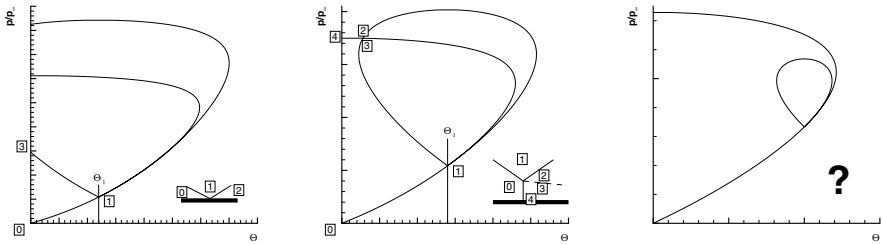

(a) (b) (c)

Fig. 1. Incident- and reflected-shock polars for: (a) regular reflection; (b) Mach reflection; and (c) von Neumann paradox.

approaches that show a solution similar to that obtained in the cases where the von Neumann triple point solution exists (see for instance the solutions obtained in [1]).

Aim of the present paper is to better understand how the solution of weak Mach reflection is obtained. The discussion is made by the help of a numerical solver including shock-fitting developed by [3]. In this way Rankine-Hugoniot relationships (that is the shock polar) are enforced on the fitted shock and thus a clearer discussion can be made.

2 Shock-capturing solution

The selected test case is an example of the von Neumann paradox with $M_\infty = 1.5$ and $\Theta_1 = 10^o$. The solution displayed in Figure 2 has been obtained by a shock capturing solver based on the Godunov approach. The isobars reported in Figure 2 show that a Mach reflection takes place with the "classical" curved shape of the Mach stem and with a reflected shock, which is not straight in the vicinity of the triple point because of the subsonic flow behind it.

Figure 2 allows a better analysis of this result; on the left the numerical solutions obtained downstream of the shocks are plotted in the plane $\Theta, p/p_\infty$ and compared with the theoretical polars; note that the hollowed squares reported on the left plot of Figure 2 represent the values of Θ and p/p_∞ in the cells downstream of the shocks. The theoretical shock polars show clearly that the present test case is a typical case of Von Neumann paradox. In fact, the incident and reflected shock polars do not intersect with each other. Nevertheless, the numerical solution provides a smooth transition between the polars with displacement from the theoretical polars in the proximity of the triple point. This behavior could be related to the effect of the numerical viscosity inside the shock thickness that here plays the same role as the physical viscosity. In fact, Navier-Stokes solutions resolving correctly the shock thickness provide the same solution [1]. An explanation can be given by considering the effect of the viscosity as responsible of a displacement of the solution across the shock from the Rankine-Hugoniot jump relationships [4].

It is worth comparing the above results with those that can be obtained in a case where the von Neumann triple point solution does exist. The results relevant to the case with $M_\infty = 2.0$ and $\Theta_1 = 14^o$ are shown in Figure 3. It is interesting to observe that in this case the numerical solution always follows the shock polars as predicted by the theory.

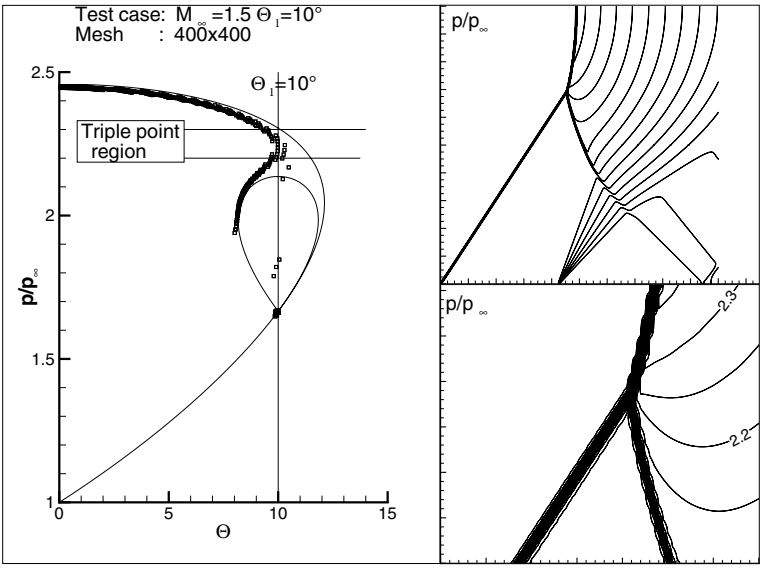

Fig. 2. Shock-capturing numerical solution for the von Neumann paradox test case with $M_\infty = 1.5$ and $\Theta_1 = 10^\circ$: shock polar (left) and pressure field with enlargement of the triple point region (right).

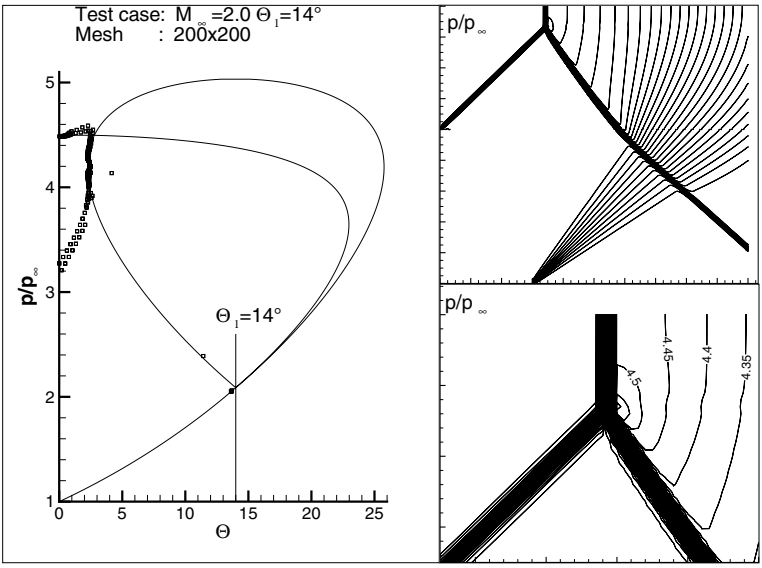

Fig. 3. Shock-capturing numerical solution for "classical Mach reflection" test case with $M_\infty = 2.0$ and $\Theta_1 = 14^\circ$: shock polar (left) and pressure field with enlargement of the triple point region (right).

3 Hybrid shock-fitting shock-capturing solution

The same test cases presented in the foregoing section have been computed with a different solver. In this case an unstructured shock-capturing solver [2] is considered, coupled with a shock-fitting technique as discussed in detail in [3]. This technique considers the shock as an internal boundary for the shock-capturing solver. Therefore the computational domain is splitted by the shock in two sub-domains where the shock-capturing solver is used. The shock-fitting technique recomputes the downstream state and the shock speed enforcing the Rankine-Hugoniot jump relationships between the two boundaries, and the updated solution and position of the shock is used as the new boundary condition for the two computational sub-domains in the next step. In the present test cases the Mach stem and the reflected shock are handled by the shock-fitting technique, whereas the incident shock is captured. Thus, the present approach represents an hybrid technique. Indeed, it does not remove completely the effect of shock thickness in the triple point region, where the Mach stem and reflected shock have zero-thickness, whereas the captured incident shock still has a finite thickness.

The results obtained for the test case with $M_\infty = 1.5$ and $\Theta_1 = 10^o$ are displayed in Figure 4. It is interesting to note that the computed result is the same typical Mach

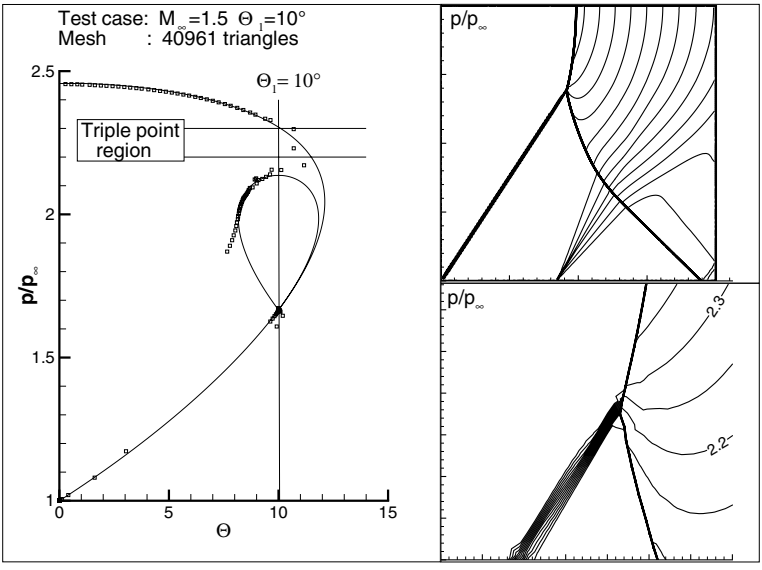

Fig. 4. Hybrid shock-fitting numerical solution for the von Neumann paradox test case with $M_\infty = 1.5$ and $\Theta_1 = 10^o$: shock polar (left) and pressure field with enlargement of the triple point region (right).

reflection as that computed by the shock-capturing approach, except that the Mach stem and the reflected shock have zero thickness. Nevertheless, the present computation allows some further comments. The enforcement of shock jump relationships should assure the absence of points outside the shock polar. On the contrary, Figure 4(left) shows that there are three points lying between the two shock polars. Because each point plotted

on the plane $\Theta - p/p_\infty$ represents the downstream state of a shock node, it is easy to prove that three anomalous states plotted in Figure 4(left) identifies the nodes where the captured incident shock, with its finite thickness, impinges on the fitted shock. In fact, to have points which lies neither on the incident- nor on the reflected-shock polar, the upstream conditions for the fitted shock must be different than those defining the two theoretical shock polars. This happens because the captured incident shock spreads the shock through a number of cells (typically three), characterized by intermediate states between its upstream and downstream conditions. Therefore the three points lying outside the shock polars belong to three different shock polars related to the flow conditions which take place "inside" the captured shock.

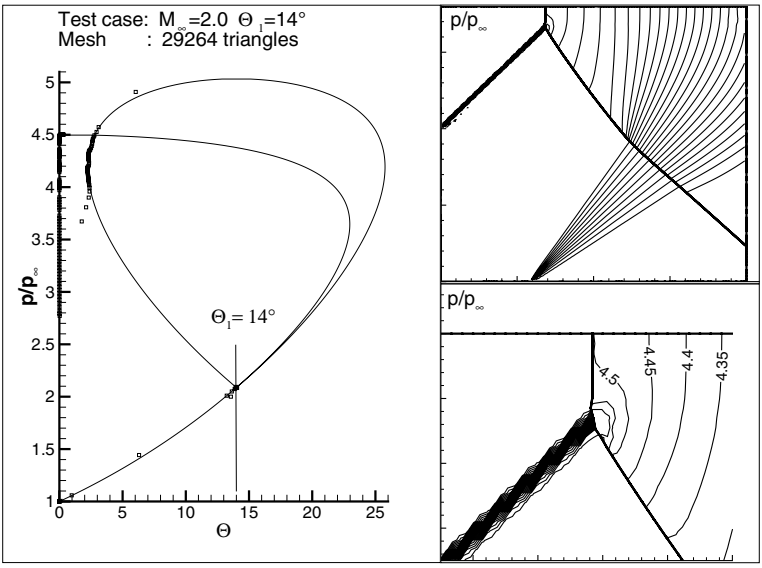

Fig. 5. Hybrid shock-fitting numerical solution for the "classical Mach reflection" test case with $M_\infty = 2.0$ and $\Theta_1 = 14°$: shock polar (left) and pressure field with enlargement of the triple point region (right).

The above discussion is confirmed by the computation of the second test case, where the von Neumann triple point solution exists, by the shock-fitting approach. The results reported in Figure 5 shows that also in this test case, there are three points about the triple point where the numerical solution is anomalous. Indeed, the downstream pressure of these shock points appears to be higher than at the intersection between the two polars. The reason is again due to the spreading of the incident shock leading to different upstream conditions for the Rankine-Hugoniot jump relationships enforced on the fitted shock. It should be also noted that in this case the above spreading of points away from the shock polars worsens the description of the Mach stem, as shown by the lack of points on the incident shock polar in the vicinity of the triple point.

4 Conclusions

Identifying one of the possible cases of the von Neumann paradox, the present study has compared the solutions obtained by a pure shock-capturing and a hybrid shock-fitting approach. The interesting result is that the a finite thickness of the incident shock is sufficient to assure a transition from the incident to the reflected shock polar. In fact, this finite thickness leads to the existence of a finite number of intermediate shock polars. The comparison between the shock-capturing and hybrid shock-fitting solutions in the von Neumann paradox test case shows that the shock-fitting approach reduces the number of cells not lying on the shock polars whereas the shock-capturing approach shows a smoother transition. The final demonstration of the role of the shock thickness in the von Neumann paradox could come from the development of a pure shock-fitting technique able to compute all shocks with the Rankine-Hugoniot jump relations and the triple point explicitly enforcing the von Neumann model. This problem is presently being faced by the authors and the results will be presented in a forthcoming paper.

References

1. Bondar Y., Ivanov M., Khotyanovsky D., Kudryavtsev A., Weak shock reflection in steady flows, Proc. 17th International Shock Interaction Symposium, 4-8 September 2006, Rome, Italy
2. Bonfiglioli A., Fluctuation splitting schemes for the compressible and incompressible Euler and Navier-Stokes equations, IJCFD 14:21–39, 2000
3. Paciorri R., Bonfiglioli A., Numerical simulation of flow with shocks through an unstructured shock-fitting solver, Proc. 26th International Symposium on Shock Waves, 2007, Goettingen, Germany
4. Sternberg J., Triple-Shock-Wave Interactions, Phys. of Fluids vol. 2, no. 2, pp. 179–206, 1959

On the ongoing quest to pinpoint the location of RR-MR transition in blast wave reflections

H. Kleine[1], E. Timofeev[2], A. Gojani[3], M. Tetreault-Friend[2], and K. Takayama[3]

[1] *School of Aerospace, Civil, and Mechanical Engineering, University of New South Wales/Australian Defence Force Academy, Canberra, ACT 2600, Australia*
[2] *Department of Mechanical Engineering, McGill University, 817 Sherbrooke Street West, Montreal, Quebec H3A2K6, Canada*
[3] *TUBERO, Tohoku University, 2-2-1 Katahira, Aoba-ku, Sendai 980-8577, Japan*

1 Introduction

Fundamental processes such as the reflection of blast waves have received considerably less attention in the open literature than the case of steady or pseudo-steady reflection phenomena [1]. The true unsteadiness of these processes complicates both the numerical/analytical and experimental treatment, and further difficulties are introduced by the inherently destructive nature of trials involving explosives with masses ranging between a few hundred grams and several thousands of kilograms. The transfer of these tests into the laboratory environment, with a reduction of charge masses into the milligram range, has opened new possibilities to tackle such problems. The advantages and constraints of such laboratory-scale tests are discussed in [2, 3].

When a blast wave impinges onto a straight surface, the wave initially reflects regularly, but at a certain horizontal distance x_{tr} from the explosion centre, the pattern changes into an irregular reflection. If one assumes that the transition from regular to irregular reflection can be described using the criteria derived from classic steady two- and three-shock theories, as it has previously been postulated [1, 4], the location of the transition point may be predicted. In numerical modeling, the high-pressure/temperature balloon model is typically used as a numerical blast source. The source can be calibrated on the basis of experimental records to ensure that the intensity of the numerical and experimental incident blast waves are the same within experimental accuracy. The subsequent numerical simulations predict the location of the transition point which agrees well with the theory [5].

Unfortunately, experimental records do not seem to confirm these predictions and reveal substantial discrepancies that cannot be explained by inevitable experimental errors or the idealized treatment of the flow as inviscid [5]. At the same time, numerical simulation indicates that after transition the size of the Mach stem remains small (less than 0.1 mm) for a relatively long distance due to the fact that the trajectory of the triple point is tangential to the reflecting surface. Thus, it may be conjectured that the early development of the Mach stem can experimentally only be visualized with great difficulty if at all.

It was the main goal of this investigation to see if the aforementioned discrepancies could be resolved by using improved experimental visualization techniques. Different approaches were taken to obtain an unambiguous signal for the onset of irregular reflection. The test scenarios correspond to the configurations tested before in similar small-scale experiments [5], while the final test series was a combination of modern high-speed photography and an adaptation of the soot trace experiment conducted by Ernst Mach in 1875 [6].

2 Experiments

All experiments were conducted with pellets of silver azide (AgN_3) with a nominal mass of 10 mg, which were ignited by laser irradiation. Details on the explosive and the ignition method are given in [2, 3]. The tests can be classified into three different categories:

- re-enactment of large-scale tests with added visualization;
- observation of the reflection process in a way only possible in laboratory tests;
- combination of high-speed photography and soot technique.

In the first category, large-scale tests are replicated on a model scale, the main difference being that complete flow field visualization by density-sensitive methods such as shadowgraph or schlieren techniques is applied. These tests are a conventional *HOB* (height of burst) scenario, where a single charge is ignited above a solid, smooth surface, or a double-charge arrangement that corresponds to the large-scale tests described in [7].

The second and third categories of tests differ from the first category inasmuch that they are only feasible within the laboratory scale. Rather than trying to determine the onset of irregular reflection by searching for the first indication of a Mach stem on the flow visualization records, it was attempted to create a system that would flag the creation of the Mach stem by a unique signal that should be largely independent of the (spatial) resolution of the used optical system. The tests of category 2 were also a conventional *HOB* scenario with a single charge – however, in this case the process was observed through a transparent ground [3]. While the Mach stem itself did not become visible in this view, its appearance changed the way the reflected wave was recorded by a schlieren system. This change depended on the setting of the optical system rather than on its resolution. The third and final set of tests was conducted after all previous tests had revealed the limitations of a 'flow-visualization-only' approach. A surface technique – observing the trace of shock waves in a soot layer, as pioneered by Ernst Mach [6] – was used for these tests. Two charges were ignited simultaneously and the propagation of their mid-air intersection point on a soot-covered plate was monitored. In this case, the high-speed-photographic record of this process provided one measurement and the post-experiment analysis of the soot trace another.

3 Results and discussion

3.1 Re-enactment of large-scale tests

Arguably the most obvious approach to investigate blast reflection processes is to scale down corresponding large-scale tests and make use of the fact that a range of density-sensitive flow visualization techniques can be applied in the laboratory, which are not available on the large scale. With an adequate visualization system and camera one can monitor the generation of all essential flow features. In the past, however, such direct optical determination of the transition point has been the subject of some controversy and conjecture, and it was hoped that improved camera technology would help to clarify some of the outstanding issues. In the conducted tests, the propagation of the blast waves was recorded by means of time-resolved schlieren visualization. Single-shot visualizations may yield a higher resolution and thus more details about the flow structure, but the loss of information about the temporal development of the waves is likely to introduce new uncertainties, which make it difficult if not impossible to determine crucial elements

of a process such as the emergence of new flow features. The potential of time-resolved visualization has recently been dramatically increased through the advent of enhanced recording technologies [8]. A new high-speed video camera, the Shimadzu HPV-1 [9], allows one to take one hundred images at frequencies of up to one million frames per second (fps) at full frame resolution. In a number of tests it has already been demonstrated that this camera is currently the best available tool for experimental visualization of highly unsteady flow phenomena, e.g., [3, 5, 9].

In the conducted tests, different imaging lenses allowed one to visualize either the whole field of view or to magnify certain areas. The smallest area that could be visualized this way had dimensions of approximately 40 mm × 30 mm. Higher magnifications were not possible with this set-up as the available light could not sufficiently expose the CCD. The results presented in [5] confirmed that the large discrepancy between experimental and numerical values for x_{tr} cannot be attributed to experimental uncertainties or the simplifying assumptions in the numerical simulation. It can be concluded that this discrepancy is, indeed, caused by the initially minuscule size and the very gradual growth of the Mach stem – an observation that holds true both for small-scale and large-scale experiments. For the studied case 10 mg AgN_3 at $HOB = 35$ mm, the value for x_{tr} obtained from theory (detachment criterion) is $x_{tr\,th} = 32.5$ mm. Numerical simulation predicted $x_{tr\,num} = 28.3$ mm, while the optical records described above gave $x_{tr\,exp} \approx 43.5$ mm at the highest image magnification. For a lower image magnification, the value for x_{tr} was considerably higher [5].

At a first glance, there is an obvious trend that increased image magnification reduces the discrepancy between experimental and numerical results for x_{tr}. The achievable improvement is, however, limited as further image magnification generates a number of problems that renders this approach ineffective: for constant size of the recording device (here: the CCD) the visualized area becomes so small that all information about the global behavior of the flow field and thus the benefits of time-resolved visualization are lost. Furthermore, as a consequence of the finite exposure time of the camera, motion blur becomes increasingly important.

The following simplified analysis illustrates these points. It is obvious that a flow element of size g can only be identified on the visualization record, if its image $m_{im} \times g$ exceeds the size p of one pixel, where m_{im} is the image magnification factor. Hence the smallest resolvable detail g_{min} is given by

$$g_{min} = p/m_{im} \ . \tag{1}$$

Two conclusions can be drawn from (1): the higher the image magnification m_{im} becomes, and the smaller the pixel size p, the higher is the chance to resolve fine details of the imaged object. With current technology, however, both m_{im} and p have clear limitations. For most commercially available digital high-speed cameras, p is of the order of tens of micrometers. Several factors limit the obtainable maximum image magnification m_{im}, with space restrictions and minimum illumination density requirements arguably being the most stringent ones. Another restriction is imposed by the application described here: typical schlieren systems require reasonably high focal lengths of the schlieren mirrors in order to obtain sufficient sensitivity, and for such systems it is rare – and difficult – to obtain imaging factors larger than unity. In fact, in the tests reported here, the highest magnification factor obtained was approximately 0.5 [5].

In addition, large values of m_{im} introduce motion blur as an image resolution-degrading factor. The exposure times of most digital high-speed cameras have a lower

limit, which may be imposed by the architecture of the recording CCD chip and/or its minimum exposure requirements. If the exposure time is given as Δt, an object moving at speed v will only be properly imaged without motion blur, if

$$m_{im} \times v \times \Delta t \leq p \quad . \tag{2}$$

In the case of the Shimadzu HPV-1, the minimum exposure time of 250 ns and the given pixel size limit m_{im} to values below 0.66 for expected object (wave) speeds of 400 m/s. According to (1), the smallest resolvable detail then has a size of 0.1 mm. All these considerations assume perfect imaging without diffraction effects. Numerical simulation of the reflection process indicates that for the given charge sizes the Mach stem initially has a size of only a few tens of micrometers and that the aforementioned 'visibility threshold' of $g_{min} > 0.1$ mm is only surpassed several millimeters downstream of the transition point.

From the above discussion of the imaging constraints in the given time-resolved schlieren visualization system it is clear that current time-resolved technology cannot resolve flow elements less than 0.1 mm in size and moving at velocities higher than 400 m/s. These are, however, exactly the conditions encountered in the transition from regular to irregular blast wave reflection. It was therefore concluded that unless time-resolved visualization with at least ten-fold larger resolution and ten times faster frame exposure times becomes available, the described small-scale re-enactment of large-scale blast wave tests will not be capable of reliably revealing the onset of irregular reflection.

3.2 Combination of high-speed photography and surface techniques

In view of the inevitable difficulties of a fully flow visualization-based determination of x_{tr}, a different approach was chosen: Ernst Mach's original soot trace experiment [6] was repeated with two explosive charges of equal mass. A sharp-edged flat plate was positioned in the plane of the two charges, which were positioned 70 mm apart, similar to the double charge tests described in [5]. The distance of the leading edge of this plate to the charges was measured with an accuracy better than 0.25 mm. A snugly fitting plexiglass insert within the plate was covered with a layer of fine soot and was illuminated from the back by a strong flashlight to be photographed with the Shimadzu HPV-1 at framing rates of 500 kfps and 1 Mfps. The used lens was a NIKON Nikkor 210 mm, set at $f22$. A picture of the central portion of the setup is given in Fig. 1a.

The idea of this arrangement is that the blast waves would remove parts of the soot layer, which would become visible as bright traces on the high-speed recording. It was expected that the intersection point of the two waves would 'carve' a distinct path into the soot layer, and that the transition to irregular reflection would become visible through a marked change of the characteristics of this path such as a sudden change in width. This approach is, in parts, similar to the tests described by Krehl [10]. It yields two records, which complement each other. The soot trace can be evaluated after the experiment, and the width of the trace can be measured (Fig. 1b). In parallel, the actual time-resolved observation of the process provides further insight as it depicts the generation of the trace. Schardin [11], an early advocate of animated display of dynamic processes, outlines as early as 1965 that the human brain is capable of extracting important qualitative information from an animated picture, which may not be revealed if one just analyzes individual frames – which shows that the movie is more than just a sum of frames.

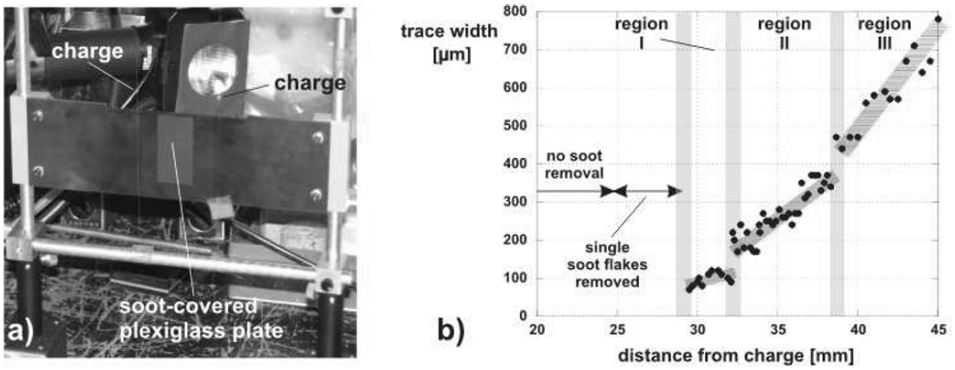

Fig. 1. a Set-up of the soot-layer / high-speed photography test. Note that the flashlight was tilted for better visibility on this picture - in the actual experiment it is positioned immediately behind the soot-covered plate; **b** Evaluated soot trace – thickness of soot trace versus distance from the charge.

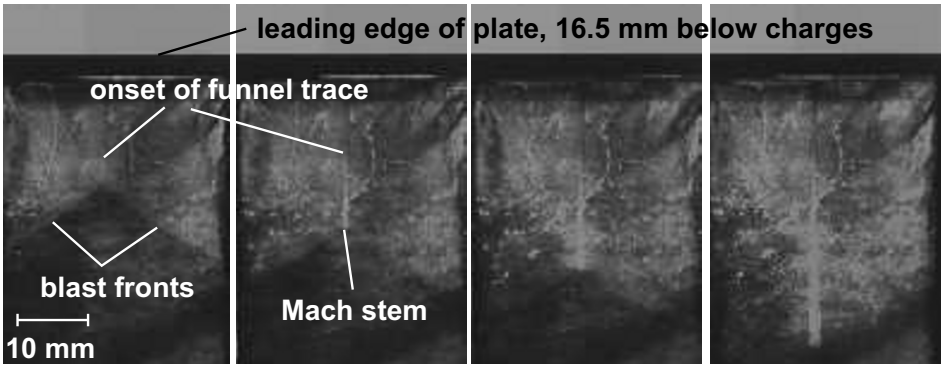

Fig. 2. Four frames of one image sequence taken with 500 000 fps. It can be seen that the trace on the soot layer becomes visibly stronger at $x \approx 31$mm, indicating a relatively sudden increase in the width of the trace. The frames indicate that each blast wave itself removes part of the soot layer, but that the evolving Mach stem leaves the strongest imprint.

From Mach's experiment it is known [6] that the ensuing Mach stem leaves a funnel-shaped imprint in the soot layer. As indicated in Fig. 2, at a certain distance from the leading edge a sharp increase in brightness was clearly visible. The subsequent microscopic inspection of the soot trace revealed that, indeed, the trace has several distinct regions where its width undergoes visible changes (Fig. 1b). The first sudden increase in width corresponds to the position at which an increase in brightness was seen on the visualisation records, at a distance of $x_{tr} \approx 32 \pm 0.5$ mm from the charges, which is considerably closer to the numerically predicted x_{tr} than the outcome of all previous visualization records. While a more detailed analysis of all traces and the records is still pending, the results so far indicate that the combined soot trace - high-speed photography approach is likely the most reliable way to detect the onset of irregular reflection.

4 Conclusions

This paper has reviewed several approaches used for an optical determination of the point where the reflection of a blast wave changes from regular to irregular. It was found that techniques, which are entirely based on the visualization of the flow, depend either on the spatial resolution of the recording medium or the sensitivity of the optical system, which limits their accuracy of measurement. For a given charge size and material, 10 mg silver azide (AgN_3), and a fixed height of burst $HOB = 35$ mm, a combination of high-speed photography and the traditional soot technique was found to provide results that agreed well with numerical predictions.

Acknowledgement. The authors would like to express their sincere thanks to Professor Andrew Higgins (McGill University, Montreal, Canada), who generously shared with us his expertise in the preparation of soot-covered surfaces. Thanks is also due to Prof. Peter Voinovich (Supercomputer Center at Ioffe Physical-Technical Institute, St. Petersburg, Russia) who advocated a long time ago the come-back of soot techniques for reflection transition studies and encouraged us to give this traditional technique a try. The study was partially supported by NSERC Discovery grant 298232-2004.

References

1. Ben-Dor G: *Shock Wave Reflection Phenomena*, Springer, New York (1991)
2. Kleine H, Dewey JM, Ohashi K, Mizukaki T, Takayama K: Shock Waves **13**(2):123 (2003)
3. Kleine H, Timofeev E, Takayama K: Shock Waves **14**(5/6):343 (2005)
4. Dewey JM: In: Ben-Dor G, Igra O, Elperin T (eds) *Handbook of Shock Waves*, vol. 2, Academic Press, San Diego, pp. 441-481 (2001)
5. Kleine H, Timofeev E, Takayama K: Proc. ISSW 24, vol. 2, Springer, New York, Heidelberg, pp.1019-1024 (2005)
6. Krehl P, van der Geest M: Shock Waves **1**(1):3 (1991)
7. Dewey JM, McMillin DJ, Classen DF: J Fluid Mech **81**:701 (1977)
8. Etoh TG, Takehara K, Okinaka T, Takano Y, Ruckelshausen A, Poggemann D: Proc. 24th Int. Congr. High Speed Photography & Photonics, SPIE, Bellingham, vol. 4183, pp. 36-47 (2001)
9. Kleine H, Hiraki K, Maruyama H, Hayashida T, Yonai J, Kitamura K, Kondo Y, Etoh TG: Shock Waves **14**(5/6):333 (2005)
10. Krehl P: Proc. ISSW19, vol. 1, Springer, Berlin, Heidelberg, New York, pp. 221-226 (1992)
11. Schardin H: VII. Int. Kongr. Kurzzeitphotographie, Helwich, Darmstadt, pp.17-23 (1967)

Shock over spheres in unsteady near-sonic free flight

J. Falcovitz[1], **T. Kikuchi**[2], **and K. Takayama**[3]

[1] *Institute of Mathematics, The Hebrew University of Jerusalem, Israel*
[2] *Interdisciplinary Shock Wave Research Laboratory, Institute of Fluid Science, Tohoku University, Sendai, Japan*
[3] *Tohoku University Biomedical Engineering Research Organization, Tohoku University, Sendai, Japan*

Summary. We focus on the determination of shock standoff distance for a spherical projectile at slightly supersonic free flight. A $40\,mm$ polycarbonate sphere was launched by a light gas gun, visualizing the free-flight flow as a double exposure holographic interferogram, from which standoff distance was read. This data is found to agree with previously published data, and reaches down to $M_0 = 1.002$ – a range where almost no previously published data exists. A large-time steady flow simulation using the GRP scheme was performed for the relatively higher speed $M_0 = 1.20$, and found to agree with experimental data. We discuss the difficulties associated with obtaining lower Mach number simulations, suggesting that a supercomputer capability is required for that. The significance of projectile deceleration at the transonic range is indicated, proposing to study this effect by using a moving-projectile simulation method.

1 Introduction

Determination of the detached shock standoff distance over spheres in steady supersonic flow is a basic research topic in shock dynamics. Early studies of detached shocks, such as those compiled by Liepmann and Roshko ([2, Sec. 4.14] and references in Fig. 4.15 therein), relied on experimental observation with Mach numbers exceeding $M_0 \approx 1.16$. In the present study we specifically focus on near-sonic free stream flow, anticipating standoff distances well beyond the sphere diameter, as indicated by the trend of the previously mentioned data [2, Fig. 4.15].

A typical steady, inviscid, supersonic flow about a sphere is depicted schematically in Fig. 1. It features a curved shock wave at a standoff distance δ, where δ/D is a function solely of the free stream Mach number M_0 and the fluid properties, due to dimensional similarity. A streamtube starting at the detached shock front passes through a sonic surface (where the flow undergoes transition from subsonic to supersonic), surrounds the sphere and proceeds to the wake region, after a transition back to subsonic speed that may involve a stopping shock wave.

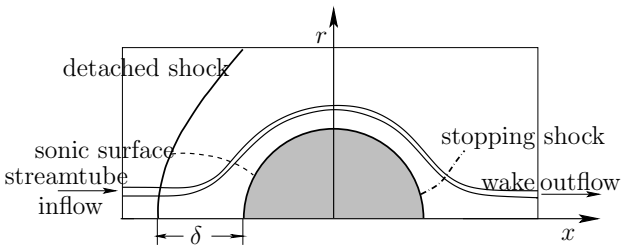

Fig. 1. Detached shock in steady supersonic flow around a stationary sphere

A steady-flow theoretical analysis of this flow field is quite complex due to the existence of *subsonic* and *supersonic* flow regions, separated by a *sonic surface*. Neither the sonic surface nor the shock fronts are known in advance. The advantage of this approach is that the upstream part of the flow field – where the detached shock is located – is not sensitive to details of the downstream part, particularly the wake which is notably difficult to calculate realistically. The resulting calculated standoff distances were found to agree well with aeroballistic measurements (see [3] and references therein).

Rather than develop a construction algorithm for the hyperbolic/elliptic flow map in the case of a detached shock ahead of a sphere, it is more practical nowadays to seek a numerical simulation by means of a large-time solution to the Euler equations, using a conservation laws scheme. The shock front is then automatically obtained by shock-capturing, and the time-integration requires solely inflow/outflow boundary conditions on a "computational rectangle" as shown schematically in Fig. 1 (along with the boundary conditions on the spherical surface). In the present study we have used the Moving Boundary Tracking version (for the stationary spherical surface) of the GRP conservation laws scheme [1]. Unfortunately, the computations were found too difficult to conduct at near-sonic speeds – they barely converged at $M_0 = 1.20$, and convergence becomes more difficult as the Mach number decreases.

Recently, ballistic experiments were conducted at the Interdisciplinary Shock Wave Research Laboratory of the Institute of Fluid Science, in Tohoku University, Sendai, Japan [4]. A sabot-mounted $D = 40mm$ spherical projectile was launched by a gas gun at slightly supersonic speed, with a trajectory nearly free of perturbations. Visualization of the detached shock was acquired by double-exposure holographic interferometry, and its speed was determined by crossing laser beams.

In the present study we consider and compare shock detachment distances as function of free flight Mach number in the range $1.0 < M_0 < 1.5$. In the next section we consider the experimental findings, following by computational simulation, drawing special attention to the issue of free-flight deceleration. We compile (in a single figure) the presently obtained shock standoff data, as well as data available from previously mentioned studies.

2 Ballistic experiments

Our free flight experiments were performed in a ballistic range at the Interdisciplinary Shock Wave Laboratory of the Institute of Fluid Science, Tohoku University. A $40mm$ diameter sphere was launched from a $51mm$ diameter gas gun in ambient air at speeds ranging from 340 to $375m/s$, with flight Mach number in the range from 1.01 to 1.10. The projectile was made of high density polycarbonate (density $1.2\,gr/cm^3$, mass $40.3\,gr$). A schematic layout diagram is given in Fig. 2, showing the projectile going through the sabot remover and blast suppression system before cutting the laser beams for velocity measurement, and at last reaching the visualization section where a double exposure holographic interferometry image is acquired [5]. A typical isopycnics image is shown in Fig. 3. We clearly see the stand-off curved shock and the smooth rotational flow downstream the front, as well as the (seemingly turbulent) wake flow behind the sphere and slight perturbation ahead of the shock front due to a precursor blast wave [4]. The standoff distance data is presented in Fig. 4, along with previously published data and a computational result obtained by a method presented in the next Section.

The issue of *projectile deceleration* arises in any free-flight testing. Starr et al. [3] tested spheres and other blunt-nose projectiles at near-sonic speeds in an aeroballistic range

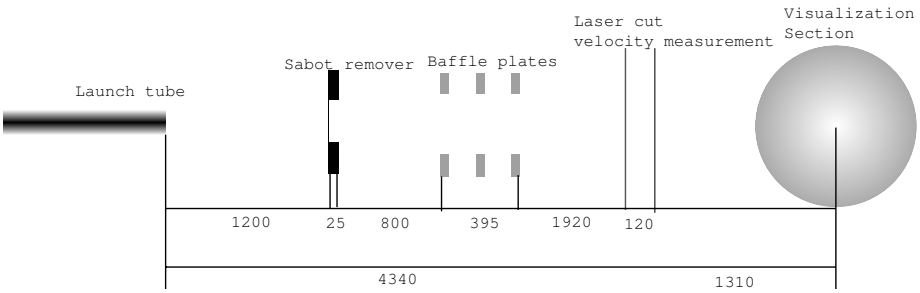

Fig. 2. Experimental layout. Distances in mm

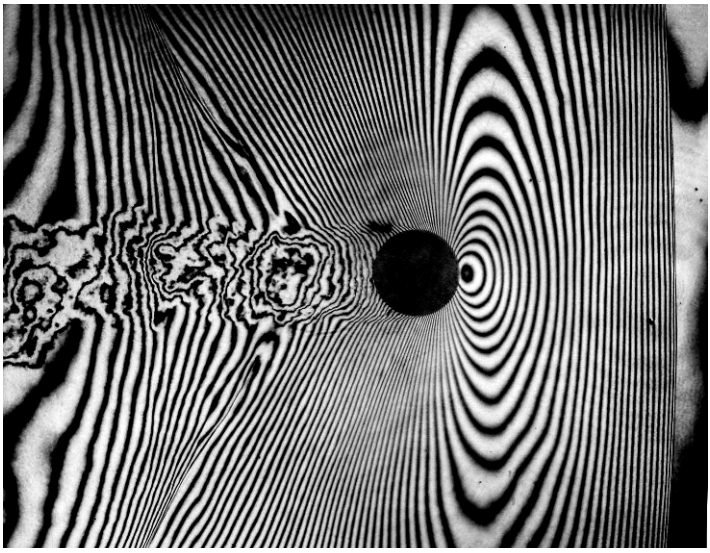

Fig. 3. Free flight isopycnics at $M_0 = 1.025$ in air

facility, contending that this effect was "avoided in the present study by a careful selection of model mass and launch velocity". However, no analysis or reference is provided in support of that contention. In our experiments, assuming a drag coefficient $C_d \approx 1$, it is readily estimated that over the free flight distance between the velocity measurement and the visualization section ($1250\,mm$) the projectile decelerates by roughly 2% (so that, for example, $M_0 = 1.02$ becomes $M_0 = 1.00$). This effect is not negligible in the considered near-sonic range. How can it be accounted for in the interpretation of acquired shock standoff data?

Generally speaking, projectile deceleration affects the shock standoff distance in two ways. First, the flow field evolves continually in time, so that it is no more stationary. In particular, the detached shock is attenuated by rarefaction waves emanating from the decelerated projectile. The second component is the change in standoff distance due solely to the projectile deceleration, over a time interval shorter than the previously discussed shock attenuation response time. It is estimated that if such deceleration commences at

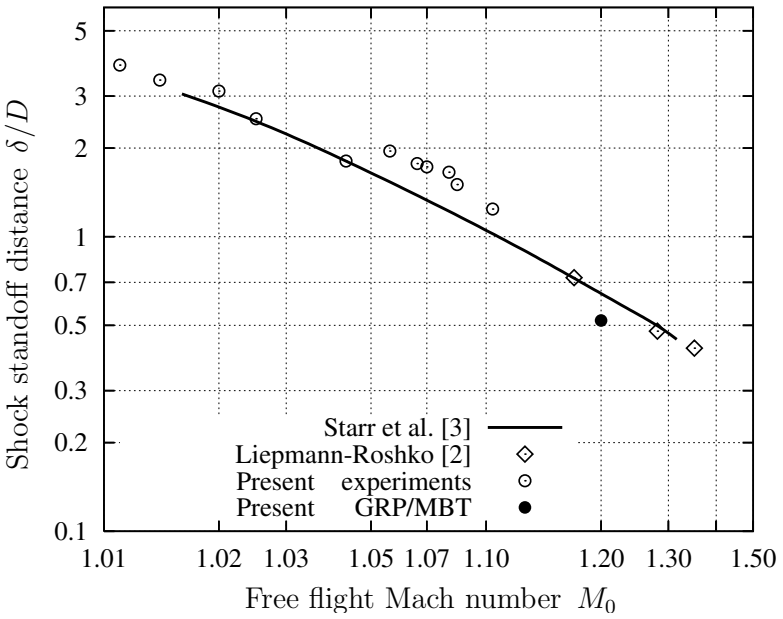

Fig. 4. Shock standoff distance for spheres in air

the velocity measurement section, then in our setup the increase in standoff distance at the visualization section is about $10^{-2}D$. This amount is relatively small when $\delta/D \approx 1$ (the largest value measured here was ≈ 3), and we are left with the shock attenuation contribution. A simple estimate of this effect seems unfeasible since it would involve calculation of rarefaction wave propagation across the entire "shock layer" region between the sphere and the shock front.

What can practically be done about the deceleration issue? Experimentally, we might repeat the tests with a much heavier sphere, thereby minimizing the effects of deceleration. Unfortunately, this would require a serious modification of the launching system. Another remedy might be a second, post-visualization, velocity measurement. It is noted, however, that even if the velocity at the moment of visualization is determined, the shock standoff data is not expected to be identical to that of the corresponding steady flow. Next we discuss the capabilities of numerical simulations of near-sonic flow about a sphere, that may help resolve the deceleration issue.

3 Numerical simulation

A steady flow numerical simulation was performed by the GRP/MBT scheme [1, Chapter 8] using a $4D \times 2.4D$ axisymmetric Cartesian grid as depicted schematically in Fig. 1, with a square-cell mesh size of $D/160$. The stationary spherical boundary was implemented by a circle embedded in the grid (intersecting the mesh cells). We show results for a flight Mach number $M_0 = 1.20$ in Figure 5, where a stand-off shock front and a separated wake flow (including shed vortex in velocity display) are clearly visible.

The flow is shown at a time where $tu/D \approx 5$ (t,u are time, free flight speed). The inflow boundary conditions is readily set at the free flight conditions, while for the upper and outflow boundaries we use an approximate "none-reflecting" boundary condition. One inherent difficulty with the simulations is that the flow never fully converged. (When the simulation time was increased by 10%, the standoff distance increased by about 2%, mostly due to evolution of the wake flow.) Reducing the free flight Mach number requires a wider computation domain, in order to minimize perturbations due to shock reflection from the upper domain boundary. Consequently, simulations by time-integration of the fluid dynamical conservation laws become increasingly difficult as the free flight Mach number is reduced to the near-sonic range.

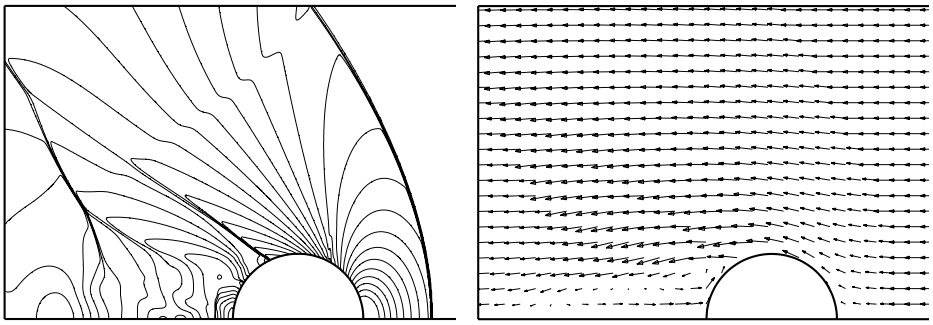

Fig. 5. GRP simulation. Isobars and velocity vectors for $M_0 = 1.20$

Can numerical simulations produce the flow field about a *decelerated* sphere? This is possible, but in a setup of *moving* sphere and stationary air, using the capabilities of a computational scheme such as the GRP/MBT method ([1, Chapter 8], and the example shown in Fig. 8.5 therein). The computation domain has to be extended continually as the sphere advances, since "non-reflecting" boundary condition at the wake side is impossible due to the fact that the flow across this boundary would be an *inflow* (hence, the normally upwind BC would be revert to a "downwind" BC, which is inherently unstable). This difficulty may be alleviated by letting the air move with a constant velocity (say, equal to the initial sphere velocity), as in the previously outlined stationary-sphere simulation. In any case, such simulation would probably require a supercomputer capability. We were unable to perform it so far, but we may do so in the future.

4 Concluding remarks

We were able to acquire clear high-resolution interferograms of the flow about a spherical projectile in free flight at slightly supersonic speeds. The quality of our imaging is superior to that of previous aeroballistic range experiments. The obtained detached shock standoff distance agrees fairly well with previous free-flight data. We raise, in particular, the issue of sphere deceleration, which appears to be non-negligible in the near-sonic range. An analysis of the deceleration effects on the interferogram and the standoff data is due, and we indicate how it can be performed by conservation-laws simulations; so far we

were unable to conduct it. Although this issue was mentioned in previous studies [3], no analysis of the effect was offered. Numerical simulations at steady flow produce a standoff distance in fair agreement, but somewhat lower than the available test data. The simulations are increasingly hard to conduct at near-sonic speeds. We offer to perform such simulations for a moving sphere, in a setup of expanding computation domain, that requires a supercomputer capability. Such simulations can be readily extended to treat a decelerated projectile, and may thus help in comparing the steady and non-steady (decelerated) shock standoff data at the near-sonic range.

References

1. Ben-Artzi M., Falcovitz J. *Generalized Riemann problems in computational fluid dynamics*, Cambridge University Press, London, 2003.
2. H. W. Liepmann, A. Roshko, *Elements of gasdynamics*, John Wiley & Sons, New York, 1957.
3. R. F. Starr, A. B. Bailey, M. O Varner, *Shock detachment distance at near sonic speeds*, AIAA Journal, 14:537–539, 1976.
4. T. Kikuchi, D. Numata, K. Takayama, M. Sun, *Shock stand-off distance over spheres flying at transonic speed ranges in air*, Presented at the 26^{th} International Symposium on Shock Waves, Göttingen, Germany, 15–20 July, 2007.
5. K. Takayama, *Applications of holographic interferometry to shock wave research*, SPIE 398:174–180, 1983.

Shock wave diffraction over complex convex walls

C. Law, B.W. Skews, and K.H. Ching

School of Mechanical, Industrial and Aeronautical Engineering, University of the Witwatersrand, PO WITS 2050, South Africa

Summary. An experimental investigation of the flow behind a shock diffracting over faceted walls with turning angles for individual facets of 22.5° and 30° has been conducted at an incident shock Mach number of 1.5. The features of the near wall flow have been identified and the early development of the flow around the wall was considered. For the Mach 1.5 case, the expansion generated at each corner was shown to have a marked effect on the separation shear layers formed after each corner. More work needs to be done using a less directionally sensitive optical system.

1 Introduction

Work on the flow behind diffracting shocks by Skews [1] and more recently by Law et al. [2] identified a number of features in the supersonic flow behind the diffracting shock. Among these features was a flow separation point that was not necessarily fixed at the corner such as that of 'A' in Fig. 1(a) and a backward facing shock ('B' in Fig. 1(a)). Fig. 1(a) is a schlieren image of a Mach 2.945 shock diffracting around a 30° corner. These features were dependent on local flow Mach number, wall angle and the pressure distribution along the wall.

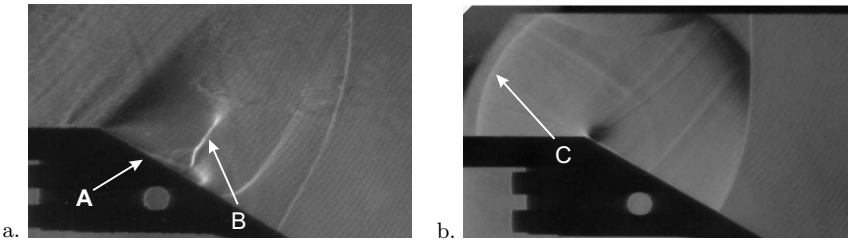

Fig. 1. Shock diffraction over a 30° wedge with **a.** $M_s = 2.945$, **b.** $M_s = 1.192$.

In the case of Fig. 1(a) the flow behind the Mach 2.945 shock is supersonic and the expansion around the corner produced a flow with an even higher Mach number near the wall. Skews [1] identifies the condition for the existence of the backward facing shock as supersonic flow along the shear layer and relative to the shock. For diffraction angles greater than 15° the lowest Mach number this was observed at was a shock Mach number of 1.46 on a 90° corner, though it appeared more as a series of shocklets along the shear layer rather than a single backward facing shock. Extrapolating the data, Skews proposed a minimum incident shock Mach number of 1.45 as the Mach number below which the

backward facing shock could not exist. The data for a 15° wall angle suggested that this minimum criterion should be higher. Where the 15° data differed from the other data was that the flow had not detached and there was thus no shear layer. This would suggest then that the shape of the shear layer is what causes the formation of the backward facing shock to occur much sooner.

From the early experimental data collected by Skews [3] for a shock diffraction around a single corner, at low initial shock Mach numbers below 1.45, the pressure distribution was insufficient to produce a backward facing shock. Fig. 1(b), shows a Mach 1.192 shock diffracting over a 30° corner producing a subsonic flow behind the shock and an expansion which propagates upstream into the flow at local sonic speed ('C'in fig. 1(b)).

This does raise the question of what effect this expansion would have on a preceding diffraction. Skews [4] examined the shape of a shock wave diffracting over 45° and 90° faceted convex walls, where the angles quoted refer to the relative angle of inclination of one facet with respect to the next. The work uses Whitham's shock dynamics method [5] to predict the shape of the shock and identifies a number of key features in the flow behind the diffracting shock. The original study only considered two wall angles and this has now been extended to look at increasing numbers of facets and thus smaller incremental turning angles. This work examines the flow behind a shock diffracting over multi-faceted walls, where the flow behind the incident shock is largely subsonic.

2 Methodology

A shock tube was used to run a range of tests over faceted walls with turning angles of 22.5° and 30° and over wedges with corresponding turning angles. The tube is currently capable of a Mach number range between 1.01 and 1.6, though it is capable of much higher Mach numbers when a partial vacuum is drawn in the test section.

A single pass schlieren system was used to capture the experimental images on a Canon 350D 8.1 megapixel digital SLR camera. Triggering was via a time delay unit connected to a Yokogawa DL850 digital oscilloscope, using two PCB pressure transducers to detect the pressure rise of the shock. Data from the scope was also used to calculate shock velocity and Mach number.

An adaptive refinement Euler code (previously described by Law et. al [6]) was used in parallel with the experimental data to better understand the flow field and improve the interpretation of the experimental images.

3 Results

The transition case where the incident Mach number is 1.45 is interesting in that the separated shear layer is characterised by a series of shocklets that form above it in a region where the flow has just become supersonic. These shocklets are still evident at a shock Mach number of 1.5, since the local Mach number is marginally higher, the shocklets are more noticeable. The result for a Mach 1.5 shock diffracting over a backward facing step is very well understood and was used as a benchmark case for testing numerical codes [7]. A Mach 1.5 case thus provides a useful framework when considering the diffraction of a shock over a faceted convex wall. The result of such a diffraction can be seen in fig. 2. The schlieren image of fig. 2(a) was focused on the near wall region so that the camera had

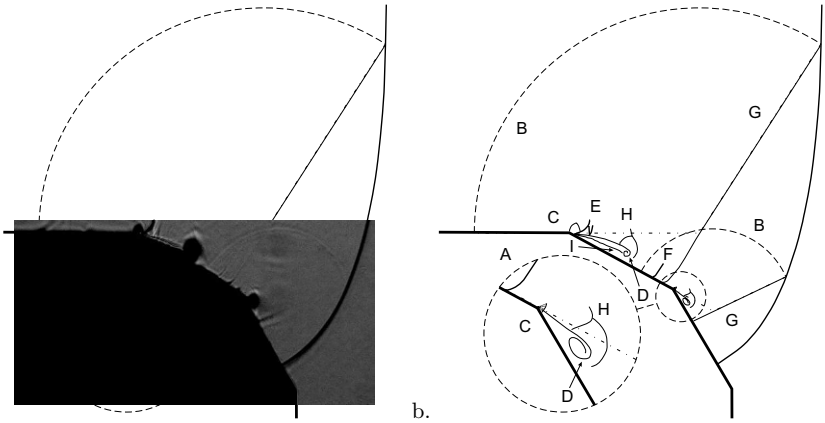

Fig. 2. Structure of a shock diffraction over a multi-faceted convex wall at $M_s = 1.52$.

sufficient resolution to resolve small flow features there. Earlier work provided sufficient information however that the shock shape sketched outside of the image frame, was inferred and while the shock shape as sketched, may not necessarily be accurate it is a reasonable approximation. Of particular interest to this study however is the flow immediately adjacent to the wall. Fig. 2(b) proposes a schematic representation of the flow in that region.

In fig. 2(b) A is an exploded view of the circled area near the wall at the second corner; B is the expansion front generated by the incident shock diffraction around the corners; C is the expansion centred at each corner and ending in a shock; D is the shear layer that starts at the separation point on each face and rolls up into a vortex; E is a series of shocklets typically found along the shear layer in a Mach 1.5 shock diffraction; F is a shocklet formed by non-uniformities in the boundary layer; G is the contact surface generated by each diffraction; H is a region of high density gradients that forms at the end of the shear layers where they roll up and I is an unstable boundary layer that grows rapidly from the separation point.

It should be noted that the shocklets at E are not present at the second diffraction. In the case of the second corner, the time scales are different and the shocklets potentially have not been given time to form at the instant captured in fig. 2. The Euler simulation results in fig. 3, show that the pressure (fig. 3(a)) decreases along each successive facet of the wall, as does the sound speed (fig. 3(c)), but the Mach number (fig. 3(b)) remains relatively constant away from the wall. The black lines on the colour flood plots of fig. 3 represent sonic contours and as expected these separate the supersonic flow at the corners from the subsonic flow everywhere else. Naturally the results of fig. 3 are invalid when considering the effects of any viscous phenomena such as the boundary layer, which can clearly be identified by comparing the CFD results to the experimental ones (Primarily F and I identified above, but indirectly H as well through the boundary layer's effect on the shear layer).

The region at the ends of the two shear layers (H) are only seen in the experiments. The shear layer is pushed away from the wall by the boundary layer and separates from the wall closer to the corner. This behaviour was previously described by Law et al. [2]

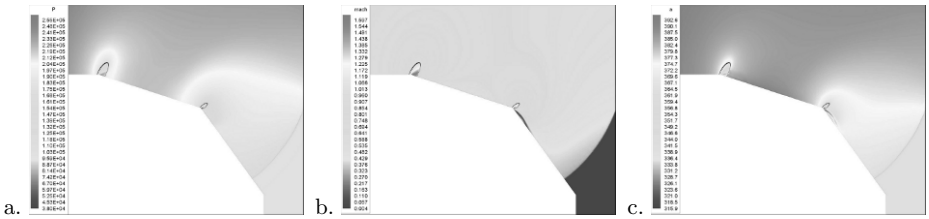

Fig. 3. Euler simulation of a $M_s = 1.52$ shock diffraction over a multi-faceted convex wall with **a.** pressure, **b.** Mach number, and **c.** sound speed flood plots.

and results in an earlier formation of the shear layer and its accompanying vortex. The unidirectional nature of the schlieren system used, means that some information about these regions has not been captured, but shadowgraph and omni-directional schlieren imaging are being investigated so as to better understand this region. At this time, it is surmised that the region is similar to the bifurcated shock region previously described by Law et al. [2] among others.

By considering the behaviour of the diffraction with time it is possible to identify the process by which the backward facing shock that was previously identified by Skews [4], is formed. This is illustrated in fig. 4 which shows the diffraction of a Mach 1.53 ±0.01 shock around a 30° faceted wall.

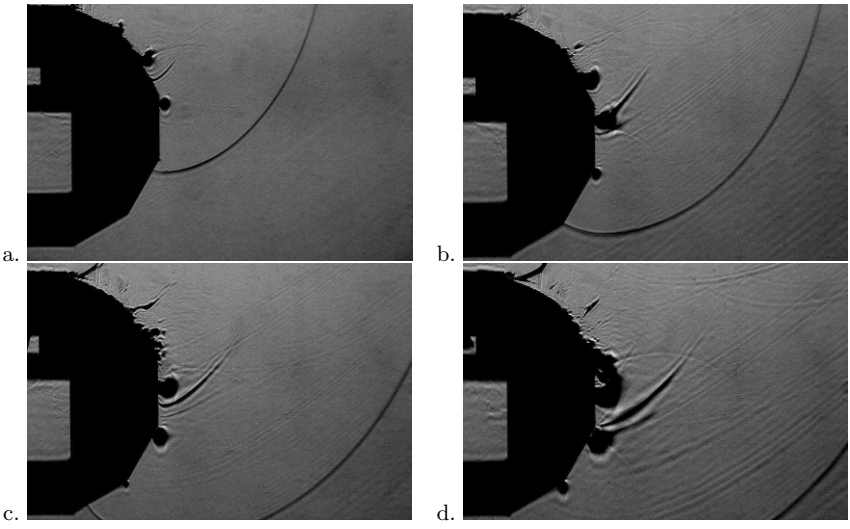

Fig. 4. Shock diffraction over a 30° multi-faceted convex wall with **a** − **c.** $M_s = 1.53$ and **d.** $M_s = 1.52$.

A shear layer created by the pressure driven separation of the flow on the second facet can be seen in fig. 3(b and c). This shear layer is pushed away from the wedge surface by the boundary layer development below it (fig. 4.a). It then rolls up into a vortex

and a backward facing shock is formed to normalise the pressure of the flow diffracting around the vortex. This shock then propagates along the face of the wedge, driven by the self similar growth of the separated flow. The shock is seen to pass through the expansion region at the end of the second facet and through the vortex formed at the upper corner of the third facet (fig. 4(b)) continuing further down the wedge to interact with the vortex at the next corner and ultimately to detach from the wall (fig. 4(d)). The shear layer also seems to propagate along the wall and then begins to move away from the wall at the third facet. There are a number of smaller shocklets that seem to form along the separated shear layers at both the first two diffraction corners. The boundary layer and shear layer off the second corner seem to interact to form a highly rotational or turbulent flow region immediately adjacent to the wall at the second facet. More diagnostic information is needed however in order to adequately be able to describe the flow in that region.

The 30° turning angle of the results in fig. 4 clearly has an effect on how quickly the shear layer forms as the flow conditions at a shallower turning angle are significantly different. This can be seen in fig. 5 where a Mach 1.52 shock is diffracted around a faceted wall with a shallower turning angle of 22.5°.

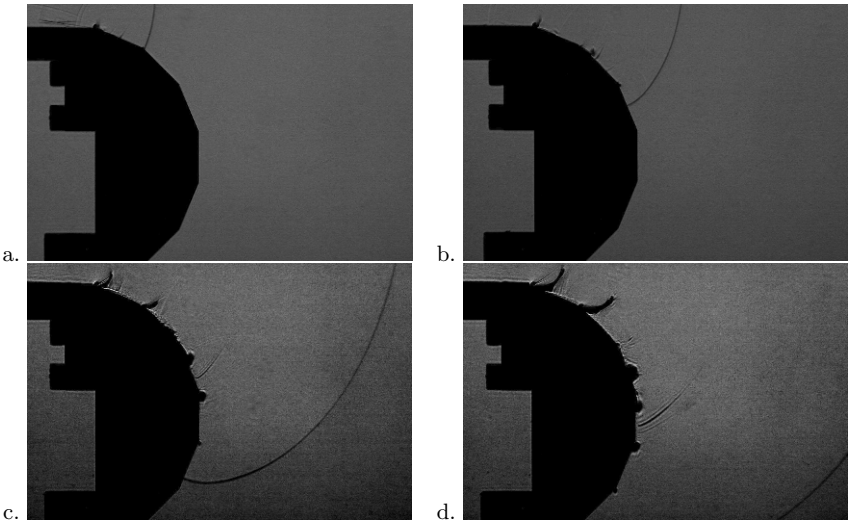

Fig. 5. Shock diffraction over a 22.5° multi-faceted convex wall with $M_s = 1.52$

Fig. 4(b) and fig. 5(c) are roughly coincident as the diffracting shocks are in the same approximate position (measured as the horizontal distance travelled by the primary shock.) The lower turning angles of fig. 5 are still characterised by the formation of shear layers near the corners and the shocklets that are typical of a Mach 1.5 diffraction, forming on the shear layers. Unlike the steeper 30° turning angle of the previous result however, the shear layers remain adjacent to the walls.

In addition, a comparison of the roughly co-incident results of fig. 4(d) with fig. 5(d) also shows that a separated shear layer terminating in a vortex and backward facing shock, has not yet had time to form in fig. 5(d) while it is clearly identifiable in fig. 4(d).

In both figures however the shocklets formed on the shear layers at each corner of the first two facets, increase in strength with time but appear to remain attached to the corners. Both fig. 4 and fig. 5 contain a backward facing shock that can be tracked through all results propagating along the wall. In fig. 5 however the turning angle is shallower and the expansion at each corner is thus much weaker. The shock must consequently also be weaker and is not enough to detach the shear layer as was the case in fig. 4. If the flow is allowed to converge to steady state, it should be noted that both cases will produce the flow pattern first identified by Skews [4].

Ordinarily the shear layers formed at each corner are expected to grow with time and to wrap up into a vortex. This process is interrupted however by the expansion created at a downstream corner which then propagates upstream. In both results the effect of the expansion on the first facet is to reattach the shear layer. For the 30° result the expansion wave is insufficient to reattach the shear layer, while on the 22.5° expansion the pressure gradient driving the separation is weaker and the expansion reattaches the shear layer.

4 Conclusion

The diffraction of a shock over a multi-faceted convex wall produces a number of complex interactions. Experimental results for Mach 1.5 shocks diffracting over 22.5° and 30° multi-faceted walls was presented and a basic flow geometry was proposed and presented schematically in fig. 2. Not all the features could be definitively identified as there was insufficient information in the optical results, but an explanation has been offered that needs to be confirmed by further experimentation and numerical simulation. The results have shown that the expansion created at each corner changes the behaviour of the shear layer formed at a corner. The effects include changing the pressure gradient along the facet face, the result of which, can be reattachment of the separated shear layer among other things.

In the limit as the number of facets increase to infinity, the wall tends to a circular arc. Further experiments are planned using increasing numbers of facets and ultimately circular arcs. Many of the experiments also need to be repeated using a multi-directional schlieren system.

References

1. Skews BW, J. Fluid Mech., 29, (1967) 705 – 719
2. Law C, Menon N, Skews BW: Near-wall features in transient compressible flow on convex walls, ISSW 25, Bangalore, India, 2005
3. Skews BW, J. Fluid Mech., 29, (1967) 297 – 304
4. Skews BW: Shock Waves **14**, 3 (2005) 137 – 146
5. Whitham GB: J. Fluid Mech., 2 (1957) 145 – 171
6. Law C, Felthun LT, Skews BW: Two-Dimensional Numerical Simulation of Shock-on-Shock Interactions, ISSW 23, Fort Worth, Texas, 2001
7. Takayama K, Inoue O: Shock Waves **1**, 4 (1991) 301 – 312

Shock waves in mini-tubes: influence of the scaling parameter S

W. Garen[1], B. Meyerer[1], S. Udagawa[2], and K. Maeno[3]

[1] *University of Applied Sciences Oldenburg/Ostfriesland/Wilhelmshaven, Constantiaplatz 4, 26723 Emden, Germany*
[2] *Graduate School of Sci. and Tech., Chiba Univ., 133 Yayoi, Inage, Chiba, 2638522, Japan*
[3] *Faculty of Engineering, Chiba Univ., 133 Yayoi, Inage, Chiba, 2638522, Japan*

Summary. Weak shock waves have been investigated in a glass tube of 1 mm diameter and a length of 600 mm. The distance between shock and contact surface is approximately 10 mm and both travel nearly with the same speed at the measuring position of 410 mm. For a laminar flow behind the shock wave an identical Mach number M_1 can be generated with two different shock strength values p_{41} as a consequence of friction effects.

1 Introduction

For shock waves in micro shock tubes the diffusive effects like shear stress and heat conduction lead to important deviation from 'normal shock behaviour' which has been described by Brouillette [1]. As a first approximation he introduced a scaling parameter S which consists of the Reynolds number Re multiplied by the tube diameter D and divided by the length $4L$. L is the distance between the moving shock wave and the following contact surface between driver and test gas. For $S \to \infty$ (big tubes, high Reynolds numbers) diffusive effects are unimportant. For $S \sim 1$ or less the friction and heat conduction are dominant and important deviation for pressure, density and temperature may be expected in the moving flow field behind the shock. To study those diffusive effects very low S-values are necessary which are combined with narrow tubes and low Reynolds numbers. Small tube diameters in the order of mm or even μm lead to problems to find suitable sensors for measuring the state variables like pressure, density and temperature in front of and behind the shock wave. Suitable sensors need a very high spatial and temporal resolution and a high sensitivity. Furthermore it is important to measure the distance L between the shock and the contact surface to calculate the scaling factor S. A further serious problem is the generation of shock waves by the diaphragm techniques. Especially for low Mach numbers (desirable to get low Reynolds numbers) it is not simple to find acceptable thin diaphragms which will rupture at low pressure differences due to the small cross section of the thin tubes. The influence of the scaling parameter S can be seen for example in the formula of the Hugoniot curve for the density change caused by the shock wave:

$$\frac{\rho_2}{\rho_1} = \frac{(\gamma_1+1)M^2 + \frac{2\gamma_1 M}{Pr}\cdot\frac{1}{S} + (\frac{1}{S})^2\frac{2\gamma_1}{Pr}}{(\gamma_1-1)M^2 + \frac{1}{S}\cdot\frac{2}{M\cdot Pr} + 2} \tag{1}$$

If S becomes infinite the well-known ideal density ratio is

$$\frac{\rho_2}{\rho_1} = \frac{(\gamma_1+1)M^2}{(\gamma_1-1)M^2+2}$$

Similar results can be found for the pressure and temperature change.

2 General considerations

2.1 Reynolds number *Re* and scaling factor *S*

Following Brouilette [1] the scaling factor is: $S = \frac{Re_1 \cdot D}{4L}$ with $Re_1 = \frac{a_1 D}{\nu_1}$
a_1 = speed of sound and ν_1 = kinematic viscosity
We changed $Re = Re_2 = \frac{u_p \cdot D}{\nu_2}$ by using the ideal gas velocity u_p behind the shock instead of a_1 to get $Re_2 \to 0$ for $M_1 \to 1$. With help of the Rankine-Hugoniot relations Re_2 can be expressed as:

$$Re_2 = \frac{a_1 \cdot D}{\nu_N} \cdot \frac{p_1}{p_N} \cdot \frac{M_1(M_1^2 - 1)}{1 + \frac{\gamma_1 - 1}{2} M_1^2} \tag{2}$$

where subscript N refers to the standard conditions. Here Re_2 (and S) depends on the tube diameter D, the initial pressure of the test gas p_1 and the shock Mach number M_1. A similar expression for the Reynolds number Re_3 can be calculated in the region 3 (behind the contact surface).

2.2 Detection of the contact surface

For calculating S it is important to measure the distance between the shock and the contact surface, which is done by a laser differential interferometer. When the contact surface strikes the interferometer beams there should be a signal if the optical paths in region 2 (behind the shock) and in region 3 (behind the contact surface) are different. The two-beam interferometer signal $\triangle U_{21}$ (jump caused by the shock wave) is:

$$u_{12} = \frac{\triangle U_{21}}{U_0 2\pi \frac{D}{\lambda} \cdot \frac{p_1}{p_N} K_1} = \left(\frac{\rho_2}{\rho_1} - 1 \right) \tag{3}$$

where p_1 is the test gas pressure, K_1 is the Gladstone-Dale constant of the test gas, p_N pressure at standard conditions and $\frac{\rho_2}{\rho_1}$ is the density ratio caused by the shock. Regarding the contact surface there can be found a signal $\triangle U_{23}$:

$$u_{23} = \frac{\triangle U_{23}}{U_0 2\pi \frac{D}{\lambda} \cdot \frac{p_1}{p_N} \cdot K_1} = \left[\frac{K_4}{K_1} \cdot \frac{a_4^2}{a_1^2} \cdot \frac{\gamma_1}{\gamma_4} \cdot \left(\frac{p_2}{p_1} \right)^{\frac{1}{\gamma_4}} - \frac{\rho_2}{\rho_1} \right] \tag{4}$$

where the subscript 4 refers to the driver gas.

Fig.1 shows the relative theoretical interferometer signal (equations 3 and 4) as a function of the Mach number M_1 for the shock and the contact surface. For air as a driver gas the signal of the contact surface is very small, in the case of helium as a driver gas the density change should be detectable. The signal is negative because the Gladstone-Dale constant for helium is one order smaller than for air.

2.3 Shock strength $\frac{p_4}{p_1}$ for micro scaling shock tubes

It is well known that for small diameter shock tubes and low initial pressures the distance between the shock and the contact surface can be very short [2] and the experimental shock-strength $p_{41} = \frac{p_4}{p_1} = \frac{driver\,pressure}{test\,gas\,pressure}$ is considerably higher than the theoretical one. With the assumption that the contact surface has a very small distance from the shock

(some mm) and travels nearly with shock velocity a higher p_{41} can be considered by wall friction of the moving driver gas in state 3 behind the contact surface with the distance between the measuring position and the high pressure section.

The ideal shock strength without friction is obtained as:

$$p_{41} = \frac{p_4}{p_1} = \left[1 + \frac{2\gamma_1}{\gamma_1 + 1}(M_1^2 - 1)\right] \cdot \left[1 - \frac{\gamma_4 - 1}{\gamma_1 + 1}\left(\frac{a_1}{a_4}\right) \cdot \frac{M_1^2 - 1}{M_1}\right]^{\frac{-2\gamma_4}{\gamma_4 - 1}}$$

where γ is the ratio of specific heat and a is the speed of sound.

The real pressure ratio including friction is:

$$p_{41}^* = p_{41} + \Delta p_{fl} = \frac{p_4}{p_1} + \frac{\Delta p_f}{p_1}$$

$$\frac{\Delta p_f}{p_1} = \frac{\lambda}{Re_3} \cdot \frac{u_{p3}^2}{2} \cdot \rho_3 = \frac{32 a_1 \cdot \eta_3}{D \cdot p_1} \cdot \frac{L^*}{D} \cdot M_1$$

$$p_{41}^* = \left[1 + \frac{2\gamma_1}{\gamma_1 + 1}(M_1^2 - 1)\right] \cdot \left[1 - \frac{\gamma_4 - 1}{\gamma_1 + 1}\left(\frac{a_1}{a_4}\right) \cdot \frac{M_1^2 - 1}{M_1}\right]^{\frac{-2\gamma_4}{\gamma_4 - 1}} + \frac{32 a_1 \cdot \eta_3}{D \cdot p_1} \cdot \frac{L^*}{D} \cdot M_1 \quad (5)$$

with $\lambda = friction$ coefficient, $\eta_3 = viscosity$ of driver gas and L^* is the distance between measuring position and high pressure chamber. Equation (5) assumes that the transport properties μ resp. η as well as γ remain constant and the particle speed u_{p3} equals the shock speed u_1.

2.4 Experimental set-up

Instead of a diaphragm we used a quickly opening valve [3]. Fig. 2 shows the schematic principle. Inside of the high pressure chamber there is a rubber ball under high pressure which separates the shock tube from the driver section p_4. The other side of the tube with the rubber ball is closed by a thin membrane. By rupturing the membrane the rubber

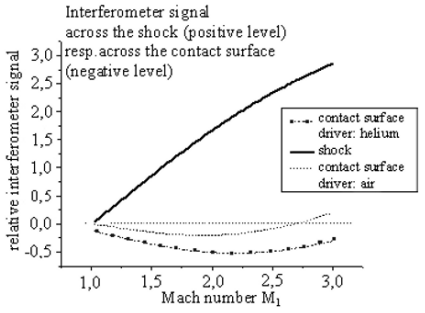

Fig. 1. Relative interferometer sensitivity for density change caused by the shock or the contact surface respectively

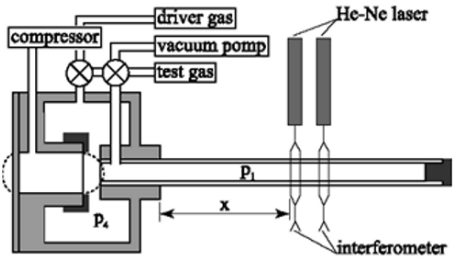

→ **Fig. 2.** Schematic experimental set-up

ball pulls back and the driver gas compresses the test gas and forms a shock wave. The dimensions of the micro glass shock tube are: diameter $D = 1$ mm, length $l = 600$ mm. For measuring the shock speed and the density change caused by the shock we used one or two special laser interferometers set up by Wollaston prisms. The beam diameters have to be only some hundreds of a millimeter inside of the glass tube to prevent optical curvature influences of the tube.

3 Results

3.1 Detection of the contact surface

Fig.3 shows a typical density trace of the two-beam interferometer. Both beams pass the shock tube with a beam distance of 5.59 mm. The first jump down is attributed to the running shock from which the shock speed and the density change can be calculated. The second jump up is caused by the contact surface which also allows the calculation of the speed and the density change of the contact surface [4]. Due to equations (3 and 4) the jumps have opposite levels. In case of air as a driver gas a detection of the contact surface was impossible which is in agreement with equation (4). It can be seen from fig.3 that the contact velocity up is nearly equal to the shock speed u_1 and the distance between shock and contact surface is nearly equal to the beam distance of the interferometer (5.59 mm), which is very short compared to the distance from the opening of the shock tube to the measurement position ($L^* = 420$ mm; $\frac{L^*}{D} = 140$). The measurements of this paper were carried out in a smaller tube of $D = 1$ mm and the distance $L^* = 410$ mm or $\frac{L^*}{D} = 410$.

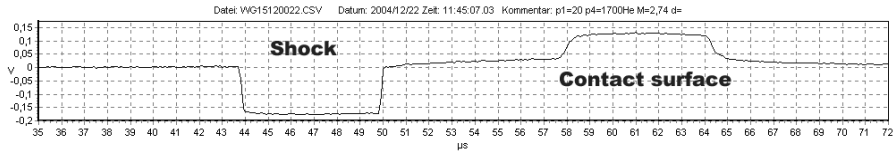

Fig. 3. Density trace behind an incident shock wave in air ($p_1 = 20mbar$) driven by helium ($p_4 = 1bar$), $M_1 = 2.74$, $D = 3mm$

3.2 Shock strength $\frac{p_4}{p_1}$ as a function of the Mach number M_1

It can be expected that the friction influences with smaller tubes and low initial pressures p_1 become important and $\frac{p_4}{p_1}$ increases for a desired Mach number M_1. From the above results we expect, that the contact surface moves with the shock speed velocity and the position is close behind the shock, at least for low pressures p_1.

Fig.4 represents measurements of the shock strength $\frac{p_4}{p_1}$ against the Mach number M_1. In these experiments the driver gas was helium with a constant pressure p_4 and the test gas was air at different initial pressures p_1 ($p_1 = 400$, 200, 100, 50, 20, 10, 5, 2 mbar). The theoretical values $\frac{p_4}{p_1}$ as a function of M_1 are much more smaller than the experimental ones. On the other hand the theoretical calculation with wall friction shows good agreement with experimental results at least for higher shock strengths. For

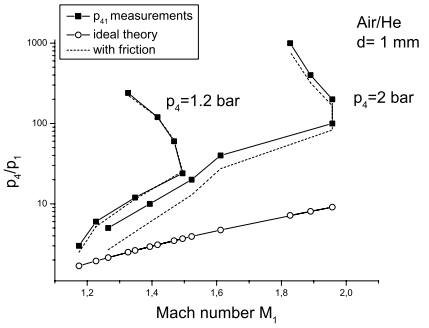

Fig. 4. Shock strength $\frac{p_4}{p_1}$ as a function of M_1: a) $p_4 = constant = 2$ bar helium b) $p_4 = constant = 1.2$ bar helium

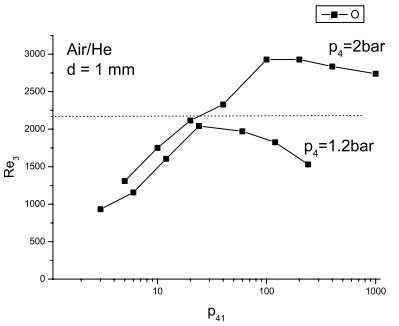

Fig. 5. Reynolds number Re_3 as a function of the shock strength p_{41}

the ideal theory the shock strength $\frac{p_4}{p_1}$ is only a function of Mach number M_1 whereas for very small tubes under real conditions the shock strength depends on the Mach number M_1, initial pressure p_1, tube diameter D and the measuring distance from the diaphragm (quickly opening valve). As a consequence:

$$p_{41} = f(M_1, Re, \frac{D}{L^*}...)$$

Fig.4 shows some surprising results: Under above conditions ($p_4 = const$ and p_1 varies) it follows:

- a maximum Mach number M_{1max}
- it seems, there is a region where two different p_{41}-values belong to the same Mach number M_1

More experiments are in progress to understand this behaviour but it seems reasonable that these results are strongly influenced by friction effects of the moving gas behind the shock. For a first explication the following assumption may be acceptable: By help of equation (3) under the condition that the pressure ratio p_{41} is nearly completely needed to move the gas against the wall friction it can be assumed:

$$p_{41}^* \approx \frac{\Delta p_f}{p_1} = \tag{6}$$

$$\left[1 + \frac{2\gamma_1}{\gamma_1 + 1}(M_{1max}^2 - 1)\right] \cdot \left[1 - \frac{\gamma_4 - 1}{\gamma_1 + 1}\left(\frac{a_1}{a_4}\right) \cdot \frac{M_{1max}^2 - 1}{M_{1max}}\right]^{\frac{-2\gamma_4}{\gamma_4 - 1}} + \frac{32 a_1 \cdot \eta_3}{D \cdot p_1} \cdot \frac{L^*}{D} \cdot M_{1max}$$

For small initial pressures p_1 the first term in equation (4) is small compared to the second one which yields to:

$$\frac{\Delta p_f}{p_1} = \frac{p_4 - p_1}{p_1} \approx \frac{32 a_1 \cdot \eta_3}{D \cdot p_1} \cdot \frac{L^*}{D} \cdot M_{1max} \tag{7}$$

or

$$p_4 - p_1 = \frac{32 a_1 \cdot \eta_3}{D} \cdot \frac{L^*}{D} \cdot M_{1max} \tag{8}$$

With: a) $p_4 = 2$ bar, $a_1 = 340$ m/s, $\eta_3 \approx 19 \cdot 10^{-6}$ kg/ms, $D = 10^{-3}m$, $M_{1max} \approx 2.35$ and b) $p_4 = 1.2$ bar, $a_1 = 340$ m/s, $\eta_3 \approx 19 \cdot 10^{-6}$ kg/ms, $D = 10^{-3}m$, $M_{1max} \approx 1.41$ This Mach numbers are quite acceptable(fig.4). Fig.5 shows the Reynolds number Re_3 versus p_{41} with the driver pressures $p_4 = 2$ bar and $p_4 = 1.2$ bar. Re_3 is only a function of the Mach number M_1 and the driver pressure p_{41}.

4 Conclusions

Weak shock waves have been produced in a small glass shock tube with a diameter of 1 mm and a length of 600 mm, the position of the interferometer (for speed and density measurements) was at 410 mm. The test gas was air and the driver gas was helium. With this combination we were also able to detect the contact surface due to the different Gadstone-Dale values of the gases. As a temporary result we found that the contact speed is nearly equal to the shock speed and both are travelling with a short distance behind each other. By lowering the initial pressure p_1 and constant driver pressure p_4 there exists a maximum Mach number M_{1max} which depends only on the (constant) driver pressure p_4, tube dimensions D and l, the viscosity η_3 of the driver gas and the sound velocity a_1 of the test gas. For driver pressures $p_{41} \leq 2$ bar there exist two different p_{41}-values, which belong to the same Mach number M_1. The lower one produces a certain Mach number and a certain Reynolds number combined with an initial pressure p_1. The higher p_{41}-value is combined with a lower Reynolds number (smaller p_1) and induced a higher friction resistance, which again leads to the same Mach number independent of the higher shock strength p_{41}. This remarkable behaviour is found only in the case of a laminar flow behind the moving shock.

Acknowledgement. The authors would like to express their gratitude to the German Academic Exchange Service (DAAD). This work was performed during a one year's stay of Mr. Shinsuke Udagawa in Emden, Germany, financed by a PhD- scholarship from DAAD.

References

1. Brouillette M.: Shock waves at microscales. In: *Shock Waves* 13, (Springer-Verlag, 2003), pp. 3-12
2. Duff R.E.: Shock-tube performance at low initial pressure. In: *Phys. Fluids* 2, (1959), pp. 207-216
3. Garen W., Synofzik R., Frohn A.: Shock tube for generating weak shock waves. **AIAA-journal.** 12, (1974), pp. 1132-1134,
4. Garen W.: A novel mini-shock tube for generating shock waves at micro scales in turbulent and lamimar gas flows. In: *25th International Symposium on Shock Waves, Bangalore.* (Springer-Verlag, 2005), pp. 746-750

Shock wave interactions inside a complex geometry

H. Zare-Behtash, D. Kounadis, and K. Kontis

The University of Manchester, School of MACE
Sackville Street, Manchester M60 1QD, UK

1 Introduction

Studies of shocks expanding into confined regions lack detailed quantitative data of major flowfield features that evolve in time. The transient behaviour of shock waves and detonations has been the subject of study of many investigators. These include phenomena such as shock reflections, diffractions and shock/vortex interactions. The mentioned phenomena have been explored by various authors, for example shock wave reflections have been studied both phenomenon experimentally and analytically by Ben-Dor and Takayama [1], Ben-Dor et al. [2] and Henderson and Lozzi [3]. The shock diffraction pattern over corners at different Mach numbers has been studied experimentally by Skews ([4], [5]) and also by Griffith and Bricklet [6]. Shock diffraction from small areas to larger ones, have been studied by authors such as, Jiang et al. [7] and Chang and Kim [8].

Detonations diffractions from smaller to large areas have especially attracted the attention of many researchers. The study into the evolution of detonation waves that suddenly expand has been motivated not only by the need to surpress accidental detonations but also in the interest of the applicability of such flows to the concept of pulse detonation engines (Papalex et al. [9], Pantow et al. [10], Ohyagi et al. [11], Glaser et al. [12]). Pulse detonation engines (PDEs) are currently being investigated as a new technology for aerospace propulsion Glaser et al. [13].

The present study involves a combination of unsteady reflections, diffractions, vortex and subvortices generation and finally shock/vortex interactions caused by the passage of a shock wave through a complex geometry. We aim to apply theory of non-reactive shock diffraction for the discussion of the behaviour of a detonation wave, derived from the visualisation of the flow. Nondetonational computational studies have highlighted the importance of the starting vortices, precursor shocks, and direct pressure loads created by the gas-dynamic (shock-tube) processes within the ejector to the overall thrust-augmentation performance of the system. These data will be valuable for calibrating computational fluid dynamics codes and ultimately for the optimisation of PDE-ejection configurations for propulsion applications (Allgood et al. [14]).

2 Experimental Setup

Experiments have been carried out using a cylindrical shock-tube, made of seamless pipe to generate the shock waves. The internal and external diameters of the shock-tube were 30 mm and 38 mm, respectively. Experiments have been performed for driver gas (air) pressures of 4, 8 and 12 bar. The pressure in the driven section was atmospheric. The driver length used was 700mm. An industrial film diaphragm has been used to divide the

two sections in the shock-tube. The bursting of the diaphragm was initiated manually with a plunger. This setup is similar to that used by An et al. [15] and [16] and Kounadis et al. [17].

In order to study the different types of reflections, the model shown in Fig. 1 was employed. This is attached to the circular shock tube via an adaptor which gradually changes the nozzle shape from circular to rectangular, allowing for the two-dimensional study of the flow. A similar approach has been employed by Allgood et al. [14]. The test section is divided into three main sections of study. As the shock wave enters the test section, it first encounters a concave section converging into an area of constant cross-section. The shock then diffracts into a region bounded by solid straight walls on the top and bottom surfaces. Perspex sheets with a thickness of 10 mm were used on both sides of the nozzle to allow the visualisation of the flow features. The reason for chosing the relatively thick dimension of the perspex sheets was the high pressures during the experiments. In order to maintain a good seal between the nozzle geometry and the perspex sheets either side, a thin layer of instant rubber gasket was apllied on the nozzle walls. The instant gasket has a high pressure and temperature tolerance providing an ideal seal. Of course manufacturing a rubber sheet of the same geometry as the nozzle was also considered for a seal, but due to the very fine geometry and also the fact that it would introduce a thickness on the side wall and affect the quality of the flow, it was decided to use the instant gasket.

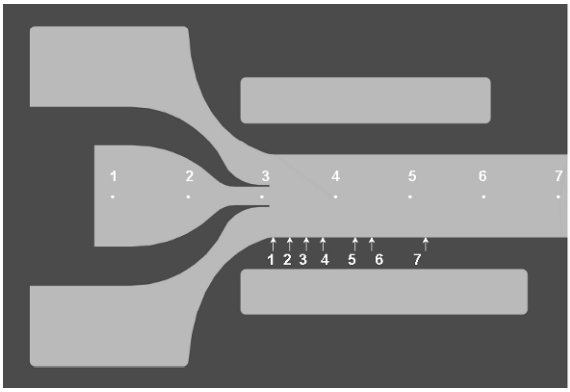

Fig. 1. Test section.

3 Results and Discussion

Figure 2 is the shadowgraph series of the events unfolded for the diaphragm pressure ratio of 8. Each frame is labeled with the corresponding time in milliseconds relative to the time the shock front arrives at the convergent-concave section of the test section.

Converging-concave section

The reflection of a planar shock wave over a cylindrical concave surface goes through four sequence of events; a direct Mach reflection, $DiMR$, a momentarily stationary Mach re-

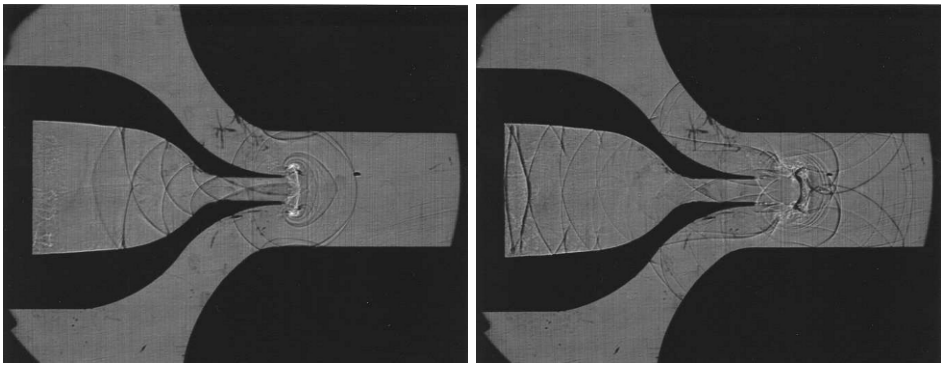

(a) (b)

Fig. 2. Shadowgraph time series for diaphragm pressure ratio of 8. a) 0.13 ms, b) 0.22 ms.

flection, $StMR$, an inverse Mach reflection, $InMR$, and finally termination of the $InMR$ and the formation of an RR. Since the RR configuration, formed after the termination of an $InMR$, has a special structure associated with it, it is referred to as a transitioned regular reflection TRR. The reflection process over a concave wedge can be summarised as follows [18]:

$$DiMR \rightarrow StMR \rightarrow InMR \rightarrow TRR$$

Uniform area section

As the incident shock travels along the concave surface it is accelerated by the area reduction of the converging nozzle and becomes stronger (Allgood et al. [14] and Chisnell [20]). As the complex shock pattern moves along the channel the reflected waves, which were once part of the Mach reflection moving along the concave walls, move towards each other and collide head on. As the reflected waves pass each other they create two focal points, one at the front just behind the incident shock and the other at the rear just before the entrance into the concave section. These waves then move towards the channel walls and are again reflected from it. The head-on collision, passing and reflection from the walls, like a bouncing motion, is continuously repeated in the flow and gives rise to an even more complicated behaviour. Each time a reflected wave moves away from the wall towards its counter reflecting counter part from the other wall, it is attached at two locations, one end is at the apex of the corner towards the convergent part of the test section and the other end is attached to the incident shock wave, this can be seen in Fig. 3 for the 12 bar case.

The point where the reflected wave is attached to the incident wave varies as the flow travels further downstream. At one instant the reflected and incident waves make contact along the surface of the channel, giving rise to a regular reflection pattern, while at some time later this attachment point moves along the incident wave away from the wall as the reflected and incident shocks merge at the stem. The wave reflecting from the opposite wall behaves in the same manner.

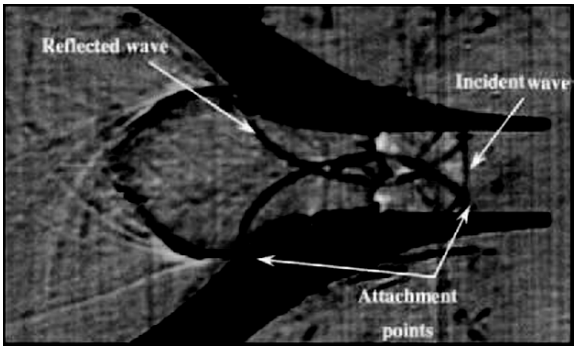

Fig. 3. Flow pattern in the constant area section.

Diffraction region

The planar shock wave undergoes transition to a cylindrical shock front as it travels through the area change. Two opposing vortex cores are formed at the corner of the area expansion and are convected downstream and expand outward slightly. These are formed once the fluid through the uniform area section encounters the area change and begins to form a 'starting jet' (Abate and Shyy [19]). The formation of the 'starting jet' gives rise to these vortices generated due to the formation of a shear layer between emerging and external fluids What is evident in Fig. 2(a) is that the initial incident wave and the first set of reflected waves exiting the nozzle go through a regular reflection pattern upon collision with the wall as they develope a cylindrical shape. The diffracted cylindrical shock wave encounters the wall head on with an initial reflection angle of 90^o. As the shock wave propagates outwards the point where it touches the reflecting surface encounters an ever decreasing effectiv reflecting wedge angle. Regular reflection is known to be impossible when the incidence angle exceeds the critical angle ($\nu_i > \nu_{cr}$). In the controversial range of incidence angles $\nu_{st} < \nu_i < \nu_{cr}$, both kinds of reflection are possible. In any event, Mach reflection would be impossible for $\nu_i < \nu_{st}$ (Kobayashi [21]). At the same time the portions of the bouncing reflected waves inside the constant area nozzle move backwards into the oncoming flow, these form a pattern which appear as a trail of spades one followed by the other.

A feature which is also present in the current study is the presence of an embedded shock wave or a 'diaphragm shock' (Fig. 2(b). For the highest driver pressure this shock wave does not appear to be stable for long and is quickly burst open due to the interaction between the shock reflection patterns that occur outside the nozze. In Fig. 2(b) we can also see that the weak rim of the diaphragm shock is drawn into the low-pressure core of the primary vortex core. From the same figure, we see the result of the interaction between a shock wave and a vortex, namely the phenomenon of shock splitting. The reflected shock waves from the upper and lower walls are diffracted by the strong circulation produced by the two vortex cores and are in a way drawn into its vortical motion.

The overall flow structure is greatly influenced by the shock strength. This is due to the non-linear interactions of the many flowfield elements which are confined in a limited flow passage (Chang and Kim [8]). The number of waves behind the diffracted precursor shock wave increases at higher Mach numbers. Each time a wave is diffracted from the uniform area section, (these waves are a consequence of the continuous bouncing

motion of the two reflected waves within the section) a shock focusing also takes place simultaneously which travels back into the oncoming flow. Therefore for the number of waves we see behind the precursor shock there exists a focused spade pattern inside the convergent-divergent section.

The pressure history at transducer 2 along the side wall is given in Fig. 4 for the three different diaphragm pressure ratios. The pressure traces appear qualitatively similar, and vary only in magnitude of the features. Examining closely these plots we can pin point some interesting features which correlate with the shadowgrams. The graphs all seem to have a gradual pressure increase until the first maxima, a reduction, and afterwards increase again. The arrival of the original incident shock wave is the first phenomenon captured by the transducers. As expected this arrival varies for the different pressure ratios, it occurs at 3.50 ms, 3.10 ms and 2.85 ms for pressure ratios of 4, 8 and 12, respectively.

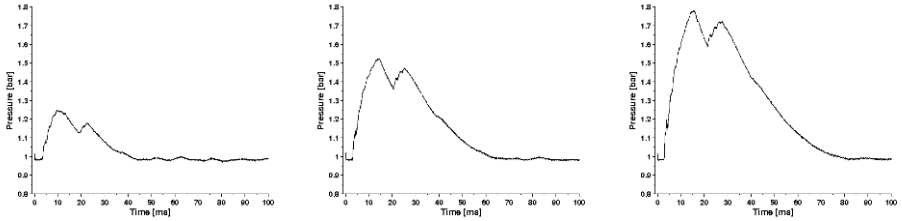

(a) (b) (c)

Fig. 4. Pressure history for transducer 2. Pressure ratios: a) 4, b) 8, c) 12. Transducer locations are depicted in Fig. 1.

After the incident shock wave has passed the transducer, the pressure behind it continues to increase upto peak values of: 1.24, 1.52 and 1.77 bar, in order of increasing pressure ratio. The pressure drop that follows the first maxima is due to the expansion of the flow generated when the two tails of the reflected shocks visible in Fig. 3 move away from each other. From the pressure histories in Fig. 4 we see that the gradient of the expansion becomes steeper at higher pressures. This is owed to the fact that the two shocks are moving away faster and thus the expansion is generated. After the drop in pressure at location T2, as mentioned above, the pressure increases again to its second maximum pressure value. But this time it does so with more pronounced step changes. By looking back at Fig. 2(a) we can see that each pressure rise represents the passage of a focused shock structure. Since the transducer is placed along the centreline of the nozzle it would be reasonable to assume that each pressure variation corresponds to a focal point.

References

1. Ben-Dor G, Takayama K., The dynamics of the transition from Mach to regular reflection over concave cylinders. Israel Journal of Technology **23**, (1986/7)
2. Ben-Dor G., Takayama K., Dewey J. M., Further analytical considerations of weak shock wave reflections over a concave wedge. Fluid Dynamics Research **2**, (1987)

3. Henderson L. F., Lozzi A., Experiments on transition of Mach reflexion. Journal of Fluid Mechanics **68**, (1975)
4. Skews B. W., The shape of a diffracted shock wave. Journal of Fluid Mechanics **29**, (1967)
5. Skews B. W., The perturbed region behind a diffracting shock wave. Journal of Fluid Mechanics **29**, (1967)
6. Griffith W., Brickl D. E., The diffraction of strong shock waves. Physical Review **89**, (1952)
7. Jiang Z., Takayama K., Babinsky H., Meguro T., Transient shock wave flows in tubes with a sudden change in cross section. Shock Waves **7**, (1997)
8. Chang K. S., Kim J. K., Numerical investigation of inviscid shock wave dynamics in an expansion tube. Shock Waves **5**, (1995)
9. Papalexandris M. V., J. F., Jacobs C., Deledicque V., Structural characteristics of detonation expansion from a small channel to a larger one. Proceedings of the Combustion Institute, (2007)
10. Pantow E. G., Fischer M., Kratzel Th., Decoupling and recoupling of detonation waves associated with sudden expansion. Shock Waves **6**, (1996)
11. Ohyagi S., Obara T., Hoshi S., Cai P., Yoshihashi T., Diffraction and re-initiation of detonations behind a backward-facing step. Shock Waves **12**, (2002)
12. Glaser A. J., Caldwell N., Gutmark E., Hoke J., Bradley R., Schauer F., Effects of tube and ejector geometry on the performance of pulse detonation engine driven ejectors. 42nd AIAA/ASME/SAE/ASEE Joint Propulsion Conference & Exhibit, (2006)
13. Glaser A. J., Caldwell N., Gutmark E., Hoke J., Bradley R., Schauer F., Experimental study of ejectors driven by a pulse detonation engine. 45th AIAA Aerospace Sciences Meeting and exhibit, (2007)
14. Allgood D., Gutmark E., A., Dean A. J., Experimental investigation of a pulse detonation engine with a two-dimensional ejector. AIAA Journal **43**, (2005)
15. An R., Kounadis D., Zare-Behtash H., Kontis K., Vortex ring interaction studies with a cylinder and sphere. 36th AIAA Fluid Dynamics Conference and Exhibit, San francisco, (2006)
16. An R., Kontis K., Edwards J. A., Compressible vortex-ring interaction studies with a number of generic body configurations. 43rd AIAA Aerospace Sciences Meeting and Exhibit, Reno, Nevada, (2006)
17. Kounadis D., An R., Zare-Behtash H., Kontis K., Head-on interactioon of shock waves and vortex rings with solid and perforated walls. 36th AIAA Fluid Dynamics Conference and Exhibit, San francisco, (2006)
18. Ben-Dor G., Shock Wave Reflection Phenomena. Springer-Verlag, (1992)
19. Abate G., W. Shyy W., Dynamic structure of confined shocks undergoing sudden expansion. Progress in Aerospace Sciences **38**, (2002)
20. Chisnell R. F., The motion of a shock wave in a channel, with applications to cylindrical and spherical shock waves. Journal of Fluid Mechanics **2**, (1957)
21. Kobayashi S., Adachi T., Suzuki T., Examination of the von Neumann paradox for a weak shock wave. Fluid Dynamics Research **17**, (1995)

Shock wave interactions with concave cavities

B.W. Skews[1] and H. Kleine[2]

[1] *University of the Witwatersrand, PO Wits, Johannesburg, 2050, South Africa*
[2] *University of New South Wales, ADFA, Canberra, ACT2600, Australia*

Summary. Recently conducted time-resolved studies of the interaction of a shock wave with a cylindrical cavity have added significantly to the understanding of shock wave reflection and focusing phenomena. Three major interaction issues are highlighted; firstly the reflection of waves off curved surfaces, secondly the details of shock focusing, and lastly the development of interesting shear layer flows, including jet formation and shear layer instabilities. Clarification of many of the processes is obtained by the tracking of weak perturbations generated from small steps on the surface of the cavity. In this paper the findings found for a circular reflector are highlighted and contrasted with those for parabolic surfaces.

1 Introduction

The recent availability of high-speed digital cameras makes it possible to examine shock wave induced flow phenomena more effectively than previously, since a single test can deliver many images, thereby removing problems arising from reproducibility of initial conditions. In this work issues of shock wave focusing and reflection off curved surfaces are revisited, and a number of new phenomena are identified.

Most previous work has concentrated on the impact of a shock wave on a parabolic cavity with a strong emphasis on the focusing properties of the wave system. Most of the investigated cavities were chosen to be shallow. The classic work is that of Sturtevant and Kulkarny [1], who were mainly interested in the motion of the triple points established during the focusing process. The other major work is that of Izumi et al. [2]. They compared experiment with simulation for a range of parabolic cavities of different depth to aperture ratios with the deepest one being for a ratio of unity. Numerical resolution was rather poor so some of the features captured in the photographs are not resolved in the simulation. The third comprehensive study [3] covered a wide variety of cavity shapes but only for the case of strong shocks. The reflector models were relatively small so that much of the flow details were not clearly visible in the presented experimental records.

Previous work on cylindrical cavities has been limited to the study of the shock wave reflection off the cylindrical surface and was not extended to times for which the shock is fully reflected. The majority of this work, done by Ben-Dor and collaborators, is summarised in his monograph [4]. The main features are the study of the transition from an initial Mach reflection (MR) to what they termed a Transitioned Regular Reflection (TRR) which will also be discussed later in the current work.

2 Experimental Details

A simple shock tube with a test section 150 mm high and 75 mm wide was used to generate plane shock waves. The test gas was air. The flow was visualised by means of

shadowgraph and omnidirectional schlieren imaging, with a Shimadzu HPV-1 high-speed digital camera as the recording device. This camera can take images at the rate of up to 1 million frames per second. Each test results in a video clip of 102 frames. Tests were conducted on two cavity profiles. The first is a semi-cylindrical surface of nominal 65 mm radius with a tangential entry for the shock. The second is a parabolic surface with the same depth to aperture ratio as the cylinder. In order to evaluate which part of the cavity surface has an effect on which part of the flow field small wall roughnesses are introduced, consisting of strips of 45 micron thick tape placed at regular intervals on the wall. With a sensitive optical system these weak wall signals may be imaged.

3 Studies on cylindrical cavities

Recent findings of a comprehensive study of the flows induced for the cylindrical cavity are presented in [5]. Three main areas of interest are pertinent, both for their inherent significance and for purposes of comparison with the data for different cavity profiles. These are: the evolution of the reflection of the plane incident wave off the curved surface, the focusing process on the plane of symmetry, and the topology and evolution of the shear layers that are generated.

3.1 The Reflection Phase

As the incident shock enters the cavity the finite radius of the cavity leading edge leads to the formation of a corner signal or lip shock as is indicated in Fig. 1a. This sequence of high sensitivity schlieren images complement the shadowgraph images in [5] as they emphasise different aspects of the same process. The top row of images is for a Mach 1.24 incident shock. As the shock propagates into the cavity successive compression waves arising from the increasing slope of the wall accumulate as is evident from the white patch developing behind the shock. This results in a part of the shock curving forward to remain normal to the wall. In frame (b) a kink begins to develop on the shock as some of the compression waves combine to form a reflected shock. This becomes visible by the small black feature close to the kink, which is the first indication of the development of a Mach reflection (MR). In frame (c), MR is fully established as is evident from the appearance of a slipstream.

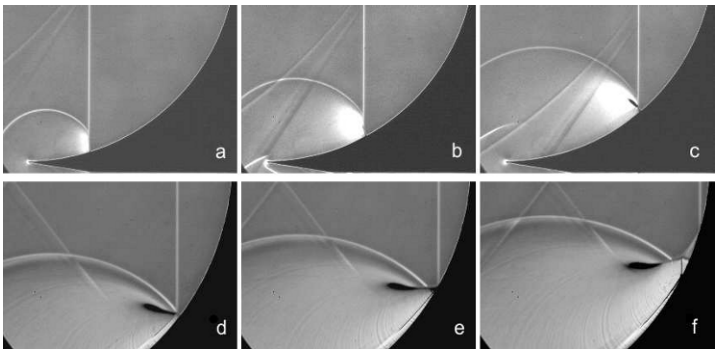

Fig. 1. The reflection evolution on a cylindrical surface. Upper row: $M = 1.24$, time between frames 26μs. Lower row: $M = 1.36$, time between frames 12μs

The lower row of images is for a stronger shock and the Mach reflection is now well established in frame (d), but is of the inverse type as the triple point is approaching the wall. It strikes the wall in frame (e) and the generation of the slipstream ceases. It is interesting to observe that the corner signal is originally ahead of the triple point (frame c), coincides with it in frame (d), after which it lags behind the triple point. This suggests that the corner signal is not responsible for transition to irregular reflection, as it is for plane wedges [6]. At frame (f) the reflection is a TRR (Transitioned Regular Reflection), as defined, and analysed, in [4]. The incident wave reflects regularly off the wall and a new three-shock system is developed behind it with a wall shock being established between the triple point and the wall in order to balance the pressures. A fresh slipstream is formed which meets the wall at the same point where the earlier slipstream terminated.

An interesting feature of using sensitive schlieren imaging for a strong shock is that small perturbations arising at slight roughness elements on the model wall become visible, as seen in the second row of Fig. 1. They clearly indicate how successive compression waves arising from the wall combine to form the reflected shock.

3.2 The focus and post-focus phases

Shock focusing is the previously most studied topic [1, 2], however, predominantly with shallow parabolic surfaces. The gas dynamic focus is taken to be where the two shear layers from the TRR on either side of the cavity collide. Figure 2 shows the development for two shock strengths from when the incident shock is fully reflected from the back of the cavity forming a converging cylindrical shock wave (first frames), through the time of focus (middle frames), to when the main reflected wave starts to develop.

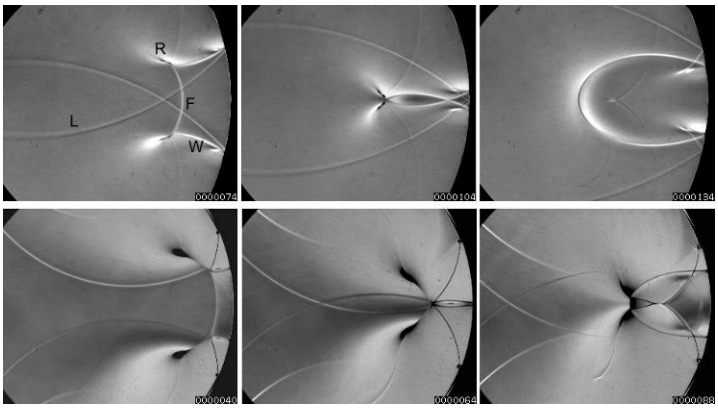

Fig. 2. Development of the flow before, at, and after focus. Top row: $M = 1.04$, Time between frames $\Delta t = 30\mu s$, Bottom row: $M = 1.37$, $\Delta t = 24\mu s$

At the time just before focus the wave system consists of the seven shocks as seen in the left column of Fig.2. The patterns are similar for shocks of different strengths. The waves are: the converging cylindrical wave (F) arising from the incident shock reflection off the back wall of the cavity, the two wall shocks (W), the two reflected waves (R), and the two weak lip shocks (L). All except the lip shock intersect symmetrically at two triple

points - note that L intersects R but neither F nor W for the high Mach number case (left bottom image of Fig. 2). These triple points leave behind two shear layers, although in the weak wave case these are very faint on the image. In the middle frame of both series the cylindrical wave is overtaken, and the remaining four waves and the shear layer meet at a point.

As shown in the final frames, the main reflected shock, which eventually emerges from the cavity, is initially made up from the two wall shocks generated earlier from the TRR. In the weak wave case the shear layers terminate in a slightly brighter spot and the original reflected waves also disappear as they are overtaken by the main reflected shock. This also occurs in the strong wave case but at much later times as will be shown subsequently. At the time of the last frame new triple points are formed in the strong wave case as the growing main reflected wave encounters the original reflected waves from the TRR. This results in two new shear layers being formed. Thus one has the original shear layers from the MR, joined to those from the TRR, which then connect up with this new pair. The subsequent evolution of these features is discussed below.

4 Shear layer behaviour

After the incident wave is fully reflected the most notable of the new features identified is the result of the meeting of the two strong shear layers that are generated from the TRR. Figure 3 shows the evolution of these features for a Mach 1.33 incident shock. The main

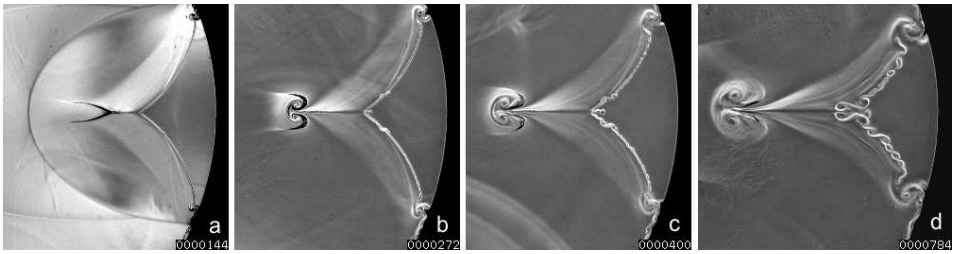

Fig. 3. The evolution of the shear layer structures showing the development of jets and Kelvin-Helmholtz instability. $M = 1.33$, $\Delta t = 128\mu s$ between first three frames, and $\Delta t = 384\mu s$ to the last frame

reflected wave absorbs the original reflected waves from the TRR leaving behind two new shear layers, and is the only wave remaining besides the original lip shocks. The two main shear layers from the TRR meet on the plane of symmetry and form a forward facing jet which couples with these new layers as shown in frame (a). However, the jet is sufficiently strong that it penetrates between these layers forming a mushroom shaped feature with a vortex on either side, frame (b). This feature continues to grow but propagates forward at a relatively low velocity. In frames (b) and (c) a second jet, facing in the opposite direction also becomes evident at the intersection of the TRR shear layers. It is thus evident that a stagnation point must develop within the shear layer confluence with part of the flow being deflected forward and the remaining backwards. The confluence point remains essentially fixed in position. At the time of frame (c) instabilities appear on the shear layers and these rapidly grow into typical Kelvin-Helmholtz patterns. At later

times these break down into turbulence. Throughout this process the schlieren images show relatively strong gradients surrounding these interactions. Similar KH instabilities occur on the jet boundaries and large vortices develop at the wall where the shear layers from the early MR meet that from the TRR, and the early shear layers also becomes unstable.

5 Comparison with a parabolic cavity using weak wave tracers

In order to obtain a better understanding of the flow processes and the development of the flow a novel weak wave tracer method is used. Thin tape is attached to the model, the edges of which form very weak, essentially acoustic, waves which can be visualised with a sensitive optical set-up.

Figure 4 shows the application of the method for two different cavity shapes: the top row for the circular arc and the bottom row for a parabolic surface of the same depth and aperture. The only previous work involving such a deep parabolic reflector is that of Izumi [2], but that study only contains a limited description of the flow processes. In the preliminary study described here rather different and interesting features appear. Both tests are run at an incident Mach number of 1.23. Comparison between the two sets is made with the centre image being at the time of focus and those on either side 20 μs earlier and later, respectively. Focus occurs 199 μs after entry to the cavity for the cylindrical case, and at 179 μs for the parabolic profile.

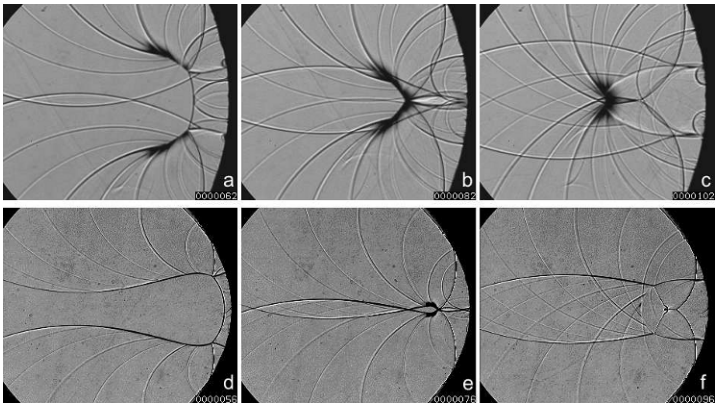

Fig. 4. Shadowgraph images showing perturbations from thin tape on the surface. Central image is at focus and others 20μs either side. Top row: cylindrical reflector. Bottom row: parabolic reflector of same depth and aperture. $M = 1.23$

Consider the pre-focus stages first. The basic reflection processes identified above are present in both cases; however, the lip shock is weak for the cylinder case and strong for the parabola because of the finite wall angle at the entrance in the latter case. In both cases the primary features arise from a TRR on each side of the cavity, being a shear layer, a reflected shock, a wall shock, and the collapsing cylindrical wave from the rear of the cavity. The weak perturbations from the tape on the wall, however, contrast the two

processes quite markedly. In the cylindrical case the lip shock overruns the reflected wave and merges with the wall shock, and waves arising from the initial portion of the surface converge on one side of the reflected wave whereas the later ones strengthen it from the other side. This gives a graphic description of how the reflected wave is formed in this case. By contrast, in the parabolic case all wavelets merge with the lip shock from one side. This effect is more marked at the time of focus where the corner signal has passed beyond the focal point for the cylindrical case but is still approaching it for the parabola. It is also noted, for the parabola, how the wavelets are much more concentrated at the focus, although they do not all meet there as they would for an acoustic incident wave. The amount of spread is thus a measure of the non-linearity and would thus be expected to be a function of Mach number. The major difference between the two cases after focus is in the new shear layers that are generated at the tip of the main jet due to the new triple points being formed. In both cases these shear layers are established by the main reflected shock passing over the original reflected shocks (R), as described in section 3.2. For the cylindrical reflector, R is relatively short and soon fans out into compression bands, which is why it is absorbed into the main reflected shock. By contrast, for the parabola, the original reflected shock is linked to the much stronger lip shock so that its interaction with the main reflected wave results in a set of slipstreams that do not only spread out much further apart but also persist.

For this parabolic case, a total of four shear layers develop as shown in Fig. 5. The first (1) is positioned close to the wall and results from the initial Mach reflection, and it is left behind when the associated triple point impacts the wall. The second (2) results from the TRR. The third (3) arises from the aforementioned interaction of the lip shock with the main reflected shock, and the last (4) forms because this reflected shock interacts with the wall as a Mach reflection.

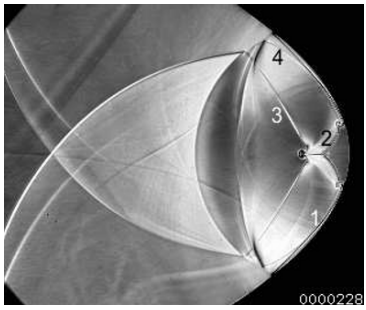

Fig. 5. Late stage development of the reflection pattern for a parabolic cavity, $M = 1.23$

References

1. Sturtevant B. & Kulkarny VA.: J. Fluid Mech. **73**, 651–671 (1976)
2. Izumi K., Aso S. & Nishida M.: Shock Waves **3**, 213–222 (1994)
3. Shugaev FV. & Shtemenko LS.: *Propagation and reflection of shock waves,*(World Scientific, 1998)
4. Ben-Dor G.: *Shock Wave Reflection Phenomena*, (Springer, 1992)
5. Skews BW. & Kleine H.: J. Fluid Mech. **In Press**, (2007)
6. Hornung H., Oertel H. & Sandeman RJ.: J. Fluid Mech. **90**, 541–560 (1979)

Shock waves dynamics investigations for surface discharge energy analysis

D.F. Latfullin[1], I.V. Mursenkova[1], I.A. Znamenskaya[1], T.V. Bazhenova[2], and A.E. Lutsky[3]

[1] *Moscow State University, Faculty of Physics, Leninskie Gory, Moscow, 119992, Russia*
[2] *Institute of Extreme-State Thermophysics UIHT RAS, Moscow, Izhorskaya st. 13/19, 127412, Russia*
[3] *Keldysh Institute of Applied Mathematics RAS, Miusskaya sq. 4, Moscow, 125047, Russia*

Summary. The distribution of the energy of a sliding discharge (plasma sheet) was obtained from the analysis of the discharge plasma radiation and the dynamics of shock waves caused by the pulsed input of the discharge energy into the gas. Non-stationary flow arising in the discharge chamber after surface discharges was visualized. Shadow and schlieren images of a flow were recorded after discharge initiation at various moments of time. CFD simulations of pulse energy release near surface were conducted and compared with experimental data.

1 Introduction

Interest in surface discharges is explained by need to develop nonequilibrium plasma for flow control. Boundary layer control using plasma technique is a method of flow pattern correction within subsonic/supersonic range. The attempts to find effective modern means to improve the streamlining and aerodynamic characteristics of supersonic and hypersonic air vehicles cause this motivation [1, 2].

A sliding surface discharge (plasma sheet) is a distributed plasma formation in the diffuse shape or in the shape of parallel channels sliding over a dielectric surface [3]. Discharges of this type are used as plasma electrodes in gas-discharge and excimer lasers and as sources of UV radiation for uniform preionization of the main discharge volume [3, 4]. The initiation of a sliding discharge in a gasdynamic flow in a shock tube makes it possible to model pulsed surface energy input into a boundary layer [5, 6]. Sliding surface discharges possess specific properties that can be used to efficiently affect gasdynamic flows. Specifically, discharge develops within a thin surface gas layer on a solid-gas dielectric interface and due to the relatively high discharge voltage and current it is capable of supplying a considerable power into the gas. Discharge duration is shorter than the characteristic times of gasdynamic processes and it can be organized over a wide surface area. It is necessary to investigate the distribution of energy input and analyze the transformation of the discharge energy into heat after discharge in order to influence of surface energy input on the flow parameters.

The initiation of a pulsed discharge is accompanied by gasdynamic perturbations caused by fast energy input into a small volume. In studying the dynamics of gas heating, an effective approach is to analyze gasdynamic perturbations arising near the discharge zone [5, 6].

The aim of the present study was to analyze the surface discharge energy rate and distribution. The spatial energy distribution model of a sliding discharge (plasma sheet) was based on the analysis of the discharge plasma glow and the analysis of shock waves from the discharge area. Shadow and schlieren visualization methods were used to analyse

non-stationary flow arising after surface discharges. To estimate the rate of pulse energy release near surface, CFD simulations were conducted and compared with experimental data.

2 Experimental setup

Experiments were carried out on the setup which consists of the special discharge chamber mounted with a shock tube (see Fig. 1 a). Two side walls of the chamber are the quarts plane glasses. Plasma sheets (size of 30×100 mm) were initiated on two opposite walls of the discharge chamber at a distance of 24 mm from one another. Pulse discharge time was about 200 ns, the voltage was 30 kV, discharge current was about 1000 A. Air is used as working gas at initial pressure of 20-200 Torr.

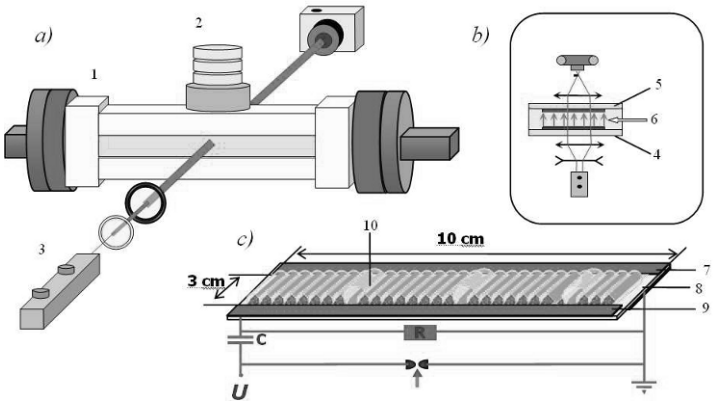

Fig. 1. a) Scheme of the experimental setup: (1) discharge chamber, (2) power supply, (3) laser; b) Optical scheme: (4) shock tube channel, (5) glasses, and (6) discharge zone; c) Discharge circuit: (7) grounded electrode, (8) dielectric, (9) high voltage electrode, (10) shock waves.

To organize a plasma sheet, we used the electrode configuration shown in Fig. 1 c. The current reached its maximum value (1-2 kA) during 50 ns, and the most of energy was input into the discharge during 100 ns after breakdown.

The integral glow of the sliding discharge was photographed through the windows of the discharge chamber, and the digital images of the glow were then processed using standard software packages. Measurements of the discharge glow were performed in quiescent air and in a gas flow behind a plane shock wave (with a Mach number of up to 3.5) at a flow velocity of up to 900 m/s (corresponding to a Mach number of up to 1.5) and gas densities of 0.03-0.40 kg/m^3. By analyzing and processing images of the discharge glow, we studied the structure of the surface discharge with and without a gas flow and determined the thickness of plasma layer and the geometry of the discharge channels.

Due to fast energy input into a thin gas layer, shock waves propagated away from the plasma sheet [5, 6]. The dynamics of perturbations propagating from the plasma sheets was studied using shadowgraphy. To visualize shock waves and to analyze the dynamics

of their motion, we took shadow and schlieren images of the flow at different instants after the initiation of discharge. The pulse laser was used as light source operating at energy of 0.64 J, pulse time 20 ns, and wavelength 0.6943 μm (see Fig. 1 a, b).

3 Experimental results

3.1 Discharge glow analysis

The glow of a distributed surface discharge was recorded in different directions. Measurements of the integral glow of the plasma sheet in quiescent air at pressures of 20-200 Torr showed that the discharge had a quasi-planar structure and consisted of a diffuse glow and a set of channels.

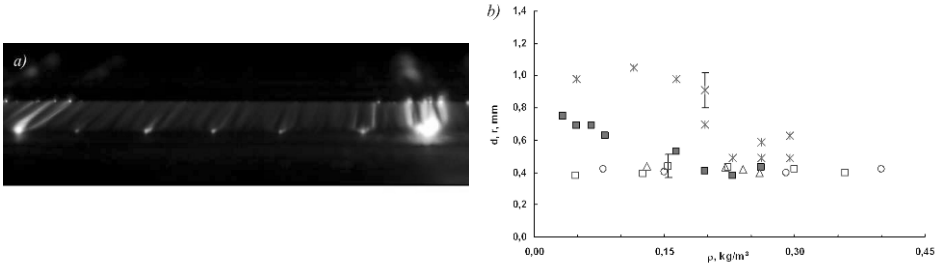

Fig. 2. a) Glow of the plasma of a surface discharge in quiescent air (ρ=0.10 kg/m^3); b) Geometrical parameters of a sliding discharge: radius r of bright channels (asterisks) and plasma layer thickness d for discharges excited in quiescent air (solid squares) and in gas flows with Mach numbers of M = 0.9 (triangles), M = 1.2 (circles), and M = 1.3 (closed squares)

Experiments showed that surface discharge structure was: 5-9 channels per 1 cm length with one more bright (intensive) channel (Fig. 2 a). In a transverse (relative to the propagation direction of the discharge channels) air flow, a more diffuse plasma glow of the surface discharge was observed behind the shock wave at transonic and supersonic velocities (M=0.9-1.3). The thickness of the plasma layer, the distance between the channels, and the number of channels per unit length depended on flow pressure.

The thickness of the plasma layer was determined by scanning images of the glow region and by processing the obtained intensity profile of the plasma glow. From the full width at half-maximum of the intensity profile, we found the thickness of the energy input zone. The radius of a bright channel was found analogously. The results of these measurements are presented in Fig. 2 b. The plasma layer thickness in a quiescent air decreased from 0.8 to 0.4 mm as the density varied from 0.03 to 0.30 kg/m^3. In the ranges of the densities and flow velocities under study, the plasma layer thickness in an air flow was almost constant value of 0.4 mm.

3.2 Shock waves analysis

The development of a pulsed surface discharge was accompanied by an abrupt change in the pressure in the energy input zone and the generation of shock waves. Experiments

showed that the development of the discharge channels led to the formation of semi-cylindrical shock waves (Fig. 3 a). The bends of the front corresponded to the semi-cylindrical shock waves (of different intensities) propagating from individual channels of discharge. Various three-shock configurations arising due to the interaction between semi-cylindrical shock fronts were visualized by the Schlieren method.

The shock waves moved away from plane discharge area at initial velocity of 800 m/s. Over the subsequent 5-6 μs, the propagation velocity decreased. The deceleration of the shock wave was apparently associated with the propagation of rarefaction waves inside the energy input layer. Fronts of these waves interfered with each other and formed quasi-planar smooth shock front (Fig. 3 b). The waves propagated at a constant velocity of 450±50 m/s 10-20 μs after discharge initiation. Further there was a counter interaction of shock waves from two plasma sheets, and during next 15-20 μs shock waves have decayed.

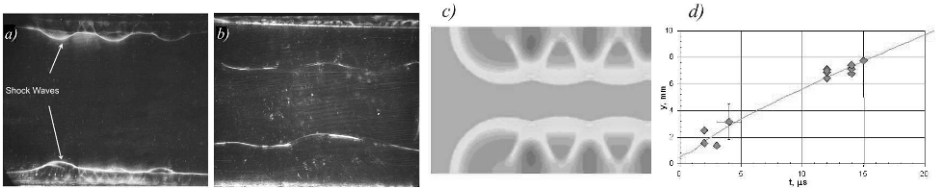

Fig. 3. a) Schlieren image, 2 μs after discharge; b) Schlieren image, 12 μs after discharge; c) Density field at 15 μs after discharge; d) Calculated (line) and experimental (points) average shock wave front position.

The dynamics of shock fronts was investigated by digital processing and analyzing of shadow and Schlieren images taken at different instants after the initiation of a surface discharge. The positions of the envelope front of a quasi-planar shock waves propagating from each plasma sheet were obtained by averaging the coordinates of the wave front over the image. In Fig. 3 d, the symbols show the measured positions of the envelope front of a shock wave as functions of time (the y-t diagram). By analyzing the coordinates of the shock front envelope line and its propagation velocity in the formation stage and in the stage of steady-state motion, we could compare the measured values of the propagation velocity with results of computer simulations.

4 Numerical simulation

In order to determine how fast the energy of a distributed surface discharge is transformed into heat, we performed numerical simulations of pulsed energy input near a surface and the development of the generated perturbations (shock waves). Comparison of numerical dynamics of shock waves movement from plasma sheets with experimental data was carried out at various values of an instant energy deposition. The gasdynamic expansion of perturbations from the zone of energy input was calculated. The numerical simulations was performed using time-dependent Euler equations (viscosity and heat conduction of the medium were ignored). For 2D, non-steady compressible flow of ideal, perfect gas:

$$
\begin{aligned}
Q_t + & E_t + F_y = 0 \\
Q &= (\rho, \rho u, \rho v, e)^T \\
E &= (\rho u, \rho u^2 + p, \rho uv, (e+p)u)^T \\
F &= (\rho v, \rho uv, \rho v^2 + p, (e+p)v)^T
\end{aligned}
$$

Hear ρ, p, E - density, pressure and total energy, u, v - velocity vector components. At realization of computer simulation the model of ideal gas with $\gamma = 1.4$ was used. The system is supplemented by the equation of a state of polytrope gas.

Equations were solved using the Godunov's generalized difference scheme with piecewise-linear time and space representations of the gasdynamic functions [7]. The energy deposition in thin layer was simulated in accordance with a real process. The gasdynamic flow pattern moving from region of energy deposition was calculated and compared to the experimental data. The discharge duration is appreciably shorter than the characteristic time of gasdynamic processes; therefore, in our calculations, we assumed that the energy was input instantly.

Energy input in air was modeled by depositing an energy in each of the two 10-cm-long layers located near two solid surfaces placed at a distance of 24 mm from one another. The simulation was conducted at 100 Torr pressure and 293 K temperature. An analysis of shadow images indicates that the resulting wave front forms due to the interference of shock fronts propagating from individual semi-cylindrical sliding discharge channels. Therefore, we performed simulations in which the deposited energy was distributed among several equidistantly spaced channels of radius d, the distance between the channel axes being 2.22d. The total deposited energy was equal to the experimentally determined value. The deposited energy was distributed over the surface in accordance with the experimental results: the ratio between the numbers of bright and diffuse channels was 1 : 8 and the energy deposited into each ninth channel was eight times as large as that input into the neighboring channels. Initially, it was assumed that the entire deposited energy was instantly transformed into heat.

Numerical simulations show that shock waves propagating into the unperturbed gas form at the boundaries of the energy input regions. A single front propagating toward the symmetry plane $y = 0$ forms as a result of interference between individual semi-cylindrical shock waves propagating from each of the channels. As time elapses, the shock front gradually becomes more plane. This is illustrated in Fig. 3 c, which presents the density distributions.

5 Discussion of the results

A comparison between the calculated flow fields and the visualized shock wave configurations indicates good agreement. Although the measured flow pattern is similar to that calculated under the assumption of 100% transformation of the discharge energy into heat, there is appreciable difference between the measured and calculated positions of the shock waves. In the experiment, the shock wave propagates considerably slower than in simulations. Apparently, this difference is associated to a large extent with the assumption that the entire energy of the electric discharge instantly transforms into the translational degrees of freedom, whereas in the experiment, electric losses, energy losses due to the excitation of the vibration and electronic degrees of freedom, radiative losses,

etc., can play a significant role. Since the propagation velocity of the shock wave is determined by the pressure increment caused by pulsed energy input, we performed a series of simulations aimed at estimating the energy fraction instantly transformed into heat. The best agreement between the calculated and measured dependencies *y(t)* was achieved at the energy fraction instantly transformed into heat being 40% (Fig. 3 d).

The simulations showed, that under these conditions, the temperature of the surface gas layer increased to 1000 K over 1-2 μs. As we assumed, fast gas heating is caused by the efficient excitation of the electronic states of nitrogen molecules, followed by their quenching at high strengths of the reduced electric field. Thus, the heating dynamics of a surface gas layer in a distributed sliding discharge is closely related to the character of kinetic processes in the gas-discharge plasma.

6 Conclusion

Analysis of the results of experimental and numerical investigation of shock waves dynamics after pulse surface energy deposition in gas showed good agreement with a thermal energy deposition model. Experimental values of the velocity of shock waves well agree with the results of calculations obtained assuming that about 40% of energy deposited in the surface layer is converted into heat instantly in the stage of energy supply. The plasma layer thickness in a quiescent air decreased from 0.8 to 0.4 mm as the density increased. In gas flows with Mach numbers of 0.9-1.3, the plasma layer thickness determined from the intensity profile of the plasma glow is independent of the gas density and amounts to 0.4 mm.

Acknowledgement. This work was supported by the program No. 9 part 2 of the Russian Academy of Sciences and the Russian Foundation for Basic Research, grant No. 06-08-01301 a.

References

1. Chernyi G.G., Some Recent Results in Aerodynamic Applications of Flows with Localized Energy Addition, AIAA Paper 1999-4819, 1999
2. Bletzinger P., Ganguly B.N., Van Wie D., Garscadden A. Plasmas in High Speed Aerodynamics, J. Phys. D: Appl. Phys. 38, R33-R57, 2005
3. Karlov N. V., Kuz'min G. P., and Prokhorov A. M., Gas Discharge Lasers with Plasma Electrodes, Izv. Akad. Nauk SSSR, Ser. Fiz. 48, 1430-1437, 1984
4. Baranov V.Yu., Borisov V.M., Davidovskii A.M., and Khristoforov O.B., Use of a discharge over a dielectric surface for preionization in excimer lasers, Sov. J. Quantum Electron. Vol. 11. No 42. P. 77-82, 1981
5. Znamenskaya I.A., Lutsky A.E., Mursenkova I.V., The surface energy deposited into gas during initiation of a pulsed plasma sheet discharge, Technical Physics Letters 30(12), 1036-1038, 2004
6. Znamenskaya I.A., , Latfullin D.F., Lutsky A.E., Mursenkova I.V. and Sysoev N.N., Development of Gasdynamic Perturbations Propagating from a Distributed Sliding Surface Discharge, Technical Physics, 2007, Vol. 52, No. 5, P. 546-554, 2007
7. Kulikovskii A. G., Pogorelov N. V. and Semenov A. Yu., Mathematical Aspects of Numerical Solution of Hyperbolic Systems, Chapman and Hall, Boca Raton, 2001

Shock-on-shock interactions over double-wedges: comparison between inviscid, viscous and nonequilibrium hypersonic flow

G. Tchuen[1], M. Fogue[1], Y. Burtschell[2], D.E. Zeitoun[2], and G. Ben-Dor[3]

[1] *Institut Universitaire de Technologie Fotso Victor, Université de Dschang, BP. 134 Bandjoun - Cameroun.*
[2] *Ecole Polytechnique Universitaire de Marseille/DME, Université de Provence, Technopole de Chateau Gombert, 13453 Marseille Cedex 13, France.*
[3] *Department of Mechanical Engineering, Ben-Gurion University of the Negev, Beer Sheva, 84105 Israel.*

1 Introduction

The interactions between shock waves and boundary layers is a phenomenon frequently encountered in hypersonic flight. The existence of such shocks interactions produces a very high localized heat-transfer rates, oscillating pressure fields on the vehicle surface and can alter the aerodynamic characteristics of the vehicle. The flowfield perturbations which result of the shock-shock interactions are an important factor in the design of the shuttle entry configuration. Using from an experimental program which employed elementary configurations, Edney [1] defined the flow phenomena which characterize the various types of shock-interaction patterns.

About a decade ago Olejniczak et al. [2] published their results of a study on the interaction of an inviscid flow with a double-wedge. The interaction between two shock waves resulted in a variety of overall shock wave configurations. The space parameter of interactions has been explored and the different Edney [1] type of interactions have been identified. The type of interaction that occurs depends on the relevant non-dimensional parameters, which for inviscid flow are the Mach number M, the ratio of specific heats γ, the ratio of the first wedge face length to the second wedge face L_2/L_1, and the two wedge angles θ_1 and θ_2.

In order to show the significance of high temperature effect in the fluid on the present flow problems, nonequilibrium air flow simulation have been performed for comparison. For the nonequilibrium air flow, the internal energies take into account one translational temperature, two vibrational temperatures and the definition of the transport properties are related to the model. The air flow is assumed to be consisting of 5 components (N_2, O_2, NO, N, O). The chemical reactions are given by the Gardiner [3] model which involves 17 reactions (dissociation and recombination). The goal of the present study is to repeated Olejniczak et al. [2] work by using home computer codes [4,5] that accounted for both viscosity and real gas effects. The influence of these two mechanisms separately and together on the results are examined.

In the present work, the computational fluid dynamics with a two-dimensional compressible Navier-Stokes solver is used to study shock interactions generated by double-wedge geometries. the nominal flow conditions are a freestream Mach number of 9.0. Two double-wedge is studied with the angles $(15^o - 45^o)$ and $(15^o - 50^o)$. The obtained shock interaction pattern is either a Type-V pattern, a Type IV pattern or a Type-VI pattern, as defined by Edney. Interest is focused not only on the overall double-wedge, but

also in particular region submitted to strong constraints which limit the performances of the structure. The comparisons have been made between the computed surface pressure along the body and Mach number contours values obtained with and without real gas effects.

2 Analysis

The full laminar time-dependent Navier-Stokes equations for two-dimensional flow and multicomponent mixture of reacting gases are written as conservation laws in the integral form:

$$\frac{\partial}{\partial t}\int_V W dV + \int_{\partial V} F \cdot n dS = \int_{\partial V} \Omega dV, \tag{1}$$

where

$$\begin{aligned}
W &= [\rho_s, \rho u, \rho v, \rho e, \rho e_{v_m}]^T, \\
F &= (F_{c_x} + F_{c_y}), \qquad F_v = (F_{v_x} + F_{v_y}), \\
F_{c_x} &= [\rho_s u, \rho u^2 + p, \rho uv, (\rho e + p)u, \rho e_{v_m} u]^T, \\
F_{v_x} &= [\rho_s V_{x_s}, \tau_{xx}, \tau_{xy}, u\tau_{xx} + v\tau_{xy} + q_x + \sum_{s=1}^{ns} \rho_s h_s V_{x_s}, q_{v_{m_x}} + \rho_m e_{v_m} V_{x_m}]^T, \\
\Omega &= [\omega_s, 0, 0, 0, \Omega_{rv_m}]^T,
\end{aligned}$$

with: $s = 1, ..., ns$; $m = 1, 2$. F_{c_y} and F_{v_y} have the same expression as F_{c_x} and F_{v_x}, respecting y direction. ns is the total number of species, and m the number of molecular vibrating species. The viscous stresses τ_{xx}, τ_{xy}, τ_{yx}, the heat flux components q_x, q_y, the species diffusion fluxes and the source term Ω can be found in detail in ref. [5].

The equation of state is needed and the mixture pressure is given by Dalton's law as the sum of partial pressure of each species regarded as perfect gas

$$p = \sum_{s=1}^{ns} \rho_s \mathcal{R} T / \hat{M}_s. \tag{2}$$

The translational temperature T is obtained by the total energy equation of the mixture per unit of volume:

$$T = \left(\sum_{s}^{ns} \rho_s C_{v,tr}^s \right)^{-1} \left[\rho E - \frac{1}{2} \sum_{s} \rho_s u_s^2 - \sum_{m=1}^{nm} \rho_m e_{v_m} - \sum_{s}^{ns} \rho_s h_s^0 \right], \tag{3}$$

where $C_{v,tr}^s$ is the specific heat of species s.

3 Numerical methods

The finite volume approach integrates governing equations over each cell in the discretized domain. The spatial derivatives of the inviscid fluxes are approximated by an upwing TVD formulation coupling with a modified form of AUFS [6] (Artificially Upstream Flux

vector Splitting) scheme, in which high temperature effect are introduced. The MUSCL approach and Mimmod limiter function are used to achieve second-order spatial accuracy. The viscous fluxes are discretized by second-order central differences. The source term Ω is treated implicitly in order to avoid the stiffness problems introduced by the small mesh increments in the boundary layer. A time predictor-corrector algorithm [5] is used to obtain second order time accuracy.

In this work, the grids have been stretched in both directions near the surface and the hinge location, to correctly computed the shock wave/boundary-layer laminar interaction. Figure 1 shows the geometry and grid used in calculations for first double-wedge. The minimum grid spacing in x and y direction are respectively equal to $\Delta x = 1.35\text{x}10^{-4}m$ and $\Delta y = 1.02\text{x}10^{-5}m$.

4 Boundary conditions

The boundary conditions are imposed along the double-wedge. A no-slip velocity condition is applied at the body surface, and an adiabatic wall is assumed for all cases. The boundary-layer approximation of a zero wall-normal pressure gradient are employed. In the case of reacting flows, the wall is assumed to be noncatalytic, i.e the concentration gradients at the wall are zero.

Freestream conditions are enforced at the farfield boundary, while zero-order extrapolation conditions are set at the supersonic out-flow. The freestream conditions of this high enthalpy real gas test-case are reported below: $L_1, L_2 = 0.05$ (m); $\theta_1 = 15^o$; $\theta_2 = 45^o$ and 50^o; $P_\infty = 10^5(P_a)$; T_∞, $T_{V_{N_2}}$, $T_{V_{O_2}} = 300$ (K); $U_\infty = 3130.137$ (m/s); $M_\infty = 9.0$; $Y_{N_2} = 0.766$; $Y_{O_2} = 0.233$. In this study $L_2/L_1 = 1$ and $\theta_1 = 15^o$ are kept constant, which allows to explore the influence of real gas effect with θ_2 parameter space.

5 Results and discussions

The details of the influence of real gas effect on double-wedge shock interaction are described. The first wedge angle, ratio of wedge face lengths, and ratio of specific heats are held constant so that we can fully explore the remaining θ_2 parameter space.

The first case concerns $15^o - 45^o$ double-wedge. Figure 2 shows the contour lines of Mach number with an enlargement of the interaction region for an inviscid flow. The structure of the shock interaction is similar to the type V interaction, following the notation of Edney. The oblique shock interact the bow shock from the second wedge and a third shock is transmitted from the interaction toward the surface. The reattachment shock intersects this transmitted shock and forming a triple point. The streamlines which pass through the triple points show the location of the contact discontinuities. A thick shear layer (region of weak gradient) is emitted from the main intersection point on the bow shock, which separate the outboard flow from the supersonic inboard flow.

The figure 3 shows the computed Mach contours for a nonequilibrium flow. In this case, viscous fluxes and thermochemical nonequilibrium are taken into account together. The shock interaction that corresponds is an Edney Type VI shock interaction. A contact discontinuity can be clearly seem. The interacting shocks are less detached causing a strong shock/boundary layer. The difference is clearly observed in the comparison of the

shock stand-off distances. In this case, the nonequilibrum effect leads to the transition from shock of the Type V for inviscid calculation to a shock of the type VI.

The figure 4 compares the computed surface pressure for an inviscid, viscous and nonequilibrium flow at M=9 with wedge of $\theta_1 = 15^o$ and $\theta_2 = 45^o$. The flow field is characterized by an underexpanded jet which impinges on the wedge and produces large-amplitude surface pressure variations. In the inviscid case, the first pressure peak (380 times free-stream value) that appears at s/L=1, is a result of the interaction with the leading edge of the second wedge and corresponds to the regular reflection of the transmitted shock on the wedge surface. This is followed by a slight variation of the pression which corresponds to a rapid expansion. The present computed inviscid surface pressure is identical to the one obtained by Olejniczak et al. [2]. In viscous case, the flow fields is also associated with oscillating pressure fields in which extremely high-pressure peaks are developed. For nonequilibrium case, the pressure is much affected by chemical reactions and a reduction in the predicted peak pressure of about 66.6% can be observed. The final abrupt drop in pressure (at $s/L = 2$) is a result of expansion onto the after body.

The second case concerns the $15^o - 50^o$ double-wedge. An enlarged view of Mach number countours over the interaction region is shown in figure 5. The flow field has a shock interaction that corresponds to an Edney Type IV shock interaction. The contours Mach number shows the extended separated region around the hinge location. The region of the interactions is close to the corner as a result of compression due to the presence of normal shock and the compression due to the interaction oblique shock/bow shock. The incident shock impinges on the bow shock and a triple point is generated. The streamlines show the presence of a sinuous contact discontinuity originates from the triple point. The results are similar to those of Olejniczak et al. [2].

These flows are complicated when the finite-rate chemical reaction are coupled to the fluid motion and that viscous effects plays a large role. So figures 6 - 8 also allow to explore progressively the influence of different effects on the flow field. The computed Mach number contours along the interaction region are showns in figure 6. The shock/shock interaction remains Type IV interaction in Edney's notation. The existent normal shock becomes more important with nonequilibrium calculation. The thickness of the shock layer using the differents models are significantly different. Figure 7 shows that the nonequilibrium shock layer is 35% less thick than the inviscid shock layer. This is due to the fact that the endotermal dissociation reactions as well as the excitation of the internal degree of freedom cause a decrease in the temperature in the flowfield, and thus an increase in the density. An expansion fan is emanated from the interaction point.

The computed inviscid, viscous and nonequilibrium surface pressure are compared in the figure 8. The pressure behind the two first shock is higher compared to the pressure behing the deflected third shock. The expansion causes a rapid decrease of the surface pressure distribution along double-wedge. After the pressure peak at $s/L = 1$, alternating pressure minima and maxima are visible along the second wedge surface, as visualized by the rounded countours centred at the extrema locations. The first three pressure peaks are associated with the two humps that are seen in figure 7. In inviscid case, the pressure peaks are again seen to decrease monotonically, from slightly more than 300 time the ambiant pressure, to about 160 times the ambiant pressure and finally to slightly below 120 times the ambient pressure.

6 Conclusion

The present study was undertaken to investigate the shock/shock and shock/boundary-layer interactions in hypersonic flow around double-wedge configurations. The main effects, which are considered, are the viscous and physico-chemical nonequilibrium processes behind the shock, which are commonly referred as high-temperature effect. Three of the interactions that occurs (Type IV, Type V, and Type VI) fit into Edney's classification scheme.

The comparisons between the present numerical results and the Olejniczak et al. [2] solutions for the type-VI and IV solutions are satisfactory on the double-wedge, both in term of pressure and Mach number. The obtained results show that the real gas effects alter significantly the structure of the shock-interaction. The computed surface pressure is deeply sensitive to the nonequilibrium effect as different results show it.

References

1. Edney, B. *Anomalous heat transfer and pressure distributions on blunt bodies at hypersonic speeds in the presence of an impinging shock* Rep.115. Flygtekniska Foroksanstalten (The aeronautical Research Institute of Sweden), Stockholm, 1968.
2. Olejniczak, J., Wright, M. J. and Candler, G. V. *Numerical study of inviscid shock interactions of double-wedge geometries* Journal of Fluid Mechanics, 352, 1-25, 1997.
3. Gardiner, W. C. *Combustion chemistry.* Springer Verlag, 1984.
4. Burtschell, Y., Zeitoun, D. E. and Ben-Dor, G. *Steady shock wave reflections in thermochemical non-equilibrium flows* International Journal of Shock Waves, 11, 15-21, 2001.
5. Tchuen, G., Burtschell, Y. and Zeitoun, D. E. *Numerical study of nonequilibrium weakly ionized air flow past blunt body* Int. J. of Numerical Methods for heat and fluid flow, 15, (6), 588 - 610, 2005.
6. Sun, M., and Takayama, K., *An artificially upstream flux vector splitting scheme for the Euler equations.* Journal of Computational Physics, Vol. 189, pp. 305-329, 2003.

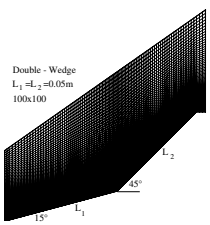

Fig. 1. Structure of grid employed

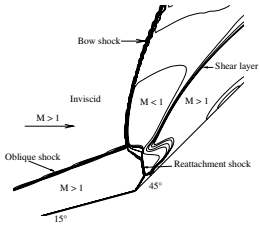

Fig. 2. enlargement of the interaction region showing Mach contours

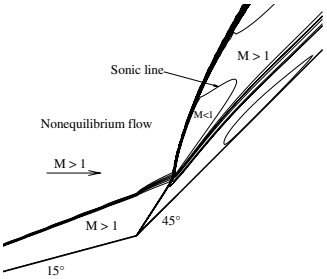

Fig. 3. Mach contours for nonequilibrium flow

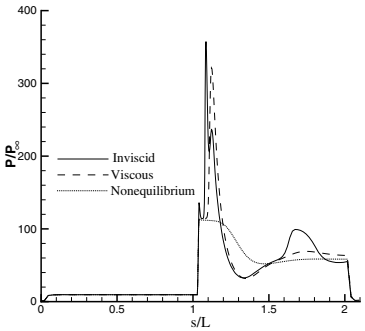

Fig. 4. Comparison of surface pressure

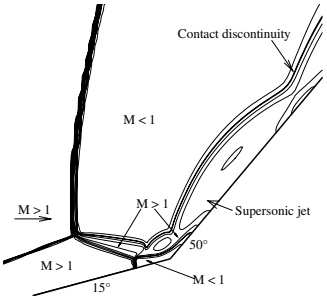

Fig. 5. contours Mach number

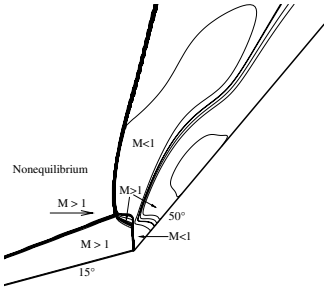

Fig. 6. Contours Mach number for non-equilibrium

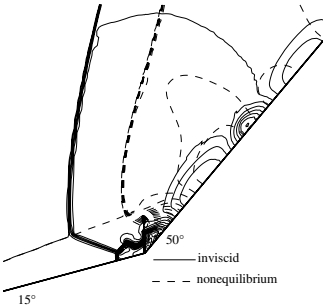

Fig. 7. Comparison of pressure contours

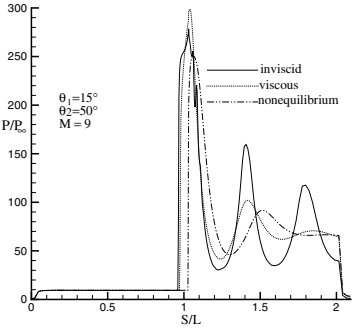

Fig. 8. Comparison of surface pressure

Simulation of forming a shock wave in the shock tube tube on the molecular level and behavior of the end of a shock-heated gas

S.V. Kulikov

Institute of Problems of Chemical Physics of Russian Academy of Sciences, Chernogolovka, 142432, Russia

Summary. Monte Carlo nonstationary method of statistical simulation (another name DSMC) was used in calculations. Simulation was carried out in the one-dimensional coordinate space and in the three-dimensional velocity space. Molecules were presented as hard spheres without internal structure. At an initial moment, the high-pressure chamber (HPC) of a shock tube was filled up by a gas with the molecular mass (μ) equal to μ of H_2. And the low-pressure channel (LPC) was filled up by the mixture of gases with μ of each gas equal to μ of Xe, O_2, He and H_2 with the ratio of concentrations 1:10:169:20 respectively At an initial moment, temperatures of gases in HPC and LPC were set equal, but the ratio of pressures was set to 100. The simulation started after removing a diaphragm between this parts. Parallel calculations were carried out by means of a multi-processor computer. Domain decompositions of a simulation region was performed. And 175 processors were used. It was found that the size of the diffuseness zone for the end of a shock-heated gas from the side of the HPC didn't change during the time of simulation.

1 Introduction

The Monte Carlo non-stationary method of statistical simulation (MCNMSS) (another name DSMC) [1] was used in calculations. It takes into account all processes of heat-mass transfer automatically. Development of computers permits now to simulate by MCNMSS a gas processes in which a local mean free path of molecules (λ) is much less than a local character size of this process (L) except a small region where $\lambda \sim$ L. Forming a shock wave in the shock tube is one of such processes. Numerical study of the process in the gas on the molecular process level is important and gives a lot of useful information.

2 Statement of problem

At an initial moment, the high-pressure chamber (HPC) of a shock tube was filled up by a gas with the molecular mass(μ) equal to μ of H_2 . And the low-pressure channel (LPC) was filled up by the mixture of gases with μ of each gas equal to μ of Xe, O_2, He and H_2 with the ratio of concentrations(n) 1:10:169:20 respectively. Molecules reflected elastically from the walls at boundaries of the simulation region. At an initial moment, temperatures (T) of gases in HPC and LPC were set equal, but the ratio of pressures was set to 100. The simulation started after removing a diaphragm between this parts of the shock tube.

3 Method of simulation

MCNMSS with constant weight factors [1] was used in calculations. Simulation was carried out in the one-dimensional coordinate space and in the three-dimensional velocity space. Molecules were presented as hard spheres without internal structure. The ratio of diameters was equal to 1.000:0.737:0.443:0.540 for Xe, O_2, He and H_2 respectively. In order to the size of spatial cell (Δx) did not exceed local λ in the gas, the value of spatial cell in HPC was 20 times smaller than the value of that in LPC at the beginning. During the simulation, that part LPC where molecules from HPC have enter, got new cells the value of which was 20 times smaller than the value of old sells. In order to use reasonable number of model particles, weight factors of H_2 were 50 times higher in HPC than in LPC. But, they were equal to 1, 10, 169 and 20 for Xe, O_2, He and H_2 respectively in LPC. The initial average number of model particles per cell (N) was equal to 360 both in LPC and in HPC, initial Δx =0.15 in LPC. Here and bellow distance is normalized to mean free path in LPC at the initial moment (λ_H). The time of splitting of collision and displacement stages was Δt=0.04. Here and bellow time is normalized to the ratio $\Delta x/u$, where u is the most probable thermal velocity of molecules of H_2 at the beginning. Parallel calculations were carried out by means of a multi-processor computer. Domain decompositions of a simulation region was performed. The modeled region spread from 2246.25 to 2246.25 Boundary between LPC and HPC was placed at x=746.25. And 175 processors were used. Standard Message Passage Interface (MPI) was used to communicate data between processors.

4 Results

Figs 1-8 shows profiles of flow characteristics of components for different moments of time.Here and bellow T was normalized to its initial value in LPC, n - to initial value of concentration of Xe in LPC. Velocities are normalized to u.

Obtained positions of the wave of rarefaction, the zone of shock-heated gas and the wave front as well as values of gas parameters behind the front complied well with results of the simple theory of shock wave [2, 3].

Component	H_2		Xe	
t	ΔT	Δn	ΔT	Δn
232.05	56	70	50	28
358.05	51	54	35	19
668.65	60	60	28	37
845.4	56	70	28	28
1059.35	58	63	42	18

Table 1. Sizes of the zones of diffuseness

Interesting obtained results are connected with behavior of an end of a shock-heated gas from the side of the HPC. Table shows the sizes of these zones of diffuseness for the temperature (ΔT) and concentration (Δn) of H_2 and Xe. Accuracy of results is equal to $\pm$ 10. One can see that the sizes didn't change during the time of simulation with statistical accuracy. The sizes of the concentration diffuseness were equal to 26, 55, 55, 63 and of the temperature diffuseness -to 37, 55, 55, 56 for Xe, O_2, He and H_2 respectively.

5 Conclusion

It is very difficult (maybe impossible) to obtain correct solution on hydrodynamic level in this case. But MCNMSS permits to calculate this problem.

It was found that the size of the diffuseness zone of the shock-heated gas from the side of the HPC didn't change during the time of simulation.

The present study was supported by the Program of Presidium of RAS "Mathematical modeling and intellectual systems (program of Presidium of RAS No 16).

References

1. Genich A. P., Kulikov S.V., Manelis G.B., Chereshnev S.L.: Thermophysics of translational relaxation in shock waves in gases. Sov. Tech. Rev.B Therm. Phys., v.4, part 1, pp. 1-69, 1992.
2. Landau, L.D., Lifshitz, E.,M. Hydrodynamics. M.:Nauka, 1986, (in Russian).
3. Losev, S.A., Osipov, A.I., Stupochenko, E.V. Relaxation Processes in the Shock Waves. M.:Nauka, 1965, (in Russian).

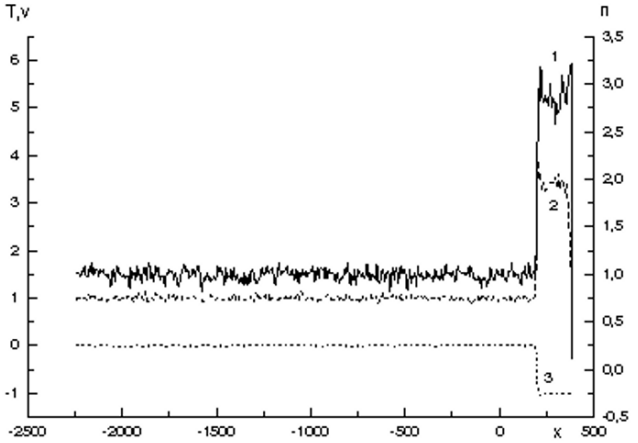

Fig. 1. Profiles of concentration(1), total kinetic temperature (2) and longitudinal velocity (3) for Xe at time 358.5.

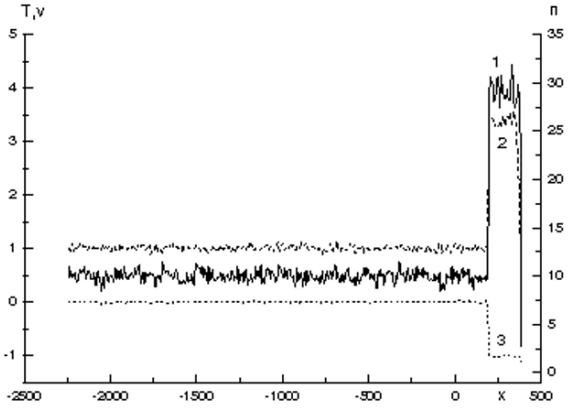

Fig. 2. Profiles of concentration(1), total kinetic temperature (2) and longitudinal velocity (3) for O_2 at time 358.5.

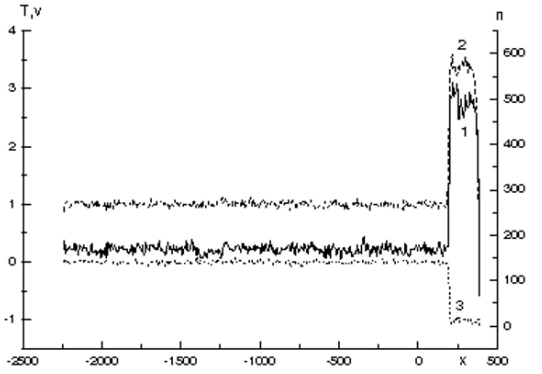

Fig. 3. Profiles of concentration(1), total kinetic temperature (2) and longitudinal velocity (3) for He at time 358.5.

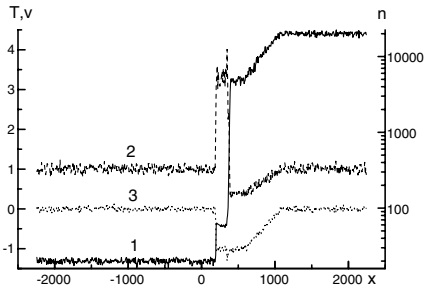

Fig. 4. Profiles of concentration(1), total kinetic temperature (2) and longitudinal velocity (3) for H_2 at time 358.5.

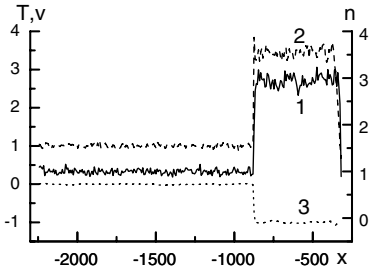

Fig. 5. Profiles of concentration(1), total kinetic temperature (2) and longitudinal velocity (3) for Xe at time 1059.3.

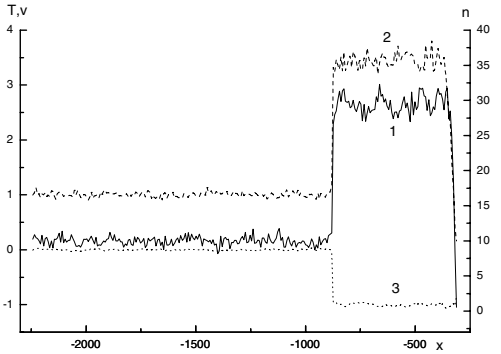

Fig. 6. Profiles of concentration(1), total kinetic temperature (2) and longitudinal velocity (3) for O_2 at time 1059.3.

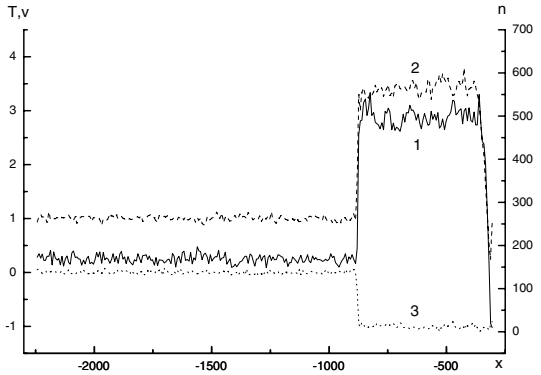

Fig. 7. Profiles of concentration(1), total kinetic temperature (2) and longitudinal velocity (3) for He at time 1059.3.

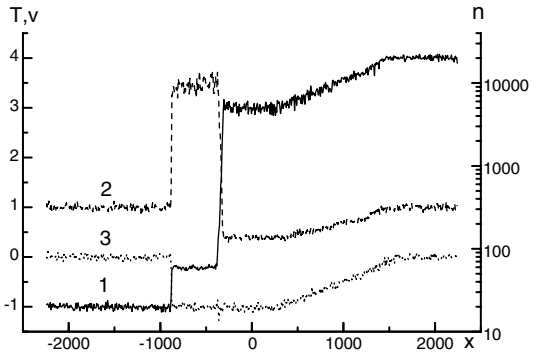

Fig. 8. Profiles of concentration(1), total kinetic temperature (2) and longitudinal velocity (3) for H_2 at time 1059.3.

Some special features of the flow in compressed layer downstream the incident shock in overexpanded jet

V.N. Uskov[1] **and M.V. Chernyshov**[2]

[1] *Baltic State Technical University, Department of Plasma and Gas Dynamics*
1st Krasnoarmeyskaya Str. 1, 190005 St. Petersburg (Russia)
[2] *Special Materials Ltd.,*
Bolshoy Sampsonievskiy Ave. 28A, 194044 Saint Petersburg (Russia)

Summary. The mathematical model for the investigation of two-dimensional overexpanded jet flow parameters in the vicinity of supersonic nozzle edge is formulated. The variation of the key parameter of this problem (i.e., the geometrical curvature of the shock emanating from the nozzle lip) is studied depending on flow conditions.

1 Introduction

A fragment of the complex study of supersonic jet flow in the vicinity of the nozzle edge (nozzle lip) is contained in this work. Spatial derivatives of various gas-dynamic variables on both sides of incident shock emanating from the nozzle lip during the exhaustion of two-dimensional (plane or axisymmetric) overexpanded jet flow into ambient space are related by local differential condition of compatibility [1]. The condition of isobaricity of the flow along the free surface of the inviscid gas (i.e., jet boundary) allows us to investigate the own geometrical curvature of the shock and jet boundary, to find the special and extremal features of the flow. The geometrical curvature of the oblique shock occurs to be key differential characteristic which determines all basic nonuniformities of the flow in the vicinity of the nozzle edge. At this study, we analyze the variation of the shock curc=vature in two-dimensional jet of the perfect gas.

The differential characteristics of the supersonic jet flow field are exactly connected with such physical effects as Taylor-Göertler instability development, the problem of the existence of the mutual transition of regular and Mach reflection at small Mach numbers, and excitations of the auto-oscillations in free and impacting jets.

2 Governing equations

Stationary shock wave AT (Figure 1) emanating from the nozzle lip with a half-angle $\theta \geq 0$ is characterized by its strength $J = 1/n$ where $n = p_a/p_n$ is jet incalculability, p_a is supersonic flow pressure some upstream the nozzle edge, p_n is ambient pressure.

Shock-wave strength J (the relations of static pressures downstream and upstream the shock) belongs to the interval $1 < J < J_m$, where $J_m = (1 + \varepsilon)\mathrm{M}^2 - \varepsilon$ is the strength of the normal shock occurring at the flow with Mach number M upstream it, $\varepsilon = (\gamma - 1)/(\gamma + 1)$, γ is the ration of specific heats (the further calculations suppose $\gamma = 1.4$), M is flow Mach number in the neighborhood of the point A.

Flow deflection angle β is determined by its strength and Mach number upstream:

$$\tan|\beta| = \sqrt{\frac{J_m - J}{J + \varepsilon}} \frac{(1 - \varepsilon)(J - 1)}{J_m + \varepsilon - (1 - \varepsilon)(J - 1)}. \tag{1}$$

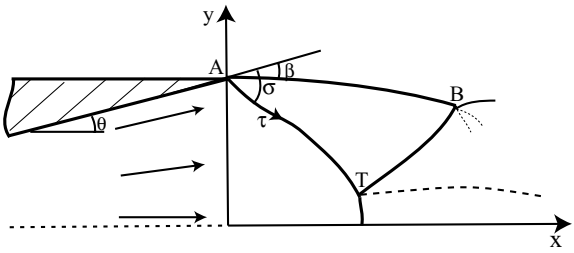

Fig. 1. The scheme of overexpanded jet flow into the motionless medium

Shock slope angle σ between the shock wave and flow deflection angle ahead and Mach number M_2 downstream are connected with M and J by the following relations:

$$J = (1+\varepsilon)\mathrm{M}^2 \sin^2\sigma - \varepsilon, \tag{2}$$

$$\mathrm{M}_2 = \sqrt{\frac{(J+\varepsilon)\mathrm{M}^2 - (1-\varepsilon)(J^2-1)}{J(1+\varepsilon J)}}. \tag{3}$$

The derivatives of flow parameters usually suffer a discontinuitgy on the incident shock. On both sides of the shock wave, they are related by local differential conditions of compatibility [1] in the form

$$N_{i2} = C_i \sum_{j=1}^{5} A_{ij} N_j, \quad i = 1 \ldots 3, \tag{4}$$

where N_{i2} and N_j are flow nonuniformities behind and ahead the shock wave, respectively; the coefficients C_i and A_{ij} depend on M, J θ. The nonuniformities $N_1 = \partial \ln p/\partial s$, $N_2 = \partial\theta/\partial s$, and $N_3 = \partial \ln p_0/\partial n$ characterize the nonisobaricity, the curvature of streamlines, and the vorticity of the flow with constant total heat, respectively; the meaning of $N_4 = \delta/y$ is the type of symmetry ($\delta = 0$ in plane flow, $\delta = 1$ in axisymmetric one); $N_5 \equiv K_\sigma$ is shock-wave curvature. Conditions (4) determine the nonuniformities of the flow in the compressed layer immediately behind the shock if the flow field ahead of the shock wave is known.

The condition of isobaricity of the flow ($N_{12} = 0$) along the free surface (jet boundary) AB (Figure 1) determines the sought curvature of the incident shock:

$$K_\sigma = -\sum_{j=1}^{4} A_{1j} N_j / A_{15}, \tag{5}$$

which, for example, affects the curvature $N_{22} \equiv K_\tau$ of the jet boundary:

$$K_\tau = C_2 \sum_{j=1}^{4} \left(A_{2j} A_{15} - A_{1j} A_{25}\right) N_j / A_{15}. \tag{6}$$

The latter parameter ([2]- [5]) influences the development of Taylor-Göertler instability.

Dependence (5), equations of two-dimensional gas flow "natural" coordinate system (s, n) ahead and behind the shock, and relations (1-3) between the shock-wave shape, its

strength, and Mach numbers on its both sides determines, after some transformations, the local changes of shock strength and Mach number downstream it in the direction τ along the shock wave:

$$\frac{dJ}{d\tau} = -2(J+\varepsilon)\left(B_1N_1 + B_2N_2 + B_3N_3 + \chi acN_4\sin\theta + qK_\sigma\right), \tag{7}$$

$$\frac{d\mathrm{M}_2}{d\tau} = -\left[1+\varepsilon(\mathrm{M}_2^2-1)\right]\cdot\left(\frac{\mathrm{M}_2N_{22}}{1-\varepsilon} + \frac{N_{32}}{(1+\varepsilon)\mathrm{M}_2}\right)\cdot\sin(\sigma-\beta).$$

Here $\chi = -1$ when the shock falls down, $c = \sqrt{(J+\varepsilon)/(J_m+\varepsilon)}$, $q = \sqrt{(J_m-J)/(J+\varepsilon)}$, and the factors B_i are

$$B_1 = \chi ac\cdot\frac{1-(1-2\varepsilon)(\mathrm{M}^2-1)}{(1+\varepsilon)\mathrm{M}^2}, B_2 = c\cdot\left(\frac{1+\varepsilon(\mathrm{M}^2-1)}{1-\varepsilon} - q^2\right), B_3 = c\cdot\frac{1+\varepsilon(\mathrm{M}^2-1)}{J_m+\varepsilon}.$$

Total pressure losses coefficient $I = p_{02}/p_0 = (JE^\gamma)^{(1-\varepsilon)/2\varepsilon}$ (p_0 and p_{02} are stagnation pressures upstream and downstream the shock, $E = \rho_0/\rho_{02} = (1+\varepsilon J)/(J+\varepsilon)$ is the reverse ratio of specific volumes) as well as the increase of the entropy $\Delta S = c_v\ln(JE^\gamma)$ of the gas (c_v is heat capacity at constant volume) are unambiguously determined and monotonically depend on shock strength. So the sign of the nonuniformity N_{32} (4) and, according to Crocco formula, the direction of vorticity of the flow with constant total heat are determined by the sign of the derivative $dJ/d\tau$ wich, in its turn, depends on the geometrical curvature of the shock according to (7).

Condition $A_{15} = 0$, when, as you can see in (5), shock-wave curvature and numerous differential flow parameters become unlimited, corresponds to shock strength equal to

$$J_p = \frac{3J_m - 2 - 3\varepsilon + \sqrt{9J_m^2 + 2\varepsilon(17+8\varepsilon)J_m + 16 + 16\varepsilon + 9\varepsilon^2}}{2(3+\varepsilon)}, \tag{8}$$

(the so-called constant-pressure point). Inequality $1 < J_p(\mathrm{M}) < J_m(\mathrm{M})$ is correct at any fixed γ and $\mathrm{M} > 1$. Flow behind the shock of such strength is always subsonic.

So the sought curvature of incident shock emanating from the nozzle lip is the basic parameters for investigation of all differential characteristics of the flow in the compressed layer downstream the shock.

3 Analytical and computational results

Let, for certainty, the parameters of isentropic flow ahead of the incident shock be described be the model of a cylindrical or a spherical source where

$$N_1 = -\frac{(1+\delta)\gamma\mathrm{M}^2\sin\theta}{y(\mathrm{M}^2-1)}, \quad N_2 = N_3 = 0, \quad N_4 = \delta/y.$$

Relation (5) make it possible to analyze the influence of the problem parameters (M, θ, $n_a = 1/J$, and γ, as well as symmetry type). Jet incalculability n and, correspondingly, shock-wave strength J can be changed most easily in practice. To change other problem parameters, we must differ the type of the gas or the shape of the nozzle. That's why we consider further the dependence of the dimensionless curvature of the shock $rK_\sigma(J)$ on

its strength (i.e., on the incalculability) at the various meanings of flow Mach number or nozzle half-angle (r is the radius or the half-width of nozzle exit section).

The shock-wave curvature depends simply on the nozzle half-angle (is proportional to $\sin\theta$) in plane jet. In further calculations relating the plane flow, we consider the dimensionless curvature $K_\sigma^- = rK_\sigma/\sin\theta$ [6].

At low Mach numbers, the value of K_σ^- is positive (the shock wave AT in Figure 1 is downward convex in the vicinity of the nozzle lip) and increases as a function of shock-wave intensity in the interval $(1; J_p)$ tending to infinity at $J \to J_p$ (Figure 2,a). For $J > J_p$, the curvature is negative. For all values of intensity other than J_p, this curvature is finite. In particular, as $J \to 1$ (degeneration into a weak discontinuity) and at $J \to J_m$ (normal shock) it equals

$$\lim_{J\to 1} K_\sigma^- = -\frac{(1-2\varepsilon)\mathrm{M}^2 - 2(1-\varepsilon) - \delta\mu(\mathrm{M})}{(1-\varepsilon)\mathrm{M}(\mathrm{M}^2-1)}, \quad \lim_{J\to J_m} K_\sigma^- = -\frac{\mathrm{M}^2 + \delta\mu(\mathrm{M})}{(1-\varepsilon)(\mathrm{M}^2-1)},$$

$\mu(M) = 1 + \varepsilon(\mathrm{M}^2 - 1)$. As Mach number increases to $\mathrm{M}_a = \sqrt{(2-\varepsilon)/(1-\varepsilon)} = 1.483$, there arises a minimum curvature (Figure 2,b), first, at the point $J = 1$. The value of the shock-wave curvature at the minimum point decreases to zero at a Mach number

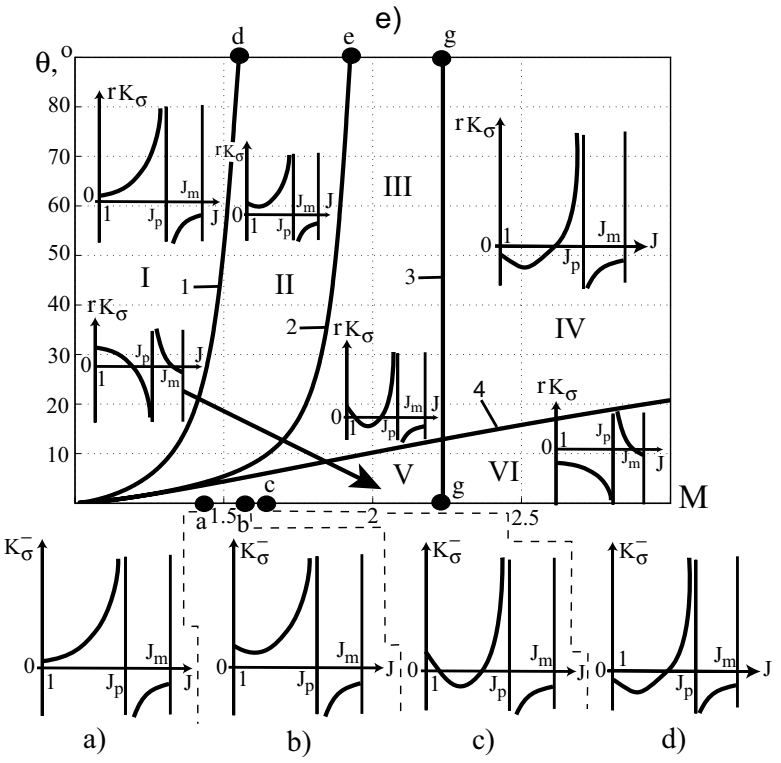

Fig. 2. Variation of the geometrical curvature of the incident shock depending on flow condtions

$\mathrm{M}_b = 1.571$ and intensity $J_b = 1.242$ and then becomes negative (Figure 2,c). For an arbitrary ratio of specific heats, the value of M_b is the greatest real root of the equation

$$(3-4\varepsilon)^2\mathrm{M}_b^8 - 8(3-6\varepsilon+4\varepsilon^2)\mathrm{M}_b^6 + 8(1-3\varepsilon+4\varepsilon^2)\mathrm{M}_b^4 + 32\varepsilon(1-\varepsilon)\mathrm{M}_b^2 + 16(1-\varepsilon)^2 = 0.$$

At a Mach number $\mathrm{M}_c = \sqrt{2(1-\varepsilon)/(1-2\varepsilon)} = 1.581$, the curvature of the shock wave degenerating into a weak discontinuity becomes negative for the first time (Figure 2,d). Another value of the strength of the shock of zero curvature at same Mach number is $J = \mathrm{M}_c^2 - 1 = 1/(1-2\varepsilon) = 1.5$. At $\mathrm{M} > \mathrm{M}_c$, the strength of the shock wave of zero curvature rapidly increases and flow downstream it becomes subsonic at $\mathrm{M} = 1.787$ and $J = 2.699$. At high Mach number, the zero curvature of the shock corresponds to the intensive shock with subsonic flow downstream it, but the flow behind the minimum curvature shock, on the contrary, is supersonic.

Unlike the plane flow, the variation of the dimensionless curvature rK_σ of the shock AT depends on the angle θ non-monotonically, so the study at the plane (M, θ) is necessary (Figure 2,e). Curves 1-4 are the borders of the regions I-VI where the dependence of shock curvature of the jet incalculability is different. In particular, curve 1, where (like in plane flow at $\mathrm{M} = \mathrm{M}_a$) mimimim of $rK_\sigma(J)$ occurs at the point $J = 1$, determined by the relation

$$\cot\theta = -\frac{3(1-\varepsilon)\mathrm{M}^4 - 2(3-\varepsilon)\mathrm{M}^2 - (1-\varepsilon)}{(1-\varepsilon)(\mathrm{M}^2-1)^{3/2}}.$$

This curve finishes at $\theta = 90^\circ$ and

$$\mathrm{M}_d = \frac{3-\varepsilon+2\sqrt{3-3\varepsilon+\varepsilon^2}}{3(1-\varepsilon)} = 1.551$$

(here we do not consider the problem of the practical realization of such flow). Curve 2 of the appearance of the shocks with moderate strength and negative curvature finishes at $\mathrm{M} = \mathrm{M}_e = 1.925$ such as

$$\sum_{k=0}^{4} b_k \mathrm{M}_e^{2k} = 0,$$

$$b_6 = -24\varepsilon(2-3\varepsilon)^2, \quad b_5 = -80 + 672\varepsilon - 1036\varepsilon^2 + 384\varepsilon^3 + 252\varepsilon^4,$$

$$b_4 = 296 - 930\varepsilon + 412\varepsilon^2 + 886\varepsilon^3 - 1096\varepsilon^4 + 48\varepsilon^5,$$

$$b_3 = -(1-\varepsilon)(101 + 609\varepsilon - 1365\varepsilon^2 + 1775\varepsilon^3 - 192\varepsilon^4),$$

$$b_2 = -3(107 - 208\varepsilon + 423\varepsilon^2 - 96\varepsilon^3)(1-\varepsilon)^2,$$

$$b_1 = (61 - 337\varepsilon + 192\varepsilon^2)(1-\varepsilon)^3, \quad b_0 = (1+48\varepsilon)(1-\varepsilon)^4.$$

Vertical line 3 of weak shock curvature direction change corresponds to Mach number $\mathrm{M}_g = 3(1-\varepsilon)/(1-3\varepsilon) = 2.236$ (the phenomenon at $\mathrm{M} = \mathrm{M}_c$ is analogous in plane flow).

The change of infinite discontinuity direction at the plot $rK_\sigma(J)$ at $J = J_p(\mathrm{M}, \gamma)$ corresponds to the following curve 4:

$$\cot\theta = -\frac{\sqrt{J_p+\varepsilon}\left[(3+\varepsilon)(9\varepsilon-1)J_p^3 + (28+34\varepsilon+82\varepsilon^2+16\varepsilon^3)J_p^2 + cJ_p + d\right]}{(1-\varepsilon)((3+\varepsilon)J_p + 2 + 4\varepsilon)(J_p-1)^{3/2}\sqrt{(1+\varepsilon J_p)(3J_p+1+4\varepsilon)}},$$

$$c = 33 + 94\varepsilon + 49\varepsilon^2 + 48\varepsilon^3, \quad d = 2(1+2\varepsilon)(3+13\varepsilon),$$

which has the horizontal asymptote at $M \to \infty$:

$$\theta = \arctan \frac{(1-\varepsilon)\sqrt{3\varepsilon}}{9\varepsilon - 1} = 49.684^\circ.$$

The variations of shock-wave curvature at zones I-IV are the same as at corresponding Mach numbers (Figure 2,a-d) at the plane flow. But these zones I-IV correspond only to rather large half-angles of the nozzle in the axisymmetric stream. When the angle θ is small (zones V-VI), the factor of flow symmtry is dominating, and the variation of shock-wave curvature has no analogue in plane flow. When the nozzle is contoured ($\theta = 0$) the only differences from adjacent regions V and VI are zero curvatures of the shock at $J \to 1$ and $J = J_m$.

The fact of the existence of the shocks with positive convexity emanating from the nozzle lip both in overexpanded and underexpanded jets at small flow Mach numbers was confirmed experimentally by Prof. V. I. Zapryagayev (private communication).

4 Conclusions

Concluded computational and analytical studies discover that, depending of plane or axisymmetric jet flow conditions from the supersonic nozzle, shock wave emanating from the nozzle lip can have the different convexity direction. Dependence of shock curvature on jet incalculability is also non-monotonous and variative. Shock wave unusually convex to the axe of the plane of symmetry realizes as a rule at small Mach number flow regions. This fact possibly allows us to connect the unusual shock convexity direction and flow parameters governed by shock curvature with the problem of regular and Mach reflection transition and the excitation of auto-oscillations. At the same time, variation of shock-wave curvature sufficiently depends of symmetry type (whether the flow is plane or axisymmetric).

This study was supported by the Russian Foundation for Basic Research (project code 07-08-00529).

References

1. Adrianov A. L., Starykh A. L., Uskov V. N. Interference of Steady Gas-Dynamic Discontinuities. Nauka, Novosibirsk, 1995, 180 p. (in Russian)
2. Glaznev V. N., Zapryagaev V. I., Uskov V. N., Terekhova N. M., Erofeev V. K., Grigoryev V. V., Kozhemyakin A. O., Kotenok V. A., Omelchenko A. V. Jets and Unsteady Flows in Gas Dynamics. Siberian Branch of the Russian Academy of Sciences, 2000, 200 p. (in Russian)
3. Terekhova N. M.: Streamwise vortices in axisymmetric jets. Dokl. Ross. Akad. Nauk, vol. 347, no. 6, 1996.
4. Zapraygaev V. I., Solotchin A. V., Kiselev N. P.: Structure of a supersonic jet with varied geometry of the nozzle entrance. Journal of Applied Mechanics and Technical Physics, vol. 43, no. 4, 2002.
5. Zapragayev V. I., Kiselev N. P., Pavlov A. A.: Effect of streamline curvature on intensity of streamwise vortices in the mixing layer of supersonic jets. Journal of Applied Mechanics and Technical Physics, vol. 45, no. 3, 2004.
6. Uskov V. N., Chernyshov M. V.: Differential characteristics of the flow field in a plane overexpanded jet in the vicinity of the nozzle lip. Journal of Applied Mechanics and Technical Physics, vol. 47, no. 3, 2006.

Studies on micro explosive driven blast wave propagation in confined domains using NONEL tubes

C. Oommen, G. Jagadeesh, and B.N. Raghunandan

Aerospace Engineering Department, Indian Institute of Science, Bangalore, India

Summary. Explosive driven micro blast waves are generated in the laboratory using NONEL tubes. The explosive mixture coated to the inner walls of the plastic Nonel tube comprises of HMX and Aluminum ($18mg/m$). The detonation is triggered electrically to generate micro blast waves from the open end of the tube. Flow visualization and over pressure measurements have been carried out to understand the propagation dynamics of these micro-blast waves in both confined and unconfined domains. The classical cubic root law used for large scale blast correlation appears to hold good even for these micro-blasts generated in the laboratory.

1 Introduction

Confined explosions from combustible and explosive fuels in grain elevators, coal mines, nuclear explosion or a pressurized vessel rupture are causes of serious concern. The blast waves produced by sudden release of energy are normally characterized by a supersonic shock front followed by an exponential type decay of the physical properties like over-pressure of the gas [1], [2]]. Unlike shock waves that attenuate as it expand spherically, the shock wave from internal blasts can diffract, reflect and get focused depending on the physical barriers in the propagation path. While it is rather impossible to carry out realistic experiments to understand such situations, with the tremendous advances in CFD it is now possible to simulate many of the destruction scenarios in large-scale explosions. But these CFD simulation tools have to be validated with the help of precise experiments aimed at understanding the basic physics associated with explosive driven shock wave propagation in both confined and unconfined domains.

Execution of large scale experiments are laborious and expensive besides the safety concerns associated with the handling and blasting of sensitive energetic materials. Small scale or micro blast experiments, on the other hand have the advantages of being safe and economical. In addition to low turn over time between experiments, many vital diagnostic tools that throw light into the shock propagation dynamics like density sensitive flow visualization techniques which may be rather difficult to implement in large scale experiments could be easily employed in micro blast experiments [3].

Recently a safe and inexpensive experimental technique using micro charge silver azide has been reported for micro blast generation in the laboratory [3]. It has been shown that the blast wave parameters, empirically derived from large scale explosions, could be scaled to charges of the order of a few milligrams. In the present work, we report our attempts to employ the NONEL tubes (M/s Dyno Nobel, Sweden) as a means of generating micro blasts for shock propagation investigations in confined and unconfined domains. Both flow visualization and over pressure measurements are used to characterize the micro-blast wave propagation.

2 Experimental

NONEL tube was procured from M/s Dyno Nobel Sweden. It is a commercially available shock tube, (explosive transfer system (ETS) or detonation transmission tubing (DTT)) used for signal transmission in mining, especially in electrically endangered areas. NONEL shock tube is a small diameter, three-layer plastic tube coated on the innermost wall with a reactive explosive compound, which, when initiated, propagates a low energy signal along the length of the tubing with minimal disturbance outside of the tube. The ignition of the reactive material coated on the inner surface of the shock tube results in the formation of a shock front. As a result of the shock front streaming past the material on the tube walls, the reactive material is assumed to undergo a turbulent dispersion towards the center of the tube. The shock front also heats up the gases in the tube. The dispersed energetic material is heated and then combust to release energy which supports the shock front at a typical rate of $6000 - 7000$ ft/sec (2000 m/sec) The combustion reaction thus would resemble that of a dust explosion. The detonation is confined to the tube along its length and the products of combustion escape from the open end. The resultant output is characterized as a high pressure impulse along with hot burning particles.

The explosive composition inside the shock tube is a mixture of Aluminum and HMX. The technical specifications of the NONEL tube used in the present study as given by the manufacturer is given in Table 1. The explosive, Beta HMX (Octol) which is crystalline and has a typical particle size around 20 microns. The mixture of HMX and aluminum, both classic fuels, has a negative oxygen balance. Thus the air in the tube provides the oxygen necessary for combustion. A precise determination of this balance is difficult as aluminium is vulnerable to oxidation. The expected reaction products of the HMX/aluminum mixtures are gaseous CO_2, NO_x and H_2O and solid Al_2O_3. Only limited information is available in the public domain on the working of this device [[4], [5], [6], [7], [8]].

Table 1. Technical Specifications of NONEL DynaLine

Composition	Octogen (HMX) 16 mg/m
	Aluminium powder 2 mg/m
Tube Specifications	Inner layer : Ionomer
	Middle and outer layer: Polyethylene

The ignition of the shock tube can be done by various means. A safe electric method was adopted during our experiments. NONEL Dynostart, an electronic blasting machine was purchased along with NONEL Dynaline. It consists of an energy source (battery), a voltage converter, a capacitor for energy accumulation, an electrode and push buttons to effect initiation. The electrical energy is converted to a powerful spark, which the electrode emits into the inside of the NONEL tube to initiate the shock wave reaction.

In the first phase of this research program a preliminary characterization of the explosive composition was carried out. A quantitative estimation of the explosive composition inside the tube was carried out from a series of firings of different lengths of shock tube. An average value of 18 mg/m was estimated from these trials. The explosive mixture was

subsequently extracted into a solvent after splicing the tube for spectral characterization. Presence of HMX was confirmed by FTIR and ^{13}C NMR spectroscopic studies. However no attempts were made to establish the presence of aluminium in the explosive mixture.

Two sets of experiments were conducted using NONEL shock tubes. In one set of experiments the shock propagation in open air was examined. Side on overpressure, in psi, immediately behind the primary shock was measured at different distances from the blast source by sensors placed side on to the flow. PCB Piezotronics pressure transducers with a sensitivity of 0.04989 V/psi was used for measuring the overpressure levels in open domain. A photograph of the experimental arrangement is shown in Fig. 1.

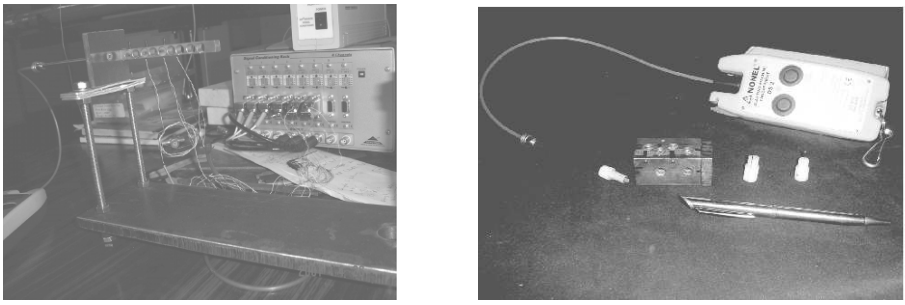

Fig. 1. Experimental arrangement for measuring overpressure levels from micro blast in open domain

A second set of experiment was conducted wherein overpressure levels in an internal blast were measured. In order to examine the shock propagation dynamics in enclosures, the NONEL tube was inserted to one end of a fabricated rectangular steel box of dimensions 65mm x 29 mm. The side on overpressure levels at different locations along the shock propagation were measured using Kulite ultraminiature pressure transducers (LQ 062 Series) placed at regular intervals. These tiny transducers have small foot print, high natural frequency, extreme resistance to vibration and shock and wide temperature range (-65^0F to 450^0F) making it ideal for the present study. A slightly bigger chamber of dimension 80mm x 50mm with toughened glass windows (6mm thickness) on either side was used for flow visualization in internal blast studies as the shock front could not be captured in the smaller dimension rectangular box used for overpressure measurements.

3 Results and Discussions

3.1 Micro blast generation

A schlieren image of the shock wave coming out from the tip of the shock tube is shown in Fig. 2. The shock emanating from the tip of the tube is spherical. It is important to note here that it is nearly impossible to initiate a secondary explosive to detonation in milligram quantities without a detonator. Further the over pressure measurement in open domain is carried out to evaluate the possibility of scaling large scale blast waves using controlled micro-explosions in the laboratory.

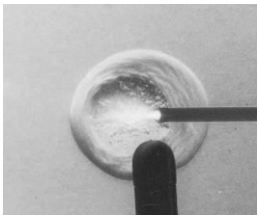

Fig. 2. Schlieren image of the shock wave emanating from the NONEL tube

3.2 Peak overpressure vs. scaled distance

When an explosive charge detonates in air a shock front is formed. The larger the explosive charge, the higher the peak shock pressure at any given distance from the charge. The peak pressure at any distance for any size of any explosive can be quite accurately estimated based upon scaling experiments using TNT [1], [2]. It is customary to plot the blast property of interest (in the present case overpressure) against the scaled distance Z.

$$Z = R/W^{\frac{1}{3}} \tag{1}$$

Where R is the distance from the center of charge and W is the TNT equivalent weight of the explosive under consideration. One method of converting explosive weight to TNT equivalent weight is as follows.

$$W_{(TNTequivalent)} = W_{exp} \frac{(\frac{P_{CJ}}{\rho})_{exp}}{(\frac{P_{CJ}}{\rho})_{TNT}} \tag{2}$$

Where ρ is the density and P_{CJ} is the C-J Pressure of the explosive.

The overpressure levels were measured at different distances (10 mm, 20 mm, 30 mm, 40 mm, 50 mm and 70 mm) from the explosion source. In order to plot the scaled distance against peak over pressure one should have an idea about the weight of the explosive. In the present case it is not straight forward to estimate the energy at the open end of the shock tube as the energy release mechanism is different from other conventional type of explosion where in the entire energy yield can be associated to a point source. In a shock tube the energy released inside the tube supports the shock front to move it at a set VOD which remains constant through out the length of the tube. The actual energy available at the open end thus remains uncertain. In order to circumvent this uncertainty different lengths (0.5m, 1 m, 2 m and 3m) of the shock tube were fired and overpressure levels at different distances were measured for each length. The overpressures measured at different distances were found to be identical irrespective of the length of the tube used for generating the blast suggesting a fixed amount of explosive responsible for the energy yield at the tip. Assuming that the micro blast follows the scaling law, the scaled distance for an experimentally observed value of overpressure was calculated from the scaling curve. From this scaled distance and actual distance the weight of explosive in TNT equivalent weight was estimated to be 1.63 mg. Based on this energy level subsequent peak overpressures were estimated from the scaling law and was found to be matching very well with the experimental values of overpressures obtained at different lengths from the micro blast. Fig. 3 shows the plot of peak overpressure versus scaling distance for TNT blasts along with the values obtained from the micro blast studies (marked in black

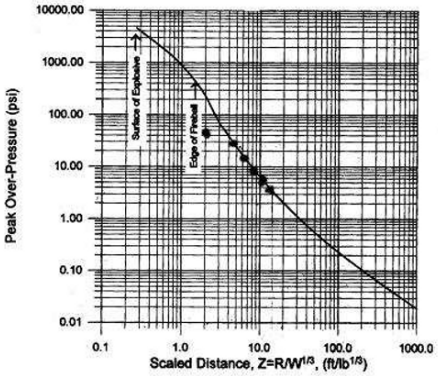

Fig. 3. Peak shock pressure vs scaled distance for TNT and microblasts

spots). The values used are averages of 12 firings. The results confirm the observations made earlier using silver azide that blast wave parameters could be scaled for charge masses varying from a few milligrams to several tons [3].

Using the TNT equivalent formula mentioned earlier the amount of HMX responsible for the energy yield at the open end of the shock tube was estimated. Aluminium being present in small quantity was not considered in the calculation. 1.6 mg of TNT was found to be equivalent to 1 mg of HMX. Assuming that the velocity of detonation inside the tube is 2000 m/sec and explosive loading inside the tube is 18 mg/m, it can be assumed that only around 55 mm length of the tube is contributing to the energy output at the open end of the shock tube in a time scale of 27 microseconds. Interestingly the reaction time scale reported in detonation transmission tubing is of this order [4].

In spite of most of the experimental values falling in the predicted range in the micro explosion, it can also be seen from Fig. 3 that the experimental peak pressure levels observed at the closest point from the explosion source (10mm) is not in the predicted range. This could be due to two reasons. One reason could be the disproportionate diaphragm size of the pressure sensor with respect to the blast wave size. It was also observed during our flow visualization studies that a well defined spherical shock front is formed only after 20 mm from the point of microblast. The second reason could be due to the low energy levels involved in the explosion. It is known that scaling curve deviate considerably at close distances depending upon the energy release levels [9].

3.3 Micro blast wave propagation in confined domains

The schlieren images of the internal blast wave propagation captured using a high speed camera is shown in Fig.4. The reflection phenomena inside the closed chamber could be clearly followed from the images. Shock coalescence near the end wall as seen from the visualization images corroborate the observed overpressure level augmentation at the chamber end. An estimation of velocity of shock wave at different instances has shown that the reflected wave from the end wall gains speed while crossing the hot debris from the shock tube. Yet another parameter that was explored was the effect of a vent on the

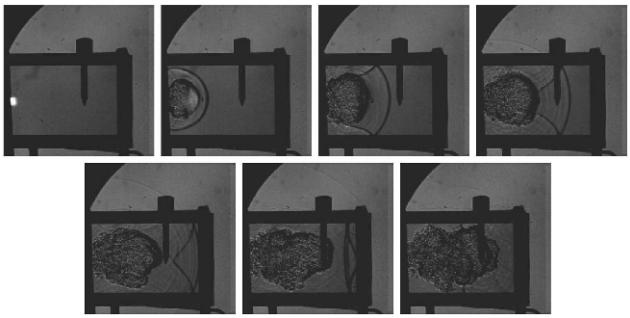

Fig. 4. Sequential images of the micro blast propagation inside a closed chamber (time delay after the trigger in micro sec. -56, -17, 21,59,97,136 and 497)

end wall of the box. A significant decrease of overpressure levels and residence time was observed in these cases. Some of the other features that are being explored in the ongoing work are shock speed amplification as the reflected wave transverse through hot debris and reflection characteristics of end wall materials.

4 Conclusions

Nonel shock tubes have been proposed as a method of generating micro blast waves in the laboratory. Flow visualization and overpressure measurements have been carried out to characterize blast wave propagation in open and confined domains. It has been found from studies in open air that the blast wave parameter, overpressure, can be scaled for charge masses varying from milligrams to several tons confirming earlier findings based on tiny blast using silver azide. High overpressure levels from shock coalescence in internal blasts have been confirmed from flow visualization studies The technique could be conveniently adapted in experiments wherein conventional shock tubes have been used hitherto to simulate blast wave propagation or blast wave loadings on materials

References

1. W E Baker, Explosions in Air, (University of Texas Press, Austin and London 1973)
2. G F Kenny and K J Graham, Explosive Shocks in Air, 2nd Edition. (Springer-Verlag, New York 1985)
3. H Kleine, J M Dewey, K Ohashi, T Mizukaki and K Takayama: Shock Waves **13**, 123 (2003)
4. D K L Tsang, Mathematical and Computer Modelling 44, 717 (2006)
5. D Sutton, A H Noble and p M Lynch, 14th Int. Pyrotech. Semianr, Jersey, 1989 pp. 627-636
6. Product Literature from ET, Inc. Subsidiary of OEA, Inc. Product: TLX Energy Transfer System, 1990
7. G F Brent, D Sutton and A H Noble, Journal of Energetic Materials, 1 (1993) 2245-260.
8. L C Yang and Ian H P Do, AIAA Journal **38**, 2260 (2000)
9. J M Dewey: Handbook of shock waves. Vol. 2 Shock wave interactions and propagation. Ed. Gabi Ben-Dor, Ozer Igra and Tov Elperin,(academic Press, San Diego 2001)

The aerodynamics of a supersonic projectile in ground effect

G. Doig[1], H. Kleine[2], A.J. Neely[2], T.J. Barber[1], E. Leonardi[1], J.P. Purdon[2], E.M. Appleby[2], and N.R. Mudford[2]

[1] *School of Mechanical and Manufacturing Engineering, University of New South Wales, Kensington, Sydney, NSW 2052, Australia*
[2] *School of Aerospace, Civil and Mechanical Engineering, University of New South Wales/Australian Defence Force Academy, Northcott Drive, Canberra, ACT 2600, Australia*

Summary. A computational aerodynamic study of a bullet travelling in ground effect at Mach 2.4 has been conducted, based on physical experiments conducted by UNSW@ADFA in Canberra, Australia. The investigation aimed to establish the way in which the aerodynamic characteristics of the bullet change due to close proximity to the ground. CFD was validated against the experimentally observed flow field and pressure measurements and was subsequently used to predict the aerodynamic forces on the projectile.

1 Introduction

Although there is some evidence to suggest that researchers have contemplated the effects of the flight of a bullet near a wall or ground plane in the past [1], the aerodynamic consequences of such a situation have never been formally addressed by the scientific community despite relevance to, for example, urban combat scenarios where bullets will be fired in close proximity to walls. In a preliminary study [2], the flowfield around a standard NATO 5.56 mm round, fired from an ADI AUSSTEYR A1/A2 rifle, passing at Mach 2.4 over a ground plane at a range of clearances, was visualised by means of time-resolved schlieren using a high-speed video camera (Shimadzu HPV-1). The video, captured at 500,000 frames per second (fps), revealed how the shock waves between the bullet and the ground reflected and interacted with either the bullet or the wake or both – an example is shown in Fig. 1. For a more detailed description of these tests and the observed salient flow features, see [3].

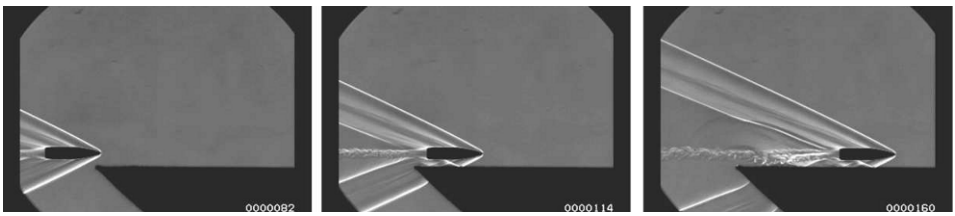

Fig. 1. Projectile at Mach 2.4 over the leading edge of the simulated wall at a height-to-diameter ground clearance $h/d = 0.75$; stills from a time-resolved schlieren sequence taken at 500,000 fps.

Although the experiments attempted to address a widely-held yet anecdotal belief in the military [2] that a bullet fired close to a wall will follow it, the field of view

in the schlieren video was not sufficient to determine any trajectory changes. The live-range experiments were followed by a wind tunnel program [4], in which an instrumented geometrically scaled up projectile was placed in the test section of the UNSW@ADFA supersonic blow-down tunnel. Flow conditions and bullet geometry were chosen in a way to nominally conserve the Reynolds and the Mach numbers of the live-range experiment, however, neither the spin of the bullet nor the correct ground boundary condition could be replicated. Ideally, the ground should be moving beneath the stationary object at the same speed as the freestream air, to simulate the free-flight case of the object moving through still air over a stationary ground. However, this is not feasible for supersonic speeds in a wind tunnel [5], and therefore a compromise of a short elevated ground plane was implemented as shown in Fig. 2.

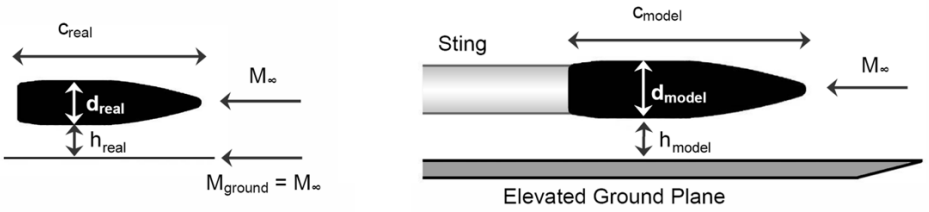

Fig. 2. Relevant properties for the live-range bullet, as simulated in CFD, with a moving ground (left) and the wind tunnel model used for obtaining quantitative data, supported by a sting extending from the base (right).

CFD was used to investigate the aerodynamics of the bullet in ground effect in more detail. Firstly, an appropriate numerical approach was established with regards to mesh resolution and turbulence modelling, based on comparisons to selected experimental cases of the bullet in free-flight. A more comprehensive comparison was made to all available ground effect wind tunnel and live-range experiments, with two goals: to prove that the wind tunnel experiments were indeed a faithful representation of the original live-range tests, and to effectively fill in the gaps in flow field data left by the physical limitations of the experiments. These simulations provided a comprehensive database for all relevant properties. They were also conducted for ground clearances and scenarios which were not examined experimentally, such that all trends were fully defined over a wide range of ground clearances.

2 Verification and validation of numerical model

The Reynolds-Averaged Navier-Stokes equations were solved using an explicit solver with multigrid on fully structured meshes. Of all solvers tested, the explicit one provided the fastest convergence without compromising accuracy. As the shock waves remain steady in location and magnitude over time, and the rotational velocity is an order of magnitude smaller than the axial velocity, a transient analysis was not required. The bullet was geometrically simplified for both the wind tunnel and the CFD model to eliminate a knurled strip that runs around the circumference halfway along the projectile surface, as its influence on the resultant forces is not significant [6].

Initially, a quarter bullet mesh with symmetry planes was used to simulate the bullet in free flight, unbounded by a ground plane, to verify the influence of the mesh on the quality of the solution. The meshes featured a concentration of cells in the bullet boundary layer such that $y+$ values of less than 1 on the surface were achieved, with local cell refinement in shock regions based on density gradients. Far-field boundary locations were tested and those depicted in Fig. 3a were settled upon. Further extension of the boundaries by two chord lengths in each direction altered the predicted forces on the bullet by less than 1 %. The finest mesh for the quarter bullet, with one level of shock adaptation, contained 3.93 million cells, meaning that the full bullet model, for free-flight simulations involving rotation, incorporated 15.72 million cells.

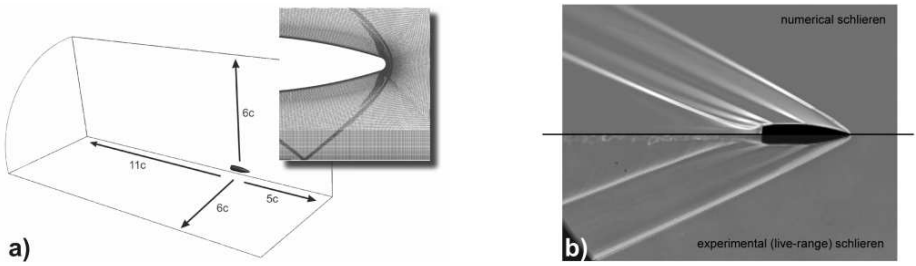

Fig. 3. a) Domain size for live-range bullet simulations. Insert shows mesh detail near bullet leading edge, featuring shock-adapted mesh refinement. The domain for the wind tunnel model simulations equalled that of the test section (area 155 mm × 90 mm) and a similar meshing strategy was implemented for consistency. b) Numerical vs. experimental schlieren for the bullet in free flight in the original experiment.

Three turbulence models were tested to verify their ability to capture the flow features: the one-equation Spalart-Allmaras , the $k-\epsilon$ RNG with enhanced wall functions, and the $k-\omega$ SST model. The lift coefficient, C_y, differed by less than 2 % across all the turbulence models, mainly due to differences in the way in which both the bow shock diffused across mesh elements and the separating flow at the base of the bullet was calculated. The base flow area had a far more marked influence on the drag force, which was around 7 to 8 % less using both the $k-\omega$ SST and $k-\epsilon$ RNG on the fine mesh. Comparisons to schlieren images of a free-flight case from the firing range, as shown in Fig. 3b, confirmed that the one-equation model was predicting all shock locations well had the advantage of faster and more stable numerical convergence. The model's authors originally tested for blunt trailing edges in transonic flow, as well as shock-induced separation, with encouraging results [7]. Coupled with the validation performed in the present study, its use for this fully supersonic case is justified.

Once the standard approach was established and validated against the free flight experiments described above, a comprehensive set of numerical results was obtained for all ground clearances tested in the wind tunnel. The CFD solutions were compared to data measured from six pressure tappings located axially along the surface of the bullet model, which could be rotated to map pressure on both upper and lower surfaces. In addition, a visual evaluation of density contours superimposed on the experimental schlieren was conducted, an example of which is shown in Fig. 4 for a ground clearance of $0.42 \times d$ (the lowest attempted in the tunnel due to the extent of the ground boundary layer). The

markedly greater spatial resolution afforded by the CFD provided more comprehensive information on the behaviour of the pressure distribution compared to what can be inferred from the data of the discrete pressure tappings used in the wind tunnel tests. From experiment and CFD it became obvious that the close proximity of the ground plane strongly influences the pressure distribution along the lower surface of the projectile while the upper surface remains largely unaffected and shows a pressure distribution essentially equivalent to that of the bullet in free flight. Results are shown in Fig. 5.

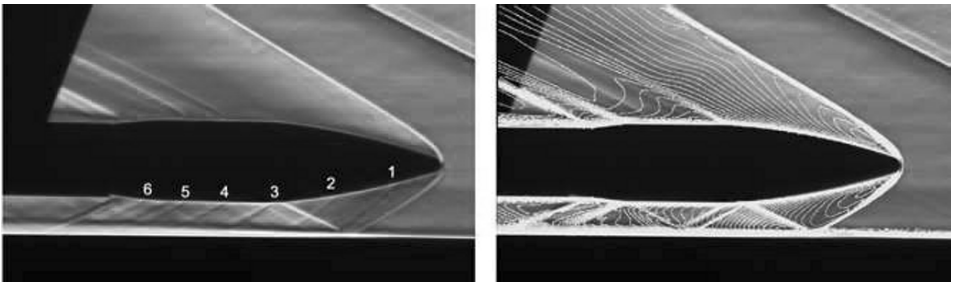

Fig. 4. Colour schlieren of the wind tunnel model at an $h/d = 0.42$ in the ADFA wind tunnel with numbers denoting pressure tapping locations (left), and with superimposed density contours from CFD (right).

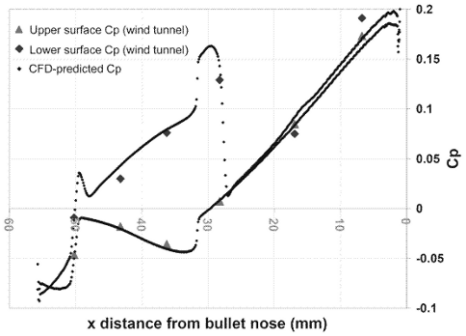

Fig. 5. Pressure coefficient along axis, experimental results and CFD, for $h/d = 0.42$.

The pressures predicted by the Spalart-Allmaras turbulence model were always within approximately 2 % of the experimental readings, that is, within the likely experimental uncertainty margin. This close agreement suggests that the CFD was reproducing the ground boundary layer accurately, since a large discrepancy in the shock-boundary layer interaction would manifest itself in differences in the strength and location of the reflected shocks. Simulations at all other ground clearances matched the experimental schlieren from both wind tunnel and live-range experiments well (further pressure data was not available at the time of writing). An additional CFD simulation was run with an idealised moving ground in the wind tunnel, to establish the influence of the unavoidable ground boundary layer. Overall, these results confirmed that the elevated ground plane was a good approximation, but the presence of the sting rendered drag coefficient predictions

inaccurate. The CFD simulations of the wind tunnel tests (without taking into account the sting) yielded approximately 5 % lower lift and drag forces than the simulation of the live-range test, which is attributed to the slight discrepancy in Reynolds number.

3 Results

Figure 6 shows force component coefficients from CFD simulations of the live-range bullet, plotted against ground clearance to conclusively establish the influence of ground effect on the bullet aerodynamics. All coefficients are based on frontal area for ease of comparison, although this serves to somewhat exaggerate the lateral component, which would normally be referenced to the side area. One can see that drag remains fairly consistent, fluctuating around the freestream value. The differences exhibited are caused by mild changes of skin friction as initially one and then two shock interactions occur, and by the influence of the reflected shocks on the near-wake region.

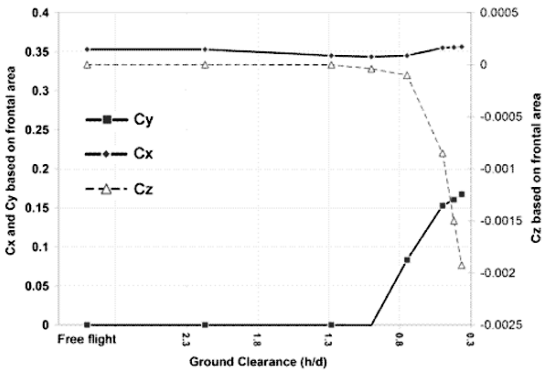

Fig. 6. CFD predictions for coefficients of drag (C_x), lift (C_y) and lateral force (C_z) for the live-range bullet at different ground clearances.

The effects on the lift coefficient, C_y, are more pronounced, with a clear trend towards a positive lift force as the projectile gets closer to the ground plane ($< 1 \times d$). This is due to the increased pressure along the lower surface of the bullet caused by the shock reflections between the ground and the bullet. The maximum observed lift force acting on the projectile, at $h/d = 0.42$, was approximately 1.56 N. While this is a relatively large force considering the small mass of the bullet, it is unlikely that it would have been sufficient to cause a visible displacement in the field of view of the original live-range experiment. A proper dynamic analysis will be undertaken at a later stage to assess the effect that the aerodynamic forces have on the projectile trajectory. It is worth noting that while the forces caused by the ground effect are comparatively large, they depend strongly on the clearance. Figure 6 shows that this effect only occurs for clearances less than one diameter because above this distance, the bow shock no longer reflects onto the bullet itself.

The lateral coefficient, C_z, shows that the bullet also experiences an increasing lateral force as ground clearance is reduced. This is purely a function of the spin of the bullet

causing an asymmetry in the flow. The force by itself is by at least two orders of magnitude smaller than all other aerodynamic forces so that it can be assumed that it has no discernable effect on the bullet.

4 Conclusions

CFD has been used to determine the effect of the presence of a wall on the aerodynamic forces acting on a bullet travelling at Mach 2.4. Comparisons to live-range experiments and wind tunnel tests allowed one to establish a suitable numerical approach which incorporated the one-equation Spalart-Allmaras turbulence model. Accurate capturing of shock reflections was problematic due to the high mesh resolutions required, but all major flow features were reproduced by the CFD simulation when compared to both the live-range and wind tunnel experiments. It was found that the elevated ground used in the wind tunnel as an approximation of a more appropriate, but unfeasible, moving ground was justified in that it replicated the actual experimental shock locations and resulted in a comparable pressure distribution around the bullet.

CFD was subsequently used to conduct a thorough study of the bullet at different ground clearances to quantify the influence of the ground on the aerodynamic forces acting on the bullet. While the effect on drag was not pronounced, a distinct lift force was produced when the bullet was modelled within one diameter off the ground plane. This reached a peak at the lowest tested ground clearance, but once the bullet was moved away from the surface to one diameter clearance or more, this lift became negligible. A lateral precession would be the likely result from the lift force, but a dynamic analysis to establish the extent of this effect is yet to be performed. Finally, it was also found that the spin of the bullet produced a lateral force in ground effect, but it was of orders of magnitude smaller than the other aerodynamic forces.

Clearly, specific results are only applicable to the projectile used. A bullet of larger diameter or length, travelling at a different Mach number, would experience different levels of alteration to lift and drag forces, although one can assume that at fully supersonic speeds, the trends described here would be broadly applicable to all such projectiles. Further research will involve a thorough dynamic analysis, moment calculations to determine the ground's influence on the important parameter bullet pitch, and a larger range of wind tunnel tests such that the CFD can be quantitatively validated for all ground clearances.

References

1. Cranz C: Deutsche Akademie der Luftfahrtforschung, **40**:5 (1939)
2. Purdon JP: Supersonic projectiles in the vicinity of solid obstacles. BE thesis, UNSW@ADFA (2006)
3. Purdon JP, Mudford NR, Kleine H: Proc. 24th Int. Congr. High-Speed Photography and Photonics, SPIE (in press) (2007)
4. Appleby EM: Pressure effects on supersonic projectiles in close proximity to a wall. BE thesis, UNSW@ADFA (2006)
5. Barber T, Beves C, Diasinos S, Doig G, Leonardi E, Neely A: Autotechnology **2**:1 (2007)
6. Silton SI: J. Spacecraft & Rockets **42**:2 (2005)
7. Spalart PR, Allmaras SR: AIAA paper 92-0439 (1992)

The interaction of supersonic and hypersonic flows with a double cone: comparison between inviscid, viscous, perfect and real gas model simulations.

M.-C. Druguet[1], **G. Ben-Dor**[2], **and D. Zeitoun**[1]

[1] *Université de Provence, IUSTI-UMR CNRS 6595,*
Polytech'Marseille, Département de Mécanique Energétique,
Technopôle de Château Gombert, 5 rue Enrico Fermi, 13453 Marseille, France
[2] *Pearlstone Center for Aeronautical Engineering Studies,*
Department of Mechanical Engineering, Faculty of Engineering Sciences,
Ben-Gurion University of the Negev, Beer Sheva, Israel

Summary. The double-cone configuration is well suited to study fondamental aspects of high-enthalpy flows, as the shock interaction resulting from the interaction of the hypersonic flow with the double cone is sensitive to the high-temperature effects. A CFD campaign to compute the flow over a double cone is performed with considering different levels of modeling the real-gas effects. Comparisons between viscous and inviscid flow model simulations past the double cone are also presented. The comparisons show the major contribution of the viscous and real gas effects, separately and together, to the resulted flow field.

1 Introduction

It is expected that highly supersonic and hypersonic flights will become common by both civil and military aircrafts in the coming decades. For this reason, investigating relevant flow fields is of great interest and importance. The hypersonic flow over a double-cone geometry, which resembles shapes of intakes and noses of supersonic and hypersonic vehicles, is a good candidate since it is associated with many complex phenomena, namely shock-on-shock interactions, Mach reflections (triple points) and re-circulation zones. These vehicles will likely have regions of separated flow, for example, near control surfaces and behind flame holders. Additionally, the shock-on-shock interactions and shocks impinging on the vehicle surface could cause high localized aerodynamic and aerothermal loads.

The double-cone flows have been widely studied in recent years, to validate both numerical methods [1] and physico-chemical models [2,3]. If the physico-chemical models have been easily validated for low-enthalpy conditions of a pure nitrogen flow [1], the validation of real gas effects in the air flow in high-enthalpy conditions is not yet finalized [2, 3]. The present work is in continuity of those past studies and aims at comparing the shock-interaction patterns, for a given double-cone geometry and given free stream conditions, computed with the following models : perfect gas inviscid flow, perfect gas viscous flow, real gas inviscid flow, and real gas viscous flow. A detailed comparison between the flow fields of these four simulations enables us to elucidate the contribution of viscous and real gas effects, separately and together, to the resulted flow field. In turn, the importance of accounting for these mechanisms separately and together in similar simulations is better understood.

2 Flow conditions, physics modeling and computational methodology

The comparison of the inviscid, viscous, perfect and real gas flow simulations is done on test cases of double-cone flow proposed in the early 2000's by Candler *et al.* [4] and Holden and Wadhams [5]. Two test cases are selected for the present study : a first test case (Run 35) corresponding to low-enthalpy ($\sim$ 3.7 MJ/kg) flow conditions, where the real-gas effects are negligible; this test case is used to compare the inviscid and viscous flow model simulations in order to show the effect of viscosity on the flowfield; a second test case (Run 43) corresponding to high-enthalpy ($\sim$ 8.9 MJ/kg) flow conditions where the high-temperature effects may be preponderant. This test case allows us to compare perfect and real gas model simulations, both for inviscid and viscous flow models. The flow conditions of the two test cases are summarized in Table 1. Both runs are done

	ρ_∞ (kg/m^3)	u_∞ (m/s)	M_∞	T_{wall} (K)	T_∞ (K)	$T_{V_{N_2\infty}} = T_{V_{O_2\infty}}$ (K)
Run 35	5.515×10^{-4}	2713.0	11.30	296.1	138.9	
Run 43	2.134×10^{-3}	4218.1	8.87	296.2	576.0	576.0
	$Y_{N_2\infty}$	$Y_{O_2\infty}$	Y_{NO_∞}	Y_{N_∞}	Y_{O_∞}	
Run 35	0.98120	0.01880	0.00000	0.00000	0.00000	
Run 43	0.73704	0.17160	0.06477	0.00000	0.02659	

Table 1. Free stream conditions for low-enthalpy Run 35 and high-enthalpy Run 43 cases. [5]

on the same geometry, a double cone that has two conical sections of 10.16-cm surface length, angles $\theta_1 = 25°$ and $\theta_2 = 55°$. Note that with this geometry and under those freestream conditions, the flow is completely laminar.

All computations are performed assuming a non-equilibrium chemistry and a non catalytic double cone wall. Reactions rate models by Park [6] for air with 5 species and 17 reactions are applied. The air flow is also assumed to be in thermal nonequilibrium. The exchange between vibrational and translation-rotational energy is modeled with the Landau-Teller approach. The vibrational relaxation times are obtained with the semi-empirical curve fit by Millikan and White [7]. The transport properties for gas mixtures in nonequilibrium require a special modeling. The viscosity and the thermal conductivity are computed with Gupta *et al.*'s model [8].

The simulations are done with the Parallel Implicit Nonequilibrium Navier-Stokes (PINENS) code, that solves the Navier-Stokes equations for chemical and vibrational nonequilibrium flows of compressible gas mixtures. It is based on a finite-volume method on structured grid, where the flux evaluation scheme is the Roe solver, with the H-correction to avoid eventual *carbuncle*-type problems ; the reconstruction of the variables at the interface between cells is done with the van-Leer scheme. This combination of numerical schemes turned out to be one of the most efficient numerical schemes to predict the flow over the double cone [1]. The implicit time resolution of the equation system is based on the DPLR solver. The computational grid used for the 2D-axisymmetric simulations consists of a 512x256 cell grid in streamwise and normal directions. This grid was found to be the best compromise for accuracy and efficiency to compute the flow past the double-cone geometry [1].

3 Results

No comparison with experimental data are shown in this paper. The validation of the numerical methods and physico-chemical models was done in previous work of Druguet *et al.* [1, 3] and Nompelis *et al.* [2] by comparison of the computed surface pressure and heat flux with the experiments of Holden [5].

3.1 Comparison inviscid/viscous flow model simulations

The comparison between inviscid and viscous flow model simulations for a perfect gas model is performed on the low-enthalpy case (Run 35) where the real gas effects are negligible. The temperature fields are shown in Figs. 1 and 2. The contribution of viscous effects to the flow field, which is clearly seen, is very significant. As a matter of fact the neglect of viscosity results in a completely different flow field: without viscosity the flow does not recirculate in the corner of the two cones.

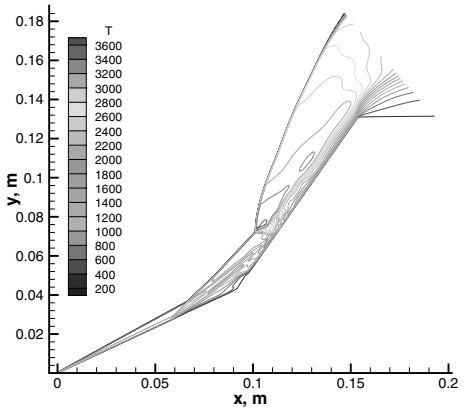

Fig. 1. The flow field (temperature) that results from the interaction of a Mach 11.3 low-enthalpy flow (Run 35) with the $25° - 55°$ double cone. Perfect gas viscous flow.

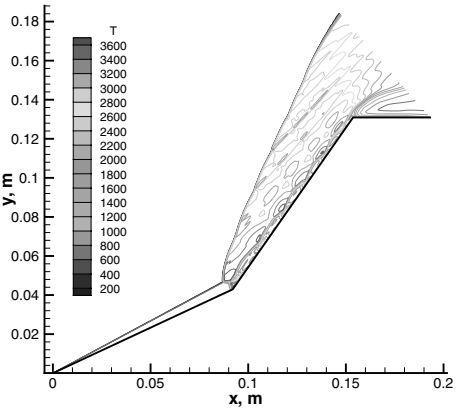

Fig. 2. The flow field (temperature) that results from the interaction of a Mach 11.3 low-enthalpy flow (Run 35) with the $25° - 55°$ double cone. Perfect gas inviscid flow.

3.2 Comparison perfect/real gas model simulations

The comparisons between perfect and real gas model simulations for inviscid and viscous flow models are performed on the high-enthalpy case (Run 43) for which the high-temperature gas effects are important. The computed flow field for various models of thermo-chemical nonequilibrium are shown in Figs. 3 and 4. The results on the left-hand side are for a viscous flow model and those on the right-hand side are for an inviscid flow model. The top figures display the temperature field and the bottom figures show the pressure coefficient along the double-cone surface. In order to efficiently measure the influence of the various components of the real-gas effects, computations are done with models including real-gas effects step by step: frozen chemistry and vibration, frozen

chemistry and vibrational equilibrium, nonequilibrium chemistry and frozen vibration, nonequilibrium chemistry and vibration, nonequilibrium chemistry and equilibrium vibration. Note that the flow field with the frozen chemistry and vibration model and the viscous flow model gets unstable and converges towards a detached shock configuration. It is therefore not shown here.

The effect of the chemistry models is shown in Fig. 3 where frozen and nonequilibrium chemistry model simulations are compared. The effect of chemical reactions is clearly seen for the viscous flow model (left, top and bottom figures). The nonequilibrium chemistry model predicts a recirculation zone much smaller than the frozen chemistry model does. This can simply be explained by the fact that the chemical reactions are mostly endothermal, therefore the part of the flow energy absorbed by the chemical reactions is no longer

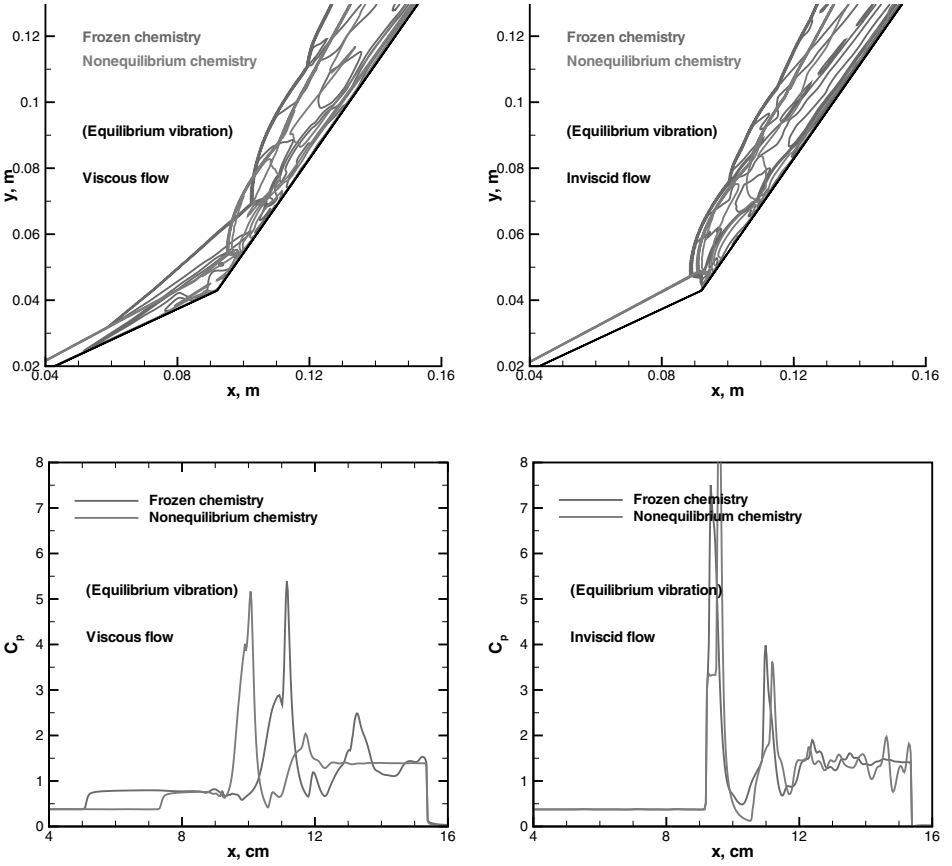

Fig. 3. The temperature field (top) and surface pressure coefficient (bottom) that result from the interaction of a Mach 8.87 high-enthalpy flow (Run 43) with the $25^\circ - 55^\circ$ double cone. Viscous (left) and inviscid (right) flow models. Comparison between frozen and nonequilibrium chemistry models.

available in the flow itself, reducing the size of the recirculation zone [1, 3]. On the other hand, the effect of the chemical reactions is not so visible for the inviscid flow model, probably because of the configuration of the shock interaction that is confined in the corner between the two cones. It would be interesting to perform the same comparison on a different double-cone geometry, where the shock interaction does not take place in the corner of the two cones.

The effect of the vibrational relaxation models is shown in Fig. 4, where frozen, nonequilibrium and equilibrium vibrational relaxation models are compared. Their effects are not as important as the effect of the chemistry models. The results with the frozen and the nonequilibrium vibrational relaxation models are very similar, and show a recirculation zone slightly larger than the one predicted by the simulation with the

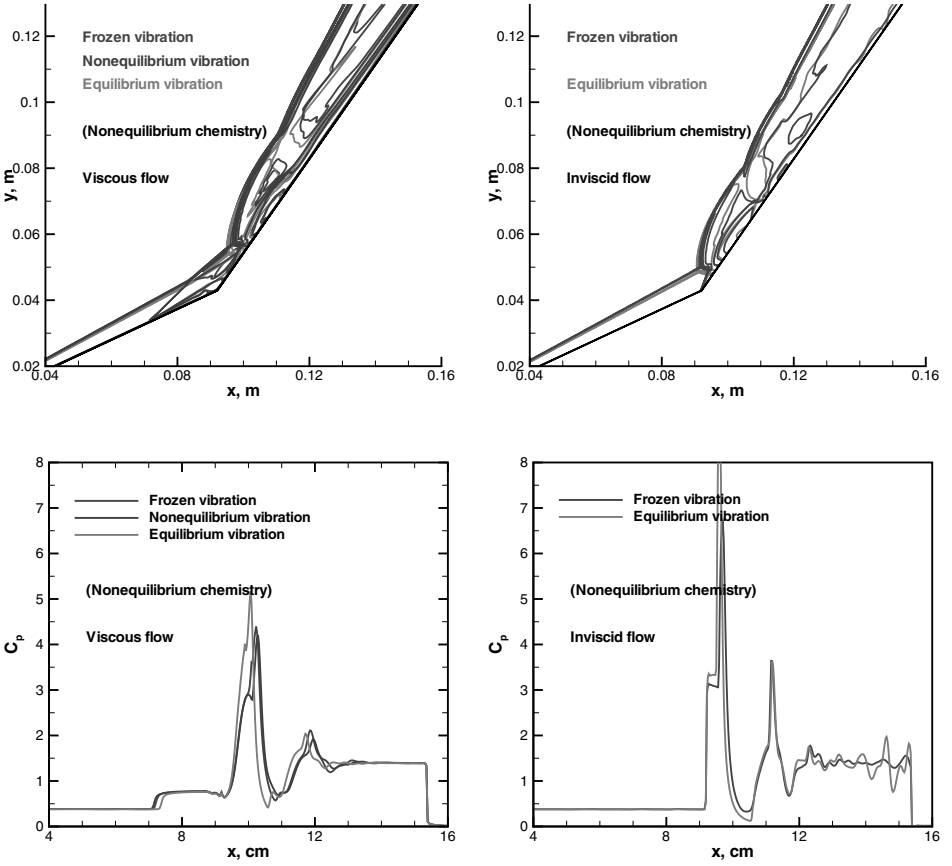

Fig. 4. The temperature field (top) and surface pressure coefficient (bottom) that result from the interaction of a Mach 8.87 high-enthalpy flow (Run 43) with the $25^\circ - 55^\circ$ double cone. Viscous (left) and inviscid (right) flow models. Comparison between frozen, nonequilibrium and equilibrium vibration models.

equilibrium vibrational relaxation model. Here again, more energy absorbed by the thermal processes, the smaller the recirculation zone is. The small difference between the results computed with the various vibration models might be due to the freestream conditions that are such that the vibrational temperatures are equal to the trans-rotational temperature.

4 Conclusions

Comparisons of inviscid, viscous flow, perfect and real gas model simulations were performed. Several conclusions can be drawn from that work: 1) the flow viscosity is necessary to the flow to recirculate and therefore has a major effect on the shock-interaction configuration; 2) among the several real gas effects computed here, the chemical nonequilibrium has the most important influence on the shock interaction; 3) in the present double-cone configuration and with the given freestream conditions, the vibrational relaxation model does not show any significant effect on the flowfield. This is probably due to the freestream conditions where the vibrational mode of the molecules is in equilibrium with the trans-rotational mode. It would be interesting to perform the same kind of comparisons for freestream conditions where the vibrational temperatures are different from the equilibrium temperature. Finally the comparison perfect/real gas model simulations show that the more is the energy absorbed by the physico-chemical processes, the smaller the recirculation zone size is.

Acknowledgement. All the computational ressources used for the present simulations were provided by the Institut du Développement et des Ressources en Informatique Scientifique (IDRIS), 91403 Orsay, France.

References

1. Druguet M.-C., Candler G.V., Nompelis I.: Effect of numerics on Navier-Stokes computations of hypersonic double-cone flows. *AIAA Journal*, **43**,(3):616–623, (2005).
2. Nompelis I., Candler G.V., Holden M.S., Wadhams T.P.: Computational investigation of hypersonic viscous-inviscid interactions in high-enthalpy flows. AIAA Paper 2003-3642.
3. Druguet M.-C., Candler G.V., Nompelis I.: Comparison of physical models in computations of high-enthalpy double-cone flows. AIAA Paper 2006-3419.
4. Candler G.V., Nompelis I., Holden M.: Computational analysis of hypersonic laminar viscous-inviscid interactions. AIAA Paper 2000-0532.
5. Holden M.S., Wadhams T.P.: Code validation study of laminar shock/boundary layer and shock/shock interactions in hypersonic flow. AIAA Paper 2001-1031A.
6. Park C.: Review of chemical-kinetic problems of future NASA missions, I: Earth entries. *Journal of Thermophysics and Heat Transfer*, **7**,3:385–398, (1993).
7. Millikan R.C., White D.R.: Systematics of vibrational relaxation. *Journal of Chemical Physics*, **39**,12, (1963).
8. Gupta R.N., Yos J.M., Thomson R.A., Lee K.-P.: A review of reaction rates and thermodynamic and transport properties for an 11-species air model for chemical and thermal nonequilibrium calculations to 30000K. *NASA-RP-1232*, (1990).

The two distinct configurations of 3-shock reflections in the domain beset by the von Neumann paradox

A. Siegenthaler

Private address: Kirchweg 57, CH-5415 Nussbaumen, Switzerland

Summary. The theory presented at the 25th ISSW is used to map out the effective boundary between regular and Mach reflection in the weak domain. Transition from one to the other being inhibited at detachment, its occurrence is found to be delayed by some extent until the requirements for it are fulfilled. This same theory is then also used to determine the change-over limit between weak Mach to Guderley reflection. These results are then discussed in the light of the fascinating results obtained by numerical computation of the whole flow field.

1 Introduction

In 1943 von Neumann (JvN) [4] pointed out that based on classic Rankine-Hugoniot (RH) shock wave theory, transition from Regular to Mach reflection (RR to MR) presents an insurmountable impasse in the weak domain (see Fig. 2). JvN referred to the experimentally observed weak MR (WMR) as extraordinary MR in contrast to ordinary MR which takes place in strong reflections ([4], pars. 45, 52 and 58). The distinction between the two cases may also be referred to as the no-solution *vs.* the dual-solution domain, although, strictly speaking, the former of the two denotations is not quite correct, for in fact there exists one trivial solution which however, in the context of reflection, does not correspond to the actually observed phenomenon.

It is astounding to read that JvN also noticed that WMR needed to be subdivided in two separate types of reflection, each displaying distinct features ([4], par. 56). A description of the individual characteristics of these two 3-shock systems may be found in Ben-Dor et al. [1] (p. 130-132). And they were investigated and discussed by Colella & Henderson [2] who demonstrated that such a subdivision is fully supported by experimental facts. However, while their dissertation of Guderley Reflection (GR - designation introduced by Skews & Ashworth [7]) is of prime significance, their theory of WMR is based on the misleading trivial solution mentioned above. As a corollary, their criterion for transition between said two regions leads to increasingly unrealistic results as weaker incident shocks are considered.

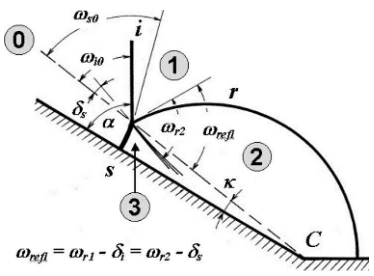

Fig. 1. Nomenclature used for the 3-shock reflection: The (circled) numbers denote the (4) flow regions, separated by three shock waves and one contact discontinuity. In regions (0) and (1) the flows are constant and uniform throughout, in (2) and (3) non-uniform and always subsonic (as a result of curved s- and r- shocks in WMR). The values indicated in this study for region (2) and (3) only apply to the direct vicinity of the triple point (e.g.: for the r-shock the departure from RH vanishes with increasing distance from the triple point)

Resorting to numerical computation, Tesdall and Hunter [9] observed the evolution of a complex structure within the wake of the shock interaction region for ramp angles off glancing incidence. These amazing flow peculiarities were subsequently confirmed experimentally in a special shock tube by [7] who then named this configuration as GR (in memory of the scientist who broadly anticipated the 'new' features).

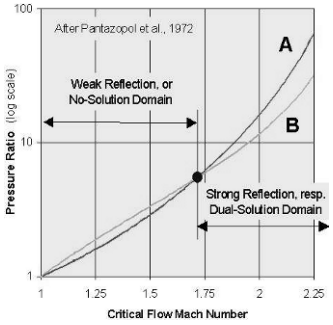

Fig. 2. Pressure mismatch which is responsible for transition from 2- to 3-shock reflection configuration to be inhibited at detachment of RR. A (red): Compounded pressure ratio p_2/p_0 across i- and r-shock pair. B (blue): Pressure ratio p_3/p_0 over a fictitious incipient Mach stem. As long as A is lower than B, the growth of a Mach stem is precluded due to lack of sufficient driving force. Using the critical flow Mach number for the abscissa accentuates the weak domain ($M_0 = \infty > M_0^* = 2.444$ for air with $\gamma = 1.402$). The intersection of the curves occurs at $M_0 = 2.2039$ (standard flow Mach number), resp. at $\xi_i = 0.4326$. In term of pressure ratio, the max. mismatch $p_3/p_2 = 1.1944$ is reached at $M_0 = 1.4642$, resp. at $\xi_i = 0.7573$. In term of pressure difference, the max. mismatch $(p_3 - p_2)/p_0 = 0.4512$ occurs at $M_0 = 1.7017$, resp. at $\xi_i = 0.6366$

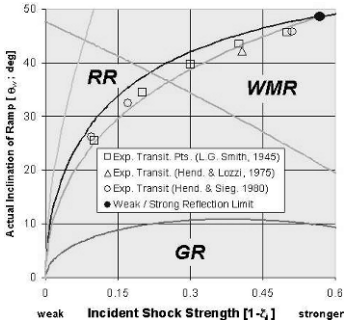

Fig. 3. Domains and calculated transition boundaries between the various types of shock reflection configurations for an ideal diatomic gas in the weak domain ($\gamma = 1.402$). The variable used for the abscissa is $(1 - \xi_i)$. This choice also strongly accentuates the weak domain. The data points represent experimentally determined 2- to 3-shock transition angles. Considering a vertical line at the abscissa of 0.3 ($\xi_i = 0.7$), from top to bottom, the curves represent the following boundaries: 1. Detachment of RR (the downstream sonic condition has been omitted); 2. Transition from PRR to WMR; 3. The erroneous transition from WMR to GR acc. to [2]; 4. Transition from WMR to GR as advocated in this study. In this representation, the limit of glancing incidence is depicted by the ramp inclination angle = 0. The round dot at the abscissa of 0.5674 demarcates the limit between weak and strong domains. The steep grey line represents the 2- to 3-shock transition as per transonic similarity approximation acc. to [9] ($a = 2^{1/2}$)

One notorious subject of discordance concerns the influence, which viscous boundary layers may have on a given reflection process. While Zakharian et al. [10] (p. 201-202) make the concluding observation that such effects do not appear to be able to perturb the shock system at the triple point, the results of [2] convincingly suggest that viscous effects do indeed exert an influence. One reliable observation of old that ought not to be overlooked in this respect is that in RR the r-shock definitely appears to be quite immune to any such disturbance. So it is difficult to imagine why and how other types of reflections could be substantially affected by viscous effects.

2 Discussion

The black line in Fig. 3 represents the detachment condition of RR. It may be useful to recall that whereas this limit can not be visualised by optical techniques, the downstream sonic condition is easily detectable as the corner signal catches up with the point of reflection. Theory on the one hand discloses that the angular difference between catch-up and detachment reaches a maximum of 0.58° at a shock strength $\xi_i = 0.878$ in air (see transition data in Table 1).

On the other hand, experimental results reported by Smith [8] (brief conference report) and by Henderson & Siegenthaler [3] reveal that a 2-shock configuration persists for up to 4° past catch-up, and that only then does an incipient Mach stem begin to appear. Now, since the flow regimes between those two narrowly spaced ramp inclinations may be expected to be closely similar, it can be concluded that viscous effects must be equivalent too. These therefore cancel out, and the argument that such effects could be responsible for persistence must be refuted. This gap of up to 4° represents an unmistakable and convincing witness that a 2-shock reflection pattern does indeed persist beyond detachment. This conclusion together with some further experimental observations provided the stimulus for elaborating a theory which takes these facts into account (Siegenthaler [6]). The result is a 2-shock pattern which consists of an r-shock whose characteristics are

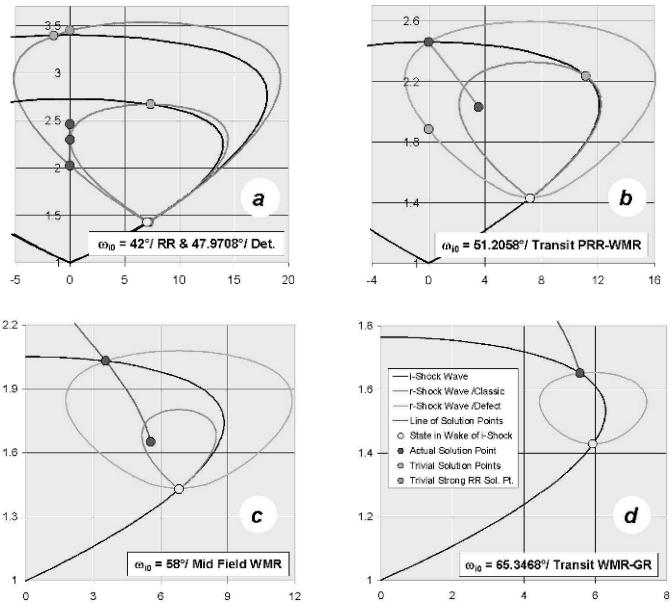

Fig. 4. Shock polar maps depicting the evolution of the solutions from RR to the point of WMR-GR transition (pressure *vs.* deflection plane). The legend shown in Fig. (d) applies to all 4 diagrams. In all 4 figures., the polars for the i-shock (black curves) are calculated for a strength of $\xi_i = 0.7$ in air and for the angle of incidence as indicated in each diagram (2 separate RR cases are drawn in Fig. (a). The parameters that pertain to the polars of the r-shocks (green curves) are: Fig. (a), $M_1 = 1.5044$ & $1.3207, X = 1$; Fig. (b), $M_1 = 1.2408, X = 0.9537$; Fig. (c), $M_1 = 1.1065, X = 0.9648$; Fig. (d), $M_1 = 1.0013, X = 0.9877$

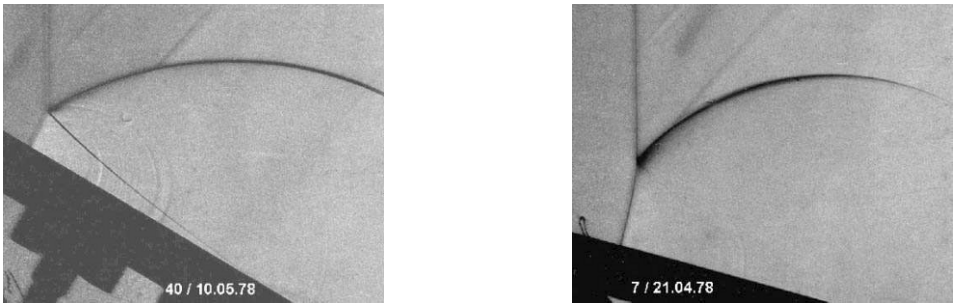

Fig. 5. Schlieren photos of a typical WMR **(l.h.s.)**, and one **(r.h.s.)** close to WMR-GR transition. The knife-edge of the optical system is inclined 30° anti-clockwise off the vertical axis. The measured parameters are (Δt = time elapsed after the incident shock passed the ramp corner): **Fig. l.h.s.**: $\xi_i = 0.48$ $\omega_{i0} = 54°10'$ $\omega_{refl} = 67°36'$ $\kappa = 5°4'$ $\Delta t = 96$ µsec; **Fig. r.h.s.**: $\xi_i = 0.50$ $\omega_{i0} = 60°39'$ $\omega_{refl} = 79°13'$ $\kappa = 13°30'$ $\Delta t = 87$ µsec; On **r.h.s**, a very faint slip-stream is still visible; calculation yields transition to take place at an angle $\omega_{i0} = 61°51.5'$; the photo appears to exhibit a mix of WMR and GR features; thus some overlapping of the characteristics pertinent to both types may have to be considered. The two weak oblique streaks which appear between the i- and the r-shocks in the upper part of the photos are disturbances produced by the cookie-cutter at the entrance into the test section - they have no influence on the reflection process

forced to deviate from the classic RH behaviour as the angle of incidence increases past detachment. And only when the pressure requirement for a Mach stem can be met, does onset of MR occur.

The crescent shaped area between the black and the red lines (Fig. 3) represents the 2-shock irregular extension and has been dubbed the Pseudo-RR region. The observations

Table 1. Calculated transition limits in the weak reflection domain for air ($\gamma = 1.402$). Note that for the shock strengths in the 2 columns on the r.h.s., the results for 2- to 3-shock transition correspond to the classic RH solutions (von Neumann condition). Notwithstanding these 2 RH solutions, the reflection at the WMR-GR transition still features a defect r-shock. This implies that in the strong domain, the r-shock of Single MR reaches detachment condition before the GR limit is reached. Therefore, WMR with a defect r-shock extends to some degree into the strong reflection domain

i-Shock Strength	ξ_i	0.90	0.80	0.70	0.60	0.50	0.43262	0.40
Sonic	ω_{i0}	60.2482	52.1829	47.4816	44.3571	42.1755	41.0869	40.6518
Condition	ω_{refl}	69.8543	62.5216	57.1774	52.7649	48.8760	46.4387	45.2944
RR	ω_{i0}	60.8258	52.7374	47.9708	44.7755	42.5250	41.3921	40.9362
Detachment	ω_{refl}	73.5458	66.9070	61.7562	57.2913	53.1951	50.5522	49.2918
PRR-WMR	ω_{i0}	65.0120	56.7671	51.2058	46.9419	43.4497	41.3921	40.8526
Transition	ω_{refl}	79.2346	73.8664	68.6863	62.9451	56.0871	50.5522	47.1417
WMR-GR	ω_{i0}	74.0342	68.6771	65.3468	63.1793	61.8590	61.3804	61.2627
Transition	ω_{refl}	86.7527	84.0818	81.1189	77.7988	74.0623	71.2715	69.8302
Glancing	ω_{i0}	74.1488	68.7979	65.4580	63.2762	61.9404	61.4511	61.3282
Incidence	ω_{refl}	88.8326	86.7510	84.0817	80.8950	77.1810	74.3491	72.8707

that transition from the 2- to the 3-shock reflection configuration occurs smoothly in experiments, and that the appearance and growth of the Mach stem is a continuous and steady process, are both respected in that model. And JvN's assumption for transition to take place under conditions where both, RR and MR (normal Mach stem) can co-exist, is also fulfilled (JvN referred to that as quasi-stationary condition; see pars. 40-45 of [4]). The key difference then, is that in the vicinity of the triple point, the r-shock departs from RH theory (thus dubbed as 'defect' shock in [6]).

The unrealistic solution that was proposed in [2] may provide some fair results for i-shocks of strength close to the weak/strong change-over limit. However, it yields increasingly erroneous answers as weaker i-shocks are being considered (see the turquoise-blue dots in Figs. 4a & 4b; in Fig. 4c this solution has vanished; see also the line labelled 3T in Fig. 4 of [3] and the lines marked C on the diagrams of [6]). The green line in Fig. 3 represents the WMR to GR transition limit as assumed in [2]. It is obvious this would lead to abstruse situations in the weaker range. That criterion together with the trivial solution therefore need to be discarded.

The evolution of the solution from RR through to GR is depicted by a series of polar diagrams (Figs. 4). With respect to WMR, the two beneficial attributes of defect shocks are to enable an increase of the streamline deflection and this is accompanied by a boost of the pressure jump. Both of these trends are clearly visible in Figs. 4b to 4d. This combination then enables transition to WMR to take place.

For 3-shock systems the relation presently used for converting the transition results from the angles of incidence ω_{i0} to the angles of ramp inclination θ_w, has been taken from [1] (p. 133). The relation becomes $\theta_w = 90 - (\omega_{i0} + \kappa) = \omega_{s0} - \omega_{i0}$

After transition to WMR has occurred, the r-shock experiences a steady decrease of the flow Mach number M_1 as the ramp inclination is being reduced. A limit is reached where the shock Mach number of the r-wave becomes equal to 1. In line with classic gas dynamics, the shock character then vanishes. In this study, this is regarded as the point where WMR-GR transition occurs. Drawing again from the theory of [6] and introducing the Mach wave condition, the blue line of Fig. 3 is obtained. On first appraisal,

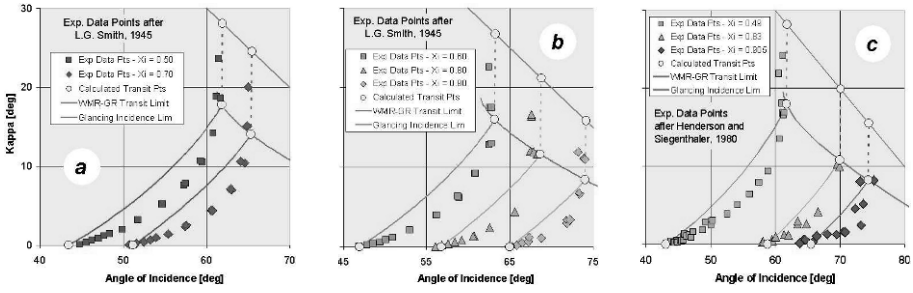

Fig. 6. Angle of the triple point path κ *vs.* the angle of incidence ω_{i0} for a series of shock strengths $0.49 < \xi_i < 0.905$. The yellow dots are calculated points of transition. Beginning from the abscissa and going up, these points are: PRR to WMR ($\kappa = 0$), WMR to GR, and glancing incidence. The solid lines which connect the lower 2 yellow dots are calculated according to a relation for MR provided in [1]. The dashed lines that join the upper 2 yellow dots are empirical; they demonstrate that for GR the angle ω_{i0} remains nearly constant while reducing the ramp inclination θ_w towards zero

comparing this limit with the experimental data per Figs. 6, the agreement appears to be surprisingly good. However, when the important data point of [7] and the results of [9] are considered, it is realised that, in the context of the highly constrained flow regime under consideration, the condition of $M_r = 1$ probably represents too stringent a limitation. On the other side, as the results of [9] suggest, it may be expected that a sequence of supersonic patches could hardly be sustained once the upstream/downstream Mach numbers begin to separate appreciably as the shock strength increases (acc. to Prandtl's velocity relation). In other words, Guderley's patch(es) might be a phenomenon which is specific to transonic flow. Finally, the idea of considering the WMR-GR transition as a sharp delineation may be an elusive conception, for indeed on re-examining Figs. 6 in the light of the results of [9], it might be appropriate to regard the change-over as a gradual process.

3 Conclusion

The necessity to discern between two types of 3-shock reflection configurations in the weak domain has been discussed. The construct of a defect r-shock as described in [6] represents an accurate theory for predicting the onset of WMR. The credible assumption that WMR ceases to exist when the shock Mach number of the r-wave reaches unity, yields a plausible and perhaps too stringent delineation for transition to GR. Although the justification for the consideration of the model used is well founded, it ought to be reminded that the understanding of its underlying mechanism remains to be elucidated through pertinent experimental research.

S. D. G.

References

1. Ben-Dor G, Igra O and Elperin T (2001): Handbook of Shock Waves. Academic Press.
2. Colella P and Henderson LF (1990): The von Neumann paradox for the diffraction of weak shock waves. J Fluid Mech, 213, 71-94.
3. Henderson LF and Siegenthaler A (1980): Experiments on the diffraction of weak blast waves: the von Neumann paradox. Proc. R. Soc. Lond., A369, 537-555.
4. von Neumann J (1943): Oblique Reflection of Shocks, etc. see: John von Neumann - Collected Works VI, Pergamon Press, 1963.
5. Pantazopol D et al. (1972): Sur les conditions d'apparition de l'effet de Mach dans la reflexion d'une onde de choc oblique en ecoulement supersonique. Comptes Rendus Hebd. des Seances de l'Academie des Sciences, 275(A), 225-228.
6. Siegenthaler A (2005): Weak Mach reflection: a bold solution backed by results from pertinent experiments. Procs. 25th ISSW, Bangalore, India.
7. Skews BW and Ashworth JT (2005): The physical nature of weak shock wave reflection. J Fluid Mech, 542, 105-114.
8. Smith LG (1946): Photographic investigation of the reflection of plane shocks in air. The Physical Review (2nd series), 69, 678 (Proc. Am. Phys. Soc., Minutes of April Meeting).
9. Tesdall AM and Hunter JK (2002): Self-similar solutions for weak shock reflection. SIAM J Appl Math 63, 42-61.
10. Zakharian AR et al. (2000): The von Neumann paradox in weak shock reflection. J Fluid Mech, 422, 193-205.

The von Neumann paradox for strong shock waves

S. Kobayashi[1], **T. Adachi**[1], **and T. Suzuki**[2]

[1] *Saitama Institute of Technology, 1690 Fusaiji, Fukaya-shi, Saitama, 369-0293, Japan*
[2] *Toyama Prefectural University, 5180 Kosugi-machi, Imizu-gun, Toyama, 939-0398, Japan*

Summary. Up to the present, the von Neumann paradox has been mentioned only for weak shock waves, and the classical theories have been considered to be valid for strong shock waves. In the present paper, we discovered experimentally that the paradox also occurs in strong shock waves for the same reason as in weak shock waves. We also explain why it has not been observed so far and demonstrate that the essence of the problem lies in the transport properties of the fluid.

1 Introduction

The *von Neumann paradox* is well-known in shock reflection phenomena [1]. In short, it is a discrepancy between von Neumann's classical theory and experiment results for weak shock waves with an incident shock Mach number M_i less than 1.46 [2].

So far, self-similarity has been taken for granted, and so a single photograph was considered sufficient for measurement for a single experiment condition. However, detailed measurement revealed that, although the triple point moves almost along a single straight line through the wedge apex, the wave angles, such as angles of incidence and reflection, vary as the incident shock proceeds [3,4]. This result demonstrates that the oblique shock reflection phenomena are non-self-similar (or, equivalently, not pseudo-steady), unlike the conventional postulation in theory and numerical computation.

Physically, this is due to the viscosity and the thermal conductivity (transport properties) of the fluid, which produce characteristic lengths in the system. Henderson et al.'s [5] numerical results considering transport properties demonstrated that the effect of the boundary is important. Adachi et al. [6] analytically investigated the effect of the boundary layer on the wedge. Our results [4] showed that the wave configuration changes towards that given by the theory, and for some cases, the von Neumann paradox resolves in the end. We also demonstrated that, when the experiment data for various wedge angles θ_w are rearranged for a fixed location of incident shock, the tendency given by past experiments [7, 8] can be reproduced. Thus, the von Neumann paradox is regarded as a discrepancy between pseudo-steady inviscid theory and actual unsteady viscous phenomena. The effect of the boundary can propagate to the triple point and affect the flow-field, since the flow behind the reflected shock and the Mach stem is subsonic relative to the triple point. Consequently, no perfect-fluid theory will explain the paradox successfully.

Although the von Neumann paradox has been mentioned only for weak shock wave, so long as the reflection is a Mach-type, the region bounded by the reflected wave and the Mach stem is subsonic with respect to the triple point. This can be visually illustrated in Fig. 1, where the wavelets issue over the rough surface (♯240) and the reflected wave is an envelope of these waves. Therefore, even for strong Mach reflection, the boundary can affect the triple point and the paradox might be possible.

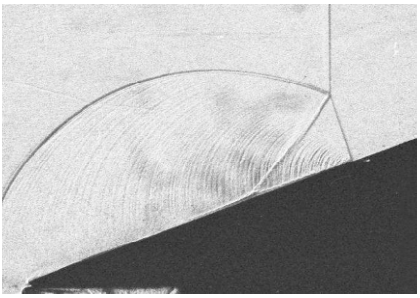

Fig. 1. Typical strong Mach reflection over a rough slope, $M_i = 1.915$, $\theta_w = 20°$, $x = 35.8$mm, where x is the distance from the wedge apex to the incident shock in the direction of propagation.

2 Experiment

We performed the experiments using a conventional shock tube in our institute (see [3] for details). The driver gas was helium, and the driven gas was air at room temperature and atmospheric pressure for each experiment run. The incident shock Mach number was $M_i = 1.915$. The models were ordinary smooth wedges of 10°, 12°, 20°, 30° and 49°. Except for the 49° wedge, the surfaces were polished with ♯2000 sand paper, and the measured surface roughness was less than 1μm. The 49° wedge was not polished, and its surface roughness is larger.

Shadowgraphy was employed to visualize the wave configuration. The light source was a xenon flash lamp with a 180ns pulse width (nanopulse light NPL-5 and its power supply NP-1A, Sugawara Laboratories, Inc.). The flash lamp was triggered by the output of the pressure gauge (601A, Kistler) installed nearest to the test section via a digital delay circuit (digital retarder RE-306, Sugawara Laboratories, Inc.). The reflection configuration at any desired instant could be photographed by regulating the delay time.

The triple-point coordinate (x, y) and the angle ω_{ir} made by the incident and reflected shocks at the triple point were measured directly from photographic negatives enlarged by a factor of about 50 using a profile projector (V-12, Nikon, Inc.). The triple-point location was easily converted in the coordinate system with the leading edge taken as the origin O, and the incident shock propagation direction as the x-axis. The y-axis was defined upward normal to the x-axis.

3 Results

3.1 Triple-point trajectory

The locations of triple point are presented in Fig. 2 for various wedge angles. The results indicate that the triple-point trajectory is a single straight line through the wedge tip for each wedge angle. However, this does not necessarily mean that self-similarity holds. Only in the case of $\theta_w = 49°$, does the transition from regular to Mach reflection occur on the wedge during the propagation (*dynamic transition* [9]). Therefore, the trajectory is not a single straight line when examined closely.

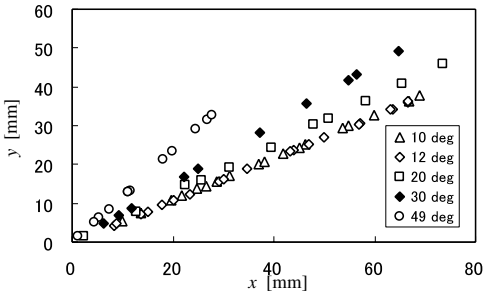

Fig. 2. Triple-point trajectories for various wedge angles, $M_i = 1.915$.

3.2 Angle between the incident and reflected waves

The angle ω_{ir} between the incident and reflected waves is presented in Fig. 3. For small wedge angles ($\theta_w = 10° \sim 30°$), the variation is large in the early stage of reflection ($0 < x < 20$mm), and the angle ω_{ir} seems to decrease asymptotically to some corresponding value. For a large wedge angle ($\theta_w = 49°$), the angle increases almost discontinuously around $x = 20$mm. This corresponds to the dynamic transition from regular to Mach reflection mentioned in 3.1.

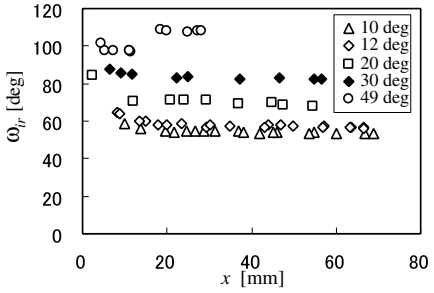

Fig. 3. Variation of the angle made by the incident and reflected shocks, $M_i = 1.915$.

3.3 Relation between angles of incidence and reflection

Figure 4 presents the relation between angles of incidence and reflection. Theory and experiment are compared in Fig. 4(a). Each arrow indicates the general direction of change for the experiment data. In all cases, experiment data varies toward the three-shock theory curve. This means that, although the discrepancy exists in an early stage, the von Neumann paradox will be resolved in the end.

The von Neumann theory can be revised by relaxing the boundary condition on the slipstream [10]. The numerical results considering the slipstream divergence δ are presented in Fig. 4(b). For $\omega_i \simeq 60°$, the effect of slipstream divergence is extremely large, since the small variation of δ causes large variation of ω_r. In fact, the experiment cited in reference [8] exhibited a slight disagreement there. For smaller ω_i , i.e., $\theta_w > 20°$,

the slipstream divergence becomes less effective. The discrepancy with the theory is conspicuous only in an early stage of reflection, for the Mach stem length is so short that the sink effect (a possible cause for slipstream divergence) over the wedge surface is strong. Since the past experiments are inferred to have been conducted for $x > 50$mm, where the steady state has been approximately attained, the discrepancy is probably unnoticed.

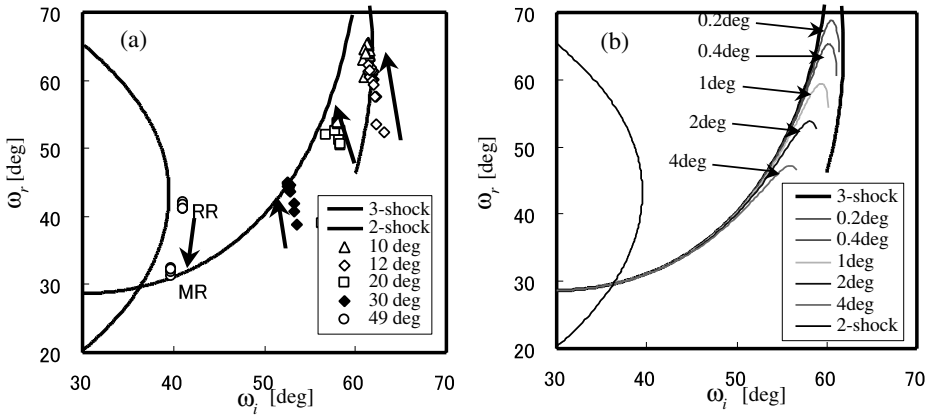

Fig. 4. Relation between angles of incidence and reflection for $M_i = 1.915$. (a) Classical theories and experiment. (b) Calculation considering the effect of slipstream divergence δ.

4 Conclusion

We conducted a series of experiments to investigate oblique shock reflection of strong shock waves, especially concentrating on the unsteady behavior. We found that the von Neumann paradox occurs even for strong shock waves. The reason why this has not been discovered so far can be explained by considering the effect of the slipstream divergence and the incident shock location where the measurement was made.

References

1. A. Sakurai, L.F. Henderson, K. Takayama, Z. Walenta, P. Colella: Fluid Dynamics Research **4**, 333-345 (1989)
2. R. Kawamura, H. Saito: J. Phys. Soc. Japan **11**, 584-592 (1956)
3. S. Kobayashi, T. Adachi, T. Suzuki: Phys. Fluids, **12**, 1869-1877 (2000)
4. S. Kobayashi, T. Adachi, T. Suzuki: Fluid Dynamics Research, **35**, 275-286 (2004)
5. L.F. Henderson, W.Y. Crutchfield, R.J. Virgona: J. Fluid Mech. **331**, 1-36 (1997)
6. T. Adachi, A. Sakurai, S. Kobayashi: Shock Waves, **11**, 271-278 (2002)
7. L.G. Smith: Photographic investigation of the reflection of plane shocks in air, OSRD Report 6271, Washington (1945)
8. W. Bleakney, A. H. Taub: Rev. Mod. Physics **21**, 584-605 (1949)
9. L.F. Henderson, K. Takayama, W.Y. Crutchfield, S. Itabashi: J. Fluid Mech. **431**, 273-296 (2001)
10. S. Kobayashi, T. Adachi, T. Suzuki: Fluid Dynamics Research, **17**, 13-25 (1995)

Unsteady Navier-Stokes simulations of regular-to-Mach reflection transition on an ideal surface

E. Timofeev[1] **and A. Merlen**[2]

[1] *Department of Mechanical Engineering, McGill University, 817 Sherbrooke St. West, Montreal, Quebec H3A2K6, Canada*
[2] *Laboratoire de Mécanique de Lille, Université des Sciences et Technologies de Lille (Lille1), Cité scientifique - Bâtiment M3, 59655 Villeneuve d'Ascq Cédex, France*

1 Introduction

Unsteady shock wave reflection from an ideal surface takes place, for instance, when a shock wave diffracts over a symmetrical body and the diffracted fronts meet behind the body and reflect from each other. The same kind of interaction is observed when two blast waves induced by a simultaneous explosion of two identical charges interact midway between the charges. The question whether or not the transition between regular (RR) and Mach (MR) reflections for such unsteady reflections can be predicted with the two- and three-shock theories based on steady flow assumption still remains open.

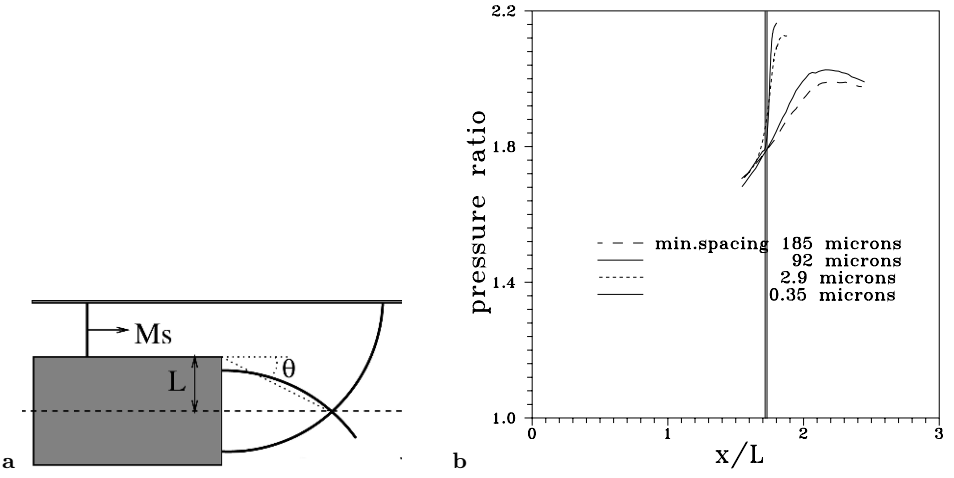

Fig. 1. The schematic and plot are reproduced from [1]. **a** Schematic of shock wave diffraction over a body and its reflection from the plane of symmetry (dashed line) behind it; **b** Pressure at the symmetry plane behind the reflection point or behind the Mach stem (after transition) for various adaptive grids; the pressure value is normalized by its value in front of the incident shock; the minimum grid spacing is given for $L = 60$ mm; $M_s = 1.336$, $\gamma = 1.4$. Two thin vertical lines correspond to the sonic (left line) and detachment (right line) points determined in [1].

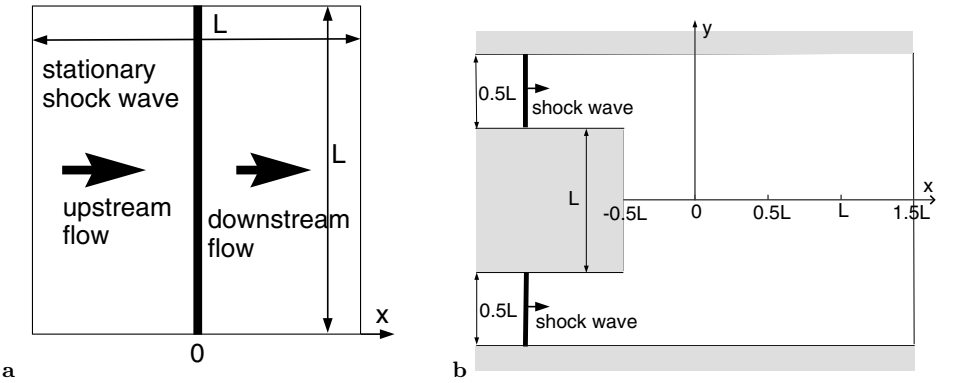

Fig. 2. The schematics of the problems simulated in the present study: **a** Stationary shock wave; **b** Shock wave diffraction over a body and its subsequent reflection from the plane of symmetry.

Timofeev et al. [1] considered the reflection of a diffracted shock wave from the plane of symmetry (Fig. 1a) using high-resolution numerical simulations with the Euler equations/perfect gas model and high-resolution holographic interferometry. Assuming that the shock wave diffraction over a 90° corner is self-similar, it was possible to determine the diffracted shock intensity using the diffracted shock geometry extracted from high-resolution simulations (or interferograms). Then, knowing the diffracted shock intensity and incident angle, the theoretical sonic and detachment points were calculated.

The paper [1] contains two major conclusions. First of all, it is established that the transition occurs after the detachment point, with a small delay of 0.3-0.4° in terms of incident shock angle. It is to be noted that the onset of Mach reflection is judged by the visual appearance of Mach stem, i.e., the reflection is considered to be of Mach type when the Mach stem is clearly at least one grid cell high. The second conclusion is that very fast pressure growth at the reflection point from the RR to MR value is observed at transition (Fig. 1b). The pressure growth rate does not exhibit grid convergence and is determined by grid spacing (note in Fig. 1b how fine the mesh should be to resolve the pressure rise at transition). All that seems to be in line with the Euler model assuming discontinuous shock fronts. Under such assumption the transition point may be viewed as a singular point at which the regular and Mach reflection (with zero-height Mach stem) exist simultaneously at the very moment of transition and an instant pressure jump takes place at the point of transition.

In the present paper the same problem is considered using a more complex physical model, namely the Navier-Stokes equations (the perfect gas assumption is retained; $\gamma = 1.4$). For that purpose, the viscous terms approximated by central differences are included into an adaptive unstructured Euler code [2]. It is widely recognized that at moderate Mach numbers the Navier-Stokes solution provides a good approximation of shock front structure, and therefore the Navier-Stokes numerical model can be used to evaluate, at least qualitatively, the influence of finite shock front thickness on the RR-MR transition.

2 CFD model and grid convergence

At the first stage, a stationary normal shock wave ($M_s = 1.336$ as in [1]) is simulated to determine grid spacings needed to achieve grid convergence (i.e. independence of the shock profile from grid step size), see Fig. 2a. The background mesh has an average grid step of $0.05L$. The results for two Reynolds numbers, 1,000 and 10,000, are shown in Fig. 3. It is seen that, as a rule of thumb, for grid convergence it is necessary to have at least 10 grid cells across the shock. This corresponds to 4 refinement levels for $Re = 1,000$ and 6 refinement levels for $Re = 10,000$ (each refinement level makes the grid two times finer). The Reynolds number is calculated using the distance L (see Fig. 2a), density ρ_1 and viscosity μ_1 of the gas in front of the shock, and the velocity $\sqrt{p_1/\rho_1}$, where p_1 is the pressure in front of the shock.

At the next stage of the investigation, the problem of shock wave diffraction and reflection shown schematically in Fig. 2b is considered (the same setup as in [1]). The computations are performed with $M_s = 1.336$, $\gamma = 1.4$ for $Re = 1,000$ and $Re = 10,000$ with the grid refinement determined above. The Reynolds number is calculated using the distance L (see Fig. 2b), density ρ_1 and viscosity μ_1 of the gas in front of the diffracted shock, and the velocity $\sqrt{p_1/\rho_1}$, where p_1 is the pressure in front of the diffracted shock.

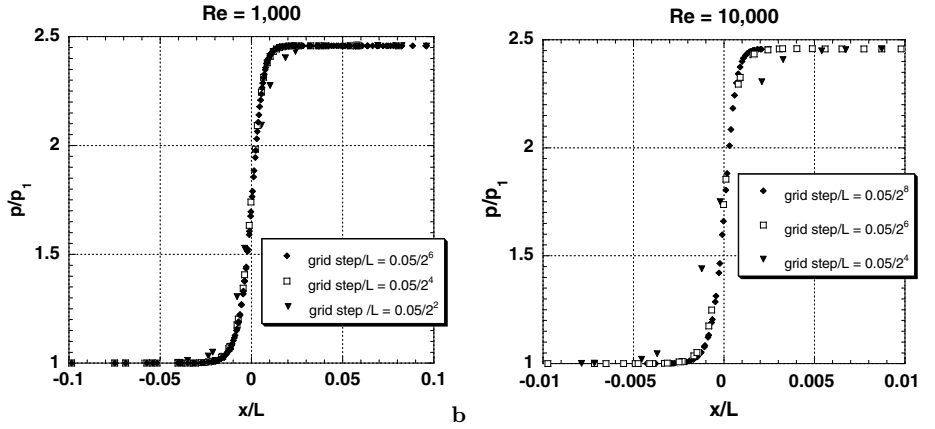

Fig. 3. Normalized pressure distributions across $M_s = 1.336$ stationary normal shock wave for **a** $Re = 1000$ and **b** $Re = 10,000$ and different grid spacings.

3 Results and discussion

The results are summarized in Figs. 4-7. Figure 4 shows instant pressure distributions along the plane of symmetry. In Figs. 5 and 6 the successive reflection patterns in the vicinity of the plane of symmetry are shown for the same time moments as the bold pressure curves in Figs. 4a,b. The respective x-t diagrams at the plane of symmetry can be found in Fig. 7. It should be emphasized that these are grid-convergent results, i.e., they will remain the same even if a finer mesh is used. The thickness of the shock fronts is determined by physical rather than numerical viscosity.

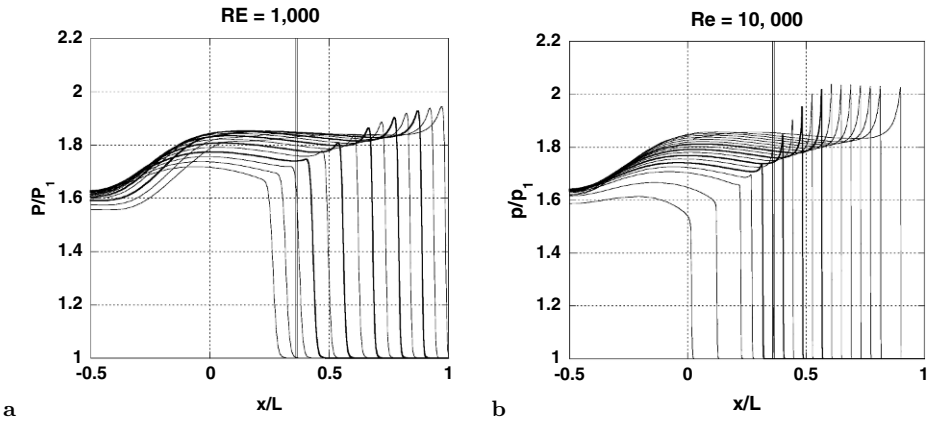

Fig. 4. Normalized instant pressure distributions along the plane of symmetry for the problem of shock wave diffraction and reflection shown in Fig. 2b for **a** $Re = 1,000$ and **b** $Re = 10,000$. The reflection patterns for time moments corresponding to the bold curves are shown in Fig. 5 and Fig. 6. Two thin vertical lines correspond to the sonic (left line) and detachment (right line) points determined in [1]. The value of x/L in the figure is related to the value in Fig. 1b ([1]) as follows: $(x/L)_{\text{Fig.4}} = (x/L)_{\text{Fig.1b}}/2 - 0.5$.

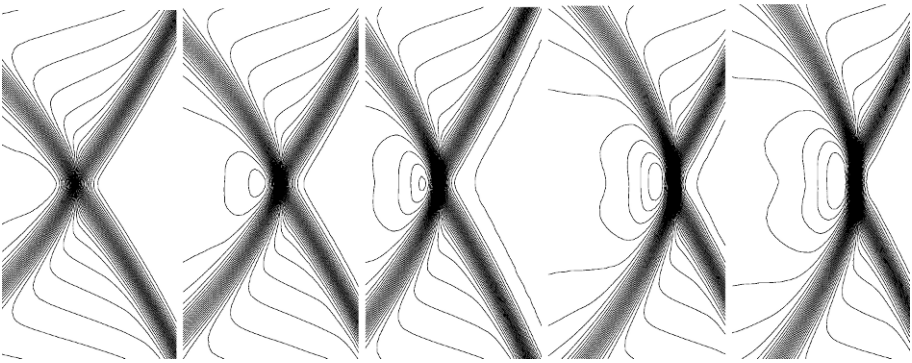

Fig. 5. Density contours in the vicinity of the plane of symmetry corresponding to the bold curves in Fig. 4a (in the same sequence from left to right). The physical size of each image is $0.2L \times 0.4L$; $Re = 1,000$.

The following observations can be made using the figures.

– If the onset of Mach reflection is determined via visual examination of reflection patterns, it is to be concluded that, for the Reynolds numbers under consideration, the finite shock front thickness due to viscous effects results in a considerable delay of transition as compared to the "inviscid" detachment point. Indeed, only the fourth reflection pattern from the left in Fig. 5 and the third from the left in Fig. 6 may be considered as emerging Mach reflections. For $Re = 1,000$ the delay is (approximately,

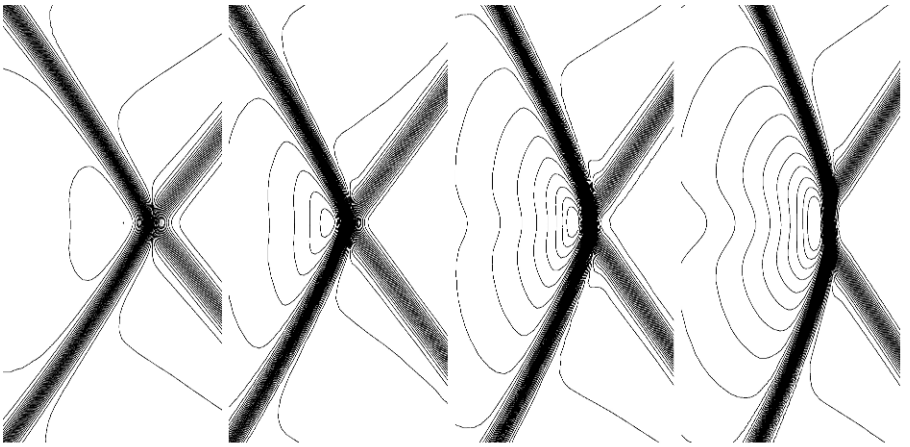

Fig. 6. Density contours in the vicinity of the plane of symmetry corresponding to the bold curves in Fig. 4b (in the same sequence from left to right). The physical size of each image is $0.03L \times 0.06L$; $Re = 10,000$.

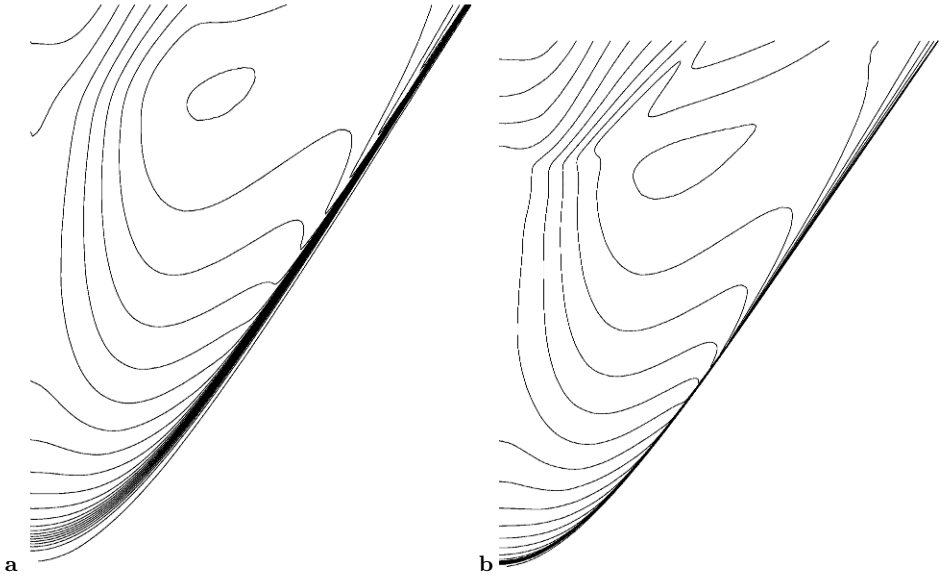

Fig. 7. x-t diagrams at the plane of symmetry for **a** $Re = 1,000$ and **b** $Re = 10,000$.

since there is no well-defined, sharp boundary) 0.4-0.5L and for $Re = 10,000$ the delay is 0.15-0.2L. It is to be noted that even though the Reynolds number increases by one order of magnitude the delay reduces only by 2-3 times. This is due to the fact that in the unsteady reflections under consideration the triple point trajectory

is tangential to the reflection surface (the plane of symmetry in this case). It could be conjectured that for Reynolds numbers of the order of 10^5-10^6 (typical for shock wave experiments) the delay may still be of the order of millimeters even though the shock front thickness would be less than one micron. The respective computations are in progress now.

– It is seen that for both Reynolds numbers the pressure and density behind the reflection zone at the plane of symmetry *gradually* rise from the values corresponding to regular reflection to the ones corresponding to Mach reflection. The intermediate values appear to be different from those defined by the inviscid two- and three-shock theories. Furthermore, the reflection zone at the plane of symmetry gradually diminishes in width from the wide zone corresponding to regular reflection (almost double value of single shock front thickness) to the narrow one corresponding to the Mach stem front. This is especially well illustrated by the x-t diagram for $Re = 1,000$ (Fig. 7a). Thus, under the Navier-Stokes model (with finite shock front thickness) it would be more meaningful to consider a *transition zone* from regular to Mach reflection (in space and time) rather than a transition point. For higher Reynolds numbers (10^5-10^6) the transition zone width will decrease. However, as explained above it is likely that it will be still much larger than the thickness of shock front and may not be neglected.

Acknowledgement. The study was partially supported by the Canadian National Science and Engineering Research Council (NSERC) Discovery grant 298232-2004, Université des Sciences et Technologies de Lille (Lille1), and France-Canada Research Foundation (2006/2007 seed grant).

References

1. Timofeev EV, Skews BW, Voinovich PA, Takayama K (1999) The influence of unsteadiness and three-dimensionality on regular-to-Mach reflection transitions: a high-resolution study. In: Ball GJ, Hillier R, Roberts GT (eds) Shock Waves, Proc. of the 22nd Intl. Symp. on Shock Waves, London, UK, 18-23 July 1999. University of Southhampton, vol. 2, pp. 1231–1236
2. Saito T, Voinovich P, Timofeev E, Takayama K (2001) Development and application of high-resolution adaptive numerical techniques in Shock Wave Research Center. In: Toro EF (ed) Godunov methods: theory and applications. Kluwer Academic/Plenum Publishers, NY, pp. 763–784

Underwater shock and bubble interactions from twin explosive charges

J.J. Lee[1], J. Gregson[3], G. Rude[1], and G.T. Paulgaard[2]

[1] *DRDC Suffield, AB, Canada*
[2] *Amtech Aeronautical Ltd, AB, Canada*
[3] *Martec Ltd, NS, Canada*

1 Introduction

The loading of a marine structure by an underwater explosion (UNDEX) has long been known to consist of two main parts: the shock from the charge detonation followed at a much later time by the strong flow and pressure waves from the collapsing detonation product bubble, Snay [1]. The shock loading from close-proximity charges is complicated by possible Mach reflection due to the interactions between the strong shocks and the structure. The loading from the bubble collapse is also complicated by the complex flow field generated by the interaction between the collapsing bubble and the rigid structure. A significant portion of the energy released by an underwater explosive displaces a large volume of water during bubble expansion and collapse, Arons et al. [2], Sternberg and Hurwitz [3]. In the presence of a nearby rigid structure, the bubble evolves into an annulus while collapsing towards the structure and produces a strong impinging jet, Klasboer et al. [4]. Measuring the near-field loading phenomenon is challenging due to both the strong shock and the high-velocity bubble jet flow. Due to the comparable shock impedances of water and a rigid structure such as a steel wall, the strong shock transmitted into the wall poses problems in embedding diagnostic gauges in the wall while decoupling them from the shock effects. In the present work, the conditions of an explosion near an infinitely-rigid wall are reproduced with two identical charges detonated simultaneously while measuring the pressure along the plane of symmetry between the charges.

Early experiments on the twin charge configuration were performed by A.M. Shanes as reported by Cole [5] with limited pressure measurements at a single location on and off the plane of symmetry. This study, along with photographic diagnostic measurements by Coleburn and Roslund [6], demonstrated the presence of Mach reflection at the shock intersection on the plane of symmetry. The experimental results in [6] were also analyzed using oblique shock theory and a number of equations of state for water with reasonable success in Enig [7]. In the present study, the interaction between the twin explosions are found to consist of a number of phenomena involving the collision of the two spherical shocks and the collapse of the detonation product bubbles onto each other. In order to further elucidate the shock and bubble interactions, the phenomena were modeled in a 2D axi-symmetric configuration with the Chinook CFD code.

2 Experimental Details

The explosive charges and pressure gauges were suspended in their intended positions using thin nylon fishing lines stretched across a 2 m-diameter rigid Aluminum ring. The charges consisted of spheres of C4 explosive, and piezo-electric tourmaline crystal gauges

were used to measure the pressure. The mass of each of the twin charges was 40 g, and one test with a single 80 g charge was conducted for comparison. To resolve the details of the pressure load distribution due to the bubble jet, several gauges were placed near the center point between the two charges where the jet was expected to impinge. The gauges (3 to 6 mm in diameter) and associated wiring were judged to be non-intrusive due to their small size. A schematic of the experimental arrangement is shown in Figure 1. The two charges were placed at separation distances of 115 mm, 537 mm, and 1074 mm. These values corresponded to distances of 0.2 R, 0.5 R, and 1.0 R respectively between the charges and the plane of symmetry, where R is the maximum bubble radius of a single charge at the test depth.

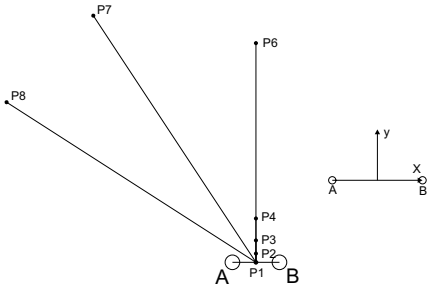

Fig. 1. Schematic diagram of the charges (A and B) and the eight pressure gauges (P1–8).

The entire charge arrangement was submerged in the UNDEX pond facility at DRDC Suffield to a depth of 3 m. The underwater explosion was filmed using a high-speed video camera enclosed in a hardened submersible casing. The video images were captured at rates of 2000 to 5000 frames-per-second.

3 Numerical Modeling

The numerical modeling was carried out using Martec Ltd's finite-volume Eulerian code Chinook. The simulations were performed in three stages. First a 1-dimensional high-resolution simulation of the explosion was performed until the shock reached the symmetry plane. That solution was then mapped onto a high-resolution 2D axisymmetric domain to simulate the shock interactions, and subsequently mapped to a much coarser 2D axisymmetric domain to model the bubble expansion and collapse. In all cases, the water was modeled using the Tait equation of state, while the explosive products were modeled with the JWL equation of state.

4 Results and Discussion

The harsh environment produced by the shock and bubble jet was found to be very severe for the pressure gauges placed close to the impingement point. Gauges placed within a radius of about 10 cm from the center point between the two charges were severed from their cables. This damage appeared to be caused mainly by the high-velocity bubble jet since some shock signals were recorded prior to gauge destruction.

4.1 Shock Pressure

Immediately after detonation of the charges, spherical shock waves radiate out from the charge locations. The shocks collide on the symmetry plane, effectively reflecting off the virtual rigid surface. Figure 2 shows a typical shock pressure history with a sharp rise and a rapid exponential decay. The experimental trace (green) shows an abrupt cutoff about 200 μs after the initial rise. This cutoff occurs when the incident shock reflects off the product bubble interface and returns towards the symmetry plane as a rarefaction wave. The numerical trace (red) reproduces the shock history features, including the cavitation cutoff, but the peak pressure is lower due to numerical diffusion.

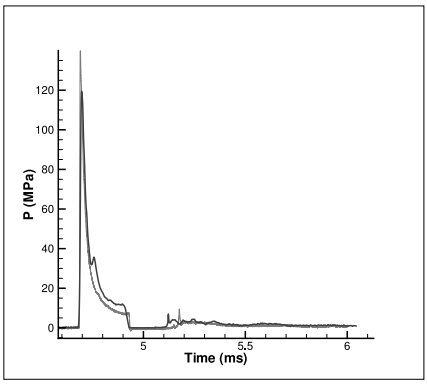

Fig. 2. Shock pressure history for a twin charge test at a 0.2 R standoff distance, with the simulation results in red and the experimental measurements in green.

For the smallest charge standoff distance of 0.2 R, the reflection conditions were favorable for the formation of a Mach stem. The contour plot in Figure 3 shows the onset of Mach stem formation as well as the general wave interactions. The rarefaction wave radiating from the product bubble interface can also be seen. The incident shock angle at the onset of Mach reflection was estimated to be 46°. This value is in good agreement with calculation using two-dimensional oblique shock theory [6] and the Walker-Sternberg equation of state [8], which provides a value for the critical angle of 47.6°.

The shock pressure is shown in Figure 4 as a function of the non-dimensional distance where **R** is the distance from the charge location to a point on the plane of symmetry and **R**$\circ$ is the radius of a charge with a mass twice that of one of the twin charges. The pressures are plotted for three standoff distances where the non-dimensional standoff distance **X** is the the charge separation divided by the radius of one of the twin charges (40 g). The **X** values of 11.8, 29.6, and 59.2 correspond to charge standoffs of 0.2 R, 0.5 R, and 1.0 R respectively. Also shown are the pressures calculated from scaled pressure relations for C4 charges, Paulgaard et al. [9]. The green dashed curve shows the reflected pressure calculated from the scaled pressure using the acoustic approximation where the reflected pressure is simply twice the incident pressure. This pressure is in good agreement with the experimental data for charge separations **X** of 29.6 and 59.2 because the standoff distance is large enough and the incident pressure is low enough for the acoustic approximation to be valid. For a charge separation of 11.8, Mach reflection occurred at incidence angles above the critical value of 46° which corresponds to a scaled

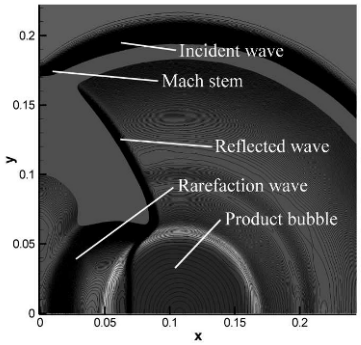

Fig. 3. Pressure and density contours from a simulation of the shock interaction between two charges at a standoff distance of 0.2 R from the plane of symmetry.

distance **R/R**○ of 17.5. This can be seen in Figure 4 as the pressure is 3.4 times the incident pressure for scaled distances above 17.5. At larger scaled distances above 22, the Mach stem weakens and the pressure approaches the acoustic value of twice the incident pressure. It can also be seen that the pressure from a single 80 g charge is lower than that from the twin charge configuration. This is not surprising because the twin charge configuration produces twice the individual charge pressure due to acoustic reflection, whereas doubling the charge mass only increases the pressure by a factor of $2^{(1/3)}$ by scaling relations.

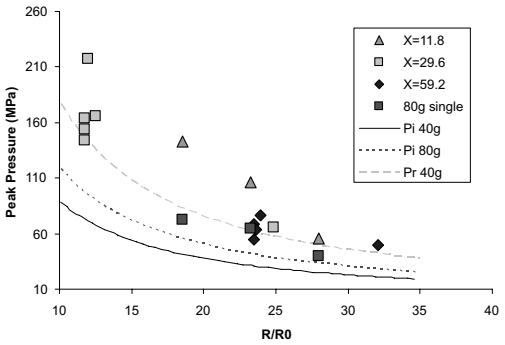

Fig. 4. Pressure in terms of non-dimensional distance on the symmetry plane.

4.2 Bubble Pressure

The first collapse of the detonation product bubble occurs about 90 ms after initiation of a 40 g charge. First the bubble expands, pushing the surrounding water radially outwards, then it collapses in a torroidal fashion against the plane of symmetry (Figure 5).

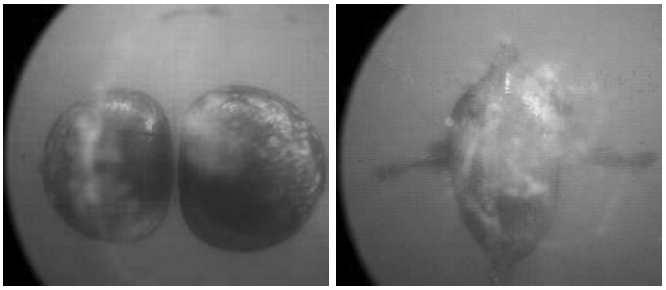

Fig. 5. Collapsing product bubbles for twin charges at a 0.5 R standoff distance.

For a free-field bubble, the pressure rise is typically gradual, with a similar gradual decay. For a twin charge configuration, the collapse is more complex, resulting in an asymmetrical pulse. The bubble collapse pressure was found to be approximately an order of magnitude smaller than the shock pressure (Figure 6), however the impulse is one to two orders of magnitude larger than the shock impulse due to the longer duration of the pulse. The impulse was also found to be larger than that of a single free-field charge of 40 g, but comparable to that of a single 80 g charge.

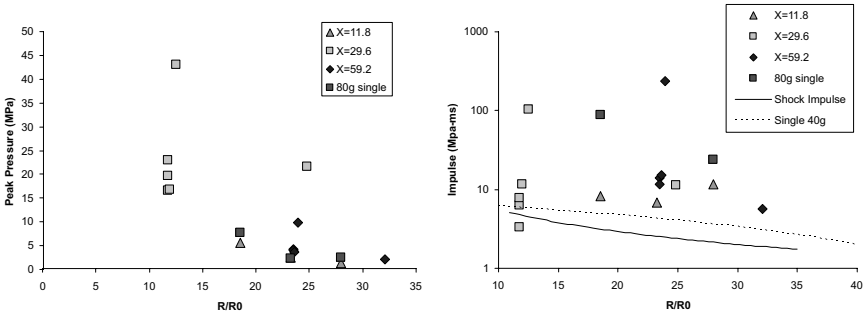

Fig. 6. Bubble collapse pressure (left) and impulse (right) in terms of non-dimensional distance on the symmetry plane.

Chinook modeling results of the bubble collapse reproduced many qualitative features of the bubble shape. This is consistent with previous near field UNDEX modeling efforts, Link et al. [10], Gregson et al. [11]. However detailed features of the bubble pulse loading were often not captured, and impulse was generally overpredicted (see Figure 7). Investigations into the cause of these differences are ongoing.

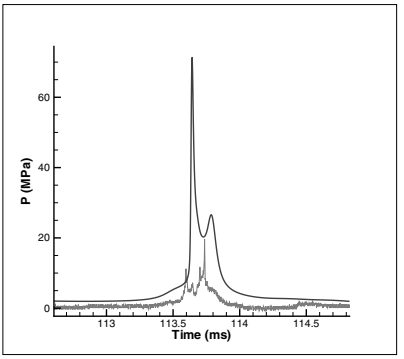

Fig. 7. Comparison of a bubble pressure loading (red) time history with corresponding experimental trace(green). Note that the simulation overpredicts the peak pressure.

5 Conclusion

The present study provides direct pressure measurements of the shock interaction and the impinging jets between the collapsing bubbles from twin underwater explosions. In spite of the harsh flow environment within the jets, pressure measurements were obtained along the plane of symmetry. The regimes of regular and Mach reflection are found to agree with oblique shock reflection theory, and the pressure histories were found to agree with CFD simulations for the shock interaction. The bubble collapse pressures were found to be much smaller than the shock pressures, however the impulses were considerably larger due to the longer duration of bubble jet phenomenon. Plans are underway to investigate the bubble jet loading regime in more detail by systematically varying the charge standoff in finer increments.

References

1. Snay HG: Hydrodynamics of underwater explosions. In: *Naval Hydrodynamics Publication 515*, (National Academy of Sciences,1957), Chap. XIII
2. Arons AB, Yennie DR: Rev. Modern Phys. **20**, 3 (1948), pp 519–536
3. Sternberg HM, Hurwitz H: Proc. 6th Symposium (Intl) on Detonation, Coronado, CA (1976), pp 528–539
4. Klaseboer E, Hung KC, Wang C, Wang CW, Khoo BC, Boyce P, Debono S, and Charlier H: J. Fluid Mech. **537**, (2005), pp 387–413
5. Cole RH: *Underwater explosions*, edition (Princeton University Press, 1948)
6. Coleburn NL, Roslund LA: Proc. 5th Symposium (Intl) on Detonation, (1970), pp 581–588
7. Enig JW: Proc. 6th Symposium (Intl) on Detonation, (1976), pp 570–588
8. Walker, Sternberg HM: Proc. 4th Symposium (Intl) on Detonation, (1965), pp 27–38
9. Paulgaard G, Slater JE, Rude G: *Experimental Underwater Explosive Performance of C4*, edition (DRDC Suffield Report TR 2007-087, 2007)
10. Link R, Jiang L, Slater JE: Proc. of the 75th Shock and Vibration Symposium, Virginia Beach, VA. SAVIAC (2004).
11. Gregson J, Link R, Lee JJ: Proc. of the 77th Shock and Vibration Symposium, Monterey, CA. SAVIAC (2006).

Viscosity effects on weak shock wave reflection

D. Khotyanovsky, A. Kudryavtsev, Y. Bondar, G. Shoev, and M. Ivanov

Institute of Theoretical and Applied Mechanics,
Siberian Branch of the Russian Academy of Sciences, Novosibirsk 630090, Russia

Summary. The effects of flow viscosity on weak shock wave reflection are investigated with the Navier–Stokes and DSMC flow solvers. It is shown that the viscosity plays crucial role in the vicinity of three-shock intersection at the parameters corresponding to the von Neumann reflection of shock waves in steady flow. Instead of a singular triple point, in viscous flow there is a smooth shock transition zone, where one-dimensional shock jump relations cannot be applied.

1 Background and motivation

Many interesting phenomena that occur in oblique shock wave reflection have been discovered in the past. Main feature herein is the existence of two possible configurations of shocks, regular and irregular. Regular reflection consists of the incident shock wave and the reflected shock wave with supersonic flow behind the reflected shock. Irregular reflection, which is in most cases called Mach reflection due to E. Mach who first discovered this phenomenon, is a complex shock wave pattern that combines the incident, reflected shock waves and the Mach stem. A contact discontinuity (slipstream) emanates from the triple point due to inequality of entropy in the flow passing through the incident and reflected shocks and the flow passing through the Mach stem. Classical theoretical methods such as shock polar analysis and the three-shock theory based on Rankine–Hugoniot jump conditions across the oblique shocks were developed by J. von Neumann to describe the shock wave configurations at various flow parameters and to predict transitions between different types of shock wave interaction. These theoretical methods predict well most of the features of shock wave interaction.

Steady shock wave reflection is very important in aerodynamics and has been extensively studied in recent years with emphasis to strong shock waves (for flow Mach number higher than 2.2 in air). However, for supersonic civil aviation the lower Mach number range is most interesting. Regular and irregular interactions of different types are inherent in such critical phenomena as off-design inlet flows, inlet starting and flow stalling. Interactions and reflections of weak shock waves are typical for supersonic inlet flows at low and moderate Mach numbers (M=1-2). There are many problems of irregular shock reflections in steady flows which are not yet investigated. One of the most exciting phenomena that occurs in irregular reflection of weak shock waves is a shock wave reflection in the range of flow parameters where the von Neumann's three-shock theory does not produce any solution whereas the experiments reveal [1] a three-shock structure similar to the Mach reflection pattern. This inconsistency is referred to as the von Neumann paradox, and the observed reflection pattern as the von Neumann reflection (vNR). Inviscid numerical simulations of the pseudo-steady shock wave reflection at the conditions of the von Neumann paradox conducted in [1] with a second-order Godunov-type scheme showed that the incident and Mach shocks "appear to form a single wave

with a continuously turning tangent". The Euler computations performed later in [2] with a specifically-designed shock-fitting algorithm argued that the grid resolution in the vicinity of the triple point is essential in this problem and found many interesting flow details.

Many efforts were made to develop a consistent inviscid theory of the vNR. Those studies were mainly concerned with the pseudo-steady reflection of a shock wave running over a wedge. As soon as the three-shock solution does not exist at the von Neumann paradox conditions, some additional gasdynamic features are introduced to solve the problem (local supersonic patch, compression wave, etc.). In the second group of works, the vNR is explained by the effects of flow viscosity ([3]). Due to finite thickness of the interacting shock waves the flow in the vicinity of the triple point is substantially different from the inviscid flow. As stated in [3], at the intersection there must be a zone of essentially two-dimensional flow, which he labels "non Rankine-Hugoniot shock wave zone", where the gradients of flow parameters in the direction tangent to the shock wave are important. This non-R-H zone acts as a buffer zone separating R-H shocks in the upper and lower domains. The size of this non-R-H zone was estimated as a few shock wave thicknesses. It is therefore impossible to confirm or reject the existence of such a viscous zone via inspection of the experimental data because of the insufficient resolution of the flow field in the experiment. We believe that the numerical computations can help clarify this.

2 Problem formulation and numerical techniques

In this study we investigate irregular reflection of weak shock waves in steady supersonic flow with Mach number M_∞ between two symmetrical wedges with equal angles of attack θ_w. The shock wave reflection occurs at the plane of symmetry half-way between the wedges. Necessary length scale is introduced in this problem due to influence of the expansion waves emanating from the trailing edges of the wedges. The wedge chord, w, was chosen as the length scale. The flow geometry is controlled with the parameter g/w, which is the ratio of the distance between the trailing edges g to the wedge chord w.

Characteristic feature of the weak shock wave reflection is that the flow behind the reflected shock wave of the Mach reflection is subsonic. For a gas with specific heats ratio γ there is a Mach number value M_c, at which the shock wave angles corresponding to the detachment α_d and the von Neumann α_N conditions coincide: $\mathrm{M}_c \approx 2.2$ for diatomic gases with $\gamma = 1.4$, and $\mathrm{M}_c \approx 2.47$ for monatomic gases with $\gamma = 5/3$. At flow Mach number $\mathrm{M}_\infty < \mathrm{M}_c$ the reflected shock wave of the MR belongs to the strong family, and hence the flow behind the reflected shock is subsonic.

It is convenient to illustrate various conditions on pressure-deflection diagrams, see Fig. 1, where different shock polar combinations for $\gamma = 5/3$ and $\mathrm{M}_\infty = 1.7$ are given. The intersection of the reflected shock polar with the incident shock polar indicates matching pressure p_{ss} and flow deflection at the slipstream θ_{ss}, and represents a three-shock solution. These solutions are listed in Table 1 for various θ_w. For reference, Mach number behind the reflected shock M_{rs} is also given in the last column of Table 1. At $\theta_w = 8.5^\circ$ the shock polar intersection yields a three-shock solution corresponding to an MR with subsonic flow behind the reflected shock wave. The deflection angle of the flow passing through the reflected shock is decreased. At $\theta_w = 9.627^\circ$ the reflected shock wave becomes normal to the flow, and the flow deflection is not changed. At higher angles,

the reflected shock wave predicted by the three-shock solution is inclined forward with respect to the flow, and the flow deflection in the reflected shock is increased. The three-shock solution obtained at $\theta_w = 13°$ predicts a forward-inclined reflected shock wave with supersonic flow behind it. Such a configuration cannot exist, and the solution should be discarded. $\theta_w = 13.5°$ does not produce any three-shock solution since the reflected shock polar does not intersect the incident shock polar. This latter case corresponds to the von Neumann paradox conditions.

In this study we investigate numerically some of these shock wave reflection configurations. The computations are conducted with both Navier–Stokes equations and the DSMC (Direct Simulation Monte Carlo) method. The computations are performed at low Reynolds number of the flow with full resolution of the internal structure of the shock waves. The Navier–Stokes code is a time-explicit shock capturing code based on WENO-5 [4] discretization of the convective terms, and the central-difference discretization of the diffusive terms. The DSMC simulations are performed with the SMILE code [5]. The grid resolution studies were made to ensure that the shock wave profiles are properly resolved.

To eliminate possible non-equilibrium effects a monatomic gas, Argon, with $\gamma = 5/3$ is considered. Power-law dependence of the viscosity coefficient on temperature with exponent 0.81 is used in the Navier–Stokes. The computations were performed at flow Mach number $M_\infty = 1.7$. Reynolds number was typically $Re = 1000$.

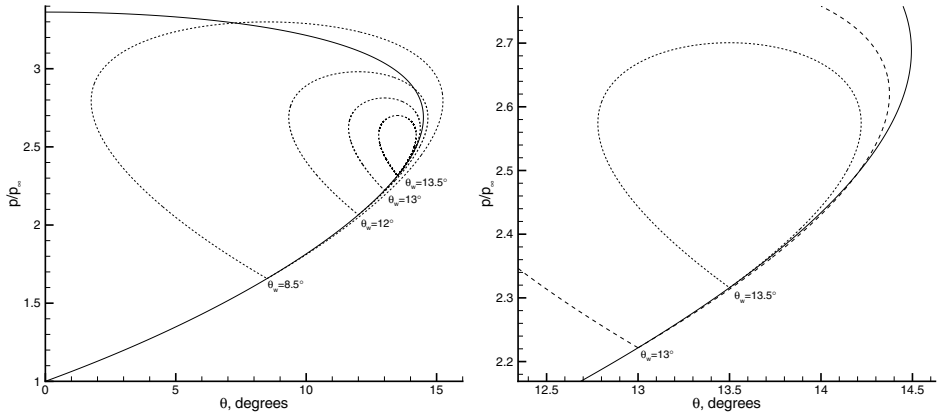

Fig. 1. Pressure-deflection diagrams for $\gamma = 5/3$, $M_\infty = 1.7$. Incident shock polar is solid, reflected shock polars for various wedge angles θ_w are dashed

Table 1. Three-shock solutions at $\gamma = 5/3$, $M_\infty = 1.7$ at various wedge angles θ_w

θ_w	p_{ss}/p_∞	θ_{ss}	M_{rs}
8.5	3.293	7.275	0.7780
9.627	3.227	9.627	0.7999
12	2.873	14.13	0.9008
13	2.495	14.20	1.011

3 Results and discussions

The results of the Navier–Stokes computations at $\theta_w = 12°$ are illustrated in Fig. 2. The obtained shock wave reflection resembles a typical MR pattern, though smeared by the flow viscosity. Instead of the triple point we have a smooth continuous transition from the Mach stem to the reflected shock, which we label the triple-shock zone. Closed subsonic region is formed behind the Mach stem and the reflected shock. The size of this region is governed by the geometry parameter g/w, which is $g/w = 1.5$ in this case. The flow portions passing through the Mach stem and the reflected shock are separated with the mixing layer. The reflected shock wave is curved due to the influence of expansion waves that cause pressure drop in the subsonic flow behind the reflected shock. An interesting observation that can be made inspecting the pressure distribution is that the pressure rise in the reflected shock wave is followed by gradual pressure increase downstream of the reflected shock. This also concerns the part of the flow just behind the triple-shock zone. This pressure rise can be explained by the influence of the disturbances from high-pressure flow behind the Mach stem that reach the flow behind the reflected shock through the subsonic region.

In Fig. 3 the distributions of pressure and flow deflection along the curve passing just behind the Mach and reflected shock are given. The pressure monotonously decreases when moving upwards along the Mach stem and the reflected shock. There is an apparent slope change in the pressure variation just behind the triple-shock zone at $y/w \approx 0.65$. The flow deflection increases when moving up behind the Mach stem, reaches its maximum behind the triple-shock region, and then decreases as the reflected shock becomes more and more curved. An interesting observation is that the flow deflection behind the triple-shock zone does not exceed the flow deflection behind the incident shock $\theta_w = 12°$. This contradicts the three-shock solution, which predicts $\theta = 14.13°$ at the slipstream given in Table 1. This is most evident in the right plot of Fig. 3, where we compared our numerical results with shock polars in the (p, θ) plane. The pressures and flow deflection are really close to shock polars far from the triple-shock region, and deviate from the shock-polar solutions in the vicinity of the shock intersection where the viscosity effects are strong. Note, that the deviation of the flow parameters from the shock polars effectively means that Rankine–Hugoniot relations are not valid within the viscous triple-shock zone.

The results of the Navier–Stokes computations at $\theta_w = 13.5°$, i.e. at the von Neumann paradox conditions, are presented in Figs. 4 and 5. Although there is no three-shock solution in this case, the Navier–Stokes computations clearly demonstrate a triple-shock pattern similar to those observed in the previous case. The reflected shock wave is much weaker in this case, since the flow Mach number behind the incident shock is close to unity $\mathrm{M} = 1.064$. The results of the DSMC computations performed at the von Neumann paradox conditions ($\gamma = 7/5$, $\mathrm{M}_\infty = 1.5$ $\theta_w = 10°$) (see Fig. 6) are in good qualitative agreement with the Navier–Stokes computations.

Our simulations performed with substantially different approaches suggest that the flow viscosity causes formation of a smooth shock transition zone in the triple-shock region, where one-dimensional shock jump relations cannot be applied.

Acknowledgement. This study was supported by the Russian Foundation for Basic Research (Grant 06-01-22000) and the Fundamental Research Program 14 of the Russian Academy of Sciences. The computations were performed at the Siberian Supercomputer Centre, Novosibirsk and the Joint Supercomputer Centre, Moscow.

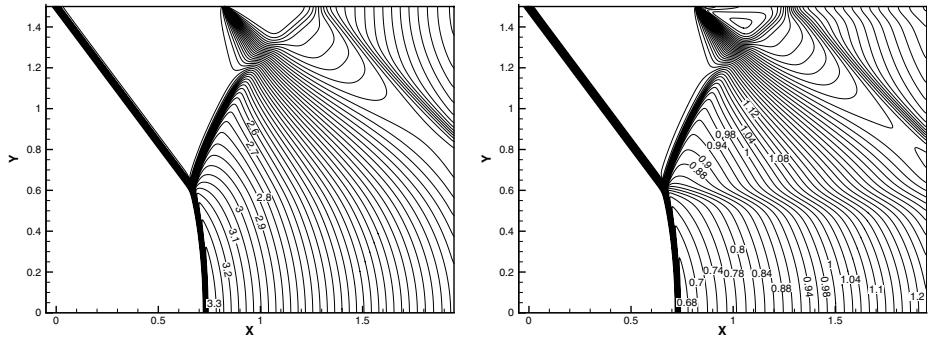

Fig. 2. Pressure contours (left) and Mach number contours (right). Navier–Stokes computations at $\gamma = 5/3$, $M_\infty = 1.7$, $Re = 1000$, $\theta_w = 12^\circ$

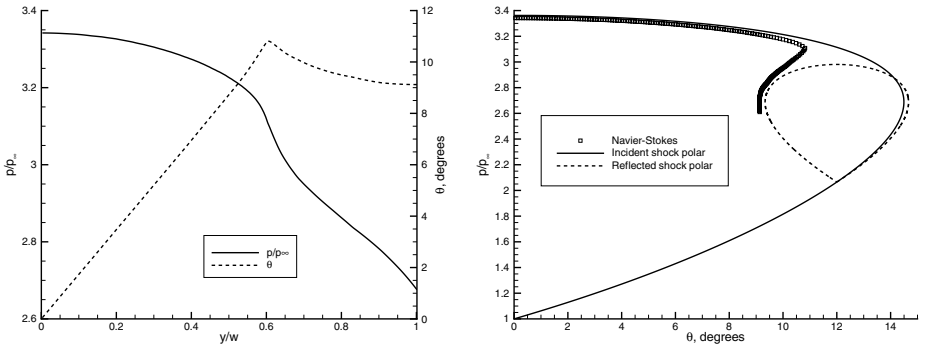

Fig. 3. Pressure and flow deflection variation along the Mach stem and reflected shock. Navier–Stokes computations at $\gamma = 5/3$, $M_\infty = 1.7$, $Re = 1000$, $\theta_w = 12^\circ$

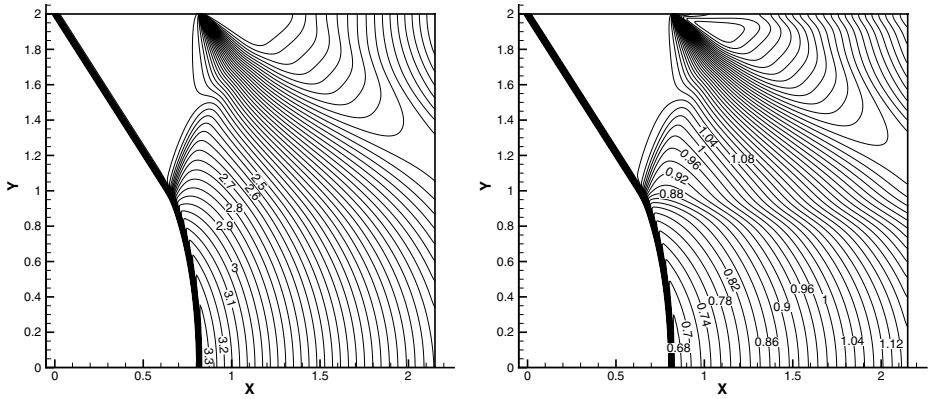

Fig. 4. Pressure contours (left) and Mach number contours (right). Navier–Stokes computations at the von Neumann paradox conditions: $\gamma = 5/3$, $M_\infty = 1.7$, $Re = 1000$, $\theta_w = 13.5^\circ$

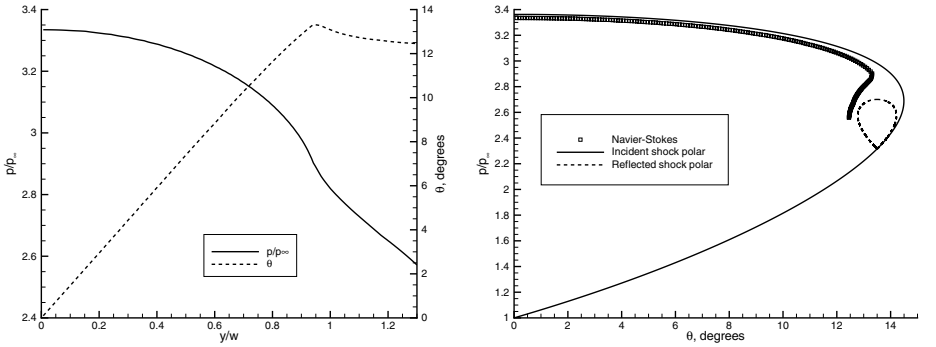

Fig. 5. Pressure and flow deflection variation along the Mach stem and reflected shock. Navier–Stokes computations at $\gamma = 5/3$, $M_\infty = 1.7$, $Re = 1000$, $\theta_w = 13.5^\circ$

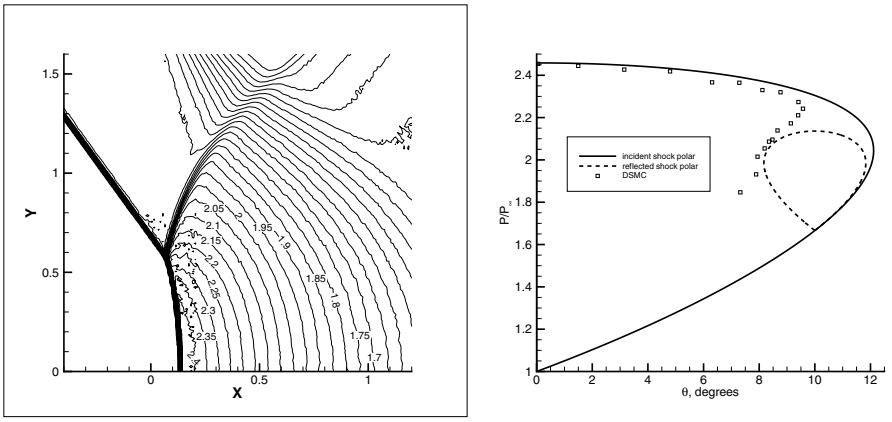

Fig. 6. Pressure contours (left) and pressure-deflection variation (right) obtained in the DSMC computations at $\gamma = 7/5$, $M_\infty = 1.5$, $Re_\infty = 1834$, $\theta_w = 10^\circ$

References

1. P. Colella, L.F. Henderson: J. Fluid Mech. **213** (1990)
2. E.I. Vasilyev, A.N. Kraiko: Computational Mathematics and Mathematical Physics **39(8)** (1999).
3. J. Sternberg: Phys. Fluids **2(2)** (1959)
4. G. Jiang, C.-W. Shu: J. Comput. Phys. **126** (1996).
5. M.S. Ivanov, G.N. Markelov, S.F. Gimelshein: AIAA Paper 98-2669, (1998).

Author Index

Keyword Index